Transactions of the ASME®

Technical Editor, **LEWIS T. WHEELER**

Department of Mechanical Engineering,
University of Houston,
Houston, TX 77204-4792

APPLIED MECHANICS DIVISION

Chairman, **C. T. HERAKOVICH**
Secretary, **T. HUGHES**
Associate Technical Editors,
J. R. BARBER (2000)
J. L. BASSANI (1999)
R. C. BENSON (2000)
M. M. CARROLL (2000)
I. M. DANIEL (1999)
W. J. DRUGAN (2000)
A. A. FERRI (2000)
J. T. JENKINS (1999)
J. W. JU (2001)
V. K. KINRA (1999)
S. KYRIAKIDES (2000)
W. K. LIU (1999)
A. K. MAL (2001)
A. NEEDLEMAN (2001)
M. ORTIZ (2001)
N. C. PERKINS (1999)
M.-J. PINDERA (2000)
K. T. RAMESH (2000)
D. A. SIGINER (2000)
C. G. SPEZIALE (2001)
M. TAYA (1999)

BOARD ON COMMUNICATIONS

Chairman and Vice-President
R. K. SHAH

OFFICERS OF THE ASME
President, **W. M. PHILLIPS**
Executive Director, **D. L. BELDEN**
Treasurer, **J. A. MASON**

PUBLISHING STAFF
Managing Director, Engineering
CHARLES W. BEARDSLEY
Director, Technical Publishing
PHILIP DI VIETRO
Managing Editor, Technical Publishing
CYNTHIA B. CLARK
Managing Editor, Transactions
CORNELIA MONAHAN
Production Coordinator
JUDITH SIERANT
Production Assistant
MARISOL ANDINO

Transactions of the ASME, Journal of Applied Mechanics (ISSN 0021-8936) is published quarterly (Mar., June, Sept., Dec.) for $240.00 per year by The American Society of Mechanical Engineers, Three Park Avenue, New York, NY 10016. Periodicals postage paid at New York, NY and additional mailing office. POSTMASTER: Send address changes to Transactions of the ASME, Journal of Applied Mechanics, c/o THE AMERICAN SOCIETY OF MECHANICAL ENGINEERS, 22 Law Drive, Box 2300, Fairfield, NJ 07007-2300. **CHANGES OF ADDRESS** must be received at Society headquarters seven weeks before they are to be effective. Please send old label and new address. **PRICES:** To members, $40.00; to nonmembers, $240.00; single issue, $96.00. Add $40.00 (airmail $60.00) for postage to countries outside the United States and Canada.

STATEMENT from By-Laws. The Society shall not be responsible for statements or opinions advanced in papers or . . . printed in its publications (B7.1, Para. 3), **COPYRIGHT © 1999** by The American Society of Mechanical Engineers. Authorization to photocopy material for internal or personal use under circumstances not falling within the fair use provisions of the Copyright Act is granted by ASME to libraries and other users registered with the Copyright Clearance Center (CCC). Transactional Reporting Service provided that the base fee of $3.00 per article is paid directly to CCC, Inc., 222 Rosewood Drive, Danvers, MA 01923. Request for special permission or bulk copying should be addressed to Reprints/Permission Department.

INDEXED by Applied Mechanics Reviews and Engineering Information, Inc. Canadian Goods & Services Tax Registration #126148048.

Journal of Applied Mechanics

Published Quarterly by The American Society of Mechanical Engineers

VOLUME 66 • NUMBER 1 • MARCH 1999

1 List of Reviewers

TECHNICAL PAPERS

3 Studies of Elastic-Plastic Instabilities
V. Tvergaard

10 Recovery Experiments for Adiabatic Shear Localization: A Novel Experimental Technique
D. R. Chichili and K. T. Ramesh

21 The Influence of a Ductile Interphase on the Overall Elastoplastic Behavior of a Fiber-Reinforced Composite
K. Ding and G. J. Weng

32 On the St. Venant Problems for Inhomogeneous Circular Bars
F. Rooney and M. Ferrari

41 Buckling of Thick Orthotropic Cylindrical Shells Under Torsion
Y. S. Kim, G. A. Kardomateas, and A. Zureick

51 On Nanobuckling of Monomolecular Layers Adhering to a Substrate
A. Chiskis and R. Parnes

55 A Geometric Approach for Establishing Dynamic Buckling Loads of Autonomous Potential Two-Degree-of-Freedom Systems
A. N. Kounadis

62 Surface Bifurcation in Anisotropic Materials With Application to Aluminum Alloys
M. D. Nestorović, E. Chu, and N. Triantafyllidis

69 A Reissner's Mixed Variational Theorem Applied to Vibration Analysis of Multilayered Shell
E. Carrera

79 Crack Propagation in a Brittle Elastic Material With Defects
M. Valentini, S. K. Serkov, D. Bigoni, and A. B. Movchan

87 Double Curvature Bending of Variable-Arc-Length Elasticas
S. Chucheepsakul, C. M. Wang, X. Q. He, and T. Monprapussorn

95 A Higher-Order Theory for Plane Stress Conditions of Laminates Consisting of Isotropic Layers
X. J. Wu and S. M. Cheng

101 A Simplified Method for Calculating the Crack-Tip Field of Functionally Graded Materials Using the Domain Integral
P. Gu, M. Dao, and R. J. Asaro

109 Nonlinear Stability Considerations in Thermoelastic Contact
J. A. Pelesko

117 Bifurcation of Elastoplastic Pressure-Sensitive Hollow Cylinders
P. Papanastasiou and D. Durban

124 A Micro/Macroscopic Analysis for Cyclic Plasticity of Dual-Phase Materials
J. Fan

137 Contact Creep of Biphasic Cartilage Layers
R. Kelkar and G. A. Ateshian

146 Anomalous Frictional Behavior in Collisions of Thin Disks
J. Calsamiglia, S. W. Kennedy, A. Chatterjee, A. Ruina, and J. T. Jenkins

153 An Axisymmetric Membrane Element With Bending Stiffness for Static Implicit Sheet Metal Forming Simulation
S. K. Esche, G. K. Kinzel, and J. K. Lee

165 The Elastic Field of an Elliptic Cylindrical Inclusion in a Laminate With Multiple Isotropic Layers
H. G. Beom and Y. Y. Earmme

172 On a Spring-Network Model and Effective Elastic Moduli of Granular Materials
K. Alzebdeh and M. Ostoja-Starzewski

181 Thermosolutal Convection in the Presence of Both Vertical and Horizontal Temperature Gradients
A. K. Sahai

(Contents continued on outside back cover)

This journal is printed on acid-free paper, which exceeds the ANSI Z39.48-1992 specification for permanence of paper and library materials. ♾ ™

♻ 85% recycled content, including 10% post-consumer fibers.

Downloaded 04 May 2010 to 171.66.16.52. Redistribution subject to ASME license or copyright; see http://www.asme.org/terms/Terms_Use.cfm

CONTENTS (CONTINUED)

197 **The Stability of a Two-Layer Inviscid Flow Between an Elastic Layer and a Rigid Boundary**
P. J. Schall and J. P. McHugh

204 **Green's Function for a Heat Source in an Infinite Region With an Arbitrary Shaped Hole**
K. Yoshikawa and N. Hasebe

211 **Lyapunov Exponents and Stochastic Stability of Quasi-Integrable-Hamiltonian Systems**
W. Q. Zhu and Z. L. Huang

218 **Analytical Vibration of Spinning, Elastic Disk-Spindle Systems**
R. G. Parker

225 **Local Similarity in Nonlinear Random Vibration**
S. Krenk and J. B. Roberts

236 **Load Identification Through Structural Modification**
P. W. Möller

242 **The Modal Formulation and Adaptive-Passive Control of the Nonself-Adjoint One-Dimensional Acoustic System With a Mass-Spring Termination**
V. Jayachandran and J. Q. Sun

250 **On Dynamic Cycle Collapse of Circular Plates**
P. D. Chinh

254 **Vibration Control of a Rotating Shaft: An Analytical Solution**
S. M. Yang and G. J. Sheu

BRIEF NOTES

Exact Connection Between Deflections of the Classical and Shear Deformation Laminated Plate Theories 260
Z.-q. Cheng and S. Kitipornchai

On the Elastic Constants of Transversely Isotropic, Quasi-Symmetric Composites 262
P. D. Chinh

A Theory of Continuum Damage Mechanics for Anisotropic Solids 264
U. Lee

Closed-Form Integrals for Constant and Linear Elements in the Eigenstrain Method 268
P. A. Kelly and D. Nowell

Comments on Stability Properties of Conservative Gyroscopic Systems 272
P. Lancaster and W. Kliem

273 A Simplified Variation of Parameters Approach to Euler's Equations
D. L. Richardson and J. W. Mitchell

276 A Circular Inhomogeneity Problem Revisited
K. W. Lee, S. T. Choi, and Y. Y. Earmme

278 Nature of Stress Singularities at the Reentrant Wedge Corner for a Branched Crack Problem
A. S. Selvarathinam and J. G. Goree

280 Synthesis of Nonlinear Constitutive Functions, Applications to the Electromagnetic Control of Snapping
S. S. Antman

ANNOUNCEMENTS AND SPECIAL NOTICES

20 17th Biennial ASME Conference on Mechanical Vibration and Noise—Call for Papers

54 Change of Address Form

180 Periodicals on ASMENET

259 CIMS 2000—Announcement

284 Worldwide Mechanics and Meetings List

286 Fourth International Conference on Vibration Problems—Announcement and Call for Papers

287 Information for Authors

Downloaded 04 May 2010 to 171.66.16.52. Redistribution subject to ASME license or copyright; see http://www.asme.org/terms/Terms_Use.cfm

Studies of Elastic-Plastic Instabilities

V. Tvergaard
Department of Solid Mechanics,
Technical University of Denmark
DK-2800 Lyngby, Denmark

Analyses of plastic instabilities are reviewed, with focus on results in structural mechanics as well as continuum mechanics. First the basic theories for bifurcation and post-bifurcation behavior are briefly presented. Then, localization of plastic flow is discussed, including shear band formation in solids, localized necking in biaxially stretched metal sheets, and the analogous phenomenon of buckling localization in structures. Also some recent results for cavitation instabilities in elastic-plastic solids are reviewed.

1 Introduction

The occurrence of instabilities in solids or structures under static loading is discussed here in a rather broad context. The elastic post-buckling theory of Koiter (1945) is an important starting point, explaining how imperfection-sensitivity is tied to bifurcation and initial post-bifurcation behaviour, and how imperfection-sensitivity plays a key role in relation to experimentally observed buckling loads. In the plastic range the understanding of uniqueness and bifurcation relies on the theory of Hill (1958, 1961), which applies to plastic buckling of structures as well as to tensile instabilities at large plastic strains. For the initial post-bifurcation behavior in the plastic range a theory has been developed by Hutchinson (1973, 1974), while the knowledge of imperfection-sensitivity in the plastic range is mainly based on numerical solutions (Needleman and Tvergaard, 1982).

Instabilities leading to localization of plastic flow are frequently observed. The most known case is that of necking in a tensile test specimen, and closely related to this kind of instability is the necking in thin metal sheets, which gives an important limitation of sheet metal formability. In the mathematical description the formation of localized shear bands in solids is quite similar to localized necking in sheets, but shear bands represent a material instability, which does not depend on constraints along the boundary of the solid. Both for analyses of shear bands and sheet necking relevant applications of nonlocal theories to incorporate additional length scales are mentioned. In addition, the analogous phenomenon of buckling localization is briefly discussed, including a few examples of such instabilities, which often occur at a secondary bifurcation point.

A cavitation instability in a metal refers to a situation, where the stress level is so high that a void in the solid grows without bounds, while the stress and strain states far away from the void remain constant. Thus, the stored elastic energy in the solid provides the work needed for plastic dissipation in the material around the growing void. Such high stress levels are not found at a sharp notch or even in front of a blunting crack tip. However, in metal-ceramic systems highly constrained plastic flow leads to plasticity under high tensile mean stress, e.g., in ductile reinforcing particles or in thin metal layers in ceramics.

Contributed by the Applied Mechanics Division of THE AMERICAN SOCIETY OF MECHANICAL ENGINEERS for publication in the ASME JOURNAL OF APPLIED MECHANICS.

Discussion on the paper should be addressed to the Technical Editor, Professor Lewis T. Wheeler, Department of Mechanical Engineering, University of Houston, Houston, TX 77204-4792, and will be accepted until four months after final publication of the paper itself in the ASME JOURNAL OF APPLIED MECHANICS.

Manuscript received and accepted by the ASME Applied Mechanics Division, Nov. 23, 1998. Associate Technical Editor: L. T. Wheeler.

2 Bifurcation and Post-Bifurcation Theories

Instabilities of a solid or structure under static loading occur at a bifurcation point or at a limit point. The basic understanding of the importance of the post-bifurcation behavior and the associated imperfection-sensitivity was obtained by the general theory of post-buckling behaviour of elastic structures developed by Koiter (1945). This theory gives an asymptotic expression for the initial post-bifurcation behaviour and asymptotic estimates of imperfection-sensitivity.

For a case in which the buckling mode is unique, Koiter's (1945) theory gives an asymptotically exact relation between the load parameter λ and the buckling mode amplitude ξ of the form

$$\left(1 - \frac{\lambda}{\lambda_c}\right)\xi + a\xi^2 + b\xi^3 + \ldots = \frac{\lambda}{\lambda_c}\,\bar{\xi} \qquad (2.1)$$

where λ_c is the critical load parameter and $\bar{\xi}$ is the amplitude of an initial imperfection in the shape of the buckling mode. If either $a \neq 0$ or $a = 0$, $b < 0$ the structure is imperfection-sensitive in the sense that an imperfection reduces the maximum support load to a value $\lambda_s < \lambda_c$. This is illustrated in Fig. 1(a) and 1(c), whereas Fig. 1(b) illustrates an initially stable post-bifurcation behavior. If there are simultaneous buckling modes, (2.1) is replaced by similar simultaneous equations for the mode amplitudes. Such cases involving nonlinear interaction between simultaneous buckling modes are usually characterized by a strong sensitivity to small imperfections, as is well known for circular cylindrical shells under axial compression (Koiter, 1963), and also for optimally designed thin-walled compression members, e.g., an eccentrically stiffened panel (Tvergaard, 1973).

For solids or structures deformed into the plastic range analyses of instabilities are governed by the general theory of bifurcation and uniqueness for elastic-plastic solids due to Hill (1958, 1961). This theory makes use of a linear comparison solid, for which the instantaneous moduli are independent of whether or not elastic unloading takes place in a material point currently on the yield surface, in order to determine a bifurcation in the actual elastic-plastic solid. With the prescribed dead loads or displacements proportional to a single parameter λ, the theory shows that bifurcation in elastic-plastic solids takes place under increasing λ, in agreement with the condition of Shanley (1947) for column buckling.

An asymptotic theory of the initial post-bifurcation behavior in the plastic range has been developed by Hutchinson (1973, 1974). In the case where the eigenmode is unique, the asymptotically exact expression for the load parameter λ in terms of the eigenmode amplitude ξ is of the form

 Copyright © 1999 by ASME

Downloaded 04 May 2010 to 171.66.16.27. Redistribution subject to ASME license or copyright; see http://www.asme.org/terms/Terms_Use.cfm

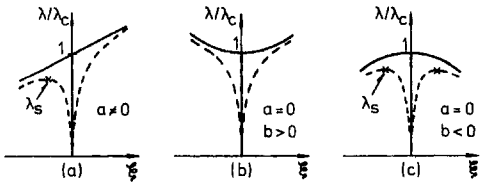

Fig. 1 Elastic initial post-buckling behavior in cases where the bifurcation mode is unique. Dashed curves show effect of small initial imperfections.

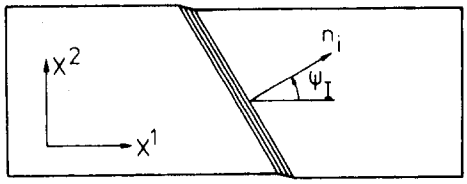

Fig. 3 Plastic flow localization in a uniformly strained solid

$$\frac{\lambda}{\lambda_c} = 1 + \lambda_1 \xi + \lambda_2 \xi^{1+\beta} + \ldots \qquad (2.2)$$

for $\xi \geq 0$ and with $0 < \beta < 1$. Except for very special cases λ_1 is positive, so that bifurcation takes place under increasing load, and λ_2 is negative. The solid curves in Fig. 2 illustrate typical post-bifurcation behaviour in the plastic range, for a symmetric case as well as an unsymmetric case. The expansion (2.2) is clearly inspired by Koiter's work (2.1), but the derivation of (2.2) is strongly complicated by the material nonlinearities, in particular by the need to account for elastic unloading zones that spread into the material as functions of ξ. The work of Hutchinson (1973, 1974) is limited to elastic-plastic solids characterized by a smooth yield surface and normality of the plastic flow rule.

Due to the complications resulting from the material nonlinearities, it has been difficult to obtain simple asymptotic estimates for the effect of imperfections, analogous to the effect of $\bar{\xi}$ in (2.1). Attempts have been made to consider the elastic-plastic material with elastic unloading neglected, i.e., a hypoelastic material, and it has been found (Needleman and Tvergaard, 1982) that an asymptotic expansion for this hypoelastic material can give a very useful indication of the imperfection-sensitivity for the elastic-plastic structure. More recently Christensen (1997) has shown that various enhanced asymptotic expansions can be used to obtain rather accurate estimates of the imperfection-sensitivity for columns. The case of simultaneous bifurcation in two or more modes has not yet been expressed in terms of asymptotic expansions. In fact, most of the current knowledge of post-bifurcation behavior and imperfection-sensitivity in the plastic range has been obtained by numerical solutions of the nonlinear field equations. This is true for elastic-plastic structural components subject to buckling under compressive loading, as well as for solids undergoing tensile instabilities at large plastic strains.

A strain-rate sensitivity of the inelastic behaviour of metals is often observed. The elastic-viscoplastic material models used to represent this rate sensitivity are usually chosen such that in the limit of no rate sensitivity they reduce to a standard time-independent elastic-plastic material model. However, the first critical bifurcation point does not smoothly approach the elastic-plastic bifurcation point as the rate-sensitivity is reduced (see Tvergaard, 1989a). When studying the uniqueness and bifurcation it is seen that the creep strain rates do not at all affect bifurcation, and therefore the first critical bifurcation is the elastic bifurcation, which usually occurs at unrealistically high stresses. However, in the presence of an unavoidable small imperfection the behavior predicted for a slightly rate sensitive inelastic material is practically identical to that predicted for the corresponding time-independent elastic-plastic material. Thus, in the case of elastic-viscoplastic materials it is important that imperfections are accounted for in studies of instabilities.

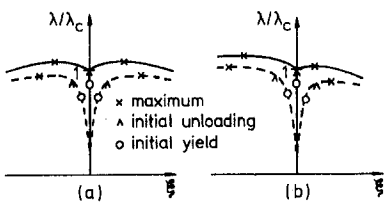

Fig. 2 Initial post-bifurcation behavior in the plastic range in cases where the bifurcation mode is unique. Dashed curves show effect of small initial imperfections.

3 Localization of Plastic Flow

The onset of necking in a tensile test specimen is the most known case where bifurcation from a uniformly stressed state in a solid leads to plastic flow localization. For a one-dimensional model Considére (1885) demonstrated that this instability occurs at the maximum load point. Hutchinson and Miles (1974) have found that due to three-dimensional effects the bifurcation point actually occurs a little after the load maximum, with a smaller delay the smaller the thickness of the bar relative to the length.

3.1 Shear Bands. The occurrence of a shear band instability in a solid represents a situation where plastic flow localization is an outcome of material response, rather than a consequence of boundary conditions. Such material instabilities are of significance as a precursor to fracture, and has been observed in a wide variety of materials (e.g., see Needleman and Tvergaard, 1992).

The basic phenomenon of shear localization can be studied by a relatively simple model problem for solids subject to uniform straining. The localized shearing is assumed to occur in a thin slice of material with reference normal n_j (see Fig. 3), while the strain fields outside this band are assumed to remain uniform throughout the deformation history. The quantities inside and outside the band are denoted by $(\ )^b$ and $(\ )^o$, respectively, and a Cartesian reference coordinate system is used. Then, with uniform deformation fields inside and outside the band, only the conditions of compatibility and equilibrium at the interface have to be required

$$u^b_{i,j} = u^o_{i,j} + c_i n_j \qquad (3.1)$$

$$(T^i)^b = (T^i)^o \qquad (3.2)$$

where u_i are displacement components, T^i are nominal traction components, and c_i are three parameters to be determined. The detailed incremental equations for $\dot{c}_i$, resulting from substituting (3.1) into the incremental version of (3.2), are specified in Tvergaard (1989a).

If there is an initial inhomogeneity inside the band, e.g., a lower yield strength or a higher degree of damage, the incremental equations for $\dot{c}_i$ are inhomogenous. Then the equations describe the gradual development of localization, and localization is said to occur when strain rate reversal occurs outside the band. On the other hand, if there is no initial inhomogeneity, the equations are homogeneous, and then a nontrivial solution for $\dot{c}_i$ can only occur at a bifurcation point. The first such bifurcation into a shear band mode coincides with loss of ellipticity of the field equations governing incremental equilibrium,

Downloaded 04 May 2010 to 171.66.16.27. Redistribution subject to ASME license or copyright; see http://www.asme.org/terms/Terms_Use.cfm

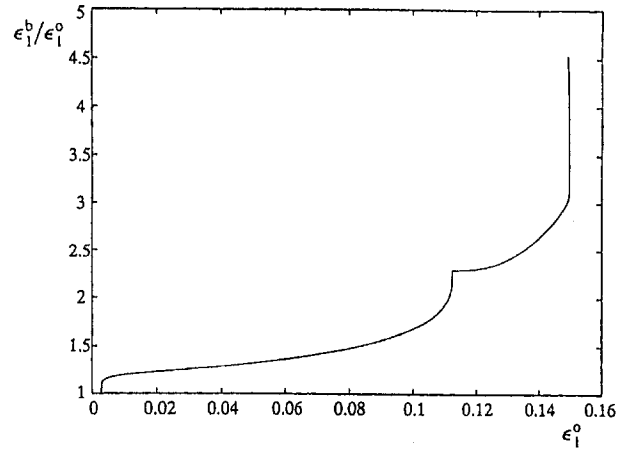

Fig. 4 Shear band development versus strain in a sintered metal for uniaxial plane strain tension, $\epsilon_3^o = 0$ and $\sigma_2^o = 0$, with $\psi_I = 37$ deg. The initial porosity is specified by $f_I = 0.05$ and $\Delta f = 0.01$. (From Redanz and Tvergaard, 1998.)

and the corresponding critical band inclination is that of the characteristics (Hadamard, 1903; Hill, 1962; Rice, 1977).

Several investigations have used this simple model problem to study the effect of different constitutive laws on the onset of localization. Some analyses, as that of Hutchinson and Tvergaard (1981) for a solid that forms a vertex on the yield surface or of Tvergaard (1982) for a solid subject to void growth, have been continued beyond the first onset of localization, and cases have been found in which the localized straining saturates after some shearing. Such behavior has also been found recently in a study of localization in a sintered metal (Redanz and Tvergaard, 1998), as illustrated in Fig. 4, showing the ratio of the maximum principal strains inside and outside the band versus the strain outside the band. It is seen that localization is first predicted at $\epsilon_1^o = 0.113$, but then plastic straining outside the band starts again, and the secondary onset of localization is predicted at $\epsilon_1^o = 0.150$.

In continuum studies of shear localization it is well known that numerical predictions show an inherent mesh sensitivity, since the softening material behavior typical of situations near final failure will tend to give localization in regions as narrow as possible within the mesh resolution. This problem can be resolved by incorporating a material length scale in the constitutive relations, and such nonlocal plasticity models have been proposed by a number of authors (e.g., Aifantis, 1984; Zbib and Aifantis, 1989; de Borst, 1993; Fleck et al., 1993, 1994). In these models the additional material length is tied to the plastic strain gradient, thus representing nonlocal effects in the deformation mechanism. Benallal and Tvergaard (1995) have shown for the plane strain tensile test that the onset of bifurcation is delayed by strain gradient plasticity. In other cases the most relevant characteristic length may be related to damage mechanisms, as suggested by Pijaudier and Bazant (1987) and Barenblatt (1992). This nonlocal damage approach has been used by Leblond et al. (1994) and by Tvergaard and Needleman (1995) for a porous ductile material, and it has been shown that also the nonlocal damage approach removes the inherent mesh sensitivity in the predictions of failure by shear localization.

In most of the nonlocal material models the material characteristic length, introduced as an additional phenomenological parameter, has not been quantitatively related to actual microstructural lengths in the material. However, for the nonlocal ductile fracture model Tvergaard and Needleman (1997) have used a void-sheet cell model study (Tvergaard, 1989b) to obtain a micromechanical basis for assigning the material characteristic length. In the case shown in Fig. 5, the void-sheet cell model predicts the onset of plastic flow localization at $\epsilon_2 = 0.075$, and it is seen that the values of the post-localization slopes predicted by the nonlocal continuum model depend strongly on the value chosen for the material length L. A good fit with the post-localization slope predicted by the micromechanical void-sheet model is obtained in Fig. 5 for L in the range between $3.25R_0$ and $4.00R_0$, where R_0 is the initial radius of the voids in the micromechanical model.

3.2 Necking in Thin Metal Sheets. In metal-forming problems involving deep drawing of thin sheets the onset of localized necking is an important failure mode that limits the sheet metal formability. When a plane stress state is assumed, both inside and outside the band, sheet necking is the plane stress analog of the shear band localization problem described in relation to Eqs. (3.1) and (3.2), with the equations modified to account for different initial sheet thickness inside and outside the band. This simple plane stress (M-K) analysis for sheet necking was first introduced by Marciniak and Kuczynski (1967), and later the strong effect of the constitutive model on sheet necking predictions was shown by Støren and Rice (1975).

Recently, the M-K model has been employed by Kuroda and Tvergaard (1998) to analyse the effect of plastic anisotropy on sheet necking. Four different phenomenological models for plastic anisotropy are used in the analyses, with the yield surfaces and hardening behavior fitted to agree with experimental results of Kuwabara et al. (1998). Earlier studies for anisotropic sheets have taken the principal tensile axes to be along the orthotropic axes of the anisotropy, but this new investigation has also focussed on tension in directions inclined (by the initial angle θ_I) to the initial orthotropic axes, so that a description of the rotation of the orthotropic axes with deformation is a necessary part of the analysis. Figure 6 shows forming limit diagrams resulting from such analyses for cases where the initial thickness imperfection is taken to be specified by $h_I^b/h_I^o = 0.999$. The forming limit diagrams are computed by assuming a fixed proportion of the principal strains outside the band, and the curves show the strain at the onset of localization. It is seen in Fig. 3 that the localization strains predicted by the different anisotropic plasticity models differ a great deal, even though all models are fitted to the same experimental data. Also, the localization strains differ a great deal depending on the direction of the

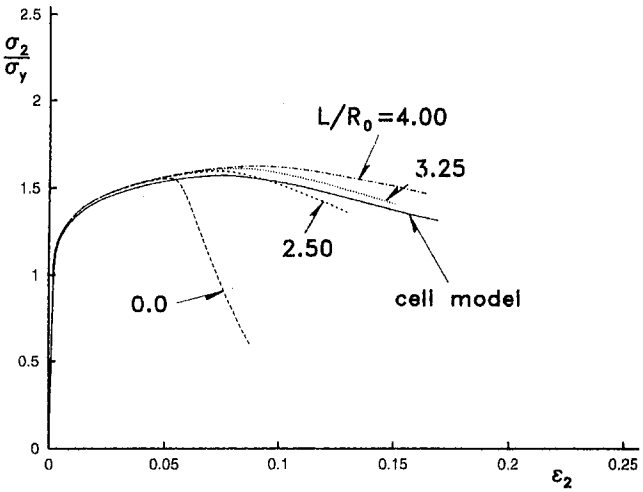

Fig. 5 Stress-strain curve for void-sheet cell model compared with shear localization predictions of nonlocal material model, for uniaxial plane strain tension, $R_0/D_0 = 0.175$, $\psi_I = 30$ deg, $f_I = 0.060$ and different values of L/R_0. (From Tvergaard and Needleman, 1997.)

Downloaded 04 May 2010 to 171.66.16.27. Redistribution subject to ASME license or copyright; see http://www.asme.org/terms/Terms_Use.cfm

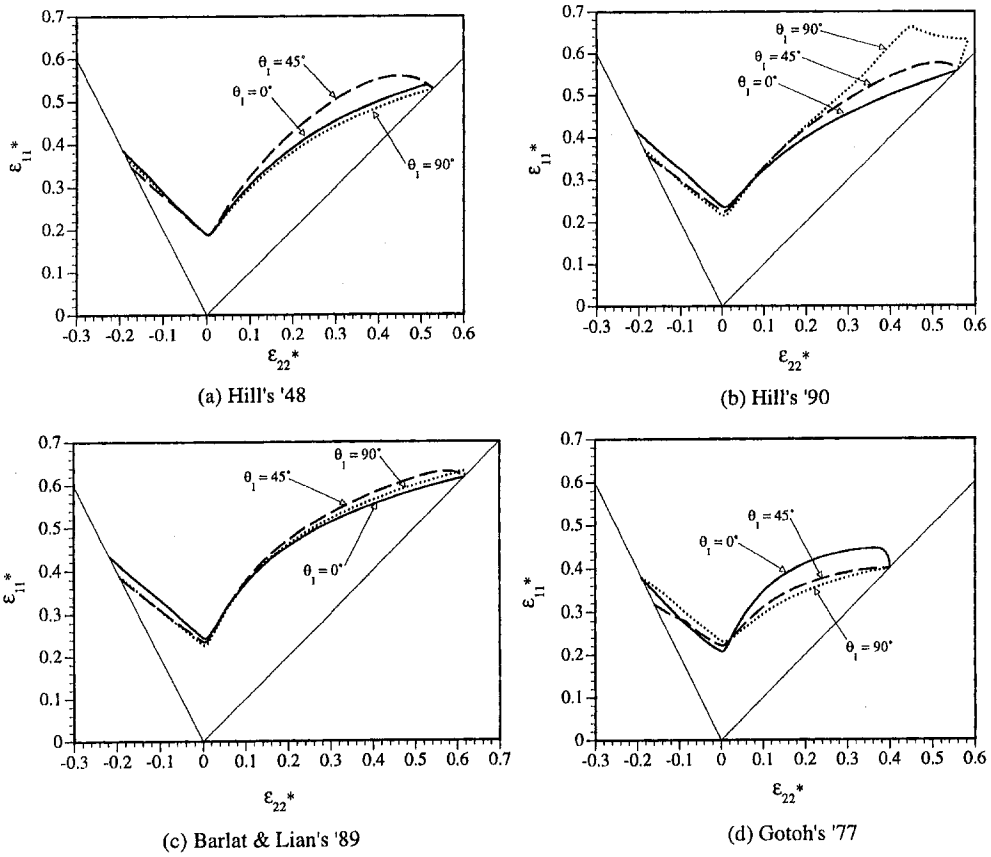

Fig. 6 Forming limit diagrams for anisotropic metal sheets. Three different tensile directions, θ_1, relative to initial orthotropic axes, with initial imperfection, $h_1^0/h_1^0 = 0.999$. (From Kuroda and Tvergaard, 1998.)

principal tensile stress relative to the orthotropic axes of the anisotropy.

The problem of necking in a thin sheet is really three-dimensional. In terms of the plane stress *M-K* model, bifurcation into a necking mode from a perfect sheet corresponds to loss of ellipticity of the governing plane stress field equations, but in terms of three-dimensional theory bifurcation occurs in a diffuse mode inside the elliptic range, according to the bifurcation theory of Hill (1958), e.g., see the analysis of Tvergaard (1993) for the case of necking in a tensile bar with rectangular cross section. The three-dimensional effects result in a delay of the onset of localization and in a fixed width of the neck band of the order of the current thickness of the sheet. In terms of a plane stress model these thickness effects can be accounted for by incorporating a material length scale in the plane stress constitutive relations, just like nonlocal three-dimensional models have used a material length to represent microstructural features of the material. Such a nonlocal plane stress model has been developed by Mikkelsen (1997), who has shown that the model can rather accurately reproduce the three-dimensional results of Tvergaard (1993). In an application to a thick-walled tube under internal pressure, earlier investigated by Larsson et al. (1982) and Tvergaard (1990), the nonlocal plane stress model has been found very useful in describing the bifurcation and localization behaviour (Mikkelsen and Tvergaard, 1999). The first bifurcation leads to the development of a localized axisymmetric bulge on the tube, and subsequently a secondary bifurcation gives localized necking on one side of the bulge, as illustrated by the nonlocal plane stress solutions in Fig. 7.

3.3 Buckling Localization. In experiments for axially compressed steel plate strips Moxham (1971) found that the final collapse mode involves one buckle, rather than the periodic buckle pattern predicted at the first bifurcation point. Subsequently, it was shown by Tvergaard and Needleman (1980) that the basic mechanism of buckling localization is associated with a bifurcation at or shortly after the maximum load point, in close analogy with the Considére (1885) result for tensile necking. Growing buckles give a reduced axial stiffness. Thus, the overall behavior of the periodically buckled structure may be represented by considering a homogeneous axially com-

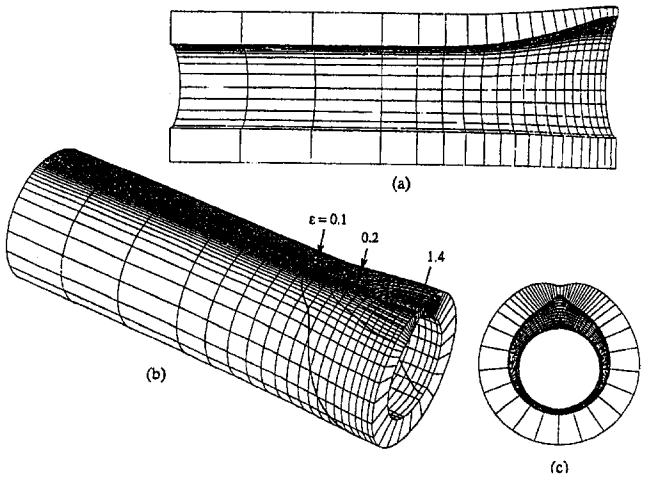

Fig. 7 Three views of deformed nonlocal membrane elements for a tube under internal pressure, with $L_0/R_0 = 8.0$, $H_0/R_0 = 0.6$, $n = 10$ and $l = 0.29H$. Contours of maximum principal logarithmic strain are included. (From Mikkelsen and Tvergaard, 1999.)

Downloaded 04 May 2010 to 171.66.16.27. Redistribution subject to ASME license or copyright; see http://www.asme.org/terms/Terms_Use.cfm

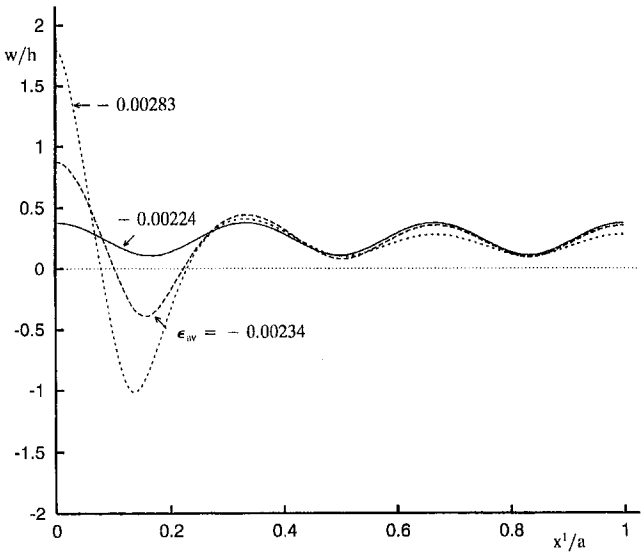

Fig. 8 Normal deflections along center line of an axially compressed elastic-plastic cylindrical panel with curvature parameter θ = 0.6 and hardening exponent n = 10. (From Tvergaard and Needleman, 1999.)

pressed bar constrained to remain straight, but free to slide in the axial direction, for which the axial stress is a nonlinear function of the strain. At a load maximum this one-dimensional bar model shows a bifurcation into a localized mode. Besides the axially compressed plate strip, this simple bar model is relevant to a broader class of periodically buckled structures under axial compression, including an elastic column on a softening foundation (Tvergaard and Needleman, 1980) and a circular cylindrical shell under axial compression (Tvergaard, 1983). In each of these cases localization is initiated at a secondary bifurcation point.

Tvergaard and Needleman (1980) also pointed out that a similar simple model applies to a tube under pure bending, where a gradually reduced bending stiffness results from ovalization of the cross section and from a short-wave buckle pattern on the compressed side of the tube. This simple model predicts a bifurcation at the point where the bending moment reaches a maximum, which results in the well-known final collapse mode, where the tube forms a sharp kink.

Recently, the post-buckling behavior of cylindrical panels under axial compression, which was first studied by Koiter (1956) for elastic panels, has been reanalyzed by Tvergaard and Needleman (1999) for elastic-plastic panels. This structural element represents an example, where either a stable or an unstable post-bifurcation behavior can result, dependent on the panel curvature and the material parameters. It is shown that in cases where a load maximum is reached, the initially periodic buckling pattern localizes (e.g., see Fig. 8), whereas no buckling localization is predicted in the cases where no load maximum is reached.

In relation to the nonlocal continuum models discussed above, it is noted that the structural buckling models already contain the characteristic length scales, which determine the width of localized regions. In fact, here the simple models used by Tvergaard and Needleman (1980) to disclose the basic mechanism of buckling localization follow the opposite trend, since these simple models neglect the characteristic material length, in order to more clearly illustrate the common feature of a broad class of structures.

4 Cavitation Instabilities

Unstable growth of a small void in a metal occurs under rather rare conditions, in which plastic flow is highly constrained, leading to mean tensile stress levels which are more than four or five times the tensile flow stress of the solid. For a cavity in an infinite elastic-plastic material under pure hydrostatic tension the critical stress was determined early on (Bishop, Hill and Mott, 1945), and the spherically symmetric problem of unstable cavity growth has also attracted much interest in the context of nonlinear elasticity (Ball, 1982; Horgan and Abeyaratne, 1986; Horgan, 1992).

A striking example of cavitation instabilities was observed by Ashby, Blunt, and Bannister (1989) in tensile experiments on highly constrained ductile wire. These instabilities did not occur under pure hydrostatic tension, and therefore the growth of an initially spherical void in an axisymmetric stress state was studied by Huang et al. (1991) and Tvergaard et al. (1992). It was found that a cavitation instability limit is still reached, as long as the stress state allows for a sufficiently high mean stress during plastic flow.

The cavitation instability limit is defined as the constant remote stress and strain state, at which the cavity grows without bounds. Then, since no external work is applied to the solid, stored elastic energy is used to balance the plastic dissipation involved in the void growth. However, in a finite solid the void cannot grow without bounds. This is illustrated by computations of void growth in a thin metal layer between ceramics (Tvergaard, 1997), where the use of remeshing has made it possible to numerically follow the growth of an initially tiny void until coalescence with neighbouring voids, where the hole has reached dimensions comparable to the thickness of the metal layer. Figure 9 shows the average tensile stress versus average strain in the metal layer, and the corresponding evolution of the void volume V. For the smallest initial void Fig. 9 shows that V grows by many orders of magnitude, while the average stress and strain remain constant, but then as the void size becomes comparable with the dimensions of the solid the growth behavior changes such that the average strain in the layer increases significantly, while the average stress decays towards zero.

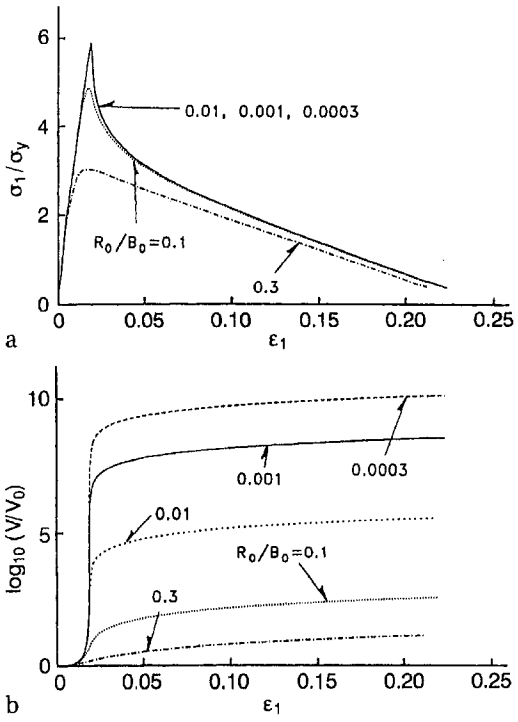

Fig. 9 Void growth in thin metal layer between ceramics. Average true stress and void volume growth versus average logarithmic strain, for hardening exponent n = 10. (From Tvergaard, 1997.)

Downloaded 04 May 2010 to 171.66.16.27. Redistribution subject to ASME license or copyright; see http://www.asme.org/terms/Terms_Use.cfm

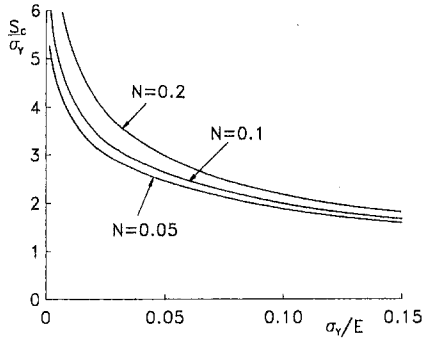

Fig. 10 Critical stress for cavitation instability versus initial yield strain, for $T/S = 0.9$, $\nu = 0.3$ and various values of hardening exponent N. (From Tvergaard, 1998.)

The studies of cavitation instabilities have focussed on a single void in a solid, but if the solid contains a distribution of voids it is of interest to know if several voids would cavitate simultaneously. A cell model study (Tvergaard, 1996), for a solid containing two populations of voids with different size, has made it possible to study the different growth rates of the two voids in the unit cell, and the studies clearly show that once a cavitation instability is reached, the two voids will not grow simultaneously. The indication is that also in a group of more than two voids in a uniform stress field, only one of them would finally grow in an unstable manner.

The cavitation instability studies of Huang et al. (1991) and Tvergaard et al. (1992) for an initially spherical void in an axisymmetric stress state have recently been extended to account for a large initial yield strain (Tvergaard, 1998). This is not realistic for metals, but large initial yield strains are of interest for polymers (e.g., see Steenbrink and van der Giessen, 1997), where somewhat different material models are used. For the power-hardening solid in a stress state with the ratio $T/S = 0.9$ between the principal stresses Fig. 10 shows that the value of the critical stress normalized by the flow stress decays significantly, as the initial yield strain increases.

References

Aifantis, E.C., 1984, "On the microstructural origin of certain inelastic models," *J. Engng. Mater. Tech.,* Vol. 106, pp. 326–334.

Ashby, M.F., Blunt, F.J., and Bannister, M., 1989, "Flow characteristics of highly constrained metal wires," *Acta Metall.,* Vol. 37, p. 1857.

Ball, J.M., 1982, "Discontinuous equilibrium solutions and cavitation in nonlinear elasticity," *Phil. Trans. R. Soc. London,* Vol. A306, pp. 557–610.

Barenblatt, G.I., 1992, "Micromechanics of fracture," *Proc. Int. Congr. Theor. Appl. Mech.,* Haifa, Israel.

Benallal, A., and Tvergaard, V., 1995, "Nonlocal continuum effects on bifurcation in the plane strain tension-compression test," *J. Mech. Phys. Solids,* Vol. 43, pp. 741–770.

Bishop, R.F., Hill, R., and Mott, N.F., 1945, "The theory of indentation and hardness tests," *Proc. Phys. Soc.,* Vol. 57, pp. 147–159.

de Borst, R., 1993, "A generalization of J_2-flow theory for polar continua," *Comput. Meth. Appl. Mech. Engng.,* Vol. 103, pp. 347–362.

Christensen, C.D., 1997, "Plastic stability and imperfection sensitivity of the Euler column," Report, Department of Structural Engineering, Technical University of Denmark.

Considére, M., 1885, "L'Emploi du fer et de l'acier dans les constructions," *Annales des Ponts et Chaussées,* Vol. 9, pp. 574–775.

Fleck, N.A., and Hutchinson, J.W., 1993, "A phenomenological theory of strain gradient plasticity," *J. Mech. Phys. Solids,* Vol. 41, pp. 1825–1857.

Fleck, N.A., Muller, G.M., Ashby, F., and Hutchinson, J.W., 1994, "Strain gradient plasticity: Theory and experiment," *Acta Metall. Mater.,* Vol. 42, pp. 475–487.

Hadamard, J., 1903, *Leçons sur la Propagation des Ondes et les Équations de L'Hydrodynamique,* Paris, Chapter 6.

Hill, R., 1958, "A general theory of uniqueness and stability in elastic-plastic solids," *J. Mech. Phys. Solids,* Vol. 6, pp. 236–249.

Hill, R., 1961, "Bifurcation and uniqueness in non-linear mechanics of continua," *Problems of Continuum Mechanics,* M.A. Lavrentiev et al., eds., Society for Industrial and Applied Mathematics, Philadelphia, PA.

Hill, R., 1962, "Acceleration waves in solids," *J. Mech. Phys. Solids,* Vol. 10, pp. 1–16.

Horgan, C.O., 1992, "Void nucleation and growth for compressible nonlinearly elastic materials: An example," *Int. J. Solids Struct.,* Vol. 29, pp. 279–291.

Horgan, C.O., and Abeyaratne, R., 1986, "A bifurcation problem for a compressible nonlinearly elastic medium: Growth of a microvoid," *J. Elasticity,* Vol. 16, pp. 189–200.

Huang, Y., Hutchinson, J.W., and Tvergaard, V., 1991, "Cavitation instabilities in elastic-plastic solids," *J. Mech. Phys. Solids,* Vol. 39, pp. 223–241.

Hutchinson, J.W., 1973, "Postbifurcation behavior in the plastic range," *J. Mech. Phys. Solids,* Vol. 21, pp. 163–190.

Hutchinson, J.W., 1974, "Plastic buckling," *Advan. Appl. Mech.,* Vol. 14, pp. 67–144.

Hutchinson, J.W., and Miles, J.W., 1974, "Bifurcation analysis of the onset of necking in an elastic-plastic cylinder under uniaxial tension," *J. Mech. Phys. Solids,* Vol. 22, pp. 61–77.

Hutchinson, J.W., and Tvergaard, V., 1981, "Shear band formation in plane strain," *Int. J. Solids Struct.,* Vol. 17, pp. 451–470.

Koiter, W.T., 1945, "Over de stabiliteit van het elastisch evenwicht," thesis, Delft, H.J. Paris, Amsterdam (English translations (a) NASA TT-F10, 1967; (b) AFFDL-TR-70-25, 1970).

Koiter, W.T., 1956, "Buckling and post-buckling behaviour of a cylindrical panel under uniaxial compression," National Luchtvaart Laboratorium, 20, Report S476, Amsterdam.

Koiter, W.T., 1963, "The effect of axisymmetric imperfections on the buckling of cylindrical shells under axial compression," *Proc. Kon. Ned. Ak. Wet.,* Vol. 66B, pp. 265–279.

Kuroda, M., and Tvergaard, V., 1998, "Forming limit diagrams for anisotropic metal sheets with different yield criteria," DCAMM Report No. 584, Technical University of Denmark.

Kuwabara, T., Ikeda, S., and Kuroda, K., 1998, "Measurement and analysis of different work hardening in cold-rolled steel sheet under biaxial tension," *J. Mater. Proc. Mech.,* Vol. 80–81, pp. 517–523.

Larsson, M., Needleman, A., Tvergaard, V., and Storåkers, B., 1982, "Instability and failure of internally pressurized ductile metal cylinders," *J. Mech. Phys. Solids,* Vol. 30, pp. 121–154.

Leblond, J.B., Perrin, G., and Devaux, J., 1994, "Bifurcation effects in ductile metals with damage delocalization," ASME JOURNAL OF APPLIED MECHANICS, Vol. 61, pp. 236–242.

Marciniak, Z., and Kuczynski, K., 1967, "Limit Strains in the Process of Stretch Forming Sheet Metal," *Int. J. Mech. Sci.,* Vol. 9, pp. 609–620.

Mikkelsen, L.P., 1997, "Post-necking behaviour modelled by a gradient dependent plasticity theory," *Int. J. Solids Struct.,* Vol. 34, pp. 4531–4546.

Mikkelsen, L.P., and Tvergaard, V., 1999, "A nonlocal two-dimensional analysis of instabilities in tubes under internal pressure," *J. Mech. Phys. Solids,* Vol. 47, pp. 953–969.

Moxham, K.E., 1971, "Buckling tests on individual welded steel plates in compression," Cambridge University Engineering Department, Report CUED/C–Struct/TR.3.

Needleman, A., and Tvergaard, V., 1982, "Aspects of plastic postbuckling behavior," *Mechanics of Solids,* The Rodney Hill 60th Anniversary Volume, H.G. Hopkins and M.J. Sewell, eds., Pergamon Press, London, pp. 453–498.

Needleman, A., and Tvergaard, V., 1992, "Analysis of plastic flow localization in metals," ASME *Applied Mechanics Reviews,* Vol. 45, pp. S3–S18.

Pijaudier-Cabot, G., and Bazant, Z.P., 1987, "Nonlocal damage theory," *J. Engng. Mech. ASCE,* Vol. 113, pp. 1512–1533.

Redanz, P., and Tvergaard, V., 1998, "Analysis of shear band instabilities in sintered metals," *Int. J. Solids Struct.,* to appear.

Rice, J.R., 1977, "The localization of plastic deformation," *Proc. 14th Int. Congr. Theoret. Appl. Mech.,* W.T. Koiter, ed., North-Holland, Amsterdam, pp. 207–220.

Shanley, F.R., 1947, "Inelastic column theory," *J. Aeronaut. Sci.,* Vol. 14, pp. 261–267.

Steenbrink, A.C., and van der Giessen, E., 1997, "Void growth in glassy polymers: Effect of yield properties on hydrostatic expansion," *Int. J. Damage Mech.,* Vol. 6, pp. 317–330.

Stören, S., and Rice, J.R., 1975, "Localized necking in thin sheets," *J. Mech. Phys. Solids,* Vol. 23, pp. 421–441.

Tvergaard, V., 1973, "Imperfection-sensitivity of a wide integrally stiffened panel under compression," *Int. J. Solids Struct.,* Vol. 9, pp. 177–192.

Tvergaard, V., 1982, "Influence of void nucleation on ductile shear fracture at a free surface," *J. Mech. Phys. Solids,* Vol. 30, pp. 399–425.

Tvergaard, V., 1983, "On the transition from a diamond mode to an axisymmetric mode of collapse in cylindrical shells," *Int. J. Solids Struct.,* Vol. 19, pp. 845–856.

Tvergaard, V., 1989, "Plasticity and creep at finite strains," *Theoretical and Applied Mechanics,* P. Germain, M. Piau, and D. Caillerie, eds., Elsevier Science Publishers B.V., Amsterdam, pp. 349–368.

Tvergaard, V., 1989, "Numerical study of localization in a void-sheet," *Int. J. Solids Struct.,* Vol. 10, pp. 1143–1156.

Tvergaard, V., 1990, "Bifurcation in elastic-plastic tubes under internal pressure," *Eur. J. Mech., A/Solids,* Vol. 9, pp. 21–35.

Tvergaard, V., 1993, "Necking in tensile bars with rectangular cross-section," *Comp. Meth. in Appl. Mech. and Engng.,* Vol. 103, pp. 273–290.

Downloaded 04 May 2010 to 171.66.16.27. Redistribution subject to ASME license or copyright; see http://www.asme.org/terms/Terms_Use.cfm

Tvergaard, V., 1996, "Effect of void size difference on growth and cavitation instabilities," *J. Mech. Phys. Solids,* Vol. 44, pp. 1237–1253.

Tvergaard, V., 1997, "Studies of void growth in a thin ductile layer between ceramics," *Computational Mechanics,* Vol. 20, pp. 186–191.

Tvergaard, V., 1998, "Effect of large elastic strains on cavitation instability predictions for elastic-plastic solids," *Int. J. Solids Struct.,* to appear.

Tvergaard, V., and Needleman, A., 1980, "On the Localization of Buckling Patterns," ASME JOURNAL OF APPLIED MECHANICS, Vol. 47, pp. 613–619.

Tvergaard, V., and Needleman, A., 1995, "Effects of nonlocal damage in porous plastic solids," *Int. J. Solids Struct.,* Vol. 32, pp. 1063–1077.

Tvergaard, V., and Needleman, A., 1997, "Nonlocal effects on localization in a void-sheet," *Int. J. Solids Struct.,* Vol. 34, pp. 2221–2238.

Tvergaard, V., and Needleman, A., 1999, "Buckling localization in a cylindrical panel under axial compression," W. T. Koiter Commemorative Issue, *Int. J. Solids Struct.,* to appear.

Tvergaard, V., Huang, Y., and Hutchinson, J.W., 1992, "Cavitation instabilities in a power hardening elastic-plastic solid," *Eur. J. Mech., A/Solids,* Vol. 11, pp. 215–231.

Zbib, H.M., and Aifantis, E.C., 1989, "A gradient-dependent flow theory of plasticity: Application to metal and solid instabilities," ASME *Applied Mechanics Reviews,* Vol. 42, pp. S295–S304.

Downloaded 04 May 2010 to 171.66.16.27. Redistribution subject to ASME license or copyright; see http://www.asme.org/terms/Terms_Use.cfm

Warner T. Koiter Medal Recipient

Conferral at the Applied Mechanics Dinner,
1998 International Mechanical Engineering Congress and Exposition

THE WARNER T. KOITER MEDAL was established in 1996 to recognize distinguished contributions to the field of solid mechanics with emphasis on the effective blending of theoretical and applied elements, and on a high degree of leadership in the international solid mechanics community.

The medal honors the late Dr. Warner T. Koiter (1914–1997), world-renowned authority in the field of solid mechanics, and it commemorates his vast contributions as research engineer and teacher.

VIGGO TVERGAARD, Dr. Techn., professor, department of solid mechanics, Technical University of Denmark, Lyngby, *for seminal contributions to the understanding of instability and failure phenomena in solids and structures.*

Dr. Tvergaard has been affiliated with the department of solid mechanics at the Technical University of Denmark in Lyngby since 1969. He has worked as a doctoral student, assistant professor, associate professor, docent, research professor and, since 1994, a professor. He was appointed visiting professor of engineering at Brown University, (Providence, R.I.) from 1989 to 1994.

Dr. Tvergaard has done research in the areas of plastic buckling of structures, mechanics of materials, fracture mechanics and micromechanics. He is currently editor in chief of *European Journal of Mechanics A/Solids,* and a member of the advisory editorial boards for the *International Journal of Thin Walled Structures, International Journal of Mechanics Science, Mechanics of Materials, Acta Mechanica Sinica, Modelling and Simulation in Material Science and Engineering, International Journal of Damage Mechanics and The Cambridge Monographs on Mechanics.*

Among the honors received by Dr. Tvergaard are the Esso Prize in 1982 for outstanding technical and scientific research and the Villum Kann Rasmussen scholarship in 1989 for technical research on material mechanics and fracture mechanics.

Dr. Tvergaard is a member of the Danish Academy of Technical Sciences, the Danish Center for Applied Mathematics and Mechanics, and The Society of Danish Engineers.

Dr. Tvergaard earned his master's degree in mechanical engineering, and Ph.D. and Dr. Techn. in solid mechanics at Technical University of Denmark. He received an honorary doctorate from the Royal Institute of Technology (Stockholm, Sweden) in 1993.

Downloaded 04 May 2010 to 171.66.16.27. Redistribution subject to ASME license or copyright; see http://www.asme.org/terms/Terms_Use.cfm

Recovery Experiments for Adiabatic Shear Localization: A Novel Experimental Technique

D. R. Chichili
Mem. ASME

K. T. Ramesh[1]
Mem. ASME

Laboratory for Impact Dynamics
and Rheology,
Department of Mechanical Engineering,
The Johns Hopkins University,
Baltimore, MD 21218

A novel experimental technique has been developed that allows the recovery of specimens within which an adiabatic shear band has been grown as the result of a single torsional pulse. The technique uses a new device called the compression-torsion Kolsky bar; this is an adaptation of the classical torsional Kolsky bar in which both compression and torsion are stored in the clamped length. Recovery of the specimen is obtained by causing the transmitted compression pulse to reflect from the free end of the output bar as a tensile pulse which then causes failure of the specimen/output-bar interface. All further pulses then cause no more than rigid motions of the specimen. Thus the specimen is recovered after it has been loaded by a single torsional pulse; microscopic examination of the recovered specimen now allows the rigorous determination of the evolution of microstructure and the identification of deformation mechanisms that are active under the dynamic shear loading. As an example of the utility of this recovery technique, its application to the study of adiabatic shear localization in alpha-titanium is presented. The technique allows a systematic study of the microscopic mechanisms that drive the initiation and growth of adiabatic shear bands by recovering samples within which shear bands have been grown under controlled conditions; further characterization through sectioning, followed by optical, scanning, and transmission electron microscopy is then possible. The technique also allows one to study the influence of the shape and size of geometric defects (for example, notch tip radius and notch depth) on the initiation of adiabatic shearing failures. The effect of normal stresses on the susceptibility of a material to shear localization can also be investigated.

Introduction and Background

The compression Kolsky bar or split Hopkinson pressure bar (Kolsky, 1949) is probably the most widely used technique for the study of material behavior at high strain rates ($\approx 10^3$–10^4 s^{-1}). This technique has subsequently been adapted to the study of shearing deformations; the adaptation is known as the torsional Kolsky bar (e.g., Hartley et al., 1985). Recently Staab and Gilat (1991) modified the torsional Kolsky bar to test specimens under dynamic tension (see also Chichili and Ramesh, 1995); other variants of the tension bar are also used (e.g., Pelletier et al., 1995). All of these techniques are used to obtain the macroscopic constitutive response (essentially the stress-strain behavior as a function of strain rate and temperature) of the material. Modified versions of these techniques have also been applied to studies of the development of dynamic failures within materials, such as adiabatic shear bands (Marchand and Duffy, 1988; Ramesh, 1994) and dynamic fracture (e.g., Couque and Lankford, 1989).

A fundamental understanding of material behavior at high strain rates also requires an understanding of the microscopic mechanisms that are active during dynamic deformations, and consequently of the evolution of microstructure with loading. However, the specimens in traditional Kolsky bar experiments are typically subjected to more than one loading pulse and hence cannot be used to characterize (post-mortem) the evolution of microstructure with dynamic loading. Thus, controlled dynamic experiments (also called dynamic recovery experiments) are essential for understanding the evolution of microstructure with the loading history. Various methods have been developed to recover samples in the compression Kolsky bar (da Silva and Ramesh 1997; Nemat-Nasser et al., 1991). In the da Silva-Ramesh modification of the compression Kolsky bar, the compression pulse that is transmitted to the output bar reflects from the free end of the output bar as a tensile pulse. By making the output bar shorter than the input bar, this tension pulse causes failure of the specimen-output bar interface before the first compressive reloading. Thus, the specimen is recovered after being subjected to a single known compressive stress pulse.

However, an equivalent recovery technique does not currently exist for the torsional Kolsky bar. The specific application of the torsional Kolsky bar of interest to this paper is the investigation of adiabatic shear localization in metals (e.g., Marchand and Duffy, 1988). In these experiments, an adiabatic shear band is developed within a thin-walled tube specimen undergoing initially homogeneous torsional deformations. This technique has the advantage of a well-characterized initial stress state, but the disadvantage is that the development of the shear band is extremely sensitive to random geometric defects in the thin-walled specimen. Further, the technique is not amenable to post-mortem microstructural characterization of the shear band, since repeated loadings drive the specimen to catastrophic failure in several modes. If the specimen fails completely during the initial torsional pulse, later torsional pulses can cause the two fractured surfaces to rub against each other. Further, if a shear band forms, and if this is followed by a crack which does not run all the way around the specimen during the first pulse (a common occurrence), the subsequent loadings do not represent pure torsion. Typically the asymmetry induced by the cracked specimen

[1] To whom correspondence should be addressed.

Contributed by the Applied Mechanics Division of THE AMERICAN SOCIETY OF MECHANICAL ENGINEERS for publication in the ASME JOURNAL OF APPLIED MECHANICS.

Discussion on the paper should be addressed to the Technical Editor, Professor Lewis T. Wheeler, Department of Mechanical Engineering, University of Houston, Houston, TX 77204-4792, and will be accepted until four months after final publication of the paper itself in the ASME JOURNAL OF APPLIED MECHANICS.

Manuscript received by the ASME Applied Mechanics Division, Sept. 30, 1997; final revision, May 28, 1998. Associate Technical Editor: L. T. Wheeler.

 Copyright © 1999 by ASME

Downloaded 04 May 2010 to 171.66.16.27. Redistribution subject to ASME license or copyright; see http://www.asme.org/terms/Terms_Use.cfm

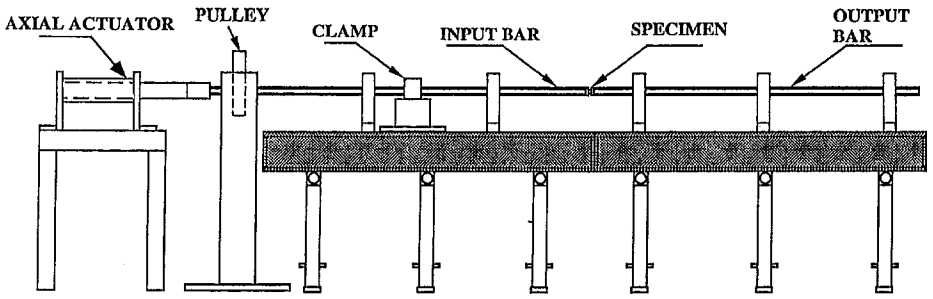

Fig. 1 Schematic diagram of a compression-torsion Kolsky bar

results in the development of a bending wave, and thus one often observes cracks that have later grown in tension and that have kinked away from the initial failure plane. As a result, the interactions between evolving microstructure, failure modes, and loading can no longer be evaluated.

Other experimental methods, such as the dynamic punching tests of Zener and Hollomon (1944) and a variant of the latter using a "hat" specimen in the split-Hopkinson pressure bar (e.g., Meyers et al., 1994) have been used to develop adiabatic shear bands for later microstructural examination. However, the stress distributions and loading histories in these experiments are very complex, and so it is difficult to relate the observed microstructures to specific features in the loading history. Bai et al. (1994) modified the classical torsional Kolsky bar for recovering specimens by attaching an "unloading bar" to the output bar using a ratchet-type connector. Once the loading pulse has passed completely into the "unloading bar," the output and unloading bars separate and thus the initial loading wave is trapped in the unloading bar. However, the amplitude of the reflected wave (within the input bar) has to be maintained at a sufficiently small level to ensure that no secondary plastic deformation is imposed on the specimen. This restricts the technique to either strong materials or low rates (because of the restriction on the magnitude of the reflected pulse).

This paper describes a novel experimental technique called the compression-torsion Kolsky bar, developed at Johns Hopkins, which allows the recovery of specimens within which adiabatic shear bands have been grown under controlled conditions. The rest of the paper describes the experimental technique in detail and illustrates the application of the technique to investigating adiabatic shear localization in alpha-titanium.

Experimental Technique

Experimental Configuration. The device (Fig. 1) consists of two long metal bars that are designed to remain elastic throughout the test. The overall design is much like that of a conventional torsional Kolsky bar (e.g., Ramesh 1994), with an "input bar," an "output bar," and a specimen. The compression-torsion Kolsky bar used for the experiments described here uses input and output bars made of 7075-T651 aluminum; the input bar is about 3.5 m long and the output bar is 2.7 m long, and they are each one inch in diameter. The torquing device consists of a pulley driven by a hydraulic system and is attached to one end of the input bar (this is the conventional torsional bar arrangement). In addition, however, a hydraulic actuator for the application of forces in an axial direction is placed at the same end of the input bar, with a pair of flat platens (one on a ball-and-socket joint) used to apply a compressive force to the input bar itself. The actuators, bars, and specimen are supported on an alignment table and specially designed bearing blocks. Strain gages are mounted on both the bars for measuring the shear strains, axial strains, and bending strains in the bars. The specimen is attached between the two bars using a very thin layer of an epoxy adhesive.

In operation, both compression and torque are applied to a short section of the input bar using the hydraulic system, while the rest of the bar is restrained from compression and rotation using a friction clamp. The yield strength of the 7075-T6 aluminum limits the maximum stored input torque to 400 N-m. The maximum compression that can be stored in the bar is in principle determined by the bar buckling limit, and is therefore dependent on the length of the clamped segment and the number of supports of that segment. In practice, however, the bar buckling limit is beyond the capability of the hydraulic loading system, and the true compression limit is determined from specimen buckling considerations. The friction clamp uses a notched bolt made of 2024-T4 aluminum that is extended until breakage by means of a separate hydraulic system. When the friction clamp is suddenly released by breaking the prenotched bolt, a compressive pulse and a torsional pulse propagate down the bar towards the specimen. Each pulse amplitude is half the corresponding stored stress and the pulse duration is determined by the length of the bar between the loading device and the clamp. The design of the friction clamp is critical; if the mechanism of release is asymmetrical, flexural waves will also be generated in the bar. Bar alignment and the clamping arrangement are adjusted until the bending waves (measured in the bars using a separate set of strain gages) are negligible.

Wave Propagation. The propagation of the waves in the bars after the release of the clamp is shown in Fig. 2; longitudinal waves are shown as solid lines, and torsional waves are shown as dashed lines. When the friction clamp is suddenly released by breaking the prenotched bolt, a compressive wave and a torsional wave propagate down the bar towards the specimen at the longitudinal bar wave velocity ($C_d = \sqrt{E/\rho} = 4.95$ m/s) and the shear wave velocity ($C_s = \sqrt{\mu/\rho} = 2.9$ m/s), respectively, while the corresponding unloading waves propagate back into the preloaded section, reducing the compressive and shear stresses there to half their initial values. Both the unloading waves reflect from the end of the input bar (which acts as a rigid end condition) thereby generating a single compressive pulse and a single torsional pulse (Fig. 2). The pulses are trapezoidal in shape: each pulse amplitude is half the corresponding stored stress, the pulse duration is determined by the length of the bar between the loading device and the clamp, and the rise and fall times are determined by the clamp release process.

Since the longitudinal pulse travels faster than the shear pulse, it arrives first at the specimen. This is an advantage, since by positioning the clamp appropriately, the torsional pulse can be set to arrive at the specimen after the compressive stresses have equilibrated along the length of the specimen. Since the specimen is designed to have a lower elastic impedance than the bar, the compressive stresses within it build up when the compressive wave arrives. The torsional pulse then loads the specimen in shear after a steady compression has developed in the specimen. By design, the amplitude of the incident torsional pulse is such that the specimen deforms plastically. Parts of the

Downloaded 04 May 2010 to 171.66.16.27. Redistribution subject to ASME license or copyright; see http://www.asme.org/terms/Terms_Use.cfm

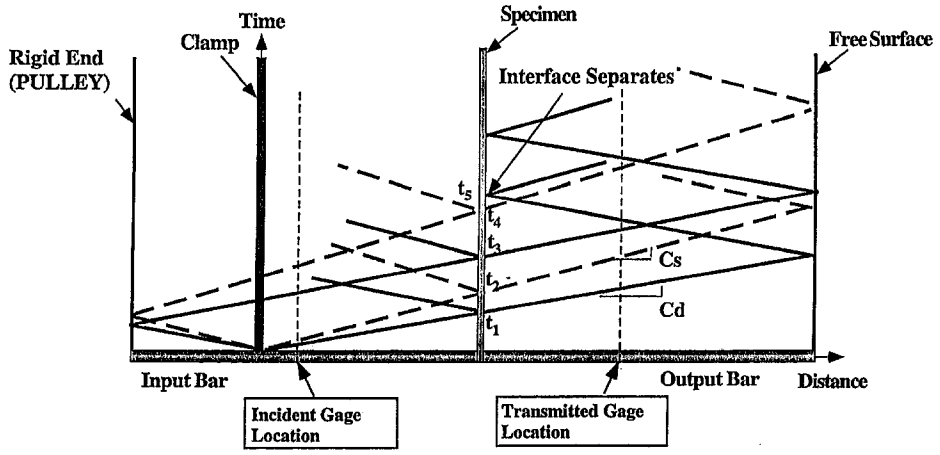

Fig. 2 Wave propagation diagram for the compression-torsion Kolsky bar in the recovery mode. The interface is separated after the initial shear unloading has gone through. The specimen is under only compression from t_1 to t_2, under combined compression and torsion from t_2 to t_3, torsion alone from t_3 to t_4 and separation occurs at t_5.

compression and torsional pulses are transmitted through the specimen into the output bar (resulting in what are known as "transmitted pulses"); part of each pulse is reflected back into the input bar as a reflected pulse. The incident torsional and axial gages are located 1.381 m and 1.454 m from the specimen, respectively, and the transmitted torsional and axial gages are located 0.975 m and 0.908 m from the specimen, respectively (Fig. 2). The strain gage signals are captured using a Nicolet MultiPro digital oscilloscope with 12-bit vertical resolution and using differential inputs, and the data processing is performed using VuPoint on an IBM compatible computer.

In the classical torsional Kolsky bar test there are no longitudinal waves, and after several reverberations of the torsional wave within the thin-walled tube specimen, the shear stress and the shear strain in the specimen become nearly homogeneous. Once a uniform stress state has been achieved, the stress in the specimen can be obtained from the transmitted shear strain signal γ_T in the output bar:

$$\tau_S = \frac{\mu R^3}{d^2 h}\,\gamma_T \tag{1}$$

and the strain rate in the specimen can be determined from the reflected shear strain signal γ_R in the input bar:

$$\dot{\gamma}_S = \frac{C_s d}{lR}\,\gamma_R. \tag{2}$$

Here μ is the shear modulus for the bars, R is the bar radius, d is the mean diameter of the thin-walled tube specimen, l is the specimen length, and h is the specimen wall thickness. The shear rate is integrated over time to obtain the shear strain, and a correlation of the stress and strain histories then provides a stress-strain curve (at a shear rate corresponding to Eq. (2)) for the specimen material. However, in the case of inhomogeneous deformations (as with shear localization), only the boundary tractions and the boundary velocities can be directly inferred (using the fact that the input and output bars remain elastic). Thus in the classic shear band tests of Marchand and Duffy (1988) the stress-strain curves are only meaningful up to the time at which the deformations become inhomogeneous, i.e., up to the time at which the shear band begins to develop. The current apparatus functions under similar constraints, in that only boundary tractions and boundary velocities can be inferred in the case of inhomogeneous deformations.

Recovery Mechanism. The intent of the new technique, however, is to allow the recovery of the specimen after it has been loaded by a single torsional pulse (in the Marchand-Duffy type test the specimen is repeatedly loaded until gross failure occurs). The mechanism that leads to recovery is as follows. The transmitted compressive pulse reflects (Fig. 2) from the free end of the output bar and returns as a tensile pulse. The key feature in the present compression-torsion Kolsky bar is that the specimen/output-bar interface separates under tensile loading, because the adhesive that is used can carry compressive and shearing stresses, but is unable to sustain tension. The clamped length and the length of the output bar can be chosen such that the separation occurs at the desired time. Note that in the configuration shown in Fig. 2, the separation occurs just after the incident shear wave has completely passed the specimen. All further pulses in the bar then result in essentially rigid motions (although the trapped shear pulse has substantial amplitude, the specimen is comparatively very short and has one end stress-free) of the specimen, and a true recovery test has been achieved. Hence, the technique provides a means to recover the specimen after it has been subjected to a single known torsional (loading) pulse. Evidence of this recovery mechanism is presented in the subsequent paragraphs.

Elastic wave propagation experiments were first performed to check the strength of the epoxy; these tests include only the adhesive joint, which now directly connects the input and output bars. Figures 3 and 4 show the typical compression and torsion signals obtained from one such test. The incident compression pulse in Fig. 3 does not unload to a zero stress level because of a deviation of the end condition of the input bar from the ideal rigid condition with regard to longitudinal waves. However, this does not affect our interpretation of the experiment since we do not need information from the reflected longitudinal pulse at all; we use the compression wave solely to generate the recovery mechanism. (If the reflected longitudinal pulse were to be used to evaluate the compressive strain rate in the sample, it would have to be corrected for the drift in the baseline. Such corrections can be made using a separate series of calibration experiments performed to evaluate the end condition alone.) Note (Fig. 3) that the incident compression pulse is completely transmitted into the output bar. This transmitted compression pulse reaches the free end of the output bar and is reflected back as a tensile pulse. Once the tensile pulse reaches the interface, the epoxy fails, the interface separates and the tensile pulse that caused the separation propagates back into the output bar as a compression pulse. The interface separation is thus evident from Fig. 3. The recovery process is much more clearly seen in Fig. 4, which shows the torsion signals during the same experiment. Since this is an elastic test, the incident shear is completely transmitted into the output bar (which also demon-

Downloaded 04 May 2010 to 171.66.16.27. Redistribution subject to ASME license or copyright; see http://www.asme.org/terms/Terms_Use.cfm

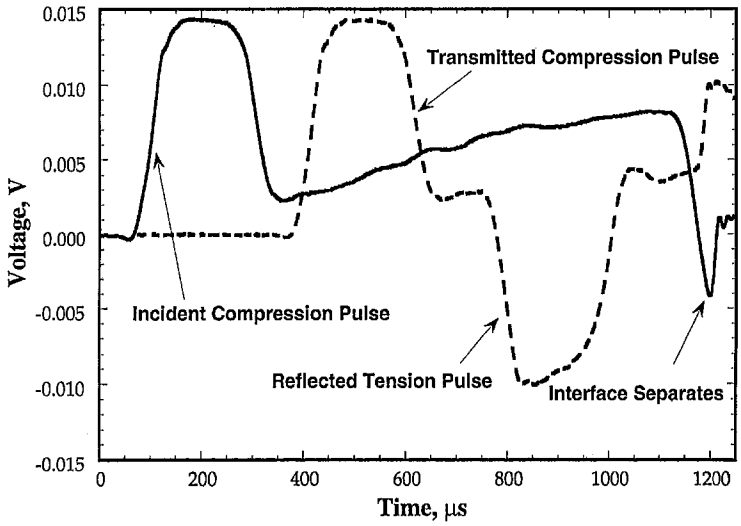

Fig. 3 Compression signals for an elastic test in the compression-torsion Kolsky bar. The initial unloading pulse does not unload to zero stress level as the pulley is not a perfect rigid end condition. Note that the reflected tensile pulse is trapped in the output bar as the interface separates under tension.

strates that the epoxy holds in shear). Examination of the incident torsional pulse shows that the pulley end condition represents a rigid end condition in torsion (unlike in compression). When the reflected shear pulse from the free end of the output bar reaches the interface, the interface has already been separated due to the tensile loading shown in Fig. 3. Thus, the reloading shear pulse is seen to be trapped in the output bar. The result is a rigid-body rotation of the output bar. The ability of the epoxy joint to provide the recovery mechanism has thus been demonstrated.

Application to Study of Normal Stress Effects. One consequence of the experimental configuration of Fig. 1, clearly evident in the wave propagation diagram of Fig. 2, is that the relative durations of the compressive and torsional pulses can be varied by changing the location of the clamp. For instance, with the experimental configuration represented in Fig. 2, the specimen is under just compression from t_1 to t_2, under combined compression and torsion from t_2 to t_3, and under torsion alone between t_3 and t_4. Separation occurs at t_5, which can be made very close to t_4. Such an arrangement could be a very useful recovery experiment if one were certain that the magnitude of the compression was irrelevant to the problem under study, so that only the single torsional loading is of interest and the on/off nature of the longitudinal mode may be ignored. However, a number of applications involve substantial normal stress effects, and the magnitude of the initial compressive loading needed to ensure separation of the adhesive interface is not small, and so one may well be concerned about the changing compressive state. This is probably the case with adiabatic shear localization, which is the application of immediate interest in this paper.

A configuration that addresses this specific issue is presented in Fig. 5. The intent now is to maintain the compression during the entire time that the specimen is plastically loaded in torsion. This can be achieved by having the tensile pulse reach the specimen-bar interface just after the time that the compressive unloading wave reaches the specimen (see the wave propagation diagram of Fig. 5). As a consequence, the specimen/output-bar interface will then separate while the specimen is still under shear. This configuration can be attained either by moving

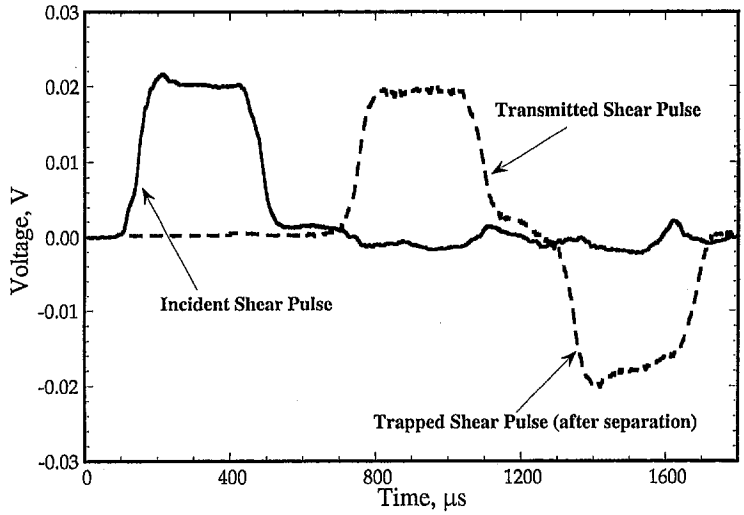

Fig. 4 Shear signals for an elastic test. Note that the entire incident shear pulse is transmitted and gets trapped in the output bar. This shows that the adhesive can sustain in shear and compression but fails in tension.

Downloaded 04 May 2010 to 171.66.16.27. Redistribution subject to ASME license or copyright; see http://www.asme.org/terms/Terms_Use.cfm

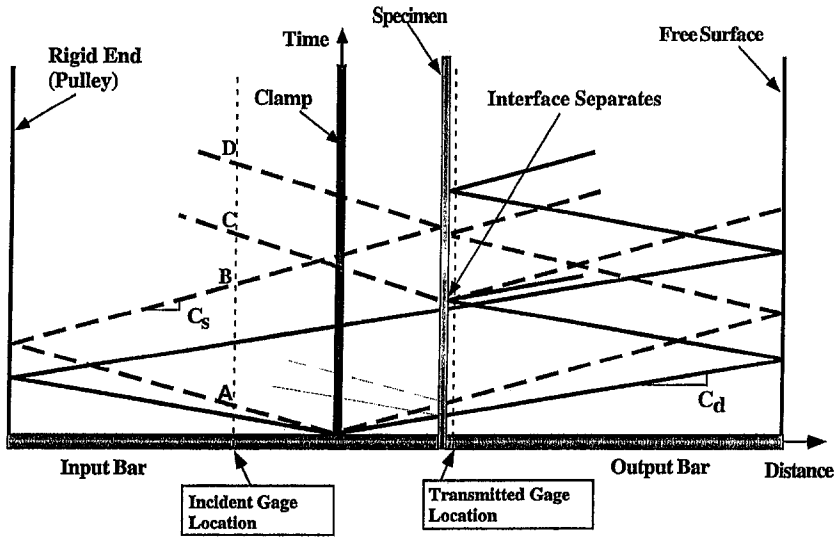

Fig. 5 Wave propagation diagram to study the effect of normal stress on the shear localization behavior of the material. The interface separates while the specimen is still under torsion. Note that the specimen is under pressure during the entire shear loading pulse.

the clamp towards the specimen (thus increasing the pulse duration) and/or adjusting the length of the output bar. Fig. 5 shows the wave propagation in the compression-torsion Kolsky bar using an increased clamped length. The torsional signals shown in Fig. 6 are developed during an elastic test with this clamped length (elastic in that there is no specimen, and the input and output bars are joined together with a thin layer of the epoxy adhesive), with strain gages located as shown in Fig. 5. The incident torsional and axial gages are located 1.381 m and 1.454 m from the specimen, respectively, and the transmitted torsional and axial gages are both located 0.089 m from the specimen. The solid line in Fig. 6 represents the torsional signal from the strain gage on the incident bar, with wave arrivals A, B, C, D, and E shown also on Fig. 5. The signal begins at zero volts because the strain gage is AC-coupled into the oscilloscope, so that the DC component corresponding to the stored torque is filtered out. Wavefront A represents the torsional unloading wave that propagates into the pre-torqued region when the clamp is released; wavefront B represents the continued unloading that results from a reflection from the rigid end condition of the pulley. Wavefront C represents the unloading signal that arises from the separation of the bars by the tensile pulse, and wavefront D is the reflected unloading wave as shown. The transmitted torsional pulse has been cut short by the separation, as shown in Fig. 5, with the true duration of the incident pulse being the sum of the durations of the transmitted pulse and the reflected pulse CD. Wavefronts E and F show the trapped shear pulse as a result of the separation (this pulse causes only rigid rotations of the specimen) and thus the utility of the compression-torsion configuration of Fig. 5 has been demonstrated.

Application to Shear Localization

This section describes the application of the recovery technique developed above to the investigation of adiabatic shear localization within materials (specifically, within commercially

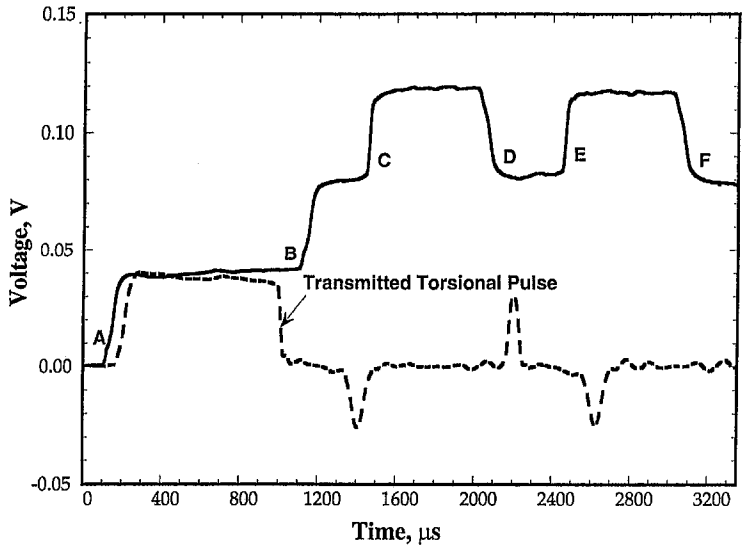

Fig. 6 Shear signals for an elastic test. Note that the amplitude of the transmitted signal is same as that of the incident shear signal. Further as the interface separates during the shear loading pulse, part of it is reflected back into the input bar (wave front CD).

Downloaded 04 May 2010 to 171.66.16.27. Redistribution subject to ASME license or copyright; see http://www.asme.org/terms/Terms_Use.cfm

Table 1 Chemical composition of alpha-titanium

C	Fe	N	O	H	Ti
0.041	0.07	0.008	0.12	0.0013	Bal.

pure titanium). The intent is to understand the initiation, development, and propagation of adiabatic shear bands with specific reference to microscopic mechanisms and microstructural influences. The entire research effort on adiabatic shear bands in titanium is too large to describe within this paper, which focuses on the technique alone; the overall results on the shear band problem are presented in another paper that is currently under preparation (Chichili, Hemker, and Ramesh, 1997b). In the following we focus on a brief description of those results that can be clearly tied to the new experimental technique.

Materials Issues. The material investigated is a commercially pure alpha titanium (grade-2) obtained from President Titanium, Inc. The material had been annealed at 705°C for two hours and then air cooled, and the resulting microstructure consisted of equiaxed grains with an average grain size of 35 μm. The chemical composition of the material (evaluated after heat treatment) is given in Table 1 (the interstitial content is a critical strengthening factor in titanium). Table 2 lists nominal values for the mechanical properties of the material in the as-received condition. The rate-dependent mechanical behavior of this material has been systematically characterized over a wide strain rate range of 10^{-5} to 10^{+5} s^{-1} using a combination of quasistatic and dynamic testing techniques in a previous work (Chichili, Ramesh, and Hemker, 1998a). Both the flow stress and the degree of strain hardening of the material increase with increasing strain rate, while the flow stress decreases with increasing temperature. The response of this alpha-titanium to high-rate shearing within the conventional torsional Kolsky bar experiment is presented in Fig. 7 for a shear strain rate of 1.3×10^3 s^{-1}. The deformations in this experiment were homogeneous until a shear strain of about 0.6, when an adiabatic shear band was formed that eventually caused complete failure of the thin-walled tube specimen. Information at smaller strains from such tests is used together with dynamic compressive and tensile Kolsky bar data and very high strain rate pressure-shear plate impact results to develop a constitutive function that represents the material behavior over a wide range of strain rates. Combined with independent data on the temperature-dependence of the flow stress, this information allows us to perform computational simulations of the development of adiabatic shear localization in this material.

Design of Recovery Experiments in Adiabatic Shear Localization. The specimens used for recovery experiments in adiabatic shear localization are circumferentially notched thick-walled cylinders (Fig. 8) with flanges for attachment to the bars. The notch provides a known strong geometric defect and thus defines the location where a shear band is likely to initiate. The shear band then propagates radially inward, with a decreasing driving force; one reason for the substantial wall thickness of the specimen is the interest in examining the shear band tip as it propagates inwards. The thick-walled cylinder geometry is also required because otherwise the applied compressive load could cause buckling.

However, a consequence of the thick-walled geometry is that the stresses in the specimen are not uniform (whereas they are uniform for the classic thin-walled cylinder specimen). Thus we cannot use Eqs. (1) and (2) to obtain the shear rate and shear stress histories in the specimen from the reflected and transmitted pulses. However, the fact that the input and output bars remain elastic allows us to obtain the boundary conditions on the specimen from the torsional pulses in the bars (a process greatly assisted by the fact that there is no dispersion in the propagation of torsional waves in elastic bars in the first torsional mode). The angular velocities ω_1, ω_2 of the specimen/input-bar and specimen/output-bar boundaries, respectively, can be computed from

$$\omega_1 = \frac{T_I - T_R}{J\rho c_S} \tag{3}$$

$$\omega_2 = \frac{T_T}{J\rho c_S} \tag{4}$$

where J is the bar polar moment of inertia (the input and output bars are assumed to be similar); ρ is the density of the bars; and the incident, reflected, and transmitted torques have magnitudes T_I, T_R, and T_T, respectively. The normal tractions applied to the specimen/bar interfaces can be computed directly from the measured longitudinal strains in the elastic bars. The corresponding initial boundary value problem for the specimen with known angular velocities and normal tractions at the specimen/bar interfaces can be solved numerically to obtain the stress, strain, and temperature distributions within the specimen (since the material properties are already known with sufficient accuracy). Of course, once an adiabatic shear band is developed within the specimen, the quality of the numerical simulation depends critically on our knowledge of material behavior under the extreme conditions that exist within the band, and on the ability of the numerical procedure to capture such severely localized deformations. Computational results of such simulations using ABAQUS/Explicit will also be presented in a forthcoming paper (Chichili, Ramesh, and Hemker, 1998b).

Elastic experiments were first performed with a solid titanium cylinder (of the same diameter as the bar and 25.4 mm in length) attached between the input and output bars with the epoxy adhesive. Such experiments were necessary to ensure that the epoxy bond could hold the aluminum-titanium interface in shear but fail in tension, and were completely successful.

Compression and torsion signals obtained during a compression-torsion Kolsky bar test using the thick-walled specimen itself are shown in Figs. 9 and 10, respectively. It is clear from Fig. 9 that the entire incident pulse is transmitted through the specimen to the output bar, indicating that the compressive stresses have completely equilibrated across the specimen. The figure also shows that separation occurs as a result of the transmitted pulse reflecting off the free end of the output bar as a tensile pulse, with separation occurring as shown in Fig. 5. Note that the amplitude of the transmitted compression pulse is all that is of interest in characterizing the compressive loading, and so the not-quite-rigid end condition on the pulley side of the input bar does not effect the result. The numerical simulation of the dynamic compressive loading of the notched thick-walled specimen shows that the hydrostatic stress at the notch root corresponds to about 1 GPa. A thin-walled cylindrical specimen would buckle under the corresponding incident compressive load. The torsional signals in Fig. 10 show that a substantial portion of the incident torsion pulse is reflected into the input bar, because of the plastic deformation of the specimen under the torsional load. The fact that the torsional pulses have been trapped in the input and output bars as a result of the tensile separation is clearly evident in the signals shown. All of these further pulses in the bar then result in only rigid motions of the specimen, and thus a true recovery test of the thick-walled cylinder has been achieved.

Table 2 Mechanical properties of alpha-titanium (as provided by the manufacturer)

Yield stress, MPa	Tensile Stress, MPa	Elongation, %
337	506	25

Downloaded 04 May 2010 to 171.66.16.27. Redistribution subject to ASME license or copyright; see http://www.asme.org/terms/Terms_Use.cfm

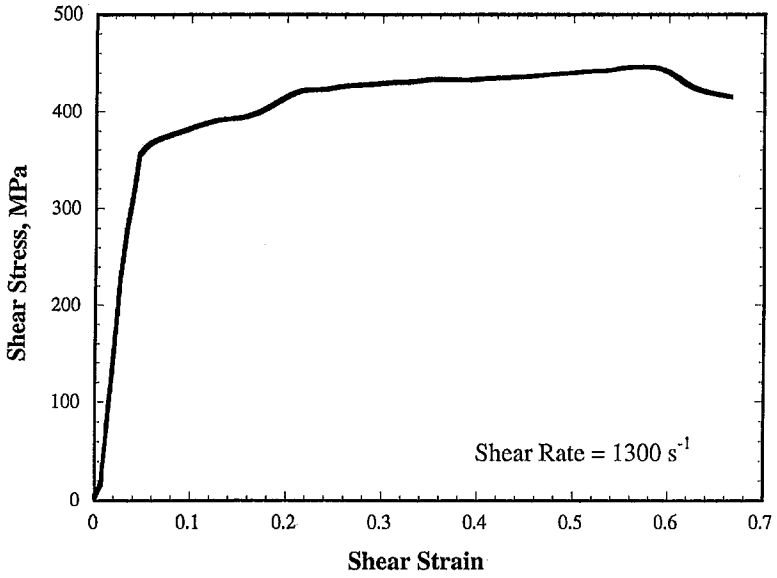

Fig. 7 A shear stress-shear strain curve obtained on the alpha-titanium during a classical torsional Kolsky bar test with a thin-walled tube specimen at a shear rate of 1.3 × 10^3 s^{-1}. Failure of the specimen by adiabatic shear localization occurs at a shear strain of nearly 0.6.

Results of Adiabatic Shear Localization Recovery Experiments. The value of the recovery approach can be clearly identified by comparing (Fig. 11) the final state of (*a*) a specimen obtained from the conventional torsional Kolsky bar test a la Duffy (a thin-walled tubular specimen), (*b*) a thick-walled specimen from a torsional Kolsky bar without the recovery mode, and (*c*) a thick-walled specimen from the recovery mode described here in the compression-torsion Kolsky bar. Adiabatic shear bands are developed in the specimen in all three cases. In the Duffy-type test the through-thickness shear band immediately causes catastrophic failure of the specimen (Fig. 11(*a*)) during the initial loading pulse, with the fracture surfaces then rubbed against each other during repeated torsional loading. As a consequence, it is extremely difficult to determine the mechanisms that are developed during the shear banding by post-mortem microstructural examination of the specimen. Thick-walled specimens tested within a conventional torsional Kolsky bar (case (*b*)) develop a shear band as well, but are driven to complete fracture (Fig. 11(*b*)) by repeated reloadings from the reflected and transmitted pulses. The fracture usually develops in an asymmetric mode, and may be accompanied by substantial bending during the later reloadings. Again, it is impossible to relate the mechanisms that can be observed in the specimen, post-mortem, to the character of any particular one of the multiple loadings that are sustained. However, specimens recovered from the recovery experiment described here

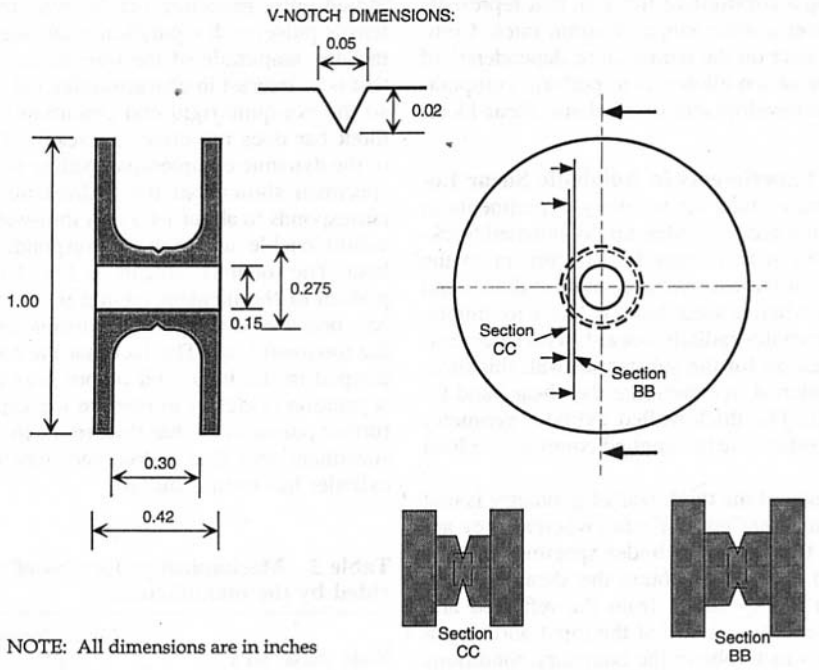

Fig. 8 The specimen geometry used in the compression-torsion Kolsky bar. Also shown are schematics of the sections cut from the specimen for optical microscopy.

Downloaded 04 May 2010 to 171.66.16.27. Redistribution subject to ASME license or copyright; see http://www.asme.org/terms/Terms_Use.cfm

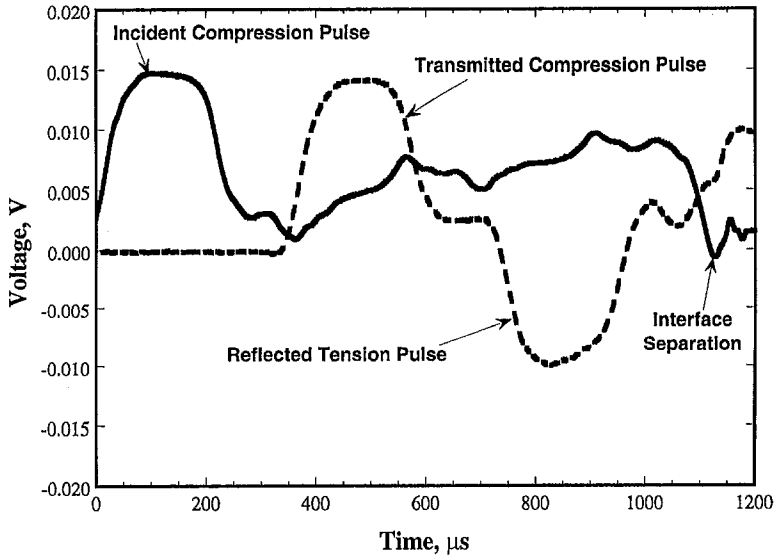

Fig. 9 Compression signals in the compression-torsion Kolsky bar with the specimen attached between the input and output bars. The reflected tension pulse causes the separation of the interface just after the incident shear wave has unloaded at the specimen.

develop a shear band, and are recovered intact (Fig. 11(*c*)) after a single torsional loading. Post-mortem microstructural examination can now be used to determine the mechanisms active during the shearing, and the extent of the microstructural change can be quantitatively related to the applied dynamic loading.

The recovered specimens are sectioned to examine the propagation of the shear band and the associated microstructural mechanisms. While a much more detailed description of the microstructural features are presented in a forthcoming paper, we present here examples of what is observed through a particular sectioning regimen and associated optical microscopy (Fig. 8 also shows the specific sections of the recovered specimen that are presented in this paper). All of the sections are made with a low-speed diamond saw along planes parallel to the specimen axis but at varying distances from the specimen axis towards the outer surface of the specimen. Since these (e.g., sections BB and CC in Fig. 8) are plane sections taken within an axisymmetric problem, the true radius actually varies across the specimen, being equal to the notch root radius at the notches and having a minimum in the center of the section. This is very important to recognize because of the inhomogeneous stress state in the thick-walled specimen (thus the shear stress and the pressure both vary along the sections). Note that the strain and temperature distributions will also vary with radius due to the inhomogeneous stress distributions within the thick-walled cylinder.

Each section from the recovered specimens is polished and etched in a solution of 5 percent HF, 20 percent HNO_3, and 75 percent H_2O for optical microscopy. Figures 12(*a*) and 12(*b*) show optical micrographs of sections CC and BB of a specimen that has developed an adiabatic shear band during an experiment

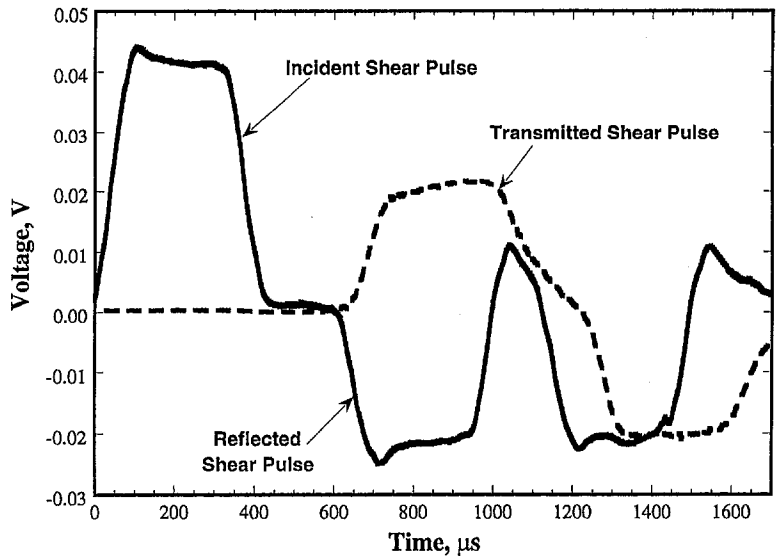

Fig. 10 Shear signals with the specimen attached between the bars. Note that the transmitted shear signal is trapped in the output bar as the specimen-output bar interface is separated before the signal reflects back from the free surface of the output bar and reaches the specimen.

Downloaded 04 May 2010 to 171.66.16.27. Redistribution subject to ASME license or copyright; see http://www.asme.org/terms/Terms_Use.cfm

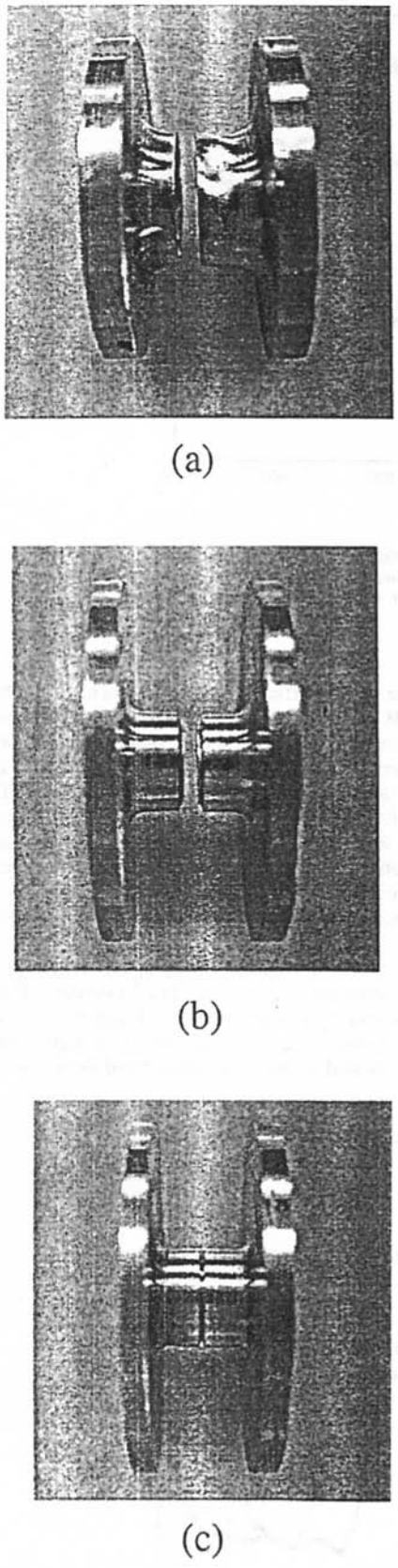

Fig. 11 Photographs of the specimens deformed using different experimental techniques (*a*) thin-walled tubular specimen obtained from the conventional torsional Kolsky bar test, (*b*) a thick-walled specimen from a torsional Kolsky bar without the recovery mode, and (*c*) a thick-walled specimen from the recovery mode described here in the compression-torsion Kolsky bar. The specimens fractured into two pieces under non-recovery mode while the specimen was intact when recovered using the present technique.

using the compression-torsion Kolsky bar in the configuration described in Fig. 2. Each micrograph occupies essentially the boxed areas shown on sections CC and BB in Fig. 8. The left and right ends of the micrograph (Section CC, ~80 μm below the notch root) of Fig. 12(*a*) originate just below the notch tip, and both areas of intense shearing and areas in which a crack has been developed are evident. The grains in the microstructure can be observed to be very heavily sheared as one approaches the band, with the grains near the band elongating and aligning themselves in the shear direction. The cracked regions are aligned along the shearing direction as well; earlier investigators have also noted a predisposition to cracking immediately after the development of a shear band in alpha-titanium (e.g., Culver, 1973). Closer examination of the material on the sides of the crack reveals that the crack has in fact propagated through a region that was heavily sheared prior to the development of the crack. Because of the severity of the defect represented by the notch, the crack is initiated at the notch tip and propagates into the already intensely deformed region. The crack runs radially inwards and terminates inside the specimen because the deformation (and stress) levels decrease as one moves towards the center of the section. This is clearly evident in Fig. 12(*b*), which shows an optical micrograph of section BB for the same specimen (note the larger distance between notch tips because of the greater depth of the section: ~135 μm below the notch root). This cross section still shows the shear band but shows much less separation of the shearing surfaces (cracking). Intermittent failure zones that appear ready to coalesce are also evident in this micrograph.

A closer examination of the literature, and our other results (e.g., with the thin-walled tube specimens), indicates that cracking is always observed in alpha-titanium immediately after shear band development when the deformations are developed in simple shearing without any additional normal stresses. On the other hand, experiments in which substantial superimposed compressive stresses exist show much more evolved shear bands with no cracks (e.g., in ballistic tests). The specimen from which the cross sections of Fig. 12(*a*) and (*b*) were obtained was tested in the configuration of Fig. 2, which resulted in a significant period of time during which the material was subjected to a pure torsional load with no superimposed compressive load before separation of the specimen-output bar interface occurs. It is therefore possible that the cracking developed in Figs. 12(*a*) and (*b*) are a consequence of the purely torsional mode (the process of crack formation involves void nucleation and coalescence, as shown by Chichili, Ramesh, and Hemker, 1998b).

To test this hypothesis, several experiments were performed with the experimental configuration of Fig. 5, where there is always a superimposed compression during the time of the torsional loading pulse (this is one reason why the experimental configuration of Fig. 5 was developed). The results of one such test (torsion with superimposed compression, which translates to a high hydrostatic pressure near the notch root) can be observed in the optical micrograph of Fig. 12(*c*), which shows section CC of the recovered specimen. Unlike in the previous test, the material is observed to undergo shear localization without subsequent fracture. Thus, the applied compressive stresses delay the onset of the fracture process within the shear band. Explicit finite element analysis of the specimen under the dynamic compressive and torsional loads indicates that the magnitude of the hydrostatic pressure at the notch root was approximately 900 MPa for this test. We believe that this is the first time that experimental evidence of normal stress effects on shear band evolution has been obtained with a clearly defined loading condition, and this has become possible as a result of the newly developed recovery technique. This is an extremely important question that must be answered for such diverse problems as armor/anti-armor interactions and machining. The torque to compression ratio has been varied to understand the

Downloaded 04 May 2010 to 171.66.16.27. Redistribution subject to ASME license or copyright; see http://www.asme.org/terms/Terms_Use.cfm

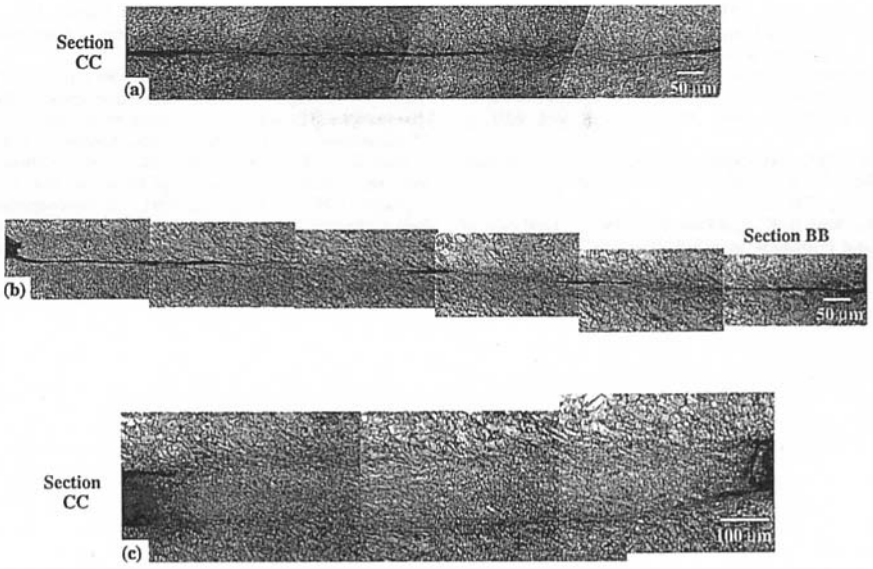

Fig. 12 Optical micrographs of specimens deformed using compression-torsion Kolsky bar. The sections are the boxed areas shown in Fig. 8. Micrographs (*a*) and (*b*) were obtained from a specimen deformed using the configuration described in Fig. 2. Micrograph (*c*) corresponds to Fig. 5, with a pressure that is superimposed for the entire duration of the shear loading pulse; it is clear that the pressure prevents the onset of the void-driven failure process within the shear band.

failure phenomenon that follows the shear localization, and to understand the influence of pressure in a quantitative manner. A complete description of the microstructural evolution within the shear band and the effect of pressure on the shear localization, coupled with numerical modeling to obtain accurate stress, strain, and temperature distributions, is reported elsewhere (Chichili, Ramesh, and Hemker, 1998b).

Thus, the compression-torsion Kolsky bar technique can be used to recover notched thick-walled specimens subjected to known torsion and compression pulses of controlled amplitude and duration. Removal of the specimen allows the examination of the following fundamental issues in adiabatic shear localization:

- A systematic study of the deformation microstructure within the shear band by recovering samples deformed to various controlled shears. The character and evolution of microstructure within the shear bands and the micromechanisms that lead to and promote the formation of adiabatic shear bands can be investigated.
- The influence of the shape and size of geometric defects (e.g., notch tip radius and notch depth). Thin-walled tube experiments using the conventional torsional Kolsky bar (e.g., by Marchand and Duffy, 1988) have demonstrated a strong sensitivity to the variations in wall thickness, which appear to act as initiating defects. Hence, by introducing a known geometric defect such as a notch, this technique can be used to study "defect sensitivities."
- Shear band energetics. By allowing the specimen to be subjected to increasing amounts of energy in the torsional pulse before separation, we are able to recover specimens in which shear bands have grown to varying lengths because of the varying amounts of energy available for band evolution.
- The specimen can be subjected to increasing amplitudes of the compressive pulse (and therefore increasing hydrostatic pressures at the notch tip). A comparison of a low normal stress recovery test with a high normal stress recovery test, both of which have the same amount of torsional energy, will show the influence of pressure on the shear localization.

Conclusions

A recovery technique based on the compression-torsion Kolsky bar has been developed for investigation of the deformation mechanisms that are active during dynamic shear loadings. As an example of the utility of this recovery technique, its application to the study of microscopic mechanisms within adiabatic shear localization in alpha-titanium is presented. The technique allows a systematic study of the microscopic mechanisms that drive the initiation and growth of adiabatic shear bands by recovering samples within which shear bands have been grown under controlled conditions; further characterization through sectioning, followed by optical, scanning, and transmission electron microscopy is then possible. The technique also allows one to study the influence of the shape and size of geometric defects (for example notch tip radius and notch depth) on the initiation of adiabatic shearing failures. Finally, and perhaps most significantly, the effect of normal stresses on the susceptibility of a material to shear localization can also be investigated.

Acknowledgments

The authors would like to acknowledge the support of the National Science Foundation's Mechanics and Materials Program through Grant No. CMS-9402618, and of the U.S. Army Research Office through Grant Nos. DAAH04-95-1-0417 and DAAH04-95-1-0272. The authors are pleased to acknowledge helpful discussions with Dr. T. W. Wright of the Army Research Laboratory and Prof. K. J. Hemker of Johns Hopkins.

References

Bai, Y., Xue, Q., Xu, Y., and Shen, L., 1994, "Characteristics and Microstructure in the Evolution of Shear Localization in Ti-6Al-4V alloy," *Mechanics of Materials,* Vol. 17, pp. 155–164.

Chichili, D. R., and Ramesh, K. T., 1995, "Dynamic Failure Mechanisms in a 6061-T6 Al/Al_2O_3 Metal-Matrix Composite," *International Journal of Solids and Structures,* Vol. 32, pp. 2609–2626.

Chichili, D. R., Ramesh, K. T., and Hemker, K. J., 1998a, "The High-Strain-Rate Response of Alpha-Titanium: Experiments, Deformation Mechanisms and Modeling," *Acta Materialia,* Vol. 46, pp. 1025–1043.

Chichili, D. R., Ramesh, K. T., and Hemker, K. J., 1998b, "Adiabatic Shear Localization in Alpha-Titanium: Experiments, Microstructural Evolution and Modeling," manuscript in preparation.

Couque, H., and Lankford, J., 1989, "Quasi-elastic versus Dynamic Fracture properties of Ceramic Fiber Reinforced Materials," *Inst. Phys. Conf. Series,* Vol. 102, p. 433.

Culver, R. S., 1973, "Thermal Instability in Dynamic Plastic Deformation," *Metallurgical Effects at High Strain Rates,* R. W. Rohde et al., eds., Plenum Press, New York, pp. 519–530.

Downloaded 04 May 2010 to 171.66.16.27. Redistribution subject to ASME license or copyright; see http://www.asme.org/terms/Terms_Use.cfm

da Silva, M., and Ramesh, K. T., 1997, "The Rate Dependent Deformations of Porous Iron," *International Journal of Plasticity,* Vol. 13, p. 587.

Hartley, K. A., Duffy, J., and Hawley, R. H., 1985, "The Torsional Kolsky Bar," *Metals Handbook,* American Society of Metals, Vol. 8, p. 218.

Kolsky, H., 1949, "An Investigation of the Mechanical Properties of Materials at Very High Rates of Loading," *Proc. Phys. Society,* Vol. 62B, p. 676.

Marchand, A., and Duffy, J., 1988, "An Experimental Study of the Formation Process of Adiabatic Shear Bands in a Structural Steel," *Journal of Mechanics and Physics of Solids,* Vol. 36, pp. 251–283.

Meyers, M. A., Subhash, G., Kad, B. K., and Prasad, L., 1994, "Evolution of Microstructure and Shear Band Formation in α-hcp Titanium," *Mechanics of Materials,* Vol. 17, pp. 175–193.

Nemat-Nasser, S., Isaacs, J. B., and Starrett, J. E., 1991, "Hopkinson Techniques for Dynamic Recovery Experiments," *Proc. Royal Society of London,* Vol. A20, pp. 371–391.

Pelletier, P., Worswick, M. J., and Weickert, C. A., 1995, "Tensile split-Hopkinson bar testing of different Armco iron stocks," *Metallurgical and Materials Applications of Shock-Wave and High-Strain-Rate Phenomena,* L. E. Murr, K. P. Staudhammer and M. A. Meyers, eds., Elsevier, Amsterdam, pp. 429–436.

Ramesh, K. T., 1994, "On the Localization of Shearing Deformations in Tungsten Heavy Alloys," *Mechanics of Materials,* Vol. 17, pp. 165–173.

Staab, G. H., and Gilat, A., 1991, "A direct-tension split Hopkinson bar for high strain-rate testing," *Experimental Mechanics,* Vol. 31, pp. 232–235.

Zener, C., and Hollomon, J. H., 1944, "Effect of Strain-Rate upon Plastic Flow in Steel," *Journal of Applied Physics,* Vol. 15, p. 22.

Downloaded 04 May 2010 to 171.66.16.27. Redistribution subject to ASME license or copyright; see http://www.asme.org/terms/Terms_Use.cfm

The Influence of a Ductile Interphase on the Overall Elastoplastic Behavior of a Fiber-Reinforced Composite

K. Ding
Graduate Student

G. J. Weng
Professor,
Fellow ASME

Department of Mechanical and Aerospace Engineering,
Rutgers University,
New Brunswick, NJ 08903

While there exist various homogenization theories for the plasticity of a fiber-reinforced composite, no such theories have been explicitly developed to account for the influence of a ductile interphase. In this paper a simple scheme is developed for such a purpose. The theory evolved out of the work of Qiu and Weng (1992) and Hu (1996), and bears an identical structure to Ponte Castañeda's (1991) variational procedure and Suquet's (1995, 1996) modified secant moduli approach. An exact solution under the plane-strain biaxial loading is also developed to assess the accuracy of the theory. It is found that, with either a soft or a hard interphase and with or without work-hardening, the homogenization theory can produce sufficiently accurate results under this condition. The theory is then used to examine the influence of the interphase volume concentration on the anisotropic behavior of the composite under axial tension, transverse tension, axial shear, and transverse shear, with both a soft and a hard interphase. The results indicate that, while the axial tensile behavior is not sensitive to the interphase concentration, the behaviors under other types of loading are greatly affected by its presence, especially when the interphase is softer than the matrix.

1 Introduction

The strength of a unidirectional fiber-reinforced composite can be greatly affected by the presence of an interphase. An interphase may develop due to chemical reaction between the fiber and the matrix, and it can also be purposefully introduced to tailor the property of the composite. In the latter case the system also belongs to the broad class of the emerging functionally graded composites (FGCs). Unlike the traditional two-phase composite, a graded composite involves spatially varying property of the material. A more commonly studied FGC has a microstructure in which the volume concentration or shape of inclusions or fibers continues to vary as a function of position (e.g., Zuiker and Dvorak, 1994a, b, and Reiter et al. 1997). Another type of FGCs involves a position-dependent matrix property. In this case Lutz and Ferrari (1993) and Lutz and Zimmerman (1996) have considered a radially dependent elastic property of a sphere and of the matrix in a particle-reinforced composite, respectively, and Mikata (1994) has analyzed the case of a fiber-reinforced system, all dealing with the symmetric loading. These recent studies have shed some new light on the behavior of this new class of materials. All of these investigations, however, are directed toward the elastic behavior of an FGC.

A fiber composite with an interphase has its distinctive value in itself, and it can also be cast in the light of the second type of FGCs with a simple step-function variation in the matrix property. While in the elastic context such a problem is not difficult to evaluate and, in fact, has been evaluated by Qiu and Weng (1991), it has never been addressed from the standpoint of an elastoplastic problem. As this is the simplest kind of FGCs, its development is likely to pave a way for the future development of a plasticity theory with a more general variation. In this study the matrix and interphase can be ideally plastic, or capable of work-hardening, and the yield stress and work-hardening strength of the interphase can be either softer or harder than the matrix. Unlike the first class of FGCs, there is a well-defined representative volume element here and one can use the composite cylinder assemblage (Hashin and Rosen, 1964) or the generalized self-consistent model (GSC, Christensen and Lo, 1979) to represent its microgeometry. Our goal here is to develop a simple homogenization scheme to examine the influence of a ductile interphase on the nonlinear behavior of the fiber-reinforced system.

The homogenization method to be presented is built upon a direct secant-moduli approach successively developed in Tandon and Weng (1988), Weng (1990), Qiu and Weng (1992, 1995), and Hu (1996). While all of these dealt with an ordinary two-phase composite, the concept of secant moduli, energy-based effective stress, and field-fluctuation method introduced there will serve as the basis for the present development. Different approaches based on the nonlinear variational principles have also been developed by Talbot and Willis (1985), Ponte Castañeda (1991, 1992), and Willis (1991, 1992), and applied to examine the plasticity of the traditional two-phase fiber-reinforced composites (Talbot and Willis, 1992; deBotton and Ponte Castañeda, 1993). Hu (1996) has proved that, when the distortional energy-based effective stress (Qiu and Weng, 1992) is evaluated by a field-fluctuation method, the direct secant-moduli approach actually coincides with Ponte Castañeda's result. This relation was first noted by Qiu and Weng (1992, 1995) with an incompressible matrix, but it was Hu who gave it a general proof regardless of the compressibility of the ductile matrix. In a separate development Suquet (1995, 1996) has used the con-

Contributed by the Applied Mechanics Division of THE AMERICAN SOCIETY OF MECHANICAL ENGINEERS for publication in the ASME JOURNAL OF APPLIED MECHANICS.

Discussion on the paper should be addressed to the Technical Editor, Professor Lewis T. Wheeler, Department of Mechanical Engineering, University of Houston, Houston, TX 77204-4792, and will be accepted until four months after final publication of the paper itself in the ASME JOURNAL OF APPLIED MECHANICS.

Manuscript received by the ASME Applied Mechanics Division, Jan. 13, 1998; final revision, July 14, 1998. Associate Technical Editor: I. M. Daniel.

 Copyright © 1999 by ASME

Downloaded 04 May 2010 to 171.66.16.27. Redistribution subject to ASME license or copyright; see http://www.asme.org/terms/Terms_Use.cfm

cept of the "second moment" of the strain and stress fields to formulate a so-called "modified secant-moduli" method, and further proved that such a formulation is exactly identical to Ponte Castañeda's variational procedure. As the concept of "second moment" is identical to Qiu and Weng's energy-based definition and Suquet's evaluation of this quantity is also identical to Hu's approach, it has become clear that the direct secant-moduli approach with the energy-based effective stress and Hu's field-fluctuation method will yield results which can also be obtained from Ponte Castañeda's variational procedure and Suquet's modified secant-moduli approach. Other micromechanical theories have also been developed by Dvorak and Bahei-El-Din (1987) and Sun and Chen (1991) from different perspectives, and an incremental version was in fact long formulated by Hill (1964). These theories do not have direct connections with the present development but they represent some interesting approaches to the plasticity of the traditional two-phase fiber composites.

The direct secant-moduli approach and the theories of Ponte Castañeda and Suquet all made use of a linear comparison composite. Based on this approach Ding and Weng (1998) have recently studied the plasticity of a particle-reinforced system with a ductile interphase. The present work is a sequel to this one and, together, they bring the interphase issue on the overall elastoplastic behavior of these two basic composites to a completion. In the following the transverse shear modulus of the elastic comparison composite will be derived from the GSC, and its transverse Young's modulus calculated from the transversely isotropic relation. The other four effective moduli will be taken directly from the exact solutions of Qiu and Weng (1991). Using these results as the starting point, the theoretical development to be unfolded will follow the work of Qiu and Weng (1992) and Hu (1996). With this same starting point, it can also be derived from Castañeda's procedure or Suquet's theory, as stated above. An exact solution will also be developed to assess the accuracy of the developed homogenization theory.

2 Constitutive Equations of the Ductile Phases

In the three-phase fiber-reinforced composite, the fiber will be referred to as phase 1, the interphase as phase 2, and the matrix as phase 3. The volume concentration of the rth phase will be denoted by c_r. The elastoplastic properties of all constituent phases will be taken to be isotropic, with the bulk and shear moduli denoted by κ_r and μ_r, respectively. The plastic stress-strain relations of the ductile phases will be represented by the modified Ludwik equation as

$$\sigma_e^{(r)} = \sigma_y^{(r)} + h_r \cdot (\epsilon_e^{p(r)})^{n_r}, \quad r = 2, 3 \tag{1}$$

where $\sigma_y^{(r)}$, h_r, and n_r ($0 \le n_r \le 1$) are the tensile yield stress, strength coefficient, and work-hardening exponent, in turn. As usual the effective stress and plastic strain are defined as

$$\sigma_e^{(r)} = [\tfrac{3}{2}\sigma_{ij}'^{(r)}\sigma_{ij}'^{(r)}]^{1/2}, \quad \epsilon_e^{p(r)} = [\tfrac{2}{3}\epsilon_{ij}^{p(r)}\epsilon_{ij}^{p(r)}]^{1/2}, \tag{2}$$

in terms of its deviatoric stress $\sigma_{ij}'^{(r)}$ and plastic strain $\epsilon_{ij}^{p(r)}$.

As the method to be unfolded makes use of a linear comparison composite whose constituent phases will possess an elastic property equal to the secant moduli of the nonlinear phase, it is useful to introduce the secant Young's modulus of the rth

$$E_r^s = \frac{\sigma_e^{(r)}}{\dfrac{\sigma_e^{(r)}}{E_r} + \left(\dfrac{\sigma_e^{(r)} - \sigma_y^{(r)}}{h_r}\right)^{1/n_r}}, \tag{3}$$

at a given σ_e, where E_r is the ordinary Young's modulus. With a linear hardening ($n_r = 1$) it is convenient to use the tangent modulus E_r^p of the bilinear stress-strain curve, with

$$\frac{1}{E_r^p} = \frac{1}{E_r} + \frac{1}{h_r}. \tag{4}$$

The secant shear modulus, secant Poisson's ratio, and plane-strain bulk modulus follow as

$$\mu_r^s = \frac{E_r^s}{2(1+\nu_r^s)}, \quad \nu_r^s = \frac{1}{2} - \left(\frac{1}{2} - \nu_r\right)\frac{E_r^s}{E_r},$$

$$k_r^s = \kappa_r + \frac{1}{3}\mu_r^s, \tag{5}$$

from the isotropic relations and plastic incompressibility. These secant moduli reduce to their elastic counterparts whenever the superscript s is deleted; conversely with the addition of the superscript s the elastic moduli would translate into their "secant" moduli. It is to be reminded that, throughout the paper, the Roman k_r represents the plane-strain bulk modulus whereas the Greek κ_r represents the ordinary three-dimensional bulk modulus.

3 Effective Elastic Moduli of the Linear Comparison Composite

The composite as a whole is taken to be transversely isotropic, with the fiber direction serving as direction 1 and plane 2-3 isotropic. To pave the way for the development of the nonlinear theory using the linear results, we shall first use the generalized self-consistent scheme to find the linear overall elastic properties of the composite. In this light the volume concentration c_r is related to the outer radius of the rth phase a_r as

$$c_1 = (a_1/a_3)^2, \; c_2 = (a_2^2 - a_1^2)/a_3^2, \; c_3 = 1 - (c_1 + c_2). \tag{6}$$

In fact the results are identical to those derived from the composite cylinder assemblage for the plane-strain bulk modulus κ_{23}, axial shear modulus μ_{12}, longitudinal Young's modulus E_{11}, and major Poisson's ratio ν_{12}. So the first four properties can be quoted directly from the exact solutions of Qiu and Weng (1991), and the result for μ_{23} can be derived using the GSC.

The overall moduli tensor L and compliance tensor M of the composite, following Walpole's (1969) notations, can be written as

$$L = (2\kappa_{23}, C_{12}, C_{11}, 2\mu_{23}, 2\mu_{12}),$$
$$M = (C_{11}/2\kappa_{23}E_{11}, -\nu_{12}/E_{11}, 1/E_{11}, 1/2\mu_{23}, 1/2\mu_{12}), \tag{7}$$

where C_{11} ($=E_{11} + 4\nu_{12}^2\kappa_{23}$) and C_{12} ($=2\nu_{12}\kappa_{23}$) are the usual elastic constants in the contracted notations. Now we recall κ_{23}, μ_{12}, E_{11}, and ν_{12}, from Qiu and Weng (1991)

$$\kappa_{23} = k_3 + (k_3 + \mu_3)[c_1(k_2 + \mu_2)(k_1 - k_3) + c_2(k_1 + \mu_2)(k_2 - k_3)/\{(k_1 + \mu_2)[(k_2 + \mu_3) + (c_1 + c_2)(k_3 - k_2)] + c_1(k_2 - k_1)[(\mu_3 - \mu_2)/(c_1 + c_2) + (k_3 + \mu_2)]\},$$

$$\mu_{12} = \mu_3 + 2\mu_3[2c_1\mu_2(\mu_1 - \mu_3) + c_2(\mu_1 + \mu_2)(\mu_2 - \mu_3)]/\{(\mu_1 + \mu_2)[(\mu_2 + \mu_3) + (c_1 + c_2)(\mu_3 - \mu_2)] + c_1(\mu_2 - \mu_1)[(\mu_3 - \mu_2)/(c_1 + c_2) + (\mu_3 + \mu_2)]\},$$

$$E_{11} = c_1E_1 + c_2E_2 + c_3E_3 + P/R,$$

$$\nu_{12} = c_1\nu_1 + c_2\nu_2 + c_3\nu_3 + Q/R,$$

Downloaded 04 May 2010 to 171.66.16.27. Redistribution subject to ASME license or copyright; see http://www.asme.org/terms/Terms_Use.cfm

$$P = 4c_1c_2(\nu_1 - \nu_2)^2\left[\left(\frac{1}{\mu_3} - \frac{1}{\mu_2}\right) + (c_1 + c_2)\left(\frac{1}{k_3} + \frac{1}{\mu_2}\right)\right]$$

$$+ 4c_1c_3(c_1 + c_2)(\nu_1 - \nu_3)^2\left(\frac{1}{k_2} + \frac{1}{\mu_2}\right)$$

$$+ 4c_2c_3(c_1 + c_2)(\nu_2 - \nu_3)^2\left(\frac{1}{k_1} + \frac{1}{\mu_2}\right),$$

$$Q = c_1c_2(\nu_1 - \nu_2)\left(\frac{1}{k_2} - \frac{1}{k_1}\right)\left(\frac{1}{\mu_3} + \frac{c_1 + c_2}{k_3}\right)$$

$$+ c_1c_3(\nu_1 - \nu_3)\left[\frac{c_1 + c_2}{k_3}\left(\frac{1}{k_2} + \frac{1}{\mu_2}\right)\right.$$

$$\left. - \left(\frac{c_1}{k_1\mu_2} + \frac{c_2}{k_2\mu_2} + \frac{c_1 + c_2}{k_1k_2}\right)\right]$$

$$+ c_2c_3(\nu_2 - \nu_3)\left[\frac{c_1 + c_2}{k_3}\left(\frac{1}{k_1} + \frac{1}{\mu_2}\right)\right.$$

$$\left. - \left(\frac{c_1}{k_1\mu_2} + \frac{c_2}{k_2\mu_2} + \frac{c_1 + c_2}{k_1k_2}\right)\right],$$

$$R = \left(\frac{1}{\mu_3} + \frac{c_1 + c_2}{k_3}\right)\left(\frac{c_1 + c_2}{\mu_2} + \frac{c_1}{k_2} + \frac{c_2}{k_1}\right)$$

$$+ c_3\left(\frac{c_1 + c_2}{k_1k_2} + \frac{c_1}{k_1\mu_2} + \frac{c_2}{k_2\mu_2}\right). \quad (8)$$

Based on the GSC, the transverse shear modulus μ_{23} can be found in a similar way as in Christensen and Lo (1979). The procedure is lengthy and is not called for, but the outcome is that, by setting the determinant of the matrix given in Appendix A equal to zero, it will yield a second-order algebraic equation in terms of μ_{23} which can be readily solved. The component $\eta_r = 3 - 4\nu_r$ for the rth phase in this listing. The procedure in arriving at this result is entirely analogous to that of an ordinary two-phase composite.

The transverse Young's modulus is a combination of the above moduli

$$\frac{1}{E_{22}} = \frac{1}{4}\left(\frac{1}{\kappa_{23}} + \frac{1}{\mu_{23}}\right) + \frac{\nu_{12}^2}{E_{11}}. \quad (9)$$

In the next section, these values will be added with a super or a subscript s to reflect the "secant" plastic state of the constituent phases in the determination of the homogenized effective stress by the field-fluctuation method.

4 Determination of the Homogenized Effective Stress of the Interphase and the Matrix

Unlike the effective stress of a homogeneously deformed phase, a certain definition is needed for the effective stress of a heterogeneously deformed ductile phase in a homogenization scheme. Following the equivalence of the distortional energy, the homogenized effective stress $\sigma_e^{(r)}$ of a ductile phase is defined as (Qiu and Weng, 1992)

$$\frac{1}{6\mu_r^s}\sigma_e^{2(r)} = \frac{1}{V_r}\int_{V_r}\frac{1}{4\mu_r^s}\sigma_{ij}'^{(r)}(\mathbf{x})\sigma_{ij}'^{(r)}(\mathbf{x})dV, \quad \text{or}$$

$$\sigma_e^{2(r)} = \langle\sigma_e^{2(r)}(\mathbf{x})\rangle, \quad (10)$$

in terms of the volume average (the angle brackets) of the "second moment" of the position $\mathbf{x}$-dependent deviatoric stress field.

Qiu and Weng (1992, 1995) have invoked the equivalence between the global elastic energy and those of the local constituent ones to evaluate this quantity. However, for the present problem there are two unknowns $\sigma_e^{(2)}$ and $\sigma_e^{(3)}$, and therefore such a single equation is not sufficient. It is now useful to introduce the field-fluctuation method originally developed by Bobeth and Diener (1986) in elasticity and recently extended to plasticity by Suquet (1995, 1996) and Hu (1996). This method also starts out with the total elastic energy equivalence between the homogenized global system and the local constituent phases, as

$$2U_s = \bar{\boldsymbol{\sigma}}M_s\bar{\boldsymbol{\sigma}} = \sum\langle\boldsymbol{\sigma}_rM_r^s\boldsymbol{\sigma}_r\rangle, \quad (11)$$

in symbolic notations, where U_s is the elastic energy of the linear comparison composite corresponding to a certain "secant" state of its constituent phases, and the boldfaced $\bar{\boldsymbol{\sigma}}$ is the stress tensor of the composite. Furthermore, M_r^s is the compliances tensor of the rth phase and the summation Σ is extended to all three phases. The overall compliances tensor M_s is given in Section 3 by adding a superscript s to each modulus. Then a variation in the shear modulus of the rth phase from μ_r^s to $\mu_r^s + \delta\mu_r^s$ will result in a variation for the overall compliance tensor from M_s to $M_s + \delta M_s$ and a stress field from $\boldsymbol{\sigma}_r(x)$ to $\boldsymbol{\sigma}_r(x) + \delta\boldsymbol{\sigma}_r(x)$. Under the same boundary traction giving rise to the same $\bar{\boldsymbol{\sigma}}$, the contribution from the additional stress field $\delta\boldsymbol{\sigma}_r(x)$ on the overall energy is zero because its associated outer traction vanishes. Then by taking a variation with respect to μ_r^s, one finds (Hu, 1996)

$$c_r\langle\boldsymbol{\sigma}_r'\boldsymbol{\sigma}_r'\rangle\delta\left(\frac{1}{2\mu_r^s}\right) = \bar{\boldsymbol{\sigma}}\delta M_s\bar{\boldsymbol{\sigma}}. \quad (12)$$

It follows that

$$\sigma_e^{2(r)} = \frac{3}{2}\langle\boldsymbol{\sigma}_r'\boldsymbol{\sigma}_r'\rangle = \bar{\boldsymbol{\sigma}}\left(\frac{-3\mu_r^{s2}}{c_r}\frac{\delta M_s}{\delta\mu_r^s}\right)\bar{\boldsymbol{\sigma}}. \quad (13)$$

To examine the influence of the ductile interphase on the anisotropy of the stress-strain relations, five separate loadings will be considered. The corresponding homogenized effective stresses for the ductile phase are given by

(i) plane-strain biaxial tension $\bar{\sigma}_{22} = \bar{\sigma}_{33} = \frac{1}{2}\bar{\sigma}_{\alpha\alpha}$

$$\sigma_e^{2(r)} = \frac{3\mu_r^{s2}\bar{\sigma}_{\alpha\alpha}^2}{4c_r\kappa_{23}^{s2}}\frac{\delta\kappa_{23}^s}{\delta\mu_r^s}; \quad (14)$$

(ii) axial tension $\bar{\sigma}_{11}$

$$\sigma_e^{2(r)} = \frac{3\mu_r^{s2}\bar{\sigma}_{11}^2}{c_rE_{11}^{s2}}\frac{\delta E_{11}^s}{\delta\mu_r^s}; \quad (15)$$

(iii) transverse tension $\bar{\sigma}_{22}$

$$\sigma_e^{2(r)} = \frac{3\mu_r^{s2}\bar{\sigma}_{22}^2}{c_rE_{22}^{s2}}\frac{\delta E_{22}^s}{\delta\mu_r^s}; \quad (16)$$

(iv) axial shear $\bar{\sigma}_{12}$

$$\sigma_e^{2(r)} = \frac{3\mu_r^{s2}\bar{\sigma}_{12}^2}{c_r\mu_{12}^{s2}}\frac{\delta\mu_{12}^s}{\delta\mu_r^s}; \quad (17)$$

(v) transverse shear $\bar{\sigma}_{23}$

$$\sigma_e^{2(r)} = \frac{3\mu_r^{s2}\bar{\sigma}_{23}^2}{c_r\mu_{23}^{s2}}\frac{\delta\mu_{23}^s}{\delta\mu_r^s}. \quad (18)$$

We shall make use of these relations in Section 6.

Downloaded 04 May 2010 to 171.66.16.27. Redistribution subject to ASME license or copyright; see http://www.asme.org/terms/Terms_Use.cfm

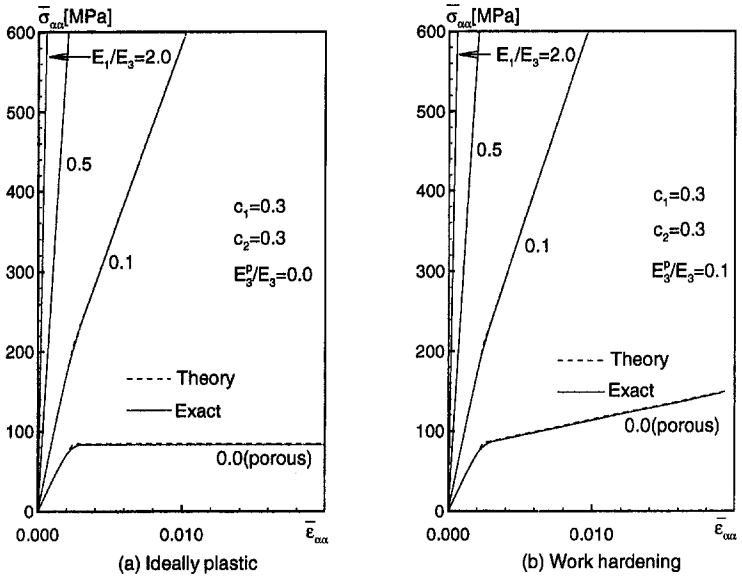

Fig. 1 Comparison between the energy approach and the mean effective stress approach in light of an exact solution with a soft interphase: (*a*) ideally plastic matrix and interphase, and (*b*) linearly work-hardening matrix and interphase

Once the homogenized effective stress $\sigma_e^{(r)}$ of a ductile phase is established in terms of the applied stress $\bar{\boldsymbol{\sigma}}$, the stress-strain curve of the fiber composite can be determined by the following procedure. At a given $\bar{\boldsymbol{\sigma}}$, the objective is to find the corresponding effective moduli L_s or compliances M_s corresponding to certain "secant" state of the interphase and the matrix so that the overall strain $\bar{\boldsymbol{\epsilon}}$ can be found. To this end one may first assume two separate values for μ_2^s and μ_3^s to begin with, and calculate the corresponding effective moduli given in Section 3 and the effective stress $\sigma_e^{(r)}$ from (13). These calculated values are then substituted into (3) to (5) to find the homogenized values of μ_2^s and μ_3^s. If these values are equal—or very close—to the originally assumed values, the answer is found. Otherwise a new set of values reflecting the calculated ones should be taken and the process repeated, until the solution is obtained.

Implicit in this iteration procedure is the assumption that the homogenized effective stress $\sigma_e^{(r)}$ and homogenized secant shear modulus μ_r^s also obey the local constitutive Eqs. (3) to (5). Such an approximation will result in some error, but as shown in the next section, it is not expected to be large.

5 An Exact Solution Under Plane-Strain Biaxial Tension

To place this established homogenization scheme in proper perspective, it is desirable that its accuracy be evaluated first in light of some exact solution. To this end we now carry out an exact elastic-plastic analysis for the three-phase system under a plane-strain biaxial loading. Both ductile phases are taken to exhibit a bilinear stress-strain curve. Care must be exercised

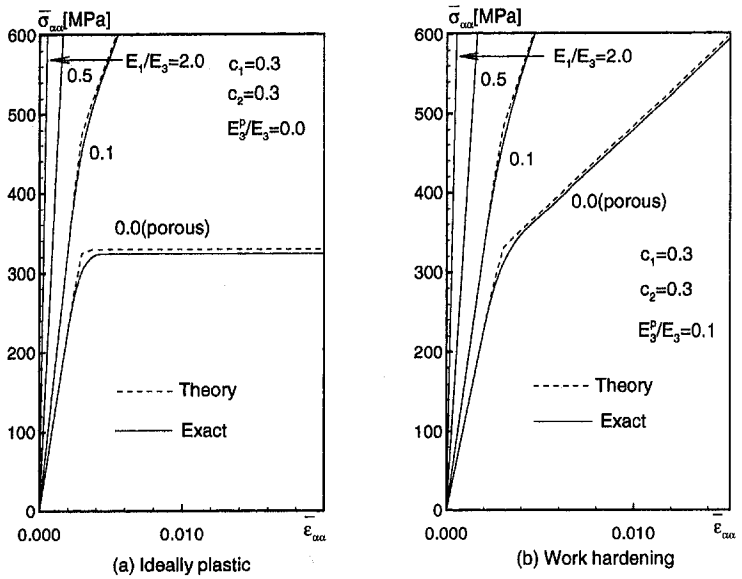

Fig. 2 Comparison between the energy approach and the mean effective stress approach in light of an exact solution with a hard interphase: (*a*) ideally plastic matrix and interphase, and (*b*) linearly work-hardening matrix and interphase

Downloaded 04 May 2010 to 171.66.16.27. Redistribution subject to ASME license or copyright; see http://www.asme.org/terms/Terms_Use.cfm

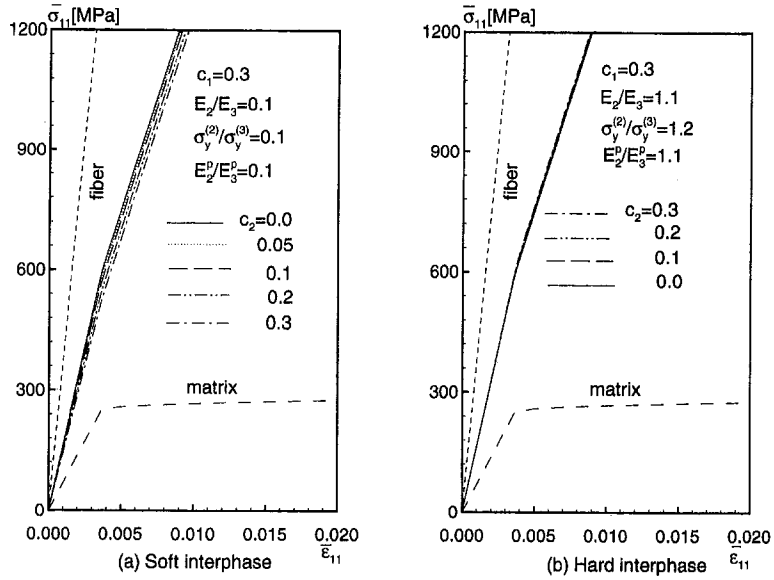

Fig. 3 Influence of the ductile interphase on the axial tensile behavior of a fiber-reinforced composite: (*a*) soft interphase, and (*b*) hard interphase

that, unlike a traditional fiber composite involving only one ductile phase, plastic deformation may ensue from the interface of either phase, and that it may start from a new phase when the elastic/plastic boundary of the already yielded phase is still progressing. The following presentation is meant to be brief, but detailed formulae are given in Appendix B.

To begin with we recall that, in the elastic state, the radial displacement in the fiber, interphase, and the matrix can be written as

$$u_r^{(1)} = A_1 r; \quad u_r^{(i)} = B_1^{(i)} r + B_2^{(i)} \frac{a_2^2}{r}, \quad i = 2, 3 \qquad (19)$$

in a cylindrical coordinate system. The corresponding strain and stress components are

$$\epsilon_{rr}^{(1)} = \epsilon_{\theta\theta}^{(1)} = A_1;$$

$$\epsilon_{rr}^{(i)} = B_1^{(i)} - B_2^{(i)} \frac{a_2^2}{r^2}, \quad \epsilon_{\theta\theta}^{(i)} = B_1^{(i)} + B_2^{(i)} \frac{a_2^2}{r^2}, \quad i = 2, 3 \qquad (20)$$

and

$$\sigma_{rr}^{(1)} = \sigma_{\theta\theta}^{(1)} = 2k_1 A_1, \quad \sigma_{zz}^{(1)} = \nu_1(\sigma_{rr}^{(1)} + \sigma_{\theta\theta}^{(1)});$$

$$\sigma_{rr}^{(i)} = 2k_i B_1^{(i)} - 2\mu_i B_2^{(i)} \frac{a_2^2}{r^2}, \quad \sigma_{\theta\theta}^{(i)} = 2k_i B_1^{(i)} + 2\mu_i B_2^{(i)} \frac{a_2^2}{r^2},$$

$$\sigma_{zz}^{(i)} = \nu_i(\sigma_{rr}^{(i)} + \sigma_{\theta\theta}^{(i)}), \quad i = 2, 3. \qquad (21)$$

The constants A_1, $B_1^{(i)}$, and $B_2^{(i)}$ can be determined from the continuity conditions at the interfaces and the boundary condition; they are given in Appendix B.

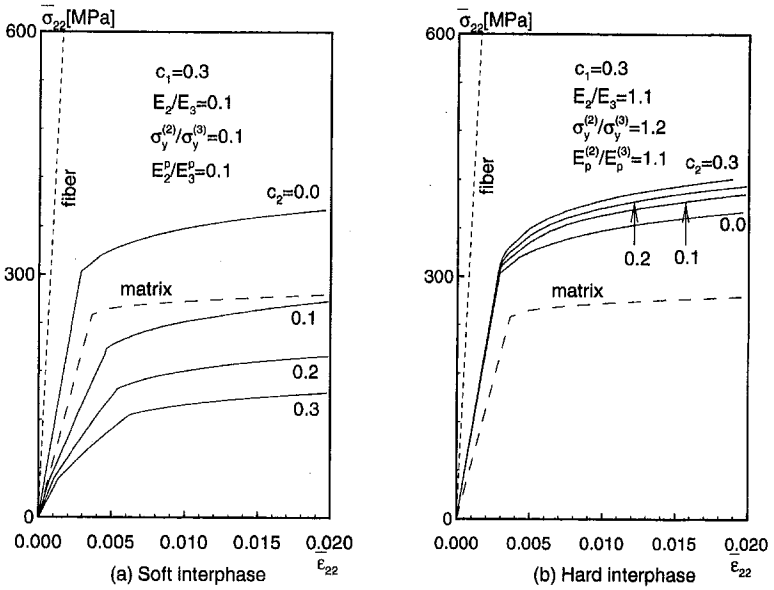

Fig. 4 Influence of the ductile interphase on the transverse tensile behavior of a fiber-reinforced composite: (*a*) soft interphase, and (*b*) hard interphase

Downloaded 04 May 2010 to 171.66.16.27. Redistribution subject to ASME license or copyright; see http://www.asme.org/terms/Terms_Use.cfm

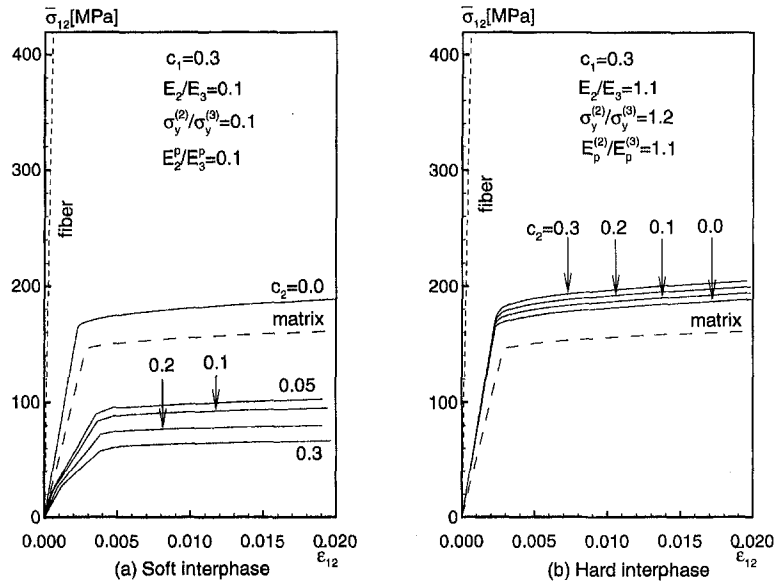

Fig. 5 Influence of the ductile interphase on the axial shear behavior of a fiber-reinforced composite: (*a*) soft interphase, and (*b*) hard interphase

Due to the complexity of the plastic deformation, we shall consider both ductile phases to be elastically incompressible as well. The effective stress is then given by

$$\sigma_e^{(i)} = \frac{\sqrt{3}}{2}(\sigma_{\theta\theta}^{(i)} - \sigma_{rr}^{(i)}). \tag{22}$$

After plastic deformation starts from the interface in one phase, two possibilities may ensue: Plastic zone will spread while the other phase remains elastic or plastic deformation will occur in the other phase soon after. Both phases will eventually become fully plastic. Assuming a linearly work-hardening interphase and matrix, one arrives at the following displacement, radial plastic strain, and stress fields in the plastic zone

$$u_r^{(i)} = -\frac{h_i + E_i}{E_i}\frac{D_i}{r}, \tag{23}$$

$$\epsilon_{rr}^{(i)p} = \frac{D_i}{r^2} + \frac{\sqrt{3}\sigma_y^{(i)}}{2(h_i + E_i)}, \tag{24}$$

$$\sigma_{rr}^{(i)} = \frac{2\sigma_y^{(i)}E_i}{\sqrt{3}(h_i + E_i)}\log r + \frac{2}{3}D_i h_i \frac{1}{r^2} + C_i, \tag{25}$$

where D_i can be further expressed in terms of the elastic-plastic boundary $r_p^{(i)}$

$$D_i = -\frac{\sqrt{3}\sigma_y^{(i)}}{2(h_i + E_i)}(r_p^{(i)})^2. \tag{26}$$

In addition, the circumferential stress in the plastic state satisfies

$$\sigma_{\theta\theta}^{(i)} - \sigma_{rr}^{(i)} = \frac{2}{\sqrt{3}}(\sigma_y^{(i)} - h_i\epsilon_{rr}^{p(i)}). \tag{27}$$

Constants C_i, A_1, $B_1^{(i)}$, and $B_2^{(i)}$ can be determined again from the interface and boundary conditions; the results are given in Appendix B. After these constants are determined, the overall biaxial strain is simply

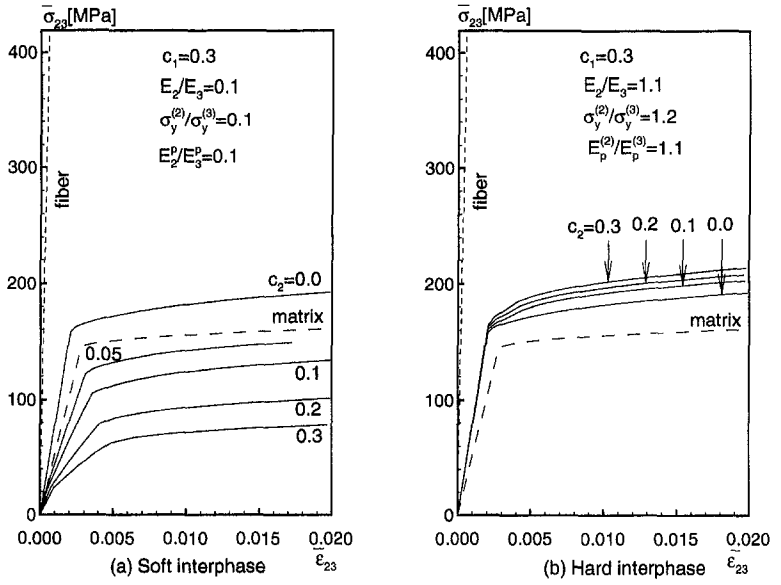

Fig. 6 Influence of the ductile interphase on the transverse shear behavior of a fiber-reinforced composite: (*a*) soft interphase, and (*b*) hard interphase

Downloaded 04 May 2010 to 171.66.16.27. Redistribution subject to ASME license or copyright; see http://www.asme.org/terms/Terms_Use.cfm

$$\bar{\epsilon}_{\alpha\alpha} = 2c_1A_1, \quad (28)$$

due to the assumption of elastic incompressibility of the ductile phases.

The biaxial tensile stress-strain relations of the composite are shown in Figs. 1 and 2, with a soft and hard interphase, respectively. For Fig. 1 the soft interphase is taken to have a property only 1/10th of that of the matrix

$$E_2 = E_3/10, \quad \sigma_y^{(2)} = \sigma_y^{(3)}/10, \quad E_2^p = E_3^p/10, \quad (29)$$

and for Fig. 2 the hard interphase is assumed to have

$$E_2 = 1.1E_3, \quad \sigma_y^{(2)} = 3\sigma_y^{(3)}, \quad E_2^p = 1.1E_3^p. \quad (30)$$

Such a choice will correspond to the two distinct yielding processes discussed in Appendix B, with the interphase yielding first and the matrix yielding first, respectively. In both cases E_3 is taken to be 68.3 GPA and $\sigma_y^{(3)}$ to be 250 MPa. It may be further noted that parts (a) and (b) of both figures correspond to the ideally plastic and linearly work-hardening state, respectively.

Results of the biaxial behavior by the exact solution and the homogenization theory are marked by "Exact" and "Theory" in both plots. In each case, the objective was to disclose the influence of fiber stiffness—as it varies from being stiffer than the matrix to being softer, and then eventually becoming porous—on the nonlinear behavior of the composite. A quick glance over all four figures indicates that the homogenization scheme could provide fairly accurate results for the biaxial behavior, especially when the interphase is softer than the matrix. From these results one is led to conclude that, when the fiber is stiffer than the matrix, the biaxial nonlinearity is negligible, and that it is only when the fiber is substantially softer than the matrix that it begins to display strong nonlinear characteristics.

6 Anisotropic Stress-Strain Relations of the Fiber-Reinforced Composite

Our theoretical calculations here are directed toward uncovering the influence of the volume concentration of the interphase on the overall response of the composite along various loading directions. Again both soft interphase and hard interphase have been considered.

As a material base 6061-T6 aluminum was taken as the matrix and silicon-carbide as fibers. These materials possess the following properties (Arsenault, 1984; Nieh and Chellman, 1984)

$$E_1 = 490 \text{ GPA}, \quad \nu_1 = 0.17,$$
$$E_3 = 68.3 \text{ GPA}, \quad \nu_3 = 0.33, \quad \sigma_y^{(3)} = 250 \text{ MPa},$$
$$h_3 = 173 \text{ MPa}, \quad n_3 = 0.455 \quad (31)$$

at room temperature. Specifically we have studied the range of volume concentrations,

$$c_1 = 0.3, \quad c_2 + c_3 = 0.7, \quad (32)$$

and let c_2 vary between 0 and 0.3, the former corresponding to an ordinary two-phase composite.

For a soft interphase we again used

$$E_2 = E_3/10, \quad \sigma_y^{(2)} = \sigma_y^{(3)}/10, \quad E_2^p = E_3^p/10, \quad (33)$$

while retaining the same Poisson's ratio and n, and for a hard interphase we took

$$E_2 = 1.1E_3, \quad \sigma_y^{(2)} = 1.2\sigma_y^{(3)}, \quad E_2^p = 1.1E_3^p. \quad (34)$$

The results for axial tension, transverse tension, axial shear, and transverse shear are displayed from Fig. 3 to Fig. 6, respectively. In each figure the left one corresponds to a soft interphase and the right one a hard interphase. The properties of the fiber and matrix are also plotted in the background as reference.

For the axial tension in Fig. 3, the presence of a soft or a hard interphase does not appear to have a significant effect on the behavior of the composite for this is a fiber-dominated mode. Thus as c_2 increases from 0 to 0.3, the results do not deviate greatly from that of an ordinary two-phase system. In comparing (a) to (b), a soft interphase does lead to a somewhat more compliant composite even though the difference is not significant either.

Such is not the case under the transverse tension as shown in Fig. 4, which reveals that, with a soft interphase, the system as a whole is very sensitive to the volume concentration of the interphase. When c_2 is greater than 0.1, the three-phase composite can become even softer than the original aluminum matrix. The dependence on c_2 as depicted in (b) is less strong when the interphase is harder than the matrix, but it is still stronger than the axial behavior in Fig. 3.

The axial shear behavior as displayed in Fig. 5 is particularly sensitive to the interphase when it is soft. Indeed even at the low concentration of $c_2 = 0.05$, the stress-strain curve is already well below that of the pure matrix. But with a hard interphase its reinforcement just increases steadily with increasing c_2. The transverse shear behavior shown in Fig. 6 also exhibits a similar pattern as in the case of axial shear, except that the decrease in the elastoplastic strength at $c_2 = 0.05$ is not as drastic as in Fig. $5(a)$. Its reinforcement with a hard interphase also increases in a steady fashion with increasing concentration.

Acknowledgment

This work was supported by the National Science Foundation, under Grant CMS-9625304, and by the Office of Naval Research, under Grant N-00014-91-J-1937.

References

Arsenault, R. J., 1984, "The Strengthening of Aluminum Alloy 6061 by Fiber and Platelet Silicon Carbide," *Materials Science and Engineering,* Vol. 64, pp. 171–181.

Bobeth, M., and Diener, G., 1986, "Field Fluctuations in Multicomponent Mixtures," *Journal of the Mechanics and Physics of Solids,* Vol. 34, pp. 1–17.

Christensen, R. M., and Lo, K. H., 1979, "Solutions for Effective Shear Properties in Three Phase Sphere and Cylinder Models," *Journal of the Mechanics and Physics of Solids,* Vol. 27, pp. 315–330.

Ding, K., and Weng, G. J., 1998, "Plasticity of Particle-Reinforced Composites with a Ductile Interphase," ASME JOURNAL OF APPLIED MECHANICS, Vol. 65, pp. 596–604.

Dvorak, G. J., and Bahei-El-Din, Y. A., 1987, "A Bimodal Plasticity Theory of Fibrous Composite Materials," *Acta Mechanica,* Vol. 69, pp. 219–241.

DeBotton, G., and Ponte Castañeda, P., 1993, "Elastoplastic Constitutive Relations for Fiber-Reinforced Solids," *International Journal of Solids and Structures,* Vol. 30, pp. 1865–1890.

Hashin, Z., and Rosen, B. W., 1964, "The Elastic Moduli of Fiber-Reinforced Materials," ASME JOURNAL OF APPLIED MECHANICS, Vol. 31, pp. 223–232.

Hashin, Z., and Shtrikman, S., 1963, "A Variational Approach to the Theory of the Elastic Behavior of Multiphase Materials," *Journal of the Mechanics and Physics of Solids,* Vol. 11, pp. 127–140.

Hill, R., 1964, "Theory of Mechanical Properties of Fiber-Strengthened Materials: II. Inelastic Behavior," *Journal of the Mechanics and Physics of Solids,* Vol. 12, pp. 214–218.

Hu, G., 1996, "A Method of Plasticity for General Aligned Spherical Void or Fiber-Reinforced Composites," *International Journal of Plasticity,* Vol. 12, pp. 439–449.

Lutz, M. P., and Ferrari, M., 1993, "Compression of a Sphere with Radially Varying Elastic Moduli," *Composite Engineering,* Vol. 3, pp. 873–884.

Lutz, M. P., and Zimmerman, R. W., 1996, "Effect of the Interphase Zone on the Bulk Modulus of a Particulate Composite," ASME JOURNAL OF APPLIED MECHANICS, Vol. 63, pp. 855–861.

Mikata, Y., 1994, "Stress Fields in a Continuous Fiber Composite With a Variable Interphase Under Thermo-Mechanical Loadings," ASME *Journal of Engineering Materials and Technology,* Vol. 116, pp. 367–377.

Nieh, T. G., and Chellman, D. J., 1984, "Modulus Measurements in Discontinuous Reinforced Aluminum Composites," *Scripta Metallurgica,* Vol. 8, pp. 925–928.

Ponte Castañeda, P., 1991, "The Effective Mechanical Properties of Nonlinear Isotropic Composites," *Journal of the Mechanics and Physics of Solids,* Vol. 39, pp. 45–71.

Ponte Castañeda, P., 1992, "New Variational Principles in Plasticity and Their Application to Composite Materials," *Journal of the Mechanics and Physics of Solids,* Vol. 40, pp. 1757–1788.

Downloaded 04 May 2010 to 171.66.16.27. Redistribution subject to ASME license or copyright; see http://www.asme.org/terms/Terms_Use.cfm

Qiu, Y. P., and Weng, G. J., 1991, "Elastic Moduli of Thickly Coated Particle and Fiber-Reinforced Composites," ASME JOURNAL OF APPLIED MECHANICS, Vol. 58, pp. 388–398.

Qiu, Y. P., and Weng, G. J., 1992, "A Theory of Plasticity for Porous Materials and Particle-Reinforced Composites," ASME JOURNAL OF APPLIED MECHANICS, Vol. 59, pp. 261–268.

Qiu, Y. P., and Weng, G. J., 1995, "An Energy Approach to the Plasticity of a Two-Phase Composite Containing Aligned Inclusions," ASME JOURNAL OF APPLIED MECHANICS, Vol. 62, pp. 1039–1046.

Reiter, T., Dvorak, G. J., and Tvergaard, V., 1997, "Micromechanical Models for Graded Composite Materials," *Journal of the Mechanics and Physics of Solids,* Vol. 45, pp. 1281–1302.

Sun, C. T., and Chen, J. L., 1991, "A Micromechanical Model for the Plastic Behavior of Fibrous Composites," *Composites Science and Technology,* Vol. 40, pp. 115–129.

Suquet, P., 1995, "Overall Properties of Nonlinear Composites: A Modified Secant Moduli Theory and Its Link with Ponte Castañeda's Nonlinear Variational Procedure," *C. R. Academie des Sciences,* Vol. 320, Series IIb, pp. 563–571.

Suquet, P., 1996, "Overall Properties of Nonlinear Composites. Remarks on Secant and Incremental Formulations," *IUTAM Symposium on Micromechanics of Plasticity and Damage of Multiphase Materials,* edited by A. Pineau and A. Zaoui, eds, Kluwer, Amsterdam, pp. 149–156.

Talbot, D. R. S., and Willis, J. R., 1985, "Variational Principles for Inhomogeneous Nonlinear Media," *IMA Journal of Applied Mathematics,* Vol. 35, pp. 39–54.

Talbot, D. R. S., and Willis, J. R., 1992, "Some Simple Explicit Bounds for the Overall Behavior of Nonlinear Composites," *International Journal of Solids and Structures,* Vol. 29, pp. 1981–1987.

Tandon, G. P., and Weng, G. J., 1988, "A Theory of Particle-Reinforced Plasticity," ASME JOURNAL OF APPLIED MECHANICS, Vol. 55, pp. 126–135.

Walpole, L. J., 1969, "On the Overall Elastic Moduli of Composite Materials," *Journal of the Mechanics and Physics of Solids,* Vol. 17, pp. 235–251.

Weng, G. J., 1990, "The Overall Elastoplastic Stress-Strain Relations of Dual-Phase Metals," *Journal of the Mechanics and Physics of Solids,* Vol. 38, pp. 419–441.

Willis, J. R., 1991, "On Methods for Bounding the Overall Properties of Nonlinear Composites," *Journal of the Mechanics and Physics of Solids,* Vol. 39, pp. 73–86.

Willis, J. R., 1992, "On Methods for Bounding the Overall Properties of Nonlinear Composites: Correction and Addition," *Journal of the Mechanics and Physics of Solids,* Vol. 40, pp. 441–445.

Zuiker, J., and Dvorak, G. J., 1994a, "The Effective Properties of Functionally Graded Composites—I. Extension of the Mori-Tanaka Method to Linearly Varying Fields," *Composites Engineering,* Vol. 4, pp. 19–35.

Zuiker, J., and Dvorak, G. J., 1994b, "The Effective Properties of Composite Materials with Constant Reinforcement Density by the Linear Mori-Tanaka Method," ASME *Journal of Engineering Materials and Technology,* Vol. 116, pp. 428–437.

Downloaded 04 May 2010 to 171.66.16.27. Redistribution subject to ASME license or copyright; see http://www.asme.org/terms/Terms_Use.cfm

Downloaded 04 May 2010 to 171.66.16.27. Redistribution subject to ASME license or copyright; see http://www.asme.org/terms/Terms_Use.cfm

APPENDIX A

Components of the Matrix for the Effective Shear Modulus in the Generalized Self-Consistent Scheme

$$
\begin{bmatrix}
0 & 0 & \mu_1(\eta_2-3)-\mu_2(\eta_1-3) & (\mu_1-\mu_2)\frac{1}{c_1} & [\mu_1(\eta_2+1)+\mu_2(\eta_1+1)]\frac{1}{c_1^2} & (\mu_1+\mu_2\eta_1)\frac{1}{c_1^3} & 0 & 0 & 0 & 0 & 0 & 0 \\
0 & 0 & \mu_1(\eta_2+3)-\mu_2(\eta_1+3) & -(\mu_1-\mu_2)\frac{1}{c_1} & -[\mu_1(\eta_2-1)-\mu_2(\eta_1-1)]\frac{1}{c_1^2} & (\mu_1+\mu_2\eta_1)\frac{1}{c_1^3} & 0 & 0 & 0 & 0 & 0 & 0 \\
0 & 1 & 0 & -1 & 4\frac{1}{c_1} & 3\frac{1}{c_1^2} & 0 & 0 & 0 & 0 & 0 & 0 \\
1 & 0 & -1 & 0 & \frac{1}{c_1^2} & \frac{1}{c_1^3} & 0 & 0 & 0 & 0 & 0 & 0 \\
0 & 0 & \mu_3(\eta_2-3)-\mu_2(\eta_3-3) & (\mu_3-\mu_2)\frac{1}{c_1+c_2} & [\mu_3(\eta_2+1)+\mu_2(\eta_3+1)]\frac{1}{(c_1+c_2)^2} & (\mu_3+\mu_2\eta_3)\frac{1}{(c_1+c_2)^3} & 0 & 0 & -2\mu_2(\eta_3+1)\frac{1}{(c_1+c_2)^2} & -\mu_2(\eta_3+1)\frac{1}{(c_1+c_2)^3} & 0 & 0 \\
0 & 0 & \mu_3(\eta_2+3)-\mu_2(\eta_3+3) & -(\mu_3-\mu_2)\frac{1}{c_1+c_2} & [-\mu_3(\eta_2-1)+\mu_2(\eta_3-1)]\frac{1}{(c_1+c_2)^2} & (\mu_3+\mu_2\eta_3)\frac{1}{(c_1+c_2)^3} & 0 & 0 & -\mu_2(\eta_3-\eta_2)\frac{1}{(c_1+c_2)^2} & -\mu_2(\eta_3+1)\frac{1}{(c_1+c_2)^3} & 0 & 0 \\
0 & 0 & 0 & 1 & -4\frac{1}{c_1+c_2} & -3\frac{1}{(c_1+c_2)^2} & 0 & -1 & 4\frac{1}{(c_1+c_2)} & 3\frac{1}{(c_1+c_2)^2} & 0 & 0 \\
0 & 0 & 1 & 0 & -4\frac{1}{(c_1+c_2)^2} & -\frac{1}{(c_1+c_3)^2} & -1 & 0 & \frac{1}{(c_1+c_2)^2} & \frac{1}{(c_1+c_2)^3} & 0 & 0 \\
0 & 0 & 0 & 0 & 0 & 0 & 6 & -1 & -2 & -3 & -2 & 3 \\
0 & 0 & 0 & 0 & 0 & 0 & 0 & -1 & 4 & 3 & -2 & -3 \\
0 & 0 & 0 & 0 & 0 & 0 & -\frac{\mu_{23}}{\mu_3}(\eta_3-3) & -\frac{\mu_{23}}{\mu_3} & -\frac{\mu_{23}}{\mu_3(\eta_3+1)} & -\frac{\mu_{23}}{\mu_3} & -2 & 1 \\
0 & 0 & 0 & 0 & 0 & 0 & -\frac{\mu_{23}}{\mu_3}(\eta_3+3) & \frac{\mu_{23}}{\mu_3} & \frac{\mu_{23}}{\mu_3}(\eta_3-1) & -\frac{\mu_{23}}{\mu_3} & 2 & 1
\end{bmatrix}
$$

APPENDIX B

Exact Local Elastic-Plastic Analysis

When both the interphase and the matrix are ductile, there exist several possibilities for the yielding process. The most common one, however, starts from the fiber/interphase interface and spreads out over the entire interphase before yielding at the matrix interface commences. Another distinct yielding process starts from the matrix until it becomes fully plastic, then followed by the interphase yielding. The following results have been derived for these two specific cases which have been used to plot Figs. 1 and 2, respectively. Regardless of the possibilities, the composite is initially in an elastic state and in this case the coefficients A_1, $B_1^{(i)}$, and $B_2^{(i)}$ are given by

$$A_1 = \frac{3}{4}\frac{\bar{\sigma}_{\alpha\alpha}}{(c_2E_2 + c_1c_3E_3)/(c_1 + c_2) + 3k_1},$$

$$B_1^{(2)} = 0, \quad B_1^{(3)} = 0,$$

$$B_2^{(2)} = \frac{3}{4}\frac{c_1\bar{\sigma}_{\alpha\alpha}}{(c_2E_2 + c_1c_3E_3)/(c_1 + c_2) + 3k_1},$$

$$B_2^{(3)} = \frac{3}{4}\frac{c_1\bar{\sigma}_{\alpha\alpha}}{(c_2E_2 + c_1c_3E_3)/(c_1 + c_2) + 3k_1}. \quad \text{(B1)}$$

B.1 Yielding From the Interphase. When the interphase is partly plastic and partly elastic but the matrix remains elastic, we let $X = [A_1, C_2, B_1^{(2)}, B_2^{(2)}, B_1^{(3)}, B_2^{(3)}]$. Then these constants can be determined in terms of the elastic-plastic boundary $r_p^{(2)}$ from the matrix equation $SX = B$, with

$$S = \begin{Bmatrix} 1 & 0 & 0 & 0 & 0 & 0 \\ \frac{E_1}{(1-2\nu_1)(1+\nu_1)} & -1 & 0 & 0 & 0 & 0 \\ 0 & 0 & 1 & \frac{1}{r_p^{2(2)}} & 0 & 0 \\ 0 & 1 & -\frac{E_2}{(1-2\nu_2)(1+\nu_2)} & \frac{E_2}{(1+\nu_2)r_p^{2(2)}} & 0 & 0 \\ 0 & 0 & 1 & \frac{1}{c_1+c_2} & -1 & -\frac{1}{c_1+c_2} \\ 0 & 0 & \frac{E_2}{(1-2\nu_2)(1+\nu_2)} & -\frac{E_2}{(1+\nu_2)(c_1+c_2)} & -\frac{E_3}{(1-2\nu_3)(1+\nu_3)} & \frac{E_3}{(1+\nu_3)(c_1+c_2)} \end{Bmatrix}, \quad \text{(B2)}$$

and

$$B = \left\{\frac{\sqrt{3}}{2}\frac{\sigma_y^{(2)}r_p^{2(2)}}{E_2c_1}, \frac{\sqrt{3}}{3}\frac{\sigma_y^{(2)}}{h_2+E_2}\left[E_2\log c_1 - \frac{h_2r_p^{2(2)}}{c_1}\right], \right.$$

$$\left.\frac{1}{2}\frac{\sigma_y^{(2)}}{E_2}, -\frac{\sqrt{3}}{3}\frac{\sigma_y^{(2)}}{h_2+E_2}[E_2\log r_p^{(2)} - h_2], 0, 0\right\}^T. \quad \text{(B3)}$$

The boundary $r_p^{(2)}$ is in turn related to the applied stress $\bar{\sigma}_{\alpha\alpha}$ through

$$\bar{\sigma}_{\alpha\alpha} = \frac{2E_3}{(1-2\nu_3)(1+\nu_3)}B_1^{(3)} - \frac{2E_3}{1+\nu_3}B_2^{(3)}. \quad \text{(B4)}$$

Therefore, corresponding to each increment of $r_p^{(2)}$, one can find out the components of X and $\bar{\sigma}_{\alpha\alpha}$.

When the interphase is fully plastic but the matrix is partly plastic and partly elastic, we let $X = [A_1, C_2, D_2, C_3, B_1^{(3)}, B_2^{(3)}]$. The coefficients in the $SX = B$ equation are

$$S = \begin{Bmatrix} 1 & 0 & \frac{h_2+E_2}{E_2c_1} & 0 & 0 & 0 \\ \frac{E_1}{(1-2\nu_1)(1+\nu_1)} & -1 & -\frac{2}{3}\frac{h_2}{c_1} & 0 & 0 & 0 \\ 0 & 0 & -\frac{h_2+E_2}{E_2} & 0 & 0 & 0 \\ 0 & 1 & \frac{2}{3}\frac{h_2}{c_1+c_2} & -1 & 0 & 0 \\ 0 & 0 & 0 & 0 & -1 & -\frac{1}{r_p^{2(3)}} \\ 0 & 0 & 0 & 1 & -\frac{E_3}{(1-2\nu_3)(1+\nu_3)} & \frac{E_3}{1+\nu_3}\frac{1}{r_p^{2(3)}} \end{Bmatrix}, \quad \text{(B5)}$$

and

$$B = \left\{0, \frac{1}{\sqrt{3}}\frac{\sigma_y^{(2)}E_2\log c_1}{h_2+E_2}, \frac{\sqrt{3}}{2}\frac{\sigma_y^{(3)}r_p^{2(3)}}{E_3}, \right.$$

$$\frac{1}{\sqrt{3}}\frac{\sigma_y^{(3)}}{h_3+E_3}\left(E_3\log(c_1+c_2) - \frac{h_3r_p^{2(3)}}{c_1+c_2}\right)$$

$$-\frac{1}{\sqrt{3}}\frac{\sigma_y^{(2)}E_2\log(c_1+c_2)}{h_2+E_2}, -\frac{\sqrt{3}}{2}\frac{\sigma_y^{(3)}}{E_3}, $$

$$\left.-\frac{\sigma_y^{(3)}}{\sqrt{3}(h_3+E_3)}(E_3\log r_p^{(3)} - h_3)\right\}. \quad \text{(B6)}$$

One can obtain X in terms of $r_p^{(3)}$, which is again related to the applied $\bar{\sigma}_{\alpha\alpha}$ through (B4). Then by increasing $r_p^{(3)}$, one can proceed in the same fashion.

When both the interphase and the matrix are in the fully plastic state, we let $X = [A_1, C_2, D_2, C_3, D_3]$. From $SX = B$, with

$$S = \begin{Bmatrix} 1 & 0 & \frac{h_2+E_2}{E_2c_1} & 0 & 0 \\ \frac{E_1}{(1-2\nu_1)(1+\nu_1)} & -1 & -\frac{2h_2}{3c_1} & 0 & 0 \\ 0 & 0 & -\frac{h_2+E_2}{E_2(c_1+c_2)} & 0 & \frac{h_3+E_3}{E_3(c_1+c_2)} \\ 0 & 1 & \frac{2h_2}{3(c_1+c_2)} & -1 & -\frac{2h_3}{3(c_1+c_2)} \\ 0 & 0 & 0 & 1 & \frac{2h_3}{3} \end{Bmatrix}, \quad \text{(B7)}$$

Downloaded 04 May 2010 to 171.66.16.27. Redistribution subject to ASME license or copyright; see http://www.asme.org/terms/Terms_Use.cfm

and

$$B = \left\{0, 0, 0, \frac{1}{\sqrt{3}}\left[\frac{\sigma_y^{(3)}E_3}{h_3 + E_3} - \frac{\sigma_y^{(2)}E_2}{h_2 + E_2}\right]\log(c_1 + c_2), \sigma_b\right\}^T, \tag{B8}$$

the final stage of the stress-strain curve can be calculated.

B.2 Yielding From the Matrix. In this case equations (B1), (B7) and (B8) remain valid, but (B2) to (B6) must be modified.

When the matrix is partly plastic and partly elastic while the interphase remains elastic, we let $X = [A_1, B_1^{(2)}, B_2^{(2)}, C_3, B_1^{(3)}, B_2^{(3)}]$. Then

$$S = \begin{Bmatrix} 1 & -1 & -\frac{1}{c_1} & 0 & 0 & 0 \\ \frac{E_1}{(1-2\nu_1)(1+\nu_1)} & -\frac{E_2}{(1-2\nu_2)(1+\nu_2)} & \frac{E_2}{(1+\nu_2)c_1} & 0 & 0 & 0 \\ 0 & 1 & \frac{1}{c_1+c_2} & 0 & 0 & 0 \\ 0 & \frac{E_2}{(1-2\nu_2)(1+\nu_2)} & -\frac{E_2}{(1+\nu_2)(c_1+c_2)} & -1 & 0 & 0 \\ 0 & 0 & 0 & 0 & -1 & -\frac{1}{r_p^{2(3)}} \\ 0 & 0 & 0 & 1 & -\frac{E_3}{(1-2\nu_3)(1+\nu_3)} & \frac{E_3}{(1+\nu_3)r_p^{2(3)}} \end{Bmatrix}, \tag{B9}$$

and

$$B = \left\{0, 0, \frac{\sqrt{3}}{2}\frac{\sigma_y^{(3)}r_p^{2(3)}}{E_3(c_1+c_2)}, \frac{\sqrt{3}}{3}\frac{\sigma^{(3)}}{h_3+E_3}\left[E_3\log(c_1+c_2) - \frac{h_3 r_p^{(3)}}{c_1+c_2}\right], -\frac{\sqrt{3}}{2}\frac{\sigma_y^{(3)}}{E_3}, -\frac{\sqrt{3}}{3}\frac{\sigma_y^{(3)}}{h_3+E_3}[2E_3\log r_p^{(3)} - h_3]\right\}^T. \tag{B10}$$

When the matrix is fully plastic but the interphase is partly plastic and partly elastic, we let $X = [A_1, C_2, B_1^{(1)}, B_2^{(1)}, C_3, D_3]$. Then

$$S = \begin{Bmatrix} 1 & 0 & 0 & 0 & 0 & 0 \\ \frac{E_1}{(1-2\nu_1)(1+\nu_1)} & -1 & 0 & 0 & 0 & 0 \\ 0 & 0 & -1 & -\frac{1}{r_p^{2(2)}} & 0 & 0 \\ 0 & 1 & -\frac{E_2}{(1-2\nu_2)(1+\nu_2)} & \frac{E_2}{(1+\nu_2)r_p^{2(2)}} & 0 & 0 \\ 0 & 0 & 1 & \frac{1}{c_1+c_2} & 0 & \frac{h_3+E_3}{E_3(c_1+c_2)} \\ 0 & 0 & \frac{E_2}{(1-2\nu_2)(1+\nu_2)} & -\frac{E_2}{(1+\nu_2)(c_1+c_2)} & -1 & -\frac{2}{3}\frac{h_3}{c_1+c_2} \end{Bmatrix}, \tag{B11}$$

and

$$B = \left\{\frac{\sqrt{3}}{2}\frac{\sigma_y^{(2)}r_p^{2(2)}}{E_2c_1}, \frac{\sqrt{3}}{3}\frac{\sigma_y^{(2)}}{h_2+E_2}\left[E_2\log c_1 - \frac{h_2 r_p^{2(2)}}{c_1}\right], -\frac{\sqrt{3}}{2}\frac{\sigma^{(2)}}{E_2}, -\frac{\sqrt{3}}{3}\frac{\sigma_y^{(2)}}{h_2+E_2}[2E_2\log r_p^{(2)} - h_2], 0, \frac{\sqrt{3}}{3}\frac{\sigma_y^{(3)}E_3\log(c_1+c_2)}{h_3+E_3}\right\}^T. \tag{B12}$$

Downloaded 04 May 2010 to 171.66.16.27. Redistribution subject to ASME license or copyright; see http://www.asme.org/terms/Terms_Use.cfm

On the St. Venant Problems for Inhomogeneous Circular Bars

F. Rooney

M. Ferrari

Biomedical Microdevices Center,
Department of Materials
Science and Mineral Engineering,
University of California,
Berkeley, CA 94720-1710

The classical St. Venant problems, i.e., simple tension, pure bending, and flexure by a transverse force, are considered for circular bars with elastic moduli that vary as a function of the radial coordinate. The problems are reduced to second-order ordinary differential equations, which are solved for a particular choice of elastic moduli. The special case of a bar with a constant shear modulus and the Poisson's ratio varying is also considered and for this situation the problems are solved completely. The solutions are then used to obtain homogeneous effective moduli for inhomogeneous cylinders. Material inhomogeneities associated with spatially variable distributions of the reinforcing phase in a composite are considered. It is demonstrated that uniform distribution of the reinforcement leads to a minimum of the Young's modulus in the class of spatial variations in the concentration considered.

Introduction

In his original paper on torsion and flexure of cylinders by end loads, St. Venant (1855) made the assertion that stress fields corresponding to statically equivalent end loads would differ negligibly except perhaps near the ends of the cylinder. In this way he could justify his solutions as good approximations to the problem with a general distribution of forces on the ends. The statement, as originally formulated, needed clarification and various authors have rendered it more precise, and derived estimates of the difference between the stresses corresponding to statically equivalent loadings (Von Mises, 1945; Sternberg, 1954; Toupin, 1965, Knowles, 1966). These analyses do not require the body to be homogeneous.

The first approaches to the St. Venant problems for inhomogeneous materials were made in the 1960s. The torsion problem was formulated in terms of a single stress function, assuming that both the shear modulus and Poisson's ratio vary, by Ely and Zienkiewicz (1960). Several solutions for various cross-section geometries and shear moduli were given by Lekhnitskii (1981). The solutions for the stresses, however, did not involve the Poisson's ratio. The problem of flexure by a transverse load was solved under the assumption that the Poisson's ratio be constant by Schile (1962) and Rooney and Ferrari (1995). The general flexure problem was considered by Reissner (1964) who proved that if the Poisson's ratio is non constant, the classical assumption of plane stress is not compatible with the existence of displacements. Thus, the general flexure problem involves an auxiliary bending component. This feature of flexure with a nonconstant Poisson's ratio was noted by Muskhelishvili (1963) in connection with compound bars. Schile and Sierakowski (1965) reduced the compatibility equations involving the six Beltrami stress functions to two equations involving two independent stress functions.

In this paper the equations obtained are further reduced to ordinary differential equations and solved for a particular choice of elastic moduli. The corresponding problems for a constant shear modulus are reduced to quadratures. The solutions obtained are then utilized to calculate effective homogeneous moduli.

Contributed by the Applied Mechanics Division of THE AMERICAN SOCIETY OF MECHANICAL ENGINEERS for publication in the ASME JOURNAL OF APPLIED MECHANICS.

Discussion on the paper should be addressed to the Technical Editor, Professor Lewis T. Wheeler, Department of Mechanical Engineering, University of Houston, Houston, TX 77204-4792, and will be accepted until four months after final publication of the paper itself in the ASME JOURNAL OF APPLIED MECHANICS.

Manuscript received by the ASME Applied Mechanics Division, May 15, 1996; final revision, Feb. 20, 1998. Associate Technical Editor: R. Abeyaratne.

Functionally graded materials, or FGMs, are composite materials with microstructural variations designed in order to tailor fit specific applications. A typical example of this technology is the use of metal matrices with continuously varying concentrations of ceramic particles, to reduce thermal wear and brittle failure in components subject to large thermal gradients, such as turbine blades and combustion chambers. FGMs have also been used to enhance adhesion properties of films on various alloys for use in the microfabrication of electrical components. The approach to designing FGMs is quite different from the usual design with homogeneous materials. Since the material properties are not fixed for FGMs, an optimum stress or temperature field can be specified a priori, then the relevant moduli can be adjusted in order to realize the given field. For an overview of the issues that arise in connection with these innovative materials, reference can be made to the International Symposia on FGMs (Yamanouchi et al., 1990; Holt et al., 1992) and the review article by Cherradi et al. (1994).

FGMs, by their very nature, are inhomogeneous and as such the traditional approach, involving the replacement of the material in question with a homogenized one, fails to model the macroscopic variation in material properties that prompts their use. The fact that the material properties vary continuously gives FGMs an advantage over laminates since there is no stress build up at the boundaries of the constituent components, leading to technological problems like debonding. Some creative ways around this hurdle are based on averaging approaches that represent the properties of relatively small physical volumes in terms of the material properties within. A critical evaluation of this effort is given by Christensen (1990). Some different later schemes are presented in Ferrari (1994) and Aboudi et al. (1993).

Motivated by the success of FGM technology, there has been a reawakening of interest in inhomogeneous elasticity and thermoelasticity. Erdogan and his co-workers have analyzed the various problems associated with cracks in inhomogeneous bodies, (Delale and Erdogan 1983, 1988; Erdogan and Ozturk, 1992a,b) and have shown, for example, that bonding dissimilar elements through a functionally graded layer which makes the material parameters continuous causes the singularities at the crack tips to disappear (Delale and Erdogan, 1983). Ferrari et al. have considered some basic elastic and thermoelastic problems (for plates, Ferrari (1992), for spheres, Lutz and Ferrari (1993), and cylinders, Rooney and Ferrari (1994, 1995)).

Basic Equations

Consider an isotropic elastic cylinder of constant cross-section Ω, with the elastic moduli varying across the cross section.

 Copyright © 1999 by ASME

Downloaded 04 May 2010 to 171.66.16.27. Redistribution subject to ASME license or copyright; see http://www.asme.org/terms/Terms_Use.cfm

Introduce a Cartesian coordinate system with the z-axis parallel to the generators of the cylinder. In accordance with St. Venant's principle any two systems of forces are considered equivalent if their resultant forces and resultant moments are equal. The resultant forces thus can be resolved into a longitudinal and a transverse component together with a moment about a transverse axis. The problem with the resultant moment about the z-axis, corresponding to torsion, has been considered elsewhere (Lekhnitskii, 1981; Rooney and Ferrari, 1995).

Assume that the stress tensor can be written in the form

$$\mathbf{T} = \mathbf{T}^{(0)}(x, y) + z\mathbf{T}^{(1)}(x, y) \tag{1}$$

with $T^{(1)}_{yz} = T^{(1)}_{xz} = 0$. The constitutive equations give the strains in the form

$$\mathbf{E} = \mathbf{E}^{(0)}(x, y) + z\mathbf{E}^{(1)}(x, y) \tag{2}$$

with $E^{(1)}_{xz} = E^{(1)}_{yz} = 0$.

If we choose the following stress function representation

$$T_{xx} = \frac{\partial^2 \Phi}{\partial y^2} \quad T_{xy} = -\frac{\partial^2 \Phi}{\partial x \partial y} \quad T_{yy} = \frac{\partial^2 \Phi}{\partial x^2}$$

$$T_{yz} = -\frac{\partial \Psi}{\partial x} \quad T_{xz} = \frac{\partial \Psi}{\partial y} - \int T^{(1)}_{zz}\, dx + f(y) \tag{3}$$

where $\Phi = \Phi^{(0)}(x, y) + z\Phi^{(1)}(x, y)$ and $\Psi = \Psi(x, y)$, then the equilibrium equations are automatically satisfied.

In light of (2), the six nontrivial compatibility equations reduce to the following:

$$\frac{\partial^2 E_{zz}}{\partial x^2} = \frac{\partial^2 E_{zz}}{\partial y^2} = \frac{\partial^2 E_{zz}}{\partial x \partial y} = 0 \tag{4}$$

$$\frac{\partial}{\partial x}\left(\frac{\partial E_{yz}}{\partial x} - \frac{\partial E_{xz}}{\partial y}\right) = \frac{\partial}{\partial z}\left(\frac{\partial E_{xx}}{\partial y} - \frac{\partial E_{xy}}{\partial x}\right) \tag{5}$$

$$\frac{\partial}{\partial y}\left(\frac{\partial E_{yz}}{\partial x} - \frac{\partial E_{xz}}{\partial y}\right) = -\frac{\partial}{\partial z}\left(\frac{\partial E_{yy}}{\partial x} - \frac{\partial E_{xy}}{\partial y}\right) \tag{6}$$

$$2\frac{\partial^2 E_{xy}}{\partial x \partial y} = \frac{\partial^2 E_{xx}}{\partial y^2} + \frac{\partial^2 E_{yy}}{\partial x^2}. \tag{7}$$

Equations (4) imply

$$E_{zz} = (A_0 + B_0 x + C_0 y) + z(A_1 + B_1 x + C_1 y) \tag{8}$$

where A_0, B_0, C_0, A_1, B_1, C_1 are constant. Using (8) and the stress function representation (3) together with the constitutive equations gives

$$T_{zz} = 2\mu(1 + \nu)E_{zz} + \nu\nabla^2\Phi. \tag{9}$$

Substituting into (5) and (6), and using the representation (3) yields

$$\nabla \cdot \left[\frac{1}{\mu}\nabla(\nabla\Phi^{(1)})\right] - \nabla\left(2\nu E_{zz} + \frac{\nu}{\mu}\nabla^2\Phi^{(1)}\right) = \nabla \times (\xi \mathbf{e}_z), \tag{10}$$

where

$$\xi = \nabla \cdot \left(\frac{1}{\mu}\nabla\Psi\right) - \frac{\partial}{\partial y}\left(\frac{1}{\mu}\int T^{(1)}_{zz}dx\right) - \frac{\partial}{\partial y}\left(\frac{f(y)}{\mu}\right). \tag{11}$$

The final compatibility Eq. (7) leads to

$$\nabla \cdot \left(\nabla \cdot \left[\frac{1}{\mu}\nabla(\nabla\Phi)\right]\right) - \nabla^2\left(\frac{\nu}{\mu}\nabla^2\Phi\right) = \nabla^2(2\nu E_{zz}) \tag{12}$$

where μ is the shear modulus and ν is Poisson's ratio.

The condition that the lateral surface of the cylinder be free of tractions reduces to

$$\frac{d}{ds}\left[\frac{\partial \Phi}{\partial x}\right] = \frac{d}{ds}\left[\frac{\partial \Phi}{\partial y}\right] = 0 \quad \text{on } \partial\Omega \tag{13}$$

$$\frac{d\Psi}{ds} = \left[\int T^{(1)}_{zz}dx - f(y)\right]\frac{dy}{ds} \quad \text{on } \partial\Omega \tag{14}$$

where s is the arc length along $\partial\Omega$ and $f(y)$ is an arbitrary function of y which can be chosen either to simplify (10) or to simplify the boundary condition (14).

The constants in (8) can be determined from the end conditions in the following situations:

(a) Simple Tension.

$$\int_\Omega \mathbf{t}dA = \mathscr{T}\mathbf{e}_z \quad \int_\Omega \mathbf{r} \times \mathbf{t}dA = \mathbf{0} \tag{15}$$

(b) Pure Bending by a Moment in the e′ Direction.

$$\int_\Omega \mathbf{t}dA = \mathbf{0} \quad \int_\Omega \mathbf{r} \times \mathbf{t}dA = \mathscr{M}\mathbf{e}' \tag{16}$$

(c) Flexure by a Force in the e′ Direction.

$$\int_\Omega \mathbf{t}dA = \mathscr{P}\mathbf{e}' \quad \int_\Omega \mathbf{r} \times \mathbf{t}dA = \mathbf{0} \tag{17}$$

where $\mathbf{t}$ is the traction vector on the end, i.e., $\mathbf{t} = \mathbf{T}\mathbf{e}_z$.

Special cases of the inhomogeneous St. Venant problems have been investigated previously. Pure torsion, which corresponds to taking $\Phi = 0$ and $E_{zz} = 0$ in our analysis, has been studied for some special geometries and particular forms of the elastic constants (Lekhnitskii, 1981; Rooney and Ferrari, 1995). Flexure with a constant Poisson's ratio is also given by $\Phi = 0$ but in this case $E_{zz} \neq 0$. This problem has been studied by Schile (1963), Reissner (1964), and Rooney and Ferrari (1995).

Circular Cylinders

Let Ω be the disk $0 \leq x^2 + y^2 \leq a^2$. Introduce r, θ as the usual polar coordinates. Let the elastic constants depend on r only.

The boundary conditions on the lateral surface $r = a$ are

$$T_{rr} = T_{r\theta} = T_{rz} = 0$$

$$\frac{1}{r}\frac{\partial \Phi}{\partial r} + \frac{1}{r}\frac{\partial^2 \Phi}{\partial \theta^2} = 0 \quad \frac{1}{r}\frac{\partial^2 \Phi}{\partial r \partial \theta} = 0 \quad T_{rz} = 0 \quad \text{at } r = a. \tag{19}$$

The end conditions for simple tension are

$$\int_\Omega T_{zz}dA = \mathscr{T}, \quad \int_\Omega r(T_{z\theta}\mathbf{e}_z - T_{zz}\mathbf{e}_\theta)dA = \mathbf{0},$$

$$\int_\Omega (T_{zr}\mathbf{e}_r + T_{z\theta}\mathbf{e}_\theta)dA = \mathbf{0}. \tag{20}$$

For pure bending in the $\mathbf{e}_y$ direction,

Downloaded 04 May 2010 to 171.66.16.27. Redistribution subject to ASME license or copyright; see http://www.asme.org/terms/Terms_Use.cfm

$$\int_\Omega T_{zz}dA = 0, \quad \int_\Omega r(T_{z\theta}\mathbf{e}_z - T_{zz}\mathbf{e}_\theta)dA = \mathcal{M}\mathbf{e}_y,$$

$$\int_\Omega (T_{zr}\mathbf{e}_r + T_{z\theta}\mathbf{e}_\theta)dA = \mathbf{0}, \tag{21}$$

and for flexure in the $\mathbf{e}_x$ direction,

$$\int_\Omega T_{zz}dA = 0, \quad \int_\Omega r(T_{z\theta}\mathbf{e}_z - T_{zz}\mathbf{e}_\theta)dA = \mathbf{0}, \tag{22}$$

$$\int_\Omega (T_{zr}\mathbf{e}_r + T_{z\theta}\mathbf{e}_\theta)dA = \mathcal{P}\mathbf{e}_x.$$

The most general system of forces on the end of the bar is a superposition of the three simple solutions. The system of equations naturally splits into two families of solutions: (1) $\Phi^{(1)} = 0$ and $\Psi = 0$ which corresponds to simple tension and pure bending; and (2) $\Phi^{(0)} = 0$ and $\Psi \neq 0$ which corresponds to flexure but with a tension/bending component dictated by compatibility (Reissner, 1964).

Simple Tension and Pure Bending

In general as pointed out by Schile and Sierakowski (1965) the tension and bending solutions are coupled, but due to the symmetry involved in this problem we can consider them separately. Let $\Phi^{(1)} = \Psi = 0$. Then (8) becomes

$$T_{zz} = 2\mu(r)(1 + \nu(r))(A_0 + B_0 r\cos\theta) + \nu(r)\nabla^2\Phi, \tag{23}$$

and the third equation of both (20) and (21) is automatically satisfied since $T_{rz} = T_{\theta z} = 0$.

(a) Simple Tension. The second of the end conditions for simple tension (20) implies the choice of $B_0 = 0$ and $\Phi = A_0 f(r)$. Then A_0 can be evaluated from the first equation

$$\mathcal{T} = 2\pi\int_0^a 2\mu(1 + \nu)A_0 rdr + 2\pi\int_0^a \nu A_0\nabla^2 f(r)rdr. \tag{24}$$

Using the divergence theorem and the boundary conditions gives

$$A_0 = \frac{\mathcal{T}}{2\pi}\Big/\left(\int_0^a 2\mu(1 + \nu)rdr - \int_0^a \nu'(r)f'(r)rdr\right). \tag{25}$$

For $\Phi = A_0 f(r)$, the compatibility equation takes the simple form

$$\frac{d}{dr}(rE_{\theta\theta}) = E_{rr}. \tag{26}$$

This leads to

$$-\frac{1}{r}\left(\frac{1}{\mu}\right)' f'(r) + \left(\frac{1 - \nu}{\mu}\nabla^2 f(r)\right)' = 2\nu'. \tag{27}$$

The boundary conditions imply $f'(a) = 0$. Let $F(r) = rf'(r)$. Since the stresses are nonsingular in Ω, $f'(r)$ must be finite thus $F(0) = 0$. Substituting this into (27) gives the following second-order ordinary differential equation for $F(r)$:

$$F'' + \left(-\frac{1}{r} - \frac{\nu'}{1 - \nu} - \frac{\mu'}{\mu}\right)F' + \frac{\mu'}{r(1 - \nu)\mu}F = \frac{2r\mu\nu'}{1 - \nu} \tag{28}$$

with $F(a) = F(0) = 0$.

(b) Pure Bending. Similarly for bending, the first of (21) is satisfied by taking $A_0 = 0$ and $\Phi = B_0 rg(r)\cos\theta$. The second condition of (21) gives an expression for B_0:

$$B_0 = \frac{\mathcal{M}}{\pi}\Big/\left(\int_0^a 2\mu(1 + \nu)r^3dr - \int_0^a \nu'(r)g'(r)r^3dr\right) \tag{29}$$

with $g(r)$ to be determined from (12) and the boundary conditions (19). In this case (12) leads to the following equation:

$$-\frac{1}{r}\left(\frac{1}{\mu}\right), r\Phi, rr - \left(\frac{1}{\mu}\right), rr\left(\frac{1}{r}\Phi, r + \frac{1}{r^2}\Phi, \theta\theta\right) + \nabla^2\left(\frac{1 - \nu}{\mu}\nabla^2\Phi\right) = \nabla^2(2\nu r\cos\theta). \tag{30}$$

Let $\Phi = B_0 rg(r)\cos\theta$ gives (after multiplying by r^2)

$$-\left[\left(\frac{1}{\mu}\right)'(r^2 g')\right]' + \left[r^3\left(\frac{1 - \nu}{r^3\mu}(r^3 g')'\right)'\right]' = 2(r^3\nu')'. \tag{31}$$

Let $G(r) = r^3 g'(r)$ and integrate once to obtain the following second-order ordinary differential equation for G:

$$G'' + \left(-\frac{3}{r} - \frac{\nu'}{1 - \nu} - \frac{\mu'}{\mu}\right)G' + \frac{\mu'}{r(1 - \nu)\mu}G = \frac{2r^3\mu\nu'}{1 - \nu} + \frac{K_2\mu}{1 - \nu} \tag{32}$$

with K_2 a constant of integration. Similarly to the situation for simple tension, the requirement that the stress be nonsingular implies that $G(0) = 0$.

Flexure

Consider a circular bar under the action of a constant force $\mathcal{P}$ acting in the $\mathbf{e}_x$ direction, with the force applied on the surface $z = 0$. Let

$$\Phi = z\Phi^{(1)}(r, \theta) \quad \Psi = \Psi(r, \theta), \tag{33}$$

and assume the shear stresses in the form

$$T_{rz} = -\frac{1}{r}\frac{\partial\Psi}{\partial\theta} \quad T_{\theta z} = \frac{\partial\Psi}{\partial r} - r\int T_{zz}^{(1)}(r, \theta)\,d\theta. \tag{34}$$

The boundary conditions (19) imply $\Psi = \text{const}$, which can be taken to be zero without loss of generality, i.e.,

$$\Psi = 0 \quad \text{on } r = a. \tag{35}$$

This ensures the z component of the equilibrium equations is identically satisfied. From the third equation of (22), using (34) and the boundary condition (35), it follows that T_{zz} must have the form

$$T_{zz} = z\sigma(r)\cos\theta. \tag{36}$$

Taking all the constants in (8) to be zero except B_1, and letting

$$\Phi^{(1)} = B_1 rh(r)\cos\theta \tag{37}$$

and defining $H(r) = r^3 h'(r)$, it follows by (36) that

$$\sigma(r) = 2\mu(1 + \nu)B_1 r + \nu B_1\frac{H'}{r^2} = B_1\tau(r). \tag{38}$$

The end conditions (22) give B_1 in the form

Downloaded 04 May 2010 to 171.66.16.27. Redistribution subject to ASME license or copyright; see http://www.asme.org/terms/Terms_Use.cfm

$$B_1 = \frac{\mathscr{P}}{\pi} \Big/ \left(\int_0^a 2\mu(1+\nu) r^3 dr - \int_0^a \nu'(r) h'(r) r^3 dr \right) \quad (39)$$

and the boundary conditions (19) and the condition of finite stresses require

$$H(0) = H(a) = 0. \quad (40)$$

The compatibility Eqs. (5) and (6) in this case can be expressed as

$$\nabla \times \left\{ \nabla \times \left[\frac{1}{\mu} (T_{rz}\mathbf{e}_r + T_{\theta z}\mathbf{e}_\theta) \right] \right\} = \nabla \cdot \left[\frac{1}{\mu} \nabla(\nabla \Phi^{(1)}) \right] + \nabla \left(2E_{zz} - \frac{\sigma}{\mu} \cos\theta \right). \quad (41)$$

Substituting the expressions for the stresses (34) leads to

$$\nabla \times \left[\left(\nabla \cdot \left(\frac{1}{\mu} \nabla \Psi \right) - \frac{1}{r} \frac{\partial}{\partial r} \left(\frac{r^2 \sigma}{\mu} \right) \sin\theta \right) \mathbf{e}_z \right] = \nabla \cdot \left[\frac{1}{\mu} \nabla(\nabla \Phi^{(1)}) \right] + \nabla \left(2E_{zz} - \frac{\sigma}{\mu} \cos\theta \right). \quad (42)$$

The other compatibility Eq. (7) gives

$$\nabla \cdot \left(\nabla \cdot \left[\frac{1}{\mu} \nabla(\nabla \Phi^{(1)}) \right] \right) - \nabla^2 \left(\frac{\sigma}{\mu} \cos\theta \right) = 0, \quad (43)$$

which leads to

$$r^3 \left(\frac{\sigma}{r\mu} \right)' = r^3 \left(\frac{H'}{r^3 \mu} \right)' - \frac{H}{r} \left(\frac{1}{\mu} \right)' + K_3 \quad (44)$$

where K_3 is an integration constant. If we substitute for σ in terms of H we can show (44) is equivalent to (32) with H substituted for G. The $\mathbf{e}_r$ component of (42) is

$$\frac{1}{r} \frac{\partial}{\partial \theta} \left[\nabla \cdot \left(\frac{1}{\mu} \nabla \Psi \right) \right] = B_1 \left[\left(\frac{H'}{r^2 \mu} \right)' - \frac{H}{r^3} \left(\frac{1}{\mu} \right)' + 2 + \frac{2\tau}{r\mu} \right] \cos\theta. \quad (45)$$

Integrating to obtain a differential equation for Ψ yields

$$\nabla \cdot \left(\frac{1}{\mu} \nabla \Psi \right) = B_1 \left[\frac{1}{r} \left(\frac{H'}{\mu} \right)' - \frac{H'}{r^2 \mu} - \frac{1}{r^2} \left(\frac{H}{\mu} \right)' + 2r + \frac{2\tau}{\mu} \right] \sin\theta. \quad (46)$$

The arbitrary function of r introduced by the θ integration can be shown to be zero by using the $\mathbf{e}_\theta$ component of (42). Letting $\Psi = B_1 j(r) \sin\theta$ then

$$\frac{1}{r} \left(\frac{rj'}{\mu} \right)' - \frac{j}{r^2 \mu} = \frac{1}{r} \left(\frac{H'}{\mu} \right)' - \frac{H'}{r^2 \mu} - \frac{1}{r^2} \left(\frac{H}{\mu} \right)' + 2r + \frac{2\tau}{\mu}. \quad (47)$$

Now let $J(r) = j(r) + H(r)/r$, to write (47) as

$$J'' + \left(\frac{1}{r} - \frac{\mu'}{\mu} \right) J' - \frac{1}{r^2} J = 2\mu(2+\nu) r - (1-2\nu) \frac{H'}{r^2}. \quad (48)$$

The boundary conditions (35) and (40) require

$$J(a) = 0. \quad (49)$$

Special Cases

Just as the problem for constant Poisson's ratio simplifies the analysis, consideration of the St. Venant problems simplifies if the shear modulus is constant. Let $\mu = \mu_0$ to reduce (12) to

$$\nabla^4 \Phi - \nabla^2(\nu \nabla^2 \Phi) = \nabla^2(2\mu_0 \nu E_{zz}), \quad (50)$$

and (10) to

$$\nabla(\nabla^2 \Phi^{(1)}) - \nabla(2\mu_0 \nu E_{zz} + \nu \nabla^2 \Phi^{(1)}) = \nabla \times (\chi \mathbf{e}_z), \quad (51)$$

with

$$\chi = \nabla^2 \Psi - \frac{\partial}{\partial y} \left(\int T_{zz}^{(1)} dx \right) - \frac{df(y)}{dy}. \quad (52)$$

A partial particular integral can be deduced from (50), and Φ can then be expressed as

$$\Phi = -\tfrac{1}{2} \mu_0 (A_0 + A_1 z + \tfrac{1}{2} [(B_0 + B_1 z)x + (C_0 + C_1 z)y]) r^2 + \zeta, \quad (53)$$

where

$$\nabla^4 \zeta - \nabla^2(\nu \nabla^2 \zeta) = 0. \quad (54)$$

The boundary conditions (13) become

$$\frac{d}{ds} \left[\frac{\partial \zeta}{\partial x} \right] = \frac{d}{ds} \left\{ \mu_0 x \left(A_0 + A_1 z + \frac{1}{2} [(B_0 + B_1 z)x + (C_0 + C_1 z)y] \right) + \frac{1}{4} \mu_0 (B_0 + B_1 z) r^2 \right\} \quad (55)$$

$$\frac{d}{ds} \left[\frac{\partial \zeta}{\partial y} \right] = \frac{d}{ds} \left\{ \mu_0 y \left(A_0 + A_1 z + \frac{1}{2} [(B_0 + B_1 z)x + (C_0 + C_1 z)y] \right) + \frac{1}{4} \mu_0 (C_0 + C_1 z) r^2 \right\}. \quad (56)$$

For flexure, (51) becomes

$$\nabla((1-\nu)\nabla^2 \zeta) = \nabla \times \left\{ \nabla^2 \Psi - \frac{\partial}{\partial y} \left(\int T_{zz}^{(1)} dx \right) - \frac{df(y)}{dy} \right\}, \quad (57)$$

with the boundary condition (14).

(a) Circular Cylinders. Consider now a circular cylinder with $\mu = \mu_0$. The solutions for all three St. Venant problems can be reduced to quadratures as follows:

Downloaded 04 May 2010 to 171.66.16.27. Redistribution subject to ASME license or copyright; see http://www.asme.org/terms/Terms_Use.cfm

(i) Simple Tension. Letting $E_{zz} = A_0$, (53) gives

$$\Phi = -\tfrac{1}{2}\mu_0 A_0 r^2 + \zeta. \tag{58}$$

Letting $\zeta = A_0 f(r)$, the boundary conditions (55) imply

$$f'(a) = \mu_0 a. \tag{59}$$

Integrating (54) for this ζ, discarding the solutions that are singular at $r = 0$ gives

$$rf'(r) = \kappa_1 \int_0^r \frac{r'}{1-\nu(r')}\,dr'. \tag{60}$$

The boundary condition (59) leads to

$$\kappa_1 = \mu_0 a^2 \Big/ \int_0^a \frac{r'}{1-\nu(r')}\,dr'. \tag{61}$$

Using the end conditions (20), A_0 is determined,

$$A_0 = \frac{\mathcal{T}}{2\pi\mu_0 a^2} \Big/ \left[1 + \int_0^a \frac{r'\nu(r')}{1-\nu(r')}\,dr' \Big/ \int_0^a \frac{r'}{1-\nu(r')}\,dr'\right]. \tag{62}$$

(ii) Pure Bending. Similarly to the above, let $E_{zz} = B_0 r\cos\theta$ to deduce

$$\Phi = -\tfrac{1}{4}\mu_0 B_0 r^3 \cos\theta + \zeta. \tag{63}$$

With $\zeta = B_0 r g(r)\cos\theta$, the boundary conditions imply

$$g'(a) = \tfrac{1}{2}\mu_0 a \quad g(a) = \tfrac{1}{4}\mu_0 a^2. \tag{64}$$

Integrating (54) gives

$$r^3 g'(r) = \kappa_2 \int_0^r \frac{r'^3}{1-\nu(r')}\,dr', \tag{65}$$

which by (64) determines κ_2 as

$$\kappa_2 = \frac{1}{2}\mu_0 a^4 \Big/ \int_0^a \frac{r'^3}{1-\nu(r')}\,dr'. \tag{66}$$

The end conditions (20) give B_0 in the form

$$B_0 = \frac{2\mathcal{M}}{\pi\mu_0 a^4} \Big/ \left[1 + \int_0^a \frac{r'^3\nu(r')}{1-\nu(r')}\,dr' \Big/ \int_0^a \frac{r'^3}{1-\nu(r')}\,dr'\right]. \tag{67}$$

(iii) Flexure. Letting $E_{zz} = B_1 zr\cos\theta$, it is found that

$$\Phi = -\tfrac{1}{4}\mu_0 B_1 z r^3 \cos\theta + \zeta. \tag{68}$$

Taking $\zeta = B_1 z r h(r)\cos\theta$, the boundary conditions give

$$h'(a) = \tfrac{1}{2}\mu_0 a \quad h(a) = \tfrac{1}{4}\mu_0 a^2. \tag{69}$$

Integrating (54) leads to

$$r^3 h'(r) = \kappa_3 \int_0^r \frac{r'^3}{1-\nu(r')}\,dr' \tag{70}$$

with κ_3 given by the boundary conditions (69) as

$$\kappa_3 = \frac{1}{2}\mu_0 a^4 \Big/ \int_0^a \frac{r'^3}{1-\nu(r')}\,dr'. \tag{71}$$

Using (9) and (68) it is found that

$$T_{zz} = B_1 zr\cos\theta\left\{2\mu_0 + \nu\frac{H'}{r^3}\right\} \tag{72}$$

where $H(r) = r^3 h'(r)$. Recalling (34) gives the shear stresses as

$$T_{rz} = -\frac{1}{r}\frac{\partial\Psi}{\partial\theta} \quad T_{\theta z} = \frac{\partial\Psi}{\partial r} - B_1 r^2\sin\theta\left\{2\mu_0 + \nu\frac{H'}{r^3}\right\}, \tag{73}$$

and the end conditions (22) give

$$B_1 = \frac{2\mathcal{P}}{\pi\mu_0 a^4} \Big/ \left[1 + \int_0^a \frac{r'^3\nu(r')}{1-\nu(r')}\,dr' \Big/ \int_0^a \frac{r'^3}{1-\nu(r')}\,dr'\right]. \tag{74}$$

Substituting (73) into (57) and integrating leads to

$$\nabla^2\Psi - \frac{1}{r}\frac{\partial}{\partial r}\left(B_1 r^3\left\{2\mu_0 + \frac{\kappa_3\nu}{1-\nu}\right\}\right)\sin\theta = B_1\kappa_3 r\sin\theta. \tag{75}$$

Letting $\Psi = B_1 rL(r)\sin\theta$,

$$r^3 L'(r) = r^4\left\{2\mu_0 + \frac{\kappa_3\nu}{1-\nu}\right\} + \frac{1}{4}\kappa_3 r^4 - \int_0^r r'^3\left\{2\mu_0 + \frac{\kappa_3\nu}{1-\nu}\right\}dr' \tag{76}$$

and L can be found by another integration, with the constant determined so that $L(a) = 0$.

Effective Moduli

By comparing the obtained results with the corresponding solutions for homogeneous bars one can use the end conditions to define effective homogeneous moduli for the inhomogeneous cylindrical element.

(1) Simple Tension. Let the longitudinal strain be $E_{zz} = A_0$ and the force on the end be $\mathcal{T}$. Then, the effective Young's modulus is defined by analogy with the homogeneous problem as

$$E_T = \frac{\mathcal{T}}{\pi A_0 a^2}. \tag{77}$$

Three situations will be considered. In case I both the elastic moduli vary across the cross section, while in cases II and III where one of the moduli is constant.

Case I: $\mu = \mu(r)$ *and* $\nu = \nu(r)$. Using Eq. (25) and (76) gives

$$\bar{E}_T = \frac{2}{a^2}\left(\int_0^a 2\mu(1+\nu)\,rdr - \int_0^a \nu'(r)F(r)\,dr\right). \tag{78}$$

Case II: $\mu = \mu_0$ *and* $\nu = \nu(r)$. Equation (77) together with (62) leads to an effective Young's Modulus in this case in the form

Downloaded 04 May 2010 to 171.66.16.27. Redistribution subject to ASME license or copyright; see http://www.asme.org/terms/Terms_Use.cfm

$$\hat{E}_T = 2\mu_0\left[1 + \int_0^a \frac{r'\nu(r')}{1-\nu(r')}\,dr'\right] \Big/ \int_0^a \frac{r'}{1-\nu(r')}\,dr'\Bigg]. \quad (79)$$

Case III: $\mu = \mu(r)$ *and* $\nu = \nu_0$. In this case the effective modulus can be obtained from (78),

$$\hat{E}_T = \frac{4(1+\nu_0)}{a^2}\int_0^a \mu(r) r dr. \quad (80)$$

(2) Pure Bending. In the homogeneous case, $E_{zz} = B_0 r\cos\theta$ where

$$B_0 = \frac{\mathscr{M}}{EI_y} \quad \text{and} \quad I_y = \int x^2 dA. \quad (81)$$

Case I: $\mu = \mu(r)$ *and* $\nu = \nu(r)$. Equating B_0 from (81) with the expression in (29) gives for the effective modulus

$$\bar{E}_B = \frac{4}{a^4}\left[\int_0^a 2\mu(1+\nu) r^3 dr - \int_0^a \nu'(r) G(r) dr\right]. \quad (82)$$

Case II: $\mu = \mu_0$ *and* $\nu = \nu(r)$. Equations (81) and (67) lead to

$$\hat{E}_B = 2\mu_0\left[1 + \int_0^a \frac{r'^3\nu(r')}{1-\nu(r')}\,dr'\right] \Big/ \int_0^a \frac{r'^3}{1-\nu(r')}\,dr'\Bigg]. \quad (83)$$

Case III: $\mu = \mu(r)$ *and* $\nu = \nu_0$. From (82) we obtain

$$\hat{E}_B = \frac{8(1+\nu_0)}{a^4}\int_0^a \mu(r) r^3 dr. \quad (84)$$

This coincides with the expression for the effective Young's modulus derived earlier from consideration of the torsion of inhomogeneous circular bars by Rooney and Ferrari (1995).

(3) Flexure. The homogeneous solution for flexure has $E_{zz} = B_1 zr\cos\theta$, with

$$B_1 = \frac{\mathscr{P}}{EI_y} \quad \text{and} \quad I_y = \int x^2 dA \quad (85)$$

where $\mathscr{P}$ is the strength of the applied load. By inspection then the effective moduli obtained from consideration of the flexure problem have the same form as the moduli derived from pure bending, mutatis mutandis.

An Example

Consider a circular cylindrical tube, of inner radius $r = \frac{1}{2}$ and outer radius $r = 1$, consisting of a matrix material reinforced by rigid spherical inclusions, undergoing simple tension. The effective Young's modulus depends on the distribution of the inclusions. The determination of macroscopic elastic constants from the details of the microstructure is an active area of research and several schemes have been proposed (Eshelby, 1957; Christensen, 1990; Aboudi et al., 1993; Ferrari, 1994). For spherical inclusions in an isotropic matrix Ferrari's poly-inclusion method leads to the same effective moduli as the Mori-Tanaka scheme.

$$\frac{\mu}{\mu_m} = 1 + \frac{c}{1-c}(1+\mathscr{A}) \quad (86)$$

and

$$\frac{\kappa}{\kappa_m} = 1 + \frac{c}{1-c}\left(1 + \frac{4}{3y}\right), \quad (87)$$

where μ_m and κ_m are the shear modulus and bulk modulus of the matrix material, $y = \mu_m/\kappa_m$, $\mathscr{A} = (9y+8)/6(y+2)$, and c is the concentration of the inclusions, i.e., the volume of the inclusions divided by the total volume.

From (86), letting $\hat{\mu} = \mu/\mu_m$ one obtains

$$c = \frac{\hat{\mu}-1}{\hat{\mu}+\mathscr{A}} \quad (88)$$

and

$$1 - \nu = \frac{1}{2} b\,\frac{\hat{\mu}-A}{\hat{\mu}-B} \quad (89)$$

where

$$A = \frac{3(4-3y)}{6y+32}, \quad B = \frac{3(4-3y)}{6y+17}, \quad b = \frac{B}{A}. \quad (90)$$

Letting the overall volume fraction be c_0 and the concentration of inclusions vary as a function of r, then it is found that

$$\int_{1/2}^1 c(r) 2r dr = \tfrac{3}{4} c_0. \quad (91)$$

Substituting (89) into (27) and letting $u = r^2$ gives

$$-\frac{1}{u}\frac{d}{du}\left[\frac{1}{\hat{\mu}}\right]F + \frac{d}{du}\left[\frac{B}{A}\,\frac{\hat{\mu}-A}{\hat{\mu}-B}\,\frac{1}{\hat{\mu}}\,\frac{dF}{du}\right] = 2\mu_m\frac{d\nu}{du} \quad (92)$$

which has the particular solution

$$F_0 = -\mu_m B u. \quad (93)$$

To make further progress the form of $c(r)$ must be made explicit.

Two choices for $c(r)$ will be considered:
Case I:

$$c(r) = 1 - \frac{1+\mathscr{A}}{\mathscr{A}}\,\frac{r^{2\rho}}{r^{2\rho}+K}, \quad (94)$$

which corresponds to a power-law distribution for the shear modulus,

$$\hat{\mu} = K\mathscr{A} u^{-\rho}. \quad (95)$$

Case II:

$$c(r) = \frac{1+\mathscr{A}}{\mathscr{A}}\,\frac{B}{B+\mathscr{A}}\,\frac{r^{2\sigma}}{r^{2\sigma}-M} - \frac{1}{\mathscr{A}}, \quad (96)$$

which corresponds to a power-law distribution for Poisson's ratio

$$v = 2\nu - 1 = -\frac{b-1}{1+B/\mathscr{A}}\,\frac{1}{M}\,u^{\sigma}. \quad (97)$$

These are illustrated in Figs. 1 and 2, respectively, corresponding to the choice $y = 13/6$ and $c_0 = \frac{1}{5}$.

Case I: Under the distribution (94), (91) gives

$$\int_{1/4}^1 \frac{u^{\rho}}{u^{\rho}+K}\,du = \frac{3\mathscr{A}}{4(1+\mathscr{A})}(1-c_0) \quad (98)$$

which serves to determine K for a given value of ρ.

Substituting (94) into (86) gives

Downloaded 04 May 2010 to 171.66.16.27. Redistribution subject to ASME license or copyright; see http://www.asme.org/terms/Terms_Use.cfm

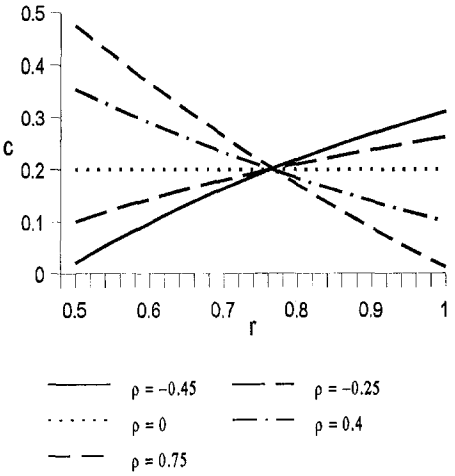

Fig. 1 Distribution of inclusions in case I for $y = 13/6$ and $c_0 = \frac{1}{5}$

$$\hat{\mu} = K\mathscr{A}u^{-\rho}. \tag{99}$$

Changing the independent variable to $v = 2\nu - 1$ in the homogeneous version of (92) leads to

$$\frac{d^2F}{dv^2} + \left[\frac{1}{\rho}\frac{1}{v} + \frac{1}{v-1} + \left(2 - \frac{1}{\rho}\right)\frac{1}{v+b-1}\right]\frac{dF}{dv} + \frac{1}{\rho}\frac{(b-1)^2}{v^2(v-1)(v+b-1)^2}F = 0. \tag{100}$$

This is a Fuchsian equation with regular singularities at 0, 1, 1-b, ∞. Thus, the solution can be expressed in the form of a Riemannian P-symbol

$$F = P\begin{pmatrix} 0 & 1 & 1-b & \infty & \\ 1 & 0 & \xi & 0 & ; \ v \\ -1/\rho & 0 & \eta & 2 & \end{pmatrix} \tag{101}$$

where $\xi, \eta = \frac{1}{2}\left[-1 + (1/\rho) \pm \sqrt{(1-(1/\rho))^2 + (4/\rho b)}\right]$.

The Eq. (100) can be reduced to Heun's equation (Ronveaux, 1995)

$$\frac{d^2y}{dz^2} + \left[\frac{\gamma}{z} + \frac{\delta}{z-1} + \frac{\epsilon}{z-a}\right]\frac{dy}{dz} + \frac{\alpha\beta z - q}{z(z-1)(z-a)}y = 0 \tag{102}$$

with $\alpha + \beta + 1 = \gamma + \delta + \epsilon$, corresponding to the P-symbol

$$y = P\begin{pmatrix} 0 & 1 & a & \infty & \\ 1 & 0 & 0 & \alpha & ; \ z \\ 1-\gamma & 1-\delta & 1-\epsilon & \beta & \end{pmatrix} \tag{103}$$

which has the solution, analogous to the hypergeometric series, corresponding to the exponent zero at $z = 0$

$$y = H1(a, q; \alpha, \beta, \gamma, \delta; z) = 1 + \alpha\beta\sum_{n=1}^{\infty}\frac{G_n(q)(z/a)^n}{n!\gamma(\gamma+1)(\gamma+n-1)} \tag{104}$$

where $G_1(q) = q$; $G_2(q) = \alpha\beta q^2 + \{(\alpha+\beta-\delta+1) + a(\gamma+\delta)\}q - \alpha\gamma G_{n+1}(q) = [n\{(\alpha+\beta-\delta+n) + a(\gamma+\delta+n-1)\} + \alpha\beta q]G_n(q) - (\alpha+n-1)(\beta+n-1)(\gamma+n-1)naG_{n-1}(q)$.

Then as long as $1/\rho$ is not an integer, two independent solutions of (100) are

$$F_1 = (v+b-1)^{\xi}vH1 \times (1-b, q_1; \xi+1, \xi+3, -1-1/\rho, 1; v) \tag{105}$$

$$F_2 = (v+b-1)^{\xi}v^{-1/\rho}H1 \times (1-b, q_2; \xi-1/\rho, \xi-1/\rho+2, 1+1/\rho, 1; v) \tag{106}$$

where $q_1 = (\xi+1)(2+1/\rho) + (1+1/\rho)(1-b)$ and $q_2 = 1/\rho^2 + \xi(1/\rho - 2)$.

Using the boundary conditions together with (93) gives

$$F(u) = \mu_m B[-u + A_1F_1(u) + A_2F_2(u)] \tag{107}$$

with

$$A_1 = \frac{F_2(1/4) - 1/4F_2(1)}{F_1(1)F_2(1/4) - F_1(1/4)F_2(1)}$$

$$A_2 = \frac{-F_1(1/4) + 1/4F_1(1)}{F_1(1)F_2(1/4) - F_1(1/4)F_2(1)}.$$

The effective Young's Modulus can then be calculated from (78) leading to

$$\bar{E}_T = \frac{8}{3}\left(\int_{1/4}^{1} 2\mu(1+\nu)du - \int_{1/4}^{1}\nu'(u)F(u)du\right). \tag{108}$$

If $\bar{E}_T^{(0)}$ is the Young's modulus corresponding to the homogeneous distribution of inclusions then

$$\bar{E}_T^{(0)} = \frac{1+\mathscr{A}c_0}{1-c_0}\left[3 + \frac{(1-b)(1+\mathscr{A}c_0)}{1+\mathscr{A}c_0 - B(1-c_0)}\right]. \tag{109}$$

Now let

$$\mathscr{E} = \bar{E}_T/\bar{E}_T^{(0)}. \tag{110}$$

Figure 3 shows the variation of $\mathscr{E}$ as a function of ρ. Examination of Fig. 3 leads to the conclusions that the qualitative response of the bar, i.e., the normalized effective Young's modulus doesn't depend strongly on the matrix material and, at least for the family of concentration profiles chosen, that the uniform distribution of inclusions gives a minimum for the effective modulus. It also appears that the magnitude of the modulus depends on the value of the maximum concentration of the distribution rather than whether it is specifically concentrated at the outer or inner surface. The apparent discrepancy in Fig. 3 is due to the choice (94). The maximum concentrations at

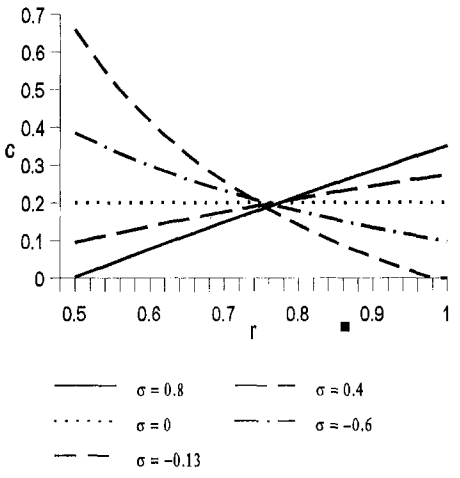

Fig. 2 Distribution of inclusions in case II for $y = 13/6$ and $c_0 = \frac{1}{5}$

Downloaded 04 May 2010 to 171.66.16.27. Redistribution subject to ASME license or copyright; see http://www.asme.org/terms/Terms_Use.cfm

the outer surface for this family are only about 50 percent of the maximum concentration at the inner surface.

Case II. Now consider the second family of distributions. Substituting (96) into (91) implies

$$\int_{1/4}^{1} \frac{u^\sigma}{u^\sigma - M}\, du = \frac{3}{4}\,\frac{1 + \mathscr{A}c_0}{1 + \mathscr{A}}\,\frac{B + \mathscr{A}}{B}. \qquad (111)$$

Substituting (96) into (86) and (87) gives

$$v = 2\nu - 1 = -\frac{b-1}{1 + B/\mathscr{A}}\,\frac{1}{M}\,u^\sigma. \qquad (112)$$

Using (112) in the homogeneous version of (92) leads to

$$\frac{d^2F}{dv^2} + \left[-\frac{1}{\sigma}\frac{1}{v} + \frac{1}{v-1} + \frac{1}{v+b-1}\right]\frac{dF}{dv}$$

$$-\frac{1}{\sigma}\,\frac{(b-1)}{v^2(v-1)(v+b-1)}\,F = 0. \qquad (113)$$

This also can be reduced to Heun's equation, and if $1/\sigma$ is not an integer two independent solutions of (113) are

$$F_1 = vH1(1-b, (2-b)(1-1/\sigma);$$

$$1, 2 - 1/\sigma, 2 - 1/\sigma, 1; v) \qquad (114)$$

$$F_2 = v^{1/\sigma}H1(1-b, 0, 1, 1/\sigma, 2 - 1/\sigma, 1; v). \qquad (115)$$

Using the boundary conditions leads to

$$F(u) = \mu_m B[-u + A_1F_1(u) + A_2F_2(u)] \qquad (116)$$

with A_1 and A_2 given by (107). Using this in Eq. (105) the effective Young's modulus can be calculated. Using (109) we can calculate the normalized Young's modulus $\mathscr{E}$ by (110).

Figure 4 shows the variation of $\mathscr{E}$ with σ. The concentration distribution (96) gives larger values of concentrations at the edges than (94). Figure 4 shows that the matrix material has some effect at the more extreme concentrations especially for $y < \frac{4}{3}$. The uniform distribution again gives a minimum. In this case it seems that if the inclusions are concentrated near the inner surface this leads to larger values for the effective Young's modulus, but this may also be because of the family of concentrations chosen. The scale on the σ-axis is purposely left uncalibrated since the range of variation of σ depends on y and, recalling the fact that $y = \frac{4}{3}$ corresponds to $\nu = \frac{1}{5}$ irrespective of the distribution of inclusions, the possible values of σ are confined to a narrowing band of values as $y \to \frac{4}{3}$.

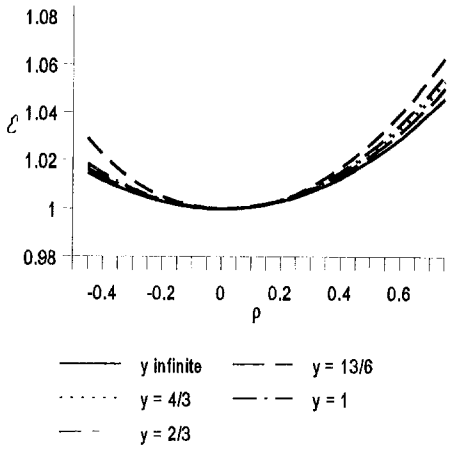

Fig. 3 Normalized effective Young's modulus for case I

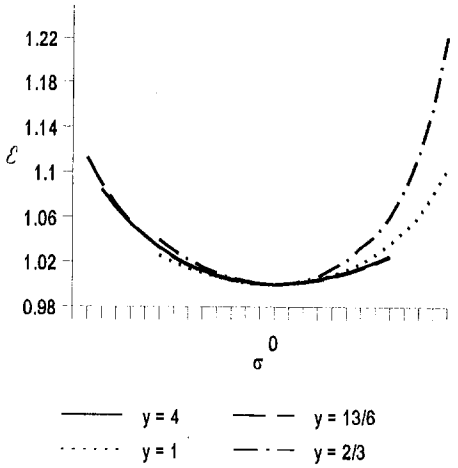

Fig. 4 Normalized effective Young's modulus for case II

Conclusions

The increasing technological importance of heterogeneous materials has led researchers to reconsider the subject of inhomogeneous elasticity. The earlier approaches to multiphase materials, involving pointwise homogenization in order to take advantage of the existing library of solutions in homogeneous elasticity, are unsatisfactory in the case of FGMs, where the inhomogeneity is an integral part of the design of the material. Even in the example given, wherein a homogenizing procedure is applied to an inhomogeneous member, it is found that the distribution of the inhomogeneity is important to the material response. In particular, it is noted that of the various possible distributions of the reinforcing material, uniform dispersion gives the least value for the effective elastic moduli.

References

Aboudi, J., Pindera, M.-J., and Arnold, S., 1993, "Thermoelastic response of metal matrix composites with large diameter fibers subjected to thermal gradients," NASA Technical Memorandum 106344.

Abramowitz, M., and Stegun, I.A., 1964, *Handbook of Mathematical Functions,* Dover, New York.

Cherradi, N., Kawasaki, A., and Gasik, M., 1994, "Worldwide trends in functional gradient materials research and development," *Composite Engineering,* Vol. 4, pp. 883–894.

Christensen, R.M., 1990, "Critical evaluation for a class of micro-mechanics models," *J. Mech. Phys. Solids,* Vol. 38, pp. 379–404.

Colchin, G.B., and Faverman, E.A., 1972, *The Theory of Elasticity of Nonhomogeneous Bodies,* Kishiniev.

Delale, F., and Erdogan, F., 1983, "The Crack Problem for a Nonhomogeneous Plane," ASME JOURNAL OF APPLIED MECHANICS, Vol. 50, pp. 609–614.

Delale, F., and Erdogan, F., 1988, "The interface crack in a nonhomogeneous medium," *Int. J. Engng. Sci.,* Vol. 28, pp. 559–568.

Ely, J.F., and Zienkiewicz, O.C., 1960, "Torsion of compound bars—A relaxation solution," *Int. J. Mech. Sci.,* Vol. 1, pp. 356–365.

Erdogan, F., and Ozturk, M., 1992a, "Diffusion problems in bonded nonhomogeneous materials with an interface cut," *Int. J. Engng. Sci.,* Vol. 30, pp. 1507–1523.

Erdogan, F., and Ozturk, M., 1992b, "Fracture mechanics of debonding in dissimilar bonds through a functionally graded interface zone," *Proceedings of the Second International Symposium on Functionally Gradient Materials,* Third International Ceramic Science & Technology Congress, San Francisco, pp. 31–38.

Eshelby, J.D., 1957, "The determination of the elastic field of an ellipsoidal inclusion, and related problems," *Proc. Roy. Soc. Lond.,* Vol. A241, pp. 276–303.

Ferrari, M., 1992, "Anisotropic layers with through-thickness thermal and material variations," *J. Thermal Stresses,* Vol. 15, pp. 439–445.

Ferrari, M., 1994, "Composite homogenization via the poly-inclusion method," *Composite Engineering,* Vol. 4, pp. 37–45.

Gradshteyn, I.S., and Ryzhik, I.N., 1980, *Table of Integrals, Series and Products.*

Gurtin, M.E., 1972, "The linear theory of elasticity," *Mechanics of Solids,* Vol. II, C. Truesdell, ed., Springer-Verlag, New York.

Holt, J.B., Koizumi, M., Hirai, T., and Munir, Z., 1992, *Proceedings of the Second International Symposium on Functionally Gradient Materials,* Third International Ceramic Science & Technology Congress, San Francisco, 1992.

Downloaded 04 May 2010 to 171.66.16.27. Redistribution subject to ASME license or copyright; see http://www.asme.org/terms/Terms_Use.cfm

Knowles, J.K., "On Saint Venant's principle in the two-dimensional linear theory of elasticity," *Arch. Rat. Mech. Anal.,* Vol. 21, pp. 1–22.

Lekhnitskii, S.G., 1981, *The Theory of Elasticity of an Anisotropic Body,* Mir, Moscow.

Lutz, M.P., and Ferrari, M., 1993, "Compression of a sphere with radially varying elastic moduli," *Composite Engineering,* Vol. 3, pp. 873–884.

Muskhelishvili, N.I., 1963, *Some Basic Problems of the Mathematical Theory of Elasticity,* Noordhoff, Groningen.

Reissner, E., 1964, "Note on the problem of St. Venant flexure," *ZAMP,* Vol. 15, pp. 198–200.

Ronveaux, A., ed., 1995, *Heun's Differential Equations,* Oxford University Press, Oxford, UK.

Rooney, F.J., and Ferrari, M., 1994, "Torsion of a functionally graded shaft with rectangular cross section," *Materials and Design Technology,* ASME, New York, pp. 285–289.

Rooney, F.J., and Ferrari, M., 1995, "Torsion and flexure of inhomogeneous elements," *Composite Engineering,* Vol. 5, pp. 901–911.

St. Venant, A.J.C.B. de, 1855, "Memoire sur la torsion des prismes," *Mem. Divers Savants Acad. Sci. Paris,* Vol. 14, pp. 233–560.

Sternberg, E., 1954, "On Saint-Venant's principle," *Quart. Appl. Math.,* Vol. 11, pp. 393–402.

Schile, R.D., 1962, "Bending of non homogeneous bars," *Int. J. Mech. Sci.,* Vol. 5, pp. 439–445.

Schile, R.D., and Sierakowski, R.L., 1965, "On the Saint Venant problem for a nonhomogeneous elastic material," *Quart. Appl. Math.,* Vol. 23, pp. 19–25.

von Mises, R., 1945, "On Saint-Venant's principle," *Bull. Amer. Math. Soc.,* Vol. 51, pp. 555–562.

Whittaker, E.T., and Watson, G.N., 1927, *A Course of Modern Analysis,* Cambridge University Press, London.

Yamanouchi, M., Koizumi, M., Hirai, T., and Shiota, I., 1990, *Proceedings of the First International Symposium on Functionally Gradient Materials,* Tokyo, 1990.

Downloaded 04 May 2010 to 171.66.16.27. Redistribution subject to ASME license or copyright; see http://www.asme.org/terms/Terms_Use.cfm

Y. S. Kim
Graduate Research Assistant,
School of Civil and Environmental Engineering.

G. A. Kardomateas
Professor,
School of Aerospace Engineering,
Fellow ASME

A. Zureick
Professor,
School of Civil and Environmental Engineering.

Georgia Institute of Technology,
Atlanta, GA 30332

Buckling of Thick Orthotropic Cylindrical Shells Under Torsion

A three-dimensional elasticity solution to the problem of buckling of orthotropic cylindrical shells under torsion is presented. A mixed form of the Galerkin method with a series of Legendre polynomials in the thickness coordinate has been applied to solve the governing differential equations. The accuracy of existing shell theory solutions has been assessed through a comparison study for both isotropic and orthotropic cylinders. For isotropic cylinders the solutions based on the Donnell shell theory were found to predict nonconservative values for the critical loads. As the circumferential wave numbers increase, shell theory solutions provide more accurate values. For orthotropic cylinders, the classical shell theory predicts much higher critical loads for a relatively short and thick cylinder, while the shear deformation theories provide results reasonably close to the elasticity solutions. Detailed data are also presented for the critical torsional loads over a wide range of length ratios and radius ratios for isotropic, glass/epoxy, and graphite/epoxy cylinders.

Introduction

Composite materials have gained widespread usage in structural applications because of their unique properties such as high strength-to-weight ratio and corrosion resistance. Both plate and shell structural laminated composite configurations have found technical applications in aircraft and marine industries. In particular, circular cylindrical shells can be used as primary load-carrying members in many industrial applications (e.g., torsion bars in automotive suspension components) and under a variety of loading configurations. It is therefore of great technical importance when designing lightweight cylindrical shells to clarify the elastic stability characteristics.

The review articles by Ambartsumian (1962), Bert and Francis (1974), Tennyson (1975), and Simitses (1986, 1996) provided detailed accounts of the evolution of the active research dealing with composite cylindrical shells. Some of works summarized in those articles employed classical shell theories and the others did refined theories including shear deformation effects. However, shell theories and formulations, be they classical or refined, are inherently approximate since they are based directly upon initial assumptions and hypotheses. Furthermore, existence of different shell theories underscores the need for elasticity solutions to use as benchmarks for comparison of predictions from the various approximate methods.

Recently, several three-dimensional elasticity-based buckling solutions have become available in the cylindrical shell literature. Babich and Kilin (1985) investigated on axisymmetric but three-dimensional form of stability loss of a three-layered orthotropic cylindrical shell under axial compression. Kardomateas (1993a) dealt with the problem of an orthotropic cylinder under uniform external pressure on the basis of the "ring assumption," in that the prebuckling stress and displacement field was axisymmetric, and the buckling modes were assumed to be two-dimensional. In a further study (Kardomateas and Chung, 1994), this ring assumption was relaxed so that a nonzero axial displacement and a full dependence of buckling modes on the three coordinates were assumed. A more thorough investigation of the thickness effect was conducted by Kardomateas (1993b) for the case of a transversely isotropic thick cylindrical shell under axial compression. In this work, he presented a closed-form solution in terms of Bessel functions.

In more recent studies, Kardomateas (1995, 1996) considered the problem of buckling of orthotropic cylindrical shells under axial compression in one case and combined axial compression and external pressure in another case. These works included comprehensive studies of the performance of shell formulations by Donnell (1933), Flügge (1960), Danielson and Simmonds (1969), and Timoshenko and Gere (1961). Other three-dimensional elasticity results that dealt with orthotropic and cross-ply laminated cylinders and cylindrical panels under combined axial compression and uniform external pressure were presented by Soldatos and Ye (1994) and Ye and Soldatos (1995). These studies provided elasticity solutions by using the successive approximation method.

An investigation of the literature presented above revealed that little information is available on the three-dimensional elasticity-based buckling analysis of orthotropic cylindrical shells under torsion. Therefore, in the current study, an orthotropic cylindrical shell with fixed ends, subjected to torsion, is studied. Employing cylindrical coordinates r, θ, and z (see Fig. 1), the nonlinear three-dimensional theory of elasticity is appropriately formulated following Kardomateas (1993a). This problem is more complicated than the pure external pressure or axial compression one due to the coupled torsional displacement modes of the first-order field (non-separable function of θ and z). Applying displacements at the prebuckling state, buckling equations are reduced to three linear homogenous differential equations in terms of the displacements of the perturbed state. A mixed-form Galerkin procedure is employed to solve these equations and to find numerical values for the critical loads. After comparing the results of this study with the ones from shell theories for a variety of example problems, an extensive parametric study of both isotropic and orthotropic cylinders is performed.

Formulation

For a homogeneous orthotropic cylindrical shell occupying a region in the three-dimensional Euclidean space referred to a cylindrical coordinate system (r, θ, z) in which the z-axis coincides with the longitudinal axis of the shell as shown in Fig. 1, the stress-strain relationships can be expressed in the form

Contributed by the Applied Mechanics Division of THE AMERICAN SOCIETY OF MECHANICAL ENGINEERS for publication in the ASME JOURNAL OF APPLIED MECHANICS.

Discussion on the paper should be addressed to the Technical Editor, Professor Lewis T. Wheeler, Department of Mechanical Engineering, University of Houston, Houston, TX 77204-4792, and will be accepted until four months after final publication of the paper itself in the ASME JOURNAL OF APPLIED MECHANICS.

Manuscript received by the ASME Applied Mechanics Division, Feb. 10, 1998; final revision, May 12, 1998. Associate Technical Editor: S. Kyriakides.

 Copyright © 1999 by ASME

Downloaded 04 May 2010 to 171.66.16.27. Redistribution subject to ASME license or copyright; see http://www.asme.org/terms/Terms_Use.cfm

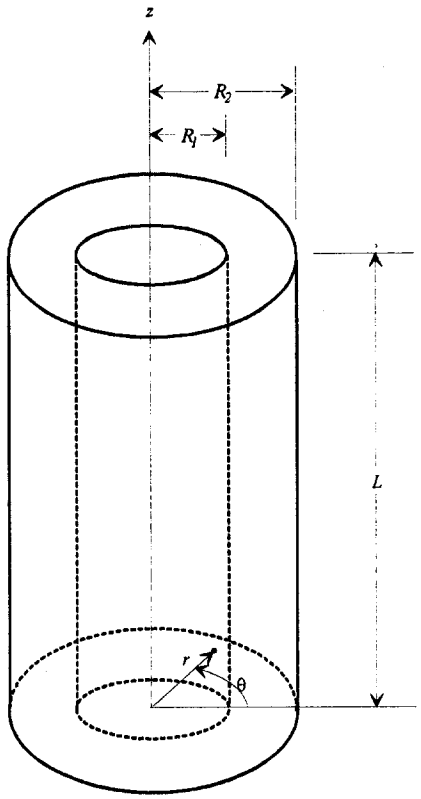

Fig. 1 Dimensions and coordinates for a cylindrical shell

$$\begin{bmatrix} \sigma_{rr} \\ \sigma_{\theta\theta} \\ \sigma_{zz} \\ \tau_{\theta z} \\ \tau_{rz} \\ \tau_{r\theta} \end{bmatrix} = \begin{bmatrix} c_{11} & c_{12} & c_{13} & 0 & 0 & 0 \\ c_{12} & c_{22} & c_{23} & 0 & 0 & 0 \\ c_{13} & c_{23} & c_{33} & 0 & 0 & 0 \\ 0 & 0 & 0 & c_{44} & 0 & 0 \\ 0 & 0 & 0 & 0 & c_{55} & 0 \\ 0 & 0 & 0 & 0 & 0 & c_{66} \end{bmatrix} \begin{bmatrix} \epsilon_{rr} \\ \epsilon_{\theta\theta} \\ \epsilon_{zz} \\ \gamma_{\theta z} \\ \gamma_{rz} \\ \gamma_{r\theta} \end{bmatrix}, \quad (1)$$

where c_{ij} are the stiffness coefficients and ϵ_{rr}, $\epsilon_{\theta\theta}$, ϵ_{zz}, $\gamma_{r\theta}$, γ_{rz}, $\gamma_{\theta z}$ are the engineering strains defined by the following nonlinear kinematic equations:

$$\epsilon_{rr} = u_{,r} + \tfrac{1}{2}(u_{,r}^2 + v_{,r}^2 + w_{,r}^2), \quad (2a)$$

$$\epsilon_{\theta\theta} = \frac{v_{,\theta}}{r} + \frac{u}{r} + \frac{1}{2r^2}[(u_{,\theta} - v)^2 + (v_{,\theta} + u)^2 + (w_{,\theta})^2], \quad (2b)$$

$$\epsilon_{zz} = w_{,z} + \tfrac{1}{2}(u_{,z}^2 + v_{,z}^2 + w_{,z}^2), \quad (2c)$$

$$\gamma_{r\theta} = \frac{u_{,\theta}}{r} + v_{,r} - \frac{v}{r} + \frac{1}{r}[u_{,r}(u_{,\theta} - v) + v_{,r}(v_{,\theta} + u) + w_{,r}(w_{,\theta})], \quad (2d)$$

$$\gamma_{rz} = u_{,z} + w_{,r} + (u_{,r}u_{,z} + v_{,r}v_{,z} + w_{,r}w_{,z}), \quad (2e)$$

$$\gamma_{\theta z} = v_{,z} + \frac{w_{,\theta}}{r} + \frac{1}{r}[u_{,z}(u_{,\theta} - v) + v_{,z}(v_{,\theta} + u) + w_{,z}(w_{,\theta})]. \quad (2f)$$

In the general stability theory of elastic solids, it is known that at the critical load there are two possible infinitely close positions of equilibrium. Denoting u_0, v_0, w_0 as the r, θ, and z components of displacement corresponding to the primary position, the displacements in the perturbed position are denoted by

$$u = u_0 + \alpha u_1(r, \theta, z); \quad v = v_0 + \alpha v_1(r, \theta, z);$$
$$w = w_0 + \alpha w_1(r, \theta, z), \quad (3)$$

where α is an infinitesimally small quantity. Here, $\alpha u_1(r, \theta, z)$, $\alpha v_1(r, \theta, z)$, and $\alpha w_1(r, \theta, z)$ are displacements that points of the body must undergo to shift them from their initial equilibrium position to their new equilibrium position. The functions $u_1(r, \theta, z)$, $v_1(r, \theta, z)$, and $w_1(r, \theta, z)$ are assumed finite and α is independent of r, θ, and z.

Substituting (3) into (2) results in the following equations for the strain components in the perturbed state:

$$\epsilon_{ij} = \epsilon_{ij}^0 + \alpha\epsilon_{ij}' + \alpha^2\epsilon_{ij}'', \quad (4)$$

where ϵ_{ij}^0 are values of the strain components in the initial position of equilibrium; ϵ_{ij}' are strain quantities that depend on derivatives of both u_0, v_0, w_0 and u_1, v_1, w_1; and ϵ_{ij}'' are parameters that depend only on derivatives of u_1, v_1, w_1 and contain only quadratic terms. Substitution of (4) into (1) yields

$$\sigma_{ij} = \sigma_{ij}^0 + \alpha\sigma_{ij}' + \alpha^2\sigma_{ij}'', \quad (5)$$

where σ_{ij}^0, σ_{ij}', and σ_{ij}'' can be expressed in the form of (1) by replacing ϵ_{ij} by ϵ_{ij}^0, ϵ_{ij}', and ϵ_{ij}'', respectively.

From three-dimensional elasticity theory (Ciarlet, 1988), the equations of equilibrium are expressed in terms of the second Piola-Kirchhoff stress tensor Σ in the form

$$\text{div}(\Sigma \cdot F^T) = 0, \quad (6)$$

where F is the deformation gradient defined by

$$F = I + (\text{grad } V)^T, \quad (7)$$

where V is the displacement vector and I is the identity tensor. The linear strains are also introduced as

$$e_{rr} = u_{,r}, \quad e_{\theta\theta} = \frac{v_{,\theta}}{r} + \frac{u}{r}, \quad e_{zz} = w_{,z}, \quad (8a)$$

$$e_{r\theta} = \frac{u_{,\theta}}{r} + v_{,r} - \frac{v}{r}, \quad e_{rz} = u_{,z} + w_{,r}, \quad e_{\theta z} = v_{,z} + \frac{w_{,\theta}}{r}, \quad (8b)$$

and the linear rotations as

$$2\omega_r = \frac{w_{,\theta}}{r} - v_{,z}, \quad 2\omega_\theta = u_{,z} - w_{,r}, \quad 2\omega_z = v_{,r} + \frac{v}{r} - \frac{u_{,\theta}}{r}. \quad (8c)$$

Following Kardomateas (1993a), the following buckling equations govern the first-order field:

$$\frac{\partial}{\partial r}(\sigma_{rr}' - \tau_{r\theta}^0\omega_z' + \tau_{rz}^0\omega_\theta') + \frac{1}{r}\frac{\partial}{\partial\theta}(\tau_{r\theta}' - \sigma_{\theta\theta}^0\omega_z' + \tau_{\theta z}^0\omega_\theta') + \frac{\partial}{\partial z}(\tau_{rz}' - \tau_{\theta z}^0\omega_z' + \sigma_{zz}^0\omega_\theta') + \frac{1}{r}(\sigma_{rr}' - \sigma_{\theta\theta}' + \tau_{rz}^0\omega_\theta' + \tau_{\theta z}^0\omega_r' - 2\tau_{r\theta}^0\omega_z') = 0, \quad (9a)$$

$$\frac{\partial}{\partial r}(\tau_{r\theta}' + \sigma_{rr}^0\omega_z' + \tau_{rz}^0\omega_r') + \frac{1}{r}\frac{\partial}{\partial\theta}(\sigma_{\theta\theta}' + \tau_{r\theta}^0\omega_z' - \tau_{\theta z}^0\omega_r') + \frac{\partial}{\partial z}(\tau_{\theta z}' + \tau_{rz}^0\omega_z' - \sigma_{zz}^0\omega_r') + \frac{1}{r}(2\tau_{r\theta}' + \sigma_{rr}^0\omega_z' - \sigma_{\theta\theta}^0\omega_z' + \tau_{\theta z}^0\omega_\theta' - \tau_{rz}^0\omega_r') = 0, \quad (9b)$$

Downloaded 04 May 2010 to 171.66.16.27. Redistribution subject to ASME license or copyright; see http://www.asme.org/terms/Terms_Use.cfm

$$\frac{\partial}{\partial r}(\tau'_{rz} - \sigma^0_{rr}\omega'_\theta + \tau^0_{r\theta}\omega'_r) + \frac{1}{r}\frac{\partial}{\partial \theta}(\tau'_{\theta z} - \tau^0_{r\theta}\omega'_\theta + \sigma^0_{\theta\theta}\omega'_r)$$

$$+ \frac{\partial}{\partial z}(\sigma'_{zz} - \tau^0_{rz}\omega'_\theta + \tau^0_{\theta z}\omega'_r)$$

$$+ \frac{1}{r}(\tau'_{rz} - \sigma^0_{rr}\omega'_\theta + \tau^0_{r\theta}\omega'_r) = 0. \quad (9c)$$

The boundary conditions associated with (6) can be expressed as

$$(F \cdot \Sigma^T) \cdot \hat{N} = t(V), \quad (10)$$

where t is the traction vector on the surface having an outward unit normal $\hat{N} = (\hat{l}, \hat{m}, \hat{n})$ before deformation. Traction vector t depends on the displacement field $V = (u, v, w)$. Again, following Kardomateas (1993a), the following boundary conditions at the lateral and end surfaces are obtained:

$$(\sigma'_{rr} - \tau^0_{r\theta}\omega'_z + \tau^0_{rz}\omega'_\theta)\hat{l} + (\tau'_{r\theta} - \sigma^0_{\theta\theta}\omega'_z + \tau^0_{\theta z}\omega'_\theta)\hat{m}$$

$$+ (\tau'_{rz} - \tau^0_{\theta z}\omega'_z + \sigma^0_{zz}\omega'_\theta)\hat{n} = 0, \quad (11a)$$

$$(\tau'_{r\theta} + \sigma^0_{rr}\omega'_z + \tau^0_{rz}\omega'_r)\hat{l} + (\sigma'_{\theta\theta} + \tau^0_{r\theta}\omega'_z - \tau^0_{\theta z}\omega'_r)\hat{m}$$

$$+ (\tau'_{\theta z} + \tau^0_{rz}\omega'_z - \sigma^0_{zz}\omega'_r)\hat{n} = 0, \quad (11b)$$

$$(\sigma'_{rr} - \tau^0_{r\theta}\omega'_z + \tau^0_{rz}\omega'_\theta)\hat{l} + (\tau'_{r\theta} - \sigma^0_{\theta\theta}\omega'_z + \tau^0_{\theta z}\omega'_\theta)\hat{m}$$

$$+ (\tau'_{rz} - \tau^0_{\theta z}\omega'_z + \sigma^0_{zz}\omega'_\theta)\hat{n} = 0. \quad (11c)$$

In an orthotropic cylindrical shell subjected to pure torsion, the cross section of the cylinder simply rotates about the longitudinal axis, and thus similar to the case of isotropy, the displacements at the initial position are expressed in the form:

$$u_0 = w_0 = 0; \quad v_0 = \frac{M}{C} rz, \quad (12)$$

where M is the torque at both ends and C is the torsional rigidity of the cylinder, defined as $C = c_{44}\pi(R_2^4 - R_1^4)/2$, where R_1 and R_2 are inner and outer radius, respectively.

Using Eqs. (1) and (8), we obtain the strain components at the prebuckling state,

$$e^0_{rr} = e^0_{\theta\theta} = e^0_{zz} = e^0_{r\theta} = e^0_{rz} = 0, \quad e^0_{\theta z} = \frac{M}{C} r, \quad (13)$$

and the stress components,

$$\sigma^0_{rr} = \sigma^0_{\theta\theta} = \sigma^0_{zz} = \tau^0_{r\theta} = \tau^0_{rz} = 0, \quad \tau^0_{\theta z} = \frac{c_{44}M}{C} r. \quad (14)$$

Substitution of (14) and the expressions for σ'_{ij} and ω'_i in terms of the displacements from (1) and (8) transforms the buckling Eqs. (9) into the following system of three linear homogenous partial differential equations with three unknown displacement functions u_1, v_1, and w_1:

$$c_{11}u_{1,rr} + c_{11}\frac{u_{1,r}}{r} + c_{66}\frac{u_{1,\theta\theta}}{r^2} + c_{55}u_{1,zz} - c_{22}\frac{u_1}{r^2} + 2\bar{M}u_{1,\theta z}$$

$$+ (c_{12} + c_{66})\frac{v_{1,r\theta}}{r} - (c_{22} + c_{66})\frac{v_{1,\theta}}{r^2} - \bar{M}(rv_{1,rz} + 2v_{1,z})$$

$$+ (c_{13} + c_{55})w_{1,rz} + (c_{13} - c_{23})\frac{w_{1,z}}{r}$$

$$- \bar{M}\left(w_{1,r\theta} - \frac{w_{1,\theta}}{r}\right) = 0, \quad (15a)$$

$$(c_{12} + c_{66})\frac{u_{1,r\theta}}{r} + (c_{22} + c_{66})\frac{u_{1,\theta}}{r^2} + \bar{M}u_{1,z} + c_{66}v_{1,rr} + c_{66}\frac{v_{1,r}}{r}$$

$$+ c_{22}\frac{v_{1,\theta\theta}}{r^2} + c_{44}v_{1,zz} - c_{66}\frac{v_1}{r^2} + \bar{M}v_{1,\theta z} + (c_{23} + c_{44})\frac{w_{1,\theta z}}{r}$$

$$- \bar{M}\left(w_{1,r} + \frac{w_{1,\theta\theta}}{r}\right) = 0, \quad (15b)$$

$$(c_{13} + c_{55})u_{1,rz} + (c_{23} + c_{55})\frac{u_{1,z}}{r} + (c_{23} + c_{44})\frac{v_{1,\theta z}}{r} - \bar{M}rv_{1,zz}$$

$$+ c_{55}w_{1,rr} + c_{55}\frac{w_{1,r}}{r} + c_{44}\frac{w_{1,\theta\theta}}{r^2} + c_{33}w_{1,zz} + \bar{M}w_{1,\theta z} = 0. \quad (15c)$$

In the same manner, three homogeneous boundary conditions can be obtained from (11) for the lateral surfaces for $\hat{m} = \hat{n} = 0$ and $\hat{l} = \pm 1$:

$$c_{11}u_{1,r} + c_{12}\frac{u_1}{r} + c_{12}\frac{v_{1,\theta}}{r} + c_{13}w_{1,z} = 0 \text{ at } r = R_1, R_2, \quad (16a)$$

$$c_{66}\frac{u_{1,\theta}}{r} + c_{66}v_{1,r} - c_{66}\frac{v_1}{r} = 0 \text{ at } r = R_1, R_2, \quad (16b)$$

$$c_{55}u_{1,z} + c_{55}w_{1,r} = 0 \text{ at } r = R_1, R_2, \quad (16c)$$

where $\bar{M} = Mc_{44}/2C$.

There is a substantial difference between Eqs. (15) and those obtained by Kardomateas (1993a, 1995) for the case of buckling of an orthotropic cylindrical shell subjected to lateral or axial compression. This difference is that in the same equation we encounter both odd and even orders of derivatives of a displacement with respect to the same independent variable. This prevents one from reducing (15) to ordinary differential equations by applying a separable form of displacement functions as in the external pressure or the axial compression loading case. Therefore, a solution procedure using the Galerkin method is employed in this study.

For convenience, equations (15) and (16) are rewritten in the form

$$L_{i1}(u_1) + L_{i2}(v_1) + L_{i3}(w_1) = 0, \quad i = 1, 2, 3, \quad (17a)$$

$$B_{i1}(u_1) + B_{i2}(v_1) + B_{i3}(w_1) = 0, \quad i = 1, 2, 3, \quad (17b)$$

where L_{ij} and B_{ij} are differential operators of second order.

Solution Methodology

In solving problems using the Galerkin technique, three methods can be used to choose trial functions: the interior method, the boundary method, and the mixed method. In this study, the mixed method (Mikhlin, 1964, Bolotin, 1963, Finlayson, 1972) is employed to overcome the complexity of finding trial functions that satisfy either the differential Eqs. (17a) or the boundary conditions (17b). Use of the Galerkin procedure requires that the interior and boundary weighted residuals vanish. For the first differential equation and boundary condition corresponding to $i = 1$ in (17), these appear as

$$\int_V \hat{u}_j[L_{11}(u_1) + L_{12}(v_1) + L_{13}(w_1)]dV = 0, \quad (18a)$$

$$\int_S \hat{u}_j[B_{11}(u_1) + B_{12}(v_1) + B_{13}(w_1)]dS = 0, \quad (18b)$$

where $\hat{u}_j$ is the jth term of the trial functions of the displacement u_1. Similarly, those residuals can be written for the second and third equations corresponding to $i = 2, 3$ in (17) by subsequently replacing $\hat{u}_j$ with $\hat{v}_j$ and $\hat{w}_j$, respectively. After per-

Downloaded 04 May 2010 to 171.66.16.27. Redistribution subject to ASME license or copyright; see http://www.asme.org/terms/Terms_Use.cfm

forming integration by parts with respect to r on (18a) and combining it with (18b), and doing similar procedures for the other two sets of equations, we can obtain the following three sets of governing equations:

$$\int_V \{\hat{u}_j[L'_{11}(u_1) + L'_{12}(v_1) + L'_{13}(w_1)] - \hat{u}_{j,r}[B'_{11}(u_1) + B'_{12}(v_1) + B'_{13}(w_1)]\}dV = 0, \quad (19a)$$

$$\int_V \{\hat{v}_j[L'_{21}(u_1) + L'_{22}(v_1) + L'_{23}(w_1)] - \hat{v}_{j,r}[B'_{21}(u_1) + B'_{22}(v_1) + B'_{23}(w_1)]\}dV = 0, \quad (19b)$$

$$\int_V \{\hat{w}_j[L'_{31}(u_1) + L'_{32}(v_1) + L'_{33}(w_1)] - \hat{w}_{j,r}[B'_{31}(u_1) + B'_{32}(v_1) + B'_{33}(w_1)]\}dV = 0, \quad (19c)$$

where the modified operators L'_{ij} and B'_{ij} are given in Appendix A.

Considering the fixed boundary conditions at the longitudinal edges $z = 0, L$, trial functions for the displacements are chosen as

$$u_1 = \sum_{k=1}^{K_1}\sum_{m=1}^{M_1} P_k(r)[A_{kmn}\,\mathrm{Sin}\,(n\theta) + B_{kmn}\,\mathrm{Cos}\,(n\theta)]\,\mathrm{Sin}\,(\lambda_m z), \quad (20a)$$

$$v_1 = \sum_{k=1}^{K_2}\sum_{m=1}^{M_2} P_k(r)[C_{kmn}\,\mathrm{Sin}\,(n\theta) + D_{kmn}\,\mathrm{Cos}\,(n\theta)]\,\mathrm{Sin}\,(\lambda_m z), \quad (20b)$$

$$w_1 = \sum_{k=0}^{K_3-1}\sum_{m=1}^{M_3} P_k(r)[E_{kmn}\,\mathrm{Sin}\,(n\theta) + F_{kmn}\,\mathrm{Cos}\,(n\theta)]\,\mathrm{Sin}\,(\lambda_m z), \quad (20c)$$

where $P_k(r)$ is a kth term set of Legendre polynomials, $\lambda_m = m\pi/L$, and A_{kmn}, B_{kmn}, C_{kmn}, D_{kmn}, E_{kmn}, F_{kmn} are unknown coefficients. The integer values n and m in Eqs. (20) represent the number of waves around the circumference and along the length of the cylinder, respectively. Upon substituting Eqs. (20) into Eqs. (19) and integrating, we obtain six sets of linear algebraic equations. The $(q + k)$th terms for the first and second sets of the $(K_1 \times M_1)$ equations are, respectively,

$$\sum_{k=1}^{K_1}\sum_{m=1}^{M_1}[(\Gamma^{(11)}_{qk} + \lambda_m^2\Gamma^{(14)}_{qk} + \Psi^{(11)}_{qk})\Phi^{(1)}_{pm}A_{kmn} - \bar{M}(\Lambda^{(11)}_{qk})\lambda_m\Phi^{(2)}_{pm}B_{kmn}] - \sum_{k=1}^{K_2}\sum_{m=1}^{M_2}[(\Gamma^{(12)}_{qk} + \Psi^{(12)}_{qk})\Phi^{(1)}_{pm}D_{kmn} - \bar{M}(\Lambda^{(12)}_{qk})\lambda_m\Phi^{(2)}_{pm}C_{kmn}] + \sum_{k=0}^{K_3-1}\sum_{m=1}^{M_3}[(\Gamma^{(13)}_{qk} + \Psi^{(13)}_{qk})\lambda_m\Phi^{(2)}_{pm}E_{kmn} - \bar{M}(\Lambda^{(13)}_{qk})\Phi^{(1)}_{pm}F_{kmn}] = 0, \quad (21a)$$

$$\sum_{k=1}^{K_1}\sum_{m=1}^{M_1}[(\Gamma^{(11)}_{qk} + \lambda_m^2\Gamma^{(14)}_{qk} + \Psi^{(11)}_{qk})\Phi^{(1)}_{pm}B_{kmn} + \bar{M}(\Lambda^{(11)}_{qk})\lambda_m\Phi^{(2)}_{pm}A_{kmn}] + \sum_{k=1}^{K_2}\sum_{m=1}^{M_2}[(\Gamma^{(12)}_{qk} + \Psi^{(12)}_{qk})\Phi^{(1)}_{pm}C_{kmn} + \bar{M}(\Lambda^{(12)}_{qk})\lambda_m\Phi^{(2)}_{pm}D_{kmn}] + \sum_{k=0}^{K_3-1}\sum_{m=1}^{M_3}[(\Gamma^{(13)}_{qk} + \Psi^{(13)}_{qk})\lambda_m\Phi^{(2)}_{pm}F_{kmn} + \bar{M}(\Lambda^{(13)}_{qk})\Phi^{(1)}_{pm}E_{kmn}] = 0, \quad (21b)$$

the $(q + k)$th terms for the third and fourth sets of the $(K_2 \times M_2)$ equations are, respectively,

$$-\sum_{k=1}^{K_1}\sum_{m=1}^{M_1}[(\Gamma^{(21)}_{qk} + \Psi^{(21)}_{qk})\Phi^{(1)}_{pm}B_{kmn} - \bar{M}(\Lambda^{(21)}_{qk})\lambda_m\Phi^{(2)}_{pm}A_{kmn}] + \sum_{k=1}^{K_2}\sum_{m=1}^{M_2}[(\Gamma^{(22)}_{qk} + \lambda_m^2\Gamma^{(24)}_{qk} + \Psi^{(22)}_{qk})\Phi^{(1)}_{pm}C_{kmn} - \bar{M}(\Lambda^{(22)}_{qk})\lambda_m\Phi^{(2)}_{pm}D_{kmn}] - \sum_{k=0}^{K_3-1}\sum_{m=1}^{M_3}[(\Gamma^{(23)}_{qk} + \Psi^{(23)}_{qk})\lambda_m\Phi^{(2)}_{pm}F_{kmn} - \bar{M}(\Lambda^{(23)}_{qk})\Phi^{(1)}_{pm}E_{kmn}] = 0, \quad (21c)$$

$$\sum_{k=1}^{K_1}\sum_{m=1}^{M_1}[(\Gamma^{(21)}_{qk} + \Psi^{(21)}_{qk})\Phi^{(1)}_{pm}A_{kmn} + \bar{M}(\Lambda^{(21)}_{qk})\lambda_m\Phi^{(2)}_{pm}B_{kmn}] + \sum_{k=1}^{K_2}\sum_{m=1}^{M_2}[(\Gamma^{(22)}_{qk} + \lambda_m^2\Gamma^{(24)}_{qk} + \Psi^{(22)}_{qk})\Phi^{(1)}_{pm}D_{kmn} + \bar{M}(\Lambda^{(22)}_{qk})\lambda_m\Phi^{(2)}_{pm}C_{kmn}] + \sum_{k=0}^{K_3-1}\sum_{m=1}^{M_3}[(\Gamma^{(23)}_{qk} + \Psi^{(23)}_{qk})\lambda_m\Phi^{(2)}_{pm}E_{kmn} + \bar{M}(\Lambda^{(23)}_{qk})\Phi^{(1)}_{pm}F_{kmn}] = 0, \quad (21d)$$

and finally, the $(q + k)$th terms for the fifth and sixth sets of the $(K_3 \times M_3)$ equations are, respectively,

$$\sum_{k=1}^{K_1}\sum_{m=1}^{M_1}[(\Gamma^{(31)}_{qk} + \Psi^{(31)}_{qk})\lambda_m\Phi^{(2)}_{pm}A_{kmn}] - \sum_{k=1}^{K_2}\sum_{m=1}^{M_2}[(\Gamma^{(32)}_{qk} + \Psi^{(32)}_{qk})\lambda_m\Phi^{(2)}_{pm}D_{kmn} - \bar{M}(\lambda_m^2\Lambda^{(32)}_{qk})\Phi^{(1)}_{pm}C_{kmn}] + \sum_{k=0}^{K_3-1}\sum_{m=1}^{M_3}[(\Gamma^{(33)}_{qk} + \lambda_m^2\Gamma^{(34)}_{qk} + \Psi^{(33)}_{qk})\Phi^{(1)}_{pm}E_{kmn} - \bar{M}(\Lambda^{(33)}_{qk})\lambda_m\Phi^{(2)}_{pm}F_{kmn}] = 0, \quad (21e)$$

$$\sum_{k=1}^{K_1}\sum_{m=1}^{M_1}[(\Gamma^{(31)}_{qk} + \Psi^{(31)}_{qk})\lambda_m\Phi^{(2)}_{pm}B_{kmn}] + \sum_{k=1}^{K_2}\sum_{m=1}^{M_2}[(\Gamma^{(32)}_{qk} + \Psi^{(32)}_{qk})\lambda_m\Phi^{(2)}_{pm}C_{kmn} + \bar{M}(\lambda_m^2\Lambda^{(32)}_{qk})\Phi^{(1)}_{pm}D_{kmn}] + \sum_{k=0}^{K_3-1}\sum_{m=1}^{M_3}[(\Gamma^{(33)}_{qk} + \lambda_m^2\Gamma^{(34)}_{qk} + \Psi^{(33)}_{qk})\Phi^{(1)}_{pm}F_{kmn} + \bar{M}(\Lambda^{(33)}_{qk})\lambda_m\Phi^{(2)}_{pm}E_{kmn}] = 0. \quad (21f)$$

In Eqs. (21) above, constants from integration of the trigonometric functions in the z direction are denoted by

$$\Phi^{(1)}_{pm} = \int_0^L \mathrm{Sin}\,(\lambda_p z)\,\mathrm{Sin}\,(\lambda_m z)dz, \quad (22a)$$

$$\Phi^{(2)}_{pm} = \int_0^L \mathrm{Sin}\,(\lambda_p z)\,\mathrm{Cos}\,(\lambda_m z)dz, \quad (22b)$$

and those from integration with respect to r are

$$\Gamma^{(ij)}_{qk} = \int_{R_1}^{R_2} P_q D^S_{ij}(P_k)rdr, \quad (23a)$$

$$\Lambda^{(ij)}_{qk} = \int_{R_1}^{R_2} P_q D^G_{ij}(P_k)rdr, \quad (23b)$$

$$\Psi^{(ij)}_{qk} = -\int_{R_1}^{R_2} P_{q,r}K_{ij}(P_k)rdr, \quad (23c)$$

where D^S_{ij} and D^G_{ij} are the ensuing r-dependent terms after substituting the trial displacement functions in (20) into the operators L'_{ij} in (19). Similarly K_{ij} are the ensuing r-dependent terms after substituting (20) into B'_{ij} in (19). D^S_{ij}, D^G_{ij}, and K_{ij} are given explicitly in Appendix B.

Equations (21) yield $2 \times (K_1 \times M_1 + K_2 \times M_2 + K_3 \times M_3)$ algebraic equations. However, it can be noted that the terms

Downloaded 04 May 2010 to 171.66.16.27. Redistribution subject to ASME license or copyright; see http://www.asme.org/terms/Terms_Use.cfm

Table 1 Aspect ratios of an isotropic cylinder corresponding to the results of Figs. 2 and 3

	L/R_c, R_c/h							
	n							
Z	2	3	4	5	6	7	8	9
10000	21.05, 23.66	14.03, 53.24	10.52, 94.64	8.419, 147.9	7.016, 212.9	6.014, 289.8	5.262, 378.6	4.677, 479.1
5000	17.28, 17.56	11.52, 39.50	8.639, 70.22	6.912, 109.7	5.760, 158.0	4.937, 215.1	4.320, 280.9	3.840, 355.5
2000	13.31, 11.84	8.870, 26.65	6.652, 47.38	5.322, 74.03	4.435, 106.6	3.801, 145.1	3.326, 189.5	2.957, 239.8
1000	10.79, 9.002	7.194, 20.25	5.396, 36.01	4.317, 56.26	3.597, 81.02	3.083, 110.3	2.698, 144.0	2.398, 182.3
500	8.671, 6.972	5.781, 15.69	4.335, 27.89	3.468, 43.57	2.890, 62.74	2.477, 85.40	2.168, 111.5	1.927, 141.2
200	6.362, 5.180	4.241, 11.66	3.181, 20.72	2.545, 32.38	2.121, 46.62	1.818, 63.46	1.590, 82.89	1.414, 104.9
100	4.948, 4.282	3.299, 9.634	2.474, 17.13	1.979, 26.76	1.649, 38.54	1.414, 52.45	1.237, 68.51	1.100, 86.71
50	3.817, 3.597	2.545, 8.094	1.909, 14.39	1.527, 22.48	1.272, 32.38	1.091, 44.07	0.954, 57.56	0.848, 72.85
20	2.733, 2.807	1.822, 6.315	1.367, 11.23	1.093, 17.54	0.911, 25.26	0.781, 34.38	0.683, 44.91	0.607, 56.83
10	2.246, 2.078	1.497, 4.675	1.123, 8.311	0.898, 12.99	0.749, 18.70	0.642, 25.45	0.562, 33.24	0.499, 42.07

including $\bar{M}$ in (21) have either A_{kmn}, D_{kmn}, E_{kmn} only or B_{kmn}, C_{kmn}, F_{kmn} only. Therefore, Eqs. (21) can be divided into two parts to reduce the dimensions of matrices to be handled. These two partitioned sets of equations are in the form

$$[P]\{\alpha\} + \bar{M}[Q]\{\beta\} = \{0\}, \tag{24a}$$

$$[S]\{\beta\} + \bar{M}[R]\{\alpha\} = \{0\}, \tag{24b}$$

where $\{\alpha\} = \lfloor A_{kmn}, D_{kmn}, E_{kmn} \rfloor^T$ and $\{\beta\} = \lfloor B_{kmn}, C_{kmn}, F_{kmn} \rfloor^T$. The matrices P, Q, R, and S have the dimension of $(K_1 \times M_1) + (K_2 \times M_2) + (K_3 \times M_3)$, respectively. From (24$a$) we obtain

$$\{\alpha\} = -\bar{M}[P]^{-1}[Q]\{\beta\}. \tag{25}$$

Substitution into (24b) yields

$$([S] - \bar{M}^2[G])\{\beta\} = \{0\}, \tag{26}$$

where $[G] = [R][P]^{-1}[Q]$.

Equation (26) constitutes a generalized eigensystem with $\bar{M}^2$ being the eigenvalue. The system has a nontrivial solution if and only if the determinant of $[S] - \bar{M}^2[G]$ vanishes.

Numerical Results and Discussion

Numerical results based on the preceding formulations have been generated for a wide range of geometrical and material parameters affecting the behavior of cylindrical shells under torsional loads. For all cases considered, the critical torsional load was computed using a QR algorithm combined with similarity reduction of general matrix to upper Hessenberg form (Wilkinson and Reinsch, 1971). When calculating eigenvalues, extended precision (28 significant figures) was used. By increasing the integer value of circumferential wave number, n, the lowest eigenvalue corresponding to the critical load was found.

Comparison With Existing Isotropic Shell Solutions. For an isotropic cylinder subjected to torsion, Yamaki (1984) presented numerical results pertaining to the critical shear stress, τ_{cr}, and the corresponding circumferential wave number parameter, $\beta = nL/\pi R_c$, where R_c and L are the radius of the midline surface and the length of the shell, respectively. He employed a direct integration method combined with an iterative technique to Donnell's buckling equations and concluded that Donnell's equations yielded sufficiently accurate results when n is greater than 4. The inaccuracy of the Donnell's equations for the cases with low values of n refers to the shallow shell approximation that omits the in-plane displacement component in certain kinematic relations. It should be noted that he specified the geometric property of the shell by only one parameter $Z = \sqrt{1-\nu^2}(L/R_c)^2(R_c/h)$, which is known as the Batdorf parameter, where h is the thickness of the shell, and then minimized eigenvalues with respect to the wave number by treating β as a continuous variable.

In order to compare Yamaki's results with those from this study, a combination of the geometric parameters with an assumed integer value of n for a particular isotropic cylinder was selected so as to correspond to the published values of Z and β by Yamaki. For convenience, these parameters (L/R_c and R_c/h) are given in Table 1. A range of n from 2 to 9 was used and R_c was set to 0.1905 m.

In addition to the shell theory results by Yamaki, those from a simplified formula derived by Donnell (1933) were also compared with the present elasticity solutions. Donnell presented the following formula for the critical shear stress of ends-fixed short and moderately long shells subjected to torsion:

$$\tau_{cr} = \frac{E}{(1-\nu^2)}\frac{h^2}{L^2}\left[4.6 + \sqrt{7.8 + 1.67\left(\sqrt{1-\nu^2}\,\frac{L^2}{2hR_c}\right)^{3/2}}\right]. \tag{27}$$

The critical torsional load, M_{cr}, can then be calculated:

$$M_{cr} = \tau_{cr}\frac{2\pi}{3}(R_2^3 - R_1^3). \tag{28}$$

Table 2 shows critical torsional loads, as predicted by the present three-dimensional elasticity formulation, compared with those predicted by Donnell's formula and Yamaki for a typical value of circumferential wave number $n = 5$. Since an isotropic cylinder was investigated, Young's modulus E was assumed to

Table 2 Comparison of results for an isotropic cylinder ($n = 5$)

	Critical torsional loads ($N \cdot m \times 10^{-7}$)		
Z	Elasticity	Donnell (% increase vs. Elasticity)	Yamaki (% increase vs. Elasticity)
10000	1.565	1.610 (2.82%)	1.578 (0.82%)
5000	3.366	3.491 (3.70%)	3.393 (0.79%)
2000	9.238	9.740 (5.44%)	9.312 (0.81%)
1000	18.95	20.32 (7.26%)	19.10 (0.79%)
500	37.58	41.20 (9.64%)	37.86 (0.74%)
200	86.97	98.96 (13.8%)	87.54 (0.65%)
100	157.2	184.8 (17.5%)	158.1 (0.57%)
50	287.0	348.0 (21.3%)	289.3 (0.80%)
20	737.3	916.7 (24.3%)	759.1 (2.95%)
10	2069	2633 (27.3%)	2271 (9.76%)

Downloaded 04 May 2010 to 171.66.16.27. Redistribution subject to ASME license or copyright; see http://www.asme.org/terms/Terms_Use.cfm

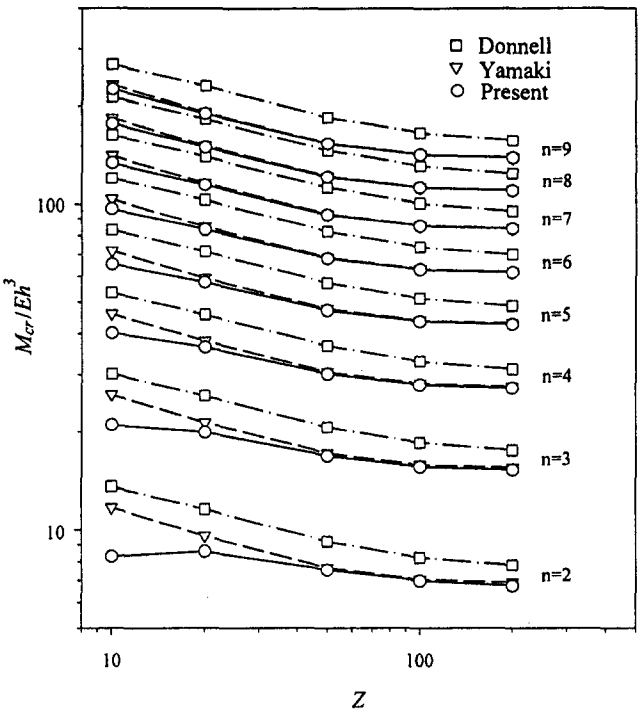

Fig. 2 Comparison of critical loads for an isotropic cylinder ($Z \leq 200$)

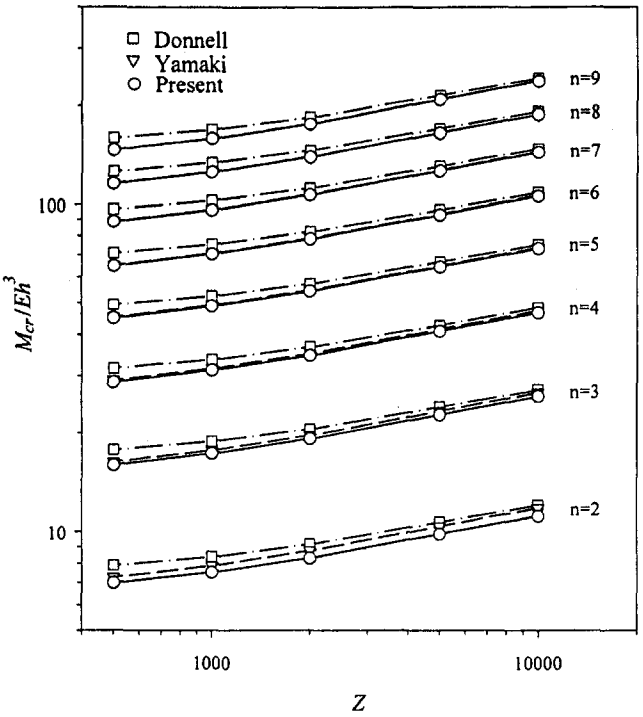

Fig. 3 Comparison of critical loads for an isotropic cylinder ($Z \geq 500$)

be unity for convenience and Poisson's ratio ν was taken as 0.3.

It is clearly seen from Table 2 that Yamaki's results are much closer to the elasticity solutions than those from the Donnell's simplified formula and that both shell theory solutions result in nonconservative critical torsional loads. Discrepancies between the elasticity solution and Donnell's formula increase as the parameter Z becomes small, as is the case for short and thick cylinders. On the other hand, differences between the Yamaki's result and elasticity solution are independent of values of Z as long as Z is greater than 50. Discrepancies increase drastically for very short and moderately thick cylinders with values of Z less than 20.

Critical torsional loads for the same isotropic cylinder that buckles into wave numbers other than 5 were also calculated and compared with those from shell theories. Results are shown graphically in Figs. 2 and 3, where the nondimensionalized critical torque M_{cr}/Eh^3 is plotted against the parameter Z. Similar observations can be made for the cases with n other than 5. In addition, the larger the wave number n for the same values of Z, the smaller the differences between both shell theory approaches and the elasticity solutions. It should be noted that circumferential wave numbers used to set the input parameters for given values of Z, are proven to correspond to the lowest eigenvalues from the elasticity solutions for all cases studied.

To examine the convergence of the present eigenvalue solution as sufficient numbers of displacement functions are retained, values for critical torsional loads for the previously discussed isotropic cylindrical shell ($Z = 10$, $L/R_c = 0.898$, $R_c/h = 12.99$, $n = 5$) were generated as the numbers of terms in r and z increase by one, respectively. The number of terms in r and in z describe numbers of the upper indices, K_i and M_i, respectively, in Eq. (20), where $i = 1, 2, 3$. Equal numbers for K_i (i.e., $K_1 = K_2 = K_3$) and M_i (i.e., $M_1 = M_2 = M_3$) were used for the displacements u_1, v_1, w_1.

Results are given in Table 3, which clearly shows that the critical torsional load is monotonically converging from above as the number of terms in r and z increases. An acceptable converged value for the critical load occurs when addition of one term in z as well as in r yields a difference between subsequent values less than 0.01 percent. Therefore, for this case the converged critical load is obtained by employing five terms in r and 21 terms in z, or 5×21 terms.

Same monotonic convergence is detected for all other studied isotropic cylinder cases, but convergence tables are not presented here because of limited space. Instead, solution sizes, which provide converged values of the critical torsional loads,

Table 3 Convergence of critical loads for an isotropic cylinder ($Z = 10$, $n = 5$)

Critical torsional loads ($N \cdot m \times 10^{-7}$)			
No. of terms in z	No. of terms in r		
	3	4	5
1	6693.7	6667.5	6667.4
2	2243.0	2208.4	2208.0
3	2167.8	2132.6	2132.3
4	2141.5	2105.7	2105.3
5	2129.3	2093.0	2092.6
6	2122.6	2085.9	2085.4
7	2118.5	2081.5	2081.0
8	2115.7	2078.6	2078.1
9	2113.9	2076.6	2076.0
10	2112.5	2075.1	2074.5
11	2111.4	2073.9	2073.4
12	2110.6	2073.1	2072.5
13	2110.0	2072.4	2071.7
14	2109.5	2071.8	2071.2
15	2109.1	2071.4	2070.7
16	2108.7	2071.0	2070.3
17	2108.4	2070.7	2070.0
18	2108.2	2070.5	2069.7
19	2108.0	2070.3	2069.5
20	2107.8	2070.1	2069.2
21	2107.6	2069.9	2069.1

Downloaded 04 May 2010 to 171.66.16.27. Redistribution subject to ASME license or copyright; see http://www.asme.org/terms/Terms_Use.cfm

Table 4 Number of terms required for convergence of critical loads for an isotropic cylinder

(No. of terms in r) x (No. of terms in z)								
	n							
Z	2	3	4	5	6	7	8	9
10000	4x30	3x31	3x34	3x34	3x35	3x35	3x36	3x36
5000	4x29	4x31	3x33	3x33	3x34	3x35	3x35	3x36
2000	4x27	4x28	4x31	4x31	3x32	3x33	3x34	3x34
1000	4x25	4x26	4x30	4x30	4x31	3x32	3x33	3x33
500	4x24	4x24	4x27	4x27	4x29	4x30	4x31	4x32
200	4x20	4x22	4x25	4x25	4x26	4x28	4x29	4x30
100	5x19	4x20	4x24	4x24	4x25	4x26	4x27	4x28
50	5x17	4x19	4x23	4x23	4x24	4x25	4x26	4x28
20	5x15	5x18	4x22	4x22	4x23	4x25	4x26	4x27
10	5x13	5x16	5x21	5x21	4x22	4x23	4x24	4x25

are summarized in Table 4. When n is larger than 5, the use of Legendre polynomials containing up to four terms provides accepted convergence values. Maximum number of terms in r for all cases considered here is 5. It is clearly seen from Table 4 that a larger number of z terms is required for a longer cylinder with a larger value of Z regardless of the circumferential wave number. However, for a given value of Z the rate of convergence is slightly slower as the wave number n increases even though a higher value of n refers to a shorter cylinder.

Comparison With Existing Orthotropic Shell Solutions. Before discussing accuracy of the shell theory results for orthotropic cylinders, it is now appropriate to quote a study performed by Etitum and Dong (1995). They calculated torsional buckling loads of cross-ply and angle-ply cylinders by using a three-dimensional semi-analytical finite element method, based on Biot's incremental deformation theory (Biot, 1965) and then compared the results with those obtained from the classical and the first-order shear deformation formulations based on the Flügge shell theory. They concluded that for thin geometry ($R_c/h = 100$), classical theory can be trusted to give accurate results over a reasonably wide range of normalized wavelength ratio L/R_c. They also showed that shell theories and three-dimensional formulation do not correlate well at all for a relatively thick cylinder ($R_c/h = 10$). In this case, shell theory results can be lower or higher than those obtained from three-dimensional theory depending upon the values of L/R_c.

In the literature, there is a limited number of shell theory based articles dealing with torsion of orthotropic cylinders having fixed ends (Simitses, 1967, 1968; Tabiei and Simitses, 1994). Tabiei and Simitses (1994) performed an extensive parametric study of laminated cylindrical shells under torsion by employing Donnell-type kinematic relations when deriving the equilibrium equations and then employing Sanders-type relations in the buckling equations. They compared numerical results from classical shell theory (CL), first-order shear deformation theory (FOSD), and higher-order shear deformation theory (HOSD).

Table 5 shows critical torsional loads of graphite/epoxy cylinders predicted by the present three-dimensional elasticity formulation along with those from Tabiei and Simitses (1994) based on the various shell theories. The material properties of the Graphite/Epoxy cylinder considered herein are

$$E_{11} = E_{22} = 9.928 \times 10^9 \text{ N/m}^2,$$

$$E_{33} = 149.617 \times 10^9 \text{ N/m}^2,$$

$$G_{12} = 2.551 \times 10^9 \text{ N/m}^2, \quad G_{13} = G_{23} = 4.481 \times 10^9 \text{ N/m}^2,$$

$$\nu_{12} = 0.45, \quad \nu_{13} = \nu_{23} = 0.0186.$$

Radius of the centerline of the cylinder, R_c is set to 0.1905 m and the length is varied such that $L/R_c = 1, 2, 5$. The thickness of the cylinder is also varied to correspond to R_c/h ratios equal to 100, 60, 30, and 15. On the third column of Table 5, Batdorf parameter $\tilde{z}$ for orthotropic cylinder, corresponding to the shell geometric parameter Z is indicated. It should be noted that $\tilde{z}$ depends not only on the geometry but also on the stiffness constants (Nemeth, 1994), and is defined as

$$\tilde{z} = \frac{L^2(Q_{11}Q_{22} - Q_{12}^2)^{1/2}}{R_c\sqrt{12}(Q_{11}Q_{22}D_{11}D_{22})^{1/4}}, \tag{29}$$

where stiffness constants Q_{ij} and flexural rigidity D_{ij} of a cylindrical shell are (1 ≡ axial, 2 ≡ circumferential),

$$Q_{11} = \frac{hE_{11}}{1 - \nu_{12}\nu_{21}}; \quad Q_{22} = \frac{hE_{22}}{1 - \nu_{12}\nu_{21}};$$

$$Q_{12} = \frac{h\nu_{12}E_{22}}{1 - \nu_{12}\nu_{21}}; \quad D_{ij} = \frac{h^2}{12}Q_{ij}. \tag{30}$$

The data in Table 5 are also shown graphically in Fig. 4 by normalizing the critical torsional load to $M_{cr}/E_{22}h^3$. It is clearly seen from Table 5 and Fig. 4 that results from shell theories are reasonably close to the elasticity solutions as long as the cylinder is long or thin. More specifically, when the ratio L/R_c is set at 5, the data from all approaches agree remarkably well over the entire range of the R_c/h ratios considered. Furthermore, all shell theories predict slightly lower values for the critical loads. However, for the case of short cylinder ($L/R_c = 1$) classical shell theory predicts much higher values when the cylinder is moderately thick ($R_c/h \leq 30$), while shear deformation theories provide reasonable values for the critical torsional loads. When L/R_c is 2, the classical theory results are higher than the elasticity solutions except for the case of $R_c/h = 60$, but shear deformation theory results are lower except $R_c/h = 100$ case.

Higher-order shear deformation theory gave conservative values for all cases except for the case of $L/R_c = 2$, $R_c/h = 100$.

Table 5 Comparison of results for an orthotropic cylinder

Critical torsional loads ($N \cdot m \times 10^4$) / Wave number						
Geometry			Elasticity	CL*	FOSD*	HOSD*
L/R_c	R_c/h	$\tilde{z}$		(% increase vs. Elasticity)	(% increase vs. Elasticity)	(% increase vs. Elasticity)
5	100	2493	.8418/7	.8277 / 7 (-1.67%)	.8277 / 7 (-1.67%)	.8277 / 7 (-1.67%)
5	60	1496	2.552/6	2.515 / 6 (-1.44%)	2.515 / 6 (-1.44%)	2.515 / 6 (-1.44%)
5	30	748.1	12.00/5	11.78 / 5 (-1.84%)	11.74 / 5 (-2.18%)	11.72 / 5 (-2.33%)
5	15	374.0	58.56/4	58.33 / 4 (-0.38%)	56.33 / 4 (-3.80%)	56.01 / 4 (-4.34%)
2	100	399.0	1.255/9	1.297 / 10 (3.42%)	1.293 / 10 (3.06%)	1.293 / 10 (3.06%)
2	60	239.4	4.217/7	4.193 / 7 (-0.55%)	4.173 / 7 (-1.04%)	4.155 / 7 (-1.47%)
2	30	119.7	23.57/6	23.96 / 6 (1.67%)	23.32 / 6 (-1.05%)	23.01 / 6 (-2.40%)
2	15	59.84	138.9/5	158.2 / 5 (13.9%)	134.6 / 5 (-3.07%)	130.0 / 5 (-6.41%)
1	100	99.74	2.429/11	2.456 / 11 (1.09%)	2.435 / 11 (0.25%)	2.396 / 11 (-1.35%)
1	60	59.84	9.605/10	9.985 / 10 (3.96%)	9.666 / 10 (0.64%)	9.504 / 10 (-1.05%)
1	30	29.92	62.32/9	73.47 / 8 (17.9%)	61.91 / 9 (-0.66%)	59.51 / 9 (-4.50%)
1	15	14.96	347.6/8	575.0 / 7 (65.4%)	329.6 / 8 (-5.17%)	309.2 / 8 (-11.0%)

* Tabiei and Simitses (1994)

Downloaded 04 May 2010 to 171.66.16.27. Redistribution subject to ASME license or copyright; see http://www.asme.org/terms/Terms_Use.cfm

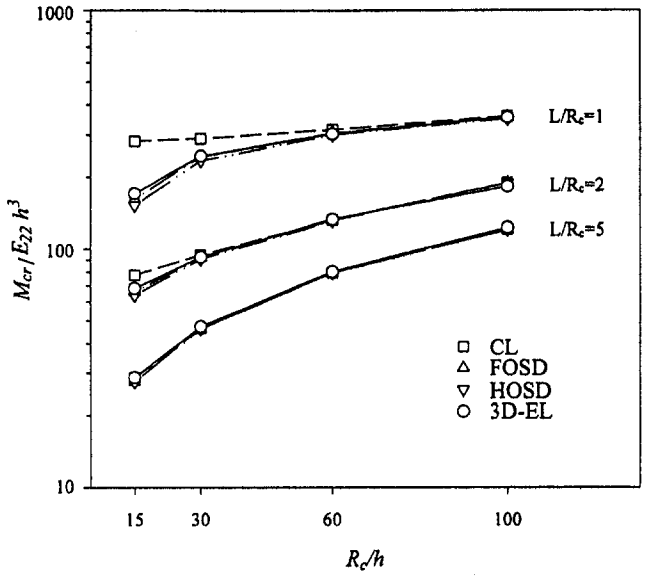

Fig. 4 Comparison of critical loads for an orthotropic cylinder

The results from classical theory and first-order shear deformation theory are higher or lower, depending on L/R_c and R_c/h. It should be mentioned on the basis of the results compared herein that there is no trend on the conservatism of the critical loads from shell theories as in the isotropic cases.

Figure 5 shows a comparison of normalized critical torsional loads with respect to the Batdorf parameter $\tilde{z}$. Even though the data from shell theories compared herein are limited, it can be noted that for the value of $\tilde{z}$ above about 100, shell theories are adequate to predict critical torsional load of an orthotropic cylinder.

The circumferential wave number n that a cylinder buckles into is also shown in Table 5. Integer wave numbers calculated from the shell theories and elasticity formulation agreed in most cases. However, all shell theories predicted different wave numbers for the case of $L/R_c = 2$, $R_c/h = 100$, and so did the classical shell theory for the cases of $L/R_c = 1$, $R_c/h = 15$ and $L/R_c = 1$, $R_c/h = 30$.

It should be noted that the critical load is also monotonically converging for all cases of orthotropic construction considered

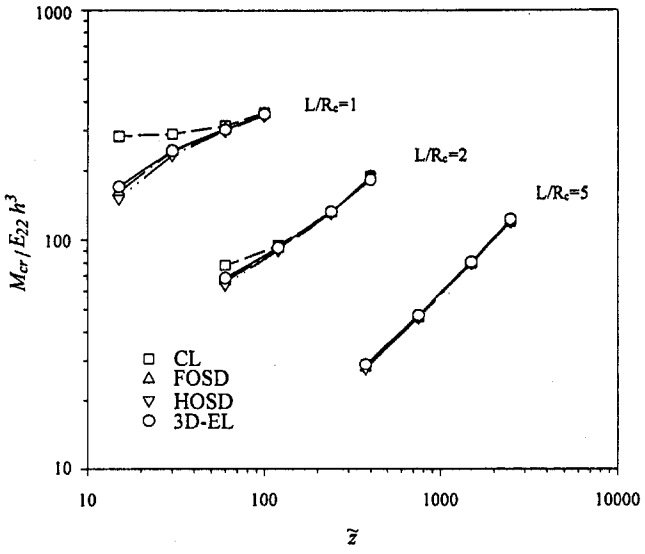

Fig. 5 Variation of critical loads for an orthotropic cylinder with respect to $\tilde{z}$

Table 6 Critical torsional loads of an isotropic cylinder

Critical torsional loads ($N \cdot m \times 10^6$) / Wave number

	R_2/R_1				
L/R_2	1.01	1.05	1.1	1.15	1.2
1	2.262/10	101.6/6	516.7/5	1238/4	2164/4
2	1.513/8	54.84/5	247.0/4	565.2/3	987.5/3
3	1.232/7	41.70/4	182.3/3	404.3/3	725.9/3
4	1.070/6	35.81/4	148.9/3	344.7/3	633.1/3
5	.9650/6	32.99/4	132.4/3	316.5/3	527.4/2
6	.8784/5	29.25/3	123.2/3	288.9/2	451.4/2
7	.8111/5	26.47/3	117.5/3	250.4/2	403.2/2
8	.7687/5	24.68/3	113.9/3	224.7/2	371.2/2
9	.7304/4	23.46/3	102.9/2	207.0/2	349.0/2
10	.6816/4	22.60/3	93.61/2	194.4/2	333.2/2

herein, as it is for an isotropic cylinder. Four terms in r are employed to provide convergence within 0.01 percent for all cases except the shortest and thickest cylinder with $L/R_c = 1$, $R_c/h = 15$, which needs five terms. Maximum number of z terms needed is 25 when $L/R_c = 1$, $R_c/h = 15$. For a given L/R_c ratio, the number of terms in z needed decreases as the ratio R_c/h becomes small.

Parametric Study. Having established confidence in the methodology and assessed the accuracy of shell theory results, an extensive parametric study is performed to provide accurate values for the critical torsional loads of isotropic and orthotropic cylindrical shells. Results presented herein can be used as references for future studies employing shell theory.

For the isotropic cylinder Young's modulus $E = 14$ GN/m^2 and Poisson's ratio $\nu = 0.3$ are assumed. Orthotropic materials considered here are typical glass/epoxy and graphite/epoxy with circumferential reinforcements, having the following properties:

$$\text{glass/epoxy: } E_{11} = E_{33} = 14.0 \times 10^9 \text{ N/m}^2,$$

$$E_{22} = 57.0 \times 10^9 \text{ N/m}^2,$$

$$G_{12} = G_{23} = 5.7 \times 10^9 \text{ N/m}^2,\ G_{13} = 5.0 \times 10^9 \text{ N/m}^2,$$

$$\nu_{12} = 0.068,\ \nu_{13} = 0.400,\ \nu_{23} = 0.277,$$

$$\text{graphite/epoxy: } E_{11} = 9.9 \times 10^9 \text{ N/m}^2,$$

$$E_{22} = 140.0 \times 10^9 \text{ N/m}^2,$$

$$E_{33} = 9.1 \times 10^9 \text{ N/m}^2,\quad G_{12} = 4.7 \times 10^9 \text{ N/m}^2,$$

$$G_{13} = 5.9 \times 10^9 \text{ N/m}^2,\quad G_{12} = 4.3 \times 10^9 \text{ N/m}^2$$

$$\nu_{12} = 0.020,\ \nu_{13} = 0.533,\ \nu_{23} = 0.300,$$

where the subscripts 1, 2, 3 correspond to r, θ, and z-directions, respectively.

The outer cylinder radius R_2 is set to 1 m and the ratio L/R_2 is varied from 1 to 10. A range of outer versus inner radii R_2/R_1 from thin (1.01) to thick (1.20) is examined.

Tables 6 through 8 show critical torsional loads and wave numbers around the circumference for the isotropic, the glass/epoxy, and the graphite/epoxy cylinders. In general, critical torsional loads of the graphite/epoxy cylinder are higher than those of the glass/epoxy cylinder because of the stronger reinforcements. As the cylinder becomes thicker or longer, it buckles into a lower circumferential wave number n. For given shell geometries, the buckling wave number of the isotropic cylinder is the highest followed by the glass/epoxy cylinder and then the graphite/epoxy cylinder.

Downloaded 04 May 2010 to 171.66.16.27. Redistribution subject to ASME license or copyright; see http://www.asme.org/terms/Terms_Use.cfm

Table 7 Critical torsional loads of a glass/epoxy cylinder

Critical torsional loads ($N \cdot m \times 10^6$) / Wave number

	R_2/R_1				
L/R_2	1.01	1.05	1.1	1.15	1.2
1	3.811/9	141.7/5	668.2/4	1560/4	2693/4
2	2.832/7	88.00/4	373.3/3	821.6/3	1434/3
3	2.423/6	74.92/4	294.3/3	672.0/3	1168/2
4	2.181/5	66.12/3	265.7/3	602.2/2	933.6/2
5	1.981/5	59.24/3	252.3/3	510.8/2	816.7/2
6	1.874/5	55.41/3	233.7/2	458.2/2	750.8/2
7	1.722/4	53.07/3	209.1/2	425.6/2	710.1/2
8	1.618/4	51.54/3	192.8/2	404.1/2	683.5/2
9	1.548/4	50.49/3	181.6/2	389.2/2	665.1/2
10	1.499/4	47.91/2	173.5/2	378.5/2	651.9/2

Table 8 Critical torsional loads of a graphite/epoxy cylinder

Critical torsional loads ($N \cdot m \times 10^6$) / Wave number

	R_2/R_1				
L/R_2	1.01	1.05	1.1	1.15	1.2
1	4.716/7	153.5/4	682.1/4	1558/4	2621/3
2	3.753/6	108.4/4	413.2/3	904.0/3	1528/3
3	3.305/5	92.00/3	361.1/3	762.8/3	1175/2
4	3.043/5	83.69/3	338.8/2	643.5/2	1015/2
5	2.767/4	79.71/3	296.2/2	585.4/2	938.7/2
6	2.587/4	77.51/3	272.0/2	553.0/2	897.1/2
7	2.479/4	73.65/2	257.0/2	533.1/2	871.8/2
8	2.367/3	67.39/2	247.1/2	520.1/2	855.4/2
9	2.201/3	63.10/2	240.3/2	511.2/2	844.2/2
10	2.085/3	60.04/2	235.4/2	504.7/2	836.1/2

Conclusion

The accuracy of shell theory solutions has been assessed through a comparison study for both isotropic and orthotropic cylinders. For isotropic cylinders it was found that Donnell's simplified formula and the direct integration techniques by Yamaki always predict nonconservative values for the critical torsional loads. The results from Donnell's formula deviate increasingly from those obtained by the present solution as the cylinder becomes shorter and thicker. On the other hand, deviation of Yamaki's results is independent of cylinder dimensions unless the shell geometry parameter, Z, is smaller than 50. As the circumferential wave numbers corresponding to the critical load increase, both shell theory solutions provide more accurate values.

The shell theory solution for orthotropic cylinders, which has been compared with the present elasticity formulation, is based on Donnell-type kinematic relations and Sanders-type buckling equations by employing classical, first-order shear deformation, and higher-order shear deformation theories. While both shear deformation theories provide results reasonably close to the three-dimensional elasticity solutions, classical theory predicts much higher critical load values for a short and thick cylinder. However, there is no observed trend regarding the conservatism of the results from the shell theories with respect to three-dimensional elasticity solutions on the basis of the data compared. In general, it can be concluded that shell theories are adequate to predict critical torsional loads of an orthotropic cylinder for the value of Batdorf parameter $\tilde{z}$ above 100.

Detailed numerical tables and figures have also been presented that show variation of critical torsional loads over a wide range of length ratio L/R_2 and radii ratio R_2/R_1 for isotropic, glass/epoxy, and graphite/epoxy cylinders. These solutions can be used to evaluate the performance of various proposed shell theories.

Acknowledgment

The financial support of the Federal Highway Administration (U.S. DOT/FHWA Contract No. 61-93-C-00012), the Office of Naval Research, Ship Structure and Systems, S&T Division (Grant N00014-91-J-1892), and the School of Civil & Environmental Engineering at Georgia Institute of Technology are gratefully acknowledged. The authors would like to thank especially Mr. Eric Munley of the Federal Highway Administration and Dr. Y. D. S. Rajapakse of the Office of Naval Research for their encouragement on this study.

References

Ambartsumian, S. A., 1962, "Contributions to the Theory of Anisotropic Layered Shells," ASME *Applied Mechanics Reviews,* Vol. 15, pp. 245–249.

Babich, I. Y., and Kilin, V. I., 1985, "Stability of a Three-Layer Orthotropic Cylindrical Shell Under Axial Compression," *Soviet Applied Mechanics,* Vol. 21, pp. 566–569.

Bert, C. W., and Francis, P. H., 1974, "Composite Material Mechanics: Structural Mechanics," *AIAA Journal,* Vol. 12, pp. 1173–1186.

Biot, M. A., 1965, *Mechanics of Incremental Deformations,* John Wiley and Sons, New York.

Bolotin, V. V., 1963, *Nonconservative Problems of the Theory of Elastic Stability,* Macmillan, New York.

Ciarlet, P. G., 1988, *Mathematical Elasticity, Vol. 1: Three-dimensional Elasticity,* North Holland, Amsterdam.

Danielson, D. A., and Simmonds, J. G., 1969, "Accurate Buckling Equations for Arbitrary and Cylindrical Elastic Shells," *International Journal of Engineering Science,* Vol. 7, pp. 459–468.

Donnell, L. H., 1933, "Stability of Thin-walled Tubes Under Torsion," NACA Report 479.

Etitum, P. and Dong, S. B., 1995, "A Comparative Study of Stability of Laminated Anisotropic Cylinders Under Axial Compression and Torsion," *International Journal of Solids and Structures,* Vol. 32, pp. 1231–1246.

Finlayson, B. A., 1972, *The Method of Weighted Residuals and Variational Principles,* Academic Press, New York.

Flügge, W., 1973, *Stress in Shells,* Springer-Verlag, Berlin.

Kardomateas, G. A., 1993a, "Buckling of Thick Orthotropic cylindrical Shells Under External Pressure," ASME JOURNAL OF APPLIED MECHANICS, Vol. 60, pp. 195–202.

Kardomateas, G. A., 1993b, "Stability Loss in Thick Transversely Isotropic Cylindrical Shells Under Axial Compression," ASME JOURNAL OF APPLIED MECHANICS, Vol. 60, pp. 506–513.

Kardomateas, G. A., and Chung, C. B., 1994, "Buckling of Thick Orthotropic Cylindrical Shells Under External Pressure Based on Non-planar Equilibrium Modes," *International Journal of Solids and Structures,* Vol. 31, pp. 2195–2210.

Kardomateas, G. A., 1995, "Bifurcation of Equilibrium in Thick Orthotropic Cylindrical Shells Under Axial Compression," ASME JOURNAL OF APPLIED MECHANICS, Vol. 62, pp. 43–52.

Kardomateas, G. A., 1996, "Benchmark Three-dimensional Elasticity Solutions for the Buckling of Thick Orthotropic Cylindrical Shells," *Composites, Part B,* Vol. 27B, pp. 569–580.

Mikhlin, S. G., 1964, *Variational Methods in Mathematical Physics,* Macmillan, New York.

Nemeth, M. P., 1994, "Nondimensional Parameters and Equations for Buckling of Anisotropic Shallow Shells," ASME JOURNAL OF APPLIED MECHANICS, Vol. 61, pp. 664–669.

Sanders, J. L. Jr., 1963, "Nonlinear Theories of Thin Shells," *Quarterly of Applied Mathematics,* Vol. 21, pp. 21–26.

Simitses, G. J., 1967, "Instability of Orthotropic cylindrical Shells Under Combined Torsion and Hydrostatic Pressure," *AIAA Journal,* Vol. 5, pp. 1463–1469.

Simitses, G. J., 1968, "Buckling of Eccentrically Stiffened Cylinders Under Torsion," *AIAA Journal,* Vol. 6, pp. 1856–1860.

Simitses, G. J., 1986, "Buckling and Postbuckling of Imperfect Cylindrical Shells," *Proceedings of the ASME Joint PVP and Computer Engineering Division Conference,* Chicago, IL, ASME PVP-119 and NDE-3, pp. 1–11.

Simitses, G. J., 1996, "Buckling of Moderately Thick Laminated Cylindrical Shells: A Review," *Composites, Part B,* Vol. 27, pp. 581–587.

Soldatos, K. P., and Ye, J., 1994, "Three-dimensional Static, Dynamic, Thermoelastic and Buckling Analysis of Homogeneous and Laminated Composite Cylinders," *Composite Structures,* Vol. 29, pp. 131–143.

Tabiei, A., and Simitses, G. J., 1994, "Buckling of Moderately thick, Laminated Cylindrical Shells Under Torsion," *AIAA Journal,* Vol. 32, pp. 639–647.

Tennyson, R. C., 1974, "Buckling of Laminated Composite Cylinders: A Review," *Composites,* Vol. 1, pp. 17–24.

Timoshenko, S. P., and Gere, J. M., 1961, *Theory of Elastic Stability,* 2nd Ed., McGraw-Hill, New York.

Downloaded 04 May 2010 to 171.66.16.27. Redistribution subject to ASME license or copyright; see http://www.asme.org/terms/Terms_Use.cfm

Wilkinson, J. H., and Reinsch, C., 1971, *Linear Algebra,* Springer-Verlag, New York.

Yamaki, N., 1984, *Elastic Stability of Circular Cylindrical Shells,* North-Holland, Amsterdam.

Ye, J., and Soldatos, K. P., 1995, "Three-dimensional Buckling Analysis of Laminated Composite Hollow Cylinders and Cylindrical Panels," *International Journal of Solids and Structures,* Vol. 32, pp. 1949–1962.

APPENDIX A

Operators L'_{ij} and B'_{ij} of Eq. (19) are

$$L'_{11}(u_1) = -c_{12}\frac{u_{1,r}}{r} - c_{22}\frac{u_1}{r^2} + c_{66}\frac{u_{1,\theta\theta}}{r^2} + c_{55}u_{1,zz} + 2\bar{M}u_{1,\theta z}, \quad \text{(A1)}$$

$$L'_{12}(v_1) = c_{66}\frac{v_{1,r\theta}}{r} - (c_{22} + c_{66})\frac{v_{1,\theta}}{r^2} - \bar{M}(rv_{1,rz} + 2v_{1,z}), \quad \text{(A2)}$$

$$L'_{13}(w_1) = c_{55}w_{1,rz} - c_{23}\frac{w_{1,z}}{r} - \bar{M}\left(w_{1,r\theta} - \frac{w_{1,\theta}}{r}\right), \quad \text{(A3)}$$

$$L'_{21}(u_1) = c_{12}\frac{u_{1,r\theta}}{r} + (c_{22} + c_{66})\frac{u_{1,\theta}}{r^2} + \bar{M}u_{1,z}, \quad \text{(A4)}$$

$$L'_{22}(v_1) = c_{66}\frac{v_{1,r}}{r} - c_{66}\frac{v_1}{r^2} + c_{22}\frac{v_{1,\theta\theta}}{r^2} + c_{44}v_{1,zz} + \bar{M}v_{1,\theta z}, \quad \text{(A5)}$$

$$L'_{23}(w_1) = (c_{23} + c_{44})\frac{w_{1,\theta z}}{r} - \bar{M}\left(w_{1,r} + \frac{w_{1,\theta\theta}}{r}\right), \quad \text{(A6)}$$

$$L'_{31}(u_1) = c_{13}u_{1,rz} + c_{23}\frac{u_{1,z}}{r}, \quad \text{(A7)}$$

$$L'_{32}(v_1) = (c_{23} + c_{44})\frac{v_{1,\theta z}}{r} - \bar{M}rv_{1,zz}, \quad \text{(A8)}$$

$$L'_{33}(w_1) = c_{44}\frac{w_{1,\theta\theta}}{r^2} + c_{33}w_{1,zz} + \bar{M}w_{1,\theta z}, \quad \text{(A9)}$$

$$B'_{11}(u_1) = c_{11}u_{1,r} + c_{12}\frac{u_1}{r}, \; B'_{12}(v_1) = c_{12}\frac{v_{1,\theta}}{r}, \; B'_{13}(w_1) = c_{13}w_{1,z}, \quad \text{(A10)}$$

$$B'_{21}(u_1) = c_{66}\frac{u_{1,\theta}}{r}, \; B'_{22}(v_1) = c_{66}v_{1,r} - c_{66}\frac{v_1}{r}, \; B'_{23}(w_1) = 0, \quad \text{(A11)}$$

$$B'_{31}(u_1) = c_{55}u_{1,z}, \; B'_{32}(v_1) = 0, \; B'_{33}(w_1) = c_{55}w_{1,r}. \quad \text{(A12)}$$

APPENDIX B

Operators D^S_{ij} and D^G_{ij} of Eq. (23) are

$$D^S_{11}(P_k) = -\left(\frac{c_{12}}{r}\right)P_{k,r} - \left(\frac{c_{22} + n^2c_{66}}{r^2}\right)P_k, \quad \text{(B1)}$$

$$D^S_{12}(P_k) = \left(\frac{nc_{66}}{r}\right)P_{k,r} - \left(\frac{nc_{22} + nc_{66}}{r^2}\right)P_k, \quad \text{(B2)}$$

$$D^S_{13}(P_k) = (c_{55})P_{k,r} - \left(\frac{c_{23}}{r}\right)P_k, \; D^S_{14}(P_k) = -(c_{55})P_k, \quad \text{(B3)}$$

$$D^S_{21}(P_k) = \left(\frac{nc_{12}}{r}\right)P_{k,r} + \left(\frac{nc_{22} + nc_{66}}{r^2}\right)P_k, \quad \text{(B4)}$$

$$D^S_{22}(P_k) = \left(\frac{c_{66}}{r}\right)P_{k,r} - \left(\frac{n^2c_{22} + c_{66}}{r^2}\right)P_k, \quad \text{(B5)}$$

$$D^S_{23}(P_k) = \left(\frac{nc_{23} + nc_{44}}{r}\right)P_k, \; D^S_{24}(P_k) = -(c_{44})P_k, \quad \text{(B6)}$$

$$D^S_{31}(P_k) = (c_{13})P_{k,r} + \left(\frac{c_{23}}{r}\right)P_k,$$

$$D^S_{32}(P_k) = \left(\frac{nc_{23} + nc_{44}}{r}\right)P_k, \quad \text{(B7)}$$

$$D^S_{33}(P_k) = -\left(\frac{n^2c_{44}}{r^2}\right)P_k, \; D^S_{34}(P_k) = -(c_{33})P_k, \quad \text{(B8)}$$

$$D^G_{11}(P_k) = (2n)P_k, \; D^G_{12}(P_k) = -(r)P_{k,r} - (2)P_k,$$
$$D^G_{13}(P_k) = -(n)P_{k,r} + \left(\frac{n}{r}\right)P_k, \quad \text{(B9)}$$

$$D^G_{21}(P_k) = (1)P_k, \; D^G_{22}(P_k) = (n)P_k,$$
$$D^G_{23}(P_k) = -(1)P_{k,r} + \left(\frac{n^2}{r}\right)P_k, \quad \text{(B10)}$$

$$D^G_{31}(P_k) = 0, \; D^G_{32}(P_k) = (r)P_k, \; D^G_{33}(P_k) = (n)P_k, \quad \text{(B11)}$$

and K_{ij} are

$$K_{11}(P_k) = (c_{11})P_{k,r} + \left(\frac{c_{12}}{r}\right)P_k, \; K_{12}(P_k) = \left(\frac{nc_{12}}{r}\right)P_k, \; K_{13}(P_k) = (c_{13})P_k, \quad \text{(B12)}$$

$$K_{21}(P_k) = \left(\frac{nc_{66}}{r}\right)P_k, \; K_{22}(P_k) = (c_{66})P_{k,r} - \left(\frac{c_{66}}{r}\right)P_k,$$
$$K_{23}(P_k) = 0, \quad \text{(B13)}$$

$$K_{31}(P_k) = (c_{55})P_k, \; K_{32}(P_k) = 0, \; K_{33}(P_k) = (c_{55})P_{k,r}. \quad \text{(B14)}$$

Downloaded 04 May 2010 to 171.66.16.27. Redistribution subject to ASME license or copyright; see http://www.asme.org/terms/Terms_Use.cfm

A. Chiskis

R. Parnes

Department of Mechanics,
Materials and Structures,
Faculty of Engineering,
Tel-Aviv University,
Ramat Aviv 69978, Israel

On Nanobuckling of Monomolecular Layers Adhering to a Substrate

It is shown that the first buckling mode corresponding to the lowest buckling force of a plane monomolecular layer glued to a substrate may not be smooth. The resulting saw-like configuration of neighboring molecules leads to corrugation on a molecular level and we name such a phenomenon nanobuckling. *A criterion governing this smooth—not smooth transition is derived. The model presented may also describe surface instability of a perfect crystal due to contraction.*

1 Introduction

We present a simple model by means of which we demonstrate a *microbuckling* phenomenon. This phenomenon may reflect interesting features of microstructures and may be applied to a rich variety of structures such as monomolecular layers (e.g., a layer of carbon atoms) strongly interacting with a substrate, or as a first approximation to describe the surface instability phenomenon of a surface (an aggregate of first atomic layers) of a perfect monocrystal due to contraction of the crystal.

While modern technology of microelectronics presently uses thin layers on the microscale, more advanced technologies may, in the future, lead to applications of molecularly thick layers (particularly, in the rapidly growing new branch of nanotechnology). Specifically, the investigation of buckling shapes of such layers (due to a mechanical force or thermal contraction) is of great interest and, as we demonstrate, they depend significantly on the material properties of the layer and the adhesion.

We note that nonquantum classical molecular dynamics and continuum mechanical treatments have been used as a tool for consideration of buckling and instability phenomena in carbon nanotubes (Falvo et al., 1997; Yakobson and Richard, 1997; Yakobson, Brabec, and Bernholc, 1996). However, stability analyses, which usually make appeal to continuum idealizations, do not take into account the discrete nature of the problem but use standard techniques as applied to rod and shell structures. Such considerations, being correct for long-wave perturbation or instabilities, fail to describe the short-wave instabilities (a 400 percent error for a corrugation wave is pointed out in Falvo et al. (1997)) which are the primary interest of the present article. According to this point of view, the buckling mode corresponding to the first buckling force is smooth (Fig. 1(a)), whereas those corresponding to the higher values of the buckling forces are less smooth, etc. This point of view takes its root, probably, in observations of the buckling of *free* elements. In such a case a continuum model may be successfully used (as an application to micromachined beams, see Fang and Wickert (1994)). However, when considering the instability of an element which is not free but which interacts with other elements of the structure, the first buckling mode may differ considerably from the buckling mode of the free element.

Below, we consider buckling of a monomolecular thin layer "glued" to the substrate. Note that a problem of transition (or sliding) of a monolayer with respect to the substrate is discussed in the present literature related to nanofriction (see Weiss and Elmer, 1996; Gyalog and Thomas, 1997) using the Frenkel-Kontorova-Tomlinson model. (Application of this model to crystal sliding and to a monolayer on a crystalline substrate is given in Franc and van der Merwe, (1949).) In the present paper we do not discuss the sliding phenomenon but rather buckling in the transverse direction. The layer is modeled by inextensible chain segments interacting with each another by means of spiral springs and with the substrate by means of usual springs (which model the adhesion). The inextensibility of the chain elements is assumed as a first approximation in order to simplify the analysis. For example, recent experiments on carbon nanotubes lead to very high estimates of Young's modulus ranging up to 4 TPa with an average value of 1.8 TPa (see Treacy et al., 1996).

We show that the first (i.e., the smallest) buckling mode may be the sharpest one, namely, having a saw shape where the neighboring molecules are shifted in the antiphase (Fig. 1(b)). We denote such a phenomenon as *nanobuckling.* Appearance of this shape as the first buckling mode depends, as we demonstrate, on the parameters of the layer and of the adhesion. Qualitatively, nanobuckling occurs when the rigidity of the "spiral spring" modeling the chain element interactions is much weaker than the spring rigidity modeling the adhesion.

2 Basic Equations and Qualitative Analysis

We consider a monomolecular layer of molecules or atoms spaced a distance a apart glued to a substrate. The layer is modeled by inextensible chain segments interacting with one another by means of spiral springs. Such springs represent the angular forces resulting from the adjustment of the electron clouds surrounding the molecules. The layer, assumed to be connected to the substrate by means of linear springs, is subjected to a compressive force, F (see Fig. 2).

Letting y_k be the displacement of the kth node in the y-direction in the buckled position, the angle of declination of the $(k-1, k)$ segment, ϕ_k, is then

$$\phi_k = \frac{y_k - y_{k-1}}{a}, \quad |\phi_k| \ll 1. \tag{1}$$

The potential energy of the spiral spring, $U_k^{(1)}$, and the potential energy of the linear spring connecting the layer with the substrate, $U_k^{(2)}$, in the node k are

Contributed by the Applied Mechanics Division of THE AMERICAN SOCIETY OF MECHANICAL ENGINEERS for publication in the ASME JOURNAL OF APPLIED MECHANICS.

Discussion on the paper should be addressed to the Technical Editor, Professor Lewis T. Wheeler, Department of Mechanical Engineering, University of Houston, Houston, TX 77204-4792, and will be accepted until four months after final publication of the paper itself in the ASME JOURNAL OF APPLIED MECHANICS.

Manuscript received by the ASME Applied Mechanics Division, July 1, 1998; final revision, Oct. 8, 1998. Associate Technical Editor: S. Kyriakides.

 Copyright © 1999 by ASME

Downloaded 04 May 2010 to 171.66.16.27. Redistribution subject to ASME license or copyright; see http://www.asme.org/terms/Terms_Use.cfm

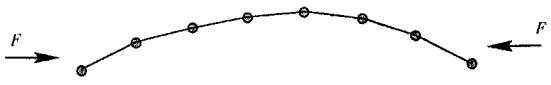

(a) Smooth buckling shape

(b) Saw-like buckling shape

Fig. 1 Buckling shapes

$$U_k^{(1)} = \frac{C}{2}(\phi_{k+1} - \phi_k)^2 = \frac{C}{2}\left(\frac{y_{k+1} - 2y_k + y_{k-1}}{a}\right)^2,$$

$$U_k^{(2)} = \frac{K}{2} y_k^2. \tag{2}$$

The total potential energy, U, and the work, A, of the applied compressive force, F, is then calculated as

$$U = \sum_k (U_k^{(1)} + U_k^{(2)}), \quad A = F\Delta = F\sum_k \Delta_k, \tag{3}$$

where, since $\Delta_k = a(1 - \cos\phi_k)$,

$$\Delta_k = \frac{(y_k - y_{k-1})^2}{2a}. \tag{4}$$

Introducing a nondimensional vertical displacement,

$$q_k = y_k/a, \tag{5}$$

we write the free energy functional, Π, in the form

$$\Pi = U - A = \sum_k \Pi_k,$$

$$\Pi_k = \frac{C}{2}(q_{k+1} - 2q_k + q_{k-1})^2 + \frac{Ka^2}{2} q_k^2 - \frac{Fa}{2}(q_k - q_{k-1})^2. \tag{6}$$

Conditions of extremum of Π, namely $\partial\Pi/\partial q_k = 0$, yield the equilibrium equations

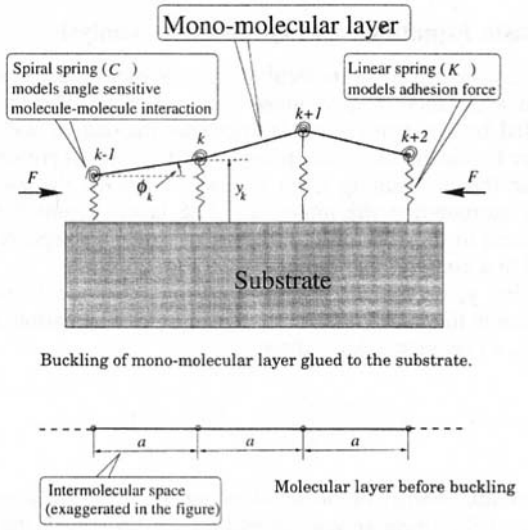

Buckling of mono-molecular layer glued to the substrate.

Fig. 2 Model of problem

$$C\mathcal{D}^{(4)}q_k + Ka^2 q_k + Fa\mathcal{D}^{(2)}q_k = 0, \tag{7}$$

where the finite difference operators are defined as

$$\mathcal{D}^{(2)}q_k = q_{k+1} - 2q_k + q_{k-1},$$

$$\mathcal{D}^{(4)}q_k = (q_{k+2} - 2q_{k+1} + q_k) - 2(q_{k+1} - 2q_k + q_{k-1}) + (q_k - 2q_{k-1} + q_{k-2}). \tag{8}$$

Note that

$$\mathcal{D}^{(4)}q_k = \mathcal{D}^{(2)}q_{k+1} - 2\mathcal{D}^{(2)}q_k + \mathcal{D}^{(2)}q_{k-1}. \tag{9}$$

While Eq. (7) is analyzed analytically in the following section, in the remaining part of the present section we demonstrate qualitatively that saw-like shapes can correspond to the lowest buckling force.

Let $\{q_k = Q_k\}$ describe a buckling shape. The corresponding buckling force is then

$$F = \frac{(C/a)\sum_k (Q_{k+1} - 2Q_k + Q_{k-1})^2 + Ka\sum_k Q_k^2}{\sum_k (Q_k - Q_{k-1})^2}. \tag{10}$$

In comparing the two terms of the numerator, we note that since $\sum_k (Q_{k+1} - 2Q_k + Q_{k-1})^2 \sim \sum_k (\phi_{k+1} - \phi_k)^2$, the first term tends to increase F when the ϕ_{k+1} and ϕ_k differ greatly, while the latter term is independent of the slopes ϕ_k. We note, too, that the denominator term $\sum_k (Q_k - Q_{k-1})^2 \sim \sum_k \phi_k^2$ tends to minimize F when the $|\phi_k|$ are as large as possible, which occurs for a saw-like shape, i.e., $(\phi_k = -\phi_{k-1})$. *Therefore, the saw-like shape minimizes the buckling force F, when the ratio*

$$R \equiv \frac{Ka^2}{C} \gg 1; \tag{11}$$

i.e., when the interaction with the substrate dominates the bending rigidity of the layer. (In the following section, we refine the range of values of R).

Choosing the saw shape

$$Q_k = Q(-1)^k, \tag{12}$$

noting then that $Q_k = Q_{k+2} = Q_{k-2} = Q$, $Q_{k-1} = Q_{k+1} = -Q$ such that $\mathcal{D}^{(4)}Q_k = 16Q$, $\mathcal{D}^{(2)}Q_k = 4Q$ and applying it to Eq. (7), we obtain

$$(16C + Ka^2 - 4Fa)Q = 0. \tag{13}$$

Since we seek a nontrivial solution, $Q \neq 0$, we arrive at

$$F = 4C/a + \frac{Ka}{4} \tag{14}$$

for the corresponding buckling force.

3 General Solution

Let us seek the solution of (7) in the form

$$q_n = Q\cos(\pi n/N), \quad N = 1, 2, 3, \ldots. \tag{15a}$$

Note that shapes corresponding to $N = 1$ or $N = 2$ are saw-like shapes. For $N = 1$, $q_n = Q(-1)^n$, $n = 1, 2, 3, \ldots$ while for $N = 2$, $q_n = Q(-1)^{n/2}$, n is even and $q_n = 0$, n odd. For increasing N, the shapes are no longer saw-like but become smoother.

It is convenient to let

$$q_n = Qe^{ikn}, \quad k = \pi/N, \quad N = 1, 2, 3 \ldots. \tag{15b}$$

Noting that

Downloaded 04 May 2010 to 171.66.16.27. Redistribution subject to ASME license or copyright; see http://www.asme.org/terms/Terms_Use.cfm

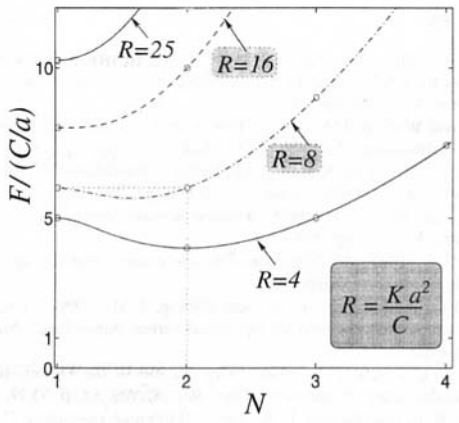

Fig. 3 Effect of parameter *R* on nondimensional *F-N* behavior

$$\mathcal{D}^{(2)}q_n = (e^{ik} - 2 + e^{-ik})Qe^{ikn} = (e^{ikn/2} - e^{-ikn/2})^2 Qe^{ikn}$$
$$= -4Q \sin^2 (k/2)e^{ikn}, \quad (16a)$$

then, due to (9),

$$\mathcal{D}^{(4)}q_n = -4Q \sin^2 (k/2)(e^{ik(n+1)} - 2e^{ikn} + e^{ik(n-1)})$$
$$= -4 \sin^2 (k/2)\mathcal{D}^{(2)}q_n = 16Q \sin^4 (k/2)e^{ikn}. \quad (16b)$$

Substituting (16) into (7) we obtain

$$(16C \sin^4 (k/2) + Ka^2 - 4Fa \sin^2 (k/2))Qe^{ikn} = 0. \quad (17)$$

Nontrivial solutions, $Q \neq 0$, lead to the characteristic equation

$$16C \sin^4 (k/2) + Ka^2 - 4Fa \sin^2 (k/2) = 0, \quad (18)$$

and hence the buckling force is given by

$$F = 4(C/a) \sin^2 (k/2) + \frac{Ka}{4 \sin^2 (k/2)}. \quad (19)$$

From (19) we immediately observe that the buckling force F depends on N (via $k = \pi/N$). To find to which N the minimal force corresponds, we investigate (19), written in the form

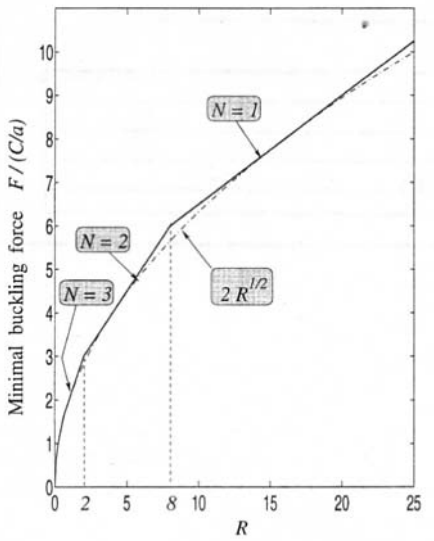

Fig. 4 Minimal buckling force as function of parameter *R* showing corresponding buckling modes. Increasing values of *R* represent increasing strength of adhesion. The dashed curve represents the continuous relation given by (19).

$$F = KaS + \frac{C/a}{S}, \quad S \equiv \frac{1}{4 \sin^2 (\pi/(2N))}, \quad (20a, b)$$

or

$$F = \frac{C}{a}\left(RS + \frac{1}{S}\right), \quad F = Ka\left(S + \frac{1}{RS}\right). \quad (20c, d)$$

Note that when N increases ($N = 1, 2, 3, \ldots$), S also increases. It is obvious that (20) has only one minimum (for $S > 0$) at $S = S_*$. Setting $dF/dS = 0$, we obtain $Ka - (C/a)/S^2 = 0$, whose root

$$S_*^2 = \frac{C}{Ka^2} \quad (21)$$

yields the minimum buckling force

$$F_* = 2(CK)^{1/2}. \quad (22a)$$

Alternatively, we may write

$$F_* = \frac{2C}{a} R^{1/2} \quad \text{or} \quad F_* = 2KaR^{-1/2}. \quad (22b, c)$$

Recalling the definition $R \equiv Ka^2/C$, relation (21) can be rewritten as

$$R = 16 \sin^4 (\pi/(2N_*)). \quad (23)$$

We first observe that for

$$R > 16 \quad (24)$$

there exists no integer N_* such that (23) holds. Therefore, for $R > 16$, $F = F(S(N))$ necessarily increases for increasing values of *real* $N > 1$ (see Fig. 3 for $R = 16$). *Thus we conclude that if $R > 16$, i.e., when the interaction with the substrate dominates the bending stiffness of the layer, the layer buckles as a saw-like shape, with $N = 1$.* While this criterion is sufficient, we show below that saw-like buckling modes occur for $R > 2$.

We now investigate the buckling shapes for $R \leq 16$. From (23) we obtain the relation

$$N_* = \frac{\pi/2}{\arcsin (R^{1/4}/2)}. \quad (25)$$

For integer N_*, $N = N_*$ determines the buckling shape, (15a). However, for any given R, N_* does not necessarily correspond to an integer. For this case let $\hat{N}$, $\hat{N} + 1$ be integers such that

$$\hat{N} < N_* < \hat{N} + 1. \quad (26)$$

Then the minimal critical force is determined by

$$\hat{F} \equiv F = \min \{F(\hat{N}), F(\hat{N} + 1)\} \quad (27)$$

and the buckling shape, determined by N, corresponds to either $\hat{N}$ or $\hat{N} + 1$, whichever produces the minimum of (27). Let us denote for brevity

$$F_N = F(S(N)) \quad S_N \equiv S(N), \quad (28)$$

where F and S are defined in (20). It is shown[1] that

$$\text{If} \quad R > (S_{\hat{N}} S_{\hat{N}+1})^{-1} \quad \text{then} \quad F = F_{\hat{N}}, N = \hat{N},$$
$$\text{If} \quad R < (S_{\hat{N}} S_{\hat{N}+1})^{-1} \quad \text{then} \quad F = F_{\hat{N}+1}, N = \hat{N} + 1. \quad (29)$$

Then, e.g., from (25) and (29),

[1] From (20), the required condition for $F_{\hat{N}+1} > F_{\hat{N}}$ is $KaS_{\hat{N}} + (C/aS_{\hat{N}}) \leq KaS_{\hat{N}+1} + (C/aS_{\hat{N}+1})$, which, after a simple transformation (taking into account (11)) gives $S_{\hat{N}+1}S_{\hat{N}}(S_{\hat{N}+1} - S_{\hat{N}})R \geq S_{\hat{N}+1} - S_{\hat{N}}$. Since $S_{\hat{N}+1} > S_{\hat{N}}$, we obtain the condition $S_{\hat{N}+1}S_{\hat{N}}R \geq 1$, i.e., $R \geq (S_{\hat{N}+1}S_{\hat{N}})^{-1}$.

Downloaded 04 May 2010 to 171.66.16.27. Redistribution subject to ASME license or copyright; see http://www.asme.org/terms/Terms_Use.cfm

$$\text{for} \quad 8 < R, \quad N = 1,$$

$$\text{for} \quad 2 < R < 8, \quad N = 2,$$

$$\text{for} \quad 0.5858 < R < 2, \quad N = 3,$$

$$\text{for} \quad 0.2238 < R < 0.5858, \quad N = 4, \text{ etc.}$$

In Fig. 4, the nondimensional buckling force is shown as a function of R. Noting the criterion (29) and relation ($20c$), F is seen to be a piecewise linear function of R.[2] We observe here the transition from a corrugated to a smoother buckling mode for a given C/a. For a fixed value of C/a, increasing values of R correspond physically to an increasing strong interaction with the substrate. Finally, we note that the buckling mode will have a saw shape ($N = 1$) if $R > 8$ and a saw shape ($N = 2$) whenever $2 < R < 8$.

[2] It is of interest to note that while the present problem is, by its very nature, discrete, similar behavior for the critical load versus normalized stiffness is known for a continuum model, namely a rod of *finite* length resting on an elastic foundation (see, e.g., Fig. 6-3 of Simitses (1967)).

References

Falvo, M. R., Clary, G. J., Taylor, R. M., Chi, V., Brooks, F. P., Washburn, S., and Superfine, R., 1997, "Bending and buckling of carbon nanotubes under large strain," *Nature,* Vol. 389, pp. 582–584.

Fang, W., and Wickert, J. A., 1994, "Post buckling of micromachined beams," *J. Micromech. Microeng.,* Vol. 4, pp. 116–122.

Franc, F. C., and van der Merwe, J. H., 1949, "One-dimensional dislocations. I. Static theory," *Proc. R. Soc. Lond.,* Vol. A198, pp. 205–216.

Gyalog, T., and Thomas, H., 1997, "Friction between atomically flat surfaces," *Europhys. Lett.,* Vol. 37, pp. 195–200.

Simitses, G. J., 1967, *An Introduction to the Elastic Stability of Structures,* Prentice-Hall, Englewood Cliffs, NJ.

Treacy, M. M. J., Ebbesen, T. W., and Gibson, J. M., 1996, "Exceptionally high Young's modulus observed for individual carbon nanotubes," *Nature,* Vol. 381, pp. 678–680.

Weiss, M., and Elmer, F. J., 1996, "Dry friction in the Frenkel-Kontorova-Tomlinson model: Static Properties," *Phys. Rev. B,* Vol. 53, p. 7539.

Yakobson, B. I., and Richard, E. S., 1997, "Fullerene nanotubes: $C_{1,000,000}$ and beyond," *American Scientist,* Vol. 85, pp. 324–337.

Yakobson, B. I., Brabec, C. J., and Bernholc, J., 1996, "Nanomechanics of carbon tubes: Instabilities beyond linear response," *Phys. Rev. Letters,* Vol. 76, pp. 2511–2514.

Downloaded 04 May 2010 to 171.66.16.27. Redistribution subject to ASME license or copyright; see http://www.asme.org/terms/Terms_Use.cfm

A Geometric Approach for Establishing Dynamic Buckling Loads of Autonomous Potential Two-Degree-of-Freedom Systems

A. N. Kounadis
National Technical University of Athens,
Structural Analysis and Steel Bridges,
42, Patission Street,
Athens 106 82, Greece

Nonlinear dynamic buckling of autonomous potential two-degree-of-freedom nondissipative systems with static unstable critical points lying on nonlinear primary equilibrium paths is studied via a geometric approach. This is based on certain salient properties of the zero level total potential energy "surface" which in conjunction with the total energy-balance equation allow establishment of new dynamic buckling criteria for planar systems. These criteria yield readily obtained "exact" dynamic buckling loads without solving the highly nonlinear initial-value problem. The simplicity, reliability, and efficiency of the proposed technique is illustrated with the aid of various dynamic buckling analyses of two two-degree-of-freedom models which are also compared with those obtained by the Verner-Runge-Kutta scheme.

1 Introduction

Consider a general N-degree-of-freedom nonlinear nondissipative system, associated with generalized coordinates q_i ($i = 1, \ldots, n$) and parameters μ_j ($j = 1, \ldots, m$) under (conservative) potential step loading of infinite duration. Lagrange equations of motion after setting

$$y_i = q_i, \; y_{n+i} = \dot{q}_i \quad (i = 1, \ldots, n) \tag{1}$$

can always be written in the form of an autonomous vector-matrix equation as follows:

$$\dot{\mathbf{y}} = \mathbf{Y}(\mathbf{y}; \boldsymbol{\mu}), \quad \mathbf{y} \in E^{2n}, \quad \boldsymbol{\mu} \in E^m \tag{2}$$

where the dots denote differentiation with respect to time t; $\mathbf{y} = (y_1, \ldots, y_{2n})^T$ is the state vector in the $2n$-dimensional Euclidean space E with T denoting transpose, while $\mathbf{Y} = (Y_1, \ldots, Y_{2n})^T$ is a nonlinear vector function; $\boldsymbol{\mu} = (\mu_1, \ldots, \mu_m)^T$ is the control parameter-vector with m independent parameters such as λ (loading), q_i^0 (initial displacements), k_j (stiffnesses), etc. $\mathbf{Y}(\mathbf{y}, \boldsymbol{\mu})$ is assumed to be an analytic function of $\mathbf{y}$ and $\boldsymbol{\mu}$, at least in the domain of interest. The $(2n + m)$-dimensional state-parameter space, E^{2n+m}, spanned by y_i and μ_j is assumed to be Euclidean. A classification of the various types of autonomous systems is given in a thorough way by Huseyin (1986). Attention is focused herein on autonomous potential systems experiencing either steady-state solutions (i.e., equilibria) or unbounded solutions (due to dynamic buckling). The points of the state-parameter space E^{2n+m} that represent equilibrium (singular) states are obtained via the equation

$$\mathbf{Y}(\mathbf{y}, \boldsymbol{\mu}) = 0 \tag{3}$$

which defines an m-dimensional equilibrium surface in E^{2n+m} (manifold) that includes stable, unstable, and critical states. A statical analysis with the aid of Eq. (3) of the above systems associated with a total potential energy V is in order for it can yield important information for the subsequent dynamic analysis.

At this point one should adopt a definition for stability necessary to elucidate the mechanism of dynamic instability. In view of the lack of a universal definition of stability, for the purposes of the present analysis the stability criterion of Laplace or Lagrange (boundedness of solution) is employed. According to this criterion, dynamic buckling (in the large) is defined as that state for which an escaped motion either becomes unbounded (overflow) or of very large amplitude which if damping is present could be captured by a remote stable equilibrium (point attractor) associated with a large displacement. The minimum load corresponding to this state is defined as the dynamic buckling load.

This work deals with the dynamics of that broad class of autonomous potential systems whose patterns of primary equilibrium paths (obtained from Eq. (3)) are nonlinear; namely dynamics of limit point systems (Fig. 1(a)) and of unstable bifurcational systems with branching points bifurcating from nonlinear paths (Fig. 1(b)) are considered. The dynamic response of these systems shown in Fig. 1(a, b) cannot be established via a local analysis by discussing the nature of Jacobian eigenvalues. Instead, a global (nonlinear) analysis must be employed. The (special) simple and easily treated case of static bifurcational systems with trivial primary paths (Kounadis, 1994) including the more complex case of multiple branching points (Kounadis and Raftoyiannis, 1997) are not discussed here.

The major difficulty for establishing the long-term response associated with dynamic buckling is the intractability of the highly nonlinear differential equations of motion. Despite the availability of high-speed computers and computational techniques, quite often one has to overcome numerical difficulties associated with large time solutions (Kounadis, 1991a, b), solutions very sensitive to initial conditions or to damping (Kounadis, 1991a, b) or solutions related to alternative narrow regions of stability and instability as the loading increases slowly (Kounadis, 1991a, 1995): difficulties due to which numerical

Contributed by the Applied Mechanics Division of THE AMERICAN SOCIETY OF MECHANICAL ENGINEERS for publication in the ASME JOURNAL OF APPLIED MECHANICS.

Discussion on the paper should be addressed to the Technical Editor, Professor Lewis T. Wheeler, Department of Mechanical Engineering, University of Houston, Houston, TX 77204-4792, and will be accepted until four months after final publication of the paper itself in the ASME JOURNAL OF APPLIED MECHANICS.

Manuscript received by the ASME Applied Mechanics Division, Feb. 2, 1998; final revision, June 4, 1998. Associate Technical Editor: S. Kyriakides.

 Copyright © 1999 by ASME

Downloaded 04 May 2010 to 171.66.16.27. Redistribution subject to ASME license or copyright; see http://www.asme.org/terms/Terms_Use.cfm

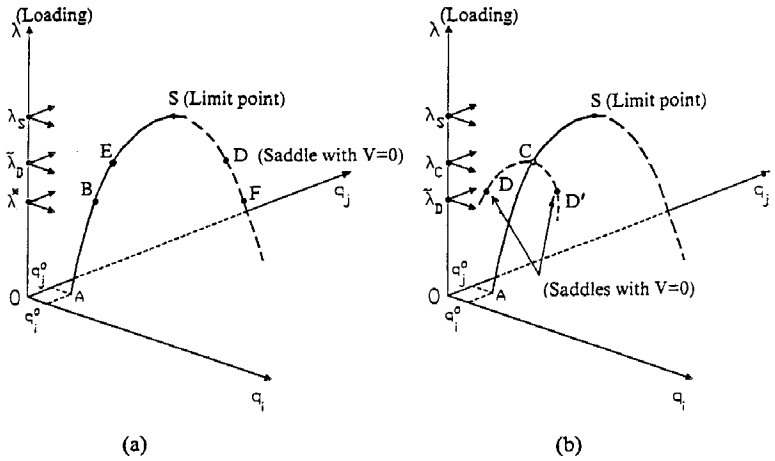

Fig. 1 Nonlinear equilibrium paths (λ versus q_i and q_j) of a typical limit point system, (*a*), and of an unstable bifurcational system, (*b*)

methods become time-consuming, sometimes less reliable, and possibly erroneous if correct solutions are missed. These drawbacks become more acute when a multiparameter investigation is needed.

A powerful, local in character, technique applicable only to the bifurcations of equilibria and periodic orbits is based on the center manifold theorem which provides a means for reducing the system dimension. However, this technique requires the transformation of the field equations into a standard form, in general, difficult to be obtained for N-degree-of-freedom systems. Analogous difficulties are associated with the application of Lyapunov-Schmidt reduction technique. Certainly, both the above, essentially approximate techniques, can be successfully applied to special cases of equations.

In view of the above, a more efficient, reliable, and readily applied technique based on energy and mainly geometric considerations (associated with a few successive coordinate transformations) is employed. This technique is illustrated with various analyses of two two-degree-of-freedom models which are checked via a modified Verner-Runge-Kutta numerical scheme.

An interesting monograph for the state of the art, starting from the early studies of Hoff (1954), Grigolyuk (1955), Humphreys and Bodner (1962) until 1990, dealing essentially with one-degree-of-freedom systems, is presented by Simitses (1990). Further work in this area referring to analyses of two-degree-of-freedom and three-degree-of-freedom dissipative/nondissipative systems is reported in the book by Kounadis and Kratzig (1995). Two qualitative analyses leading to exact, approximate, and upper-lower bound buckling estimates for autonomous potential systems were recently presented by Kounadis (1996a, b).

The objective of this work is by extending the last two studies to establish a comprehensive and readily applied geometric approach leading to exact dynamic buckling loads for two-degree-of-freedom systems. This is successfully achieved by studying certain salient properties of the curve $V = 0$ (or surface or hypersurface for higher dimensions) which vary as the loading increases above a certain level. This is very conveniently established by using (a few) successive coordinate transformations of a Cartesian system sliding slowly along the length of the stable primary path.

2 Statement of the Problem

Subsequently we consider a general N-degree-of-freedom nonlinear system with nonlinear primary path of the type of Fig. 1(*a*) or Fig. 1(*b*), the static response of which is described by an analytic and single-valued total potential energy function $V(q_i, \lambda; q_i^0)$, nonlinear with respect to q_i and linear in the conservative loading λ, where q_i^0 are initial displacements. One could also include other parameters, but for the sake of simplifying the notation we have restricted ourselves only to q_i^0. For a fixed value of λ the total potential energy V represents a "hypersurface" in the $(n + 1)$-dimensional configuration space spanned by V and q_i $(i = 1, \ldots, n)$. Equilibrium paths are the

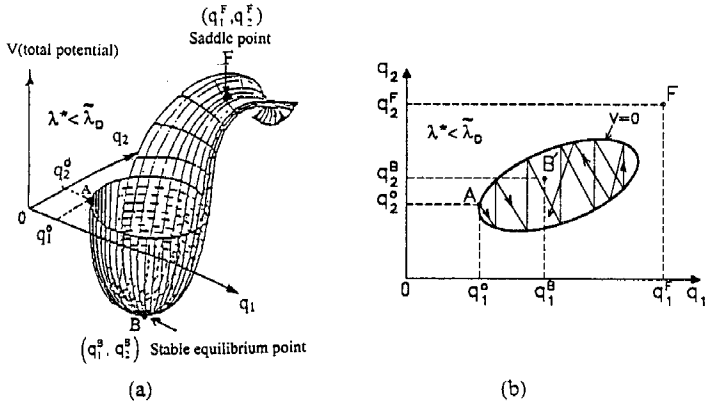

Fig. 2 (*a*) Energy surface V (at $\lambda^* < \tilde{\lambda}_D$) for a two-degree-of-freedom system and (*b*) projection of motion in 0 q_1q_2-plane

Downloaded 04 May 2010 to 171.66.16.27. Redistribution subject to ASME license or copyright; see http://www.asme.org/terms/Terms_Use.cfm

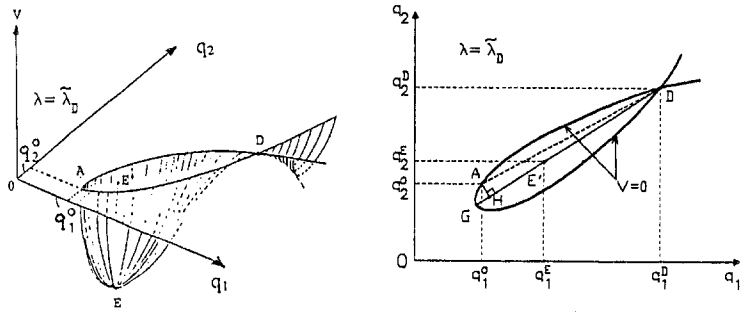

Fig. 3 (*a*) **Total potential surface** $V \leq 0$ **at** $\lambda = \tilde{\lambda}_D$, **and** (*b*) **its intersection with the** $0q_1q_2$**-plane for a two-degree-of-freedom system**

loci of equilibrium (singular) points of these "energy surfaces" which are obtained from Eq. (3) or equivalently from

$$V_i(q_i, \lambda; q_i^0) = 0, \quad (i = 1, \ldots, n) \tag{4}$$

where the subscript i indicates partial differentiation with respect to the corresponding q_i. We can now assume that one solution of Eqs. (4), $q_i = q_i^F(\lambda)$, defines a nonlinear fundamental (primary) path in the load-displacement space which is single-valued.

We are interested in the global stability and dynamic buckling of the above types of systems (Fig. 1(*a*, *b*)) when they are subjected to a step load of infinite duration. The analysis can be easily extented to the cases of a step load of finite duration, of an impulsive loading (Kounadis and Raftoyiannis, 1990) or of an impact loading (Kounadis, Gantes, and Simitses, 1997). For both the above two types of systems we can assume for the aforementioned types of dynamic loading the following initial ($t = 0$) conditions:

$$q_i(0) = q_i^0, \dot{q}_i(0) = 0 \quad (i = 1, \ldots, n). \tag{5}$$

Equations (5) define the position of the starting point of motion A (Fig. 1(*a*, *b*)). Then, the total energy equation of the above autonomous potential systems (including loss of energy) at any time $t > 0$ (being the first integral of Lagrange equations of motion) is given by (Kounadis, 1993)

$$E = K + V + 2\int_0^t F dt' = 0 \tag{6}$$

where $K = (\frac{1}{2})a_{ij}\dot{q}_i\dot{q}_j$ is the positive definite function of the total kinetic energy; $V = (q_i, \lambda; q_i^0)$ is the above total potential energy; and $F = (\frac{1}{2})c_{ij}\dot{q}_i\dot{q}_j$ is a non-negative definite Rayleigh dissipation function. Dummy-suffix summation convention is employed herein with summations ranging from 1 to n. From Eq. (6) it is clear that throughout the motion (including dynamic buckling, being an escaped motion)

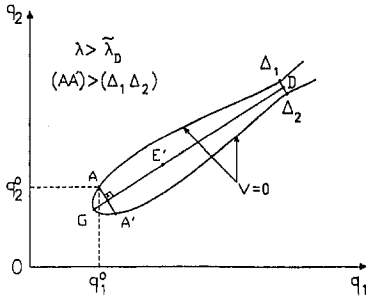

Fig. 4 Curve $V = 0$ for $\lambda > \tilde{\lambda}_D$

$$V(q_i, \lambda; q_i^0) \leq 0 \tag{7}$$

while if $V > 0$ there is no motion, and hence dynamic buckling.

According to the criterion for dynamic buckling adopted in the Introduction it should be added (Kounadis, 1996a, b) that dynamic buckling for the above N-degree-of-freedom systems (Fig. 1(*a*)) occurs via a saddle point D (with zero V) or via a neighborhood of D (with very small negative V). For the systems of Fig. 1(*b*) (associated with an unstable symmetric branching point) there are two saddle points D' and D with $V = 0$. Loading λ, corresponding to saddles D (Fig. 1(*a*)) or D and D' (Fig. 1(*b*)) for which $V = 0$, is denoted by $\tilde{\lambda}_D$. This load in case of nondissipative systems of one degree-of-freedom coincides with the exact dynamic buckling loads λ_D, while for nondissipative N-degree-of-freedom systems $\tilde{\lambda}_D$ is, in general, a lower bound dynamic buckling estimate (Kounadis, 1996a), i.e., $\tilde{\lambda}_D < \lambda_D$ (exact dynamic buckling load).

3 Geometric Approach

The lower bound dynamic buckling loads $\tilde{\lambda}_D$ (for the above two types of nondissipative systems) and the corresponding saddle q^D (on the unstable path, Fig. 1(*a*)) or saddles q^D and $q^{D'}$ (on the two unstable paths, Fig. 1(*b*)) are obtained for given initial (displacements) conditions q^0 by solving the system of $(n + 1)$-equations (Kounadis, 1996a, b)

$$\left.\begin{aligned} V_i(q_i, \lambda; q_i^0) &= 0 \\ V(q_i, \lambda; q_i^0) &= 0 \end{aligned}\right\} \quad i = 1, \ldots, n \tag{8}$$

with respect to q_i $(i = 1, \ldots, n)$ and λ.

Energy and geometric criteria for an a priori qualitative prediction of the degree of accuracy of $\tilde{\lambda}_D$ have been presented in the last two studies. Moreover, simple formulas for determining the error between $\tilde{\lambda}_D$ and the exact dynamic buckling load λ_D for two systems of two degree-of-freedom were recently proposed (Gantes, Kounadis, and Mallis, 1996).

On the unstable path SDF (Fig. 1(*a*)) and on the unstable paths CD and CD' (Fig. 1(*b*)), the total potential energy V is indefinite (Kounadis, 1996a, b) associated with saddles increasing with decreasing λ along these falling paths. At point D as well as at D and D' we have $V = 0$ (yielding $\tilde{\lambda}_D$), while for $\lambda < \tilde{\lambda}_D$ the function V on the unstable path becomes positive increasing with decreasing λ. Hence, for $V > 0$ there is *no motion* and thus dynamic buckling (escaped motion) is ruled out.

Two Degree-of-Freedom Systems. The error (difference) $E = \lambda_D - \tilde{\lambda}_D$ can be more conveniently established by considering two-degree-of-freedom systems for which one has a simple geometric picture of the energy potential surface $V(q_i, \lambda; q_i^0)$

Downloaded 04 May 2010 to 171.66.16.27. Redistribution subject to ASME license or copyright; see http://www.asme.org/terms/Terms_Use.cfm

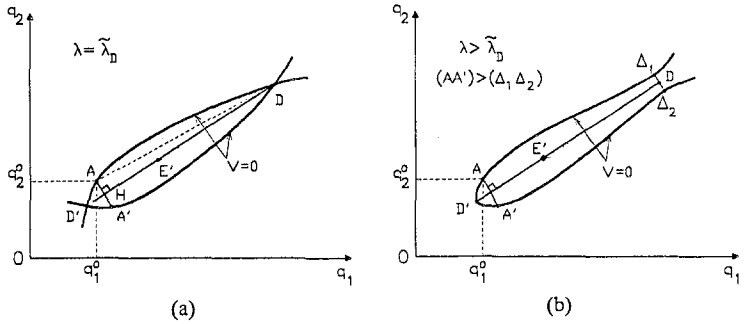

Fig. 5 Curve $V = 0$: (*a*) at $\lambda = \tilde{\lambda}_D$ with two saddles *D* and *D'*, and (*b*) at $\lambda > \tilde{\lambda}_D$ with one saddle

in the V-displacement space. For a typical two-degree-of-freedom model (corresponding to Fig. 1(*a*)), the energy surface V (at a fixed load $\lambda^* < \tilde{\lambda}_D$) passing through the points A (defined by the initial conditions q_1^0 and q_2^0), the stable equilibrium point $B(q_1^B, q_2^B)$ and the saddle $F(q_1^F, q_2^F)$ are shown in Fig. 2(*a*). The points B and F both correspond to λ^*. Clearly, at point B the surface V experiences a minimum, at point A there corresponds $V = 0$, while at the saddle F the total potential energy V is positive and maximum (as V varies in the vertical plane passing through points B and F). One can visualize the motion in the Vq_1q_2-space (for fixed $\lambda^* < \tilde{\lambda}_D$) by the frictionless motion of a point-ball with unit mass which starts from point A and moves on the interior "surface" of the total potential, where $V \leq 0$. Fig. 2(*b*) shows the projection of a typical motion (in the horizontal plane $0q_1q_2$) which is surrounded by the plane (closed) curve $V = 0$, being the intersection of the "surface" V with the horizontal plane $0q_1q_2$. In planar systems the width of the enclosed plane region by this curve is very small compared to the length of its longitudinal axis. The geometry of this curve and the positions of the points A, B, and F, relative to each other, depend on the level of the loading λ. The unit mass, initially located at point A, falls sharply into the interior of the "surface" $V \leq 0$, following the trajectory of the steepest descent. If $\lambda < \tilde{\lambda}_D$, any motion starting from A cannot escape through $F(q_1^F, q_2^F)$, since above the horizontal plane $V > 0$, and hence there is no motion leading to dynamic buckling. However, as λ increases, the saddle F approaches the horizontal plane $0q_1q_2$. At a certain value, $\lambda = \tilde{\lambda}_D$ (for which $V = 0$) the surface V touches the plane $0q_1q_2$ at the saddle D (Fig. 3(*a*)). Then, for λ infinitesimally greater than $\tilde{\lambda}_D$ (so that $V(D) < 0$), the unit mass escapes through the saddle $D(q_1^D, q_2^D)$ *provided* that it will be directed from point A to point D (being the escape passage). In this case $\tilde{\lambda}_D \equiv \lambda_D$. However, this is possible only when the points A (with $V = 0$), E (with $V_{\min}$) and D (with $V = 0$) lie in the same vertical plane which implies the existence of one (unique) trajectory starting from A, passing through E and then escaping via the saddle D (see Fig. 3(*b*)). The principal directions of the matrix $[V_{ij}]$ of the 2nd variation, $\delta^2 V$, correspond to the direction $E'D$ (associated with the smallest eigenvalue of $[V_{ij}]$), and to its normal direction (associated with the greatest eigenvalue of $[V_{ij}]$). Nevertheless, the existence of such a unique trajectory is not usually the case, because if the unit mass starts from a point A on the curve $V = 0$, not lying in the above vertical plane or on the straight line $E'D$, it cannot reach point D but it will stop at a point along the line $E'D$, where the width of the enclosed region by curve $V = 0$ is smaller than that at point A. Then, the unit mass will go back and forth between these two points around the stable equilibrium point E which is a center. As the point A moves away from the vertical plane (passing through the points E and D), so the difference between λ_D and $\tilde{\lambda}_D$ increases (Kounadis, 1996a, b). However, by slightly increasing λ (above $\tilde{\lambda}_D$) the closed curve $V = 0$ becomes an open curve, exhibiting an opening at the corresponding new saddle D (Fig. 4). If the width (AA') at point A, corresponding to the new open curve $V = 0$, is still greater than the width $(\Delta_1\Delta_2)$ at the saddle D [namely, if $(AA') > (\Delta_1\Delta_2)$], an escape motion (and hence dynamic buckling) is impossible. Then, we further increase the load λ so that the width at point A of the corresponding new curve $V = 0$ is equal to the width of the same curve at the corresponding new saddle D. In this case, an escape motion (and thus dynamic buckling) will occur. The corresponding load λ to this situation is the dynamic buckling load.

For a two-degree-of-freedom system of the type shown in Fig. 1(*b*) the intersection of the total potential surface V with the horizontal plane $0q_1q_2$ for $\lambda = \tilde{\lambda}_D$, is also a closed curve $V = 0$ but with two saddles D and D'. The maximum width of the plane region described by the curve $V = 0$ is also very small compared to the length of the longitudinal axis DD'. For λ slightly greater than $\tilde{\lambda}_D$ one of the saddles disappears (see Fig. 5(*b*)), while at the other (new) saddle the new curve $V = 0$ exhibits an opening, exactly in the same way as in Fig. 4 (corresponding to the system of Fig. 1(*a*)). If $(AA') > (\Delta_1\Delta_2)$ escaped motion (i.e., dynamic buckling) through the neighborhood of D is impossible. However, at a certain level of λ, the width of the plane region enclosed by the curve $V = 0$ at A [i.e., (AA')] becomes equal to the width $\Delta_1\Delta_2$ at D, a situation which leads to dynamic buckling. This load is the dynamic buckling load.

In view of the above, it may happen that $\tilde{\lambda}_D$ becomes equal or practically equal to the exact dynamic buckling load λ_D (e.g., correct to four significant figures). This can be known a priori depending on the proximity of point A to point G or D' (see Figs. 3(*b*), 5(*a*)). Such a proximity can be determined explicitly by means of the magnitude of the angle $A\hat{D}H \equiv A\hat{D}E'$ (Gantes, Kounadis, and Mallis, 1996). The above accuracy of $\tilde{\lambda}_D$ is always assured if this angle is less than 1 deg or 0.0175 rad. If this is not the case, we increase the load λ (above $\tilde{\lambda}_D$) according to the procedure outlined below.

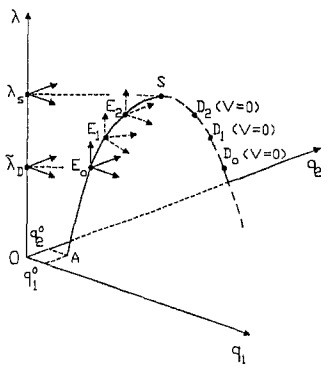

Fig. 6 Sliding and rotating Cartesian coordinate system for $\lambda \geq \tilde{\lambda}_D$

Downloaded 04 May 2010 to 171.66.16.27. Redistribution subject to ASME license or copyright; see http://www.asme.org/terms/Terms_Use.cfm

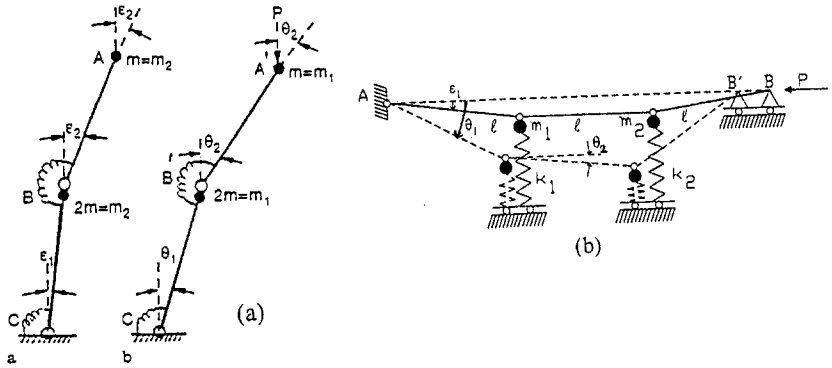

Fig. 7 Two-degree-of-freedom systems: (*a*) limit point system and (*b*) unstable bifurcational system

Coordinate Transformations. The analysis that follows is valid for both systems shown in Fig. 1(a, b). Solving Eqs. (8) for $i = 1, 2$ we find the load $\lambda = \tilde{\lambda}_D$ and the corresponding saddle D (see Fig. 1(a)) or saddles D and D' (see Fig. 1(b)). If the angle $A\hat{D}H$ is higher than 1 deg or 0.0175 rad (Fig. 3(b), Fig. 5(a)) we apply the following procedure: We determine the stable equilibrium E, say $E = E_0$ and the saddle D_0 both corresponding to $\lambda = \tilde{\lambda}_D$. Next, we choose E_0 as the new origin of a Cartesian coordinate system slowly sliding along the primary (stable) equilibrium path (Fig. 6). This is performed with the aid of the following transformation of variables:

$$\lambda_1 = \tilde{\lambda}_D + \delta\lambda \tag{9}$$

$$q_1 = q_1^{E_0} + Q_1, \quad q_2 = q_2^{E_0} + Q_2. \tag{10}$$

Using the above transformation (10) with $\delta\lambda = \delta\lambda_0$ (small positive increment), $E = E_0$ and $D = D_0$, Eqs. (8) become

$$V_i(Q_1, Q_2; \tilde{\lambda}_D + \delta\lambda_0; Q_1^0; Q_2^0) = 0, \quad i = 1, 2 \tag{11}$$

$$V(Q_1, Q_2; \tilde{\lambda}_D + \delta\lambda_0; Q_1^0; Q_2^0) = 0 \tag{12}$$

where the new position of A in terms of Q_i^0 ($i = 1, 2$) is defined by

$$Q_1^0 = q_1^0 - q_1^{E_0}, \quad Q_2^0 = q_2^0 - q_2^{E_0}. \tag{13}$$

From Eqs. (11) we find the new equilibria $E_1(Q_1^{E_1}, Q_2^{E_1})$ and $D_1(Q_1^{D_1}, Q_2^{D_1})$ corresponding to $\lambda_1 = \tilde{\lambda}_D + \delta\lambda_0$, while from Eq. (12) we can establish the new curve $V = 0$ which now is open (as in Fig. 4 or Fig. 5(b)). Then, we can compare the width (AA') of the enclosed region described by the curve $V = 0$ at A with the width ($\Delta_1\Delta_2$) at the saddle D_1. If (AA') is greater than the opening ($\Delta_1\Delta_2$), we increase the load λ_1 by $\delta\lambda_1 > \delta\lambda_0$ (>0), after choosing E_1 as new origin and making use of the following transformation of variables:

$$\left.\begin{aligned} \lambda_2 &= \tilde{\lambda}_D + \delta\lambda_1 \\ Q_1^{(0)} &= Q_1^{(1)} + Q_1^{E_1}, \; Q_2^{(0)} = Q_2^{(1)} + Q_2^{E_1} \end{aligned}\right\}. \tag{14}$$

Thereafter, we repeat the previous procedure. Namely, we find the new position of point A, the new equilibria $E_2(Q_1^{E_2}, Q_2^{E_2})$ and $D_2(Q_1^{D_2}, Q_2^{D_2})$, and finally the new curve $V = 0$ corresponding to $\lambda_2 = \tilde{\lambda}_D + \delta\lambda_1$. If the width ($AA'$) at point A is equal to the width ($\Delta_1\Delta_2$) at the new saddle D_2, then λ_2 is the dynamic buckling load; otherwise, we further increase (or possibly decrease) λ_2 to achieve the equality of the widths (AA') and ($\Delta_1\Delta_2$).

Note that the above procedure for determining dynamic buckling loads (associated with the condition (AA') = ($\Delta_1\Delta_2$)) does not involve error accumulation. This is so, since the transition to this final state E_i ($i = 1, 2, \ldots$) is directly derivable from the initial equilibrium point E_0 without intermediate steps.

4 Numerical Examples

Subsequently, numerical results in tabular and graphical form are presented related to dynamic buckling analyses of the two two-degree-of-freedom models shown in Fig. 7(a, b) corresponding to the typical cases of Fig. 1(a, b), respectively. Both models are subjected to a step load λ of infinite duration.

Equations of Motion. Lagrange equations of motion, in dimensionless form, for the above two nondissipative models, are given by Kounadis (1995),

$$\left.\begin{aligned} (1+m)\ddot{\theta}_1 + \ddot{\theta}_2\cos(\theta_1 - \theta_2) \\ + \dot{\theta}_2^2\sin(\theta_1 - \theta_2) + V_1 = 0 \\ \ddot{\theta}_2 + \ddot{\theta}_1\cos(\theta_1 - \theta_2) - \dot{\theta}_1^2\sin(\theta_1 - \theta_2) + V_2 = 0 \end{aligned}\right\}, \tag{15}$$

where $V_1 = V_2 = 0$ are the nonlinear equilibrium equations related to the following total potential functions V:

Table 1 Static buckling loads (SBLs) λ_s and dynamic buckling loads (DBLs) λ_D, $\tilde{\lambda}_D$, λ_D^* and pertinent errors for $m = 2$, $\delta_1 = -2.5$, $\delta_2 = -0.75$, $\gamma_1 = \gamma_2 = 0$, $\epsilon_1 = 0.05$, and various values of ϵ_2

		DBLs			Error percent	
ϵ_2	SBLs λ_s	Runge-Kutta λ_D	$V = 0$ $\tilde{\lambda}_D$	Geom. Approach λ_D^*	$(\lambda_D - \tilde{\lambda}_D)/\lambda_D$	$(\lambda_D - \lambda_D^*)/\lambda_D$
−0.03	0.3484997	0.34234608	0.3240248	0.341593	5.4%	0.22%
−0.02	0.3055120	0.29465561	0.2915148	0.294535	1.0%	0.04%
−0.01	0.2836452	0.27028147	0.2692948	0.270348	0.4%	0.02%
0	0.2677128	0.25262317	0.2523081	0.252799	0.2%	0.07%
0.01	0.2549430	0.23855465	0.2384910	0.238869	0.1%	0.13%
0.02	0.2442086	0.22679802	0.2268233	(*)	0.01%	—
0.03	0.2349196	0.21668189	0.2166727	(*)	0.01%	—

(*) implies $\lambda_D^* \equiv \tilde{\lambda}_D$ since angle $A\hat{D}E'$ is less than 1 deg.

Downloaded 04 May 2010 to 171.66.16.27. Redistribution subject to ASME license or copyright; see http://www.asme.org/terms/Terms_Use.cfm

Table 2 Static buckling loads (SBLs) λ_s and dynamic buckling loads (DBLs) λ_D, $\tilde{\lambda}_D$, λ_D^* and pertinent errors for $m = 2$, $\gamma_1 = \gamma_2 = -0.4364$, $\delta_1 = \delta_2 = 0$, $\epsilon_2 = 0.05$, and various values of ϵ_2

		DBLs			Error percent	
ϵ_2	SBLs λ_s	Runge-Kutta λ_D	$V = 0$ $\tilde{\lambda}_D$	Geom. approach λ_D^*	$(\lambda_D - \tilde{\lambda}_D)/\lambda_D$	$(\lambda_D - \lambda_D^*)/\lambda_D$
−0.03	0.3802254	0.3798435	0.3790879	0.379827	0.19%	0.004%
−0.02	0.3743722	0.3718727	0.3717223	0.371869	0.04%	0.001%
−0.01	0.3706676	0.3663773	0.3663055	0.366382	0.08%	0.001%
0	0.3676076	0.3616716	0.3616375	0.361686	0.01%	0.004%
0.01	0.3649324	0.3574471	0.3574312	0.357479	0.01%	0.008%
0.02	0.3625302	0.3535689	0.3535564	(*)	0.001%	—
0.03	0.3603394	0.3499611	0.3499570	(*)	0.004%	—

(*) implies $\lambda_D^* \equiv \tilde{\lambda}_D$ since angle $A\hat{D}E'$ is less than 0.4 deg.

Table 3 Static buckling loads (SBLs) λ_s and dynamic buckling loads (DBLs) λ_D, $\tilde{\lambda}_D$, λ_D^* and pertinent errors for $m = 1$, $\gamma_1 = \gamma_2 = \gamma = 1$, $\epsilon_2 = 0$, and various values of ϵ_1

		DBLs			Error percent	
ϵ_1	SBLs λ_C	Runge-Kutta λ_D	$V = 0$ $\tilde{\lambda}_D$	Geom. approach λ_D^*	$(\lambda_D - \tilde{\lambda}_D)/\lambda_D$	$(\lambda_D - \lambda_D^*)/\lambda_D$
0.01	0.999813	0.999680	0.990793	0.999602	0.9%	0.008%
0.02	0.999251	0.998725	0.981442	0.998226	1.7%	0.05%
0.05	0.995321	0.992199	0.952552	0.991107	4.0%	0.11%
0.07	0.990844	0.985073	0.932653	0.983497	5.5%	0.16%
0.10	0.981372	0.970476	0.901910	0.968729	7.4%	0.18%
0.12	0.973263	0.959723	0.881006	0.957612	8.7%	0.22%
0.15	0.958449	0.941011	0.802937	0.938847	16.7%	0.23%
0.20	0.926991	0.907976	0.793951	0.905434	14.1%	0.27%

Model in Fig. 7(a).

$$V = \tfrac{1}{2}(\theta_1 - \epsilon_1)^2 + \tfrac{1}{3}\delta_1(\theta_1 - \epsilon_1)^3 + \tfrac{1}{4}\gamma_1(\theta_1 - \epsilon_1)^4 + \tfrac{1}{2}(\theta_1 - \epsilon_1 - \theta_2 + \epsilon_2)^2 - \tfrac{1}{3}\delta_2(\theta_1 - \epsilon_1 - \theta_2 + \epsilon_2)^3 + \tfrac{1}{4}\gamma_2(\theta_1 - \epsilon_1 - \theta_2 + \epsilon_2)^4 - \lambda(\cos\epsilon_1 + \cos\epsilon_2 - \cos\theta_1 - \cos\theta_2) \quad (16)$$

In this model, shown in Fig. 7(a), quadratic and cubic (soft-type) nonlinearities δ_i and γ_i $(i = 1, 2)$ are included.

Model in Fig. 7(b).

$$V = \frac{1}{2}(\sin\theta_1 - \sin\epsilon_1)^2 - \frac{\gamma_1}{4}(\sin\theta_1 - \sin\epsilon_1)^4 + \frac{1}{2}(\sin\theta_1 - \sin\epsilon_1 + \sin\theta_2 - \sin\epsilon_2)^2$$

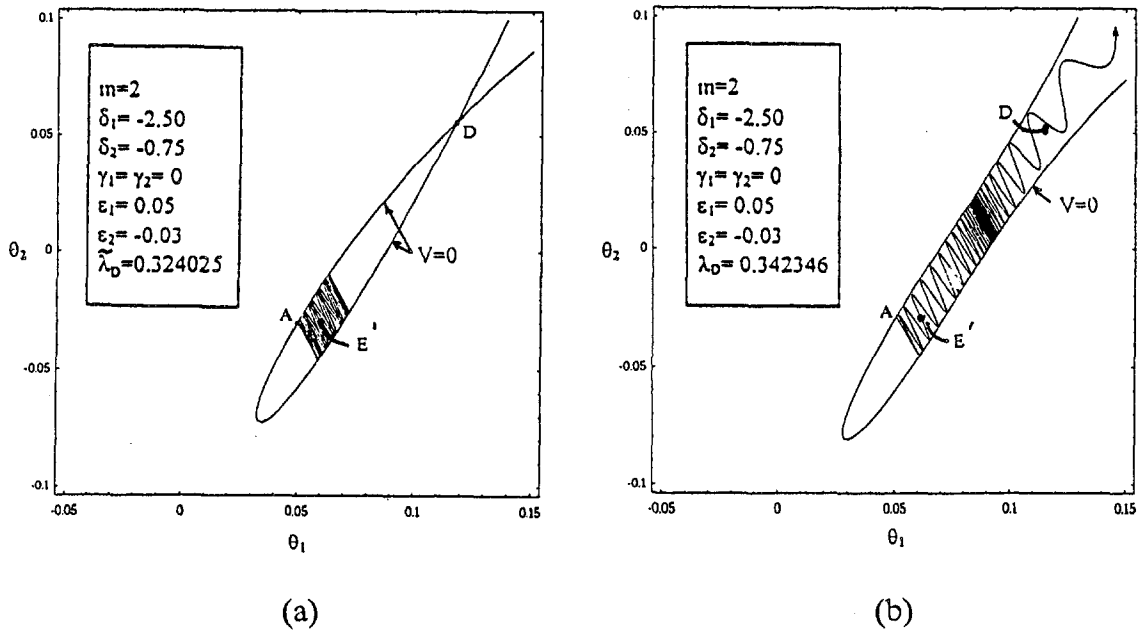

Fig. 8 Motion projection on horizontal plane: (*a*) at $\tilde{\lambda}_D = 0.324025$, (*b*) at $\lambda_D = 0.342346$ (exact dynamic buckling load)

Downloaded 04 May 2010 to 171.66.16.27. Redistribution subject to ASME license or copyright; see http://www.asme.org/terms/Terms_Use.cfm

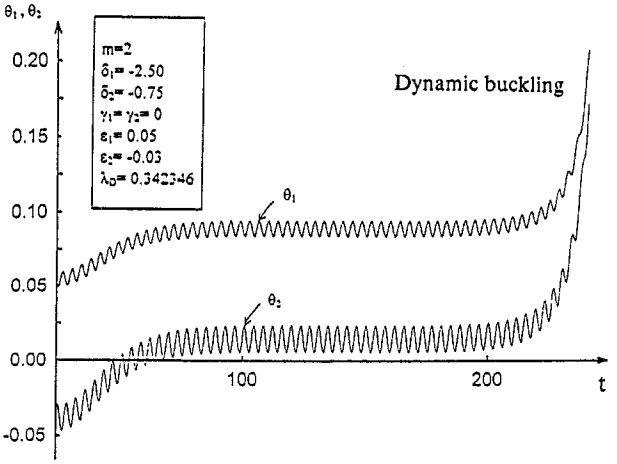

Fig. 9 Time series θ_i (i = 1.2) versus time t at the instant of dynamic buckling

$$- \frac{\gamma_2}{4}(\sin\theta_1 - \sin\epsilon_1 + \sin\theta_2 - \sin\epsilon_2)^4$$

$$- \lambda[\cos\epsilon_1 - \cos\theta_1 + \cos\epsilon_2$$

$$- \cos\theta_2 + \sqrt{1 - (\sin\epsilon_1 + \sin\epsilon_2)^2}$$

$$- \sqrt{1 - (\sin\theta_1 + \sin\theta_2)^2}] \quad (17)$$

The model shown in Fig. 7(b) corresponds to the above V with $\epsilon_2 = 0$ and cubic nonlinearities γ_i (i = 1, 2).

As is known, systems made from nonlinearly elastic material of soft quadratic type (associated with asymmetric bifurcations) are more sensitive to imperfections than those made from materials of soft cubic type nonlinearities (associated with symmetric unstable bifurcations).

Table 1 (with $\gamma_i = 0$) and Table 2 (with $\delta_i = 0$) refer to the model in Fig. 7(a), while Table 3 refers to the model in Fig. 7(b). These tables give various numerical results for nondissipative systems from which one can compare the values of SBLs (static buckling loads) and dynamic buckling loads obtained by the Runge-Kutta scheme and by the proposed geometric approach.

From the last column of Table 1 (quadratic model) it is clear that the *maximum* difference between λ_D (Runge-Kutta) and λ_D^* (geometric approach) is 0.22 percent. For $\epsilon_2 \geq 0.02$ we have $\lambda_D^* \equiv \tilde{\lambda}_D$ since angle $A\hat{D}E'$ is 0.8 deg (for $\epsilon_2 = 0.02$) and 1 deg (for $\epsilon_2 = 0.03$).

Analogous results are given in Table 2 (cubic model).

In Table 2 the dynamic buckling loads λ_D^* are much closer to those obtained by the Runge-Kutta scheme compared to the corresponding ones in Table 1. In this case $A\hat{D}E' < 0.4$ deg.

From Table 3, referring to the cubic bifurcational system, the deviation of $\tilde{\lambda}_D$ from λ_D may be unacceptable for structural design purposes, while the proposed dynamic buckling load λ_D^* is practically equal (within four significant figures of accuracy) to λ_D obtained by the Runge-Kutta scheme and thus may be considered as the exact dynamic buckling load.

In Fig. 8(a, b) one can see the projection of the motion on the horizontal plane $V = 0$ at the level $\lambda = \tilde{\lambda}_D$ and at the level of the "exact" dynamic buckling load $\lambda = \lambda_D$ [where (AA') $= (\Delta_1\Delta_2)$] for the cantilever model with $m = 2$, $\gamma_1 = \gamma_2 = 0$, $\delta_1 = -2.50$, $\delta_2 = -0.75$, $\epsilon_1 = 0.05$, and $\epsilon_2 = -0.03$ (see Table 1). Time series θ_i versus t (i = 1, 2) shown in Fig. 9 correspond to the lower and higher eigenvalues of matrix $[V_{ij}]$. The direction $HE'D$ (Fig. 3(b)) corresponds to the lower eigenvalue, while its normal direction to the higher eigenvalue.

The proposed technique can be extended to systems with more than two degrees-of-freedom. The curve $V = 0$ at a fixed load λ becomes a surface for a 3-degree-of-freedom model or a hypersurface (for an N-degree-of-freedom model with $N > 3$). If the segment (AA'), normal to the direction ED', becomes equal to the parallel segment $(\Delta_1\Delta_2)$ passing through the saddle D, then dynamic buckling occurs according to this analysis.

In the above analyses the mass distribution is uniform or nearly uniform, and thus its effect on the dynamic buckling load is negligible. However, from existing numerical results (Kounadis, 1996b) it was found that even in case of a profound nonuniform mass distribution the exact dynamic buckling load practically remains unchanged.

In view of the above one concludes that the proposed static approach can practically provides the exact dynamic buckling load.

References

Gantes, Ch., Kounadis, A. N., and Mallis, J., 1996, "Dynamic Stability of Discrete Systems via Geometric and Energy Considerations Using Mathematica," *2nd Greek National Congress on Computational Mechanics,* Chania, Crete, June 26–28, pp. 384–391.

Grigolyuk, E. I., 1995, "Nonlinear Vibration and Stability of Shallow Shells," *Izvestia Akademi Nauk. SSSR,* Vol. 30, No. 33 (translated from Russian in Appl. Mech. Series 131, Inst. Eng. Research, University of California, 1960).

Hoff, N. J., and Bruce, V. J., 1954, "Dynamic Analyses of the Buckling of Laterally Loaded Arches," *J. Math. Physics,* Vol. 32, No. 4, pp. 276–288.

Humphreys, J. S., and Bodner, S. R., 1962, "Dynamic Buckling of Shallow Shells Under Impulsive Loading," *J. Eng. Mech. Div.,* Vol. 88, No. Em2, pp. 17–36.

Huseyin, K., 1986, *Multiple-Parameter Stability Theory and its Applications,* Clarendon Press, Oxford, UK.

Kounadis, A. N., 1991a, "Chaoticlike Phenomena in the Nonlinear Dynamic Stability of Discrete Damped or Undamped Systems Under Step Loading," *Int. J. Non-Linear Mechanics,* Vol. 26, No. 3–4, pp. 301–311.

Kounadis, A. N., 1991b, "On the Reliability of Postbuckling Analyses for Nonconservative Imperfect Systems," *Arch. Mech.,* Vol. 43, No. 1, pp. 95–105.

Kournadis, A. N., 1991c, "Some New Instability Aspects for Nonconservative Systems Under Follower Loads," *Int. J. Mech. Sci.,* No. 4, pp. 297–311.

Kournadis, A. N., 1993, "Static and Dynamic, Local and Global, Bifurcations in Nonlinear Autonomous Structural Systems," *AIAA J.,* Vol. 31, No. 8, pp. 1468–1477.

Kounadis, A. N., 1994, "A Qualitative Analysis for the Local and Global Dynamic Buckling and Stability of Autonomous Discrete Systems," *Z. J. Mech. Appl. Math.,* Vol. 47, Pt. 2, pp. 269–295.

Kounadis, A. N., 1995, "Nonlinear Stability and Dynamic Buckling of Autonomous Dissipative Systems," *ZAMM,* Vol. 75, No. 4, pp. 283–293.

Kounadis, A. N., 1996a, "On the Nonlinear Dynamic Buckling Mechanism of Autonomous Dissipative/Nondissipative Discrete Systems," *Archive of Appl. Mech.,* Vol. 66, pp. 395–906.

Kounadis, A. N., 1996b, "Qualitative Criteria in Nonlinear Dynamic Buckling and Stability of Autonomous Dissipative Systems," *Int. J. Non-Linear Mechanics,* Vol. 31, No. 6, pp. 887–906.

Kounadis, A. N., and Kratzig, W. B., 1995, *Stability of Structures, Theory and Computational Techniques* (CISM Courses and Lectures), Springer-Verlag, Wien, pp. 73–143.

Kounadis, A. N., and Raftoyiannis, J., 1990, "Dynamic Stability Criteria of Nonlinear Elastic Damped or Undamped Systems Under Step Loading," *AIAA J.,* Vol. 28, pp. 1217–1223.

Kounadis, A. N., and Raftoyiannis, J., 1997, "Dynamic Buckling and Global Stability of Dissipative/Nondissipative Systems Exhibiting Mode Coupling Under Static Loading," XXII Yugoslav Congress of Theoretical and Applied Mechanics, June 2–7, Venjacka Banja, invited lectures, pp. 15–30.

Simitses, G. J., 1990, *Dynamic Stability of Suddenly Loaded Structures,* Springer-Verlag, New York.

Downloaded 04 May 2010 to 171.66.16.27. Redistribution subject to ASME license or copyright; see http://www.asme.org/terms/Terms_Use.cfm

Surface Bifurcation in Anisotropic Materials With Application to Aluminum Alloys

M. D. Nestorović

E. Chu

N. Triantafyllidis
Fellow ASME

Department of Aerospace Engineering,
The University of Michigan,
3042 FXB Building,
Ann Arbor, MI 48109-2140

Surface bifurcation is an instability mechanism which appears in the form of surface waviness on traction-free surfaces in ductile solids subjected to large strains. In sheet metal forming, the practical interest in this phenomenon stems from the fact that it occurs past the onset of localization, i.e., the forming limit, but prior to the local fracture failure in a quasi-static, monotonic loading process. In this work, we apply the general theory for surface bifurcation in a homogeneously strained, anisotropic, rate-independent, elastoplastic half-space, to study the influence of material anisotropy on the onset of surface instabilities. In particular, we calculate the critical principal strains ϵ_1^c, ϵ_2^c and the corresponding eigenmode orientation angle Ω_c when the principal strain axes are at a fixed angle α with respect to the rolling direction of the solid. The presented calculations are for a 2024-T3 aluminum alloy, whose constitutive properties have been determined experimentally. It is found that by varying the strain orientation angle α, the surface bifurcation strains can vary up to an order of 80 percent for in-plane principal strains of a different sign, but only up to an order of ten percent for principal strains of the same sign. The eigenmode orientation angle Ω_c is calculated for a particular strain orientation ($\alpha = \pi/6$), for which case it is found that Ω_c is close to the forming limit angle ψ_c only for positive principal strains. The presentation is concluded by a discussion of the influence of the anisotropy and the yield surface parameters of the constitutive model on surface bifurcation.

1 Introduction and Motivation

An instability phenomenon occurring during a quasi-static loading of ductile solids at adequately high levels of strain, is the development of surface waviness on the previously smooth traction-free boundaries. The resulting surface roughness is in the form of same orientation surface wrinkles of a very short wavelength. Upon further straining, the development of microcracks at the bottom of the wave troughs, which eventually leads to fracture, justifies the interest in surface bifurcation as a precursor phenomenon to the ultimate failure by fracture.

The credit for the theoretical explanation of this phenomenon within the context of large strain continuum mechanics goes to Biot (1965), who was the first to show the possibility of a bifurcation instability occurring in an elastic, traction-free half-space subjected to large in-plane stresses. The corresponding eigenmode decays exponentially away from the surface, but the analysis provides no characteristic wavelength for the mode. Subsequent investigations at large deformations in finite-size elastoplastic solids showed that surface bifurcations always appear on the free surfaces after an adequate amount of straining in compression as well as in tension. Examples of surface bifurcations in structures include the elastoplastic rectangular block under tension and compression by Hill and Hutchinson (1975) and Young (1976), respectively, the pure bending of elastic and elastoplastic rectangular bars by Triantafyllidis (1980) and the internal pressurization of cylindrical tubes by Larsson et al. (1982). It should be emphasized at this point that the roughness resulting from a bifurcation, and which appears at high levels of strain in the form of similarly oriented wavelets, is due to the interaction between the finite strain kinematics and the nonlinearity of the constitutive law. This phenomenon should not be confused with the surface roughness which can appear at any initially smooth surface and which grows linearly with strain in the small strain regime, in the form of "orange peel" with no preferred orientation observed. The latter phenomenon is due to the orientation mismatch of the surface grains in metal polycrystals and requires micromechanical descriptions of the solid at the grain level, as the interested reader can see from the recent work by Becker (1997).

The critical load at surface bifurcation is strongly dependent on the constitutive model as well as on the in-plane stress state. For isotropic, incompressible, rate-independent solids, Hutchinson and Tvergaard (1980) have studied the surface bifurcation of a traction-free half-space under proportional straining conditions, using a finite strain generalization of the J_2 deformation theory of plasticity. Their analysis is capable of finding the lowest strain surface bifurcation only for isotropic solids, due to a particular form assumed for the eigenmode. In a subsequent work, Triantafyllidis (1984) presented the general analysis for the surface bifurcation in any anisotropic, rate-independent, traction-free half-space. The latter work investigates all the possible modes in order to find the wanted critical load. In the same work it is shown that the bifurcation mode is polarized along a certain direction, i.e., it consists of waves whose crests are parallel lines, exactly as observed in experiments involving approximately homogeneous principal strain fields as in the case of bending of bars or bursting of internally pressurized tubes (see the corresponding pictures in Hutchinson and Tvergaard (1980) and Larsson et al. (1982)).

The present work is motivated by problems in sheet metal forming involving alloys subjected to finite strain and for which a high quality of the finished surface is required. Since the alloys in question are in general anisotropic, the investigation

Contributed by the Applied Mechanics Division of THE AMERICAN SOCIETY OF MECHANICAL ENGINEERS for publication in the ASME JOURNAL OF APPLIED MECHANICS.

Discussion on the paper should be addressed to the Technical Editor, Professor Lewis T. Wheeler, Department of Mechanical Engineering, University of Houston, Houston, TX 77204-4792, and will be accepted until four months after final publication of the paper itself in the ASME JOURNAL OF APPLIED MECHANICS.

Manuscript received by the ASME Applied Mechanics Division, Dec. 12, 1997; final revision, May 7, 1998. Associate Technical Editor: S. Kyriakides.

 Copyright © 1999 by ASME

Downloaded 04 May 2010 to 171.66.16.27. Redistribution subject to ASME license or copyright; see http://www.asme.org/terms/Terms_Use.cfm

of surface bifurcation requires the general methodology given by Triantafyllidis (1984). Of particular interest is the influence of anisotropy, measured by the angle α formed between the principal strains and the rolling direction, on the surface bifurcation. All the corresponding calculations are based on the recently proposed anisotropic plasticity theories by Karafillis and Boyce (1993). The numerical results presented in this work correspond to a particular aluminum alloy 2024-T3 whose material properties have been determined experimentally by Barlat et al. (1991).

Results are presented for three different values of the principal strain orientation angle α and show a strong influence of plastic anisotropy on the critical strains for principal strains of a different sign. The eigenmode orientation angle Ω_c is also calculated as a function of the principal strain ratio tan φ for a particular value of the principal strain orientation angle α. Finally, to study the influence of the yield surface, the critical strains for the anisotropic material are compared to their counterparts of two fictious isotropic materials, both with the same uniaxial stress-strain curve in the rolling direction as the alloy under investigation.

2 General Theory for Surface Bifurcation

The general theory for the surface bifurcation of a traction-free half-space, consisting of an anisotropic, homogeneous, rate-independent material, which is subjected to a homogeneous, in-plane state of stress, has been derived by Triantafyllidis (1984). However, for reasons of completeness, a brief outline of this theory is presented here.

In the current configuration, a Cartesian coordinate system is used, in which the solid occupies the half-space $x_3 \leq 0$. An updated Lagrangian formulation of the problem is presented, with Δf denoting the perturbation of any field quantity from the spatially constant principal solution whose uniqueness is under investigation. The perturbed equilibrium equations and the traction-free surface boundary conditions are expressed in terms of the first Piola-Kirchhoff stress $\mathbf{\Pi}$ as follows:

$$\Delta\Pi_{ij,i} = 0 \quad (x_\alpha \in \Re,\ x_3 \leq 0)^1 \tag{1}$$

$$\Delta\Pi_{3i} = 0 \quad (x_\alpha \in \Re,\ x_3 = 0). \tag{2}$$

For any rate-independent material, the perturbation of the first Piola-Kirchhoff stress is related to the perturbation of the deformation gradient $\mathbf{F}$ by the linearized constitutive relation

$$\Delta\Pi_{ji} = L_{ijkl}\Delta F_{kl} \tag{3}$$

$$\Delta F_{kl} = \Delta u_{k,l} \tag{4}$$

where $\Delta\mathbf{u}$ is the perturbation of the displacement.

The incremental moduli tensor $\mathbf{L}$ is a function of the material properties and the current state of stress. Explicit expressions for the case of some finitely strained aluminum alloys will be given in the next section. At this point it suffices to say that the half-space is assumed homogeneous, incrementally linear and under a spatially constant state of stress which has been achieved through a given strain history. The loading path in question is parameterized by a "time-like" scalar λ which increases monotonically from zero and is assumed to uniquely characterize the present state of the material. Consequently the components of the incremental moduli tensor are λ-dependent constants $L_{ijkl}(\lambda)$.

The governing Eqs. (1), (3), (4) and the boundary conditions (2) have to be complemented by the requirement of bounded displacement and deformation gradient perturbations, which in addition must decay to zero away from the surface, i.e.,

$$\Delta u_i \to 0, \quad \Delta F_{ij} \to 0, \quad \text{as } x_3 \to -\infty. \tag{5}$$

The above system of linear partial differential equations with constant coefficients can be reduced to a system of ordinary differential equations in x_3 by considering its Fourier transform with respect to x_α. By substituting the constitutive (3) and kinematic Eqs. (4) into the equilibrium Eqs. (1) and subsequently considering the Fourier transform of the resulting equations with respect to x_α, we obtain the following system of ordinary differential equations in x_3:

$$(i\omega_\alpha)(i\omega_\beta)L_{i\alpha k\beta}\Delta\hat{u}_k + (i\omega_\gamma)(L_{i3k\gamma} + L_{i\gamma k3})\Delta\hat{u}_{k,3} + L_{i3k3}\Delta\hat{u}_{k,33} = 0 \tag{6}$$

where $\Delta\hat{u}_k(\omega_\alpha, x_3)$ is the double Fourier transform of $\Delta u_k(x_\alpha, x_3)$, with ω_α the Fourier transform variable corresponding to x_α. In deriving (6) it is tacitly assumed that the perturbation fields Δu_k are adequately smooth (at least twice continuously differentiable) and uniformly bounded with respect to all coordinates. The boundedness requirement for Δu_k implies that the Fourier transforms $\Delta\hat{u}_k$ are not functions of their arguments in the classical sense, but distributions in the ω_α plane.

The general solution to the system of ordinary differential equations with constant coefficients in (6) is found to be the sum of three linearly independent partial solutions

$$\Delta\hat{u}_k(\omega_\alpha, x_3) = \sum_{j=1}^{3} \xi_{(j)}(\omega_\alpha)A_k^{(j)} \exp\left[i\omega z_{(j)}x_3\right] \tag{7}$$

where the following notations have been employed: The quantity ω is the norm of the vector ω_α (i.e., $\omega \equiv |\omega_\alpha\omega_\alpha|^{1/2}$) and $z_{(j)}$ denote the three roots with negative imaginary part of the following sixth-order polynomial in z,

$$\det\left[L_{i\alpha k\beta}n_\alpha n_\beta + (L_{i3k\gamma} + L_{i\gamma k3})n_\gamma z + L_{i3k3}z^2\right] = 0, \tag{8}$$

where $\omega_\alpha = \omega n_\alpha$, $n_1 = \cos\Omega$, $n_2 = \sin\Omega$ and $z_{(j)} = a_{(j)}(\Omega, \lambda) + ib_{(j)}(\Omega, \lambda)$ such that $b_{(j)} < 0$ $(j = 1 - 3)$.

The requirement that for the load parameter λ values of interest no real roots of (8) are allowed for any angle Ω, stems from the fact that we seek surface instabilities occurring in the elliptic regime of the material response, i.e., prior to the occurrence of any localized mode of deformation. Recall (e.g., Rice, 1976) that the mathematical expression for the strong ellipticity condition is $L_{ijkl}(\lambda)n_jn_l > 0$ for all three-dimensional unit vectors $\mathbf{n}$, which implies the necessity of nonreal roots for (8). The selection of the three roots of the sixth order polynomial in (8) which have a negative imaginary part, follows from (5) which requires the perturbation to decay away from the free surface. The unit vector $\mathbf{A}^{(j)}$, which is associated with the root $z_{(j)}$ is the eigenvector of the following 3×3 matrix:

$$\left[L_{i\alpha k\beta}n_\alpha n_\beta + (L_{i3k\gamma} + L_{i\gamma k3})n_\gamma z_{(j)} + L_{i3k3}z_{(j)}^2\right]A_k^{(j)} = 0. \tag{9}$$

For a simple root $z_{(j)}$, the corresponding eigenvector $\mathbf{A}^{(j)}$ in (9) is unique, while for a double root, one has two corresponding eigenvectors which are chosen to be mutually orthogonal[2]. Finally, $\xi_{(j)}(\omega_\alpha)$ is the amplitude of the jth partial solution $A_k^{(j)} \exp[i\omega z_{(j)}x_3]$ and is a distribution defined in the Fourier transform space ω_α to be specified subsequently.

The Fourier transform of the surface boundary conditions (2), after substituting the constitutive (3) and kinematic Eqs. (4) and the general expression for the transform of the displacement perturbation in (7), gives the following result:

[1] Here and subsequently, Latin indexes range from 1 to 3, while Greek indexes range from 1 to 2. Einstein's summation convention is implied over repeated indexes. Repeated indexes in parentheses are not summed, unless indicated explicitly.

[2] This choice is always possible in the case where the moduli have the major symmetry $L_{ijkl}(\lambda) = L_{klij}(\lambda)$, a condition met in all plasticity theories leading to self-adjoint problems.

Downloaded 04 May 2010 to 171.66.16.27. Redistribution subject to ASME license or copyright; see http://www.asme.org/terms/Terms_Use.cfm

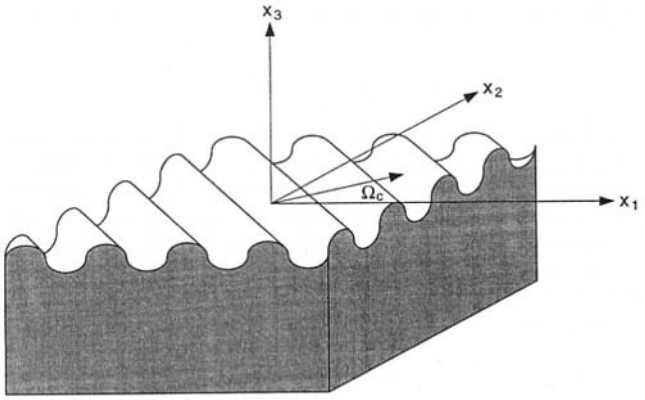

Fig. 1 Schematic representation of the half-space indicating orientation angle Ω_c of the surface mode

$$\sum_{j=1}^{3} S_{ij}(\Omega, \lambda)\xi_{(j)}(\omega_\alpha) = 0,$$

$$S_{ij}(\Omega, \lambda) \equiv [L_{i3k\alpha}(\lambda)n_\alpha + L_{i3k3}(\lambda)z_{(j)}]A_k^{(j)}. \quad (10)$$

For the homogeneous system in (10) to admit a nontrivial solution $\xi_{(j)}(\omega_\alpha)$, the matrix of constants S_{ij} must be singular. Thus, onset of the surface bifurcation corresponds to the first such occurrence of a singular matrix S_{ij} (at a load level λ_c and for an angle Ω_c), as the load parameter λ increases from zero. Hence

$$\det [S_{ij}(\Omega_c, \lambda_c)] = 0;$$

$$\det [S_{ij}(\Omega, \lambda)] \neq 0,$$

$$\text{for } \Omega \in [0, \pi) \quad \text{and} \quad 0 \leq \lambda < \lambda_c. \quad (11)$$

Note that in the above procedure of searching for the critical load λ_c, only the domain $[0, \pi)$ has to be scanned for Ω, at each increment of λ. Indeed from (8), one obtains that $z_{(j)}(\Omega + \pi) = -z_{(j)}(\Omega)$, which will result in the equivalent condition $\det [\bar{S}_{ij}(\Omega_c, \lambda_c)] = 0$ at criticality.

At this point we present an important remark about the shape of the eigenmode. For the homogeneous system in (10), to admit at λ_c a nontrivial solution in the ω_α plane, the corresponding eigenmode $\xi_{(j)}$ should vanish in all points except those along the direction $\omega_2/\omega_1 = \tan \Omega_c$. In this case the distribution $\xi_{(j)}(\omega_\alpha)$ has a line support along the above-mentioned direction, i.e.,

$$\xi_{(j)}(\omega_\alpha) = \Xi_{(j)}f, \quad \text{supp } f = \{\omega_\alpha | \omega_2/\omega_1 = \tan \Omega_c\} \quad (12)$$

where $\Xi_{(j)}$ is a unit vector obtained from (10), at λ_c, Ω_c, and f is a scalar distribution in the Fourier plane ω_α, with a line support indicated in (12). It follows from (12) and (7) that upon inversion of the Fourier transform for the perturbed displacement one obtains

$$\Delta u_k(x_1, x_2, x_3) = \Delta u_k(x_1 \cos \Omega_c + x_2 \sin \Omega_c, x_3), \quad (13)$$

i.e., the bifurcation eigenmode is in the form of waves polarized along the direction $\tan \Omega_c$, which is graphically represented in Fig. 1. The amplitude of these waves as well as their shape cannot be specified by this analysis in view of the arbitrariness of the distribution f in (12).

To complete the general theory, one needs to specify the loading path followed from the stress-free configuration. An in-plane stress state is required, which dictates that the Kirchhoff stress[3] components on the free surface vanish, namely

$$\tau_{3i}(\lambda) = 0. \quad (14)$$

The stress state in the half-space is achieved through a proportional straining path, where the in-plane principal logarithmic strains ϵ_α are oriented at a fixed angle α with respect to the x_i material axis of orthotropy and have a constant ratio $\tan \varphi$, i.e.,

$$\epsilon_1 = \lambda \cos \varphi, \quad \epsilon_2 = \lambda \sin \varphi \quad (15)$$

while the in-plane components of the strain rate tensor $D_{\alpha\beta}$ are given by

$$D_{\alpha\beta} = \begin{bmatrix} \cos\alpha & -\sin\alpha \\ \sin\alpha & \cos\alpha \end{bmatrix} \begin{bmatrix} \cos\varphi & 0 \\ 0 & \sin\varphi \end{bmatrix} \begin{bmatrix} \cos\alpha & \sin\alpha \\ -\sin\alpha & \cos\alpha \end{bmatrix}. \quad (16)$$

From the above relations (14)–(16) for the loading path, one can calculate the stress state $\boldsymbol{\tau}(\lambda)$ and consequently the incremental moduli $\mathbf{L}(\lambda)$ in (3) which are given as functions of the current stress state. The functional dependence $\mathbf{L}(\boldsymbol{\tau})$ depends on the constitutive model adopted and a specific selection for aluminum alloys will be proposed in the next section. At this point it suffices to say, that for finitely strained elastoplastic solids a convenient form of the constitutive law is given by the incremental moduli tensor $\mathcal{L}(\boldsymbol{\tau})$ which relates the Jaumann rate of the Kirchhoff stress $\overset{\nabla}{\boldsymbol{\tau}}$ to the strain rate tensor $\mathbf{D}$. In the absence of a rigid-body rotation of the solid, $\overset{\nabla}{\boldsymbol{\tau}} = d\boldsymbol{\tau}/d\lambda$, and hence

$$\frac{d\tau_{ij}}{d\lambda} = \mathcal{L}_{ijkl}(\tau(\lambda))D_{kl}. \quad (17)$$

From (17) the relations between the known constant strain rates $D_{\alpha\beta}$ and the nonzero stress rate components are

$$\frac{d\tau_{\alpha\beta}}{d\lambda} = \mathcal{P}_{\alpha\beta\gamma\delta}(\boldsymbol{\tau}(\lambda))D_{\gamma\delta}, \quad \mathcal{P}_{\alpha\beta\gamma\delta} \equiv \mathcal{L}_{\alpha\beta\gamma\delta} - \frac{\mathcal{L}_{\alpha\beta33}\mathcal{L}_{33\gamma\delta}}{\mathcal{L}_{3333}}. \quad (18)$$

In deriving the plane-stress incremental equations in (18) it is tacitly assumed that x_3 is a material axis of orthotropy, a property which when combined with the plane stress assumption (14) gives for the out of plane-strain rates $D_{3\alpha} = 0$, $D_{33} = -\mathcal{L}_{33\gamma\delta}D_{\gamma\delta}/\mathcal{L}_{3333}$ and hence the expressions for the plane-stress moduli $\mathcal{P}(\boldsymbol{\tau})$ recorded in (18).

The determination of the stress state $\boldsymbol{\tau}(\lambda)$ from (16) and (18) leads to the calculation of the complete moduli tensor $\mathcal{L}(\boldsymbol{\tau})$ from which one can find the moduli tensor $\mathbf{L}(\lambda)$, required by the general analysis in (3) to be

$$L_{ijkl} = \mathcal{L}_{ijkl} - \tfrac{1}{2}(\tau_{ik}\delta_{jl} + \tau_{il}\delta_{jk} + \tau_{jk}\delta_{il} - \tau_{jl}\delta_{ik}). \quad (19)$$

The above result follows from the definitions of the moduli $\mathbf{L}(d\Pi_{ji}/d\lambda = L_{ijkl}(\lambda)(dF_{kl}/d\lambda))$ and $\mathcal{L}$ in (17), the relations between the two stress measures $(\boldsymbol{\Pi}, \boldsymbol{\tau})$ and their work conjugate strain rate measures $(d\mathbf{F}/d\lambda, \mathbf{D})$, and is a straightforward calculation in continuum mechanics. The above discussion gives the physical meaning of the time-like parameter λ as a measure of the principal strain size (see (15)) and provides an explicit methodology for the determination of the moduli $\mathbf{L}(\lambda)$ which enter the calculations for the onset of the surface bifurcation.

3 Constitutive Model

As mentioned above, the application of the general surface bifurcation analysis to a specific solid requires the material properties of the solid, which enter through the incremental moduli tensor $\mathcal{L}(\boldsymbol{\tau})$ that relates the Jaumann rate of the Kirchhoff stress $\overset{\nabla}{\boldsymbol{\tau}}$ to the strain rate tensor $\mathbf{D}$. For buckling problems in metals, which occur during a proportional loading path, as is the case here, it has been established that the deformation

[3] Use of the Kirchhoff stress measure leads to the incremental moduli $\mathbf{L}$ with the major symmetry $L_{ijkl} = L_{klij}$ if the same symmetry is adopted for the incremental moduli $\mathcal{L}$.

Downloaded 04 May 2010 to 171.66.16.27. Redistribution subject to ASME license or copyright; see http://www.asme.org/terms/Terms_Use.cfm

theory of plasticity gives better correlation to experiments, as compared to the standard flow theory with a smooth yield surface (see the review article by Hutchinson (1974)). Following Stören and Rice (1975), an attractive way to obtain a finite strain version of the deformation theory of plasticity is by assuming that the incremental moduli, derived for deformation theory of plasticity is by assuming that the incremental moduli, derived for deformation theory under a small strain assumption, are also the ones relating the Jaumann rate of the Kirchhoff stress to the strain rate. Their method, which also assumed a von Mises isotropic yield function $\Phi(\boldsymbol{\tau})$, was applied to the prediction of the forming limit diagrams of biaxially stretched metallic sheets. The generalization of this model for the case of anisotropic yield functions $\Phi(\boldsymbol{\tau})$, which has been used by Triantafyllidis and Needleman (1980) for wrinkling calculations in the cup drawing test, is adopted for our purpose and has the following incremental moduli tensor $\mathcal{L}(\boldsymbol{\tau})$ components:

$$\mathcal{L}_{ijkl} = Q^{-1}_{ijkl} - \frac{[Q^{-1}_{ijmn}(\partial\tau_e/\partial\tau_{mn})][(\partial\tau_e/\partial\tau_{pq})Q^{-1}_{pqkl}]}{[(E_t)^{-1} - (E_s)^{-1}]^{-1} + [(\partial\tau_e/\partial\tau_{pq})Q^{-1}_{pqrs}(\partial\tau_e/\partial\tau_{rs})]} \tag{20}$$

$$Q_{ijkl} = \frac{1+\nu}{E}\left[\frac{1}{2}(\delta_{ik}\delta_{jl} + \delta_{il}\delta_{jk}) - \frac{\nu}{1+\nu}\delta_{ij}\delta_{kl}\right] + \left(\frac{1}{E_s} - \frac{1}{E}\right)\left(\frac{\partial\tau_e}{\partial\tau_{ij}}\frac{\partial\tau_e}{\partial\tau_{kl}} + \frac{\partial^2\tau_e}{\partial\tau_{ij}\partial\tau_{kl}}\right). \tag{21}$$

In the above expressions, E is the Young's modulus, ν the Poisson's ratio of the material's uniaxial response, and $\tau_e(\boldsymbol{\tau})$ is the effective stress (τ_e is a function of Φ) which is a homogeneous function of $\boldsymbol{\tau}$, of degree one. In addition, $E_s(\tau_e)$ and $E_t(\tau_e)$ are the secant and tangent moduli evaluated at a stress level τ_e on the uniaxial stress-strain curve. Finally, the rank four tensor $\mathbf{Q}^{-1}$ is the inverse of $\mathbf{Q}$ in (21) and is assumed to have the same symmetries as $\mathbf{Q}$, i.e., $Q_{ijpq}Q^{-1}_{pqkl} = (\frac{1}{2})(\delta_{ik}\delta_{jl} + \delta_{il}\delta_{jk})$ and $Q^{-1}_{ijkl} = Q^{-1}_{klij} = Q^{-1}_{jikl} = Q^{-1}_{ijlk}$. It should also be mentioned that the moduli in (20) and (21) assume loading of the solid in the plastic regime of the response, i.e., $\tau_e \geq \tau_y$, where τ_y is the yield stress.

The above proposed formulation is applicable to anisotropic rate-independent elastoplastic materials which do not exhibit the Bauschinger effect, i.e., materials which exhibit no difference between their tensile and compressive responses. Instead of expressing the equivalent stress τ_e, or the yield function Φ ($\tau_e = (\Phi/2)^{1/m}$)[4] as anisotropic functions of $\boldsymbol{\tau}$ (e.g., Hill, 1950), Karafillis and Boyce (1993) have proposed the concept of an "Isotropic Plasticity Equivalent" (IPE) material, for which τ_e is an isotropic function of the IPE material's stress. The IPE material's stress tensor $\mathbf{s}$ is related to the actual stress tensor $\boldsymbol{\tau}$ of the anisotropic material by a rank four symmetric tensor $\mathbf{A}$ which characterizes the anisotropy of the material. Thus, it is assumed that

$$\tau_e = \left(\frac{|s_1 - s_2|^m + |s_2 - s_3|^m + |s_3 - s_1|^m}{2}\right)^{1/m} \tag{22}$$

where s_I are the principal values of $s_{ij} = A_{ijkl}\tau_{kl}$.

The specific choice of $\tau_e(\mathbf{s})$ in (22) used here has also been employed by Barlat et al. (1991) and was first proposed for isotropic materials by Hershey (1954). For the case of orthotropic materials, like the aluminum alloys of interest, the transformation tensor $\mathbf{A}$ contains only six independent nonzero components c_J, namely

$$\begin{aligned} A_{1111} &= (c_2 + c_3)/3,\ A_{2222} = (c_1 + c_3)/3,\\ A_{3333} &= (c_1 + c_2)/3,\\ A_{1122} &= A_{2211} = -c_3/3,\ A_{1133} = A_{3311} = -c_2/3,\\ A_{2233} &= A_{3322} = -c_1/3,\\ A_{2323} &= A_{2332} = A_{3223} = A_{3232} = c_4/2,\\ A_{1313} &= A_{1331} = A_{3113} = A_{3131} = c_5/2,\\ A_{1212} &= A_{1221} = A_{2112} = A_{2121} = c_6/2. \end{aligned} \tag{23}$$

In addition to the Eqs. (20) – (23), the complete characterization of the material model requires the uniaxial stress-strain curve of the material, which is determined experimentally, as are the constant exponent m, appearing in the equivalent stress determination in (22), and the six anisotropy coefficients c_J in (23).

4 Results and Discussion

The numerical calculation of the critical load λ_c at the onset of surface bifurcation and of the corresponding eigenmode direction Ω_c proceeds as follows:

The construction of the stability matrix $S_{ij}(\Omega, \lambda)$ defined in (10), which is required for the calculation of λ_c and Ω_c according to (11), involves the determination of the current stress state $\tau_{\alpha\beta}(\lambda)$. The calculation of the stress state at load parameter λ is based on the system of first order ordinary differential equations in (18), which are numerically integrated using a second-order Runge-Kutta method with a step size $\Delta\lambda = 10^{-4}$. To verify the accuracy of the numerical stress integration algorithm, the results have been compared with the known analytical solution for the special case of a von Mises isotropic material. For this isotropic material, the constitutive equations reduce to the J_2 deformation theory, i.e., the exponent in the definition of the equivalent stress τ_e in (22) is $m = 2$ and the all six coefficients in (23) which characterize the orthotropy of the material are $c_J = 1$. For this case it can be shown (e.g., Triantafyllidis et al., 1982) that the principal stresses τ_α are related to the principal strains ϵ_α by

$$\tau_\alpha = \frac{E_s}{1-\nu_s^2}[(1-\nu_s)\epsilon_\alpha + \nu_s(\epsilon_1 + \epsilon_2)]$$
$$\nu_s = \frac{1}{2} + \frac{E_s}{E}\left(\nu - \frac{1}{2}\right) \tag{24}$$

where $E_s(\tau_e)$ is the secant modulus evaluated at the equivalent stress $\tau_e = (\tau_1^2 - \tau_1\tau_2 + \tau_2^2)^{1/2}$. When comparing the stresses obtained by the previously described numerical integration algorithm to their exact counterparts in (24), for the isotropic material case, the error in the stresses is of the order 0.1 percent.

The numerical determination of the critical load λ_c is based on the evaluation of the minimum value, with respect to the angle Ω, of the determinant of the stability matrix in (11) every ten load increments. The Ω minimum of the determinant is also obtained numerically by scanning the $[0, \pi)$ interval in 315 equal increments. Further verification of the accuracy of our algorithm is obtained by comparing our results with those of Hutchinson and Tvergaard (1980) for an isotropic, incompressible, rate-independent material with a hardening exponent of $n = 0.1$.

The material investigated for surface bifurcation is a 2024-T3 aluminum alloy, whose anisotropy coefficients c_J and exponent m appearing in the definition of the equivalent stress τ_e have been experimentally determined by Barlat et al. (1991). The alloy's experimentally obtained uniaxial stress-strain re-

[4] Φ is usually a homogeneous polynomial in $\boldsymbol{\tau}$ of order m. For the von Mises case $m = 2$.

Downloaded 04 May 2010 to 171.66.16.27. Redistribution subject to ASME license or copyright; see http://www.asme.org/terms/Terms_Use.cfm

Table 1 Coefficients of the anisotropic yield function

Material	m	c_1	c_2	c_3	c_4	c_5	c_6
2024-T3	8	1.378	1.044	0.955	1.000	1.000	1.210

sponse along the rolling direction ($\alpha = 0$) is fitted to a power law of the type $(\tau/\tau_y) = (\epsilon/\epsilon_y)^n$ or equivalently $\tau = K\epsilon^n$ where $\tau_y = E\epsilon_y$. The numerical values used in the calculations are summarized in Table 1 for the anisotropic yield function coefficients and the uniaxial stress-strain constants are: $E = 69000$ MPa, $\nu = 0.31$, $K = 667.69$ MPa, and $n = 0.114$.

The results of the calculations are plotted in the principal logarithmic strain space $\epsilon_1 - \epsilon_2$ in Figs. 2–4 and Fig. 6 with the surface bifurcation points in each figure corresponding to the solid curve. The dashed curve represents the loss of ellipticity in the three-dimensional incremental equilibrium equations, i.e., the possibility of the onset of a localized deformation band in three-dimensions. The corresponding load parameter λ for each point on the dashed curve is the lowest load parameter at which $L_{ijkl}(\lambda)n_j n_l$ loses positive definiteness on the radial loading path in question. According to the general theory presented in Section 2, we seek surface bifurcations in the elliptic regime of the material, which explains why the surface bifurcation curves are entirely inside the loss of ellipticity curves. For comparison purposes we also plot by a dotted curve, in the same figures, the forming limit curve which corresponds to the onset of localized necking in a biaxially stretched thin sheet. The corresponding load parameter λ for each point on the dotted curve is the lowest load parameter at which $P_{\alpha\beta\gamma\delta}(\lambda)n_\beta n_\delta$ loses positive definiteness on the radial loading path in question, where the plane stress incremental moduli $\mathbf{P}(\lambda)$ are derived from their three-dimensional counterpart $\mathbf{L}(\lambda)$ by

$$P_{\alpha\beta\gamma\delta} = L_{\alpha\beta\gamma\delta} - \frac{L_{\alpha\beta 33}L_{33\gamma\delta}}{L_{3333}}. \tag{25}$$

The forming limit curves are meaningful for tensile principal stresses and hence are plotted only for $\sigma_1 > 0$ and $\sigma_2 > 0$. It should be remarked here that the plotting of the forming limit curve in the principal strain space is a popular tool for assessing the formability of alloys in sheet metal forming industry and the corresponding diagrams, termed forming limit diagrams (FLD) have been produced experimentally and predicted analytically for an infinite variety of alloys (see discussion in Stören and Rice (1975)).

The results in Figs. 2–4 correspond to straining paths with the principal axes oriented at $\alpha = 0, \pi/6$ and $\pi/4$, respectively, to the rolling direction of the alloy. It should be mentioned here

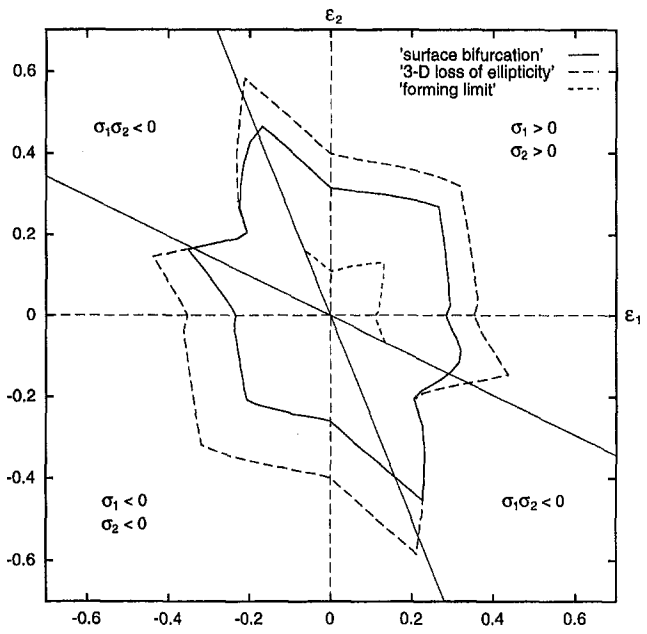

Fig. 3 Surface bifurcation depicted by a solid line, three-dimensional loss of ellipticity and forming limit curves depicted by a dashed and a dotted line, respectively, are plotted in principal strain space for a 2024-T3 aluminum alloy strained at an angle $\alpha = \pi/6$ with respect to its rolling direction

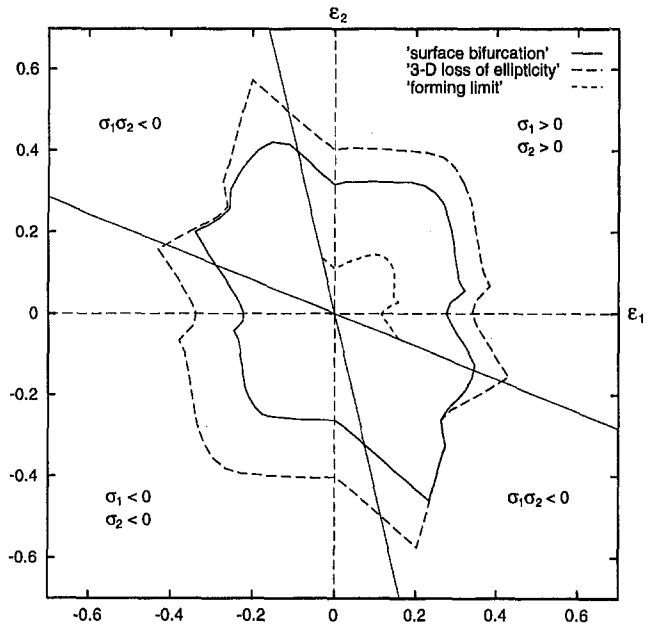

Fig. 2 Surface bifurcation depicted by a solid line, three-dimensional loss of ellipticity and forming limit curves depicted by a dashed and a dotted line respectively, are plotted in principal strain space for a 2024-T3 aluminum alloy strained at an angle $\alpha = 0$ with respect to its rolling direction

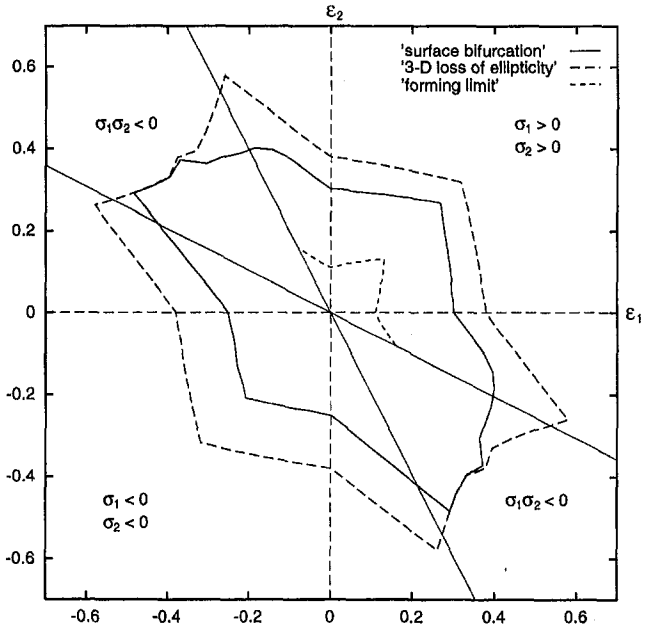

Fig. 4 Surface bifurcation depicted by a solid line, three-dimensional loss of ellipticity and forming limit curves depicted by a dashed and a dotted line, respectively, are plotted in principal strain space for a 2024-T3 aluminum alloy strained at an angle $\alpha = \pi/4$ with respect to its rolling direction

Downloaded 04 May 2010 to 171.66.16.27. Redistribution subject to ASME license or copyright; see http://www.asme.org/terms/Terms_Use.cfm

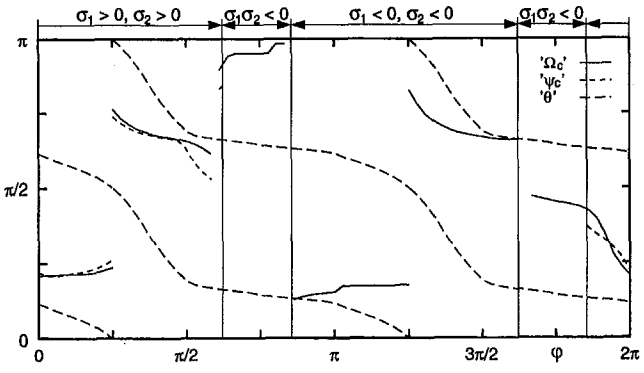

Fig. 5 Orientation angle Ω_c for the onset of surface bifurcation depicted by a solid line and angle ψ_c for the onset of plane stress necking, i.e., forming limit, depicted by a dotted line, are plotted as functions of the principal strain ratio angle φ. The principal stress orientation angle θ which is essentially constant during proportional straining is plotted in a dashed line.

that due to the orthotropy of the material the results are symmetric about $\alpha = \pi/4$. For the principal strains of the same sign $\epsilon_1\epsilon_2 > 0$ (first and fourth quadrant of the graphs) the effects of the change of the orientation angle α are not that pronounced, i.e., the forming limit, surface instability and loss of three-dimensional ellipticity results never differ by more than 12 percent between the three different values of α, except in a small region near $\varphi = \pi/18$. Notice the discontinuity in the slope of the curves for $\varphi = \pi/18$ when $\alpha = 0$ and for $\varphi = \pi/4, 5\pi/4$ when $\alpha = \pi/6, \pi/4$. For $\epsilon_1 = \epsilon_2$ ($\varphi = \pi/4, 5\pi/4$), the forming limit, surface instability and loss of ellipticity curves in Figs. 2–4 all coincide, respectively, as expected from the resulting isotropic strain state.

The influence of the orientation angle α is considerably more pronounced in the case of the principal strains of a different sign $\epsilon_1\epsilon_2 < 0$ (second and fourth quadrant of the graphs). The biggest changes, for the different orientation angles, occur in the neighborhood of $\varphi = 3\pi/4, 7\pi/4$. Notice in particular the changes in the critical surface strains between $\alpha = \pi/6$ and $\alpha = \pi/4$, which can differ by up to 83 percent between the two cases. It should also be remarked that unlike the case of the principal strains of the same sign, for certain strain paths with $\epsilon_1\epsilon_2 < 0$ the loss of ellipticity and surface instability curves coincide, i.e., there is no surface instability in the elliptic regime of the material response.

A typical graph for the orientation angle of the surface mode Ω_c as a function of the load path angle φ is depicted by a solid line in Fig. 5 and corresponds to the principal strains oriented at $\alpha = \pi/6$ with respect to the rolling direction. On the same graph is also plotted in a dashed line the orientation angle θ of the principal stresses corresponding to the onset of the surface bifurcation and the forming limit curve, since the orientation of the principal stresses remains almost constant during a proportional straining path. The orientation angle of the localized failure zone corresponding to the forming limit curve ψ_c is plotted in a dotted line for $\sigma_1 > 0$ and $\sigma_2 > 0$. It is interesting to note that the orientation angles Ω_c and ψ_c do not coincide, but are close for positive principal strains, and are both different from the principal stress orientation angle θ. The two curves for θ as a function of φ are due to the fact that one corresponds to σ_1 and the other to σ_2. It is also worth mentioning that for each load orientation angle φ there is only one value of Ω_c and ψ_c with the obvious exception of the hydrostatic straining at $\varphi = \pi/4, 5\pi/4$, due to symmetry, and near three of the four locations of the change of sign in the principal stresses.

All of the above reported calculations correspond to a 2024-T3 anisotropic aluminum alloy with a yield surface exponent $m = 8$. The influence of the anisotropy and the yield surface exponent m on the surface bifurcation curves is investigated in Fig. 6, which depicts the surface bifurcation results for the 2024-T3 alloy plus two additional hypothetical comparison materials. An isotropic solid $c_J = 1$ with the same yield surface exponent $m = 8$ as the actual 2024-T3 alloy and a J_2 isotropic material $c_J = 1$ with $m = 2$ which only shares the same uniaxial stress-strain curve as the actual alloy for $\alpha = 0$. Notice the significant influence of m which results in a consistent overprediction of surface bifurcation by the isotropic J_2 deformation theory by as much as 30 percent for the isotropic straining case. In comparing the $m = 8$ isotropic to the anisotropic cases the changes are not monotonic. In addition to the expected differences between the critical strain predictions for principal strains of the opposite sign, notice the significant differences (maximized for $\varphi = \pi/4$) in the predictions of the two different isotropic comparison solids for principal strains of the same sign. The latter observation indicates that the correct yield surface characterization is more important for the prediction of surface bifurcation than the anisotropy for the same sign principal strains.

5 Conclusion

The development of strain-induced surface roughness is an important factor which limits formability of alloys with a desired high-quality surface finish. For small strains, the development of surface roughness is due to the surface grain misorientation and appears in the form of random "orange peel." This effect can be reduced by surface treatment which results in the smaller grain size. Surface roughness for large strains, which appears in the form of same orientation wavelets several grains wide, is a surface bifurcation instability due to the nonlinear kinematics and the constitutive response of the solid. This instability is inevitable at high strains and is a precursor to the ultimate fracture failure of the material. Unlike the previous phenomenon, it is amenable to a continuum description which admits analytical solutions for the case of a half-space idealization.

Surface bifurcation is extremely sensitive to the constitutive description of the material. Past work was available only for the

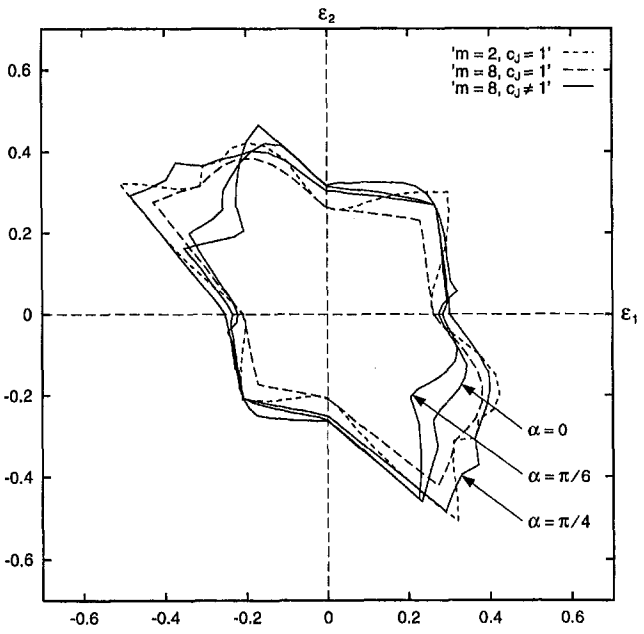

Fig. 6 Surface bifurcation curves plotted by solid lines in principal strain space for a 2024-T3 aluminum alloy strained at $\alpha = 0$, $\pi/6$ and $\pi/4$ with respect to its rolling direction. For comparison purposes, surface bifurcation of two isotropic materials with the same uniaxial stress-strain curve as the actual alloy for $\alpha = 0$ are also plotted. The dotted curve corresponds to the finite strain generalization of J_2 deformation theory of plasticity while the dashed curve corresponds to an isotropic material which shares the same yields surface with the actual alloy.

Downloaded 04 May 2010 to 171.66.16.27. Redistribution subject to ASME license or copyright; see http://www.asme.org/terms/Terms_Use.cfm

von Mises-type isotropic materials, thus motivating the present study on the influence of anisotropy on surface bifurcation. The present calculations for an actual aluminum alloy, although indicative due to the extreme difficulty in obtaining experimental verification, show that anisotropy is extremely important for the case of principal strains of the opposite sign. Moreover, it is also found that the yield surface characterization plays an important role near balanced biaxial strains.

The above proposed continuum approach can be improved by the incorporation of grain size effects to predict the characteristic length of the surface mode. Improvements on the continuum approach always provide an analytically tractable alternative to the full-scale micromechanical calculations in three dimensions which involve fine meshing of many grains.

Acknowledgments

The partial support of ALCOA and NSF under grant G-CMS-9503956 are gratefully acknowledged.

References

Barlat, F., Lege, D. J., and Brem, J. C., 1991, "A Six-Component Yield Function for Anisotropic Materials," *Int. J. Plasticity,* Vol. 7, pp. 693–712.

Becker, R., 1997, "Effects of Strain Localization on Surface Roughening During Sheet Forming," *Acta Materialia,* to appear.

Biot, M. A., 1965, *Mechanics of Incremental Deformations,* John Wiley and Sons, New York.

Hershey, A. V., 1954, "The Plasticity of an Isotropic Aggregate of Anisotropic Face Centered Cubic Crystals," ASME JOURNAL OF APPLIED MECHANICS, Vol. 21, pp. 241–249.

Hill, R., 1950, *The Mathematical Theory of Plasticity,* Clarendon Press, Oxford.

Hill, R., and Hutchinson, J. W., 1975, "Bifurcation Phenomena in the Plane Tension Test," *J. Mech. Phys. Solids,* Vol. 23, pp. 239–264.

Hutchinson, J. W., 1974, "Plastic Buckling," *Adv. Appl. Mechanics,* Vol. 14, pp. 67–144.

Hutchinson, J. W., and Tvergaard, V., 1980, "Surface Instabilities on Statically Strained Plastic Solids," *Int. J. Mech. Sciences,* Vol. 22, pp. 339–354.

Karafillis, A. P., and Boyce, M. C., 1993, "A General Anisotropic Yield Criterion Using Bounds and a Transformation Weighting Tensor," *J. Mech. Phys. Solids,* Vol. 41, pp. 1859–1886.

Larsson, M., Needleman, A., Tvergaard, V., and Storakers, B., 1982, "Instability and Failure of Internally Pressurized Ductile Metal Cylinders," *J. Mech. Phys. Solids,* Vol. 30, pp. 121–154.

Rice, J. R., 1976, "The Localization of Plastic Deformation," *Theoretical and Applied Mechanics,* W. T. Koiter, ed., pp. 207–220.

Stören, S., and Rice, J. R., 1975, "Localized Necking in Thin Sheets," *J. Mech. Phys. Solids,* Vol. 23, pp. 421–441.

Triantafyllidis, N., 1980, "Bifurcation Phenomena in Pure Bending," *J. Mech. Phys. Solids,* Vol. 28, pp. 221–245.

Triantafyllidis, N., 1984, "Surface Instabilities in Finitely Strained Solids Under Static Loading," *Int. J. Eng. Science,* Vol. 22, pp. 1187–1192.

Triantafyllidis, N., and Needleman, A., 1980, "Analysis of Wrinkling in the Swift Cup Test," ASME *Journal of Engineering Materials and Technology,* Vol. 102, pp. 241–248.

Triantafyllidis, N., Needleman, A., and Tvergaard, V., 1982, "On the Development of Shear Bands in Pure Bending," *Int. J. Solids Structures,* Vol. 18, pp. 121–138.

Young, N. J. B., 1976, "Bifurcation Phenomena in the Plane Compression Test," *J. Mech. Phys. Solids,* Vol. 24, pp. 77–91.

Downloaded 04 May 2010 to 171.66.16.27. Redistribution subject to ASME license or copyright; see http://www.asme.org/terms/Terms_Use.cfm

A Reissner's Mixed Variational Theorem Applied to Vibration Analysis of Multilayered Shell

E. Carrera
Department of Aeronautics and Aerospace Engineering,
Politecnico di Torino,
Corso Duca degli Abruzzi, 24,
10129 Torino, Italy
e-mail: carrera@polito.it

A comprehensive model of anisotropic multilayered double curved shells fulfilling a priori the interlaminar continuity requirements for the transverse shear and transverse normal stress as well as the static conditions on the bounding surfaces of the shell is developed in this paper. To this end, Reissner's mixed variational theorem is employed to derive the equations governing the dynamic equilibrium and compatibility of each layer, while the interlaminar continuity conditions are used to drive the equations at the multilayered level. No assumptions have been made concerning the terms of type thickness to radii shell ratio h/R. *Classical displacement formulations and related equivalent single layer equations have been derived for comparison purposes. Comparison of frequency predictions based upon the presented structural model with a number of results spread throughout the specialized literature and obtained via other models reveals that this advanced model provides results in excellent agreement with the ones based on three-dimensional elasticity theory, and better as compared to the ones violating the interlaminar stress continuity requirements and/or transverse normal stress and related effects.*

1 Introduction

Due to the noncontinuous distribution of thermomechanical material properties in the thickness direction, the multilayered shells exhibits low values of the transverse properties relative to the in-plane ones and a directional nature of the elastic behavior which is exploited to design material as well as structural properties. Examples of multilayered shell structures used in modern aerospace, automotive, and ship vehicles are laminated constructions made of anisotropic composite materials, sandwich panels, layered structures used as thermal protection or intelligent structural systems embedding piezo-layers. In the recent years, considerable attention is being paid to the development of appropriate two-dimensional shell theories that can accurately describe the static and dynamic response of multilayered anisotropic thick shells. Exhaustive overviews were given in the articles by Kapania (1989) and by Noor and Burton (1990) (see also the recent article by Timarci and Soldatos; 1995).

The directional nature of multilayered structures leads to higher transverse shear and normal stress deformability with respect to traditional isotropic cases. Therefore, further requisites become essential towards a reliable modeling of layered structures. Among them, the fulfillment of both continuity of displacement and transverse shear and normal stresses at the interface between two adjacent layers are such a necessary desideratum. In Carrera, (1995) these requisites were referred to by the acronyms C_z^0-requirements which state that both displacements and transverse stress components are C^0-continuous functions in the thickness shell coordinate z. Approximated and exact three-dimensional solutions by Mirsky (1964), Chau and Achenbach (1972), Srinivas (1974), Noor and co-author (Noor and Rarig, 1974; Noor and Peters, 1989a, 1989b), Ren (1987), Varadan and Bhaskar (1991), and Ye and Soldatos (1994) have numerically confirmed the need of the above-mentioned refinements for static and dynamic analysis of shell problems. In particular, the fundamental role played by transverse normal stress σ_{zz} was underlined. Exact elasticity solutions are known for particular cases only, concerning simple configurations. In the most general cases and to minimize the computational effort, two-dimensional models are preferred in practice. Attempts to introduce C_z^0 requirements in a two-dimensional model have been done by many investigators in the last three decades. Both layer-wise models (LWMs) (it is intended the number of the unknown variables remains dependent on the number of layers) and equivalent single layer models (ESLMs) (these models preserve the independence of the number of the independent variables from the numbers of the layers) have been proposed. Exhaustive overview can be read in the aforementioned review articles by Kapania (1989) and Noor and Burton (1990). More recent works have been reviewed by Soldatos and Timarci (1993) and Timarci and Soldatos (1995). A few of the most important contributions are reviewed in what follows. These are related to works addressing dynamic analysis.

The free-vibration analysis of layered anisotropic shells has been studied by many investigators. Classical ESLM theories were employed by Weingarten (1964), Dong (1968), Bert, Baker, and Egle (1969), and Stavsky and Loewy (1971). Shear deformable models were employed by Soldatos (1985), Reddy (1984), and Carrera (1991). Refined models were implemented by Sun and Whitney (1974). Top and bottom shell surface homogeneous conditions were considered by Reddy and Liu (1985) and by Librescu, Kheider, and Frederick (1989). Rath and Das (1973) fulfilled a priori the interlaminar transverse shear continuity and described the so called zig-zag form for the in-plane displacements in a ESL-theory; the particular case of symmetrical through the thickness response of a layered shell was considered by Di Sciuva (1987) and Di Sciuva and Carrera (1992). A refinement of these last models were proposed by Cho and Parmerter (1993) for the plates case. Further refinements with application to laminated shells were provided by Soldatos and Timarci (1993), Timarci and Soldatos (1995), and Librescu and Lin (1996).

Based on the theory by Ambartsumian (1958), Hsu and Wang (1971) have derived the equations for the free-vibration

Contributed by the Applied Mechanics Division of THE AMERICAN SOCIETY OF MECHANICAL ENGINEERS for publication in the ASME JOURNAL OF APPLIED MECHANICS.

Discussion on the paper should be addressed to the Technical Editor, Professor Lewis T. Wheeler, Department of Mechanical Engineering, University of Houston, Houston, TX 77204-4792, and will be accepted until four months after final publication of the paper itself in the ASME JOURNAL OF APPLIED MECHANICS.

Manuscript received by the ASME Applied Mechanics Division, Apr. 1, 1998; final revision, June 17, 1998. Associate Technical Editor: J. N. Reddy.

 Copyright © 1999 by ASME

Downloaded 04 May 2010 to 171.66.16.27. Redistribution subject to ASME license or copyright; see http://www.asme.org/terms/Terms_Use.cfm

analysis of layered orthotropic cylindrical shell considering each layer separately; e.g., a LW description was referred to. Other LW approaches were adopted by Cheung and Wu (1972), Alam and Asnani (1984), and Barbero, Reddy, and Teply (1990). All the mentioned theories being based on the displacement approach cannot describe completely and a priori the C_z^0-requirements.

For the case of plates, the author in recent articles (Carrera 1995, 1997, 1998a, b) has shown the convenience to refer to a Reissner's mixed variational theorem (RMVT) (Reissner, 1986) as a tool to furnish quasi-three-dimensional evaluations of stresses, displacements, and vibration response of multilayered thick structures. Similar discussion and conclusions were reported in the overview paper by Grigolyuk and Kulikov (1988). RMVT was also applied by Murakami (1986) and Toledano and Murakami (1986; 1987a, b) to the static analysis of plates and extended to shell by Jing and Tzeng (1993). In particular the mentioned author's works have shown that the use of RMVT require a layer-wise description in thick plate analyses. On the bases of the good results obtained for plates (Carrera 1998a, b), this paper extends the dynamic analysis to double curved shell structures. The equations governing the dynamic equilibrium of theories which are based on classical displacement formulation are given, in the Appendix, for comparison purposes.

2 Preliminary

The salient features of shell geometry are shown in Fig. 1. A laminated shell composed of N_l layers is considered. The integer k, used as superscript or subscript, denotes the layer number which starts from the shell bottom. The layer geometry is denoted by the same symbols as those used for the whole multilayered shell and vice versa. α_k and β_k are the curvilinear orthogonal coordinates (coinciding with principal curvature lines) on the layer reference surface Ω_k (middle surface of the k-layer). z_k denotes the rectilinear coordinate in the direction normal to Ω_k. Γ_k is the Ω_k boundary: Γ_k^g and Γ_k^m are those parts of Γ_k on which geometrical and mechanical boundary conditions are imposed, respectively; these boundary are herein considered parallel to α_k or β_k. The further dimensionless thickness coordinate is introduced, $\zeta_k = 2z_k/h_k$; where h_k denotes the thickness in the A_k domain. The following relation holds in the given orthogonal system of curvilinear coordinates for the square of line element, for the area of an infinitesimal rectangle on Ω_k, and for an infinitesimal volume, respectively (Kraus, 1967):

$$ds_k^2 = H_\alpha^k d\alpha_k^2 + H_\beta^k d\beta_k^2 + H_z^k dz_k^2$$

$$d\Omega_k = H_\alpha^k H_\beta^k d\alpha_k d\beta_k$$

$$dV = H_\alpha^k H_\beta^k H_z^k d\alpha_k d\beta_k dz_k \qquad (1)$$

where $H_\alpha^k = A^k(1 + z_k/R_\alpha^k)$, $H_\beta^k = B^k(1 + z_k/R_\beta^k)$, $H_z^k = 1$. R_α^k and R_β^k are the radii of curvature in the directions of α_k and β_k, respectively. A^k and B^k are the coefficients of the first fundamental form of Ω_k. For the sake of simplicity attention is herein restricted to a shell with a constant curvature, i.e., doubly curved shell (cylindrical, spherical, toroidal geometries) for which $A^k = B^k = 1$.

The laminae are considered to be homogeneous and to operate in the linear elastic range. By employing stiffness coefficients, Hooke's law for the anisotropic k-lamina is written in the form $\sigma_i = \tilde{C}_{ij}\epsilon_j$ where the subindices i and j, ranging from 1 to 6, stand for the index couples 11, 22, 33, 13, 23, and 12, respectively. The material is assumed to be orthotropic, as specified, by $\tilde{C}_{14} = \tilde{C}_{24} = \tilde{C}_{34} = \tilde{C}_{64} = \tilde{C}_{15} = \tilde{C}_{25} = \tilde{C}_{35} = \tilde{C}_{65} = 0$. This implies that $\sigma_{\alpha z}^k$ and $\sigma_{\beta z}^k$ depend only on $\epsilon_{\alpha z}^k$ and $\epsilon_{\beta z}^k$. In matrix form

$$\boldsymbol{\sigma}_{pH_d}^k = \tilde{\mathbf{C}}_{pp}^k \boldsymbol{\epsilon}_{pG}^k + \tilde{\mathbf{C}}_{pn}^k \boldsymbol{\epsilon}_{nG}^k$$

$$\boldsymbol{\sigma}_{nH_d}^k = \tilde{\mathbf{C}}_{np}^k \boldsymbol{\epsilon}_{pG}^k + \tilde{\mathbf{C}}_{nn}^k \boldsymbol{\epsilon}_{nG}^k \qquad (2)$$

where

$$\tilde{\mathbf{C}}_{pp}^k = \begin{bmatrix} \tilde{C}_{11}^k & \tilde{C}_{12}^k & \tilde{C}_{16}^k \\ \tilde{C}_{12}^k & \tilde{C}_{22}^k & \tilde{C}_{26}^k \\ \tilde{C}_{16}^k & \tilde{C}_{26}^k & \tilde{C}_{66}^k \end{bmatrix}, \quad \tilde{\mathbf{C}}_{pn}^k = \tilde{\mathbf{C}}_{np}^{kT} = \begin{bmatrix} 0 & 0 & \tilde{C}_{13}^k \\ 0 & 0 & \tilde{C}_{23}^k \\ 0 & 0 & \tilde{C}_{36}^k \end{bmatrix},$$

$$\tilde{\mathbf{C}}_{nn}^k = \begin{bmatrix} \tilde{C}_{44}^k & \tilde{C}_{45}^k & 0 \\ \tilde{C}_{45}^k & \tilde{C}_{55}^k & 0 \\ 0 & 0 & \tilde{C}_{66}^k \end{bmatrix}.$$

Boldface letters denote arrays. The superscript T signifies array transposition. The subscripts n and p denote transverse (out-of-plane, normal) and in-plane values, respectively. Therefore $\boldsymbol{\sigma}_p^k = \{\sigma_{\alpha\alpha}^k, \sigma_{\beta\beta}^k, \sigma_{\alpha\beta}^k\}$, $\boldsymbol{\sigma}_n^k = \{\sigma_{\alpha z}^k, \sigma_{\beta z}^k, \sigma_{zz}^k\}$ and $\boldsymbol{\epsilon}_p^k = \{\epsilon_{\alpha\alpha}^k, \epsilon_{\beta\beta}^k, \epsilon_{\alpha\beta}^k\}$, $\boldsymbol{\epsilon}_n^k = \epsilon_{\alpha z}^k, \epsilon_{\beta z}^k, \epsilon_{zz}^k\}$. Subscript H denotes stresses evaluated by Hooke's law while subscript G denotes strain from the geometrical relation Eq. (4). The further subscript d signifies values employed in the displacement formulation (see Appendix). For the adopted mixed solution procedure, the stress-strain relationships are conveniently put in the following mixed form (Librescu, 1975):

$$\boldsymbol{\sigma}_{pH}^k = \mathbf{C}_{pp}^k \boldsymbol{\epsilon}_{pG}^k + \mathbf{C}_{pn}^k \boldsymbol{\sigma}_{nM}^k$$

$$\boldsymbol{\epsilon}_{nH}^k = \mathbf{C}_{np}^k \boldsymbol{\epsilon}_{pG}^k + \mathbf{C}_{nn}^k \boldsymbol{\sigma}_{nM}^k \qquad (3)$$

where both stiffness and compliance coefficients are employed. The subscript M states that the transverse stresses are those of the assumed model in Eq. (5) (see the next section). The relation between the arrays of coefficients in the two forms of Hooke's law is simply found,

$$\mathbf{C}_{pp}^k = \tilde{\mathbf{C}}_{pp}^k - \tilde{\mathbf{C}}_{pn}^k \tilde{\mathbf{C}}_{nn}^{k^{-1}} \tilde{\mathbf{C}}_{np}^k, \quad \mathbf{C}_{pn}^k = \tilde{\mathbf{C}}_{pn}^k \tilde{\mathbf{C}}_{nn}^{k^{-1}}$$

$$\mathbf{C}_{np}^k = -\tilde{\mathbf{C}}_{nn}^{k^{-1}} \tilde{\mathbf{C}}_{np}^k, \quad \mathbf{C}_{nn}^k = \tilde{\mathbf{C}}_{nn}^{k^{-1}}.$$

Superscript -1 denotes an inversion of the array.

As one remains within the small deformation field, the strain components $\boldsymbol{\epsilon}_p^k$, $\boldsymbol{\epsilon}_n^k$ are linearly related to the displacements $\mathbf{u}^k$ ($\mathbf{u}^k = u_\alpha^k, u_\beta^k, u_z^k$), according to the following geometrical relations (Kraus, 1967):

$$\boldsymbol{\epsilon}_{pG}^k = \mathbf{D}_p \mathbf{u}^k + \mathbf{A}_p \mathbf{u}^k, \quad \boldsymbol{\epsilon}_{nG}^k = \mathbf{D}_{n\Omega} \mathbf{u}^k + \lambda_D \mathbf{A}_n \mathbf{u}^k + \mathbf{D}_{nz} \mathbf{u}^k \qquad (4)$$

where

$$\mathbf{D}_p = \begin{bmatrix} \dfrac{\partial_\alpha}{H_\alpha^k} & 0 & 0 \\ 0 & \dfrac{\partial_\beta}{H_\beta^k} & 0 \\ \dfrac{\partial_\beta}{H_\beta^k} & \dfrac{\partial_\alpha}{H_\alpha^k} & 0 \end{bmatrix}, \quad \mathbf{A}_p = \begin{bmatrix} 0 & 0 & \dfrac{1}{H_\alpha^k R_\alpha^k} \\ 0 & 0 & \dfrac{1}{H_\beta^k R_\beta^k} \\ 0 & 0 & 0 \end{bmatrix},$$

$$\mathbf{D}_{n\Omega} = \begin{bmatrix} 0 & 0 & \dfrac{\partial_\alpha}{H_\alpha^k} \\ 0 & 0 & \dfrac{\partial_\beta}{H_\beta^k} \\ 0 & 0 & 0 \end{bmatrix}, \quad \mathbf{A}_n = \begin{bmatrix} -\dfrac{1}{H_\alpha^k R_\alpha^k} & 0 & 0 \\ 0 & -\dfrac{1}{H_\beta^k R_\beta^k} & 0 \\ 0 & 0 & 0 \end{bmatrix},$$

$$\mathbf{D}_{nz} = \begin{bmatrix} \partial_z & 0 & 0 \\ 0 & \partial_z & 0 \\ 0 & 0 & \partial_z \end{bmatrix}.$$

λ_D is a trace operator which can assume the values 0 or 1.

Downloaded 04 May 2010 to 171.66.16.27. Redistribution subject to ASME license or copyright; see http://www.asme.org/terms/Terms_Use.cfm

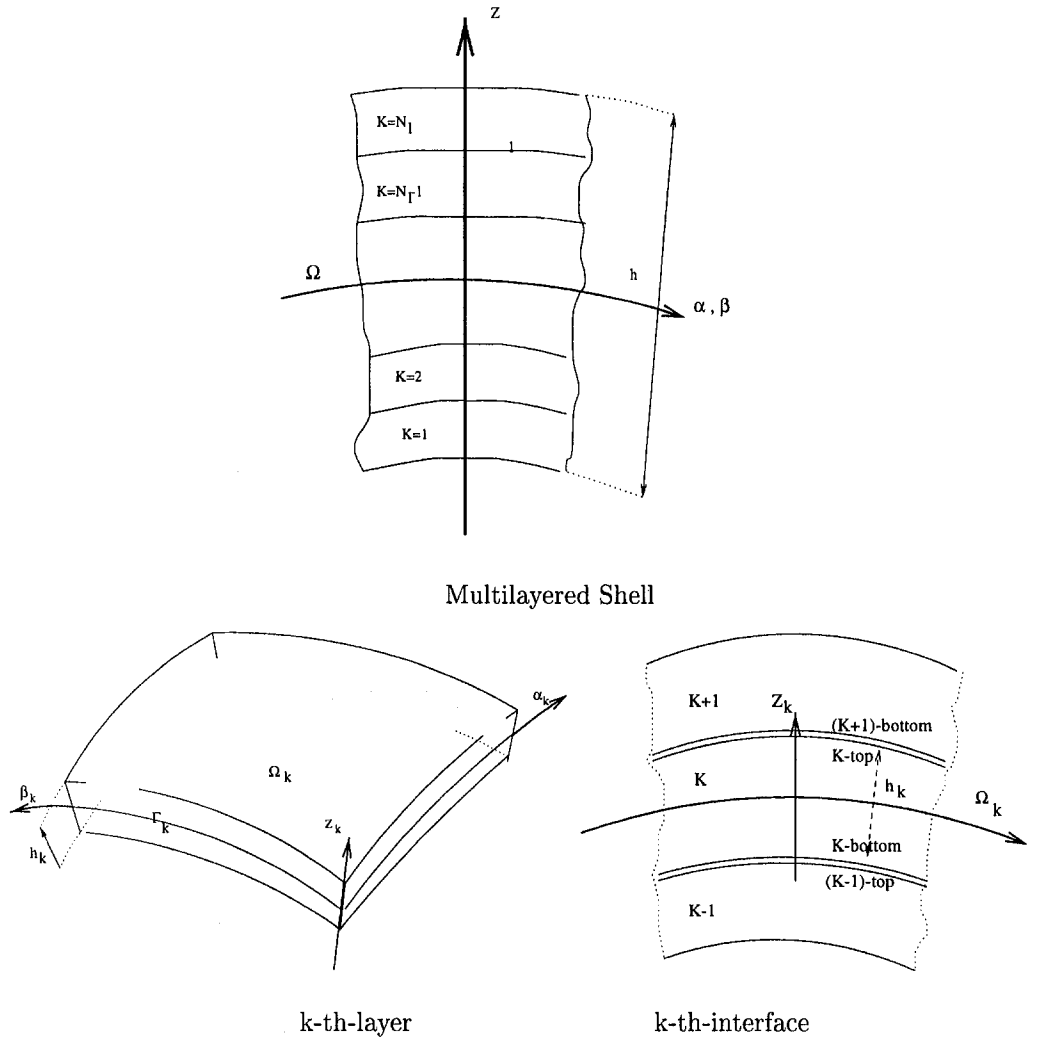

Fig. 1 Geometry and notation of multilayered shells

This has been introduced in order to identify terms which are neglected in the Donnell-type shallow shell theory (Kraus, 1967) which is therefore obtained by putting $\lambda_D = 0$. No assumption have been made for those terms which are divided by H_α^k and H_β^k which are not expanded as Taylor series (Kraus, 1967; Soldatos, 1985; Carrera, 1991). That is, curvature terms have been entirely retained in the following developments.

3 Displacement and Transverse Stress Fields

According to what was carried out for plates (Carrera, 1995, 1998a, b), the C_z^0-requirements are fulfilled completely and a priori by assuming a layer-wise model for both displacement $\mathbf{u}^k$ and transverse stress fields $\boldsymbol{\sigma}_n^k$. The following N-order expansions has been chosen in the thickness direction of each k-layer:

$$\mathbf{u}^k = F_t\mathbf{u}_t^k + F_b\mathbf{u}_b^k + F_r\mathbf{u}_r^k = F_\tau\mathbf{u}_\tau^k$$

$$\boldsymbol{\sigma}_{nM}^k = F_t\boldsymbol{\sigma}_{nt}^k + F_b\boldsymbol{\sigma}_{nb}^k + F_r\boldsymbol{\sigma}_{nr}^k = F_\tau\boldsymbol{\sigma}_{n\tau}^k$$

$$\tau = t, b, r \quad r = 2, 3, \ldots, N \quad k = 1, 2, \ldots, N_l. \quad (5)$$

N is a free parameter of the model. Subscripts t and b denote values related to the layer top and bottom surface, respectively. They consist of the linear part of the expansion. Higher order distributions in the z-direction (parabolic, cubic, etc.) are introduced by the r-polynomials. The repeated indexes τ are summed over their ranges. The thickness functions $F_\tau(\zeta_k)$ have been defined by

$$F_t = \frac{P_0 + P_1}{2}, \quad F_b = \frac{P_0 - P_1}{2},$$

$$F_r = P_r - P_{r-2}, \quad r = 2, 3, \ldots, N$$

in which $P_j = P_j(\zeta_k)$ is the Legendre polynomial of the j-order defined in the ζ_k-domain: $-1 \le \zeta_k \le 1$. The top and bottom values have been used as unknown variables. The C_z^0-requirements can therefore be easily linked: The compatibility of the displacement and the equilibrium for the transverse stress components read

$$\mathbf{u}_t^k = \mathbf{u}_b^{(k+1)}, \quad k = 1, N_l - 1$$

$$\boldsymbol{\sigma}_{nt}^k = \boldsymbol{\sigma}_{nb}^{(k+1)}, \quad k = 1, N_l - 1$$

$$\boldsymbol{\sigma}_{nb}^1 = \bar{\boldsymbol{\sigma}}_{nb}, \quad \boldsymbol{\sigma}_{nt}^{N_l} = \bar{\boldsymbol{\sigma}}_{nt} \quad (6)$$

where the overbar denotes imposed values in correspondence to static conditions on the bounding surfaces of the shells.

Equations (5) refers to the same order of expansion as the three components for both displacements and transverse stresses. In order to meet well-known results from literature (Kraus, 1967; Sun and Whitney, 1974) or the author's discussion reported in Carrera (1995, 1997), different polynomial orders should be used in developments that are presented in the subsequent sections. Trace operators that would lead to a shortening of the resulting arrays in Eqs. (10), (23) could be introduced for this aim. For the sake of brevity, the results

Downloaded 04 May 2010 to 171.66.16.27. Redistribution subject to ASME license or copyright; see http://www.asme.org/terms/Terms_Use.cfm

related to these aspects have not been discussed. These could be more conveniently reported in future works.

4 Governing Equations

The equilibrium and compatibility are formulated in terms of the $\mathbf{u}^k$ and $\boldsymbol{\sigma}_n^k$ unknowns via Reissner's mixed variational theorem (Reissner, 1986) that in the shell dynamic case is herein written as

$$\sum_{k=1}^{N_l}\int_{\Omega_k}\int_{\Lambda_k}(\delta\boldsymbol{\epsilon}_{p_G}^{k^T}\boldsymbol{\sigma}_{p_H}^k+\delta\boldsymbol{\epsilon}_{n_G}^{k^T}\boldsymbol{\sigma}_{n_M}^k+\delta\boldsymbol{\sigma}_{n_M}^{k^T}(\boldsymbol{\epsilon}_{n_G}^k-\boldsymbol{\epsilon}_{n_H}^k))d\Omega_k dz = \sum_{k=1}^{N_l}\int_{\Omega_k}\int_{\Lambda_k}\rho^k\delta\mathbf{u}^k\ddot{\mathbf{u}}^k dV+\delta L^e. \quad (7)$$

δ signifies variational symbol. ρ_k denotes mass density. The variation of the internal work has been split into in-plane and out-of-plane parts and involves stress coming from Hooke's Law and strain coming from geometrical relations. δL_e is the virtual variation of the work done by external surface forces $\mathbf{p}^k = \{p_\alpha^k,\ p_\beta^k,\ p_z^k\}$. The L.H.S. includes the variations of the internal work in the shell: The first two terms come from the displacement formulation, they will lead to variationally consistent equilibrium conditions; the third "mixed" term variationally enforces the compatibility of the transverse strains components.

4.1 Equilibrium and Constitutive Equations for the k-layers. In contrast with most of the available shell literature and to the previous author's works related to plates, in the present analysis the definition of stress or strain resultants in the shell thickness direction has been omitted. Such a choice is mainly due to the author's wish of preserving the terms H_α^k, H_β^k in the strain Eqs. (4). In fact, if the Love's approximations $H_\alpha^k = H_\beta^k = 1$ are not introduced, as is the case in the present article, the definition of stress and strain resultants still remains possible, but according to the author's opinion, not convenient. As a result, along with this paper, the governing equations will be directly written in terms of the introduced stress and displacement variables. By using the array formula for the integration by parts similar to those introduced in Carrera (1998), the RMVT work equations Eq. (7) assumes the following form:

$$\begin{aligned}\sum_{k=1}^{N_l}\Bigg(&\int_{\Omega_k}\{\delta\mathbf{u}_\tau^{k^T}[(-F_{\tau}\mathbf{D}_p^T+F_{\tau}\mathbf{A}_p^T)\mathbf{C}_{pp}(F_s\mathbf{D}_p+F_s\mathbf{A}_p)\mathbf{u}_s^k\\&+(-F_{\tau}\mathbf{D}_p^T+F_{\tau}\mathbf{A}_p^T)\mathbf{C}_{pn}F_s\boldsymbol{\sigma}_{ns}^k\\&+(-F_{\tau}\mathbf{D}_{n\Omega}^T+\lambda_D F_{\tau}\mathbf{A}_n^T+F_{\tau_z})F_s\boldsymbol{\sigma}_{ns}^k]\delta\boldsymbol{\sigma}_\tau^{k^T}[(F_{\tau}F_s\mathbf{D}_{n\Omega}\\&+\lambda_D F_{\tau}F_s\mathbf{A}_n+F_{\tau}F_{s_z}-F_{\tau}\mathbf{C}_{np}(F_s\mathbf{D}_p+F_s\mathbf{A}_p))\mathbf{u}_s^k\\&-F_{\tau}F_s\mathbf{C}_{nn}\boldsymbol{\sigma}_{ns}^k]\}d\Omega_k\\&+\int_{\Gamma_k}\int_{\Lambda_k}\delta\mathbf{u}_\tau^{k^T}[F_{\tau}\mathbf{I}_p^T\mathbf{C}_{pp}(F_s\mathbf{D}_p+F_s\mathbf{A}_p)\mathbf{u}_s^k\\&+F_{\tau}F_s\mathbf{I}_p^T\mathbf{C}_{pn}\boldsymbol{\sigma}_{ns}^k+F_{\tau}F_s\mathbf{I}_{n\Omega}^T\boldsymbol{\sigma}_{ns}^k]d\Gamma_k\Bigg)\\&=\sum_{k=1}^{N_l}\int_{\Omega_k}\delta\mathbf{u}_\tau^{k^T}\mathbf{p}_\tau^k d\Omega_k+\sum_{k=1}^{N_l}\int_{\Omega_k}\delta\mathbf{u}_\tau^{k^T}\rho^k F_{\tau}F_s\ddot{\mathbf{u}}^k d\Omega_k \quad (8)\end{aligned}$$

where

$$\mathbf{I}_p=\begin{bmatrix}\frac{1}{H_\alpha^k}&0&0\\0&\frac{1}{H_\beta^k}&0\\\frac{1}{H_\beta^k}&\frac{1}{H_\alpha^k}&0\end{bmatrix};\quad \mathbf{I}_{n\Omega}=\begin{bmatrix}0&0&\frac{1}{H_\alpha^k}\\0&0&\frac{1}{H_\beta^k}\\0&0&0\end{bmatrix}$$

and $\mathbf{p}_\tau^k = \{p_{x\tau}^k,\ p_{y\tau}^k,\ p_{z\tau}^k\}$ are the variatianally consistent load vectors coming from the applied loadings $\mathbf{p}^k$. Of practical interest could be the case in which both shearing ($p_{\alpha t}^k$, $p_{\beta t}^k$, $p_{\alpha b}^k$, $p_{\beta b}^k$) and normal (p_{zt}^k, p_{zb}^k) surface forces are applied with correspondence to the top and or bottom surface of the layer, $d\Omega_k^p = d\Omega_k^t = (1+(h_k/2R_\alpha^k))(1+(h_k/2R_\beta^k))d\Omega_k$ and $d\Omega_k^n = d\Omega_k^b = (1-(h_k/2R_\beta^k))d\Omega_k$. By imposing the definition of virtual variations for the unknown stress and displacement variables, the differential system of governing equations and related boundary conditions for the $N_l k$-layers in each Ω_k domain are found. The equilibrium and compatibility equations are

$$\begin{aligned}\delta\mathbf{u}_\tau^k:&\quad \mathbf{K}_{uu}^{k\tau s}\mathbf{u}_s^k+\mathbf{K}_{u\sigma}^{k\tau s}\boldsymbol{\sigma}_{ns}^k=\mathbf{M}^{k\tau s}\ddot{\mathbf{u}}_s^k+\mathbf{p}_\tau^k\\ \delta\boldsymbol{\sigma}_{n\tau}^k:&\quad \mathbf{K}_{\sigma u}^{k\tau s}\mathbf{u}_s^k+\mathbf{K}_{\sigma\sigma}^{k\tau s}\boldsymbol{\sigma}_{ns}^k=0\end{aligned} \quad (9)$$

with boundary conditions

$$\text{geometrical on } \Gamma_k^g \quad \text{mechanical on } \Gamma_k^m$$

$$\mathbf{u}_\tau^k=\bar{\mathbf{u}}_\tau^k \quad \text{or} \quad \boldsymbol{\Pi}_u^{k\tau s}\mathbf{u}_s^k+\boldsymbol{\Pi}_\sigma^{k\tau s}\boldsymbol{\sigma}_{ns}^k=\boldsymbol{\Pi}_u^{k\tau s}\bar{\mathbf{u}}_s^k+\boldsymbol{\Pi}_\sigma^{k\tau s}\bar{\boldsymbol{\sigma}}_{ns}^k \quad (10)$$

in which the bar denotes the assigned. The introduced differential arrays are given by the following relations:

$$\begin{aligned}\mathbf{K}_{uu}^{k\tau s}&=\int_{\Lambda_k}(-F_{\tau}\mathbf{D}_p^T+F_{\tau}\mathbf{A}_p^T)\mathbf{C}_{pp}^k(F_s\mathbf{D}_p+F_s\mathbf{A}_p)H_\alpha^k H_\beta^k dz_k\\ \mathbf{K}_{u\sigma}^{k\tau s}&=\int_{\Lambda_k}[(-F_{\tau}\mathbf{D}_p^T+F_{\tau}\mathbf{A}_p^T)\mathbf{C}_{pn}^k F_s+F_{\tau_z}F_s\mathbf{I}\\&\qquad+\lambda_D F_{\tau}F_s\mathbf{A}_n-F_{\tau}F_s\mathbf{D}_{n\Omega}^T]H_\alpha^k H_\beta^k dz_k\\ \mathbf{K}_{\sigma u}^{k\tau s}&=\int_{\Lambda_k}\{F_{\tau}F_s\mathbf{D}_{n\Omega}+\lambda_D F_{\tau}F_s\mathbf{A}_n+F_{\tau}F_{s_z}\mathbf{I}\\&\qquad-\mathbf{C}_{np}^{k\tau s}(F_{\tau}F_s\mathbf{D}_p+F_{\tau}F_s\mathbf{A}_p)\}H_\alpha^k H_\beta^k dz_k\\ \mathbf{K}_{\sigma\sigma}^{k\tau s}&=-\int_{\Lambda_k}F_{\tau}F_s\mathbf{C}_{nn}^{k\tau s}H_\alpha^k H_\beta^k dz_k\\ \boldsymbol{\Pi}_u^{k\tau s}&=\int_{\Lambda_k}F_{\tau}\mathbf{I}_p^T\mathbf{C}_{pp}(F_s\mathbf{D}_p+F_s\mathbf{A}_p)\mathbf{I}_p^T H_\alpha^k H_\beta^k dz_k\\ \boldsymbol{\Pi}_\sigma^{k\tau s}&=\int_{\Lambda_k}(F_{\tau}F_s\mathbf{I}_p^T\mathbf{C}_{pn}+F_{\tau}F_s\mathbf{I}_{n\Omega}^T)H_\alpha^k;\quad H_\beta^k dz_k\\ \mathbf{M}^{k\tau s}&=\int_{\Lambda_k}\rho^k F_{\tau}F_s\mathbf{I}H_\alpha^k H_\beta^k dz_k.\end{aligned} \quad (11)$$

$\mathbf{I}$ is the unit array. As usual in two-dimensional modelings, the integration in the thickness direction can be made a priori by introducing the following layer-integrals (the further integrals related to the displacement formulation, (see Appendix) are also introduced),

$$(J^{k\tau s},\ J_\alpha^{k\tau s},\ J_\beta^{k\tau s},\ J_{\alpha/\beta}^{k\tau s},\ J_{\beta/\alpha}^{k\tau s},\ J_{\alpha\beta}^{k\tau s})=\int_{\Lambda_k}F_{\tau}F_s\left(1,\ H_\alpha^k,\ H_\beta^k,\ \frac{H_\alpha^k}{H_\beta^k},\ \frac{H_\beta^k}{H_\alpha^k},\ H_\alpha^k H_\beta^k\right)dz$$

$$(J^{k\tau_z s},\ J_\alpha^{k\tau_z s},\ J_\beta^{k\tau_z s},\ J_{\alpha\beta}^{k\tau_z s})=\int_{\Lambda_k}F_{\tau_z}F_s(1,\ H_\alpha^k,\ H_\beta^k,\ H_\alpha^k H_\beta^k)dz$$

Downloaded 04 May 2010 to 171.66.16.27. Redistribution subject to ASME license or copyright; see http://www.asme.org/terms/Terms_Use.cfm

$$(J^{k\tau s_z},\ J^{k\tau s_z}_{\alpha},\ J^{k\tau s_z}_{\beta},\ J^{k\tau s_z}_{\alpha\beta}) = \int_{A_k} F_\tau F_{s_z}(1,\ H^k_\alpha,\ H^k_\beta,\ H^k_\alpha H^k_\beta)dz$$

$$(J^{k\tau_z s_z},\ J^{k\tau_z s_z}_{\alpha\beta}) = \int_{A_k} F_{\tau_z} F_{s_z}(1,\ H^k_\alpha H^k_\beta)dz. \qquad (12)$$

As a further step, the differential and algebraic operators can be conveniently split in the two terms related to the H^k_α and H^k_α, respectively,

$$(\mathbf{D}_p,\ \mathbf{A}_p,\ \mathbf{D}_{n\Omega},\ \mathbf{A}_n,\ \mathbf{I}_p,\ \mathbf{I}_{n\Omega}) = \frac{1}{H_\alpha}(\mathbf{D}^\alpha_p,\ \mathbf{A}^\alpha_p,\ \mathbf{D}^\alpha_{n\Omega},\ \mathbf{A}^\alpha_n,\ \mathbf{I}_p,\ \mathbf{I}_{n\Omega}) + \frac{1}{H_\beta}(\mathbf{D}^\beta_p,\ \mathbf{A}^\beta_p,\ \mathbf{D}^\beta_{n\Omega},\ \mathbf{A}^\beta_n,\ \mathbf{I}^\beta_p,\ \mathbf{I}^\beta_{n\Omega}). \qquad (13)$$

Therefore, the differential operators of Eqs. (11) are written

$$\mathbf{K}^{k\tau s}_{uu} = (-\mathbf{D}^{\alpha T}_p + \mathbf{A}^{\alpha T}_p)\mathbf{C}_{pp} \times [J^{k\tau s}_{\beta/\alpha}(\mathbf{D}^\alpha_p + \mathbf{A}^\alpha_p) + J^{k\tau s}(\mathbf{D}^\beta_p + \mathbf{A}^\beta_p)] + (-\mathbf{D}^{\beta T}_p + \mathbf{A}^{\beta T}_p)\mathbf{C}_{pp}[J^{k\tau s}_{\alpha/\beta}(\mathbf{D}^\alpha_p + \mathbf{A}^\alpha_p) + J^{k\tau s}(\mathbf{D}^\beta_p + \mathbf{A}^\beta_p)]$$

$$\mathbf{K}^{k\tau s}_{u\sigma} = (-J^{k\tau s}_\beta \mathbf{D}^{\alpha T}_p - J^{k\tau s}_\alpha \mathbf{D}^{\beta T}_p + J^{k\tau s}_\alpha \mathbf{A}^{\beta T}_p + J^{k\tau s}_\beta \mathbf{A}^{\alpha T}_p)\mathbf{C}^k_{pn} + J^{k\tau_z s}_{\alpha\beta}\mathbf{I} + \lambda_D(J^{k\tau s}_\beta \mathbf{A}^{\alpha T}_n + J^{k\tau s}_\alpha \mathbf{A}^{\beta T}_n) - J^{k\tau s}_\beta \mathbf{D}^{\alpha T}_{n\Omega} - J^{k\tau s}_\alpha \mathbf{D}^{\beta T}_{n\Omega}$$

$$\mathbf{K}^{k\tau s}_{\sigma u} = -\mathbf{C}^k_{np}(J^{k\tau s}_\beta \mathbf{D}^\alpha_p + J^{k\tau s}_\alpha \mathbf{D}^\beta_p + J^{k\tau s}_\alpha \mathbf{A}^\beta_p + J^{k\tau s}_\beta \mathbf{A}^\alpha_p) + J^{k\tau s_z}_{\alpha\beta}\mathbf{I} + \lambda_D(J^{k\tau s}_\beta \mathbf{A}^\alpha_n + J^{k\tau s}_\alpha \mathbf{A}^{\beta_n}) + J^{k\tau s}_\beta \mathbf{D}^\alpha_{n\Omega} + J^{k\tau s}_\alpha \mathbf{D}^\beta_{n\Omega}$$

$$\mathbf{K}^{k\tau s}_{\sigma\sigma} = -J^{k\tau s}_{\alpha_\beta} C^{k\tau s}_{nn}$$

$$\mathbf{\Pi}^{k\tau s}_u = (J^{k\tau s}_{\beta/\alpha}\mathbf{I}^{\alpha T}_p + J^{k\tau s}\mathbf{I}^{\beta T}_p)\mathbf{C}_{pp}(\mathbf{D}^\alpha_p + \mathbf{A}^\alpha_p) + (J^{k\tau s}\mathbf{I}^{\alpha T}_p + J^{k\tau s}_{\alpha/\beta}\mathbf{I}^{\beta T}_p)\mathbf{C}_{pp}(\mathbf{D}^\beta_p + \mathbf{A}^\beta_p)$$

$$\mathbf{\Pi}^{k\tau s}_\sigma = (J^{k\tau s}_\beta \mathbf{I}^{\alpha T}_p + J^{k\tau s}_\alpha \mathbf{I}^{\beta T}_p)\mathbf{C}_{pn} + J^{k\tau s}_\beta \mathbf{I}^{\alpha T}_{n\Omega} + J^{k\tau s}_\alpha \mathbf{I}^{\beta T}_{n\Omega}. \qquad (14)$$

The inertia array is found

$$\mathbf{M}^{k\tau s}_{ij} = J^{k\tau s}_{\alpha\beta}\delta_{ij}, \quad i, j = 1, 3 \qquad (15)$$

where the Kroneker symbol δ_{ij} has been introduced. Cylindrical shell equations are simply obtained by enforcing $R_\alpha = \infty$ (or $R_\beta = \infty$) while spherical shell geometries correspond to the case $R_\alpha = R_\beta$. Discarding the terms multiplied by the trace operators λ_D, the corresponding Donnell's shallow shell equations are obtained. Neglecting all the curvature terms the governing equation written for multilayered plates (Carrera 1998b) are given as particular cases.

4.2 Fulfillment of C^0_z-Requirements and Governing Equations at a Multilayered Level. In the preceding sections the governing shell equations have been considered to be independent of the N_l layers. Interlaminar continuity conditions, i.e., C^0_z-requirements in Eqs. (6) must be used to drive the governing equations for the whole multilayered shell. This can be done by following the same steps described in previous works (Carrera, 1995, 1998a, b). Here it is only remarked that in contrast to plates, it is essential to have the same product of type $d\alpha^* d\beta^*$ in each k-layer equations for shell geometry due to the curvature changes. This can be done by choosing the value on the reference shell surface $\Omega d\alpha d\beta$ as $d\alpha^* d\beta^*$. Each $d\alpha_k d\beta_k$ defined on Ω_k is therefore written as $d\alpha_k d\beta_k = (R_\alpha R_\beta / R^k_\alpha R^k_\beta)d\alpha\ d\beta$. The following shell arrays for the displacement and stress unknowns are introduced at the very end,

$$\mathbf{u} = \{\mathbf{u}^{1T}_b, \mathbf{u}^{1T}_t, \mathbf{u}^{1T}_r;\ \mathbf{u}^{2T}_t, \mathbf{u}^{2T}_r;\ \ldots\ \mathbf{u}^{kT}_t, \mathbf{u}^{kT}_r;\ \mathbf{u}^{(k+1)T}_t, \mathbf{u}^{(k+1)T}_r;\ \ldots\ \mathbf{u}^{(N_l-1)T}_t, \mathbf{u}^{(N_l-1)T}_r;\ \mathbf{u}^{N_l T}_t, \mathbf{u}^{N_l T}_r\}$$

$$\boldsymbol{\sigma}_n = \{\boldsymbol{\sigma}^{1T}_{nt}, \boldsymbol{\sigma}^{1T}_{nr};\ \boldsymbol{\sigma}^{2T}_{nt}, \boldsymbol{\sigma}^{2T}_{nr};\ \ldots\ \boldsymbol{\sigma}^{kT}_{nt}, \boldsymbol{\sigma}^{kT}_{nr};\ \boldsymbol{\sigma}^{(k+1)T}_{nt}, \boldsymbol{\sigma}^{(k+1)T}_{nr};\ \ldots\ \boldsymbol{\sigma}^{(N_l-1)T}_{nt}, \boldsymbol{\sigma}^{(N_l-1)T}_{nr};\ \boldsymbol{\sigma}^{N_l T}_{nr}\}, \qquad (16)$$

in which the top and r-variables have been chosen as layer unknowns. The dimensions M_u and M_σ of these two arrays depend on the number of layers N_l as well as on the order of the used expansion N according to the following formula:

$$M_u = 3(N_l + 1) + 3\,NN_l, \quad M_\sigma = M_u - 6.$$

Therefore, the governing system of differential equations at a multilayered level is formally written in the following final form:

$$\mathbf{K}_{uu}\mathbf{u} + \mathbf{K}_{u\sigma}\boldsymbol{\sigma}_n = \mathbf{M}\ddot{\mathbf{u}} + \mathbf{p} + \mathbf{p}^{1N_l}_u$$
$$\mathbf{K}_{\sigma u}\mathbf{u} + \mathbf{K}_{\sigma\sigma}\boldsymbol{\sigma}_n = \mathbf{p}^{1N_l}_\sigma, \qquad (17)$$

while the boundary conditions are

$$\mathbf{u} = \bar{\mathbf{u}} \quad \text{or} \quad \mathbf{\Pi}_u\mathbf{u} + \mathbf{\Pi}_\sigma\boldsymbol{\sigma}_n = \mathbf{\Pi}_u\bar{\mathbf{u}} + \mathbf{\Pi}_\sigma\bar{\boldsymbol{\sigma}}_n + \mathbf{q}^{1N_l}_\sigma. \qquad (18)$$

$\mathbf{p}^{1N_l}_u$, $\mathbf{p}^{1N_l}_\sigma$, and $\mathbf{q}^{1N_l}_\sigma$ are arrays coming from transverse stress values imposed at the top/bottom of the shell surfaces.

4.3 Closed-Form Solutions for Shells Composed of Orthotropic Layers. The boundary value problem governed by Eqs. (17), (18) in the most general case of geometry, boundary conditions, and layouts, could be solved by only implementing approximate solution procedures. In order to assess the proposed models these equations are herein solved for a special case in which closed-form solutions are given. The particular case in which the material has the following properties (as it is the case of cross-ply shells) $\tilde{C}_{16} = \tilde{C}_{26} = \tilde{C}_{36} = \tilde{C}_{45} = 0$ has been considered, for which Navier-type closed-form solutions can be found by assuming the following harmonic forms for the applied loadings $\mathbf{p}^k = \{p^k_{\alpha_\tau}, p^k_{\beta_\tau}, p^k_{z_\tau}\}$ and unknown displacement $\mathbf{u}^k = \{u^k_{\alpha_\tau}, u^k_{\beta_\tau}, u^k_{z_\tau}\}$ and stress $\boldsymbol{\sigma}^k_n = \{\sigma^k_{\alpha z_\tau}, \sigma^k_{\beta z_\tau}, \sigma^k_{zz_\tau},\}$ variables in each k-layer:

$$(u^k_{\alpha_\tau}, \sigma^k_{\alpha z_\tau}, p^k_{\alpha_\tau}) = \sum_{m,n}(U^k_\alpha, S^k_{\alpha z_\tau}, P^k_{\alpha_\tau}) \cos\frac{m\pi\alpha_k}{a_k} \sin\frac{n\pi\beta_k}{b_k} e^{i\omega_{mn}\hat{t}} \quad k = 1, N_l$$

$$(u^k_{\beta_\tau}, \sigma^k_{\beta z_\tau}, p^k_{\beta_\tau}) = \sum_{m,n}(U^k_\beta, S^k_{\beta z_\tau}, P^k_{\beta_\tau}) \sin\frac{m\pi\alpha_k}{a_k} \cos\frac{n\pi\beta_k}{b_k} e^{i\omega_{mn}\hat{t}} \quad \tau = t, b, r$$

$$(u^k_{z_\tau}, \sigma^k_{zz_\tau}, p^k_{z_\tau}) = \sum_{m,n}(U^k_z, S^k_{zz_\tau}, P^k_{z_\tau}) \sin\frac{m\pi\alpha_k}{a_k} \sin\frac{n\pi\beta_k}{b_k} e^{i\omega_{mn}\hat{t}} \quad r = 2, N \qquad (19)$$

which correspond to simply supported boundary conditions. a_k and b_k are the shell lengths in the α_k and β_k directions, respectively, while m and n are the correspondent wave numbers; $i = \sqrt{-1}$, $\hat{t}$ is the time and ω_{mn} is the circular frequency. Capital letters at R.H.S. denote correspondent maximum amplitudes. Upon substitution of Eqns. (19), the governing equations assume the form of a linear system of ordinary differential equations in the time domain. The free-vibration response leads to an eigenvalue problem. Upon eliminations of the stress unknowns, the mixed case leads to

$$\|\hat{\mathbf{K}}_{uu} - (\hat{\mathbf{K}}_{u\sigma}(\hat{\mathbf{K}}_{\sigma\sigma})^{-1}\hat{\mathbf{K}}_{\sigma u}) - \omega^2_{mn}\hat{\mathbf{M}}\| = 0. \qquad (20)$$

The double bar denotes determinant, while the hat indicates arrays constituted by real numbers.

5 Results and Discussion

As an attempt to test and evaluate the foregoing mixed models, the theories were applied to a large number of homogeneous and laminated cylindrical and spherical shell problems. The most significant results are described in the following analysis.

Downloaded 04 May 2010 to 171.66.16.27. Redistribution subject to ASME license or copyright; see http://www.asme.org/terms/Terms_Use.cfm

Table 1 List of the acronyms used to denote shell theories, in alphabetic order

D-l$^{N_l^*}$, D-p$^{N_l^*}$	Present LWMs based on displacements formulation, p and l refer to parabolic and linear expansion, N_l^* is the numbers of mathematical interfaces
ESLM	Present Equivalent Single Layer Model
E-l, E-p	Present ESLM with linear and parabolic displacements fields.
E-l.b	E-l neglecting transverse normal stress
3D	Three dimensional solution
LWM	Layer Wise Model
M-p$^{N_l^*}$,M-l$^{N_l^*}$	Present Mixed LWMs.
.Δ	Donnell-Type Approximations

The free-vibrational response of simply supported, cross-ply laminated cylindrical and spherical shells has been analyzed. Three-dimensional solutions as well as related analyses based on displacement formulations (of layer-wise LW and equivalent single-layer ESLM type), is compared. A compendium of the used acronyms to denote the theories have been given in Table 1. Continuous reference to these acronyms is made in the subsequent discussion. In a few cases the reported tables quote results related to Donnell's type approximations. Static conditions on the bounding surfaces of the shell could not be imposed for the mixed linear expansion (M-1) of Eqs. (5). In fact, their linkage would require discarding the stiffness and/or compliance contributions related to the top and bottom shell layers. These conditions have therefore not been considered in all the quoted M-1 results. Fictitious mathematical interfaces have been introduced in the calculation in order to both improve the displacement and stress fields and to reduce the curvature approximations related to the thickness to radii shell ratio h/R. The total number of interfaces is denoted by N_l^*. If it is different to N_l, it will be put as a superscript in correspondence to the acronyms of the considered layer-wise results. Mostly the case $N_l^* = 2 \times N_l$ has been implemented.

As a preliminary result a static problem has been solved. The effectiveness of the layer-wise mixed analysis to describe a priori the transverse stress field has been shown in Fig. 2. A cross-ply laminated cylinder, loaded by harmonic distribution of transverse pressure of amplitude $P^1_{z_b}$, applied at the inner surface has been considered. Exact solutions were given by Varadan and Bhaskar (1991). A comparison has been made with further results by the same authors (Bhaskar and Varadan, 1992) in which the Reissner's theorem was used in the field of ESLM analysis. An excellent agreement between the exact studies and the present M-p a priori evaluations can be seen. A poor description was found for the ESLM analysis by Bhaskar and Varadan (1992) even though the transverse shear stresses were evaluated via integration of the three-dimensional indefinite equilibrium equations (H.b-B&V). Furthermore, the related transverse shear stresses evaluated a priori (H.a-B&V) demonstrate, as it was found for plates (Carrera, 1998a), that such an evaluation requires a layer-wise description.

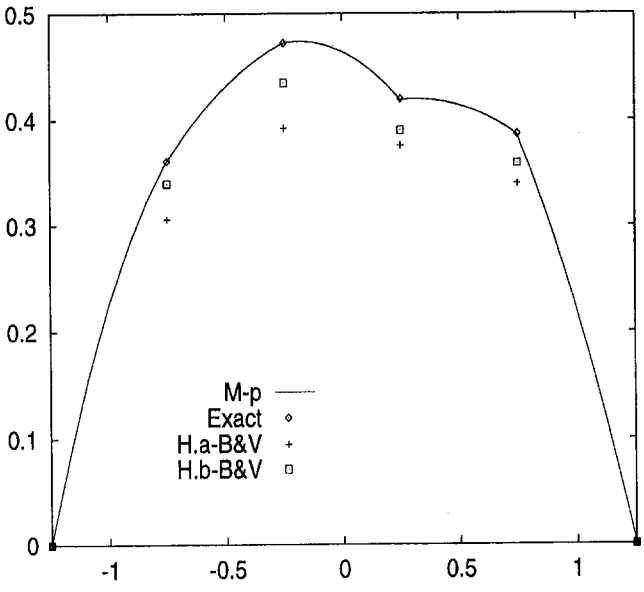

Fig. 2 Amplitude of transverse shear stress $\bar{S}_{\alpha z} = |S_{\alpha z} \times 10h/P^1_{z_b}R_\beta|$ versus z. Varadan and Bhaskar's (1991) cylindrical shells with $R_\beta/h = 4$, $h = 2.5$, $m = 1$, $n = 8$. Five layers case, $E_L/E_T = 25$, $G_{LT}/E_T = .5$, $G_{TT} = .2$, $\nu_{LT} = \nu_{TT} = .25$.

Table 2 Effect of degree of orthotropy of the individual layers E_L/E_T on $\omega \times 10\sqrt{\rho h^2/E_T}$. Comparison to three-dimensional solutions by Noor and Rarig (1974). $h/R_\beta = 0.2$, $a/R_\beta = 1$, $m = 1$, $n = 4$.

	N_l	E_L/E_T 3	10	40
3D	2	2.3141	2.5464	2.9262
M-p		2.3139	2.5461	2.9248
M-p^4		2.3141	2.5464	2.9260
M-l		2.3217	2.5538	2.9328
D-p		2.3150	2.5514	2.9594
D-l		2.3292	2.5626	2.9666
E-p		2.3219	2.5589	2.9822
E-l		2.3450	2.5826	3.0367
E-l.b		2.3812	2.6019	3.0756
3D	3	2.3173	2.6542	3.1675
M-p		2.3173	2.6541	3.1663
M-p^6		2.3173	2.6542	3.1673
M-l		2.3153	2.6472	3.1358
D-p		2.3181	2.6589	3.1979
D-l		2.3522	2.6665	3.2087
E-p		2.3266	2.6842	3.3205
E-l		2.3577	2.7066	3.3322
E-l.b		2.3798	2.7186	3.3497
3D	5	2.3767	2.8245	3.4631
M-p		2.3768	2.8245	3.7506
M-p^{10}		2.3767	2.8245	3.4633
M-l		2.3768	2.8264	3.7538
D-p		2.3768	2.8248	3.7507
D-l		2.3808	2.8364	3.7611
E-p		2.3908	2.8805	3.8972
E-l		2.4201	2.8981	3.9198
E-l.b		2.5761	3.2320	4.0927
3D	10	2.4357	2.9856	3.7506
M-p		2.4357	2.9856	3.7506
M-p^{20}		2.4357	2.9856	3.7506
M-l		2.4358	2.9863	3.7538
D-p		2.4357	2.9856	3.7507
D-l		2.4366	2.9885	3.7611
E-p		2.4488	3.0281	3.8972
E-l		2.4768	3.0467	3.9198
E-l.b		2.4975	3.0548	3.9281

A few parametric studies have been presented to provide some insight into the effects of variation in material and geometric characteristics of laminated shells on their vibration characteristic. Tables 2–5 consider laminated circular cylinders having both symmetric and skew-symmetric lamination with respect to the middle surface for which approximate three-dimensional solution were given by Noor and Rarig (1974) and Noor and Peters (1989b). The fibers of the different layers alternate between the longitudinal α and circumferential β directions, with the fibers of the top layer running in the circumferential direction. The total thickness of the circumferential and longitudinal layers in each shell was the same. The material characteristics of the individual layers were taken to be those of typical of high-modulus fibrous composites, namely $G_{LT}/E_T = G_{Lz}/E_T = .6$, $G_{TT}/E_T = .5$, $\nu_{LT} = \nu_{TT} = .25$, where the subscripts L refer to the direction of fibers and subscript T refers to the transverse

Downloaded 04 May 2010 to 171.66.16.27. Redistribution subject to ASME license or copyright; see http://www.asme.org/terms/Terms_Use.cfm

Table 3 Effect of thickness to radii ratio h/R_β on $\omega \times 10\sqrt{\rho h^2/E_T}$. Comparison to three-dimensional solutions by Noor and Rarig (1974). $E_L/E_T = 30$, $a/R_\beta = 1$, $m = 1$.

	h/R_β	n		
		2	4	6
		N_l=2		
3D	.05	0.8165	0.5385	0.4218
M-p		0.8165	0.5385	0.4218
D-p		0.8166	0.5387	0.4220
E-l		0.8169	0.5394	0.4238
M-p.Δ		0.8213	0.5450	0.4309
3D	.25	4.4910	3.8047	4.1584
M-p		4.4903	3.8023	4.1539
D-p		4.5194	3.8498	4.2196
E-l		4.6020	3.9952	4.4293
M-p.Δ		4.5772	3.9556	4.4368
3D	.40	7.5953	6.9568	7.9209
M-p		7.5873	6.9410	7.8976
M-p[4]		7.5948	6.9537	7.9156
M-p[8]		7.5970	6.9572	7.9202
D-p		7.6780	7.0766	8.0744
D-p[4]		7.6051	6.9690	7.9353
D-p[8]		7.5979	6.9584	7.9218
E-l		7.9928	7.5598	8.6944
M-p.Δ		7.7572	7.2678	8.3377
		N_l=10		
3D	.05	0.8410	0.5832	0.5027
M-p		0.8410	0.5832	0.5027
D-p		0.8410	0.5832	0.5027
E-l		0.8414	0.5844	0.5055
M-p.Δ		0.8422	0.5881	0.5148
3D	.25	5.1280	4.7990	5.4710
M-p		5.1281	4.7992	5.4712
D-p		5.1283	4.7993	5.4714
E-l		5.2651	5.0361	5.8226
M-p.Δ		5.1604	4.9648	5.7233
3D	.40	8.6111	8.4732	9.8040
M-p		8.6116	8.4736	9.8043
D-p		8.6119	8.4742	9.8053
E-l		8.9576	9.0508	10.0629
M-p.Δ		8.6928	8.8329	10.2779

Table 4 Effect of length to radii ratio a/R_β on $\omega \times 10\sqrt{\rho h^2/E_T}$. Comparison to three-dimensional solutions by Noor and Rarig (1974). $N_l = 10$, $E_L/E_T = 30$, $h/R_\beta = .2$, $m = 1$.

	a/R_β	n		
		2	4	6
3D	.5	8.5280	8.0598	8.1694
M-p		8.5280	8.0597	8.1693
D-p		8.5285	8.0602	8.1699
E-l		8.9135	8.5952	8.7780
M-p.Δ		8.5440	8.1194	8.2645
3D	1.	3.9756	3.5961	4.0428
M-p		3.9757	3.5962	4.0429
D-p		3.9758	3.5962	4.0430
E-l		4.0538	3.7355	4.2559
M-p.Δ		3.9966	3.7062	4.2239
3D	5.	0.6627	1.0499	2.3511
M-p		0.6632	1.0503	2.3512
D-p		0.6632	1.0503	2.3513
E-l		0.6634	1.0877	2.4932
M-p.Δ		0.7226	1.3530	2.6408
3D	20.	0.1039	0.9663	2.3294
M-p		0.1065	0.9667	2.3295
D-p		0.1066	0.9668	2.3296
E-l		0.1066	1.0061	2.4719
M-p.Δ		0.3073	1.2882	2.6215

direction; ν_{LT} is the major Poisson's ratio. Three parameters were varied in these tables, namely the degree of orthotropy of the individual layers E_L/E_T, the thickness ratio h/R and the

Table 5 Effect of longitudinal and circumferential wave numbers on $\omega \times \sqrt{\rho h^2/E_T}$. Comparison to three-dimensional solutions by Noor and Peters (1989b). $N_l = 40$, $E_L/E_T = 15$, $G_{LT}/E_T = .5$, $G_{TT}/E_T = .35$, $\nu_{LT} = \nu_{TT} = .3$ $a/R_\beta = 5.$, $h/R_\beta = .2$.

	m	n		
		0	4	10
3D	1	0.08886	0.08365	0.4489
M-p		0.08886	0.08365	0.4489
D-p		0.08886	0.08365	0.4489
E-l		0.08886	0.08596	0.4789
3D	2	0.1777	0.1175	0.4545
M-p		0.1777	0.1175	0.4545
D-p		0.1777	0.1175	0.4545
E-l		0.1777	0.1199	0.4847
3D	3	0.2666	0.1695	0.4681
M-p		0.2666	0.1695	0.4681
D-p		0.2666	0.1695	0.4681
E-l		0.2666	0.1728	0.4987

length to thickness ratio a/R as well as circumferential and longitudinal modes m and n. As a main fact one remarks that the present layer-wise mixed analyses are, in general, in very good agreement with three-dimensional results even though very thick shells are considered. It is of further interest to notice that stress and displacement formulations lead to a lower and higher estimate of the shell stiffness as far as the three-dimensional solutions are concerned. In fact, D-p and D-1 frequency values are always higher than the exact ones. In the mixed cases a unique conclusion cannot be drawn: This very much depends on the relative role played by the in-plane and out-of-plane energy and the results obviously become problem-dependent. For most of the considered problems it has been found that mixed and displacements solutions lead to lower and higher approximations for the fundamental and higher order frequencies, respectively. The following further comments can be made about the results of these tables. Thickness, E_L/E_t and N_l decreasing the ESLMs results improve. Lower accuracy should be registered for both higher circumferential and longitudinal modes. In some cases ESLM results related to parabolic expansion (E-p) could be better than those related to LW analysis with linear expansion in each layer (D-1). Transverse normal stress effects can remarked by comparing E-1 to E-1.b results. No shear correction factors have been used for the quoted ESLM results. As demonstrated by Noor and Peters (1989a, b), the values of exact shear correction factors is problem-dependent. Therefore, the use of a fixed value could be meaningless as long as thick shells are analyzed. On the other hand, the accuracy of LW results increase by N_l increasing (the numbers of the unknown variables increases). In fact, fictitious interfaces (Tables 2, 3) show major benefits for laminates composed by two or three layers as well as for thicker shells. The increasing accuracy obtained by using fictitious interfaces confirm the convergence of the proposed layer-wise models to the three-dimensional solutions. One-dimensional effects along the longitudinal directions become predominant in long cylinders and M-p and D-p merge in such cases (Table 4). This is confirmed by the results related to the $n = 0$ analysis, e.g., pure longitudinal vibrations (Table 5). Donnell's shallow shell approximations are not affected by h/R_β and in general the related curvature terms should be retained for thicker as well as thin closed cylinders. The errors introduced by such approximations could be not conservative. In other words, two-dimensional refinements of the classical model could be meaningless unless curvature terms are discarded (see also Carrera, 1991).

A comparison to the recent three-dimensional exact solution by Ye and Soldatos (1994) and to several refined models quoted in Timarci and Soldatos (1995) and Di Sciuva and Carrera (1992) have been provided in Table 6. A three-layered moderately thick cylindrical shell has been considered. An excellent

Downloaded 04 May 2010 to 171.66.16.27. Redistribution subject to ASME license or copyright; see http://www.asme.org/terms/Terms_Use.cfm

Table 6 Effect of radii to length ratio R/a on $\omega \times a^2\sqrt{\rho/h^2E_T}$. Comparison to three-dimensional exact solution by Ye and Soldatos (1994) and to other refined ESLM analyses (Timarci and Soldatos, 1995; Di Sciuva and Carrera, 1992). $a/h = 10$, $m = 1$, $n = 2$ unless given in brackets. $N_l = 3$, $h_1 = h_3 = h_2/2$. $E_L/E_T = 25$, $G_{LT}/E_T = .5$, $G_{TT}/E_T = .2$, $\nu_{LT} = \nu_{TT} = .25$.

R_β/a	5	10	20	50	100
3D	10.305	10.027	9.902	9.834	9.815
	(14)	(22)	(30)	(24)	
M-p	10.305	10.027	9.902	9.834	9.815
	(14)	(22)	(30)	(24)	
D-p	10.306	10.028	9.903	9.835	9.816
	(14)	(22)	(30)	(24)	
PAR_{ds}	10.496	10.223	10.099	10.032	10.013
			(28)	(26)	
HYP_{ds}	10.496	10.226	10.103)	10.036	10.018
			(28)	(26)	
UNI_{cs}	10.462	10.187	10.063	9.996	9.977
			(28)	(26)	
PAR_{cs}	10.329	10.051	9.927	9.859	9.840
				(26)	
HYP_{cs}	10.328	10.050	9.925	9.858	9.839
				(26)	
ZZL	10.462	10.187	10.063	9.996	9.971
	(14)	(24)	(28)	(16)	(4)

agreement between present mixed analysis M-p and an exact solution has to be registered. Better results with respect to standard displacement formulation D-p are found. The value quoted in brackets accompanying some of the numerical results in Table 6 indicates the circumferential wave number, n, for which the fundamental frequency was detected. All the theories considered in the above-mentioned references belong to the ESLM family. Further, they all do neglect transverse normal stress effects. Uniform UNI, parabolic PAR, and hyperbolic HYP transverse shear stress distribution in the thickness shell direction where considered as well as the two cases of interlaminar discontinuous *ds* and continuous *cs* shear stresses (see Timarci and Soldatos, 1995, for further details). Uniform distribution cases do not fulfill static conditions at the top and bottom shell surfaces. ZZL results refer to Di Sciuva and Carrera's (1992) analysis which is the same as that of UNI_{cs}. The fundamental mode, e.g., n-values can be erroneously predicted by ESLM analysis. The importance of fulfilling the interlaminar transverse shear stress continuity has been confirmed by the present analysis (see the interesting discussion in Timarci and Soldatos (1995)). Nevertheless, the role played by the transverse normal stress should be underlined. Such a role could become more predominant for thicker shells. The numerical analysis of this aspect could be the subject of future investigations.

Only a few results for square spherical shell panels have been considered in Tables 7–8. Table 7 gives a comparison of the present studies with the first-order shear deformation theories (FSDT) by Reddy (1984) the higher-order shear deformation Theory (HSDT) by Reddy and Liu (1984), for three-layer cross-plied panels. Classical lamination theories (CLT) results were taken from (Carrera, 1991). Increasing $R = R_\alpha = R_\beta$

Table 7 Effect of radii to length ratio R/a on $\omega \times \sqrt{a^4\rho/h^2E_T}$. Spherical, square cross-plied panels. $a/h = 10$, $m = n = 1$. $N_l = 3$, $a/R_\beta = 5.$, $h/R_\beta = .2$, material of Table 6.

R/a	1	2	5	10	plate
M-p	16.043	12.889	11.720	11.531	11.457
D-p	16.048	12.896	11.727	11.538	11.464
E-l	16.271	13.714	12.785	12.641	12.593
M-p.Δ	16.682	13.122	11.762	11.542	11.457
D-p.Δ	16.688	13.129	11.790	11.549	11.464
E-l.Δ	17.010	13.975	12.832	12.653	12.593
HSDT	-	-	12.060	11.860	11.790
FSDT	16.115	13.382	12.372	12.215	12.162
CLT	17.820	15.878	15.233	15.136	15.104

Table 8 Effect of radii to length ratio R/a on $\omega \times \sqrt{\rho h^2/E_T}$. Spherical, square cross-plied panels. Material data are those of Tables 2–4 with $E1/Et = 40$. $a/h = 5$, $m = n = 1$.

	N_l	R/a		
		.5	1	10
M-p	2	.5478	.4232	.3441
M-p[4]		.5471	.4233	.3441
D-p		.5505	.4290	.3510
E-l		.4828	.4062	.3662
M-p.Δ		.6081	.4487	.3445
D-p.Δ		.6142	.4553	.3513
E-l.Δ		.5315	.4315	.3666
M-p	3	.5546	.4683	.4291
M-p[6]		.5539	.4681	.4292
D-p		.5557	.4712	.4323
E-l		.4978	.4650	.4588
M-p.Δ		.6205	.4999	.4296
D-p.Δ		.6229	.5031	.4327
E-l.Δ		.5446	.4989	.4592

values are considered. Quite different results were found from the referenced ESLM analyses. As R/a is increased better results are furnished by Donnell's descriptions. Thicker, symmetric, and unsymmetric cross-ply laminated spherical shells are considered in Table 8. Larger difference between LW and ESLM analysis have been found with respect to Table 7. To confirm the importance of the curvature terms in LW analysis one should observe the lower discrepancy of the layer-wise results related to the different N_l^* when R/a (i.e., R/h) increases (Table 8).

6 Concluding Remarks

Layer-wise theories have been presented for the dynamic analysis of multilayered shells made by orthotropic layers. The theories have been formulated on the bases of a Reissner's mixed variational theorem. Classical displacement formulations and related equivalent single-layer equations have been also considered for comparison purposes. With respect to existing theories, the proposed mixed models permit fulfilling completely and a priori the continuity conditions at the interfaces for both displacement and transverse stress components (transverse displacement and transverse normal stress included). That is, no post-processing techniques are requested to compute transverse stresses. No assumptions have been made concerning the terms related to the thickness-to-radii h/R shell ratio. The equations related to the Donnell's shallow shell-type approximations have been derived for all the considered theories.

Parametric studies were made of the effects of variations in the lamination and geometric parameters of cylindrical and spherical simply supported shells on their free-vibration characteristics. Solutions obtained by the proposed mixed models were compared with those related to available three-dimensional elasticity analysis as well as with those of available and implemented ESLM and LW results. The conducted analysis confirm that the proposed mixed models furnish an excellent agreement to exact three-dimensional even though very thick anisotropic shells were considered.

As a drawback the layer-wise description requires the use of unknown variables, the number of which depends on the number of layers. Such a drawback should be taken into account wherever computational models, e.g., finite element applications have to be developed. Nevertheless, the most expensive layer-wise analysis performed in this article (which is based on simple closed-form solution procedures) took only a few c.p.u. seconds on a standard personal computer. However, the mixed layer-wise theories preserve the advantages of two-dimensional modeling and lead to an excellent agreement with exact three-dimensional results. This fact should encourage the use of the proposed theories to design vibrational response of multilayered

Downloaded 04 May 2010 to 171.66.16.27. Redistribution subject to ASME license or copyright; see http://www.asme.org/terms/Terms_Use.cfm

structures or their use to provide reference solutions in order to assess simplified models.

References

Alam, Asnani, N.T., 1984, "Vibration and Damping Analysis of a Multilayered Cylindrical Shells, Part I: Theoretical Analysis," *American Institute of Aeronautics and Astronautics Journal,* Vol. 22, pp. 803–810.

Ambartsumian, S.A., 1968, "On General Theory of Anisotropic Shells," *Journal of Applied Mathematics and Mechanics,* (translation of PMM Prikladnaia Matematika I Mekhanika, Vol. 22, No. 2, pp. 226–237).

Barbero, E.J., Reddy, J.N., and Teply, J.L., 1990, "General Two-Dimensional Theory of laminated Cylindrical Shells," *American Institute of Aeronautics and Astronautics Journal,* Vol. 28, pp. 544–553.

Bert, C.W., Baker, J.L., and Egle, D.L., 1969, "Free Vibration of Multilayer Anisotropic Cylindrical Shells," *Journal of Composite Materials,* Vol. 3, pp. 480–500.

Bhaskar, K., and Varadan, T.K., 1992, "Reissner's New Mixed Variational Principle Applied to Laminated Cylindrical Shells," ASME *Journal of Pressure Vessel Technology,* Vol. 114, pp. 115–119.

Carrera, E., 1991, "The Effects of Shear Deformation and Curvature on Buckling and Vibrations of Cross-Ply Laminated Composite Shells," *Journal of Sound and Vibration,* Vol. 151, pp. 405–433.

Carrera, E., 1995, "A class of Two Dimensional Theories for Multilayered Plates Analysis," *Atti Accademia delle Scienze di Torino, Mem Sci. Fis.,* No. 19–20, pp. 49–87.

Carrera, E., 1997, "C_z^0-Requirements: Models for the Two-Dimensional Analysis of Multilayered Structures," *Composite Structures,* Vol. 37, pp. 373–383.

Carrera, E., 1998a, "Evaluation of Layer-Wise Mixed Theories for Laminated Plates Analysis," *American Institute of Aeronautics and Astronautics Journal,* Vol. 5, pp. 830–839.

Carrera, E., 1998b, "Layer-Wise Mixed Models for Accurate Vibration Analysis of Multilayered Plates," ASME JOURNAL OF APPLIED MECHANICS, Vol. 65, pp. 820–828.

Cheung, Y.K., and Wu, C.I., 1972, "Free Vibrations of Thick, Layered Cylinders Having Finite Length with Various Boundary Conditions," *Journal of Sound and Vibration,* Vol. 24, pp. 189–200.

Cho, M., and Parmerter, R.R., 1993, "Efficient Higher Order Composite Plate Theory for General Lamination Configurations," *American Institute of Aeronautics and Astronautics Journal,* Vol. 31, pp. 1299–1305.

Chou, F.H., and Achenbach, J.D., 1972, "Free Three-dimensional Vibrations of Orthotropic Cylinders," *Journal of Sound and Vibration,* Vol. 98, pp. 813–822.

Di Sciuva, M., 1987, "An Improved Shear Deformation Theory for Moderately Thick Multilayered Anisotropic Shells and Plates," ASME JOURNAL OF APPLIED MECHANICS, Vol. 54, pp. 589–596.

Di Sciuva, M., and Carrera, E., 1992, "Elasto-Dynamic Behavior of Relatively Thick, Symmetrically Laminated, Anisotropic Circular Cylindrical Shells," ASME JOURNAL OF APPLIED MECHANICS, Vol. 59, pp. 222–223.

Dong, S.B., 1968, "Free Vibration of Laminated Orthotropic Cylindrical Shells," *Journal of Acoustical Society of America,* Vol. 44, pp. 1628–1635.

Grigolyuk, E.I., and Kulikov, G.M., 1988, "General Direction of the Development of the Theory of Shells," *Mekhanica Kompozitnykh Materialov,* No. 2, pp. 287–298.

Hsu, T., and Wang, J.T., 1971, "Rotationally Symmetric Vibrations of Orthotropic Layered Cylindrical Shells," *Journal of Sound and Vibration,* Vol. 16, pp. 473–487.

Jing, H., and Tzeng, K., 1993, "Refined Shear Deformation Theory of Laminated Shells," *American Institute of Aeronautics and Astronautics Journal,* Vol. 31, pp. 765–773.

Kapania, R.K., 1989, "A Review on the Analysis of Laminated Shells," ASME *Journal of Pressure Vessel Technology,* Vol. 111, pp. 88–96.

Kraus, H., 1967, *Thin Elastic Shells,* John Wiley and Sons, New York.

Librescu, L., 1975, *Elasto-statics and Kinetics of Anisotropic and Heterogeneous Shell-Type Structures,* Noordhoff, Leyden, Netherlands.

Librescu, L., Khdeir, A.A., and Frederick, D., 1989, "A Shear Deformable Theory of Laminated Composite Shallow Shell-Type Panels and Their Response Analysis. Part I: Vibration and Buckling," *Acta Mechanica,* Vol. 77, pp. 1–12.

Librescu, L., and Lin, W., 1996, "Two Models of Shear Deformable Laminated Plates and Shells and Their Use in Prediction of Global Response Behavior," *European Journal of Mechanics, Part A: Solids,* Vol. 15, pp. 1095–1120.

Murakami, H., 1986, "Laminated Composite Plate Theory With Improved In-Plane Response," ASME JOURNAL OF APPLIED MECHANICS, Vol. 53, pp. 661–666.

Noor, A.K., and Rarig, P.L., 1974, "Three-Dimensional Solutions of Laminated Cylinders," *Computer Methods in Applied Mechanics and Engineering,* Vol. 3, pp. 319–334.

Noor, A.K., and Peters, W.S., 1989a, "Stress, Vibration and Buckling of Multilayered Cylinders," *Journal of Structural Engineering, ASCE,* Vol. 115, pp. 69–89.

Noor, A.K., and Peters, W.S., 1989b, "A Posteriori Estimates for Shear Correction Factors in Multilayered Composite Cylinders," *Journal of Engineering Mechanics, ASCE,* Vol. 115, 1989, pp. 1225–1245.

Noor, A.K., and Burton, W.S., 1990, "Assessment of Computational Models for Multilayered Composite Shells," ASME *Applied Mechanics Reviews,* Vol. 43, pp. 67–97.

Rath, B.K., and Das, Y.C., 1973, "Vibration of Layered Shells," *Journal of Sound and Vibration,* Vol. 28, pp. 737–757.

Reddy, J.N., 1984, "Exact Solution of Moderately Thick Laminated Shells," *Journal of Engineering Mechanics, ASCE,* Vol. 110, pp. 769–809.

Reddy, J.N., and Liu, C.F., 1985, "A Higher-Order Shear Deformation Theory of Laminated Elastic Shells," *International Journal of Engineering Sciences,* Vol. 23, pp. 319–330.

Reissner, E., 1986, "On a Mixed Variational Theorem and on a Shear Deformable Plate Theory," *International Journal for Numerical Methods in Engineering,* Vol. 23, pp. 193–198.

Ren, J.G., 1987, "Exact Solutions for Laminated Cylindrical Shells in Cylindrical Bending," *Composites Science and Technology,* Vol. 29, pp. 169–187.

Soldatos, K.P., 1985, "On the Theories used for Wave Propagation in Laminated Composite thin Elastic Shells," *Journal of Applied Mathematics and Physics, ZAMP,* Vol. 36, pp. 120–133.

Soldatos, K.P., and Timarci, T., 1993, "A Unified Formulation of Laminated Composites, Shear Deformable, Five-Degrees-of-Freedom Cylindrical Shell Theories," *Composite Structures,* Vol. 25, pp. 165–171.

Srinivas, S., 1974, "Analysis of Laminated, Composite, Circular Cylindrical Shell with General Boundary Conditions," NASA TR R-412.

Stavsky, Y., and Loewy, R., 1971, "On Vibration of Heterogeneous Orthotropic Cylindrical Shells," *Journal of Sound and Vibration,* Vol. 15, pp. 235–256.

Varadan, T.K., and Bhaskar, K., 1991, "Bending of Laminated Orthotropic Cylindrical Shells—An Elasticity Approach," *Composite Structures,* Vol. 17, pp. 141–156.

Sun, C.T., and Whitney, J.M., 1974, "Axisymmetric Vibrations of Laminated Composite Cylindrical Shells," *Journal of Acoustical Society of America,* Vol. 55, pp. 1238–1245.

Timarci, T., and Soldatos, K.P., 1995, "Comparative Dynamic Studies for Symmetric Cross-Ply Circular Cylindrical Shells on the Basis a Unified Shear Deformable Shell Theories," *Journal of Sound and Vibration,* Vol. 187, pp. 609–624.

Toledano, A., and Murakami, H., 1986, "Shear Deformable Two-Layer Plate Theory With Interlayer Slip," *Journal of Engineering Mechanics Division, ASCE,* Vol. 114, pp. 604–623.

Toledano, A., and Murakami, H., 1987a, "A Composite Plate Theory for Arbitrary Laminated Configurations," ASME JOURNAL OF APPLIED MECHANICS, Vol. 54, pp. 181–189.

Toledano, A., and Murakami, H., 1987b, "A Higher-Order Laminated Plate Theory with Improved In-Plane Responses," *International Journal of Solids and Structures,* Vol. 23, pp. 111–131.

Weingarten, V.I., 1964, "Free Vibration of Multilayered Cylindrical Shells," *Experimental Mechanics,* Vol. 4, pp. 200–205.

Ye, J.Q., and Soldatos, K.P., 1994, "Three-Dimensional Vibration of Laminated Cylinders and Cylindrical Panels With Symmetric or Antisymmetric Cross-Ply Lay-Up," *Composites Engineering,* Vol. 4, pp. 429–444.

APPENDIX

Related Theories Based on Displacement Formulation Layer-Wise Models

The displacement approach is formulated in terms of $\mathbf{u}^k$ by variatianally imposing the equilibrium via classical principle of virtual displacements,

$$\sum_{k=1}^{N_l}\int_{\Omega_k}\int_{A_k}(\delta\boldsymbol{\epsilon}_{p_G}^{k^T}\boldsymbol{\sigma}_{p_{H_d}}^{k}+\delta\boldsymbol{\epsilon}_{n_G}^{k^T}\boldsymbol{\sigma}_{n_{H_d}}^{k})d\Omega_k dz = \sum_{k=1}^{N_l}\int_{\Omega_k}\int_{A_k}\rho^k\delta\mathbf{u}^k\ddot{\mathbf{u}}^k dV+\delta L^e. \quad (21)$$

Upon introducing Eqs. (3), (5), and (4) and following the same procedure developed for the mixed case, the Eq. (21) leads to

$$\begin{aligned}\sum_{k=1}^{N_l}\Bigg(&\int_{\Omega_k}\int_{A_k}\delta\mathbf{u}_\tau^{k^T}\{(-F_\tau\mathbf{D}_p^T+F_\tau\mathbf{A}_p^T)[\tilde{\mathbf{C}}_{pp}(F_s\mathbf{D}_p+F_s\mathbf{A}_p)\\&+\tilde{\mathbf{C}}_{pp}(F_s\mathbf{D}_{n\Omega}+\lambda_D F_s\mathbf{A}_n+F_{s_z})]\\&+(-F_\tau\mathbf{D}_{n\Omega}^T+\lambda_D F_\tau\mathbf{A}_n^T+F_{\tau_z})[\tilde{\mathbf{C}}_{np}(F_s\mathbf{D}_p+F_s\mathbf{A}_p)\\&+\tilde{\mathbf{C}}_{nn}(F_s\mathbf{D}_{n\Omega}+\lambda_D F_s\mathbf{A}_n+F_{s_z})]\}\mathbf{u}_s d\Omega_k\\&+\int_{\Gamma_k}\int_{A_k}\delta\mathbf{u}_\tau^{k^T}\{F_\tau\mathbf{I}_p^T[\tilde{\mathbf{C}}_{pp}(F_s\mathbf{D}_p+F_s\mathbf{A}_p)\\&+\tilde{\mathbf{C}}_{pp}(F_s\mathbf{D}_{n\Omega}+\lambda_D F_s\mathbf{A}_n+F_{s_z})]\\&+F_\tau\mathbf{I}_{n\Omega}^T[\tilde{\mathbf{C}}_{np}(F_s\mathbf{D}_p+F_s\mathbf{A}_p)\end{aligned}$$

Downloaded 04 May 2010 to 171.66.16.27. Redistribution subject to ASME license or copyright; see http://www.asme.org/terms/Terms_Use.cfm

$$+ \tilde{\mathbf{C}}_{nn}(F_s\mathbf{D}_{n\Omega} + \lambda_D F_s\mathbf{A}_n + F_{s_z})]\}\mathbf{u}_s d\Gamma_k\Big)$$

$$= \sum_{k=1}^{N_l}\int_{\Omega_k}\delta\mathbf{u}_\tau^{kT}\mathbf{p}_\tau^k d\Omega_k^p + \sum_{k=1}^{N_l}\int_{\Omega_k}\delta\mathbf{u}_\tau^{kT}\rho^k F_\tau F_s\ddot{\mathbf{u}}^k. \quad (22)$$

The differential system of governing equations and related boundary conditions follows.

$$\delta\mathbf{u}_\tau^k: \quad \mathbf{K}_d^{k\tau s}\mathbf{u}_s^k = \mathbf{M}^{k\tau s}\ddot{\mathbf{u}}_s^k + \mathbf{p}_\tau^k$$

$$\text{geometrical on } \Gamma_k^g \quad \text{mechanical on } \Gamma_k^m$$

$$\mathbf{u}_\tau^k = \bar{\mathbf{u}}_\tau^k \quad \text{or} \quad \mathbf{\Pi}_{\mathrm{l}d}^{k\tau s}\mathbf{u}_s^k = \mathbf{\Pi}_d^{k\tau s}\bar{\mathbf{u}}_s^k \quad (23)$$

The introduced differential arrays are

$$\mathbf{K}_d^{k\tau s} = \int_{A_k}\{(-F_\tau\mathbf{D}_p^T + F_\tau\mathbf{A}_p^T)[\tilde{\mathbf{C}}_{pp}(F_s\mathbf{D}_p + F_s\mathbf{A}_p)$$
$$+ \tilde{\mathbf{C}}_{pn}(F_s\mathbf{D}_{n\Omega} + \lambda_D F_s\mathbf{A}_n + F_{s_z})]$$
$$+ (-F_\tau\mathbf{D}_{n\Omega}^T + \lambda_D F_\tau\mathbf{A}_n^T + F_{\tau_z})[\tilde{\mathbf{C}}_{np}(F_s\mathbf{D}_p + F_s\mathbf{A}_p)$$
$$+ \tilde{\mathbf{C}}_{nn}(F_s\mathbf{D}_{n\Omega} + F_s\mathbf{A}_n + F_{s_z})]\}H_\alpha^k H_\beta^k dz_k$$

$$\mathbf{\Pi}_d^{k\tau s} = \int_{A_k}\{F_\tau\mathbf{I}_p^T[\tilde{\mathbf{C}}_{pp}(F_s\mathbf{D}_p + F_s\mathbf{A}_p)$$
$$+ \tilde{\mathbf{C}}_{pp}(F_s\mathbf{D}_{n\Omega} + \lambda_D F_s\mathbf{A}_n + F_{s_z})]$$
$$+ F_\tau\mathbf{I}_{n\Omega}^T[\tilde{\mathbf{C}}_{np}(F_s\mathbf{D}_p + F_s\mathbf{A}_p)$$
$$+ \tilde{\mathbf{C}}_{nn}(F_s\mathbf{D}_{n\Omega} + \lambda_D F_s\mathbf{A}_n + F_{s_z})]\}H_\alpha^k H_\beta^k dz_k. \quad (24)$$

The definitions given by Eqs. (12) and (13) can be introduced in the previous arrays in a similar to what done for the mixed case. For the sake of brevity the resulting formula are not given.

Equivalent Single-Layer Models. As in classical shell analysis, the assumed model Eq. (5) can also be written at a multilayered level,

$$\mathbf{u} = F_t\mathbf{u}_t + F_b\mathbf{u}_b + F_r\mathbf{u}_r = F_\tau\mathbf{u}_\tau$$
$$\boldsymbol{\sigma}_{nM} = F_t\boldsymbol{\sigma}_{nt} + F_b\boldsymbol{\sigma}_{nb} + F_r\boldsymbol{\sigma}_{nr} = F_\tau\boldsymbol{\sigma}_{n\tau}, \quad (25)$$

in which the functions F_τ are expressed in terms of the shell coordinate $\zeta = 2z/h$ and correspondent ESLM theories can be derived. The use of top and bottom values as variables is not mandatory for standard displacement formulation. Classical Taylor expansions are more convenient for this purpose. In such a case $F_t = 1$, $F_b = z$, $F_r = z^r$; $\mathbf{u}^t$ becomes the displacement vector of a shell point lying on Ω and $\mathbf{u}^b$, $\mathbf{u}^r$ their higher order derivatives.

By repeating what has been done for the layer-wise case, the governing equations are formally written in the same manner. In fact, it is sufficient to introduce the following multilayered 3×3 stiffness arrays:

$$(\mathbf{E}_{ij}^{\tau s}, \mathbf{E}_{\alpha ij}^{\tau s}, \mathbf{E}_{\beta ij}^{\tau s}, \mathbf{E}_{\alpha l\beta_{ij}}^{\tau s}, \mathbf{E}_{\beta l\alpha_{ij}}^{\tau s}, \mathbf{E}_{\alpha\beta_{ij}}^{\tau s})$$
$$= \sum_{k=1}^{N_l}\tilde{\mathbf{C}}_{ij}^k(J^{k\tau s}, J_\alpha^{k\tau s}, J_\beta^{k\tau s}, J_{\alpha l\beta}^{k\tau s}, J_{\beta l\alpha}^{k\tau s}, J_{\alpha\beta}^{k\tau s})$$

$$(\mathbf{E}_{ij}^{\tau z^s}, \mathbf{E}_{\alpha ij}^{\tau z^s}, \mathbf{E}_{\beta ij}^{\tau z^s}, \mathbf{E}_{\alpha\beta_{ij}}^{\tau z^s}) = \sum_{k=1}^{N_l}\tilde{\mathbf{C}}_{ij}^k(J^{k\tau z^s}, J_\alpha^{k\tau z^s}, J_{z\beta}^{k\tau z^s}, J_{\alpha\beta}^{k\tau z^s})$$

$$(\mathbf{E}_{ij}^{\tau s_z}, \mathbf{E}_{\alpha ij}^{\tau s_z}, \mathbf{E}_{\beta ij}^{\tau s_z}, \mathbf{E}_{\alpha\beta_{ij}}^{\tau s_z}) = \sum_{k=1}^{N_l}\tilde{\mathbf{C}}_{ij}^k(J^{k\tau s_z}, J_\alpha^{k\tau s_z}, J_\beta^{k\tau s_z}, J_{\alpha\beta}^{k\tau s_z})$$

$$(\mathbf{E}_{ij}^{\tau z^{s_z}}, \mathbf{E}_{\alpha\beta_{ij}}^{\tau z^{s_z}}) = \sum_{k=1}^{N_l}\tilde{\mathbf{C}}_{ij}^k(J^{k\tau z^{s_z}}, J_{\alpha\beta}^{k\tau z^{s_z}})$$

$$\mathbf{E}_\rho^{\tau s} = \sum_{k=1}^{N_l}\mathbf{I}\rho_k J_{\alpha\beta}^{k\tau s}. \quad (26)$$

They consist of a 3×3 array for each τ, s couple and they result in a four index array. The index coupled ij can assume the four expressions pp, pn, np, nn and are related to Hooke's law in Eq. (3). It is intended that both function F_τ, F_s and terms H_α^k and H_β^k in J^k-type integrals, have to be considered as functions of the whole shell coordinate z for ESLM cases.

Downloaded 04 May 2010 to 171.66.16.27. Redistribution subject to ASME license or copyright; see http://www.asme.org/terms/Terms_Use.cfm

M. Valentini
Department of Mechanical and Structural Engineering, Faculty of Engineering, University of Trento, Via Mesiano 77, 38050 Povo, Trento, Italy

S. K. Serkov
Department of Mathematics, University of Utah, Salt Lake City, UT 84112

D. Bigoni
Department of Mechanical and Structural Engineering, Faculty of Engineering, University of Trento, Via Mesiano 77, 38050 Povo, Trento, Italy

A. B. Movchan[1]
Department of Mathematical Sciences, University of Liverpool, Liverpool L69 3BX, UK

Crack Propagation in a Brittle Elastic Material With Defects

A two-dimensional asymptotic solution is presented for determination of the trajectory of a crack propagating in a brittle-elastic, isotropic medium containing small defects. Brittleness of the material is characterized by the assumption of the pure Mode I propagation criterion. The defects are described by Pólya-Szegö matrices, and examples for small elliptical cavities and circular inclusions are given. The results of the asymptotic analysis, which agree well with existing numerical solutions, give qualitative description of crack trajectories observed in brittle materials with defects, such as porous ceramics.

1 Introduction

The analysis of failure mechanisms of brittle-composite materials has design implications in a broad range of contexts. These include defects—containing, porous, and particulate, or fiber-reinforced materials. Examples of these materials are: structural and traditional ceramics, which may contain flaws or pores, fibrous biological materials, porous rocks, porous high-strength metals at low temperature and ceramic or metal composites. In other materials, like concrete or certain rocks, stiff inclusions co-exist in a soft matrix with pores and microcracks. In this context, fracture propagation is the dominant failure mechanism at the microscale.

It is obvious that fracture propagation is affected by the presence of inhomogeneities, which modify the crack trajectory and, consequently, the toughness of the material. For instance, the toughening effect of a diluted porosity remains controversial (see, e.g., Claussen, (1976) and Duan et al. (1995) where the porosity consists of small cracks). In fact, on one hand, pores may act as stress concentrators and initiate strain localization and microcracking between cavities. On the other hand, pores may deviate the crack path from linearity and, when the crack tip intersects a cavity, this may produce a stress release. From the latter point of view, pores yield a shielding effect on crack propagation.

The above discussion elucidates the theoretical and practical relevance of developing analytical models capable of describing the fracture mechanisms of brittle materials containing voids or inclusions. This problem, numerically analyzed by Rubinstein (1986) and Rose (1986), is the focus of the present paper. In particular, an asymptotic solution is presented for the determination of the trajectory of a crack growing in an elastic-brittle isotropic material, under generalized plane conditions. With the term "brittle" we mean a material in which the fracture propagates according to the pure Mode I criterion or "criterion of local symmetry," i.e., $K_{II} = 0$ (Banichuk, 1970; Goldstein and Salganik, 1974). Two perturbed solutions are employed, one of which concerns the modification of the near-tip fields due to a perturbation from rectilinearity in the crack trajectory. In the other perturbed solution, defects are introduced and the modification on the near-tip field is evaluated. The former analysis is similar to some extent to that presented by Cotterell and Rice (1980). The latter analysis was initiated by Movchan, Nazarov, and Polyakova (1991) and is based on the concept of the Pólya-Szegö (1951) matrix, which characterizes the effect of the inclusion.

The model described in this article makes possible to investigate the effects of a number of inclusions on the trajectory of a crack. It is assumed that the characteristic size of defects is small compared to the distance from the crack trajectory and no interaction takes place between the defects. Examples are presented where defects are described by circular elastic inclusions and elliptical voids. Results are shown to agree with those presented by Rubinstein (1986) and are qualitatively consistent with crack patterns in brittle materials.

2 Problem Formulation

2.1 Crack Geometry and Field Equations. A quasi-static semi-infinite plane crack is considered, smoothly curved in the portion extending from the tip to a reference point where the crack profile becomes rectilinear, as indicated in Fig. 1. With respect to a coordinate system having the origin in the reference point and the axis x_1 tangent to the rectilinear crack profile, the crack tip has abscissa l. If the curved portion of the crack is sufficiently regular and close to rectilinearity, it can be

[1] To whom correspondence should be addressed. e-mail: abm@liv.ac.uk.

Contributed by the Applied Mechanics Division of THE AMERICAN SOCIETY OF MECHANICAL ENGINEERS for publication in the ASME JOURNAL OF APPLIED MECHANICS.

Discussion on the paper should be addressed to the Technical Editor, Professor Lewis T. Wheeler, Department of Mechanical Engineering, University of Houston, Houston, TX 77204-4792, and will be accepted until four months after final publication of the paper itself in the ASME JOURNAL OF APPLIED MECHANICS.

Manuscript received by the ASME Applied Mechanics Division, July 29, 1996; final revision, Aug. 3, 1998. Associate Technical Editor: J. L. Bassani.

 Copyright © 1999 by ASME

Downloaded 04 May 2010 to 171.66.16.27. Redistribution subject to ASME license or copyright; see http://www.asme.org/terms/Terms_Use.cfm

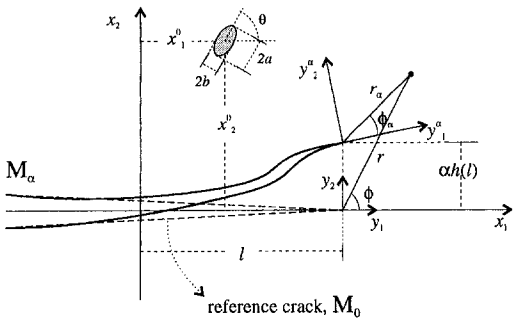

Fig. 1 Crack geometry

treated as *a perturbed straight crack.* In this case, the crack geometry can be specified by introducing a smooth function h of x_1, which, multiplied by a perturbation parameter α, specifies the x_2-coordinate of the curved portion of the crack. Therefore, the semi-infinite crack is described by the set $M_\alpha(l) := \{(x_1, x_2)\colon x_1 < l,\ x_2 = \alpha h(x_1)\}$, with $0 < \alpha \ll 1$. A defect is considered in the form of a cavity or an elastic inclusion, and is indicated by Ω_ϵ. The position of the defect is to some extent arbitrary, in the sense that it can be placed in an arbitrary point, but the ratio between the diameter of the defect and the minimal distance from crack trajectory has to be small enough to allow the use of a perturbation technique, that will be clarified in the following. It is therefore assumed that $\epsilon = \frac{1}{2}$ diam Ω_ϵ/dist $(\Omega_\epsilon, M_\alpha) \ll 1$.

The crack problem regards plane strain (or stress) deformation of linear elastic, isotropic materials, characterized by the Lamé constants λ, μ, for the matrix material, and λ_0, μ_0, for the inclusion.

Vectors $\mathbf{u}$ and $\mathbf{u}^{(0)}$, representing the displacement fields in the matrix and inside the defect, respectively, are required to satisfy the Lamé equations

$$\mathbf{Lu} := \mu\Delta\mathbf{u} + (\lambda + \mu)\nabla\nabla\cdot\mathbf{u} = \mathbf{0}, \qquad \mathbf{x} \in \mathbf{R}^2\backslash(\Omega_\epsilon \cup M_\alpha), \quad (1)$$

$$\mathbf{L}^{(0)}\mathbf{u}^{(0)} := \mu_0\Delta\mathbf{u}^{(0)} + (\lambda_0 + \mu_0)\nabla\nabla\cdot\mathbf{u}^{(0)} = \mathbf{0}, \qquad \mathbf{x} \in \Omega_\epsilon, \quad (2)$$

and the boundary conditions. These consist of the traction-free condition at the crack faces

$$\boldsymbol{\sigma}^{(\mathbf{n})}(\mathbf{u}; \mathbf{x}) = \mathbf{0}, \quad \mathbf{x} \in M_\alpha^{\pm}, \quad (3)$$

(where $\boldsymbol{\sigma}^{(\mathbf{n})}$ is the stress vector relative to the elementary area of unit normal $\mathbf{n}$) and of two interface conditions at the inclusion boundary

$$\boldsymbol{\sigma}^{(\mathbf{n})}(\mathbf{u}; \mathbf{x}) = \boldsymbol{\sigma}^{(\mathbf{n},0)}(\mathbf{u}^{(0)}; \mathbf{x}), \quad \mathbf{u} = \mathbf{u}^{(0)}, \quad \mathbf{x} \in \partial\Omega_\epsilon. \quad (4)$$

In the case of a cavity, conditions (4) are replaced by the traction boundary condition

$$\boldsymbol{\sigma}^{(\mathbf{n})}(\mathbf{u}; \mathbf{x}) = \mathbf{0}, \quad \mathbf{x} \in \partial\Omega_\epsilon. \quad (5)$$

When the distance r from the crack tip tends to infinite, the displacement field is supposed to have the following asymptotic form:

$$\mathbf{u}(\mathbf{x}) \sim K_I^\infty r^{1/2}\boldsymbol{\Phi}^I(\phi), \quad \text{as} \quad r \to \infty, \quad (6)$$

where the stress intensity factor K_I^∞ is given, and the polar components of the vector function $\boldsymbol{\Phi}^I = (\Phi_r^I, \Phi_\phi^I)^t$ are specified by

$$\Phi_r^I(\phi) = \frac{1}{4\mu\sqrt{2\pi}}\left[(2\kappa - 1)\cos\frac{\phi}{2} - \cos\frac{3\phi}{2}\right],$$

$$\Phi_\phi^I(\phi) = \frac{1}{4\mu\sqrt{2\pi}}\left[\sin\frac{3\phi}{2} - (2\kappa + 1)\sin\frac{\phi}{2}\right], \quad (7)$$

where $\kappa = (\lambda + 3\mu)(\lambda + \mu)^{-1}$ for plane strain and $\kappa = (5\lambda + 6\mu)(3\lambda + 2\mu)^{-1}$ for plane stress.

2.2 Unperturbed Crack. The perturbation introduced by a defect on the near-tip crack fields is considered for a rectilinear crack M_0 (note that $\alpha = 0$ has been considered). For this problem, following Movchan et al. (1991) and Movchan and Movchan (1995) the displacement field *near the crack tip* can be represented as

$$\mathbf{u}(\mathbf{x}) \sim \mathbf{v}(\mathbf{x}) + \epsilon^2\mathbf{w}(\mathbf{x}), \quad (8)$$

where $\mathbf{v}(\mathbf{x}) = K_I r^{1/2}\boldsymbol{\Phi}^I(\phi)$ is the displacement field corresponding to a rectilinear crack in a plane without inclusion, and $\epsilon^2\mathbf{w}$ represents the correction term associated with the perturbation field produced by the small defect Ω_ϵ. The reason why the corrective term is second order in ϵ can be appreciated by considering the Neumann boundary value problem of a homogeneous elastic isotropic solid containing a defect (Movchan and Movchan, 1995, Section 1.3). The vector field $\mathbf{w}$ satisfies

$$\mathbf{Lw}(\mathbf{x}) = -\sum_{j,k=1}^{3}[(\mathbf{V}_{(\partial/\partial\mathbf{x})}^{(j)})^t\mathbf{v}(\mathbf{x})]_{\mathbf{x}=\mathbf{x}^0}\mathcal{P}_{jk}\mathbf{V}_{(\partial/\partial\mathbf{x})}^{(k)}\delta(\mathbf{x} - \mathbf{x}^0), \qquad \mathbf{x} \in R^2\backslash M_0, \quad (9)$$

(where $\mathbf{x}^0$ is the centre of the defect, and δ the Dirac function) and the homogeneous traction boundary conditions on the crack faces

$$\boldsymbol{\sigma}^{(\mathbf{n})}(\mathbf{w}; \mathbf{x}) = \mathbf{0}, \quad \mathbf{x} \in M_0^{\pm}. \quad (10)$$

In Eq. (9) $\mathcal{P}_{jk}$ are components of the Pólya-Szegö matrix of the defect and vectors $\mathbf{V}_{(\partial/\partial\mathbf{x})}^{(j)}$ are defined as

$$\mathbf{V}_{(\partial/\partial\mathbf{x})}^{(1)} := \begin{pmatrix} \dfrac{\partial}{\partial x_1} \\ 0 \end{pmatrix}, \quad \mathbf{V}_{(\partial/\partial\mathbf{x})}^{(2)} := \begin{pmatrix} 0 \\ \dfrac{\partial}{\partial x_2} \end{pmatrix},$$

$$\mathbf{V}_{(\partial/\partial\mathbf{x})}^{(3)} := \frac{1}{\sqrt{2}}\begin{pmatrix} \dfrac{\partial}{\partial x_2} \\ \dfrac{\partial}{\partial x_1} \end{pmatrix}. \quad (11)$$

Detailed discussion related to the structure of the matrix $\mathcal{P}$ will be given in Section 3.

2.3 Perturbation of the Crack Trajectory. We are now in a position to investigate the main problem, namely, perturbation of the crack trajectory induced by the presence of a defect. In the absence of defects, the crack would propagate rectilinearly under Mode I loading, a condition which trivially satisfies the criterion $K_{II} = 0$. The presence of a defect, even small, produces a perturbation in terms of a smooth deflection from linearity of crack trajectory.

Let us consider the asymptotic expansion of the displacement field near the tip of perturbed crack M_α. A local system of coordinates $\mathbf{y}^\alpha$ can be introduced, which has the origin centered in the tip of the perturbed crack (i.e., in the point of coordinates $(l, \alpha h(l))$) and axis y_1^α tangent to the crack trajectory at the crack tip (Fig. 1):

Downloaded 04 May 2010 to 171.66.16.27. Redistribution subject to ASME license or copyright; see http://www.asme.org/terms/Terms_Use.cfm

$$\mathbf{y}^{\alpha} = \begin{pmatrix} 1 & \alpha h'(l) \\ -\alpha h'(l) & 1 \end{pmatrix} \mathbf{y} - \begin{pmatrix} 0 \\ \alpha h(l) \end{pmatrix}, \qquad (12)$$

where $\mathbf{y}$ is a system of coordinates translated with respect to $\mathbf{x}$, in particular, $\mathbf{y} = (y_1, y_2) = (x_1 - l, x_2)$.

In the polar coordinate system $\mathbf{y}^{\alpha}$ (Fig. 1), the asymptotic expansion of the displacement vector $\mathbf{u}$, relative to the perturbed crack, can be represented as follows:

$$\mathbf{u}(\mathbf{y}^{\alpha}) \sim \sum_{j=I,II} r_{\alpha}^{1/2} K_j(\alpha) \boldsymbol{\Phi}^{(j)}(\phi_{\alpha}),$$

$$K_j(\alpha) \sim K_j(l) + \alpha K_j'(l), \qquad (13)$$

where quantities evaluated in l are referred to the unperturbed problem, so that $K_{II}(l) = 0$ by definition.

Moreover, displacement $\mathbf{u}(\mathbf{y}^{\alpha})$ may be represented in the system $\mathbf{y}$ through a rotation, i.e.,

$$\mathbf{u}(\mathbf{y}, \alpha) = \begin{pmatrix} 1 & -\alpha h'(l) \\ \alpha h'(l) & 1 \end{pmatrix} \mathbf{u}(\mathbf{y}^{\alpha}), \qquad (14)$$

and, a Taylor series expansion of (14) can be performed near $\alpha = 0$:

$$\mathbf{u}(\mathbf{y}, \alpha) = \mathbf{u}(\mathbf{y}, 0) + \alpha \left.\frac{\partial \mathbf{u}(\mathbf{y}, \alpha)}{\partial \alpha}\right|_{\alpha=0} + O(\alpha^2). \qquad (15)$$

Therefore, using Eqs. (13), (14), Eq. (15) becomes

$$\mathbf{u}(\mathbf{y}, \alpha) = \mathbf{u}(\mathbf{y}, 0) + \alpha \left\{ \begin{pmatrix} 0 & -h'(l) \\ h'(l) & 0 \end{pmatrix} \mathbf{v}(\mathbf{y}) + \left.\frac{\partial \mathbf{u}}{\partial y_1^{\alpha}} \frac{\partial y_1^{\alpha}}{\partial \alpha}\right|_{\alpha=0} + \left.\frac{\partial \mathbf{u}}{\partial y_2^{\alpha}} \frac{\partial y_2^{\alpha}}{\partial \alpha}\right|_{\alpha=0} + \left.\frac{\partial \mathbf{u}}{\partial K_I(\alpha)} \frac{\partial K_I(\alpha)}{\partial \alpha}\right|_{\alpha=0} + \left.\frac{\partial \mathbf{u}}{\partial K_{II}(\alpha)} \frac{\partial K_{II}(\alpha)}{\partial \alpha}\right|_{\alpha=0} \right\} + O(\alpha^2), \qquad (16)$$

where $\mathbf{v}(\mathbf{y})$ is the same of Eq. (8).

The coefficient of the term multiplying α in Eq. (16) can be written as

$$\mathbf{u}'(\mathbf{y}) := -\frac{1+\kappa}{4\mu} h(l) K_I(l) r^{-1/2} \boldsymbol{\Psi}^{II}(\phi) + K_I'(l) r^{1/2} \boldsymbol{\Phi}^{I}(\phi) + \left[K_{II}'(l) - \frac{1}{2} K_I(l) h'(l) \right] r^{1/2} \boldsymbol{\Phi}^{II}(\phi), \qquad (17)$$

where the components of the vector function $\boldsymbol{\Phi}^{I}$ are given by (7) and

$$\Phi_r^{II}(\phi) = \frac{1}{4\mu\sqrt{2\pi}} \left[(1 - 2\kappa) \sin\frac{\phi}{2} + 3 \sin\frac{3\phi}{2} \right],$$

$$\Phi_{\phi}^{II}(\phi) = \frac{1}{4\mu\sqrt{2\pi}} \left[3 \cos\frac{3\phi}{2} - (1 + 2\kappa) \cos\frac{\phi}{2} \right],$$

$$\Psi_r^{II}(\phi) = \frac{1}{\sqrt{8\pi}(1+\kappa)} \left[(1 + 2\kappa) \sin\frac{3\phi}{2} - \sin\frac{\phi}{2} \right],$$

$$\Psi_{\phi}^{II}(\phi) = \frac{1}{\sqrt{8\pi}(1+\kappa)} \left[(2\kappa - 1) \cos\frac{3\phi}{2} - \cos\frac{\phi}{2} \right]. \qquad (18)$$

The stress components associated with (17) exhibit an unphysical strong singularity, and this fact indicates the presence of the boundary layer in the vicinity of the crack tip. This singularity may be eliminated in the way exposed in the following. First, let us introduce the weight function

$$\boldsymbol{\zeta}^{II}(\mathbf{y}) := r^{-1/2} \boldsymbol{\Psi}^{II}(\phi), \qquad (19)$$

and therefore define

$$\mathbf{w}^*(\mathbf{y}) := \mathbf{u}'(\mathbf{y}) + \frac{1+\kappa}{4\mu} h(l) K_I(l) \boldsymbol{\zeta}^{II}(\mathbf{y}), \qquad (20)$$

which satisfies the Lamé system (1) and the same boundary conditions on $M_0^{\pm}$ as $\mathbf{u}'$, but does not have a singularity at the crack tip $(l, 0)$.

Let us consider the ring $\Xi_R = \{\mathbf{y}: (1/R) \leq \|\mathbf{y}\| \leq R\}$, surrounding the reference crack tip, and the integral

$$\int_{\Xi_R \setminus M_0} [\boldsymbol{\zeta}^{II}(\mathbf{y}) \cdot \mathbf{L}\mathbf{u}(\mathbf{y}) - \mathbf{u}(\mathbf{y}) \cdot \mathbf{L}\boldsymbol{\zeta}^{II}(\mathbf{y})] dy. \qquad (21)$$

If the defect is far enough from the reference crack tip, representation (8) holds and therefore

$$\int_{\Xi_R \setminus M_0} [\boldsymbol{\zeta}^{II}(\mathbf{y}) \cdot \mathbf{L}\mathbf{u}(\mathbf{y}) - \mathbf{u}(\mathbf{y}) \cdot \mathbf{L}\boldsymbol{\zeta}^{II}(\mathbf{y})] d\mathbf{y} = -\epsilon^2 \int_{\Xi_R \setminus M_0} [\boldsymbol{\zeta}^{II} \sum_{j,k=1}^{3} [(\mathbf{V}_{(\partial/\partial \mathbf{y})}^{(j)})^t \mathbf{v}]_{\mathbf{y}=\mathbf{y}^0} \mathcal{P}_{jk} \mathbf{V}_{(\partial/\partial \mathbf{y})}^{(k)}] \times \delta(\mathbf{y} - \mathbf{y}_0) d\mathbf{y} = \epsilon^2 \sum_{j,k=1}^{3} \mathcal{P}_{jk} \mathcal{F}_{jk}(\mathbf{v}, \boldsymbol{\zeta}^{II}; \mathbf{y}^0), \qquad (22)$$

where

$$\mathcal{F}_{jk}(\mathbf{v}, \boldsymbol{\zeta}^{II}; \mathbf{y}^0) := (\mathbf{V}_{(\partial/\partial \mathbf{y})}^{(j)})^t \mathbf{v}(\mathbf{y}^0) \mathbf{V}_{(\partial/\partial \mathbf{y})}^{(k)} \boldsymbol{\zeta}^{II}(\mathbf{y}^0). \qquad (23)$$

If we reconsider integral (21), apply the Betti formula, and take the limit when R tends to infinity, we obtain

$$\lim_{R\to\infty} \int_{\Xi_R \setminus M_0} [\boldsymbol{\zeta}^{II}(\mathbf{y}) \cdot \mathbf{L}\mathbf{u}(\mathbf{y}) - \mathbf{u}(\mathbf{y}) \cdot \mathbf{L}\boldsymbol{\zeta}^{II}(\mathbf{y})] dy = \lim_{R\to\infty} \left\{ \int_{C_1} [\zeta_r^{II} \sigma_{rr}(\mathbf{u}) + \zeta_{\phi}^{II} \sigma_{r\phi}(\mathbf{u}) - u_r \sigma_{rr}(\boldsymbol{\zeta}^{II}) - u_{\phi} \sigma_{r\phi}(\boldsymbol{\zeta}^{II})] ds - \int_{C_2} [\zeta_r^{II} \sigma_{rr}(\mathbf{u}(\mathbf{y}, 0) + \alpha \mathbf{w}_r^*(\mathbf{y})) + \zeta_{\phi}^{II} \sigma_{r\phi}(\mathbf{u}(\mathbf{y}, 0) + \alpha \mathbf{w}_r^*(\mathbf{y})) - (u_r(\mathbf{y}, 0) + \alpha w_r^*(\mathbf{y})) \sigma_{rr}(\boldsymbol{\zeta}^{II}) - (u_{\phi}(\mathbf{y}, 0) + \alpha w_{\phi}^*(\mathbf{y})) \sigma_{r\phi}(\boldsymbol{\zeta}^{II})] ds + \sum_{\pm} \int_{M_0} [\zeta_1^{II} \sigma_{12}(\mathbf{u}) + \zeta_2^{II} \sigma_{22}(\mathbf{u}) - u_1 \sigma_{12}(\boldsymbol{\zeta}^{II}) - u_2 \sigma_{22}(\boldsymbol{\zeta}^{II})] ds \right\} = 0 + \alpha \{ \tfrac{1}{2} h'(l) K_I(l) - K_{II}'(l) \} + 0, \qquad (24)$$

where $C_1(R) = \{\mathbf{y}: \|\mathbf{y}\| = R\}$ and $C_2 = \{\mathbf{y}: \|\mathbf{y}\| = 1/R\}$.

Note that in the integral along C_1, the field $\mathbf{u}$ corresponds to (6), whereas in the integral along C_2 the approximation (17), regularized via the weight function, is used. Finally, the integral along M_0 is null because of the traction free boundary conditions. Matching (24) with (22) it is concluded that $\alpha = \epsilon^2$, and the derivative of K_{II} is evaluated in the form

$$K_{II}'(l) = K_I(l) [\tfrac{1}{2} h'(l) - \sum_{j,k=1}^{3} \mathcal{P}_{jk} \mathcal{F}_{jk}(r^{-1/2} \boldsymbol{\Psi}^{II}, r^{1/2} \boldsymbol{\Phi}^{I}; \mathbf{y}^0)]. \qquad (25)$$

Note that if the crack remains straight, i.e., if $h = 0$, relation (25) can be used to compare the present asymptotic solution

Downloaded 04 May 2010 to 171.66.16.27. Redistribution subject to ASME license or copyright; see http://www.asme.org/terms/Terms_Use.cfm

to the numerical results of Rubinstein (1986) referred to the influence of defects on the near-tip fields of a rectilinear crack.

If the pure Mode I criterion of fracture is adopted, the orientation of the crack has to be chosen in such a way that $K_{II}(\alpha) = 0$, and therefore

$$K_{II}(\alpha) \sim \alpha K'_{II}(l) = 0, \tag{26}$$

which can be substituted into Eq. (25) to get

$$h'(l) = 2 \sum_{j,k=1}^{3} \mathcal{P}_{jk}\mathcal{F}_{jk}(r^{-1/2}\Psi^{II}, r^{1/2}\Phi^{I}; \mathbf{y}^0). \tag{27}$$

Equation (27) can be easily integrated[2] to obtain the solution for the crack deflection function in the case when the center of the inclusion is placed at the generic point (x_1^0, x_2^0):

$$h(l) = \frac{4\mu}{x_2^0(\kappa + 1)} \{\cos\phi \mathcal{L}^t(\phi)\mathcal{P}\mathcal{L}(\phi) - \mathcal{L}^t(0)\mathcal{P}\mathcal{L}(0)\}, \tag{28}$$

where $\cos\phi = (x_1^0 - l)[(x_2^0)^2 + (x_1^0 - l)^2]^{-1/2}$, and[3]

$$\mathcal{L}(\phi) = \begin{pmatrix} \frac{1}{4\mu\sqrt{2\pi}} \cos\frac{\phi}{2}\left[\kappa - 1 - 2\sin\frac{\phi}{2}\sin\frac{3\phi}{2}\right] \\ \frac{1}{4\mu\sqrt{2\pi}} \cos\frac{\phi}{2}\left[\kappa - 1 + 2\sin\frac{\phi}{2}\sin\frac{3\phi}{2}\right] \\ \frac{1}{4\mu\sqrt{\pi}} \sin\phi\cos\frac{3\phi}{2} \end{pmatrix}. \tag{29}$$

It may be important to remark that the problem of the interaction of a crack with more than one defect can be solved in a straightforward way in the present framework, when it is assumed that defects do not interact. In particular, when a number of defects is considered, their effect consists in a modification of Eq. (8), where the sum of the perturbative terms relative to all defects replaces the single term $\epsilon^2\mathbf{w}$.

3 The Pólya-Szegö Matrices

The Pólya-Szegö matrix $\mathcal{P}$ characterizes the morphology of the inclusion and its elastic properties. The properties of the dipole tensors for boundary value problems related to the Laplacian were given by Pólya and Szegö (1951). For problems of elasticity, the dipole tensors were analyzed by Zorin et al. (1988), Babich et al. (1989), Movchan (1992), and Movchan and Serkov (1991). In this section we briefly discuss the definitions and give explicit representation for the dipole matrices corresponding to circular inclusions and elliptical cavities.

Definitions. Let us go back to the problem of an infinite plane with a finite inclusion or cavity Ω_ϵ, presented in Section 2.2. In that section, the unperturbed, i.e., without defect solution was identified with the solution corresponding to a static rectilinear crack in a plane. In the case of a plane with a defect, the solution can be represented as a linear combination of the vectors $\mathbf{U}^{(j)}$ $(j = 1, 2, 3)$, satisfying the homogeneous Lamé system and admitting the representation

$$\mathbf{U}^{(j)}(\mathbf{x}) = \mathbf{V}_{\mathbf{x}}^{(j)} + \mathbf{W}^{(j)}(\mathbf{x}), \tag{30}$$

where

$$\mathbf{V}_{\mathbf{x}}^{(1)} = (x_1, 0)', \quad \mathbf{V}_{\mathbf{x}}^{(2)} = (0, x_2)',$$

$$\mathbf{V}_{\mathbf{x}}^{(3)} = 2^{-1/2}(x_2, x_1)', \tag{31}$$

and the vector field $\mathbf{W}^{(j)}$, decaying at infinity, can be expressed as

$$\mathbf{W}^{(j)} = \sum_{k=1}^{3} \mathcal{P}_{jk}[\mathbf{V}_{(\partial/\partial\mathbf{x})}^{(k)}]'\mathbf{T}(\mathbf{x}) + O(|\mathbf{x}|^{-2}). \tag{32}$$

Apart from factor ϵ^2 which is now included in $\mathcal{P}$, this matrix is the Polya-Szegö matrix defined in Section 2.2, whereas $\mathbf{T}$ is the Kelvin-Somigliana matrix (Fichera, 1972) defined as

$$\mathbf{T}(\mathbf{x}) = \frac{\lambda + \mu}{8\pi\mu(\lambda + 2\mu)} \begin{pmatrix} -2\kappa \ln\sqrt{x_1^2 + x_2^2} + \frac{2x_1^2}{x_1^2 + x_2^2} & \frac{2x_1x_2}{x_1^2 + x_2^2} \\ \frac{2x_1x_2}{x_1^2 + x_2^2} & -2\kappa \ln\sqrt{x_1^2 + x_2^2} + \frac{2x_2^2}{x_1^2 + x_2^2} \end{pmatrix}. \tag{33}$$

A Circular Inclusion. In the case of an elastic circular inclusion of radius R, having Lamé constants λ_0, μ_0, the outside-inclusion displacement field $\mathbf{u} = (u_1, u_2)$ can be represented, via complex Kolosov-Muskhelishvili (1953) potentials $\varphi(z)$ and $\psi(z)$, as

$$u_1 + iu_2 = (2\mu)^{-1}[\kappa\varphi(z) - z\overline{\varphi'(z)} - \overline{\psi(z)}], \tag{34}$$

where

$$\varphi(z) = \alpha z + \frac{\bar{\gamma}R^2}{z}\frac{\mu_0 - \mu}{\kappa\mu_0 + \mu},$$

$$\psi(z) = \gamma z + \frac{\mathrm{Re}\,(\alpha)R^2}{z}\frac{2\mu_0(\kappa - 1) - 2\mu(\kappa_0 - 1)}{\mu(\kappa_0 - 1) + 2\mu_0} + \frac{\bar{\gamma}R^4}{z^3}\frac{\mu_0 - \mu}{\kappa\mu_0 + \mu}. \tag{35}$$

Constants α and γ in Eq. (35) can be determined from the conditions at infinity. In particular, when the displacement field behaves like $\mathbf{V}_{\mathbf{x}}^{(j)}$ + smaller terms, as $\|\mathbf{x}\| \to \infty$, it can be shown that

[2] The following auxiliary identity may be helpful in the integration

$$\zeta^{II} = \frac{4\mu}{\kappa + 1}\frac{\partial(r^{1/2}\Phi^I)}{\partial y_2}.$$

[3] It may be noted that Cartesian components of the vector $\mathcal{L}$ are given by

$$\mathcal{L}_k = r^{1/2}((\mathbf{V}_{(\partial/\partial\mathbf{y})}^{(k)})'(r^{1/2}\Phi^I(\phi)))_{\mathbf{y}=\mathbf{y}^0}.$$

Downloaded 04 May 2010 to 171.66.16.27. Redistribution subject to ASME license or copyright; see http://www.asme.org/terms/Terms_Use.cfm

$$\alpha = \frac{\mu}{\kappa - 1}, \quad \gamma = -\mu, \quad \text{for} \quad j = 1,$$

$$\alpha = \frac{\mu}{\kappa - 1}, \quad \gamma = \mu, \quad \text{for} \quad j = 2,$$

$$\alpha = 0, \quad \gamma = i\mu\sqrt{2}, \quad \text{for} \quad j = 3. \tag{36}$$

In addition to representation (34), the displacement field at infinity can be represented as a linear combination of vectors $\mathbf{U}^{(j)}$ (30), plus smaller terms. The asymptotic expression (32) for the field $\mathbf{W}^{(j)}$ can be rewritten via the complex variable $z = x_1 + ix_2$ in the form

$$W_1^{(j)} + iW_2^{(j)} = \mathcal{P}_{j1}\left(\frac{\partial}{\partial z}[T_{11} + iT_{12}] + \frac{\partial}{\partial \bar{z}}[T_{11} + iT_{12}]\right)$$

$$+ \mathcal{P}_{j2}\left(\frac{\partial}{\partial z}[-T_{22} + iT_{12}] + \left(\frac{\partial}{\partial \bar{z}}[T_{22} - iT_{12}]\right)\right.$$

$$+ \frac{1}{\sqrt{2}}\mathcal{P}_{j3}\left(\frac{\partial}{\partial z}[iT_{11} + iT_{22}]\right.$$

$$\left.\left. + \left(\frac{\partial}{\partial \bar{z}}[2T_{12} + i(T_{22} - T_{11})]\right)\right) + O\left(\frac{1}{|z|^2}\right), \tag{37}$$

where

$$\mathbf{T} = \frac{\lambda + \mu}{8\pi\mu(\lambda + 2\mu)}\begin{pmatrix} -2\kappa \ln|z| + \dfrac{z^2 + \bar{z}^2 + 2z\bar{z}}{2z\bar{z}} & \dfrac{z^2 - \bar{z}^2}{2iz\bar{z}} \\ \dfrac{z^2 - \bar{z}^2}{2iz\bar{z}} & -2\kappa \ln|z| - \dfrac{z^2 + \bar{z}^2 - 2z\bar{z}}{2z\bar{z}} \end{pmatrix}, \tag{38}$$

is the complex variable representation of the Kelvin-Somigliana matrix.

Comparing relations (34) and (37), it is concluded that the Pólya-Szegö matrix for the given elastic circular inclusion can be expressed in the form

$$\mathcal{P} = \frac{R^2}{4q}\begin{pmatrix} \Xi + \Theta & \Xi - \Theta & 0 \\ \Xi - \Theta & \Xi + \Theta & 0 \\ 0 & 0 & 2\Theta \end{pmatrix}, \tag{39}$$

where

$$q = \frac{\lambda + \mu}{8\pi\mu(\lambda + 2\mu)}, \quad \Theta = \frac{\mu_0 - \mu}{\kappa\mu_0 + \mu},$$

$$\Xi = \frac{1}{(\kappa - 1)^2}\frac{2\mu_0(\kappa - 1) - 2\mu(\kappa_0 - 1)}{\mu(\kappa_0 - 1) + 2\mu_0}. \tag{40}$$

An Elliptical Cavity. In the case of an elliptical cavity in an isotropic elastic plane, we denote with a and b the large and small semi-axes of ellipse, respectively, and with θ the angle between the x_1-axis and the largest axis of the ellipse. The conformal mapping of the exterior of the unit disk into the exterior of the elliptical cavity can be given as

$$\omega(\xi) = \frac{a + b}{2}\left(\xi + m\frac{e^{2i\theta}}{\xi}\right), \quad m = \frac{a - b}{a + b}, \tag{41}$$

and therefore, the solution $\mathbf{u}$, expressed via complex potentials, becomes

$$u_1 + iu_2 = (2\mu)^{-1}\left[\kappa\varphi(\xi) - \frac{\omega(\xi)}{\overline{\omega'(\xi)}}\overline{\varphi'(\xi)} - \overline{\psi(\xi)}\right]. \tag{42}$$

Taking into account the condition at infinity and the traction-free boundary condition at the cavity boundary, the Pólya-Szegö matrix can be obtained in the following form (Movchan[4], 1992):

$$\mathcal{P} = -\frac{1}{4\mu}(a + b)^2\pi(\lambda + 2\mu) \times \begin{pmatrix} \Xi + \Theta + \Sigma & \Xi - \Theta & \Lambda \\ \Xi - \Theta & \Xi + \Theta - \Sigma & \Lambda \\ \Lambda & \Lambda & 2\Theta \end{pmatrix}, \tag{43}$$

where

$$\Theta = \frac{2\mu^2}{\lambda + \mu}, \quad \Xi = (\lambda + \mu)(1 + m^2),$$

$$\Sigma = -4\mu m \cos 2\theta, \quad \Lambda = -2\sqrt{2}\mu m \sin 2\theta. \tag{44}$$

4 Interaction Between a Semi-infinite Crack and a Cavity

As a first application of the presented theory, we consider the case of interaction of a semi-infinite crack and an elliptical cavity Ω_ϵ with the largest axis inclined at the angle θ to the x_1-axis. The center of the ellipse is located at (x_1^0, x_2^0). Substituting (43) into (28) we obtain

$$H(l) = \epsilon^2 h(l) = \frac{R^2}{2x_2^0}[2(1 + m^2) - z(2 + z - z^2 + m^2(1 + z) + 2m\cos 2\theta(1 + 2z)(1 - z^2) - 2m \sin 2\theta(2z - 1)(1 + z)\sqrt{1 - z^2})], \tag{45}$$

where

$$z = \frac{-l + x_1^0}{\sqrt{(x_2^0)^2 + (-l + x_1^0)^2}}, \quad R = \frac{a + b}{2}.$$

It should be noted that conditions $m = 0$ and $m = 1$ correspond to the relevant cases of a circular void and of a Griffith crack, respectively.

The crack trajectories $h(l)$, as obtained from (45), are reported in Fig. 2. In particular, the crack trajectory is plotted in Fig. 2(a) resulting from the interaction of a semi-infinite crack with an ellipse having the major axis parallel to x_1 and center at (0, 1). Different aspect ratio are investigated. Figure 2(b) pertains to the case of a semi-infinite crack interacting with a Griffith crack inclined at different angles.

It should be noted that in the case of a circular cavity, $m = 0$, $H(l)$ takes positive values for every l. Therefore, a circular cavity always "attracts" a crack. In the case of an elliptical void, the situation is more complicated. In fact the trajectory of the crack is influenced by the orientation of the ellipse and

[4] Note that in the formula analogous to (43) of the paper by Movchan (1992), the $\sqrt{2}$ factor was missed in the term Λ.

Downloaded 04 May 2010 to 171.66.16.27. Redistribution subject to ASME license or copyright; see http://www.asme.org/terms/Terms_Use.cfm

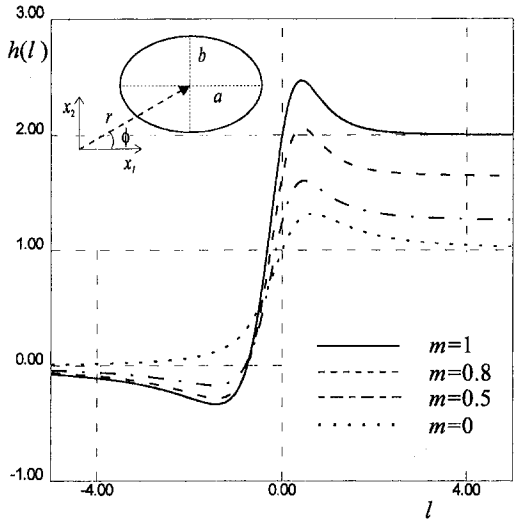

Fig. 2(*a*) Elliptic cavity, with major axis parallel to the main crack. Results reported for different aspect ratios.

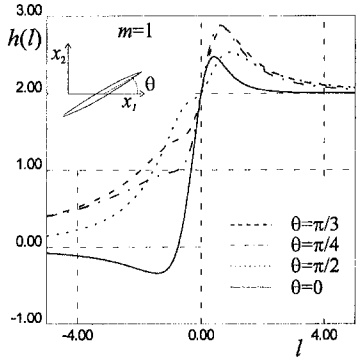

Fig. 2(*b*) Griffith crack at different inclinations

Fig. 2 Crack trajectory $h(l)$ versus crack-tip position l, resulting from interaction with a cavity

by the aspect ratio a/b. In particular, the crack may suffer a slight repulsion, followed by a strong attraction (so that curves relative to Fig. 2(a) have a minimum followed by a maximum). In any case, the deflection at infinity always corresponds to attraction. This can be verified by observing that the limit $l \to +\infty$ of (28)

$$H_\infty = -\frac{\epsilon^2 4\mu}{\kappa + 1}\,[\mathcal{L}(0)\mathcal{P}\mathcal{L}(0)] = \frac{R^2}{x_2^0}(1 + m^2), \quad (46)$$

is always positive, the dipole matrix $\mathcal{P}$ being negative definite for any cavity of finite dimension. Moreover, H_∞ increases when parameter m increases (Fig. 2(a)). This means that the deflection due to interaction with a thin ellipse is greater than the deflection produced by a circular cavity with diameter equal to the crack length.

Note from Fig. 2(b), that for any orientation of the Griffith crack, all crack trajectories intersect at the point corresponding to $l = 0$. Moreover, $H(0) = H_\infty$ and therefore the crack deflection at infinity is independent of the orientation of the small defect. However, the change of the angle θ affects the shape of the crack trajectory in the vicinity of the origin.

A SEM photograph is reported in Fig. 3(a) of a crack path induced by Vicker indenter in a sample of porcelain stoneware. This particular ceramic contains a dilute concentration of near-ellipsoidal voids. These voids have been modeled as ellipses in Fig. 3(b), where the crack trajectory has been obtained using the solution developed above. Obviously, certain approximations of the model may be anticipated. In particular, interactions between voids has been neglected; moreover, the assumption of small ratio between void dimension and distance from the crack tip is often forced. Perhaps more important, the model refers to a situation of plane strain, whereas the physical problem may be three-dimensional. However, we note from Fig. 3 that, in spite of all the approximations, the mathematical model gives an excellent description of the physical situation.

In closure of this section, a comparison is presented of the theory developed in this article to numerical solution of the singular integral equation for the complex crack opening given by Rubinstein (1986). To this purpose, $h'(l) = 0$ is considered in Eq. (25), which gives the the normalised Mode II stress intensity factor in the case when the unperturbed state corresponds to the Mode I load (characterized by the stress infinity factor K_I^∞)

$$K_{II}/K_I^\infty \sim \frac{R^2}{r^2}\sum_{j,k=1}^{3} \mathcal{P}_{jk}\mathcal{F}_{jk}(r, \phi), \quad (47)$$

with (r, ϕ) being polar coordinates of a small defect.

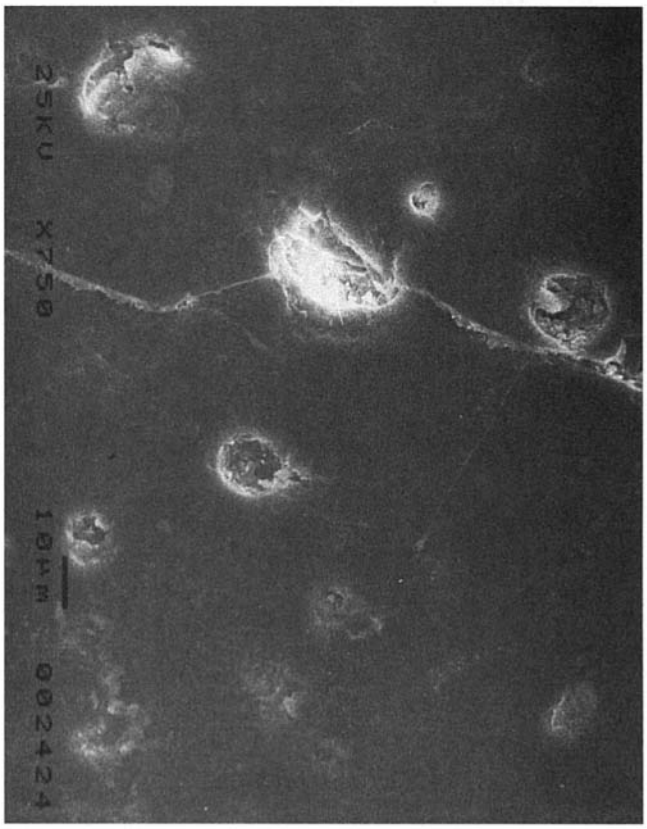

Fig. 3(*a*) SEM photograph of a crack in a porcelain stoneware

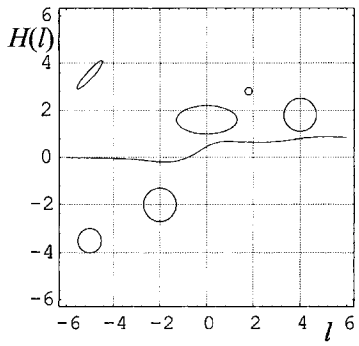

Fig. 3(*b*) Model prediction

Downloaded 04 May 2010 to 171.66.16.27. Redistribution subject to ASME license or copyright; see http://www.asme.org/terms/Terms_Use.cfm

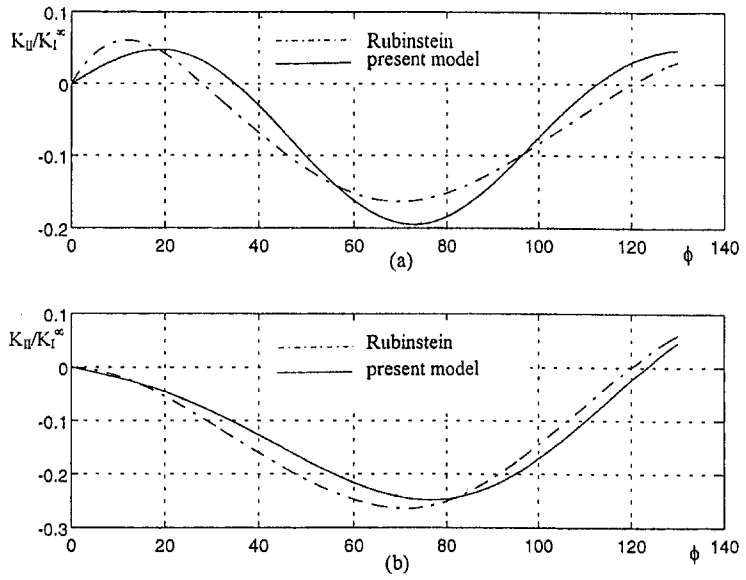

Fig. 4 Comparison with Rubinstein's results, Mode II normalized stress intensity factor versus defect position ϕ; (*a*) interaction with a Griffith crack, (*b*) interaction with a circular cavity

Comparison with Rubinstein's results is reported in Fig. 4(*a*) and (*b*), where the cases of a Griffith crack and a circular cavity are considered, respectively. Note that the Mode II normalised stress intensity factors are reported versus ϕ, the angle of orientation of the position vector relative to the small defect (Fig. 1). Obviously, since (47) is an approximate asymptotic formula, a discrepancy with the numerical results of Rubinstein can be expected. The error is however quite small and the results of explicit asymptotic analysis show the right qualitative behaviour of the stress intensity factor as a function of the angular variable ϕ.

5 Interaction Between a Semi-infinite Crack and a Circular Elastic Inclusion

In the case of a circular inclusion, the Pólya-Szegö matrix $\mathcal{P}$ is given by (39). Consequently, formula (28) gives

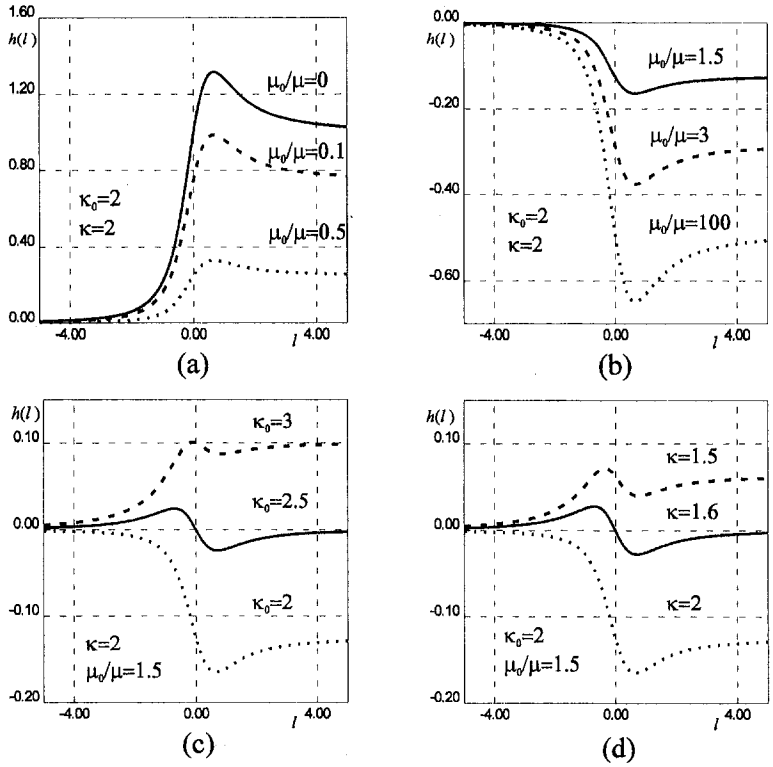

Fig. 5 Crack trajectory $h(l)$ versus crack-tip position l, resulting from interaction with an elastic circular inclusion; (*a*) inclusion more rigid than the matrix, (*b*) inclusion less rigid than the matrix, (*c*) and (*d*) cases in which $\mathcal{P}$ is indefinite.

Downloaded 04 May 2010 to 171.66.16.27. Redistribution subject to ASME license or copyright; see http://www.asme.org/terms/Terms_Use.cfm

$$H(l) = \epsilon^2 h(l)$$

$$= \frac{R^2}{2x_2^0}\left[(z^2 + z - 2)\frac{\mu_0(\kappa - 1) - \mu(\kappa_0 - 1)}{\mu(\kappa_0 - 1) + 2\mu_0} + (z - z^3)\frac{\mu_0 - \mu}{\kappa\mu_0 + \mu}\right], \quad (48)$$

where R is the radius of the inclusion and

$$z = \frac{-l + x_1^0}{\sqrt{(x_2^0)^2 + (-l + x_1^0)^2}}.$$

In the particular case when $\mu_0 = 0$, Eq. (48) reduces to Eq. (45) with $m = 0$, which corresponds to the case of a circular cavity. In plain strain, the Pólya-Szegö matrix $\mathcal{P}$ of a circular inclusion is positive definite when

$$\frac{\mu_0}{\mu} > 1 \quad \text{and} \quad \frac{\lambda_0 + \mu_0}{\lambda + \mu} > 1, \quad (49)$$

and is negative definite when the inequalities (49) are both reversed. Otherwise, the matrix $\mathcal{P}$ is indefinite.

The crack deflection at infinity is given by

$$H_\infty = \epsilon^2 h_\infty = \frac{R^2}{x_2^0}\left\{1 - \frac{\mu_0(\kappa + 1)}{2\mu_0 + (\kappa_0 - 1)\mu}\right\}. \quad (50)$$

Crack trajectories $h(l)$ relative to the interaction of a semi-infinite crack with an elastic circular inclusion centered at (0, 1) are reported in Fig. 5, for different values of elastic parameters. It can be noted that the defect tends to attract the crack in the case of an inclusion less rigid than the matrix (Fig. 5(a)), whereas in the opposite case of an inclusion more rigid than the matrix, the crack tends to be repelled by the defect (Fig. 5(b)). Figures 5(c) and (d) refer to cases in which matrix $\mathcal{P}$ is indefinite. Note in this case that a set of parameters can be chosen, for which the deflection at infinity is equal to zero.

6 Conclusions

Application of perturbative techniques to the problem of fracture propagation in an elastic material has been shown to be relevant in obtaining approximate solutions of interaction of a semi-infinite crack with defects.

Accepting the hypotheses of noninteracting defects and small ratio between defect diameter and distance to the crack, an analytical solution for the crack trajectory has been presented. This solution gives qualitative information on crack path in brittle materials. In particular, inclusions less rigid than the matrix generally "attract" the crack, whereas an opposite effect is observed in the case of inclusions more rigid than the matrix. In conclusion, a model has been presented to obtain the shape of crack trajectory as influenced by number, position, form, and elastic constants of the defects.

Acknowledgments

The authors would like to thank Prof. J.R. Willis (Cambridge University) for helpful discussions and Dr. A. Tucci and Dr. L. Esposito (Ceramic Centre, Bologna) for assistance with the experiment. M. V. acknowledges the financial support of the TMR European fund (Contr. ERBCHRXCT930383) and is grateful to Bath University (School of Mathematical Sciences) for provision of computing facilities. D. B. and M. V. acknowledge the financial support of Italian MURST 60%.

References

Babich, V.M., Zorin, I.S., Ivanov, M.I., Movchan, A.B., and Nazarov, S.A., 1989, "Integral characteristics in problems of elasticity," *Steklov Mathematical Institute (LOMI)*, preprint P-6-89, Leningrad, (in Russian).

Banichuk, N.V., 1970, "Determination of the Form of a Curvilinear Crack by Small Parameter Technique," *Izv. An SSR, MTT 7*, Vol. 2, pp. 130–137 (in Russian).

Claussen, N., 1976, "Fracture toughness of Al_2O_3 with an unstabilized ZrO_2 dispersed phase," *J. Am. Ceram. Soc.*, Vol. 59, pp. 49–51.

Cotterell, B., and Rice, J.R., 1980, "Slightly curved or kinked cracks," *Int. Journal of Fracture*, Vol. 16, No. 2, pp. 155–169.

Duan, K., Mai, Y.W., and Cotterel, B., 1976, "On the paradox between crack bridging and crack interaction in quasi-brittle materials," *J. Europ. Ceram. Soc.*, Vol. 15, pp. 1061–1064.

Fichera, G., 1972, "Unilateral constraints in elasticity," *Handbuch der Physik*, Vol. VI a/2, S. Flügge, ed., Springer-Verlag, Berlin.

Goldstein, R.V., and Salganik, R.L., 1974, "Brittle fracture of solids with arbitrary cracks," *Int. J. Fracture*, Vol. 10, pp. 507–523.

Movchan, A.B., 1992, "Integral characteristics of elastic inclusions and cavities in the two-dimensional theory of elasticity," *Eur. J. Appl. Math.*, Vol. 3, pp. 21–30.

Movchan, A.B., Nazarov, S.A., and Polyakova, O.R., 1991, "The quasi-static growth of a semi-infinite crack in a plane containing small defects," *Comptes Rendus de L'Academie des Sciences. Paris, Série II*, Vol. 313, pp. 1223–1228.

Movchan, A.B., and Movchan, N.V., 1995, *Mathematical modelling of solids with non regular boundaries*, CRC Press, Boca Raton, FL.

Movchan, A.B., and Serkov, S.K., 1991, "Elastic polarisation matrices for polygonal domains," *Mech. Solids*, Vol. 26, No. 3, pp. 63–68.

Muskhelishvili, N.I., 1953, *Some basic problems of the mathematical theory of elasticity*, Noordhoff, Groningen.

Pólya, G., and Szegö, G., 1951, *Isoperimetric inequalities in mathematical physics*, Princeton, University Press, Princeton, NJ.

Rose, L.R.F., 1986, "Microcrack interaction with a main crack," *Int. J. Fracture*, Vol. 31, pp. 233–242.

Rubinstein, A.A., 1986, "Macro-crack—Micro-defect Interaction," ASME JOURNAL OF APPLIED MECHANICS, Vol. 53, pp. 505–510.

Zorin, I.S., Movchan, A.B., and Nazarov, S.A., 1988, "The use of the elastic polarisation tensor in problems of crack mechanics," *USSR Izvestiya Mechanics of Solids*, Vol. 26, No. 6, pp. 128–134 (in Russian).

Downloaded 04 May 2010 to 171.66.16.27. Redistribution subject to ASME license or copyright; see http://www.asme.org/terms/Terms_Use.cfm

S. Chucheepsakul
Department of Civil Engineering,
King Mongkut's University of
Technology Thonburi,
Bangkok 10140, Thailand
Mem. ASME

C. M. Wang
Department of Civil Engineering

X. Q. He
Department of Mechanical and
Production Engineering

The National University of Singapore,
Kent Ridge 119260, Singapore

T. Monprapussorn
Department of Civil Engineering,
King Mongkut's University of
Technology Thonburi,
Bangkok 10140, Thailand

Double Curvature Bending of Variable-Arc-Length Elasticas

This paper deals with the double curvature bending of variable arc-length elasticas under two applied moments at fixed support locations. One end of the elastica is held while the other end portion of the elastica may slide freely on a frictionless support at a prescribed distance from the held end. Thus, the variable deformed length of the elastica between the end support and the frictionless support depends on the relative magnitude of the applied moments. To solve this difficult and highly nonlinear problem, two approaches have been used. In the first approach, the elliptic integrals are formulated based on the governing nonlinear equation of the problem. The pertinent equations obtained from applying the boundary conditions are then solved iteratively for solution. In the second approach, the shooting-optimization method is employed in which the set of governing differential equations is numerically integrated using the Runge-Kutta algorithm and the error norm of the terminal boundary conditions is minimized using a direct optimization technique. Both methods furnish almost the same stable and unstable equilibrium solutions. An interesting feature of this kind of bending problem is that the elastica can form a single loop or snap-back bending for some cases of the unstable equilibrium configuration.

1 Introduction

The class of elastica problems for which the equilibrium deformed arc-length between stationary supports is to be determined may be referred to as variable arc-length elastica problems. Early studies on variable arc-length elasticas include the work by Gospodnetic (1959) and Conway (1947) who obtained closed-form solutions for elasticas under a central point load while Schile and Sierakowski (1967) treated elasticas under two symmetrically located point loads. The variable arc-length of the elasticas studied by these early researchers arise from the fact that both end portions of the beams are allowed to slide on their rigid supports. More recently, Chucheepsakul et al. (1994, 1995, 1996, 1997a, b) and Wang et al. (1997) investigated the bending of variable-arc-length elasticas under moment gradient and a noncentral point load. Unlike the aforementioned earlier studies, the variableness of the arc-length is due to the fact that one end of the elastica is now held while the other end portion of the elastica is allowed to slide on a support. This type of variable-arc-length elastica problems, which has applications in marine risers and cables, has drawn the attention of a number of researchers as shown in recent discussions in the open literature (see Hartono, 1997; Golley, 1997).

The present paper continues in this line of research by considering the double curvature bending of the variable arc-length elasticas under two applied moments in the same direction applied at the supports. In offshore engineering operations, the double curvature bending configuration of elasticas is known as an "S" shaped of the suspended pipe laying system or pipe drilling system. The lower portion of pipe develops sag-bend while the upper portion is hog-bend. The class of flexible rods such as robot manipulator arms or deployable flexible space structures, during operations, may experience this bending configuration as well. Large bending on either portion of the pipe or rod may cause the failure of the structural system. This investigation complements earlier studies that confined bending to one of a single curvature-type bending. The governing nonlinear differential equation for elasticas subjected to such a double curvature bending is first derived. Together with the boundary condition, the equation is solved exactly using the elliptic integral technique. As an independent check, the shooting optimization method is also used to obtain the solutions. In this method, the set of governing differential equations is numerically integrated using the fifth-order Cash-Karp Runge-Kutta method and the error norm minimized by an optimization algorithm. Extensive bending results are presented and salient feature of such a problem are highlighted.

2 Governing Equation

Figure 1(a) shows an elastica of uniform flexural rigidity EI. It is hinged at end A and supported on a frictionless support at B located at a distance L from end A. This beam is subjected to a clockwise moment $M_A = (1 - \beta)M_0$ at the hinged end A and a clockwise moment $M_B = \beta M_0$ at B. The scalar parameter β proportions the magnitude of the moments applied at A and B.

The constitutive relation and the geometric relations are given by

$$M = -EI\frac{d\theta}{ds}; \quad \frac{dy}{ds} = \sin\theta; \quad \frac{dx}{ds} = \cos\theta \quad (1a,b,c)$$

where x, y are the Cartesian rectangular coordinates measured from end A and θ is the slope of the centroidal axis of the elastica with respect to the horizontal.

Figure 1(b) shows the deformed configuration of elastica under the clockwise moments, the elastica will bend in a double curvature mode for $0 < \beta < 1$ with point C being the point of contraflexure. Considering a free-body diagram of the elastica (Fig. 1(c)), the bending moment is given by

Contributed by the Applied Mechanics Division of THE AMERICAN SOCIETY OF MECHANICAL ENGINEERS for publication in the ASME JOURNAL OF APPLIED MECHANICS.

Discussion on the paper should be addressed to the Technical Editor, Professor Lewis T. Wheeler, Department of Mechanical Engineering, University of Houston, Houston, TX 77204-4792, and will be accepted until four months after final publication of the paper itself in the ASME JOURNAL OF APPLIED MECHANICS.

Manuscript received by the ASME Applied Mechanics Division, Feb. 11, 1998; final revision, Sept. 25, 1998. Associate Technical Editor: R. C. Benson.

 Copyright © 1999 by ASME

Downloaded 04 May 2010 to 171.66.16.27. Redistribution subject to ASME license or copyright; see http://www.asme.org/terms/Terms_Use.cfm

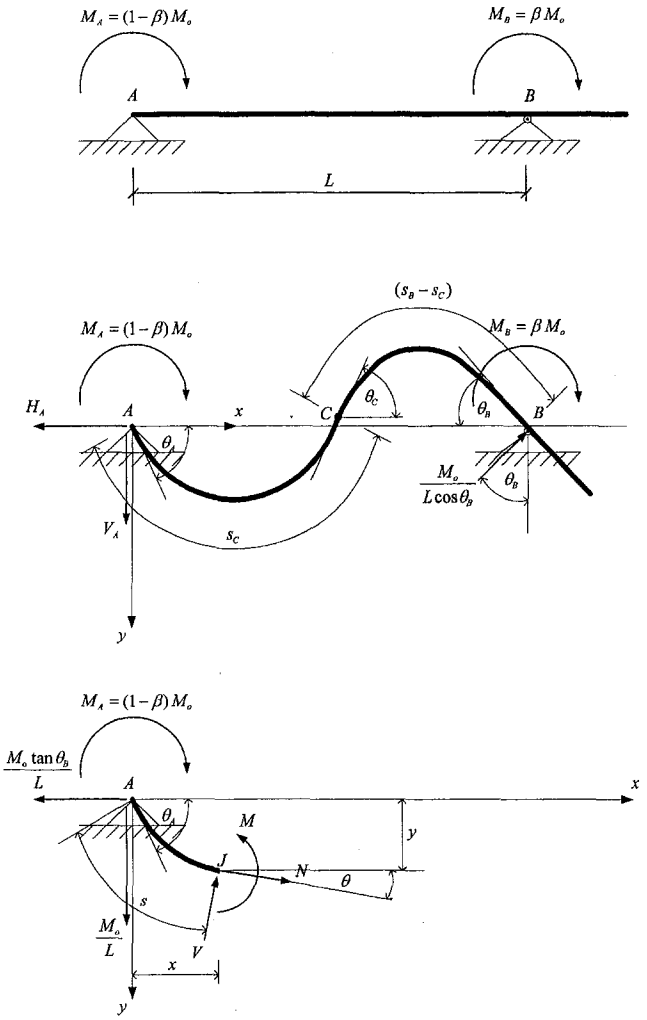

Fig. 1 (*a*) Undeformed configuration of elastica; (*b*) deformed configuration of elastica under clockwise moments; (*c*) free body of elastica segment

$$M(s) = (1 - \beta)M_0 - \frac{M_0}{L} y \tan\theta_B - \frac{M_0}{L} x. \qquad (2)$$

In view of Eqs. (1) with some algebraic manipulations, Eq. (2) may be written as

$$EI \frac{d^2\theta}{ds^2} = \frac{M_0}{L} [\tan\theta_B \sin\theta + \cos\theta]. \qquad (3)$$

Then the governing equation, the boundary conditions, and the inflection condition written in a nondimensional form are as follows:

$$\frac{d^2\theta}{d\bar{s}^2} = \bar{M}[\tan\theta_B \sin\theta + \cos\theta] \qquad (4)$$

$$\left.\frac{d\theta}{d\bar{s}}\right|_{\theta=\theta_A} = -(1 - \beta)\bar{M};$$

$$\left.\frac{d\theta}{d\bar{s}}\right|_{\theta=\theta_B} = -\beta\bar{M}; \quad \left.\frac{d\theta}{d\bar{s}}\right|_{\theta=\theta_C} = 0 \qquad (5a,b,c)$$

$$\bar{x}|_{\theta=\theta_A} = 0; \quad \bar{y}|_{\theta=\theta_A} = 0;$$

$$\bar{x}|_{\theta=\theta_B} = 1; \quad \bar{y}|_{\theta=\theta_B} = 0 \qquad (6a,b,c,d)$$

where

$$\bar{x} = \frac{x}{L}, \quad \bar{y} = \frac{y}{L}, \quad \bar{s} = \frac{s}{L}, \quad \text{and} \quad \bar{M} = \frac{M_0 L}{EI}.$$

3 Elliptic Integrals Method

Upon integrating Eq. (4) and applying boundary conditions given in Eqs. (5*a–c*), the set of first-order differential equations, Eqs. (7*a–c*), and two constraint equations, Eqs. (8) and (9), are obtained.

$$\frac{d\theta}{d\bar{s}} = \pm\sqrt{2\bar{M}\left(-\tan\theta_B \cos\theta + \sin\theta + \frac{\beta^2\bar{M}}{2}\right)} \qquad (7a)$$

$$\frac{d\bar{x}}{d\bar{s}} = \cos\theta; \quad \frac{d\bar{y}}{d\bar{s}} = \sin\theta \qquad (7b,c)$$

$$2\sin(\theta_A - \theta_B) = (1 - 2\beta)\bar{M}\cos\theta_B \qquad (8)$$

$$2\sin(\theta_B - \theta_C) = \beta^2\bar{M}\cos\theta_B \qquad (9)$$

The minus sign (−) in Eq. (7*a*) applies for $-\theta_C \le \theta \le \theta_A$ and the plus sign (+) applies for $-\theta_C \le \theta \le \theta_B$.

For convenience and generality, the following nondimensional parameters are used:

$$\left.\begin{aligned} &\Omega = \mu_1 \cos\theta + \sin\theta + \mu_2; \quad \mu_1 = -\tan\theta_B; \quad \mu_2 = \frac{\beta^2\bar{M}}{2} \\ &\nu = \sqrt{1 + \mu_1^2}; \quad \tau = \cos^{-1}\left(\frac{1}{\nu}\right) = \sin^{-1}\left(\frac{\mu_1}{\nu}\right) \end{aligned}\right\}. \qquad (10a,\ldots,e)$$

In view of the foregoing nondimensional terms, the integrations of the curvature expression in Eq. (7*a*) and the longitudinal and transverse coordinate in Eqs. (7*b*) and (7*c*) with respect to the arc-length parameter $\bar{s}$ yield the following pertinent equations:

Case I: $\mu_2 \le \nu$ or $\bar{M} \le 2 \sec\theta_B/\beta^2$.

For $-\theta_C \le \theta \le \theta_A$

$$\bar{s} = -\frac{1}{\sqrt{2\bar{M}}}\int_{\theta_A}^{\theta}\frac{d\theta}{\sqrt{\Omega}} = -\frac{1}{\sqrt{\nu\bar{M}}}[F(\Phi, k) - F(\Phi_A, k)] \qquad (11)$$

$$\left.\begin{aligned} \bar{x} &= -\frac{1}{\sqrt{2\bar{M}}}\int_{\theta_A}^{\theta}\frac{\cos\theta}{\sqrt{\Omega}}\,d\theta \\ &= -\frac{\sin\tau}{\sqrt{\nu\bar{M}}}\{2[E(\Phi, k) - E(\Phi_A, k)] \\ &\quad - [F(\Phi, k) - F(\Phi_A, k)]\} \\ &\quad - \frac{2k\cos\tau}{\sqrt{\nu\bar{M}}}\{\cos\Phi - \cos\Phi_A\} \end{aligned}\right\} \qquad (12)$$

$$\left.\begin{aligned} \bar{y} &= -\frac{1}{\sqrt{2\bar{M}}}\int_{\theta_A}^{\theta}\frac{\sin\theta}{\sqrt{\Omega}}\,d\theta \\ &= -\frac{\cos\tau}{\sqrt{\nu\bar{M}}}\{2[E(\Phi, k) - E(\Phi_A, k)] \\ &\quad - [F(\Phi, k) - F(\Phi_A, k)]\} \\ &\quad + \frac{2k\sin\tau}{\sqrt{\nu\bar{M}}}\{\cos\Phi - \cos\Phi_A\} \end{aligned}\right\} \qquad (13)$$

Downloaded 04 May 2010 to 171.66.16.27. Redistribution subject to ASME license or copyright; see http://www.asme.org/terms/Terms_Use.cfm

For $-\theta_C \le \theta \le \theta_B$

$$\bar{s} = \bar{s}_C + \frac{1}{\sqrt{2\bar{M}}}\int_{-\theta_C}^{\theta}\frac{d\theta}{\sqrt{\Omega}} = -\frac{1}{\sqrt{\nu\bar{M}}}[2F(\Phi_C, k) - F(\Phi_A, k) - F(\Phi, k)] \quad (14)$$

$$\left.\begin{aligned}\bar{x} &= \bar{x}_C + \frac{1}{\sqrt{2\bar{M}}}\int_{-\theta_C}^{\theta}\frac{\cos\theta}{\sqrt{\Omega}}\,d\theta \\ &= -\frac{\sin\tau}{\sqrt{\nu\bar{M}}}\{2[2E(\Phi_C, k) - E(\Phi_A, k) - E(\Phi, k)] \\ &\quad - [2F(\Phi_C, k) - F(\Phi_A, k) - F(\Phi, k)]\} \\ &\quad - \frac{2k\cos\tau}{\sqrt{\nu\bar{M}}}\{2\cos\Phi_C - \cos\Phi_A - \cos\Phi\}\end{aligned}\right\} \quad (15)$$

$$\left.\begin{aligned}\bar{y} &= \bar{y}_C + \frac{1}{\sqrt{2\bar{M}}}\int_{-\theta_C}^{\theta}\frac{\sin\theta}{\sqrt{\Omega}}\,d\theta \\ &= -\frac{\cos\tau}{\sqrt{\nu\bar{M}}}\{2[2E(\Phi_C, k) - E(\Phi_A, k) - E(\Phi, k)] \\ &\quad - [2F(\Phi_C, k) - F(\Phi_A, k) - F(\Phi, k)]\} \\ &\quad + \frac{2k\sin\tau}{\sqrt{\nu\bar{M}}}\{2\cos\Phi_C - \cos\Phi_A - \cos\Phi\}\end{aligned}\right\} \quad (16)$$

where $F(\Phi, k)$ and $E(\Phi, k)$ are the adjustable elliptic integrals of the first and second kind, respectively (Byrd and Friedman, 1971) and define as

$F(\Phi, k)$ = sgn (θ) × the Jacobi's standard elliptic integral of first kind (17*a*)

$E(\Phi, k)$ = sgn (θ) × the Jacobi's standard elliptic integral of second kind (17*b*)

where

$$\text{sgn}(\theta) = \begin{cases} 1 & \text{if } \cos(\tau + \theta) \le 0 \\ -1 & \text{if } \cos(\tau + \theta) > 0 \end{cases} \quad (17c)$$

$$\Phi_i = \sin^{-1}\sqrt{\frac{\nu[1 - \sin(\tau + \theta_i)]}{\nu + \mu_2}} \quad (i = A, B, \text{and } C) \quad (17d)$$

and

$$k = \sqrt{\frac{\mu_2 + \nu}{2\nu}}. \quad (17e)$$

The subscripts A, C, and B denote quantities evaluated at end A, at the point of contraflexure C, and at end B.

Case II: $\mu_2 \ge \nu$ or $\bar{M} \ge 2\sec\theta_B/\beta^2$.

For $-\theta_C \le \theta \le \theta_A$

$$\bar{s} = -\frac{1}{\sqrt{2\bar{M}}}\int_{\theta_A}^{\theta}\frac{d\theta}{\sqrt{\Omega}} = -\sqrt{\frac{2}{(\mu_2 + \nu)\bar{M}}}[F(\Phi, k) - F(\Phi_A, k)] \quad (18)$$

$$\left.\begin{aligned}\bar{x} &= -\frac{1}{\sqrt{2\bar{M}}}\int_{\theta_A}^{\theta}\frac{\cos\theta}{\sqrt{\Omega}}\,d\theta \\ &= -\sqrt{\frac{\mu_2 + \nu}{2\bar{M}}}\frac{\sin\tau}{\nu}\left\{[E(\Phi, k) - E(\Phi_A, k)] - \left(\frac{\mu_2}{\mu_2 + \nu}\right)[F(\Phi, k) - F(\Phi_A, k)]\right\} \\ &\quad - \sqrt{\frac{\mu_2 + \nu}{2\bar{M}}}\frac{\cos\tau}{\nu}\{\sqrt{1 - k^2\sin^2\Phi} - \sqrt{1 - k^2\sin^2\Phi_A}\}\end{aligned}\right\} \quad (19)$$

$$\left.\begin{aligned}\bar{y} &= -\frac{1}{\sqrt{2\bar{M}}}\int_{\theta_A}^{\theta}\frac{\sin\theta}{\sqrt{\Omega}}\,d\theta \\ &= -\sqrt{\frac{\mu_2 + \nu}{2\bar{M}}}\frac{\cos\tau}{\nu}\left\{[E(\Phi, k) - E(\Phi_A, k)] - \left(\frac{\mu_2}{\mu_2 + \nu}\right)[F(\Phi, k) - F(\Phi_A, k)]\right\} \\ &\quad + \sqrt{\frac{\mu_2 + \nu}{2\bar{M}}}\frac{\sin\tau}{\nu}\{\sqrt{1 - k^2\sin^2\Phi} - \sqrt{1 - k^2\sin^2\Phi_A}\}\end{aligned}\right\} \quad (20)$$

For $-\theta_C \le \theta \le \theta_B$

$$\bar{s} = \bar{s}_C + \frac{1}{\sqrt{2\bar{M}}}\int_{-\theta_C}^{\theta}\frac{d\theta}{\sqrt{\Omega}} = -\sqrt{\frac{2}{(\mu_2 + \nu)\bar{M}}} \times [2F(\Phi_C, k) - F(\Phi_A, k) - F(\Phi, k)] \quad (21)$$

$$\left.\begin{aligned}\bar{x} &= \bar{x}_C + \frac{1}{\sqrt{2\bar{M}}}\int_{-\theta_C}^{\theta}\frac{\cos\theta}{\sqrt{\Omega}}\,d\theta \\ &= -\sqrt{\frac{\mu_2 + \nu}{2\bar{M}}}\frac{\sin\tau}{\nu}\left\{[2E(\Phi_C, k) - E(\Phi_A, k) - E(\Phi, k)] - \left(\frac{\mu_2}{\mu_2 + \nu}\right)[2F(\Phi_C, k) - F(\Phi_A, k) - F(\Phi, k)]\right\} \\ &\quad - \sqrt{\frac{\mu_2 + \nu}{2\bar{M}}}\frac{\cos\tau}{\nu}\{2\sqrt{1 - k^2\sin^2\Phi_C} - \sqrt{1 - k^2\sin^2\Phi_A} - \sqrt{1 - k^2\sin^2\Phi}\}\end{aligned}\right\} \quad (22)$$

$$\left.\begin{aligned}\bar{y} &= \bar{y}_C + \frac{1}{\sqrt{2\bar{M}}}\int_{-\theta_C}^{\theta}\frac{\sin\theta}{\sqrt{\Omega}}\,d\theta \\ &= -\sqrt{\frac{\mu_2 + \nu}{2\bar{M}}}\frac{\cos\tau}{\nu}\left\{[2E(\Phi_C, k) - E(\Phi_A, k) - E(\Phi, k)] - \left(\frac{\mu_2}{\mu_2 + \nu}\right)[2F(\Phi_C, k) - F(\Phi_A, k) - F(\Phi, k)]\right\} \\ &\quad + \sqrt{\frac{\mu_2 + \nu}{2\bar{M}}}\frac{\sin\tau}{\nu}\{2\sqrt{1 - k^2\sin^2\Phi_C} - \sqrt{1 - k^2\sin^2\Phi_A} - \sqrt{1 - k^2\sin^2\Phi}\}\end{aligned}\right\} \quad (23)$$

Downloaded 04 May 2010 to 171.66.16.27. Redistribution subject to ASME license or copyright; see http://www.asme.org/terms/Terms_Use.cfm

Table 1 Comparison of results for $\bar{M} = 3$

Scaling parameter β	Rotation at end A θ_A (rad.)				Rotation at inflection point C θ_C (rad.)				Rotation at end B θ_B (rad.)				Arc-length between end A and end B s_B / L			
	Stable		Unstable		Stable		Unstable		Stable		Unstable		Stable		Unstable	
	EIM	SOM	EIM	SOM	EIM	SOM	EIM	SOM	EIM	SOM	EIM	SOM	EIM	SOM	EIM	SOM
0.2	0.809178	0.809178	1.676451	1.676451	-0.308262	-0.308261	-0.774967	-0.774968	-0.250095	-0.250095	-0.730252	-0.730253	1.057947	1.057947	1.389155	1.389157
0.3	0.582261	0.582261	1.935173	1.935176	-0.195065	-0.195065	-0.852140	-0.852141	-0.059895	-0.059895	-0.753528	-0.753528	1.024429	1.024429	1.571777	1.571778
0.4	0.404192	0.404192	2.200021	2.200024	-0.139999	-0.139999	-0.895187	-0.895187	0.101105	0.101105	-0.712570	-0.712570	1.010185	1.010185	1.795838	1.795839
0.5	0.248962	0.248962	2.563713	2.563716	-0.122994	-0.122994	-0.897397	-0.897397	0.248962	0.248962	-0.577880	-0.577879	1.006148	1.006148	2.131044	2.131044
0.6	0.107839	0.107839	3.211004	3.211009	-0.134068	-0.134068	-0.781243	-0.781241	0.389108	0.389108	-0.227209	-0.227208	1.009265	1.009265	2.683418	2.683420
0.7	-0.022824	-0.022823	4.034156	4.034159	-0.166414	-0.166414	-0.507650	-0.507648	0.523583	0.523583	0.277445	0.277446	1.018010	1.018010	3.133527	3.133527
0.8	-0.144274	-0.144274	4.584228	4.584237	-0.215100	-0.215099	-0.271359	-0.271355	0.652506	0.652506	0.622864	0.622866	1.031259	1.031259	3.205925	3.205925
0.9	-0.256301	-0.256301	4.910267	4.910275	-0.277533	-0.277532	-0.104692	-0.104688	0.774510	0.774510	0.840437	0.840439	1.047787	1.047788	3.126340	3.126340
1.0	-0.357892	-0.357891	5.102634	5.102641	-0.357892	-0.357891	0.011884	0.011888	0.887168	0.887168	0.986463	0.986465	1.066052	1.066052	3.004975	3.004975

EIM = Elliptic integrals method

SOM = Shooting-optimization method

Table 2 Comparison of results for $\bar{M} = 4$

Scaling parameter β	Rotation at end A θ_A (rad.)				Rotation at inflection point C θ_C (rad.)				Rotation at end B θ_B (rad.)				Arc-length between end A and end B s_B / L			
	Stable		Unstable		Stable		Unstable		Stable		Unstable		Stable		Unstable	
	EIM	SOM	EIM	SOM	EIM	SOM	EIM	SOM	EIM	SOM	EIM	SOM	EIM	SOM	EIM	SOM
0.3	0.825429	0.825429	1.838025	1.838032	-0.275928	-0.275928	-0.710531	-0.710532	-0.095780	-0.095780	-0.557152	-0.557154	1.050532	1.050532	1.406683	1.406685
0.4	0.543462	0.543461	2.271076	2.271081	-0.186644	-0.186644	-0.797177	-0.797177	0.135969	0.135969	-0.514942	-0.514943	1.018374	1.018374	1.683169	1.683171
0.5	0.330743	0.330743	2.845593	2.845597	-0.161837	-0.161837	-0.794667	-0.794667	0.330743	0.330743	-0.296000	-0.295999	1.010778	1.010777	2.090479	2.090480
0.6	0.150575	0.150575	3.715098	3.715102	-0.172847	-0.172847	-0.621146	-0.621145	0.507668	0.507669	0.168135	0.168136	1.015525	1.015525	2.590702	2.590704
0.7	-0.006984	-0.006984	4.454271	4.454278	-0.205004	-0.205003	-0.382895	-0.382893	0.670480	0.670480	0.578994	0.578995	1.028092	1.028092	2.779393	2.779394
0.8	-0.144723	-0.144723	4.913399	4.913407	-0.248341	-0.248340	-0.200994	-0.200991	0.817771	0.817771	0.834135	0.834136	1.045181	1.045182	2.748219	2.748219
0.9	-0.263226	-0.263226	5.187674	5.187683	-0.297909	-0.297908	-0.070484	-0.070479	0.946332	0.946333	0.998837	0.998839	1.063600	1.063600	2.650107	2.650107
1.0	-0.363395	-0.363394	5.342972	5.342977	-0.363395	-0.363391	0.021717	0.021721	1.053967	1.053968	1.111548	1.111550	1.080591	1.080593	2.538994	2.538995

EIM = Elliptic integrals method

SOM = Shooting-optimization method

where

$$\Phi_i = \sin^{-1}\sqrt{\frac{\nu[1-\sin(\tau+\theta_i)]}{2}} \quad (i = A, B, \text{and } C) \tag{24a}$$

$$k = \sqrt{\frac{2\nu}{\mu_2+\nu}}. \tag{24b}$$

In view of the foregoing elliptic integral formulation, there are four independent variables (θ_A, θ_B, θ_C, $\bar{M}$). In practical problems, quite often the moment $\bar{M}$ is assigned and the displacements θ_A, θ_B, and θ_C are to be determined. However, if the given value of $\bar{M}$ is greater than the critical or maximum value $\bar{M}_{cr}$ (see definition below), there is no solution possible. Therefore, instead of assigning $\bar{M}$, the value of θ_B has been assigned and the unknowns to be solved are θ_A, θ_C, and $\bar{M}$. Three independent equations are required for solution, for instance Eqs. (6*d*), (8), and (9) with the assistance of either Eq. (16) or (23). The system of nonlinear equations is written as follows:

$$f_1 = 2\sin(\theta_A - \theta_B) - (1-2\beta)\bar{M}\cos\theta_B = 0 \tag{25}$$

$$f_2 = 2\sin(\theta_B - \theta_C) - \beta^2\bar{M}\cos\theta_B = 0 \tag{26}$$

$$f_3 = -\int_{\theta_A}^{-\theta_C}\frac{\sin\theta}{\sqrt{\Omega}}\,d\theta + \int_{-\theta_C}^{\theta_B}\frac{\sin\theta}{\sqrt{\Omega}}\,d\theta = 0. \tag{27}$$

Equation (27) can be expressed in terms of elliptic integrals as

$$\left.\begin{aligned} f_3 = &-\sqrt{\frac{2}{\nu}}\cdot\cos\tau\{2[2E(\Phi_C,k) - E(\Phi_A,k) - E(\Phi_B,k)] \\ &- [2F(\Phi_C,k) - F(\Phi_A,k) - F(\Phi_B,k)]\} \\ &+ \sqrt{\frac{2}{\nu}}\cdot 2k\sin\tau\{2\cos\Phi_C - \cos\Phi_A - \cos\Phi_B\}, \end{aligned}\right\}$$

$$\text{if } \mu_2 \le \nu \tag{28a}$$

Downloaded 04 May 2010 to 171.66.16.27. Redistribution subject to ASME license or copyright; see http://www.asme.org/terms/Terms_Use.cfm

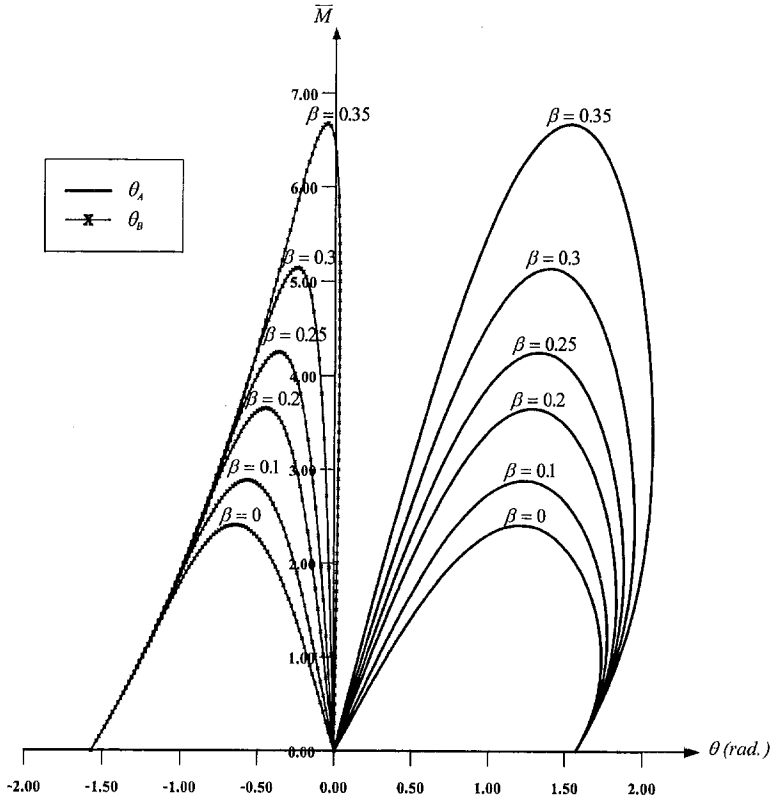

Fig. 2 Relationship between $\bar{M}$ and θ_A, and θ_B for $0 \leq \beta \leq 0.35$

or

$$f_3 = -\frac{\sqrt{\mu_2 + \nu}}{\nu}\cdot\cos\tau\Big\{[2E(\Phi_C, k) - E(\Phi_A, k) - E(\Phi_B, k)] - \left(\frac{\mu_2}{\mu_2 + \nu}\right)[2F(\Phi_C, k) - F(\Phi_A, k) - F(\Phi_B, k)]\Big\} + \frac{\sqrt{\mu_2 + \nu}}{\nu}\cdot\sin\tau\{2\sqrt{1 - k^2\sin^2\Phi_C} - \sqrt{1 - k^2\sin^2\Phi_A} - \sqrt{1 - k^2\sin^2\Phi_B}\},$$

if $\mu_2 \geq \nu$. (28b)

The unknowns θ_A, θ_C, and $\bar{M}$ can be determined by solving iteratively the Eqs. (25) to (27) for the given parameters θ_B and β. The procedure to solve the nonlinear equations is as follows:

Step 1 Assign a value for θ_B, $(0 \leq \theta_B \leq \pi/2)$ and set the initial values of θ_A, θ_C, and $\bar{M}$ from the linear beam theory.

Step 2 Evaluate Eqs. (25) to (27) and check if the results are satisfied within the specified tolerance $\epsilon = 10^{-12}$, i.e.,

$$|f_i| \leq \epsilon \text{ when } i = 1, 2, 3. \quad (29)$$

Step 3 If the tolerance specification is not satisfied, θ_A, θ_C, and $\bar{M}$ are adjusted by using the Newton approach, i.e., let $\{x_1, x_2, x_3\} = \{\theta_A, \theta_C, \bar{M}\}$

$$x_i^{k+1} = x_i^k + \Delta x_i^{k+1} \text{ when } i = 1, 2, 3 \quad (30)$$

where Δx_i^{k+1} has been solved from

$$\sum_{j=1}^{3} \frac{\partial f_i}{\partial x_j}\Delta x_j = -f_i. \quad (31)$$

Step 4 Check if $|\Delta x_i^{k+1}| \leq \epsilon$, if not, repeat Steps 2–4 until the specified tolerance set is achieved.

Step 5 Once θ_A, θ_C, and $\bar{M}$ are determined and the deflection $\bar{y}$ at any distance $\bar{x}$ can be obtained from either Eqs. (12), (13), (15), (16) or Eqs. (19), (20), (22), (23).

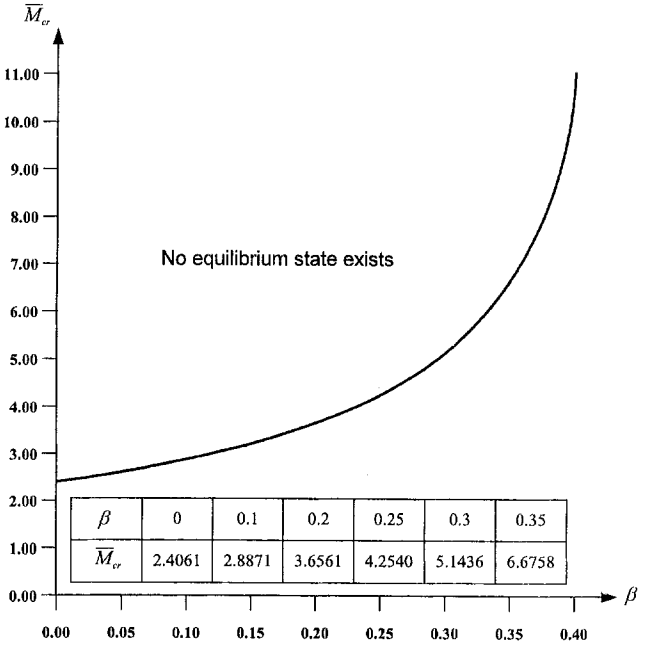

β	0	0.1	0.2	0.25	0.3	0.35
$\bar{M}_{cr}$	2.4061	2.8871	3.6561	4.2540	5.1436	6.6758

Fig. 3 Relationship between $\bar{M}_{cr}$ and β

Downloaded 04 May 2010 to 171.66.16.27. Redistribution subject to ASME license or copyright; see http://www.asme.org/terms/Terms_Use.cfm

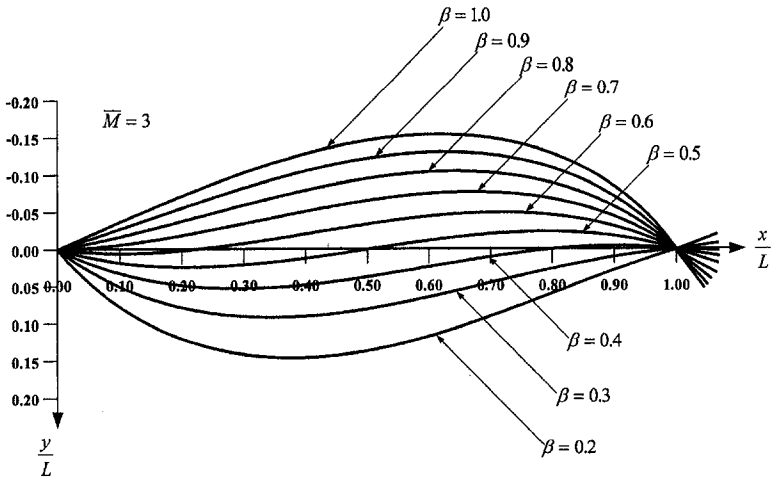

Fig. 4 Stable equilibrium configurations for $\bar{M} = 3$

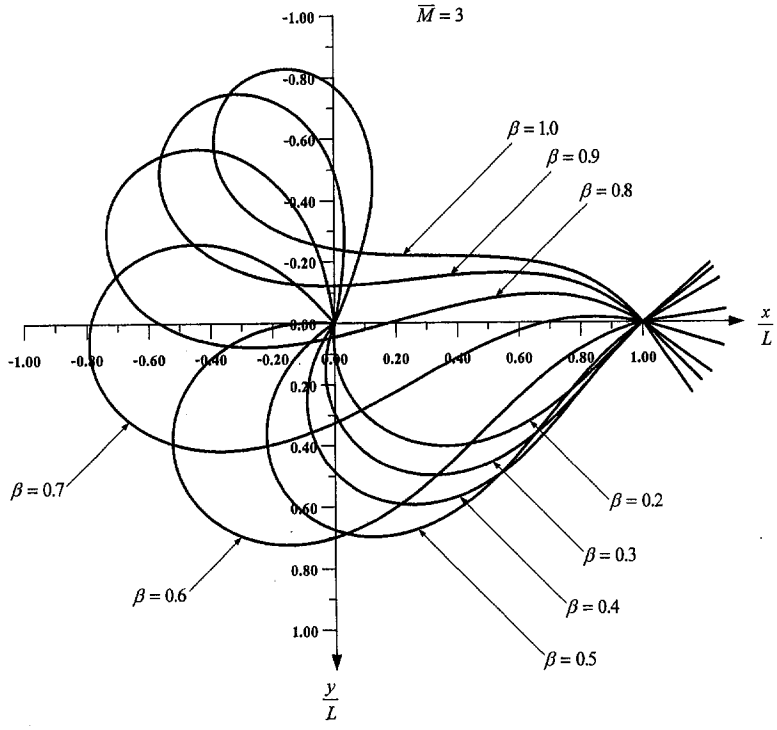

Fig. 5 Unstable equilibrium configurations for $\bar{M} = 3$

The value of $\bar{s}_B = s_B/L$ is determined from either Eqs. (11), (14) or Eqs. (18), (21).

Step 6 Add an incremental $\Delta\theta_B$ to θ_B and repeat Steps 2–5 to construct the curves of $\bar{M}$ versus θ_A and θ_B.

4 Shooting-Optimization Method

In view of Eqs. (1) and (2) and setting forth additional dimensionless quantities $s^* = s/s_B$, $\bar{s}_B = s_B/L$, another form of the governing differential equations and the boundary conditions can be written in a nondimensional form as

$$\frac{d\theta}{ds^*} = \bar{s}_B\bar{M}[\bar{x} + \bar{y}\tan\theta_B - (1 - \beta)] \qquad (32a)$$

$$\left.\frac{d\theta}{ds^*}\right|_{s^*=0} = -(1 - \beta)\bar{s}_B\bar{M}; \quad \left.\frac{d\theta}{ds^*}\right|_{s^*=1} = -\beta\bar{s}_B\bar{M};$$

$$\left.\frac{d\theta}{ds^*}\right|_{s^*=s_C^*} = 0 \qquad (32b,c,d)$$

$$\frac{d\bar{x}}{ds^*} = \bar{s}_B\cos\theta; \quad \bar{x}(0) = 0; \quad \bar{x}(1) = 1 \qquad (33a,b,c)$$

$$\frac{d\bar{y}}{ds^*} = \bar{s}_B\sin\theta; \quad \bar{y}(0) = 0; \quad \bar{y}(1) = 0. \qquad (34a,b,c)$$

For a given value of $\bar{M}$, there are four unknowns (θ, $\bar{x}$, $\bar{y}$, and $\bar{s}_B$) to be evaluated from the three first-order differential equations together with four end conditions ($\bar{x}(0) = 0$; $\bar{y}(0) = 0$; $\bar{x}(1) = 1$; $\bar{y}(1) = 0$). However, if the given value of $\bar{M}$ is greater than the critical or maximum value, the solution does not exist. Therefore, instead of assigning $\bar{M}$, the value of θ has been assigned and thus the unknowns to be solved are ($\bar{x}$, $\bar{y}$, $\bar{M}$, and $\bar{s}_B$). The solution steps are as follows:

Downloaded 04 May 2010 to 171.66.16.27. Redistribution subject to ASME license or copyright; see http://www.asme.org/terms/Terms_Use.cfm

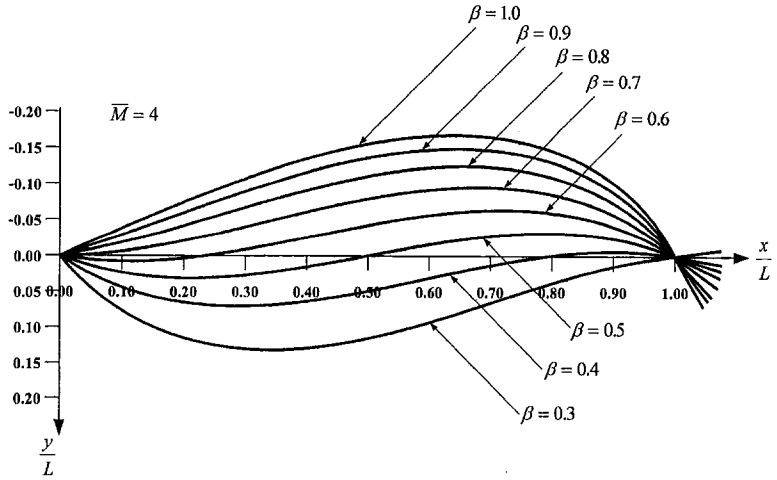

Fig. 6 Stable equilibrium configurations for $\bar{M} = 4$

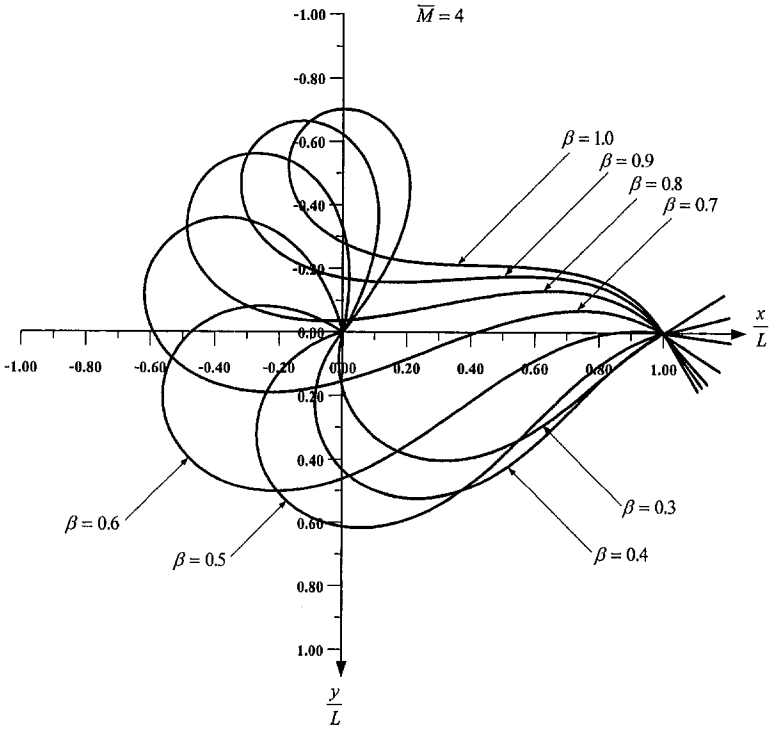

Fig. 7 Unstable equilibrium configurations for $\bar{M} = 4$

Step 1 Set the initial step size of integration and the initial values of $s^*(1) = 1$, $\bar{x}(1) = 1$, $\bar{y}(1) = 0$, and $\theta(1) = \theta_B$.

Step 2 Given θ_B, one guesses $\bar{M}$ and $\bar{s}_B$ at the first iteration from the linear small displacement theory.

Step 3 Integrate Eqs. (32a), (33a) and (34a) from $s^* = 1$ to 0 using the fifth-order Cash-Karp Runge-Kutta with adaptive step size control following Fehlberg method (Press et al. 1992).

Step 4 Minimize the error norm using the Nelder and Mead simplex method (Nelder and Mead, 1965) with respect to $\bar{M}$ and $\bar{s}_B$. The objective function Φ for the minimization process is

$$\underset{\bar{M},\bar{s}_B}{\text{Min}}\ \Phi = |\bar{x}(0)| + |\bar{y}(0)|. \tag{35}$$

Step 5 Once the value of $\bar{M}$, θ_A, and θ_B are obtained, the value of θ_C is calculated using Eq. (9).

Step 6 Add an incremental $\Delta\theta_B$ to θ_B and repeat Steps 3–5 to construct the curves of $\bar{M}$ versus θ_A and θ_B.

5 Results and Discussion

It has been found that there are two equilibrium configurations under the applied moments. One equilibrium state is stable while the other is unstable. Numerical results of θ_A, θ_C, θ_B, and s_B/L for both equilibrium states computed from the elliptic integrals method and the shooting-optimization method are compared in Tables 1 and 2 for $\bar{M} = 3$ and 4, and for values of β ranging from 0.2 to 1.0. There is generally an excellent agreement between the results obtained from the two methods, thus confirming the validity of the solution.

Figure 2 shows the variations of the moment parameter $\bar{M}$ with respect to θ_A and θ_B for values of β up to 0.35. The curves indicate that there are at least two solutions for a given value of $\bar{M}$ and β. Physically, it can be seen that as $\bar{M}$ initially in-

Downloaded 04 May 2010 to 171.66.16.27. Redistribution subject to ASME license or copyright; see http://www.asme.org/terms/Terms_Use.cfm

creases from zero, the end rotation θ_A (or $|\theta_B|$) increases from zero as well. As $\bar{M}$ reaches a maximum resisting value of beam, an infinitesimal increase in $\bar{M}$ will initiate continuous beam motion. Furthermore, an increment of rotation θ_A (or $|\theta_B|$) requires no increment of $\bar{M}$, and for the equilibrium $\bar{M}$ should be reduced instead of being increased. At this state the equilibrium is unstable, since a small disturbance will initiate continuous beam motion. Therefore, the peak value of $\bar{M}$ for each β is known as the maximum or critical value of $\bar{M}$ or $\bar{M}_{cr}$. This value can be determined numerically using the Dichotomous search algorithm (Kempf, 1987) during calculations in Step 5. A plot of $\bar{M}_{cr}$ against β is given in Fig. 3. It can be seen that the critical moment value increases rapidly when $\beta > 0.35$. The critical moment values for β greater than 0.35 are somewhat difficult to obtain because their magnitudes are relatively very large.

Owing to the presence of a critical moment parameter, there is therefore a critical value of β associated with a moment value where no solution exists. For example, when $\bar{M} = 3$, β must be greater than about 0.1 before an equilibrium configuration can exists and for $\bar{M} = 4$, β must be greater than about 0.2.

The stable and unstable equilibrium configurations for $\bar{M}_{cr} = 3$ and 4 are shown in Figs. 4–7. It can be seen that, for the unstable cases, the elasticas snap back and form single loops when β is greater than 0.8.

6 Concluding Remarks

The governing equations and solutions for double curvature bending of variable-arc-length elasticas are presented. The two approaches used to solve the problem, namely the elliptic integrals method and the shooting-optimization method, yield almost the same solutions. The problem involves two possible equilibrium configurations, one that is stable while the other unstable. The stable ones are associated with the smaller slope values while the unstable ones are associated with the larger slope values.

Critical moment parameter values $\bar{M}_{cr}$ are computed for various values of β. Equilibrium states for the variable arc-length elasticas do not exist when the moment parameter values are greater than these critical moment values.

This study also shows the interesting snap-back equilibrium solutions involving single loops in the cases of unstable equilibrium configurations for which the scaling parameter β is close to unity.

Acknowledgment

The authors would like to acknowledge the reviewers for their many useful comments which lead to improvements in the revised manuscript.

References

Byrd, P. F., and Friedman, M. D., 1971, *Handbook of Elliptic Integrals for Engineers and Scientists,* 2nd Ed., Springer-Verlag, Berlin.

Conway, H. D., 1974, "The large deflection of a simply supported beam," *Phil. Mag., Series* 7, Vol. 38, pp. 905–911.

Chucheepsakul, S., Bunchareon, S., and Wang, C. M., 1994, "Large deflection of beams under moment gradient," *J. Engrg. Mech., ASCE,* Vol. 120, pp. 1848–1860.

Chucheepsakul, S., Bunchareon, S., and Huang, T., 1995, "Elastica of simple variable-arc-length beam subjected to an end moment," *J. Engrg. Mech., ASCE,* Vol. 121, pp. 767–772.

Chucheepsakul, S., Theppitak, G., and Wang, C. M., 1996, "Large deflection of simple variable-arc-length beam subjected to a point load," *Struct. Engrg. & Mech.,* Vol. 4, No. 1, pp. 49–59.

Chucheepsakul, S., and Huang, T., 1997a, "Finite-element solution of variable-arc-length beams under a point load," *J. Struct. Engrg., ASCE,* Vol. 123, No. 7, pp. 968–970.

Chucheepsakul, S., Theppitak, G., and Wang, C. M., 1997b, "Exact solutions of variable-arc-length elasticas under moment gradient," *Struct. Engrg. & Mech.,* Vol. 5, No. 5, pp. 529–539.

Golley, B. W., 1997, Discussion on "Elastica of simple variable-arc-length beam subjected to end moment," *J. Engrg. Mech., ASCE,* Vol. 123, No. 1, pp. 93–94.

Gospodnetic, D., 1959, "Deflection Curve of a Simply Supported Beam," ASME JOURNAL OF APPLIED MECHANICS, Vol. 26, pp. 675–676.

Hartono, W., 1997, Discussion on "Elastica of simple variable-arc-length beam subjected to end moment," *J. Engrg. Mech., ASCE,* Vol. 123, No. 1 pp. 92–93.

Kempf, J., 1987, *Numerical Solfware Tools in C,* Prentice-Hall, Englewood Criffs, NJ, pp. 178–180.

Nelder, J. A., and Mead, R., 1965, "A simplex method for function minimization," *Comp. J.,* Vol. 7, pp. 308–313.

Press, W. H., Teukolsky, S. A., Vettering, W. T., and Flannery, B. P., 1992, *Numerical Recipes in Fortran,* 2nd Ed., Cambridge University Press, pp. 708–716, 372–381, 401–406.

Schile, R. D., and Sierakowski, R. L., 1967, "Large deflection of a beam loaded and supported at two points," *Int. J. Non-linear Mech.,* Vol. 2, pp. 61–68.

Wang, C. M., Lam, K. Y., He, X. Q., and Chucheepsakul, S., 1997, "Large deflections of an end supported beam subjected to a point load," *Int. J. Nonlinear Mechanics,* Vol. 31, No. 1, pp. 63–72.

Wang, T. M., 1968, "Nonlinear bending of beams with concentrated loads," *J. of Franklin Institute,* Vol. 285, pp. 386–390.

Downloaded 04 May 2010 to 171.66.16.27. Redistribution subject to ASME license or copyright; see http://www.asme.org/terms/Terms_Use.cfm

A Higher-Order Theory for Plane Stress Conditions of Laminates Consisting of Isotropic Layers

X. J. Wu

S. M. Cheng[1]
Assoc. Mem. ASME

Structures, Materials and Propulsion Laboratory,
Institute of Aerospace Research,
National Research Council of Canada,
Ottawa, Ontario K1A 0R6, Canada

In this paper, a higher-order theory is derived for laminates consisting of isotropic layers, on the basis of three-dimensional elasticity with displacements as higher-order functions of z in the thickness direction. The theory employs three stress potentials, Ψ (an Airy function), p (a harmonic function), and its conjugate q, to satisfy all conditions of stress equilibrium and compatibility. Interlaminar shear stresses, i.e., antiplane stresses, are shown to be present at the interfaces, especially near material discontinuities where gradients of in-plane stresses are usually high. For illustrating its practical application, the problem of a plate containing a hole patched with an intact plate is solved.

Introduction

In the current context of composite mechanics, assumptions are often made such that a multilayer composite is treated as a homogeneous and anisotropic body. Under the generalized plane-stress conditions, the gross stresses can be solved using the classical theory of plane-stress elasticity and then partitioned in each individual layer, according to the uniform strain partitioning rule (Tsai, 1980). In such a description, antiplane stresses are not considered. These antiplane stresses happen to be the interlaminar stresses, which are known to play an important role in delamination and fracture of multilayer composites. Therefore, it is indispensable to solve these interlaminar stresses for assessment of fracture and damage tolerance of composite materials.

It has been recognized that interlaminar stresses are present in regions where in-plane stress gradient exists (Pipes and Pagano, 1970; Pagano, 1978), especially near the free edges, holes, and cracks. Some analytical methods have been proposed to calculate interlaminar stresses at free edges (Kassapoglu and Lagace, 1986; Bhat and Lagace, 1994). However, these treatments assume the condition that in-plane stresses do not vary along one direction in the plane. These methods mostly apply to infinite straight edges but have limitations in addressing problems of holes and cracks in composite materials. Some approximate theories (e.g., Pagano, 1978), which use the "sublayer" concept to model the stress distribution in one physical layer, have been developed to address the general three-dimensional stress states in laminates. Higher-order theories are needed to include antiplane stress terms for more accurate description of lamination problems.

To appreciate the theoretical significance, it should be pointed out that the difficulties arise from the classical theory itself. The classical plane-stress theory employs one stress function, Ψ (Airy function), to satisfy only one in-plane compatibility condition, and ignores all the out-of-plane strain compatibility conditions. Rigorously speaking, the classical plane-stress theory is only applicable to a single-layer plate of zero thickness. In composite materials, the compatibility at the interfaces between different materials is very important, because wherever incompatibility exists, interfacial flaws or delamination will form.

In the present treatment, dealing with thin laminates consisting of isotropic layers, we will show that antiplane stresses are required to be present to satisfy the interfacial compatibility conditions. The new theory only assumes that each layer is homogeneous and isotropic, there is no pressure acting normal to the lamination plane, i.e., $\sigma_z = 0$, the displacements can be expanded up to second order of the coordinate z (the coordinate in the thickness direction), as in the Taylor series. Based on this displacement assumption under the condition of $\sigma_z = 0$, all the stress-equilibrium and strain-compatibility conditions in an isotropic body are met by three stress potentials: an Airy function Ψ and two conjugate harmonic stress functions, p and q. Using these stress potentials, a quasi-three-dimensional formulation is obtained for the elasticity of laminates consisting of isotropic layers under the generalized plane-stress conditions. As an example, the boundary value problem of an infinite plate containing a circular cutout patched with an intact plate is solved.

Stress and Displacement Functions

In the present treatment we consider a thin composite laminate consisting of isotropic layers, as shown in Fig. 1 (only two layers are drawn for simplicity without losing generality). The thickness of the laminate is small compared to the planar dimensions of the body. We assume that body forces are absent in the composite and the stress normal to the x-y plane, σ_z, is zero. In a plate of finite thickness, stresses and displacements as functions of coordinate z can generally be expanded into Taylor series. The zero-order terms of u and v represent the membrane problem (Timoshenko and Goodier, 1970); the zero-order term of w and the first-order terms of u and v represent the bending problem (Timoshenko, and Woinowsky-Krieger, 1959), which we do not consider here. To satisfy all the compatibility requirements for a composite laminate, second-order terms of u and v must be considered as follows:

$$u = u(x, y) + z^2\beta_1(x, y), \quad v = v(x, y) + z^2\beta_2(x, y),$$

$$w = w_0 - \frac{\nu z}{E}(\sigma_x + \sigma_y) \tag{1}$$

where w_0 is a rigid-body movement.

When $\sigma_z = 0$, the stress-strain relations for an isotropic layer are described by Hooke's law, as

[1] To whom correspondence should be addressed.

Contributed by the Applied Mechanics Division of THE AMERICAN SOCIETY OF MECHANICAL ENGINEERS for publication in the ASME JOURNAL OF APPLIED MECHANICS.

Discussion on the paper should be addressed to the Technical Editor, Professor Lewis T. Wheeler, Department of Mechanical Engineering, University of Houston, Houston, TX 77204-4792, and will be accepted until four months after final publication of the paper itself in the ASME JOURNAL OF APPLIED MECHANICS.

Manuscript received by the ASME Applied Mechanics Division, Jan. 21, 1998; final revision, June 25, 1998. Associate Technical Editor: J. W. Ju.

 Copyright © 1999 by ASME

Downloaded 04 May 2010 to 171.66.16.27. Redistribution subject to ASME license or copyright; see http://www.asme.org/terms/Terms_Use.cfm

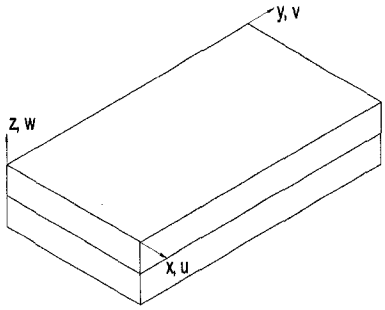

Fig. 1 Schematic of a two-layer composite

$$\epsilon_x = \frac{1}{E}(\sigma_x - \nu\sigma_y), \quad \epsilon_y = \frac{1}{E}(\sigma_y - \nu\sigma_x), \quad \epsilon_z = -\frac{\nu}{E}(\sigma_x + \sigma_y)$$

$$\gamma_{xy} = \frac{\tau_{xy}}{\mu}, \quad \gamma_{xz} = \frac{\tau_{xz}}{\mu}, \quad \gamma_{xy} = \frac{\tau_{yz}}{\mu}. \tag{2}$$

From the antiplane stress-strain relationships, we can find that the anti-plane shear stresses are linear functions of the coordinate z:

$$\tau_{xz} = -zf_1(x, y), \quad \tau_{yz} = -zf_2(x, y). \tag{3}$$

Here, the plane of $z = 0$ is defined as the neutral plane: for a surface layer, it is the unattached free surface of the lamina, and for an inner layer, it is the midplane of the lamina in a symmetrical configuration of layer lay-up.

The stresses in each layer must satisfy the equilibrium conditions

$$\frac{\partial\sigma_x}{\partial x} + \frac{\partial\tau_{xy}}{\partial y} + \frac{\partial\tau_{xz}}{\partial z} = 0 \tag{4a}$$

$$\frac{\partial\tau_{xy}}{\partial x} + \frac{\partial\sigma_y}{\partial y} + \frac{\partial\tau_{yz}}{\partial z} = 0 \tag{4b}$$

$$\frac{\partial\tau_{xz}}{\partial x} + \frac{\partial\tau_{yz}}{\partial y} = 0 \tag{4c}$$

which can be decomposed into two sets of conditions:
(i) for the zero-order equilibrium,

$$\frac{\partial\sigma_x}{\partial x} + \frac{\partial\tau_{xy}}{\partial y} = f_1(x, y) \tag{5a}$$

$$\frac{\partial\tau_{xy}}{\partial x} + \frac{\partial\sigma_y}{\partial y} = f_2(x, y) \tag{5b}$$

$$\frac{\partial f_1}{\partial x} + \frac{\partial f_2}{\partial y} = 0; \tag{5c}$$

(ii) for the second-order equilibrium,

$$\frac{\partial^2\beta_1}{\partial x^2} + \frac{1+\nu}{2}\frac{\partial^2\beta_2}{\partial x\partial y} + \frac{1-\nu}{2}\frac{\partial^2\beta_1}{\partial y^2} = 0 \tag{6a}$$

$$\frac{\partial^2\beta_2}{\partial y^2} + \frac{1+\nu}{2}\frac{\partial^2\beta_1}{\partial x\partial y} + \frac{1-\nu}{2}\frac{\partial^2\beta_2}{\partial x^2} = 0. \tag{6b}$$

We choose three stress potentials, Ψ, p, and q, such that

$$\sigma_x = \frac{\partial^2\Psi}{\partial y^2} + p, \quad \sigma_y = \frac{\partial^2\Psi}{\partial x^2} + p, \quad \tau_{xy} = -\frac{\partial^2\Psi}{\partial x\partial y} \tag{7}$$

$$f_1 = \frac{\partial q}{\partial y} = \frac{\partial p}{\partial x}, \quad f_2 = -\frac{\partial q}{\partial x} = \frac{\partial p}{\partial y} \tag{8}$$

Here and in later text, the notions, σ_x, σ_y, and τ_{xy} only refer to the membrane stresses in the plane of $z = 0$, unless otherwise specified.

Given the definitions in Eq. (7) and (8), it can be shown that the equilibrium conditions, Eq. (5), are automatically satisfied. In the following, we will first show that, by satisfying the compatibility conditions, Ψ is an Airy function (or bi-harmonic function), p and q are conjugate harmonic functions. We will also show that Eq. (6) can be automatically satisfied with the above choice of stress potentials.

In problems of elasticity, stress potentials must satisfy all the compatibility equations for representing the true stress state in a three-dimensional body (Timoshenko and Goodier, 1970). The six compatibility conditions are expressed as

$$\frac{\partial^2\epsilon_x}{\partial y^2} + \frac{\partial^2\epsilon_y}{\partial x^2} = \frac{\partial^2\gamma_{xy}}{\partial x\partial y} \tag{9a}$$

$$\frac{\partial^2\epsilon_z}{\partial y^2} + \frac{\partial^2\epsilon_y}{\partial z^2} = \frac{\partial^2\gamma_{yz}}{\partial y\partial z} \tag{9b}$$

$$\frac{\partial^2\epsilon_x}{\partial z^2} + \frac{\partial^2\epsilon_z}{\partial x^2} = \frac{\partial^2\gamma_{xz}}{\partial x\partial z} \tag{9c}$$

$$2\frac{\partial^2\epsilon_x}{\partial y\partial z} = \frac{\partial}{\partial x}\left(-\frac{\partial\gamma_{yz}}{\partial x} + \frac{\partial\gamma_{xz}}{\partial y} + \frac{\partial\gamma_{xy}}{\partial z}\right) \tag{9d}$$

$$2\frac{\partial^2\epsilon_y}{\partial x\partial z} = \frac{\partial}{\partial y}\left(\frac{\partial\gamma_{yz}}{\partial x} - \frac{\partial\gamma_{xz}}{\partial y} + \frac{\partial\gamma_{xy}}{\partial z}\right) \tag{9e}$$

$$2\frac{\partial^2\epsilon_z}{\partial x\partial y} = \frac{\partial}{\partial z}\left(\frac{\partial\gamma_{yz}}{\partial x} + \frac{\partial\gamma_{xz}}{\partial y} - \frac{\partial\gamma_{xy}}{\partial z}\right). \tag{9f}$$

Upon substituting Eqs. (2), (3), (7), and (8) into Eq. (9), Eq. (9a) becomes

$$\nabla^4\Psi + (1-\nu)\nabla^2 p = 0. \tag{10}$$

Meanwhile, Eqs. (9b) and (9c) are automatically satisfied with

$$E\beta_1 = \frac{\partial}{\partial x}\left(\frac{\nu}{2}\nabla^2\Psi - p\right), \quad E\beta_2 = \frac{\partial}{\partial y}\left(\frac{\nu}{2}\nabla^2\Psi - p\right) \tag{11}$$

which are actually the antiplane stress-strain relations, in Eq. (2), expressed in terms of the stress potentials.

Substituting Eq. (11) into Eq. (6), we have

$$\nabla^2\left(\frac{\nu}{2}\nabla^2\Psi - p\right) = 0, \quad p = p_1 + \frac{\nu}{2}\nabla^2\Psi \tag{12}$$

where p_1 is a harmonic function.

Substituting Eq. (12) into Eq. (10), we have

$$\nabla^4\Psi = 0. \tag{13}$$

So far we have shown that Ψ is a bi-harmonic function and p is a harmonic function. It is easy to prove that Eq. (9f) is automatically satisfied with the above functions.

The compatibility condition Eqs. (9d) and (9e) can be rewritten as

$$2\frac{\partial\beta_1}{\partial y} = \frac{(1+\nu)}{E}\nabla^2 q + \left(\frac{\partial\beta_1}{\partial y} + \frac{\partial\beta_2}{\partial x}\right) \tag{14a}$$

$$2\frac{\partial\beta_2}{\partial x} = -\frac{(1+\nu)}{E}\nabla^2 q + \left(\frac{\partial\beta_1}{\partial y} + \frac{\partial\beta_2}{\partial x}\right) \tag{14b}$$

which lead to

Downloaded 04 May 2010 to 171.66.16.27. Redistribution subject to ASME license or copyright; see http://www.asme.org/terms/Terms_Use.cfm

$$\frac{(1+\nu)}{E}\nabla^2 q = \frac{\partial \beta_1}{\partial y} - \frac{\partial \beta_2}{\partial x}. \tag{15}$$

Equation (15) is automatically satisfied with β_1 and β_2 as defined in Eq. (11) and (8). Therefore,

$$\nabla^2 q = 0 \tag{16}$$

and hence, q is also a harmonic function. Furthermore, by the Cauchy-Riemann relations in Eq. (8), p and q are conjugate to each other.

In the plane-stress problems of a single-sheet material, the antiplane shear stresses are zero because the two surfaces are free. Then, we choose $p_1 = -\nu/2\nabla^2\Psi$, and hence $p = 0$, for the material. In laminated composites, however, the compatibility conditions at the laminar interfaces may impose conditions that require the existence of a nonzero potential p. From this, using Eq. (3) and (8), interlaminar shear stresses can be derived. Under the generalized plane-stress conditions, the averages of the antiplane shear stresses, τ_{xz} and τ_{yz}, over the laminate thickness are zero. These conditions are naturally satisfied because τ_{xz} and τ_{yz} are asymmetrical functions of z and the laminate has two surface layers.

By now, we have shown that p and q are harmonic functions and that Ψ is an Airy function. These stress potentials satisfy all the six strain compatibility conditions. Therefore, the solution derived from Ψ and p (or q) should represent a true stress state for each layer in the laminate. The last, but not the least, problem is to choose particular stress functions to meet the prescribed boundary conditions and interfacial compatibility conditions.

For that purpose, if we take advantage of the mathematical properties of harmonic and bi-harmonic functions, we can formulate a complex variable approach, in parallel to that developed by Muskhelishvili (1953). By satisfying the Cauchy-Riemann conditions in Eq. (8), p and q can be considered as the real and imaginary part of a complex variable function, $\chi(x + iy) = p + iq$, respectively. This complex function should be *analytic* within the region S occupied by the body. According to Muskhelishvili, the Airy function Ψ can be expressed in terms of two analytical functions, as

$$2\Psi = \bar{\xi}\Omega(\xi) + \omega(\xi) + \xi\bar{\Omega}(\bar{\xi}) + \bar{\omega}(\bar{\xi}) \tag{17}$$

where $\xi = x + iy$ is the complex variable and $\bar{\xi}$ denotes its conjugate, the same meaning also applies to complex functions. For antiplane shear stress potential p, we introduce another complex function ψ such that

$$2p = \chi(\xi) + \bar{\chi}(\bar{\xi}) = \psi'(\xi) + \overline{\psi'}(\bar{\xi}). \tag{18}$$

Using Eq. (7) and the complex variable mathematics similar to that in Muskhelishvili's book, we can express the in-plane stress components as

$$\sigma_x + \sigma_y = 2[\Omega'(\xi) + \bar{\Omega}'(\bar{\xi})] + \psi'(\xi) + \overline{\psi'}(\bar{\xi}) \tag{19a}$$

$$\sigma_y - \sigma_x + 2i\tau_{xy} = 2[\bar{\xi}\Omega''(\xi) + \omega''(\xi)] \tag{19b}$$

and the displacements (at $z = 0$) as

$$2\mu(u + iv) = \kappa\Omega(\xi) - [\xi\bar{\Omega}'(\bar{\xi}) + \overline{\omega'}(\bar{\xi})] + k\psi(\xi) \tag{20}$$

where μ is the shear modulus, $\kappa = (3 - \nu)/(1 + \nu)$, $k = (1 - \nu)/(1 + \nu)$. Using Eqs. (3) and (8), the antiplane shear stresses can be derived as

$$\tau_{xz} + i\tau_{yz} = -z\overline{\chi'}(\bar{\xi}) = -z\overline{\psi''}(\bar{\xi}). \tag{21}$$

Using Eq. (11), the second-order displacement can be derived as

$$E(\beta_1 + i\beta_2)z^2 = [2\nu\bar{\Omega}''(\bar{\xi}) - \overline{\psi''}(\bar{\xi})]z^2. \tag{22}$$

In the next section we will use the above complex variable formula to solve the boundary value problem of patching a circular cutout in a plate.

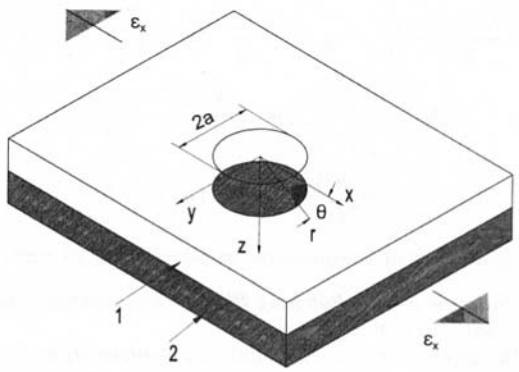

Fig. 2 A plate containing a circular cutout is patched with an intact plate. The composite structure is subjected to uniform strain at the remote ends.

A Boundary Value Problem Example

In this section we will solve a practical problem—patching a circular cutout—as an example of the boundary value problem formulation. We consider an infinite plate containing a circular hole of diameter $2a$, patched with an intact plate, as shown in Fig. 2. (This asymmetrical patching can be considered as one-half of the symmetrical patching of a hole-weakened plate with two intact plates on both sides.) The two plates are isotropic materials having different elastic modulus ($E_1 \neq E_2$) but the same Poisson's ratio ($\nu_1 = \nu_2 = \nu$). They are immediately bonded (or glued) such that antiplane shear stresses can transmit across the interface everywhere in the bonded region ($r > a$).

At infinity, the straining of the two plates is uniform and compatible, i.e.,

$$\epsilon_x^{(1)} = \frac{S^{(1)}}{E_1} = \epsilon_x^{(2)} = \frac{S^{(2)}}{E_2};$$

$$\epsilon_y^{(1)} = -\frac{\nu S^{(1)}}{E_1} = \epsilon_y^{(2)} = -\frac{\nu S^{(2)}}{E_2}; \tag{23}$$

where $S^{(1)}$ and $S^{(2)}$ are the stresses at infinity in the two plates, respectively.

Now, for mathematical treatment, we consider that the two plates are separately subjected to uniaxial tension with interlamilar shear stresses acting on the interface.

1 Solution for the Plate Containing A Circular Hole. For general solution, the stress potential can be written in Laurent series as

$$\Omega_1(\xi) = \frac{S^{(1)}}{4}\xi + \sum_{m=1}^{\infty}\frac{a_m}{\xi^m},$$

$$\omega_1'(\xi) = -\frac{S^{(1)}}{2}\xi + \sum_{m=1}^{\infty}\frac{b_m}{\xi^m}, \quad \psi_1(\xi) = \sum_{m=1}^{\infty}\frac{c_m}{\xi^m} \tag{24}$$

where a_m, b_m, and c_m are real constants.

Along the free edge of the hole, these stress potentials must satisfy the boundary condition

$$\Omega_1(\xi) + \xi\bar{\Omega}_1'(\bar{\xi}) + \overline{\omega_1'}(\bar{\xi}) + \int_\Gamma p_1 d\xi = 0. \tag{25}$$

Substituting (24) into (25) and integrating $p_1 = [\psi_1'(\xi) + \overline{\psi_1'}(\bar{\xi})]/2$ along the arc, we obtain the following relations, by comparing the coefficients of the Fourier series.

Downloaded 04 May 2010 to 171.66.16.27. Redistribution subject to ASME license or copyright; see http://www.asme.org/terms/Terms_Use.cfm

$$a_1 = \frac{S^{(1)}a^2}{2} - \frac{c_1}{2}, \quad a_m = -\frac{c_m}{2} \quad (m = 3, 5, 7 \ldots) \quad (26a)$$

$$b_1 = \frac{S^{(1)}a^2}{2}, \quad b_3 = \frac{S^{(1)}a^4}{2} - \frac{c_1 a^2}{3},$$

$$b_{m+2} = -\frac{m(m+1)c_m a^2}{2(m+2)} \quad (m = 3, 5, 7 \ldots) \quad (26b)$$

The coefficients of even-number subscripts are all zero.

2 Solution for the Patching Plate. The patching plate can be divided into two regions:

(i) the region of $r < a$ where only the in-plane stress functions exist because the upper and lower surfaces of the region are free of antiplane shear traction, then

$$\Omega_0(\xi) = \sum_{m=1}^{\infty} \delta_m \xi^m, \quad \omega_0'(\xi) = \sum_{m=1}^{\infty} \gamma_m \xi^m; \quad (27)$$

(ii) the region of $r > a$ where

$$\Omega_2(\xi) = \frac{S^{(2)}}{4}\xi + \sum_{m=1}^{\infty} \frac{\alpha_m}{\xi^m},$$

$$\omega_2'(\xi) = -\frac{S^{(2)}}{2}\xi + \sum_{m=1}^{\infty} \frac{\beta_m}{\xi^m}, \quad \psi_2(\xi) = \sum_{m=1}^{\infty} \frac{d_m}{\xi^m}. \quad (28)$$

α_m, β_m, δ_m, γ_m, and d_m are real constants.

Along the circular contour of $r = a$ between the two regions, stresses and displacements should be continuous:

$$\sigma_r|_{r^-=a} = \sigma_r|_{r^+=a}, \quad \tau_{r\theta}|_{r^-=a} = \tau_{r\theta}|_{r^+=a}$$
$$u|_{r^-=a} = u_{r^+=a}, \quad v|_{r^-=a} = v|_{r^+=a}, \quad (29)$$

which, according to Eqs. (19) and (20), can be written into

$$(\sigma_r - i\tau_{r\theta})|_{r=a} = \Omega_0'(\xi) + \overline{\Omega_0'}(\bar{\xi}) - [\bar{\xi}\Omega_0''(\xi) + \omega_0''(\xi)]e^{2i\theta}$$
$$= \Omega_2'(\xi) + \overline{\Omega_2'}(\bar{\xi}) + \tfrac{1}{2}(\psi'(\xi) + \overline{\psi'}(\bar{\xi}))$$
$$- [\bar{\xi}\Omega_2''(\xi) + \omega_2''(\xi)]e^{2i\theta} \quad (30)$$

and

$$2\mu(u + iv)|_{r=a} = \kappa\Omega_0(\xi) - [\xi\overline{\Omega_0'}(\bar{\xi}) + \overline{\omega_0'}(\bar{\xi})]$$
$$= \kappa\Omega_2(\xi) - [\xi\overline{\Omega_2'}(\bar{\xi}) + \overline{\omega_0'}(\bar{\xi})] + k\psi_2(\xi). \quad (31)$$

Substituting Eqs. (27) and (28) into Eqs. (30) and (31), and comparing the coefficients of the Fourier series, we obtain

$$\delta_1 = \frac{S^{(2)}}{4}, \quad \beta_1 = 0, \quad \gamma_1 = -\frac{S^{(2)}}{2} + \frac{1}{(\kappa+1)}\frac{d_1}{a^2}$$

$$\alpha_m = -\frac{\kappa}{\kappa+1}\frac{d_m}{2}, \quad (m = 1, 3, 5, \ldots)$$

$$\beta_{m+2} = -\frac{1}{2}\frac{\kappa}{\kappa+1}\frac{m(m+1)}{(m+2)}d_m a^2 \quad (m = 1, 3, 5, \ldots)$$

$$\delta_{m+2} = -\frac{1}{2}\frac{m}{(\kappa+1)(m+2)}\frac{d_m}{r^{2(m+1)}}, \quad (m = 1, 3, 5, \ldots)$$

$$\gamma_m = \frac{m+1}{\kappa+1}\frac{d_m}{2a^{2m}} \quad (m = 3, 5, \ldots). \quad (32)$$

3 Continuity at the Interface. The two plates are immediately bonded together such that τ_{xz} and τ_{yz}, as given by Eq. (21), are continuous across the interface everywhere in the region of $r > a$. This continuity condition requires that

Table 1 Values of the coefficient c_m

c_1	c_3	c_5	c_7	c_9	c_{11}	c_{13}
23.3560	1.7510	−0.2207	1.6290	−0.3733	1.5298	−0.4337

$$-h_1\psi_1'' = h_2\psi_2'' \quad (33)$$

which can be satisfied with

$$d_m = -\frac{h_1}{h_2}c_m \quad (m = 1, 3, 5, \ldots). \quad (34)$$

Now, we shall consider the conditions of displacement continuity, from which constants c_m or d_m will be determined. Using Eq. (20), the complex displacement field in the plate containing a hole can be written as

$$2\mu_1(u + iv)^{(1)}$$
$$= \frac{S^{(1)}}{4}\left[(\kappa - 1)\xi + 2\bar{\xi} + 2a^2\left(\frac{\kappa}{\xi} + \frac{1}{\bar{\xi}} + \frac{\xi}{\bar{\xi}^2} - \frac{a^2}{\bar{\xi}^3}\right)\right]$$
$$- \frac{1}{2}\sum_{m=1,3,\ldots} c_m\left(\frac{1}{\xi^m} + \frac{m\xi}{\bar{\xi}^{m+1}} - \frac{m(m+1)}{m+2}\frac{a^2}{\bar{\xi}^{m+2}}\right) \quad (35)$$

and that in the patching plate can be written as

$$2\mu_2(u + iv)^{(2)} = \frac{S^{(2)}}{4}[(\kappa - 1)\xi + 2\bar{\xi}] + \frac{1}{2(\kappa+1)}$$
$$\times\left(\frac{h_1}{h_2}\right)\sum_{m=1,3,\ldots} c_m\left(\frac{1}{\xi^m} + \frac{\kappa m\xi}{\bar{\xi}^{m+1}} - \frac{\kappa m(m+1)}{m+2}\frac{a^2}{\bar{\xi}^{m+2}}\right). \quad (36)$$

Here, the second-order displacements given by Eq. (22) are neglected, apparently because they are in the order of $(h/a)^2 \ll 1$, compared to that given by Eq. (35) and (36). Therefore, the displacement continuity condition at the interface can be written as

$$(u + iv)^{(1)} = (u + iv)^{(2)}. \quad (37)$$

When Eqs. (35) and (36) are substituted into Eq. (37) for equality, however, analytical expressions of c_m cannot be obtained in general. We use the least-square allocation method to determine these constants numerically from Eq. (37) at discrete points. Hypothetically, given any number of continuity points in the x-y plane, it is possible to find the corresponding number of c_m, since Eq. (37) have infinite terms. But, in practice, this hypothetical accuracy cannot be achieved because any computing tool has limited capacity and finite errors. In this study, we take m up to 13 in both Eqs. (35) and (36), and use the least-square method to solve for c_m. From a 10,000-point mesh (100 equally spaced points from $r/a = 1$ to 10 at each of the 100 equally divided values of θ from 0 to $\pi/2$). For numerical illustration, we assume that both plates have a Poisson's ratio of 0.3 but their stiffness ratio is $(E_1h_1)/(E_2h_2) = 0.5$, one contains a hole of $a = 1$ and the other is intact, and the remote stress in layer 1 is $S^{(1)} = 100$ MPa. The values of c_m, evaluated by computer software, are given in Table 1.

From Table 1 it can be perceived that only the first term of the antiplane shear potential series dominates in the region near the cutout. Higher-index terms will vanish rapidly away from the edge of the hole. Additional calculations that includes terms of m up to 29 yields results very close to the above sample calculation (with an error of one percent for the first term).

Downloaded 04 May 2010 to 171.66.16.27. Redistribution subject to ASME license or copyright; see http://www.asme.org/terms/Terms_Use.cfm

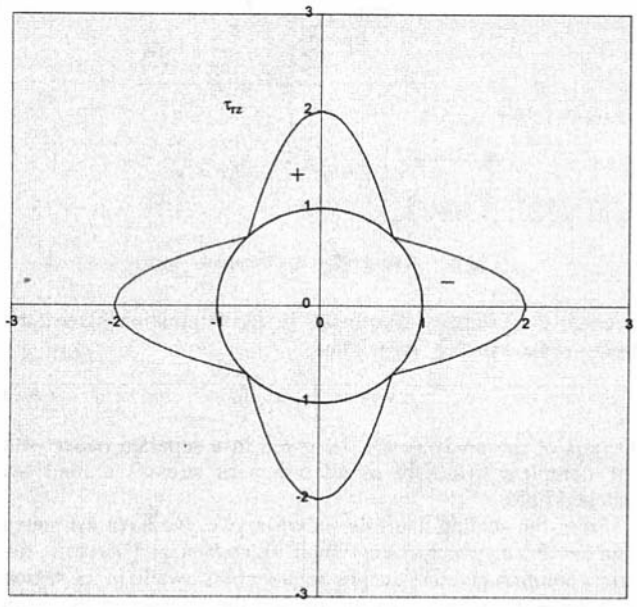

Fig. 3 Distribution of the interlaminar stress τ_{rz} around the hole of a = 1. The abscissa is parallel to the x-axis and the ordinate is parallel to the y-axis. The maximum interlaminar shear stress is normalized to be unity.

Figure 3 shows the distribution of the interlaminar τ_{rz} (at $z = h_1$), derived from the first term in Eq. (21) and normalized to unity, around the circular cutout. We note that, along the x-axis ($\theta = 0$), τ_{rz} (or τ_{xz}) reaches its maximum. The negative sign indicates that this shear stress acts against the stretching of the hole-weakened plate over the patching plate. The distribution of $\tau_{\theta z}$ has a 45-deg angle shift relative to the distribution of τ_{rz}. According to the formula of (21), the antiplane shear τ_{rz} in each plate does not vanish at the free boundary of $r = a$, but the two-layer average is zero. This only satisfies the condition (or assumption) of the generalized plane stress, a method of correction for the antiplane shear stress in the so-called boundary layer is discussed in the Appendix. A complete treatment to all stress components will be given in a separate paper.

Discussion

In this paper a higher-order plane-stress theory is derived for laminates consisting of isotropic layers under the condition of $\sigma_z = 0$. The new theory employs three stress potentials, Ψ (Airy function), p and q (conjugated harmonic functions), to describe the stress state (including antiplane shear stresses) in a laminate of finite thickness. These stress potentials satisfy the three-dimensional compatibility conditions as well as the equilibrium equations within each constituent layer. Therefore, by the theory of elasticity, the formulation represents an exact stress state in each layer, as long as the prescribed boundary conditions, including interfacial continuity conditions, are met. In the present treatment, the continuity of interlaminar shear stresses is satisfied everywhere in the lamination plane, but the continuity of displacement at the interface is only satisfied in the least-square sense. This weakness of the theory is perhaps due to the assumption of $\sigma_z = 0$, which obviously simplifies the true stress state near material discontinuities or in regions of high-stress gradients across dissimilar materials in laminates. More stringent requirements of displacement continuity would cause a singularity of σ_z near the free edges (Pagano and Pipes, 1970; Pagano, 1978). Comparing to other treatments (e.g., finite element methods) that set displacements to be continuous everywhere in the lamination plane, the least-square satisfaction seems to correspond to weak interfacial conditions that allow the existence of "dislocations" or viscous sliding to remove the stress singularity. Therefore, the present theory seems to apply to laminates that are weakly bonded ("weak" is relative to the strong continuity within the laminar). Weak interfaces such as grain boundaries and glue layers are most commonly seen in the real world. Nevertheless, σ_z should be present in the free-edge boundary region, but it is apparently not included in the present formulation. This discrepancy can be corrected by incorporating a so-called boundary layer along the free edge where the average σ_z can be estimated, as shown in the Appendix.

The great advantage of the present theory over other lamination theories comes with the mathematical power of its complex-variable formulation to solve the quasi-three-dimensional stress problems of thin laminates. Extending Muskhelishvili's formulation for the classical plane elasticity problems, we have developed a complex variable boundary value problem formulation including antiplane shear potential functions. This approach can be used to address various boundary value problems of thin laminates, of course with the limitations of the generalized plane-stress assumption (Sokolnikoff, 1956).

In the example of patching a circular cutout discussed in this paper, it is shown that interlaminar stresses exist by the requirement of compatibility, and the existence of these interlaminar stress affects the in-plane stresses in the adjacent layers. A complete stress analysis for the problem will be given in a separate paper. In this paper the example is merely shown here of how a boundary value problem of a laminate can be solved using the present theory. Particularly relevant to lamination problems, the interfacial continuity conditions of antiplane shear stresses and in-plane displacement are considered, as given in Eqs. (33) and (37). In general, the magnitude and distribution of the interlaminar shear stresses depend on the displacement continuity conditions at the interface. This implies that interlaminar shear stresses depend on the quality of interfacial bonding, which is true in reality. The present theory also allows one to deal with interfaces that contain some delaminated regions. Further discussions on these topics are out of the scope of the present paper.

Acknowledgment

The work was partially conducted at the Structures, Materials and Propulsion Laboratory, Institute for Aerospace Research, National Research Council of Canada.

References

Bhat, N.V., and Lagace, P.A., 1994, "An Analytical Method for the Evaluation of Interlaminar Stresses Due to Material Discontinuities," *Journal of Composite Materials,* Vol. 28, pp. 190–210.

Kassapoglou, C., and Lagace, P.A., 1986, "An Effective Method for the Calculation of Interlaminar Stresses in Composite Materials," ASME JOURNAL OF APPLIED MECHANICS, Vol. 53, pp. 744–750.

Muskhelishvili, N.I., 1953, *Some Basic Problems of The Mathematical Theory of Elasticity* Noordhoff, Groningen, Holland (translated by J.R.M. Radok).

Pagano, N.J., 1978, "Stress Fields in Composite Laminates," *International Journal of Solids and Structures,* Vol. 14, pp. 385–400.

Pipes, B.R., and Pagano, N.J., 1970, "Interlaminar Stresses in Composite Materials under Uniform Axial Extension," *Journal of Composite Materials,* Vol. 4, pp. 538–548.

Sokolnikoff, I.S., 1956, *Mathematical Theory of Elasticity,* McGraw-Hill, New York.

Timoshenko, S.P., and Goodier, J.N., 1970, *Theory of Elasticity,* 3rd Ed., McGraw-Hill, New York, Chapters 2 and 8.

Timoshenko, S.P., and Woinowsky-Krieger, S., 1959, *Theory of Plates and Shells,* 2nd Ed., McGraw-Hill, New York, Chapter 2.

Tsai, S.W., and Hahn, H.T., 1980, *Introduction to Composite Mechanics,* Technomic Publishing Co., Lancaster, PA.

APPENDIX

Boundary Layer at the Free Edge

We notice that the interlaminar stress τ_{rz}, as derived from Eq. (21), is nonzero at the free edge of the hole, but its average

Downloaded 04 May 2010 to 171.66.16.27. Redistribution subject to ASME license or copyright; see http://www.asme.org/terms/Terms_Use.cfm

over the two layers is zero under the generalized plane-stress condition. One may be interested to what the stress condition is, if the edge of the hole is absolutely free. In this case, a *boundary layer* needs to be considered to modify the stress distribution.

Let us take an element of the boundary layer for consideration, as shown in Fig. A1. On the inner side of this element there exist surface tractions of the antiplane shear stress and the second-order in-plane stress σ_r (the main component of σ_r has already vanished), which can be known from the present theory. The outer side, which is the edge of the hole, is absolutely stress-free. The stress distribution within this element is generally three-dimensional. For simplicity, we only consider the force balance along the r and z directions for the boundary layer element.

Suppose that the boundary layer has a thickness of t and assume $t \ll a$. The force equilibrium in the r-direction is

$$\int_0^h \sigma_r dz + \int_0^t \tau_{rz} dr = 0. \tag{A1}$$

We assume that, as first approximation, τ_{rz} decreases linearly to zero at the boundary of the hole. Then, t can be estimated from integration of Eq. (A1).

From the second-order displacement functions, using Eqs. (1), (2), and (22), we can obtain the second-order σ_r, which is in the order of $(h/a)^2$, and hence t is proportional to h^2/a, which is indeed small compared to the radius of the hole.

Now, we consider the force balance in the z direction. We assume that the singularity of σ_z has been removed and an

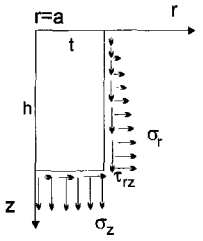

Fig. A1 A section of the boundary layer

average is uniformly distributed in the lamination plane (the bottom plane in Fig. A1). Then,

$$\sigma_z t = -\int_0^{h_1} \tau_{rz} dz. \tag{A2}$$

Details of the analysis will be given in a separate paper with the complete treatment of all orders of stresses around the patched hole.

From the scaling analysis shown above, we have estimated that $t \sim h^2/a$, which is very small since $h \ll a$. Therefore, the stress solution given in the previous section is valid in the region $r > (a + t)$, which also means that the stresses in the main body are practically unaltered by the presence of the boundary layer. Within this boundary layer, the stress state is no longer plane stress.

In the light of the above discussion, with the incorporation of a boundary layer, we shall consider that the present theory formulates a rather accurate approximation to the true stress state near material discontinuities in composite laminates.

Downloaded 04 May 2010 to 171.66.16.27. Redistribution subject to ASME license or copyright; see http://www.asme.org/terms/Terms_Use.cfm

A Simplified Method for Calculating the Crack-Tip Field of Functionally Graded Materials Using the Domain Integral

P. Gu[1]

M. Dao
Assoc. Mem. ASME

R. J. Asaro

Division of Structural Engineering,
University of California at San Diego,
La Jolla, CA 92093-0085

A finite element based method is proposed for calculating stress intensity factors of functionally graded materials (FGMs). We show that the standard domain integral is sufficiently accurate when applied to FGMs; the nonhomogeneous term in the domain integral for nonhomogeneous materials is very small compared to the first term (the standard domain integral). In order to obtain it, the domain integral is evaluated around the crack tip using sufficiently fine mesh. We have estimated the error in neglecting the second term in terms of the radius of the domain for the domain integration, the material properties and their gradients. The advantage of the proposed method is that, besides its accuracy, it does not require the input of material gradients, derivatives of material properties; and existing finite element codes can be used for FGMs without much additional work. The numerical examples show that it is accurate and efficient. Also, a discussion on the fracture of the FGM interlayer structure is given.

1 Introduction

The mechanics of functionally graded materials (FGM), including crack problems, have been intensively studied recently. It has been shown that for FGM crack problems the crack tip has a regular square-root singularity, the stress and displacement near-tip fields are of the same forms as those for homogeneous materials (see Delale and Erdogan, 1983, 1988; Gu and Asaro, 1997a, b). So the influence of material gradients at the near tip manifests itself through the stress intensity factors. In other words, the stress intensity factors uniquely characterize the near-tip field. Knowing the structure of the crack-tip field, it is important to accurately calculate the stress intensity factors and determine the effect of material gradients on them for different geometries and loadings, including those often-used specimens. Finite element analysis which can handle difficult material behaviors and geometries as well as various loadings provides useful and the most often-used way to solve mechanical and thermal problems including those involving FGMs. In this paper, we present a simple and sufficiently accurate finite element method for calculating the crack-tip field for FGMs, which can be easily incorporated into existing finite element codes and commercial software packages without much additional work.

The often-used method to calculate the crack-tip field, stress intensity factors (elastic case), and energy release rate (elastic or plastic case), involves evaluating the J-integral (Rice, 1968) using the solved stress and deformation fields around crack tip. For homogeneous materials, this has been an efficient way since the path independence of the J-integral allows us to perform the calculation along a path not too close to the tip so that the inaccuracy of field variables at the tip region due to the singularity can be avoided. Later, the domain integral method has been developed to perform the calculation of the J-integral (Li, Shih and Needleman, 1985; Shih, Moran and Nakamura, 1986; Moran and Shih, 1987). The domain integral method has been shown to be more efficient and more accurate than direct calculation of the J-integral, since the domain integration comes more naturally than the line integration of the two-dimensional space and the surface integration of the three dimensional space in finite element analysis. Works along similar line as the domain integral can be found in the early papers by Parks (1974, 1977), Hellen (1975) and deLorenzi (1982), whose virtual crack extension method is the special case of the domain integral. The domain integral method has been implemented in numerous programs to solve crack mechanics, including the well-known commercial package ABAQUS. In this paper, we use the domain integral methodology to treat the FGM case. In the non-homogeneous case, there is an additional term besides the regular one due to the variation of material properties. In our analysis of two-dimensional elastic crack problems of non-homogeneous materials, to capture the singularity and material property variation, the mesh is designed such that the smallest elements at the crack tip are very small, about 10^{-5} times a characteristic length, which is usually the crack length, and even much smaller for inelastic problems. The material variation is achieved by using corresponding material properties at Gauss integration points (different Gauss points have different properties). For such mesh design, to perform the domain integration, the domains can be chosen as the circular regions formed by the first few rings of elements. In such a situation, we show that the second term in the domain integral for nonhomogeneity is very small compared to the first term, the standard domain integral, and may be neglected. Therefore the domain integral can be calculated numerically in the same way as that for homogeneous materials, using the standard domain integral. From the numerical point of view, this allows us to apply existing finite element programs for homogeneous materials to nonhomogeneous materials, avoiding the additional programming work.

The current study is focused on elastic two-dimensional and three-dimensional problems. The method may also be extended

[1] MARC Analysis Research Corporation, 4330 La Jolla Village Drive, Suite 320, San Diego, CA 92122.

Contributed by the Applied Mechanics Division of THE AMERICAN SOCIETY OF MECHANICAL ENGINEERS for publication in the ASME JOURNAL OF APPLIED MECHANICS.

Discussion on the paper should be addressed to the Technical Editor, Professor Lewis T. Wheeler, Department of Mechanical Engineering, University of Houston, Houston, TX 77204-4792, and will be accepted until four months after final publication of the paper itself in the ASME JOURNAL OF APPLIED MECHANICS.

Manuscript received by the ASME Applied Mechanics Division, Mar. 9, 1998; final revision, July 14, 1998. Associate Technical Editor: M.-J. Pindera.

 Copyright © 1999 by ASME

Downloaded 04 May 2010 to 171.66.16.27. Redistribution subject to ASME license or copyright; see http://www.asme.org/terms/Terms_Use.cfm

to the nonlinear material behavior. The numerical examples given include a sandwiched structure with a FGM interlayer, which illustrates the advantage of using FGM to reduce material mismatch between the upper and lower layers. For such structures, cracks may form at one side and propagate to the other side through the FGM interlayer when the microscopic defects and external loading are favorable. The crack in the sandwiched structure solved in this paper is along the layers' thickness direction with the crack tip inside the FGM, and the loading includes remote bending, three-point bending, and four-point bending. This kind of configuration may also be good for fracture testing of FGMs since the FGMs are usually very thin so that mechanical testing may be handled when bonding them to two bulk materials. In general, the solutions to the three-point bending and four-point bending specimens depend on several parameters, including geometry, loading, and material variation. We write them in a compact form such that the functionality of each parameter may be clearly understood. These examples show a way to systemically present the solutions so that they can be documented and are easy to use in practice.

The paper consists of three sections. Besides this Introduction, Section 2 is the discussion of the domain integral method in which we estimate the second term due to nonhomogeneity and show that based on the analysis, the term can be neglected. Section 3 contains numerical examples.

2 Numerical Method

The crack-tip stress field in a FGM has a regular singularity (see Delale and Erdogan, 1983, 1988; Gu and Asaro, 1997a, b) and the singular term for plane problems is given by

$$\sigma_{ij} = \frac{K_I}{\sqrt{2\pi r}}\,\sigma_{ij}^{I}(\theta) + \frac{K_{II}}{\sqrt{2\pi r}}\,\sigma_{ij}^{II}(\theta) \tag{1}$$

where the angular functions σ_{ij}^{I} and σ_{ij}^{II} are independent of material properties and their variations and are the same as those for homogeneous materials. The displacement singular term is given by

$$u_i = \frac{K_I}{2\mu_0}\sqrt{\frac{r}{2\pi}}\,u_i^{I}(\theta) + \frac{K_{II}}{2\mu_0}\sqrt{\frac{r}{2\pi}}\,u_i^{II}(\theta). \tag{2}$$

Here, μ_0 is the shear modulus at the crack tip. The angular functions u_i^{I} and u_i^{II} are also independent of material gradients, and are the same as those for homogeneous materials. Material gradients only affect the near-tip fields through the mode I and mode II stress intensity factors, K_I and K_{II}. The energy release rate is defined as

$$G = -\frac{\partial \Pi}{\partial a} \tag{3}$$

which is related to the near-tip field by

$$G = \frac{K_I^2}{E_0} + \frac{K_{II}^2}{E_0} \tag{4}$$

where E_0 is Young's modulus at the crack tip. The energy release rate can be represented by the following line integral:

$$J = \lim_{\Gamma \to 0} \int_{\Gamma} (W\delta_{1i} - \sigma_{ij}u_{j,1})n_i\,dC \tag{5}$$

where W is the strain energy density and n_i is the outward normal of the path Γ, which starts from a point on the lower crack face and ends at another point on the upper crack face. For the homogeneous case, the integral under the limit is divergence free; therefore, it is path independent and the limit is not needed. In this case, the J in (5) is Rice's J-integral (Rice, 1968). For nonhomogeneous materials, path independence occurs when the crack is perpendicular to the material property variation direction, since in this case the integral is still divergence free.

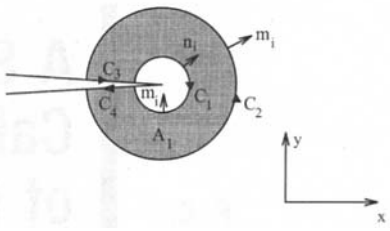

Fig. 1 A simply connected domain A_I enclosed by the contour C ($C = C_1 + C_2 + C_3 + C_4$) near crack tip. The domain is where the domain integral is evaluated.

There are usually several ways to calculate stress intensity factors after the stress and displacement fields are obtained. In the stress matching and displacement matching, the stress intensity factors are obtained by extrapolating from the stresses or displacements ahead of the crack tip using (1) or (2). For example, K_I is obtained by substituting the obtained normal stress ahead of the crack tip into (1). The matching method has the advantage that almost no additional calculation is required even in the FGM case, but it requires a high degree of mesh refinement and often suffers from instability as the crack tip is approached (see Anderson, 1995). Another way, the domain integral method, which is an energy approach based on the J-integral and which has been proved to be efficient for homogeneous materials, is the focus of our numerical study here.

In the domain integral method, the energy release rate J is calculated through an area integral in the two-dimensional case and stress intensity factors are then obtained using (4). The area integral approach provides much better accuracy than directly evaluating the contour integral in (5), and is easier to implement numerically. Early works along the line of the energy approach were given by Parks (1974, 1977), Hellen (1975), and deLorenzi (1982). Shih and his co-workers (see Li, Shih, and Needleman, 1985; Shih, Moran, and Nakamura, 1986; Moran and Shih, 1987) formulated the domain integral methodology in a general way. For homogeneous materials, it has been applied in above works to elastic and plastic material responses, mechanical and thermal loadings, and two-dimensional and three-dimensional spaces. We will discuss the application of the domain integral to nonhomogeneous materials. In particular, we will show that the integral term representing the effect of nonhomogeneity may be neglected when evaluating the integration at a region close the crack tip; therefore, the standard domain integral for homogeneous materials gives sufficient accuracy. We will discuss the elastic case; the conclusion may be extended to the power-law hardening case, i.e., HRR singularity (Hutchinson, 1968; Rice and Rosengren, 1968).

Consider an annular region A_I around the crack tip in the two-dimensional case, as shown in Fig. 1. For simplicity in the discussion, we consider that the material variation is along the x-axis; and only one of the two material parameters, the Young's modulus, has a gradient where the Poisson's ratio is taken as a constant since its variation is usually small compared to the former. The conclusion obtained below can be extended to the general material variation case. Both the inner and outer boundary of the region A_I are sufficiently close to the crack tip. The J given in (5) can be written in terms of the boundary integral,

$$J = \oint_C (\sigma_{ij}u_{i,1} - W\delta_{1j})qm_j ds \tag{6}$$

where $C = C_2 + C_3 + C_1 + C_4$ is the boundary of A_I; m_j is the outward normal of A_I; on C_1, $m_j = -n_j$, and on C_2, $m_j = n_j$; and q is a smooth function which has the value of unity on C_1 and zero on C_2. Applying the divergence theorem to (6) gives

Downloaded 04 May 2010 to 171.66.16.27. Redistribution subject to ASME license or copyright; see http://www.asme.org/terms/Terms_Use.cfm

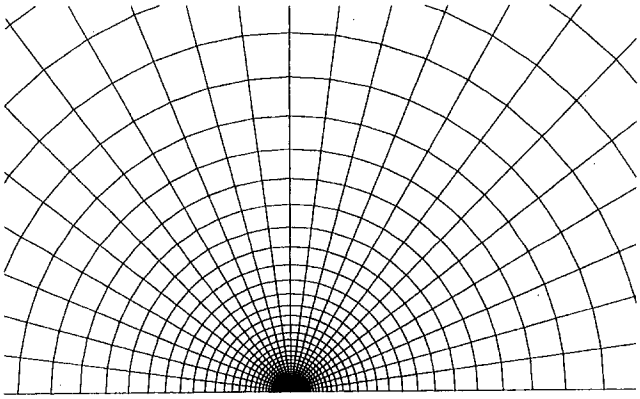

Fig. 2 Finite element mesh of the crack-tip region. In our calculation four-node bilinear elements are used. The smallest element at the tip is 10^{-5} times a characteristic length.

$$J = \int_{A_I} (\sigma_{ij} u_{i,1} - W\delta_{1j}) q_{,j} dA - \int_{A_I} W_{,1} q dA. \tag{7}$$

Here, $W = W[E(x), \epsilon(x, y)]$. The derivative of W under the second integral is with respect to the coordinate x in $E(x)$. Comparing with the homogeneous case, the second integral is an additional term which represents the effect of nonhomogeneity.

In numerical implementation, the inner contour C_1 is usually taken as the crack tip, and the outer boundary C_2 is taken to be the same as element boundaries. The function q defined above is an arbitrary function as long as it gives the correct values at the boundaries, C_1 and C_2. It was shown by Shih and his coworkers in the previously mentioned papers that the calculated J is insensitive to the choice of q. The value of it within an element may be taken as

$$q = \sum_{i=1}^{n} N_i q_i \tag{8}$$

where N_i are the shape functions of the element, n is the number of nodes per element, and q_i are the nodal values of q, which are assigned in accordance with a smooth function varying from zero at the outer boundary to unity at the crack tip. The derivative of q with respect to the coordinate x_i is

$$\frac{\partial q}{\partial x_i} = \sum_{i=1}^{n} \sum_{k=1}^{2} \frac{\partial N_i}{\partial \eta_k} \frac{\partial \eta_k}{\partial x_i} q_i \tag{9}$$

where η_k are the coordinates in the isoparametric space. Evaluating the quantity under the integral in (7) at the Gauss integration points, J is obtained numerically by

$$J = \sum_{A_I} \sum_{p=1}^{n} \left\{ [(\sigma_{ij} u_{i,1} - W\delta_{1j}) q_{,j} - W_{,1} q] \det \left(\frac{\partial x_k}{\partial \eta_k} \right) \right\}_p w_p. \tag{10}$$

Here, w_p is the weight function of integration, and det $(\cdot)$ is the determinant of Jacobian matrix.

The mesh design for our nonhomogeneous problems is a standard mesh design for crack problems. The crack tip is surrounded by an arrangement of wedge-shaped isoparametric elements. The same type of elements makes circular rings which surround the wedge-shaped elements at the tip (see Fig. 2). In this region, the size of the elements increases along the radial direction according to the exponential scale which gives the unit aspect ratio of the elements. The smallest elements at the crack tip are smaller or equal to $10^{-5}a$, where a is a characteristic length. Between the circular region and the region far away from the tip where the stresses vary regularly, there is a transition zone in which the element shape changes gradually from the curved polygon to the regular element shape. The geometry of a typical mesh of this kind was shown in the previously mentioned papers (also see Shih and Asaro, 1989). It is noted that near the tip the mesh needs to be refined to account for the high-stress gradients associated with the singularity; in the FGM case, also to account for the material property variation.

Using this type of mesh, we show here that if we evaluate the domain integral in the region sufficiently small around the crack tip, the value of the second term in (7) involving the derivative of W is very small, essentially negligible. The domain integral in practice can be calculated in the region close to the crack tip (the circular domain consisting of the first 10 or 20 circular rings of elements at the crack tip zone) as demonstrated in the next section. In our calculations, as mentioned above, the smallest element is in the size of $10^{-5}a$, where a is the characteristic length. In such a situation, the second integral in (7) may be estimated as follows. Using the above mesh design, the first 10 or 20 rings of elements are arranged within the radius $10^{-4}a$ from the crack tip. The weight functions for the two integrals in the expression (7) are q and $q_{,j}$. If the pyramid shape for the function q (Fig. 3(a)) is used, its derivative with respect to the coordinates is on the order of $10^4 a^{-1}$ considering that the domain is within a circle with radius $10^{-4}a$. Then, the weight functions of the first and second integrals are of the orders 10^4 and 1, respectively. Note that a^{-1} in the derivative of q has been moved to the integrand of the first integral. The first integral is overweighted by its weight function compared to that of the second. On the other hand, the two integrands are not likely to differ by such a large amount as that of the weight functions, i.e., to be of the same order. This is due to the following: (a) they both are essentially energy density terms (energy density unit/length) calculated using stress and strain fields; (b) both are proportional to the loading, the square of the stress intensity factor K_I^2; and (c) the first is proportional to the inverse of the modulus and the second is proportional to the derivative of the modulus divided by the square of the modulus. Since such a small domain for the domain integral is well within the K-dominance zone, the asymptotic expressions (1) and (2) are valid within it. The K-dominance zone for FGMs has been examined in Gu and Asaro (1997b), where it has been shown that within the distance of a few percent of the characteristic length, the difference of the stress fields of the asymptotic and full solutions are within a few percent. Substituting (1) and (2) into the two integrands, (b) and (c) can be confirmed. This permits us to write

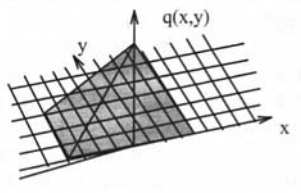

(a) pyramid function

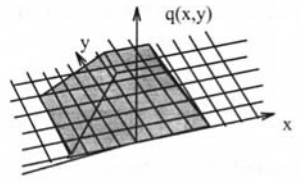

(b) plateau function

Fig. 3 The two often used shapes of q function

Downloaded 04 May 2010 to 171.66.16.27. Redistribution subject to ASME license or copyright; see http://www.asme.org/terms/Terms_Use.cfm

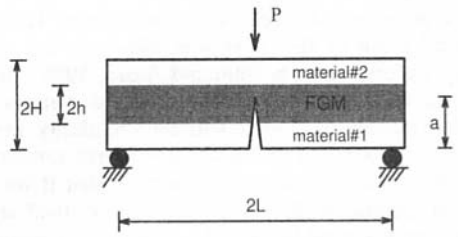

Fig. 4(a)

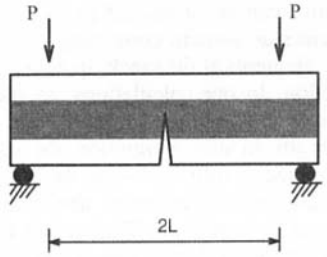

Fig. 4(b)

Fig. 4 Two sandwiched bending specimens with FGM interlayer: (a) three-point bending; (b) four-point bending

$$[\text{first integrand}] = \frac{K_I^2}{E_0 a}\frac{f_1(\theta)}{r}$$

$$[\text{second integrand}] = \frac{K_I^2 E_0'}{E_0^2}\frac{f_2(\theta)}{r}. \qquad (11)$$

In (11), E_0' is the derivative of the Young modulus at the crack tip; f_1 and f_2 are obtained from angular functions in (1) and (2), and therefore they do not have much effect on the magnitudes of the two integrands. In our discussion, we assume that there is only mode I loading. However, one can obtain the same conclusion for mixed-mode presentation through similar steps. Also, $E_0'a$ is roughly proportional to E_0 as can be seen from the following example. Consider the FGM interlayer in Fig. 4 with linear modulus variation, we have $E_0 = (E_2 + E_1)/2$ and $E_0'a = E_0 a\zeta/2/h$ when the crack tip is at the middle of the FGM interlayer, where the subscripts denote the properties for material #1 and #2, and $\zeta = (E_2 - E_1)/(E_2 + E_1)$. The variation of the multiplier ζ, as E_2/E_1 varies, is small. So, the two scale factors in the above expression (11) would not differ much as long as a and h do not differ much, and this is similar for other material variation forms. Note that if h is the smallest length compared to other dimensional lengths, one could chose the characteristic length a to be h so that $a/h = 1$. If E_0 and $E_0'a$ are of the same order, from the above analysis we estimate that the first integral is 10^4 times the second integral. In general, the difference between E_0 and $E_0'a$ is not significant at all, compared to that of the two weight functions and therefore the second term in (7) may be neglected. It may also be shown that the conclusion is true by a similar step if the plateau shape for the q function (Fig. 3(b)) is used.

Suppose that r_D is the radius of domain where the domain integral is evaluated and within it the field can be well represented by the singular field (1) and (2), then from the above analysis the error of neglecting the second term can be estimated as

$$e \approx \frac{r_D E_0'/E_0}{1 + r_D E_0'/E_0}. \qquad (12)$$

The error is very small if we choose r_D to be sufficiently small. The simplified method has the following advantages: (a) it gives the same accuracy for the stress intensity factors as the domain integral for homogeneous materials, as we shall see in numerical examples; (b) the input of the derivatives of the material properties (gradients) is not required such that in the numerical implantation only material properties need to be assigned to elements or Gauss integration points and this is easy to achieve; and (c) no additional calculations are required as compared to the homogeneous case.

When the gradient of the thermal expansion coefficient of the FGM does not vanish and thermal loading (temperature change) is applied, the additional term related to the gradient of the thermal expansion coefficient is an integrand under the second integral in (7) which can be written as

$$[\text{thermal term under second integral}] = K_I T_0 \alpha_0' \frac{f_3(\theta)}{\sqrt{r}} \qquad (13)$$

where T_0 is temperature change at the crack tip, α_0' is the gradient of thermal expansion coefficient at the crack tip, and f_3 is obtained from the angular function in (1). This term may also be neglected due to the following reasons. First, it is under the second integral in (7). As analyzed before, the first integral is overweighted. Second, the $1/r$ factor in first integrand, given in (11), is much larger than the $1/\sqrt{r}$ factor in (13), in the domain with radius $10^{-4}a$. Third, since the stress solution only depends on the ratio of the muduli of the two bulk materials for traction problems (as we shall see in next section), the two moduli may be chosen in the calculation such that $1/E_0$ in (11) is in a normal range. Having these, we can estimate that the magnitude of (13) and that of the first expression of (11) do not differ much.

We have gone a rigorous way to show that the standard domain integral can be directly used for nonhomogeneous materials. A simple way to argue this is that since the asymptotic expressions (1) and (2) are the same as those for homogeneous materials with the material properties being those at the crack tip, there exists a small homogeneous zone which may be regarded as the K-dominance zone so that the standard domain integral is valid there. But from this simple way it is impossible to obtain the above error analysis. When the second term is neglected, the expression to numerically calculate domain integral becomes

$$J = \sum_{A_I}\sum_{p=1}^{n}\left\{[(\sigma_{ij}u_{i,1} - W\delta_{1j})q_{,j}]\det\left(\frac{\partial x_k}{\partial \eta_k}\right)\right\}_p w_p, \qquad (14)$$

which is the same as that for the homogeneous case.

When the domain integral is obtained, the stress intensity factors can be evaluated using (4). If there is only mode I stress intensity factor at the tip due to the symmetric material properties, the geometry and the loading, it can be evaluated directly from (4). If it is a mixed-mode problem, the interaction energy release rate defined in Shih and Asaro (1989) may be evaluated instead of the energy release rate in (4). Using the interaction energy release rate, modes I and II can be separated.

3 Numerical Results

We have extensively tested the numerical method using many crack geometries and loadings. The results have been compared with those obtained by other methods, such as displacement-matching and singular integral equations. All showed the method to be accurate, convergent to the correct solution. The domain integral evaluated from the domains near the tip is stable, independent of the domain chosen. The following are four examples that illustrate this.

The first example is an edge-cracked plate made of a FGM, subject to remote constant strain. It has been solved previously by Erdogan and Wu (1993), using the singular integral equation method. We use it to check the accuracy of our scheme. The second and the third are three-point bending and four-point bending specimens made of sandwiched structures with the in-

Downloaded 04 May 2010 to 171.66.16.27. Redistribution subject to ASME license or copyright; see http://www.asme.org/terms/Terms_Use.cfm

terlayers being FGMs (Fig. 4). The interlayer is a zone of transition wherein the material properties change smoothly from the upper layer to the lower layer. The length $2L$ is assumed to be sufficiently large so that it would not affect the solutions. The height of the bars is $2H$, the crack length a, and the height of the interlayers $2h$. The crack is perpendicular to the upper and lower boundaries, and its tip is inside the FGM. The sandwiched structures can be used to study either the fracture of FGMs or the interface behavior when the interlayer thickness is small compared to those of the two bulk layers. The geometry of the first example is the same as Fig. 4, and the only difference is that it is a single piece of FGM for the constant strain problem.

The mesh design was discussed in the previous section. The four-node bilinear elements are used in the study. We have extensively tested the numerical method by changing the material properties, the loadings, and the specimen dimensions. We also have changed the size of the domain by changing the number of rings of elements. All of the stress intensity factors evaluated from the domain integral have shown the accuracy of the scheme. The convergence study results will be provided in tabular form later in the section. The material property variation is achieved by using corresponding material properties at Gauss integration points of each element. We use the software package ABAQUS to perform the calculation, and only the user-subroutine UMAT is required for the material variation. The J-integral is also calculated using the standard domain integral function provided in ABAQUS.

For real FGMs, the property variation along the thickness can be linear, exponential, or some other form. For elastic problems, both Young's modulus and Poisson's ratio vary with the position in general. It is assumed in all examples in this section that the former has the major effect and the latter is taken to be constant. It is reasonable to do so since the variation of the Poisson's ratios is usually small compared to that of the moduli. For the problems studied (see Fig. 4), the Young's modulus is expressed by the following:

$$E(y) = Ay + B$$
$$E(y) = A \exp(By) \tag{15}$$

where A and B are material constants which represent material gradients. The origin of the coordinates is at the center of these specimens and y is along the thickness direction. The first expression in (15) is a linear form, whereas the second is an exponential form. Given the moduli of the lower and upper layer, E_1 and E_2, the two constants are expressed as

$$A = \frac{E_2 - E_1}{2h}, \quad B = \frac{E_2 + E_1}{2} \tag{16}$$

for the linear gradient, and

$$A = \sqrt{E_1 E_2}, \quad B = \frac{1}{2h} \log\left(\frac{E_2}{E_1}\right) \tag{17}$$

for the exponential variation.

In the first example, material variation along the thickness is taken to be the exponential form in (15). The loading is a constant strain ϵ_0 far away from the crack at the two ends which gives rise to a remote stress field, $\sigma = \sigma_0 \exp(By)$, where $\sigma_0 = A\epsilon_0/(1 - \nu^2)$. The energy release rate was calculated from the domains formed by the first 20 rings, using the J-integral evaluation function in ABAQUS. The results from the first ten rings are shown in Table 1, given for different E_2/E_1 ratios, and the results from the domains formed by the remaining ten rings of elements basically are the same as those of column 9 and 10 in the table. The ratio E_2/E_1 is the modulus of the upper boundary over that of the lower boundary. In the calculation we choose $\sigma_0 = 1$ and the crack length $a = 1$. From the table, the convergence of the numerical method is clearly seen. When the ratio is 1, it represents homogeneous material. In the strong material variation case, the ratio is 10. We see that in both cases the convergence behavior is the same. So, we may conclude that the convergence of using the standard domain integral for FGMs is the same as that for homogeneous materials. The domain integral scheme has been proved to be a useful one in the numerical analysis of the homogeneous fracture. Note that those results from the domains formed by the first two rings usually have a relatively large error in both the homogeneous and FGM case, due to the inaccuracy of the innermost elements. Thus, those results from the domains formed by the first two rings may be disregarded. The stress intensity factors obtained from the four cases in the table, in which the ratio is equal to 0.1, 0.2, 5, and 10, are 4.01, 4.22, 6.49, and 7.48, respectively. These results are the same as those obtained from the singular integral equation method provided by Erdogan and Wu (1993).

Due to the symmetric geometries and symmetric material properties with respect to the crack line for the two specimens in Fig. 4, there is only mode I stress intensity factor at the crack tip for the second and third examples. Since the near-tip fields are of the same form as those for homogeneous materials, the generic form of the stress intensity factor may be written as

$$K_I = Ta^{1/2} Y\left(\frac{E_2}{E_1}, \frac{a}{H}, \frac{h}{H}, \wp\right) \tag{18}$$

where T is a representative stress magnitude, a is a characteristic length (can be taken as the crack length) and Y is a dimensionless function which is related to the geometries of the problems and material properties: the ratio of the moduli and $\wp$, the form of material variation. There are four independent variables in the dimensionless function Y. For known material variation $\wp$ and the thickness of the FGM h/H, the solution Y depends on the modulus ratio and the position of the crack tip a/H, and may be systemically presented by tables or figures. For example, if using tables, each table contains the solution for given $\wp$ and h/H, where the row represents E_2/E_1 and the column represents a/H. If using figures, each figure contains the solution for given $\wp$ and h/H, and in the figure each curve corresponds to a value E_2/E_1 with the x-axis being a/H. Given the representatives of $\wp$ and h/H, we construct the complete solution in above ways for others to use. For homogeneous materials, Y is only related to a/H. It is obtained in terms of a figure or empirical expressions which are given in the handbook by Tada et al. (1985).

Figure 5 shows the solution of mode I stress intensity factor versus the position of the crack tip in the FGM for linear mate-

Table 1 Convergence for the Remote Constant Strain Problem

	Energy release rate calculated from the first ten rings [in units of $\sigma_0^2 a/E_1$]									
E_2/E_1	1	2	3	4	5	6	7	8	9	10
0.1	42.43	46.15	46.21	46.24	46.25	46.26	46.26	46.26	46.28	46.27
0.2	33.26	36.17	36.22	36.24	36.25	36.26	36.26	36.26	36.27	36.27
1	20.99	22.83	22.86	22.88	22.88	22.89	22.89	22.89	22.90	22.90
5	15.76	17.14	17.16	17.17	17.18	17.18	17.18	17.18	17.19	17.19
10	14.78	16.07	16.09	16.10	16.11	16.11	16.11	16.11	16.12	16.12

Downloaded 04 May 2010 to 171.66.16.27. Redistribution subject to ASME license or copyright; see http://www.asme.org/terms/Terms_Use.cfm

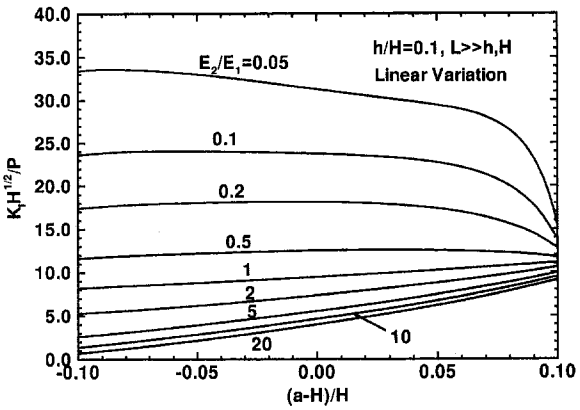

Fig. 5 Stress intensity factor versus crack-tip position in the FGM interlayer for three-point bending with $h/H = 0.1$

rial variation in the three-point bending specimen, where $h/H = 0.1$. The geometry represents the case where the interlayer of FGM is considerably thin compared to the two bulk materials. It is seen that the curves in the figure are the nondimensional function Y in (18) if the characteristic length is taken to be H. The solutions of this kind for various h/H and $\wp$ form a complete solution for the three-point bending specimen. Usually tough materials such as metals have a lower modulus than brittle materials such as ceramics. From this figure, when the crack travels from a tough side (the side with smaller modulus) to a brittle side (the side with larger modulus) the crack-tip stresses increase. The energy release rate calculated from the domains formed by the first ten rings of elements is listed in Table 2 for both linear and exponential material variations. The stable results in the table again show the convergence of the numerical scheme. When the toughness of the two bulk materials is different, it is expected to vary along the thickness of the FGM and can be written as $\Gamma((a - H)/H)$ in the FGM. Then, for stable growth in the FGM interlayer we have

$$G\left(\frac{a-H}{H}\right) = \frac{K_I^2\left(\frac{a-H}{H}\right)}{E\left(\frac{a-H}{H}\right)} = \Gamma\left(\frac{a-H}{H}\right)$$

$$\frac{\partial G\left(\frac{a-H}{H}\right)}{\partial a} < \frac{\partial \Gamma\left(\frac{a-H}{H}\right)}{\partial a}. \qquad (19)$$

For unstable growth, in the second equation "<" is replaced by ">." Let's consider a special case where the toughness is constant across the thickness of the FGM. From the figure, we see in this special case that when material #2 is much softer than material #1, $E_2/E_1 \ll 1$, the crack growth is likely to be stable. This is especially true when the crack tip is close to material #2. When material #2 is stiffer than material #1, the crack growth is likely to be unstable. In general, if the toughness varies with position and the crack is close to material #2 with $E_2/E_1 \ll 1$, it is a stable growth when the decrease of the slope in the figure overcomes the decrease of the toughness. Figure 6 represents the case when $h/H = 0.5$ and other parameters are the same as Fig. 5. From the two figures we see that the trend of these curves has a dramatic change as the percentage of the FGM changes, and this is especially true for those curves with $E_2/E_1 < 1$. For many crack-tip positions in Fig. 6 the stress intensity factor increases as the crack length increases. This means that if the increase of the toughness at the crack tip as the crack length increases is not as fast as the stress intensity factor, it is an unstable growth for the crack tip traveling in those positions. In the above discussion of the crack growth, we have assumed that the crack propagates along the original direction, since these are the cases where geometry, loading, and material are symmetric with respect to the crack line. A first-order approximation model, which is based on local homogeneity, has been used to examine the crack propagating direction for several cracked FGM geometries (Gu and Asaro, 1997b). The model also predicts that a crack grows along its original direction when everything is symmetric.

For the four-point bending specimen shown in Fig. 4, the two ends far away from the crack line is in a pure bending state, where the bending moment $M = Pl$ and l is the distance between the applied force and the support of the beam. The neutral axis changes with material properties, material variation, and layer's thicknesses and is known when these are given. Our numerical results show very good convergence as those listed in Table 1 and 2. Figures 7(a) and (b) illustrate the stress intensity factor versus the interlayer thickness for the crack tip at the center of the beam and linear material variation. It is recognized that these curves are the function Y in (18) if the characteristic length is chosen as H. Compared to Fig. 5, this is another way to present the solution: each curve represents a case for a value E_2/E_1, given $\wp$ and a/H. In these two figures, for a fixed H and as h/H increases, the K_I increases when $E_2/E_1 > 1$ and decreases when $E_2/E_1 < 1$. When h/H is zero, it is the bimaterial solution. The figure tells us that although the increase of the percentage of the FGM in the structure due to the increase of interlayer thickness reduces the mismatch between the two bulk materials, it may not reduce the stress intensities at the crack tip. The increase or decrease of the stress intensities depends on the crack position. As far as the crack propagation is concerned, at this point we do not know how the toughness changes with the FGM percentage increase (note that the increase of the percentage reduces the material gradients). So we do not know if the increase of FGM percentage can prevent the crack growth. However, under the special case that the toughness is constant for FGM, we may conclude that the increase of FGM percentage may not be good to prevent crack growth. In another paper (Dao et al., 1997) we have shown that the increase of FGM percentage may not reduce microstress concentration at the grain size level under thermal loading for a perfect FGM without cracking. The conclusion of the microstress concentration was obtained from a statistically based analysis.

Using a similar analysis, the method can be extended to the three-dimensional case. In three-dimensional space, the domain can be chosen such that its boundary is a tube, which surrounds the crack tip and whose radius of the cross section is sufficiently

Table 2 Convergence for the Three-Point Bending Specimen*

	Energy release rate calculated from the first ten rings [in units of $P^2/(HE_1)$]									
$\wp$	1	2	3	4	5	6	7	8	9	10
linear	466.8	507.7	508.4	508.7	508.8	508.9	508.9	508.9	509.1	509.1
exponential	542.7	590.2	591.1	591.4	591.6	591.6	591.7	591.7	591.9	591.8

* The numerical results in the table are for $h/H = 0.1$, $(a - H)/H = -0.1$ and $E_2/E_1 = 0.1$

Downloaded 04 May 2010 to 171.66.16.27. Redistribution subject to ASME license or copyright; see http://www.asme.org/terms/Terms_Use.cfm

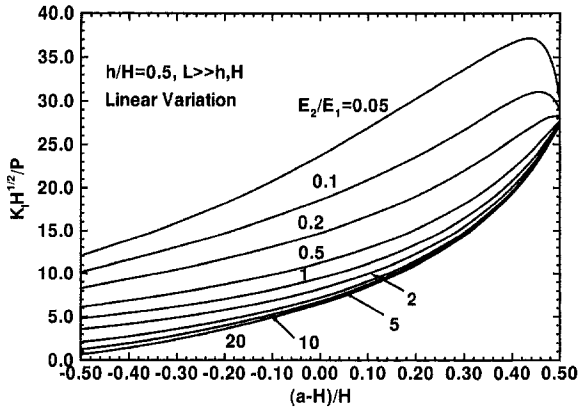

Fig. 6 Stress intensity factor versus crack-tip position in the FGM interlayer for three-point bending with $h/H = 0.5$

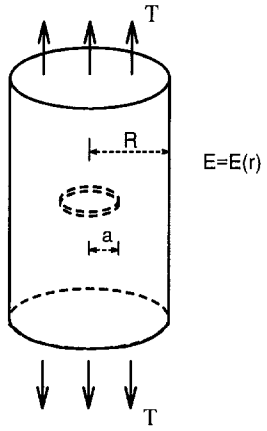

Fig. 8 Penny-shaped crack in a cylindrical FGM solid

small such that the analysis similar to the two-dimensional case can be applied. Detailed discussion of the three-dimensional standard domain integral can be found in previously mentioned papers on the domain integral. The reason for which the simplified method is true is exactly the same as that for the two-dimensional case, i.e., the standard domain integral is overweighted compared to the nonhomogeneous terms. Here we will only give an example of a special version in three-dimensional space, an asymmetric problem shown in Fig. 8. The detailed discussion of the general three-dimensional problem will be given in a separate article elsewhere. The penny-shaped crack (Fig. 8) is in a cylindrical solid. The radius of the crack is a, the radius of the cross section is R, and the length of the solid is so large as not to affect the solution. The Young's modulus is considered to vary along the radius direction, $E = E(r)$. By the structure of the crack-tip field and dimensional consideration, the solution is given in the form

$$K_I = Ta^{1/2}Y\left(\frac{E_2}{E_1}, \frac{a}{R}, \wp\right) \tag{20}$$

where E_2 is the modulus at the outer boundary and E_1 is the modulus at the asymmetric line. The solution to the problem can be easily documented compared to the three-layer bending bars, since we have fewer dependent parameters in the nondimensional function Y here. For given material variation $\wp$, the solution can be presented by a table or a figure. Table 3 shows the convergence for linear and exponential variations, where $E_2/E_1 = 20$ and $a/R = 0.5$. The convergence is very much similar to the two-dimensional case. Except for the first one or two rings, others give the accurate solution.

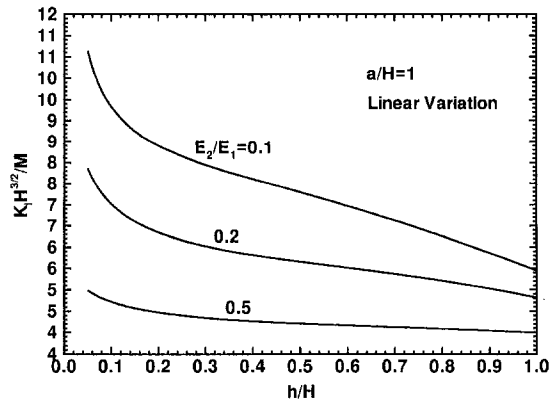

Fig. 7(*a*)

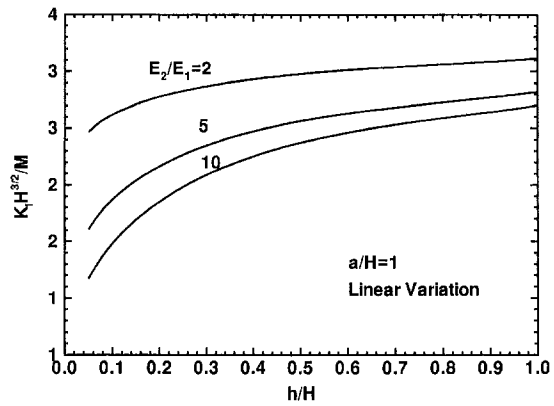

Fig. 7(*b*)

Fig. 7 Stress intensity factor versus thickness of the FGM interlayer for four-point bending

4 Concluding Remarks

We have shown that the standard domain integral can be used to evaluate the crack-tip field for nonhomogeneous materials, such as FGMs. The method requires a sufficiently fine mesh near the crack tip as shown. However, the error induced by the method is estimated such that one can control the error by controlling the size of the domain where the domain integral is evaluated. From the numerical solutions given in the previous section, we have seen that the energy release rate calculated from the domains formed by the rings of elements around the crack tip in this way is very stable and accurate. The examples are all in mode I where both loading, geometry, and material variation are symmetric with respect to the crack face, but the method can be used to calculate the modes I and II stress intensity factors for the mixed-mode case using a defined interaction energy release rate by Shih and Asaro (1989). The method may also be extended to the nonlinear case, such as plastic crack problems. These all suggest that this simplified method, without the input of material gradients and without many changes of the existing finite element code for homogeneous materials, may be well suited for crack mechanics analysis of FGMs where the materials possess gradients. In the examples of the sandwiched structure we have presented the solution in a compact functional form which can be used to easily document a complete solution for other study and design purpose. Finally, it is noted that the material variation is assumed to be continuous across the thickness of the FGM in this study. For real FGMs, the material variation is created by the spatial distribution of one material phase relative to the other. The continuous approach, the proposed numerical method and the fracture behav-

Downloaded 04 May 2010 to 171.66.16.27. Redistribution subject to ASME license or copyright; see http://www.asme.org/terms/Terms_Use.cfm

Table 3 Convergence for Penny-Shaped Crack in a Cylindrical Solid*

	Energy release rate calculated from the first ten rings [in units of T^2a/E_1]									
$\wp$	1	2	3	4	5	6	7	8	9	10
linear	0.04260	0.04633	0.04640	0.04642	0.04644	0.04644	0.04645	0.04645	0.04646	0.04646
exponential	0.03286	0.03574	0.03579	0.03581	0.03582	0.03583	0.03583	0.03583	0.03584	0.03584

* The numerical results in the table are for $a/R = 0.5$ and $E_2/E_1 = 20$

ior analysis in the previous section, implies that the particle size of the phases that make the FGMs is very small compared to the crack length and other geometrical lengths, and the microstructure of the FGMs is sufficiently fine. In the above condition, the effect of the particle size in the mechanics analysis may be neglected.

Acknowledgment

This work was supported by the Office of Naval Research through grant N00014-93-1-1164. We are grateful to Prof. C. F. Shih of Brown University with whom we had helpful discussions. We are also grateful to Dr. Q. S. Yu of UCSD who made helpful suggestions in the presentation of the material.

References

Anderson, T. L., 1995, *Fracture Mechanics—Fundamentals and Applications,* 2nd Ed., CRC Press, Boca Raton, FL.

Dao, M., Gu, P., Maewal, A., and Asaro, R. J., 1997, "A Micromechanical Study of Residual Stresses in Functionally Graded Materials," *Acta Metallurgica,* Vol. 45, pp. 3265–3276.

Delale, F., and Erdogan, F., 1983, "The Crack Problem for a Nonhomogeneous Plane," ASME JOURNAL OF APPLIED MECHANICS, Vol. 50, pp. 609–614.

Delale, F., and Erdogan, F., 1988, "On the Mechanical Modeling of the Interfacial Region in Bonded Half-Planes," ASME JOURNAL OF APPLIED MECHANICS, Vol. 55, pp. 317–324.

deLorenzi, H. G., 1982, "On Energy Release Rate and the *J*-Integral for 3-D Crack Configurations," *International Journal of Fracture,* Vol. 19, pp. 183–193.

Erdogan, F., and Wu, B. H., 1993, "Analysis of FGM Specimens for Fracture Toughness Testing," *Ceramic Transactions,* Vol. 34, J. B. Holt et al., eds., The American Ceramic Society, Westerville, OH.

Gu, P., and Asaro, R. J., 1997a, "Cracks in Functionally Graded Materials," *International Journal of Solids and Structures,* Vol. 34, pp. 1–17.

Gu, P., and Asaro, R. J., 1997b, "Crack Deflection in Functionally Graded Materials," *International Journal of Solids and Structures,* Vol. 34, pp. 3085–3098.

Hellen, T. K., 1975, "On The Method of Virtual Crack Extension," *International Journal of Numerical Methods in Engineering,* Vol. 9, pp. 187–207.

Hutchinson, J. W., 1968, "Singular Behavior at the End of a Tensile Crack Tip in a Hardening Material," *Journal of the Mechanics and Physics of Solids,* Vol. 16, pp. 13–31.

Li, F. Z., Shih, C. F., and Needleman, A., 1985, "A Comparison of Methods for Calculating Energy Release Rates," *Engineering Fracture Mechanics,* Vol. 21, pp. 405–421.

Moran, B., and Shih, C. F., 1987, "A General Treatment of Crack Tip Contour Integrals," *International Journal Fracture,* Vol. 35, pp. 295–310.

Parks, D. M., 1974, "A Stiffness Derivative Finite Element Technique for Determination of Crack Tip Stress Intensity Factors," *International Journal Fracture,* Vol. 10, pp. 487–502.

Parks, D. M., 1977, "The Virtual Crack Extension Method for Nonlinear Material Behavior," *Computational Method in Applied Mechanics and Engineering,* Vol. 12, pp. 353–365.

Rice, J. R., 1968, "A Path Independent Integral and The Approximate Analysis of Strain Concentration by Notches and Cracks," ASME JOURNAL OF APPLIED MECHANICS, Vol. 35, pp. 379–386.

Rice, J. R., and Rosengren, G. F., 1968, "Plane Strain Deformation near a Crack Tip in a Power-Law Hardening Material," *Journal of the Mechanics and Physics of Solids,* Vol. 16, pp. 1–12.

Shih, C. F., Moran, B., and Nakamura, T., 1986, "Energy Release Rate along a Three-Dimensional Crack Front in A Thermally Stressed Body," *International Journal Fracture,* Vol. 30, pp. 79–102.

Shih, C. F., and Asaro, R. J., 1989, "Elastic-plastic Analysis of Cracks on Bimaterial Interfaces: Part I—small Scale Yielding," ASME JOURNAL APPLIED MECHANICS, Vol. 55, pp. 299–316.

Tada, H., Paris, P. C., and Irwin, G. R., 1985, *The Stress Analysis of Cracks Handbook,* 2nd Ed., Paris Publications, St. Louis, MO.

Downloaded 04 May 2010 to 171.66.16.27. Redistribution subject to ASME license or copyright; see http://www.asme.org/terms/Terms_Use.cfm

Nonlinear Stability Considerations in Thermoelastic Contact

J. A. Pelesko
Applied Mathematics,
California Institute of Technology,
Pasadena, CA 91125

The behavior of a one-dimensional thermoelastic rod is modeled and analyzed. The rod is held fixed and at constant temperature at one end, while at the other end it is free to separate from or make contact with a rigid wall. At this free end a pressure and gap-dependent thermal boundary condition is imposed which couples the thermal and elastic problems. Such systems have previously been shown to undergo a bifurcation from a unique linearly stable steady-state solution to multiple steady-state solutions with alternating stability. Here, the system is studied using a two-timing or multiple-scale singular perturbation technique. In this manner, the analysis is extended into the nonlinear regime and dynamic information about the history dependence and temporal evolution of the solution is obtained.

1 Introduction

Thermoelastic contact problems arise in areas as diverse as the study of automotive disk brakes (Lee and Barber, 1993), the production of metals (Richmond, Hector, Jr., and Fridy, 1990), and the analysis of heat exchangers (Srinivasan and France, 1985). In 1978, it was pointed out by J. R. Barber (Barber, 1978) that the solution of such problems posed certain difficulties. In particular, the assumption of perfect insulation during a separated phase and perfect thermal contact during contact led to models with solutions which were unacceptable on physical grounds. Rejecting such solutions, Barber conjectured that these models failed to capture relevant physics and introduced a pressure-dependent thermal boundary condition. This condition, which has become known as the Barber condition, allowed for a smooth transition between the insulated and perfect thermal contact states. Studying a linearized version of a thermal contact problem which included the Barber condition, he showed that the paradoxes inherent in simpler models could be avoided and physically relevant solutions recovered.

In 1980 Comninou and Dundurs (Cominou and Dundurs, 1980), again using the assumption of perfect insulation during separation and perfect thermal contact during contact, explicitly constructed multiple steady-state solutions to a thermal contact problem. They showed that for two half-spaces, there existed steady states in which the entire region between the two materials remained in contact and that there also existed steady-states consisting of alternating regions of contact and separation. They pointed out that the existence of such solutions raised important questions about the stability of steady states and about the history dependence of solutions to thermal contact problems.

Again in 1980, Barber, Dundurs, and Comninou (Barber, Dundurs, and Comninou, 1980) investigated a thermal contact problem which combined the Barber condition with nonunique steady-state solutions in a one-dimensional model of a thermoelastic rod. Imposing a temperature gradient across the rod, they demonstrated that the system underwent a bifurcation from a unique linearly stable steady-state solution to multiple solutions with alternating stability as the magnitude of the thermal gradient was varied.

Since that time, various authors have explored the Barber condition and its implications for thermal contact problems. While such analyses have been extended to multiple materials (Panek, 1980; Barber, 1981; Zhang and Barber, 1990) various geometries (Yeo and Barber, 1995; Li and Barber, 1997), and to numerical simulations (Olesiak, 1996), all theoretical work to date has relied upon linear stability theory. While this provides useful information about the existence of steady states and their stability to infinitesimal perturbations, it fails to provide information about dynamics, history dependence, and nonlinear effects.

In this paper, we use a multiple scale or two-timing method to study a one-dimensional thermal contact model. We show how standard ideas from nonlinear stability theory, for example as discussed in Kevorkian and Cole (1996) and Matkowsky (1970), may be applied to thermal contact problems. We begin in Section 2 by formulating the governing equations for our model. We make the standard assumption that quasi-static uncoupled thermoelasticity is valid and use the Signorini contact condition to capture periods of separation and contact. However, we do not impose the Barber condition on the thermal part of the problem. Rather, we impose a pressure and gap-dependent Dirichlet boundary condition. This condition is chosen for simplicity in the later analysis, but provides us with a model with the same qualitative features as seen in other thermal contact problems. In Section 3 we investigate the linear theory for our model. We show that as in previous rod models (Barber, 1978; Barber, Dundurs, and Comninou, 1980) the system undergoes a bifurcation from a single linearly stable steady-state solution to multiple steady-state solutions. Finally, in Section 4, we study the behavior of our system near the bifurcation point. That is, we inquire as to what happens when the system is started nearby the now linearly unstable steady-state solution. Linear theory, of course, predicts an exponentially growing solution which is only valid for small time. Using multiple scale techniques, we incorporate the effect of stabilizing nonlinear terms into our theory and obtain information about the dynamics and history dependence of the solution. We show that as conjectured, the solution does indeed approach one of the stable solutions obtained in the linear theory.

2 Formulation of the Model

We consider a one-dimensional thermoelastic rod of length L suspended between two rigid walls as pictured in Fig. 1.

Contributed by the Applied Mechanics Division of THE AMERICAN SOCIETY OF MECHANICAL ENGINEERS for publication in the ASME JOURNAL OF APPLIED MECHANICS.

Discussion on the paper should be addressed to the Technical Editor, Professor Lewis T. Wheeler, Department of Mechanical Engineering, University of Houston, Houston, TX 77204-4792, and will be accepted until four months after final publication of the paper itself in the ASME JOURNAL OF APPLIED MECHANICS.

Manuscript received by the ASME Applied Mechanics Division, June 20, 1998; final revision, Aug. 31, 1998. Associate Technical Editor: S. Kyriakides.

 Copyright © 1999 by ASME

Downloaded 04 May 2010 to 171.66.16.27. Redistribution subject to ASME license or copyright; see http://www.asme.org/terms/Terms_Use.cfm

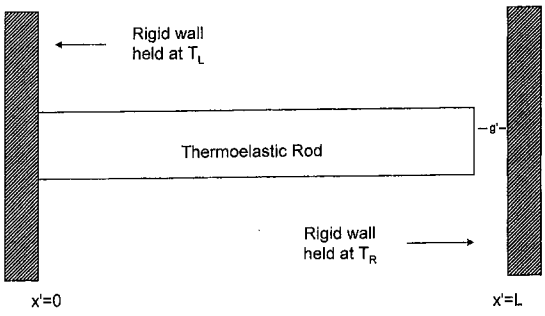

Fig. 1 Sketch of the model geometry

We assume that the rod possesses constant thermal and elastic material properties, is homogeneous and isotropic, and that uncoupled quasi-static thermoelastic theory is valid. With these assumptions in mind, we formulate the equations governing the temperature distribution, elastic displacement, and stress within the rod. The temperature of the rod, T, satisfies

$$\rho c_p \frac{\partial T}{\partial t'} = \kappa \frac{\partial^2 T}{\partial x'^2} \quad 0 < x' < L. \tag{2.1}$$

Here ρ is the density, c_p the specific heat, and κ the thermal conductivity. The elastic displacement, u', is related to the temperature distribution through

$$\frac{\partial^2 u'}{\partial x'^2} = \alpha \frac{\partial T}{\partial x'} \quad 0 < x' < L \tag{2.2}$$

where here α is the coefficient of thermal expansion. The stress, σ', is related to the displacement and temperature fields through the Duhamel-Neuman relation

$$\sigma' = E \frac{\partial u'}{\partial x'} - E\alpha(T - T_L) \quad 0 < x' < L \tag{2.3}$$

where here E is the Young's modulus of the elastic rod. The left end of the rod is assumed to be firmly attached to a rigid wall which is held at temperature T_L. Hence at this end we impose the Dirichlet boundary conditions

$$T(0, t') = T_L \tag{2.4}$$

and

$$u'(0, t') = 0. \tag{2.5}$$

In contrast, the right end of the rod is assumed free and may be separated from or in contact with a rigid wall held at temperature T_R. The rod is assumed to have length $L - g'$ when uniformly at the temperature T_L. To capture the possibility of a gap or of contact, we impose the Signorini contact condition on the displacement and stress

$$\left\{ \begin{array}{c} u' \le g' \\ \sigma' \le 0 \\ (u' - g')\sigma' = 0 \end{array} \right\} \quad \text{at } x' = L. \tag{2.6}$$

Finally, we need a boundary condition on the temperature at $x' = L$. We impose a "variable" Dirichlet condition in the form

$$T(L, t') = T_0 f(g'/L - u'(L, t')/L + \sigma'(L, t')/E). \tag{2.7}$$

Here T_0 is a scale factor and f is a dimensionless function of the dimensionless variable $\eta = g'/L - u'(L, t')/L + \sigma'(L, t')/E$. We note that η measures the relative gap size during periods of separation or the relative contact pressure during periods of contact. This boundary condition may be interpreted as modeling the temperature that the rod "feels" at its free end according as its degree of separation from the wall or as the strength of its contact with the wall. We assume that $T_0 f(\eta) \to T_R$ as $\eta \to -\infty$. That is, the temperature the rod feels is precisely that of the wall as the contact pressure becomes infinite. On the other hand, we define T_A as the limit of $T_0 f(\eta)$ as $\eta \to \infty$. That is, in the case of maximum separation, we assume that the rod feels some temperature T_A, perhaps the ambient temperature of the surrounding environment, or perhaps some effective temperature modeling radiative and convective effects. In general, to complete the formulation of the problem, we must also specify initial conditions. Since our intent is to consider steady-state solutions and perturbations about these steady states, we leave the formulation of initial conditions until later in the Discussion.

Next, we introduce dimensionless variables and rewrite our governing equations in dimensionless form. We define

$$\theta = \frac{T - T_L}{T_L - T_A}, \quad t = \frac{\kappa}{\rho c_p L^2} t',$$

$$x = \frac{x'}{L}, \quad u = \frac{u'}{L}, \quad \sigma = \frac{\sigma'}{E}, \tag{2.8}$$

and substitute these into Eqs. (2.1)–(2.7). This yields

$$\frac{\partial \theta}{\partial t} = \frac{\partial^2 \theta}{\partial x^2} \quad 0 < x < 1 \tag{2.9}$$

$$\frac{\partial^2 u}{\partial x^2} = \delta \frac{\partial \theta}{\partial x} \quad 0 < x < 1 \tag{2.10}$$

$$\sigma = \frac{\partial u}{\partial x} - \delta\theta \quad 0 < x < 1 \tag{2.11}$$

$$\theta(0, t) = 0 \tag{2.12}$$

$$u(0, t) = 0 \tag{2.13}$$

$$\left\{ \begin{array}{c} u \le g \\ \sigma \le 0 \\ (u - g)\sigma = 0 \end{array} \right\} \text{ at } x = 1 \tag{2.14}$$

$$\theta(1, t) = \frac{T_0 f(g - u(1, t) + \sigma(1, t)) - T_L}{T_L - T_A} \tag{2.15}$$

where here

$$\delta = \alpha(T_L - T_A), \quad g = \frac{g'}{L}. \tag{2.16}$$

Note that δ may be interpreted as a nondimensional coefficient of thermal expansion or as a dimensionless measure of a thermal gradient in the problem, while g is a dimensionless measure of the reference state gap width.

Now, we note that the problems for u and σ are linear with linear boundary conditions and hence may be solved exactly. That is, we may integrate Eq. (2.10) twice and use Eqs. (2.11), (2.13) and (2.14) to solve for u and σ. We find

$$u(x, t) = \delta \int_0^x \theta(\zeta, t) d\zeta - x \max \{\delta \int_0^1 \theta(\zeta, t) d\zeta - g, 0\} \tag{2.17}$$

and

$$\sigma(x, t) = -\max \{\delta \int_0^1 \theta(\zeta, t) d\zeta - g, 0\}. \tag{2.18}$$

Using these solutions, we may evaluate η, i.e.,

$$\eta = g - u(1, t) + \sigma(1, t) = g - \delta \int_0^1 \theta(\zeta, t) d\zeta. \tag{2.19}$$

Downloaded 04 May 2010 to 171.66.16.27. Redistribution subject to ASME license or copyright; see http://www.asme.org/terms/Terms_Use.cfm

Hence, we have reduced the problem to one for θ only. That is, we are left with

$$\frac{\partial\theta}{\partial t} = \frac{\partial^2\theta}{\partial x^2} \quad 0 < x < 1 \tag{2.20}$$

$$\theta(0, t) = 0 \tag{2.21}$$

$$\theta(1, t) = \frac{T_0 f\left(g - \delta\int_0^1 \theta(\zeta, t)d\zeta\right) - T_L}{T_L - T_A}. \tag{2.22}$$

Finally, for illustrative purposes, we choose a specific, symmetric form for f. In particular, we take

$$T_0 = T_L, \quad f(\eta) = 1 + \frac{T_L - T_A}{T_L}\tanh\,(2(g - \eta)). \tag{2.23}$$

We note that this corresponds to the assumption that $T_A < T_L < T_R$ and that $T_R = 2T_L - T_A$. Hence, the boundary condition at $x = 1$, i.e., Eq. (2.22), becomes

$$\theta(1, t) = \tanh\left(2\delta\int_0^1 \theta(\zeta, t)d\zeta\right). \tag{2.24}$$

3 Linear Theory

In this section we compute the steady-state solutions of the system (2.20), (2.21), (2.24) and examine their linear stability. We begin by setting the time derivative to zero in Eq. (2.20), integrating the resulting ode and using the boundary conditions, Eqs. (2.21), (2.24), to determine that steady solutions must have the form

$$\theta^*(x) = ax \tag{3.1}$$

where a satisfies

$$a = \tanh\,(\delta a). \tag{3.2}$$

We immediately see that $a = 0$ always satisfies Eq. (3.2) hence $\theta^*(x) = 0$ is always a steady-state solution of our problem. Next, we notice that for $\delta < 1$, $a = 0$ is the only solution to Eq. (3.2), but that as δ passes through one, two additional roots appear. This is easy to see graphically; the reader is referred to Fig. 2. Hence, $\delta = 1$ is a bifurcation point for our problem, that is, as δ passes through one we undergo a transition from a single steady-state solution to three steady-state solutions.

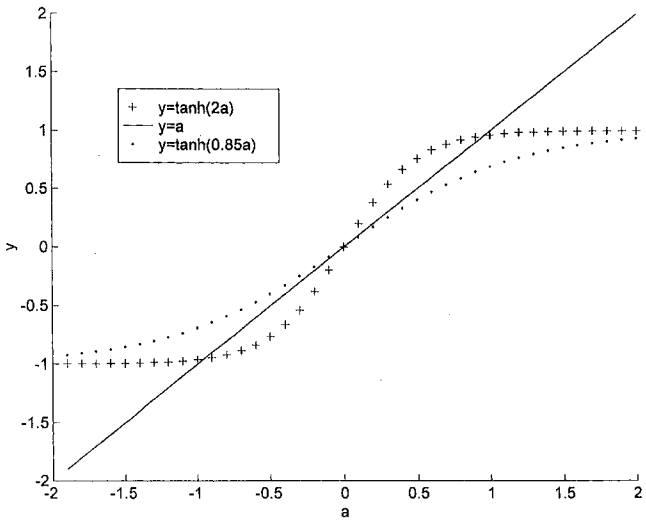

Fig. 2 Graphical solution for steady states for different values of the bifurcation parameter

Next, we investigate the linear stability of these steady states. Accordingly, we seek a solution to (2.20), (2.21), (2.24) in the form

$$\theta(x, t) = ax + \phi(x)e^{-\lambda^2 t} \tag{3.3}$$

where $|\phi(x)| \ll 1$ and a satisfies Eq. (3.2). Inserting this ansatz into our governing equations, expanding the nonlinear terms in Taylor series, and omitting quadratic and higher order terms in ϕ, we obtain the eigenvalue problem

$$\frac{d^2\phi}{dx^2} + \lambda^2\phi = 0 \tag{3.4}$$

$$\phi(0) = 0 \tag{3.5}$$

$$\phi(1) = 2\delta\,\mathrm{sech}^2(\delta a)\int_0^1 \phi(\zeta)d\zeta. \tag{3.6}$$

This linear eigenvalue problem has a solution ϕ when λ satisfies

$$\frac{\lambda}{2} = \delta\,\mathrm{sech}^2(\delta a)\tan\left(\frac{\lambda}{2}\right). \tag{3.7}$$

The solutions of this equation in conjunction with Eq. (3.3) determine the stability of the perturbation ϕ; if $\mathrm{Re}(\lambda^2) > 0 (<0)$, then the steady state is linearly stable (unstable). We note that using Eq. (3.2) and trigonometric identities we may rewrite Eq. (3.7) in the form

$$\frac{\lambda}{2} = \delta(1 - a^2)\tan\left(\frac{\lambda}{2}\right). \tag{3.8}$$

In Appendix A we prove that solutions to Eq. (3.8) are either pure real or pure imaginary. Since purely real solutions for λ correspond to exponential decay of the perturbation we need only focus on the existence of pure imaginary roots. Setting $\lambda = i\alpha$ in Eq. (3.8), where α is assumed real, leads us to consider

$$\frac{\alpha}{2} = \delta(1 - a^2)\tanh\left(\frac{\alpha}{2}\right). \tag{3.9}$$

Clearly, if $a = 0$, this equation has a nonzero solution only when $\delta > 1$. Further, we note that $\lambda = 0$ is an eigenvalue if and only if $\delta = 1$. Hence we immediately conclude that the zero solution is stable for $0 < \delta < 1$, marginally stable for $\delta = 1$ and unstable for $\delta > 1$. On the other hand, for $a \neq 0$, we may solve Eq. (3.2) for δ and obtain

$$\delta = \frac{\tanh^{-1}(a)}{a}. \tag{3.10}$$

We note that $\tanh^{-1}$ is well defined since $|a| < 1$. Then, using this expression for δ in Eq. (3.9) we find

$$\frac{\alpha}{2} = \frac{(1 - a^2)\tanh^{-1}(a)}{a}\tanh\left(\frac{\alpha}{2}\right). \tag{3.11}$$

Now, noting that for any a such that $|a| < 1$, the coefficient in front of tanh is also less than one, we conclude that our two nonzero solutions are stable for all $\delta \geq 1$. The conclusions of this linear theory are summarized in the bifurcation diagram sketched in Fig. 3.

4 Nonlinear Theory

In the previous section we found and investigated the linear stability of steady-state solutions to our model, i.e., Eqs. (2.20), (2.21), and (2.24). We determined that $\theta^*(x) = 0$ was a solution for all positive values of the parameter δ, and that the linear stability of this solution changed as δ passed through one. In particular, for $\delta < 1$, this solution was found to be linearly stable, while for $\delta > 1$, linear theory predicts that any infinitesimal perturbation will grow exponentially. Clearly, in this pa-

Downloaded 04 May 2010 to 171.66.16.27. Redistribution subject to ASME license or copyright; see http://www.asme.org/terms/Terms_Use.cfm

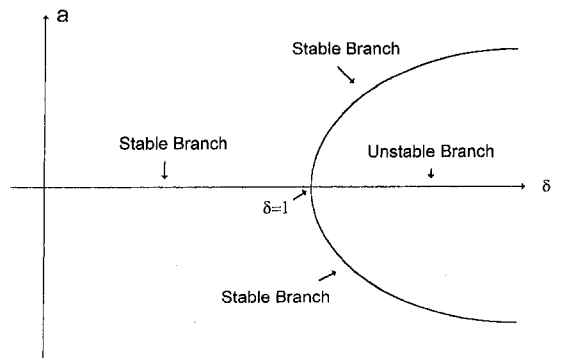

Fig. 3 Bifurcation diagram indicating existance and stability of steady-state solutions as a function of the parameter, delta

rameter range, the linear theory is only valid for a limited time. In this section, we use the method of multiple scales, or two-timing, to extend our analysis into the nonlinear regime. That is, we investigate the nature of the solution to our governing equations when δ is nearby, but greater than one, and the initial conditions are such that the system starts near the now unstable zero solution. Our goal is to develop an approximate solution which is valid for all time, thereby allowing us to understand the dynamics and history dependence of solutions near this bifurcation point.

We begin by imposing the initial condition

$$\theta(x, 0) = \epsilon h(x). \tag{4.1}$$

Here, $\epsilon \ll 1$ and $h(x)$ is an arbitrary $O(1)$ function. Note that this defines ϵ and starts our system near the zero solution. It is now convenient to rescale by setting $\theta = \epsilon v$. Introducing this rescaling into Eqs. (2.20), (2.21), (2.24), and (4.1), expanding the nonlinear terms in a Taylor series and retaining terms up to $O(\epsilon^2)$ we obtain

$$\frac{\partial v}{\partial t} = \frac{\partial^2 v}{\partial x^2} \tag{4.2}$$

$$v(0, t) = 0 \tag{4.3}$$

$$v(1, t) = 2\delta \int_0^1 v(\zeta, t)d\zeta - \frac{8\epsilon^2\delta^3}{3}\left(\int_0^1 v(\zeta, t)d\zeta\right)^3 \tag{4.4}$$

$$v(x, 0) = h(x). \tag{4.5}$$

Next, we let $\delta = 1 + \epsilon^2\gamma$ where γ is $O(1)$, and seek a solution for v in the form

$$v(x, t, \tau) \sim v_0(x, t, \tau) + \epsilon^2 v_1(x, t, \tau) + \cdots \tag{4.6}$$

where the long time scale τ is defined by $\tau = \epsilon^2 t$. We note that the choice of scale for τ, δ, and the expansion of v is made in order to bring in the effect of the cubic nonlinearity, the deviation from $\delta = 1$ and the slow time scale at the same order. Now, inserting the expansion for v, i.e., Eq. (4.6), into Eqs. (4.2)–(4.5), treating t and τ as independent variables, and equating to zero coefficients of powers of orders of ϵ^2, we obtain an infinite set of equations which sequentially determine the v_n. We list the first two, which are sufficient to determine the leading-order behavior. We have

$$\frac{\partial v_0}{\partial t} = \frac{\partial^2 v_0}{\partial x^2} \tag{4.7}$$

$$v_0(0, t, \tau) = 0 \tag{4.8}$$

$$v_0(1, t, \tau) = 2\int_0^1 v_0(\zeta, t, \tau)d\zeta \tag{4.9}$$

$$v_0(x, t, \tau) = h(x) \tag{4.10}$$

and

$$\frac{\partial v_1}{\partial t} = \frac{\partial^2 v_1}{\partial x^2} - \frac{\partial v_0}{\partial \tau} \tag{4.11}$$

$$v_1(0, t, \tau) = 0 \tag{4.12}$$

$$v_1(1, t, \tau) = 2\int_0^1 v_1(\zeta, t, \tau)d\zeta + 2\gamma\int_0^1 v_0(\zeta, t, \tau)d\zeta - \frac{8}{3}\left(\int_0^1 v_0(\zeta, t, \tau)d\zeta\right)^3 \tag{4.13}$$

$$v_0(x, t, \tau) = 0. \tag{4.14}$$

Now we must construct a solution to the leading order problem. An eigenfunction approach is reasonable; we seek solutions in the form $A(t, \tau)\phi(x)$, separate variables, and obtain the following problem for the spatial eigenfunctions:

$$\frac{d^2\phi}{dx^2} + \lambda^2\phi = 0 \tag{4.15}$$

$$\phi(0) = 0 \tag{4.16}$$

$$\phi(1) = 2\int_0^1 \phi(\zeta)d\zeta. \tag{4.17}$$

We note that this is the same as the eigenfunction problem of the linear theory for $a = 0$, $\delta = 1$ and hence the eigenvalues are given by

$$\frac{\lambda}{2} = \tan\left(\frac{\lambda}{2}\right). \tag{4.18}$$

Further, from the linear theory, we note that zero is an eigenvalue, and that all other eigenvalues are pure real. In contrast to the linear theory, here we must explicitly construct our eigenfunctions and establish an eigenfunction expansion theorem. Towards this end, we remove the integral from our boundary condition (4.17) by integrating Eq. (4.15) across the rod, solving for the integral, and eliminating the integral from Eq. (4.17). Hence we may study the equivalent system

$$\frac{d^2\phi}{dx^2} + \lambda^2\phi = 0 \tag{4.19}$$

$$\phi(0) = 0 \tag{4.20}$$

$$\frac{d\phi}{dx}(0) - \frac{d\phi}{dx}(1) = \frac{\lambda^2}{2}\phi(1). \tag{4.21}$$

We note that there is no difficulty with $\lambda = 0$ as it is an eigenvalue of this system as well as the original system. However, having rewritten our system in the form (4.19)–(4.21), we recognize that we are faced with a nonstandard eigenvalue problem. That is, the eigenvalue, λ, appears in the boundary conditions. Consequently, we cannot simply consider the operator $L = d^2/dx^2$ and recast our problem as a special case of $L\phi = -\lambda^2\phi$. Rather, we must exercise care in defining an operator, constructing an adjoint, and finding an expansion theorem. We follow a classical approach, outlined, for example, in Friedman (1990).

We begin by considering the space of two component vectors U, whose first component is a real valued C^2 function, $u(x)$, and whose second component is a real number, u_1. We define the inner product of two vectors in this space by

$$\langle U, V\rangle = \int_0^1 u(x)v(x)dx + u_1v_1. \tag{4.22}$$

Next, we restrict our attention to the subspace, D, of vectors U

Downloaded 04 May 2010 to 171.66.16.27. Redistribution subject to ASME license or copyright; see http://www.asme.org/terms/Terms_Use.cfm

such that $u(0) = 0$ and $u_1 = u(1)$. Then we define an operator L acting on elements U of D by

$$LU = \begin{pmatrix} -\dfrac{d^2u}{dx^2} \\ 2\left(\dfrac{du}{dx}(0) - \dfrac{du}{dx}(1)\right) \end{pmatrix}. \tag{4.23}$$

Note that our eigenvalue problem, Eqs. (4.19)–(4.21), is now simply stated as: find a vector U in D such that $LU = \lambda^2 U$. Further, we may define an adjoint operator, L^*, where

$$L^*V = \begin{pmatrix} -\dfrac{d^2v}{dx^2} \\ \dfrac{dv}{dx}(1) \end{pmatrix} \tag{4.24}$$

and acts on elements, V, of the subspace D^* defined as two component vectors satisfying $v(0) = v(1)$ and $v_1 = -v(1)/2$. The reader may easily verify that with the inner product, (4.22), we have $\langle LU, V\rangle = \langle U, L^*V\rangle$.

Next, we may attempt to derive an expansion theorem and solve our leading-order problem. First, we note, of course, that the discrete spectrum of L is given by Eq. (4.18). That fact that our operator is not self-adjoint raises the possibility that L also possesses a continuous spectrum which would effect the nature of an eigenfunction expansion. In Appendix B, we use the Green's function approach to show that the discrete spectrum is the entire spectrum and is defined by Eq. (4.18). This having been said, we now construct eigenvectors. We find

$$U_n = \begin{pmatrix} \dfrac{a_n \sin(\lambda_n x)}{\lambda_n} \\ \dfrac{a_n \sin(\lambda_n)}{\lambda_n} \end{pmatrix} \tag{4.25}$$

where $\lambda_0 = 0$ and the remaining λ_ns are the real nonzero solutions of Eq. (4.18). Similarly, we can construct the following adjoint eigenfunctions from our adjoint eigenvalue problem

$$V_n = \begin{pmatrix} \dfrac{\sin(\lambda_n x) - \sin(\lambda_n(x-1))}{\lambda_n} \\ -\dfrac{\sin(\lambda_n)}{2\lambda_n} \end{pmatrix} \tag{4.26}$$

where, of course, the λ_ns are the same as above. We note that the following orthogonality properties hold:

$$\langle U_n, V_m\rangle = 0 \quad \text{for all} \quad n \neq m \tag{4.27}$$

$$\langle U_n, V_m\rangle \neq 0 \quad \text{for all} \quad n \neq 0 \tag{4.28}$$

and

$$\langle U_0, V_0\rangle = 0. \tag{4.29}$$

Further, we choose the a_ns, for $n \neq 0$ so that

$$\langle U_n, V_n\rangle = 1 \tag{4.30}$$

and we choose a_0 so that

$$\langle U_0, U_0\rangle = 1. \tag{4.31}$$

Now we can construct a solution to our leading order problem by using the eigenvectors and the adjoint eigenvectors just defined. We seek a solution lying in the subspace D in the following form:

$$\begin{pmatrix} v_0(x, t, \tau) \\ v_0(1, t, \tau) \end{pmatrix} = \sum_{n=0}^{\infty} A_n(\tau) e^{-\lambda_n^2 t} U_n. \tag{4.32}$$

The governing equation and the boundary conditions are of course satisfied, while the A_ns are unknown amplitude functions depending on the slow time scale τ. They will be determined by requiring that our perturbation expansion be bounded at the next order. However, before doing this, we still must impose the initial condition. We require

$$\begin{pmatrix} v_0(x, 0, 0) \\ v_0(1, 0, 0) \end{pmatrix} = \begin{pmatrix} h(x) \\ h_1 \end{pmatrix} = \sum_{n=0}^{\infty} A_n(0) U_n \tag{4.33}$$

where h_1 and the $A_n(0)$ are yet to be determined. If we take an inner product with V_m, where $m \neq 0$, we find

$$A_m(0) = \langle H, V_m\rangle \tag{4.34}$$

where

$$H = \begin{pmatrix} h(x) \\ h_1 \end{pmatrix}. \tag{4.35}$$

Next, we take an inner product with V_0 and find

$$\langle H, V_0\rangle = 0 \tag{4.36}$$

which implies

$$\int_0^1 h(x)dx = \frac{h_1}{2} \tag{4.37}$$

and hence uniquely determines h_1. Now, $A_0(0)$ is still undetermined. To remedy this situation, we take an inner product with U_0 across Eq. (4.33) and solve for $A_0(0)$ to find

$$A_0(0) = \langle H, U_0\rangle - \sum_{n=1}^{\infty} A_n(0)\langle U_n, U_0\rangle. \tag{4.38}$$

Now, we turn to the task of determining the $A_n(\tau)$. Towards this end, let us consider our $O(\epsilon^2)$ problem, Eqs. (4.11)–(4.14). It is convenient to homogenize the boundary conditions by seeking a solution for v_1 in the form

$$v_1(x, t, \tau) = w(x, t, \tau) + \left(6\gamma \int_0^1 v_0(\zeta, t, \tau)d\zeta - 8\left(\int_0^1 v_0(\zeta, t, \tau)d\zeta\right)^3\right)x^2. \tag{4.39}$$

Now, w satisfies

$$\frac{\partial w}{\partial t} = \frac{\partial^2 w}{\partial x^2} + f(x, t, \tau) \tag{4.40}$$

$$w(0, t, \tau) = 0 \tag{4.41}$$

$$w(1, t, \tau) = 2\int_0^1 w(\zeta, t, \tau)d\zeta \tag{4.42}$$

where

$$f(x, t, \tau) = -\frac{\partial}{\partial t}\left(\left(6\gamma \int_0^1 v_0(\zeta, t, \tau)d\zeta - 8\left(\int_0^1 v_0(\zeta, t, \tau)d\zeta\right)^3\right)x^2\right) + 12\gamma \int_0^1 v_0(\zeta, t, \tau)d\zeta - 16\left(\int_0^1 v_0(\zeta, t, \tau)d\zeta\right)^3 - \frac{\partial v_0}{\partial \tau}.$$

We seek a solution for w in the form

Downloaded 04 May 2010 to 171.66.16.27. Redistribution subject to ASME license or copyright; see http://www.asme.org/terms/Terms_Use.cfm

$$\begin{pmatrix} w(x, t, \tau) \\ w(1, t, \tau) \end{pmatrix} = \sum_{n=0}^{\infty} B_n(t, \tau) U_n. \tag{4.43}$$

Our governing Eq. (4.40) requires that

$$\sum_{n=0}^{\infty} \left[\frac{\partial B_n}{\partial t} + \lambda_n^2 B_n \right] \frac{a_n \sin(\lambda_n x)}{\lambda_n} = f(x, t, \tau). \tag{4.44}$$

While we cannot expect this equation to hold at $x = 1$, we can expect the sum on the left to converge at $x = 1$. That is, we can set

$$f_1 = \sum_{n=0}^{\infty} \left[\frac{\partial B_n}{\partial t} + \lambda_n^2 B_n \right] \frac{a_n \sin(\lambda_n)}{\lambda_n} \tag{4.45}$$

which allows us to write the vector equation

$$\sum_{n=0}^{\infty} \left[\frac{\partial B_n}{\partial t} + \lambda_n^2 B_n \right] U_n = \begin{pmatrix} f(x, t, \tau) \\ f_1(t, \tau) \end{pmatrix}. \tag{4.46}$$

Now, if we take an inner product with V_0 across Eq. (4.46), we find

$$\langle F, V_0 \rangle = 0 \tag{4.47}$$

where

$$F = \begin{pmatrix} f(x, t, \tau) \\ f_1(t, \tau) \end{pmatrix}. \tag{4.48}$$

This uniquely determines f_1, in particular,

$$\frac{f_1}{2} = \int_0^1 f(x, t, \tau) dx. \tag{4.49}$$

Finally, we may derive amplitude equations for the $A_n(\tau)$ by requiring that the solution for w be free of secular terms. That is, we want to suppress terms proportional to t or $te^{-\lambda_n^2 t}$ from the solution for w. Taking an inner product with V_n across Eq. (4.46) yields

$$\frac{\partial B_n}{\partial t} + \lambda_n^2 B_n = \langle F, V_n \rangle. \tag{4.50}$$

Setting to zero the coefficients of $e^{-\lambda_n^2 t}$ on the right-hand side yields the following amplitude equation for A_n, $n \neq 0$:

$$\frac{dA_n}{d\tau} + \frac{4\lambda_n^2 \sin(\lambda_n)}{\lambda_n - \sin(\lambda_n)} \left(\frac{3A_0^2}{4} - 1 \right) A_n = 0. \tag{4.51}$$

Now, taking an inner product across Eq. (4.46) with U_0 yields

$$\frac{\partial B_0}{\partial t} = \langle F, U_0 \rangle - \sum_{n=1}^{\infty} \langle F, V_n \rangle \langle U_n, U_0 \rangle. \tag{4.52}$$

Removing terms on the right which are independent of t yields the amplitude equation for A_0

$$\frac{dA_0}{d\tau} - \frac{45\gamma}{4} A_0 + \frac{45}{16} A_0^3 = 0. \tag{4.53}$$

The leading-order solution, i.e., $v_0(x, t, \tau)$, is now completely determined.

5 Discussion

We began by constructing a model of a one-dimensional thermoelastic rod subjected to conditions which allowed for thermoelastic contact. We introduced a boundary condition, similar in spirit to the Barber condition, which captured the fact that thermal effects at the free end of the rod are strongly dependent upon the rod's state. That is, the temperature at the right end of the rod was assumed to be a function of the size of the gap between the rod and the wall during separation, and the contact pressure during contact. Solving explicitly for the displacement and the stress, we reduced the problem to a diffusion equation with a nonlinear and nonlocal boundary condition. Choosing a particular form for the nonlinearity, we set out to attempt both a linear and a nonlinear analysis of our model.

The linear theory revealed that our thermoelastic contact model possesses the same features that make other such models of interest. In particular, we showed that our system underwent a bifurcation from a single steady-state solution to three steady-state solutions as the dimensionless parameter δ was varied. Further, we investigated the linear stability of these steady states. The reader's attention is again directed toward Fig. 3. We found that when the steady state was unique it was stable, while when multiple solutions existed, two were stable, and the previously stable zero solution was now linearly unstable.

Next, we noted that our linear analysis suggested several interesting questions. In particular, if we started in a neighborhood of the zero solution, but with the control parameter δ such that the zero solution was unstable, linear theory predicted that the solution would grow exponentially with time. Noting that such a result can only be valid for small time led us to inquire as to the effect of the neglected nonlinear terms. That is; do nonlinear terms stabilize this growing solution? Does the solution approach one of the stable solutions found in the linear theory? How does it get there? How do the initial conditions influence the final state? We used the method of multiple scales, or two-timing, to address these questions. We derived the following asymptotic approximation for the solution, which we again note is uniformly valid in time,

$$\theta(x, t, \tau) \sim \epsilon \sum_{n=0}^{\infty} A_n(\tau) e^{-\lambda_n^2 t} \frac{a_n \sin(\lambda_n x)}{\lambda_n} + O(\epsilon^2). \tag{5.1}$$

The A_n's satisfy the amplitude, or Landau equations

$$\frac{dA_n}{d\tau} + \frac{4\lambda_n^2 \sin(\lambda_n)}{\lambda_n - \sin(\lambda_n)} \left(\frac{3A_0^2}{4} - 1 \right) A_n = 0 \tag{5.2}$$

for $n \neq 0$ and

$$\frac{dA_0}{d\tau} - \frac{45\gamma}{4} A_0 + \frac{45}{16} A_0^3 = 0. \tag{5.3}$$

Since all but the $n = 0$ mode decay exponentially with time, we may answer many of our questions by examining the amplitude equation for A_0. We first note that this equation includes the effect of the cubic nonlinearity and this nonlinear term exerts a stabilizing influence on the solution. In Fig. 4 we sketch the phase plane for the A_0 amplitude equation. We see that A_0 approaches $\pm 2\sqrt{\gamma}$ according as its initial condition is positive or negative. This implies that θ approaches $\pm \sqrt{3\gamma} x$ as $t \to \infty$. We note that these are the stable solutions found in the linear theory when δ is near one. The criteria for where θ goes, i.e., the dependence on initial conditions is quite natural. If $A_0(0) > 0$ (<0) the rod is initially stretched (contracted) and θ tends to a state of contact (separation). Further the dynamics are easily obtained by integrating the amplitude equation. We also note that inspection of the amplitude equations for the A_n reveals a mode coupling. That is, inspecting Eq. (5.2), we see that the coefficient in front of the A_n depends upon $A_0(\tau)$. Hence, even though all other modes are decaying, how they decay is influenced by the behavior of the $n = 0$ mode. Physically this is not unexpected as the A_0 mode tends to stretch or contract the rod. This means that the right end of the rod experiences different conditions according as the behavior of A_0 which in turn effects the behavior of the higher-order modes.

Downloaded 04 May 2010 to 171.66.16.27. Redistribution subject to ASME license or copyright; see http://www.asme.org/terms/Terms_Use.cfm

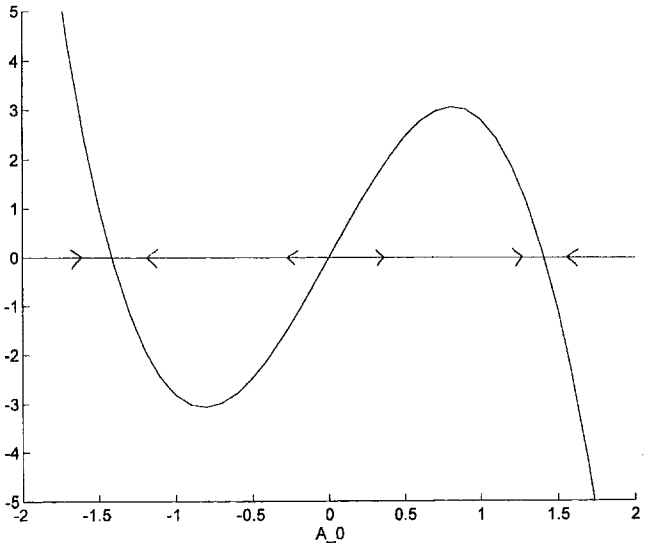

Fig. 4 Phase plane for the dominant amplitude equation illustrating the behavior of $A_0(\tau)$ and its dependence on initial conditions

Finally, we suggest that the above type analysis may be fruitfully applied to other thermoelastic contact problems. In particular, it would be of interest to see the results of such an analysis for a multidimensional problem where steady-state solutions are not so easy to construct. The author is currently attempting to extend this analysis to include the Barber condition and to apply this analysis to multidimensional thermoelastic contact problems.

Acknowledgment

The author gratefully acknowledges Dr. Louis G. Hector, Jr. for introducing him to this field and Prof. Donald S. Cohen for numerous useful discussions.

References

Barber, J. R., 1978, "Contact Problems Involving a Cooled Punch," *Journal of Elasticity,* Vol. 8, pp. 409–423.

Barber, J. R., 1981, "Stability of Thermoelastic Contact for the Aldo Model," ASME JOURNAL OF APPLIED MECHANICS, Vol. 48, pp. 555–558.

Barber, J. R., Dundurs, J., and Comninou, M., 1980, "Stability Considerations in Thermoelastic Contact," ASME JOURNAL OF APPLIED MECHANICS, Vol. 47, pp. 871–874.

Barber, J. R., and Zhang, R., 1988, "Transient Behavior and Stability for the Thermoelastic Contact of Two Rods of Dissimilar Materials," *Int. J. Mech. Sci.,* Vol. 30, pp. 691–704.

Comninou, M., and Dundurs, J., 1980, "On Lack of Uniqueness in Heat Conduction Through a Solid to Solid Contact," ASME *Journal of Heat Transfer,* Vol. 102, pp. 319–323.

Friedman, B., 1990, *Principles and Techniques of Applied Mathematics,* Dover, New York.

Kevorkian, J., and Cole, J. D., 1996, *Multiple Scale and Singular Perturbation Methods,* Springer-Verlag, New York.

Lee, K., and Barber, J. R., 1993, "Frictionally Excited Thermoelastic Instability in Automotive Disk Breaks," ASME *Journal of Tribology,* Vol. 115, pp. 607–614.

Li, C., and Barber, J. R., 1997, "Stability of Thermoelastic Contact of Two Layers of Dissimilar Materials," *Journal of Thermal Stresses,* Vol. 20, pp. 169–184.

Matkowsky, B. J., 1970, "A Simple Nonlinear Dynamic Stability Problem," *Bulletin of the American Mathematical Society,* Vol. 76, pp. 620–625.

Olesiak, Z. S., and Pyryev, Y. A., 1996, "Transient Response in a One-Dimensional Model of Thermoelastic Contact," ASME JOURNAL OF APPLIED MECHANICS, Vol. 63, pp. 575–581.

Panek, C., 1980, "A Thermomechanical Example of Autooscillation," ASME JOURNAL OF APPLIED MECHANICS, Vol. 47, pp. 875–878.

Richmond, O., Hector, L. G., Jr., Fridy, J. M., 1990, "Growth Instability During Nonuniform Directional Solidification of Pure Metals," ASME JOURNAL OF APPLIED MECHANICS, Vol. 57, pp. 529–536.

Srinivasan, M. G., and France, D. M., 1985, "Nonuniqueness in Steady State Heat Transfer in Prestressed Duplex Tubes: Analysis and Case History," ASME JOURNAL OF APPLIED MECHANICS, Vol. 48, pp. 555–558.

Yeo, T., and Barber, J. R., 1995, "Stability of a Semi-infinite Strip in Thermoelastic Contact With a Rigid Wall," *Int. J. Solids Structures,* Vol. 32, pp. 553–567.

Zhang, R., and Barber, J. R., 1990, "Effect of Material Properties on the Stability of Static Thermoelastic Contact," ASME JOURNAL OF APPLIED MECHANICS, Vol. 57, pp. 365–369.

APPENDIX A

In this appendix, we show that solutions to

$$\lambda = \mu \tan(\lambda) \tag{6.1}$$

are either pure real or pure imaginary. Here, μ is a real number. To obtain this result, we consider the eigenvalue problem

$$\frac{d^2\phi}{dx^2} + \lambda^2\phi = 0 \tag{6.2}$$

$$\frac{d\phi}{dx}(0) = 0 \tag{6.3}$$

$$\mu\frac{d\phi}{dx}(1) + \lambda^2\phi(1) = 0. \tag{6.4}$$

It is easy to see that this problem has a solution if and only if λ satisfies Eq. (6.1). Now, we multiply Eq. (6.2) by the complex conjugate of ϕ, which we denote by ϕ^*, and integrate from $x = 0$ to $x = 1$. This yields

$$\lambda^2(\|\phi\|^2 - \mu|\phi(1)|^2) = \|\phi'\|^2 \tag{6.5}$$

where here

$$\|\phi\|^2 = \int_0^1 \phi(x)\phi^*(x)dx, \tag{6.6}$$

$$|\phi(1)|^2 = \phi(1)\phi^*(1) \tag{6.7}$$

and primes denote differentiation with respect to x. Now, if $\|\phi\|^2 \neq \mu|\phi(1)|^2$, then we may solve for λ^2 to find

$$\lambda^2 = \frac{\|\phi'\|^2}{(\|\phi\|^2 - \mu|\phi(1)|^2)}. \tag{6.8}$$

Since the right-hand side of this expression is real, λ^2 must be as well. Hence in this case, λ is either pure real or pure imaginary. On the other hand, if $\|\phi\|^2 = \mu|\phi(1)|^2$, we are left with $\|\phi'\|^2 = 0$, and hence can conclude that ϕ is constant. But then for ϕ to be a nontrivial eigenfunction, we must conclude that $\lambda^2 = 0$ and hence again, λ is pure real or pure imaginary.

APPENDIX B

In this appendix, we construct the Green's function for, and study the spectrum of, the operator L which was introduced in Section 4. Recall that we are interested in the space of two component vectors U, whose first component is a real-valued C^2 function, $u(x)$, and whose second component is a real number, u_1. Further, recall that the operator L is defined by

$$LU = \begin{pmatrix} -\dfrac{d^2u}{dx^2} \\ 2\left(\dfrac{du}{dx}(0) - \dfrac{du}{dx}(1)\right) \end{pmatrix} \tag{7.1}$$

and that L's domain is the space of two component vectors U, such that $u(0) = 0$ and $u_1 = u(1)$. The Green's function, G, for our operator will be a two by two matrix whose components we define as

Downloaded 04 May 2010 to 171.66.16.27. Redistribution subject to ASME license or copyright; see http://www.asme.org/terms/Terms_Use.cfm

$$G(x, \zeta, \lambda) = \begin{pmatrix} g_1(x, \zeta, \lambda) & g_3(x, \lambda) \\ g_2(\zeta, \lambda) & g_4(\lambda) \end{pmatrix}. \quad (7.2)$$

The Green's function satisfies the equation

$$(L - \lambda^2)G = \begin{pmatrix} \delta(x - \zeta) & 0 \\ 0 & 1 \end{pmatrix} \quad (7.3)$$

and the boundary conditions

$$g_1(0, \zeta, \lambda) = 0 \quad (7.4)$$

$$g_3(0, \zeta, \lambda) = 0 \quad (7.5)$$

$$g_2(\zeta, \lambda) = g_1(1, \zeta, \lambda) \quad (7.6)$$

$$g_4(\lambda) = g_3(1, \lambda) \quad (7.7)$$

ensuring that each column of G lies in the domain of the operator L. Now, we may easily solve for each component. We find

$$g_1(x, \zeta, \lambda) = \begin{Bmatrix} A \sin(\lambda x) & x < \zeta \\ C \sin(\lambda x) + D \cos(\lambda x) & x > \zeta \end{Bmatrix} \quad (7.8)$$

$$g_2(\zeta, \lambda) = C \sin(\lambda) + D \cos(\lambda) \quad (7.9)$$

$$g_3(x, \zeta, \lambda) = \frac{\sin(\lambda x)}{\lambda(2(1 - \cos(\lambda)) - \lambda \sin(\lambda))} \quad (7.10)$$

$$g_4(\zeta, \lambda) = \frac{\sin(\lambda)}{\lambda(2(1 - \cos(\lambda)) - \lambda \sin(\lambda))} \quad (7.11)$$

where here

$$A = \frac{\cos(\lambda\zeta)(2\cos(\lambda) + \lambda \sin(\lambda)) - \sin(\lambda\zeta)(\lambda \cos(\lambda) - 2\sin(\lambda))}{\lambda(\lambda \sin(\lambda) - 2(1 - \cos(\lambda)))} \quad (7.12)$$

$$C = \frac{2\cos(\lambda\zeta) + 2\sin(\lambda\zeta)\sin(\lambda) + \lambda \sin(\lambda\zeta)\cos(\lambda)}{\lambda(\lambda \sin(\lambda) - 2(1 - \cos(\lambda)))} \quad (7.13)$$

and

$$D = \frac{\sin(\lambda\zeta)}{\lambda}. \quad (7.14)$$

The spectrum of L may now be obtained by considering the integral of the Green's function over a large circle in the complex λ plane, i.e., we need to consider

$$\frac{1}{2\pi i} \oint G d\lambda. \quad (7.15)$$

This integral may be evaluated by residues. It is clear that G has no branch cuts, and that the location of the poles of G are defined by

$$\frac{\lambda}{2} = \tan\left(\frac{\lambda}{2}\right). \quad (7.16)$$

Hence the spectrum of L is purely discrete and is as discussed in Section 4.

Downloaded 04 May 2010 to 171.66.16.27. Redistribution subject to ASME license or copyright; see http://www.asme.org/terms/Terms_Use.cfm

Bifurcation of Elastoplastic Pressure-Sensitive Hollow Cylinders

P. Papanastasiou
Schlumberger Cambridge Research,
Cambridge CB3 0EL, England

D. Durban
Faculty of Aerospace Engineering,
Technion,
Haifa 32000, Israel
Mem. ASME

A linear bifurcation analysis is presented for pressure sensitive elastoplastic hollow cylinders under radial surface loads. Material response is modeled by flow and deformation theories of the Drucker-Prager solid accounting for arbitrary hardening. Sample calculations are given for cylinders that deform in axially symmetric patterns under uniform radial pressure applied at the boundaries. No bifurcation points were found with flow theory in the realistic range of stress though the primary equilibrium path is nearly identical for both theories. For thick-walled cylinders the dominant bifurcation mode predicted by deformation theory appears to be a circumferential surface instability. Deformation theory results for bifurcations are apparently not sensitive to deviations from associativity.

1 Introduction

Collapse and failure of wellbores, including the emergence of concentrated shear bands and sanding, are closely associated with possible bifurcation away from the equilibrium state of stress. However, while the onset of bifurcation modes along the primary path of (axially symmetric) deforming hollow cylinders have been examined in detail for elastoplastic metals (Chu, 1979; Tomita et al., 1981; Larsson et al., 1982; Reddy, 1982; Tvergaard, 1990) there appear to be relatively few studies available for bifurcation of hollow cylinders made of pressure-sensitive materials. Interest in such problems rises from modern technologies in sintered powder metals manufacturing as well as from the classical field of borehole stability within the context of geomechanics. An early exception is the doctoral dissertation by Papanastasiou (1990) where borehole bifurcation and failure due to high stresses in geomaterials was investigated. Studies of bifurcation problems for the borehole, based on conventional perturbation methods for a rigid/plastic material, for either classical plasticity (Vardoulakis and Papanastasiou, 1988) or for Cosserat plasticity (Papanastasiou and Vardoulakis, 1989) are also available. Furthermore, Papanastasiou and Vardoulakis (1992) carried out a post-bifurcation analysis with a Cosserat finite element model incorporating material softening in the constitutive equations of elastoplasticity in order to trigger localization of deformation and to model progressive failure. More recently, Chau (1992, 1993) examined in detail a wide spectrum of bifurcations in axially symmetric stressed full cylinders, made of pressure-sensitive materials, with transverse isotropy (thus excluding plastic nonassociativity). In the present study emphasis is placed on enhancing the constitutive modeling to include nonassociated response within the framework of both flow and deformation theories.

This paper presents a systematic, though preliminary, study of bifurcation phenomena in hollow cylinders which admit a pressure-sensitive elastoplastic response. The analysis is based on the complete formulation of incremental (rate) continuum mechanics with finite strains along with objective incremental constitutive equations for elastoplastic pressure sensitive solids. The basic setting is that of a hollow thick-walled cylinder which deforms in an axially symmetric pattern under uniform normal loads applied at the boundaries.

The perturbed field equations are derived in the next section together with appropriate boundary data for traction rates and velocities. In Section 3 we discuss eigenmodes that admit separation of variables representation and show that the governing equations for the perturbed field are reduced to an eigenvalue system with three ordinary differential equations of second order each. Material behavior is modeled by flow and deformation theories of a nonassociated Drucker-Prager pressure-sensitive solid. The formulation is within the framework of large strains accounting for arbitrary hardening (or softening) response of the plastic constitutive branch.

Numerical examples are provided in Section 4, for Castlegate sandstone, over a range of hollow cylinder problems. These include bifurcations under increasing external pressure (the hollow cylinder test) and decreasing internal pressure from a background uniform confining pressure (to simulate wellbore drilling).

The main findings from the numerical examples are that deformation theory predicts bifurcations at stress levels which are considerably below flow theory results—the latter occur at unrealistically high loads—and that for thick cylinders the dominant bifurcation mode is a surface instability in the circumferential direction. No axial waves appear to enter the critical bifurcation modes, resulting in a plane-strain response of the perturbed field. Bifurcation modes develop in the presence of strain hardening and it was found that nonassociativity has negligible effect on the critical loads.

2 Perturbed Equilibrium Equations

We examine a hollow circular cylinder which deforms in an orthogonal pattern under the action of uniform normal boundary loads. Let (r, θ, z) be a current Eulerian polar system of coordinates with associated unit base vectors $(\mathbf{e}_r, \mathbf{e}_\theta, \mathbf{e}_z)$. Then the deformed configuration of the cylinder is bounded by $(a \le r \le b, 0 \le z \le l)$ and the primary state of stress is simply

$$\boldsymbol{\sigma} = \sigma_{rr}\mathbf{e}_r\mathbf{e}_r + \sigma_{\theta\theta}\mathbf{e}_\theta\mathbf{e}_\theta + \sigma_{zz}\mathbf{e}_z\mathbf{e}_z \qquad (1)$$

where the stress components may depend on r, and $\boldsymbol{\sigma}$ satisfies the equilibrium equation

$$\nabla \cdot \boldsymbol{\sigma} = \mathbf{0}. \qquad (2)$$

Possible modes of bifurcation along the primary path are governed by the rate form of (2), namely

Contributed by the Applied Mechanics Division of THE AMERICAN SOCIETY OF MECHANICAL ENGINEERS for publication in the ASME JOURNAL OF APPLIED MECHANICS.

Discussion on the paper should be addressed to the Technical Editor, Professor Lewis T. Wheeler, Department of Mechanical Engineering, University of Houston, Houston, TX 77204-4792, and will be accepted until four months after final publication of the paper itself in the ASME JOURNAL OF APPLIED MECHANICS.

Manuscript received by the ASME Applied Mechanics Division, Dec. 23, 1997; final revision, Sept. 7, 1998. Associate Technical Editor: M. M. Carroll.

 Copyright © 1999 by ASME

Downloaded 04 May 2010 to 171.66.16.27. Redistribution subject to ASME license or copyright; see http://www.asme.org/terms/Terms_Use.cfm

$$\nabla\cdot(\overset{\nabla}{\boldsymbol{\sigma}} - \mathbf{D}\cdot\boldsymbol{\sigma} + \boldsymbol{\sigma}\cdot\mathbf{W} + \mathbf{I}\cdot\cdot\mathbf{D}\boldsymbol{\sigma}) = \mathbf{0} \tag{3}$$

where the Eulerian strain rate $\mathbf{D}$ and the spin $\mathbf{W}$ are related to the perturbed velocity vector $\mathbf{V}$ by

$$\mathbf{D} = \tfrac{1}{2}(\nabla\mathbf{V} + \mathbf{V}\nabla)$$

$$\mathbf{W} = \tfrac{1}{2}(\nabla\mathbf{V} - \mathbf{V}\nabla). \tag{4}$$

$\mathbf{I}$ is the second-order unit tensor and $\overset{\nabla}{\boldsymbol{\sigma}}$ denotes the Jaumann stress rate defined as

$$\overset{\nabla}{\boldsymbol{\sigma}} = \dot{\boldsymbol{\sigma}} + \mathbf{W}\cdot\boldsymbol{\sigma} - \boldsymbol{\sigma}\cdot\mathbf{W} \tag{5}$$

with the superposed dot standing for differentiation with respect to a time-like parameter. Material behavior is here described by the instantaneous (incremental) linear relation

$$\overset{\nabla}{\boldsymbol{\sigma}} = \mathcal{L}\cdot\cdot\mathbf{D} \tag{6}$$

where $\mathcal{L}$ is the instantaneous moduli tensor and depends on the stress history. Equation (3) is supplemented by the boundary data, for traction rates or velocities,

$$\mathbf{n}\cdot(\overset{\nabla}{\boldsymbol{\sigma}} - \mathbf{D}\cdot\boldsymbol{\sigma} + \boldsymbol{\sigma}\cdot\mathbf{W} + d_{nn}\boldsymbol{\sigma}) = \mathbf{0} \quad \text{or} \quad \mathbf{n}\cdot\mathbf{V} = 0, \tag{7}$$

where $\mathbf{n}$ is the outward unit normal vector at the boundary and

$$d_{nn} = \mathbf{nn}\cdot\cdot\mathbf{D}. \tag{8}$$

Now, denoting by (u, v, w) the (r, θ, z) components of the perturbed velocity vector $\mathbf{V}$ we have

$$\mathbf{V} = u\mathbf{e}_r + v\mathbf{e}_\theta + w\mathbf{e}_z \tag{9}$$

implying that the Eulerian strain rate tensor $(4)_a$ is

$$\mathbf{D} = d_{rr}\mathbf{e}_r\mathbf{e}_r + d_{\theta\theta}\mathbf{e}_\theta\mathbf{e}_\theta + d_{zz}\mathbf{e}_z\mathbf{e}_z + d_{r\theta}(\mathbf{e}_r\mathbf{e}_\theta + \mathbf{e}_\theta\mathbf{e}_r) + d_{\theta z}(\mathbf{e}_\theta\mathbf{e}_z + \mathbf{e}_z\mathbf{e}_\theta) + d_{zr}(\mathbf{e}_z\mathbf{e}_r + \mathbf{e}_r\mathbf{e}_z) \tag{10}$$

with the strain rate components

$$d_{rr} = u_{,r} \quad d_{\theta\theta} = \frac{1}{r}(u + v_{,\theta}) \quad d_{zz} = w_{,z}$$

$$d_{r\theta} = \frac{1}{2}\left(\frac{u_{,\theta}}{r} + v_{,r} - \frac{v}{r}\right) \quad d_{\theta z} = \frac{1}{2}\left(v_{,z} + \frac{w_{,\theta}}{r}\right)$$

$$d_{zr} = \frac{1}{2}(u_{,z} + w_{,r}). \tag{11}$$

Similarly, the spin tensor $(4)_b$ can be written as

$$\mathbf{W} = \omega_{r\theta}(\mathbf{e}_r\mathbf{e}_\theta - \mathbf{e}_\theta\mathbf{e}_r) + \omega_{\theta z}(\mathbf{e}_\theta\mathbf{e}_z - \mathbf{e}_z\mathbf{e}_\theta) + \omega_{zr}(\mathbf{e}_z\mathbf{e}_r - \mathbf{e}_r\mathbf{e}_z) \tag{12}$$

with the components

$$\omega_{r\theta} = \frac{1}{2}\left(-\frac{u_{,\theta}}{r} + v_{,r} + \frac{v}{r}\right) \quad \omega_{\theta z} = \frac{1}{2}\left(-v_{,z} + \frac{w_{,\theta}}{r}\right)$$

$$\omega_{zr} = \frac{1}{2}(u_{,z} - w_{,r}). \tag{13}$$

Inserting the stress tensor (1), along with (10) and (12), in the rate equilibrium equation we obtain the three scalar equations

$$\overset{\nabla}{\sigma}_{rr,r} + \frac{1}{r}(\overset{\nabla}{\sigma}_{rr} - \overset{\nabla}{\sigma}_{\theta\theta}) + \frac{1}{r}\overset{\nabla}{\sigma}_{r\theta,\theta} + \overset{\nabla}{\sigma}_{rz,z} + [\sigma_{rr}(d_{\theta\theta} + d_{zz})]_{,r} + \frac{1}{r}[\sigma_{rr}(d_{\theta\theta} + d_{zz}) - \sigma_{\theta\theta}(d_{zz} + d_{rr})] - \frac{1}{r}(\sigma_{\theta\theta}\omega_{r\theta} + \sigma_{rr}d_{r\theta})_{,\theta} + (\sigma_{zz}\omega_{zr} - \sigma_{rr}d_{zr})_{,z} = 0 \tag{14}$$

$$\overset{\nabla}{\sigma}_{r\theta,r} + \frac{2}{r}\overset{\nabla}{\sigma}_{r\theta} + \frac{1}{r}\overset{\nabla}{\sigma}_{\theta\theta,\theta} + \overset{\nabla}{\sigma}_{\theta z,z} + (\sigma_{rr}\omega_{r\theta} - \sigma_{\theta\theta}d_{r\theta})_{,r} + \frac{1}{r}\sigma_{\theta\theta}(d_{zz} + d_{rr})_{,\theta} - \frac{1}{r}(\sigma_{rr} + \sigma_{\theta\theta})d_{r\theta} + \frac{1}{r}(\sigma_{rr} - \sigma_{\theta\theta})\omega_{r\theta} - (\sigma_{zz}\omega_{\theta z} + \sigma_{\theta\theta}d_{\theta z})_{,z} = 0 \tag{15}$$

$$\overset{\nabla}{\sigma}_{zr,r} + \frac{1}{r}\overset{\nabla}{\sigma}_{zr} + \frac{1}{r}\overset{\nabla}{\sigma}_{\theta z,\theta} + \overset{\nabla}{\sigma}_{zz,z} - (\sigma_{rr}\omega_{zr} + \sigma_{zz}d_{zr})_{,r} + \frac{1}{r}(\sigma_{\theta\theta}\omega_{\theta z} - \sigma_{zz}d_{\theta z})_{,\theta} - \frac{1}{r}(\sigma_{rr}\omega_{zr} + \sigma_{zz}d_{zr}) + \sigma_{zz}(d_{rr} + d_{\theta\theta})_{,z} = 0 \tag{16}$$

where $\overset{\nabla}{\sigma}_{ij}$, $(i, j = r, \theta, z)$ are the Jaumann stress rate components. The boundary data (7) follow as

$$\begin{aligned}
r = a, b: \quad & \overset{\nabla}{\sigma}_{rr} = 0 \quad \text{or} && u = 0\\
& \overset{\nabla}{\sigma}_{r\theta} + \sigma_{rr}\omega_{r\theta} - \sigma_{\theta\theta}d_{r\theta} = 0 \quad \text{or} && v = 0\\
& \overset{\nabla}{\sigma}_{zr} - \sigma_{rr}\omega_{zr} - \sigma_{zz}d_{zr} = 0 \quad \text{or} && w = 0
\end{aligned} \tag{17}$$

$$\begin{aligned}
r = 0, l: \quad & \overset{\nabla}{\sigma}_{zr} + \sigma_{zz}\omega_{zr} - \sigma_{rr}d_{zr} = 0 \quad \text{or} && u = 0\\
& \overset{\nabla}{\sigma}_{\theta z} - \sigma_{zz}\omega_{\theta z} - \sigma_{\theta\theta}d_{\theta z} = 0 \quad \text{or} && v = 0\\
& \overset{\nabla}{\sigma}_{zz} = 0 \quad \text{or} && w = 0.
\end{aligned} \tag{18}$$

Material behavior in this study is modeled by the flow and deformation theories of the Drucker-Prager solid (Durban and Fleck 1997; Durban and Papanastasiou 1997a, 1997b) where the constitutive relation (6) becomes

$$\begin{aligned}
\overset{\nabla}{\sigma}_{rr} &= L_{rr}d_{rr} + L_{r\theta}d_{\theta\theta} + L_{rz}d_{zz}\\
\overset{\nabla}{\sigma}_{\theta\theta} &= L_{\theta r}d_{rr} + L_{\theta\theta}d_{\theta\theta} + L_{\theta z}d_{zz}\\
\overset{\nabla}{\sigma}_{zz} &= L_{zr}d_{rr} + L_{z\theta}d_{\theta\theta} + L_{zz}d_{zz}
\end{aligned} \tag{19}$$

$$\overset{\nabla}{\sigma}_{r\theta} = 2G_{r\theta}d_{r\theta} \quad \overset{\nabla}{\sigma}_{\theta z} = 2G_{\theta z}d_{\theta z} \quad \overset{\nabla}{\sigma}_{zr} = 2G_{zr}d_{zr}. \tag{20}$$

Here the instantaneous moduli L_{ij}, G_{ij} $(i, j = r, \theta, z)$ may depend on the primary states of stress and strain and are therefore known functions of the radial coordinate r. Inserting the stress rates (19)–(20) in the rate equilibrium Eqs. (14)–(16) and boundary conditions (17)–(18), and substituting the strain rate component (11) and spin components (13), we arrive at an eigenvalue system for the onset of bifurcation.

Of course, this incremental formulation can be used to trace the pre-bifurcation axially symmetric deformation pattern. With the plane-strain constraint Eqs. (14)–(16) simplify to

$$\frac{d}{dr}\overset{\nabla}{\sigma}_{rr} + \frac{1}{r}(\overset{\nabla}{\sigma}_{rr} - \overset{\nabla}{\sigma}_{\theta\theta}) + \frac{d}{dr}(\sigma_{rr}d_{\theta\theta}) + \frac{1}{r}(\sigma_{rr}d_{\theta\theta} - \sigma_{\theta\theta}d_{rr}) = 0 \tag{21}$$

Downloaded 04 May 2010 to 171.66.16.27. Redistribution subject to ASME license or copyright; see http://www.asme.org/terms/Terms_Use.cfm

along with specified radial traction rates $\overset{\nabla}{\sigma}_{rr}$ at $r = a, b$. No shear and no spin are activated during that path and the only non-vanishing strain rates are, by (11),

$$d_{rr} = \frac{du}{dr} \qquad d_{\theta\theta} = \frac{u}{r}. \tag{22}$$

Thus, by (19), (21) is related to a second-order equation for the radial velocity $u(r)$.

3 Eigenmodes Solution and Constitutive Specification

Possible eigenfields of the homogeneous system (14)–(18) are given by the separation of variables solution

$$u = U(r) \cos m\theta \cos \frac{k\pi z}{l} \tag{23}$$

$$v = V(r) \sin m\theta \cos \frac{k\pi z}{l} \tag{24}$$

$$w = W(r) \cos m\theta \sin \frac{k\pi z}{l} \tag{25}$$

where the radial profiles $U(r), V(r), W(r)$ are to be determined and $m, k = 0, 1, 2, \ldots$ are the circumferential and axial wave numbers. This velocity field complies with conditions (18) of vanishing shear traction rates and axial velocity at $z = 0, l$. Substituting the velocities (23)–(25) in the rate equilibrium Eqs. (14)–(16) we obtain three ordinary differential equations for the radial profiles, viz

$$L_{rr}U'' + \left[L'_{rr} + \frac{1}{r}(L_{rr} + L_{r\theta} - L_{\theta r}) + \frac{1}{r}(\sigma_{rr} - \sigma_{\theta\theta})\right]U'$$
$$+ \left[\frac{1}{r}(L_{r\theta} + \sigma_{rr})' - \frac{1}{r^2}L_{\theta\theta} - \left(\frac{m}{r}\right)^2\left(G_{r\theta} - \frac{1}{2}(\sigma_{rr} - \sigma_{\theta\theta})\right) - \left(\frac{k\pi}{l}\right)^2\left(G_{zr} - \frac{1}{2}(\sigma_{rr} - \sigma_{zz})\right)\right]U$$
$$+ \left(\frac{m}{r}\right)\left[L_{r\theta} + G_{r\theta} + \frac{1}{2}(\sigma_{rr} - \sigma_{\theta\theta})\right]V' + m\left[\frac{1}{r}L'_{r\theta} - \frac{1}{r^2}\left(L_{\theta\theta} + G_{r\theta} + \frac{1}{2}(\sigma_{rr} - \sigma_{\theta\theta})\right)\right]V + \left(\frac{k\pi}{l}\right)\left[L_{rz} + G_{zr} + \frac{1}{2}(\sigma_{rr} - \sigma_{zz})\right]W'$$
$$+ \left(\frac{k\pi}{l}\right)\left[L'_{rz} + \frac{1}{r}(L_{rz} - L_{\theta z})\right]W = 0 \tag{26}$$

$$-\left(\frac{m}{r}\right)\left[L_{\theta r} + G_{r\theta} - \frac{1}{2}(\sigma_{rr} - \sigma_{\theta\theta})\right]U' - \left(\frac{m}{r}\right)\left[\left(G_{r\theta} - \frac{1}{2}\sigma_{\theta\theta}\right)' + \frac{1}{r}(L_{\theta\theta} + G_{r\theta})\right]U$$
$$+ \left[G_{r\theta} + \frac{1}{2}(\sigma_{rr} - \sigma_{\theta\theta})\right]V''$$
$$+ \left[\left(G_{r\theta} + \frac{1}{2}(\sigma_{rr} - \sigma_{\theta\theta})\right)' + \frac{1}{r}\left(G_{r\theta} + \frac{1}{2}(\sigma_{rr} - \sigma_{\theta\theta})\right)\right]V' - \left[\frac{1}{r}\left(G_{r\theta} - \frac{1}{2}\sigma_{\theta\theta}\right)' + \frac{1}{r^2}G_{r\theta} + \left(\frac{m}{r}\right)^2 L_{\theta\theta} + \left(\frac{k\pi}{l}\right)^2\left(G_{\theta z} - \frac{1}{2}(\sigma_{\theta\theta} - \sigma_{zz})\right)\right]V - \left(\frac{m}{r}\right)\left(\frac{k\pi}{l}\right)\left[L_{\theta z} + G_{\theta z} + \frac{1}{2}(\sigma_{\theta\theta} - \sigma_{zz})\right]W = 0 \tag{27}$$

$$-\left(\frac{k\pi}{l}\right)\left[L_{zr} + G_{zr} - \frac{1}{2}(\sigma_{rr} - \sigma_{zz})\right]U' - \left(\frac{k\pi}{l}\right)\left[\left(G_{zr} - \frac{1}{2}(\sigma_{rr} + \sigma_{zz})\right)' + \frac{1}{r}\left(L_{z\theta} + G_{zr} - \frac{1}{2}(\sigma_{rr} - \sigma_{zz})\right)\right]U$$
$$- \left(\frac{m}{r}\right)\left(\frac{k\pi}{l}\right)\left[L_{z\theta} + G_{\theta z} - \frac{1}{2}(\sigma_{\theta\theta} - \sigma_{zz})\right]V$$
$$+ \left[G_{zr} + \frac{1}{2}(\sigma_{rr} - \sigma_{zz})\right]W'' + \left[\left(G_{zr} + \frac{1}{2}(\sigma_{rr} - \sigma_{zz})\right)' + \frac{1}{r}\left(G_{zr} + \frac{1}{2}(\sigma_{rr} - \sigma_{zz})\right)\right]W' - \left[\left(\frac{m}{r}\right)^2\left(G_{\theta z} + \frac{1}{2}(\sigma_{\theta\theta} - \sigma_{zz})\right) + \left(\frac{k\pi}{l}\right)^2 L_{zz}\right]W = 0 \tag{28}$$

where the prime denotes partial differentiation with respect to r.

Similarly, the traction-rate free boundary conditions of (17) take the form, at $r = a, b$,

$$L_{rr}U' + \frac{1}{r}L_{r\theta}U + \left(\frac{m}{r}\right)L_{r\theta}V + \left(\frac{k\pi}{l}\right)L_{rz}W = 0$$
$$-\left(\frac{m}{r}\right)\left[G_{r\theta} - \frac{1}{2}(\sigma_{rr} + \sigma_{\theta\theta})\right]U + \left[G_{r\theta} + \frac{1}{2}(\sigma_{rr} - \sigma_{\theta\theta})\right]V' - \frac{1}{r}\left[G_{r\theta} - \frac{1}{2}(\sigma_{rr} + \sigma_{\theta\theta})\right]V = 0 \tag{29}$$
$$-\left(\frac{k\pi}{l}\right)\left[G_{zr} - \frac{1}{2}(\sigma_{rr} + \sigma_{zz})\right]U + \left[G_{zr} + \frac{1}{2}(\sigma_{rr} - \sigma_{zz})\right]W' = 0.$$

The eigensystem (26)–(29) covers a wide range of solids described by (19)–(20) and is valid for all axially symmetric (torsionless) primary paths. The pre-bifurcation deformation pattern is recovered from (26)–(28) with $m = 0$ and $k = 0$, implying that both v and w of (24)–(25) vanish, which reduce to the single second-order equation

$$L_{rr}U'' + \left[L'_{rr} + \frac{1}{r}(L_{rr} + L_{r\theta} - L_{\theta r}) + \frac{1}{r}(\sigma_{rr} - \sigma_{\theta\theta})\right]U' + \left[\frac{1}{r}(L_{r\theta} + \sigma_{rr})' - \frac{1}{r^2}L_{\theta\theta}\right]U = 0 \tag{30}$$

Downloaded 04 May 2010 to 171.66.16.27. Redistribution subject to ASME license or copyright; see http://www.asme.org/terms/Terms_Use.cfm

along with the specified traction rate ($\overset{\nabla}{\sigma}_{rr}$) boundary conditions, via (29), at $r = a, b$

$$L_{rr}U' + \frac{1}{r}L_{r\theta}U = \overset{\nabla}{\sigma}_{rr}. \tag{31}$$

The uniform axial velocity which may accompany the solution of (30) – (31), unless the plane-strain constraint is imposed on the primary path, is linear in z and is superimposed on the radial velocity U.

The Drucker-Prager constitutive relations for elastoplastic pressure sensitive solids originate from an effective stress σ_e and a plastic potential ϕ defined by (Durban and Fleck, 1977)

$$\sigma_e = Q + \mu\sigma_h \qquad \phi = Q + \eta\sigma_h \tag{32}$$

where $Q = (\frac{3}{2}\mathbf{S}\cdot\cdot\mathbf{S})^{1/2}$ is the von Mises effective stress, $\mathbf{S}$ being the stress deviator, σ_h is the hydrostatic stress ($\frac{1}{3}\mathbf{I}\cdot\cdot\boldsymbol{\sigma}$) and ($\mu$, η) are material parameters that reflect the pressure sensitivity of the material. For associated solids $\mu = \eta$ and for the Mises model $\mu = \eta = 0$. Normality of plastic strain rates, plastic power equivalence and linear decomposition of the elastic-plastic strain rate generate a flow theory of the type (6) with the instantaneous moduli tensor

$$\mathcal{L} = 2GJ + \lambda\mathbf{II} - \Gamma_t\left(\frac{3\mathbf{S}}{2Q} + \frac{\eta K}{2G}\mathbf{I}\right)\left(\frac{3\mathbf{S}}{2Q} + \frac{\mu K}{2G}\mathbf{I}\right) \tag{33}$$

where J is the fourth-order unit tensor, (G, λ, K) are the usual elastic constants (with ν and E denoting the Poisson ratio and elastic modulus, respectively),

$$G = \frac{E}{2(1+\nu)} \qquad \lambda = \frac{\nu E}{(1+\nu)(1-2\nu)}$$

$$K = \frac{E}{3(1-2\nu)} \tag{34}$$

and

$$\Gamma_t = \frac{4(G - G_t)/3}{1 + (K/K_t - 1)G_t/G} \tag{35}$$

with the instantaneous shear (G_t) and bulk (K_t) moduli defined as

$$\frac{1}{G_t} = \frac{1}{G} + 3\left(\frac{\sigma_e}{\phi}\right)\frac{d\epsilon_p}{d\sigma_e} \quad \frac{1}{K_t} = \frac{1}{K} + \mu\eta\left(\frac{\sigma_e}{\phi}\right)\frac{d\epsilon_p}{d\sigma_e}. \tag{36}$$

Here, the total plastic strain ϵ_p is a known function of the effective stress σ_e, representing hardening or softening of the material. It is worth mentioning that the definitions of G_t and K_t follow from the power production identity

$$\boldsymbol{\sigma}\cdot\cdot\mathbf{D} = \frac{1}{3G_t}Q\dot{Q} + \frac{1}{K_t}\sigma_h\dot{\sigma}_h + \frac{\sigma_e}{\phi}\left(\frac{d\epsilon_p}{d\sigma_e}\right)(\mu Q\dot{\sigma}_h + \eta\sigma_h\dot{Q}). \tag{37}$$

For the axially symmetric primary path of the hollow cylinder we obtain from (33) the instantaneous moduli, defined in (19) – (20),

$$L_{ij} = 2G\delta_{ij} + \lambda - \Gamma_t N_i M_j \quad i, j = r, \theta, z$$

$$G_{r\theta} = G_{\theta z} = G_{zr} = G \tag{38}$$

with

$$M_i = \frac{3S_{ii}}{2Q} + \frac{\mu K}{2G} \qquad N_i = \frac{3S_{ii}}{2Q} + \frac{\eta K}{2G}$$

$$i = r, \theta, z \quad \text{no sum.} \tag{39}$$

Notice that for nonassociated solids $M_i \neq N_i$ implying that $L_{ij} \neq L_{ji}$ when $i \neq j$.

The deformation theory version of the Drucker-Prager solid has been formulated in Durban and Fleck (1997) and can be cast in the form

$$\mathbf{E}_L = \frac{1}{2G_s}\boldsymbol{\sigma} - \left(\frac{1}{2G_s} - \frac{1}{3K_s}\right)\sigma_h\mathbf{I} + \frac{p_0}{3K}\mathbf{I} \tag{40}$$

where $\mathbf{E}_L$ is the finite logarithmic strain tensor, (G_s, K_s) are the secant shear and bulk moduli, respectively, defined as

$$\frac{1}{G_s} = \frac{1}{G} + \frac{3\sigma_e\epsilon_p}{\phi Q} \qquad \frac{1}{K_s} = \frac{1}{K} + \eta\frac{\sigma_e\epsilon_p}{\phi\sigma_h}, \tag{41}$$

and p_0 is the background hydrostatic pressure. The rate version of (40) is obtained (Durban and Papanastasiou, 1997b) by taking the Jaumann rate of (40) which generates the relation

$$\overset{\nabla}{\boldsymbol{\sigma}} = \mathcal{L}_d\cdot\cdot\overset{\nabla}{\mathbf{E}}_L \tag{42}$$

where the Jaumann rate of the logarithmic strain tensor is related to the Eulerian strain rate tensor by (Durban and Papanastasiou, 1997b)

$$\overset{\nabla}{\mathbf{E}}_L = \mathcal{A}\cdot\cdot\mathbf{D} \quad \mathcal{A} = J + \frac{1}{2}\left(\frac{a_j^2 + a_k^2}{a_j^2 - a_k^2}\ln\frac{a_j}{a_k} - 1\right)\mathbf{S}_i\mathbf{S}_i \tag{43}$$

and $\mathcal{L}_d$ is a fourth-order material tensor. Here a_i are the principal stretches and $\mathbf{S}_i$ the shear unit tensors (e.g., $\mathbf{S}_1 = \mathbf{n}_2\mathbf{n}_3 + \mathbf{n}_3\mathbf{n}_2$ where $\mathbf{n}_i$ are the principal unit vectors associated with $\boldsymbol{\sigma}$). In the expression for $\mathcal{A}$ (43) summation is carried over i with (j, k) taking the corresponding cyclic values.

The material tensor $\mathcal{L}_d$ in (42) can be put in a form which resembles the flow theory tensor (33), viz

$$\mathcal{L}_d = 2G_sJ + \lambda_d\mathbf{II} - \Gamma_d\left(\frac{3\mathbf{S}}{2Q} + \frac{\eta_d K}{2G_s}\mathbf{I}\right)\left(\frac{3\mathbf{S}}{2Q} + \frac{\mu_d K}{2G_s}\mathbf{I}\right) \tag{44}$$

where

$$\lambda_d = \frac{(1 - G_d/G_s)K}{1 + (G_d/G)(K/K_d - 1) - (G_dK)/(G_sK_d)} - \frac{2}{3}G_s \tag{45}$$

$$\Gamma_d = \frac{(4G_s/3)[1 + (G_d/G)(K/K_d - 1) - (G_dK)/(G_sK_d)]}{1 + (G_d/G)(K/K_d - 1)} \tag{46}$$

$$\eta_d = \frac{\eta(1 - G_d/G)}{1 + (G_d/G)(K/K_d - 1) - (G_dK)/(G_sK_d)} \tag{47}$$

$$\mu_d = \frac{(3/\eta)G_d(1/K_d - 1/K)}{1 + (G_d/G)(K/K_d - 1) - (G_dK)/(G_sK_d)} \tag{48}$$

with the instantaneous shear (G_d) and bulk (K_d) moduli given by

$$\frac{1}{G_d} = \frac{1}{G} + 3\left[\left(\frac{1}{\phi}\right)\frac{d(\sigma_e\epsilon_p)}{d\sigma_e} - \frac{\sigma_e\epsilon_p}{\phi^2}\right] \tag{49}$$

$$\frac{1}{K_d} = \frac{1}{K} + \eta\left[\left(\frac{\mu}{\phi}\right)\frac{d(\sigma_e\epsilon_p)}{d\sigma_e} - \eta\frac{\sigma_e\epsilon_p}{\phi^2}\right]. \tag{50}$$

These definitions for G_d and K_d follow from a plastic power identity similar to (37).

Downloaded 04 May 2010 to 171.66.16.27. Redistribution subject to ASME license or copyright; see http://www.asme.org/terms/Terms_Use.cfm

Combining (43) with (42) we find that the instantaneous moduli tensor defined in (6) takes here the form

$$\mathcal{L} = \mathcal{L}_d \cdot\cdot \mathcal{A} \tag{51}$$

with $\mathcal{L}_d$ expressed by (44). It follows that the material moduli of (19)–(20) for the deformation theory version of the Drucker-Prager material become

$$L_{ij} = 2G_s\delta_{ij} + \lambda_d - \Gamma_d N_i M_j \quad i, j = r, \theta, z$$

$$G_{r\theta} = G_s\left(\frac{a_r^2 + a_\theta^2}{a_r^2 - a_\theta^2}\ln\frac{a_r}{a_\theta}\right) \quad G_{\theta z} = G_s\left(\frac{a_\theta^2 + a_z^2}{a_\theta^2 - a_z^2}\ln\frac{a_\theta}{a_z}\right)$$

$$G_{zr} = G_s\left(\frac{a_z^2 + a_r^2}{a_z^2 - a_r^2}\ln\frac{a_z}{a_r}\right) \tag{52}$$

with

$$M_i = \frac{3S_{ii}}{2Q} + \frac{\mu_d K}{2G_s} \qquad N_i = \frac{3S_{ii}}{2Q} + \frac{\eta_d K}{2G_s}$$

$$i = r, \theta, z \quad \text{no sum.} \tag{53}$$

Thus, the deformation theory relations (52)–(53) are on equal footing with the flow theory relations (38)–(39). In fact moduli L_{ij} of (52) could be recovered from (38) with the transformations $G \to G_s$, $\lambda \to \lambda_d$, $\Gamma_t \to \Gamma_d$, $\mu \to \mu_d$, $\eta \to \eta_d$, along with the large strain factors in the shear moduli of (52). The latter, incidentally, can be removed by replacing $\overset{\nabla}{\mathbf{E}}_L$ in (42) by $\mathbf{D}$ and thereby constructing a hypoelastic nonholonomic model based on the Drucker-Prager deformation theory.

For associated solids with $\eta = \mu$ ($\phi = \sigma_e$) we find from (36) and (49)–(50) that

$$\frac{1}{G_d} = \frac{1}{G_t} = \frac{1}{G} + 3\frac{d\epsilon_p}{d\sigma_e} \qquad \frac{1}{K_d} = \frac{1}{K_t} = \frac{1}{K} + \mu^2\frac{d\epsilon_p}{d\sigma_e} \tag{54}$$

with a further reduction to the Mises solid when $\mu = 0$. With (54) we have from (47)–(48) that $\eta_d = \mu_d$ and the deformation theory tensor (51) becomes symmetric, $\mathcal{L}^T = \mathcal{L}$.

The deformation theory instantaneous moduli are smaller than their flow theory counterparts hence describing weaker plastic response. For that reason, bifurcations predicted by flow theory are usually at much higher levels of load when compared to deformation theory results (Durban and Papanastasiou, 1997b).

In the absence of pressure sensitivity ($\mu = \eta = 0 \Rightarrow \mu_d = \eta_d = 0$) we recover from (33) the standard J_2 flow theory tensor

$$\mathcal{L} = 2GJ + \lambda\mathbf{II} - \frac{3(G - G_t)}{\sigma_e^2}\mathbf{SS} \tag{55}$$

and, similarly, tensor (44) is reduced to the J_2 deformation theory version

$$\mathcal{L} = 2G_sJ + \lambda\mathbf{II} - \frac{3(G_s - G_t)}{\sigma_e^2}\mathbf{SS} \tag{56}$$

with $\sigma_e = Q$.

4 Numerical Examples

Sample calculations were performed for Castlegate sandstone with the material parameters

$$E = 8100 \text{ MPa} \quad \nu = 0.35 \quad \mu = \eta = 0.912$$

along with the hardening characteristic

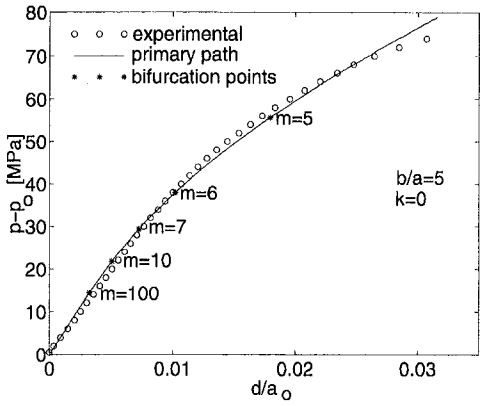

Fig. 1 Axially symmetric deformation of a hollow cylinder under increasing external pressure p with constant internal pressure $p_0 = 2$ MPa. Circumferential wave numbers (m) are indicated near the bifurcation points. In all cases $k = 0$. Hole closure is denoted by d.

$$\epsilon_p = 0 \quad \text{for} \quad \sigma_e \le Y, \quad Y = 9.80 \text{ MPa}$$

$$\epsilon_p = \epsilon_0\left(\frac{\sigma_e}{Y} - 1\right)^n \quad \text{for} \quad \sigma_e \ge Y, \quad \epsilon_0 = 2.22\ 10^{-2}, \quad n = 3.547.$$

Here Y is the yield stress and n is the hardening exponent. These parameters were made to fit the triaxial calibration test as predicted by the Drucker-Prager inner cone model (Durban and Papanastasiou, 1997a).

The plane-strain constraint has been imposed on the primary path in the cases examined here. No significant difference between flow and deformation theory predictions for the pre-bifurcation axially symmetric patterns have been found. That path is evaluated from (30) and (31), though the incremental procedure can be avoided for the deformation theory model by direct use of the finite strain constitutive Eqs. (40)–(41) together with the radial component of equilibrium (2).

Eigenvalues and bifurcation points along the primary path were evaluated by employing a Galerkin finite element procedure to solve the system (26)–(28) with the appropriate boundary data (29). This scheme is combined with a searching technique to trace the minimizing pair (k, m) for which the smallest eigenvalue is attained. No bifurcation points were found with flow theory in the realistic range of stresses. This finding is consistent with earlier observations by Papanastasiou and Vardoulakis (1992) who implemented material softening in flow theory of plasticity in order to predict bifurcation modes. Deformation theory predictions for onset of bifurcation were at realistic load levels. Nearly all bifurcations modes that were detected here show that the smallest load at bifurcation is attained with $k = 0$, implying via (23)–(25) plane-strain bifurcation eigenfunctions.

Figure 1 shows the primary axially symmetric loading history in terms of increasing external pressure p (with a constant level of internal pressure $p_0 = 2$ MPa) vs normalized hole closure for a hollow cylinder with initial dimensions of $a = a_0 = 5$ mm, $b/a = 5$ and $l/b = 1$. Correlation of experimental data with theoretical predictions for the primary path (with both flow and deformation theories) appears to be good. Also indicated are bifurcation points with the lowest one being a surface instability ($m = 100$). It should be mentioned, however, that in experiments on small size hole there is a considerable scale effect (Papamichos and van den Hoek, 1995) resulting in bifurcation with much smaller wave numbers m (Papanastasiou and Vardoulakis, 1989, 1992). The lowest bifurcation point predicted by our analysis ($m = 100$) can only be compared with the failure point of a large hole. The present study predicts

Downloaded 04 May 2010 to 171.66.16.27. Redistribution subject to ASME license or copyright; see http://www.asme.org/terms/Terms_Use.cfm

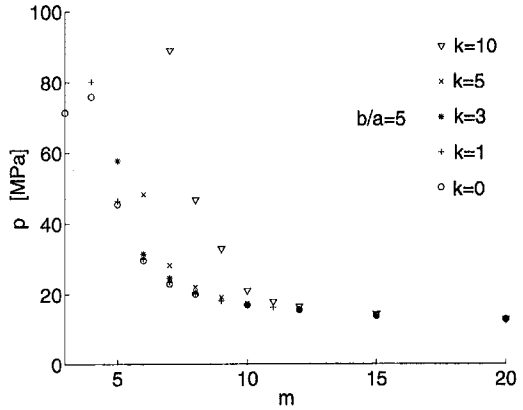

Fig. 2 Influence of wave number on bifurcations for an externally pressurized hollow cylinder. Earliest bifurcation is with $m \to \infty$ and $k = 0$.

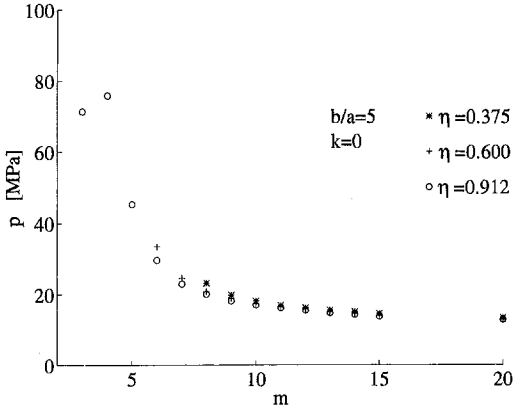

Fig. 4 Bifurcation under increasing external pressure p at different values of nonassociativity. In all cases $\mu = 0.912$.

surface instabilities ($m = 100$) at $p - p_o = 12.40$ MPa (Fig. 1) where as initial failure in Castlegate sandstone hollow cylinder experiments with large hole, $a = 180$ mm, was observed at 15 MPa (Papamichos and van den Hoek, 1995).

Convergence of the smallest eigenvalue with increasing circumferential wave number m is illustrated in Fig. 2 for the case of loading with external pressure, under zero internal pressure (for the same cylinder as in Fig. 1). During the calculations we have confirmed the half-space plane-strain surface instability (Durban and Papanastasiou, 1997b) at a hoop stress σ_θ ($r = a$) = 79.6 MPa with m, $k \to \infty$. However, as $m \to \infty$ Fig. 2 suggests that the earliest bifurcation occurs with $k = 0$.

Bifurcation loads for different values of the ratio of external to internal radii, b/a, (but with identical ratio $l/b = 1$) are shown in Fig. 3 for externally pressurized cylinders. Here again the critical eigenvalues for thick cylinders are obtained with $k = 0$ and $m \to \infty$. For thick cylinders, the bifurcation load approaches the asymptotic value of an externally pressurized cavity embedded in an infinite medium. Thus, bifurcation data in Fig. 3 for $b/a = 5$ is almost identical with the results for $b/a = 10$. For thin-walled cylinders, Fig. 3 suggests that the lowest bifurcation points occur at modes with finite m; $m = 3$ for $b/a = 3$ and $m = 4$ for $b/a = 2$.

No appreciable sensitivity of the bifurcation loads to the level of nonassociativity has been found (Fig. 4). This observation is in agreement with results reported in Durban and Papanastasiou (1997b) on surface instabilities in plane-strain compression. The geometrical dimensions here are as in Fig. 1. Figure 4 shows that the bifurcation points obtained with the associated model ($\eta = 0.912$) are slightly lower than the bifurcation points obtained with the nonassociated solids. This is because an associated solid leads to higher stress concentration (increased hoop stress) at the hole wall, which in turn may lead to surface instabilities at lower stress level than in a nonassociated solid (Papanastasiou and Vardoulakis, 1992).

Finally, in Fig. 5, we examine the case of decreasing internal pressure from two initial states of hydrostatic (30 MPa and 50 MPa) compression. These results are for a circular cylindrical cavity embedded in an infinite medium ($a/b \to 0$) with $l/a = 10$. This deformation pattern simulates drilling of a wellbore with the onset of surface bifurcations suggesting the level of mud pressure required to prevent collapse of the wellbore. Only few of the bifurcation modes are marked in Fig. 5 since they are highly condensed and clustered together.

5 Conclusion

A linear bifurcation analysis has been presented for pressure sensitive elastoplastic hollow cylinders. Material response is modelled by flow and deformation theories of the Drucker-Prager solid. The main conclusions that emerge from this study are that: (a) deformation theory predicts bifurcation in the realistic stress region whereas no bifurcation points were obtained with flow theory, (b) bifurcations are dominated by surface instabilities in the circumferential direction with no axial waves developing, (c) deformation theory predictions are not sensitive to deviations from associativity, and (d) deformation theory predicts bifurcation of pressure sensitive solids in the strain-hardening range.

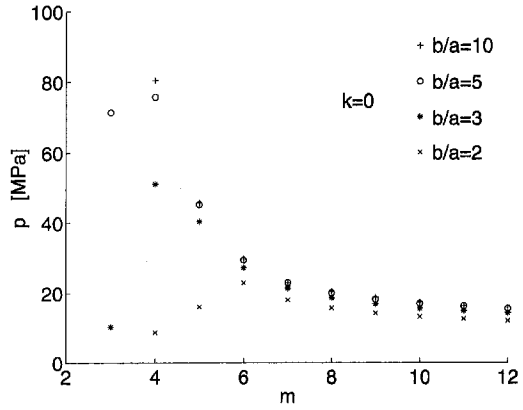

Fig. 3 Bifurcation under increasing external pressure p at different values of cylinder thickness ratio b/a

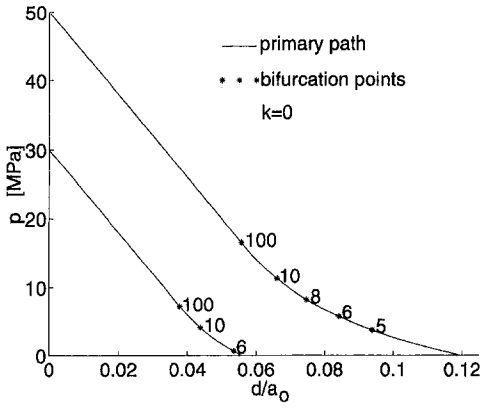

Fig. 5 Decreasing internal pressure p from two initial states of hydrostatic compression. Circumferential wave numbers (m) are indicated near the bifurcation points. Results are for a cavity embedded in an infinite medium. Initial radius of cavity is a_0 and d denotes hole closure.

Downloaded 04 May 2010 to 171.66.16.27. Redistribution subject to ASME license or copyright; see http://www.asme.org/terms/Terms_Use.cfm

Acknowledgment

The authors wish to thank Schlumberger for supporting this research. Part of this study was supported by the fund for promotion of research at the Technion.

References

Chau, K.-T., 1992, "Non-Normality and Bifurcation in a Compressible Pressure-Sensitive Circular Cylinder Under Axisymmetric Tension and Compression," *Int. J. Solids Struct.*, Vol. 29, pp. 801–824.

Chau, K.-T., 1993, "Axisymmetric Bifurcation in a Compressible Pressure-Sensitive Circular Cylinder Under Axisymmetric Tension and Compression," ASME JOURNAL OF APPLIED MECHANICS, Vol. 60, pp. 282–289.

Chu, C. C., 1979, "Bifurcation of Elastic-Plastic Circular Cylindrical Shells Under Internal Pressure," ASME JOURNAL OF APPLIED MECHANICS, Vol. 46, pp. 889–894.

Durban, D., and Fleck, N. A., 1997, "Spherical Cavity Expansion in a Drucker-Prager Solid," ASME JOURNAL OF APPLIED MECHANICS, Vol. 64, pp. 743–750.

Durban, D., and Papanastasiou, P., 1997a, "Cylindrical Cavity Expansion and Contraction in Pressure Sensitive Geomaterials," *Acta Mechanica,* Vol. 122, pp. 99–122.

Durban, D., and Papanastasiou, P., 1997b, "Elastoplastic Response of Pressure Sensitive Solids," *Int. J. Num. Anal. Meth. Geomech.*, Vol. 21, pp. 423–441.

Larsson, M., Needleman, A., Tvergaard, V., and Storakers, B., 1982, "Instability and Failure of Internally Pressurized Ductile Metal Cylinders," *J. Mech. Phys. Solids,* Vol. 30, pp. 121–154.

Papamichos, E., and van den Hoek, P., 1995, "Size Dependency of Castlegate and Berea Sandstone Hollow Cylinder Strength on the Basis of Bifurcation Theory," *Proceedings 35th U.S. Symp. Rock Mechanics,* pp. 301–306.

Papanastasiou, P., 1990, "Numerical Analysis of Localization Phenomena with Application in Deep Boreholes," Doctoral dissertation, University of Minnesota.

Papanastasiou, P., and Vardoulakis, I., 1989, "Bifurcation Analysis of Deep Boreholes: II. Scale Effect," *Int. J. Num. Anal. Meth. Geomech.*, Vol. 13, pp. 183–198.

Papanastasiou, P., and Vardoulakis, I., 1992, "Numerical Treatment of Progressive Localization in Relation to Borehole Stability," *Int. J. Num. Anal. Meth. Geomech.*, Vol. 16, pp. 389–424.

Reddy, B. D., 1982, "A Deformation Theory Analysis of the Bifurcation of Pressurized Thick-Walled Cylinders," *Quart. J. Mech. Appl. Math.*, Vol. 35, pp. 183–196.

Tomita, Y., Shindo, A., and Kitagawa, H., 1981, "Bifurcation and Post Bifurcation Behaviour of Internally Pressurized Elastic-Plastic Circular Tubes Under Plane Strain Conditions," *Int. J. Mech. Sci.*, Vol. 23, pp. 723–732.

Tvergaard, V., 1990, "Bifurcation in Elastic-Plastic Tubes Under Internal Pressure," *European J. Mech., A/Solids,* Vol. 9, pp. 21–35.

Vardoulakis, I., and Papanastasiou, P., 1988, "Bifurcation analysis of deep boreholes: I. Surface Instabilities," *Int. J. Num. Anal. Meth. Geomech.*, Vol. 12, pp. 379–399.

Downloaded 04 May 2010 to 171.66.16.27. Redistribution subject to ASME license or copyright; see http://www.asme.org/terms/Terms_Use.cfm

A Micro/Macroscopic Analysis for Cyclic Plasticity of Dual-Phase Materials

J. Fan*
The George W. Woodruff School of Mechanical Engineering, Georgia Institute of Technology, Atlanta, GA 30332-0405
Mem. ASME

In this paper, a methodology is developed to simulate cyclic micro/macroscopic responses of dual-phase materials based on an extension of the self-consistent scheme. This extension is significant because it makes the self-consistent scheme capable of determining overall responses of materials as well as local stress evolution in microstructure. Results show satisfactory agreement between the cyclic responses up to 50 cycles predicted by the present methodology and the experimental data of Bower (1989). The heterogeneous feature of distributions of cyclic stress, strain and energy in microstructure, as well as the essential role of the strong-energy-absorption-capability of the thin layers on the material behavior, and the high strength of the thin-layer microstructure are exploited. The possible impact of this work on issues such as ratchetting of the dual-phase material and the ductile and fatigue behavior of its hard phase, as well as the significance on plasticity modeling of constituents and effective homogeneous inclusions are also mentioned.

1 Introduction

This paper is concerned with the development of a method for micro/macroscopic analysis of cyclic plasticity. It is hoped that this method is capable of determining the overall responses of materials, as well as local stress evolution in microstructure under cyclic loading. This effort is consistent with the recent understanding that local anisotropy and heterogeneity associated with microstructure have significant influence on material behavior and fatigue life (McDowell, 1997). It is believed that without in-depth knowledge of the characteristics of stress and strain evolution in microstructures, issues which exist for a long time in cyclic behavior and fatigue may be difficult clarify and solve.

One way to meet the challenge of consistently carrying on the cyclic analysis across micro/macroscopic scales is to apply the self-consistent scheme (SCS) for the analysis. Traditionally, however, the SCS cannot include local analysis because the premise of the SCS requires the inclusion to be homogeneous media. This limits the application of SCS to problems involving heterogeneity and anisotropy associated with microstructures of engineering materials. Weng (1990, 1993) and Qiu and Weng (1991) applied Mori-Tanaka's mean field theory to improve the SCS analysis (e.g., Hutchinson, 1970) for investigating interactions between two constituents. They concluded that a mean-field approach to a nonlinear system is usually not as accurate as the local approach, and that it overestimates the yield stress and underestimates the maximum local stress. On the other hand, the extension of Berveiller and Zaoui (1979) to Hill's (1965) and K-B-W's (1961, 1962) SCS models cannot be applied to cyclic loading because they use the secant approach for their analysis.

This work focuses on a further extension of the SCS. This extension makes the SCS capable of determining overall responses of materials as well as local stress evolution in microstructures under complicated applied loading conditions. While this extension keeps the advantage of Hill's weakening constraint power of matrix, it is convenient for application. This is a tangential modulus-type approach, so that it can be applied for cyclic loading. This approach is exemplified by layer structured dual phase metal. This class of materials includes certain types of pearlitic steel, such as the standard high-carbon pearlitic rail steel (BS11), with fine randomly oriented layers of the elastioplastic hard and soft phases.

2 An Extension of the Self-Consistent Scheme for Cyclic Plasticity

Now consider a representative unit cell of a statistically homogeneous and plastically incompressible dual-phase material. It is assumed that the overall representative unit cell is an aggregate of a large number of randomly oriented ellipsoidal or spherical inclusions, and that each inclusion is composed of a relatively large number of two alternatively arranged and perfectly bonded layered materials (Fig. 1(a), (b)). This assumption makes it reasonable to obtain the macroscopic stress and strain by volume average over all orientations. It also makes it reasonable to consider an inclusion to be an effectively homogeneous media in which the detailed microstructure is smeared out. Therefore, the interaction of every inclusion with its surrounding aggregate is calculated individually by taking the inclusion under consideration as an effectively homogeneous ellipsoid or sphere. This effectively homogeneous inclusion is embedded in a homogeneous medium whose incremental moduli $\mathbf{L}$ is the overall moduli of the dual-phase metal. On the other hand, constitutive relations of the effectively homogeneous inclusion are obtained from the analysis of interactions of their constituents. Both of them are elastoplastic materials with plastic incompressibility being assumed, and the direct interactions between them are through their interfaces. In the following, quantities which are associated with the effectively homogeneous inclusions and the whole aggregate are denoted by superscript c and a bar over the quantities, respectively. A fourth-order tensor is denoted by a bold capital Latin letter; specifically, $\mathbf{I}$ is the unit tensor and $\mathbf{S}$ the Eshelby tensor. A second-order tensor is denoted by a bar under the quantities. Index expressions are also used for tensors. Furthermore, quantities in the two phases are distinguished by a superscript i (i = 1,

Contributed by the Applied Mechanics Division of THE AMERICAN SOCIETY OF MECHANICAL ENGINEERS for publication in the ASME JOURNAL OF APPLIED MECHANICS.

Discussion on the paper should be addressed to the Technical Editor, Professor Lewis T. Wheeler, Department of Mechanical Engineering, University of Houston, Houston, TX 77204-4792, and will be accepted until four months after final publication of the paper itself in the ASME JOURNAL OF APPLIED MECHANICS.

Manuscript received by the ASME Applied Mechanics Division, Apr. 22, 1997; final revision, July 20, 1998. Associate Technical Editor: J. L. Bassani.

 Copyright © 1999 by ASME

Downloaded 04 May 2010 to 171.66.16.27. Redistribution subject to ASME license or copyright; see http://www.asme.org/terms/Terms_Use.cfm

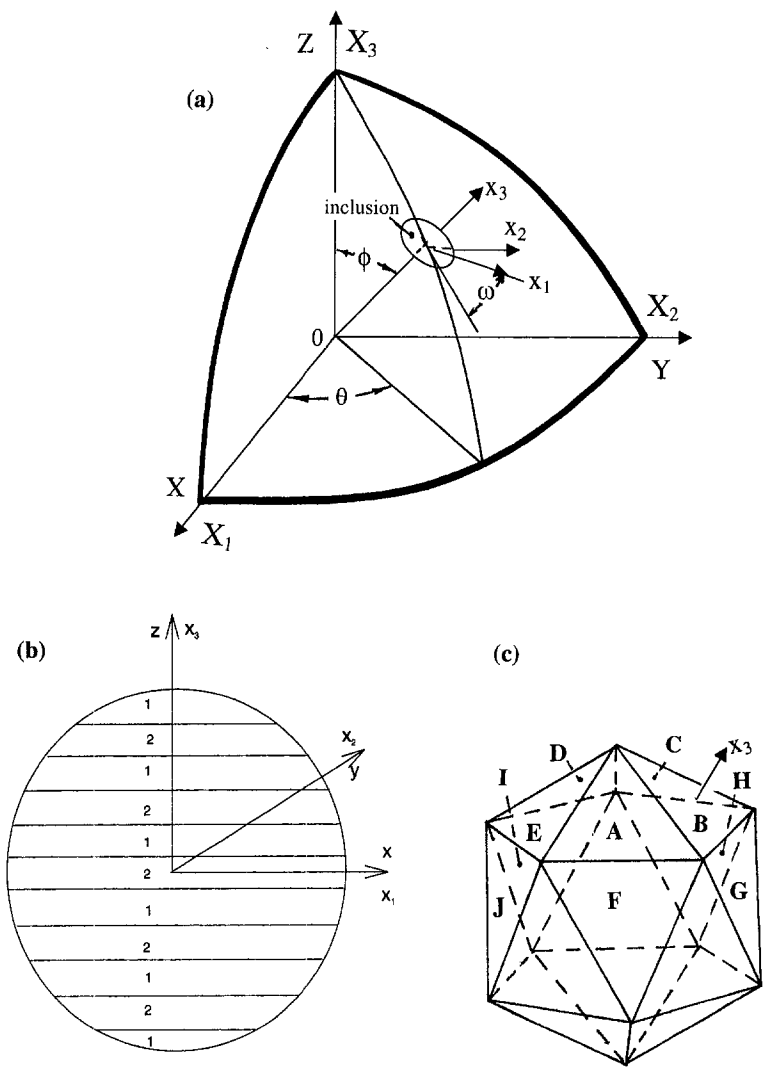

Fig. 1 Homogenized inclusion and 20 planes with spatially uniformly distributed normal directions; (*a*) the embedded inclusion in the aggregate with local and global coordinates, (*b*) the layered microstructure of the homogenized inclusion, (*c*) the 20 spatially uniformly placed planes

2) within a parenthesis; $i = 1$ is for the hard phase and $i = 2$ for the soft phase. The superscripts e and p over the symbol ϵ denote elastic and plastic strain, respectively.

Following Berveiller and Zaoui (1979), the "constraint" tensor L^* in Hill's basic relation is replaced by a tangential "constraint" tensor $\mathbf{L}_t^*$, so that the interaction between a single inclusion of homogeneous media and its surrounding aggregate can be expressed as

$$d\underline{\bar{\sigma}} - d\underline{\sigma}^c = -\mathbf{L}_t^*(d\underline{\bar{\epsilon}} - d\underline{\epsilon}^c) \tag{2.1}$$

$$\mathbf{L}_t^*\mathbf{S} = \mathbf{L}_t(\mathbf{I} - \mathbf{S}) \tag{2.2}$$

where $\mathbf{L}_t$ is an isotropic approximation of the incremental moduli, $\mathbf{L}$, of the aggregate. Under this approximation of the overall isotropy of the aggregate, $\mathbf{L}_t$ is taken as

$$\mathbf{L}_{t_{IJKL}} = \mu'\left[\frac{2\nu'}{1-2\nu'}\delta_{IJ}\delta_{KL} + \delta_{IK}\delta_{JL} + \delta_{IL}\delta_{JK}\right] \tag{2.3}$$

where μ' and ν' are the tangential elastoplastic shear modulus and Poisson's ratio of the assumed isotropic aggregate, respectively. Substituting this expression of $\mathbf{L}_t$ and Eshelby's solution of $\mathbf{S}$ for spherical inclusion into (2.2), $\mathbf{L}_t^*$ can be explicitly expressed as follows (see Appendix of Berveiller and Zaoui, 1979, and Appendix of Hutchinson, 1970):

$$\mathbf{L}'^*_{t_{IJKL}} = A\delta_{IJ}\delta_{KL} + B(\delta_{IK}\delta_{JL} + \delta_{IL}\delta_{JK}) \tag{2.4}$$

with

$$A = \frac{\mu'(3-5\nu')}{4-5\nu'}, \quad B = \frac{\mu'(7-5\nu')}{2(4-5\nu')}. \tag{2.5a,b}$$

Applying (2.4) for (2.1), the following relationship is obtained:

$$d\bar{\sigma}_{IJ} - d\sigma^c_{IJ} = -A(d\bar{\epsilon}_{KK} - d\epsilon^c_{KK})\delta_{IJ} - B(d\bar{\epsilon}_{IJ} - d\epsilon^c_{IJ}). \tag{2.6}$$

Since ν' does not change much, but μ' decreases quickly, A and B are decreasing coefficients when the macroscopic plastic strain increases. This fact indicates a weakening constraint power of the aggregate on the inclusion at hand. Keep in mind that with the plastic incompressibility conditions, (2.6) can be rewritten as follows:

$$d\bar{\sigma}_{IJ} - d\sigma^c_{IJ} = -A(d\bar{\epsilon}^e_{KK} - d\epsilon^{ec}_{KK})\delta_{IJ} - B(d\bar{\epsilon}^e_{IJ} + d\bar{\epsilon}^p_{IJ} - d\epsilon^c_{IJ}). \tag{2.7}$$

Downloaded 04 May 2010 to 171.66.16.27. Redistribution subject to ASME license or copyright; see http://www.asme.org/terms/Terms_Use.cfm

Since the aggregate is assumed to be a macroscopically isotropic material, we have

$$d\bar{\epsilon}^e_{IJ} = \frac{1}{2\bar{G}}\left(d\bar{\sigma}_{IJ} - \frac{\bar{\nu}}{1-\bar{\nu}}\, d\bar{\sigma}_{KK}\delta_{IJ}\right),$$

$$d\bar{\epsilon}^e_{KK} = \frac{1}{3\bar{K}}\, d\bar{\sigma}_{KK} \qquad (2.8a, b)$$

where $\bar{\nu}$, $\bar{G}$, and $\bar{K}$ are elastic Poisson's ratio, elastic shear, and volumetric modulus of the aggregate. With the aid of (2.8a, b) and setting the collection of all terms of the aggregate to be $d\bar{Q}_{IJ}$, (2.7) can be rewritten as

$$d\bar{Q}_{IJ} = d\sigma^c_{IJ} + Ad\epsilon^{ec}_{KK}\delta_{IJ} + Bd\epsilon^c_{IJ}. \qquad (2.9)$$

The explicit expression for $d\bar{Q}_{IJ}$ is

$$d\bar{Q}_{IJ} = \left(1 + \frac{B}{2\bar{G}}\right)d\bar{\sigma}_{IJ} + \left(\frac{A}{3\bar{K}} - \frac{B\bar{\nu}}{2\bar{G}(1+\bar{\nu})}\right)d\bar{\sigma}_{KK}\delta_{IJ} + Bd\bar{\epsilon}^p_{IJ}. \qquad (2.10)$$

Joining with (2.10), (2.9) is the constraint law used in the present self-consistent scheme. Equations (2.9) and (2.10) offer a link between the global deformation process of the aggregate and the local deformation process in inclusions. More specifically, after the applied loading is given, $d\bar{Q}_{IJ}$ can be obtained by (2.10) through an iterative process. Each value of $d\bar{Q}_{IJ}$ is taken to be an input for the calculation of stresses and strains in inclusions. The first step in carrying on this local analysis is to transform (2.10) from the global coordinate system X_I to the local coordinate system x_i by a coordinate transformation. After this transformation, (2.9) can be written in matrix form in the local coordinate system

$$\{dQ^c\} = \{d\sigma^c\} + Ad\epsilon^{ec}_{kk}\{\delta\} + B\{d\epsilon^c\} \qquad (2.11)$$

where $\{\delta\} = \{1, 1, 1, 0, 0, 0\}^T$. Equation (2.11) is a local form of the constraint law and can be specified after the constitutive law of the generic inclusion is given.

Actually, the determination of $d\bar{Q}_{IJ}$ or $\{dQ^c\}$ is within a global iterative process. In this process, the key is to determine the macroscopic plastic strain $\Delta\bar{\epsilon}^p_{IJ}$. Suppose the current step is the kth iteration of the Ith incremental loading, in which the stress increment $\Delta\bar{\sigma}_{IJ}$ is given and fixed. The values of $\Delta\bar{\epsilon}^p_{IJ}$ obtained from the last step, (k-1), are taken to calculate $\Delta\bar{Q}^k_{IJ}$ by (2.10). The obtained $\Delta\bar{Q}^k_{IJ}$ is then used to start the local iteration process through which $\Delta\epsilon^{pc}_{IJ}$ of each inclusion can be obtained. The macroscopic plastic strain $\Delta\bar{\epsilon}^p_{IJ}$ of the aggregate is determined by a volume average of $\Delta\epsilon^{pc}_{IJ}$ as follows:

$$\Delta\bar{\epsilon}^p_{IJ} = \frac{1}{V}\int_V (\Delta\epsilon^{pc}_{IJ})d\nu \qquad (2.12)$$

where V is the volume of the aggregate. The obtained $\Delta\bar{\epsilon}^p_{IJ}$ combined with $\Delta\bar{\sigma}_{IJ}$ are then used to determine $\Delta\bar{Q}^{*k}_{IJ}$ at the end of the kth iteration by (2.10). The process is repeated until the following criterion of convergence is satisfied:

$$\frac{\|\Delta\bar{Q}^{*k}_{IJ} - \Delta\bar{Q}^k_{IJ}\|}{\|\Delta\bar{Q}^{*k}_{IJ}\|} < \epsilon \qquad (2.13)$$

where symbol $\|.\|$ denotes an Euclidean norm such as $\|\Delta Q^k_{IJ}\| = (\Delta Q^k_{IJ}\Delta Q^k_{IJ})^{1/2}$, and ϵ is the tolerance. In the case of cyclic loading, ϵ is taken as 0.1 percent. This choice is a compromise between accuracy and consumed CPU time.

In (2.12), it can be seen that volume averages are necessary to obtain the macroscopic plastic strain $\Delta\bar{\epsilon}^p_{IJ}$. Since inclusions are assumed to be randomly oriented, these volume averages can be done by an average over all directions. More specifically, if the position coordinates of each inclusion are described by its Euler coordinates, θ, ϕ, ω (see Fig. 1(a)), the volume average $\bar{A}$ of a quantity A^C can be expressed by an average of A^C over all directions. One approximate way to do it is through the following integration (Hwang and Sun, 1995):

$$\Delta\bar{\epsilon}^p_{mn} = \frac{1}{8\pi^2}\int_0^{2\pi} d\theta \int_0^{\pi} \sin\varphi d\varphi \int_0^{2\pi} (\Delta\epsilon^{pc}_{mn})d\omega, \qquad (2.14)$$

and then calculated by the Guassian quadrature approach. In this work a mixed method of Gaussian quadrature and arithmetic average (Zheng, 1996) is adopted. To make the volume average in the θ, ϕ direction more accurate than the Gaussian quadrature used for (2.14), 20 spatially and uniformly distributed directions are chosen for the x_3-axis of the local coordinates. These directions are obtained from the normal vectors of the 20 planes of an isosahedron (Fig. 1(c)). The 20 planes themselves are taken to be the basic planes of x_1x_2 in which the angle ω varies. This choice makes the average over the 20 directions an arithmetic one. It is assumed that in each of these 20 planes there are infinite inclusions with randomly distributed orientations, so that

$$\Delta\bar{\epsilon}^p_{mn} = \frac{1}{20}\sum_{i=1}^{20}\left[\frac{1}{2\pi}\int_{-\pi}^{\pi} \Delta\epsilon^{pc}_{mn}(\theta_i, \varphi_i, \omega)d\omega\right]. \qquad (2.15)$$

Using the Gaussian quadrature for the integration of ω we obtain

$$\Delta\bar{\epsilon}^p_{mn} = \tfrac{1}{40}\sum_{i=1}^{20}\sum_{j=0}^{3} A^{\omega}_j \Delta\epsilon^{pc}_{mn}(\theta_i, \varphi_i, \omega_j) \qquad (2.16)$$

where A^{ω}_j, ω_j are the weighting factors and the coordinates of the four Gaussian points in the first quadrant of x_1x_2-plane, respectively. The sum of A^{ω}_j is equal to 2, which causes the number 20 in the denominator of (2.15) to be 40 in (2.16). The mixed approach is more accurate and convenient for application than the one totally based on Gussian quadrature. The values of θ_i, ϕ_i, ω_i are given in Tables 1 and 2. As seen in that table, only ten planes above the XOY coordinate plane are independent; each of the other ten planes below the XOY-plane is parallel to one of the ten independent planes. This fact makes the calculation even simpler.

3 Constitutive Relations for Constituents and the Inclusion

In a series of papers, Fan (1987), Fan and Peng (1991), and Peng, Fan, and Zheng (1996) proposed nonclassical constitutive relations of plasticity (NCP). These relations closely relate to several plasticity models with and without yield surface, but the microscopic aspects are emphasized. Therefore, the framework of the NCP will be applied here for the development of constitutive relations of the hard and soft phases; it will then be applied for the homogenized inclusion.

3.1 Cyclic Constitutive Equations for the Hard and Soft Phases. One of the essential premises of the classical mathematical theory of plasticity (CP) is the assumption, or an idealization, of an a priori existence of a yield surface. It has been found, however, that for some materials, such as dual-phase materials, there does not exist a distinct yield point. Therefore, one should be in a good position to develop theories, alternative to CP, which do not use this a priori idealization, but then should encompass the plasticity theories with yield surface. There have been several models developed along this direction, for instance, Valanis (1971, 1980), Bonder and Partom (1975), Hart (1976), and Krempl (1987), to name a few.

The basic framework of NCP and its relations with CP can be easily explained by a simple mechanical model shown in Fig. 2 for simulating the material response under applied devia-

Downloaded 04 May 2010 to 171.66.16.27. Redistribution subject to ASME license or copyright; see http://www.asme.org/terms/Terms_Use.cfm

Table 1 Euler coordinates θ and ϕ for the centers of 20 spatially and uniformly distributed planes x_1x_2

	A	B	C	D	E	F	G	H	I	J
θ	0 deg	72 deg	144 deg	216 deg	288 deg	0 deg	72 deg	144 deg	216 deg	288 deg
ϕ	37.4 deg	37.4 deg	37.4 deg	37.4 deg	37.4 deg	79.2 deg	79.2 deg	79.2 deg	79.2 deg	79.2 deg
	K	L	M	N	O	P	Q	R	S	T
θ	36 deg	108 deg	180 deg	252 deg	324 deg	36 deg	108 deg	180 deg	252 deg	324 deg
ϕ	142.6 deg	142.6 deg	142.6 deg	142.6 deg	142.6 deg	100.8 deg	100.8 deg	100.8 deg	100.8 deg	100.8 deg

Table 2 Weighting factors A_j^ω and Euler coordinates ω_j of the Gaussian points in the first quadrant of spatially and uniformly distributed planes x_1x_2

ω_1	ω_2	ω_3	ω_4	A_1^ω	A_2^ω	A_3^ω	A_4^ω
6.3 deg	29.7 deg	60.3 deg	83.8 deg	0.347855	0.652145	0.652145	0.347855

toric stress $\underline{s}$. This model is for initially isotropic and plastically incompressible materials under the condition of isothermal and small deformation. The rth dissipative mechanism of the material is described by a Maxwell-type chain which consists of a spring C_r (with stiffness C_r) and a dashpot-like plastic block a_r (with the initial plastic damping factor or frictional coefficient a_r^0). For the present work of layered structures, this dissipative mechanism is described by a chain shown in Fig. 2(c) where an additional spring E_r (with stiffness E_r) is included. C_r and E_r are related to the stochastic internal structure of the material

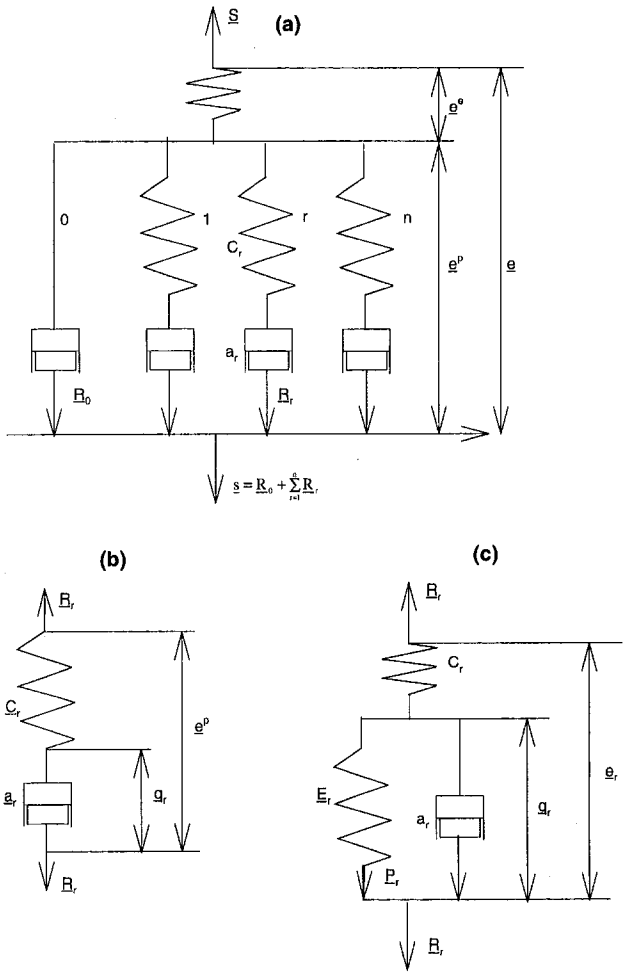

Fig. 2 A mechanical model for the proposed constitutive equations of constituents

and make no contribution to the average elastic modulus. In other words, it can be considered as a disturbed lattice structure to the spring **E**, where **E** represents the regular lattice structure whose stiffness is the average shear modulus μ. The energy stored in the spring C_r and E_r corresponds to the energy stored in the rth stochastic microstress field. This stress field is caused by the respective pattern of lattice defects, for instance, dislocations. Due to different values of parameters, each chain takes different role in the different deformation stages. The number $n^{(i)}$ of chains is determined by the material at hand as well as the accuracy required. In general, the soft phase may need more chains to describe its nonlinear behavior than the hard phase needs. It is found that two or three chains are sufficient for the case of small deformation.

Corresponding to the spring-block model in Fig. 2

$$\underline{s}^{(i)} = \underline{R}_0^{(i)} + \sum_{r=1}^{n} \underline{R}_r^{(i)} \tag{3.1}$$

$$\underline{R}_r^{(i)} = c_r^{(i)}(\underline{e}^{p(i)} - \underline{q}_r^{(i)}) \quad (r = 1, 2 \ldots n^{(i)}) \tag{3.2}$$

$$\underline{e}^{p(i)} = e^{(i)} - \underline{e}^{e(i)} = e^{(i)} - \underline{s}^{(i)}/2\mu^{(i)}. \tag{3.3}$$

As we can see later, $\sum_{r=1}^{n} \underline{R}_r^{(i)}$ is back stress and $\underline{R}_0^{(i)}$ relates to yield stress. In these equations, $\underline{q}_r^{(i)}$ and $\underline{R}_r^{(i)}$ denote the displacement of the plastic block and the driving force for the motion of the rth block, respectively. From a physical point of view, $\underline{q}_r^{(i)}$ indicates the rth internal variable. The set of internal variables, $\underline{q}_r^{(i)}$ ($r = 0, 1 \ldots n^{(i)}$) describes material internal structure caused by irreversible deformation. This set together with external variables such as strain and temperature determine the thermodynamic state of the phase at hand. The force, $\underline{R}_r^{(i)}$, is a generalized driving force for the change of the internal structure or for the evolution of the internal variables $\underline{q}_r^{(i)}$. Its value is assumed to be a linear function of the generalized rate of internal variable $\underline{q}_r^{(i)}$ with respect to the accumulative plastic strain, $p^{(i)}$, defined as

$$dp^{(i)} \equiv \sqrt{d\epsilon_{ij}^{p(i)} d\epsilon_{ij}^{p(i)}} = \sqrt{de_{ij}^{p(i)} de_{ij}^{p(i)}} \tag{3.4}$$

$dp^{(i)}$ is also called the equivalent plastic strain increment. Mathematically, this assumption can be expressed as

$$\underline{R}_r^{(i)} = a_r^{0(i)} f_r^{(i)}(p^{(i)}) \frac{d\underline{q}_r^{(i)}}{dp^{(i)}} + \underline{P}_r^{(i)} \quad r \text{ not summed.} \tag{3.5}$$

At first, let's discuss the case when $\underline{P}_r^{(i)} = 0$. In this case, the driving force and the generalized rate of internal variable is proportional. This indicates that as $dp^{(i)}$ increases for a certain value of $d\underline{q}_r^{(i)}$, the corresponding force $\underline{R}_r^{(i)}$ decreases, because

Downloaded 04 May 2010 to 171.66.16.27. Redistribution subject to ASME license or copyright; see http://www.asme.org/terms/Terms_Use.cfm

the corresponding material state is more plastically deformable. The product $a_r^{0(i)} f_r^{(i)}$ multiplied by $(d\underline{q}_r^{(i)}/dp^{(i)})$ represents the current frictional coefficients of the plastic block. The factor a_r^0 controls material resistance of the rth mechanism at the very beginning; the larger the a_r^0, the more driving force is required to overcome the barrier related to strain hardening of that mechanism. For most cases, $f_r^{(i)}(p^{(i)})$ is an increasing function with plastic deformation and is called the hardening function. This hardening induced by dislocation tangles is attributed to the interaction between the active dislocations and dislocation forests. The associated microscopic stress field is short-ranged and less directional. This type of hardening strongly depends on the slip history and the current state of dislocations at all slip systems. Based on this physical origin, $f_r^{(i)}(p^{(i)})$ is taken as a function of the accumulative plastic strain, $p^{(i)}$, to describe the isotropic hardening.

Secondly, let's discuss the case where $\underline{P}_r^{(i)} \neq 0$ which corresponds to the case in Fig. 2(c). Before discussing the physical meaning of the additional term an important capability of thin layers, namely the strong-energy-absorption-capability, may need to be mentioned. This is the capability of thin layers to absorb a relatively large amount of deformation energy before their failure. This capability results in the in situ strength of thin layers being very high. According to the calculation given by Fan and Zhang (1993), the in situ strength of a thin lamina in a laminate can be as high as 2.9 times the strength tested in free condition. This means that the maximum stored energy of a thin layer in the constraint condition can be approximately 8.4 times the energy stored in the free condition. This capability of thin layers was verified by indirect experimental observation, and microscopically explained by Langford (1979). He reported that "at very small interlamellar spacing, generation of the dislocations required in the pileups will absorb a significant fraction of the work of deformation." As we know, dislocation pileups at grain boundaries form obstacles against active dislocations. The associated long-range stress is back stress which is directional and the hardening caused by this stress is called kinematic hardening. Since the absorbed deformation energy is stored in the dislocation pileups, Langford's report implicitly means that the additional term $\underline{P}_r^{(i)}$ is necessary to describe the increase of back stress. The greater the back stress $\underline{R}_r^{(i)}$ due to the thin layer deformation, the greater the additional force $\underline{P}_r^{(i)}$ should be. Following Bower (1989), it is assumed that the generalized evolution rate of $\underline{P}_r^{(i)}$ is proportional to the difference between $\underline{R}_r^{(i)}$ and $\underline{P}_r^{(i)}$, i.e.,

$$d\underline{P}_r^{(i)}/dp^{(i)} = \gamma(\underline{R}_r^{(i)} - \underline{P}_r^{(i)})/f^{(i)}(p^{(i)}) \tag{3.6}$$

where γ is a material constant. Equation (3.6) ensures that $\underline{P}_r^{(i)}$ follows the back stress $\underline{R}_r^{(i)}$ during the cyclic plastic process. Combining (3.5) and (3.6) one obtains

$$d\underline{P}_r^{(i)} = \gamma a_r^{0(i)} d\underline{q}_r^{(i)}. \tag{3.7}$$

This relation indicates that $\underline{P}_r^{(i)}$ in the mechanical model represents the force of a spring with spring constant as $\gamma a_r^{0(i)}$. This spring is parallel to the dashpot a_r as shown in Fig. 2(c). The existence of this additional spring describes well the strong-energy-absorption-capability of thin layers. Combining (3.2) and (3.5) we obtain

$$d\underline{R}_r^{(i)} = c_r^{(i)} d\underline{e}^{p(i)} - \alpha_r^{(i)}(\underline{R}_r^{(i)} - \underline{P}_r^{(i)}) dp^{(i)}/f_r^{(i)}(p^{(i)}) \quad r \text{ not summed} \tag{3.8}$$

$$\alpha_r^{(i)} = c_r^{(i)}/a_r^{0(i)}. \tag{3.9}$$

The third, a connection between NCP and CP, is briefly pointed out as follows. For the chain $r = 0$ in Fig. 2(a), there is no spring (or the spring stiffness is infinite) which results in $d\underline{q}_0^{(i)} = d\underline{e}^{p(i)}$. Combining these results with (3.4) and (3.5) and noticing $\underline{P}_r^{(i)} = 0$, the norm of the deviatoric yield stress can be obtained as follows:

$$\|\underline{R}_0^{(i)}\| = a_0^{(i)} f_0^{(i)}(p^{(i)}). \tag{3.10a}$$

This equation indicates that $a_0^{(i)}$ is the initial deviatoric yield stress and $f_r^{(i)}(p^{(i)})$ describes the expansion of the yield surface in terms of the plastic strain accumulation. If $a_0^{(i)} = 0$ the norm will be equal to zero, which indicates material responses without a yield surface. Therefore, the difference in the model for materials with and without yield surface corresponds to the model with (or without) the chain $r = 0$. This shows the general connections of the NCP and CP in the model. More specifically, if $n^{(i)} = 1$, $f_1^{(i)} = 1$ and $\underline{P}_r^{(i)} = 0$, Eq. (3.8) reduces to the nonlinear kinematic hardening law of Armstrong and Freederick (1966); if $n^{(i)} = 1$, $f_1^{(i)} = 1$ and $\underline{P}_r^{(i)} \neq 0$, (3.8) reduces to the modified nonlinear kinematic hardening law of Armstrong and Frederick, proposed by Bower (1989). If $f_r^{(i)} = 1$ for $r = 1, 2 \ldots n$ and $\underline{P}_r^{(i)} = 0$, (3.8) reduces to the nonlinear kinematic hardening law proposed by Chaboche et al. (1979). With the help of (3.1) and (3.10a) we have

$$\|\underline{S} - \sum_{r=1}^{n^{(i)}} \underline{R}_r^{(i)}\| = a_0^{(i)} f_0^{(i)}(p^{(i)}) \tag{3.10b}$$

where $\sum_{r=1}^{n^{(i)}} \underline{R}_r^{(i)}$ and $a_0^{(i)} f_0^{(i)}$ represent, respectively, the evolution of the center and the radius of the yield surface. This fact makes it clear macroscopically that the back stress $\sum_{r=1}^{n^{(i)}} \underline{R}_r^{(i)}$ describes the kinematic hardening caused by the deformation induced anisotropy, and $f_r^{(i)}(p^{(i)})$ describe the isotropic hardening caused by plastic strain accumulation. This is the same result obtained by Valanis (1980). If $\underline{P}_r^{(i)} = 0$ and $\underline{f}_r^{(i)} = 1/w_r^{(i)}$, the Eq. (3.9$a$) is identical with the generalized Chaboche's hardening law (Jiang and Sehitoglu, 1996). Furthermore, if $w_r^{(i)}$ is taken as a power function, the constitutive equation of Ohno and Wang (1993) are recast.

Finally, to simplify the nonlinear analysis, a material time, $z^{(i)}$, originally proposed by Valanis (1980), will be introduced as follows to describe the irreversible deformation process in each phase:

$$dz^{(i)} = dp^{(i)}/f^{(i)}(p^{(i)}) \tag{3.11}$$

where $f^{(i)} = f_1^{(i)} = \ldots f_r^{(i)} = f_n^{(i)}$ is assumed and the evolution equation of $f^{(i)}$ proposed by Fan and Peng (1991) is adopted based on the previous discussion on its physical origin. This equation is

$$df^{(i)}/dz^{(i)} = \beta(d - f^{(i)}) \tag{3.12}$$

where d and β are two material parameters representing the saturation value of $f^{(i)}$ and the rate for $f^{(i)}$ to approach d, respectively. Substituting (3.11) into (3.8) and then into (3.1) with $\underline{R}_0 = 0$, the constitutive equations of each phase without yield surface can be obtained as follows:

$$d\underline{s}^{(i)} = \rho_0^{(i)} d\underline{e}^{p(i)} + \underline{h}^{(i)}(z) dz^{(i)} \tag{3.13}$$

$$\rho_0^{(i)} = \sum_{r=1}^{n^{(i)}} c_r^{(i)}, \quad \underline{h}^{(i)} = -\sum_{r=1}^{n^{(i)}} \alpha_r^{(i)}(\underline{R}_r^{(i)} - \underline{P}_r^{(i)}). \tag{3.14a, b}$$

Equation (3.13) is the constitutive equation proposed by Valanis and Fan (1983). The difference from the original one is that in the present case $\underline{P}_r^{(i)}$ is introduced in (3.14b).

3.2 The Stress-Strain Relations for an Effective Homogeneous Inclusion. Since the layers are very thin, the variation of stress and strain components across the thickness of

Downloaded 04 May 2010 to 171.66.16.27. Redistribution subject to ASME license or copyright; see http://www.asme.org/terms/Terms_Use.cfm

each layer is small. This fact, and the compatibility conditions at the interfaces of two layers require the approximate equality of in-plane strain components, as well as out-of-plane stress components in the two layers, i.e.,

$$d\epsilon_{ij}^{c} = d\epsilon_{ij}^{(1)} = d\epsilon_{ij}^{(2)} \quad (ij = 11, 22, 12) \tag{3.15}$$

$$d\sigma_{ij}^{c} = d\sigma_{ij}^{(1)} = d\sigma_{ij}^{(2)} \quad (ij = 13, 23, 33). \tag{3.16}$$

Denoting volume fractions as $V_f^{(i)}$, the in-plane stress and out-of-plane strain components of the inclusion can be obtained by volume average as follows:

$$d\sigma_{ij}^{C} = \sum_{m=1}^{2} V_f^{(m)} d\sigma_{ij}^{(m)} \quad (ij = 11, 22, 12) \tag{3.17}$$

$$d\epsilon_{mn}^{C} = \sum_{1}^{2} V_f^{(i)} d\epsilon_{mn}^{(i)} \quad (ij = 13, 23, 33). \tag{3.18}$$

Since each individual phase is assumed to be initially isotropic, plastically incompressible, and with a small deformation, we have the following expressions:

$$dS_{mn}^{(i)} = d\sigma_{mn}^{(i)} - \frac{d\sigma_{kk}}{3}\sigma_{mn}^{(i)}, \tag{3.19}$$

$$de_{mn}^{e(i)} = d\epsilon_{mn}^{(i)} - \frac{d\epsilon_{kk}}{3}\delta_{mn}^{(i)} \tag{3.20}$$

$$d\epsilon_{mn}^{(i)} = d\epsilon_{mn}^{e(i)} + d\epsilon_{mn}^{p(i)}, \quad de_{mn}^{p(i)} = de_{mn}^{p(i)} \tag{3.21a, b}$$

where δ_{mn} is the Kronecker delta. From Hooke's law, (3.13) and (3.21b), we have

$$d\epsilon_{mn}^{e(i)} = \frac{1}{2G^{(i)}}\left(d\sigma_{mn}^{(i)} - \frac{\nu^{(i)}}{1-\nu^{(i)}} d\sigma_{mn}^{(i)}\delta_{mn}\right) \tag{3.22}$$

$$d\epsilon_{mn}^{p(i)} = \frac{1}{\rho_0^{(i)}}(ds_{mn}^{(i)} - h_{mn}^{(i)}(z)dz^{(i)}). \tag{3.23}$$

Substituting (3.22) and (3.23) into (3.21a) and with the aid of (3.19), it results in

$$d\sigma_{mn}^{(i)}/2\mu_p^{(i)} = d\epsilon_{mn}^{(i)} + a^{(i)}d\epsilon_{kk}^{(i)}\delta_{mn} + h_{mn}^{(i)}dz^{(i)}/\rho_0^{(i)} \tag{3.24}$$

where

$$2\mu_p^{(i)} = \frac{\rho_0^{(i)}}{1 + \rho_0^{(i)}/2G^{(i)}} \tag{3.25}$$

$$a^{(i)} = \frac{k^{(i)}}{\rho_0^{(i)}} + \frac{\nu^{(i)}}{1-2\nu^{(i)}}, \quad k^{(i)} = \frac{2G^{(i)}(1+\nu^{(i)})}{3(1-2\nu^{(i)})}. \tag{3.26a, b}$$

It merits notice that the total number of stress and strain components of the two phases and the effective inclusion together is 36. Equations (3.15) to (3.18) offer 24 equations and (3.24) offer 12. Therefore, combining these equations will result in six new equations that are the constitutive equations of the effective inclusion. They can be expressed explicitly in matrix form as follows:

$$\{d\epsilon^{C}\} = [M]^{ep}\{d\sigma^{C}\} + \{dH\} \tag{3.27}$$

$$\{dH\} = \{dH_{11}, dH_{22}, dH_{33}, dH_{23}, dH_{13}, dH_{12}\}^{T} \tag{3.28}$$

$$[M]^{ep} = \begin{bmatrix} A/D & -B/D & -CF/D & 0 & 0 & 0 \\ -B/D & A/D & -CF/D & 0 & 0 & 0 \\ -CF/D & -CF/D & c_0 + 2c^2F/D & 0 & 0 & 0 \\ 0 & 0 & 0 & 1/P & 0 & 0 \\ 0 & 0 & 0 & 0 & 1/P & 0 \\ 0 & 0 & 0 & 0 & 0 & 1/P_0 \end{bmatrix}. \tag{3.29}$$

$[M]^{ep}$ is the elastoplastic compliance matrix which accounts for instantaneous elastoplastic responses. On the other hand, the deformation history-dependent plastic responses are accounted for by $\{dH\}$ via $h_{mn}^{(i)}(z^{(i)})$, whose values are determined through (3.14b) with the aid of (3.6) and (3.12). The explicit expressions of H_{ij} and parameters D, F, A, B, C, C_o, P_o, and P are listed in the Appendix. From (3.25) we can see when $\rho_0^{(i)} \to \infty$, $\mu_p^{(i)} \to G^{(i)}$, and then $[M]^{ep}$ reduces to the elastic compliance matrix $[M]^{e}$. This situation indicates that the instantaneous responses are pure elastic. In this case, the elastic strain matrix $[d\epsilon^{C}]^{e}$ of the inclusion can be expressed as

$$[d\epsilon^{eC}] = [M]^{e}\{d\sigma^{c}\}. \tag{3.30}$$

With the aid of (3.27) and (3.30), the plastic strain matrix of the homogenized inclusion can be expressed by

$$\{d\epsilon^{pC}\} = ([M]^{ep} - [M]^{e})\{d\sigma^{C}\} + \{dH\}. \tag{3.31}$$

Furthermore, using (3.15) to (3.18) and (3.24), the stresses and strains in each phase can be explicitly expressed.

3.3 A Local Iterative Process for Determining Inclusion's Plastic Strain. From (3.30) $d\epsilon_{kk}^{ec}$ can be determined. Substituting it and (3.27) into (2.11) we obtain

$$\{dQ^{c}\} = ([I] + A[\bar{\bar{M}}]^{e} + B[M]^{ep})\{d\sigma^{c}\} + B\{dH\}. \tag{3.32}$$

The nonzero entries of $[\bar{\bar{M}}]_{6\times6}^{e}$ can be determined from $[M]^{e}$ as follows:

$$\bar{\bar{M}}_{mn}^{e} = M_{1n}^{e} + M_{2n}^{e} + M_{3n}^{e}$$

$$\text{for } m = 1 - 3 \quad \text{and} \quad n = 1 - 3. \tag{3.33}$$

Equation (3.32) can be rewritten as

$$\{d\sigma^{c}\} = [M^{*}]^{-1}\{dQ^{*}\} \tag{3.34}$$

where

$$\{dQ^{*}\} = \{dQ^{c}\} - B\{dH\} \tag{3.35}$$

$$[M^{*}] = [[I] + A[\bar{\bar{M}}]^{e} + B[M]^{ep}]. \tag{3.36}$$

After obtaining the matrix $\{dQ^{*}\}$, $\{d\sigma^{c}\}$ of the effectively homogeneous inclusion under given applied loading can be obtained from (3.34). Actually, this calculation is conducted through a local iterative process of the inclusion at hand, and is necessary for determining $\Delta\epsilon_{mn}^{pc}$ to complete the global iteration process. In this local process, the key is the determination of the plastic strain $\Delta\epsilon_{mn}^{p(i)}$ $(i = 1, 2)$ of constituents. Their initial values can be given by the values of the last iteration. Based on these values and using (3.4), (3.11), and (3.12), the initial material time in the iterative step, $dz^{(i)}$, can be determined, so that $\{dH\}$ can be determined from the Appendix and relations of h_{mn}, $\rho_0^{(i)}$ in (3.14a, b). From (3.27) and (3.31), the strain $\{d\epsilon^{c}\}$ and plastic strain $\{d\epsilon^{pC}\}$ of each inclusion can be obtained and, in turn, using (3.15) to (3.18) and (3.24), the stress and strain components in each phase can be determined. Furthermore, with the aid of (3.21a) and (3.22), the plastic strain $\Delta\epsilon_{mn}^{p(i)}$ after the current iteration step can be obtained, and then the ending material time $dz^{*(i)}$ in that step can be determined. This process will be repeated until some convergence criterion related to the difference of $dz^{(i)}$ and $dz^{*(i)}$ is satisfied. This process is similar to the one for global iteration discussed in the end of the last section; also, the convergence criterion of $dz^{(i)}$ $(i = 1, 2)$ is similar to (2.13) for $\Delta\bar{Q}_{IJ}^{(k)}$.

4 Numerical Results and Discussion

In the present work, numerical analysis is conducted for BS11 steel. In this material the cementite layer is the hard phase and

Downloaded 04 May 2010 to 171.66.16.27. Redistribution subject to ASME license or copyright; see http://www.asme.org/terms/Terms_Use.cfm

Table 3 Material constants for numerical analysis

$\mu^{(1)} = \mu^{(2)} = 80.12$ GPa, $\nu^{(1)} = \nu^{(2)} = 0.267$, $V_f^{(1)} = 0.89$, $V_f^{(2)} = 0.11$
$(c_1^{(1)}, c_1^{(2)}, c_2^{(2)}) = (100, 8.5, 0.0435)$ GPa, $(\alpha_1^{(1)}, \alpha_1^{(2)}, \alpha_2^{(2)}) = (120, 123, 0.385)*10^3$ $\beta = 160$, $d = 1.9$, $\gamma = 17.5$

the ferrite layer is the soft phase. Since there is no explicit yield point in the stress-strain curve of this material we have

$$\underline{R}_0^{(i)} = 0 \quad (i = 1, 2) \tag{4.1}$$

and the constitutive equations used for individual phases and the effective inclusion are (3.13) and (3.27). This choice is very convenient for numerical analysis because the loading and unloading process can be addressed with in a unified fashion (Valanis and Fan, 1983; Fan and Peng, 1991). The link between global and local analysis is through (2.10) and (3.32) by global and local iterative processes. To describe the plastic behavior of the soft phase, it is found that two chains in Fig. 2(*c*) are necessary (i.e., $n^{(2)} = 2$), while for the plastic behavior of the hard phase one chain may be suitable ($n^{(1)} = 1$). This choice results in the following nine material parameters for description of the plastic behavior of both the hard and soft phases:

$$c_1^{(1)}, \alpha_1^{(1)}, c_1^{(2)}, \alpha_1^{(2)}, c_2^{(2)}, \alpha_2^{(2)}, \beta, d, \gamma.$$

In the above list, the first six parameters are from (3.14*a*, *b*),

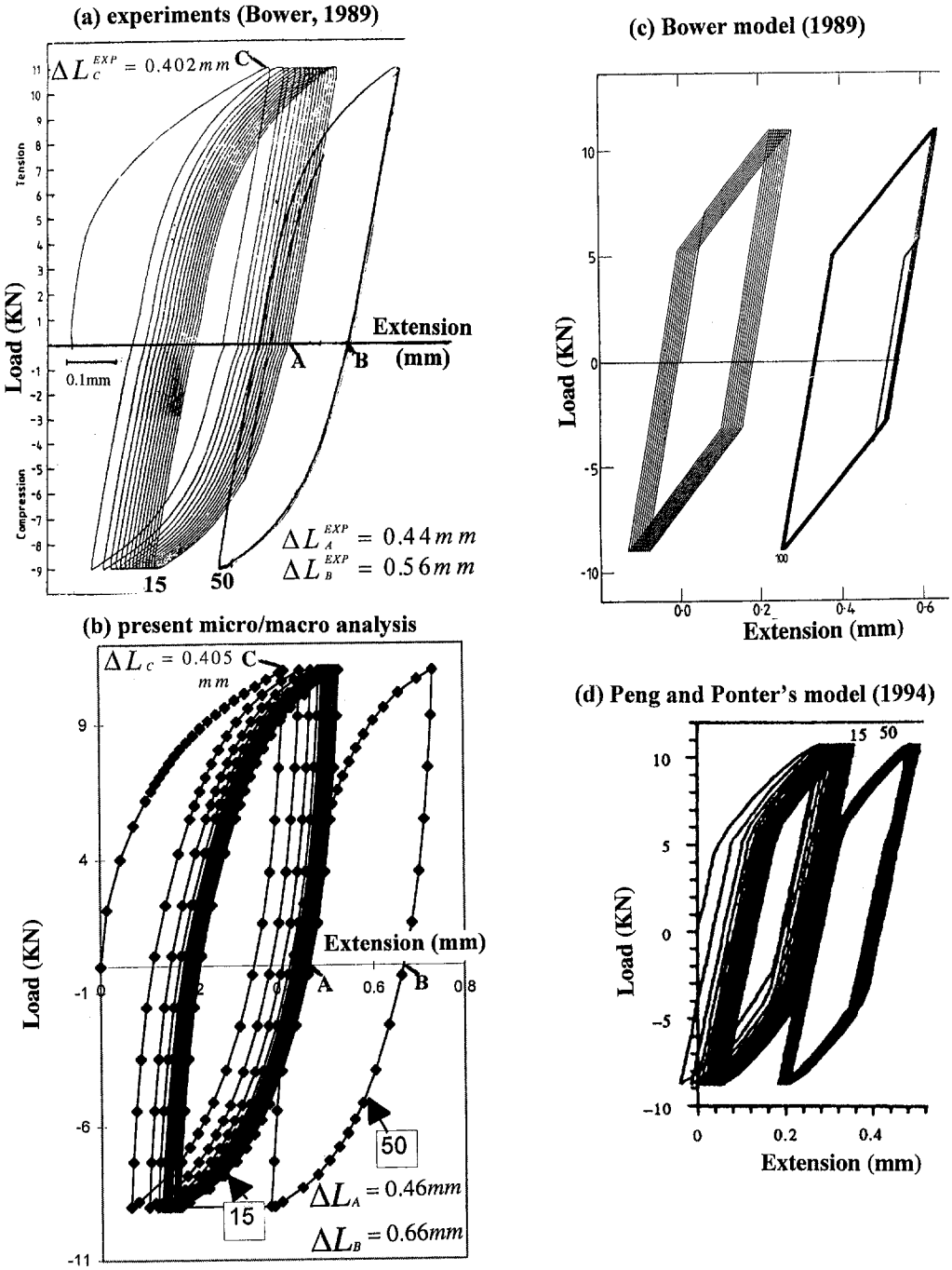

Fig. 3 Responses of the BS11 rail steel specimen under uniaxial cyclic loading, 10 ± 1 KN (σ = 56 ± 562 MPa); (*a*) experiments (Bower, 1989), (*b*) present micro/macro analysis (c) Bower model (1989), (*d*) Peng and Ponter's model (1994)

Downloaded 04 May 2010 to 171.66.16.27. Redistribution subject to ASME license or copyright; see http://www.asme.org/terms/Terms_Use.cfm

Table 4 Quantitative comparison of the specimen extension for the critical points, A, B, C between experimental results (Bower, 1989) and the present analysis

	A (unloading point at reversal 15)	B (unloading point at reversal 50)	C (peak point at first reversal)
Experiments	0.44 mm	0.56 mm	0.402 mm
Present analysis	0.46 mm	0.66 mm	0.405 mm

while other three come from the evolution laws of (3.6) and (3.12). The first six material constants are mainly determined by the stress-strain curve of the first reversal, and the last three constants are determined by the stress-strain curve of the second reversal as well as the ratchetting rate. There are interactive effects between the two material sets. Therefore, a curve-fitting process is required to make an optimized choice. It is reported (Langford, 1977) that the cementite layer has a volume fraction of about 0.1–0.15 and there are no significant differences in elastic constants between these two phases. Therefore, elastic constants are taken to be the same as the aggregate. Material constants and volume fractions used in the numerical simulation are listed in Table 3.

In the numerical analysis, the number of iterations for each step of global and local iterations is around 5. The axial strain under the applied stress along the Z-axis is compared with the corresponding strain under the same amount of applied stress along the X-axis. The maximum relative error in the two cases is only within 0.8 percent, indicating a satisfactory simulation for the macroscopic isotropy of the aggregate. In the following, all results presented are obtained by cyclic loading along the X-axis of the horizontal XOY-plane (Fig. 1(a)). Only results for cyclic number less than 50 are reported here. Since conclusions obtained for a small cyclic number may not be suitable for a large number of cycles, one must be careful when extending the conclusion drawn here to a large cyclic number.

First, the micro/macroscopic cyclic responses of the BS11 steel specimen under unsymmetric axial loading of 1 ± 10 KN (56 ± 562 MPa) are calculated by the proposed method. This is the case for which Bower (1989) reported the complete set of cyclic stress-strain curves measured in his experiments. The experimental curve of the first 15 cycles and the hysteresis loop of the full 50th cycle are given in Fig. 3(a). Theoretical results around the range of those cycles are shown in Fig. 3(b), (c), (d), which are calculated, respectively, by the present micro/macroscopic analysis, Bower's model (1989) and the model of Peng and Ponter (1994). The last two models were designed more specially to correlate the experimental data in relatively large cycles, and there is a lack of calculated results within the first 50 cycles for the two models. Therefore, a quantitative comparison with the experimental data listed in Table 4 at the critical points A, B, C of the cyclic curves (see Fig. 3(a), (b)) is only for the present analysis. It seems that the present numerical result satisfactorily compares with the experimental data. This is essential, since there is a lack of a direct approach, such as microscopic experiments, to check the accuracy of the microscopic analysis. Hence, the result that the macroscopic counterpart matches well with the measured stress-strain curve offers confidence for the reasonable accuracy of the microscopic analysis. However, this does not mean that the microscopic analysis for the hard and soft phases is equally accurate to the prediction of the overall load-deflection curve. Direct or indirect evidence should be found in the future to verify closely the accuracy of the microscopic calculations.

Figures 4–6 show the inhomogeneous feature of distributions of elastic energy, effective stress, and effective plastic strain in the hard and soft phases of microstructures. On the horizontal axes of these figures, ten microstructure elements are placed. These ten elements are located on 10 spatially and uniformly distributed planes, labeled from A to J. These planes are shown in Fig. 1(c) where planes A, B, E, F, G, and J are in the front of the paper plane, and planes I, D, C, and H are in the back. The centers of these ten microstructure elements are coincident with the first Gaussian points of the ten planes whose Euler coordinates, θ and ϕ are shown in A–J of Table 1, with ω being 6.3 deg (Table 2). For simplicity, these ten elements are denoted as the label of the plane on which the element is located. In these figures, five columns indicate the evolution of the variables at five reversal points, with reversal point 1 being the left and 5 the right. Here, the effective stress and effective plastic strain are defined, respectively, as follows:

$$\sigma_{\text{eff}}^{(i)} = \sqrt{\frac{3}{2} s_{mn}^{(i)} s_{mn}^{(i)}} \quad (i = 1, 2) \tag{4.2}$$

$$\epsilon_{\text{eff}}^{P(i)} = \sqrt{\frac{2}{3} \epsilon_{mn}^{P} \epsilon_{mn}^{P}} \quad (i = 1, 2). \tag{4.3}$$

Except for Fig. 5, all results in these figures are obtained under an unsymmetric cyclic loading (56 ± 562 MPa), which corresponds to the loading in Fig. 3(a). From these figures, we can see that the distribution of energy, stress and strain and their evolution with reversals are quite different from one another. More specifically, Figs. 4 and 6(a) show distribution of elastic energy density and effective stress, respectively, in the hard phase among the ten microstructure elements. Reversals 1, 3, 5 correspond to positive applied stress of 618 MPa, and reversal 2, 4 correspond to the negative applied stress of -506 MPa. The two figures are similar in manner. However, since elastic energy is a quadratic function of stress the variation of corresponding values in Fig. 4 is more abrupt than that in Fig. 6(a). The evolution patterns of the variables in these figures can be classified as the following three groups:

Group 1 (elements B, E, J): the values of variables at the first reversal point of this group are very large, and gradually reduce with the number of odd reversals. These elements may be important for strength under monotonic loading.
Group 2 (elements D, F): the corresponding values at the odd reversal points monotonically increase with the number of odd reversals. These elements may be important for fatigue life under cyclic loading.
Group 3 (elements A, C, G, H, I): the corresponding values increase first, and then reduce with the odd reversals.

Figure 6(b) shows a more evenly distributed effective stress in the soft phase than in the hard phase. Basically, the ten elements can also be classified in the same three groups as the above, but the increase (or decrease) tendency is basically opposite to that in the hard phase. Figure 5 shows the distribution of effective stress in the hard phase among the ten elements of microstructure under symmetric cyclic loading. The comparison between Fig. 5 and Fig. 6(a) shows that there is no significant difference concerning the distribution of the effective stresses between the case of symmetric loading and unsymmetric loading, but there is a significant difference in their values. Take the maximum local stress as an example; this maximum effective stress in both cases occurs in element D at reversal point 5. In the symmetric case, it is 3950 MPa, and in the unsymmetric case 3500 MPa. This result means that the stressing of the microstructure element in a symmetric case is stronger than that in an unsymmetric case. This result is consistent with the fact that fatigue life is generally shorter in a symmetric case than that in an unsymmetric loading if the stress amplitude is the same.

It merits notice that the element with maximum stress under cyclic loading is different from the one in monotonic loading. In the former case, it is the element D and in the latter case it is the element B. The Euler angles of elements D and B are, respectively, as (216 deg, 37.4 deg, 6.3 deg) and (72 deg, 37.4 deg, 6.3 deg). More important is the finding that the ratio χ of

Downloaded 04 May 2010 to 171.66.16.27. Redistribution subject to ASME license or copyright; see http://www.asme.org/terms/Terms_Use.cfm

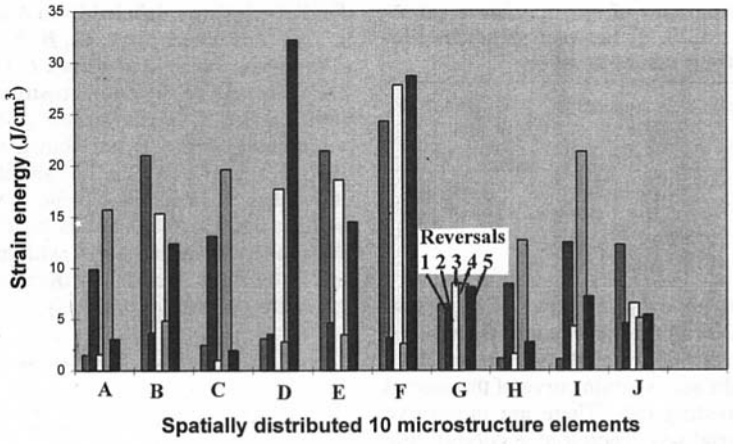

Fig. 4 Distribution of elastic energy density in hard phase of 10 microstructure elements at 1–5 reversals under unsymmetric loading (56 ± 562 MPa)

the largest local stress over the applied stress in cyclic loading is much larger than that in monotonic loading. In fact, the largest local stress at the first reversal point of Fig. 6(*a*) is found to occur in element *B* and *E* with the ratio χ to be 4.22. However, at the fifth reversal point of cyclic loading the largest local stress occurs in element *D*; its stress ratio χ is 5.67. How can one make a judgment on the effects of high local stress on the strength of materials? This is a difficult question, because the material strength of a heterogeneous microstructure can be quite different from that of macroscopically homogeneous media. In the latter case, the material strength is determined by, for instance, the uniaxial tensile test of a specimen, but in the case of microstructure the layered phase is fully constrained by the neighboring layers. These constraint effects are higher in the thinner layer than in the thicker layer, which makes the in situ strength of the thinner layer much larger, say three times, than tested in the free condition (Fan and Zhang, 1993). Therefore, the high value of the largest local stress is realistic, and its value is important for a sophisticated fatigue and strength analysis of materials.

One thing related to the high value of the local stress of the cementite layer is that the constraint effects of the thick ferrite layers on the cementite layer can significantly change the stress state of these layers. Figs. 7(*a*), (*b*) show, respectively, the hysteresis loop of 2–3 reversal and 30–31 reversal for the element *B*. In the cycle of 2–3 reversal, the local stress σ_y is arranged about ±450 MPa in the soft phase and from −1100 to 2150 MPa in the hard phase. However, in the cycle of 30–31 reversals the stress in the hard phase is totally in compression and ranges from −3900 to −1000 MPa, while the soft phase is totally in tension and arranged around 250–1100 MPa (Fig. 7(*b*)). Since the hard phase is the brittle cementile layer, this phase is able to sustain large compressive stress. This may be the other reason why the layered microstructure of pearlitic steel can undertake stress that is several times larger than the nominal applied stress.

Figure 8 shows the evolution of effective plastic strain in the hard and soft phases at reversals of cyclic loading for the element *B* under unsymmetric cyclic loading (56 ± 562 MPa). It is seen from this figure that the range of plastic effective strain between two successive reversal points in the hard phase is much smaller than that in the soft phase at the first 25 reversals. On the other hand, in the hard phase the plastic strain accumulates with cycles in the same direction, but this is not the case in the soft phase where the maximum effective plastic strain oscillates with cycles. It is interesting to notice that the different strain accumulation patterns in the hard and soft phases result in a larger plastic strain in the hard phase than that in the soft phase when it reaches the 16th reversal. Then the average effective plastic strain of the soft phase in the range of 16–28 reversals develops in the same direction as the one in the hard phase. This tendency may change again. Eventually, the ratchetting rate and direction of the material will be determined by the competition of the evolution of the plastic strain in both the hard and soft phases. These results may shine a light on the investigation of the complicated mechanism of the ratchetting effects.

In fact, a detailed calculation on the energy absorption and transferring process of the two phases shows that the deforma-

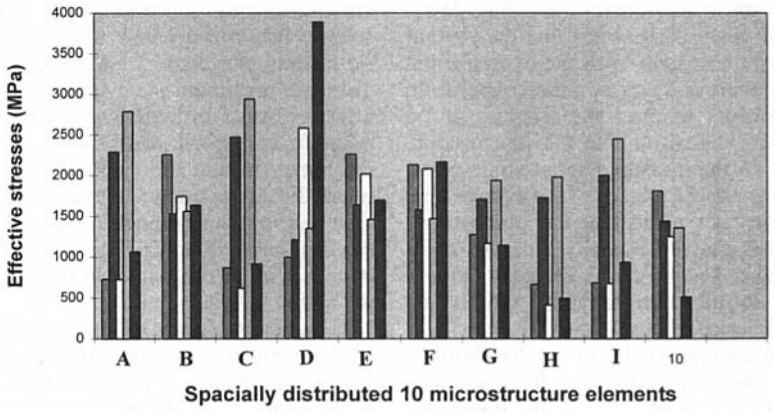

Fig. 5 Distribution of effective stresses in hard phase of 10 microstructure elements at 1–5 reversals under symmetric loading (±562 MPa)

Downloaded 04 May 2010 to 171.66.16.27. Redistribution subject to ASME license or copyright; see http://www.asme.org/terms/Terms_Use.cfm

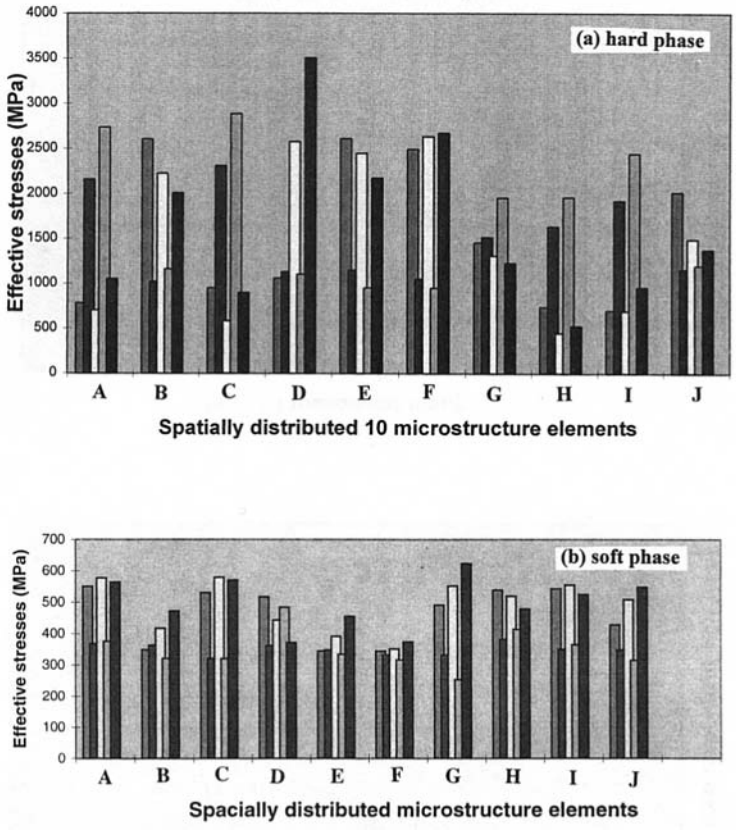

Fig. 6 Distribution of effective stresses in hard and soft phases of 10 microstructure elements at 1–5 reversals under unsymmetric loading (56 ± 562 MPa); (*a*) hard phase, (*b*) soft phase

tion energy stored in the thin layer of the hard phase (or in the spring $E_r^{(1)}$) during the first cycle can release with the cycles followed as we can see from Fig. 9. In this figure, G^T denotes the input energy density, or the total energy density. Its value equals the sum of the volume average density G^c of the inclusion and the interaction energy density G^I between the inclusion and the aggregate. $G^{c(1)}$ and $G^{c(2)}$ are the volume average density absorbed by the hard and soft phases of the inclusion. From this figure, we can see that the absorbed energy, $G^{c(1)}/G^T$, of the hard phase is reduced from 20 percent at the beginning to about 0 at reversal 100, followed by negative ratios. The reduction of the absorbed energy in the hard phase during the cyclic loading indicates that some energy stored previously is released with cycles. This energy release will reduce the external energy needed for continuously developing plastic deformation of the material. Given that the input energy of each cycle is approximately proportional to the product of the width and height of the hysteresis loop, the reduction of the input energy indicates the reduction of the width of the hysteresis loop when the amplitude of the applied stress is fixed. This fact means that the ratchetting rate is reduced. It is obvious that this reduced energy is limited and, in turn, the reduction of the ratchetting rate is also limited. It may reach a steady ratcheting after a relatively large cyclic number if there is no other disturbance. This is the phenomenon observed in Bower's experiments (1989).

It is worthwhile to briefly discuss the fatigue behavior of the brittle cementite layer based on the obtained numerical results. It is known that the cyclic number, N_{Inc}, of fatigue crack nucleation takes a relatively large percent of fatigue life in high-cycle fatigue. According to Fan, McDowell, and Horstemeyer (1998), this number can be calculated as follows:

$$N_{\text{Inc}}^{\alpha}\Delta\Gamma_{\max} = C \tag{4.4}$$

where $\Delta\Gamma_{\max}$ is related to the maximum shear plastic strain range, $\Delta\gamma_{\max}^{p}$, at the site of cyclic strain intensification by the following equation:

$$\Delta\Gamma_{\max} = \Delta\gamma_{\max}^{P}(1 + K\sigma_n^{\max}/\sigma_y) \tag{4.5}$$

where σ_y is the yield stress or reference stress, $\sigma_n^{\max}$-maximum normal peak stress perpendicular to the slip plane, C, K, and α are material parameters. This is a type of Coffin-Mason law but it is for heterogeneous material with all stress and plastic strain taken from the local analysis. From this formula we can see that the smaller the $\Delta\gamma_{\max}^{p}$ the larger the N_{Inc}. Keeping in mind the results shown in Fig. 8 that the cementite layer has a small plastic strain range between two successive peaks, we can see that this layer may sustain a relatively large number of cycles for fatigue crack nucleation.

5 Summary and Conclusion

While it is known that local anisotropy and heterogeneity associated with microstructure have profound influences on material strength and fatigue life, little information related to distribution and evolution of stress, strain and energy in microstructure can be found in the existing literature. This is mainly due to all of the difficulties involved in the analysis, especially in the case of cyclic loading. In this paper, a methodology is developed for analysis of cyclic stress and strain across micro/macroscopic scales. A summary and conclusions for this work follows.

1 The SCS has been extended to include local analysis and has been applied for cyclic loading with weakening constraint capability and calculation convenience. This extension makes the SCS capable of determining overall responses of material as well as local stress evolution in microstructures. The key in the extension is the concept of the effective homogeneous inclusion in which detailed microstructure is smeared out when

Downloaded 04 May 2010 to 171.66.16.27. Redistribution subject to ASME license or copyright; see http://www.asme.org/terms/Terms_Use.cfm

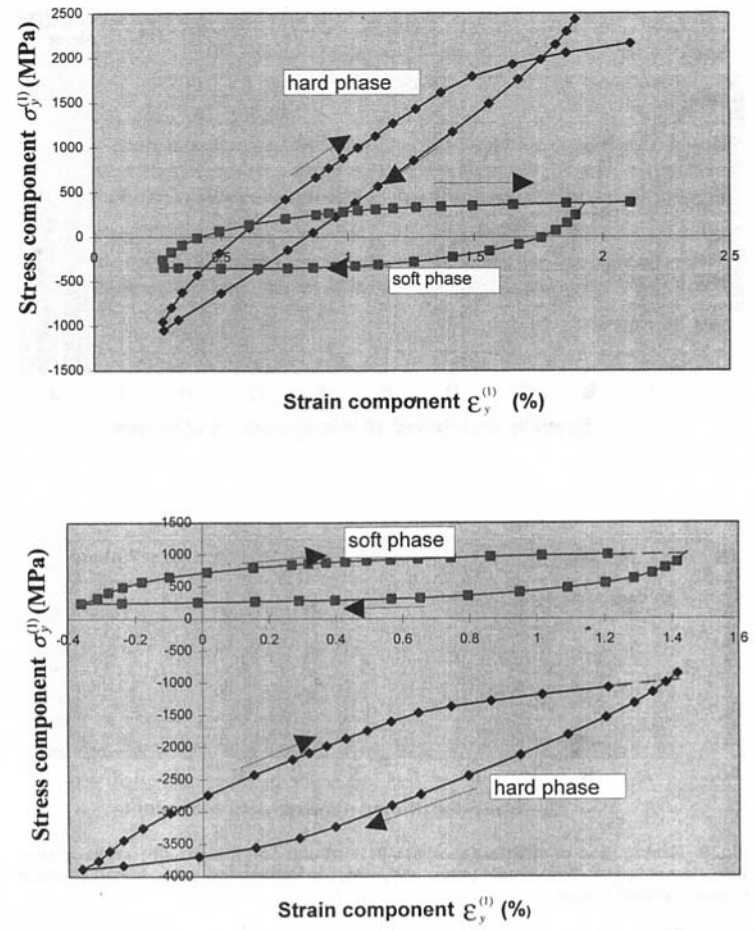

Fig. 7 Hysteresis loop of microstructure element *B* during unsymmetric loading (56 ± 562 MPa); (*a*) stress-strain loop $\sigma_y^{(1)} - \epsilon_y^{(1)}$ of 2–3 reversals for hard and soft phases, (*b*) stress-strain loop $\sigma_y^{(1)} - \epsilon_y^{(1)}$ of 30–31 reversals for hard and soft phases

investigating the interaction of the inclusion with its surrounding aggregate. However, the influence of microstructure on stress and strain evolution will be accounted for through incorporating its heterogeneity and anisotropy into constitutive relations of the effective homogeneous inclusion. By this approach the individual constitutive behavior of each phase of the microstructure and the compatibility conditions at the interface between different phases can be accounted for. Since the effective homogeneous inclusion can consist of microstructures at different scales and with different phase properties, this extension offers the possibility for investigating microscopic stress, strain and cracking of a wide scope of microstructures. They can range from cells with domain walls, laminae, and needle structures to grain and grain boundaries.

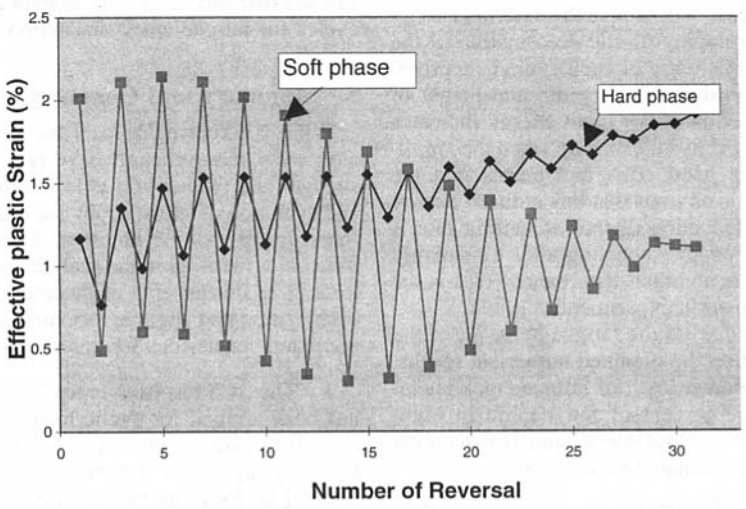

Fig. 8 Evolution of effective plastic strain with reversal numbers for the microstructure element *B* under unsymmetric loading (56 ± 562 MPa)

Downloaded 04 May 2010 to 171.66.16.27. Redistribution subject to ASME license or copyright; see http://www.asme.org/terms/Terms_Use.cfm

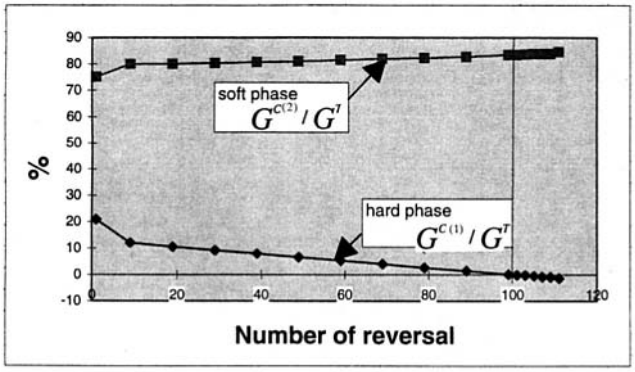

Fig. 9 Variations of absorbed energy densities for the hard and soft phases

2 The proposed method is exemplified by layer structured dual phase metal such as pearlitic rail steel with fine randomly oriented layers of the hard and soft phases. Elastoplastic constitutive equations of each phase without yield surface are taken as examples to show how to formulate the constitutive equation of the effective homogeneous inclusion and how to apply it to the SES through Eqs. (2.10) and (3.32). The numerical algorithm for the local and global iteration processes as well as the approach using isosahedron to simplify and improve the volume averaging technique are also introduced. it is found that the constitutive law without yield surface is convenient for cyclic analysis because the loading and unloading process can be addressed with in a unified fashion. The comparison between the experimental load-extension curve obtained by Bower (1989) and the results calculated by the present method show a good agreement up to 50 cycles. This comparison is significant because it offers confidence that the distribution of microscopic stress in both the hard and soft phases obtained from the present microscopic analysis may have a reasonable accuracy.

3 Results show that the distribution of elastic energy, effective stress and plastic strain and their evolution pattern are quite inhomogeneous in both the hard and soft phases, no matter whether the applied loading is symmetric or unsymmetric. The microstructure elements with different orientations are divided into three groups according to the evolution tendency of their maximum stress. Results show that the maximum local stress under symmetric loading is larger than that in unsymmetric loading under fixed amplitude of the applied loading. It is also found that the cementite hard layer can accumulate a relatively large plastic strain, even though the range of its plastic strain at each cycle is much smaller than that in the soft phase. This finding is significant for understanding the issue of whether or why the brittle cementite layer in pearlitic steel can sustain a relatively large plastic deformation and fatigue life. Controversial opinions and experimental results on this issue have been reported for many years (Langford, 1977).

4 There are findings that the maximum local stress ratio over applied stress in the hard phase can be very large. Due to the internal constraint effects, the existence of a high value of local stress may be realistic. This ratio depends on the amplitude of applied loading and is caused by intensification of the local plastic flow of the soft phase in which more loading is transferred cycle by cycle to the hard phase. While the findings of high value and heterogeneous distribution feature of stress in microstructure are significant for exploring some important issues in sophisticated strength and fatigue analysis, the failure criterion of the microstructure cannot be simply based on traditional strength theory and experiments. This area has been overlooked and is explored in this work.

5 The physically based plasticity model introduced in this work is effective in describing complicated elastoplastic behavior. Several plasticity models such as the models of Amstrong and Freedrick (1966), Bower (1989), Valanis (1980), Chaboche (1979), Ohno and Wang (1993), and Jiang and Sehitoglu (1996) as well as common classical plasticity models can be derived from this simple mechanical model. In this work, the underlying microscopic aspects of this model have been emphasized. More specifically, concepts of internal variables and their generalized driving force are introduced through the generalized displacements of a series of dashpot-like plastic blocks. The hardening function, $f^{(i)}$, is introduced through the generalized frictional coefficients and explained physically by the obstacles formed from tangles of dislocations through the interactions of the active dislocations and dislocation forests. This explanation makes it understandable that this hardening function is isotropic in nature. In this model, stochastic microscopic fields such as dislocation pile-ups are simulated by small springs C_r and E_r. Each of these springs is a disturbance to the global lattice structure and can absorb and release deformation energy. These springs take essential role in distributing generalized forces to different internal variables at different deformation stages. The function of these springs is exemplified through the spring E_r. This spring offers back stress for the kinematic hardening and can describe the strong-energy-absorption-capability of the thin layer. The significance of the energy release from this spring on investigating the ratchetting effects is also shown. Furthermore, the difference in this model for materials with and without yield surface is proved to be correspondent to the model with and without the first chain in the mechanical model. This result offers a simple and clear connection between plasticity models of CP and NCP.

Acknowledgments

Financial support from the Chinese National Science Foundation through the contract of 19772076 and Prof. Z. Gao's suggestions and contributions are much appreciated.

Reference

Armstrong, R. J., and Frederick, C. O., 1966, "A Mathematical Representation of the Multiaxial Bauschinger Effect," Report/RD/B/N 731, Central Electricity Generating Board.

Berveiller, M., and Zaoui, A., 1979, "An Extension of the Self-Consistent Scheme to Plastically Flowing Polycrystals," *J. Mech. Phys. Solids,* Vol. 26, pp. 325–344.

Bodner, S. R., and Pardom, Y., 1975, "Constitutive Equations for Elastoplastic Strain Hardening Materials," ASME *Journal of Applied Mechanics,* Vol. 42, pp. 385–389.

Bower, A. F., 1989, "Cyclic Hardening Properties of Hard-Drawn Copper and Rail Steel," *J. Mech. Phys. Solids,* Vol. 37, No. 4, pp. 455–470.

Bower, A. F., and Johnson, K. L., 1989, "The Influence of Strain Hardening on Cumulative Plastic Deformation in Rolling and Sliding Line Contact," *J. Mech. Phys. Solids,* Vol. 37, No. 4, pp. 471–493.

Budiansky, B., and Wu, T. T., 1962, "Theoretical Prediction of Plastic Strains of Polycrystals," *Proc. 4th U.S. Nat. Cong. Appl. Mech.,* p. 1175.

Chaboche, J. L., Dang Van. K., and Cordier, G., 1979, "Modelization of the Strain Memory Effect on the Hardening of 316 Stainless Steel," *Structural Mechanics in Reactor Technology,* Div. L. Berlin, L11/3.

Fan, J., 1987, "On a Thermomechanical Constitutive Theory and its Application to CDM, Fatigue, Fracture, and Composites," *Thermomechanical Coupling in Solids,* Elsevier Science Publications B. V. (9th Holland), IUTAM, 223–237.

Fan, J., McDowell, D., and Horstemeyer, M., 1998, "Micromechanics of Fatigue in Cast Al Alloys," *Proceedings of 1st International Aluminum Casting Technology Symposium,* pp. 153–163.

Fan, J., and Peng, X., 1991, "A Physically Based Constitutive Laws for Nonproportional Cyclic Plasticity," *J. Engng. Mat. Tech.,* Vol. 113, pp. 254–262.

Fan, J., and Zhang, Z., 1993, "In-Situ Damage Evolution and Micro/Macro Transition for Laminated Composites," *Composites Science and Technology,* Vol. 47, No. 2, pp. 107–118.

Hart, E. R., 1976, "Constitutive Relation for Nonelastic Deformation of Metals," *J. Engng. Mat. Tech.,* Vol. 98, pp. 193–202.

Hill, R., 1965, "Continuum Micro-Mechanics of Elastoplastic Polycrystals," *J. Mech. Phys. Solids,* Vol. 13, pp. 89–101.

Hutchinson, J. W., 1970, "Elasto-plastic Behavior of Polycrystalline Metals and Composites," *Proc. Roy. Soc.,* London, A319, pp. 247–272.

Hwang, K., and Sun, S., 1994, "Micromechanical Modeling of Cyclic Plasticity," *Advances in Engineering Plasticity,* pp. 41–48, International Academic Publishers, Beijing, China.

Downloaded 04 May 2010 to 171.66.16.27. Redistribution subject to ASME license or copyright; see http://www.asme.org/terms/Terms_Use.cfm

Jiang, Y., and Sehitoglu, H., 1994a, "Cyclic Ratchetting of 1070 Steel Under Multiaxial Stress State," *Int. J. of Plasticity,* Vol. 10, No. 5, pp. 579–608.

Jiang, Y., and Sehitoglu, H., 1994b, "Multiaxial Cyclic Ratchetting Under Multiple Step Loading," *Int. J. of Plasticity,* Vol. 10, No. 8, pp. 849–870.

Jiang, Y., and Sehitoglu, H., 1996, "Modeling of Cyclic Ratchetting Plasticity, Part 1: Development of Constitutive Relations," *J. of Applied Mechanics,* Vol. 63, pp. 720–725.

Krempl, E., 1987, "Models of Viscoplasticity, Some Comments on Equilibrium Stress and Drag Stress," *Acta Mechanica,* Vol. 69, pp. 25–42.

Kroner, E., 1961, "Zur Plastischen Vaerfurmungdes Vielkrisalls," *Acta Metall.,* Vol. 9, p. 155.

McDowell, D. L., 1997, "An Engineering Model for Propagation of Small Crack in Fatigue," *Engineering Fracture Mechanics,* Vol. 56, No. 3, pp. 357–377.

Ohno, N., and Wang, T. D., 1993, "Kinematic Hardening Rules With Critical State of Dynamic Recovery: Part 1—Formulation and Basic Features for Ratchetting Behavior," *Int. J. of Plasticity,* Vol. 9, pp. 375–390.

Peng, X., Fan, J., and Zeng, X., 1996, "Analysis for Plastic Buckling of Thin-Walled Cylinders Via Non-Classical Constitutive Theory of Plasticity," *Int. J. Solids Structures,* Vol. 33, No. 33, pp. 4495–4509.

Peng, X., and Ponter, A. R. S., 1994, "A Constitutive Law for a Class of Two-Phase Materials With Experimental Verification," *Int. J. Solids Structures,* Vol. 31, No. 8, pp. 1099–1111.

Qiu, Y. P., and Weng, G. J., 1991, "The Influence of Inclusion Shape on the Overall Elastoplastic Behavior of a Two-Phase Isotropic Composite," *Int. J. Solids Structures,* Vol. 27, pp. 1537–1580.

Valanis, K. C., 1971, "A Theory of Viscoplasticity Without a Yield Surface. Part I: General Theory. Part II: Application to mechanical behavior of metals," *Archives of Mechanics,* Vol. 23, pp. 517–551.

Valanis, K. C., 1980, "Fundamental Consequences on New Intrinsic Time Measure as a Limit of Endochronic Theory," *Arch Mech.,* Vol. 32, pp. 171–190.

Valanis, K. C., and Fan, J., 1983, "Endochronic Analysis of Cyclic Elastoplastic Strain Fields in a Notched Plate," *J. Appl. Mech.,* Vol. 50, pp. 789–794.

Weng, G. J., 1990, "The Overall Elastoplastic Stress-Strain Relations of Dual-Phase Metals," *J. Mech. Phys. Solids,* Vol. 38, pp. 419–441.

Weng, G. J., 1993, "A Self-Consistent Relation for the Time-Depending Creep of Polycrystals," *Int. J. of Plasticity,* Vol. 9, pp. 181–198.

Zheng, X., 1996, "Microscopic and Phenomenological Study on Polycrystal Plasticity and Creep," Ph.D. dissertation, Chongqing University.

APPENDIX

$$dH_{11} = \sum_{i=1}^{2} [Fh_{33}^{(i)}\chi^{(i)} + (Bh_{22}^{(i)} - Ah_{11}^{(i)})]\phi^{(i)}dz^{(i)} \quad (A.1)$$

$$dH_{22} = \sum_{i=1}^{2} [Fh_{33}^{(i)}\chi^{(i)} + (Bh_{11}^{(i)} - Ah_{22}^{(i)})]\phi^{(i)}dz^{(i)} \quad (A.2)$$

$$dH_{33} = \sum_{i=1}^{2} \left[cF(h_{11}^{(i)} + h_{22}^{(i)}) - \left(2a^{(i)}cF + \frac{Dh_{33}^{(i)}}{2\mu_p^{(i)}(1 + a^{(i)})} \right) \right] \phi^{(i)}dz^{(i)} \quad (A.3)$$

$$dH_{23} = -\sum_{i=1}^{2} \frac{h_{23}^{(i)}V_f^{(i)}dz^{(i)}}{\rho_0^{(i)}} \quad (A.4)$$

$$dH_{13} = -\sum_{i=1}^{2} \frac{h_{13}^{(i)}V_f^{(i)}dz^{(i)}}{\rho_0^{(i)}} \quad (A.5)$$

$$dH_{12} = -\sum_{i=1}^{2} \frac{2\mu_P^{(i)}h_{12}^{(i)}V_f^{(i)}dz^{(i)}}{P_0\rho_0^{(i)}} \quad (A.6)$$

with

$$D = A^2 - B^2, \quad F = A - B,$$

$$A = 2\sum_{i=1}^{2} \mu_p^{(i)} \left(1 + \frac{a^{(i)}}{1 + a^{(i)}} \right) V_f^{(i)} \quad (A.7)$$

$$B = 2\sum_{i=1}^{2} \mu_p^{(i)} \frac{a^{(i)}}{1 + a^{(i)}} V_f^{(i)}, \quad C = \sum_{i=1}^{2} \frac{a^{(i)}}{1 + a^{(i)}} V_f^{(i)},$$

$$Co = \sum_{i=1}^{2} \frac{V_f^{(i)}}{2\mu_p^{(i)}(1 + a^{(i)})} \quad (A.8)$$

$$P_o = 2\sum_{i=1}^{2} \mu_p^{(i)}V^{(i)} \quad P = 1/\sum_{i=1}^{2} V^{(i)}/2\mu^{p(i)} \quad (A.9a, b)$$

$$\chi^{(i)} = \frac{a^{(i)}}{1 + a^{(i)}}, \quad \phi^{(i)} = \frac{2\mu_P^{(i)}V_f^{(i)}dz^{(i)}}{D\rho_0^{(i)}} \quad (A.10a, b)$$

Downloaded 04 May 2010 to 171.66.16.27. Redistribution subject to ASME license or copyright; see http://www.asme.org/terms/Terms_Use.cfm

Contact Creep of Biphasic Cartilage Layers

R. Kelkar
Assoc. Mem. ASME

G. A. Ateshian
Mem. ASME

Department of Mechanical Engineering,
Columbia University,
New York, NY 10027-6699

Integral transform methods are used to solve the contact creep problem between two identical cylindrical biphasic cartilage layers bonded to rigid impermeable subchondral bone substrates. The biphasic model employed for cartilage consists of a binary mixture of an incompressible porous-permeable solid phase and an incompressible fluid phase. Solutions are obtained as a function of time, from the instantaneous to the equilibrium responses of the tissue. A significant result of this analysis is that under application of a step load, fluid pressurization may support upward of 96 percent of the total applied load for more congruent joints, shielding the solid collagen-proteoglycan matrix of the tissue from excessive stresses during physiological loading durations. The protection imparted by interstitial fluid pressurization to the solid collagen-proteoglycan matrix of cartilage is investigated, and the influence of material properties and osteoarthritic changes on the potential loss of this protective effect is discussed.

1 Introduction

Articular cartilage is the load-bearing material that covers the ends of the bones that comprise diarthrodial joints, and normally provides nearly frictionless contact over a lifetime of regular loading. The response of articular cartilage to load has been studied by several researchers investigating the longevity and load-bearing capacity of the tissue. Several of the hypotheses proposed to explain the eventual cartilage degeneration that does occur, especially in the large weight-bearing and load-bearing joints, center around the development of abnormal tissue stresses (Brown et al., 1984; Mow et al., 1992; Radin et al., 1984), which depend on both the material properties and geometries (i.e., thicknesses and congruence) of the contacting bodies (Johnson, 1985).

Recently, canine models for experimental osteoarthritis have confirmed that there is a significant change in the properties of degenerate cartilage compared to those of normal controls (Guilak et al., 1994; Setton et al., 1994). To obtain a better understanding of the normal function and load-support mechanism present in synovial joints, it is important to determine the influence of changes in the material properties, load magnitude, and geometry on the state of stress within articulating cartilage layers.

There have been several studies that have used elastic models for articular cartilage (Armstrong, 1986; Brown et al., 1984; Eberhardt, et al., 1990; Hayes et al., 1972; Hirsch, 1944; Kelly and O'Connor, 1996; Kempson et al., 1971; Sokoloff, 1966). However, elastic models cannot account for the role of interstitial fluid, which may constitute more than 80 percent of cartilage, and which has been shown to play an important role in the load support mechanism of this tissue (Ateshian et al., 1994; Ateshian and Wang, 1995; Macirowski et al., 1994). Furthermore, elastic constitutive relations cannot be employed to investigate the consequences of degenerative changes in such material parameters as tissue permeability, on the time-dependent cartilage stresses, deformation and flow fields. Poroelastic (Macirowski et al., 1994; van der Voet et al., 1993) and biphasic mixture formulations (Mow et al., 1980) have been successfully employed to model cartilage, with much analytical and experimental work having been done with the biphasic theory (e.g., Ateshian et al., 1992, 1994; Ateshian and Wang, 1995; Donzelli and Spilker, 1994; Hou et al., 1989; Kelkar and Ateshian, 1995; Mak et al., 1987; Mow et al., 1989). Contact problems using the biphasic theory include frictionless (Mak et al., 1987; Mow et al., 1989) and fully adhesive (Spilker et al., 1992; Suh and Spilker, 1994) indentation of a biphasic cartilage layer bonded to a rigid impermeable substrate using a flat cylindrical porous indenter; contact of cylindrical or spherical (Ateshian et al., 1992, 1994) biphasic layers bonded to rigid impermeable substrates using thin-layer approximations; rolling and sliding contact of cylindrical biphasic layers (Ateshian and Wang, 1995); and finite element analysis of three-body contact simulating the articular layers and menisci of the tibiofemoral joint (Donzelli, 1995; Donzelli and Spilker, 1995). Contact of poroelastic cartilage layers bonded to rigid impermeable substrates has also been analyzed by the finite element method (Macirowski et al., 1994; van der Voet et al., 1993).

The objective of this study is to obtain the frictionless contact creep response of two cylindrical biphasic cartilage layers bonded to rigid bony substrates, and to investigate the influence of material properties, joint congruence, and joint load on the tissue response. The solution procedure combines the approaches of Mak et al. (1987), Ateshian and Wang (1991), and Agbezuge and Deresiewicz (1974), and is valid for all times and arbitrary layer thicknesses.

2 Linear Biphasic Theory

The linear biphasic theory of Mow et al. (1980) is based on the theory of mixtures (Bowen, 1976; Kenyon, 1976), and models cartilage as being composed of a linearly elastic, intrinsically incompressible solid phase (consisting mainly of a collagen matrix, chondrocytes, and proteoglycan molecules) and an incompressible fluid phase (mainly interstitial water). The assumption of intrinsic incompressibility of the phases under physiologic pressures has been demonstrated experimentally (Bachrach et al., 1998; Guilak et al., 1988). Hence, volume changes in the tissue result from fluid exudation and imbibition from the solid matrix (Mow et al., 1992). The constitutive relations for the solid and fluid stresses are

$$\boldsymbol{\sigma}^s = -\varphi^s p\mathbf{I} + \boldsymbol{\sigma}^e, \tag{2.1}$$

$$\boldsymbol{\sigma}^f = -\varphi^f p\mathbf{I}, \tag{2.2}$$

Contributed by the Applied Mechanics Division of THE AMERICAN SOCIETY OF MECHANICAL ENGINEERS for publication in the ASME JOURNAL OF APPLIED MECHANICS.

Discussion on the paper should be addressed to the Technical Editor, Professor Lewis T. Wheeler, Department of Mechanical Engineering, University of Houston, Houston, TX 77204-4792, and will be accepted until four months after final publication of the paper itself in the ASME JOURNAL OF APPLIED MECHANICS.

Manuscript received by the ASME Applied Mechanics Division, Oct. 7, 1996; final revision, July 1, 1998. Associate Technical Editor: J. T. Jenkins.

 Copyright © 1999 by ASME

Downloaded 04 May 2010 to 171.66.16.27. Redistribution subject to ASME license or copyright; see http://www.asme.org/terms/Terms_Use.cfm

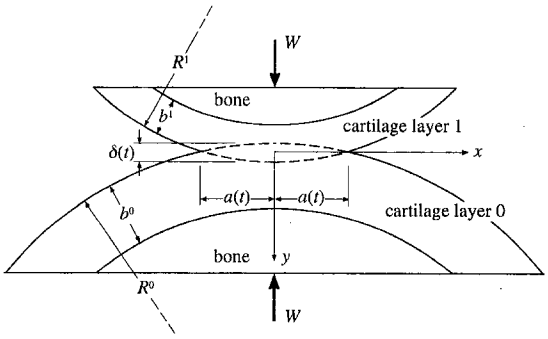

Fig. 1 Geometry of contact configuration. Two identical cylindrical biphasic layers, bonded to impermeable rigid subchondral bone substrates, are subjected to a step load intensity W. Each layer has a radius of curvature R^i and thickness b^i.

where $\boldsymbol{\sigma}^s$ and $\boldsymbol{\sigma}^f$ are the solid and fluid stresses, respectively, φ^s and φ^f are the solid and fluid volume fractions, respectively, p is the pressure, and $\mathbf{I}$ is the identity tensor; $\boldsymbol{\sigma}^e$ is the effective stress of the solid matrix, which for a linear isotropic material, is given by

$$\boldsymbol{\sigma}^e = \lambda_s \operatorname{tr}(\boldsymbol{\epsilon})\mathbf{I} + 2\mu_s\boldsymbol{\epsilon}, \tag{2.3}$$

where λ_s and μ_s are the Lamé constants, and $\boldsymbol{\epsilon}$ is the strain tensor of the solid phase. The continuity and quasi-static momentum equations for the solid and fluid phases are given by

$$\operatorname{div}(\varphi^s\mathbf{v}^s + \varphi^f\mathbf{v}^f) = \mathbf{0}, \tag{2.4}$$

$$\operatorname{div}\boldsymbol{\sigma}^s + K(\mathbf{v}^f - \mathbf{v}^s) = \mathbf{0}, \tag{2.5}$$

$$\operatorname{div}\boldsymbol{\sigma}^f - K(\mathbf{v}^f - \mathbf{v}^s) = \mathbf{0}, \tag{2.6}$$

where the diffusive drag constant, K, is related to the hydraulic permeability of the tissue, k, by $k = {\varphi^f}^2/K$ [34]. The solid velocity, $\mathbf{v}^s$, is the material derivative of the solid displacement, $\mathbf{u}$, with respect to the solid phase, $\mathbf{v}^s = D^s\mathbf{u}/Dt$, though for small velocities $\mathbf{v}^s \approx \partial\mathbf{u}/\partial t$. Note that under these conditions, the above equations are consistent (Ateshian et al., 1994; Mow and Lai, 1980) with Biot's poroelasticity theory (Biot, 1962). Adding Eqs. (2.5) and (2.6) together and substituting Eqs. (2.1)–(2.3) into the result produces

$$-\operatorname{grad} p + (\lambda_s + \mu_s)\operatorname{grad}(\operatorname{div}\mathbf{u}) + \mu_s\nabla^2\mathbf{u} = \mathbf{0}. \tag{2.7}$$

Substituting Eq. (2.2) into Eq. (2.6) results in

$$\mathbf{w} = -k\operatorname{grad} p, \tag{2.8}$$

where $\mathbf{w}$ is the relative fluid flux, $\mathbf{w} = \varphi^f(\mathbf{v}^f - \mathbf{v}^s)$. Taking the divergence of this equation and substituting it in Eq. (2.4) produces

$$\frac{\partial(\operatorname{div}\mathbf{u})}{\partial t} = k\nabla^2 p. \tag{2.9}$$

Hence, a complete determination of the pressure and displacement fields, p and $\mathbf{u}$, respectively, is sufficient to characterize the fluid velocity, $\mathbf{v}^f$.

2.1 Contact Problem. A plane-strain analysis is employed in this study (Fig. 1). For each layer i ($i = 0, 1$), the pressure, p^i, and displacement components, u_x^i, u_y^i, can be expressed in terms of potential functions Φ^i and Ψ^i, as described by McNamee and Gibson (1960):

$$u_x^i = \frac{\partial\Psi^i}{\partial x} + y\left(\frac{\partial\Phi^i}{\partial x}\right), \tag{2.10}$$

$$u_y^i = \frac{\partial\Psi^i}{\partial y} + y\left(\frac{\partial\Phi^i}{\partial y}\right) - \Phi^i, \tag{2.11}$$

$$p^i = 2\mu_s^i\left(\frac{\partial\Phi^i}{\partial y} + \eta_s^i\nabla^2\Psi^i\right), \tag{2.12}$$

where $\eta_s^i = (\lambda_s^i + 2\mu_s^i)/2\mu_s^i = (1 - \nu_s^i)/(1 - 2\nu_s^i)$, and ν_s^i is the drained Poisson ratio for the solid matrix. This potential function representation has been used successfully by several authors in the solution of biphasic or poroelastic contact problems (Agbezuge and Deresiewicz, 1974; Ateshian et al., 1994; Kelkar and Ateshian, 1995; Mak et al., 1987). These functions must satisfy the following set of equations (McNamee and Gibson, 1960):

$$\nabla^2\Phi^i = 0, \tag{2.13}$$

$$\nabla^4\Psi^i = \frac{1}{2\mu_s^i\eta_s^i k^i}\nabla^2\left(\frac{\partial\Psi^i}{\partial t}\right). \tag{2.14}$$

The boundary conditions at the interface between biphasic media have been derived by Hou et al. (1989) using mixture theory, and have been employed for solving biphasic contact problems (Ateshian et al., 1992, 1994; Ateshian and Wang, 1995; Donzelli and Spilker, 1994; Donzelli, 1995; Kelkar and Ateshian, 1995). At a contact interface Γ, with unit normal $\mathbf{n}$, the interface boundary conditions to be satisfied are given by

$$[[\mathbf{u}]]\cdot\mathbf{n} = 0, \tag{2.15}$$

$$[[p]] = 0, \tag{2.16}$$

$$[[\mathbf{w}]]\cdot\mathbf{n} = 0, \tag{2.17}$$

$$[[\boldsymbol{\sigma}^e]]\mathbf{n} = \mathbf{0}, \tag{2.18}$$

where $[[\cdot]]$ denotes the difference of the enclosed entity across Γ (e.g., $[[p]] = p^1 - p^0$, where p^1 and p^0 are the values of the pressure on either side of Γ). These conditions require that the normal displacement, effective traction, fluid pressure, and normal fluid flux be continuous across the interface.

In this study frictionless contact is assumed, hence the shear component of the effective traction is prescribed to be zero at the contact interface; the remaining interface traction components which are a priori unknown are the interfacial fluid pressure, $p_a(x, t)$ and effective normal traction $t_a(x, t)$. These tractions are applied over the a priori unknown, time-dependent contact width, $-a(t) \le x \le a(t)$; outside of this contact interface, all components of the surface tractions reduce to zero. At the cartilage-bone interfaces, the biphasic layers, of thickness b^i, are bonded to their respective rigid impermeable substrates. A step compressive normal load intensity, of magnitude W and units of load per unit length, is applied across the articular layers and maintained constant as the tissue creeps; this load must balance the resultant of the total traction at the contact interface, at all times. This is mathematically written as

$$W = \int_{-a(t)}^{a(t)} [p_a(x, t) - t_a(x, t)]dx. \tag{2.19}$$

2.2 Nondimensionalization. The variables are nondimensionalized as follows:

$$\hat{x} = \frac{x}{b}, \ \hat{y} = \frac{y}{b}, \ \hat{a} = \frac{a}{b}, \ \hat{\mathbf{u}}^i = \frac{\mathbf{u}^i}{b},$$

$$\hat{\boldsymbol{\sigma}}^{e^i} = \frac{\boldsymbol{\sigma}^{e^i}}{2\mu}, \ \hat{p}^i = \frac{p^i}{2\mu}, \tag{2.20}$$

$$\hat{\mathbf{w}}^i = \frac{b\mathbf{w}^i}{H_A k}, \ \hat{\Psi}^i = \frac{\Psi^i}{b^2}, \ \hat{\Phi}^i = \frac{\Phi^i}{b},$$

$$\hat{t} = \frac{H_A k t}{b^2}, \ \hat{W} = \frac{W}{2\mu b}, \tag{2.21}$$

Downloaded 04 May 2010 to 171.66.16.27. Redistribution subject to ASME license or copyright; see http://www.asme.org/terms/Terms_Use.cfm

where

$$b = \tfrac{1}{2}(b^0 + b^1),\ \mu = \tfrac{1}{2}(\mu_s^0 + \mu_s^1),\ k = \tfrac{1}{2}(k^0 + k^1),$$

$$H_A = \tfrac{1}{2}(2\eta_s^0\mu_s^0 + 2\eta_s^1\mu_s^1) = 2\eta\mu. \tag{2.22}$$

By substituting these nondimensional variables into Eqs. (2.1), (2.12), (2.13), and (2.14), the following equations are obtained:

$$\hat{u}_x^i = \frac{\partial\hat{\Psi}^i}{\partial\hat{x}} + \hat{y}\frac{\partial\hat{\Phi}^i}{\partial\hat{x}}, \tag{2.23}$$

$$\hat{u}_y^i = \frac{\partial\hat{\Psi}^i}{\partial\hat{y}} + \hat{y}\frac{\partial\hat{\Phi}^i}{\partial\hat{y}} - \hat{\Phi}^i, \tag{2.24}$$

$$\hat{p}^i = \hat{\mu}_s^i\left(\frac{\partial\hat{\Phi}^i}{\partial\hat{y}} + \hat{\eta}_s^i\nabla^2\hat{\Psi}^i\right), \tag{2.25}$$

$$\hat{w}_x^i = \frac{\hat{k}^i}{\eta}\frac{\partial\hat{p}^i}{\partial\hat{x}},\ \hat{w}_y^i = \frac{\hat{k}^i}{\eta}\frac{\partial\hat{p}^i}{\partial\hat{y}}, \tag{2.26}$$

$$\hat{\boldsymbol{\sigma}}^{e^i} = \hat{\mu}_s^i[(\eta^i - 1)\ \mathrm{tr}\ \boldsymbol{\epsilon}^i\mathbf{I} + \boldsymbol{\epsilon}^i], \tag{2.27}$$

and, in nondimensional form, Eqs. (2.13)–(2.14) reduce to

$$\nabla^2\hat{\Phi}^i = 0, \tag{2.28}$$

$$\nabla^4\hat{\Psi}^i = \frac{\hat{b}^{i^2}}{\hat{\mu}_s^i\eta_s^i\hat{k}^i}\nabla^2\left(\frac{\partial\hat{\Psi}^i}{\partial t}\right), \tag{2.29}$$

where $\hat{b}^i = b^i/b$, $\hat{\mu}_s^i = \mu_s^i/\mu$, and $\hat{k}^i = k^i/\eta k$. In nondimensional form, the boundary conditions are given by the following.

At $\hat{y} = 0$

$$\hat{u}_y^0 + \hat{u}_y^1 = \hat{\delta}(\hat{t}) - \frac{\hat{x}^2}{2\hat{R}},\quad \hat{w}_y^0 + \hat{w}_y^1 = 0,$$

$$-\hat{a}(\hat{t}) \le \hat{x} \le \hat{a}(\hat{t}), \tag{2.30}$$

$$\hat{p}^i = \hat{p}_a^i,\quad \hat{\sigma}_{yy}^{e^i} = \hat{\imath}_a,\quad \hat{\sigma}_{xy}^{e^i} = 0,\quad -\hat{a}(\hat{t}) \le \hat{x} \le \hat{a}(\hat{t}), \tag{2.31}$$

$$\hat{p}^i = \hat{\sigma}_{yy}^{e^i} = \hat{\sigma}_{xy}^{e^i} = 0,\quad \hat{x} < -\hat{a}(\hat{t}),\ \hat{x} > \hat{a}(\hat{t}), \tag{2.32}$$

where $\hat{\delta}(\hat{t})$ is the nondimensional normal approach ($\hat{\delta} = \delta/b$), or creep, of the contacting layers, and $\hat{R}$ is the nondimensional equivalent radius of curvature of the surfaces ($\hat{R} = R/b$ where $R = R^0R^1/(R^0 + R^1)$; note that the cylindrical profiles have been approximated by a quadratic relation.

At $\hat{y} = \hat{b}^i$

$$\hat{u}_x^i = \hat{u}_y^i = \hat{w}_y^i = 0 \quad -\infty < \hat{x} < \infty. \tag{2.33}$$

Furthermore, the relation between the nondimensional normal load intensity $\hat{W}$ and total traction at the contact interface is given by

$$\hat{W} = \int_{-\hat{a}(\hat{t})}^{\hat{a}(\hat{t})}[\hat{p}_a(\hat{x}, \hat{t}) - \hat{\imath}_a(\hat{x}, \hat{t})]d\hat{x}. \tag{2.34}$$

The contact semiwidth $\hat{a}(\hat{t})$ is obtained by satisfying the condition that the total traction reduces to zero at the contact edge:

$$\hat{p}_a(\hat{a}, \hat{t}) - \hat{\imath}_a(\hat{a}, \hat{t}) = 0. \tag{2.35}$$

Finally, it is noted that the solution of this problem is governed by seven nondimensional parameters, namely $\hat{b}^0$ (or $\hat{b}^1 = 2 - \hat{b}^0$), $\hat{k}^0$ (or $\hat{k}^1 = 2/\eta - \hat{k}^0$), $\hat{\mu}_s^0$ (or $\hat{\mu}_s^1 = 2 - \hat{\mu}_s^0$), ν_s^0, ν_s^1, $\hat{W}$, and $\hat{R}$, as can be observed from Eqs. (2.29), (2.30), (2.33), and (2.34). When the two contacting layers are identical, the number of governing nondimensional parameters reduces to three ($\hat{W}$, $\hat{R}$, $\nu_s = \nu_s^0 = \nu_s^1$).

2.3 Solution Method. The nondimensional variables are substituted into Eqs. (2.10)–(2.14), and double Fourier-Laplace transforms are applied to yield the following ordinary differential equations:

$$\left(\frac{d^2}{d\hat{y}^2} - \omega^2\right)\left(\frac{d^2}{d\hat{y}^2} - \omega^2 - \frac{s\hat{b}^{i^2}}{\hat{\mu}_s^i\eta_s^i\hat{k}^i}\right)\bar{\Psi}^i = 0, \tag{2.36}$$

$$\left(\frac{d^2}{d\hat{y}^2} - \omega^2\right)\bar{\Phi}^i = 0, \tag{2.37}$$

where $\bar{\Psi}^i(\omega, \hat{y}, s)$ and $\bar{\Phi}^i(\omega, \hat{y}, s)$ are the double-transformed potential functions, and where the double transform $\bar{\mathscr{X}}(\omega, \hat{y}, s)$ of any variable $\hat{\mathscr{X}}(\hat{x}, \hat{y}, \hat{t})$ is defined as

$$\bar{\mathscr{X}}(\omega, \hat{y}, s) \equiv \int_0^\infty e^{-s\hat{t}}\int_{-\infty}^{\infty}\hat{\mathscr{X}}(\hat{x}, \hat{y}, \hat{t})e^{j\omega\hat{x}}d\hat{x}d\hat{t}, \tag{2.38}$$

where s is the Laplace transform variable, and ω is the Fourier transform variable. These ordinary differential equations yield solutions of the form

$$\bar{\Psi}^i = B_1^i e^{\omega\hat{y}} + B_2^i e^{-\omega\hat{y}} + B_3^i e^{\zeta\hat{y}} + B_4^i e^{-\zeta\hat{y}}, \tag{2.39}$$

$$\bar{\Phi}^i = B_5^i e^{\omega\hat{y}} + B_6^i e^{-\omega\hat{y}}, \tag{2.40}$$

where $\zeta^2 = \omega^2 + s\hat{b}^{i^2}/(\hat{\mu}_s^i\eta_s^i\hat{k}^i)$, and $B_1^i(\omega, s) - B_6^i(\omega, s)$ are integration functions to be determined from double transforms of the boundary conditions of Eqs. (2.31) and (2.33) (Kelkar, 1996). This system can be solved symbolically (using a symbolic manipulator such as Macsyma) and the solution substituted into Eqs. (2.39)–(2.40) to yield expressions for $\bar{\Psi}^i$ and $\bar{\Phi}^i$. These expressions in turn may be substituted into the nondimensionalized double transforms of Eqs. (2.10)–(2.12) to provide general solutions for $\bar{u}_y(\omega, \hat{y}, s)$ and $\bar{w}_y(\omega, \hat{y}, s)$:

$$\bar{u}_y^i(\omega, \hat{y}, s) = \bar{M}_p^i(\omega, \hat{y}, s)\bar{p}_a(\omega, s) + \bar{M}_t^i(\omega, \hat{y}, s)\bar{\imath}_a(\omega, s), \tag{2.41}$$

$$\bar{w}_y^i(\omega, \hat{y}, s) = \bar{N}_p^i(\omega, \hat{y}, s)\bar{p}_a(\omega, s) + \bar{N}_t^i(\omega, \hat{y}, s)\bar{\imath}_a(\omega, s), \tag{2.42}$$

where the coefficient functions of the unknown $\bar{p}_a(\omega, s)$ and $\bar{\imath}_a(\omega, s)$, are explicitly known. To satisfy Eq. (2.30), the inverse Fourier-Laplace transforms of Eqs. (2.41)–(2.42) are required at $\hat{y} = 0$; this process is achieved in two steps, starting first by obtaining inverse Laplace transforms of these equations using the convolution theorem:

$$\tilde{u}_y^0(\omega, 0, \hat{t}) + \tilde{u}_y^1(\omega, 0, \hat{t}) = \int_0^{\hat{t}}\tilde{M}_p(\omega, 0, \tau)\tilde{p}_a(\omega, \hat{t} - \tau)d\tau + \int_0^{\hat{t}}\tilde{M}_t(\omega, 0, \tau)\tilde{\imath}_a(\omega, \hat{t} - \tau)d\tau, \tag{2.43}$$

$$\tilde{w}_y^0(\omega, 0, \hat{t}) + \tilde{w}_y^1(\omega, 0, \hat{t}) = \int_0^{\hat{t}}\tilde{N}_p(\omega, 0, \tau)\tilde{p}_a(\omega, \hat{t} - \tau)d\tau + \int_0^{\hat{t}}\tilde{N}_t(\omega, 0, \tau)\tilde{\imath}_a(\omega, \hat{t} - \tau)d\tau, \tag{2.44}$$

where a tilde ($\tilde{\ }$) denotes a Fourier transform alone, and $\tilde{M}_p = \tilde{M}_p^0 + \tilde{M}_p^1$, $\tilde{M}_t = \tilde{M}_t^0 + \tilde{M}_t^1$, $\tilde{N}_p = \tilde{N}_p^0 + \tilde{N}_p^1$, and $\tilde{N}_t = \tilde{N}_t^0 + \tilde{N}_t^1$. Prior to proceeding with the second step, which consists of obtaining the inverse Fourier transforms of Eqs. (2.43)–(2.44), the simplification procedure of Agbezuge and Deresiewicz (1974) is applied. These authors, who analyzed the contact of poroelastic half-spaces, demonstrated that in their problem, the functions $\tilde{p}_a$ and $\tilde{\imath}_a$ were relatively slow-varying temporally compared to the kernel functions $\tilde{M}_p$, $\tilde{M}_t$, $\tilde{N}_p$, and $\tilde{N}_t$; hence, $\tilde{p}_a$ and $\tilde{\imath}_a$ could be taken out of their respective integrals. The same approach is used in this study, and verification of this assump-

Downloaded 04 May 2010 to 171.66.16.27. Redistribution subject to ASME license or copyright; see http://www.asme.org/terms/Terms_Use.cfm

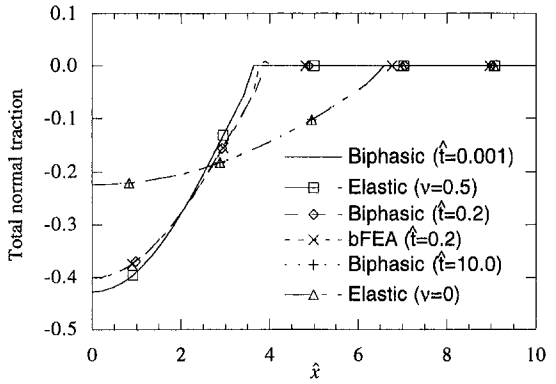

Fig. 2 Total normal contact traction, $-\hat{p}_a(\hat{x}, \hat{t}) + \hat{t}_a(\hat{x}, \hat{t})$, at three increments of time ($\hat{t}$ = 0.001, 0.2, 10.0), demonstrating the excellent agreement between (*a*) the early-time response ($\hat{t}$ = 0.001) and the incompressible elastic layer contact solution (ν = 0.5); (*b*) an intermediate time response and the biphasic finite element analysis (bFEA) of Donzelli (1995) at $\hat{t}$ = 0.2; and (*c*) the near-equilibrium response ($\hat{t}$ = 10.0) and the compressible elastic layer contact solution (ν = 0). ($\hat{R}$ = 100, $\hat{W}$ = 2, ν_s = 0.)

tion is provided with a comparison to finite element results (Donzelli, 1995).

Using the above simplification procedure, and satisfying the remaining boundary conditions in Eq. (2.32), yields the following quad integral system:

For $\hat{x} < \hat{a}(\hat{t})$ and $\hat{x} > \hat{a}(\hat{t})$,

$$\frac{1}{2\pi}\int_{-\infty}^{\infty} \tilde{p}_a(\omega, \hat{t}) e^{-j\omega\hat{x}} d\omega = 0, \tag{2.45}$$

$$\frac{1}{2\pi}\int_{-\infty}^{\infty} \tilde{t}_a(\omega, \hat{t}) e^{-j\omega\hat{x}} d\omega = 0. \tag{2.46}$$

For $-\hat{a}(\hat{t}) \le \hat{x} \le \hat{a}(\hat{t})$,

$$\frac{1}{2\pi}\int_{-\infty}^{\infty} \left\{ \left[\int_0^{\hat{t}} \tilde{M}_p(\omega, 0, \tau) d\tau \right] \tilde{p}_a(\omega, \hat{t}) + \left[\int_0^{\hat{t}} \tilde{M}_t(\omega, 0, \tau) d\tau \right] \tilde{t}_a(\omega, \hat{t}) \right\} e^{-j\omega\hat{x}} d\omega = \hat{\delta}(\hat{t}) - \hat{x}^2/2\hat{R}, \tag{2.47}$$

$$\frac{1}{2\pi}\int_{-\infty}^{\infty} \left\{ \left[\int_0^{\hat{t}} \tilde{N}_p(\omega, 0, \tau) d\tau \right] \tilde{p}_a(\omega, \hat{t}) + \left[\int_0^{\hat{t}} \tilde{N}_t(\omega, 0, \tau) d\tau \right] \tilde{t}_a(\omega, \hat{t}) \right\} e^{-j\omega\hat{x}} d\omega = 0. \tag{2.48}$$

The integrals of the functions $\tilde{M}_p$, $\tilde{M}_t$, $\tilde{N}_p$, and $\tilde{N}_t$ with respect to time can be evaluated from the numerical inverse Laplace transforms of $\bar{M}_p/s$, $\bar{N}_p/s$, $\bar{M}_t/s$, and $\bar{N}_t/s$, at any desired time step (e.g., using FORTRAN subroutine DINLAP, IMSL, Inc). Note that the simplification procedure introduced above makes it possible to solve the above system for the functions $\tilde{p}_a(\omega, \hat{t})$, $\tilde{t}_a(\omega, \hat{t})$, independently at each time step. These functions are obtained by discretizing the integrals into summations over discrete and uniformly distributed ω and $\hat{x}$ values, using an iterative guess for $\hat{a}(\hat{t})$; the normal approach $\hat{\delta}(\hat{t})$ is solved as part of the unknowns, using the Fourier transform of Eq. (2.34) as an additional equation. At each time step, inverse Fourier transforms of the discretized values of $\tilde{p}_a(\omega, \hat{t})$ and $\tilde{t}_a(\omega, \hat{t})$ are obtained using a Fast Fourier Transform scheme, and the iterative guess on $\hat{a}(\hat{t})$ is refined until it satisfies the constraint of Eq. (2.35). The details of these numerical procedure are analogous to those described in Ateshian and Wang (1995).

The solution of the system of quad integral equations is obtained for nondimensional step loads $\hat{W}$ of varying magnitudes, and for configurations of varying congruence (achieved by changing the nondimensional equivalent radius of curvature, $\hat{R}$). The effect of these parameters on the contact creep response is analyzed by varying each of them, and observing the resulting stresses, strains, displacements, fluid fluxes, and load partition.

2.4 Specification of Model Parameters. In this study, results are presented for layers with identical material properties and geometric parameters, and thus only results for a single layer will be shown. Poisson's ratio, ν_s, is assumed equal to 0 based on experimental findings for typical human cartilage (Athanasiou et al., 1991), and the results for the dependence of the creep response on the remaining nondimensional parameters ($\hat{W}$ and $\hat{R}$) will be presented. Since the solutions in each layer are identical, the superscripts i have been dropped from the names of the parameters and variables. The following typical dimensional material properties for the layers were chosen: H_A = 0.5 MPa, μ_s = 0.25 MPa, $k = 4.0 \times 10^{-15}$ m^4/N.s. A typical cartilage thickness, b, of 2.0 mm was chosen. These properties were based on those determined in experimental studies of normal human cartilage (Athanasiou et al., 1991). Using these material properties, the nondimensional time $\hat{t}$ is 10^{-3} times the dimensional time t in seconds.

3 Results

The normal component of the total contact interface traction ($-\hat{p}_a(\hat{x}, \hat{t}) + \hat{t}_a(\hat{x}, \hat{t})$) is presented in Fig. 2, for $\hat{W}$ = 2, and $\hat{R}$ = 100, at three time steps ($\hat{t}$ = 0.001, 0.2, and 10). These three time steps are representative of the instantaneous, intermediate, and equilibrium responses of the cartilage layers. To assess the validity of the approximation made in evaluating the inverse Laplace transform in Eqs. (2.43)–(2.44), the current solution is compared to the recent biphasic finite element solution of Donzelli and Spilker (1995) (Fig. 2). The nonlinear correlation coefficient between the two solutions is r^2 = 1.000, indicating agreement with the finite element solution at this arbitrarily selected intermediate time, and confirming that the approximation of Agbezuge and Deresiewicz (1974) provides an accurate and efficient inversion method. The normal traction for the instantaneous response of the biphasic layers agrees with that of the contact of two incompressible elastic layers (having ν = 0.5) with r^2 = 0.997 as confirmed by the results of Fig. 2; the equivalence of the instantaneous response of a biphasic material with that of an incompressible elastic material has been established previously (e.g., Ateshian et al., 1994; Ateshian and Wang, 1995; Mak et al., 1987; Mow et al., 1989). Similarly,

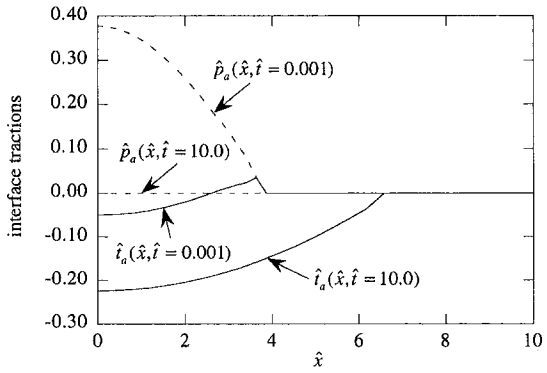

Fig. 3 Interfacial fluid pressure, $\hat{p}_a(\hat{x}, \hat{t})$, and normal effective traction, $\hat{t}_a(\hat{x}, \hat{t})$, at $\hat{t}$ = 0.001 and $\hat{t}$ = 10.0. Note that $\hat{p}_a$ is essentially zero near equilibrium. ($\hat{R}$ = 100, $\hat{W}$ = 2, ν_s = 0.)

Downloaded 04 May 2010 to 171.66.16.27. Redistribution subject to ASME license or copyright; see http://www.asme.org/terms/Terms_Use.cfm

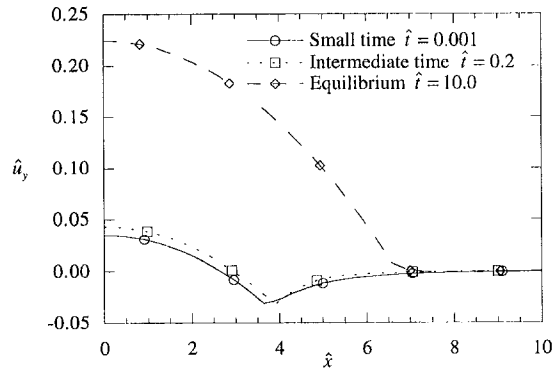

Fig. 4 Axial displacement, $\hat{u}_y$, at three time increments. ($\hat{R} = 100$, $\hat{W} = 2$, $\nu_s = 0$.)

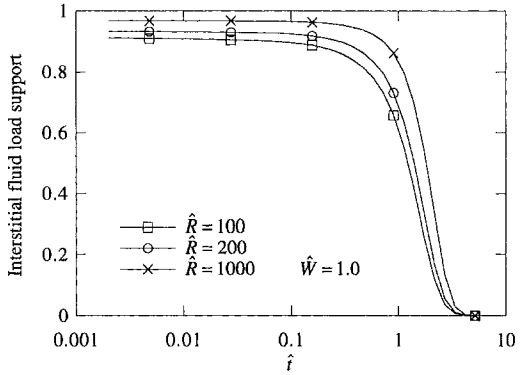

Fig. 6 Fraction of load supported by fluid pressurization, as a function of time and congruence, $\hat{R}$. ($\hat{W} = 1$, $\nu_s = 0$.)

the equilibrium response for the biphasic layers is seen to be the same as that of two contacting compressible elastic layers (having $\nu = 0$) with $r^2 = 1.000$ (Ateshian et al., 1994; Ateshian and Wang, 1995; Mak et al., 1987; Mow et al., 1989). The agreement of the current solution with these elastic solutions also serves to confirm the validity of the approximation and numerical schemes employed here. Note also from Fig. 2 that the contact semiwidth increases appreciably with time, while the peak value of the total traction decreases.

The components $\hat{p}_a(\hat{x}, \hat{t})$ and $\hat{t}_a(\hat{x}, \hat{t})$ of the total traction are shown separately in Fig. 3, for two representative time steps ($\hat{t} = 0.001, \hat{t} = 10.0$). These results demonstrate that the interstitial fluid pressure $\hat{p}_a$ supports the majority of the applied load immediately after load application. The fluid pressurization then decreases with increasing time, eventually dropping to zero at equilibrium. Correspondingly, because the applied load intensity remains constant, the effective solid traction $\hat{t}_a$ can be seen to increase with increasing time.

The surface displacement in the $\hat{y}$ direction, $\hat{u}_y$, at $\hat{t} = 0.001$, 0.2, and 10.0, is illustrated in Fig. 4. As the interstitial fluid pressure subsides, the tissue consolidates and the equilibrium surface deformation increases substantially from the instantaneous response, as evident from this figure. Another measure of this consolidation is given by the creep displacement, or normal approach $\hat{\delta}(\hat{t})$, as shown in Fig. 5 for two different congruences, $\hat{R} = 100$ and 1000, with $\hat{W} = 1$. These results confirm that increasing congruence decreases the total creep deformation, as the load is being supported over a larger contact width. The congruence regulates the onset of equilibrium, as can be assessed by the "time constant" for reaching equilibrium (i.e., that value of $\hat{t}$ at which the response has reached 63.2 percent of its equilibrium value); for $\hat{R} = 100$ it is $\hat{t} = 1.41$, and for $\hat{R} = 1000$ it is $\hat{t} = 1.92$. hence, creep equilibrium occurs later for more congruent joints.

As with the creep, the semicontact width $\hat{a}(\hat{t})$ also varies with time, eventually reaching an equilibrium value. The time dependence of the semicontact width on congruence is demonstrated in Fig. 5, confirming that the onset of equilibrium is delayed with increasing congruence (time constants of 1.30 and 1.72 for $\hat{R} = 100$ and $\hat{R} = 1000$, respectively). Immediately after load application, the normal approach and contact semiwidth do not change appreciably (Fig. 5) for a physiologically long period (up to dimensional times of a few hundred seconds for healthy cartilage). After this period, the fluid pressurization begins to drop appreciably, and there is a corresponding increase in the creep and contact semiwidth.

It has already been demonstrated from Fig. 3 that the fluid pressure decreases and the effective traction increases with increasing time. The fraction of the applied load intensity $\hat{W}$ which is supported by the integrated resultant of the interfacial fluid pressure ($\int_{-\hat{a}(\hat{t})}^{\hat{a}(\hat{t})} \hat{p}_a(\hat{x}, \hat{t})\, d\hat{x}$) is shown in Fig. 6 as a function of time, for several values of $\hat{R}$, and $\hat{W} = 1$. These results indicate that greater joint congruence promotes greater interstitial fluid load support (up to 96 percent for the early time response when $\hat{R} = 1000$). In addition, fluid pressurization is maintained longer with increased congruence (time constants of 1.56, 1.73, and 2.12 for $\hat{R} = 100$, 200, and 1000, respectively). Similar results are observed for increased applied loads (Fig. 7, time constants of 1.95, 2.12, and 2.29 for $\hat{W} = 0.5$, 1.0, and 2.0 respectively). Of particular interest is the fact that the fraction of fluid load support becomes greater as the applied load increases (Fig. 7).

The stresses and strains also vary with time throughout the thickness of the contacting layers. Though not shown in the

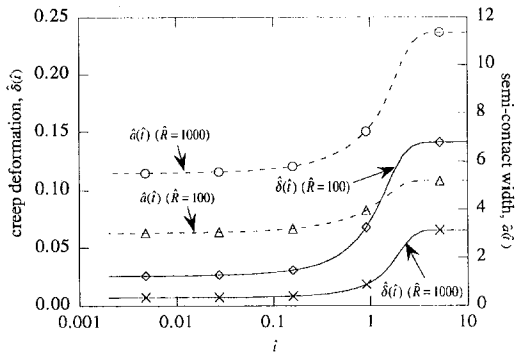

Fig. 5 Creep deformation (normal approach), $\hat{\delta}(\hat{t})$, and semi-contact width, $\hat{a}(\hat{t})$, as a function of time, for various congruences, $\hat{R}$. ($\hat{W} = 1$, $\nu_s = 0$.)

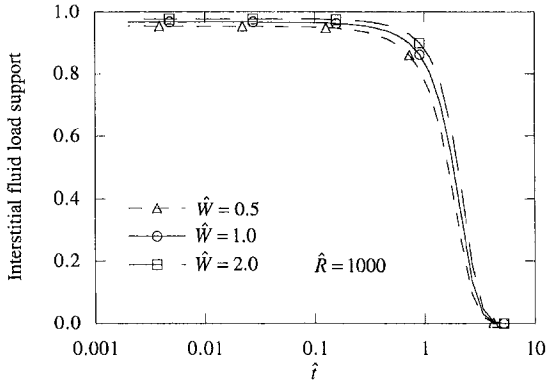

Fig. 7 Fraction of load supported by fluid pressurization, as a function of time and nondimensional load, $\hat{W}$. ($\hat{R} = 1000$, $\nu_s = 0$.)

Downloaded 04 May 2010 to 171.66.16.27. Redistribution subject to ASME license or copyright; see http://www.asme.org/terms/Terms_Use.cfm

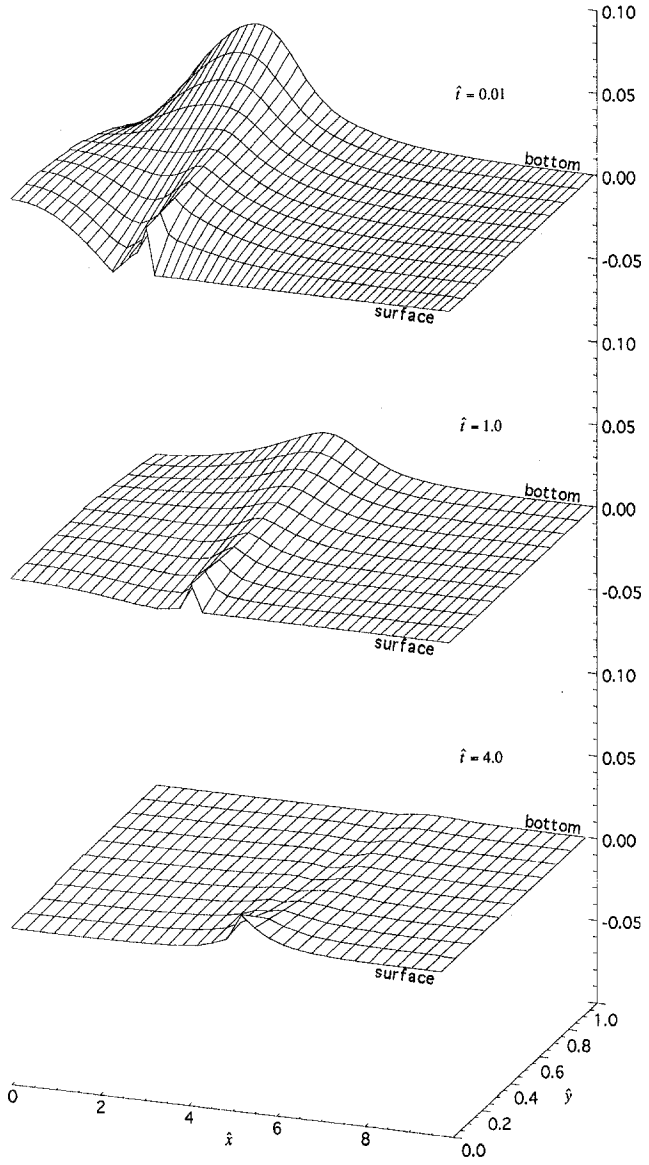

Fig. 8 Maximum principal effective stresses inside the cartilage layer, at three time steps ($\hat{t}$ = 0.01, 1.0, 4.0). The layers are in contact at the surface ($\hat{y}$ = 0), and are bonded to the rigid impermeable subchondral bone substrate at the bottom ($\hat{y}$ = 1). All units are nondimensional. ($\hat{R}$ = 100, $\hat{W}$ = 1, ν_s = 0.)

figures, the interstitial fluid pressure is found to be nearly uniform through the depth of the tissue, for the congruences analyzed in this study. Principal normal stresses and maximum shear stresses of the effective stress tensor, $\hat{\boldsymbol{\sigma}}^e$, are plotted for three time steps, $\hat{t}$ = 0.01, 1.0, 4.0, in Figs. 8–10, for $\hat{R}$ = 100 and $\hat{W}$ = 1. it is observed from these figures that in the early time response ($\hat{t}$ = 0.01), the peak magnitudes of the (nondimensional) principal maximum, principal minimum, and maximum shear stresses are all similar (approximately 0.066) and occur at the cartilage-bone interface (Figs. 8–10). From Fig. 8, it is apparent that the maximum principal normal stress is always tensile and decreases in magnitude with increasing time to become nearly uniformly zero at equilibrium, save for a localized value of 0.018 near the surface, at the edge of the contact interface. In contrast, the minimum principal normal stress (Fig. 9), which is always compressive, increases in magnitude with increasing time, becoming uniform with depth at equilibrium. Eventually, the peak magnitude of the minimum principal stress (0.141) becomes twice that of the instantaneous response. The maximum shear stress (Fig. 10) also becomes more uniform with depth as time progresses, though its peak magnitude of 0.070 at equilibrium is only six percent greater than the instantaneous response. In summary, as time progresses from the instantaneous to the equilibrium responses, the compressive component of the stress essentially doubles in magnitude, the shear stress increases by six percent, and the tensile stress decreases by a factor of 3.7.

4 Discussion

The ability of normal articular cartilage to withstand a lifetime of regular use is of interest to researchers investigating its remarkable wear properties. Furthermore, understanding the effect of normal variations in layer properties, and changes due to disease, is central to determining the relative importance of these factors on the tissue response. In this study, a solution for the potential function formulation of the time-dependent contact creep response of identical cartilage layers is presented. The most salient result of this analysis is the significant fluid pressurization which occurs immediately after load application, which supports up to 96 percent of the applied load intensity in more

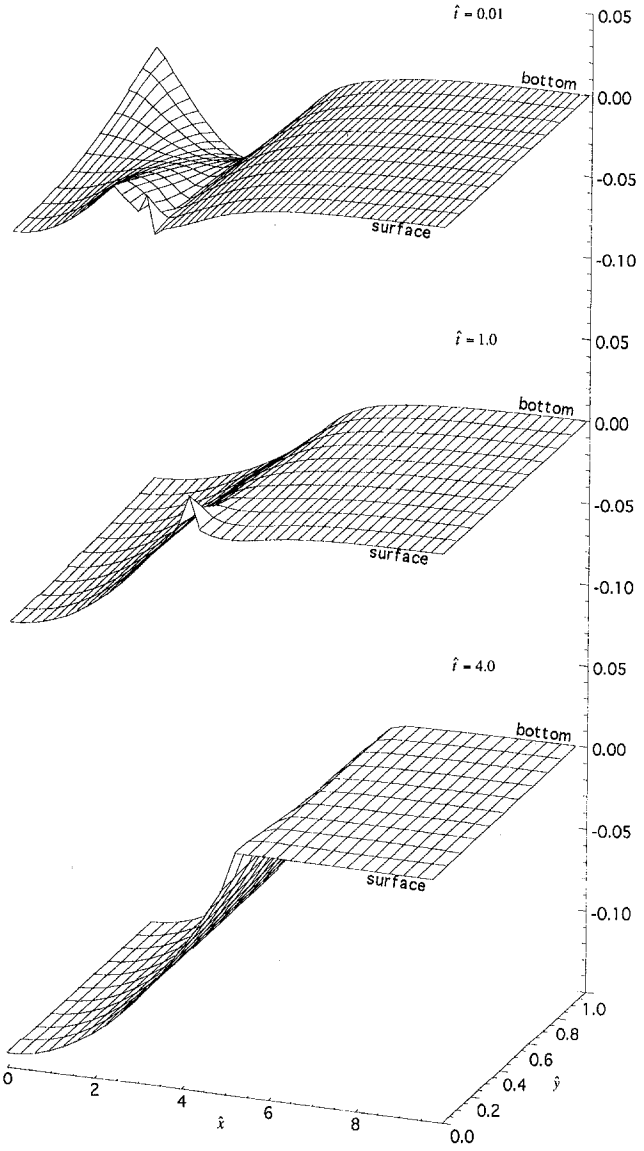

Fig. 9 Minimum principal effective stresses inside the cartilage layer, at three time steps ($\hat{t}$ = 0.01, 1.0, 4.0). ($\hat{R}$ = 100, $\hat{W}$ = 1, ν_s = 0.)

Downloaded 04 May 2010 to 171.66.16.27. Redistribution subject to ASME license or copyright; see http://www.asme.org/terms/Terms_Use.cfm

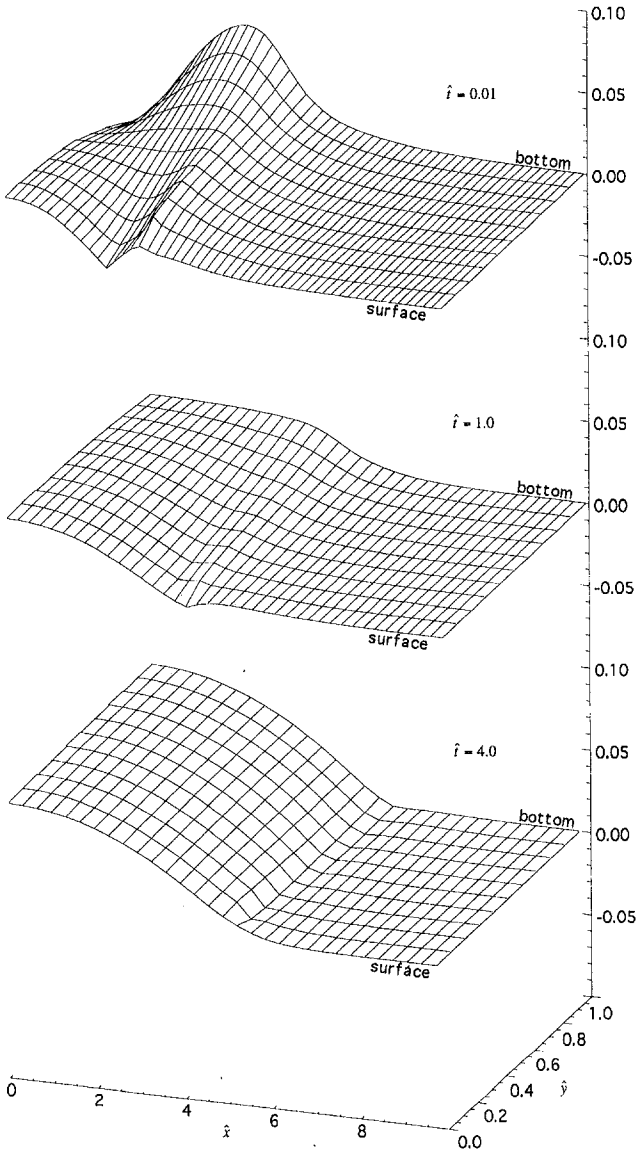

Fig. 10 Maximum effective shear stresses inside the cartilage layer, at three time steps ($\hat{t}$ = 0.01, 1.0, 4.0). ($\hat{R}$ = 100, $\hat{W}$ = 1, ν_s = 0.)

congruent joints (Fig. 6). While the importance of cartilage interstitial fluid pressurization has been observed for various configurations of joint contact in previous studies (e.g., Ateshian et al., 1992, 1994; Ateshian and Wang, 1995; Macirowski et al., 1984; van der Voet et al., 1993), the present analysis demonstrates the dependence of this pressurization on the joint congruence, the applied load, and the elapsed time following load application.

Since the constitutents of cartilage are intrinsically incompressible (Guilak et al., 1988; Bachrach et al., 1998) the hydrostatic component contributed by the interstitial fluid pressure is not likely to damage the solid matrix, and thus provides a shielding effect. Importantly, the fraction of the total applied load supported by fluid pressurization increases with increased joint congruence, and with increased applied load (Figs. 6 and 7). The high congruence of articulating surfaces in most diarthrodial joints (e.g., the hip and shoulder) possibly reflects an adaptive response by which these joints are better suited to support the high loads under which they are subjected, while maintaining their functional needs.

It is important to note that while the solution presented in this study is governed explicitly by three nondimensional parameters ($\hat{R}$, $\hat{W}$, ν_s), it is also indirectly dependent on the gel diffusion time (Holmes, 1986), $\tau_d = b^2/H_A k$, which is used to nondimensionalize the independent time variable (Eq. (2.21), $\hat{t} = t/\tau_d$). Indeed, when a dimensional solution is sought from the time-dependent responses reported in Figs. 2–10, the interpretation of these results take significantly different meanings depending on the actual value of τ_d. As presented above, for example, healthy cartilage has a gel diffusion time constant of approximately 1,000 seconds, which is considerably greater than the typical duration of most physiological activities of daily living. In arthritic cartilage, however, the permeability, k, of the tissue may increase substantially from its normative value, and typically at a rate which exceeds the concomitant decrease in the aggregate modulus, H_A (Guilak et al., 1994; Setton et al., 1994); furthermore, with advanced tissue degradation, the thickness of cartilage can also decrease substantially. Thus, a reduction of τ_d down to 500, 100, or worse to 10 seconds, signifies that the protective role imparted by interstitial fluid pressurization lasts for shorter durations than for normal cartilage; despite the ability of the tissue to recover (re-hydrate) when unloaded, a single day's range of normal activities would result in greater consolidation in that joint whose gel constant is smaller. The cumulative effect of this reduced protection over the million or so cycles of loading which diarthrodial joints typically undergo each year may contribute significantly to the mechanical pathway of osteoarthritis progression. The results of Fig. 9 suggest that the compressive stresses could potentially double in magnitude if considerable consolidation occurs. Mechanically, to the extent that traditional engineering concepts of fatigue failure apply to the solid collagen-proteoglycan matrix of articular cartilage, and with the understanding that cartilage has a limited ability to repair itself, this increased stress on the tissue may indeed contribute to the greater rate of tissue degradation typically observed in osteoarthritis. Biochemically, experiments on live cartilage explants have demonstrated that quasi-static compressive strains produce tissue responses that can be interpreted as degradative changes or attempts for repair (e.g., Gray et al., 1988; Guilak, Meyer, Ratcliffe, and Mow, 1994; Jones et al., 1982; Palmoski and Brandt, 1984) suggesting that such prolonged and possibly excessive stresses may have highly detrimental effects on the tissue. If the rate of tissue degradation exceeds the rate at which it can repair, the mechanical and biochemical pathways would together contribute to further disruption of the collagen-proteoglycan matrix.

The results of this study indicate that joint congruence promotes interstitial fluid pressurization and shielding of the solid matrix (Figs. 5–6). The clinical implications of this observation are notable with regard to surgical interventions where changes in congruence may be an unintended outcome of the procedure, e.g., meniscectomies, mismatched meniscal allografts, or mismatched hemiarthroplasties. Since higher loads lead to more intimate contact, it is interesting to note that they also promote greater shielding of the solid matrix (Fig. 7). Interstitial fluid pressurization has also been proposed to play an important role in reducing the friction coefficient of articular cartilage (Ateshian, 1995, 1997; Malcom, 1976; McCutchen, 1962). In recent theoretical predictions, it has been shown that interstitial fluid pressurization can explain the remarkable reduction of the friction coefficient during the early loading response of the tissue (Ateshian, 1995, 1997); hence, the protective effect of interstitial fluid pressurization may also extend to the wear properties of cartilage.

The sites of maximum tissue stresses observed during the early response of the tissue (Figs. 8–10), are nearly identical with the results of an asymptotic analysis of biphasic contact reported in earlier studies (Ateshian et al., 1992, 1994). As noted previously, these theoretical results are in good agreement with experimental reports of blunt trauma which have demonstrated that the cartilage layer may separate from the bony sub-

Downloaded 04 May 2010 to 171.66.16.27. Redistribution subject to ASME license or copyright; see http://www.asme.org/terms/Terms_Use.cfm

strate (Armstrong et al., 1985; Meachim and Bentley, 1978; Radin et al., 1984).

Finally, it must be recalled that simplifying assumptions have been made in relation to the modeling of this problem. First, the tissue has been assumed to behave isotropically and has been modeled as homogeneous, while cartilage is known to exhibit anisotropy and inhomogeneity. A complete characterization of its complex properties is not readily available and may vary considerably from site to site and joint to joint, even within the same species. Thus, the use of an isotropic homogeneous model is intended as a first approximation toward the understanding of the mechanical regulatory mechanisms which are involved in cartilage osteoarthritis. Second, the use of cylindrical cartilage layers of uniform thickness is clearly a simplification of the true geometry of diarthrodial joints; once again, these simplifications must be viewed in the context of the investigation of general criteria which affect the tissue response (load, congruence, material properties), rather than the response of a particular joint. Third, the relatively low values of $\hat{W}$ chosen in this analysis were selected to ensure that the equilibrium tissue strains, which are greater than in the instantaneous response, remained within the bounds of the infinitesimal deformation linear biphasic theory. For most physiologic loading periods ($\hat{t} \leq 0.01$), the choice of loads applied in this analysis can be considerably higher without approaching finite deformation. It should be emphasized that the geometric parameter of importance in this analysis is the relative curvature $\hat{R}$ and not the individual curvatures of the articular surfaces. Though the schematic of Fig. 1 shows two convex surfaces, the present analysis is equally valid for concave surfaces, or for the most commonly encountered convex-concave mating articular surfaces of most diarthrodial joints; this is true as long as the contact width is much smaller than the relative radius of curvature ($\hat{a}/\hat{R} \ll 1$), as can be verified for this study from Fig. 5.

5 Conclusion

A potential function solution of the plane-strain contact problem between two identical biphasic cartilage layers has been presented. A useful approximation, based on the work by Agbezuge and Deresiewicz (1974) was made to perform the inverse Laplace transform integration, and the validity of this approximation has been demonstrated by the excellent agreement of the current solution with the corresponding biphasic finite element analysis solution. Further validation has been provided by the excellent agreement of the current solution instantaneously and at equilibrium with the incompressible and compressible elastic solutions respectively. A significant result of this analysis is that under application of a step load, fluid pressurization may support upward of 96 percent of the total applied load for more congruent joints, shielding the solid collagen-proteoglycan matrix of the tissue from excessive stresses during physiological loading durations. This analysis also demonstrates that the contribution of fluid pressurization to the total load support increases with greater congruence of the contacting surfaces, and with increased load across the contact interface. The duration of the protective effect thus imparted by interstitial fluid is directly dependent on the tissue properties, whose degradation can lead to a progressive and irreversible chain of mechanical and biochemical events toward osteoarthritis. This study provides an improved understanding of normal and abnormal joint contact mechanics, by determining the features of the joint that affect the creep response of articular cartilage.

Acknowledgments

This study was supported in part by the National Institutes of Health, R29 AR43628 and R01 AR42850.

References

Agbezuge, L. K., and Deresiewicz, H., 1974, "On the Indentation of a Consolidating Half-Space," *Isr. J. Tech.,* Vol. 12, pp. 322–338.

Armstrong, C. G., 1986, "An Analysis of the Stresses in a Thin Layer of Articular Cartilage in a Synovial Joint," *Eng. Med.,* Vol. 15, pp. 55–61.

Armstrong, C. G., Mow, V. C., and Wirth, C. R., 1985, "Biomechanics of Impact-Induced Microdamage to Articular Cartilage: A Possible Genesis for Chondromalacia Patella," *AAOS Symposium on Sports Medicine: The Knee,* G. A. M. Finerman, ed., C. V. Mosby Co., St. Louis, MO, pp. 70–84.

Ateshian, G. A., 1995, "Continuity Requirements Across a Contact Interface in the Formulation of a Boundary Friction Model for Biphasic Articular Cartilage," *Bioengineering Conference,* ASME, New York, BED-Vol. 29, pp. 147–148.

Ateshian, G. A., 1997, "A Theoretical Formulation for Boundary Friction in Articular Cartilage," ASME *Journal of Biomechanical Engineering,* Vol. 119, pp. 81–86.

Ateshian, G. A., Lai, W. M., Zhu, W. B., and Mow, V. C., 1992, "A Biphasic Model for Contact in Diarthrodial Joints," *Adv. Bioeng.,* ASME, New York, BED-Vol. 22, pp. 191–194.

Ateshian, G. A., Lai, W. M., Zhu, W. B., and Mow, V. C., 1994, "An Asymptotic Solution for the Contact of Two Biphasic Cartilage Layers," *J. Biomech.,* Vol. 27, pp. 1347–1360.

Ateshian, G. A., and Wang, H., 1995, "A Theoretical Solution for the Moving Contact of Cylindrical Biphasic Articular Cartilage Layers," *J. Biomech.,* Vol. 28, pp. 1341–1355.

Athanasiou, K. A., Rosenwasser, M. P., Buckwalter, J. A., Malinin, T. I., and Mow, V. C., 1991, "Interspecies Comparisons of in situ Intrinsic Mechanical Properties of Distal Femoral Cartilage," *J. Orthop. Res.,* Vol. 9, pp. 330–340.

Bachrach, N. W., Mow, V. C., and Guilak, F., 1998, "Incompressibility of the Solid Matrix of Articular Cartilage Under Hydrostatic Load," *J. Biomech.,* Vol. 31, pp. 445–451.

Biot, M. A., 1962, "Mechanics of Deformation of Acoustic Propagation in Porous Media," *J. Appl. Phys.,* Vol. 33, pp. 1482–1498.

Bowen, R. M., 1976, *Continuum Physics,* Vol. 3, A. E. Eringen, ed., Academic Press, San Diego, CA, pp. 1–127.

Brown, T. D., Radin, E. L., Martin, R. B., and Burr, D., 1984, "Finite Element Studies of Some Juxtarticular Stress Changes due to Localized Subchondral Stiffening," *J. Biomech.,* Vol. 17, pp. 11–24.

Donzelli, P. S., 1995, "A Mixed-Penalty Contact Finite Element Formulation for Biphasic Soft Tissues," Ph.D. thesis, Department of Mechanical, Aeronautical Engineering and Mechanics, Rensselaer Polytechnic Institute, Troy, New York.

Donzelli, P. S., and Spilker, R. L., 1994, "A Mixed-Penalty Contact Finite Element Formulation With Applications to the Biphasic Tissues of the Knee," *Adv. Bioeng.,* ASME, New York, BED-Vol. 28, pp. 13–14.

Donzelli, P. S., and Spilker, R. L., 1995, "Iterative Contact Detection Algorithm for a Mixed-Penalty Biphasic Finite Element," *Bioengineering Conference,* ASME New York, BED-Vol. 29, pp. 169–170.

Eberhardt, A. W., Keer, L. M., Lewis, J. L., and Vithoontien, V., 1990, "An Analytical Model of Joint Contact," ASME *Journal of Biomechanical Engineering,* Vol. 112, pp. 407–413.

Gray, M. L., Pizzanelli, A. M., Grodzinsky, A. J., and Lee, R. C., 1988, "Mechanical and Physicochemical Determinants of the Chondrocyte Biosynthetic Response," *J. Orthop. Res.,* Vol. 6, pp. 777–792.

Guilak, F., Hou, J. S., Ratcliffe, A., and Mow, V. C., "Articular Cartilage Under Hydrostatic Loading," *Adv. Bioeng.,* ASME, New York, Vol. BED-Vol. 8, pp. 183–186.

Guilak, F., Meyer, B. C., Ratcliffe, A., and Mow, V. C., 1994, "The Effects of Matrix Compression on Proteoglycan Metabolism in Articular Cartilage Explants," *Osteoarthritis and Cartilage,* Vol. 2, pp. 91–101.

Guilak, F., Ratcliffe, A., Lane, N., Rossenwasser, M. P., and Mow, V. C., 1994, "Mechanical and Biochemical Changes in the Superficial Zone of Articular Cartilage in a Canine Model of Osteoarthritis," *J. Orthop. Res.,* Vol. 12, pp. 474–484.

Hayes, W. C., Keer, L. M., Herrmann, G., and Mockros, L. F., 1992, "A Mathematical Analysis for Indentation Tests of Articular Cartilage," *J. Biomech.,* Vol. 11, pp. 407–419.

Hirsch, C., 1944, "The Pathogenesis of Chondromalacia of the Patella," *Acta. Chir. Scand. Suppl.,* Vol. 83, pp. 1–106.

Holmes, M. H., 1986, "Finite Deformation of Soft Tissue: Analysis of a Mixture Model in Uni-axial Compression," ASME *Journal of Biomechanical Engineering,* Vol. 108, pp. 372–381.

Hou, J. S., Holmes, M. H., Lai, W. M., and Mow, V. C., 1989, "Boundary Conditions at the Cartilage-Synovial Fluid Interface for Joint Lubrication and Theoretical Verifications," ASME *Journal of Biomechanical Engineering,* Vol. 111, pp. 78–87.

Johnson, K. L., 1985, Contact Mechanics, Cambridge University Press, Cambridge, UK, pp. 302–306.

Jones, I. L., Klamfeldt, A., and Sanstrom, T., "The Effect of Continuous Mechanical Pressure Upon the Turnover of Articular Cartilage Proteoglycans in Vitro," *Clin. Orthop.,* Vol. 165, pp. 283–289.

Kelkar, R., 1996, "Normal and Abnormal Mechanics of the Shoulder: Studies of Articular Geometry, Contact and Kinematics, Ph.D. thesis, Columbia University, New York, pp. 250–251.

Kelkar, R., and Ateshian, G. A., "Contact Creep Response Between a Rigid Impermeable Cylinder and a Biphasic Cartilage Layer Using Integral Transform," *Bioengineering Conference,* ASME, New York, BED-Vol. 29, pp. 313–314.

Kelly, P. A., and O'Connor, J. J., 1996, "Transmission of Rapidly Applied Loads Through Articular Cartilage, Part I: Uncracked Cartilage," *Proc. Inst. Mech. Engrs.,* Vol. 210, pp. 27–37.

Downloaded 04 May 2010 to 171.66.16.27. Redistribution subject to ASME license or copyright; see http://www.asme.org/terms/Terms_Use.cfm

Kempson, G. E., Freeman, M. A. R., and Swanson, S. A. V., 1971, "The Determination of a Creep Modulus for Articular Cartilage From Indentation Tests on the Human Femoral Head," *J. Biomech.,* Vol. 4, pp. 239–250.

Kenyon, D. E., 1976, "The Theory of an Incompressible Solid-Fluid Mixture," *Arch. Rat. Mech. Anal.,* Vol. 62, pp. 131–147.

Lai, W. M., and Mow, V. C., 1980, "Drag-Induced Compression of Articular Cartilage During a Permeation Experiment," *Biorheology,* Vol. 17, pp. 111–123.

Macirowski, T., Tepic, S., and Mann, R. W., 1994, "Cartilage Stresses in the Human Hip Joint," ASME *Journal of Biomechanical Engineering,* Vol. 116, pp. 10–18.

Mak, A. F., Lai, W. M., and Mow, V. C., 1987, "Biphasic Indentation of Articular Cartilage. Part I: Theoretical Analysis," *J. Biomech.,* Vol. 20, pp. 703–714.

Malcom, L. L., 1976, "An Experimental Investigation of the Frictional and Deformational Responses of Articular Cartilage Interfaces to Static and Dynamic Loading," Ph.D. thesis, University of California, San Diego, La Jolla, CA.

McCutchen, C. W., 1962, "The Frictional Properties of Animal Joints," *Wear,* Vol. 5, pp. 1–17.

McNamee, J., and Gibson, R. E., 1960, "Displacement Functions and Linear Transforms Applied to Diffusion Through Porous Elastic Media," *Quart. J. Mech. Appl. Math.,* Vol. 13, pp. 98–111.

Meachim, G., and Bentley, G., 1978, "Horizontal Splitting in Patellar Articular Cartilage," *Arth. Rheum.,* Vol. 21, pp. 669–674.

Mow, V. C., Gibbs, M. C., Lai, W. M., Zhu, W. B., and Athanasiou, K. A., 1989, "Biphasic Indentation of Articular Cartilage, Part II: A Numerical Algorithm and an Experimental Study," *J. Biomech.,* Vol. 22, pp. 853–861.

Mow, V. C., Kuei, S. C., Lai, W. M., and Armstrong, C. G., 1980, "Biphasic Creep and Stress Relaxation of Articular Cartilage: Theory and Experiment," ASME *Journal of Biomechanical Engineering,* Vol. 102, Vol. 73–84.

Mow, V. C., and Lai, W. M., 1980, "Recent Developments in Synovial Joint Biomechanics," "*SIAM Review,* Vol. 22, pp. 275–317.

Mow, V. C., Ratcliffe, A., and Poole, A. R., "Cartilage and Diarthrodial Joints as Paradigms for Hierarchical Materials and Structures," *Biomaterials,* Vol. 13, pp. 67–97.

Palmoski, M. J., and Brandt, K. D., 1984, "Effect of Static and Cyclic Compressive Loading on Articular Cartilage Plugs in Vitro," *Arthritis Rheum.,* Vol. 27, pp. 675–681.

Radin, E. L., Martin, R. B., Burr, D. B., Caterson, B., Boyd, R. D., and Goodwin, C., 1984, "Effects of Mechanical Loading on the Tissues of the Rabbit Knee," *J. Orthop. Res.,* Vol. 2, pp. 221–234.

Setton, L. A., Mow, V. C., Muller, F. J., Pita, J. C., and Howell, D. S., 1994, "Mechanical Properties of Canine Articular Cartilage are Significantly Altered Following Transection of the Anterior Cruciate Ligament," *J. Orothop. Res.,* Vol. 12, pp. 451–463.

Sokoloff, L., 1966, "Elasticity of Aging Cartilage," *Fed. Proc. Am. Socs. Exp. Biol.,* Vol. 25, pp. 1089–1095.

Spilker, R. L., Suh, J. K., and Mow, V. C., 1992, "A Finite Element Analysis of the Indentation Stress-Relaxation Response of Linear Biphasic Articular Cartilage," ASME *Journal of Biomechanical Engineering,* Vol. 114, pp. 191–201.

Suh, J. K., and Spilker, R. L., 1994, "Indentation Analysis of Biphasic Articular Cartilage: Nonlinear Phenomena Under Finite Deformation," ASME *Journal of Biomechanical Engineering,* Vol. 116, pp. 1–9.

van der Voet, A. F., Shrive, N. G., and Schachar, N. S., 1993, "Numerical Modelling of Articular Cartilage in Synovial Joints: Poroelasticity and Boundary Conditions," *Recent Advances in Computer Methods in Biomechanics and Biomedical Engineering,* J. Middleton, G. N. Pande, K. R. Williams, eds., Books & Journals International, Ltd., UK, pp. 200–209.

Downloaded 04 May 2010 to 171.66.16.27. Redistribution subject to ASME license or copyright; see http://www.asme.org/terms/Terms_Use.cfm

J. Calsamiglia
Helsinki Institute of Physics,
Laser Physics and Quantum Optics Project,
FIN-00014 Helsingin Yliopisto,
Finland

S. W. Kennedy
Engineering and Applied Sciences,
Harvard University,
Cambridge, MA 02139

A. Chatterjee
Engineering Science and Mechanics,
Penn State University,
University Park, PA 16802

A. Ruina

J. T. Jenkins

Theoretical and Applied Mechanics,
Cornell University,
Ithaca, NY 14853

Anomalous Frictional Behavior in Collisions of Thin Disks

We report on two-dimensional collision experiments with nine thin Delrin disks with variable axisymmetric mass distributions. The disks floated on an air table, and collided at speeds of about 0.5 to 1.0 m/s with a flat-walled stationary thick steel plate clamped to the table. The collision angle was varied. The observed normal restitution was roughly independent of angle, consistent with other studies. The frictional interaction differed from that reported for spheres and thick disks, and from predictions of most standard rigid-body collision models. For "sliding" two-dimensional collisions, most authors assume the ratio of tangential to normal impulse equals μ (friction coefficient). The observed impulse ratio was appreciably lower: roughly 0.5 μ slightly into the sliding regime, approaching μ only for nearly grazing collisions. Separate experiments were conducted to estimate μ; check its invariance with force magnitude; and check that the anomalies observed are not strongly dependent on velocity magnitude. We speculate that these slightly anomalous findings are related to the two-dimensional deformation fields in thin disks, and with the disks being only "impulse-response" rigid and not "force-response" rigid.

1 Introduction

Although the prediction of the outcome of collisions of approximately rigid bodies is of use for many purposes, there is not much collisional data on which to base or test predictive laws. Stoianovici and Hurmuzlu (1996) showed that for an apparently simple system, steel rods hitting an anvil, the collisional interaction is more complex than can be captured with known simple rigid body collision laws. Towards the end of better understanding basic issues, we set out to test collisions of an even simpler system, one for which the collisional mass matrix is diagonal (a "central collision") and were surprised to find that even for this system some common rigid body collision assumptions are not applicable.

The experimental results presented in this paper were previously presented in Calsamiglia et al. (1997).

2 Sliding Collisions in Two Dimensions

We define here some sliding-related terms for two-dimensional, frictional, single-point collisions: (1) in a *sliding* collision, the tangential components of pre and post-collision relative velocity at the contact point are both non-zero and in the same direction; (2) in "single-point" collisions, actual contact occurs over a small region. The *contact region* at any instant is the region occupied by the material points (on the two bodies) that are in contact at that instant; (3) at all times during a *fully sliding* collision, all points in the contact region have a nonzero relative tangential velocity in the same direction as the pre-collision relative tangential velocity; and (4) a sliding collision that is not fully sliding is *partially sliding*.

In collisions of real objects some portions of the contact region might stop or reverse their tangential velocity for part of the collision, yet resume sliding in the original direction by the end of the collision when transients are dead. Such a collision would naturally be partially sliding. If the frictional contact is governed by Coulomb friction, then the ratio of tangential impulse to normal impulse in a sliding collision will be less than μ only if the collision is partially sliding.

Our definition of partial sliding is more macroscopic than that used by some authors. For example, in Mindlin and Deresiewicz (1953), partial sliding corresponds to some portions of the contact region sticking while others slip. In our experiments we can only distinguish between collisions where the ratio of tangential to normal impulse is roughly equal to μ (treating them as fully sliding) from collisions where that ratio is convincingly less than μ (treating them as partially sliding). We do not know the details of which parts of the contact surface are or are not sliding.

Predictions for general three-dimensional frictional single-point collisions vary from model to model. However, for sliding collisions, if there is no inertial coupling between the normal and tangential directions[1] (as for collisions of axisymmetric disks or spheres with rigid walls), practically all authors assume the tangential impulse transmitted in the collision opposes the tangential velocity and is equal to μ times the normal impulse. This is equivalent to assuming that central, sliding collisions cannot be partially sliding (this is one main point of this paper—our data shows that they can). Some more general rigid body collision models also explicitly or implicitly disallow partially sliding collisions. In Routh's (1897) model for example, the "contact point" has a unique tangential relative velocity at all times during the collision; in two dimension, if the tangential relative velocity ever becomes zero during the collision, then it must either stay zero or reverse direction (by Routh's model). Thus, partial sliding is explicitly disallowed in two dimensions. In the models of Whittaker (1944), Kane and Levinson (1985),

Contributed by the Electrical and Electronic Packaging Division (EEPD) of THE AMERICAN SOCIETY OF MECHANICAL ENGINEERS for publication in the ASME JOURNAL OF APPLIED MECHANICS.

Discussion on this paper should be addressed to the Technical Editor, Professor Lewis T. Wheeler, Department of Mechanical Engineering, University Houston, Houston, TX 77204-4792, and will be accepted until four months after final publication of the paper itself in the ASME JOURNAL OF APPLIED MECHANICS.

Manuscript received by the Applied Mechanics Division July 22, 1997; final revision August 13, 1998. Associate Technical Editor: L. T. Wheeler.

[1] Such collisions are sometimes called "central collisions".

 Copyright © 1999 by ASME

Downloaded 04 May 2010 to 171.66.16.27. Redistribution subject to ASME license or copyright; see http://www.asme.org/terms/Terms_Use.cfm

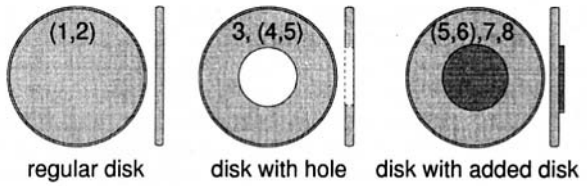

Fig. 1 Axisymmetric delrin disks, with holes or added disks

Smith (1991), and in the treatment of disk collisions by Brach[2] (1991), it is assumed that the ratio of impulses in a two-dimensional sliding collision is always equal to the friction coefficient (thus partial sliding is implicitly disallowed). In the treatment of collisions of thick disks by Maw et al. (1981), based on the incremental contact analysis of Mindlin and Deresiewicz (1953), partial sliding is not disallowed a priori. However, the solution predicts an impulse ratio of μ for all sliding collisions (and some that are "almost" sliding). The same occurs for disk collisions modeled using ad hoc localized compliances along the normal and tangential directions, as in Stronge (1994a). In the new algebraic rigid body collision model presented in Chatterjee and Ruina (1998b), it is possible to predict partially sliding disk collisions for suitable choices of the tangential restitution parameter e_t. However, that model also does not capture the present data with a single value of e_t for any one disk over the range of collision angles.

3 Description of Experiments

We now describe the disks studied and the experiments conducted (for more details, see Chatterjee, 1997).

3.1 Disks. All nine disks were cut from a rod of Delrin stock,[3] and finished on a lathe to achieve a smooth surface. The edge of each disk was rounded to ensure "point" contact (see Fig. 1). Three of the disks had holes in their centers, and four disks had smaller aluminum disks glued to their centers. The disks were blackened and marked with two white dots: one near the edge and one at the center. The disks with holes in them had thin circular pieces of paper stuck to their lower faces to help them float on the air table. Table 1 outlines the properties of each disk. Note that disk pairs (1, 2), (4, 5), and (6, 7) were made very similar (nearly identical) as a consistency check.

3.2 Procedure. The disks moved on an effectively frictionless[4] air table and collided against a steel plate clamped to the air table. The plate (40.6 cm × 20.3 cm × 1.9 cm), about 130 times more massive than the most massive disk, is treated as infinitely massive in the analysis. Pictures of the moving disks were taken using a strobe lamp and a digital camera.[5] The strobe rate was held at about 8.8 Hz. This rate provided two to three images of the disk before and after each collision on one frame. The measurement precision was about 0.23 mm/pixel determined by number of pixels in digital camera, lens focal length, and distance of camera from table surface (we made no checks of possible lens distortion errors). The launch speed of the disks was kept roughly consistent by using a simple rubber-band powered launcher, which also released the disks approximately without initial spin.

3.3 Kinematic Measurements. Digital pictures of the collisions were downloaded from the Kodak DCS and data was retrieved using the software NIHImage.[6] For each collision, we used four positions of the disk: two before and two after the collision. For each position, the x and y coordinates of the two marker points on the disk were recorded. Each set of coordinates (before, and after) was used to calculate the linear and angular velocities of the disk, before and after the collision.

3.4 Calculations. The quantities calculated for each collision were (1) the normal and tangential components of the pre and post-collision velocities of the contact point, (2) the angle made by the pre-collision contact point velocity with the plate edge normal, (the "incidence angle" θ), (3) the coefficient of normal restitution e (ratio of normal separation velocity to normal approach velocity),[7] (4) the "tangential restitution coefficient," defined here as the negative of the ratio of post-collision to pre-collision tangential contact point relative velocity, (5) the collision impulse from the steel plate to the disk, and (6) the ratio of the tangential to the normal components of the impulse (the "impulse ratio").

3.5 Note on Error Bars. The error bars shown in the figures indicate estimated upper bounds on the errors in the plotted quantities. These bounds were obtained as follows.

For each collision, the measured quantities were the x and y coordinates of eight points, i.e., 16 scalar quantities. Each calculated quantity, such as the coefficient of restitution or the angle of incidence, is thus a scalar function of 16 variables. For a function $f(q_1, q_2, \ldots, q_n)$, if the measured quantities $q_1, q_2, \ldots, q_n$ have errors $\Delta q_1, \Delta q_2, \ldots, \Delta q_n$, then the error in the calculated value of f is given to first order by the expression

$$\Delta f \approx \frac{\partial f}{\partial q_1}\Delta q_1 + \ldots + \frac{\partial f}{\partial q_n}\Delta q_n = \nabla f \cdot \Delta \mathbf{q}.$$

Now each of the Δq_i would typically be about one pixel or less (the precision of the digital imaging system). However, we took the error to be about two pixels. From this, we obtain the estimated error bound

$$|\Delta f| \le \sum \left|\frac{\partial f}{\partial q_i}\Delta q_i\right| \le h \sum \left|\frac{\partial f}{\partial q_i}\right|,$$

where h is twice the data acquisition precision (length/pixel).

In the foregoing analysis, we neglected plate misalignment errors. We assume negligible error in the plate's flatness, be-

[2] Brach's (1991) approach, in its most general form, suggests that the impulse ratio be treated as a tangential collision parameter that is not constant over all collisions between a given pair of bodies but that depends on initial conditions, e.g., the incidence angle. Therefore, this approach is neither supported nor contradicted by our data. Brach's claims about planar collisions with Coulomb friction being either fully sliding or terminated at a "rolling" condition are contradicted by our data.

[3] *General Properties:* low moisture absorption; abrasion resistance; dimensional stability and toughness; easy to machine.

[4] Based on the constancy of velocity and angular velocity before collision, the frictional effects were not greater than our measurement inaccuracy.

[5] Nikon F3 with attached Kodak Professional DCS (Digital Camera System).

[6] Available via anonymous ftp at the following internet address: zippy.nimh.nih.gov

[7] There are other "definitions" of the coefficient of restitution (see, e.g., Smith and Liu (1992)), but the popular ones are equivalent for central collisions.

Table 1 Properties of axisymmetric disks used (dimensions in mm, mass in gm, I in gm-cm^2). "I" values were measured experimentally (Chatterjee, 1997).

	Disk No.	radius R	radius of added disk or hole	thickness	mass m	I	$2I/mR^2$
Regular	1	49.1	0	6.4	67.8	827	1.01
	2	49.1	0	6.4	67.2	820	1.01
With hole	3	49.7	19.7	6.9	59.2	830	1.14
	4	49.6	29.4	6.9	45.4	745	1.33
	5	49.5	29.4	6.9	46.2	761	1.34
With added disk	6	49.1	30.5	6.5	92.0	902	.81
	7	49.2	30.5	6.4	91.5	900	.81
	8	49.2	25.4	6.3	82.8	837	.83
	9	49.1	20.3	6.2	74.6	800	.89

Downloaded 04 May 2010 to 171.66.16.27. Redistribution subject to ASME license or copyright; see http://www.asme.org/terms/Terms_Use.cfm

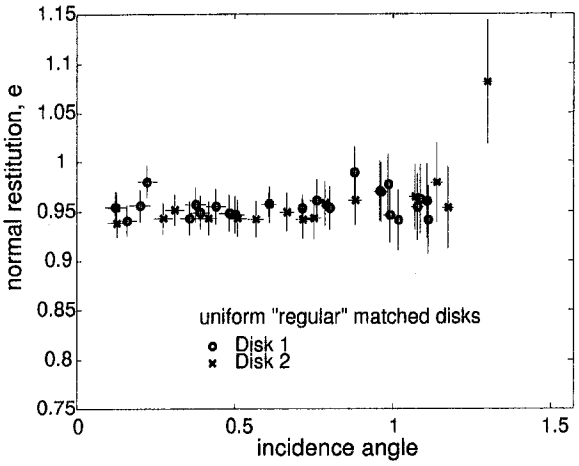

Fig. 2 The coefficient of normal restitution for disks 1 and 2

cause the edge was machined flat specifically for the experiment. The surface normal was estimated by picking off the positions of two previously marked points on the plate edge. These points were about 880 pixels apart in the digital camera; incorrectly locating them by, say, two pixels causes an error in estimating the normal direction by about .0023 radians. The plate edge was located separately for each picture, so the systematic error was probably even smaller. The horizontal error bars in the plots are several times bigger than 0.0023 near grazing incidence, and still larger in other places. So plate misalignment error does not contribute substantially. In any case, since the plate was used to select axes, if the plate angle was off by a small amount, then the "true" coordinates would change by correspondingly small amounts given by a rotation of axes formula. As such, the error from incorrectly orienting the plate is equivalent to incorrectly estimating the positions of various points, by amounts comparable to pixel size.

4 Results

For axisymmetric disks, all contact points are identical. Based on previous studies of disk and sphere collisions at moderate velocities (such as Maw et al. (1981) and Foerster et al. (1994)), we expect nondimensional collision quantities like the normal restitution coefficient e to be roughly independent of the pre-collision contact point velocity magnitude. So, for a given disk, each collision is approximately characterized by the incidence angle θ alone. Quantities of interest in collisions of axisymmetric objects like disks are the normal restitution coefficient e and the ratio of tangential to normal impulse. Also of interest is the coefficient of tangential restitution, particularly for small incidence angles.

4.1 Normal Restitution. We found e to be fairly high (typically between about 0.92 and 0.96), roughly independent of θ, and roughly the same for all nine disks. This was as expected from the literature on experiments with thick disks (e.g., Maw et al., 1981) and spheres (e.g., Foerster et al., 1994). The results for disks 1 and 2 are shown in Fig. 2, and are representative of all nine disks. The single data point at $e \approx 1.08$ is interesting because it is greater than one, though perhaps not convincingly so (given our error estimates). We mention that there is no fundamental reason why e, as defined in this paper, cannot be greater than one in frictional collisions (Smith and Liu (1992) report values as high as 2.3 from finite element method simulations, and as high as 1.4 from experiments). See, e.g., Chatterjee and Ruina (1998b) for a discussion about the relation between $e >, =, < 1$ and fundamental restrictions on collisional impulses.

4.2 Tangential Restitution. The tangential restitution coefficient is shown for three pairs of disks in Fig. 3. In the figure, positive tangential restitution corresponds to tangential velocity reversal, which is not allowed by some rigid body collision models such as in Routh (1897), Whittaker (1944), or Kane and Levinson (1985). Tangential restitution effects, caused by tangential compliance effects, have previously been observed experimentally (Maw et al., 1981; Foerster et al., 1994). Observe that, as expected, the tangential restitution is roughly consistent between the nominally identical disks: disks 1 and 2, disks 4 and 5, and disks 6 and 7. However, there is less consistency across disk pairs, and so the different disks have different tangential restitution graphs. For all disks (including the three not shown) and $\theta > \approx 0.5$, all collisions were sliding. That all

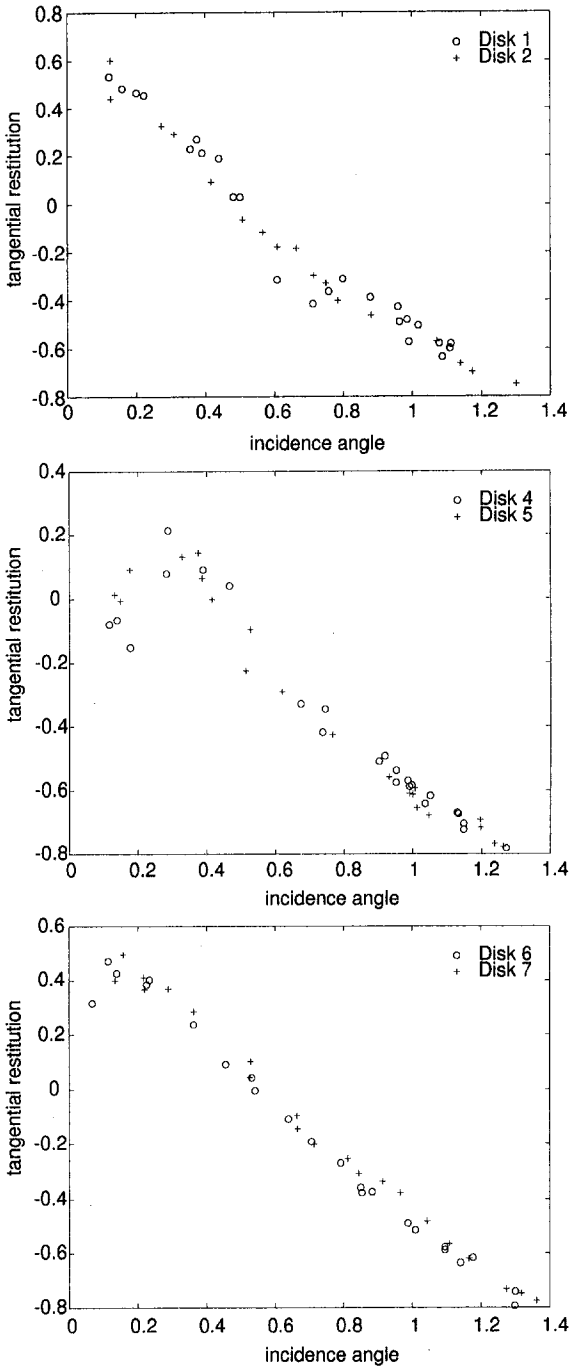

Fig. 3 Tangential restitution for disks 1 and 2, 4 and 5, 6, and 7

Downloaded 04 May 2010 to 171.66.16.27. Redistribution subject to ASME license or copyright; see http://www.asme.org/terms/Terms_Use.cfm

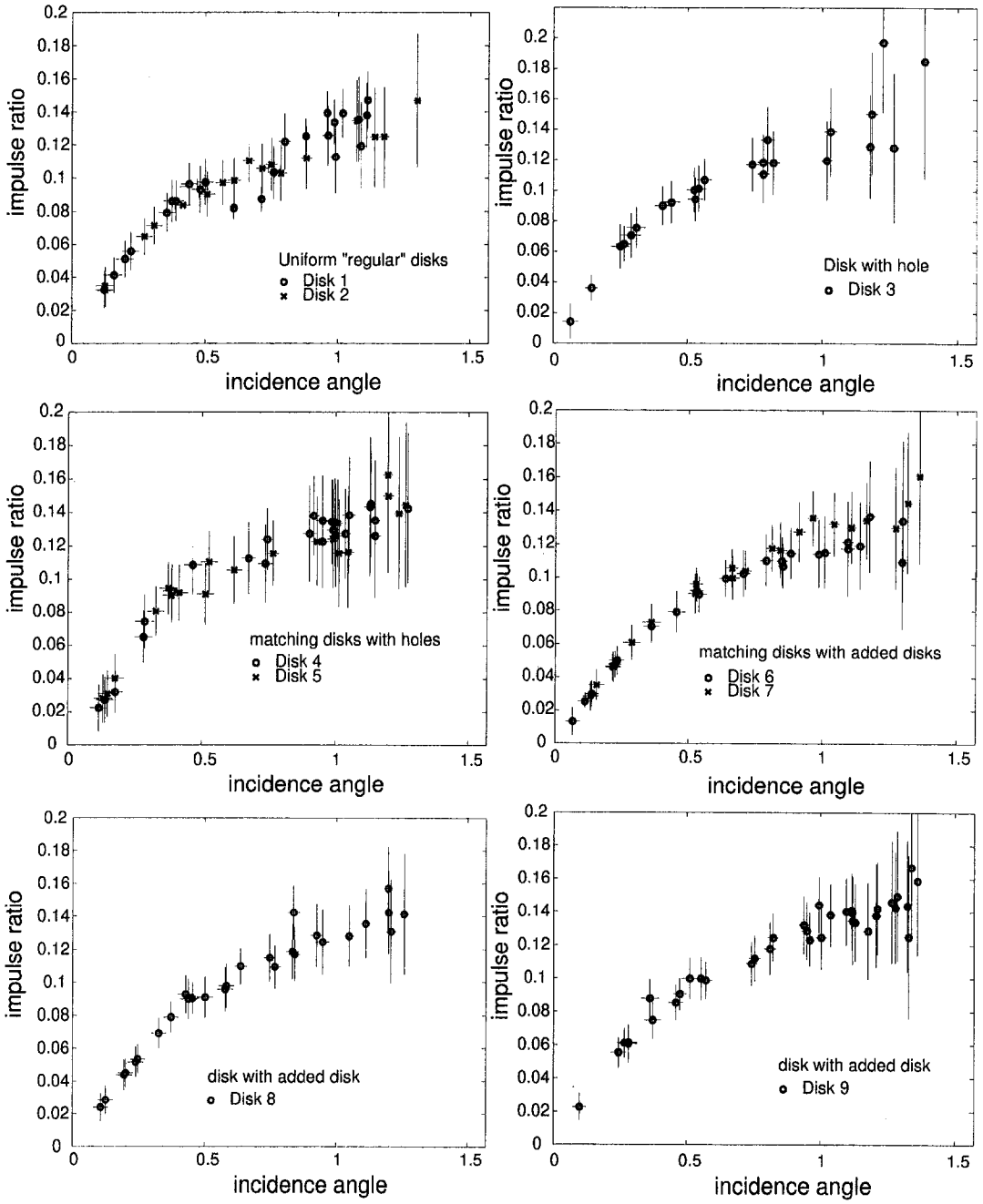

Fig. 4 The impulse ratio for disks 1 through 9

collisions for these disks should be sliding beyond $\theta \approx 0.5$ is not predicted by standard collision models.

4.3 The Impulse Ratio. The observed ratio of tangential to normal impulse is shown in Fig. 4. In each case, it is seen that the impulse ratio increases steadily with θ, approaching about 0.16 in the limit of grazing incidence. Figure 5 shows the impulse ratio for all nine disks on the same plot (without error bars for easier visibility). The degree of consistency between the data for the nine nonidentical disks is worth noting. The data can be fairly well captured using, say, a bilinear fit, with a corner at slightly under $\theta = 0.5$. As mentioned above, that is roughly where the transition occurs from tangential velocity reversal to sliding collisions.

In the sliding range, the impulse ratio is not constant but varies by roughly a factor of 2 as θ goes from 0.5 to $\pi/2$. This variation is directly opposed to the usual predictions of standard rigid body collision models as well as a detailed solution by Maw et al. (1981). For comparison, the predicted impulse ratios for the cases of Routh's law (1897), Kane and Levinson's law (1985) (essentially the same as Whittaker (1944)), and Smith's law (1991), using $e = 0.92$, for a uniform disk, and using a fitted coefficient of friction ≈ 0.162, are plotted against incidence angle θ in Fig. 5. The experimental data is represented by a bilinear curve. Note the mismatch of the bilinear fit to our data with the predictions of the conventional laws. We remark that as per several rigid body collision models, the "knee point" marking the transition from tangential velocity reversal to sliding, in collisions of disks with rigid walls, occurs at an incidence angle that depends on the coefficient of friction, normal and tangential restitution behavior, as well as the radius of gyration. Since the radii of gyration of the disks were different (see the last column of Table 1) while contact conditions were approximately the same, one might expect these knee points to occur

Downloaded 04 May 2010 to 171.66.16.27. Redistribution subject to ASME license or copyright; see http://www.asme.org/terms/Terms_Use.cfm

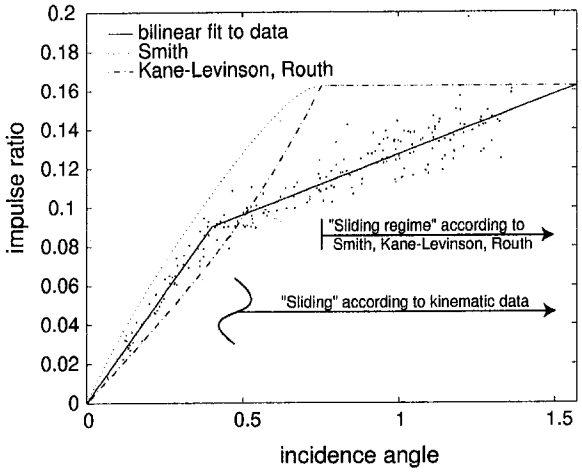

Fig. 5 The impulse ratio for all nine disks, The impulse ratio predicted by some collision laws, compared with a bilinear fit to experiment

at different incidence angles for these disks (which is apparently not the case; see Fig. 5). The typically predicted knee point for a uniform disk is far from that observed here (see Fig. 5).

5 Subsequent Experiments

5.1 Validity of the Coulomb Friction Contact Model. A year after the collision experiments we conducted some experiments to check the validity of the Coulomb model for the frictional interaction between the disks and the steel plate.

The original steel plate was lost, so we used another, similar plate. The coefficient of friction between the Delrin disks and the second plate was about 0.18. For the second plate, a pair of disks held side by side in one plane were attached together, constraining them to prevent rotation. Different steady normal loads were applied on them, and the tangential force needed to maintain sliding was measured. Within experimental precision, the sliding coefficient was found to be independent of normal force magnitude over about one order of magnitude. We can thus talk about "the" coefficient of friction, in that Coulomb friction apparently described the contact interaction quite well, with a single friction coefficient μ that is not dependent on the magnitude of the normal pressure.

For not-near-grazing collisions impact data does not allow an easy way to measure a friction coefficient. At other than grazing incidence, not all portions of the contact region may be sliding at any given instant. If the impulse ratio for near-grazing incidence is taken to be "the" coefficient, then our data (Fig. 4) for the first plate gives our estimate of about 0.16. Microscopic determination of the shear and normal tractions acting over the contact region and of where and when points of contact were slipping would require more sophisticated local measurements than we could make in this limited study. Thus, more direct measurement of the friction coefficient acting during collision was not possible for these experiments.

5.2 Possible Velocity Dependence of the Impulse Ratio. In our experiments, the velocity magnitude was roughly constant while the incidence angle θ was varied. Therefore, the normal component of collision velocity was roughly proportional to $\cos\theta$, i.e., a function of incidence angle. We would have liked to conduct similar experiments where the normal component of velocity was kept constant over all θ. We were unable to conduct such experiments due to our inability to launch the disks accurately at arbitrarily specified speeds.

Possible dependence on normal velocity magnitude was investigated by studying a few more collisions of disk 2 with the new (second) plate. In these collisions, the incidence angle was held roughly constant while the magnitude of pre-collision velocity was changed (two sets of collisions, one at roughly 0.5 m/s and the other at roughly 0.9 m/s). Figure 6 shows the results obtained, compared with the previous measurements for that disk. It is seen that changing the velocity magnitude by a factor of about 1.8 apparently changes the average impulse ratio by only a slight amount (smaller than the inherent scatter in the data points themselves). The new data points for both velocity magnitudes lie a little higher than the old data points, by an amount roughly equal to the estimated difference in the coefficients of friction for the two plates (supporting an estimate of $\mu \approx 0.16$ for the first plate and our measurement of $\mu \approx 0.18$ for the second plate).

Moreover, the new data points for both speeds lie below the estimated limiting value for grazing incidence (i.e., 0.18). Thus, the data points for each speed corroborate the increasing trend in the impulse ratio seen in the first series of experiments.

We remark that the new data points for the lower speed (0.5 m/s) lie slightly higher, on average, than those for the higher speed (0.9 m/s). While not conclusive, this observation is consistent with theory in that for disks of fixed thickness and rounded edges, as the incidence velocity magnitude is made smaller and smaller, the localized three-dimensional Hertz contact based solution (Maw et al., 1981; Mindlin and Deresiewicz, 1953) is expected to become accurate: for sufficiently small velocity magnitudes, the impulse ratio graph is expected to be flat in the sliding regime.

5.3 Significance of Subsequent Experiments. The subsequent experiments described in this section roughly demonstrate two things. First, they show that a constant μ (independent of normal force) is reasonable for the contact friction. By the discussion in Section 2, this implies that except in the limit of grazing incidence, the sliding collisions observed were only partially sliding collisions and not fully sliding collisions.

Second, somewhat less conclusively, the velocity variation experiments indicate that dependence of the impulse ratio on pre-collision velocity magnitude is small. This approximate constancy is consistent with the usual assumption that collisional impulses are homogeneous of degree one in the velocities (impulse magnitude varies linearly with velocity magnitude for any fixed velocity direction, for fixed values of collision "parameters").

6 On Rigidity in Collisions

The fundamental assumptions of rigid body collision modeling are that the time of interaction is small, displacements during the collision are small, contact forces are large, and accelera-

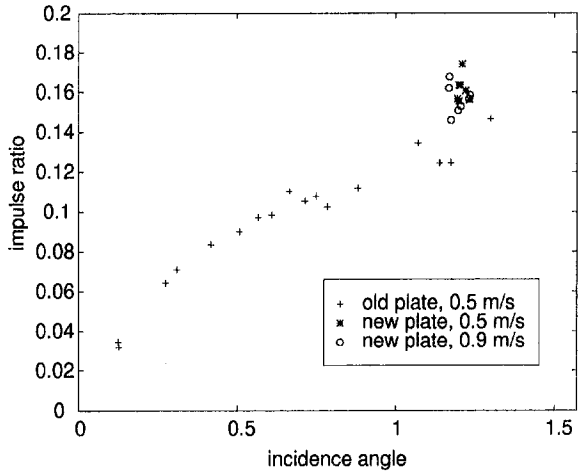

Fig. 6 The impulse ratio for disk 2, for two velocities

Downloaded 04 May 2010 to 171.66.16.27. Redistribution subject to ASME license or copyright; see http://www.asme.org/terms/Terms_Use.cfm

tions are large; that the net interaction can be described by rigid body impulse-momentum relations. Further, for "single-point" collisions, it is assumed that the size of the contact region is small compared to the overall dimensions of the colliding objects. These assumptions are reasonably applicable for the disks studied. However, specific rigid body collision models include extra hypotheses about the collision impulse. The particular assumptions made vary; so do the predicted results. The contradiction between our experimental observations and the predictions of most standard rigid body collision models should be viewed as a demonstration of the weakness of specific assumptions of these particular collision models, and not inaccuracy of the fundamental assumptions of the rigid body approach.

In a collision between any pair of real objects, contact occurs over a region (possibly small). The velocity distribution of material points in the contact region need not be uniform. Apparently the common assumption of a constant μ in the contact region is reasonable. If the relative tangential motion of all portions of the contact region is always in the same vectorial direction (with possible reversals), and the net tangential impulse is less than μ times the normal impulse, then some portions of the contact region must have stuck or reversed direction for some part of the collision, even though the whole contact region might again be moving in the original direction at the end of the collision.

If contact deformations are strongly localized, as in (say) Hertzian contact of spheres or thick slices thereof, then the whole body moves essentially like a rigid body while the contact region acts like a small, pseudostatic interaction mechanism. Such objects, where at all instants of time including during the collision, the small contact region essentially behaves like a point on an ideal rigid body, are force-response rigid (see Chatterjee, 1997; or Chatterjee and Ruina, 1998a). Since any tangential (possibly rate-dependent) compliance is of the same order as normal compliance, these objects are expected to be slipping over the whole contact area throughout the collision for collisions that are sufficiently far from normal. For such objects, in two-dimensional sliding collisions, the tangential impulse is expected to be μ times the normal impulse.

In contrast, if contact deformations are not so strongly localized, so that the motions of points at small distances from the contact region are not effectively identical to those of a point on a rigid body during the collision, but the motion of the body before and after the collision looks like that of a rigid body, and if all displacements during the collision are very small compared to the dimensions of the body, then the body is only impulse-response rigid (see Chatterjee (1997) or Chatterjee and Ruina (1998a)). In this case much more complex contact interactions can take place involving vibration and wave phenomena. Perhaps with such interactions the tangential relative velocity might reverse direction or stop during a collision (just as the normal component reverses direction multiple times in the data of Stoianovici and Hurmuzlu, 1996). For such objects, in two-dimensional sliding collisions, it might happen that the tangential impulse is less than μ times the normal impulse. As discussed in Chatterjee and Ruina (1998a) thin disks like in our experiments might only be well described as impulse-response rigid, while thick disks (as in Maw et al. (1981)) might be well described as force-response rigid. In particular consider a slice of thickness H, cut from a sphere of radius R. Then the three-dimensional Hertz-contact compliance (see Johnson, 1985) due to the rounded edges depends only on R and not on H, but the two-dimensional compliance (or the "thinness" effect of the disk) is proportional to $1/H$. For a given contact force magnitude, if H is made smaller, the two (three-dimensional and two-dimensional compliances) can become comparable.

Note that the data of Foerster et al. (1994) and Maw et al. (1981) clearly showed tangential restitution, like our disks. Our observations are not new in this regard. However, for the spheres and (presumably thick) disks studied in these works, it was found that the impulse ratio was equal to the friction coefficient for sliding collisions, i.e., in those studies, sliding collisions were fully sliding. In contrast, in our study of thin disks, we have found sliding collisions to be only partially sliding.

7 Conclusions

The fact that even in apparently "sliding" collisions, sliding need not persist throughout the collision, is relevant to general rigid body collision modeling. Contradiction of specific collision models, however, does not negate the basic rigid body approach to modeling collisions. We hope that our results will help to broaden the often restricted ideas about rigid body collisions that are promoted, in part, by several recent papers devoted to analyses of Routh's incremental model or variations thereof, examples of which include Keller (1986), Wang and Mason (1992), Stronge (1994b), Bhatt and Koechling (1995), Marghitu and Hurmuzlu (1995), and Batlle and Cardona (1997).

The details of the actual mechanical interactions in the collisions studied here were not resolvable. These interactions might be better understood through some combination of experiments with micromeasurements, detailed numerical simulations, and approximate analytical solutions.

Acknowledgments

The authors thank Michel Louge for the loan of the digital camera system, the National Science Foundation (REU program) for summer support for Calsamiglia and Kennedy, and the Department of Energy (Granular Flow Advanced Research Objective) for one summer's support for Chatterjee.

References

Batlle, J. A., and Cardona, S., 1998, "The Jamb (Self-Locking) Process in Three-Dimensional Rough Collisions," ASME JOURNAL OF APPLIED MECHANICS, Vol. 65, pp. 417–423.

Bhatt, V., and Koechling, J., 1995, "Three-Dimensional Frictional Rigid-Body Impact," ASME JOURNAL OF APPLIED MECHANICS, Vol. 62, pp. 893–898.

Brach, R. M., 1991, *Mechanical Impact Dynamics: Rigid Body Collisions,* John Wiley and Sons, Inc., New York.

Calsamiglia, J., Kennedy, S., Chatterjee, A., Ruina, A., and Jenkins, J., 1997, "Anomalous Frictional Behavior in Collisions of Thin Disks," Proceedings, ASME Winter Annual Meeting, Dallas, TX, ASME PVP-Vol. 369, pp. 57–63.

Chatterjee, A., 1997, "Rigid Body Collisions: Some General Considerations, New Collision Laws, and Some Experimental Data," Ph.D. thesis, Cornell University, Ithaca, NY.

Chatterjee, A., and Ruina, A., 1998a, "Two Interpretations of Rigidity in Rigid Body Collisions," ASME JOURNAL OF APPLIED MECHANICS, Vol. 65, pp. 894–900.

Chatterjee, A., and Ruina, A., 1998b, "A New Algebraic Rigid Body Collision Law Based on Impulse Space Considerations," ASME JOURNAL OF APPLIED MECHANICS, Vol. 65, pp. 939–951.

Foerster, S. F., Louge, M. Y., Chang, H., and Allia, K., 1994, "Measurement of the Collision Properties of Small Spheres," *Physics of Fluids,* Vol. 6, No. 3, pp. 1108–1115.

Johnson, K. L., 1985, *Contact Mechanics,* Cambridge University Press, Cambridge, UK.

Kane, T. R., and Levinson, D. A., 1985, *Dynamics: Theory and Applications,* McGraw-Hill, New York.

Keller, J. B., 1986, "Impact With Friction," ASME JOURNAL OF APPLIED MECHANICS, Vol. 53, pp. 1–4.

Marghitu, D. B., and Hurmuzlu, Y., 1995, "Three-Dimensional Rigid-Body Collisions With Multiple Contact Points," ASME JOURNAL OF APPLIED MECHANICS, Vol. 62, pp. 725–732.

Maw, N., Barber, J. R., and Fawcett, J. N., 1981, "The Role of Elastic Tangential Compliance in Oblique Impact," *Journal of Lubrication Technology,* Vol. 103, pp. 74–80.

Mindlin, R. D., and Deresiewicz, H., 1953, "Elastic Spheres in Contact Under Varying Oblique Forces," ASME JOURNAL OF APPLIED MECHANICS, Vol. 20, pp. 327–344.

Routh, E. J., 1897, *Dynamics of a System of Rigid Bodies,* 6th ed., Macmillan and Co., London.

Smith, C. E., 1991, "Predicting Rebounds Using Rigid-Body Dynamics," ASME JOURNAL OF APPLIED MECHANICS, Vol. 58, pp. 754–758.

Downloaded 04 May 2010 to 171.66.16.27. Redistribution subject to ASME license or copyright; see http://www.asme.org/terms/Terms_Use.cfm

Smith, C. E., and Liu, P-. P., 1992, "Coefficients of Restitution," ASME JOURNAL OF APPLIED MECHANICS, Vol. 59, pp. 963–969.

Stoianovici, D., and Hurmuzlu, Y., 1996, "A Critical Study of the Applicability of Rigid-Body Collision Theory," ASME JOURNAL OF APPLIED MECHANICS, Vol. 63, pp. 307–316.

Stronge, W. J., 1994a, "Planar Impact of Rough Compliant Bodies," *International Journal of Impact Engineering,* Vol. 15, No. 4, pp. 435–450.

Stronge, W. J., 1994b, "Swerve During Three-Dimensional Impact of Rough Bodies," ASME JOURNAL OF APPLIED MECHANICS, Vol. 61, pp. 605–611.

Wang, T., and Mason, M. T., 1992, "Two-Dimensional Rigid-Body Collisions With Friction," ASME JOURNAL OF APPLIED MECHANICS, Vol. 59, pp. 635–642.

Whittaker, E. T., 1944, *A Treatise on the Analytical Dynamics of Particles and Rigid Bodies,* 4th Ed., Dover, New York.

Downloaded 04 May 2010 to 171.66.16.27. Redistribution subject to ASME license or copyright; see http://www.asme.org/terms/Terms_Use.cfm

S. K. Esche
Department of Mechanical Engineering,
Stevens Institute of Technology,
Hoboken, NJ 07030
Assoc. Mem. ASME

G. K. Kinzel
Department of Mechanical Engineering,
Mem. ASME

J. K. Lee
Department of Aerospace Engineering,
Applied Mechanics, and Aviation,
Mem. ASME

The Ohio State University,
Columbus, OH 43210

An Axisymmetric Membrane Element With Bending Stiffness for Static Implicit Sheet Metal Forming Simulation

This paper reviews techniques to include the bending behavior of sheet metals into finite element method formulations. A new, numerically efficient bending correction for the implementation into axisymmetric membrane elements is developed. This bending correction is based on a number of simplifying assumptions. The accuracy of the implementation is demonstrated by analyzing two round cup drawings for which experimental measurements were available from the literature. The range of applicability of the proposed approach is discussed.

1 Introduction

A large variety of sheet metal stampings is required for automotive applications, consumer products, aerospace parts as well as a wealth of other products. Therefore, sheet metal parts are produced in large quantities using special tooling and high-volume production techniques. Traditionally, the process and tooling design for these stampings was a trial-and-error procedure based on the skills of experienced die and tool makers. This approach resulted in high development costs and long lead times conflicting with today's highly competitive global world market demanding reduced lead times, introduction of new materials for which no experience is available, greater emphasis on cost effectiveness, and increased part complexity. Therefore, new computer-aided technologies are being developed in an effort to transform sheet metal forming from an art into a science.

Section analysis has been recognized as a valuable technique applicable during sheet metal part and process design. Even though intensive research has gone into computationally efficient and numerically robust implementations, the existing two-dimensional finite element method section analysis programs still exhibit some significant limitations. This work focuses on the development of a numerically efficient approach for introducing bending stiffness into axisymmetric membrane elements of static implicit finite element programs. While pure membrane elements are known to provide accurate and computationally efficient solutions for stretch-dominated sheet metal forming problems, it is essential to include bending characteristics into the formulation when simulating bending-dominated problems and in cases when the exact shape of the final part is of importance. In addition, it has been shown by Esche (1997) that numerical buckling effects make it impossible to analyze redrawing processes as applied to achieve high drawing ratios in round cup drawings with pure membrane elements.

The paper first reviews a series of different methods for the modeling of the bending behavior of sheet metals. Then, the essentials of the formulation of the axisymmetric membrane element that formed the basis for this work are summarized. In the next section, the axisymmetric bending correction is developed. The resulting computer implementation of the method developed here is then checked against experimental data. The paper ends with conclusions and suggestions for future developments.

2 Modeling of Bending Effects in Sheet Metals

There exist three fundamental finite element types to model the deformation of thin sheets, namely membrane, shell, and continuum elements. The membrane model captures only the capability of a sheet to resist stretching while not including the bending stiffness. The sheet is assumed to be in a plane stress state where the only nonzero stress components are parallel to the surface of the sheet. The sheet thickness must therefore be defined based on the strain components parallel to the sheet surface. Usually, the material is assumed to be incompressible. While useful information can be extracted from the membrane formulation for stretch-dominated problems, adequate simulation of bending-dominated cases requires the incorporation of bending terms. Similarly, modeling of the bending behavior is essential when investigating the wrinkling and springback phenomena. Furthermore, limitations of membrane formulations exist also with respect to the minimum bending radius–sheet thickness ratio as discussed by Wang and Wagoner (1991).

There are several general strategies for modeling accurately the bending behavior of sheet metals. Like any other structure, a sheet is also a three-dimensional continuum and can therefore be modeled by continuum elements. This approach accounts for both membrane and bending effects but at a very high computational cost. Other drawbacks of continuum elements were said to be the difficulties with imposing the plastic incompressibility conditions and the need to use several layers of elements through the thickness to model accurately bending effects which leads to extensive run times.

The second approach for modeling the bending behavior in sheet metals is to use shell theory. While this approach is also much less computationally efficient than the membrane formulation due to the need for numerical integration through the shell thickness and an increased number of degrees-of-freedom, it is still preferable to continuum elements from the efficiency standpoint. Therefore, shell elements have become the most popular element type employed to model the sheet metal deformation process.

Contributed by the Applied Mechanics Division of THE AMERICAN SOCIETY OF MECHANICAL ENGINEERS for publication in the ASME JOURNAL OF APPLIED MECHANICS.

Discussion on the paper should be addressed to the Technical Editor, Professor Lewis T. Wheeler, Department of Mechanical Engineering, University of Houston, Houston, TX 77204-4792, and will be accepted until four months after final publication of the paper itself in the ASME JOURNAL OF APPLIED MECHANICS.

Manuscript received by the ASME Applied Mechanics Division, Nov. 7, 1997; final revision, Aug. 20, 1998. Associate Technical Editor: M. Ortiz.

 Copyright © 1999 by ASME

Downloaded 04 May 2010 to 171.66.16.27. Redistribution subject to ASME license or copyright; see http://www.asme.org/terms/Terms_Use.cfm

Different approaches have been developed to further improve the numerical efficiency of shell formulations. Oñate et al. (1989), Agelet de Saracibar and Oñate (1990), and Oñate and Agelet de Saracibar (1990) proposed to selectively employ shell elements only in areas of high curvature. In areas where the ratio of membrane energy to total energy is large, the shell elements are degenerated into membrane elements. Similarly, Quoirin (1992) presented a shell formulation that automatically degenerates into a membrane formulation in stretch-dominated zones basing the transition to degenerated shell elements on the comparison of the in-plane strain components at different integration points through the sheet thickness. The general idea of reducing the number of nodal degrees-of-freedom while retaining bending stiffness terms in the formulation has been approached in several ways. Lee et al. (1991) reduced the number of nodal degrees-of-freedom in their implicit program for plane-strain problems by assuming a linear variation within each element for one of the components of the displacement increment vector. Nakamachi (1992) and Nakamachi and Wagoner (1992) presented an efficient Mindlin-type shell formulation for dynamic explicit programs. In this formulation, the curvature tensor needed to evaluate the bending terms is obtained by the jewel patch method, and thus, the bending effects are incorporated without introducing additional degrees-of-freedom beyond those required in a membrane element (even though an increase in the bandwidth cannot be avoided). Similar formulations were reported by Oñate and Cervera (1993) and Oñate et al. (1996).

Another general approach is to include bending effects into membrane elements in an approximate fashion. Stoughton (1985) incorporated the effect of bending on the global deformation pattern based on a stiffness reduction factor computed from the drawbead model by Wang (1982). In addition, he corrected the final strain distribution by adding corrective terms locally in the regions of high curvature which he assumed to be restricted to the tool contact zones. Following Stoughton's example, Pourboghrat and Chandorkar (1992) also used the curvature of the tooling to adjust the membrane solution for bending effects. In their implicit formulation, Huh et al. (1993, 1994) and Han and Huh (1995) assumed that the strain can be decomposed additively into its membrane and bending parts. Then, they approximated the curvature needed for the bending terms using the difference of the kink angles of two neighboring elements. In an alternative approach, Yoo et al. (1994) and Yang et al. (1995) proposed a class of bending energy augmented membrane elements where the bending energy is approximated by introducing artificial discrete nodal or edge springs opposing the relative rotation of neighboring elements. The spring constants are determined using an average of the tangent modulus and Young's modulus. Again, the bandwidth is increased here while not increasing the total number of degrees-of-freedom compared with a membrane formulation. Brunet and Sabourin (1995) developed a triangular element for their dynamic explicit program where a constant curvature is assumed along the common sides of neighboring elements and the approximate bending forces are computed based on an elastic constitutive law using only displacement degrees-of-freedom.

For plane-strain deformation, Zhou (1993) and Zhou and Wagoner (1995) proposed an approach, which approximates the bending resistance by an equivalent bending group technique. They assumed the neutral fiber to stay in the middle surface of the sheet. Then, they computed an approximation for the curvature of the sheet by fitting a circle through three consecutive nodes and writing the engineering bending strain based on the assumption of a linear strain distribution through the sheet thickness. They evaluated the resulting bending moment and represented it by equivalent bending force couples, which were then incorporated into the force vector. Because a strain distribution is assumed which is symmetric about the middle surface of the sheet, no effective bending strain increment was accumulated. However, a true equilibrium state was reached after each increment. This approach was extended by Sadagopan (1997) for the three-dimensional case.

In an alternative approach, for the plane-strain case, Wang (1993) considered an approximation for the shifting of the neutral axis resulting in a bending strain distribution which is not symmetric about the sheet middle plane. By averaging this bending strain distribution over the sheet thickness, he arrived at some approximation of an effective bending strain. As opposed to the method by Zhou (1993), bending forces were not computed, and a standard membrane solution was obtained first. Then, the averaged effective bending strain was added to the effective membrane strain without a further equilibrium iteration, and the sheet thickness was corrected. Therefore, no equilibrium state is achieved after the bending correction, but the accumulated effective bending strain increment enters the iteration process for the next incremental step.

3 Membrane Formulation

The starting point for the current work was a family of two-dimensional (plane-strain) and three-dimensional sheet metal forming programs developed at The Ohio State University. The formulation of these programs employing membrane theory was based on the development by Wang (1984). The evolution of the codes at OSU was documented in a series of publications, for example by Germain et al. (1989), Saran et al. (1991), and Saran and Wagoner (1991).

The program developed here is based on a quasi-static incremental formulation with an implicit time integration scheme employing the Newton-Raphson method to iteratively solve the nonlinear equilibrium equations in each incremental step. The domain is discretized by linear constant strain elements. The tools are assumed to be rigid. The punch moves with constant velocity while the die is stationary. The contact is enforced using a consistent stiffness matrix formulation where the friction at the sheet–tool interfaces is included using a modified Coulomb friction law. The blankholder effects are represented by a set of statically equivalent nodal forces. The sheet material is modeled as rigid-viscoplastic considering isotropic strain and strain rate hardening and obeying Hill's new yield criterion.

Time Discretization. The deformation process of the sheet is assumed to start at the initial time ${}^0t$ and is described by a sequence of incremental time steps ${}^i\Delta t$. Here, it is worth noting that these incremental time steps ${}^i\Delta t$ are small but finite (not infinitesimal), and they can vary from increment to increment. Then, the total time ${}^nt$ elapsed at the end of the nth incremental step follows from

$$ {}^nt = {}^0t + \sum_{i=1}^{n} {}^i\Delta t. \tag{1} $$

In the following, a pre-superscript n at a quantity emphasizes the fact that this is the quantity at time ${}^nt$.

Kinematics of Deformation. To describe the kinematics of the deformation process, a fixed global (X_1, X_2, X_3) coordinate system and a local coordinate system for each element are defined. For the axisymmetric case considered in this paper, the X_1, X_2, and X_3-axes correspond to the r, θ, and z directions, respectively. In the following, the index indicating the directional component of a vectorial quantity is placed as a post-subscript. The local coordinate system is attached to the center of the element, its x_1-axis is collinear with the element, its x_3-axis is normal to that in the sheet thickness direction, while the x_2-axis is normal to both the x_1 and x_3-axes to form a right-handed coordinate system.

During time step $n + 1$, the body is deformed from its configuration ${}^nC$ at time ${}^nt$ into the configuration ${}^{n+1}C$ at time ${}^{n+1}t$.

Downloaded 04 May 2010 to 171.66.16.27. Redistribution subject to ASME license or copyright; see http://www.asme.org/terms/Terms_Use.cfm

In the following, the position of node i at time ${}^0t$ is described by vector $\mathbf{S}_i$ which is defined as

$$\mathbf{S}_i = \begin{pmatrix} S_{i1} \\ S_{i3} \end{pmatrix} \tag{2}$$

while at time ${}^nt$, its position vector is denoted by ${}^n\mathbf{s}_i$ which is defined as

$${}^n\mathbf{s}_i = \begin{pmatrix} {}^ns_{i1} \\ {}^ns_{i3} \end{pmatrix} \tag{3}$$

Note that in the axisymmetric case considered here, the 2 component (corresponding to the θ direction) is identically zero and will therefore be omitted in all equations. It would be considered in an analogous way in the case of a three-dimensional development.

Furthermore, the nodal incremental displacement vector for the time interval $t = {}^nt \ldots {}^{n+1}t$ is defined as

$${}^{n+1}\Delta\mathbf{u}_i = \begin{pmatrix} {}^{n+1}\Delta u_{i1} \\ {}^{n+1}\Delta u_{i3} \end{pmatrix} \tag{4}$$

and the nodal total displacement vector for node i is defined as

$${}^n\mathbf{u}_i = \begin{pmatrix} {}^nu_{i1} \\ {}^nu_{i3} \end{pmatrix} = \sum_{j=1}^{n} {}^j\Delta\mathbf{u}_i . \tag{5}$$

Then, the nodal position vector ${}^{n+1}\mathbf{s}_i$ of node i at time ${}^{n+1}t$ is related to the nodal position vector $\mathbf{S}_i$ at time ${}^0t$, the nodal total displacement vector ${}^n\mathbf{u}_i$ at time ${}^nt$, and the nodal incremental displacement vector ${}^{n+1}\Delta\mathbf{u}_i$ during the time interval $t = {}^nt \ldots {}^{n+1}t$ as follows:

$${}^{n+1}\mathbf{s}_i = {}^n\mathbf{s}_i + {}^{n+1}\Delta\mathbf{u}_i = \mathbf{S}_i + {}^n\mathbf{u}_i + {}^{n+1}\Delta\mathbf{u}_i = \mathbf{S}_i + {}^{n+1}\mathbf{u}_i . \tag{6}$$

Two-noded straight-line elements are used in the current formulation where each node has two displacement degrees-of-freedom corresponding to the X_1 and X_3-directions. Furthermore, standard linear shape functions are employed which implies the assumption of a constant strain distribution within each element.

Without loss of generality, it is assumed that all nodes of the mesh are ordered by increasing X_1 coordinates. Then, element i is composed of the two consecutive nodes i and $i + 1$. The element length of element i at time ${}^nt$ can then be computed as

$$\begin{aligned} {}^n1_i &= |{}^n\mathbf{s}_{i+1} - {}^n\mathbf{s}_i| \\ &= [({}^ns_{(i+1)1} - {}^ns_{i1})^2 + ({}^ns_{(i+1)3} - {}^ns_{i3})^2]^{1/2}. \end{aligned} \tag{7}$$

The principal true strain increments in the radial and circumferential directions are calculated using standard shell theory. The details are omitted here. For a treatment of the general shell theory see Budiansky (1968) and Chung (1988), and for the special case of axisymmetric shells refer to Makowski and Nolte (1987). In the following, the subscripts 1 and 2 denote the radial and circumferential directions, respectively. In accordance with Kim et al. (1978) for example, the principal true strain increments are found to be

$${}^{n+1}\Delta\epsilon_{i1} = \frac{1}{2}\ln\left(\frac{{}^{n+1}1_i^2}{{}^n1_i^2}\right) \tag{8}$$

$${}^{n+1}\Delta\epsilon_{i2} = \frac{1}{2}\ln\left(\frac{{}^{n+1}r_i^2}{{}^nr_i^2}\right) \tag{9}$$

where l_i is the length of element i given in (7) while ${}^nr_i$ and ${}^{n+1}r_i$ are the radial coordinates of the center point of element i at times t and $t + \Delta t$, respectively, which are defined as

$${}^nr_i = \frac{{}^ns_{i1} + {}^ns_{(i+1)1}}{2}$$

$${}^{n+1}r_i = \frac{{}^ns_{i1} + {}^{n+1}\Delta u_{i1} + {}^ns_{(i+1)1} + {}^{n+1}\Delta u_{(i+1)1}}{2}. \tag{10}$$

Substituting the expressions for the element length of element i given previously into (8) and (9), the equations for the principal strain increments can be written in a form, which explicitly reveals the dependence on the displacement increments:

$$\begin{aligned} &{}^{n+1}\Delta\epsilon_{i1} \\ &= \frac{1}{2}\ln\left\{\frac{[({}^ns_{(i+1)1} + {}^{n+1}\Delta u_{(i+1)1}) - ({}^ns_{i1} + {}^{n+1}\Delta u_{i1})]^2}{{}^n1_i}\right. \\ &\quad \left. + \frac{[({}^ns_{(i+1)3} + {}^{n+1}\Delta u_{(i+1)3}) - ({}^ns_{i3} + {}^{n+1}\Delta u_{i3})]^2}{{}^n1_i}\right\} \end{aligned} \tag{11}$$

$$\begin{aligned} &{}^{n+1}\Delta\epsilon_{i2} \\ &= \frac{1}{2}\ln\left\{\frac{[({}^ns_{(i+1)1} + {}^{n+1}\Delta u_{(i+1)1}) + ({}^ns_{i1} + {}^{n+1}\Delta u_{i1})]^2}{{}^nr_i}\right\}. \end{aligned} \tag{12}$$

From these relations, the derivatives with respect to the displacement increments can be obtained in a straightforward fashion.

Force Equilibrium Equations. For each node i, a nodal external force vector ${}^n\mathbf{F}_{Ei}$ and a nodal internal force vector ${}^n\mathbf{F}_{Ii}$ are defined at time ${}^nt$ as

$${}^n\mathbf{F}_{Ei} = \begin{pmatrix} {}^nF_{Ei1} \\ {}^nF_{Ei3} \end{pmatrix} \tag{13}$$

and

$${}^n\mathbf{F}_{Ii} = \begin{pmatrix} {}^nF_{Ii1} \\ {}^nF_{Ii3} \end{pmatrix}. \tag{14}$$

Furthermore, the nodal external force vector ${}^n\mathbf{F}_{Ei}$ can be split into a nonconservative part ${}^n\mathbf{F}_{\mathrm{NON}i}$ resulting from frictional contact and a conservative part ${}^n\mathbf{F}_{\mathrm{CON}i}$ resulting from drawbeads and blankholders as follows:

$${}^n\mathbf{F}_{Ei} = {}^n\mathbf{F}_{\mathrm{NON}i} + {}^n\mathbf{F}_{\mathrm{CON}i} \tag{15}$$

where

$${}^n\mathbf{F}_{\mathrm{CON}i} = \begin{pmatrix} {}^nF_{\mathrm{CON}i1} \\ {}^nF_{\mathrm{CON}i3} \end{pmatrix} \tag{16}$$

$${}^n\mathbf{F}_{\mathrm{NON}i} = \begin{pmatrix} {}^nF_{\mathrm{NON}i1} \\ {}^nF_{\mathrm{NON}i3} \end{pmatrix}. \tag{17}$$

For node i to be in equilibrium at time ${}^nt$, the applied external forces must balance the internal forces resulting in the nodal force equilibrium equations

$${}^n\mathbf{F}_{\mathrm{NON}i} + {}^n\mathbf{F}_{\mathrm{CON}i} - {}^n\mathbf{F}_{Ii} = \mathbf{0} \tag{18}$$

where the difference between the nodal external and internal force vectors will also be referred to as nodal residual force vector

$${}^n\mathbf{R}_{Fi} = {}^n\mathbf{F}_{\mathrm{NON}i} + {}^n\mathbf{F}_{\mathrm{CON}i} - {}^n\mathbf{F}_{Ii}. \tag{19}$$

For future reference, let us also define the global residual force vector ${}^n\mathbf{R}_F$, which is assembled from all nodal residual vectors ${}^n\mathbf{R}_{Fi}$ in the standard way:

Downloaded 04 May 2010 to 171.66.16.27. Redistribution subject to ASME license or copyright; see http://www.asme.org/terms/Terms_Use.cfm

$$ {}^{n}\mathbf{R}_F = \begin{pmatrix} {}^{n}\mathbf{R}_{F1} \\ {}^{n}\mathbf{R}_{F2} \\ \vdots \\ {}^{n}\mathbf{R}_{FNN} \end{pmatrix}. \tag{20} $$

Internal Force Vector. The derivation of the internal force vector follows the presentations by Germain et al. (1989) and by Saran and Wagoner (1991). The incremental plastic work associated with the deformation from time t to $t + \Delta t$ is

$$ \Delta W_P = \int_V \int_t^{t+\Delta t} \tau^{ij} D_{ij} dt dV \tag{21} $$

where τ^{ij} is the Kirchhoff stress tensor, D_{ij} is the rate of deformation tensor, and the integration is performed over the current volume. Assuming isotropic strain-hardening and the equivalent plastic work principle to hold true, the incremental plastic work can be rewritten as

$$ \Delta W_P = \int_V \int_t^{t+\Delta t} \bar{\sigma}\dot{\bar{\epsilon}} dt dV \tag{22} $$

where $\bar{\sigma}$ and $\dot{\bar{\epsilon}}$ denote the scalar effective stress and effective strain rate, respectively. Then, the effective strain increment $\Delta\bar{\epsilon}$ is defined by integrating the effective strain rate over the time increment

$$ \Delta\bar{\epsilon} = \int_t^{t+\Delta t} \dot{\bar{\epsilon}} dt. \tag{23} $$

To avoid the numerical integration of this equation, a minimum plastic work path, which is based on the assumptions that the principal directions of the rate of deformation tensor are parallel to the same material lines and the ratio of its principal values remains constant throughout the time increment, is adopted, and the effective strain rate is assumed to be constant during the time step:

$$ \Delta\dot{\bar{\epsilon}} = \frac{\Delta\bar{\epsilon}}{\Delta t}. \tag{24} $$

Under these assumptions and for a given displacement increment $\Delta\mathbf{u}$, the effective strain increment becomes a fixed function of the incremental strain tensor which can be obtained explicitly for most common yield functions. After integration over time, the variation of the incremental plastic work takes the form

$$ \delta\Delta W_P = \int_V \bar{\sigma} \frac{\partial\Delta\bar{\epsilon}}{\partial\Delta\mathbf{u}} \delta\Delta\mathbf{u} dV \tag{25} $$

resulting in the following expression for the internal force vector:

$$ \mathbf{F}_I = \int_V \bar{\sigma} \frac{\partial\Delta\bar{\epsilon}}{\partial\Delta\mathbf{u}} dV. \tag{26} $$

Using the yield criterion proposed by Hill (1979)

$$ \bar{\sigma} = [2(1 + \bar{R})]^{-1/M}[|\sigma_1 + \sigma_2|^M + (1 + 2\bar{R})|\sigma_1 - \sigma_2|^M]^{1/M} \tag{27} $$

and the equivalent plastic work principle, the associated effective strain increment can be expressed as

$$ \Delta\bar{\epsilon} = C_1[|\Delta\epsilon_1 + \Delta\epsilon_2|^{M/(M-1)} + C_2|\Delta\epsilon_1 - \Delta\epsilon_2|^{M/(M-1)}]^{(M-1)/M} $$

$$ C_1 = \tfrac{1}{2}[2(1 + \bar{R})]^{1/M} \quad C_2 = (1 + 2\bar{R})^{-[1/(M-1)]}. \tag{28} $$

Furthermore, the isotropic strain and strain rate hardening is characterized by the following relation:

$$ \bar{\sigma} = K(\bar{\epsilon} + \bar{\epsilon}_0)^n \left(\frac{\dot{\bar{\epsilon}}}{\gamma}\right)^m. \tag{29} $$

For the axisymmetric element considered here, the internal force in element i is found by integrating (26) over the current volume. An infinitesimal volume element is defined as depicted in Fig. 1:

$$ dV = rdsdtd\theta = \frac{r}{\cos\alpha_i} drdtd\theta \tag{30} $$

where

$$ \cos\alpha_i = \frac{s_{(i+1)1} - s_{i1}}{\sqrt{(s_{(i+1)1} - s_{i1})^2 + (s_{(i+1)3} - s_{i3})^2}} = \frac{s_{(i+1)1} - s_{i1}}{l_i}. \tag{31} $$

Then, the internal force is written as

$$ \mathbf{F}_{Ii} = \int_{V_i} \bar{\sigma}_i \frac{\partial\Delta\bar{\epsilon}_i}{\partial\Delta\mathbf{u}_i} dV = \int_0^{2\pi} \int_0^{t_i} \int_{s_{i1}}^{s_{(i+1)1}} \bar{\sigma}_i(r) \frac{\partial\Delta\bar{\epsilon}_i(r)}{\partial\Delta\mathbf{u}_i} \frac{r}{\cos\alpha_i} drdtd\theta = 2\pi t_i \int_{s_{i1}}^{s_{(i+1)1}} \bar{\sigma}_i(r) \frac{\partial\Delta\bar{\epsilon}_i(r)}{\partial\Delta\mathbf{u}_i} \frac{r}{\cos\alpha_i} dr. \tag{32} $$

Performing the linear transformation

$$ r(\xi) = \frac{s_{(i+1)1} - s_{i1}}{2}\xi + \frac{s_{(i+1)1} + s_{i1}}{2} \quad -1 \le \xi \le 1 \tag{33} $$

results in the following expression for the internal force vector:

$$ \mathbf{F}_{Ii} = \pi t_i l_i \int_{-1}^{1} \bar{\sigma}(\xi) \frac{\partial\Delta\bar{\epsilon}_i(\xi)}{\partial\Delta\mathbf{u}_i} \left(\frac{s_{(i+1)1} - s_{i1}}{2}\xi + \frac{s_{(i+1)1} + s_{i1}}{2}\right) d\xi = \pi t_i l_i \int_{-1}^{1} \Phi(\xi) d\xi. \tag{34} $$

Note that the integrand is a highly nonlinear function of ξ. Therefore, it is not possible to solve this integral analytically and Gauss quadrature is applied resulting in the following relation:

$$ \mathbf{F}_{Ii} = \pi t_i l_i \sum_{j=1}^{NG} w_i \Phi(\xi_i) \tag{35} $$

where ξ_i and w_i are the coordinates and the associated weights of the Gauss points and NG denotes the number of Gauss points. Using only one Gauss point with $NG = 1$, $w_1 = 2$, and $\xi_1 = 0$, the internal force vector can be found as

$$ \mathbf{F}_{Ii} = 2\pi t_i l_i \Phi(0). \tag{36} $$

External Force Vector. Let us now decompose the nonconservative nodal external force vector ${}^{n}\mathbf{F}_{\mathrm{NON}i}$ into its normal and tangential parts as follows:

$$ {}^{n}\mathbf{F}_{\mathrm{NON}i} = {}^{n}\mathbf{F}_{ni} + {}^{n}\mathbf{F}_{ti} \tag{37} $$

where

$$ {}^{n}\mathbf{F}_{ni} = \begin{pmatrix} {}^{n}F_{ni1} \\ {}^{n}F_{ni3} \end{pmatrix} \tag{38} $$

$$ {}^{n}\mathbf{F}_{ti} = \begin{pmatrix} {}^{n}F_{ti1} \\ {}^{n}F_{ti3} \end{pmatrix}. \tag{39} $$

Downloaded 04 May 2010 to 171.66.16.27. Redistribution subject to ASME license or copyright; see http://www.asme.org/terms/Terms_Use.cfm

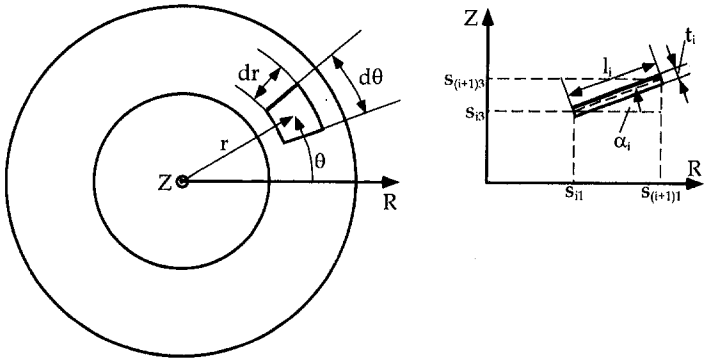

Fig. 1 Quantities used in derivation of internal force

Furthermore, let us define the magnitude of the normal component of the nonconservative nodal external force vector of contact node i as

$$ {}^{n}P_i = |{}^{n}\mathbf{F}_{ni}| = ({}^{n}F_{ni1}^2 + {}^{n}F_{ni3}^2)^{1/2}. \tag{40} $$

Then, the ever-slipping modification of Coulomb's friction law proposed by Oden and Pires (1983) is adopted to circumvent the complexities of formulating stick-slip conditions and to avoid the convergence problems associated with the discontinuous friction behavior arising from such a stick-slip friction law. This modified Coulomb friction law is governed by a smooth function of the relative displacement increment $\Delta\mathbf{u}_{\text{reltan}}$ between the node and the tool surface in the following form:

$$ \phi_i(\Delta u_{\text{reltan}i}) = \tanh\left(\frac{3|\Delta u_{\text{reltan}i}|}{\delta}\right) \tag{41} $$

In this function, δ is a small parameter. The contact force can then be written in the form:

$$ {}^{n}\mathbf{F}_{\text{NON}i} = ({}^{n}\mathbf{n}_i - \mu_i\phi_i {}^{n}\mathbf{t}_i){}^{n}P_i. \tag{42} $$

Here, ${}^{n}\mathbf{n}_i$ and ${}^{n}\mathbf{t}_i$ are the unit normal and tangential vectors at node i, and μ_i denotes the Coulomb friction coefficient at the material–tool interface which can be specified differently at all interfaces. Note that the contact force for nodes that are not in contact with the tools are set to zero. Furthermore, for future reference it is convenient to define the global vector ${}^{n}\mathbf{P}$ containing the normal contact force magnitudes of all nodes as

$$ {}^{n}\mathbf{P} = \begin{pmatrix} {}^{n}P_1 \\ {}^{n}P_2 \\ \vdots \\ {}^{n}P_{NN} \end{pmatrix}. \tag{43} $$

To express the friction forces at the sheet–tool interface, it is necessary to define normal and tangential vectors at each contact node of the mesh. As it was shown by Keum et al. (1990), it is advantageous to base the definition of these normal and tangential vectors on the geometry of the mesh rather than on that of the tool surfaces. Their definition of these nodal normal and tangential vectors was based on the slope of the mesh leading to numerical problems in vertical or near-vertical zones of the mesh. Therefore, in the current work, a different approach which avoids any reference to the slope of the mesh is used.

Tool Description. The tools are represented by functions $S(s_1)$ which are piecewise continuously differentiable everywhere in the domain except at a finite number of points representing vertical walls. Without loss of generality, the punch is assumed to move in the positive X_3-direction while the die is assumed to be stationary. Then, the die surface is defined as

$$ S_D = S_D(s_1) \tag{44} $$

and the punch surface at time ${}^{0}t$ is defined as

$$ {}^{0}S_P = {}^{0}S_P(s_1). \tag{45} $$

Assuming that the punch moves with constant velocity v_P, the total punch displacement at time ${}^{n}t$ can be calculated as

$$ {}^{n}u_P = v_P {}^{n}t \tag{46} $$

and the punch surface has translated to

$$ {}^{n}S_P(s_1, {}^{n}t) = {}^{0}S_P(s_1) + {}^{n}u_P({}^{n}t). \tag{47} $$

Contact Conditions. Consider now the frictional contact conditions at the interface between the deformable workpiece and a rigid tool surface. At equilibrium, all external and internal nodal forces have to be balanced (see (18)). At each contact node i, an additional geometric constraint has to be satisfied:

$$ {}^{n}D_i = 0, \tag{48} $$

where ${}^{n}D_i$ is the nodal distance defined as a constant multiplied by the magnitude of the nodal distance vector ${}^{n}\mathbf{d}_i$ from contact node i to the point where its normal vector intersects the tool surface. The position vector of the intersection point ${}^{n}\mathbf{s}_{Ii}$ between the normal vector of contact node i and the tool surface is defined as

$$ {}^{n}\mathbf{s}_{Ii} = \begin{pmatrix} {}^{n}s_{Ii1} \\ {}^{n}s_{Ii3} \end{pmatrix}. \tag{49} $$

Then, the nodal distance vector can be computed as

$$ {}^{n}\mathbf{d}_i = \begin{pmatrix} {}^{n}d_{i1} \\ {}^{n}d_{i3} \end{pmatrix} = {}^{n}\mathbf{s}_{Ii} - {}^{n}\mathbf{s}_i \tag{50} $$

and its absolute value follows from

$$ {}^{n}D_i = c_i|{}^{n}\mathbf{d}_i| = c_i({}^{n}d_{i1}^2 + {}^{n}d_{i3}^2)^{1/2}. \tag{51} $$

The constant c_i determines whether a contact node has intruded the tool or is located outside of the tool. It is determined uniquely by the following relation:

$$ c_i = -\text{sign}\,(\mathbf{d}_i \cdot \mathbf{n}_i). \tag{52} $$

Therefore, the nodal distance is negative for nodes that have intruded the tool and positive for nodes located outside of the tool. Note that for a node, which is not in contact with the tools, ${}^{n}D_i$ is set to zero.

For future reference, it is convenient to introduce also the global vector ${}^{n}\mathbf{D}$ containing all absolute values ${}^{n}D_i$ of the nodal distance vectors ${}^{n}\mathbf{d}_i$ as

Downloaded 04 May 2010 to 171.66.16.27. Redistribution subject to ASME license or copyright; see http://www.asme.org/terms/Terms_Use.cfm

$$ {}^{n}\mathbf{D} = \begin{pmatrix} {}^{n}D_1 \\ {}^{n}D_2 \\ \vdots \\ {}^{n}D_{NN} \end{pmatrix}. \tag{53} $$

Generalized Coordinates. At each node i, the two unknown total nodal displacement components ${}^{n}u_{i1}$, ${}^{n}u_{i3}$, and the unknown total nodal normal contact force magnitude ${}^{n}P_i$ can be combined to a vector of generalized coordinates ${}^{n}\mathbf{q}_i$ as follows:

$$ {}^{n}\mathbf{q}_i = \begin{pmatrix} {}^{n}u_{i1} \\ {}^{n}u_{i3} \\ {}^{n}P_i \end{pmatrix}. \tag{54} $$

Also, the two nodal displacement increments ${}^{n}\Delta u_{i1}$, ${}^{n}\Delta u_{i3}$, and the increment of the nodal normal contact force magnitude ${}^{n}\Delta P_i$ can be combined to a vector of generalized increments ${}^{n}\Delta\mathbf{q}_i$ as follows:

$$ {}^{n}\Delta\mathbf{q}_i = \begin{pmatrix} {}^{n}\Delta u_{i1} \\ {}^{n}\Delta u_{i3} \\ {}^{n}\Delta P_i \end{pmatrix}. \tag{55} $$

Similarly, generalized internal and external nodal force vectors which account for the additional geometric constraint can be defined for contact node i as

$$ {}^{n}\mathbf{Q}_{Ii} = \begin{pmatrix} {}^{n}\mathbf{F}_{Ii} \\ 0 \end{pmatrix} \tag{56} $$

$$ {}^{n}\mathbf{Q}_{Ei} = \begin{pmatrix} {}^{n}\mathbf{F}_{Ei} \\ {}^{n}D_i \end{pmatrix}. \tag{57} $$

The governing equations at node i can then be written as

$$ {}^{n}\mathbf{Q}_{Ei} - {}^{n}\mathbf{Q}_{Ii} = \mathbf{0}. \tag{58} $$

Introducing the nodal generalized residual vector ${}^{n}\mathbf{R}_i$ as

$$ {}^{n}\mathbf{R}_i = {}^{n}\mathbf{Q}_{Ei} - {}^{n}\mathbf{Q}_{Ii} \tag{59} $$

the governing equations at node i take the form

$$ {}^{n}\mathbf{R}_i = \mathbf{0}. \tag{60} $$

The governing equations for all NN nodes are then assembled to the consistent full set of governing equations for the system in the usual way:

$$ {}^{n}\mathbf{R}({}^{n}\Delta\mathbf{q}) = \begin{pmatrix} {}^{n}\mathbf{R}_1({}^{n}\Delta\mathbf{q}) \\ {}^{n}\mathbf{R}_2({}^{n}\Delta\mathbf{q}) \\ \vdots \\ {}^{n}\mathbf{R}_{NN}({}^{n}\Delta\mathbf{q}) \end{pmatrix} = \mathbf{0} \tag{61} $$

where in the most general case all nodal residual vectors ${}^{n}\mathbf{R}_i$ are assumed to depend on the complete global vector of generalized increments ${}^{n}\Delta\mathbf{q}$ which is assembled from all nodal vectors of generalized increments ${}^{n}\Delta\mathbf{q}_i$ as

$$ {}^{n}\Delta\mathbf{q} = \begin{pmatrix} {}^{n}\Delta\mathbf{q}_1 \\ {}^{n}\Delta\mathbf{q}_2 \\ \vdots \\ {}^{n}\Delta\mathbf{q}_{NN} \end{pmatrix}. \tag{62} $$

Equivalently, the governing equations can be expressed in terms of the conservative and nonconservative parts of the global external force vector ${}^{n}\mathbf{F}_{CON}$ and ${}^{n}\mathbf{F}_{NON}$, the global internal force vector ${}^{n}\mathbf{F}_I$ and the global distance vector ${}^{n}\mathbf{D}$ as follows:

$$ \begin{pmatrix} {}^{n}\mathbf{F}_{CON} \\ \mathbf{0} \end{pmatrix} + \begin{pmatrix} {}^{n}\mathbf{F}_{NON}({}^{n}\Delta\mathbf{u}, {}^{n}\Delta\mathbf{P}) \\ {}^{n}\mathbf{D}({}^{n}\Delta\mathbf{u}) \end{pmatrix} - \begin{pmatrix} {}^{n}\mathbf{F}_I({}^{n}\Delta\mathbf{u}) \\ \mathbf{0} \end{pmatrix} = \begin{pmatrix} \mathbf{0} \\ \mathbf{0} \end{pmatrix} \tag{63} $$

where the dependencies on the global incremental displacement vector ${}^{n}\Delta\mathbf{u}$ and the global vector ${}^{n}\Delta\mathbf{P}$ containing all incremental normal contact force magnitudes are explicitly shown.

Nonlinear Equation Solver. To solve the set of nonlinear equations (see (61)) at time ${}^{n}t$, a Taylor series expansion of the global residual vector ${}^{n}\mathbf{R}({}^{n}\Delta\mathbf{q})$ about a trial solution ${}^{n}\Delta\mathbf{q}^*$ is performed:

$$ {}^{n}\mathbf{R}({}^{n}\Delta\mathbf{q}) = {}^{n}\mathbf{R}({}^{n}\Delta\mathbf{q})|_{{}^{n}\Delta\mathbf{q}={}^{n}\Delta\mathbf{q}^*} + \left.\frac{\partial {}^{n}\mathbf{R}({}^{n}\Delta\mathbf{q})}{\partial {}^{n}\Delta\mathbf{q}}\right|_{{}^{n}\Delta\mathbf{q}={}^{n}\Delta\mathbf{q}^*} ({}^{n}\Delta\mathbf{q} - {}^{n}\Delta\mathbf{q}^*) + \ldots. \tag{64} $$

By neglecting all higher order terms and defining the global correction vector

$$ {}^{n}\delta\Delta\mathbf{q} = {}^{n}\Delta\mathbf{q} - {}^{n}\Delta\mathbf{q}^* \tag{65} $$

which makes the residual vector ${}^{n}\mathbf{R}({}^{n}\Delta\mathbf{q})$ vanish, the set of governing equations can be brought into the following form:

$$ -\left.\frac{\partial {}^{n}\mathbf{R}({}^{n}\Delta\mathbf{q})}{\partial {}^{n}\Delta\mathbf{q}}\right|_{{}^{n}\Delta\mathbf{q}={}^{n}\Delta\mathbf{q}^*} {}^{n}\delta\Delta\mathbf{q} = {}^{n}\mathbf{R}({}^{n}\Delta\mathbf{q})|_{{}^{n}\Delta\mathbf{q}={}^{n}\Delta\mathbf{q}^*}. \tag{66} $$

Then, the standard Newton-Raphson method is employed which proceeds iteratively starting from an initial guess for the global vector of generalized increments. In iteration i, a global correction vector ${}^{n}\delta\Delta\mathbf{q}^i$ is computed based on vector ${}^{n}\Delta\mathbf{q}^{i-1}$ from the previous iteration as follows:

$$ -\left.\frac{\partial {}^{n}\mathbf{R}({}^{n}\Delta\mathbf{q})}{\partial {}^{n}\Delta\mathbf{q}}\right|_{{}^{n}\Delta\mathbf{q}={}^{n}\Delta\mathbf{q}^{i-1}} {}^{n}\delta\Delta\mathbf{q}^i = {}^{n}\mathbf{R}({}^{n}\Delta\mathbf{q})|_{{}^{n}\Delta\mathbf{q}={}^{n}\Delta\mathbf{q}^{i-1}} \tag{67} $$

and then the vector of generalized increments is updated as

$$ {}^{n}\Delta\mathbf{q}^i = {}^{n}\Delta\mathbf{q}^{i-1} + {}^{n}\delta\Delta\mathbf{q}^i. \tag{68} $$

Note that the index indicating the current iteration number is shown as a post-superscript.

The iteration process is continued until certain stopping criteria are satisfied as discussed by Esche et al. (1997). Due to the nature of the present formulation, where the force-related components of the global residual vector are by several orders of magnitude larger than the distance related components, separate convergence tolerances are introduced as

$$ |{}^{n}\mathbf{F}_E^{i+1} - {}^{n}\mathbf{F}_I^{i+1}| \le \epsilon_F \tag{69} $$

$$ |{}^{n}\mathbf{D}^{i+1}| \le \epsilon_D \tag{70} $$

$$ \frac{|{}^{n}\delta\Delta\mathbf{u}^{i+1}|}{|{}^{n}\Delta\mathbf{u}^{i}|} \le \epsilon_u \tag{71} $$

$$ \frac{|{}^{n}\delta\Delta\mathbf{P}^{i+1}|}{|{}^{n}\Delta\mathbf{P}^{i}|} \le \epsilon_P \tag{72} $$

and the iteration is terminated when all four tolerance criteria are satisfied.

Finally, after achieving convergence of the increment, the global vector of generalized increments ${}^{n}\Delta\mathbf{q}$ is accumulated to the global vector of generalized coordinates ${}^{n}\mathbf{q}$ as

$$ {}^{n}\mathbf{q} = {}^{n-1}\mathbf{q} + {}^{n}\Delta\mathbf{q} \tag{73} $$

Downloaded 04 May 2010 to 171.66.16.27. Redistribution subject to ASME license or copyright; see http://www.asme.org/terms/Terms_Use.cfm

where

$$ {}^n\mathbf{q} = \begin{pmatrix} {}^n\mathbf{q}_1 \\ {}^n\mathbf{q}_2 \\ \vdots \\ {}^n\mathbf{q}_{NN} \end{pmatrix} . \tag{74} $$

In view of (63), the Newton-Raphson procedure can finally be written as

$$ \begin{bmatrix} {}^n\mathbf{K}_I^{i-1} - {}^n\mathbf{K}_{\mathrm{NON}}^{i-1} & {}^n\mathbf{N}^{i-1} \\ {}^n\mathbf{C}^{i-1} & \mathbf{0} \end{bmatrix} \begin{pmatrix} {}^n\delta\Delta\mathbf{u}^i \\ {}^n\delta\Delta\mathbf{P}^i \end{pmatrix} $$

$$ = \begin{pmatrix} {}^n\mathbf{F}_{\mathrm{CON}}^{i-1} \\ \mathbf{0} \end{pmatrix} + \begin{pmatrix} {}^n\mathbf{F}_{\mathrm{NON}}^{i-1} \\ {}^n\mathbf{D}^{i-1} \end{pmatrix} - \begin{pmatrix} {}^n\mathbf{F}_I^{i-1} \\ \mathbf{0} \end{pmatrix} \tag{75} $$

where the following notations are introduced:

$$ {}^n\mathbf{F}_I^{i-1} = {}^n\mathbf{F}_I({}^n\Delta\mathbf{u})|_{{}^n\Delta\mathbf{u}={}^n\Delta\mathbf{u}^{i-1}} \tag{76} $$

$$ {}^n\mathbf{K}_I^{i-1} = \frac{\partial {}^n\mathbf{F}_I^{i-1}}{\partial {}^n\Delta\mathbf{u}} = \left.\frac{\partial {}^n\mathbf{F}_I({}^n\Delta\mathbf{n})}{\partial {}^n\Delta\mathbf{n}}\right|_{{}^n\Delta\mathbf{u}={}^n\Delta\mathbf{u}^{i-1}} \tag{77} $$

$$ {}^n\mathbf{F}_{\mathrm{NON}}^{i-1} = {}^n\mathbf{F}_{\mathrm{NON}}({}^n\Delta\mathbf{u}, {}^n\Delta\mathbf{P})|_{{}^n\Delta\mathbf{u}={}^n\Delta\mathbf{u}^{i-1},{}^n\Delta\mathbf{P}={}^n\Delta\mathbf{P}^{i-1}} \tag{78} $$

$$ {}^n\mathbf{K}_{\mathrm{NON}}^{i-1} = \frac{\partial {}^n\mathbf{F}_{NON}^{i-1}}{\partial {}^n\Delta\mathbf{u}} $$

$$ = \left.\frac{\partial {}^n\mathbf{F}_{\mathrm{NON}}({}^n\Delta\mathbf{u}, {}^n\Delta\mathbf{P})}{\partial {}^n\Delta\mathbf{u}}\right|_{{}^n\Delta\mathbf{u}={}^n\Delta\mathbf{u}^{i-1},{}^n\Delta\mathbf{P}={}^n\Delta\mathbf{P}^{i-1}} \tag{79} $$

$$ {}^n\mathbf{N}^{i-1} = \frac{\partial {}^n\mathbf{F}_{\mathrm{NON}}^{i-1}}{\partial {}^n\Delta\mathbf{P}} = \left.\frac{\partial {}^n\mathbf{F}_{\mathrm{NON}}({}^n\Delta\mathbf{u}, {}^n\Delta\mathbf{P})}{\partial {}^n\Delta\mathbf{P}}\right|_{{}^n\Delta\mathbf{u}={}^n\Delta\mathbf{u}^{i-1},{}^n\Delta\mathbf{P}={}^n\Delta\mathbf{P}^{i-1}} \tag{80} $$

$$ {}^n\mathbf{D}^{i-1} = {}^n\mathbf{D}({}^n\Delta\mathbf{u})|_{{}^n\Delta\mathbf{u}={}^n\Delta\mathbf{u}^{i-1}} \tag{81} $$

$$ {}^n\mathbf{C}^{i-1} = \frac{\partial {}^n\mathbf{D}^{i-1}}{\partial {}^n\Delta\mathbf{u}} = \left.\frac{\partial {}^n\mathbf{D}({}^n\Delta\mathbf{u})}{\partial {}^n\Delta\mathbf{u}}\right|_{{}^n\Delta\mathbf{u}={}^n\Delta\mathbf{u}^{i-1}} . \tag{82} $$

The derivatives needed to evaluate the stiffness matrices $\mathbf{K}_I$, $\mathbf{K}_{\mathrm{NON}}$, $\mathbf{N}$, and $\mathbf{C}$ are straightforward to obtain. They can be found in the publication by Esche (1997) and are therefore omitted here.

4 Axisymmetric Bending Correction

In the current work, the method by Zhou (1993) will be extended for axisymmetric membrane elements. The formulation is based on the assumption that the bending strain is distributed linearly through the sheet thickness. The shift of the neutral fiber is neglected and thus the strain distribution is assumed to be symmetric about the middle plane of the sheet. Furthermore, it is assumed that the membrane and bending parts of the strain can be uncoupled.

The bending strain increments for the nth increment are approximated by the engineering strain increments:

$$ {}^n\Delta\epsilon_i = z\,{}^n\Delta\rho_i = z({}^n\rho_i - {}^{n-1}\rho_i) \quad i = 1, 2 \tag{83} $$

where z is the local coordinate in the sheet thickness direction, $\Delta\epsilon_1$ and $\Delta\epsilon_2$ are the principal strain increments, and $\Delta\rho_1$ and $\Delta\rho_2$ are the changes of the principal curvatures in the meridional and circumferential directions, respectively.

The principal curvatures in the radial direction are approximated by the curvatures of circles fitted through three consecutive nodes k, l, and m. The radii of these circles can be computed by two different methods. In the approach used by Zhou (1993), a system of three nonlinear equations defining the circle through the three nodes is written which is then solved for the radius and the two center point coordinates of the circle. An alternative approach is used here which is computationally more efficient. In this approach, the linear equations defining the perpendicular bisectors of the two elements that form an equivalent bending group are written.

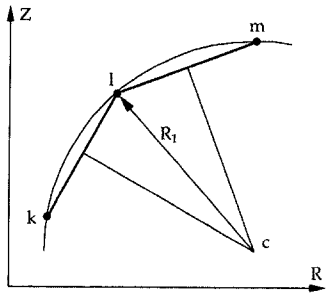

Fig. 2 Radius of curvature in radial direction based on perpendicular bisectors of elements

The intersection point of the two perpendicular bisectors is the center c of the circle through the nodes k, l, and m as depicted in Fig. 2. The coordinates of the center point are

$$ s_{c1} = \frac{\mathrm{num1}}{\mathrm{den}} \tag{84} $$

$$ s_{c3} = \frac{\mathrm{num2}}{\mathrm{den}} \tag{85} $$

where the numerators and denominator are defined as

$$ \mathrm{num1} = \tfrac{1}{2}[(s_{11}^2 - s_{k1}^2 + s_{13}^2 - s_{k3}^2)(s_{m3} - s_{13}) $$

$$ - (s_{m1}^2 - s_{11}^2 + s_{m3}^2 - s_{13}^2)(s_{13} - s_{k3})] \tag{86} $$

$$ \mathrm{num2} = \tfrac{1}{2}[(s_{m1}^2 - s_{11}^2 + s_{m3}^2 - s_{13}^2)(s_{11} - s_{k1}) $$

$$ - (s_{11}^2 - s_{k1}^2 + s_{13}^2 - s_{k3}^2)(s_{m1} - s_{11})] \tag{87} $$

$$ \mathrm{den} = (s_{11} - s_{k1})(s_{m3} - s_{13}) - (s_{m1} - s_{11})(s_{13} - s_{k3}). \tag{88} $$

The radius of curvature in the radial direction R_1 is then found from

$$ R_1 = [(s_{k1} - s_{c1})^2 + (s_{k2} - s_{c3})^2]^{1/2}. \tag{89} $$

Note that the radius of curvature R_1 determined by the equation above is always positive. Therefore, only the magnitude of the principal curvature in the radial direction is found from the inverse of the radius of curvature

$$ |\rho_1| = \frac{1}{R_1} . \tag{90} $$

The sign of the curvature is chosen from the sign of the following determinant:

$$ \mathrm{sign}\,(\rho_1) = \mathrm{sign} \begin{vmatrix} s_{k1} & s_{11} & s_{m1} \\ 1 & 1 & 1 \\ s_{k3} & s_{13} & s_{m3} \end{vmatrix} = \mathrm{sign}\,[s_{k1}(s_{m3} - s_{13}) $$

$$ - s_{11}(s_{m3} - s_{k3}) + s_{m1}(s_{13} - s_{k3})]. \tag{91} $$

Finally, the principal curvature in the radial direction can be expressed as

$$ \rho_1 = \mathrm{sign}\,(\rho_1)|\rho_1|. \tag{92} $$

The radius of curvature in the circumferential direction R_2 is identified as the radial coordinate of node l. Therefore,

Downloaded 04 May 2010 to 171.66.16.27. Redistribution subject to ASME license or copyright; see http://www.asme.org/terms/Terms_Use.cfm

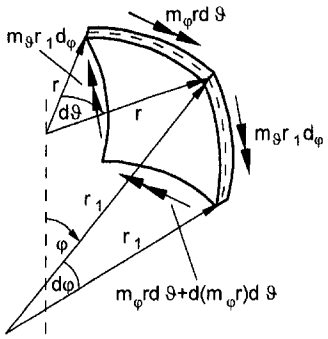

Fig. 3 Moment equilibrium for an infinitesimal axisymmetric shell element

$$^{n}\Delta\rho_2 = \frac{1}{^{n}s_{11}} - \frac{1}{^{n-1}s_{11}}. \tag{93}$$

Due to the assumed symmetry of the strain distribution with respect to the middle fiber of the sheet, only the positive range of the sheet thickness coordinate z is considered in the following derivations. Then, the effective strain increment according to the normally anisotropic yield function by Hill (1979) can be expressed as

$$\Delta\bar{\varepsilon} = Bz \tag{94}$$

where the factor B (depending both on the yield surface parameters and on the curvature changes in the meridional and circumferential directions) is defined as

$$B = \tfrac{1}{2}[2(1 + \bar{R})]^{1/M}[|\Delta\rho_1 + \Delta\rho_2|^{M/(M-1)} + (1 + 2\bar{R})^{-[1/(M-1)]}|\Delta\rho_1 - \Delta\rho_2|^{M/(M-1)}]^{(M-1)/M}. \tag{95}$$

Neglecting the strain rate dependence from (29) for reasons discussed later, the effective stress can be written as

$$\bar{\sigma} = \begin{cases} K(A + F\delta)^n \dfrac{Bz}{F\delta} & Bz \le F\delta \\ K(A + Bz)^n & Bz > F\delta \end{cases}. \tag{96}$$

If the effective strain increment Bz is less than a threshold value $F\delta$ defined here in accordance with the development by Zhou (1993), a linear pseudo-elastic behavior is assumed as proposed by Germain et al. (1989) to overcome the inherent instability problem of rigid-plastic formulations for the case of unloading regions. Otherwise, the material is assumed to follow the standard plastic hardening curve. Then, the principal stresses in the meridional and circumferential directions can be expressed as

$$\sigma_1 = \tfrac{1}{2}D_1\bar{\sigma} \quad \sigma_2 = \tfrac{1}{2}D_2\bar{\sigma} \tag{97}$$

where the constants D_1 and D_2 depend on the yield function parameters and the principal curvature changes as follows:

$$D_1 = \text{sign}\,(\Delta\rho_1 + \Delta\rho_2)\left[\frac{(1 + \bar{R})|\Delta\rho_1 + \Delta\rho_2|}{B}\right]^{1/(M-1)} + \text{sign}\,(\Delta\rho_1 - \Delta\rho_2)\left[\frac{(1 + \bar{R})|\Delta\rho_1 - \Delta\rho_2|}{(1 + 2\bar{R})B}\right]^{1/(M-1)}$$

$$D_2 = \text{sign}\,(\Delta\rho_1 + \Delta\rho_2)\left[\frac{(1 + \bar{R})|\Delta\rho_1 + \Delta\rho_2|}{B}\right]^{1/(M-1)} - \text{sign}\,(\Delta\rho_1 - \Delta\rho_2)\left[\frac{(1 + \bar{R})|\Delta\rho_1 - \Delta\rho_2|}{(1 + 2\bar{R})B}\right]^{1/(M-1)}. \tag{98}$$

To determine the bending moments causing the curvature changes above, let us consider the static moment equilibrium about an axis, which is tangential to the circumference of an infinitesimal axisymmetric shell element as shown in Fig. 3. This represents standard shell theory as discussed by Göldner (1989).

Then, the moment balance can be written as follows:

$$m_\varphi r d\vartheta - [m_\varphi r + d(m_\varphi r)]d\vartheta - m_\varphi \cos\varphi r_1 d\varphi d\vartheta = 0 \tag{99}$$

where the moments per arc length are defined as

$$m_\varphi = \int_{-t/2}^{t/2} \sigma_\varphi z dz \quad m_\vartheta = \int_{-t/2}^{t/2} \sigma_\vartheta z dz. \tag{100}$$

Then, (99) is integrated in the circumferential direction. The first term represents the total bending moment at the upper rim of the conical surface of infinitesimal height

$$M_\varphi = \int_0^{2\pi} m_\varphi r d\vartheta = 2\pi r m_\varphi. \tag{101}$$

The second term represents the total bending moment at the lower rim of this surface

$$M_\varphi + dM_\varphi = \int_0^{2\pi} [m_\varphi r + d(m_\varphi r + d(m_\varphi r)]d\vartheta = 2\pi r m_\varphi + 2\pi d(m_\varphi r). \tag{102}$$

Integrating the third term gives

$$\int_0^{2\pi} m_\vartheta \cos\varphi r_1 d\varphi d\vartheta = 2\pi \cos\varphi r_1 d\varphi m_\vartheta. \tag{103}$$

Canceling M_ϑ from the equation shows that

$$dM_\varphi = 2\pi d(m_\varphi r) = 2\pi \cos\varphi r_1 d\varphi m_\vartheta. \tag{104}$$

Replacing the infinitesimal axisymmetric shell element considered above by a group of two finite elements i and $i + 1$ formed by the nodes i, $i + 1$, and $i + 2$ with the radial coordinates r_i, r_{i+1}, and r_{i+2} as depicted in Fig. 4, and by associating the meridional arc length $r_1 d\varphi$ with the sum of the lengths l_i and l_{i+1} of the two finite elements as shown in Fig. 4, the corresponding moments can be written as

$$M = 2\pi r_{i+1} 2\int_0^{t/2} \sigma_1 z dz = 2\pi r_{i+1} D_1 \int_0^{t/2} \bar{\sigma} z dz \tag{105}$$

$$\Delta M = 2\pi(1_i + 1_{i+1}) \cos\varphi 2 \int_0^{t/2} \sigma_2 z dz = 2\pi(1_i + 1_{i+1}) \cos\varphi D_2 \int_0^{t/2} \bar{\sigma} z dz. \tag{106}$$

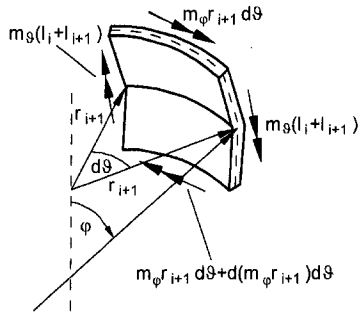

Fig. 4 Statically equivalent axisymmetric bending group

Downloaded 04 May 2010 to 171.66.16.27. Redistribution subject to ASME license or copyright; see http://www.asme.org/terms/Terms_Use.cfm

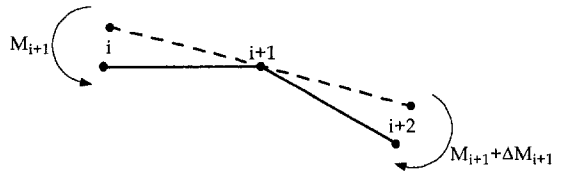

Fig. 5 Equivalent bending group

To determine the bending moments, the principal bending stress has to be integrated through the sheet thickness. Due to the assumed symmetry of the strain distribution about the middle plane of the sheet, the integration is performed only for the positive range of z and the resulting integral values are doubled. Two cases are distinguished for the integrations. In the first case, where the effective bending strain increment at the outer tension fiber is less than or equal to the threshold value, the bending moments become

$$M = \frac{2\pi r_{i+1} D_1 KB}{F\delta}(A + F\delta)^n \int_0^{t/2} z^2 dz = \frac{\pi r_{i+1} D_1 KBt^3}{12F\delta}(A + F\delta)^n \tag{107}$$

$$\Delta M = \frac{2\pi(l_i + l_{i+1})\cos\varphi D_2 KB}{F\delta}(A + F\delta)^n \int_0^{t/2} z^2 dz = \frac{\pi(l_i + l_{i+1})\cos\varphi D_2 KBt^3}{12F\delta}(A + F\delta)^n. \tag{108}$$

In the other case, where the effective bending strain increment at the outer tension fiber is larger than the threshold value, the integrations lead to

$$\begin{aligned} M &= 2\pi r_{i+1} D_1 \int_0^{F\delta/B} \bar{\sigma} z dz + 2\pi r_{i+1} D_1 \int_{F\delta/B}^{t/2} \bar{\sigma} z dz \\ &= \frac{2\pi r_{i+1} D_1 KB}{F\delta}(A + F\delta)^n \int_0^{F\delta/B} z^2 dz \\ &\quad + 2\pi r_{i+1} D_1 K \int_{F\delta/B}^{t/2} (A + Bz)^n z dz \\ &= \frac{2\pi r_{i+1} D_1 KF^2\delta^2}{3B^2}(A + F\delta)^n + 2\pi r_{i+1} D_1 K \\ &\quad \times \left[\frac{t\left(A + B\frac{t}{2}\right)^{n+1}}{2B(n+1)} - \frac{F\delta(A + F\delta)^{n+1}}{B^2(n+1)} \right. \\ &\quad \left. + \frac{(A + F\delta)^{n+2}}{B^2(n+1)(n+2)} - \frac{\left(A + B\frac{t}{2}\right)^{n+2}}{B^2(n+1)(n+2)} \right] \end{aligned} \tag{109}$$

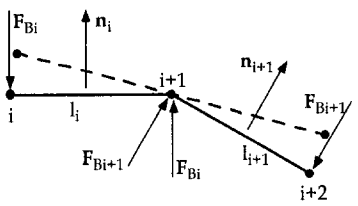

Fig. 6 Statically equivalent bending force couples

Table 1 Material parameters for aluminum AA1100-O

Density	2.7 g/cm^3
Young's modulus	68.95 GPa
Poisson's ratio	0.33
Yield strength	34.48 MPa
Normal anisotropy	0.8955
Hill's yield surface shape factor	2
Strength coefficient	161.6 MPa
Initial strain	0
Strain hardening exponent	0.2297
Strain rate hardening exponent	0

$$\begin{aligned} \Delta M &= 2\pi(l_i + l_{i+1})\cos\varphi D_2 \int_0^{F\delta/B} \bar{\sigma} z dz \\ &\quad + 2\pi(l_i + l_{i+1})\cos\varphi D_2 \int_{F\delta/B}^{t/2} \bar{\sigma} z dz \\ &= \frac{2\pi(l_i + l_{i+1})\cos\varphi D_2 KB}{F\delta}(A + F\delta)^n \int_0^{F\delta/B} z^2 dz \\ &\quad + 2\pi(l_i + l_{i+1})\cos\varphi D_2 K \int_{F\delta/B}^{t/2} (A + Bz)^n z dz \\ &= \frac{2\pi(l_i + l_{i+1})\cos\varphi KD_2 F^2\delta^2}{3B^2}(A + F\delta)^n \\ &\quad + 2\pi(l_i + l_{i+1})\cos\varphi D_2 K \\ &\quad \times \left[\frac{t\left(A + B\frac{t}{2}\right)^{n+1}}{2B(n+1)} - \frac{F\delta(A + F\delta)^{n+1}}{B^2(n+1)} \right. \\ &\quad \left. + \frac{(A + F\delta)^{n+2}}{B^2(n+1)(n+2)} - \frac{\left(A + B\frac{t}{2}\right)^{n+2}}{B^2(n+1)(n+2)} \right]. \end{aligned} \tag{110}$$

While in the first case the integrals can be solved straightforwardly, the second couple of integrals have to be solved using integration by parts. In order to be able to perform this integration analytically (thus avoiding numerical integration through the sheet thickness), the strain-rate-dependent factor of the hardening law used in the membrane element (refer to (29)) has been neglected in (96). Neglecting this term is justifiable since the errors introduced by decoupling the membrane and bending strains and by using the engineering strain increments (refer to (83)) instead of the true strain increments in (8) and (9) are likely to be larger than the error made by neglecting the strain-rate dependence (for common values of the strain-rate sensitivity exponent m).

Finally, the bending moments M_{i+1} and ΔM_{i+1} for each equivalent bending group containing elements i and $i + 1$ formed by nodes i, $i + 1$, and $i + 2$ (see Fig. 5) are converted into two statically equivalent nodal bending force couples $\mathbf{F}_{Bi}$ and $\mathbf{F}_{Bi+1}$ using the element lengths l_i and l_{i+1} (refer to (7)) and normal vectors $\mathbf{n}_i$ and $\mathbf{n}_{i+1}$ of the two elements forming the equivalent bending group (see Fig. 6):

$$\mathbf{F}_{Bi} = \frac{M_{i+1}}{l_i}\mathbf{n}_i \quad \mathbf{F}_{Bi+1} = \frac{M_{i+1} + \Delta M_{i+1}}{l_{i+1}}\mathbf{n}_{i+1}. \tag{111}$$

5 Numerical Verification

To verify numerically the axisymmetric bending correction derived above, two cup drawings with different geometries and

Table 2 Process parameters for cup drawing from aluminum AA1100-O

Friction coefficient	0.09
Blankholder force	38.2 kN
Total punch travel	86 mm

Downloaded 04 May 2010 to 171.66.16.27. Redistribution subject to ASME license or copyright; see http://www.asme.org/terms/Terms_Use.cfm

Table 3 Blank and tool geometries for cup drawing from aluminum AA1100-O

Blank diameter	254 mm
Blank thickness	0.81 mm
Die opening diameter	158.2 mm
Die corner radius	16 mm
Punch diameter	152.4 mm
Punch corner radius	20 mm

from different materials are simulated here applying the new membrane element with bending correction. The draw-in of the cup rim and the punch force as functions of the punch travel as well as the true radial and circumferential strain distributions for the solutions with and without bending correction are compared with experimental data whenever available.

The first example chosen here is the drawing of a round cup from aluminum AA1100-O as performed by Ahmetoglu (1993). The blank is fully drawn to a punch travel of 86 mm without any flange left. The material properties are summarized in Table 1, and the process parameters are shown in Table 2. The blank and tool geometries are given in Table 3. For a mesh with 21 elements, the simulation took 4 s on an IBM Risc 6000 workstation for the pure membrane case and about three times longer using the element with bending correction.

In Fig. 7, the draw-in of the cup rim is displayed for the drawing of the aluminum AA1100-O cup. Only the simulation results are plotted because experimental data for the draw-in were not available. Both elements give virtually identical draw-in curves.

The punch force curves for the aluminum AA1100-O cup drawing are given in Fig. 8. As expected, the introduction of additional stiffness slightly increases the peak value of the punch force. Figure 9 compares the true radial and circumferential strain distributions for the aluminum AA1100-O cup drawing. The experimentally determined circumferential strain distribution was not available. Since in this example the tool radii are large compared with the sheet thickness, the bending is not expected to have any influence on the strain distributions. This is confirmed by the close proximity of the strain curves, which slightly underpredict the peak radial strain compared with the experimental findings. The results are within engineering accuracy. Note that a friction coefficient of 0.09 was used in the simulations as suggested by Ahmetoglu (1993). A sensitivity analysis performed by Esche and Kinzel (1998) revealed that the slight discrepancy in the maximum punch force value can be compensated without causing significant changes in the draw-in curves and strain distributions by varying slightly the friction coefficient.

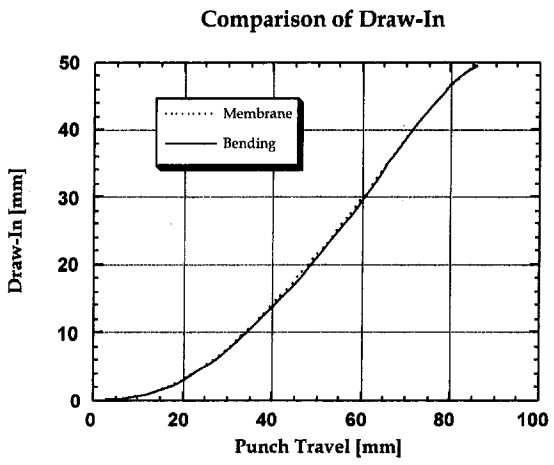

Fig. 7 Draw-in with and without bending for cup drawing from aluminum AA1100-O

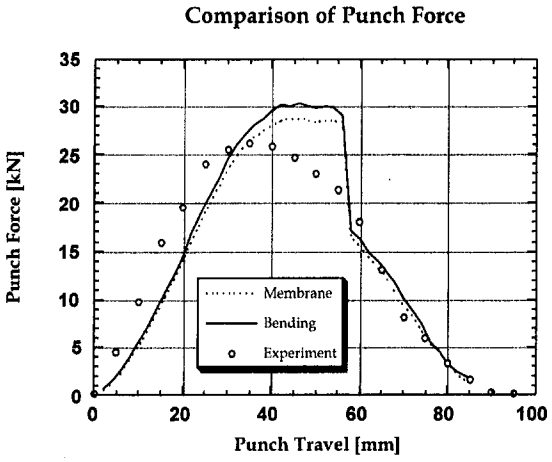

Fig. 8 Punch force with and without bending for cup drawing from aluminum AA1100-O

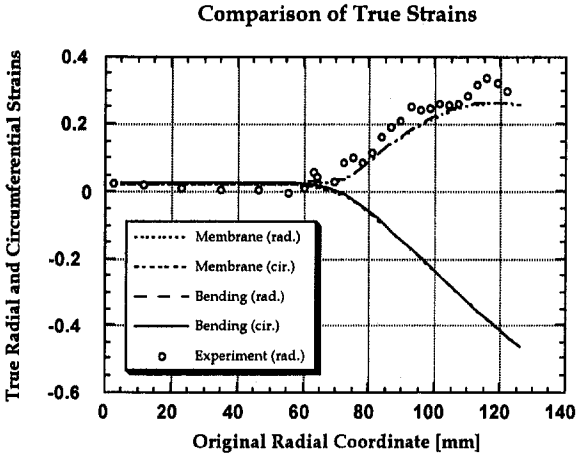

Fig. 9 True strains with and without bending for cup drawing from aluminum AA1100-O

The second experiment simulated here is the partial drawing of a round cup from deep-drawing quality steel as reported by Saran et al. (1990). The blank is formed into a partially drawn cup with a total punch travel of 40 mm. The material characteristics of this low carbon steel for automotive applications are summarized in Table 4, and the process parameters are given in Table 5. Note that a friction coefficient of 0.14 was used in

Table 4 Material parameters for deep drawing quality steel

Density	7.85 g/cm^3
Young's modulus	210 GPa
Poisson's ratio	0.3
Yield strength	220 MPa
Normal anisotropy	1.65
Hill's yield surface shape factor	2
Strength coefficient	547 MPa
Initial strain	0
Strain hardening exponent	0.18
Strain rate hardening exponent	0

Table 5 Process parameters for cup drawing from deep drawing quality steel

Friction coefficient	0.14
Blankholder force	80 kN
Total punch travel	40 mm

Downloaded 04 May 2010 to 171.66.16.27. Redistribution subject to ASME license or copyright; see http://www.asme.org/terms/Terms_Use.cfm

Table 6 Blank and tool geometries for cup drawing from deep drawing quality steel

Blank diameter	200 mm
Blank thickness	0.7 mm
Die opening diameter	102.5 mm
Die corner radius	5 mm
Punch diameter	100 mm
Punch corner radius	13 mm

the simulations contrary to the value of 0.22 suggested by the authors of the above paper since the higher friction coefficient led to strain localization for both the formulations with and without bending correction. The blank and tool geometries are shown in Table 6. The simulation with 38 pure membrane elements required a CPU time of 12 s on an IBM Risc 6000 workstation while the inclusion of the bending terms increased that time by a factor of about three.

In the second example considered here, the die corner radius is relatively small compared with the sheet thickness. Therefore, the bending is expected to cause a noticeable change compared with the pure membrane results. This is confirmed in Fig. 10 where the draw-in of the sheet rim of the deep-drawing quality steel cup is slightly lower when including the bending stiffness. Both simulations produce close approximations of the experimental measurements. In Fig. 11, the punch force is plotted as a function of the punch travel. Both simulations give good estimates for the measured punch force curves and again, the bending correction causes a slight increase in the maximum punch force as depicted in Fig. 11. The true radial and circumferential strain distributions shown in Fig. 12 are in good agreement with the experimental measurements for both strain components. When including the bending terms into the formulation, the radial strain is seen to increase slightly in the cup wall while at the same time decreasing by a small amount in the flange. The circumferential strain drops slightly.

In summary, it can be stated that for round cup drawings with common geometries the bending correction has very little influence on the draw-in of the sheet rim and the strain distributions while requiring significantly more CPU time. This phenomenon is due mainly to three reasons: First, the bending terms of the internal force vector and the internal stiffness matrix have to be evaluated in addition to the membrane terms. Second, a number of nodes that for the membrane formulation stay in contact with one of the tool surfaces lift up due to the bending stiffness. This leads to additional CPU time spent on establishing the appropriate contact status for all nodes. Third, the inclusion of the bending terms increases the bandwidth of the linear

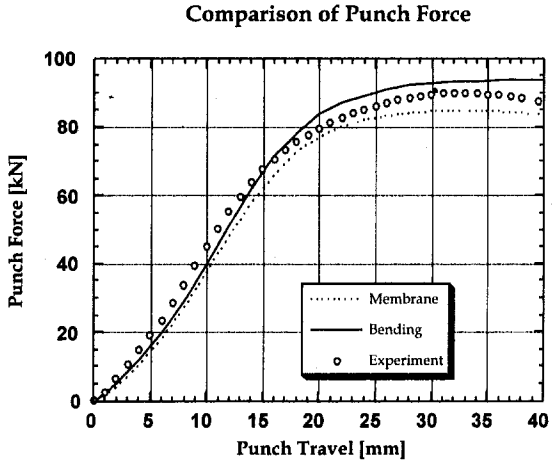

Fig. 11 Punch force with and without bending for cup drawing from deep drawing quality steel

system of equations to be solved in each iteration. Therefore, the inclusion of the bending terms into the membrane element is only recommended for cases with very sharp tool corners and for the simulation of multistage drawing operations where its application prevents numerical buckling observed with pure membrane formulations.

6 Summary and Conclusions

The correct modeling of the bending characteristics of sheet metals is crucial for the simulation of deep drawing processes with the finite element method, especially for processes with small ratios of radius of curvature to thickness of the sheet and when the exact shape of the final part is of importance. In addition, numerical buckling effects prevent simulations of redrawing processes of round cups from being performed successfully with pure membrane finite elements. This paper reviews techniques to include the bending behavior of sheet metals into finite element method formulations. Then, a new, numerically efficient bending correction for the implementation into axisymmetric membrane elements is developed. The accuracy of the implementation of this bending correction into an implicit finite element program is demonstrated by analyzing two round cup drawings for which experimental measurements were available from the literature. For large radius of curvature-to-thickness ratios, the draw-in of the sheet rim and the radial and circumferential strain distributions were shown to be almost unaffected

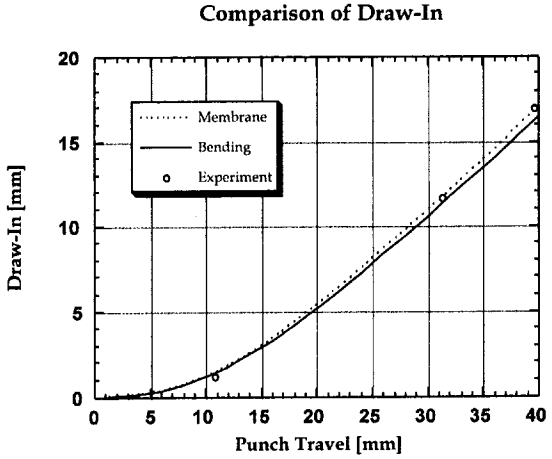

Fig. 10 Draw-in with and without bending for cup drawing from deep drawing quality steel

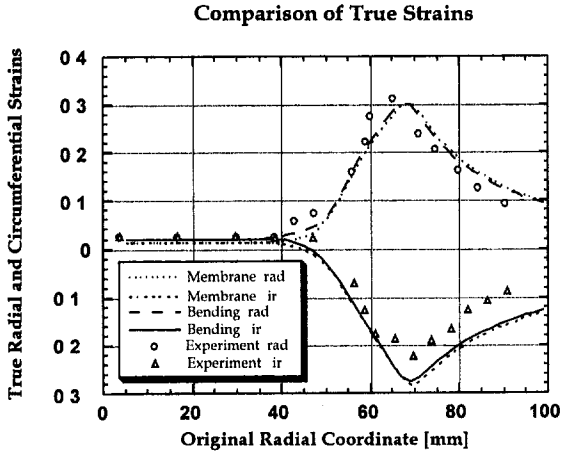

Fig. 12 True strains with and without bending for cup drawing from deep drawing quality steel

Downloaded 04 May 2010 to 171.66.16.27. Redistribution subject to ASME license or copyright; see http://www.asme.org/terms/Terms_Use.cfm

by the bending correction, while for small ratios, the differences become noticeable. The punch force was shown elsewhere to be mainly influenced by the friction coefficient at the sheet tool interfaces for which accurate values are hard to obtain. Due to the additional computational effort compared with a pure membrane formulation, the application of the proposed bending correction is suggested to be used only for bending-dominated cases. Furthermore, this bending correction is a computationally efficient approach to overcome the numerical buckling phenomena encountered in simulations of multistage drawing processes with pure membrane formulations.

Acknowledgment

This work was funded by the Engineering Research Center for Net Shape Manufacturing (ERC/NSM) at The Ohio State University, by the Edison Materials Technology Center (EMTEC) and by the Center for Advanced Materials and Manufacturing of Automotive Components (CAMMAC). This financial support is gratefully acknowledged. Furthermore, we are indebted to Dr. Mustafa A. Ahmetoglu for allowing us to use his experimental data as test cases for the developed software.

References

Agelet de Saracibar, C., and Oñate, E., 1990, "Finite element analysis of sheet metal forming problems using a selective bending/membrane formulation," *Proceedings of the 3rd ICTP,* Vol. 3, pp. 1409–1416.

Ahmetoglu, M. A., 1993, "A computer-aided engineering system for process design in sheet metal forming," Ph.D. dissertation, The Ohio State University, Columbus, OH.

Brunet, M., and Sabourin, F., 1995, "Simplified triangular shell element with a necking criterion for 3-D sheet-forming analysis," *Journal of Materials Processing Technology,* Vol. 50, pp. 238–251.

Budiansky, B., 1968, "Notes on Nonlinear Shell Theory," ASME JOURNAL OF APPLIED MECHANICS, Vol. 35, pp. 393–401.

Chung, T. J., 1988, *Continuum Mechanics,* Prentice-Hall, Englewood Cliffs, NJ.

Esche, S. K., 1997, "Developments for two-dimensional sheet metal forming analysis," Ph.D. dissertation, The Ohio State University, Columbus, OH.

Esche, S. K., Kinzel, G. L., and Altan, T., 1997, "Issues in convergence improvements for nonlinear finite element programs," *International Journal for Numerical Methods in Engineering,* Vol. 40, pp. 4577–4594.

Esche, S. K., and Kinzel, G. L., 1998, "The effect of modeling parameters and bending on two-dimensional sheet metal forming simulation," *Developments in Sheet Metal Stamping,* SAE SP-1322, pp. 87–98.

Germain, Y., Chung, K., and Wagoner, R. H., 1989, "A rigid-viscoplastic finite element program for sheet metal forming analysis," *International Journal of Mechanical Sciences,* Vol. 31, pp. 1–24.

Göldner, H., 1989, *Lehrbuch Höhere Festigkeitslehre,* VEB Fachbuchverlag, Leipzig.

Han, S. S., and Huh, H., 1995, "Modified-membrane finite-element simulation of square cup drawing processes considering influence of geometric parameters," *Journal of Materials Processing Technology,* Vol. 48, pp. 81–87.

Hill, R., 1979, "Theoretical plasticity of textured aggregates," *Mathematical Proceedings of the Cambridge Philosophical Society,* Vol. 85, pp. 179–191.

Huh, H., Han, S. S., and Yang, D. Y., 1993, "Rational finite element formulation for a membrane element in sheet metal forming analysis," *Proceedings of the 4th ICTP,* Vol. 3, pp. 1529–1534.

Huh, H., Han, S. S., and Yang, D. Y., 1994, "Modified membrane finite element formulation considering bending effect in sheet metal forming analysis," *International Journal of Mechanical Sciences,* Vol. 36, pp. 659–671.

Keum, Y. T., Nakamachi, E., Wagoner, R. H., and Lee, J. K., 1990, "Compatible description of tool surfaces and FEM meshes for analyzing sheet forming operations," *International Journal for Numerical Methods in Engineering,* Vol. 30, pp. 1471–1502.

Kim, J. H., Oh, S. I., and Kobayashi, S., 1978, "Analysis of stretching of sheet metals with hemispherical punch," *International Journal of Machine Tool Design and Research,* Vol. 18, pp. 209–226.

Lee, J. K., Cho, U. Y., Hambrecht, J., and Choudhry, S., 1991, "Recent advances in sheet metal forming analysis," *Advances in Finite Deformation Problems in Materials Processing and Structures,* Winter Annual Meeting of the ASME, AMD-Vol. 125, pp. 119–130.

Makowski, J., and Nolte, L.-P., 1987, "Simple equations in terms of displacements for finite axisymmetric deflections of shells of revolution," *International Journal of Non-Linear Mechanics,* Vol. 22, pp. 1–13.

Nakamachi, E., 1992, "Anisotropic elastic-plastic finite element simulation of 3-D sheet forming processes," *Proceedings of the 4th International Conference on Numerical Methods in Industrial Forming Processes: NUMIFORM 92,* pp. 509–514.

Nakamachi, E., and Wagoner, R. H., 1992, "Finite element simulation of sheet forming using an efficient shell model," *Proceedings of the 3rd International Conference on Computational Plasticity: COMPLAS 92,* pp. 1263–1276.

Oden, J. T., and Pires, E. B., 1983, "Nonlocal and Nonlinear Friction Law and Variational Principles for Contact Problems in Elasticity," ASME JOURNAL OF APPLIED MECHANICS, Vol. 50, pp. 67–76.

Oñate, E., Agelet de Saracibar, C., and Dalin, J. B., 1989, "Finite element analysis of sheet metal forming problems using a selective voided viscous shell membrane formulation," *Proceedings of the 4th International Conference on Numerical Methods in Industrial Forming Processes: NUMIFORM 89,* pp. 23–30.

Oñate, E., and Agelet de Saracibar, C., 1990, "Finite element analysis of sheet metal forming problems using a selective viscous bending/membrane formulation," *International Journal for Numerical Methods in Engineering,* Vol. 30, pp. 1577–1593.

Oñate, E., Cendoya, P., Rojek, J., and Miquel, J., 1996, "A simple thin shell triangle with translational degrees of freedom for sheet stamping analysis," *Proceedings of the 3rd International Conference on Numerical Simulation of 3-D Sheet Metal Forming, NUMISHEET 96,* pp. 102–111.

Oñate, E., and Cervera, M., 1993, "Derivation of thin plate bending elements with one degree of freedom per node: A simple three node triangle," *Engineering Computations,* Vol. 10, pp. 543–561.

Pourboghrat, F., and Chandorkar, K., 1992, "Springback calculation for plane strain sheet forming using finite element membrane solution," *Numerical Methods for Simulation of Industrial Metal Forming Processes,* M. J. Saran, A. B. Pifko, N. Kikuchi, and K. K. Tamma, eds., ASME, CED-Vol. 5, pp. 85–93.

Quoirin, D., 1992, "FEM modeling of 2D sheet metal forming processes," *Proceedings of the 4th International Conference on Numerical Methods in Industrial Forming Processes: NUMIFORM 92,* pp. 527–533.

Sadagopan, S., 1997, "Adding bending resistance to 3-d membrane finite element programs," Ph.D. dissertation, The Ohio State University, Columbus, OH.

Saran, M. J., Keum, Y. T., and Wagoner, R. H., 1991, "Section analysis with irregular tools and arbitrary draw-in conditions for numerical simulation of sheet forming," *International Journal of Mechanical Sciences,* Vol. 33, pp. 893–909.

Saran, M. J., Schedin, E., Samuelsson, A., Melander, A., and Gustafsson, C., 1990, "Numerical and experimental investigations of deep drawing of metal sheets," ASME *Journal of Engineering for Industry,* Vol. 112, pp. 272–277.

Saran, M. J., and Wagoner, R. H., 1991, "A Consistent Implicit Formulation for Nonlinear Finite Element Modeling With Contact and Friction: Part I—Theory," ASME JOURNAL OF APPLIED MECHANICS, Vol. 58, pp. 499–506.

Stoughton, T. B., 1985, "Finite element modeling of 1008 AK sheet steel stretched over a rectangular punch with bending effects. Computer modeling of sheet metal forming process; theory, verification and application," N. M. Wang, and S. C. Tang, eds., *Publication of The Metallurgical Society of AIME,* pp. 143–159.

Wang, C., 1993, "Mechanics of bending, flanging, and deep drawing and a computer-aided modeling system for predictions of strain, fracture, wrinkling and springback in sheet metal forming," Ph.D. dissertation, The Ohio State University, Columbus, OH.

Wang, C., and Wagoner, R. H., 1991, "Square punch forming: section analysis and bending study," *SAE Transactions,* Vol. 100, pp. 742–750.

Wang, N. M., 1982, "A mathematical model of draw bead forces in sheet metal forming," *Journal of Applied Metalworking,* Vol. 2, pp. 193–199.

Wang, N. M., 1984, "A rigid-plastic rate-sensitive finite element method for modeling sheet metal forming processes," *Numerical Analysis of Forming Processes,* J. F. T. Pittman, O. C. Zienkiewicz, R. D. Wood, and J. M. Alexander, eds., John Wiley and Sons, New York, pp. 117–164.

Yang, D. Y., Jung, D. W., Song, I. S., Yoo, D. J., and Lee, J. H., 1995, "Comparative investigation into implicit, explicit, and iterative implicit/explicit schemes for the simulation of sheet-metal forming processes," *Journal of Materials Processing Technology,* Vol. 50, pp. 39–53.

Yoo, D. J., Song, I. S., Yang, D. Y., and Lee, J. H., 1994, "Rigid-plastic finite element analysis of sheet metal forming processes using continuous contact treatment and membrane elements incorporating bending effects," *International Journal of Mechanical Sciences,* Vol. 36, pp. 513–546.

Zhou, D., 1993, "Development and testing of a new algorithm for FEM of sheet forming," Ph.D. dissertation, The Ohio State University, Columbus, OH.

Zhou, D., and Wagoner, R. H., 1995, "Development and application of sheet forming simulation," *Journal of Materials Processing Technology,* Vol. 50, pp. 1–16.

Downloaded 04 May 2010 to 171.66.16.27. Redistribution subject to ASME license or copyright; see http://www.asme.org/terms/Terms_Use.cfm

The Elastic Field of an Elliptic Cylindrical Inclusion in a Laminate With Multiple Isotropic Layers

H. G. Beom[1]
Department of Mechanical Engineering,
College of Engineering,
Chonnam National University,
300, Yongbong-dong,
Kwangju 500-757, Korea

Y. Y. Earmme
Department of Mechanical Engineering,
Korea Advanced Institute of
Science and Technology,
Kusong-dong, Yusung-gu,
Taejon 305-701, Korea

An elliptic cylindrical inclusion with an eigenstrain in an infinite laminate composed of multiple isotropic layers is analyzed. The problem is formulated by using the classical laminated plate theory in which displacement fields in the laminated plate are expressed in terms of in-plane displacements on the main plane and transverse displacement. Employing a method based on influence functions, an integral type solution to the equilibrium equation is expressed in terms of the eigenstrain. Closed-form solutions for the elastic fields are obtained by evaluating the integrals explicitly for interior points and exterior points of the ellipse. The elastic fields caused by an elliptic cylindrical inhomogeneity with an eigenstrain in the infinite laminate are determined by the equivalent eigenstrain method. Solutions for a finite laminate with an eigenstrain in a circular cylindrical inhomogeneity are also obtained in terms of material and geometric parameters for each layer composing the laminate.

1 Introduction

Studies on an ellipsoidal inclusion or inhomogeneity embedded in a three-dimensional elastic solid have been widely performed since the pioneering work of Eshelby (1957) for an ellipsoidal inclusion in which a uniform eigenstrain is prescribed. The remarkable solution has found a wide range of applications in various kinds of mechanical problems such as inclusions, inhomogeneity, cracks, and effective material properties. A detailed exposition of the topic in the mechanical context can be found in the book by Mura (1987). These works, however, are concerned with a three-dimensional solid containing an eigenstrain. The problem of a thin laminate containing an eigenstrain has not yet been solved.

Multilayers bonded together have found wide engineering applications such as in microelectronic devices (Lau, 1993). Deformation of multilayers containing inclusions has recently gained importance in the microelectronic industry, due to its potential application in various kinds of technological problems (Finot and Suresh, 1996; Freund, 1996). These layered structures used in electronics packages are assembled at elevated temperatures and then cooled. The different coefficients of thermal expansion of the constituent materials can cause the laminate to bend. Warpage of the multilayered plate containing inclusion causes assembly problems.

Recently, Beom (1998) solved the elastic field due to eigencurvature in an elliptic inclusion surrounded by an infinite single layer plate. The analysis of an uncoupled plate, such as a single layer plate or a symmetric laminate, usually entails two uncoupled problems, the one of pure in-plane deformations and the other of transverse deformations. However, the in-plane and transverse displacements of a laminated plate are in general coupled. This coupling makes it difficult to obtain exact closed-form solutions, while on the other hand the analytical solutions for a single layer can be generated without too much difficulty in some instances because of simpler mathematics involved.

It is the purpose of this study to investigate the problem of an infinite laminate with an eigenstrain in an elliptic cylindrical zone. The laminate is composed of isotropic linear elastic materials. The eigenstrain varies through the thickness of the laminate. The problem is formulated by using classical laminated plate theory in which the displacement fields in the laminated plate are expressed in terms of the in-plane displacements on the main plane and the transverse displacement. Employing a method based on influence functions, which is an extension of the Maysel's relation (Maysel, 1941; Nowacki, 1962; Ziegler and Irschik, 1987) to laminate problems, an integral type solution to the equilibrium equation is expressed in terms of the eigenstrain. Closed-form solutions for the elastic fields are then obtained by evaluating the integrals explicitly for the interior points and exterior points of the ellipse. An infinite laminate containing an elliptic cylindrical inhomogeneity in which an eigenstrain is prescribed through the thickness is considered. The elastic fields caused by the inhomogeneity with the eigenstrain are determined by the equivalent eigenstrain method, which is an extension of the equivalent inclusion method proposed for an ellipsoidal inhomogeneity problem by Eshelby (1957). Solutions for a laminate with the eigenstrain in a circular cylindrical zone are obtained as a special case and presented in terms of material and geometric parameters for each layer composing the laminate. Thermal deformation of a circular laminate is also considered to illustrate the effect of inhomogeneity on in-plane deformation and warpage of the laminate.

2 Formulation

Consider a deformation of an infinite plate composed of thin layers of isotropic linear elastic materials. The cross section of such a plate is shown schematically in Fig. 1. The plate has a constant thickness h. The tractions vanish at infinity. An eigenstrain ϵ_{ij}^{*} is prescribed in an elliptic cylindrical inclusion with a height h and a constant elliptic cross section Ω. The eigenstrain ϵ_{ij}^{*} is assumed to vary only through the thickness.

[1] To whom correspondence should be addressed.

Contributed by the Applied Mechanics Division of THE AMERICAN SOCIETY OF MECHANICAL ENGINEERS for publication in the ASME JOURNAL OF APPLIED MECHANICS.

Discussion on the paper should be addressed to the Technical Editor, Professor Lewis T. Wheeler, Department of Mechanical Engineering, University of Houston, Houston, TX 77204-4792, and will be accepted until four months after final publication of the paper itself in the ASME JOURNAL OF APPLIED MECHANICS.

Manuscript received by the ASME Applied Mechanics Division, Nov. 26, 1997; final revision, July 13, 1998. Associate Technical Editor: M.-J. Pindera.

 Copyright © 1999 by ASME

Downloaded 04 May 2010 to 171.66.16.27. Redistribution subject to ASME license or copyright; see http://www.asme.org/terms/Terms_Use.cfm

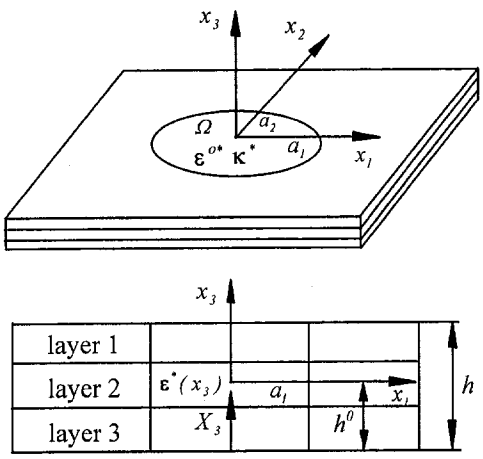

Fig. 1 Infinite plate containing an elliptic cylindrical inclusion with an eigenstrain

According to the classical laminated plate theory, the displacements at any point of a plate are written as (Jones, 1975)

$$u_i = u_i^0 - x_3 w_{,i}(x_1, x_2), \quad (i = 1, 2),$$
$$u_3 = w(x_1, x_2), \tag{1}$$

where u_i and u_3 are the in-plane and transverse displacements, respectively, u_i^0 is the in-plane displacement on *the main plane* which will be defined exactly later, and the subscript comma (,) denotes a partial derivative with respective to the in-plane Cartesian coordinates, x_1 and x_2. The constitutive relations for the laminated plate can be written as

$$N_{ij} = A_{ijkl}(\epsilon_{kl}^0 - \epsilon_{kl}^{0*}) + B_{ijkl}\kappa_{kl},$$
$$M_{ij} = B_{ijkl}\epsilon_{kl}^0 + D_{ijkl}(\kappa_{kl} - \kappa_{kl}^*). \tag{2}$$

Here N_{ij} and M_{ij} are the resultant stress and moment defined as $N_{ij} = \int_{-h^0}^{h-h^0} \sigma_{ij} dx_3$ and $M_{ij} = \int_{-h^0}^{h-h^0} x_3\sigma_{ij} dx_3$, respectively. ϵ_{kl}^0 and κ_{kl} are the main plane strain and the curvature defined as $\epsilon_{kl}^0 = 1/2(u_{k,l}^0 + u_{l,k}^0)$ and $\kappa_{kl} = -w_{,kl}$, respectively. A_{ijkl}, B_{ijkl}, and D_{ijkl} are the extensional, coupling, and bending stiffness tensors, respectively, given as

$$A_{ijkl} = A_{12}\delta_{ij}\delta_{kl} + \tfrac{1}{2}(A_{11} - A_{12})(\delta_{ik}\delta_{jl} + \delta_{il}\delta_{jk}),$$
$$B_{ijkl} = B_{12}\delta_{ij}\delta_{kl} - \tfrac{1}{2}B_{12}(\delta_{ik}\delta_{jl} + \delta_{il}\delta_{jk}),$$
$$D_{ijkl} = D_{12}\delta_{ij}\delta_{kl} + \tfrac{1}{2}(D_{11} - D_{12})(\delta_{ik}\delta_{jl} + \delta_{il}\delta_{jk}). \tag{3}$$

Here δ_{ij} is the Kronecker delta, and $A_{ij} = \int_{-h^0}^{h-h^0} C_{ij} dx_3$, $B_{ij} = \int_{-h^0}^{h-h^0} x_3 C_{ij} dx_3$ and $D_{ij} = \int_{-h^0}^{h-h^0} x_3^2 C_{ij} dx_3$ $(ij = 11, 12)$, where C_{11} and C_{12} can be written in terms of Young's modulus E and Poisson's ratio ν of the layer as $C_{11} = E/(1 - \nu^2)$ and $C_{12} = \nu E/(1 - \nu^2)$. The main plane $(x_3 = 0)$ is placed at the distance $h^0 = \int_0^h X_3 C_{11} dX_3 / \int_0^h C_{11} dX_3$ from the lower surface of the plate, which is equivalent to the condition $B_{11} = \int_{-h^0}^{h-h^0} x_3 C_{11} dx_3 = 0$. Here, X_3 $(= x_3 + h^0)$ is the vertical coordinate of the given point from the lowest surface of the plate. In this paper, the repetition of an index in a term denotes a summation with respect to that index over its range 1 to 2 for a lowercase Roman letter unless indicated otherwise, and boldfaced symbols represent vectors or matrices. The main plane eigenstrain and the eigencurvature are defined, respectively, as

$$\epsilon_{ij}^{0*} = \frac{1}{A_{11} - A_{12}} \int_{-h^0}^{h-h^0} \left[\frac{A_{11}C_{12} - A_{12}C_{11}}{A_{11} + A_{12}} \epsilon_{kk}^* \delta_{ij} + (C_{11} - C_{12})\epsilon_{ij}^* \right] dx_3,$$
$$\kappa_{ij}^* = \frac{1}{D_{11} - D_{12}} \int_{-h^0}^{h-h^0} \left[\frac{D_{11}C_{12} - D_{12}C_{11}}{D_{11} + D_{12}} \epsilon_{kk}^* \delta_{ij} + (C_{11} - C_{12})\epsilon_{ij}^* \right] x_3 dx_3. \tag{4}$$

It is noted that the main plane eigenstrain and the eigencurvature for the laminate are uniform since the eigenstrain ϵ_{ij}^* is a function of only x_3. The main plane eigenstrain and the eigencurvature defined by (4) are the generalized eigenstrains for a laminate composed of multiple isotropic layers.

Employing a method based on the influence functions, which is an extension of the Maysel's relation (Maysel, 1941; Ziegler and Irschik, 1987) to laminate problems, it can be shown that integral type solutions for the displacements are expressed as (see Appendix A for details)

$$u_i^0(x_1, x_2) = \int_\Omega \tilde{N}_{kl}^{[i]}(\xi_1, \xi_2; x_1, x_2)\epsilon_{kl}^{0*} dA,$$
$$w(x_1, x_2) = \int_\Omega \tilde{M}_{kl}^{[3]}(\xi_1, \xi_2; x_1, x_2)\kappa_{kl}^* dA. \tag{5}$$

The influence functions $\tilde{N}_{kl}^{[i]}$ and $\tilde{M}_{kl}^{[3]}$ of the infinite plate are the resultant stress and moment given as

$$\tilde{N}_{kl}^{[i]} = A_{klmn}\tilde{\epsilon}_{mn}^{0[i]}, \quad \tilde{M}_{kl}^{[3]} = D_{klmn}\tilde{\kappa}_{mn}^{[3]}, \tag{6}$$

where $\tilde{\epsilon}_{kl}^{0[i]} = 1/2((\partial\tilde{u}_k^{0[i]}/\partial\xi_l + \partial\tilde{u}_l^{0[i]}/\partial\xi_k))$ and $\tilde{\kappa}_{kl}^{[3]} = -(\partial\tilde{u}_3^{[3]}/\partial\xi_k\partial\xi_l)$ in which the displacements can be written in closed form as (Beom and Earmme, 1998)

$$\tilde{u}_k^{0[i]}(\xi_1, \xi_2; x_1, x_2) = \frac{1}{8\pi\mu}\left[-(3 - \nu^A)\ln\rho\,\delta_{ki} + (1 + \nu^A)\frac{(\xi_k - x_k)(\xi_i - x_i)}{\rho^2} \right],$$
$$\tilde{u}_3^{[i]}(\xi_1, \xi_2; x_1, x_2) = 0,$$
$$\tilde{u}_k^{0[3]}(\xi_1, \xi_2; x_1, x_2) = 0,$$
$$\tilde{u}_3^{[3]}(\xi_1, \xi_2; x_1, x_2) = \frac{1}{8\pi D_{11}}\rho^2 \ln\rho. \tag{7}$$

Here $\mu = \frac{1}{2}(A_{11} - A_{12})$, $\nu^A = A_{12}/A_{11}$ and $\rho = \{(\xi_m - x_m)(\xi_m - x_m)\}^{1/2}$. $\tilde{u}_\alpha^{0[i]}(\xi_1, \xi_2; x_1, x_2)$ and $\tilde{u}_\alpha^{[3]}(\xi_1, \xi_2; x_1, x_2)$ are the displacement components at point ξ when unit concentrated forces in the x_i-direction and the x_3-direction, respectively, are applied at point $\mathbf{x}$ in the infinite plate. It is seen from (5), (6) and (7) that *the main plane displacements u_i^0 and the transverse displacement w do not depend on the coupling stiffness* and are identical for the problem of a symmetric laminate with the same stiffnesses A_{ijkl} and D_{ijkl}. It is also worth mentioning that the main plane displacements u_i^0 for the laminate with nonzero coupling stiffness depend on only ϵ_{ij}^{0*} not κ_{ij}^*, whereas the transverse displacement w depends on only κ_{ij}^* not ϵ_{ij}^{0*}.

3 Analytic Solution

3.1 Homogeneous Infinite Plate. We consider a homogeneous infinite plate containing an elliptic cylindrical inclusion in which an eigenstrain $\epsilon_{ij}^*(x_3)$ is prescribed. The generalized eigenstrains ϵ_{kl}^{0*} and κ_{kl}^* are thus uniform in the elliptic subre-

Downloaded 04 May 2010 to 171.66.16.27. Redistribution subject to ASME license or copyright; see http://www.asme.org/terms/Terms_Use.cfm

gion Ω, as shown in Fig. 1. The major and minor semi-axes of the ellipse are a_1 and a_2, respectively. Introducing integrals H and H_{kl} defined, respectively, by

$$H(x_1, x_2) = \int_\Omega \ln \rho dA,$$

$$H_{kl}(x_1, x_2) = \int_\Omega \frac{(\xi_k - x_k)(\xi_l - x_l)}{\rho^2} dA, \tag{8}$$

the expression for the displacements in (5) is rewritten as

$$u_i^0 = \frac{1}{8\pi}\{4\nu^A H_{,l}\delta_{kl} + (3 - \nu^A)(H_{,l}\delta_{ik} + H_{,k}\delta_{il}) - (1 + \nu^A)(H_{ik,l} + H_{il,k})\}\epsilon_{kl}^{0*}$$

$$u_3 = -\frac{1}{4\pi}\{(1 + \nu^D)H\delta_{kl} + (1 - \nu^D)H_{kl}\}\kappa_{kl}^*, \tag{9}$$

where $\nu^D = D_{12}/D_{11}$.

Expressions for the solution are different for the interior points and exterior points of the ellipse. Thus, we consider separately the solution for the interior points and exterior points of the ellipse. The integrals H and H_{kl} in (9) can be performed explicitly for $\mathbf{x}$ located in Ω as well as for $\mathbf{x}$ located out of Ω. The closed forms of H and H_{kl} are presented in Beom (1998). For the uniform main plane eigenstrain ϵ_{ij}^{0*} and the uniform eigencurvature κ_{ij}^* in the elliptic zone, the main plane strain and the curvature are given by

$$\epsilon_{ij}^0 = S_{ijkl}\epsilon_{kl}^{0*}, \quad \kappa_{ij} = K_{ijkl}\kappa_{kl}^*, \tag{10}$$

where

$$S_{ijkl} = \frac{\nu^A}{2\pi}H_{,ij}\delta_{kl} + \frac{3 - \nu^A}{16\pi}(H_{,ik}\delta_{jl} + H_{,jl}\delta_{ik} + H_{,il}\delta_{jk} + H_{,jk}\delta_{il}) - \frac{1 + \nu^A}{16\pi}(H_{ik,jl} + H_{jl,ik} + H_{il,jk} + H_{jk,il}),$$

$$K_{ijkl} = \frac{1 + \nu^D}{4\pi}H_{,ij}\delta_{kl} + \frac{1 - \nu^D}{4\pi}H_{kl,ij}. \tag{11}$$

The tensors S_{ijkl} and K_{ijkl} are symmetric with respect to interchange of i and j or k and l, i.e., $S_{ijkl} = S_{jikl} = S_{ijlk}$ and $K_{ijkl} = K_{jikl} = K_{ijlk}$. The tensors S_{ijkl} and K_{ijkl} for $\mathbf{x}$ in Ω, which correspond to Eshelby's tensor in three-dimensional elasticity for an ellipsoidal inclusion embedded in an infinite elastic medium, depend only on the ratio of a_1 and a_2, ν^A and ν^D, which are presented in Appendix B. Therefore, we have an attractive conclusion that the resultant stress and resultant moment are uniform inside the inclusion as in the case of three dimensional elastic problem (Eshelby, 1957). Hermann and Achenbach (1968) dealt with a laminated material represented as micropolar one. Cheng and He (1995) extended Eshelby's equivalent inclusion method to micropolar materials. They showed that generalized Eshelby tensors for a spherical inclusion in a micropolar material vary inside the inclusion. Thus, the theory of laminate with eigenstrains can not be interpreted as models describing the behavior of a micropolar material with eigenstrains. The resultant stress and moment can be evaluated from (2) and (10), which results in

$$N_{ij} = (A_{ijmn}S_{mnkl} - A_{ijkl})\epsilon_{kl}^{0*} + B_{ijmn}K_{mnkl}\kappa_{kl}^*,$$

$$M_{ij} = B_{ijmn}S_{mnkl}\epsilon_{kl}^{0*} + (D_{ijmn}K_{mnkl} - D_{ijkl})\kappa_{kl}^*. \tag{12}$$

3.2 Infinite Plate With Inhomogeneity. Consider an infinite plate solid with the stiffnesses A_{ijkl}, B_{ijkl}, and D_{ijkl} containing an elliptic cylindrical inhomogeneity with the stiffnesses A_{ijkl}^*, B_{ijkl}^*, and D_{ijkl}^*. An eigenstrain $\epsilon_{kl}^*(x_3)$ is prescribed in the elliptic cylindrical inhomogeneity. The generalized eigenstrains ϵ_{kl}^{0*} and κ_{kl}^* are thus uniform in the elliptic subregion Ω,

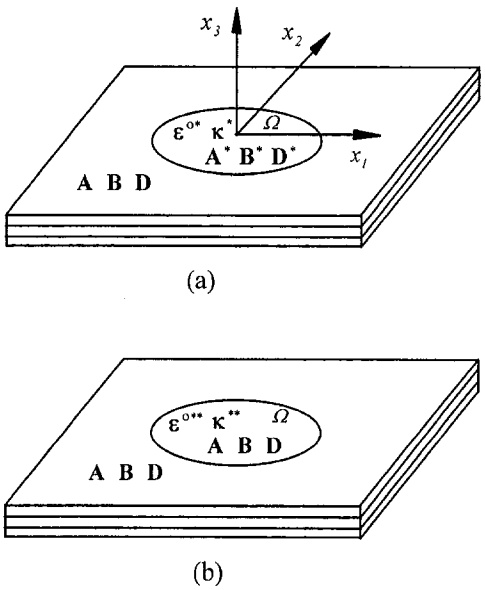

Fig. 2 Elliptic cylindrical inhomogeneity containing an eigenstrain; (*a*) infinite plate with an inhomogeneity, (*b*) infinite plate with an equivalent eigenstrain

as shown in Fig. 2. The major and minor semi-axes of the ellipse are a_1 and a_2, respectively.

The elastic fields due to the inhomogeneity can be determined by the equivalent eigenstrain method, which is an extension of the equivalent inclusion method proposed for an ellipsoidal inhomogeneity problem by Eshelby (1957). The resultant moment due to the presence of an inhomogeneity with the eigenstrain ϵ_{kl}^{0*} and eigencurvature κ_{kl}^* can be simulated by a resultant stress and moment caused by an inclusion when the eigenstrain and the eigencurvature are chosen properly, as follows: The constitutive relation for the inhomogeneity problem is written as

$$N_{ij} = A_{ijkl}^*(\epsilon_{kl}^0 - \epsilon_{kl}^{0*}) + B_{ijkl}^*\kappa_{kl},$$

$$M_{ij} = B_{ijkl}^*\epsilon_{kl}^0 + D_{ijkl}^*(\kappa_{kl} - \kappa_{kl}^*) \text{ for } \mathbf{x} \text{ in } \Omega,$$

$$N_{ij} = A_{ijkl}\epsilon_{kl}^0 + B_{ijkl}\kappa_{kl},$$

$$M_{ij} = B_{ijkl}\epsilon_{kl}^0 + D_{ijkl}\kappa_{kl} \text{ for } \mathbf{x} \text{ out of } \Omega. \tag{13}$$

Introducing an eigenstrain ϵ_{kl}^{0**} and an eigencurvature κ_{kl}^{**} in order to simulate the inhomogeneity problem in a manner analogous to the equivalent inclusion method in three dimensional elasticity (Eshelby, 1957), the constitutive relation for the homogeneous problem is written as

$$N_{ij} = A_{ijkl}(\epsilon_{kl}^0 - \epsilon_{kl}^{0**}) + B_{ijkl}\kappa_{kl},$$

$$M_{ij} = B_{ijkl}\epsilon_{kl}^0 + D_{ijkl}(\kappa_{kl} - \kappa_{kl}^{**}) \text{ for } \mathbf{x} \text{ in } \Omega,$$

$$N_{ij} = A_{ijkl}\epsilon_{kl}^0 + B_{ijkl}\kappa_{kl},$$

$$M_{ij} = B_{ijkl}\epsilon_{kl}^0 + D_{ijkl}\kappa_{kl} \text{ for } \mathbf{x} \text{ out of } \Omega. \tag{14}$$

The conditions for the equivalency of the resultant stress and moment in the two problems of inhomogeneity and homogeneity above are

$$A_{ijkl}^*(\epsilon_{kl}^0 - \epsilon_{kl}^{0*}) + B_{ijkl}^*\kappa_{kl} = A_{ijkl}(\epsilon_{kl}^0 - \epsilon_{kl}^{0**}) + B_{ijkl}\kappa_{kl}$$

$$B_{ijkl}^*\epsilon_{kl}^0 + D_{ijkl}^*(\kappa_{kl} - \kappa_{kl}^*) = B_{ijkl}\epsilon_{kl}^0 + D_{ijkl}(\kappa_{kl} - \kappa_{kl}^{**}). \tag{15}$$

As mentioned earlier, ϵ_{kl}^0 and κ_{kl} in the equation above can be obtained as known functions of ϵ_{kl}^{0**} and κ_{kl}^{**} when the eigenstrain problem in the homogeneous material is solved. Thus, (15) determines ϵ_{kl}^{0**} and κ_{kl}^{**} for a given ϵ_{kl}^{0*} and κ_{kl}^*, in such a manner that the equivalency holds. Introducing contracted

Downloaded 04 May 2010 to 171.66.16.27. Redistribution subject to ASME license or copyright; see http://www.asme.org/terms/Terms_Use.cfm

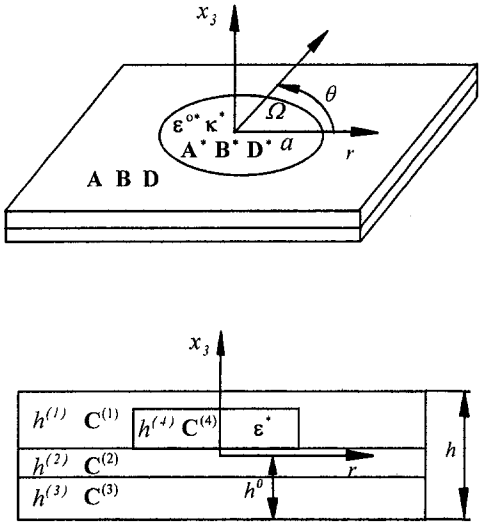

Fig. 3 Infinite plate containing a circular cylindrical inclusion with an eigenstrain

notation for the strain and the curvature, the equivalent eigenstrain and eigencurvature may be written in a matrix from as

$$\boldsymbol{\epsilon}^{0**} = \mathbf{F}^{11}\boldsymbol{\epsilon}^{0*} + \mathbf{F}^{12}\boldsymbol{\kappa}^*, \quad \boldsymbol{\kappa}^{**} = \mathbf{F}^{21}\boldsymbol{\epsilon}^{0*} + \mathbf{F}^{22}\boldsymbol{\kappa}^*, \quad (16)$$

where $\boldsymbol{\epsilon}$ and $\boldsymbol{\kappa}$ are the vectors defined by $\boldsymbol{\epsilon} = \{\epsilon_{11} \quad \epsilon_{22} \quad 2\epsilon_{12}\}^T$ and $\boldsymbol{\kappa} = \{\kappa_{11} \quad \kappa_{22} \quad 2\kappa_{12}\}^T$, and $\mathbf{F}^{ij}$ $(i, j = 1, 2)$ are the 3×3 matrices, which are presented in Appendix C. For the special case in which $\mathbf{B} = \mathbf{B}^* = \mathbf{0}$ and $\boldsymbol{\kappa}^* = \mathbf{0}$, it can be shown that the solution of the elastic fields for the infinite plate with inhomogeneity reduce to the plane-stress version of the Eshelby solution in both interior and exterior points of the elliptic inhomogeneity. The plane-stress version of the Eshelby solution is obtained by replacing ν^A by $\nu^A/(1 + \nu^A)$ in the plane-strain version of the Eshelby solution.

Before proceeding, it is noted that the approach via the through-thickness averaging approach in the lamination theory has a limitation, i.e., it cannot determine the local fields which appear at the three junctions between the individual layers and the elastic inhomogeneity. However, the solution obtained above is useful in the analysis of the fabrication cool down of microelectronic laminated components containing inhomogeneity and unsymmetric lay ups with the individual layers possessing different coefficients of thermal expansion.

4 Circular Cylindrical Inhomogeneity

To gain additional physical insight, we consider a problem of a circular cylindrical inhomogeneity as a special case of the problem of the elliptic cylindrical inhomogeneity. We consider this special case because simple expressions can be obtained for the force and moment resultants and the displacement field in terms of geometric and material parameters. The circular cylindrical inhomogeneity with a radius a and a thickness $h^{(4)}$ is embedded in an infinite triple layered plate with a thickness h, as shown in Fig. 3. The thicknesses of the three layers composing the laminate are $h^{(1)}$, $h^{(2)}$, and $h^{(3)}$, respectively. An eigenstrain ϵ_{ij}^* is prescribed in the circular cylindrical inhomogeneity with a height $h^{(4)}$. The eigenstrain is assumed to be $\epsilon_{ij}^* = \epsilon^*\delta_{ij}$ for simplicity, which is a typical case of thermal eigenstrain in an isotropic material.

The distance from the lowest surface of the plate to the main plane, h^0 is given by

$$h^0 = \frac{1}{2}\frac{\{h^2 - (h^{(2)} + h^{(3)})^2\}C_{11}^{(1)} + \{(h^{(2)} + h^{(3)})^2 - h^{(3)2}\}C_{11}^{(2)} + h^{(3)2}C_{11}^{(3)}}{h^{(1)}C_{11}^{(1)} + h^{(2)}C_{11}^{(2)} + h^{(3)}C_{11}^{(3)}}. \quad (17)$$

Here the superscripts 1, 2, 3, and 4 in the parentheses represent the quantities associated with the layers 1, 2, 3 and the inhomogeneity, respectively. The stiffness tensors of the bilayered plate A_{ijkl}, B_{ijkl}, and D_{ijkl}, and the stiffness tensors of the laminate containing the circular cylindrical inhomogeneity A_{ijkl}^*, B_{ijkl}^*, and D_{ijkl}^* can be easily written in terms of $h^{(\alpha)}$, $C_{11}^{(\alpha)}$, and $C_{12}^{(\alpha)}$ $(\alpha = 1, 2, 3, 4)$ from the definitions in the Section 2. The main plane eigenstrain ϵ_{ij}^{0*} and the eigencurvature κ_{ij}^* have the form: $\epsilon_{ij}^{0*} = \epsilon^{0*}\delta_{ij}$ and $\kappa_{ij}^* = \kappa^*\delta_{ij}$, where ϵ^{0*} and κ^* can be obtained easily from (4).

The displacement field for the infinite plate containing eigenstrain can be obtained by the equivalent eigenstrain method. The equivalent eigenstrain and the equivalent eigencurvature for the infinite plate are given in (16) as $\epsilon_{ij}^{0**} = \epsilon^{0**}\delta_{ij}$ and $\kappa_{ij}^{**} = \kappa^{**}\delta_{ij}$, respectively. Here

$$\begin{Bmatrix} \epsilon^{0**} \\ \kappa^{**} \end{Bmatrix} = \begin{bmatrix} F_{11} & F_{12} \\ F_{21} & F_{22} \end{bmatrix} \begin{Bmatrix} \epsilon^{0*} \\ \kappa^* \end{Bmatrix}, \quad (18)$$

where F_{ij} are presented in Appendix C. The solution for the displacement field in an infinite plate containing the uniform equivalent eigenstrain in the circular region with a radius a is obtained from (12) as

$$u_r^0 = \frac{1 + \nu^A}{2} r\epsilon^{0**}, \quad u_\theta^0 = 0,$$

$$u_3(r) = -\frac{1}{4}(1 + \nu^D)r^2\kappa^{**} \quad \text{for } \mathbf{x} \text{ in } \Omega,$$

$$u_r^0 = \frac{1 + \nu^A}{2}\frac{a^2}{r}\epsilon^{0**}, \quad u_\theta^0 = 0,$$

$$u_3 = -\frac{1}{4}(1 + \nu^D)a^2(2 \ln r/a + 1)\kappa^{**}$$

$$\text{for } \mathbf{x} \text{ out of } \Omega. \quad (19)$$

The corresponding resultant stress and moment are given as

$$N_{rr} = N_{\theta\theta} = -\tfrac{1}{2}A_{11}\{1 - (\nu^A)^2\}\epsilon^{0**} + \tfrac{1}{2}B_{12}\{1 + \nu^D\}\kappa^{**},$$

$$M_{rr} = M_{\theta\theta} = \tfrac{1}{2}B_{12}\{1 + \nu^A\}\epsilon^{0**} - \tfrac{1}{2}D_{11}\{1 - (\nu^D)^2\}\kappa^{**},$$

$$N_{r\theta} = M_{r\theta} = 0 \text{ for } \mathbf{x} \text{ in } \Omega,$$

$$N_{rr} = -N_{\theta\theta} = -\frac{1}{2}A_{11}\{1 - (\nu^A)^2\}\frac{a^2}{r^2}\epsilon^{0**} + \frac{1}{2}B_{12}\{1 + \nu^D\}\frac{a^2}{r^2}\kappa^{**},$$

$$M_{rr} = -M_{\theta\theta} = \frac{1}{2}B_{12}\{1 + \nu^A\}\frac{a^2}{r^2}\epsilon^{0**} - \frac{1}{2}D_{11}\{1 - (\nu^D)^2\}\frac{a^2}{r^2}\kappa^{**},$$

$$N_{r\theta} = M_{r\theta} = 0 \text{ for } \mathbf{x} \text{ out of } \Omega. \quad (20)$$

Next, consider deformation of a circular finite plate with a

Downloaded 04 May 2010 to 171.66.16.27. Redistribution subject to ASME license or copyright; see http://www.asme.org/terms/Terms_Use.cfm

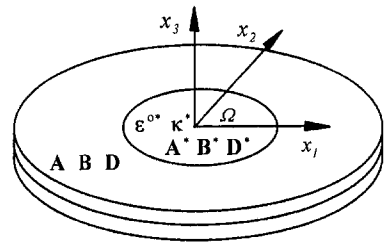

(a)

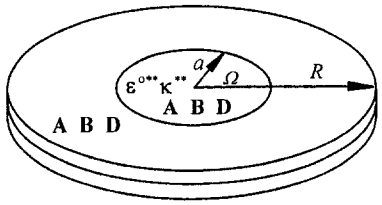

(b)

Fig. 4 Circular plate with an inhomogeneity; (*a*) circular plate with an inhomogeneity, (*b*) circular plate with an equivalent eigenstrain

radius R as shown in Fig. 4. The circular plate has the stiffness tensors A_{ijkl}, B_{ijkl}, and D_{ijkl}, and the stiffness tensors of the circular inhomogeneity with a radius a are A^*_{ijkl}, B^*_{ijkl}, and D^*_{ijkl}. The main plane eigenstrain ϵ^{0*}_{ij} and the eigencurvature κ^*_{ij} prescribed in the circular inhomogeneity are assumed to be $\epsilon^{0*}_{ij} = \epsilon^{0*}\delta_{ij}$ and $\kappa^*_{ij} = \kappa^*\delta_{ij}$. The displacement fields for the circular plate due to the inhomogeneity can be determined by the equivalent eigenstrain method as shown in Fig. 4. Applying the superposition principle, we can calculate the solution for the finite plate with the equivalent eigenstrain in the circular region. The complete solution for the displacement field for the circular plate containing the uniform equivalent eigenstrain in the circular region may be written as

$$u^0_r = \left\{\frac{1+\nu^A}{2} + p_{11}\right\} r\epsilon^{0**} + p_{12} r\kappa^{**},\ u^0_\theta = 0,$$

$$u_3(r) = -\frac{1}{2}\left[p_{21} r^2 \epsilon^{0**} + \left\{\frac{1}{2}(1+\nu^D) + p_{22}\right\} r^2 \kappa^{**}\right]$$

for $\mathbf{x}$ in Ω

$$u^0_r = \left\{\frac{1+\nu^A}{2}\frac{a^2}{r} + p_{11} r\right\} \epsilon^{0**} + p_{12} r\kappa^{**},\ u^0_\theta = 0,$$

$$u_3 = -\frac{1}{2}\left[p_{21} r^2 \epsilon^{0**} + \left\{\frac{1}{2}(1+\nu^D) a^2 (2\ln r/a + 1) + p_{22} r^2\right\}\kappa^{**}\right] \text{ for } \mathbf{x} \text{ out of } \Omega. \quad (21)$$

Here ϵ^{0**} and κ^{**} are the equivalent eigenstrain and the equivalent eigencurvature for the circular plate, which will be obtained in terms of ϵ^{0*} and κ^*. The constants p_{ij} are presented in Appendix D. The main plane strain and the curvature in the inhomogeneity are given from (21) as $\epsilon^0_{ij} = \epsilon^0\delta_{ij}$ and $\kappa_{ij} = \kappa\delta_{ij}$, in which

$$\begin{Bmatrix}\epsilon^0\\ \kappa\end{Bmatrix} = \begin{bmatrix} q_{11} & q_{12}\\ q_{21} & q_{22}\end{bmatrix}\begin{Bmatrix}\epsilon^{0**}\\ \kappa^{**}\end{Bmatrix}, \quad (22)$$

where $q_{11} = p_{11} + (1+\nu^A)/2$, $q_{12} = p_{12}$, $q_{21} = p_{21}$ and $q_{22} = p_{22} + (1+\nu^D)/2$. It is noted that the main plane strain and the curvature in the inhomogeneity for the finite plate depend on ϵ^{0**} and κ^{**}, in contrast to an infinite plate. The equivalent eigenstrain ϵ^{0**} and the equivalent eigencurvature κ^{**} for the circular plate are given by

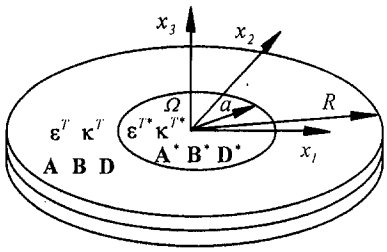

Fig. 5 Circular plate with eigenstrains

$$\begin{Bmatrix}\epsilon^{0**}\\ \kappa^{**}\end{Bmatrix} = \begin{bmatrix} F^R_{11} & F^R_{12}\\ F^R_{21} & F^R_{22}\end{bmatrix}\begin{Bmatrix}\epsilon^{0*}\\ \kappa^{*}\end{Bmatrix}, \quad (23)$$

where F^R_{ij} are presented in Appendix D.

Next, we consider thermal deformation of a circular laminate with a radius R as shown in Fig. 5, which is of particular importance in the electronic packages. This layered structure is assembled at elevated temperature and then cooled. The temperature difference is T. The main plane eigenstrain and the eigencurvature prescribed in the laminate are $\epsilon^T_{ij} = \epsilon^T\delta_{ij}$, $\kappa^T_{ij} = \kappa^T\delta_{ij}$ for $\mathbf{x}$ in Ω and $\epsilon^{T*}_{ij} = \epsilon^{T*}\delta_{ij}$, $\kappa^{T*}_{ij} = \kappa^{T*}\delta_{ij}$ for $\mathbf{x}$ out of Ω, respectively, which are given by

$$\epsilon^T = \frac{1}{A_{11}+A_{12}}\int_{-h^0}^{h-h^0}(C_{11}+C_{12})\alpha T dx_3,$$

$$\kappa^T = \frac{1}{D_{11}+D_{12}}\int_{-h^0}^{h-h^0}(C_{11}+C_{12})\alpha T x_3 dx_3,$$

$$\epsilon^{T*} = \frac{1}{A^*_{11}+A^*_{12}}\int_{-h^0}^{h-h^0}(C^*_{11}+C^*_{12})\alpha^* T dx_3,$$

$$\kappa^{T*} = \frac{1}{D^*_{11}+D^*_{12}}\int_{-h^0}^{h-h^0}(C^*_{11}+C^*_{12})\alpha^* T x_3 dx_3, \quad (24)$$

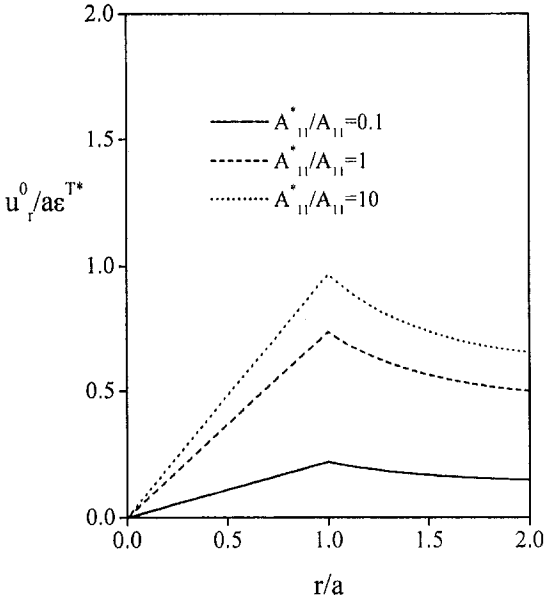

Fig. 6 Normalized radial displacement as a function of *r/a*

Downloaded 04 May 2010 to 171.66.16.27. Redistribution subject to ASME license or copyright; see http://www.asme.org/terms/Terms_Use.cfm

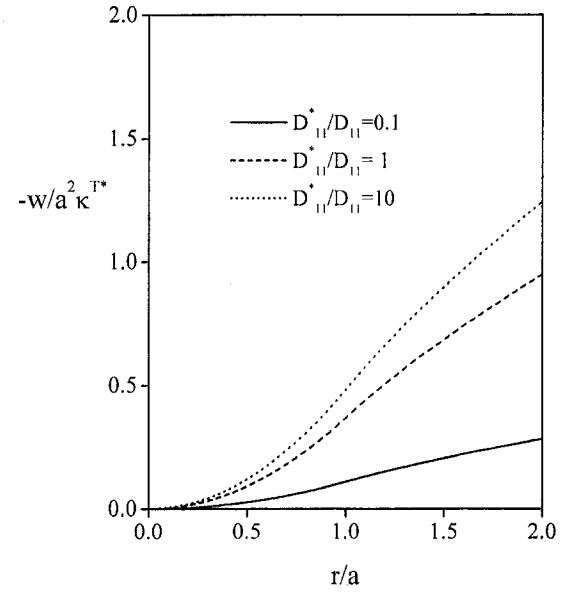

Fig. 7 Normalized transverse displacement as a function of r/a

where α is a coefficient of thermal expansion for each layer composing the laminate. The circular plate has the stiffness tensors A_{ijkl}, B_{ijkl}, and D_{ijkl}, and the stiffness tensors of the circular inhomogeneity with a radius a are A^*_{ijkl}, B^*_{ijkl}, and D^*_{ijkl}. We restrict out attention to the case of $B_{12} = B^*_{11} = B^*_{12} = 0$ for simplicity. Applying an appropriate superposition method, it can be shown that the complete solution for the displacement field for the circular plate may be written as

$$u^0_r = \epsilon^T r + \left\{\frac{1+\nu^A}{2} + p_{11}\right\}\epsilon^{0**} r,\ u^0_\theta = 0,$$

$$u_3(r) = -\tfrac{1}{2}\left[\kappa^T + \left\{\tfrac{1}{2}(1+\nu^D) + p_{22}\right\}\kappa^{**}\right] r^2 \text{ for } \mathbf{x} \text{ in } \Omega,$$

$$u^0_r = \epsilon^T r + \left\{\frac{1+\nu^A}{2}\frac{a^2}{r} + p_{11} r\right\}\epsilon^{0**},\ u^0_\theta = 0,$$

$$u_3 = -\tfrac{1}{2}\Big[\kappa^T r^2 + \Big\{\tfrac{1}{2}(1+\nu^D)a^2(2\ln r/a + 1) + p_{22} r^2\Big\}\kappa^{**}\Big] \text{ for } \mathbf{x} \text{ out of } \Omega. \quad (25)$$

where $\epsilon^{0**} = F^R_{11}(\epsilon^{T*} - \epsilon^T)$ and $\kappa^{**} = F^R_{22}(\kappa^{T*} - \kappa^T)$. In obtaining (25), (21) has been used. For three specific values of A^*_{11}/A_{11}, the normalized radial displacement $u^0_r/a\epsilon^{T*}$ is plotted as a function of r/a in Fig. 6. The normalized transverse displacement $-w/a^2\kappa^{T*}$ is plotted in Fig. 7 as r/a varies, for three specific values of D^*_{11}/D_{11}. Here the numerical values used in the computation are as follows: $\nu^A = \nu^D = 0.3$, $\nu^{A*} = \nu^{D*} = 0.3$, $\epsilon^T = \kappa^T = 0$, and $R/a = 2$. Figures 6 and 7 illustrate the effect of inhomogeneity on in-plane deformation and warpage of the laminate. It is seen from Figs. 6 and 7 that deformations induced by the eigenstrain prescribed in the inhomogeneity become larger as the stiffness of inhomogeneity increases.

5 Conclusions

An infinite laminate with an eigenstrain in an elliptic cylindrical inclusion is analyzed. The problem is formulated by using the classical laminated plate theory in which the displacement fields in the laminated plate are expressed in terms of the in-plane displacements on the main plane and transverse displacement. Employing a method based on influence functions, which is an extension of the Maysel's relation (Maysel, 1941; Ziegler and Irschik, 1987) to laminate problems, an integral type solution to the equilibrium equation is expressed in terms of the eigenstrain. Closed-form solutions of the elastic fields are obtained by evaluating the integrals explicitly for interior points and exterior points of the ellipse.

An infinite laminate containing an elliptic cylindrical inhomogeneity in which an eigenstrain varying through the thickness is prescribed is considered. The elastic fields caused by the inhomogeneity with the eigenstrain are determined by the equivalent eigenstrain method, which is an extension of the equivalent inclusion method proposed for an ellipsoidal inhomogeneity problem by Eshelby (1957). Solution for a finite laminate with an eigenstrain in a circular cylindrical inhomogeneity is obtained in terms of the material and geometric parameters for each layer composing the laminate. Thermal deformation of a circular laminate is also considered to illustrate the effect of inhomogeneity on in-plane deformation and warpage of the laminate.

Acknowledgment

The first author acknowledges the support of academic research fund from the Korea Science and Engineering Foundation. The authors are also grateful to Prof. M.-J. Pindera of The University of Virginia for valuable comments on revising the manuscript.

References

Beom, H. G., 1998, "Analysis of a Plate Containing an Elliptic Inclusion With Eigencurvatures," *Archive of Applied Mechanics,* Vol. 68, pp. 422–432.

Beom, H. G., and Earmme, Y. Y., 1998, "Complex Variable Method for Problems of a Laminate Composed of Multiple Isotropic Layers," *International Journal of Fracture,* accepted for publication.

Cheng, Z. Q., and He, L. H., 1995, "Micropolar Elastic Fields Due to a Spherical Inclusion," *International Journal of Engineering Science,* Vol. 33, pp. 389–397.

Eshelby, J. D., 1957, "The Determination of the Elastic Field of an Ellipsoidal Inclusion, and Related Problems," *Proceedings of the Royal Society,* Vol. A241, pp. 376–396.

Finot, M., and Suresh, S., 1996, "Small and Large Deformation of Thick and Thin-Film Multi-Layers: Effects of Layer Geometry, Plasticity and Compositional Gradients," *Journal of the Mechanics and Physics of Solids,* Vol. 44, pp. 683–721.

Freund, L. B., 1996, "Some Elementary Connections Between Curvature and Mismatch Strain in Compositionally Graded Thin Film," *Journal of the Mechanics and Physics of Solids,* Vol. 44, pp. 723–736.

Herrmann, G., and Achenbach, J. D., 1968, "Application of Theories of Generalized Cosserat Continua to the Dynamics of Composite Materials," *Mechanics of Generalized Continua: Proceedings of IUTAM Symposium,* E. Kroener, ed., Springer, Berlin, pp. 69–79.

Jones, R. M., 1975, *Mechanics of Composite Materials,* McGraw-Hill, New York.

Lau, J. H., 1993, *Thermal Stress and Strain in Microelectronics Packaging,* Van Nostrand Reinhold, New York.

Maysel, V. M., 1941, "A Generalization of the Betti-Maxwell Theorem to the case of the Thermal Stresses and Some Applications," *Doklady Akademii Science USSR,* Vol. 30, pp. 115–118 (in Russian).

Mura, T., 1987, *Mechanics of Defects in Solids,* Martinus Nijhoff, London.

Nowacki, W., 1962, *Thermoelasticity,* Pergamon Press, Oxford.

Ziegler, F., and Irschik, H., 1987, "Thermal Stress Analysis Based on Maysel's Formula," *Mechanics and Mathematical Methods,* Vol. 2, R. B. Hetnarski, ed., North-Holland, Amsterdam, pp. 119–188.

APPENDIX A

We consider two independent equilibrium states of an elastically deformed laminate. One set of displacements, resultant stresses, and resultant moments are denoted by u_i, N_{ij}, and M_{ij}, respectively, which satisfy both (2) and the equations of equilibrium

$$N_{ij,j} = 0, \quad Q_{i,i} = 0. \quad (A1)$$

Here Q_i is the transversal shearing force, which can be obtained from $Q_i = M_{ij,j}$. A second set of displacements, resultant stresses, and resultant moments are denoted by $\tilde{u}_i$, $\tilde{N}_{ij}$, and $\tilde{M}_{ij}$,

Downloaded 04 May 2010 to 171.66.16.27. Redistribution subject to ASME license or copyright; see http://www.asme.org/terms/Terms_Use.cfm

respectively, which satisfy the following equilibrium equations and constitutive equations:

$$\tilde{N}_{ij,j} + \tilde{p}_i = 0, \quad \tilde{Q}_{i,i} + \tilde{p}_3 = 0,$$
$$\tilde{N}_{ij} = A_{ijkl}\tilde{\epsilon}^0_{kl} + B_{ijkl}\tilde{\kappa}_{kl}, \quad \tilde{M}_{ij} = B_{ijkl}\tilde{\epsilon}^0_{kl} + D_{ijkl}\tilde{\kappa}_{kl}. \quad \text{(A2)}$$

Using the divergence theorem, it can be shown that

$$\int_A (\tilde{p}_i u_i^0 + \tilde{p}_3 u_3)\,dA = \int_A (A_{ijkl}\tilde{\epsilon}^0_{ij}\epsilon^{0*}_{kl} + D_{ijkl}\tilde{\kappa}_{ij}\kappa^*_{kl})\,dA + \int_{\partial A} [(N_{ij}n_j\tilde{u}_i^0 + Q_i n_i \tilde{u}_3 - M_{ij}n_j\tilde{u}_{3,i}) - (\tilde{N}_{ij}n_j u_i^0 + \tilde{Q}_i n_i u_3 - \tilde{M}_{ij}n_j u_{3,i})]\,ds. \quad \text{(A3)}$$

The relation between two elastic states of the same body, (A3) represents an extension of the Maysel' relation to laminate problems. (A3), with the aid of (6) and (7), then leads to the result (5).

APPENDIX B

The tensors S_{ijkl} and K_{ijkl} are symmetric with respect to interchange of i and j or k and l, i.e., $S_{ijkl} = S_{jikl} = S_{ijlk}$ and $K_{ijkl} = K_{jikl} = K_{ijlk}$. The nonzero components of S_{ijkl} and K_{ijkl} for $\mathbf{x}$ in Ω can be expressed as

$$S_{1111} = \frac{1}{2}\left\{(3+\nu^A)\frac{a_2}{a_1+a_2} - (1+\nu^A)\left(\frac{a_2}{a_1+a_2}\right)^2\right\},$$
$$S_{1122} = \frac{1}{2}\left\{(-1+\nu^A)\frac{a_2}{a_1+a_2} + (1+\nu^A)\left(\frac{a_2}{a_1+a_2}\right)^2\right\},$$
$$S_{2211} = \frac{1}{2}\left\{(-1+\nu^A)\frac{a_1}{a_1+a_2} + (1+\nu^A)\left(\frac{a_1}{a_1+a_2}\right)^2\right\},$$
$$S_{2222} = \frac{1}{2}\left\{(3+\nu^A)\frac{a_1}{a_1+a_2} - (1+\nu^A)\left(\frac{a_1}{a_1+a_2}\right)^2\right\},$$
$$S_{1212} = \frac{1}{2} - \frac{1+\nu^A}{2}\frac{a_1a_2}{(a_1+a_2)^2}, \quad \text{(B1)}$$
$$K_{1111} = \frac{1}{2}\left\{(1+\nu^D)\frac{a_2}{a_1+a_2} + (1-\nu^D)\left(\frac{a_2}{a_1+a_2}\right)^2\right\},$$
$$K_{1122} = \frac{1}{2}\left\{(1+\nu^D)\frac{a_2}{a_1+a_2} - (1-\nu^D)\left(\frac{a_2}{a_1+a_2}\right)^2\right\},$$
$$K_{2211} = \frac{1}{2}\left\{(1+\nu^D)\frac{a_1}{a_1+a_2} - (1-\nu^D)\left(\frac{a_1}{a_1+a_2}\right)^2\right\},$$
$$K_{2222} = \frac{1}{2}\left\{(1+\nu^D)\frac{a_1}{a_1+a_2} + (1-\nu^D)\left(\frac{a_1}{a_1+a_2}\right)^2\right\},$$
$$K_{1212} = \frac{1}{2}(1-\nu^D)\frac{a_1a_2}{(a_1+a_2)^2}. \quad \text{(B2)}$$

APPENDIX C

The matrices $\mathbf{F}^{ij}$ $(i, j = 1, 2)$ are

$$\mathbf{F}^{11} = [\{(\mathbf{A}^* - \mathbf{A})\mathbf{S} + \mathbf{A}\} - \{(\mathbf{B}^* - \mathbf{B})\mathbf{K}\}\{(\mathbf{D}^* - \mathbf{D})\mathbf{K} + \mathbf{D}\}^{-1}\{(\mathbf{B}^* - \mathbf{B})\mathbf{S}\}]^{-1}\mathbf{A}^*,$$
$$\mathbf{F}^{22} = [\{(\mathbf{D}^* - \mathbf{D})\mathbf{K} + \mathbf{D}\} - \{(\mathbf{B}^* - \mathbf{B})\mathbf{S}\}\{(\mathbf{A}^* - \mathbf{A})\mathbf{S} + \mathbf{A}\}^{-1}\{(\mathbf{B}^* - \mathbf{B})\mathbf{K}\}]^{-1}\mathbf{D}^*,$$
$$\mathbf{F}^{12} = -\mathbf{F}^{11}\mathbf{A}^{*-1}\{(\mathbf{B}^* - \mathbf{B})\mathbf{K}\}\{(\mathbf{D}^* - \mathbf{D})\mathbf{K} + \mathbf{D}\}^{-1}\mathbf{D}^*,$$
$$\mathbf{F}^{21} = -\mathbf{F}^{22}\mathbf{D}^{*-1}\{(\mathbf{B}^* - \mathbf{B})\mathbf{S}\}\{(\mathbf{A}^* - \mathbf{A})\mathbf{S} + \mathbf{A}\}^{-1}\mathbf{A}^*. \quad \text{(C1)}$$

Here the elements of the matrix $\mathbf{A}$ and the matrix $\mathbf{S}$ for interior points to Ω are given by

$$\mathbf{A} = \begin{bmatrix} A_{1111} & A_{1122} & A_{1112} \\ A_{2211} & A_{2222} & A_{2212} \\ A_{1211} & A_{1222} & A_{1212} \end{bmatrix},$$
$$\mathbf{S} = \begin{bmatrix} S_{1111} & S_{1122} & S_{1112} \\ S_{2211} & S_{2222} & S_{2212} \\ 2S_{1211} & 2S_{1222} & 2S_{1212} \end{bmatrix}. \quad \text{(C2)}$$

The elements of the matrices $\mathbf{B}$ and $\mathbf{D}$ are given in the same manner as $\mathbf{A}$, and the elements of the matrix $\mathbf{K}$ for the interior points to Ω are given in the same manner as $\mathbf{S}$.

When the eigenstrain ϵ^{0*}_{kl} and the eigencurvature κ^*_{kl} have the form $\epsilon^{0*}_{kl} = \epsilon^{0*}\delta_{kl}$ and $\kappa^*_{kl} = \kappa^*\delta_{kl}$, (16) reduces to (18). Here the matrix $\mathbf{F}$ is given by $\mathbf{F} = \mathbf{L}^{-1}$, where the components of L_{ij} are

$$L_{11} = \frac{1}{\hat{A}^*}\left\{\frac{1+\nu^A}{2}(\hat{A}^* - \hat{A}) + \hat{A}\right\},$$
$$L_{12} = \frac{1}{\hat{A}^*}\left\{\frac{1+\nu^D}{2}(\hat{B}^* - \hat{B})\right\},$$
$$L_{21} = \frac{1}{\hat{D}^*}\left\{\frac{1+\nu^A}{2}(\hat{B}^* - \hat{B})\right\},$$
$$L_{22} = \frac{1}{\hat{D}^*}\left\{\frac{1+\nu^D}{2}(\hat{D}^* - \hat{D}) + \hat{D}\right\}, \quad \text{(C3)}$$

where $\hat{A} = A_{11} + A_{12}$, $\hat{B} = B_{11} + B_{12}$ and $\hat{D} = D_{11} + D_{12}$.

APPENDIX D

The constants p_{ij} are

$$p_{11} = \frac{1+\nu^A}{2J}\frac{a^2}{R^2}[\hat{D}A_{11}(1-\nu^A) + B_{12}^2],$$
$$p_{12} = -\frac{1+\nu^D}{2J}\frac{a^2}{R^2}[\hat{D} + D_{11}(1-\nu^D)]B_{12},$$
$$p_{21} = -\frac{1+\nu^A}{2J}\frac{a^2}{R^2}[A_{11}(1-\nu^A) + \hat{A}]B_{12},$$
$$p_{22} = \frac{1+\nu^D}{2J}\frac{a^2}{R^2}[B_{12}^2 + \hat{A}D_{11}(1-\nu^D)], \quad \text{(D1)}$$

where $J = \hat{A}\hat{D} - B_{12}^2$. The matrix $\mathbf{F^R}$ is given by $\mathbf{F^R} = (\mathbf{L}^R)^{-1}$, where the components of L^R_{ij} are

$$L^R_{11} = \frac{1}{\hat{A}^*}\{(\hat{A}^* - \hat{A})q_{11} + (\hat{B}^* - \hat{B})q_{21} + \hat{A}\},$$
$$L^R_{12} = \frac{1}{\hat{A}^*}\{(\hat{A}^* - \hat{A})q_{12} + (\hat{B}^* - \hat{B})q_{22}\},$$
$$L^R_{21} = \frac{1}{\hat{D}^*}\{(\hat{B}^* - \hat{B})q_{11} + (\hat{D}^* - \hat{D})q_{21}\},$$
$$L^R_{22} = \frac{1}{\hat{D}^*}\{(\hat{B}^* - \hat{B})q_{12} + (\hat{D}^* - \hat{D})q_{22} + \hat{D}\}. \quad \text{(D2)}$$

Downloaded 04 May 2010 to 171.66.16.27. Redistribution subject to ASME license or copyright; see http://www.asme.org/terms/Terms_Use.cfm

On a Spring-Network Model and Effective Elastic Moduli of Granular Materials

K. Alzebdeh
Ergotron, Inc.,
1181 Trapp Road,
St. Paul, MN 55121
Mem. ASME

M. Ostoja-Starzewski
Institute of Paper Science and Technology
and Georgia Institute of Technology,
500 10th Street, N.W.,
Atlanta, GA 30318-5794
Mem. ASME

Two challenges in mechanics of granular media are taken up in this paper: (i) development of adequate numerical discrete element models of topologically disordered granular assemblies, and (ii) calculation of macroscopic elastic moduli of such materials using effective medium theories. Consideration of the first one leads to an adaptation of a spring-network (Kirkwood) model of solid-state physics to disordered systems, which is developed in the context of planar Delaunay networks. The model employs two linear springs: a normal one along an edge connecting two neighboring vertices (grain centers) which accounts for normal interactions between the grains, as well as an angular one which accounts for angle changes between two edges incident onto the same vertex; edges remain straight and grain rotations do not appear. This model is then used to predict elastic moduli of two-phase granular materials—random mixtures of soft and stiff grains—for high coordination numbers. It is found here that an effective Poisson's ratio, ν^{eff}, of such a mixture is a convex function of the volume fraction, so that ν^{eff} may become negative when the individual Poisson's ratios of both phases are both positive. Additionally, the usefulness of three effective medium theories—perfect disks, symmetric ellipses, and asymmetric ellipses—is tested.

1 Introduction

The effects of grain-grain interactions and random geometry of granular materials on their mechanical response have been a subject of many works, e.g., Shen et al. (1992). For the past two decades, a role complementary to the experimental investigations has been played by large computer simulations of disk assemblies and by various analytical studies aimed at deriving effective medium theories of the constitutive behavior. The principal method in the area of computer simulations, dating back to Cundall and Strack (1978), is the so-called discrete element (DE) model. A complete version of the DE model accounts for a normal force F, a shear force $\tilde{F}$, and a moment M at the contact between two contiguous grains (Fig. 1(*c*)). There is also a restricted model which accounts for normal and shear forces only (Bathurst and Rothenburg, 1988, 1999), but this neglect of the contact moment is justified by the fact that only small numerical errors are thus caused in problems of interest in granular materials (Rothenburg, 1994). In the case of a regular, triangular array of disks, this model is equivalent to a classical Born model of crystal lattices which is well known to lack the rotational invariance (Jagota and Benison, 1994).

The shortcoming of the Born model had been removed in several other models of crystal lattices. As a starting point, we have a central-force model, which is specified by one central (i.e., normal) force spring constant k^n, and thus fixes the value of an effective Poisson's ratio for a given lattice geometry. By introducing the so-called *three-point interactions,* one can account for the storage of energy due to the angle changes in shear deformations, and, in fact, there are two ways of doing it—according to Kirkwood or Keating, the first of which will be employed below. With two spring constants—normal k^n and angular k^a—one can now vary the Poisson's ratio.

Let us here employ a graph representation of the planar granular medium: a graph $G(V, E)$, whereby vertices of the set V signify grain centers and edges of the set E represent the existing grain-grain interactions. If we fix an r-θ polar coordinate system at a grain's center, we observe that the limitation of the conventional DE models, whether complete or restricted, is a lack of inclusion of the $\theta\theta$-type strains and stresses in any grain, which corresponds to the change of an angle formed by the lines joining the vertex V_1 of the grain 1 with the vertices V_2 and V_3 of two adjacent and mutually contiguous grains 2 and 3. Such three grains (1, 2, 3) are shown in Fig. 1(*a*), while Fig. 1(*b*) displays the normal and shear forces and moments exerted onto 1 by 2 and 3. In a classical DE model three-spring constants are being introduced at each contact—they correspond to F, $\tilde{F}$, and M, respectively. It is well known (Satake, 1978) that such a model is micropolar. However, in Fig. 1(*c*) we indicate one more interaction, of a spring constant k^a, which accounts for the energy storage due to an angle change between the edges $V_1 - V_2$ and $V_1 - V_3$.

In the present paper we shall consider a special case of the general model of Fig. 1(*c*). Namely, we admit central (or normal) force interactions, and augment them by the angular resistances of Kirkwood (1939) type (Fig. 1(*d*)). That is, shearing and bending of edges of the E set is not allowed, and no energy is stored in such a deformation mode. Consequently, the kinematics of graph $G(V, E)$ is described by displacements (regardless of rotations) of all the vertices of the V set, and the mechanics is classical rather than micropolar. Caution: a large part of the 1980s and 1990s condensed matter physics literature concerned with mechanics of heterogeneous media uses the terms "bond bending" for the presence of k^a springs; this is a misnomer.

All the interactions in this model are assumed to occur along the edges (bonds) of planar Delaunay networks (Fig. 2) and through the aforementioned angular changes. Topologically, the grains occupy all the cells of a Voronoi mosaic (Ostoja-Starzewski and Wang, 1989, 1990). On the theoretical side, this

Contributed by the Applied Mechanics Division of THE AMERICAN SOCIETY OF MECHANICAL ENGINEERS for publication in the ASME JOURNAL OF APPLIED MECHANICS.

Discussion on the paper should be addressed to the Technical Editor, Professor Lewis T. Wheeler, Department of Mechanical Engineering, University of Houston, Houston, TX 77204-4792, and will be accepted until four months after final publication of the paper itself in the ASME JOURNAL OF APPLIED MECHANICS.

Manuscript received by the ASME Applied Mechanics Division, Dec. 3, 1997; final revision, Apr. 17, 1998. Associate Technical Editor: R. C. Becker.

 Copyright © 1999 by ASME

Downloaded 04 May 2010 to 171.66.16.27. Redistribution subject to ASME license or copyright; see http://www.asme.org/terms/Terms_Use.cfm

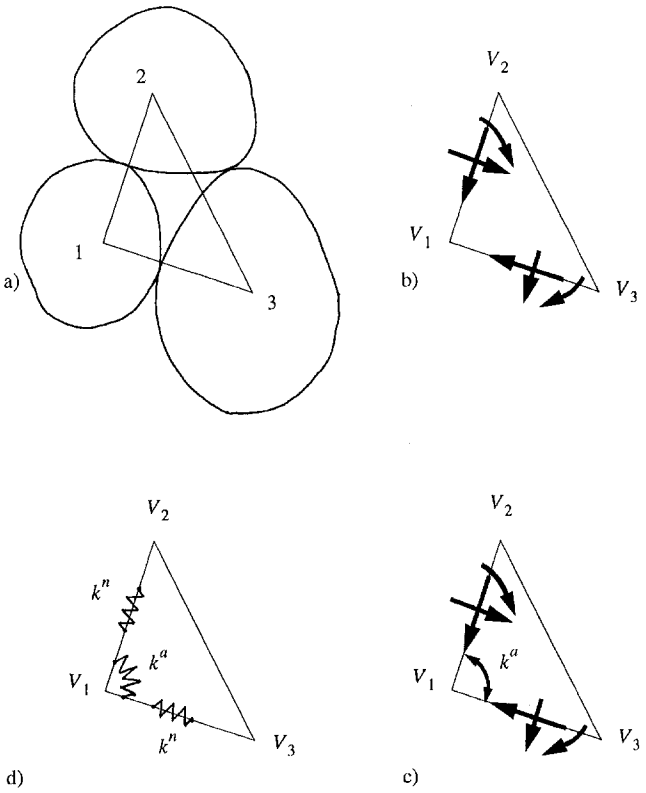

Fig. 1 (*a*) A cluster of three grains (1, 2, 3) showing the three lines of interactions; (*b*) a discrete element model showing the normal force, the shear force, and the moment exerted by grains 2 and 3 each onto the grain 1; (*c*) a most general model showing the same grain-grain interactions as before but augmented by an internal, angular spring constant k^a; (*d*) a simplified model adopted in this paper, showing only normal (k^n) and angular (k^a) effects

model is thus a generalization of the Kirkwood model to disordered geometries, whereas on the application side it is an investigation of the effect of storage of strain energy in all the grains due to the angular changes vis-à-vis the energy storage in normal grain-grain compression only. While the micro level properties are locally anisotropic and fluctuating, the statistics of Delaunay networks are homogeneous and isotropic, so that, on the macroscale, an isotropic, constitutive law (involving, say, the bulk and shear moduli) is sought. To determine it, a computational model that can handle several thousand grains under periodic boundary conditions has been developed (Alzebdeh, 1994). The model is then applied to a two-phase granular medium, a mixture of two types of grains: soft and stiff.

The present paper also critically examines the applicability of three effective medium theories by testing them against the computational model results. The effective medium theories are as follows: a self-consistent method for circular disks, a symmetric self-consistent approximation, and an asymmetric self-consistent approximation for elliptical disks, all with perfect bonding. While in Ostoja-Starzewski et al. (1995) they were restricted to a single value of the macroscopic Poisson's ratio of ~0.38 because of the presence of normal springs only, here we extend this study to a wider range of Poisson's ratios.

2 A Planar Spring Network With Central and Angular Interactions

2.1 Central Interactions. Following the basic discussion in the Introduction, we focus on a Delaunay graph $G(V, E)$ whose edges carry central forces only. Thus, the response law along any edge e between two neighboring vertices is

$$F_i = \Phi_{ij}^{(e)} u_j \quad \Phi_{ij}^{(e)} = k^{n^{(e)}} n_i^{(e)} n_j^{(e)} \quad i, j = 1, 2 \tag{2.1}$$

where F_i and u_j are the bond's force and relative displacement components, while $n_i^{(e)}$ is a unit vector along the edge. Also, $k^{n^{(e)}}$ is a central (normal) force spring constant of the half-length of the edge e. The energy stored in a single Voronoi cell is

$$U^{\text{central}} = \sum_{e=1}^{e_{\text{total}}} \tfrac{1}{2} F_i^{(e)} u_i^{(e)} \tag{2.2}$$

where the sum is carried out over all the edges (1 through e_{total}) incident onto the given vertex.

Considering the fact that the mean number of neighbors in Voronoi tessellations is six, we may focus on a regular triangular lattice of spacing $s = 2l$ with hexagonal unit cells. By setting the strain energy stored in such a cell equal to the energy of an elastic continuum $U = C_{ijkm}\epsilon_{ij}\epsilon_{km}/2$ of the same area $A = 2\sqrt{3}l^2$, under homogeneous strains, we obtain from (2.1) and (2.2) the effective moduli

$$C_{ijkm} = \frac{l^2}{A} \sum_{e=1}^{e_{\text{total}}} k^{n^{(e)}} n_i^{(e)} n_j^{(e)} n_k^{(e)} n_m^{(e)} \tag{2.3}$$

of a continuum varying on fine length scale of the granular microstructure. The above is obtained by assuming homogeneous strains—a postulate which is correct in the case of a regular, periodic network with, say, three different spring constants assigned, respectively, in three directions.

In the most basic case of 60-deg angles and identical spring constants for all the edges, we arrive at

$$C_{1111} = C_{2222} = \frac{9}{8\sqrt{3}} k^n \quad C_{1122} = C_{2211} = \frac{3}{8\sqrt{3}} k^n$$

$$C_{1212} = \frac{3}{8\sqrt{3}} k^n. \tag{2.4}$$

It is readily observed that these C_{ijkm}'s satisfy the condition

$$2C_{1212} = C_{1111} - C_{1122} \tag{2.5}$$

so that the modeled continuum is isotropic. Its planar bulk and shear moduli are

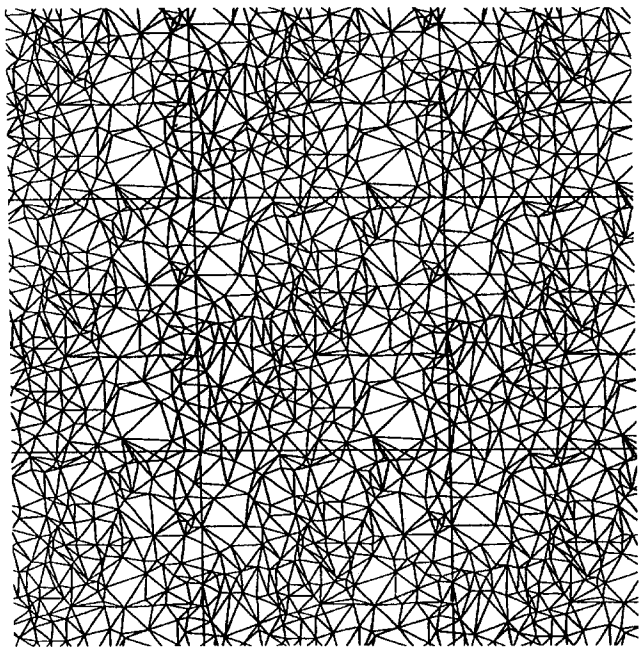

Fig. 2 A periodic Delaunay network with 200 vertices; actual simulations employed networks with up to 2000 vertices

Downloaded 04 May 2010 to 171.66.16.27. Redistribution subject to ASME license or copyright; see http://www.asme.org/terms/Terms_Use.cfm

$$\kappa = \frac{\sqrt{3}}{4} k^n \quad \mu = \frac{\sqrt{3}}{8} k^n. \tag{2.6}$$

By noting the expressions for a planar Young's modulus and a planar Poisson's ratio

$$E = \frac{4\kappa\mu}{\kappa + \mu} \quad \nu = \frac{\kappa - \mu}{\kappa + \mu}, \tag{2.7}$$

we observe that the fact that this system has just one spring constant, k^n, limits the number of free (i.e., adjustable) continuum elastic moduli to one, and thus, Poisson's ratio is fixed at 1/3.

The relation between planar and three-dimensional moduli depends on the interpretation of the spring network as a three-dimensional system in plane stress or plane strain (see also Thorpe and Jasiuk, 1992). We point out here that the continuum equivalent of an elastic planar spring network is a planar elasticity; its Navier's equation has a form different from the one commonly known from three-dimensional elasticity, that is

$$\mu u_{i,jj} + \kappa u_{j,ji} = 0 \quad i, j = 1, 2 \tag{2.8}$$

and its corresponding constitutive law is

$$\epsilon_{ij} = \frac{1 + \nu}{E} \left[\sigma_{ij} - \frac{\nu}{1 + \nu} \sigma_{kk} \delta_{ij} \right]. \tag{2.9}$$

2.2 Central and Angular Interactions. Continuum mechanics tells us that $\epsilon_{\theta\theta}$ equals $(\partial v/\partial\theta)/r + u/r$. This shows that the angular changes $\Delta\phi/\phi$ between two adjacent edges $V_1 - V_2$ and $V_1 - V_3$ in Fig. 1 correspond to $(\partial v/\partial\theta)/r$ in the r-θ polar coordinate system fixed at a grain's center. This term does not show up in two other expressions for ϵ_{rr} and $\epsilon_{r\theta}$. However, u/r is due to a radial displacement, and so $\Delta\phi/\phi$ does not exactly equal $\epsilon_{\theta\theta}$, which leads us to call it a $\theta\theta$-type strain. Following the basic discussion in the Introduction, we adapt the so-called Kirkwood model to account for $\Delta\phi/\phi$ in addition to the normal grain-grain interactions. Thus, we introduce angular springs of constant k^a acting between the edges $V_1 - V_2$ and $V_1 - V_3$ incident onto the node V_1, Fig. 1(d); the edges remain straight throughout deformation.

It now follows that the angular interaction energy stored in the Voronoi cell is a sum of energies of all the springs (1 through e_{total}), that is

$$U^{\text{angular}} = \sum_{e=1}^{e_{\text{total}}} \tfrac{1}{2} k^{a(e)} |\Delta\phi|^2$$
$$= \sum_{e=1}^{e_{\text{total}}} \tfrac{1}{2} k^{a(e)} \{ e_{kij} \epsilon_{jp} (n_i^{(e+1)} n_p^{(e+1)} - n_i^{(e)} n_p^{(e)}) \}^2 \tag{2.10}$$

where e_{kij} is a permutation tensor. The total strain energy stored in a single Voronoi cell is

$$U = U^{\text{central}} + U^{\text{angular}} \tag{2.11}$$

where U^{central} is given by (2.2). By setting the sum (2.12) equal to the energy of an elastic continuum as before, again under a postulate of homogeneous strains, a general expression of the effective moduli of the Voronoi cell can be derived. From the equilateral lattice case (Grah et al., 1996; Ostoja-Starzewski et al., 1996), with all identical k^n and k^a springs, we obtain condition (2.5), and we now really get two independent elastic moduli

$$\kappa = \frac{\sqrt{3}}{4} k^n \quad \mu = \frac{\sqrt{3}}{4} \left(\frac{1}{2} k^n + \frac{3}{l^2} k^a \right). \tag{2.12}$$

As expected, the presence of angular springs does not affect the dilatational response. From $(2.7)_2$ we find

$$\nu = \frac{\kappa - \mu}{\kappa + \mu} = \left(1 - \frac{3k^a}{k^n l^2} \right) \Big/ \left(3 + \frac{3k^a}{k^n l^2} \right) \tag{2.13}$$

which gives the full range of Poisson's ratio, between two extreme cases, that can be covered with this model

$$\nu = \frac{1}{3} \quad \text{if} \quad \frac{k^a}{k^n l^2} \to 0 \quad k^n - \text{model}$$

$$\nu = -1 \quad \text{if} \quad \frac{k^a}{k^n l^2} \to \infty \quad k^a - \text{model}. \tag{2.14}$$

It is noted here that for the Poisson's ratio between $-1/3$ and 1/3 one may also use a Keating (1966) model which employs a different calculation of the energy stored in angular springs. The case of ν higher than 1/3 is not very relevant for granular materials, but, we mention here for completeness, that it can be accomplished by a superposition of three honeycomb lattices, each with a different central force spring, thus resulting in a triangular lattice (e.g., Day et al., 1992).

2.3 Central and Bending Interactions. As mentioned in the Introduction, the DE models involve normal force, shear force, and bending moment interactions between contiguous grains, Fig. 1(b). In that case, the total energy stored in the Voronoi cell is a sum total

$$U = U^{\text{central}} + U^{\text{shear}} + U^{\text{moment}}. \tag{2.15}$$

Thus, any edge is modeled as a beam rather than as a straight rod, and the approximating continuum is a micropolar one. Setting (2.15) equal to the energy $U = C_{ijkm}\epsilon_{ij}\epsilon_{km}/2 + \kappa_{i3} D_{i3k3} \kappa_{k3}/2$, $i, j, k, m = 1, 2$, effective classical and micropolar moduli, C_{ijkm} and D_{i3k3}, can be found under conditions of homogeneous strain and curvature. The case of an equilateral lattice has been discussed in Ostoja-Starzewski et al. (1996); see also Woźniak (1970). If the vertex rotations are disregarded, the model (a restricted version of the DE model) stores energy under rigid-body rotations.

It is important to note that this model also offers a possibility of attaining Poisson's ratios other than 1/3: an increase of the cross-sectional area of such beams—i.e., a relative increase of flexural vis-à-vis axial effects—decreases ν.

3 A Two-Phase Granular Microstructure

Let us now consider a disordered, planar, granular medium, whose microstructural connectivity is modeled by a Delaunay planar tessellation graph. As is well known, a realization of the latter is generated by throwing a finite number of Poisson points in a region of $\mathbf{R}^2$ plane and defining the domains of all the points that lie closest to a given Poisson point. The resulting Poisson point field of intensity λ, as specified by ($|A|$ is a Lebesgue measure of the set A)

$$P\{N(A) = k\} = e^{-\lambda|A|} \frac{\lambda|A|}{k!} \quad A \subset \mathbf{R}^2 \tag{3.1}$$

occurs on the entire plane, and so, its numerical simulation is done on a compact subset, which actually involves a binomial point process (Stoyan et al., 1987).

These domains are called Voronoi polygons thus forming a Poisson-Voronoi tessellation, while the Poisson points and their nearest-neighbor connections are called a Poisson-Delaunay network. Figure 2 shows a special case of such a network—periodic Delaunay network—which, as elaborated below, is perfectly suited to the determination of macroscopic, effective moduli. Each Voronoi cell is occupied by a grain, and thus the topology of all the grain-grain interactions between the grains is represented by a Delaunay graph network. In accordance with Section 2.2, there are two types of interactions, both being

Downloaded 04 May 2010 to 171.66.16.27. Redistribution subject to ASME license or copyright; see http://www.asme.org/terms/Terms_Use.cfm

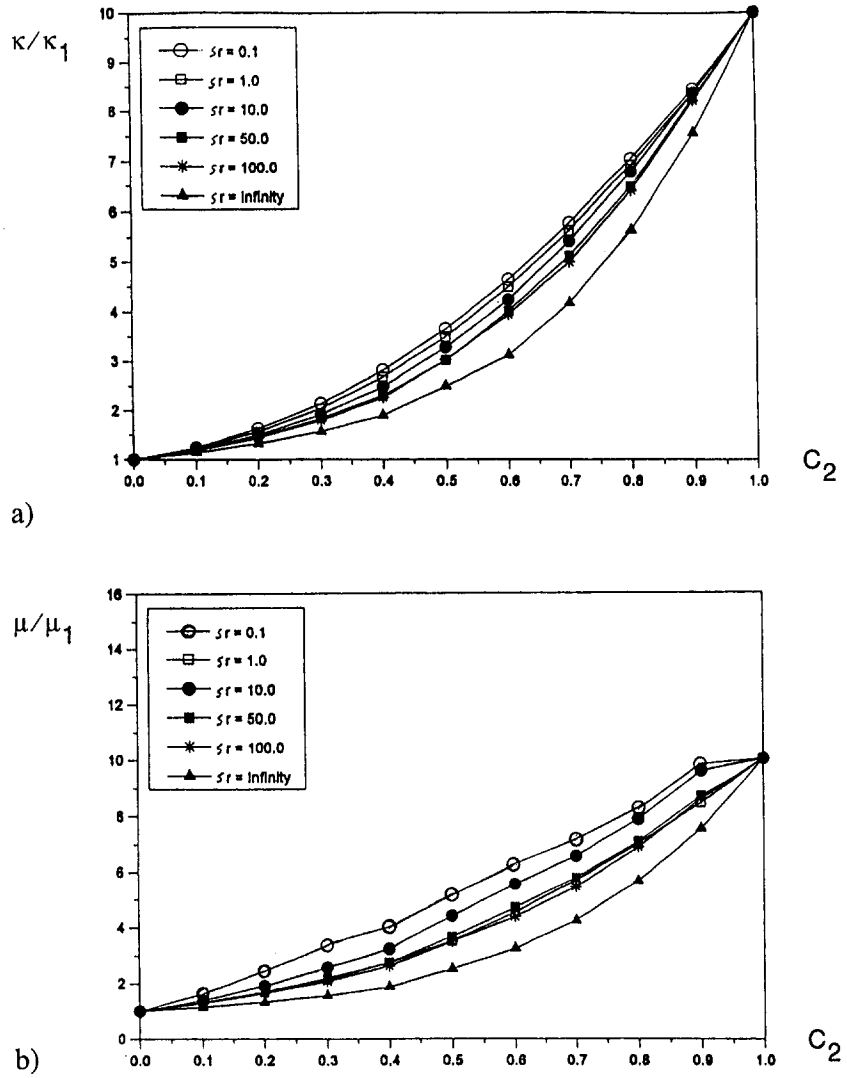

Fig. 3 Effective bulk (*a*) and shear (*b*) moduli at contrast 10 for different values of *sr*

modeled by linear elastic springs, normal with a constant k^n, and angular with a constant k^a.

The actual assignment of k^n and k^a depends on the specification of a particular grain as either soft (1) or stiff (2). Their respective volume fractions in this two-phase network are c_1 and c_2. Thus, type 1 (or 2) vertex implies that the halves of all edges incident onto it are soft (or stiff), and are specified by k_1^n (or k_2^n). Furthermore, the stiffness of any half-length, $l = s/2$, of a given edge is given by k_i^n/l, where $i = 1$ or 2. The stiffness ratio $r = k_2^n/k_1^n$ of stiff to soft spring constants is termed a contrast. Finally, the angular springs k_i^a are assigned simply according as they belong in a type-1 or type-2 grain.

Due to the geometric disorder of a Delaunay network, we cannot determine the effective, macroscopic moduli C_{ijkl}^{eff} analytically because the strain field under uniform-strain boundary conditions is nonuniform—this is why a computational model is necessary. First, we expect isotropy of C_{ijkl}^{eff} due to the spatial isotropy of the underlying Poisson point field. Next, the results for a triangular, equilateral lattice provide some guidelines here. In view of (2.14), by varying the $k^a/k^n l^2$ ratio, the present model can cover a range of media with Poisson's ratios from ~ 0.38 down to -1; the value ~ 0.38, rather than $1/3$ of a regular triangular network, is caused by the geometric disorder (Ostoja-Starzewski et al., 1995).

Following the methodology of that reference we proceed to find the overall, macroscopic, effective moduli C_{ijkl}^{eff} of periodic Delaunay networks from periodic boundary conditions

$$u_i(\mathbf{x} + \mathbf{L}) = u_i(\mathbf{x}) + \overline{\epsilon}_{ij} x_j \quad \forall \mathbf{x} \in \partial \mathbf{B}$$

$$t_i(\mathbf{x}) = -t_i(\mathbf{x} + \mathbf{L}) \quad \forall \mathbf{x} \in \partial \mathbf{B}. \tag{3.2}$$

Here $\overline{\epsilon}_{ij}$ is the macroscopic strain, t_i is the traction on $\partial \mathbf{B}$, and $\mathbf{L} = L\mathbf{e}_i$, with $\mathbf{e}_i$ being a unit base vector. The periodicity means that the network topology is modified so as to repeat itself with some periodicity L in x_1 and x_2 directions, whereby L is taken much larger than the grain size. A typical realization $\mathbf{B}(\omega)$ of a periodic Delaunay network, numbering 200 vertices, is shown in Fig. 2. A set of all such realizations $\{\mathbf{B}(\omega); \omega \in \Omega\}$, where Ω is a sample space, forms a random medium $\mathbf{B}$; a single ω indicates one realization of the Poisson point field and a chosen assignment of spring constants. In actual simulations only a minute subset of the entire sample space can be investigated, but by the standard Monte Carlo and ergodicity arguments, this subset is representative of the whole system. Thus, already the response of a single network much larger than the grain size is sufficient to gain a good estimate of C_{ijkl}^{eff}.

The procedure to calculate the effective moduli κ and μ is as follows: a given $\mathbf{B}(\omega)$ realization of the Delaunay network, is subjected, separately, to two tests:

- a biaxial extension, corresponding to a macroscopic strain state $\overline{\epsilon}_{11} = \overline{\epsilon}_{22}$,
- a shear deformation, corresponding to a macroscopic strain state $\overline{\epsilon}_{11} = -\overline{\epsilon}_{22}$.

Downloaded 04 May 2010 to 171.66.16.27. Redistribution subject to ASME license or copyright; see http://www.asme.org/terms/Terms_Use.cfm

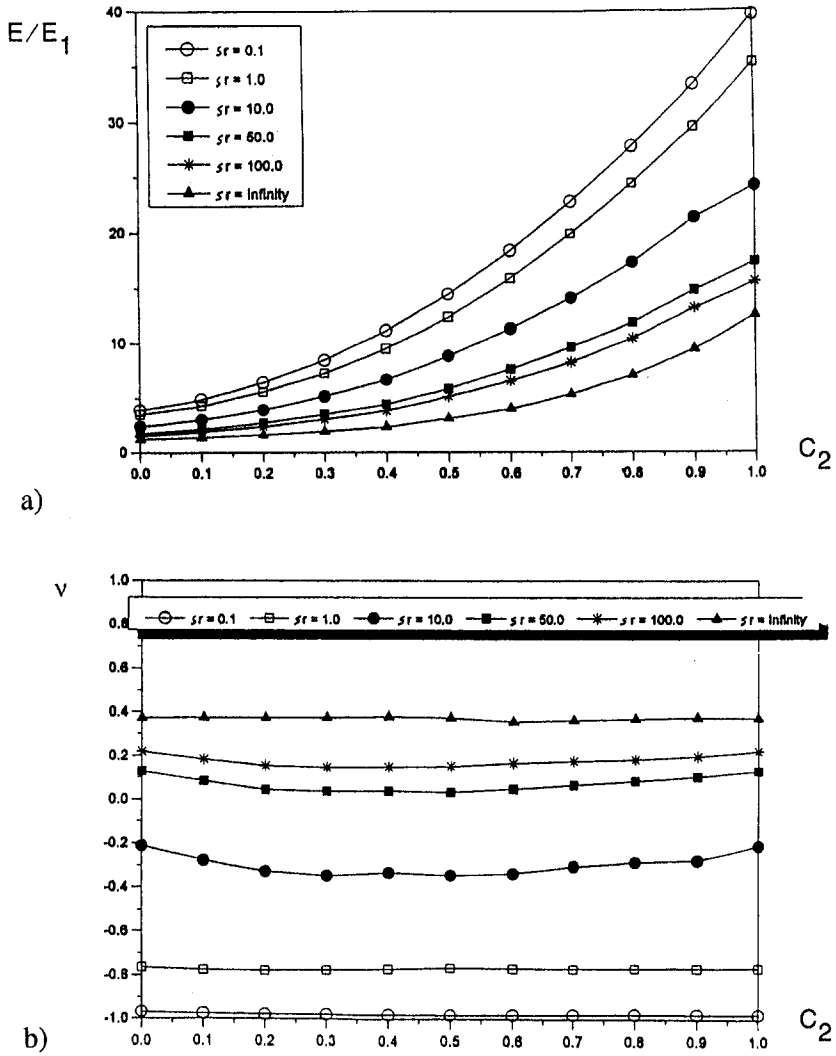

Fig. 4 Effective Young's modulus (*a*) and Poisson's ratio (*b*) at contrast 10 for the same range of values of *sr* as in Fig. 3

Actual equilibrium state is found using a conjugate gradient method. Next, by equating in each test the network's energy to that of a two-dimensional linear elastic equivalent continuum of volume (i.e., area) $V = L^2$,

$$U = \frac{V}{2}\left[\kappa\bar{\epsilon}_{ii}\bar{\epsilon}_{jj} + 2\mu\left(\bar{\epsilon}_{ij}\bar{\epsilon}_{ij} - \frac{1}{2}\bar{\epsilon}_{ii}\bar{\epsilon}_{jj}\right)\right], \qquad (3.3)$$

the bulk and shear moduli, respectively, can be calculated directly. Repeating this process in a Monte Carlo sense for a sufficient number of realizations, the effective bulk and shear moduli of the medium are obtained.

4 Numerical Results and Effective Medium Models

With the present Kirkwood-type model we have an additional parameter, the angular stiffness k^a, beyond the central force models studied in Ostoja-Starzewski et al. (1989, 1990, 1995). We shall therefore introduce a dimensionless ratio $sr \equiv k^n l^2/k^a$, in order to examine the effect of a progressive change from k^a nonexistent to k^a dominant on the effective elastic moduli of Delaunay networks. In terms of the Poisson's ratio—recall (2.14)—this corresponds to a change from about 1/3 to −1.

In the following, six particular values of *sr* are chosen: ∞, 100, 50, 10, 1.0, 0.1, whereby the first value corresponds to the central force case and the last one to angular interactions being much stronger than the central ones. Figure 3(*a*) shows the results of the effective bulk modulus κ normalized by κ_1 for a whole range of volume fraction (C_2) between 0.0 and 1.0 at 0.1 increments. Fig. 3(*b*) shows the corresponding effective shear modulus μ normalized by μ_1. Examining all these curves we observe that an increase in the *sr* parameter leads to an overall relative stiffening in terms of the effective bulk and shear moduli; this is consistent with what one might expect—introducing angular springs into a network increases its stiffness relative to a system with normal springs only.

Let us recall from (2.12) that in a perfectly homogeneous one-phase system (i.e., the regular, periodic lattice) the bulk modulus is not affected by the presence of k^a springs. On the other hand, the system of two types of grains mixed at random undergoes nonaffine deformations, a fact which influences the bulk-type response. It is therefore not surprising that κ in Fig. 3(*a*) is affected by the presence of the angular springs, albeit not as much as μ.

In Figs. 4(*a*) and (*b*) we show the effective Young's modulus and Poisson's ratio, computed from (2.7), at contrast 10 for the same range of values of *sr* as in Fig. 3. While the behavior of *E*

Downloaded 04 May 2010 to 171.66.16.27. Redistribution subject to ASME license or copyright; see http://www.asme.org/terms/Terms_Use.cfm

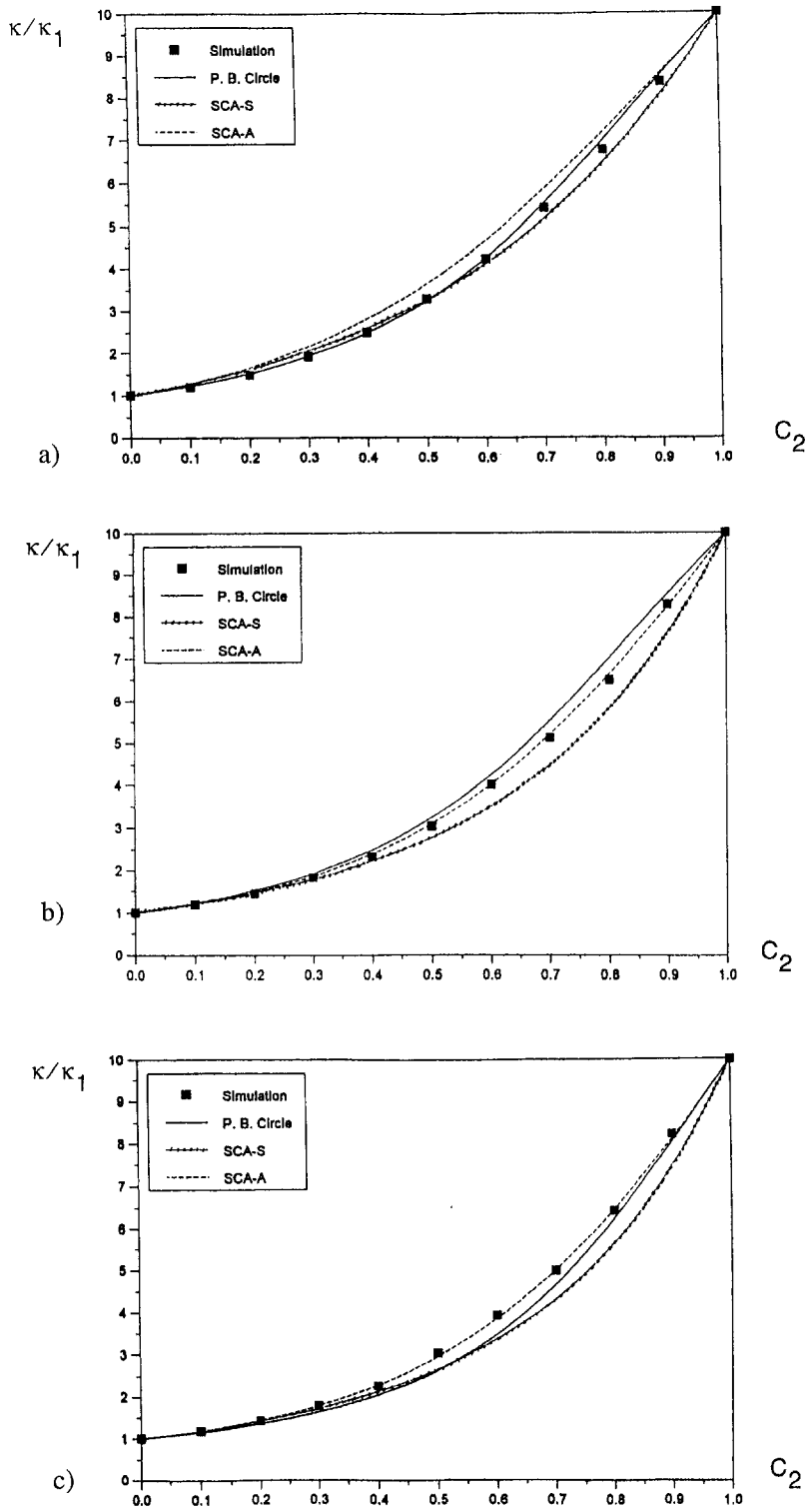

Fig. 5 Effective bulk modulus at contrast 10 from the spring network simulations and self-consistent models for *sr* = 100 (*a*), *sr* = 50 (*b*), *sr* = 10 (*c*)

is expected—it increases with the angular spring stiffness going up—the one of ν is more interesting. Namely, we observe that, a decrease in the *sr* parameter leads, for moderate values of this ratio, to a decrease of the effective Poisson's ratio ν, with respect to the one (i.e., ~0.38) of either phase, in the middle range of the volume fraction C_2, and then, for high values of *sr*, to a leveling off at −1.0, the lowest possible value of ν. This means that the effective Poisson's ratio of a mixture of two phases is a convex function of the volume fraction, so that it may become negative when ν_1 and ν_2 are still both positive. This behavior of ν is a consequence of the dependencies of κ and μ on C_2 and *sr* displayed in Fig. 3. That is, if we observe that μ increases initially more rapidly with *sr* going down than κ does, then, through a nonlinear relation $(2.7)_2$, ν of a mixture at $C_2 = 0.5$ is lower than ν of either pure phase at $C_2 = 0.0$ or 1.0. One more thing to keep in mind here is that given the 6-connectedness of the Delaunay

Downloaded 04 May 2010 to 171.66.16.27. Redistribution subject to ASME license or copyright; see http://www.asme.org/terms/Terms_Use.cfm

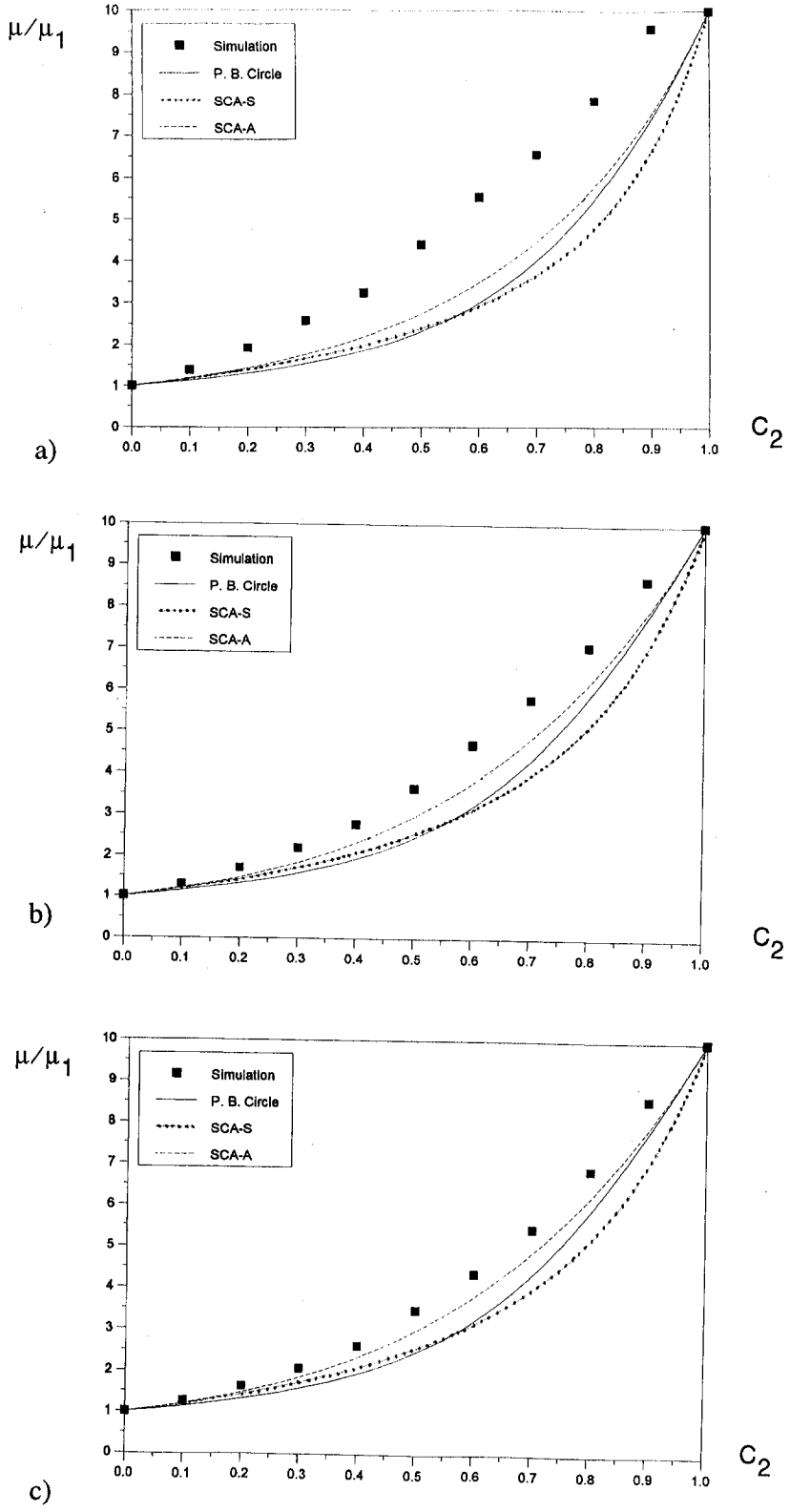

Fig. 6 Effective shear modulus at contrast 10 from the spring network simulations and self-consistent models for *sr* = 100 (*a*), *sr* = 50 (*b*), *sr* = 10 (*c*)

network, the case of $C_2 = 0.5$ is a situation of percolation of both phases, soft and stiff.

The last issue we want to discuss is a possibility of fitting the results of this type by the effective medium models. The potential for application of self-consistent models developed for composite materials hinges on a so-called spider-inclusion analogy, which is based on an observation that a single grain interacting with its neighbors is analogous to an inclusion embedded in a continuum matrix (Ostoja-Starzewski, 1993; Ostoja-Starzewski et al., 1995). The most obvious approach to employ is the classical self-consistent model of circular inclusions with perfectly bonded interfaces (PB). According to Hill

Downloaded 04 May 2010 to 171.66.16.27. Redistribution subject to ASME license or copyright; see http://www.asme.org/terms/Terms_Use.cfm

(1965) and Budiansky (1965) the formulas for bulk and shear moduli are

$$\frac{1}{\kappa} = \frac{1}{\kappa_1} + c_2\left(\frac{1}{\kappa_2} - \frac{1}{\kappa_1}\right)\frac{\frac{1}{\mu} + \frac{1}{\kappa}}{\frac{1}{\mu} + \frac{1}{\kappa_2}}$$

$$\frac{1}{\mu} = \frac{1}{\mu_1} + 2c_2\left(\frac{1}{\mu_2} - \frac{1}{\mu_1}\right)\frac{\frac{1}{\mu} + \frac{1}{\kappa}}{\frac{1}{\mu} + \frac{1}{\mu_2} + \frac{2}{\kappa}}. \quad (4.1)$$

However, in view of the shape randomness of all the Voronoi cells, we may consider the inclusions to be somewhat elongated rather than circular. This leads to an extension of the PB model to elliptical inclusions (Thorpe and Sen, 1985). In particular, two versions of the self-consistent approximations (SCA) are of interest to us:

- a Symmetric Self-Consistent Approximation (SCA-S), which treats the medium as a mixture of N phases without distinguishing any one as a matrix,
- an Asymmetric Self-Consistent Approximation (SCA-A), which treats the medium as a system of N-1 types of inclusions embedded in a matrix.

The SCA-S is specified by the following equations:

$$\sum_{i=1}^{N} c_i P_i(\kappa - \kappa_i) = 0 \quad \sum_{i=1}^{N} c_i Q_i(\mu - \mu_i) = 0 \quad (4.2)$$

while the SCA-A is given by

$$\frac{1}{\kappa} = \frac{1}{\kappa_1}\left[1 + \sum_{i=2}^{N} c_i P_i\left(\frac{\kappa_1 - \kappa_i}{\kappa}\right)\right]$$

$$\frac{1}{\mu} = \frac{1}{\mu_1}\left[1 + \sum_{i=2}^{N} c_i Q_i\left(\frac{\mu_1 - \mu_i}{\mu}\right)\right] \quad (4.3)$$

where the matrix phase (i.e., $i = 1$) serves as a reference. In the above, coefficients P_i and Q_i are given by

$$P_i = \left[1 + Z_i - \frac{Z_i Y_i}{X_i + Y_i}\left(\frac{1 - s}{1 + s}\right)^2\right]^{-1}$$

$$2Q_i = P_i\frac{1 + Z_i}{X_i + Y_i} + (2 + A_i - X_i)^{-1} \quad (4.4)$$

where s is the ellipse aspect ratio and

$$X_i = 1 + \frac{A_i s(1 + \nu)}{(1 + s)^2} \quad Y_i = \frac{A_i(1 - \nu)}{2}$$

$$Z_i = \frac{C_i(1 + \nu)}{2} \quad (4.5)$$

and

$$A_i = \frac{\mu_i}{\mu} - 1 \quad C_i = \frac{\kappa_i}{\kappa} - 1 \quad \nu = \frac{\kappa - \mu}{\kappa + \mu}. \quad (4.6)$$

Since we seek the simplest analytical model, we specialize these results to the case of two phases $N = 2$. The two governing formulas—i.e., (4.2) or (4.3)—are coupled and, hence, must be solved by iteration. Both models, SCA-S and SCA-A, collapse to the PB model when $s = 1$.

In the following we choose three cases of sr: 100, 50, 10. In Fig. 5 we show the dependence of the effective bulk modulus at contrast 10, for the volume fraction C_2 varying continuously from 0.0 through 1.0, computed from the spring network simulations and by the self-consistent models. This is followed by Fig. 6 which gives an effective shear modulus. In both figures we plot the results of SCA-S and SCA-A (both at aspect ratio $s = 2$), as well as PB models; this value of s was found to result in the best fits. We conclude that all three models give roughly same, equally good approximations for the bulk modulus, and rather poor approximations for the shear modulus.

5 Closure

Research reported in this paper has primarily been motivated by the fact that conventional computational mechanics models of granular materials do not account for angular resistance of grains. This angular resistance of a grain is called, in the language of condensed matter physics, a three-point interaction, and presents an additional contribution beyond the two-point interaction. For example, a recent book on doublet mechanics (Ferrari et al., 1997) presents models for a range of phenomena with two-point interactions, but cannot claim a full generality as it misses this three-point contribution. Our model admits only the displacements as possible degrees of freedom per grain, and thus results in a classical (non-polar continuum). Existing discrete element models possess a grain's rotation as an additional degree of freedom, and are therefore micropolar. We argue that the three-point interaction should be introduced in them to better represent the micromechanics to make, in accordance with Fig. 1(c), the strain energy stored in a single Voronoi cell a combination of (2.11) and (2.15),

$$U = U^{\text{central}} + U^{\text{shear}} + U^{\text{moment}} + U^{\text{angular}}. \quad (5.1)$$

The question of how to model the elasticity of a granular mass reflects a basic dilemma in mechanics of discrete (not only granular) materials: how best to represent a piecewise-continuous medium by a discrete mechanical model on a graph $G(V, E)$? We hope that the present paper is a useful contribution to this subject. Additionally, the presented model may also have applications in mechanics of other media, such as cellular or fibrous materials (e.g., Hansen et al., 1996).

Acknowledgment

The presentation of this work benefited from the reviewers' comments. Support of this research by the NSF under grants MSS 9202772 and CMS-9713764 is gratefully acknowledged.

References

Alzebdeh, K., 1994, "Computational Methods in Stochastic Micromechanics of Heterogeneous Solids," Ph.D. thesis, Michigan State University.

Bathurst, R. J., and Rothenburg, L., 1988, "Micromechanical Aspects of Isotropic Granular Assemblies With Linear Contact Interactions," ASME JOURNAL OF APPLIED MECHANICS, Vol. 55, pp. 17–23.

Bathurst, R. J., and Rothenburg, L., 1989, "Note on a random isotropic granular material with negative Poisson's ratio," *Intl. J. Engng. Sci.*, Vol. 26, pp. 373–383.

Budiansky, B., 1965, "On the elastic moduli of some heterogeneous materials," *J. Mech. Phys. Solids*, Vol. 13, pp. 223–227.

Cundall, P. A., and Strack, O. D. L., 1979, "A Discrete Numerical Model for Granular Assemblies," *Geotechnique*, Vol. 29, No. 1, pp. 47–65.

Day, A. R., Snyder, K. A., Garboczi, E. J., and Thorpe, M. F., 1992, "The elastic moduli of a sheet containing circular holes," *J. Mech. Phys. Solids*, Vol. 40, pp. 1031–1051.

Ferrari, M., Granik, V. T., Imam, A., and Nadeau, J. C., eds., 1997, *Advances in Doublet Mechanics*, Springer-Verlag, New York.

Grah, M., Alzebdeh, K., Sheng, P. Y., Vaudin, M. D., Bowman, K. J., and Ostoja-Starzewski, M., 1996, "Brittle intergranular failure in 2D microstructures: experiments and computer simulations," *Acta Mater.*, Vol. 44, No. 10, pp. 4003–4018.

Hansen, J. C., Chien, S., Skalak, R., and Hoger, A., 1996, "An elastic network model based on the structure of the red blood cell membrane skeleton," *Biophys. J.*, Vol. 70, pp. 146–166.

Hill, R., 1965, "A self-consistent mechanics of composite materials," *J. Mech. Phys. Solids*, Vol. 13, pp. 213–222.

Jagota, A., and Benison, S. J., 1994, "Spring-network and finite-element models for elasticity and fracture," *Non-linearity and Breakdown in Soft Condensed*

Downloaded 04 May 2010 to 171.66.16.27. Redistribution subject to ASME license or copyright; see http://www.asme.org/terms/Terms_Use.cfm

Matter, K. K. Bardhan, B. K. Chakrabarti, and A. Hansen, eds., *Lecture Notes in Physics,* Vol. 437, pp. 186–201, Springer-Verlag, New York.

Keating, P. N., 1966, "Effect of invariance requirements on the elastic strain energy of crystals with application to the diamond structure," *Phys. Rev.,* Vol. 145, pp. 637–645.

Kirkwood, J. G., 1939, "The skeletal modes of vibration of long chain molecules," *J. Chem. Phys.,* Vol. 7, pp. 506–509.

Ostoja-Starzewski, M., 1993, "Random fields and processes in mechanics of granular materials," *Mech. Mater.,* Vol. 16, No. 1–2, pp. 55–64.

Ostoja-Starzewski, M., and Wang, C., 1989, "Linear elasticity of planar Delaunay networks: Random field characterization of effective moduli," *Acta Mech.,* Vol. 80, pp. 61–80.

Ostoja-Starzewski, M., and Wang, C., 1990, "Linear elasticity of planar Delaunay networks. II: Voigt and Reuss bounds, and modification for centroids," *Acta Mech.,* Vol. 84, pp. 47–61.

Ostoja-Starzewski, M., Alzebdeh, K., and Jasiuk, I., 1995, "Linear elasticity of planar Delaunay networks—III: Self-consistent approximations," *Acta Mech.,* Vol. 110, pp. 57–72.

Ostoja-Starzewski, M., Sheng, P. Y., and Alzebdeh, K., 1996, "Spring network models in elasticity and fracture of composites and polycrystals," *Comput. Mater. Sci.,* Vol. 7, Nos. 1 and 2, pp. 82–93.

Rothenburg, L., 1994, private communication.

Satake, M., 1978, "Constitution of mechanics of granular materials through graph representation," *Theor. Appl. Mech.,* Vol. 26, University of Tokyo Press, Tokyo, Japan.

Shen, H. H., Satake, M., Mehrabadi, M., Chang, C. S., Campbell, eds., 1992, *Advances in Micromechanics of Granular Materials, Stud. Appl. Mech.,* Vol. 31, Elsevier, New York.

Stoyan, D., Kendall, W. S., and Mecke, J., 1987, *Stochastic Geometry and its Applications,* John Wiley and Sons, New York.

Thorpe, M. F., and Sen, P. N., 1985, "Elastic moduli of two-dimensional composite continua with elliptical inclusions," *J. Acoust. Soc. Am.,* Vol. 77, No. 5, pp. 1674–1680.

Thorpe, M. F., and Jasiuk, I., 1992, "New Results in the Theory of Elasticity of Two-Dimensional Composites," *Proc. Soc. Lond.,* Vol. A438, pp. 531–544.

Woźniak, C., 1970, *Surface Lattice Structures,* PWN–Polish Sci. Publ., Warsaw (in Polish).

Downloaded 04 May 2010 to 171.66.16.27. Redistribution subject to ASME license or copyright; see http://www.asme.org/terms/Terms_Use.cfm

Thermosolutal Convection in the Presence of Both Vertical and Horizontal Temperature Gradients

A. K. Sahai
Climate & Global Modeling Division,
Indian Institute of Tropical Meteorology,
Dr. Homi Bhabha Road,
Pashan,
Pune-411 008, India

The occurrence of stationary and oscillatory solutions in a horizontal layer of fluid in the presence of horizontal and vertical temperature gradients and also in the presence of a vertical solute concentration gradient is investigated. The critical Rayleigh number for oscillatory and stationary solutions is derived numerically for a wide range of values of parameters and it is found that the marginal state is of periodic character in almost all the cases except for very small values of horizontal temperature gradient, solute gradient, and Prandtl number. The effect of horizontal gradient of temperature on the stability of the system is both stabilizing as well as destabilizing. For a large value of horizontal temperature gradient the system first exhibits oscillatory motion and in subsequent time oscillations die down.

Introduction

The onset of convection in a horizontal layer of fluid due to the applied vertical temperature gradient was theoretically investigated by Benard (1900), Rayleigh (1916), and various other workers. A comprehensive account of these theoretical and experimental investigations were presented by Chandrasekhar (1961). It has been observed that the convection sets in when the applied temperature gradient, expressed in terms of Rayleigh number, exceeds a certain critical value. Krishnamurti (1973) showed experimentally that oscillatory convection occurs in liquid metals contained in the Benard cell at Rayleigh number of the order of, or only very slightly greater than, that expected for the stationary convection. Experiments of Skafel (1972) and Hurle et al. (1974) showed that the thermal convective motions of the system occur due to the horizontal temperature gradients, even very small ones. This is the reason why in the process of growing metal and semiconductor crystals from a liquid melt, spontaneous oscillations in the temperature of liquid melt have been found to occur, which lead to undesirable properties in the solid crystal produced. Hart (1972) has numerically investigated the stability of a simple parallel flow with horizontal temperature gradient and has established that longitudinal oscillatory modes are possible for small Prandtl number fluids. Gill (1974) has used a mean field approximation to study analytically the existence of thermal oscillations and has obtained results which were in agreement with the numerical investigations of Hart (1972) and comparable with experiments (Skafel, 1972; Hurle et al., 1974). Sweet et al. (1977) extended the analysis of Gill to include an adverse vertical temperature gradient and also examined the occurrence of stationary solutions as a function of the vertical and horizontal temperature gradient ratio and Prandtl number. Singhal and Srivastava (1982) have studied the effect of a magnetic field in the presence of vertical and horizontal temperature gradients and the same authors (1984) have studied the thermal oscillations of a particle fluid mixture with horizontal temperature gradients.

Instabilities which arise solely as a result of differential diffusion of different components of two component fluids are of considerable geophysical relevance. A very common example of this type of instability occurs in a fluid stratified jointly by heat and salt. Instabilities develop as a result of the disparity in diffusion rates of salt and heat even when the overall density distribution is stable. Stern (1960), while explaining the mechanism of salt fingers formation, showed that a gravitationally stable stratification of salinity and temperature (cold fresh water below warm saline water), such as observed in the oceans, is

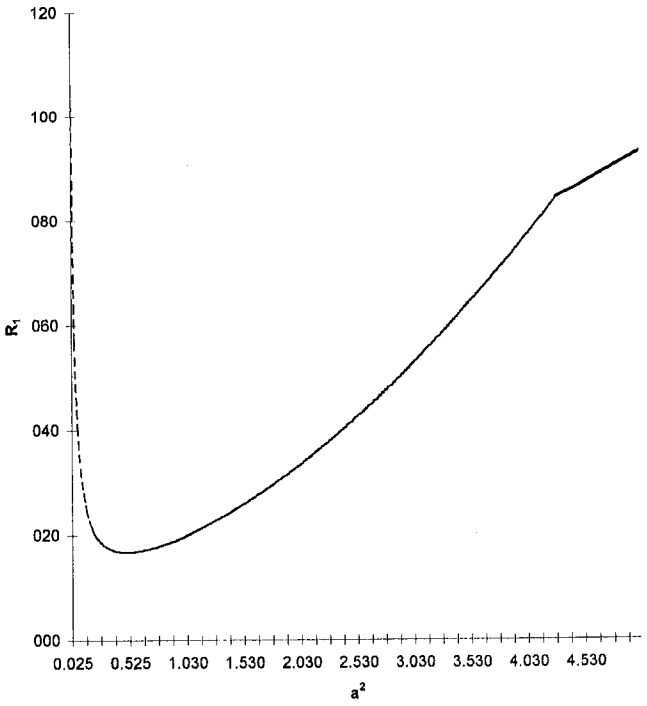

Fig. 1 Neutral stability curve for oscillatory convection, Eq. (27)--- and stationary convection, Eq. (25) ———. $R_1' = 50$, $p = 0.007$, $K^2 = 0.25 \times 10^{-8}$, $\tau = 0.01$.

Contributed by the Applied Mechanics Division of THE AMERICAN SOCIETY OF MECHANICAL ENGINEERS for publication in the ASME JOURNAL OF APPLIED MECHANICS.

Discussion on the paper should be addressed to the Technical Editor, Professor Lewis T. Wheeler, Department of Mechanical Engineering, University of Houston, Houston, TX 77204-4792, and will be accepted until four months after final publication of the paper itself in the ASME JOURNAL OF APPLIED MECHANICS.

Manuscript received by the ASME Applied Mechanics Division, May 4, 1995; final revision, July 15, 1998. Associate Technical Editor: S. A. Berger.

 Copyright © 1999 by ASME

Downloaded 04 May 2010 to 171.66.16.27. Redistribution subject to ASME license or copyright; see http://www.asme.org/terms/Terms_Use.cfm

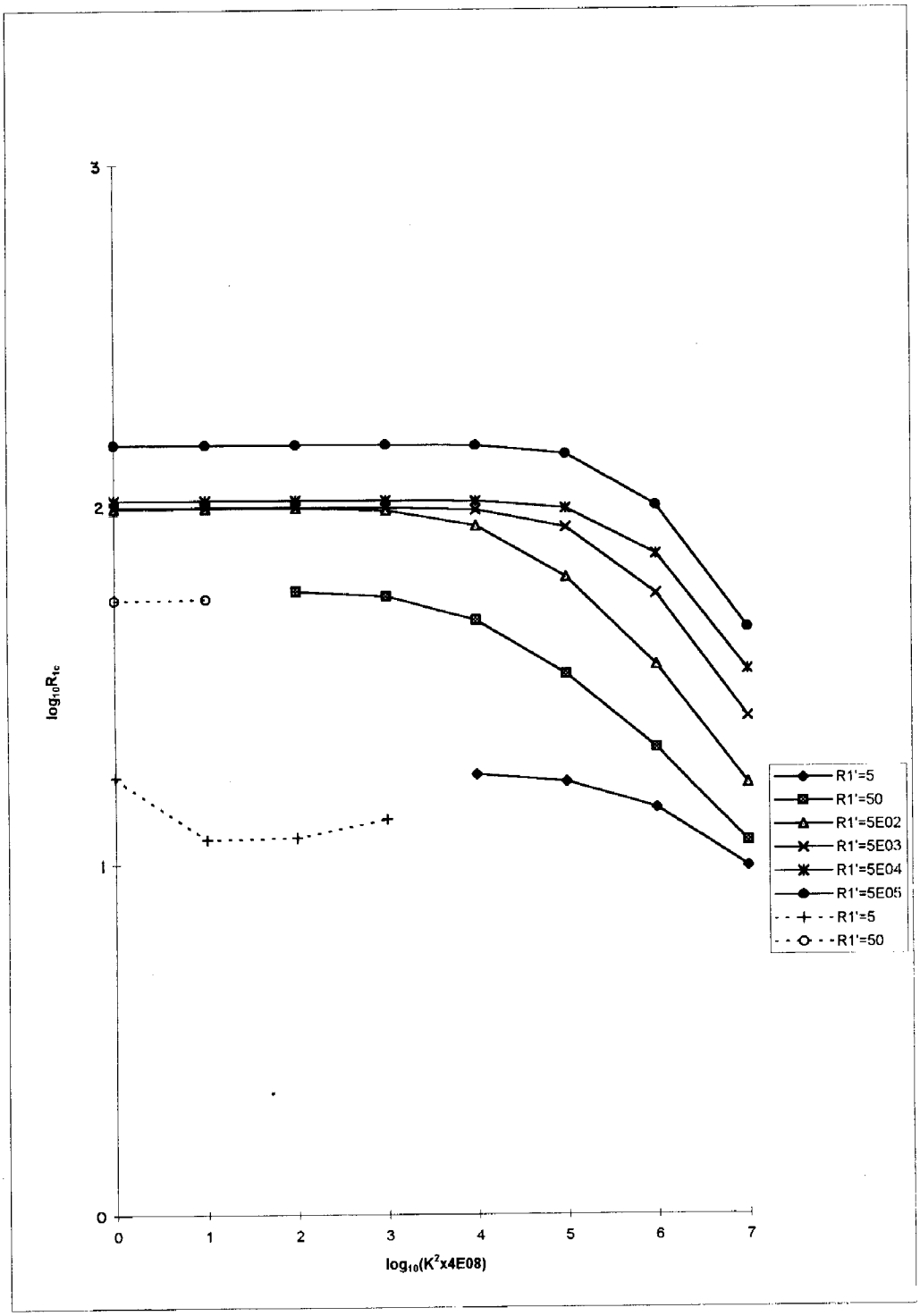

Fig. 2 Critical Rayleigh number R_c as a function of the ratio of the applied temperature gradients (K^2) for different values of R_1' for stationary convection --- and oscillatory convection ———. p = 0.0007, τ = 0.01.

actually unstable. Physically it can be explained as if a particle is displaced vertically it will lose its temperature excess much more rapidly than its salinity excess (the coefficient of diffusion of heat is a hundred times greater than that of salt), the resulting buoyant force may be sufficient to keep the particle moving in the direction of displacement. That is, any displacement will grow directly with time leading to a stationary convection. Stern (1960) has shown that the process involving salt fingers alone could redistribute the salt throughout the vertical and bring about a vertically isohaline distribution in a matter of days. That it is not observed in nature is due to an instability in which salt fingers are destroyed. Thus salt fingers are continuously created and destroyed, and the natural situation in the oceans appears to be much the same as would exist if the process were absent. Veronis (1965) considered the gravitationally opposite case (i.e., warm saline water below the fresh cold water) and showed that an instability to infinitesimal perturbations will occur first as overstable motions. The physical explanation of this can be given as follows. When a fluid particle is displaced upwards it will adjust its temperature to the local value relatively quickly

Downloaded 04 May 2010 to 171.66.16.27. Redistribution subject to ASME license or copyright; see http://www.asme.org/terms/Terms_Use.cfm

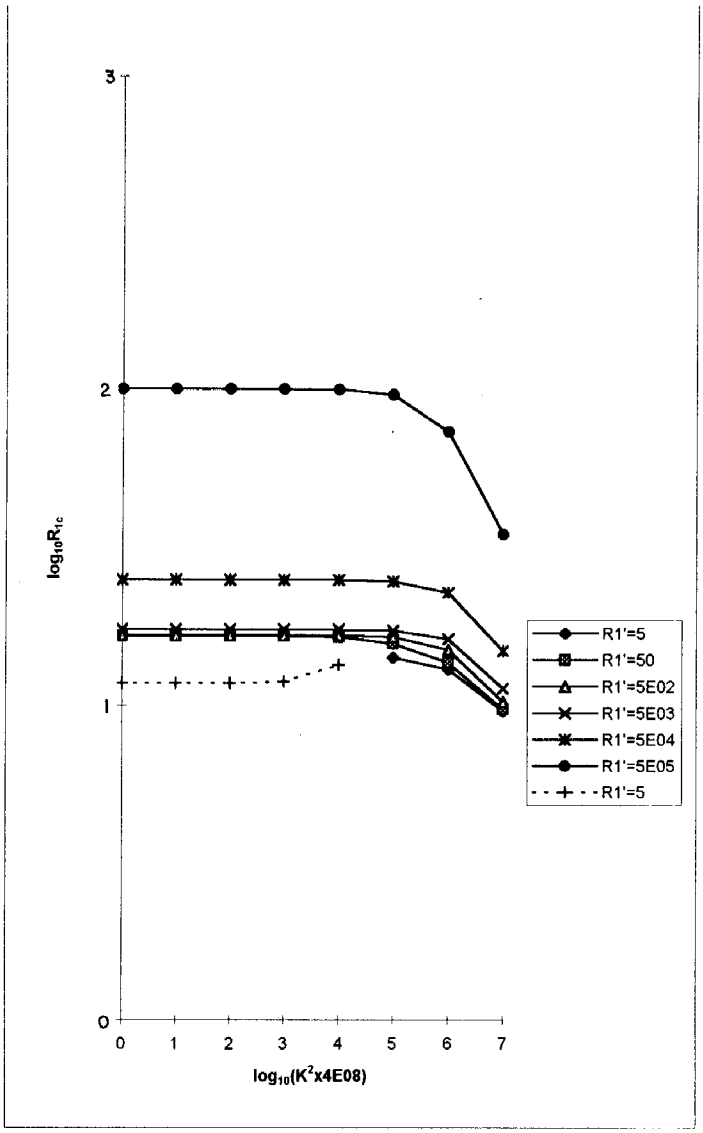

Fig. 3 Critical Rayleigh number R_c as a function of the ratio of the applied temperature gradients (K^2) for different values of R_1' for stationary convection --- and oscillatory convection ———. p = 0.007, τ = 0.01.

but the particle remains locally heavy by virtue of its excess salinity and it is forced to sink to its original position and overshoot. In its new position it experiences an upward force because of its local salinity difficiency so that it begins to oscillate about its original position, experiencing buoyancy restoring forces at the extreme points in its motion. Because of the lag in temperature between the particle and its surrounding fluid (thermal diffusivity though large but still finite), the particle always leaves either of the limiting positions faster than it arrives. This results in an increase in the amplitude of the oscillation leading to an oscillatory convection. Veronis (1965) has concluded that once the system becomes unstable, the developed state of convection will be steady and he has also pointed out that if the initial condition of warm salty water underlying cold fresh water does in fact exist, the finite amplitude instability would take place so as to destroy the initial condition, and the final configuration would be an essentially isohaline distribution. As far as the applicability of the models of Stern and Veronis is concerned, the latter author has remarked that though the situation considered by the former exits over most of the ocean, i.e., salty warm water usually lies above fresher cold water, configuration considered by him can be expected to exist (i) near coastal regions where tidal effects could carry salty warm water in under fresher cold water or (ii) in areas such as the eastern Atlantic where salty Mediterranean water flows out through the Strait of Gibralter into the ocean.

In the present communication the effect of a vertical solute gradient is studied on the convection in the presence of horizontal and vertical temperature gradients. This can be considered either as the extention of Veronis (1965) by including horizontal temperature gradients or the extention of Sweet et al. (1977) by including vertical solute gradients. Therefore, this extention is relevant and may find its application (i) in the study of the process of growing crystals of a binary alloy melt and to study the small-scale transitions that determine the physical and electrical properties of the resulting materials and (ii) in the study of geophysical problems. Observations of Stommell and Fedorov (1967) and many other workers have shown that in the main thermocline and in the mixed layer of oceans, horizontal gradients of temperature and salinity are present and a

Downloaded 04 May 2010 to 171.66.16.27. Redistribution subject to ASME license or copyright; see http://www.asme.org/terms/Terms_Use.cfm

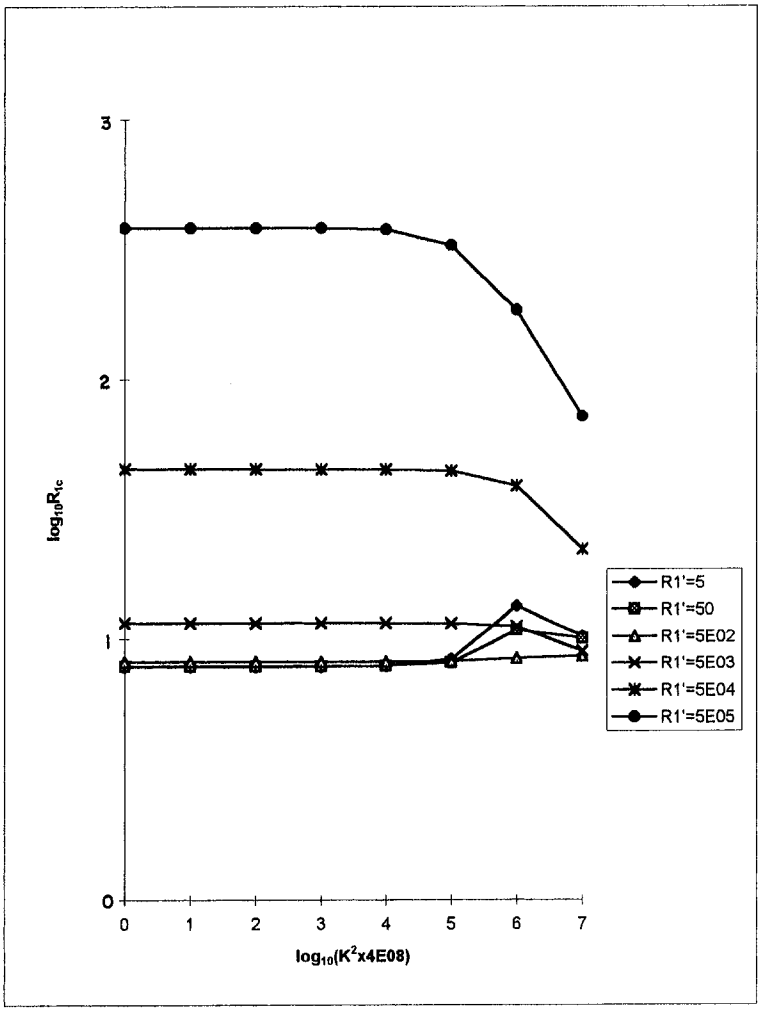

Fig. 4 Critical Rayleigh number R_c as a function of the ratio of the applied temperature gradients (K^2) for different values of R_1' for oscillatory convection. $p = 0.07$, $\tau = 0.01$.

layered structure is a characteristic of the ocean and also of some lakes. Interesting experiments related to laboratory simulation of thermohaline convection (Thorpe et al., 1969; Turner, 1968) have investigated the effects of horizontal temperature gradients on thermohaline convection. When a stable salinity gradient is subjected to a horizontal temperature gradient, resulting instability can be explained as follows. A fluid particle near the wall is forced to move upwards by thermally induced buoyancy, but the distance it can travel in this direction is limited by its salinity as in the case of Veronis (1965). It is therefore forced to move horizontally into the interior of the fluid, cooling as it does so, until it returns in a cellular manner to the hot wall. The process is identical to all fluid particles in the vicinity of the heated wall so that a stack of two-dimensional longitudinal rolls is formed simultaneously, each having a depth which is typically small compared with the overall fluid depth and a layered structure is developed. The experiments of Turner (1968), in which the experimental conditions were similar to Veronis (1965), have shown that in the bottom of the tank (i.e., on the heated surface) first oscillations appeared and then died away. A short time later, many cycles of an oscillation with steadily increasing amplitude were observed until finally the amplitude increased and the layer broke into convective motion. These experiments indicated that the convective motion occurs in horizontal layers or bands of fluid with a large horizontal scale. Shirtcliffe (1967) investigated experimentally the oscillatory instability characterizing the diffusion regime near-marginal stability. In his experiments, as the marginal state was reached, an oscillatory instability was detected near the heated surface, the amplitude of oscillations growing with time. As the imposed temperature gradient increased further the oscillations took on an increasing irregular form and a steady cellular structure becomes visible in the lower part of the fluid region.

The motivation of the present communication is to see whether these experimental results can be explained theoretically by considering temperature gradients from the side boundaries.

Formulation of the Problem

Let us consider a horizontal layer of an incompressible, viscous fluid, infinitely extending in the x-y directions and bounded by the planes at $z = d/2$ and the layer is heated laterally and vertically such that a temperature gradient β_1 in the positive x-direction and a temperature gradient β_2 in the negative z-direction are present, where the z-axis points vertically upwards. Also let the fluid be soluted from below such that a solute gradient β_3 is present in the z-direction. Then the equations of motion, continuity, heat transport, and solute concentration under Boussinesq approximations are

$$\frac{\partial \mathbf{q}}{\partial t} + (\mathbf{q}\cdot\nabla)\mathbf{q} = -\frac{\nabla p}{\rho_0} + v\nabla^2\mathbf{q} - \left(1 + \frac{\delta\rho}{\rho_0}\right)g\hat{k} \quad (1)$$

$$\nabla\cdot\mathbf{q} = 0 \quad (2)$$

Downloaded 04 May 2010 to 171.66.16.27. Redistribution subject to ASME license or copyright; see http://www.asme.org/terms/Terms_Use.cfm

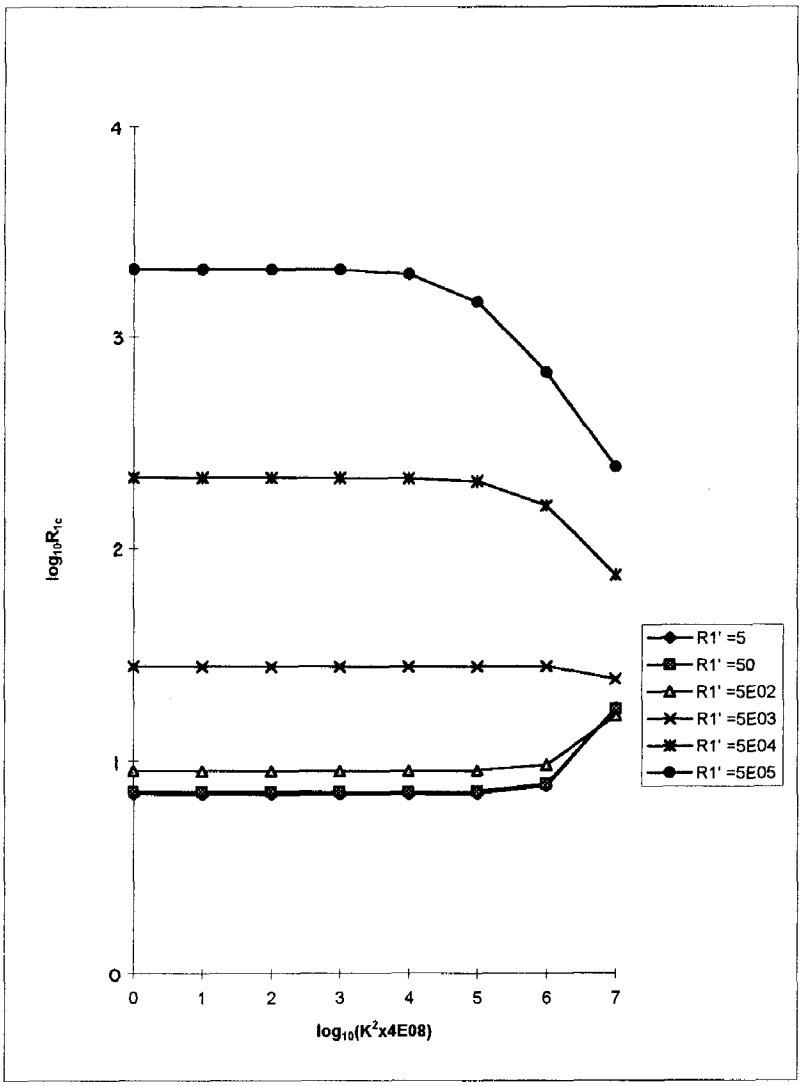

Fig. 5 Critical Rayleigh number R_c as a function of the ratio of the applied temperature gradients (K^2) for different values of R_1' for oscillatory convection. $p = 0.7$, $\tau = 0.01$.

$$\frac{\partial T}{\partial t} + (\mathbf{q}\cdot\nabla)T = K_T\nabla^2 T \tag{3}$$

$$\frac{\partial S}{\partial t} + (\mathbf{q}\cdot\nabla)S = K_S\nabla^2 S \tag{4}$$

where

$$\frac{\delta\rho}{\rho_0} = \alpha(T_0 - T) - \alpha'(S_0 - S). \tag{5}$$

Here $\mathbf{q}$, v, p, ρ, g, $\hat{k}$, T, S, K_T, K_S, α, and α' are, respectively, the fluid velocity, coefficient of kinematic viscosity, pressure, density, acceleration due to gravity, unit vector along the z-axis, temperature, solute concentration, coefficient of thermal diffusivity, coefficient of solute diffusivity, and thermal and solute expansion coefficients. Also ρ_0, T_0, and S_0 are some properly chosen mean density, mean temperature, and mean solute concentration, respectively.

From Eq. (1) the vorticity equation can be written as

$$\frac{\partial\boldsymbol{\xi}}{\partial t} + \nabla\times[(\mathbf{q}\cdot\nabla)\mathbf{q}] = v\nabla^2\boldsymbol{\xi} - \frac{g}{\rho_0}(\nabla\times\delta\rho\hat{k}) \tag{6}$$

where $\boldsymbol{\xi} = \nabla\times\mathbf{q}$.

Basic State. Let the basic state be steady. The horizontal buoyancy gradient will generate a vorticity leading to a shear dU/dz, and in turn the associated velocity field by advection generates a vertical temperature gradient $d\Theta/dz$. Therefore, an exact solution of Eqs. (1)–(4) in basic state are

$$\left.\begin{aligned}\bar{\mathbf{q}} &= (U(z), 0, 0)\\ \bar{p} &= p(z)\\ \bar{S} &= S_0 - \beta_3 z\\ \bar{T} &= T_0 + \beta_1 x - \beta_2 z + \Theta(z)\end{aligned}\right\} \tag{7}$$

where U and Θ satisfy

$$v\frac{d^3U}{dz^3} = \alpha g\beta_1, \quad K_T\frac{d^2\Theta}{dz^2} = U\beta_1. \tag{8}$$

The solutions of Eq. (8) are

$$\left.\begin{aligned}U(z) &= \frac{\alpha g\beta_1}{v}\frac{z^2}{6} + A_1z^2 + A_2z + A_3\\ \Theta(z) &= \frac{\beta_1}{K_T}\left[\frac{\alpha g\beta_1}{v}\frac{z^5}{120} + \frac{A_1z^4}{12} + \frac{A_2z^3}{6} + \frac{A_3z^2}{2}\right]\\ &\quad + A_4z + A_5\end{aligned}\right\}. \tag{9}$$

Downloaded 04 May 2010 to 171.66.16.27. Redistribution subject to ASME license or copyright; see http://www.asme.org/terms/Terms_Use.cfm

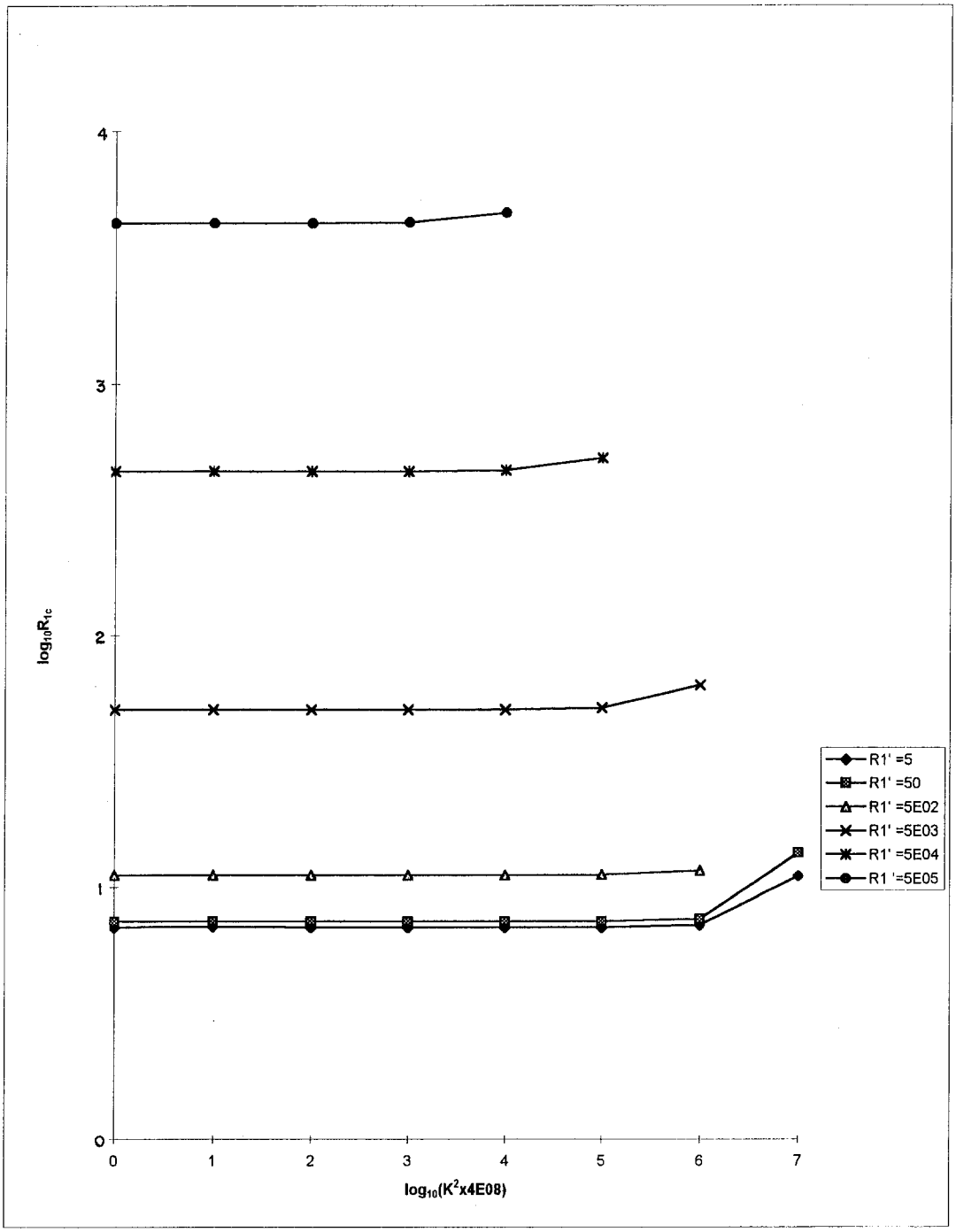

Fig. 6 Critical Rayleigh number R_c as a function of the ratio of the applied temperature gradients (K^2) for different values of R_1' for oscillatory convection. p = 7.0, τ = 0.01.

Thus U is cubic in z and Θ is quintic in z. The coefficients A_1, A_2, A_3, A_4, and A_5 depend upon the boundary conditions applied at the plane horizontal boundaries at $z = \pm d/2$.

Perturbation Equations. Let the basic state defined by Eq. (7) be slightly perturbed so that the various physical quantities undergo a change given by

$$\bar{\mathbf{q}} \to \bar{\mathbf{q}} + q', \bar{p} \to \bar{p} + p', \bar{T} \to \bar{T} + \theta, \bar{S} \to \bar{S} + \gamma. \quad (10)$$

Let the perturbed quantities $\mathbf{q}'(u, v, w)$, θ, γ, and p' be functions of y, z, and t only. This idea that the perturbed quantities are independent of x but varies in a vertical plane perpendicular to the basic flow came from the measurements of Hurle et al. (1974) and Gill (1974). Then a stream function ψ can be defined from the equation of continuity for a perturbed flow in the y–z plane with

$$v = -\frac{\partial \psi}{\partial z}, \quad w = \frac{\partial \psi}{\partial y}. \quad (11)$$

Then from the x-component of momentum and vorticity equation we get

$$\frac{\partial u}{\partial t} + \frac{dU}{dz}\frac{\partial \psi}{\partial y} = v\nabla^2 u \quad (12)$$

Downloaded 04 May 2010 to 171.66.16.27. Redistribution subject to ASME license or copyright; see http://www.asme.org/terms/Terms_Use.cfm

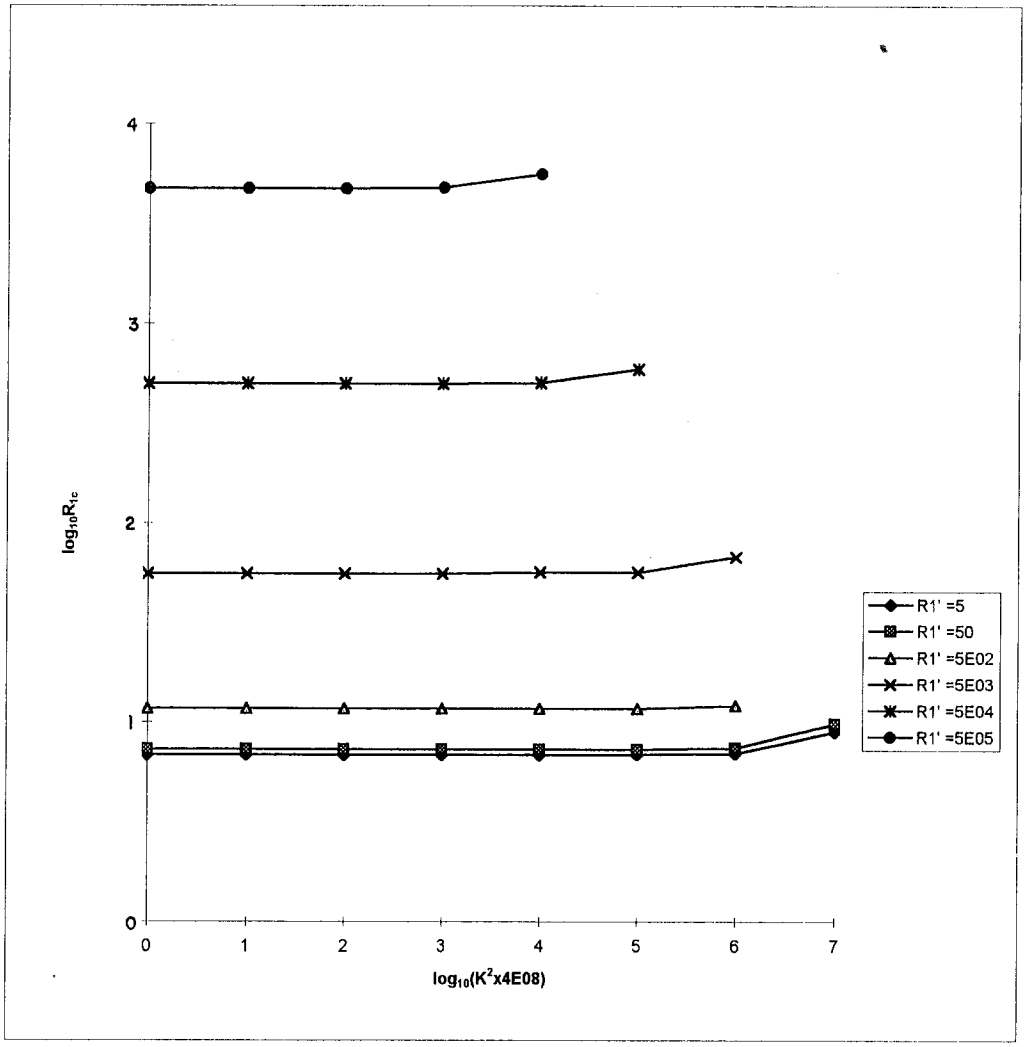

Fig. 7 Critical Rayleigh number R_c as a function of the ratio of the applied temperature gradients (K^2) for different values of R_1' for oscillatory convection. $p = 70.0$, $\tau = 0.01$.

$$\nabla^2 \frac{\partial \psi}{\partial t} = v\nabla^4\psi + g\alpha \frac{\partial \theta}{\partial y} - g\alpha' \frac{\partial \gamma}{\partial y} \tag{13}$$

where

$$\nabla^2\psi = \frac{\partial^2\psi}{\partial y^2} + \frac{\partial^2\psi}{\partial z^2}, \tag{14}$$

and from the equation of heat transport and solute concentration we get

$$\frac{\partial \theta}{\partial t} - \beta_2 \frac{\partial \psi}{\partial y} + \frac{d\Theta}{dz}\frac{\partial \psi}{\partial y} + u\beta_1 = K_T\nabla^2\theta \tag{15}$$

$$\frac{\partial \gamma}{\partial t} - \beta_3 \frac{\partial \psi}{\partial y} = K_S\nabla^2\gamma. \tag{16}$$

Eliminating all the variables from Eqs. (12) to (16) in favor of a single variable ψ, we get

$$\left[\frac{\partial}{\partial t} - v\nabla^2\right]^2 \left[\frac{\partial}{\partial t} - K_T\nabla^2\right]\left[\frac{\partial}{\partial t} - K_S\nabla^2\right]\nabla^2\psi$$

$$+ g\alpha\left[\frac{\partial}{\partial t} - v\nabla^2\right]\left[\frac{\partial}{\partial t} - K_S\nabla^2\right]\left[\frac{d\Theta}{dz} - \beta_2\right]\frac{\partial^2\psi}{\partial y^2}$$

$$- g\alpha\beta_1\left[\frac{\partial}{\partial t} - K_S\nabla^2\right]\frac{dU}{dz}\frac{\partial\psi^2}{\partial y^2}$$

$$+ g\alpha'\beta_3\left[\frac{\partial}{\partial t} - v\nabla^2\right]\left[\frac{\partial}{\partial t} - K_T\nabla^2\right]\frac{\partial\psi^2}{\partial y^2} = 0. \tag{17}$$

Solutions of Eq. (17) are obtained by using normal modes and the stream function in this case is written as

$$\psi = \hat{\psi}(z)e^{\sigma t}\sin(ly) \tag{18}$$

where σ is in general complex given by $\sigma = \sigma_r + i\sigma_i$, σ_r is the growth rate, and σ_i is the frequency of oscillation; also, l is the associated wave number. The substitution of Eq. (18) into (17) reduces the later into an ordinary differential equation of tenth order and the discussion of stability of the problem reduces in finding the eigenvalue of σ for which the approximate boundary condition is satisfied. Instability occurs when there exists an eigenvalue of σ with positive real part. Putting Eq. (18) in (17) we get

$$(\sigma_* - P^{1/2}\Delta_*)^2(\Delta_* - \sigma_* P^{1/2})(\sigma_* P^{1/2} - \tau\Delta_*)\Delta_*\hat{\psi}$$

$$+ l_*^2 A^2\left[(\sigma_* P^{1/2} - \tau\Delta_*)\right.$$

Downloaded 04 May 2010 to 171.66.16.27. Redistribution subject to ASME license or copyright; see http://www.asme.org/terms/Terms_Use.cfm

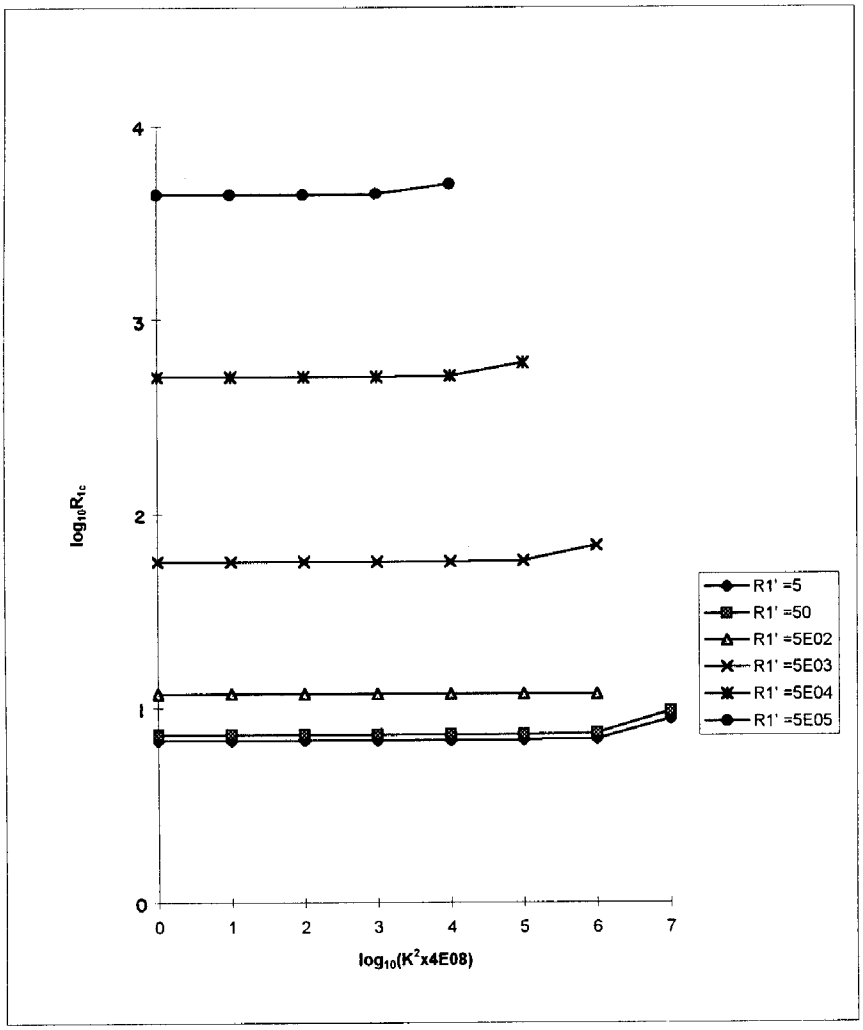

Fig. 8 Critical Rayleigh number R_c as a function of the ratio of the applied temperature gradients (K^2) for different values of R_1' for oscillatory convection. p = 700.0, τ = 0.01.

$$\times \left\{ u_* \hat{\psi} + P^{1/2}(\sigma_* - P^{1/2}\Delta_*)\left(T_* - \frac{R}{A^2}\right)\hat{\psi} \right\}$$

$$+ \frac{P^{1/2}R'\tau}{A^2}(\sigma_* - P^{1/2}\Delta_*)(\sigma_* P^{1/2} - \Delta_*)\hat{\psi} \Big] = 0. \quad (19)$$

Equation (19) is in dimensionless form. The nondimensional quantities are

$$\left.\begin{aligned} z_* = z/d,\ l_* = ld,\ \sigma_* = \sigma d^2(\upsilon K_T)^{-1/2}, \\ u_* = -\left(\frac{dU}{dz}\right)d^2/(K_T A), \\ T_* = \left(\frac{d\theta}{dz}\right)\Big/ A\beta_1,\ A = (g\alpha\beta_1 d^4)/(\nu K_T), \\ R = (g\alpha\beta_2 d^4)/(\upsilon K_T), \\ R' = (g\alpha\beta_3 d^4)/(\upsilon K_S),\ \tau = K_S/K_T, \\ P = \upsilon/K_T \text{ and } \Delta_* = \frac{d^2}{dz^2} - l_*^2 \end{aligned}\right\} \quad (20)$$

Here R, R', A, P, and τ are, respectively, the vertical Rayleigh number, solute Rayleigh number, horizontal Rayleigh number, Prandtl number, and Lewis number.

Approximate Solution of the Stability Problem

Equation (19), which is the governing equation of the problem, involves u_* and T_* which are functions of z, and is difficult to solve exactly. Following Gill (1974) and others (Sweet et al., 1977; Singhal and Srivastava, 1982, 1984) one can find the approximate solutions to Eq. (19) by replacing u_* and T_* by constants $\bar{u}$ and $\bar{T}$, respectively, which are approximately the weighted mean value of the corresponding quantities defined as

$$\bar{u} = \frac{4c^2}{\pi^2},\ \bar{T} = \frac{c^2}{\pi^4} \quad (21)$$

where

$$c^2 = \begin{cases} 1/16 & \text{for rigid conducting boundaries} \\ (1 + \pi^2/3)/16 & \text{for free conducting boundaries.} \end{cases} \quad (22)$$

Then Eq. (19) has sinusoidal solutions in z. A vertical scale can be set by assuming that the depth of the fluid will be approximately half a wavelength. Then the operator Δ_* can be replaced by

Downloaded 04 May 2010 to 171.66.16.27. Redistribution subject to ASME license or copyright; see http://www.asme.org/terms/Terms_Use.cfm

Table 1 Critical values of various parameters for oscillatory and stationary solution. $\tau = 0.01$.

R_1'	K^2	p	a_{oc}^2	R_{oc}	ω_c	a_{sc}^2	R_{sc}
5	0.25×10^{-8}	0.0007	0.5	18.186	imaginary	0.5	11.7504
		0.007	0.5	16.541	imaginary	0.475	11.7549
		0.07	0.5	7.7952	0.1105	0.475	11.6987
		0.7	0.5	6.9358	0.0969	-----	----
		7	0.475	6.8711	0.0534	0.125	15.8109
		70	0.5	6.8678	0.0150	0.2	11.3791
		700	0.5	6.8675	0.0053	0.175	11.8632
	0.25×10^{-7}	0.0007	0.5	18.185	imaginary	0.5	11.7632
		0.007	0.5	14.486	imaginary	0.5	11.7508
		0.07	0.5	7.7952	0.1104	0.475	11.7587
		0.7	0.5	6.9358	0.0938	-----	----
		7	0.425	6.9303	0.0426	0.375	11.7897
		70	0.5	6.8678	0.015	0.475	11.4763
		700	0.5	6.8675	0.0053	0.325	11.8698
	0.25×10^{-6}	0.0007	0.5	18.184	imaginary	0.5	11.8845
		0.007	0.5	16.388	imaginary	0.5	11.7632
		0.07	0.5	7.7956	0.1105	0.5	11.7516
		0.7	0.5	6.9358	0.0969	0.5	11.7486
		7	0.475	6.8711	0.0534	0.55	11.7584
		70	0.5	6.8678	0.0151	0.425	11.8052
		700	0.5	6.8675	0.0055	0.45	11.7554
	0.25×10^{-5}	0.0007	0.5	18.173	imaginary	0.575	13.4316
		0.007	0.5	16.053	imaginary	0.5	11.8849
		0.07	0.5	7.7999	0.1105	0.5	11.7635
		0.7	0.5	6.9363	0.0969	0.5	11.7511
		7	0.5	6.8712	0.0451	0.5	11.7487
		70	0.5	6.8679	0.0151	0.5	11.7476
		700	0.5	6.8676	0.0055	0.475	11.7562
	0.25×10^{-4}	0.0007	0.5	18.063	0.0778	----	----
		0.007	0.5	15.288	imaginary	0.575	13.4369
		0.07	0.5	7.8429	0.111	0.5	13.4912
		0.7	0.5	6.9415	0.0969	0.5	11.7667
		7	0.5	6.8727	0.0450	0.5	11.7547
		70	0.5	6.869	0.0151	0.5	11.7533
		700	0.5	6.8687	0.0050	0.5	11.7534
	0.25×10^{-3}	0.0007	0.5	17.231	0.2594	----	-----
		0.007	0.5	14.173	0.2032	----	-----
		0.07	0.525	8.3271	0.1184	0.575	13.4912
		0.7	0.5	6.9935	0.0971	0.5	11.9209
		7	0.5	6.8874	0.0451	0.5	11.7981
		70	0.5	6.8801	0.0149	0.5	11.7861
		700	0.5	6.8794	0.0049	0.5	11.7848
	0.25×10^{-2}	0.0007	0.45	14.484	0.6757	-----	----
		0.007	0.475	13.009	0.6057	-----	----
		0.07	0.5	13.358	0.4882	-----	----
		0.7	0.525	7.6174	0.1009	0.575	14.0927
		7	0.5	7.0422	0.0451	0.525	12.2698
		70	0.5	6.9948	0.0149	0.5	12.132
		700	0.5	6.9901	0.0056	0.5	12.1186
	0.25×10^{-1}	0.0007	0.4	9.8273	1.4073	----	----
		0.007	0.4	9.603	1.3672	----	----
		0.07	0.4	10.25	1.3714	-----	----
		0.7	0.4	17.861	1.5718	----	----
		7	0.55	11.125	0.0468	----	----
		70	0.5	8.9437	0.0151	----	----
		700	0.5	8.8195	0.0052	----	----

Downloaded 04 May 2010 to 171.66.16.27. Redistribution subject to ASME license or copyright; see http://www.asme.org/terms/Terms_Use.cfm

Table 1 Continued

R_1'	K^2	p	a_{oc}^2	R_{oc}	ω	a_{sc}^2	R_{sc}
50	$0.25x10^{-8}$	0.0007	0.5	60.269	imaginary	0.5	56.7809
		0.007	0.5	16.565	0.3629	0.475	56.7489
		0.07	0.5	7.8288	0.3886	0.5	56.8746
		0.7	0.5	7.1232	0.3111	----	--- -
		7	0.5	7.2654	0.1434	0.225	56.9029
		70	0.5	7.3115	0.0482	0.175	56.8404
		700	0.5	7.3169	0.0153	0.125	59.3034
	$0.25x10^{-7}$	0.0007	0.5	60.247	imaginary	0.5	57.0602
		0.007	0.5	16.565	0.3629	0.5	56.7813
		0.07	0.5	7.8288	0.3886	0.5	56.7457
		0.7	0.5	7.1237	0.3110	-----	----
		7	0.5	7.2654	0.1435	-----	----
		70	0.5	7.3115	0.0482	0.3	57.095
		700	0.5	7.3169	0.0153	0.3	56.9747
	$0.25x10^{-6}$	0.0007	0.5	60.031	0.0082	0.625	60.0351
		0.007	0.5	16.564	0.3630	0.5	57.0609
		0.07	0.5	7.8291	0.3886	0.5	56.7823
		0.7	0.5	7.1238	0.3110	0.525	56.7535
		7	0.5	7.2654	0.1435	0.6	56.8315
		70	0.5	7.3115	0.0482	0.5	56.7283
		700	0.5	7.3169	0.0154	0.45	56.7584
	$0.25x10^{-5}$	0.0007	0.475	58.17	0.1141	----	----
		0.007	0.5	16.552	0.3638	0.65	60.0411
		0.07	0.5	7.8313	0.3887	0.5	57.0683
		0.7	0.5	7.1243	0.3110	0.5	56.7899
		7	0.5	7.2655	0.1433	0.5	56.7580
		70	0.5	7.3116	0.0482	0.525	56.7623
		700	0.5	7.317	0.0155	0.5	56.7539
	$0.25x10^{-4}$	0.0007	0.45	49.631	0.2945	----	----
		0.007	0.5	16.439	0.3719	----	----
		0.07	0.5	7.8541	0.3894	0.65	60.132
		0.7	0.5	7.1294	0.3111	0.5	57.1426
		7	0.5	7.2672	0.1435	0.5	56.8616
		70	0.5	7.3129	0.0482	0.5	56.8340
		700	0.5	7.3182	0.0155	0.5	56.8311
	$0.25x10^{-3}$	0.0007	0.425	34.815	0.5754	----	----
		0.007	0.5	15.684	0.4362	----	----
		0.07	0.5	8.0912	0.3974	-----	----
		0.7	0.5	7.181	0.3117	0.65	61.0728
		7	0.5	7.2837	0.1435	0.5	57.9077
		70	0.5	7.3254	0.0482	0.5	57.6114
		700	0.5	7.3304	0.0152	0.5	57.5821
	$0.25x10^{-2}$	0.0007	0.4	21.426	1.0230	-----	----
		0.007	0.475	13.645	0.7365	-----	----
		0.07	0.525	10.8	0.5665	-----	----
		0.7	0.525	7.7939	0.3237	-----	----
		7	0.5	7.4571	0.1436	0.75	76.6093
		70	0.5	7.4558	0.0481	0.525	69.1619
		700	0.5	7.4564	0.0154	0.5	68.5386
	$0.25x10^{-1}$	0.0007	0.375	11.59	1.6686	----	----
		0.007	0.4	9.7122	1.4273	----	----
		0.07	0.4	10.043	1.3885	-----	----
		0.7	0.4	17.676	1.5835	----	----
		7	0.575	13.679	0.1526	----	----
		70	0.5	9.808	0.0482	----	----
		700	0.5	9.6574	0.1537	----	----

Downloaded 04 May 2010 to 171.66.16.27. Redistribution subject to ASME license or copyright; see http://www.asme.org/terms/Terms_Use.cfm

Table 1 Continued

R_1'	K^2	p	a_{oc}^2	R_{oc}	ω	a_{sc}^2	R_{sc}
500	0.25×10^{-8}	0.0007	0.5	104.26	1.1522	0.6	509.1414
		0.007	0.5	16.641	1.2674	0.5	506.9836
		0.07	0.5	8.1653	1.2405	----	----
		0.7	0.5	9.0031	0.9850	----	----
		7	0.5	11.208	0.4542	----	----
		70	0.5	11.749	0.1523	0.425	504.2984
		700	0.5	11.811	0.0477	0.125	510.0095
	0.25×10^{-7}	0.0007	0.5	104.25	1.1523	----	----
		0.007	0.5	16.641	1.2674	0.6	509.1469
		0.07	0.5	8.1653	1.2405	0.5	506.9909
		0.7	0.5	9.0031	0.9850	----	----
		7	0.5	11.208	0.4542	----	----
		70	0.5	11.749	0.1523	0.625	506.7027
		700	0.5	11.811	0.0477	0.35	506.8781
	0.25×10^{-6}	0.0007	0.5	104.1	1.1534	----	----
		0.007	0.5	16.641	1.2674	----	----
		0.07	0.5	8.1653	1.2405	----	----
		0.7	0.5	9.0032	0.9850	0.5	507.049
		7	0.5	11.209	0.4540	0.575	506.9063
		70	0.5	11.749	0.1523	0.525	506.8405
		700	0.5	11.811	0.4777	0.475	506.8218
	0.25×10^{-5}	0.0007	0.5	102.66	1.1646	----	----
		0.007	0.5	16.639	1.2677	----	----
		0.07	0.5	8.1656	1.2406	----	----
		0.7	0.5	9.0037	0.9850	0.6	509.7982
		7	0.5	11.209	0.4541	0.525	507.6449
		70	0.5	11.749	0.1525	0.5	507.4199
		700	0.5	11.811	0.0483	0.5	507.3888
	0.25×10^{-4}	0.0007	0.475	92.71	1.228	----	----
		0.007	0.5	16.619	1.2699	----	----
		0.07	0.5	8.1682	1.2410	----	----
		0.7	0.5	9.0087	0.9852	----	----
		7	0.5	11.213	0.4541	0.6	515.8549
		70	0.5	11.752	0.1525	0.5	513.5956
		700	0.5	11.814	0.0486	0.5	513.3635
	0.25×10^{-3}	0.0007	0.425	65.761	1.4859	----	----
		0.007	0.5	16.425	1.2909	----	----
		0.07	0.5	8.1945	1.2456	----	----
		0.7	0.5	9.0589	0.9871	----	----
		7	0.5	11.252	0.4541	----	----
		70	0.5	11.758	0.1523	0.65	600.0403
		700	0.5	11.846	0.0481	0.525	595.8461
	0.25×10^{-2}	0.0007	0.375	36.999	1.9939	----	----
		0.007	0.475	15.001	1.4295	----	----
		0.07	0.5	8.4367	1.2939	----	----
		0.7	0.525	9.6193	1.0248	----	----
		7	0.5	11.676	0.4546	----	----
		70	0.5	12.131	0.1523	----	----
		700	0.5	11.811	0.2461	----	----
	0.25×10^{-1}	0.0007	0.3	17.021	2.4975	----	----
		0.007	0.4	10.259	1.8756	----	----
		0.07	0.45	8.5862	1.6841	----	----
		0.7	0.425	16.4	1.7748	----	----
		7	----	-----	-----	----	-----
		70	----	-----	-----	----	-----
		700	----	-----	-----	----	-----

Downloaded 04 May 2010 to 171.66.16.27. Redistribution subject to ASME license or copyright; see http://www.asme.org/terms/Terms_Use.cfm

Table 1 Continued

R_1'	K^2	p	a_{oc}^2	R_{oc}	ω	a_{sc}^2	R_{sc}
$5x10^{-3}$	$0.25x10^{-8}$	0.0007	0.5	104.76	4.0208	----	----
		0.007	0.5	17.401	4.0439	----	----
		0.07	0.5	11.53	3.9264	----	----
		0.7	0.5	27.797	3.1154	----	----
		7	0.5	50.64	1.4361	----	----
		70	0.5	56.121	0.4821	----	----
		700	0.5	56.747	0.1534	0.2	5006.79
	$0.25x10^{-7}$	0.0007	0.5	104.74	4.0209	----	----
		0.007	0.5	17.401	4.0439	----	----
		0.07	0.5	11.53	3.9265	----	----
		0.7	0.5	27.797	3.1154	----	----
		7	0.5	50.64	1.4361	----	----
		70	0.5	56.121	0.4821	----	----
		700	0.5	56.747	0.1540	----	----
	$0.25x10^{-6}$	0.0007	0.5	104.73	4.0211	----	----
		0.007	0.5	17.401	4.0439	----	----
		0.07	0.5	11.53	3.9265	----	----
		0.7	0.5	27.797	3.1154	----	----
		7	0.5	50.641	1.4361	0.675	5015.325
		70	0.5	56.122	0.4823	0.5	5013.221
		700	0.5	56.748	0.1538	0.525	5013.04
	$0.25x10^{-5}$	0.0007	0.5	104.56	4.0239	----	----
		0.007	0.5	17.4	4.044	----	----
		0.07	0.5	11.529	3.9265	----	----
		0.7	0.5	27.798	3.1155	----	----
		7	0.5	50.648	1.4316	----	----
		70	0.5	56.129	0.4821	0.575	5073.475
		700	0.5	56.755	0.1535	0.5	5071.287
	$0.25x10^{-4}$	0.0007	0.5	103.00	4.0506	----	----
		0.007	0.5	17.387	4.0447	----	----
		0.07	0.5	11.526	3.9268	----	----
		0.7	0.5	27.801	3.1168	----	----
		7	0.5	50.723	1.4364	----	----
		70	0.5	56.963	0.4821	----	----
		700	0.5	56.828	0.1534	0.625	5871.867
	$0.25x10^{-3}$	0.0007	0.475	91.714	4.1817	----	----
		0.007	0.5	17.266	4.0520	----	----
		0.07	0.5	11.492	3.9300	----	----
		0.7	0.5	27.83	3.1293	----	-----
		7	0.5	51.5	1.4391	-----	----
		70	0.5	56.963	0.4821	----	-----
		700	0.5	57.579	0.1534	----	-----
	$0.25x10^{-2}$	0.0007	0.375	59.074	4.4977	----	----
		0.007	0.475	16.201	4.0458	----	----
		0.07	0.475	11.169	3.8919	----	----
		0.7	0.45	28.00	3.1457	----	-----
		7	0.6	63.631	1.5696	-----	----
		70	0.525	68.183	0.4902	----	-----
		700	0.5	68.534	0.1534	----	-----
	$0.25x10^{-1}$	0.0007	0.3	26.334	4.8580	----	----
		0.007	0.4	11.317	4.0761	----	----
		0.07	0.4	8.9854	3.8398	----	----
		0.7	0.3	24.335	3.5161	----	----
		7	-----	-----	----	----	----
		70	-----	-----	----	----	----
		700	-----	-----	----	----	----

Downloaded 04 May 2010 to 171.66.16.27. Redistribution subject to ASME license or copyright; see http://www.asme.org/terms/Terms_Use.cfm

Table 1 Continued

R_1'	K^2	p	a_{oc}^2	R_{oc}	ω	a_{sc}^2	R_{sc}
$5x10^4$	$0.25x10^{-8}$	0.0007	0.5	109.56	12.8282	----	----
		0.007	0.5	24.998	12.7993	----	-----
		0.07	0.5	45.174	12.4178	----	----
		0.7	0.525	215.74	10.0121	----	----
		7	0.5	444.95	4.5415	----	---
		70	0.475	499.85	1.4986	----	----
		700	0.5	506.11	0.4855	0.825	50650.67
	$0.25x10^{-7}$	0.0007	0.5	109.56	12.8282	----	----
		0.007	0.5	24.998	12.7993	----	----
		0.07	0.5	45.174	12.4178	----	----
		0.7	0.525	215.74	10.0121	----	-----
		7	0.525	444.96	4.6154	-----	----
		70	0.5	499.85	1.5246	----	-----
		700	0.525	506.12	0.4936	----	-----
	$0.25x10^{-6}$	0.0007	0.5	109.55	12.8283	----	----
		0.007	0.5	24.997	12.7993	----	----
		0.07	0.5	45.174	12.4178	----	----
		0.7	0.5	215.73	9.8521	----	----
		7	0.5	445.0	4.5418	----	----
		70	0.5	499.91	1.5278	----	----
		700	0.5	506.18	0.4844	----	----
	$0.25x10^{-5}$	0.0007	0.5	109.49	12.8293	----	----
		0.007	0.5	24.995	12.7993	----	----
		0.07	0.5	45.167	12.418	----	----
		0.7	0.5	215.68	9.8549	----	----
		7	0.5	445.44	4.5448	----	----
		70	0.525	500.5	1.5493	----	----
		700	0.525	506.76	0.4933	----	----
	$0.25x10^{-4}$	0.0007	0.5	108.92	12.8385	----	----
		0.007	0.5	24.972	12.7998	----	----
		0.07	0.5	45.10	12.4200	----	----
		0.7	0.45	215.14	9.5362	----	----
		7	0.5	449.87	4.5768	----	----
		70	0.525	506.5	1.5496	----	----
		700	0.525	512.71	0.4547	----	----
	$0.25x10^{-3}$	0.0007	0.475	103.73	12.7018	----	----
		0.007	0.5	24.743	12.8045	----	----
		0.07	0.475	44.442	12.2220	----	----
		0.7	0.25	208.44	7.8901	----	----
		7	0.425	504.9	4.7480	----	----
		70	0.625	589.94	1.6428	----	----
		700	0.525	594.93	0.4937	----	----
	$0.25x10^{-2}$	0.0007	0.4	76.724	12.3724	----	----
		0.007	0.45	22.78	12.3946	----	----
		0.07	0.3	38.905	10.4529	----	----
		0.7	0.125	159.47	6.8449	----	-----
		7	----	----	-----	-----	----
		70	----	----	-----	----	-----
		700	----	----	-----	----	-----
	$0.25x10^{-1}$	0.0007	0.325	35.741	12.0313	----	----
		0.007	0.35	14.861	11.4729	----	----
		0.07	0.175	22.116	8.6421	----	----
		0.7	0.1	75.635	7.3383	----	----
		7	----	----	----	----	----
		70	----	----	----	----	----
		700	----	----	----	----	----

Downloaded 04 May 2010 to 171.66.16.27. Redistribution subject to ASME license or copyright; see http://www.asme.org/terms/Terms_Use.cfm

Table 1 Continued

R_1'	K^2	p	a_{oc}^2	R_{oc}	ω	a_{sc}^2	R_{sc}
$5x10^5$	$0.25x10^{-8}$	0.0007	0.5	157.67	40.6020	----	-----
		0.007	0.5	100.97	40.4784	----	-----
		0.07	0.5	381.62	39.2690	----	----
		0.7	0.5	2095.1	31.1544	----	-----
		7	0.55	4296.1	15.3236	----	-----
		70	0.5	4768	7.1509	----	-----
		700	0.5	4370.1	10.3552	----	-----
	$0.25x10^{-7}$	0.0007	0.5	157.67	40.6020	----	-----
		0.007	0.5	100.97	40.4784	----	-----
		0.07	0.525	381.62	39.9076	----	----
		0.7	0.575	2095.1	32.6050	----	-----
		7	0.55	4296.5	15.3245	----	-----
		70	0.525	4769.3	7.2653	----	-----
		700	0.525	4370.9	10.5206	----	-----
	$0.25x10^{-6}$	0.0007	0.5	157.66	40.6021	----	-----
		0.007	0.5	100.96	40.4784	----	-----
		0.07	0.5	381.59	39.2694	----	----
		0.7	0.5	2094.5	31.1635	----	-----
		7	0.525	4300.0	15.1061	----	-----
		70	0.5	4774.7	7.1481	----	-----
		700	0.5	4374.7	10.3565	----	-----
	$0.25x10^{-5}$	0.0007	0.5	157.57	40.6027	----	-----
		0.007	0.5	100.92	40.4787	----	-----
		0.07	0.475	381.07	38.6015	----	----
		0.7	0.225	2086.8	23.2089	----	-----
		7	0.425	4335.8	14.1774	----	-----
		70	0.5	4831.6	7.1222	----	-----
		700	0.5	4416.7	10.3737	----	-----
	$0.25x10^{-4}$	0.0007	0.5	156.62	40.6087	----	-----
		0.007	0.5	100.55	40.4811	----	-----
		0.07	0.325	375.68	33.7218	----	-----
		0.7	0.075	1990.2	14.7720	----	-----
		7	0.175	4731.8	11.2368	----	-----
		70	0.525	5634.2	6.7512	----	-----
		700	0.5	4978.8	10.4618	----	-----
	$0.25x10^{-3}$	0.0007	0.475	148.11	39.3142	----	-----
		0.007	0.425	96.908	38.3142	----	-----
		0.07	0.125	325.62	22.7867	----	-----
		0.7	0.04	1463.5	12.5829	----	-----
		7	-----	----	-----	----	-----
		70	----	----	----	----	-----
		700	----	----	----	----	-----
	$0.25x10^{-2}$	0.0007	0.35	105.68	36.1056	----	-----
		0.007	0.225	73.845	30.1821	----	-----
		0.07	0.075	184.07	18.5284	----	----
		0.7	<0.025		12.7063	----	-----
		7	----	----	-----	----	-----
		70	----	----	-----	----	-----
		700	----	----	-----	----	-----
	$0.25x10^{-1}$	0.0007	0.275	47.241	33.2326	----	-----
		0.007	0.15	34.816	25.4330	----	-----
		0.07	0.05	71.883	15.5623	----	-----
		0.7	0.025	244.91	12.4330	----	-----
		7	----	----	----	----	-----
		70	----	----	----	----	-----
		700	----	----	----	----	-----

Downloaded 04 May 2010 to 171.66.16.27. Redistribution subject to ASME license or copyright; see http://www.asme.org/terms/Terms_Use.cfm

$$\Delta_* = -\pi^2 - l_*^2 = -k^2. \tag{23}$$

Then Eq. (19) becomes

$$(\sigma_* P^{1/2} + k^2)(\sigma_* + P^{1/2}k^2)^2(\sigma_* P^{1/2} + \tau k^2)k^2 + l_*^2 A^2 \times \left[(\sigma_* P^{1/2} + \tau k^2)\left\{ \bar{u} + (\sigma P^{1/2} + Pk^2)\left(\bar{T} - \frac{R}{A^2} \right) \right\} + (\sigma_* P^{1/2} + Pk^2)(\sigma_* P^{1/2} + k^2)\frac{R'\tau}{A^2} \right] = 0. \tag{24}$$

The marginal state defined by Eq. (24) may be steady or periodic.

Steady Marginal State. The neutral stability curve for stationary convection solutions (putting $\sigma_* = 0$ in Eq. (24)) is given by

$$R_{1(\text{Steady})} = \frac{P(1 + a^2)}{2K^2\{4 + P(1 + a^2)\}} \times \left(1 \pm \left\{ 1 - \frac{4K^2}{a^2 P}\left[(1 + a^2)^2 + \frac{a^2 R_1'}{(1 + a^2)} \right] \times [4 + (1 + a^2)] \right\}^{1/2} \right) \tag{25}$$

where

$$R_1 = R/\pi^4,\ A_1 = A/\pi^4,\ R_1' = R'/\pi^4,\quad a^2 = l_*^2/\pi^2 \quad \text{and} \quad K = \frac{cA_1}{R_1} \tag{26}$$

When $R_1' \to 0$, Eq. (25) is in agreement with Sweet et al. (1977).

Overstable Marginal State. The neutral stability curve in the marginal state for overstable solutions can be obtained by putting $\sigma_* = i\omega\pi^2$ in Eq. (24)). $R_{1(\text{Oscillatory})}$ satisfies the following forth-degree equation

$$E_0 R_1^4 + E_1 R_1^3 + E_2 R_1^2 + E_3 R_1 + E_4 = 0 \tag{27}$$

where

$$\left.\begin{aligned} E_0 &= K^4(B_1 D_0^2 - B_0 D_0),\\ E_1 &= K^2(B_0 D_0 - B_0 D_1 - 2B_1 D_0 D_1)\\ E_2 &= C_0 K^2 + 2B_1 D_0 D_2 K^2 + B_1 D_1^2\\ &\quad - D_2 B_0 K^2 - B_0 D_1 - B_2 D_0 K^2\\ E_3 &= D_1 B_2 + B_0 D_2 - C_1 - 2B_1 D_1 D_2,\\ E_4 &= C_2 + B_1 D_1^2 - B_2 D_2\\ B_0 &= Pa^2, \quad B_1 = Pb^2\\ B_2 &= b^6\{P^2 + \tau + 2P(1 + \tau)\} + B_0 \tau R_1',\\ C_0 &= \tau a^2 b^2(4 + Pb^2)\\ C_1 &= B_0 \tau b^4, \quad C_2 = P\tau b^{10}\\ D_0 &= \{4a^2 + a^2 b^2(P + \tau)\}/b^2 D_3\\ D_1 &= a^2(P + \tau)/D_3\\ D_2 &= \{(2\tau + P + P\tau)b^6 + a^2\tau(1 + P)R_1'\}/D_3,\\ D_3 &= b^2(2P + 1 + \tau), \quad b^2 = 1 + a^2 \end{aligned}\right\} \tag{28}$$

and the associated frequency ω satisfies the equation

$$\omega^2 = D_0 R_1 K^2 - D_1 R_1 + D_2. \tag{29}$$

There will be four roots of Eq. (27), but we will be interested in the lowest positive real root and that will be the value of R_1 for overstable solutions. For discussion of stability, R_1 must be real and positive for stationary and oscillatory convection in addition to this ω should also be real for oscillatory convection. We see from Eqs. (25) and (27) that R_1 will depend on the values of P, K, R_1', a and τ which will vary from problem to problem. If R_1 and ω are real still then whether the instability will set in via stationary or oscillatory convection will depend on the lower critical values of R_1 calculated from Eqs. (25) and (27). It is not possible to have an analytical solution for the critical values of R_1; therefore numerical calculations were done for a wide range of values of parameters and presented in the form of Figs. 1–8 and Table 1. For all numerical calculations $\tau = 0.01$ and the values given as R_{oc}, a_{oc}, and ω_c are critical Rayleigh number, critical wave number, and critical frequency of oscillation for oscillatory convection, respectively, and R_{sc}, and a_{sc} are critical Rayleigh number and critical wave number for stationary convection.

Results and Discussions

The following results can be derived from Figs. 1–8 and Table 1:

1 The critical Rayleigh number for oscillatory convection remains almost unchanged for lower values of K^2 and changes very significantly for higher values of K^2 Figs. 2–8.

2 Square of the critical wave number remains the same (= 0.5, in accordance with the analytical results of Veronis (1965)) in most of the cases. But for higher values of K^2 it increases in some cases when $p > 1$ and decreases when $p < 1$ (Table 1).

3 There is not a definite trend in the behavior of frequency of oscillations (Table 1).

4 The critical Rayleigh number increases with increasing R_1' for all fixed values of K^2 and p, indicating that solute gradients in this case will always have a stabilizing effect.

5 Instability sets in as stationary convection only when R_1', p, and K^2 are very small. In this case instability first sets in as stationary convection and remains stationary.

6 For lower values of R_1' and K^2 Eqs. (25) and (27) gives real values of R_1 with real frequency of oscillation, but the critical value of the Rayleigh number for stationary convection is larger than that of oscillatory convection, instability first sets in as oscillatory convection and later becomes stationary (Fig. 1) as predected by Veronis (1965) and shown experimentally by Shirtcliffe (1967).

7 When $p < 1$, the critical Rayleigh number for overstable solutions generally decreases with increasing K^2 whereas it increases with increasing K^2 for $p > 1$, for almost all the values of R_1'. This indicates that the horizontal temperature gradient has a stabilizing effect on the motion for $p > 1$ whereas it has a destabilizing effect for $p < 1$. This is a very important result, because while discussing the effect of horizontal temperature gradient Thorpe et al. (1969) had conjectured that horizontal temperature gradients will tend to destabilize the motion.

8 For higher values of K^2, the Rayleigh number increases with a beyond its critical value but after a sufficiently large value of a we could not find real values of the Rayleigh number either for oscillatory or for stationary convection. This implies that oscillations are not growing and the developed state will not be a steady one as predicted by Veronis (1965) but the oscillations will die down as observed by Turner (1968) for the intermediate state.

9 For higher values of R_1' and lower values of K^2 the system remains oscillatory.

Downloaded 04 May 2010 to 171.66.16.27. Redistribution subject to ASME license or copyright; see http://www.asme.org/terms/Terms_Use.cfm

Conclusion

It is shown here that horizontal temperature gradients will have a stabilizing effect on high Prandtl number fluids and a destabilizing effect on low Prandtl number fluids. But in each case for a high value of K^2, the system becomes stable with respect to infinitesimal perturbations in such a way that the system first becomes oscillatory and later on oscillations die down when the Rayleigh number is sufficiently increased from its critical value. This is only partly in agreement with the experimental observations of Turner (1968) because theoretically we have not shown the occurrence of convection after a sufficient time when the oscillations died. This may be due to the horizontal temperature gradients of the order of vertical temperature gradients.

Acknowledgments

The author is indebted to Prof. H. C. Khare, University of Allahabad, Allahabad and the anonymous reviewers for their valuable suggestions. Also he is very much thankful to Dr. G. B. Pant, Director, Indian Institute of Tropical Meteorology (IITM), Pune, for extending various facilities during the revision and Dr. R. Krishnan, A.D., Climate and Global Modelling Division, IITM, for valuable discussions. The work was carried out under the Climate Research Project funded by the Department of Science and Technology, Government of India.

References

Benard, H., 1900, "Les Tourbillons cellulires dons une nappe liquide," *Revue general des Sciences Pures et appliquees,* Vol. 11, pp. 1261, 1309.

Chandrasekhar, S., 1961, *Hydrodynamic and Hydromagnetic Stability,* Dover, New York, pp. 9–218.

Gill, A. E., 1974, "A theory of thermal oscillations in liquid metals," *J. Fluid Mech.,* Vol. 64, p. 577.

Hart, J. E., 1972, "Stability of thin non-rotating Hadley Circulation," *J. Atmos. Sci.,* Vol. 29, p. 687.

Hurle, D. T. J., Jakeman, E., and Johnson, C. P., 1974, "Convective temperature oscillations in molten gallium," *J. Fluid Mech.,* Vol. 64, p. 565.

Krishnamurti, R., 1973, "Some further studies on the transition to turbulent convection," *J. Fluid Mech.,* Vol. 60, p. 285.

Lord, Rayleigh, 1916, "On convective currents in a horizontal layer of fluid when the higher temperature on the underside," *Phil. Mag.,* Vol. 32, p. 529.

Shirtcliffe, T. G. L., 1967, "Thermosolutal convection: observation of an overstable mode," *Nature,* Vol. 213, p. 489.

Singhal, R., and Srivastava, K. M., 1982, "Free convection in MHD with vertical and horizontal temperature gradients," *Astrophys. Space Sc.,* Vol. 86, p. 33.

Singhal, R., and Srivastava, K. M., 1984, "Thermal oscillations of a particle fluid mixture with horizontal temperature gradients," *Appl. Sc. Res.,* Vol. 41, p. 155.

Skafel, M. G., 1972, Ph.D. thesis, University of Cambridge, Cambridge, UK.

Stern, M. E., 1960, "The Salt Fountain and Thermohaline Convection," *Tellus,* Vol. 12, p. 172.

Stommell, H., and Fedorov, K. N., 1967, "Small scale structure in temperature and salinity near Timor and Mindanao," *Tellus,* Vol. 19, p. 306.

Sweet, D., Jakeman, E., and Hurle, D. T. J., 1977, "Free convection in the presence of both vertical and horizontal temperature gradients," *Phys. Fluids,* Vol. 20, p. 1412.

Thorpe, S. A., Hutt, P. K., and Soulsby, R., 1969, "The effect of horizontal gradients on thermohaline convection," *J. Fluid Mech.,* Vol. 28, p. 375.

Turner, J. S., 1968, "The behaviour of a stable salinity gradient heated from below," *J. Fluid Mech.,* Vol. 33, p. 183.

Veronis, G., 1965, "On Finite Amplitude Instability in Thermohaline Convection," *J. Marine Res.,* Vol. 23, p. 1.

Downloaded 04 May 2010 to 171.66.16.27. Redistribution subject to ASME license or copyright; see http://www.asme.org/terms/Terms_Use.cfm

The Stability of a Two-Layer Inviscid Flow Between an Elastic Layer and a Rigid Boundary

P. J. Schall
Assoc. Mem. ASME

J. P. McHugh
Assoc. Mem. ASME

Department of Mechanical Engineering,
University of New Hampshire,
Durham, NH 03824

The linear stability of two-layer flow over an infinite elastic substrate is considered. The problem is motivated by coating flow in a printing press. The flow is assumed to be inviscid and irrotational. Surface tension between the fluid layers is included, but gravity is neglected. The results show two unstable modes: one mode associated with the interface between the elastic layer and the fluid (mode 1), and the other concentrated on the interface between the two fluids (mode 2). The behavior of the unstable modes is examined while varying the elastic parameters, and it is found that mode 1 can be made stable, but mode 2 remains unstable at small wavenumber, similar to the classic Kelvin–Helmholtz mode.

1 Introduction

The stability of flow over a flexible layer is considered. The problem is motivated by coating flow in a modern high-speed lithographic printing press. A printing press contains many parallel cylindrical rollers, each in contact with two other rollers. The rollers are arranged into two groups. One group of rollers transports ink to the printing surface, while the other group transports water. Ink has the properties of oil and is immiscible in water. The fluids in an ideal printing press are intended to remain on separate roller groups until they reach the printing object, but ink and water eventually contaminate both groups of rollers.

Some of the rollers are covered by a surface layer of compliant material, such as neoprene, so that adjoining rollers are never the same material. The compliant coating has been found in practice to improve the ability of the system to meter the thickness of the various layers of fluid. The fluid in the contact region between any two rollers is thus bounded by a rigid wall and a flexible wall.

A variety of complicated behavior can occur in the contact region between two rollers, the so-called "nip" region. One problem is splitting, where the thickness of the layers of fluid entering the contact region is different from the thickness of the fluid layers exiting the contact region. Experience has shown that splitting occurs when water has contaminated the ink in the contact region, suggesting a two-fluid model. The flow is very thin and suggests lubrication theory. However, the flexible layer allows vertical motion, even though the layer is thin. In practice, splitting variations with speed indicate that inertia is important. Hence, the inertial terms are retained in the present work.

A simple model of the flow in the contact region is treated here. The flow is modeled as two layers of fluid between a rigid and a flexible boundary, the linear stability of which is considered. The layers of fluid have constant density in each layer, constant velocity in each layer without the perturbation, and the flow is assumed to be inviscid and irrotational. The curvature of the domain in the actual nip region is not included; the boundaries are assumed to be straight.

Contributed by the Applied Mechanics Division of THE AMERICAN SOCIETY OF MECHANICAL ENGINEERS for publication in the JOURNAL OF APPLIED MECHANICS.
Discussion on the paper should be addressed to the Technical Editor, Professor Lewis T. Wheeler, Department of Mechanical Engineering, University of Houston, Houston, TX 77204-4792, and will be accepted until four months after final publication of the paper itself in the ASME JOURNAL OF APPLIED MECHANICS.
Manuscript received by the ASME Applied Mechanics Division, July 30, 1997; final revision, May 28, 1998. Associate Technical Editor: S. Lichter.

The elastic layer in the present model is assumed to have an infinite depth. In practice the flexible coating is approximately 100 times thicker than the fluid layers. Only very long waves (longer than the nip region) on the interface of the two fluids will have significant motion that penetrates the elastic layer. The material is generally neoprene, which does exhibit some viscoelastic character. However, this is of second order, and is neglected.

The problem treated here is similar to the Kelvin–Helmholtz problem and the Rayleigh capillary instability. The Kelvin–Helmholtz problem is the instability of two inviscid layers of fluid separated by an immiscible interface, and has been studied at length; see for example the books by Craik [9], Drazin and Reid [11], and Chandrasekhar [8]. The Rayleigh capillary instability [19] is the same as the Kelvin–Helmholtz problem except the layers have finite depth and the boundaries are rigid. The problem considered here differs in that one boundary is the infinite elastic substrate.

Another important and related topic is the instability of flow over compliant coatings. The flow over compliant coatings has been extensively studied in recent years; see Benjamin [2, 3, 4], Landahl [16], Duncan et al. [12, 13, 14, 15], Carpenter et al. [5, 6, 7], and Yeo [21, 22]. The thrust of the research has been the drag reduction that may be experienced when a rigid surface is coated by a compliant layer, such as neoprene.

Benjamin [3] considered boundary layer flow over a compliant coating, using a simple model of the coating. The linear analysis of Benjamin produced three modes, which he named A, B, and C waves. Duncan et al. [14] considered a uniform flow over finite depth elastic and viscoelastic layers. A detailed discussion of the A, B, C wave classification for a uniform flow, which applies to the current problem as well, is provided in Duncan et al. [14].

The three-layer model studied here shows that there are three nontrivial modes: a mode concentrated on the interface between the two fluids, a mode concentrated on the interface between the fluid and the elastic layer, and a sound wave in the elastic layer. The unstable mode on the interface between the fluid and the elastic layer can be stabilized by an appropriate choice of material constants. However, the mode on the fluid–fluid interface remains unstable at small wavenumber.

2 Governing Equations

Consider two incompressible, irrotational and inviscid fluid layers moving at constant velocities U_1 and U_2 (subscripts 1 and 2 are for the upper and lower fluid layers, respectively). The fluid is bounded by a flat plate on the top, and by an infinite

 Copyright © 1999 by ASME

Downloaded 04 May 2010 to 171.66.16.27. Redistribution subject to ASME license or copyright; see http://www.asme.org/terms/Terms_Use.cfm

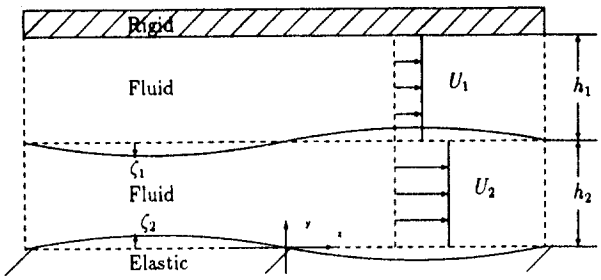

Fig. 1 Geometry and coordinate system for the model

depth elastic layer on the bottom. The geometry and coordinate system are shown in Fig. 1.

The governing equation in the fluid is Laplace's equation in each layer,

$$\nabla^2\phi_1 = 0, \tag{1}$$

$$\nabla^2\phi_2 = 0, \tag{2}$$

where ϕ is the velocity potential.

The elastic layer is governed by the Navier equations; see [17, 20]. For small displacement gradient and small particle velocity the two-dimensional Navier equations are

$$\frac{\partial^2\eta}{\partial t^2} = (\mu + \lambda)\frac{\partial^2\xi}{\partial X\partial Y} + (2\mu + \lambda)\frac{\partial^2\eta}{\partial X^2} + \mu\frac{\partial^2\eta}{\partial Y^2}, \tag{3}$$

$$\frac{\partial^2\xi}{\partial t^2} = \mu\frac{\partial^2\xi}{\partial X^2} + (2\mu + \lambda)\frac{\partial^2\xi}{\partial Y^2} + (\mu + \lambda)\frac{\partial^2\eta}{\partial Y\partial X}, \tag{4}$$

where (η, ξ) are the components of the Lagrangian displacement in the (X, Y) directions, respectively, μ and λ are the Lamé parameters, and (X, Y) are the material coordinates.

There are ten boundary conditions. The boundary condition at the flat plate $(y = h_1 + h_2)$ is zero normal velocity,

$$\frac{\partial\phi_1}{\partial y} = 0. \tag{5}$$

There are three boundary conditions at the fluid–fluid interface $(y = h_2 + \zeta_1)$. Two conditions are the continuity of normal velocity (kinematic) and the third condition is the continuity of pressure (dynamic). The kinematic conditions are

$$\frac{\partial\zeta_1}{\partial t} + \frac{\partial\phi_1}{\partial x}\frac{\partial\zeta_1}{\partial x} = \frac{\partial\phi_1}{\partial y}, \tag{6}$$

$$\frac{\partial\zeta_1}{\partial t} + \frac{\partial\phi_2}{\partial x}\frac{\partial\zeta_1}{\partial x} = \frac{\partial\phi_2}{\partial y}, \tag{7}$$

on $y = h_2 + \zeta_1$, where ζ_1 is the displacement of the fluid–fluid interface. The dynamic condition is

$$p_1 - p_2 = T\frac{\partial^2\zeta_1}{\partial x^2}, \tag{8}$$

on $y = h_2 + \zeta_1$, where T is the surface tension and p is the pressure. The pressure is evaluated with Bernoulli's equation to obtain

$$\rho_2\left(\frac{\partial\phi_2}{\partial t} + \frac{1}{2}(\nabla\phi_2\cdot\nabla\phi_2)\right) - \rho_1\left(\frac{\partial\phi_1}{\partial t} + \frac{1}{2}(\nabla\phi_1\cdot\nabla\phi_1)\right) = T\frac{\partial^2\zeta_1}{\partial x^2}. \tag{9}$$

There are four boundary conditions at the interface between the lower fluid and the elastic layer $(y = Y = \zeta_2)$. The two kinematic conditions are

$$\frac{\partial\zeta_2}{\partial t} + \frac{\partial\phi_2}{\partial x}\frac{\partial\zeta_2}{\partial x} = \frac{\partial\phi_2}{\partial y}, \tag{10}$$

$$\frac{\partial\zeta_2}{\partial t} = \frac{\partial\xi}{\partial t}, \tag{11}$$

on $y = Y = \zeta_2$, where ζ_2 is the Eulerian displacement of the fluid-elastic layer interface. The two dynamic conditions are zero shear stress,

$$\frac{\partial\eta}{\partial y} + \frac{\partial\xi}{\partial x} = 0, \tag{12}$$

and the fluid pressure is balanced by the normal stress,

$$\rho_2\left(\frac{\partial\phi_2}{\partial t} + \frac{1}{2}(\nabla\phi_2\cdot\nabla\phi_2)\right) = \lambda\frac{\partial\eta}{\partial x} + (2\mu + \lambda)\frac{\partial\xi}{\partial y}, \tag{13}$$

on $y = Y = \zeta_2$.

The remaining two boundary conditions are

$$\eta = 0, \tag{14}$$

$$\xi = 0, \tag{15}$$

as $Y \to -\infty$.

3 Linear Stability Analysis

A normal mode linear stability analysis is considered. A perturbation is added to the primary flow,

$$\phi = \bar{\phi} + \phi', \tag{16}$$

$$\eta = \bar{\eta} + \eta', \tag{17}$$

$$\xi = \bar{\xi} + \xi', \tag{18}$$

where the overbar indicates a primary flow quantity.

The perturbation quantities, by separation of variables, are assumed to have following forms:

$$\phi_1' = (D_1e^{\alpha y} + G_1e^{-\alpha y})e^{i\alpha(x-ct)}, \tag{19}$$

$$\phi_2' = (D_2e^{\alpha y} + G_2e^{-\alpha y})e^{i\alpha(x-ct)}, \tag{20}$$

$$\zeta_1 = A_1e^{i\alpha(x-ct)}, \tag{21}$$

$$\zeta_2 = A_2e^{i\alpha(x-ct)}, \tag{22}$$

$$\eta'(X, Y, t) = U(Y)e^{(i\alpha)(X-ct)}, \tag{23}$$

$$\xi'(X, Y, t) = V(Y)e^{(i\alpha)(X-ct)}. \tag{24}$$

The form of Eqs. (19) and (20) has been chosen to satisfy the governing equations for the fluid, Eqs. (1) and (2).

We substitute Eqs. (17), (18), (23), and (24) into the governing equations for the elastic layer, Eqs. (3) and (4), and subtract the primary solution to get

$$0 = (c^2 - 2\mu - \lambda)\alpha^2U(Y) + \mu\frac{\partial^2}{\partial Y^2}U(Y) + (\mu + \lambda)\alpha i\frac{\partial}{\partial Y}V(Y), \tag{25}$$

$$0 = (\mu + \lambda)\alpha i\frac{\partial}{\partial Y}U(Y) + (c^2 - \mu)\alpha^2V(Y) + (2\mu + \lambda)\frac{\partial^2}{\partial Y^2}V(Y). \tag{26}$$

We eliminate U between Eqs. (25) and (26) to obtain

Downloaded 04 May 2010 to 171.66.16.27. Redistribution subject to ASME license or copyright; see http://www.asme.org/terms/Terms_Use.cfm

$$(c^4 - [3\mu + \lambda]c^2 + [2\mu + \lambda]\mu)\alpha^4 V(Y) + [(3\mu + \lambda)c^2 - 2(2\mu + \lambda)\mu]\alpha^2 \frac{\partial^2}{\partial Y^2} V(Y) + (2\mu + \lambda)\mu \frac{\partial^4}{\partial Y^4} V(Y) = 0. \quad (27)$$

Assuming the displacement has the form $V(Y) = e^{\gamma Y}$ produces four roots:

$$\gamma_1 = \alpha \sqrt{1 - \frac{c^2}{\mu}}, \quad (28)$$

$$\gamma_2 = -\gamma_1, \quad (29)$$

$$\gamma_3 = \alpha \sqrt{1 - \frac{c^2}{2\mu + \lambda}}, \quad (30)$$

and

$$\gamma_4 = -\gamma_3. \quad (31)$$

Since the roots are distinct, the general solution to Eq. (27) is

$$V(Y) = B_1 e^{\gamma_1 Y} + B_2 e^{\gamma_2 Y} + B_3 e^{\gamma_3 Y} + B_4 e^{\gamma_4 Y}. \quad (32)$$

The boundary conditions given by Eqs. (14) and (15) can only be satisfied by choosing $B_2 = B_4 = 0$, reducing Eq. (32) to

$$V(Y) = B_1 e^{\gamma_1 Y} + B_3 e^{\gamma_3 Y}. \quad (33)$$

We substitute these expressions into the eight remaining boundary conditions, (5), (6), (7), (9), (10), (11), (12), and (13), linearize, and subtract the primary solution. In matrix form, the result is

$$\begin{bmatrix} 0 & 0 & 0 & 0 & e^{\alpha[h+1]} & 0 & -e^{-\alpha[h+1]} & 0 \\ i(U-c) & 0 & 0 & 0 & -e^{\alpha} & 0 & e^{-\alpha} & 0 \\ i(1-c) & 0 & 0 & 0 & 0 & -e^{\alpha} & 0 & e^{-\alpha} \\ -i\alpha S & 0 & 0 & 0 & R_1 & R_2 & R_3 & R_4 \\ 0 & i(1-c) & 0 & 0 & 0 & -1 & 0 & 1 \\ 0 & -1 & 1 & 1 & 0 & 0 & 0 & 0 \\ 0 & 0 & 2\mu - c^2 & 2\mu & 0 & 0 & 0 & 0 \\ 0 & 0 & R_5 & R_6 & 0 & R_7 & 0 & R_7 \end{bmatrix} \begin{bmatrix} A_1 \\ A_2 \\ B_1 \\ B_3 \\ D_1 \\ D_2 \\ G_1 \\ G_2 \end{bmatrix} = \begin{bmatrix} 0 \\ 0 \\ 0 \\ 0 \\ 0 \\ 0 \\ 0 \\ 0 \end{bmatrix} \quad (34)$$

where R_i are defined by

$$R_1 = -\rho(U - c)e^{\alpha}, \quad (35)$$

$$R_2 = (1 - c)e^{\alpha}, \quad (36)$$

$$R_3 = -\rho(U - c)e^{-\alpha}, \quad (37)$$

$$R_4 = (1 - c)e^{-\alpha}, \quad (38)$$

$$R_5 = 2[c^2 - (2\mu + \lambda)]\mu \sqrt{1 - \frac{c^2}{\mu}}, \quad (39)$$

$$R_6 = (2\mu + \lambda)[c^2 - 2\mu] \sqrt{1 - \frac{c^2}{2\mu + \lambda}}, \quad (40)$$

$$R_7 = [(2\mu + \lambda - c^2)(1 - c)]i. \quad (41)$$

Since the boundary conditions are homogeneous, the determinant of the matrix (34) must be zero. The resulting characteristic equation is a function of the complex wave speed, c, and the dimensionless parameters given below:

$$S = \frac{T}{U_2^2 \rho_2 h_2} \quad \text{(surface tension parameter)},$$

$$\mu = \frac{\mu_d}{\rho_2 U_2^2} \quad \text{(Lamé parameter) (shear modulus)},$$

$$\lambda = \frac{\lambda_d}{\rho_2 U_2^2} \quad \text{(Lamé parameter)},$$

$$\alpha = \frac{2\pi h_2}{l} \quad \text{(wavenumber)},$$

$$\rho = \frac{\rho_1}{\rho_2} \quad \text{(density ratio)},$$

$$U = \frac{U_1}{U_2} \quad \text{(velocity ratio)},$$

$$h = \frac{h_1}{h_2} \quad \text{(thickness ratio)},$$

where l is the wavelength of the disturbance.

Discarding one layer of fluid reduces the problem to the dynamics of a single interface between a fluid and a solid. The boundary conditions for this case are

$$\begin{bmatrix} 0 & 0 & 0 & \exp(\alpha) & -\exp(-\alpha) \\ i(1-c) & 0 & 0 & -1 & 1 \\ -1 & 1 & 1 & 0 & 0 \\ 0 & 2\mu - c^2 & 2\mu & 0 & 0 \\ 0 & R_5 & R_6 & R_7 & R_7 \end{bmatrix} \begin{bmatrix} A_2 \\ B_1 \\ B_3 \\ D_2 \\ G_2 \end{bmatrix} = \begin{bmatrix} 0 \\ 0 \\ 0 \\ 0 \\ 0 \end{bmatrix}. \quad (42)$$

4 Results

The characteristic equation that determines the eigenvalue is given by the determinant of the matrix in Eq. (34). This characteristic equation is algebraic with the eigenvalue appearing to the eighth power, which means there is no analytic solution. The equation is not a polynomial, however, due to the square root, hence there are not necessarily eight solutions for a chosen set of parameters. The eigenvalues are obtained numerically using the method of Delves and Lyness [10], which was also used by McHugh [18] and Duncan et al. [14]. The method of Delves and Lyness successfully finds the roots of functions that are analytic in the neighborhood of a root. A simple search routine is also employed on occasion.

Before discussing the two fluid layer problem, it is expedient first to consider results with no fluid layers and one fluid layer. An infinite elastic substrate with no fluid layers is well-known to support both pressure waves and surface waves [17, 1]. The pressure waves are stable nondispersive sound waves, and have a wavespeed given by

$$c = \sqrt{2\mu + \lambda}. \quad (43)$$

These sound waves appear as eigenmodes of the system [with eigenvalue given exactly by Eq. (43)] for the cases with one or more layers of fluid, and are never unstable.

Downloaded 04 May 2010 to 171.66.16.27. Redistribution subject to ASME license or copyright; see http://www.asme.org/terms/Terms_Use.cfm

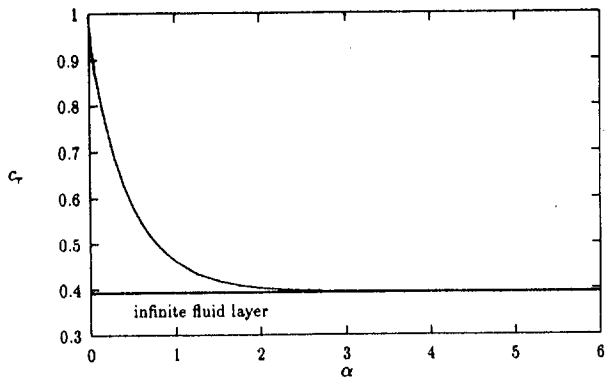

Fig. 2 c_r versus α for mode 1 with a single fluid layer ($\mu = 0.2$, $\lambda = 10$)

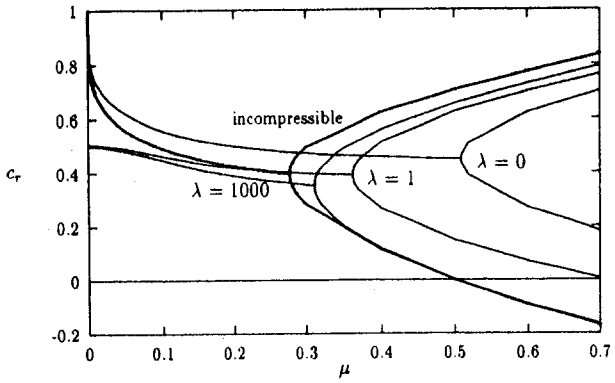

Fig. 4 c_r versus μ with several values of λ for mode 1 with a single infinite layer of fluid

The surface waves are the classic Rayleigh surface waves [17, 1], whose restoring force is the elasticity of the medium. The wavespeed is the solution to a fourth-order algebraic equation, which is difficult to express analytically. However, a valuable approximation [1] is

$$c_r = \sqrt{\mu}, \tag{44}$$

after rescaling as in section 3. Note that Rayleigh surface waves without a moving fluid layer are nondispersive and neutrally stable.

If a fluid layer of finite thickness moving at a uniform velocity is added adjacent to the infinite elastic layer, the eigenvalues are given by the determinant of Eq. (42), which is

$$4\mu^2(2\mu + \lambda - c^2)\tanh\alpha\sqrt{1 - \frac{c^2}{\mu}} - (2\mu + \lambda)(c^2 - 2\mu)^2\tanh\alpha\sqrt{1 - \frac{c^2}{2\mu + \lambda}} - c^2(c - 1)^2(2\mu + \lambda - c^2) = 0. \tag{45}$$

This characteristic equation produces two nontrivial pairs of modes. One mode is merely the sound waves mentioned above, with the wavespeed given by Eq. (43). The other mode, which will be called mode 1, is the Rayleigh surface wave, altered by the presence of the fluid layer. Eigenvalues for mode 1 are shown in Figs. 2 and 3 versus wavenumber for an example case. Note that a positive value of c_i indicates instability. For the chosen values of elastic constants, Fig. 3 shows that mode 1 is unstable for the wavenumber interval shown. Hence the presence of a moving fluid layer can make Rayleigh surface waves unstable.

The moving fluid layer does not always make mode 1 unstable. The instability of mode 1 can be controlled by the choice of elastic parameters. Figures 4 and 5 examine the effect of the elastic constants on the real and imaginary parts of the wavespeed, respectively. There is a bifurcation point where the mode 1 eigenvalues change from complex to purely real. The flow is unstable for μ less that the critical value, and stable otherwise. The eigenvalues behave in a similar manner as λ varies while μ is held constant. In general, a firmer elastic layer leads to a more stable mode 1.

Note that as μ increases, the upper branch of c_r shown in Fig. 4 approaches $c_r = \sqrt{\mu}$, which is the approximate wavespeed for Rayleigh surface waves. An increase in μ, which is the Lamé constant rescaled with the flow velocity, is equivalent to a decrease in the flow, and it follows that the eigenvalue should match $\sqrt{\mu}$.

Duncan et al. [14] previously considered the stability of uniform flow over an elastic layer. The elastic layer of Duncan had a finite thickness, and the single layer of fluid was infinitely thick. Duncan found that an infinite set of modes exist for his case, all related to mode 1 found here. The infinite set of modes are associated with an increasing level of complexity through the elastic layer. With the infinite elastic layer considered here, there is only one mode, and that mode is analogous to the first of Duncan's infinite set.

Duncan mentions the effect of allowing the thickness of the elastic layer to approach infinity, and he provides a value of the wavespeed that is independent of α. If the elastic layer has an infinite length, then there is no length scale, since the fluid layer is already infinite. The waves are then nondispersive and Duncan's wavespeed is valid. In the present problem, the fluid layer is bounded instead of the elastic layer. The result is a

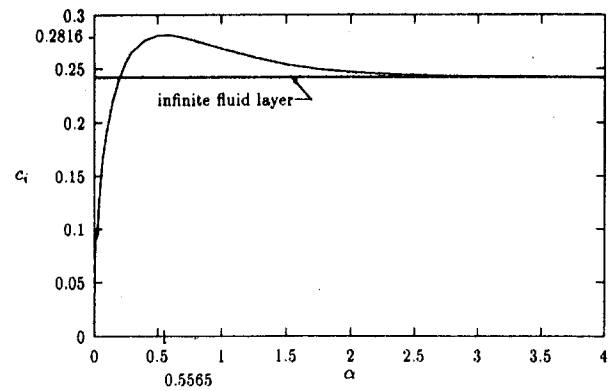

Fig. 3 c_i versus α for mode 1 with a single fluid layer ($\mu = 0.2$, $\lambda = 10$)

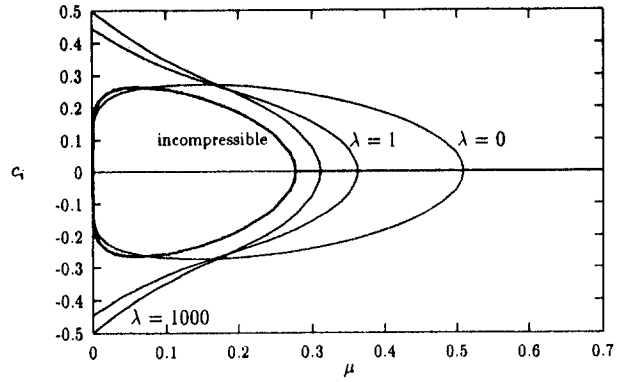

Fig. 5 c_i versus μ with several values of λ for mode 1 with a single infinite layer of fluid

Downloaded 04 May 2010 to 171.66.16.27. Redistribution subject to ASME license or copyright; see http://www.asme.org/terms/Terms_Use.cfm

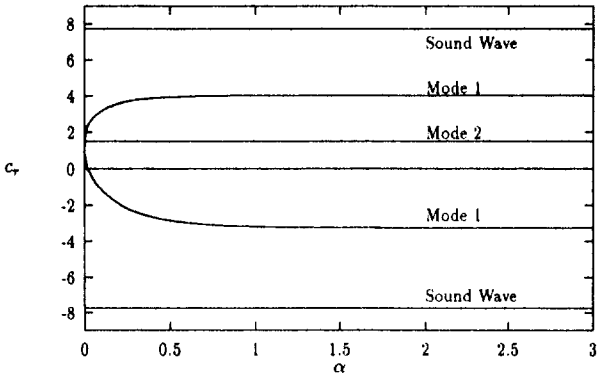

Fig. 6 c_r for mode 1 and 2 with two fluid layers (U = 1.5, h = 1, ρ = 1, μ = 25, λ = 10, S = 0.0015)

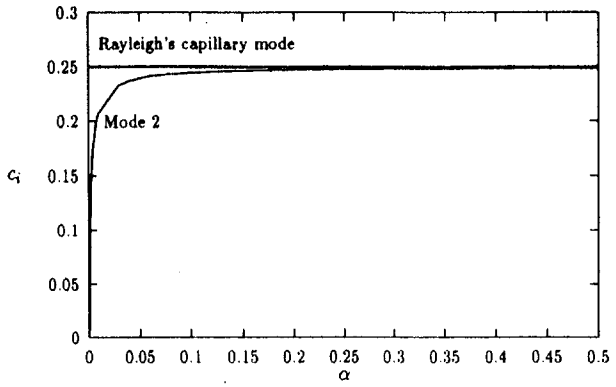

Fig. 8 c_i for the Kelvin–Helmholtz instability, Rayleigh's capillary instability, and mode 2 with two fluid layers

single mode, instead of the infinite set of Duncan, and our single mode is dispersive, as can be seen in Fig. 2.

Despite the differences between the present problem and that of Duncan, the results with one layer of fluid found here do agree qualitatively with the results for the lowest mode shown in Fig. 2 of Duncan. The two results agree exactly as $\alpha \to \infty$.

Now consider two layers of fluid. Figures 6 and 7 show the real and imaginary part of the eigenvalue versus the wavenumber for a typical set of parameters. The chosen parameters match approximate operating regions of modern printing presses. Three nontrivial pairs of eigenvalues are found. One mode is again merely the neutral sound waves, with wavespeed given by Eq. (43). Another mode is analogous to mode 1 found in the flow of a single fluid layer. Note that mode 1 is stable for the parameters of Figs. 6 and 7.

The remaining mode, mode 2, is associated with the interface between the two fluids, and is analogous to the Kelvin–Helmholtz instability and Rayleigh's capillary problem. The wavespeed for Rayleigh's capillary instability is given by

$$c = \frac{\coth \alpha + \rho U \coth \alpha h}{\coth \alpha + \rho \coth \alpha h} \pm \sqrt{\frac{\alpha S}{\coth \alpha + \rho \coth \alpha h} - \rho \coth \alpha h \coth \alpha \left(\frac{U - 1}{\coth \alpha + \rho \coth \alpha h} \right)^2}, \tag{46}$$

as in Rayleigh [19]. If $\alpha \to \infty$, then Eq. (46) gives the eigenvalue for the Kelvin–Helmholtz instability.

Figure 8 shows a comparison of c_i between Rayleigh's capillary mode, the Kelvin–Helmholtz mode, and mode 2. Note that the Kelvin–Helmholtz eigenvalue is indistinguishable from the Rayleigh capillary eigenvalue for the scale of the ordinate in Fig. 8. For small α, the effect of the elastic layer is to reduce the strength of the instability greatly, as shown in Fig. 8. The value of c_i does not become positive, hence the mode remains unstable. But c_i approaches zero for mode 2 as $\alpha \to 0$.

It is also demonstrated in Fig. 8 that the value of c for mode 2, the Kelvin–Helmholtz mode, and the Rayleigh capillary mode merge as the wavenumber increases. This is expected, since large wavenumber means short waves, and short waves would not penetrate very far into either layer, thereby making the boundaries distant and unimportant. Note that the value of c_i in Fig. 8 approaches zero as α approaches a critical value; α_{cr} = 83.33 for the parameter values of Fig. 8 (which is beyond the scale of the abscissa). Mode 2 is stable for $\alpha > \alpha_{cr}$. This trend is exactly the behavior of the classic Kelvin–Helmholtz mode.

The effect of a variation in the elastic constants on mode 2 is shown in Figs. 9 and 10, which are values of c_r and c_i for different elastic parameters at an example wavenumber. The value of c_i for mode 2 can be reduced by reducing the value of μ, as shown in Fig. 10. However, the value of c_i is still in the unstable region for the chosen wavenumber. The elastic constants can be chosen to stabilize mode 2 at other wavenumbers; the effect of a change in elastic parameters is a shift in α_{cr}. But the numerical results found here show that it is not possible to stabilize mode 2 at all wavenumbers. There is always a nonzero α_{cr} for any combination of other parameters such that mode 2 for $\alpha < \alpha_{cr}$ is unstable.

Mode 1 with two fluid layers behaves qualitatively the same as mode 1 with one fluid layer. The effect of the second layer of fluid on mode 1 is shown in Figs. 11 and 12 by varying the parameter h. With h = 0, the two-layer model is identical to the single layer model with a finite depth fluid layer.

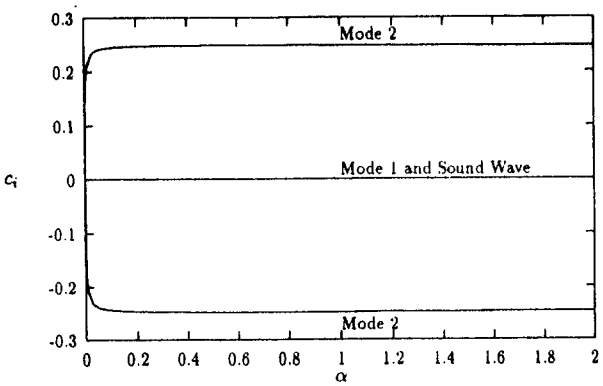

Fig. 7 c_i for mode 1 and 2 with two fluid layers (U = 1.5, h = 1, ρ = 1, μ = 25, λ = 10, S = 0.0015)

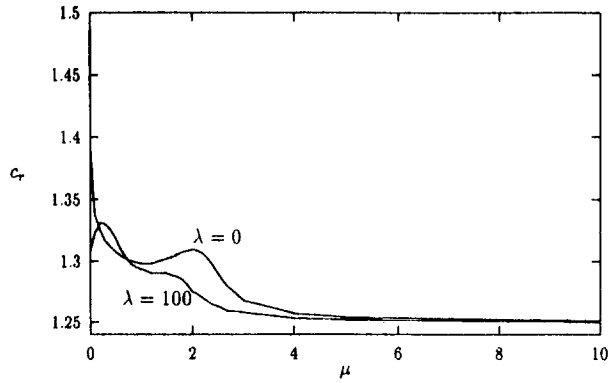

Fig. 9 The effect of the elastic parameters on c_r for mode 2 with two fluid layers (U = 1.5, h = 1, ρ = 1, α = 0.15, S = 0.0015)

Downloaded 04 May 2010 to 171.66.16.27. Redistribution subject to ASME license or copyright; see http://www.asme.org/terms/Terms_Use.cfm

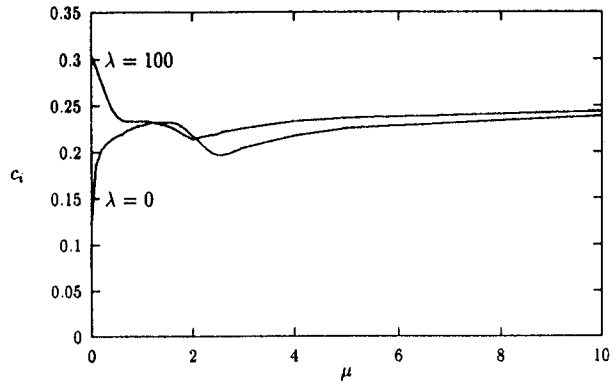

Fig. 10 The effect of the elastic parameters on c_i for mode 2 with two fluid layers ($U = 1.5$, $h = 1$, $\rho = 1$, $\alpha = 0.15$, $S = 0.0015$)

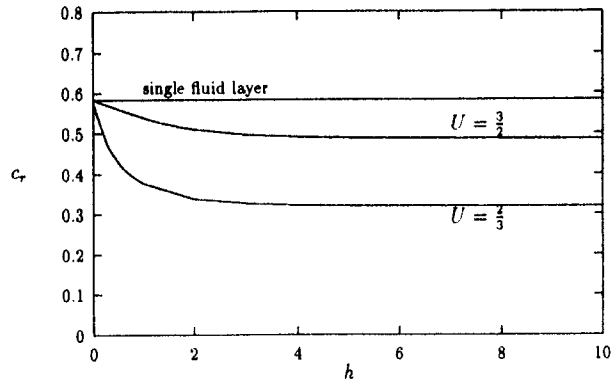

Fig. 11 The effect of the depth ratio on c_r for mode 1 with two fluid layers ($\alpha = 0.5$, $\rho = 1$, $\mu = 25$, $\lambda = 10$, $S = 0.0015$)

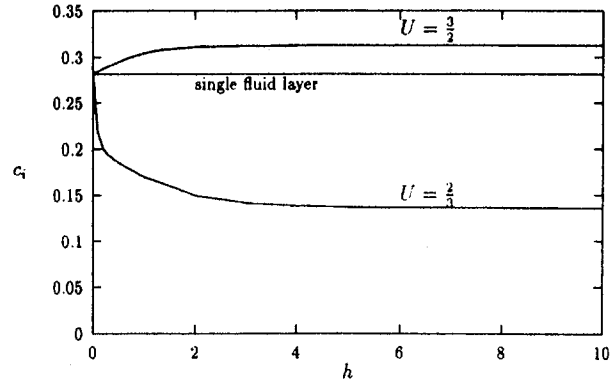

Fig. 12 The effect of the depth ratio on c_i for mode 1 with two fluid layers ($\alpha = 0.5$, $\rho = 1$, $\mu = 25$, $\lambda = 10$, $S = 0.0015$)

Two cases are shown in Figs. 11 and 12; $U = \frac{3}{2}$ and $\frac{2}{3}$. The case with $U = \frac{3}{2}$ has the fluid adjacent to the elastic layer, the "lower" layer, moving at $\frac{2}{3}$ the speed of the "upper" layer. Note that as h increases, which means that lower layer is getting thinner, the eigenvalue approaches a constant value. Hence the thickness ratio for thin lower layers is no longer important.

Adding the second layer of fluid may strengthen or weaken the instability of mode 1, depending on U. If $U > 1$, which means the upper fluid is moving faster, then mode 1 is less stable. The strongest instability occurs with a thick fast-moving upper layer and a thin slow lower layer.

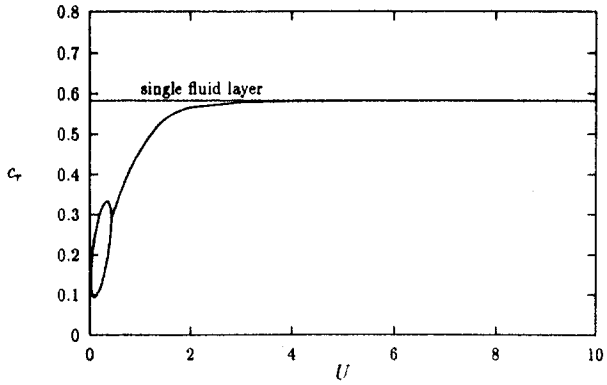

Fig. 13 The effect of velocity ratio on c_r for mode 1 with two fluid layers ($\alpha = 0.5$, $\rho = 1$, $\mu = 25$, $\lambda = 10$, $S = 0.0015$)

The velocity ratio can be chosen to stabilize mode 1 for a given wavenumber, as shown in Figs. 13 and 14. Small values of U are seen in Fig. 14 to stabilize mode 1. The elastic parameters may also be chosen to stabilize mode 1 with two fluid layers, similar to mode 1 for one fluid layer, as previously discussed. However mode 2 is still unstable at small α, making the physical problem unstable.

5 Discussion

An important question concerning application to flow between spinning rollers is whether both unstable modes can be made stable by appropriate choice of the parameters, in particular, the elastic constants. Can the elastic layer stabilize the flow? The answer according to the simple model of two fluid layers on an infinite elastic substrate is: no! The unstable mode on the interface between the fluid and the elastic layer can be stabilized, but the mode on the fluid–fluid interface remains unstable at small wavenumber.

However, one must consider the shortcomings of the present model. In particular, the fluid layers in the present model are assumed to have an infinite length. The length of the contact region between two rollers, the so-called "nip" region, is finite, of course. One might conclude that therefore the longest wave that would be excited according to the mode 2 mechanism is not longer than the length of the nip region. Therefore, the unstable long waves would not be excited. If this were true, then the flow could be stabilized by appropriate choice of elastic constants.

On the other hand, the "edge" of the nip region is not constrained by a rigid boundary. The elastic layer and fluid layers extend beyond the nip region. Such a geometry will support

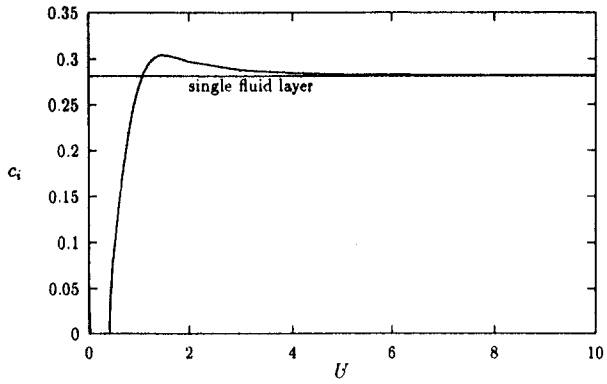

Fig. 14 The effect of velocity ratio on c_i for mode 1 with two fluid layers ($\alpha = 0.5$, $\rho = 1$, $\mu = 25$, $\lambda = 10$, $S = 0.0015$)

Downloaded 04 May 2010 to 171.66.16.27. Redistribution subject to ASME license or copyright; see http://www.asme.org/terms/Terms_Use.cfm

wave modes with a wavelength longer than the nip region, and perhaps a mode 2 at small α could be excited.

Acknowledgment

This research was sponsored by Heidelberg-Harris, Inc.

References

1 Achenbach, J. D., *Wave Propagation in Elastic Solids,* North-Holland, 1973.

2 Benjamin, T. Brooke, "Shearing Flow Over a Wavy Boundary," *Journal of Fluid Mechanics,* Vol. 6, 1959.

3 Benjamin, T. Brooke, "Effects of a Flexible Boundary on Hydrodynamic Stability," *Journal of Fluid Mechanics,* Vol. 9, 1960.

4 Benjamin, T. Brooke, "Threefold Classification of Unstable Disturbances in Flexible Surfaces Bounding Inviscid Flows," *Journal of Fluid Mechanics,* Vol. 16, 1963.

5 Carpenter, P. W., and Garrad, A. D., "Hydrodynamic Stability of Flow Over Kramer-Type Compliant Surfaces. Part 1—Tollmien–Schlichting Instabilities," *Journal of Fluid Mechanics,* Vol. 155, 1985.

6 Carpenter, P. W., and Garrad, A. D., "Hydrodynamic Stability of Flow Over Kramer-Type Compliant Surfaces. Part 2—Flow-Induced Surface Instabilities," *Journal of Fluid Mechanics,* Vol. 170, 1986.

7 Carpenter, Peter W., and Morris, Philip J., "Effect of Anisotropic Wall Compliance on Boundary-Layer Stability and Transition," *Journal of Fluid Mechanics,* Vol. 218, 1990.

8 Chandrasekhar, S., *Hydrodynamic and Hydromagnetic Stability,* Dover Publications, Inc., New York, 1961.

9 Craik, Alex D. D., *Wave Interactions and Fluid Flows,* Cambridge University Press, Cambridge, United Kingdom, 1985.

10 Delves, L. M., and Lyness, J. N., "A Numerical Method for Locating the Zeros of an Analytic Function," *Mathematics of Computation,* Vol. 21, 1967.

11 Drazin, P. G., and Reid, W. H., *Hydrodynamic Stability,* Cambridge University Press, New York, 1981.

12 Duncan, J. H., "Comparison of Wave Propagation on the Surfaces of Simple Membrane Walls and Elastic Coating Bounded by a Fluid Flow," *Journal of Sound and Vibration,* Vol. 119, 1987.

13 Duncan, J. H., "Dynamics of Waves at the Interface Between a Two-Layer Viscoelastic Coating and a Fluid Flow," *Journal of Fluids and Structures,* Vol. 2, 1988.

14 Duncan, J. H., Waxman, A. M., and Tulin, M. P., "Dynamics of Waves at the Interface Between a Viscoelastic Coating and a Fluid Flow," *Journal of Fluid Mechanics,* Vol. 158, 1985.

15 Duncan, James H., "Response of an Incompressible, Viscoelastic Coating to Pressure Fluctuations in a Turbulent Boundary Layer," *Journal of Fluid Mechanics,* Vol. 171, 1986.

16 Landahl, Martin, "On the Stability of a Laminar Incompressible Boundary Layer Over a Flexible Surface," *Journal of Fluid Mechanics,* Vol. 13, 1963.

17 Love, A. E. H., *A Treatise on the Mathematical Theory of Elasticity,* Dover Publications, Inc., New York, 1944.

18 McHugh, J. P., "Stability and Waves on a Two-Dimensional Inviscid Shear Flow," *Computers and Fluids,* Vol. 24, 1995.

19 Rayleigh, John, *The Theory of Sound,* Vol. 2, Dover Publications, Inc., New York, 1945.

20 Timoshenko, S. P., and Goodier, J. N., *Theory of Elasticity,* McGraw-Hill, New York, 1934.

21 Yeo, K. S., "Stability of Boundary-Layer Flow Over Single and Multilayer Viscoelastic Walls," *Journal of Fluid Mechanics,* Vol. 196, 1988.

22 Yeo, K. S., and Dowling, A. P., "Stability of Inviscid Flows Over Passive Compliant Walls," *Journal of Fluid Mechanics,* Vol. 183, 1987.

Downloaded 04 May 2010 to 171.66.16.27. Redistribution subject to ASME license or copyright; see http://www.asme.org/terms/Terms_Use.cfm

Green's Function for a Heat Source in an Infinite Region With an Arbitrary Shaped Hole

K. Yoshikawa
Civil Engineering and Design Division,
Tokyu Construction Co., Ltd.,
1-16-14 Shibuya, Sibuya-ku,
Tokyo 150-8340, Japan

N. Hasebe
Professor,
Department of Civil Engineering,
Nagoya Institute of Technology,
Gokiso-cho, Showa-ku,
Nagoya 466-0061, Japan

In two-dimensional thermoelasticity, Green's functions of the external force boundary value problem are derived for an infinite plane with an arbitrary shaped hole under adiabatic and isothermal boundary conditions subjected to heat sources in two cases as follows. One is the case of a heat source and a heat sink arbitrarily located within the plane, the other is the case of a heat source arbitrarily located within the plane and a heat sink at infinity. Complex stress functions, temperature function, a rational mapping function, and the thermal dislocation method are used for the analysis. In analytical examples, distributions of temperature, heat flux, and stresses are shown for an infinite plane with a rectangular hole under adiabatic and isothermal boundary conditions.

1 Introduction

In two-dimensional thermoelasticity, the general solution for a steady-state point heat source contained in an infinite plane having a hole finds applications in the thermal stress analysis for welding, as well as in the boundary element method as a fundamental solution (Green's function). The thermoelasticity problem of point heat sources is one of the fundamental problems. The fundamental solutions used in the boundary element method are restricted to extremely simple geometries; for complicated geometries only a few such fundamental solutions exist. Consequently any fundamental solution developed with respect to a complicated geometry will be of significant importance in applications, due to the small computation content and high accuracy it brings about.

As examples of analytic work concerning point heat sources in infinite domains Fukui et al., (1970) treated an infinite plane with a circular hole, where heat flux produced from a heat source flows out via the hole boundary, on which an isothermal boundary condition is stipulated. The problem of an adiabatic crack in an infinite plane, thermally deformed in a temperature field caused by a heat source, was solved by Zhang and Hasebe (1993). Fukui and Fukui (1974) obtained a solution for an infinite plane with a circular inclusion, in which heat flux generated from a heat source passes through the inclusion and flows into a heat sink. In another development, employing a basic solution for a point heat source in an infinite plane without a hole, Nisitani et al. (1991) developed a solution for an infinite plane having a circular hole and under uniform heat flow, by summing up the basic solutions for heat sources of various intensity distributed over the boundary in such a manner that the boundary condition on the hole is satisfied (the body force method). However, these references generally deal only with relatively simple geometries (circular and elliptic holes, crack); while the general solution for an arbitrarily shaped hole, it appears, still remains to be explored.

In view of the above situation, the present paper treats with an infinite plane with a hole of arbitrary shape for which adiabatic or isothermal conditions hold on the boundary. When a heat source and a heat sink are arbitrarily located within the plane, including the special case when the heat sink is at infinity, general solutions for the temperature function (complex thermal function) and the stress functions are derived. To develop the solution, a mapping function is used which maps the domain outside the hole in the original plane into the domain outside a unit circle in the mapped plane, as well as two complex stress functions that are regular outside the unit circle. The thermal dislocation method (Florence and Goodier, 1960), is also employed. In analytical examples, an infinite plane with a rectangular hole under adiabatic or isothermal boundary conditions is considered; for the case when a heat source and a heat sink are arbitrarily located in the plane, distributions of temperature, heat flux, and stresses are worked out and demonstrated graphically.

2 Stress Functions for a Point Heat Source in an Infinite Plane

In preparation for the analysis of the problem of a point heat source in an infinite plane with a hole, we derive the complex stress functions for a point heat source in an infinite plane without a hole.

For two-dimensional steady-state thermal conduction, the temperature $\Theta(z, \bar{z})$, heat flux q_x and q_y can be expressed via a temperature function $\Omega_0(z)$ (Hasebe et al., 1988)

$$\Theta(z, \bar{z}) = \tfrac{1}{2}\left[\Omega_0(z) + \overline{\Omega_0(z)}\right] \tag{1}$$

$$q_x - iq_y = -k\Omega_0'(z) \tag{2}$$

where k denotes the thermal conductivity of the material, and $\overline{[\ ]}$ stands for the conjugate of [ ]. Designating the coordinate and the intensity of the point heat source, shown in Fig. 1, by z_0 and M, respectively, the temperature function for the point heat source is given by the following formula:

$$\Omega_0(z) = -\frac{M}{2\pi k}\log(z - z_0). \tag{3}$$

Due to the presence of the point heat source, displacements caused by thermal expansion occur. These displacements are expressible in the form

$$u_0 + iv_0 = \alpha' \int \Omega_0(z)dz$$

$$= -\frac{\alpha' M}{2\pi k}(z - z_0)\{\log(z - z_0) - 1\} \tag{4}$$

Contributed by the Applied Mechanics Division of THE AMERICAN SOCIETY OF MECHANICAL ENGINEERS for publication in the ASME JOURNAL OF APPLIED MECHANICS.

Discussion on the paper should be addressed to the Technical Editor, Professor Lewis T. Wheeler, Department of Mechanical Engineering, University of Houston, Houston, TX 77204-4792, and will be accepted until four months after final publication of the paper itself in the ASME JOURNAL OF APPLIED MECHANICS.

Manuscript received by the ASME Applied Mechanics Division, Jan. 13, 1998; final revision, Apr. 27, 1998. Associate Technical Editor: M.-J. Pindera.

 Copyright © 1999 by ASME

Downloaded 04 May 2010 to 171.66.16.27. Redistribution subject to ASME license or copyright; see http://www.asme.org/terms/Terms_Use.cfm

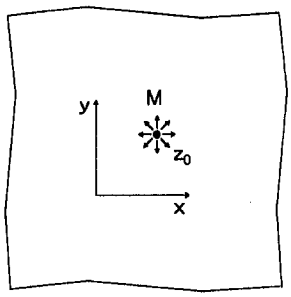

Fig. 1 Heat source located in an infinite region

where $\alpha' = \alpha(1 + \nu)$, $\kappa = 3 - 4\nu$ for plane strain and $\alpha' = \alpha$, $\kappa = (3 - \nu)/(1 + \nu)$ for generalized plane stress, with α and ν being the linear thermal expansion coefficient of the material and the Poisson's ratio of the material, respectively.

On the other hand, with use of the complex stress functions $\phi(z)$ and $\psi(z)$, as well as the displacements induced by the temperature field shown in (4), forces and displacements for the problem can be expressed as follows (Muskhelishvili, 1963):

$$\phi(z) + z\overline{\phi'(z)} + \overline{\psi(z)} = i\int (p_x + ip_y)ds \tag{5}$$

$$\kappa\phi(z) - z\overline{\phi'(z)} - \overline{\psi(z)} + 2G\alpha'\int \Omega_0(z)dz = 2G(u + iv) \tag{6}$$

where p_x and p_y are forces, u and v displacements in the x and y directions, respectively, and G is the shear modulus of the material. Based on (4)–(6) and taking the single-valuedness of forces and displacements into consideration around point z_0, the complex stress functions for the point heat source have been worked out and given in the following equations (Nisitani et al., 1991):

$$\phi_h(z) = \frac{\alpha MGR}{4\pi k}(z - z_0)\{\log(z - z_0) - 1\} \tag{7a}$$

$$\psi_h(z) = -\frac{\alpha MGR}{4\pi k}\overline{z_0}\log(z - z_0) \tag{7b}$$

where $R = (1 + \nu)/(1 - \nu)$ for plane strain and $R = 1 + \nu$ for generalized plane stress.

3 Mapping Functions

As an example the method of the derivation of the rational mapping function is demonstrated with the illustration of a special rational mapping function which maps an infinite plane with a rectangular hole in the z-plane into the exterior of a unit circle in the ζ-plane (see Fig. 2). Using of the Schwarz-Christoffel's transformation formula, this mapping function can be expressed in the following equation:

$$z = \omega(\zeta) = K\int \frac{(\zeta - 1)^{0.5}(\zeta - i)^{0.5}(\zeta + 1)^{0.5}(\zeta + i)^{0.5}}{\zeta^2}d\zeta = K\int\left(1 - \frac{1}{\zeta^4}\right)^{0.5}d\zeta \tag{8}$$

where K is a factor depending on the size of the hole. Expanding the integrand in (8) into a Taylor series, and carrying out the integration term by term, (8) turns out in the following form:

$$z = \omega(\zeta) = K\left\{\zeta + \frac{a_1}{\zeta^3} + \frac{a_2}{\zeta^7} + \frac{a_3}{\zeta^{11}} + \ldots\right\}. \tag{9}$$

Next, we consider the summation of the following fractional terms:

$$\sum_{j=1}^{N}\frac{B_j\beta_j/\zeta^3}{1 - \beta_j/\zeta^4} = \sum_{j=1}^{N}\left\{\frac{B_j\beta_j}{\zeta^3} + \frac{B_j\beta_j^2}{\zeta^7} + \frac{B_j\beta_j^3}{\zeta^{11}} + \ldots\right\} \tag{10}$$

where, for the validity of the power series expansion, we must have $|\beta_j| < 1$. The constants B_j and β_j should be determined such that the right-hand sides of (9) and (10) are approximately equal. The following equations are used:

$$\sum_{j=1}^{N} B_j\beta_j^k = a_k \quad (k = 1, 2, 3, \ldots, 2N) \tag{11}$$

which are established by comparing and equating the coefficients of the second and subsequent terms in (9) to those of the corresponding terms in (10). Equation (11) is solved via the following procedure (Hasebe and Inohara, 1981).

Consider the simultaneous equations with coefficients a_k and of n unknowns,

$$\begin{aligned} &a_1x_1 + a_2x_2 + \ldots \quad \ldots + a_nx_n + a_{n+1} = 0\\ &a_2x_1 + a_3x_2 + \ldots \quad \ldots + a_{n+1}x_n + a_{n+2} = 0\\ &\quad\vdots \qquad\qquad\qquad\quad \vdots\\ &a_nx_1 + a_{n+1}x_2 + \ldots \quad \ldots + a_{2n-1}x_n + a_{2n} = 0 \end{aligned} \tag{12}$$

β_j's should be fixed by solving the following equation of order n and with coefficients $x_1, x_2, \ldots, x_n$ which are obtained from the solution of (12):

$$\beta^n + x_n\beta^{n-1} + \ldots \quad \ldots + x_2\beta + x_1 = 0. \tag{13}$$

Substituting the β_j's obtained from the solution of (13) into (11) and solving the resulting simultaneous equations of n unknowns yields the values of B_j's. Finally, by obtaining B_j and β_j the mapping function can be written as

$$\begin{aligned} z = \omega(\zeta) &= K\left\{\zeta + \sum_{j=1}^{N}\frac{B_j\beta_j/\zeta^3}{1 - \beta_j/\zeta^4} + \text{const}\right\}\\ &= K\left[\zeta + \sum_{j=1}^{N}\left\{\frac{-\frac{B_j\sqrt{\beta_j}}{4}}{\beta_j^{1/4} - \zeta} + \frac{-\frac{B_j\sqrt{\beta_j}}{4}}{-\beta_j^{1/4} - \zeta} + \frac{\frac{B_j\sqrt{\beta_j}}{4}}{i\beta_j^{1/4} - \zeta} + \frac{\frac{B_j\sqrt{\beta_j}}{4}}{-i\beta_j^{1/4} - \zeta}\right\} + \text{const}\right]\\ &\equiv E_0\zeta + \sum_{k=1}^{n}\frac{E_k}{\zeta_k - \zeta} + E_{-1} \quad (n = 4N). \end{aligned} \tag{14}$$

Taking $E_0 \neq 0$ ($E_0 = a$, a is the radius of a circle), $E_k = 0$ ($k = 1, 2, \ldots, n$) in the general expression (14), the mapping function reduces to that for a circle; likewise, it reduces to that for an ellipse when $E_0 \neq 0$, $E_1 \neq 0$ ($E_0 = (a + b)/2$, $E_1 = (a - b)/2$, a and b are the lengths of the semi-axes of an ellipse on the x and y-axes, respectively), $\zeta_1 = 0$ and $E_k = 0$ ($k = 2$,

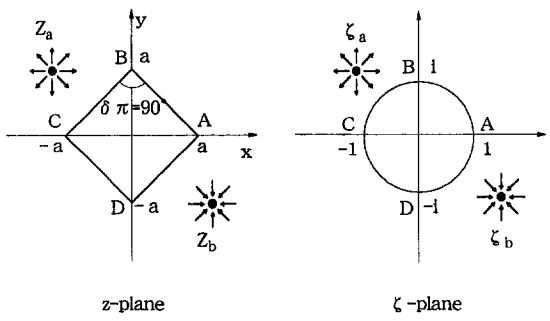

Fig. 2 Rectangular hole and unit circle, heat source, and sink source in an arbitrary point

Downloaded 04 May 2010 to 171.66.16.27. Redistribution subject to ASME license or copyright; see http://www.asme.org/terms/Terms_Use.cfm

3, . . . , n) are taken. In the following, we derive the solution to our problem with the mapping function being expressed in the form of (14).

4 Temperature Analysis

Expressions for Temperature and Heat Flux Components. Using the mapping function $\omega(\zeta)$, the temperature and heat flux components can be expressed as (Hasebe et al., 1988)

$$\Omega_0(z) = \Omega_0[\,\omega(\zeta)\,] \equiv \Omega(\zeta)$$
$$\Theta(\zeta, \bar{\zeta}) = \tfrac{1}{2}\,[\,\Omega(\zeta) + \overline{\Omega(\zeta)}\,] \tag{15}$$

$$q_x - iq_y = -k\,\frac{\Omega'(\zeta)}{\omega'(\zeta)},$$

$$q_r - iq_\theta = \frac{\zeta\omega'(\zeta)}{|\zeta\omega'(\zeta)|}\,(q_x - iq_y) \tag{16}$$

where q_r and q_θ are the heat flux components in the normal and tangential directions, respectively, in an orthogonal curvilinear coordinate system, given by the mapping function. Once the temperature function is found, the temperature and the components of the heat flux can readily be obtained from (15) and (16).

Derivation of the Complex Temperature Function. Temperature functions are derived herein for the cases when no heat is transmitted through the boundary (adibatic state), and when on the boundary the temperature is stipulated (isothermal state).

Denoting q_n as the heat flux flowing out or into the boundary, the heat flux boundary condition is expressed as follows (Hasebe et al., 1988):

$$-k\,\{\,\Omega(\sigma) - \overline{\Omega(\sigma)}\,\} = 2i\int q_n ds + \text{const} \tag{17}$$

where σ is the coordinate ζ on the unit circle, and the integration with respect to s on the right-hand side of the equation should be conducted along the path of the boundary.

Using (15), the temperature boundary condition is written in the form

$$\Omega(\sigma) + \overline{\Omega(\sigma)} = 2\Theta(\sigma, \bar{\sigma}). \tag{18}$$

Without loss of generality, we can take $q_n = 0$ in (17) (adiabatic) and $\Omega(\sigma, \bar{\sigma}) = 0$ in (18) (isothermal) as boundary conditions for consideration. Therefore the boundary conditions (17) and (18) reduce to the following form:

$$\Omega(\sigma) - \Gamma\overline{\Omega(\sigma)} = 0 \tag{19}$$

where $\Gamma = 1$ for the adiabatic and $\Gamma = -1$ for the isothermal problems, respectively.

Heat Source and Heat Sink at Arbitrary Positions. Consider the infinite domain (z-plane) having a hole of arbitrary shape with the coordinates of the point heat source and the point heat sink being denoted by z_a and z_b shown in Fig. 2, respectively. From (3) and (14), the corresponding coordinates in the mapped ζ-plane can be determined and are denoted by ζ_a and ζ_b, respectively. Now the temperature function $\Omega(\zeta)$ can be put in the form

$$\Omega(\zeta) = \Omega_1(\zeta) + \Omega_2(\zeta),$$
$$\Omega_1(\zeta) = -\frac{M}{2\pi k}\log\left(\frac{\zeta - \zeta_a}{\zeta - \zeta_b}\right) \tag{20}$$

where M is the intensity of the heat source in the infinite plane, $+M$ is the generating heat source and $-M$ is the absorbing heat sink. Substitution of (20) into the boundary condition (19) and multiplication of the resulting equation by the factor $d\sigma/[\,2\pi i(\sigma - \zeta)\,]$, followed by an integration of the Cauchy integral along the circumference of the unit circle finally yields the required function $\Omega(\zeta)$ as

$$\Omega(\zeta) = -\frac{M}{2\pi k}\left\{\log\frac{(\zeta - \zeta_a)}{(\zeta - \zeta_b)} + \Gamma\log\frac{(\zeta - \zeta_a')}{(\zeta - \zeta_b')}\right\} + \text{const} \tag{21}$$

where $\zeta_a' \equiv 1/\bar{\zeta}_a$ and $\zeta_b' \equiv 1/\bar{\zeta}_b$.

Heat Source Arbitrarily Positioned, Heat Sink at Infinity. Consider the infinite domain (z-plane) having a hole of arbitrary shape shown in Fig. 3(b), where the coordinate of the point heat source is denoted by z_a and the heat sink lies at infinity. With the use of the temperature function $\Psi_1(\zeta)$ for the heat source of intensity M at ζ_a, the required temperature function can be put in the form

$$\Omega(\zeta) = \Omega_1(\zeta) + \Omega_2(\zeta),$$
$$\Omega_1(\zeta) = -\frac{M}{2\pi k}\log(\zeta - \zeta_a). \tag{22}$$

Substitution of (22) into the boundary condition (19) and multiplication of the resulting equation by the factor $d\sigma/[\,2\pi i(\sigma - \zeta)\,]$, and integration of the Cauchy integral along the circumference of the unit circle finally gives the required function

$$\Omega(\zeta) = -\frac{M}{2\pi k}\left\{\log(\zeta - \zeta_a) + \Gamma\log\frac{(\zeta - \zeta_a')}{\zeta}\right\} + \text{const} \tag{23}$$

where $\zeta_a' \equiv 1/\bar{\zeta}_a$.

5 Thermal Stress Analysis

Heat Source and Heat Sink at Respective Arbitrary Positions. For the infinite plane with a hole of arbitrary shape, in which a heat source of intensity M and a heat sink of intensity $-M$ exist at respective arbitrary positions shown in Fig. 2, the general solution for the complex stress functions is derived in this subsection.

Denoting $\phi(\zeta)$ and $\psi(\zeta)$ as the complex stress functions regular outside the unit circle, the external traction boundary condition on the unit circle ($\zeta = \sigma$) can be written in the following equation (Muskhelishvili, 1963):

$$\phi(\sigma) + \frac{\omega(\sigma)}{\overline{\omega'(\sigma)}}\,\overline{\phi'(\sigma)} + \overline{\psi(\sigma)} = i\int (p_x + ip_y)ds \tag{24}$$

where p_x and p_y are the external tractions in the x and y directions, respectively, and the integration should be conducted along the path of the boundary. Since the external traction and the thermal problems can be treated separately without loss of generality, we can assume $p_x = p_y = 0$.

Using the complex stress functions $\phi(\zeta)$, $\psi(\zeta)$ and the temperature function $\Omega(\zeta)$, the displacement expression can be put into the following form:

$$\kappa\phi(\zeta) - \frac{\omega(\zeta)}{\overline{\omega'(\zeta)}}\,\overline{\phi'(\zeta)} - \overline{\psi(\zeta)} + 2G\alpha'\int \Omega(\zeta)\omega'(\zeta)d\zeta = 2G(u + iv) \tag{25}$$

where u and v are displacements in the x and y directions, respectively. The fourth term on the left-hand side of (25) accounts for the displacements relating to the temperature function. From this integral term, multivalued functions (logarithmic functions) are brought about; as a result, mismatch in displacement (thermal dislocation) appears. For the sake of satisfying

Downloaded 04 May 2010 to 171.66.16.27. Redistribution subject to ASME license or copyright; see http://www.asme.org/terms/Terms_Use.cfm

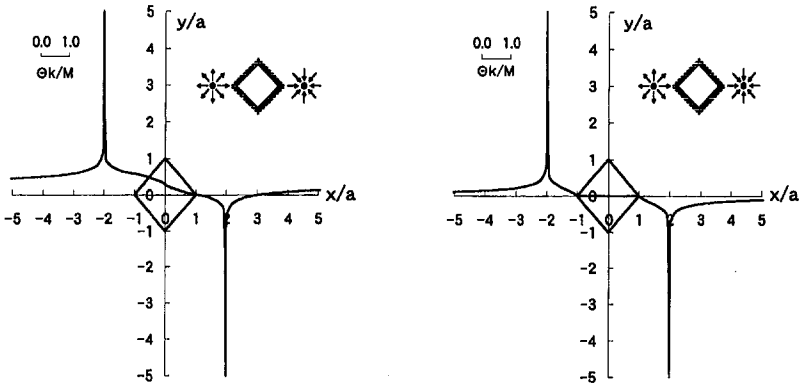

Fig. 3 Temperature distribution on the x-axis and the rectangular hole, heat source (−2a, 0), sink source (2a, 0); (a) adiabatic condition (Γ = 1), (b) isothermal condition (Γ = −1)

the condition of single-valuedness for displacements, additional functions that can be used to eliminate the mismatch in displacement should be considered. Substituting the mapping function into (7) for the point heat source, and combining it with the logarithmic functions introduced to eliminate the mismatch in displacement, we obtain $\phi_1(\zeta)$ and $\psi_1(\zeta)$. Using these functions, the required complex stress functions $\phi(\zeta)$ and $\psi(\zeta)$ can be written as

$$\phi(\zeta) = \phi_1(\zeta) + \phi_2(\zeta), \quad \psi(\zeta) = \psi_1(\zeta) + \psi_2(\zeta) \tag{26}$$

$$\phi_1(\zeta) = \frac{\alpha MGR}{4\pi k}\left[\{ \omega(\zeta) - \omega(\zeta_a) \} \log (\zeta - \zeta_a) - \{ \omega(\zeta) - \omega(\zeta_b) \} \log (\zeta - \zeta_b) \right] + A \log \zeta \tag{27a}$$

$$\psi_1(\zeta) = -\frac{\alpha MGR}{4\pi k}\left[\overline{\omega(\zeta_a)} \log (\zeta - \zeta_a) - \overline{\omega(\zeta_b)} \log (\zeta - \zeta_b) \right] + B \log \zeta. \tag{27b}$$

Moreover, since external tractions are absent on the boundary, by an analytic continuation on the external traction boundary, we obtain (Muskhelishvili, 1963)

$$\psi(\zeta) = -\overline{\phi(1/\bar{\zeta})} - \frac{\overline{\omega(1/\bar{\zeta})}}{\omega'(\zeta)}\phi'(\zeta). \tag{28}$$

Introducing (26) – (28) into the external traction boundary condition (24), and moving around the unit circle once, the requirement that the stress must be single-valued gives

$$B = \bar{A}. \tag{29}$$

Substituting (26) – (28) into the displacement expression (25), after moving around the unit circle once, the displacements must recover their initial values; on account of this, the mismatch in displacement must be eliminated. This requirement fixes the constant A in the following expression:

$$A = \frac{\alpha MGR}{4\pi k}\left\{ -\Gamma E_0(\zeta_a' - \zeta_b') + \sum_{k=1}^{n}\frac{E_k}{\zeta_k - \zeta_a} - \sum_{k=1}^{n}\frac{E_k}{\zeta_k - \zeta_b}\right\}. \tag{30}$$

Substituting (26) and (27) into the external traction boundary condition (24), noticing that $p_x = p_y = 0$ and $\bar{\sigma} = 1/\sigma$ on the boundary, multiplying both sides of the resulting equation by the factor $d\sigma/[2\pi i(\sigma - \zeta)]$, and carrying out the Cauchy integration around the boundary of the unit circle, the values of various integrals can be obtained and expressed in the following equations:

$$\frac{1}{2\pi i}\int \frac{\phi_1(\sigma)}{\sigma - \zeta}\, d\sigma = \frac{\alpha MGR}{4\pi k}\left\{ \sum_{k=1}^{n}\frac{E_k}{\zeta_k - \zeta}\log\left(\frac{\zeta_k - \zeta_a}{\zeta_k - \zeta_b}\right)\right\} + \frac{1}{2\pi i}\int \frac{A \log \sigma}{\sigma - \zeta}\, d\sigma \tag{31a}$$

$$\frac{1}{2\pi i}\int \frac{\phi_2(\sigma)}{\sigma - \zeta}\, d\sigma = \phi_2(\zeta) \tag{31b}$$

$$\frac{1}{2\pi i}\int \frac{\omega(\sigma)}{\overline{\omega'(\sigma)}}\frac{\overline{\phi_1'(\sigma)}}{(\sigma - \zeta)}\, d\sigma = \frac{\alpha MGR}{4\pi k}\left[\omega(\zeta)\log\left(\frac{1/\zeta - \overline{\zeta_a}}{1/\zeta - \overline{\zeta_b}}\right) - E_0\zeta \log\left(\frac{\overline{\zeta_a}}{\overline{\zeta_b}}\right) + \sum_{j=1}^{n}\frac{B_j}{\zeta_j - \zeta} \times \left\{ \sum_{k=1}^{n}\frac{\overline{E_k}}{(\overline{\zeta_k} - \overline{\zeta_j'})(\overline{\zeta_k} - \overline{\zeta_a})} - \frac{\overline{E_k}}{(\overline{\zeta_k} - \overline{\zeta_j'})(\overline{\zeta_k} - \overline{\zeta_b})}\right\} + E_0\left(\frac{1}{\overline{\zeta_a}} - \frac{1}{\overline{\zeta_b}}\right)\right] + \sum_{k=1}^{n}\frac{\bar{A}\zeta_k B_k}{\zeta_k - \zeta} \tag{31c}$$

$$\frac{1}{2\pi i}\int \frac{\omega(\sigma)}{\overline{\omega'(\sigma)}}\frac{\overline{\phi_2'(\sigma)}}{(\sigma - \zeta)}\, d\sigma = \sum_{k=1}^{n}\frac{\overline{A_k}B_k}{\zeta_k - \zeta} \tag{31d}$$

$$\frac{1}{2\pi i}\int \frac{\overline{\psi_1(\sigma)}}{\sigma - \zeta}\, d\sigma = -\frac{\alpha MGR}{4\pi k} \times \left\{ \omega(\zeta_a)\log\left(\frac{1}{\zeta} - \overline{\zeta_a}\right) - \omega(\zeta_b)\log\left(\frac{1}{\zeta} - \overline{\zeta_b}\right)\right\} + \frac{1}{2\pi i}\int \frac{\bar{B}\log(1/\sigma)}{\sigma - \zeta}\, d\sigma \tag{31e}$$

$$\frac{1}{2\pi i}\int \frac{\overline{\psi_2(\sigma)}}{\sigma - \zeta}\, d\sigma = \overline{\psi_2}(0) \tag{31f}$$

where $B_k \equiv E_k/\overline{\omega'(\zeta_k')}$, $\zeta_k' \equiv 1/\overline{\zeta_k}$ and $A_k \equiv \phi_2'(\zeta_k')$ $(k = 1, 2, \ldots, n)$. On account of (30), the second term on the right side of (31a) and that of (31e) cancel each other. The required complex stress function $\phi_2(\zeta)$ can then be obtained from the following equation:

Downloaded 04 May 2010 to 171.66.16.27. Redistribution subject to ASME license or copyright; see http://www.asme.org/terms/Terms_Use.cfm

$$\phi_2(\zeta) = -\frac{\alpha MGR}{4\pi k}\Bigg[\{\omega(\zeta)-\omega(\zeta_a)\}\log\left(\frac{1}{\zeta}-\zeta_a\right) - \{\omega(\zeta)-\omega(\zeta_b)\}\log\left(\frac{1}{\zeta}-\zeta_b\right) - E_0\zeta\log\left(\frac{\zeta_a}{\zeta_b}\right) + \sum_{k=1}^{n}\frac{E_k}{\zeta_k-\zeta}\log\left(\frac{\zeta_k-\zeta_a}{\zeta_k-\zeta_b}\right) + \sum_{j=1}^{n}\frac{B_j}{\zeta_j-\zeta} \times \sum_{k=1}^{n}\left\{\frac{\overline{E_k}}{(\overline{\zeta_k}-\overline{\zeta_j'})(\overline{\zeta_k}-\overline{\zeta_a})} - \frac{\overline{E_k}}{(\overline{\zeta_k}-\overline{\zeta_j'})(\overline{\zeta_k}-\overline{\zeta_b})}\right\}\Bigg] - \sum_{k=1}^{n}\frac{(\overline{A_k}+\overline{A}\zeta_k)B_k}{\zeta_k-\zeta} + \text{const.} \quad (32)$$

The unknown complex constants A_k, can be determined by solving $2n$ simultaneous equations obtained from separating the real and imaginary parts of equations $A_k \equiv \phi_2'(\zeta_k')$ $(k = 1, 2, \ldots, n)$. Eventually, the general solution for the stress function $\phi(\zeta)$ is derived by substituting (27) and (32) into (26), as follows:

$$\phi(\zeta) = \frac{\alpha MGR}{4\pi k}[\{\omega(\zeta)-\omega(\zeta_a)\}\log(\zeta-\zeta_a) - \{\omega(\zeta)-\omega(\zeta_b)\}\log(\zeta-\zeta_b)] + A\log\zeta - \frac{\alpha MGR}{4\pi k}\Bigg[\{\omega(\zeta)-\omega(\zeta_a)\}\log\left(\frac{1}{\zeta}-\overline{\zeta_a}\right) - \{\omega(\zeta)-\omega(\zeta_b)\}\log\left(\frac{1}{\zeta}-\overline{\zeta_b}\right) - E_0\zeta\log\left(\frac{\zeta_a}{\zeta_b}\right) + \sum_{k=1}^{n}\frac{E_k}{\zeta_k-\zeta}\log\left(\frac{\zeta_k-\zeta_a}{\zeta_k-\zeta_b}\right) + \sum_{j=1}^{n}\frac{B_j}{\zeta_j-\zeta}\sum_{k=1}^{n}\left\{\frac{\overline{E_k}}{(\overline{\zeta_k}-\overline{\zeta_j'})(\overline{\zeta_k}-\overline{\zeta_a})} - \frac{\overline{E_k}}{(\overline{\zeta_k}-\overline{\zeta_j'})(\overline{\zeta_k}-\overline{\zeta_b})}\right\}\Bigg] - \sum_{k=1}^{n}\frac{(\overline{A_k}+\overline{A}\zeta_k)B_k}{\zeta_k-\zeta} \quad (33)$$

where a constant term has been neglected.

When the heat source and the heat sink are located, respectively, on the boundary, taking σ_a and σ_b as the coordinates of these thermal positions and introducing $\zeta_a = \sigma_a$ and $\zeta_b = \sigma_b$ into (33) yields

$$\phi(\zeta) = A\log\zeta - \frac{\alpha MGR}{4\pi k}[\{\omega(\sigma_a)-\omega(\sigma_b)\}\log\zeta + \sum_{k=1}^{n}\frac{E_k}{\zeta_k-\zeta}\log\left\{\left(\frac{\zeta_k-\sigma_a}{\zeta_k-\sigma_b}\right)\left(\frac{\sigma_b}{\sigma_a}\right)\right\} + \sum_{j=1}^{n}\frac{B_j}{\zeta_j-\zeta} \times \sum_{k=1}^{n}\left\{\frac{\overline{E_k}}{(\overline{\zeta_k}-\overline{\zeta_j'})(\overline{\zeta_k}-\overline{\sigma_a})} - \frac{\overline{E_k}}{(\overline{\zeta_k}-\overline{\zeta_j'})(\overline{\zeta_k}-\overline{\sigma_b})}\right\}\Bigg] - \sum_{k=1}^{n}\frac{(\overline{A_k}+\overline{A}\zeta_k)B_k}{\zeta_k-\zeta}. \quad (34)$$

The above equation reveals that when the heat source and the heat sink exist on the boundary, the points for their positions, $\zeta = \sigma_a$ and $\zeta = \sigma_b$, do not have stress singularities since constraints on displacements are absent on the boundary.

The other stress function $\psi(\zeta)$ is given by (28), obtained via an analytical continuation on the boundary, because there are no external tractions on the boundary.

Heat Source Arbitrarily Positioned, Heat Sink at Infinity. In this subsection, the stress functions are derived for the case when the generating heat source of intensity M exists in the region, while the absorbing heat sink is at infinity.

Following an analysis similar to that in the previous subsection, by employing the stress functions for the heat source and the logarithmic functions used to eliminate the mismatch in displacement caused by the heat source, the complex stress functions can be written as

$$\phi(\zeta) = \phi_1(\zeta) + \phi_2(\zeta), \quad \psi(\zeta) = \psi_1(\zeta) + \psi_2(\zeta) \quad (35)$$

$$\phi_1(\zeta) = \frac{\alpha MGR}{4\pi k}[\{\omega(\zeta)-\omega(\zeta_a)\}\{\log(\zeta-\zeta_a)-1\}] + A\log\zeta \quad (36a)$$

$$\psi_1(\zeta) = -\frac{\alpha MGR}{4\pi k}[\overline{\omega(\zeta_a)}\log(\zeta-\zeta_a)] + B\log\zeta. \quad (36b)$$

In (36), the first terms of $\phi_1(\zeta)$ and $\psi_1(\zeta)$ are the stress functions for the heat source, and the second terms are functions invoked to eliminate the mismatch in displacement caused by the heat source. Substituting (35), (36), and (28) into the external traction boundary condition (24), and moving around the unit circle once, the following relation is obtainable from the condition that the stress must be single-valued,

$$B = \bar{A}. \quad (37)$$

Substituting (35), (36), and (28) into the displacement expression (25), and moving around the unit circle once, the condition that the displacements must be single-valued fixes the constant A in the following equation:

$$A = \frac{\alpha MGR}{4\pi k}\left\{-\Gamma E_0\zeta_a' + \sum_{k=1}^{n}\frac{E_k}{\zeta_k-\zeta_a}\right\}. \quad (38)$$

Substituting (35) and (36) into the external traction boundary condition (24), noticing that $p_x = p_y = 0$ and $\bar{\sigma} = 1/\sigma$ on the boundary, multiplying both sides of the resulting equation by the factor $d\sigma/[2\pi i(\sigma-\zeta)]$, and carrying out the Cauchy integration on the unit circle, the required complex stress function $\phi_2(\zeta)$ can then be obtained from the following equation:

$$\phi_2(\zeta) = -\frac{\alpha MGR}{4\pi k}\Bigg[\{\omega(\zeta)-\omega(\zeta_a)\}\log\left(\frac{1}{\zeta}-\overline{\zeta_a}\right) - E_0\zeta\log(-\overline{\zeta_a}) + \sum_{k=1}^{n}\frac{E_k}{\zeta_k-\zeta}\log(\zeta_k-\zeta_a) - 2\sum_{k=1}^{n}\frac{E_k}{\zeta_k-\zeta} + \sum_{j=1}^{n}\frac{B_j}{\zeta_j-\zeta} \times \left\{\overline{E_0} + \sum_{k=1}^{n}\frac{\overline{E_k}}{(\overline{\zeta_k}-\overline{\zeta_j'})(\overline{\zeta_k}-\overline{\zeta_a})}\right\}\Bigg] - \sum_{k=1}^{n}\frac{(\overline{A_k}+\overline{A}\zeta_k)B_k}{\zeta_k-\zeta} + \text{const} \quad (39)$$

where $B_k \equiv E_k/\overline{\omega'(\zeta_k')}$, $\zeta_k' \equiv 1/\overline{\zeta_k}$ and $A_k \equiv \phi_2'(\zeta_k')$ $(k = 1, 2, \ldots, n)$. The unknown complex constants A_k, can be determined by solving $2n$ simultaneous equations, obtained from separating the real and imaginery parts of equations $A_k \equiv \phi_2'(\zeta_k')$ $(k = 1, 2, \ldots, n)$. Finally, the general solution for the stress function $\phi(\zeta)$ can be obtained by substituting (36) and (39) into (35).

Downloaded 04 May 2010 to 171.66.16.27. Redistribution subject to ASME license or copyright; see http://www.asme.org/terms/Terms_Use.cfm

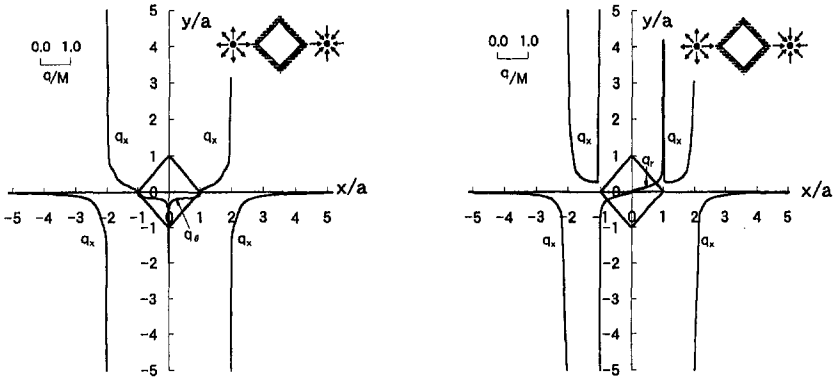

(a) Adiabatic condition (Γ =1) (b) Isothermal condition (Γ = −1)

Fig. 4 Heat flux distribution on the x-axis and the rectangular hole, heat source ($-2a$, 0), sink source ($2a$, 0); (a) adiabatic condition (Γ = 1), (b) isothermal condition (Γ = −1)

If the solution for a heat sink (this can be obtained by replacing ζ_a and M, the intensity of the heat source, with ζ_b and $-M$, respectively) is superposed in (35) on the solution for a heat source, then (33), the solution for the two coexisting thermal sources (the heat source and the heat sink), is once again obtained. However, when only the terms associated with ζ_a are retained in (34), the solution for the two thermal sources, (35) does not follow. This is because in the superposition, several terms in (35) are cancelled by the counteractions between the heat source and the heat sink.

When the heat source is located on the boundary, it is seen that the heat source is not a singular stress point.

5 Analytic Examples

In the analytic examples, we consider an infinite plane with a rectangular hole, within which a point heat source $A(-2a, 0)$ and a point heat sink $B(2a, 0)$ lie on the x-axis. In the following, for $\kappa = 2$, (corresponding to $\nu = \frac{1}{3}$ for plane strain and $\nu = 0.25$ for plane stress, ν being the Poisson's ratio of the material), the temperature, heat flux, and stress distributions on the x-axis and on the boundary (for the portion $y > 0$) are demonstrated in the respective figures.

Temperature Distributions. Dimensionless temperature distributions for the adiabatic and isothermal states on the boundary are shown in Figs. 3(a) and 3(b), respectively. The temperatures shown in the distributions are relative ones with respect to the temperature at point $A(a, 0)$, which is taken to be zero. It can be seen that the relative temperatures increase steeply near the heat source, and around the heat sink they decrease sharply in numerical value. Moreover, Fig. 3(b) shows the relative temperature is constant (zero) along the boundary, which indicates that the isothermal boundary condition has been satisfied.

Heat Flux Distributions. Dimensionless heat flux distributions for the adiabatic and isothermal states on the boundary are shown in Figs. 4(a) and 4(b), respectively. The direction of heat flux q_θ is taken to be positive, when it flows counterclockwise along the boundary; the positive directions for heat flux q_x and q_y are the x and y directions, respectively. In the adiabatic condition, the heat flux normal to the boundary, q_r, is zero; while in the isothermal condition, the heat flux in the tangential direction, q_θ, vanishes along the boundary.

Stress Distributions. Dimensionless stress distributions for the adiabatic and isothermal states on the boundary are shown in Figs. 5(a) and 5(b), respectively. σ_x and σ_y are the axial stress components in the x and y directions, respectively; τ_{xy} is the shear stress; σ_r, σ_θ and $\tau_{r\theta}$ stand for the stresses in the normal and tangential directions, and the shear stress on the boundary, respectively. The signs of the axial stresses are taken to be positive for the tensile, and negative for the compressive stress. In accordance with the steep temperature variation, compressive and tensile stress concentrations occur around the heat source and the heat sink, respectively. Comparing the stress distribution for the adiabatic case with that for the isothermal

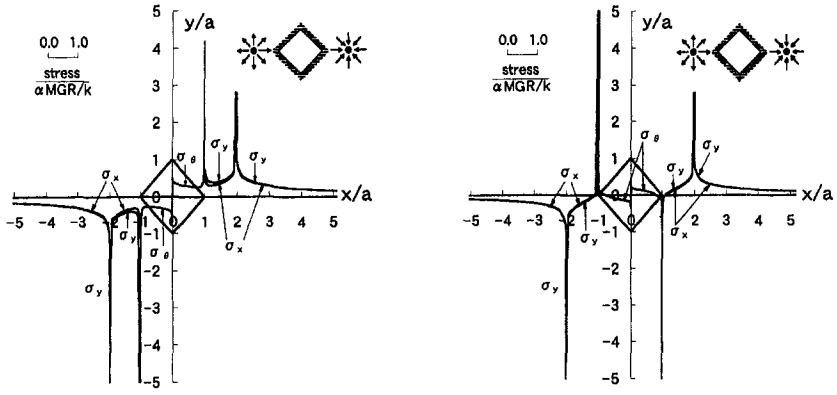

(a) Adiabatic condition (Γ =1) (b) Isothermal condition (Γ = −1)

Fig. 5 Stress distribution on the x-axis and the rectangular hole, heat source ($-2a$, 0), sink source ($2a$, 0); (a) adiabatic condition (Γ = 1), (b) isothermal condition (Γ = −1)

Downloaded 04 May 2010 to 171.66.16.27. Redistribution subject to ASME license or copyright; see http://www.asme.org/terms/Terms_Use.cfm

condition, it is seen that they differ from each other clearly in the proximity of the boundary.

6 Concluding Remarks

An infinite plane with a hole of arbitrary shape, within which a heat source and a heat sink are arbitrarily located, including the special case when the heat sink is at infinity, is considered in this paper. For adiabatic and isothermal boundary conditions, general solutions for the complex thermal function (temperature function) and the stress functions were derived and presented in (21), (23) and (33), (35), respectively. Superposing the solution (35) for a heat source M (intensity) at point z_a and a heat sink $-M$ (intensity) at point z_b, the resulting solutions are found to be identical to (33), the solution for the heat source and the heat sink coexisting at respective arbitrary points in the infinite plane. In case the heat sources are located on the boundary, the corresponding solutions were given, from which it is shown that there is no stress singularity at and around the heat sources.

The general solution developed herein is the fundamental solution (Green's function) for point heat sources lying within an infinite plane with a hole of arbitrary shape. Rational mapping functions (14) can be formed for other relatively arbitrary geometries, for example (Hasebe and Ueda, 1980; Hasebe et al., 1984, 1991). Furthermore, the solutions for circular and elliptic holes (Yoshikawa and Hasebe, 1998) are produced, when the corresponding mapping functions are inserted into (33) and (35).

References

Florence, A. L., and Goodier, J. N., 1960, "Thermal Stresses due to Disturbance of Uniform Heat Flow by an Insulated Ovaloid Hole," ASME JOURNAL OF APPLIED MECHANICS, Vol. 27, pp. 635–639.

Fukui, K., Fukui, T., and Kaibori, H., 1970, "Thermal Stresses of the Elastic Plane With a Circular Hole, Including One Heat Source," *Transactions of the Japan Society of Mechanical Engineers,* Vol. 36, No. 291, pp. 1772–1776.

Fukui, T., and Fukui, K., 1974, "Thermal Stresses Around Circular Inclusion Due to Heat Source and Sink One," *Transactions of the Japan Society of Mechanical Engineers,* Vol. 40, No. 340, pp. 3275–3283.

Hasebe, N., and Ueda, M., 1980, "Crack Originating from a Corner of a Square Hole," *Engineering Fracture Mechanics,* Vol. 13, pp. 913–923.

Hasebe, N., and Inohara, S., 1981, "Stress Intensity Factor at a Bilaterally-Bent Crack in the Bending Problem of Thin Plane," *Engineering Fracture Mechanics,* Vol. 14, No. 3, pp. 607–616.

Hasebe, N., Keer, L. M., and Nemat-Nasser, S., 1984, "Stress Analysis of a Kinked Crack Initiating from a Rigid Line Inclusion, Part I: Formulation," *Mechanics of Materials,* Vol. 3, pp. 131–145.

Hasebe, N., Tomida, A., and Nakamura, T., 1988, "Thermal Stresses of a Cracked Circular Hole due to Uniform Heat Flux," *Journal of Thermal Stresses,* Vol. 11, pp. 381–391.

Hasebe, N., Irikura, H., and Nakamura, T., 1991, "A Solution of the Mixed Boundary Value Problem for an Infinite Plane With a Hole Under Uniform Heat Flux," ASME JOURNAL OF APPLIED MECHANICS, Vol. 113, pp. 996–1000.

Muskhelishvili, N. I., 1963, *Some Basic Problems of Mathematical Theory of Elasticity,* 4th ed., Martinus Noordhoff, Dordrecht, The Netherlands.

Nisitani, H., Saimoto, A., Noguchi, H., and Chen, D. H., 1991, "Method of Analysis of Two-Dimensional Stationary Thermo-elastic Problem by a Body Force Method (1st Report, The Basic Theory)," *Transactions of the Japan Society of Mechanical Engineers,* Vol. 57, No. 542, pp. 2561–2567.

Yoshikawa, K., and Hasebe, N., 1998, "Heat Source in Infinite Plane with Elliptical Rigid Inclusion and Hole," *ASCE Journal of Engineering Mechanics,* submitted for publication.

Zhang, X., and Hasebe, N., 1993, "Basic Singular Thermoelastic Solutions for a Crack," *International Journal of Fracture,* Vol. 62, pp. 97–118.

Downloaded 04 May 2010 to 171.66.16.27. Redistribution subject to ASME license or copyright; see http://www.asme.org/terms/Terms_Use.cfm

Lyapunov Exponents and Stochastic Stability of Quasi-Integrable-Hamiltonian Systems

W. Q. Zhu
Professor

Z. L. Huang
Associate Professor

Department of Mechanics,
Zhejiang University,
Hangzhou 310027,
P.R. China

The averaged equations of integrable and nonresonant Hamiltonian systems of multi-degree-of-freedom subject to light damping and real noise excitations of small intensities are first derived. Then, the expression for the largest Lyapunov exponent of the square root of the Hamiltonian is formulated by generalizing the well-known procedure due to Khasminskii to the averaged equations, from which the stochastic stability and bifurcation phenomena of the original systems can be determined approximately. Linear and nonlinear stochastic systems of two degrees-of-freedom are investigated to illustrate the application of the proposed combination approach of the stochastic averaging method for quasi-integrable Hamiltonian systems and Khasminskii's procedure.

1 Introduction

In recent years there has been considerable interest in the study of stochastic stability and bifurcation phenomena in stochastic dynamical systems. There are several stability definitions for random dynamical systems and, among them, almost sure stability and pth moment stability have been widely used. Associated with the two stability definitions, there are two kinds of Lyapunov exponents: Lyapunov exponent and moment Lyapunov exponent. The former was first introduced by Oseledec (1968) for random dynamic systems and the largest Lyapunov exponent describes almost-sure stability. The latter was first introduced by Arnold (1984) and it describes moment stability. Both the two types of stability and their associated Lyapunov exponents are defined in terms of a norm that is homogeneous in all coordinate components. They are suitable specially for linear or linearized random dynamical systems.

For linear systems of Itô stochastic differential equations, a necessary and sufficient condition for almost-sure asymptotic stability was given by Khasminskii (1967). According to the multiplicative ergodic theorem of Oseledec (1968), vanishing of the largest Lyapunov exponent implies a change in the almost-sure asymptotic stability of the systems. Hence, the Khasminskii's theorem (1967) actually presented a procedure to evaluate the largest Lyapunov exponent for linear systems of Itô stochastic differential equations. This procedure has been successfully employed to determine numerically the Lyapunov exponent, almost-sure asymptotic stability and bifurcation of certain two-dimensional linear stochastic systems (Kozin and Prodromou, 1971; Mitchell and Kozin, 1974; Nishioka, 1976; Pardoux and Wihstutz, 1988; Sri Namachchivaya, 1991a, b; Sri Namachchivaya and Talwer, 1993; Wedig, 1988, 1989, 1990; Ariaratnam and Xie, 1989, 1990; and others). The procedure is also applicable to a special type of nonlinear stochastic system, for which the drift and diffusion coefficients of Itô equations are homogeneous of order one (Kozin and Zhang, 1990).

The direct use of Khasminskii's procedure to the systems of dimension higher than 2 has not met with much success principally due to the difficulty of discussing diffusion processes occurring on surfaces of unit hyperspheres in higher dimensional spaces. However, the method of stochastic averaging can be used to reduce a stochastic dynamical system to a system of Itô stochastic differential equations of lower dimension under certain conditions. Thus, a combination of the stochastic averaging method and Khasminskii's procedure is a powerful approach to evaluate the largest Lyapunov exponent of higher dimensional systems. Using the combination approach of Stratonovich stochastic averaging method and Khasiminskii's procedure, the largest Lyapunov exponent and almost-sure asymptotic stochastic stability have been studied for viscoelastic systems by Ariaratnam (1993, 1996) and for coupled linear systems under white noise excitation and under real noise excitation, respectively, by Ariaratnam, et al. (1990) and by Ariaratnam and Xie (1992).

Recently, the method of stochastic averaging first proposed by Stratonovich (1963) and Khasminskii (1964) was generalized to quasi-Hamiltonian systems (Zhu and Yang, 1997; Zhu et al., 1997). For a quasi-integrable and nonresonant Hamiltonian system of n degree-of-freedom, a set of n Itô stochastic differential equations for action variables or for integrals of motion can be obtained by using the stochastic averaging method. The averaging equations are usually much more simpler than original ones and, under certain conditions, can be used to evaluate the largest Lyapunov exponent by applying Khasminskii's procedure. In doing so, one has to introduce a new norm in terms of n action variables or n integrals of motion to define the stability and its associated Lyapunov exponent. For linear stochastic dynamical systems, the new norm is substantially the same as the conventional one. For nonlinear systems, however, they are different. Since n action variables or n integrals of motion completely characterize a quasi-integrable and nonresonant Hamiltonian system, the stability and its associated Lyapunov exponent defined in terms of the new norm are physically significant.

In the present paper, the stochastic averaging method for quasi-integrable and nonresonant Hamiltonian systems is first generalized to the case of real noise excitations. Then, the expression for the largest Lyapunov exponent in terms of new norm is formulated by generalizing the Khasminskii's procedure to the averaged equations under certain conditions. It is shown that the stability and bifurcation of original systems can be determined approximately by the largest Lyapunov exponent obtained by using the combination approach of the stochastic averaging method for quasi-integrable Hamiltonian systems and the Khasminskii's procedure. Finally, a coupled linear oscilla-

Contributed by the Applied Mechanics Division of THE AMERICAN SOCIETY OF MECHANICAL ENGINEERS for publication in the ASME JOURNAL OF APPLIED MECHANICS.

Discussion on the paper should be addressed to the Technical Editor, Professor Lewis T. Wheeler, Department of Mechanical Engineering, University of Houston, Houston, TX 77204-4792, and will be accepted until four months after final publication of the paper itself in the ASME JOURNAL OF APPLIED MECHANICS.

Manuscript received by the ASME Applied Mechanics Division, Aug. 4, 1997; final revision, July 8, 1998. Associate Technical Editor: N. C. Perkins.

 Copyright © 1999 by ASME

Downloaded 04 May 2010 to 171.66.16.27. Redistribution subject to ASME license or copyright; see http://www.asme.org/terms/Terms_Use.cfm

tors and a coupled linear and nonlinear oscillators subject to randomly parametric excitations are investigated to illustrate the application of the present approach.

2 Averaged Equations of Quasi-Integrable-Hamiltonian Systems With Real Noise Excitations

The method of stochastic averaging for multidegree-of-freedom quasi-integrable-Hamiltonian systems has been developed recently by Zhu et al. (1997) for both nonresonant and resonant Hamiltonian systems in the case of white noise excitations. Here, we derive the averaged equations for integrable and nonresonant Hamiltonian systems subject to light damping and real noise excitation of small intensities. Consider a quasi-Hamiltonian system of n degree-of-freedom governed by the following equations of motion:

$$\dot{Q}_i = \frac{\partial H}{\partial P_i}$$

$$\dot{P}_i = -\frac{\partial H}{\partial Q_i} - \epsilon c_{ij}\frac{\partial H}{\partial P_j} + \epsilon^{1/2} f_{ik}\xi_k(t)$$

$$i, j = 1, 2, \ldots, n; \quad k = 1, 2, \ldots, 1 \tag{1}$$

where Q_i and P_i are generalized displacements and momenta, respectively; $H = H(\mathbf{Q}, \mathbf{P})$ is twice differentiable Hamiltonian; $c_{ij} = c_{ij}(\mathbf{Q}, \mathbf{P})$ are differentiable functions representing damping coefficients; $f_{ik} = f_{ik}(\mathbf{Q}, \mathbf{P})$ are twice differentiable functions representing excitation amplitudes; ϵ is a small positive parameter; $\xi_k(t)$ are jointly stationary and ergodic random processes with correlation functions $E[\xi_k(t)\xi_l(t+\tau)] = R_{kl}(\tau)$.

Suppose that the Hamiltonian system governed by Eq. (1) with $\epsilon = 0$ is integrable and nonresonant, and that the motion of the system is quasi-periodic. Then action-angle variables, I_r and θ_r, can be introduced through canonical transformations (Tabor, 1989)

$$I_r = I_r(\mathbf{Q}, \mathbf{P})$$

$$\theta_r = \theta_r(\mathbf{Q}, \mathbf{P})$$

$$r = 1, 2, \ldots, n \tag{2}$$

such that the transformed equations of the Hamiltonian system are of the form

$$\dot{I}_r = 0$$

$$\dot{\theta}_r = \frac{\partial H(\mathbf{I})}{\partial I_r} = \omega_r(\mathbf{I})$$

$$r = 1, 2, \ldots, n \tag{3}$$

where $H(\mathbf{I})$ is the transformed Hamiltonian independent of θ_r; $\omega_r(\mathbf{I})$ are frequencies depending on I_r and not rationally related. After the canonical transformations, Eq. (1) becomes

$$\dot{I}_r = -\epsilon c_{ij}\frac{\partial I_r}{\partial P_i}\frac{\partial H}{\partial P_j} + \epsilon^{1/2} f_{ik}\frac{\partial I_r}{\partial P_i}\xi_k(t)$$

$$\dot{\theta}_r = \omega_r - \epsilon c_{ij}\frac{\partial \theta_r}{\partial P_i}\frac{\partial H}{\partial P_j} + \epsilon^{1/2} f_{ik}\frac{\partial \theta_r}{\partial P_i}\xi_k(t)$$

$$r, i, j = 1, 2, \ldots, n; \quad k = 1, 2, \ldots, l \tag{4}$$

where Q_r and P_r on the right-hand sides of Eq. (4) should be replaced by I_r and θ_r in terms of Eq. (2). It is seen from Eq. (4) that action processes I_r are slowly varying while angle processes θ_r rapidly varying. Assume that the frequency bands of random excitations $\xi_k(t)$ are sufficiently wide so that the correlation times of the excitations are much shorter than the relaxation times of action processes. It can be shown (Khasminskii, 1966; Lin and Cai, 1995; Stratonovich, 1963) that action vector $\mathbf{I} = [I_1, I_2, \ldots, I_n]^T$ converges in probability to an n-dimensional vector diffusion process as $\epsilon \to 0$ in time interval $0 \le t \le T$, where $T \sim o(\epsilon^{-1})$. The Itô stochastic differential equations for this vector diffusion process can be obtained by stochastic averaging as follows:

$$dI_r = \epsilon F_r(\mathbf{I})dt + \epsilon^{1/2} G_{ru}(\mathbf{I})dB_u(t)$$

$$r = 1, 2, \ldots, n; \quad u = 1, 2, \ldots, m \tag{5}$$

where $B_u(t)$ are independent unit Wiener processes,

$$F_r(\mathbf{I}) = \left\langle -c_{ij}\frac{\partial I_r}{\partial p_i}\frac{\partial H}{\partial p_j} + \int_{-\infty}^{0}\left[g_{sl}(t+\tau)\frac{\partial g_{rk}(t)}{\partial I_s} + \mathrm{h}_{sl}(t+\tau)\frac{\partial g_{rk}(t)}{\partial \theta_s}\right] R_{kl}(\tau)dt\right\rangle_t$$

$$G_{ru}(\mathbf{I})G_{su}(\mathbf{I}) = \left\langle \int_{-\infty}^{\infty} g_{sl}(t+\tau)g_{rk}(t)R_{kl}(\tau)d\tau\right\rangle_t \tag{6}$$

and

$$g_{rk} = f_{ik}\frac{\partial I_r}{\partial p_i}$$

$$h_{rk} = f_{ik}\frac{\partial \theta_r}{\partial p_i}. \tag{7}$$

$\langle\cdot\rangle_t$ in Eq. (6) denotes the time averaging under the condition of constant I_r. Note that g_{rk} and h_{rk} are quasi-periodic functions with n incommensurable periods $T_r = 2\pi/\omega_r(\mathbf{I})$ and can be expressed as n-fold fourier series, i.e.,

$$f(\mathbf{I}, t) = f_0(\mathbf{I}) + \sum_{\alpha=1}^{\infty}\sum_{|\mathbf{u}|=\alpha}[f_u(\mathbf{I})\cos(\mathbf{u}, \theta) + \bar{f}_u(\mathbf{I})\sin(\mathbf{u}, \theta)] \tag{8}$$

where f stands for g_{rk} or h_{rk}, $\mathbf{u} = [u_1, u_2, \ldots, u_n]^T$, u_r are positive integers, $|u| = \sum_{r=1}^{n} u_r$, $\theta = [\theta_1, \theta_2, \ldots, \theta_n]^T$, $\theta_r = \omega_r(\mathbf{I})t$, $(\mathbf{u}, \theta) = \sum_{r=1}^{n} u_r\theta_r$. Inserting the Fourier expansions of g_{rk} and h_{rk} in the form of Eq. (8) into Eq. (6) and accomplishing the integration and time averaging one obtains $F_r(\mathbf{I})$ and $G_{ru}(\mathbf{I})$.

In many cases it is more easier to obtain n integrals of motion rather than n action variables. Furthermore, n integrals of motion are related to n action variables only and are independent of n angle variables. For example, this is the case when n linear and/or nonlinear oscillators are coupled by dampings and/or parametric excitations. In this case the procedure to derive the averaged equations for I_r described in this section is also applicable to derive the averaged equations for H_r provided that I_r in Eqs. (2)–(8) are replaced by H_r.

In the case of white noise excitations, $R_{kl}(\tau) = 2D_{kl}\delta(\tau)$. Since the flow of an integrable and nonresonant Hamiltonian systems is ergodic on n-dimensional torus, the time averaging in Eq. (6) may be replaced by spatial averaging with respect to θ_r, i.e.,

$$\langle\cdot\rangle_t = \frac{1}{(2\pi)^n}\int_0^{2\pi}\cdot\, d\theta \tag{9}$$

where $\int_0^{2\pi}\cdot\, d\theta$ stands for an n-fold integral with respect to θ_r, $r = 1, 2, \ldots, n$.

Downloaded 04 May 2010 to 171.66.16.27. Redistribution subject to ASME license or copyright; see http://www.asme.org/terms/Terms_Use.cfm

3 The Largest Lyapunov Exponent of Averaged Equations

Now consider Itô equations of averaged integrals of motion

$$dH_r = \epsilon F_r(\mathbf{H})dt + \epsilon^{1/2} G_{ru}(\mathbf{H})dB_u(t)$$
$$r = 1, 2, \ldots, n; \quad u = 1, 2, \ldots, m \tag{10}$$

where $F_r(\mathbf{H})$ and $G_{ru}(\mathbf{H})$ are obtained in a similar way as those in Eq. (6). Note that the averaged vector $\mathbf{H}$ is an n-dimensional diffusion process. Assume that the Hamiltonian is a sum of n independent integrals of motion, i.e.,

$$H = \sum_{r=1}^{n} H_r(\mathbf{Q}, \mathbf{P}). \tag{11}$$

For most mechanical systems, Eq. (11) implies that the total energy of the system is a sum of n component energies. Furthermore, assume that the drift and diffusion coefficients of Eq. (10) satisfy the following conditions:

$$\lim_{|\mathbf{H}|\to 0} F_r(\mathbf{H}) = 0; \quad \lim_{|\mathbf{H}|\to 0} G_{ru}(\mathbf{H}) = 0 \tag{12a}$$

$$(\mathbf{G}(\mathbf{H})\mathbf{G}(\mathbf{H})^T\mathbf{a}, \mathbf{a}) \geq c|\mathbf{H}|^2|\mathbf{a}|^2 \tag{12b}$$

$$kF_r(\mathbf{H}) = F_r(k\mathbf{H}), \quad kG_{ru}(\mathbf{H}) = G_{ru}(k\mathbf{H}), \quad k > 0 \tag{12c}$$
$$r = 1, 2, \ldots, n; \quad u = 1, 2, \ldots, m$$

where $\mathbf{a}$ is an arbitrary vector and $c > 0$ is a scalar. Equation (12c) implies that the drift and diffusion coefficients of Eq. (10) are homogeneous in H_r of degree one. These properties permit us to derive an expression for the largest Lyapunov exponent of averaged Eqs. (10) using a procedure similar to that of Khasminskii (1967). To this end, introduce the following new variables:

$$\rho = \tfrac{1}{2}\log H \tag{13}$$

and

$$\alpha_r = H_r/H, \quad r = 1, 2, \ldots, n. \tag{14}$$

The Itô equations for ρ and α_r are obtained from Eq. (10) by using Itô differential rule as follows:

$$d\rho = \epsilon Q(\mathbf{a})dt + \epsilon^{1/2}\Sigma_u(\mathbf{a})dB_u(t) \tag{15}$$

$$d\alpha_r = \epsilon m_r(\mathbf{a})dt + \epsilon^{1/2}\sigma_{ru}(\mathbf{a})dB_u(t) \tag{16}$$
$$r = 1, 2, \ldots, n; \quad u = 1, 2, \ldots, m$$

where $\mathbf{a} = [\alpha_1, \alpha_2, \ldots, \alpha_n]^T$ and

$$Q(\mathbf{a}) = \tfrac{1}{2}\sum_{r=1}^{n} F_r(\mathbf{a}) - \tfrac{1}{4}\sum_{r,s=1}^{n}\sum_{u=1}^{m} G_{ru}(\mathbf{a})G_{su}(\mathbf{a}) \tag{17}$$

$$m_r(\mathbf{a}) = -\alpha_r \sum_{s=1}^{n} F_s(\mathbf{a}) + F_r(\mathbf{a})$$
$$+ \tfrac{1}{2}\alpha_r \sum_{i,j=1}^{n}\sum_{u=1}^{m} G_{iu}(\mathbf{a})G_{ju}(\mathbf{a}) - \tfrac{1}{2}\sum_{j=1}^{n}\sum_{u=1}^{m} G_{ru}(\mathbf{a})G_{ju}(\mathbf{a}) \tag{18}$$

$$\sigma_{ru}(\mathbf{a}) = G_{ru}(\mathbf{a}) - \alpha_r \sum_{j=1}^{n} G_{ju}(\mathbf{a}). \tag{19}$$

Note that $\sum_{r=1}^{n} \alpha_r = 1$, so only n-1 equations for α_r in Eq. (16) are independent. In the following we take the first n-1 equations for $\alpha_1, \alpha_2, \ldots, \alpha_{n-1}$ as independent equations. Let $\mathbf{a}' = [\alpha_1, \alpha_2, \ldots, \alpha_{n-1}]$ be an (n-1) dimensional vector diffusion process with α_n replaced by $\alpha_n = 1 - \sum_{r=1}^{n-1} \alpha_r$.

Define the Lyapunov exponent of original system (1) and averaged system (10) as the asymptotic rate of exponential growth of the square-root of the Hamiltonian (or the total energy)

$$\lambda = \lim_{t\to\infty} \frac{1}{2t}\log H \tag{20}$$

which is essentially the same as the almost sure Lyapunov exponent usually defined in terms of Euclidean norm for linear Hamiltonian systems (see the following example 1), but different for nonlinear Hamiltonian systems (see the following example 2). Although this definition is not completely consistent with current one, it is physically meaningful yet simple for the evaluation of the largest Lyapunov exponent.

Integrating Eq. (15) from 0 to t, we obtain

$$\rho(t) - \rho(0) = \int_0^t \epsilon Q[\mathbf{a}(\tau)]d\tau + \int_0^t \epsilon^{1/2}\Sigma_u[\mathbf{a}(\tau)]dB_u(\tau). \tag{21}$$

Dividing Eq. (21) by t, one obtains

$$\frac{1}{2t}\log H(t) = \frac{1}{2t}\log H(0) + \frac{1}{t}\int_0^t \epsilon Q[\mathbf{a}(\tau)]d\tau + \frac{1}{t}\int_0^t \epsilon^{1/2}\Sigma_u[\mathbf{a}(\tau)]dB_u(\tau). \tag{22}$$

As $t \to \infty$, the first term in Eq. (22) vanishes. The last term also vanishes, since $\Sigma_u[\mathbf{a}(\tau)]$ is bounded while $B_u(\tau)$ grows as $[\tau \log\log \tau]^{1/2}$.

Suppose that (n-1)-dimensional vector diffusion process $\mathbf{a}'$ is ergodic over the interval $0 \leq \alpha_r \leq 1$, $r = 1, 2, \ldots, n-1$, and the invariant measure (or stationary probability density) of this vector process can be obtained from the reduced Fokker-Planck equation associated with the first n-1 equations of Itô Eqs. (16). The time averaging in Eq. (22) can be replaced by assembly averaging. The Lyapunov exponent of averaged system (10) is then given by

$$\lambda = E[\epsilon Q(\mathbf{a}')] = \int \epsilon Q(\mathbf{a}')p(\mathbf{a}')d\mathbf{a}'. \tag{23}$$

For an n-dimensional Eq. (10), there exists n Lyapunov exponents. However, Eq. (22) converges to the largest Lyapunov exponent $\lambda_{\max}$, provided that $\mathbf{a}'$ is ergodic on the entire intervals $0 \leq \alpha_r \leq 1$, $r = 1, 2, \ldots, n-1$. In the special case of two-degree-of-freedom quasi-integrable-Hamiltonian systems, diffusion process $\mathbf{a}'$ is one-dimensional, and the stationary probability density can be obtained easily. In this case, we can obtain the explicit expression for the largest Lyapunov exponent.

Unfortunately, diffusion process $\mathbf{a}'$ may not be ergodic over the entire intervals $0 \leq \alpha_r \leq 1$, $r = 1, 2, \ldots, n-1$. In this case, the intervals are divided into subintervals by singular boundaries. Some subintervals may not admit ergodic solution, while some other subintervals may be noncommunicative and admit different ergodic solutions. The stationary probability density and the largest Lyapunov exponent may depend on the subinterval in which the initial state of the system is located. In this case, special investigation is necessary. Some examples for one-dimensional diffusion process with singularities may be found in Ariaratnam and Xie (1992) and Lin and Cai (1995).

The largest Lyapunov exponent evaluated from Eq. (23) can be used to investigate in the first approximation the stochastic stability and bifurcation phenomena of the original systems governed by Eq. (1). The boundary between stability and instability regions of the trivial solution of the original systems is approximately determined by $\lambda_{\max} = 0$. Note that to be consistent with the Lyapunov exponent defined in Eq. (20) here the stochastic stability is defined also in terms of the square-root of Hamiltonian rather than Euclidean norm. When the Hamiltonian system

Downloaded 04 May 2010 to 171.66.16.27. Redistribution subject to ASME license or copyright; see http://www.asme.org/terms/Terms_Use.cfm

associated with system (1) is linear, it is almost-sure asymptotic stability. If the associated Hamiltonian system is nonlinear, then it is asymptotic stability in the sense of square-root of total energy of the system with probability 1.

4 Examples

Example 1. As the first example of the application of the present approach to evaluate the largest Lyapunov exponent of quasi-integrable-Hamiltonian systems, consider a coupled linear system of n degree-of-freedom under parametric excitation of a real noise, which has been studied by Ariaratnam and Xie (1992). The system is governed by differential equations of the form

$$\ddot{X}_i + 2\beta_{ij}\dot{X}_j + \omega_i^2 X_i + \omega_i \xi(t) k_{ij} X_j = 0$$
$$i, j = 1, 2, \ldots, n \tag{1.1}$$

where X_i are generalized coordinates; β_{ij} are damping constants; ω_i are natural frequencies; and k_{ij} are constants; $\xi(t)$ is an stationary and ergodic random process with zero mean and sufficient short correlation time. It is assumed that $\beta_{ij} = O(\epsilon)$ and $k_{ij} = O(\epsilon^{1/2})$. The problem is to evaluate the largest Lyapunov exponent and to study the almost-sure asymptotic stability of the system about the equilibrium configuration $X_i = 0$.

The Hamiltonian of the system is separable,

$$H = \sum_{i=1}^{n} H_i = \tfrac{1}{2} \sum_{i=1}^{n} (\dot{X}_i^2 + \omega_i^2 X_i^2). \tag{1.2}$$

Introducing generalized displacements $Q_i = X_i$ and generalized momenta $P_i = \dot{X}_i$, Eqs. (1.1) can be rewritten as quasi-integrable-Hamiltonian system of the form of Eq. (1) with $\epsilon c_{ij} = 2\beta_{ij}$ and $\epsilon^{1/2} f_i = \omega_i \sum_{j=1}^{n} k_{ij} Q_j$. In nonresonant case, i.e., any linear combination of ω_i with small integers as coefficients may not be a small quantity of order ϵ, the averaged Itô equations of system (1.1) are of the form

$$dH_r = F_r(\mathbf{H})dt + G_{ru}(\mathbf{H})dB_u(t)$$
$$r = 1, 2, \ldots, n; \quad u = 1, 2, \ldots, n \tag{1.3}$$

where

$$F_r(\mathbf{H}) = \left[-2\beta_{rr} + \frac{1}{2} k_{rr}^2 S(2\omega_r) + \frac{1}{4} \sum_{s=1; s\neq r}^{n} k_{rs} k_{sr} S_{rs}^{-} \right] H_r + \frac{1}{4} \omega_r^2 \sum_{s=1; s\neq r}^{n} \frac{k_{rs}^2}{\omega_s^2} S_{rs}^{+} H_s$$

$$b_{rr}(\mathbf{H}) = [GG^T]_{rr} = \frac{1}{2} k_{rr}^2 S(2\omega_r) H_r^2 + \frac{1}{2} \omega_r^2 H_r \sum_{s=1; s\neq r}^{n} \frac{k_{rs}^2}{\omega_s^2} S_{rs}^{+} H_s$$

$$b_{rs}(\mathbf{H}) = [GG^T]_{rs} = \tfrac{1}{2} k_{rs} k_{sr} S_{sr}^{-} H_r H_s$$

$$S_{rs}^{\pm} = S(\omega_r + \omega_s) \pm S(\omega_r - \omega_s)$$

$$S(\omega) = 2 \int_0^{\infty} R(\tau) \cos(\omega\tau) d\tau. \tag{1.4}$$

It is seen from Eq. (1.4) that the drift and diffusion coefficients of the averaged system are homogeneous in H_r of degree one. The conditions in Eq. (12) are satisfied and the approach proposed in the last section for evaluating the largest Lyapunov exponent is applicable to the averaged system governed by Eq. (1.3). For simplicity, in the following only the result for the special case of two-degree-of-freedom systems is presented. In this case, the averaged equations are of the form

$$dH_1 = F_1(H_1, H_2)dt + G_{11}(H_1, H_2)dB_1(t) + G_{12}(H_1, H_2)dB_2(t)$$

$$dH_2 = F_2(H_1, H_2)dt + G_{21}(H_1, H_2)dB_1(t) + G_{22}(H_1, H_2)dB_2(t) \tag{1.5}$$

where

$$F_1(H_1, H_2) = \left[-2\beta_{11} + \frac{1}{2} k_{11}^2 S(2\omega_1) \pm \frac{1}{4} k^2 S^{-} \right] H_1 + \frac{k^2}{4} S^{+} \left(\frac{\omega_1}{\omega_2} \right)^2 H_2$$

$$F_2(H_1, H_2) = \left[-2\beta_{22} + \frac{1}{2} k_{22}^2 S(2\omega_2) \pm \frac{1}{4} k^2 S^{-} \right] H_2 + \frac{k^2}{4} S^{+} \left(\frac{\omega_2}{\omega_1} \right)^2 H_1$$

$$b_{11}(H_1, H_2) = \frac{1}{2} k_{11}^2 S(2\omega_1) H_1^2 + \frac{k^2}{2} S^{+} \left(\frac{\omega_1}{\omega_2} \right)^2 H_1 H_2$$

$$b_{22}(H_1, H_2) = \frac{1}{2} k_{22}^2 S(2\omega_2) H_2^2 + \frac{k^2}{2} S^{+} \left(\frac{\omega_2}{\omega_1} \right)^2 H_1 H_2$$

$$b_{12}(H_1, H_2) = b_{21}(H_1, H_2) = \pm \frac{k^2}{2} S^{-} H_1 H_2$$

$$k_{12} = \pm k_{21} = k > 0; \quad S^{\pm} = S_{12}^{\pm}. \tag{1.6}$$

Let

$$\rho = \tfrac{1}{2} \log H \tag{1.7}$$

and

$$\alpha_1 = H_1 / H. \tag{1.8}$$

The Itô equations for ρ and α_1 are obtained from Eq. (1.5) by using Itô differential rule as follows:

$$d\rho = Q(\alpha_1)dt + \Sigma(\alpha_1)dB(t) \tag{1.9}$$

$$d\alpha_1 = m(\alpha_1)dt + \sigma(\alpha_1)dB(t) \tag{1.10}$$

where

$$Q(\alpha_1) = \lambda_1 \alpha_1 + \lambda_2(1 - \alpha_1) \pm \tfrac{1}{8} k^2 S^{-} + \tfrac{1}{4} \varphi(\alpha_1)$$

$$m(\alpha_1) = \tfrac{1}{2}(1 - 2\alpha_1)\varphi(\alpha_1) + 2\alpha_1(1 - \alpha_1)(\lambda_1 - \lambda_2)$$

$$\sigma^2(\alpha_1) = \alpha_1(1 - \alpha_1)\varphi(\alpha_1)$$

$$\varphi(\alpha_1) = a\alpha_1^2 + b\alpha_1 + c$$

$$a = \frac{1}{2} k^2 S^{+} \left[\left(\frac{\omega_1}{\omega_2} \right)^2 + \left(\frac{\omega_2}{\omega_1} \right)^2 \right] - \frac{1}{2} k_{11}^2 S(2\omega_1) - \frac{1}{2} k_{22}^2 S(2\omega_2) \pm k^2 S^{-}$$

$$b = \frac{1}{2} k_{11}^2 S(2\omega_1) + \frac{1}{2} k_{22}^2 S(2\omega_2) \mp k^2 S^{+} - k^2 S^{+} \left(\frac{\omega_1}{\omega_2} \right)^2$$

$$c = \frac{1}{2} k^2 S^{+} \left(\frac{\omega_1}{\omega_2} \right)^2$$

Downloaded 04 May 2010 to 171.66.16.27. Redistribution subject to ASME license or copyright; see http://www.asme.org/terms/Terms_Use.cfm

$$\Delta = b^2 - 4ac$$

$$= [\tfrac{1}{2}k_{11}^2 S(2\omega_1) + \tfrac{1}{2}k_{22}^2 S(2\omega_2) + 2k^2 S(\omega_1 \mp \omega_2)]$$

$$\times [\tfrac{1}{2}k_{11}^2 S(2\omega_1) + \tfrac{1}{2}k_{22}^2 S(2\omega_2) - 2k^2 S(\omega_1 \pm \omega_2)]$$

$$\lambda_1 = -\beta_{11} + \tfrac{1}{8}k_{11}^2 S(2\omega_1)$$

$$\lambda_2 = -\beta_{22} + \tfrac{1}{8}k_{22}^2 S(2\omega_2). \tag{1.11}$$

Generally, $\sigma(\alpha_1)$ does not vanish in interval $0 < \alpha_1 < 1$ and vanishes at boundaries $\alpha_1 = 0, 1$. They are the singular boundaries of the first kind for diffusion process α_1 defined by Eq. (1.10). Further classification of such a boundary can be made based on the limiting behaviors of the drift and diffusion coefficients near the boundary (Zhang and Kozin, 1990; Lin and Cai, 1995). Since $m(0) > 0$ and $m(1) < 0$, the two boundaries are shunt. Furthermore, it can be shown that both the two boundaries are entrance points since diffusion exponents $\alpha^{(0)} = \alpha^{(1)} = 1$ and character values $c^{(0)} = c^{(1)} = 1$. Thus, there is no accumulation of probability mass at the two boundaries and process α_1 is ergodic throughout the interval $0 \leq \alpha_1 \leq 1$. The invariant measure or the stationary probability density $p(\alpha_1)$ can be obtained from the reduced Fokker-Planck equation associated with Itô Eq. (1.10). The result is

$$p(\alpha_1) = \frac{C}{\varphi(\alpha_1)} \exp\left[4(\lambda_1 - \lambda_2)\int \frac{d\alpha_1}{\varphi(\alpha_1)}\right]$$

$$= \frac{C}{\varphi(\alpha_1)} F(\alpha_1) \tag{1.12}$$

where

$$C = \frac{4(\lambda_1 - \lambda_2)}{F(1) - F(0)}. \tag{1.13}$$

According to Eq. (23), the largest Lyapunov exponent is

$$\lambda_{\max} = E[Q(\alpha_1)] = \int_0^1 Q(\alpha_1)p(\alpha_1)d\alpha_1$$

$$= \frac{1}{2}(\lambda_1 + \lambda_2) \pm \frac{1}{8}k^2 S^-$$

$$+ \frac{1}{2}(\lambda_1 - \lambda_2)\frac{F(1) + F(0)}{F(1) - F(0)}. \tag{1.14}$$

The value of the integral in Eq. (1.12) depends on the sign of Δ in Eq. (1.11). The expressions of $F(\alpha_1)$ for three cases of Δ are

$$F(\alpha_1)$$

$$= \exp\left[\frac{8(\lambda_1 - \lambda_2)}{\sqrt{\Delta}} \tanh^{-1}\frac{b + 2a\alpha_1}{\sqrt{\Delta}}\right]; \quad (\Delta > 0) \tag{1.15}$$

$$F(\alpha_1)$$

$$= \exp\left[\frac{8(\lambda_1 - \lambda_2)}{\sqrt{-\Delta}} \tan^{-1}\frac{b + 2a\alpha_1}{\sqrt{-\Delta}}\right]; \quad (\Delta < 0) \tag{1.16}$$

$$F(\alpha_1) = \exp\left[-\frac{8(\lambda_1 - \lambda_2)}{b + 2a\alpha_1}\right]; \quad (\Delta = 0). \tag{1.17}$$

It can be shown that after further derivation the present expression for the largest Lyapunov exponent in Eq. (1.14) is the same as that in Ariaratnam and Xie (1992).

The case where diffusion process α_1 is singular in the interval $0 < \alpha_1 < 1$ and the case of white noise excitation can be discussed similarly as in Ariaratnam and Xie (1992). The results are not presented here due to the limitation of paper length.

Example 2. As the second example, consider a linear oscillator coupled with a nonlinear oscillator by dampings and stochastically parametric excitations. The equations of motion of the system is of the form

$$\ddot{X}_1 + \beta_{11}\dot{X}_1 + \beta_{12}\dot{X}_2 + \omega_1^2 X_1 = k_{11}X_1 W_1(t) + k_{12}X_2^2 W_2(t)$$

$$\ddot{X}_2 + \beta_{21}\dot{X}_1 + \beta_{22}\dot{X}_2 + \gamma X_2^3$$

$$= k_{21}X_1 W_1(t) + k_{22}X_2^2 W_2(t) \tag{2.1}$$

where X_i are generalized coordinates; β_{ij} are damping constants; k_{ij} are constants; ω_1 is the natural frequency of the linear oscillator; $\gamma > 0$ is a constant; $W_i(t)$ are independent Gaussian white noises in the sense of Stratonovich with small intensities $2D_{ii}$.

The Hamiltonian of the system is separable

$$H = H_1 + H_2 \tag{2.2}$$

where

$$H_1 = \tfrac{1}{2}(\dot{X}_1^2 + \omega_1^2 X_1^2)$$

$$H_2 = \tfrac{1}{2}(\dot{X}_2^2 + \tfrac{1}{2}\gamma X_2^4). \tag{2.3}$$

Equation (2.1) can be rewritten as quasi-integrable-Hamiltonian system Eqs. (1a) and (1b) with $Q_i = X_i$, $P_i = \dot{X}_i$, $\epsilon c_{ij} = \beta_{ij}$ and $\epsilon^{1/2} f_{ij} = k_{ij}Q_j$, $i, j = 1, 2$. The averaged equations of H_i can be obtained by using the technique described in Section 2 of the present paper or that in Zhu et al. (1997). The result is

$$dH_r = F_r(H_1, H_2)dt + G_{ru}(H_1, H_2)dB_u(t)$$

$$r = 1, 2, \quad u = 1, 2 \tag{2.4}$$

where

$$F_1(H_1, H_2) = -\beta_{11}H_1 + \frac{k_{11}^2 D_{11}}{\omega_1^2}H_1 + k_{12}^2\delta_1 D_{22}H_2$$

$$F_2(H_1, H_2) = -\beta_{22}\delta_2 H_2 + \frac{k_{21}^2 D_{11}}{\omega_1^2}H_1 + k_{22}^2\delta_1 D_{22}H_2$$

$$[GG^T]_{11} = \frac{k_{11}^2 D_{11}}{\omega_1^2}H_1^2$$

$$[GG^T]_{22} = 2k_{22}^2\delta_3 D_{22}H_2^2$$

$$[GG^T]_{12} = [GG^T]_{21} = 0$$

$$\delta_1 = \frac{2}{3}\sqrt{\frac{2}{\gamma}}\Big/\int_0^1 \frac{dt}{\sqrt{1 - t^4}};$$

$$\delta_2 = 2\int_0^1 \sqrt{1 - t^4}\,dt \Big/ \int_0^1 \frac{dt}{\sqrt{1 - t^4}}$$

$$\delta_3 = \frac{8}{\gamma}\int_0^1 t^4\sqrt{1 - t^4}dt \Big/ \int_0^1 \frac{dt}{\sqrt{1 - t^4}}. \tag{2.5}$$

Note that the drift and diffusion coefficients in Eq. (2.5) are homogeneous in H_r of order one. The condition in Eq. (12) are satisfied and the proposed approach for evaluating the largest Lyapunov exponent is applicable. Defining ρ and α_1 as in Eq. (1.7) and (1.8), the Itô equations of ρ and α_1 are of the form

$$d\rho = Q(\alpha_1)dt + \Sigma(\alpha_1)dB(t) \tag{2.6}$$

$$d\alpha_1 = m(\alpha_1)dt + \sigma(\alpha_1)dB(t) \tag{2.7}$$

Downloaded 04 May 2010 to 171.66.16.27. Redistribution subject to ASME license or copyright; see http://www.asme.org/terms/Terms_Use.cfm

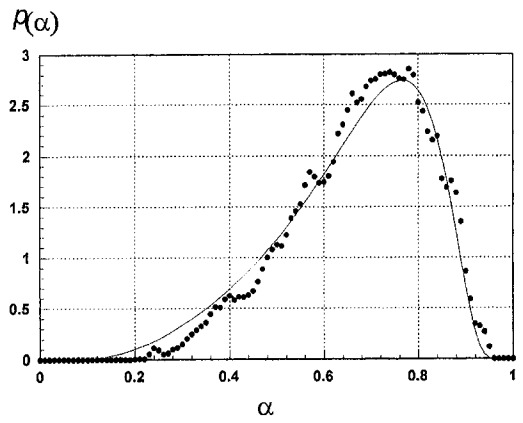

Fig. 1 Probability density $p(\alpha) = p(\alpha_1)$ in example 2. $\omega = \gamma = k_{ij} = 1$; $D_{11} = D_{22} = 0.005$; $\beta_{11} = \beta_{22} = 0.02$. ● digit simulation; — exact solution.

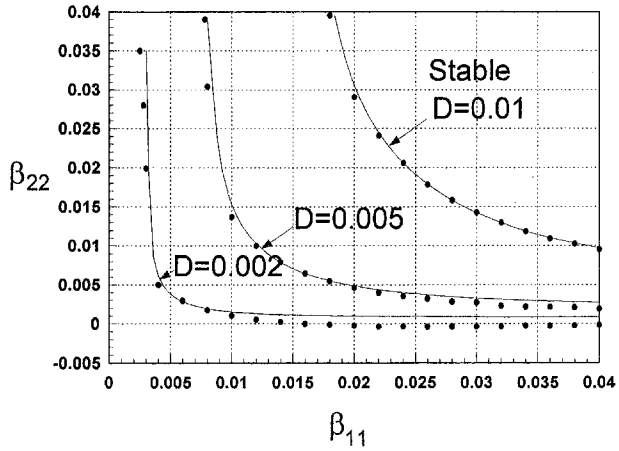

Fig. 2 Stability boundaries for different values of parameter $D = D_{11} = D_{22}$; $\omega = \gamma = k_{ij} = 1$; $(i, j = 1, 2)$. ● digit simulation; — exact solution.

where

$$Q(\alpha_1) = \left(\lambda_1 + \frac{k_{21}^2 D_{11}}{\omega_1^2}\right)\alpha_1 + (\lambda_2 + k_{12}^2\delta_1 D_{22})(1 - \alpha_1) + \frac{1}{4}A\alpha_1(1 - \alpha_1)$$

$$m(\alpha_1) = \left[2(\lambda_1 - \lambda_2) + \frac{1}{2}A(1 - 2\alpha_1)\right]\alpha_1(1 - \alpha_1) + K_{12}^2\delta_1 D_{22}(1 - \alpha_1)^2 - \frac{k_{21}^2 D_{11}}{\omega_1^2}\alpha_1^2$$

$$\sigma^2(\alpha_1) = A\alpha_1^2(1 - \alpha_1)^2$$

$$\lambda_1 = -\frac{1}{2}\beta_{11} + \frac{1}{4}\frac{k_{11}^2 D_{11}}{\omega_1^2}$$

$$\lambda_2 = -\tfrac{1}{2}\delta_2\beta_{22} + \tfrac{1}{2}(\delta_1 - \delta_3)k_{22}^2 D_{22}$$

$$A = \frac{k_{11}^2 D_{11}}{\omega_1^2} + 2\delta_3 k_{22}^2 D_{22}. \tag{2.8}$$

Generally, $\sigma(\alpha_1)$ does not vanish in interval $0 < \alpha_1 < 1$ and vanishes at boundaries $\alpha_1 = 0, 1$. It can be shown as in the first example that both the two boundaries are entrance points. So diffusion process α_1 is ergodic throughout the interval $0 \le \alpha_1 \le 1$. The invariant measure is obtained from the reduced Fokker-Planck equation associated with Itô Eqs. (2.7) as follows:

$$p(\alpha_1) = \frac{C}{\alpha_1(1 - \alpha_1)}\left(\frac{\alpha_1}{1 - \alpha_1}\right)^{4(\lambda_1 - \lambda_2)/A} \times \exp\left[-\frac{2}{A}\left(\frac{k_{12}^2\delta_1 D_{22}}{\alpha_1} + \frac{k_{21}^2 D_{11}}{\omega_1^2(1 - \alpha_1)}\right)\right] \tag{2.9}$$

where C is a normalization constant. The largest Lyapunov exponent is then

$$\lambda_{\max} = \int_0^1 Q(\alpha_1)p(\alpha_1)d\alpha_1. \tag{2.10}$$

Note that the definition of Lyapunov exponent here is

$$\lambda = \lim_{t\to\infty}\frac{1}{2t}\log\frac{1}{2}\left[\dot{X}_1^2 + \omega_1^2 X_1^2 + \dot{X}_2^2 + \frac{1}{2}\gamma X_2^4\right] \tag{2.11}$$

which is different from that usually defined in terms of Euclidean norm in that the fourth term in log is proportional to X_2^4 rather than X_2^2.

A typical stationary probability density $p(\alpha_1)$ in Eq. (2.9) is shown in Fig. 1. The stability boundaries in the plane of parameters β_{11} and β_{22} for different values of D_{ii}, γ, $k_{12} = k_{21} = k$, respectively, are shown in Figs. 2–4. It is seen from Figs. 2–4 that the stable regions increase as the stochastic excitation intensities D_{ii} or the coupled coefficients $k_{12} = k_{21} = k$ decrease. The results from Monte-Carlo simulation are also shown in Figs. 1–4. Good agreements of analytical results with the corre-

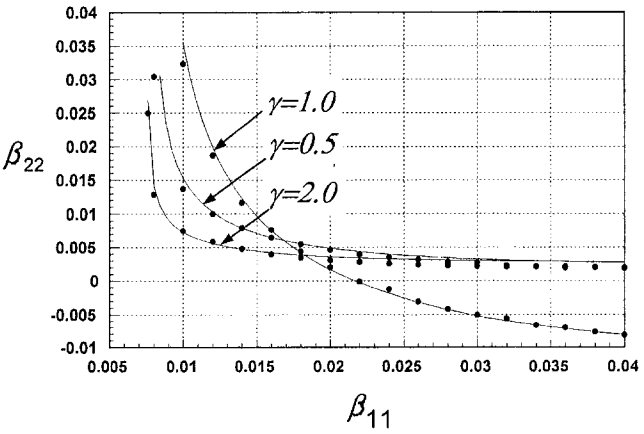

Fig. 3 Stability boundaries for different values of parameter γ; $\omega = k_{ij} = 1$; $D_{ii} = 0.005$; $(i, j = 1, 2)$. ● digit simulation; — exact solution.

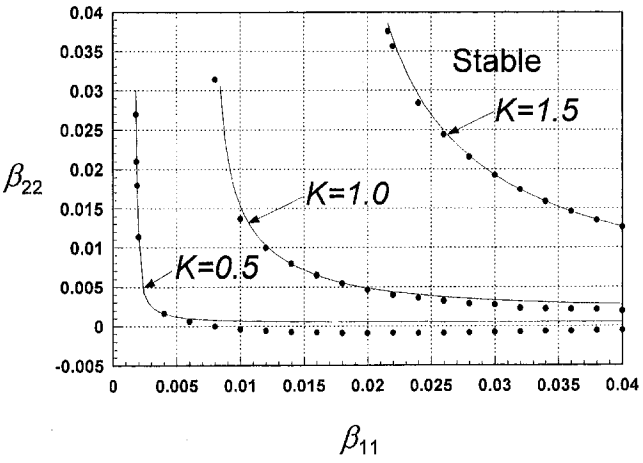

Fig. 4 Stability boundaries for different values of parameter $k = k_{12} = k_{21}$; $\omega = \gamma = 1$; $D_{ii} = 0.005$; $(i = 1, 2)$. ● digit simulation; — exact solution.

Downloaded 04 May 2010 to 171.66.16.27. Redistribution subject to ASME license or copyright; see http://www.asme.org/terms/Terms_Use.cfm

sponding results from simulation substantiate the effectiveness of the proposed approach.

5 Concluding Remarks

The averaged equations of quasi-integrable and nonresonant Hamiltonian systems of multi-degrees-of-freedom subject to light damping and real noise excitations of small intensities have been derived, which can be viewed as the generalization of those in Zhu et al. (1997). The Lyapunov exponents of stochastic systems have been defined as the asymptotic rate of exponential growth of the square-root of Hamiltonian or total energy, which are essentially the same as those usually defined in terms of Euclidean norm for linear Hamiltonian systems and different for nonlinear Hamiltonian systems. Correspondingly, the stochastic stability is defined also in terms of the square-root of Hamiltonian. The present definitions are meaningful physically and yet simple for evaluating the largest Lyapunov exponent. The expression for the largest Lyapunov exponent has been formulated for the averaged systems by generalizing the Khasminskii's procedure to the averaged equations under the conditions that the Hamiltonian is a sum of n independent integrals of motion and that the drift and diffusion coefficients of the averaged Itô equations are homogeneous in H_r of degree one. The largest Lyapunov exponent of the averaged systems can be used to determine in the first approximation the stochastic stability and bifurcation phenomena of the original systems. The present approach is applicable to multidegree-of-freedom linear and nonlinear stochastic systems, and has been illustrated with two examples.

Acknowledgment

The work reported in this paper is supported by the National Natural Science Foundation of China under grant No. 19672054, the Special Fund for Doctor Program in Institutions of Higher Learning of China and the Cao Guang Biao High Science & Technology Development Foundation of Zhejiang University.

References

Ariaratnam, S.T., 1993, "Stochastic Stability of Linear Viscoelastic Systems," *Probabilistic Engineering Mechanics,* Vol. 8, pp. 153–155.

Ariaratnam, S.T., 1996, "Stochastic Stability of Viscoelastic Systems Under Bounded Noise Excitation," *TUTAM Symposium on Advances in Nonlinear Stochastic Mechanics,* A. Naess and S. Krenk, eds., Kluwer, Dordrecht, The Netherlands, pp. 11–18.

Ariaratnam, S.T., Tam, D.S.F., and Xie, W.C., 1991, "Lyapunov Exponents and Stochastic Stability of Coupled Linear Systems," *Probabilistic Engineering Mechanics,* Vol. 6, pp. 151–156.

Ariaratnam, S.T., and Xie, W.C., 1989, "Stochastic Perturbation of Pitchfork Bifurcation," *Structure Safety,* Vol. 6, pp. 205–210.

Ariaratnam, S.T., and Xie, W.C., 1990, "Lyapunov Exponent and Rotation Number of a Two-Dimensional Nilpotent Stochastic Systems," *Dynamics and Stability of Systems,* Vol. 5, pp. 1–9.

Ariaratnam, S.T., and Xie, W.C., 1992, "Lyapunov Exponents and Stochastic Stability of Coupled Linear Systems Under Real Noise Excitation," ASME JOURNAL OF APPLIED MECHANICS, Vol. 59, pp. 664–673.

Arnold, L., 1984, "A Formula Connecting Sample and Moment Stability of Linear Stochastic System," *SIAM Journal of Applied Mathematics,* Vol. 44, pp. 793–802.

Khasminskii, R.Z., 1964, "On the Behavior of a Conservative System with Small Friction and Small Random Noise," *Prikladnaya Matematika Mechanica (Applied Mathematics and Mechanics),* Vol. 28, pp. 1126–1130 (in Russian).

Khasminskii, R.Z., 1966, "A Limit Theorem for the Solution of Differential Equations with Random Hand Sides," *Theory of Probability and Applications,* Vol. 11, No. 3, pp. 390–405.

Khasminskii, R.Z., 1967, "Sufficient and Necessary Conditions of Almost Sure Asymptotic Stability of a Linear Stochastic System," *Theory of Probability and Applications,* Vol. 11, pp. 390–405.

Kozin, F., and Prodromou, S., 1971, "Necessary and Sufficient Conditions for Almost Sure Sample Stability of Linear Itô Equations," *SIAM Journal of Applied Mathematics,* Vol. 21, pp. 413–424.

Kozin, F., and Zhang, Z. Y., 1990, "On Almost Sure Sample Stability of Nonlinear Itô Differential Equations," *Stochastic Structural Dynamics, Vol. 1: New Theoretical Developments,* Y.K. Lin and I. Elishakoff, eds., Springer-Verlag, Berlin, pp. 147–154.

Lin, Y.K., and Cai, G.Q., 1995, *Probabilistic Structural Dynamics, Advanced Theory and Applications,* McGraw-Hill, New York.

Mitchell, R.R., and Kozin, F., 1974, "Sample Stability of Second Order Linear Differential Equations with Wide Band Noise Coefficients," *SIAM Journal of Applied Mathematics,* Vol. 27, pp. 571–604.

Nishioka, K., 1976, "On the Stability of Two-Dimensional Linear Stochastic Systems," *Kodai Mathematics Seminar Report,* Vol. 27, pp. 211–230.

Oseledec, V.I., 1968, "A Multiplicative Ergodic Theorem: Lyapunov Characteristic Number for Dynamic Systems," *Transaction of the Moscow Mathematical Society,* Vol. 19, pp. 197–231.

Pardoux, E., and Wihstutz, V., 1988, "Lyapunov Exponent and Rotation Number of Two-Dimensional Linear Stochastic Systems with Small Diffusion," *SIAM Journal of Applied Mathematics,* Vol. 48, pp. 442–457.

Sri Namachchivaya, N., 1991a, "Almost Sure Stability of Stochastic Dynamical Systems under Combined Harmonic and Stochastic Excitations," *Journal of Sound and Vibration,* Vol. 151, pp. 77–90.

Sri Namachchivaya, N., 1991b, "Co-Dimensional Two Bifurcation in Presence of Noise," ASME JOURNAL OF APPLIED MECHANICS, Vol. 58, pp. 259–265.

Sri Namachchivaya, N., and Talwer, S., 1993, "Maximal Lyapunov Exponent and Rotation Number of Stochastically Perturbed Co-Dimension Two Bifurcation," *Journal of Sound and Vibration,* Vol. 169, pp. 349–372.

Stratonovich, R.L., 1963, *Topics in the Theory of Random Noise,* Vol. 1, Gordon and Breach, New York.

Wedig, W.V., 1988, "Lyapunov Exponents of Stochastic Systems and Related Bifurcation Problems," *Stochastic Structural Dynamics, Progress in Theory and Application,* S.T. Ariaratnam, et al., eds., Elsevier Applied Science, London, pp. 315–327.

Wedig, W.V., 1989, "Analysis and Simulation of Nonlinear Stochastic Systems," *Nonlinear Dynamics in Engineering Systems,* W. Schiehlen, ed., Springer-Verlag, Berlin, pp. 337–344.

Wedig, W.V., 1990, "Dynamic Stability of Beams Under Axial Forces: Lyapunov Exponents for General Fluctuating Loads," *Structural Dynamics,* W.B. Kratzig, et al., eds., Balkema, Rotterdam, pp. 141–148.

Zhang, Z.Y., and Kozin, F., 1990, "On Almost Sure Sample Stability of Nonlinear Stochastic Dynamic Systems," *Proceedings of the IEEE International Conference on System Engineering,* Pittsburgh, PA, Aug. 9–11.

Zhu, W.Q., Huang, Z.L., and Yang, Y.Q., 1997, "Stochastic Averaging of Quasi-Integrable-Hamiltonian Systems," ASME JOURNAL OF APPLIED MECHANICS, Vol. 64, pp. 975–984.

Zhu, W.Q., and Yang, Y.Q., 1997, "Stochastic Averaging of Quasi-Nonintegrable-Hamiltonian Systems," ASME JOURNAL OF APPLIED MECHANICS, Vol. 64, pp. 157–164.

Downloaded 04 May 2010 to 171.66.16.27. Redistribution subject to ASME license or copyright; see http://www.asme.org/terms/Terms_Use.cfm

Analytical Vibration of Spinning, Elastic Disk-Spindle Systems

R. G. Parker
Department of Mechanical Engineering,
Ohio State University,
206 W. 18th Ave.,
Columbus, OH 43210-1107
parker.242@osu.edu
Mem. ASME

This work develops the dynamic equations of motion for a spinning disk-spindle system and casts them in a structured formulation that reveals the classical gyroscopic nature of the system. The disk and spindle are modeled as elastic continua coupled by a rigid, three-dimensional clamp. The inherent structure of the system is clarified with the definition of extended operators that collect the component disk, spindle, and clamp equations of motion into a compact analytical form. The extended operators are easily identified as the inertia, elastic bending stiffness, gyroscopic, and rotational stiffness operators, and they possess the symmetry and definiteness characteristics that define gyroscopic continua. Consequently, well-known analytical methods for gyroscopic systems are readily applied to disk-spindle systems. Qualitative eigensolution properties, an exact, closed-form response analysis, and the Galerkin discretization that follow naturally from the structured formulation are discussed. A free and forced vibration example is presented.

Introduction

High-speed applications such as turbomachinery, disk drives, rotor dynamics, circular saws, and geared transmissions have motivated substantial research on the dynamics of spinning systems. Research on these and similar applications has generated major bodies of literature on the dynamics of spinning shafts and spinning disks. Developments in these two areas have occurred largely independently of each other despite the common features deriving from the rotational effects. Virtually all of the spinning shaft vibration analyses assume that attachments to the spinning shaft are rigid. A similar majority of the spinning disk research neglects the dynamics of the supporting structure. Only limited research addresses the current spinning system problem wherein an elastic disk is mounted on an elastic spindle via a rigid clamp (Fig. 1). The continuing trends toward higher operating speeds and lighter, more flexible devices necessitate such a model for high-precision machinery.

This work examines the coupled disk-spindle system of Fig. 1, including certain asymmetries of practical importance. The complexity of the coupled governing equations makes closed-form solution difficult, and the set of coupled disk, spindle, and clamp component equations of motion are not amenable to approximate methods. To address this problem, the equations are recast using a novel formulation in terms of extended operators acting on an extended variable. The classical gyroscopic continuum structure of the disk-spindle system is clear in the extended operator formulation. In particular, one obtains a symmetric and positive-definite inertia operator, symmetric stiffness operator, and skew-symmetric gyroscopic operator. Cast in this form, known analytical and approximate tools for gyroscopic system stability and forced response analyses can be applied to disk-spindle systems. This is a powerful result because these techniques are not readily applicable to the component equations. This work takes advantage of the extended operator formulation to 1) discuss qualitative properties of the eigensolutions, 2) obtain the closed-form forced response in terms of a generalization of the gyroscopic system Green's function to systems described by extended operators, and 3) develop a Galerkin discretization that highlights one example of the analytical methods that are straightforward with the extended operator formulation, but not feasible without it.

Previous research on coupled disk-spindle systems has focused on free vibration and stability. Chivens and Nelson (1975) examined the natural frequencies and critical speeds of an axisymmetric, rotating disk-spindle system with zero clamp thickness. Wilgen and Schlack (1979) applied Lyapunov stability theory to the same system to further investigate the critical speeds. Flowers and Wu (1992, 1996) examine coupled disk-spindle dynamics for turbomachinery applications. The importance of disk-spindle coupling in rotor-dynamics is discussed by Klompas (1978), Dopkin and Shoup (1974), and Vance (1988). The current work extends the stationary system analysis of Parker and Mote (1996), where the extended operator formulation was used to obtain closed-form eigensolutions and to investigate how disk boundary condition asymmetry couples disk and spindle dynamics. They also discuss qualitative characteristics of the stationary system eigensolutions. Shen and Ku (1997) recently examined the related problem of vibration of multiple elastic disks mounted on a rigid spindle supported by flexible bearings.

Model and Equations of Motion

Figure 1 depicts the disk-spindle system wherein the disk is a uniform Kirchhoff plate augmented by membrane stress contributions, the spindle is a uniform Euler-Bernoulli beam, and the coupling clamp is a three-dimensional rigid body. The system rotates with steady speed $\bar{\Omega}$ about the fixed axis passing through the spindle end supports. The following effects are incorporated: 1) disk and clamp center of mass offsets from the rotation axis, 2) nondiagonal clamp and disk inertia tensors, and 3) differing spindle stiffnesses in the two bending planes.

The following orthonormal bases describe the kinematics: $\{\mathbf{i}, \mathbf{j}, \mathbf{k}\}$ is an inertial basis with origin at $Z = 0$, $\{\mathbf{E}_i\}$ is obtained by rotation of $\{\mathbf{i}, \mathbf{j}, \mathbf{k}\}$ an angle $\bar{\Omega}T$ about $\mathbf{k} = \mathbf{E}_3$, and $\{\mathbf{e}_i\}$ is a corotational clamp basis with origin at C, the intersection of the planar disk with the undeformed neutral axis of the spindle. Rotation of $\{\mathbf{E}_i\}$ to $\{\mathbf{e}_i\}$ in the deflected state requires the Euler rotations φ about $\mathbf{E}_2$ and $-\psi$ about the intermediate basis vector $\tilde{\mathbf{e}}_1$. These rotations are small and subsequent results reflect linearization for $\varphi, \psi \ll 1$. The following invertible transformation relates the bases:

Contributed by the Applied Mechanics Division of THE AMERICAN SOCIETY OF MECHANICAL ENGINEERS for publication in the ASME JOURNAL OF APPLIED MECHANICS.

Discussion on the paper should be addressed to the Technical Editor, Professor Lewis T. Wheeler, Department of Mechanical Engineering, University of Houston, Houston, TX 77204-4792, and will be accepted until four months after final publication of the paper itself in the ASME JOURNAL OF APPLIED MECHANICS.

Manuscript received by the ASME Applied Mechanics Division, Sept. 3, 1997; final revision, Aug. 17, 1998. Associate Technical Editor: V. K. Kinra.

 Copyright © 1999 by ASME

Downloaded 04 May 2010 to 171.66.16.27. Redistribution subject to ASME license or copyright; see http://www.asme.org/terms/Terms_Use.cfm

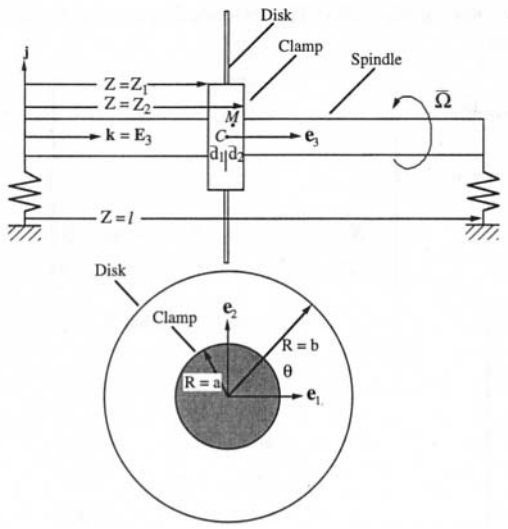

Fig. 1 Rotating disk-spindle system

$$\mathbf{E}_1 = \mathbf{e}_1 + \psi\mathbf{e}_3 \quad \mathbf{E}_2 = \mathbf{e}_2 + \psi\mathbf{e}_3 \quad \mathbf{E}_3 = -\varphi\mathbf{e}_1 - \psi\mathbf{e}_2 + \mathbf{e}_3 \quad (1)$$

The angular velocities ω_s of $\{\mathbf{E}_i\}$ and ω_c of $\{\mathbf{e}_i\}$ are

$$\omega_s = \bar{\Omega}\mathbf{E}_3 \quad \omega_c = (-\dot{\psi} - \bar{\Omega}\varphi)\mathbf{e}_1 + (\dot{\varphi} - \bar{\Omega}\psi)\mathbf{e}_2 + \bar{\Omega}\mathbf{e}_3 \quad (2)$$

The position vector of a material point on the spindle is

$$\mathbf{p}_s = U(Z, T)\mathbf{E}_1 + V(Z, T)\mathbf{E}_2 + Z\mathbf{E}_3 \quad (3)$$

where Z is the axial coordinate and U, V are elastic spindle deflections in rotating coordinates. The clamp orientation is fixed by the three Euler angles $\bar{\Omega}T$, φ, and $-\psi$. Geometric compatibility at the spindle-clamp interfaces imposes the following conditions on the clamp Euler angles:

$$\varphi(T) \approx U_Z(Z_1, T) = U_Z(Z_2, T)$$
$$\psi(T) \approx V_Z(Z_1, T) = V_Z(Z_2, T) \quad (4)$$

where the subscript denotes partial differentiation. Euler-Bernoulli modeling of the spindle restricts φ and ψ to be small as noted earlier. Rigidity of the clamp constrains the motion of point C, such that

$$\mathbf{p}_c = \mathbf{p}_s(Z_1, T) + \bar{d}_1\mathbf{e}_3$$
$$= U^c(T)\mathbf{E}_1 + V^c(T)\mathbf{E}_2 + (Z_1 + \bar{d}_1)\mathbf{E}_3 \quad (5)$$
$$U^c(T) = U(Z_1, T) + \bar{d}_1\varphi(T)$$
$$V^c(T) = V(Z_1, T) + \bar{d}_1\psi(T) \quad (6)$$

The position of the combined disk-clamp center of mass M is $\mathbf{p}_m = \mathbf{p}_c + \bar{\delta}$ where $\bar{\delta} = \bar{\delta}_1\mathbf{e}_1 + \bar{\delta}_2\mathbf{e}_2 + \bar{\delta}_3\mathbf{e}_3$ represents a center of mass offset and the $\bar{\delta}_i$ are constants. The position of a material point on the disk is

$$\mathbf{p}_d = \mathbf{p}_c + \mathbf{p}_{d/c}$$
$$= \mathbf{p}_c + R\cos\theta\mathbf{e}_1 + R\sin\theta\mathbf{e}_2 + W(R, \theta, T)\mathbf{e}_3 \quad (7)$$

where R and θ are polar coordinates that rotate with the disk, and W is the elastic disk deflection. With the angular velocity vectors (2), material point accelerations necessary for Newtonian mechanics derivation of the equations of motion are readily calculated from (3), $\mathbf{p}_m = \mathbf{p}_c + \bar{\delta}$, (5), and (7). The foregoing kinematics are defined in terms of W, U, V, U^c, V^c, φ, and ψ. Although it is convenient for subsequent analysis to retain all of these variables, the system deflection, including the clamp motion, is specified completely by U, V, W, (4), and (6).

Elastic restoring forces of the disk and spindle yield the Kirchhoff, membrane stress, and Euler-Bernoulli stiffness operators. The dynamic equations are

$$D\nabla^4 W - h\bar{\Omega}^2\bar{\chi}(W) + \rho_d\ddot{\mathbf{p}}_d\cdot\mathbf{e}_3 = \bar{q}_d(R, \theta, T)$$
$$\bar{\chi}(W) = \frac{1}{R}(R\bar{\sigma}^R W_R + \bar{\sigma}^{R\theta}W_\theta)_R + \frac{1}{R}\left(\frac{1}{R}\bar{\sigma}^\theta W_\theta + \bar{\sigma}^{R\theta}W_R\right)_\theta \quad (8)$$

$$EIU_{ZZZZ} + \rho_s\ddot{\mathbf{p}}_s\cdot\mathbf{E}_1 = \bar{q}_U(Z, T)$$
$$\xi EIV_{ZZZZ} + \rho_s\ddot{\mathbf{p}}_s\cdot\mathbf{E}_2 = \bar{q}_V(Z, T) \quad (9)$$

where $\rho_{d,s}$ are the disk areal density and spindle linear density, D is the flexural rigidity, EI and ξEI are spindle bending stiffnesses, $\bar{q}_d$ is the transverse disk loading in rotating coordinates, $\bar{q}_U$ and $\bar{q}_V$ are spindle forces in rotating coordinates, h is the disk thickness, and $\bar{\sigma}^{ij} = \hat{\sigma}^{ij}/\bar{\Omega}^2$ represent the rotational membrane stresses $\hat{\sigma}^{ij}$. The clamp motion is governed by the linear and angular momentum balances

$$\bar{\mathbf{F}} = m\ddot{\mathbf{p}}_m = m(\ddot{\mathbf{p}}_c + \ddot{\bar{\delta}})$$
$$\bar{\mathbf{M}}_c = \dot{\mathbf{H}}_c + m\bar{\delta}\times\ddot{\mathbf{p}}_c$$
$$= \bar{\mathbf{J}}_c\omega_c + \int_{\bar{P}}\rho_d\mathbf{p}_{d/c}\times\dot{\mathbf{p}}_{d/c}dA + m\bar{\delta}\times\ddot{\mathbf{p}}_c \quad (10)$$

where $m = m_c + m_d$ is the combined clamp-disk mass, $\mathbf{H}_c$ is the total angular momentum of the clamp and disk with respect to C, $\bar{\mathbf{J}}_c = [\bar{J}^c_{ij}]$ is the clamp inertia tensor with respect to C, $\bar{\mathbf{F}}$ is the resultant clamp force, and $\bar{\mathbf{M}}_c$ is the resultant clamp moment with respect to C. Admitting the applied clamp force $\bar{F}_1\mathbf{e}_1 + \bar{F}_2\mathbf{e}_2$ and moment $\bar{M}_1\mathbf{e}_1 + \bar{M}_2\mathbf{e}_2$, these resultants are

$$\bar{\mathbf{F}} = -EIU_{ZZZ}|_{Z_1}^{Z_2}\mathbf{e}_1 - \xi EIV_{ZZZ}|_{Z_1}^{Z_2}\mathbf{e}_2 + \bar{F}_1\mathbf{e}_1 + \bar{F}_2\mathbf{e}_2 \quad (11)$$

$$\bar{\mathbf{M}}_c = -\xi EIV_{ZZ}|_{Z_1}^{Z_2}\mathbf{e}_1 + EIU_{ZZ}|_{Z_1}^{Z_2}\mathbf{e}_2 + \bar{d}_2\mathbf{e}_3$$
$$\times(-EIU_{ZZZ}|_{Z_2}\mathbf{e}_1 - \xi EIV_{ZZZ}|_{Z_2}\mathbf{e}_2) - \bar{d}_1\mathbf{e}_3$$
$$\times(EIU_{ZZZ}|_{Z_1}\mathbf{e}_1 + \xi EIV_{ZZZ}|_{Z_1}\mathbf{e}_2) + \bar{M}_1\mathbf{e}_1 + \bar{M}_2\mathbf{e}_2 \quad (12)$$

The disk inertia components $\bar{J}^d_{12} = \int_{\bar{P}}\rho_d R^2\cos\theta\sin\theta dA$, $\bar{J}^d_{11} = \int_{\bar{P}}\rho_d(R\sin\theta)^2 dA$, and $\bar{J}^d_{22} = \int_{\bar{P}}\rho_d(R\cos\theta)^2 dA$ are used subsequently. Defining the dimensionless quantities

$$u, v, z = \frac{U, V, Z}{l} \quad w, r = \frac{W, R}{b}$$

$$t = \sqrt{\frac{D}{\rho_d b^4}}T \quad \Omega = \sqrt{\frac{\rho_d b^4}{D}}\bar{\Omega} \quad \gamma = \frac{a}{b}$$

$$\sigma^{ij} = \frac{\bar{\sigma}^{ij}}{(\rho_d b^2)/h} \quad q_d = \frac{\bar{q}_d}{D/b^3} \quad q_{u,v} = \frac{\bar{q}_{U,V}}{D/l^2}$$

$$F_i = \frac{\bar{F}_i}{D/l} \quad M_i = \frac{\bar{M}_i}{D} \quad K = \frac{EI/l}{D}$$

$$\rho = \frac{\rho_s l^3}{\rho_d b^4} \quad \alpha = \frac{ml^2}{\rho_d b^4} \quad J^{c,d}_{ij} = \frac{\bar{J}^{c,d}_{ij}}{\rho_d b^4} \quad \delta_i = \frac{\bar{\delta}_i}{l} \quad d_i = \frac{\bar{d}_i}{l} \quad (13)$$

where l is the spindle length and a, b are the disk inner and outer radii, (8) – (12) and the compatibility requirements (4) and (6) yield the complete set of linearized governing equations

Downloaded 04 May 2010 to 171.66.16.27. Redistribution subject to ASME license or copyright; see http://www.asme.org/terms/Terms_Use.cfm

$$\nabla^4 w - \Omega^2\chi(w) + w_{tt} - r\cos\theta(\ddot{\varphi} + \Omega^2\varphi) - r\sin\theta(\ddot{\psi} + \Omega^2\psi) = q_d(r, \theta, t)$$

$$\chi(w) = \frac{1}{r}(r\sigma^r w_r + \sigma^{r\theta} w_\theta)_r + \frac{1}{r}\left(\frac{1}{r}\sigma^\theta w_\theta + \sigma^{r\theta} w_r\right)_\theta \quad (14)$$

$$Ku_{zzzz} + \rho[u_{tt} - 2\Omega v_t - \Omega^2 u] = q_u(z, t)$$

$$\xi K v_{zzzz} + \rho[v_{tt} + 2\Omega u_t - \Omega^2 v] = q_v(z, t) \quad (15)$$

$$Ku_{zzz}|_{z_1}^{z_2} + \alpha[\ddot{u}^c - 2\Omega\dot{v}^c - \Omega^2 u^c + \delta_3(\ddot{\varphi} - 2\Omega\dot{\psi} - \Omega^2\varphi)] = F_1(t) + \alpha\delta_1\Omega^2$$

$$\xi K v_{zzz}|_{z_1}^{z_2} + \alpha[\ddot{v}^c + 2\Omega\dot{u}^c - \Omega^2 v^c + \delta_3(\ddot{\psi} + 2\Omega\dot{\varphi} - \Omega^2\psi)] = F_2(t) + \alpha\delta_2\Omega^2 \quad (16)$$

$$-K(u_{zz}|_{z_1}^{z_2} - d_2 u_{zzz}|_{z_2} - d_1 u_{zzz}|_{z_1}) + (J_{22}^c + J_{22}^d)\ddot{\varphi} - (J_{12}^c + J_{12}^d)\ddot{\psi} - (J_{11}^c + J_{22}^c - J_{33}^c)\Omega\dot{\psi} - (J_{11}^c - J_{33}^c - J_{22}^d)\Omega^2\varphi - (J_{12}^c + J_{12}^d)\Omega^2\psi + \alpha\delta_3(\ddot{u}^c - 2\Omega\dot{v}^c - \Omega^2 u^c) - \int_P r\cos\theta(w_{tt} + \Omega^2 w)dA = M_2(t) - \Omega^2 J_{13}^c \quad (17)$$

$$-\xi K(v_{zz}|_{z_1}^{z_2} - d_2 v_{zzz}|_{z_2} - d_1 v_{zzz}|_{z_1}) + (J_{11}^c + J_{11}^d)\ddot{\psi} - (J_{12}^c + J_{12}^d)\ddot{\varphi} + (J_{11}^c + J_{22}^c - J_{33}^c)\Omega\dot{\varphi} - (J_{22}^c - J_{33}^c - J_{11}^d)\Omega^2\psi - (J_{12}^c + J_{12}^d)\Omega^2\varphi + \alpha\delta_3(\ddot{v}^c + 2\Omega\dot{u}^c - \Omega^2 v^c) - \int_P r\sin\theta(w_{tt} + \Omega^2 w)dA = -M_1(t) - \Omega^2 J_{23}^c \quad (18)$$

$$\varphi(t) = u_z(z_1, t) = u_z(z_2, t) \quad \psi(t) = v_z(z_1, t) = v_z(z_2, t)$$

$$u^c(t) = u(z_1, t) + d_1\varphi(t) \quad v^c(t) = v(z_1, t) + d_1\psi(t) \quad (19)$$

$$B_i w = 0 \quad r = \gamma, 1$$

$$C_i(u, v) = 0 \quad z = 0, 1 \quad (20)$$

B_i and C_i in (20) are linear boundary operators representing disk and spindle support conditions. The rotational stresses in (14) are (Eversman, 1968)

$$\sigma^r = \frac{\mu_2}{r^2}(1 - r^2)\left(r^2 + \frac{\mu_1}{\mu_2}\right)$$

$$\sigma^\theta = \frac{\mu_2}{r^2}\left[\left(1 - \frac{\mu_1}{\mu_2}\right)r^2 - \frac{\mu_1}{\mu_2} - \frac{1 + 3\nu}{3 + \nu}r^4\right] \quad \sigma^{r\theta} = 0$$

$$\mu_1 = \frac{1 - \nu}{8}\left[\frac{(3 + \nu)\gamma^2 - (1 + \nu)\gamma^4}{(1 + \nu)\gamma^2 + (1 - \nu)\gamma^4}\right] \quad \mu_2 = \frac{3 + \nu}{8} \quad (21)$$

Extended Operator Formulation. The gyroscopic system structure of the disk-spindle equations is apparent with the use of extended operators that are shown subsequently to have the necessary symmetry and definiteness properties. The system deformation is represented by the extended variable (Parker and Mote, 1996)

$$\mathbf{h}(r, \theta, z, t) = [w(r, \theta, t), u(z, t), v(z, t), u^c(t), v^c(t), \phi(t), \psi(t)]^T \quad (22)$$

$\mathbf{h}$ is an element of the function space H consisting of all vectors with components $h_1 \in L_2(P)$, $h_{2,3} \in L_2(S)$, and complex numbers $h_{4,5,6,7}$. Elements of H are further restricted such that the components satisfy (19). The extended operators defined on $\mathbf{h} \in H$ are

$$\mathbf{Lh} = \begin{Bmatrix} \nabla^4 w \\ Ku_{zzzz} \\ \xi K v_{zzzz} \\ Ku_{zzz}|_{z_1}^{z_2} \\ \xi K v_{zzz}|_{z_1}^{z_2} \\ -K(u_{zz}|_{z_1}^{z_2} - d_2 u_{zzz}|_{z_2} - d_1 u_{zzz}|_{z_1}) \\ -\xi K(v_{zz}|_{z_1}^{z_2} - d_2 v_{zzz}|_{z_2} - d_1 v_{zzz}|_{z_1}) \end{Bmatrix}$$

$$\mathbf{Mh} = \begin{Bmatrix} w - r\varphi\cos\theta - r\psi\sin\theta \\ \rho u \\ \rho v \\ \alpha(u^c + \delta_3\varphi) \\ \alpha(v^c + \delta_3\psi) \\ (J_{22}^c + J_{22}^d)\varphi - (J_{12}^c + J_{12}^d)\psi + \alpha\delta_3 u^c - \int_P r\cos\theta w dA \\ (J_{11}^c + J_{11}^d)\psi - (J_{12}^c + J_{12}^d)\varphi + \alpha\delta_3 v^c - \int_P r\sin\theta w dA \end{Bmatrix} \quad (23)$$

$$\mathbf{Gh} = \begin{Bmatrix} 0 \\ -2\rho v \\ 2\rho u \\ -2\alpha(v^c + \delta_3\psi) \\ 2\alpha(u^c + \delta_3\varphi) \\ -(J_{11}^c + J_{22}^c - J_{33}^c)\psi - 2\alpha\delta_3 v^c \\ (J_{11}^c + J_{22}^c - J_{33}^c)\varphi + 2\alpha\delta_3 u^c \end{Bmatrix}$$

$$\tilde{\mathbf{L}}\mathbf{h} = \begin{Bmatrix} \chi(w) + r\varphi\cos\theta + r\psi\sin\theta \\ \rho u \\ \rho v \\ \alpha(u^c + \delta_3\varphi) \\ \alpha(v^c + \delta_3\psi) \\ (J_{11}^c - J_{33}^c - J_{22}^d)\varphi + (J_{12}^c + J_{12}^d)\psi + \alpha\delta_3 u^c + \int_P r\cos\theta w dA \\ (J_{22}^c - J_{33}^c - J_{11}^d)\psi + (J_{12}^c + J_{12}^d)\varphi + \alpha\delta_3 v^c + \int_P r\sin\theta w dA \end{Bmatrix} \quad (24)$$

The extended operators $\mathbf{M}$ and $\mathbf{L}$ represent inertia and elastic stiffness contributions that are independent of rotation. Rotation introduces the gyroscopic and rotational stiffness operators $\mathbf{G}$ and $\tilde{\mathbf{L}}$. The extended excitation vector is

$$\mathbf{f}(r, \theta, z, t) = [q_d, q_u, q_v, F_1 + \alpha\Omega^2\delta_1, F_2 + \alpha\Omega^2\delta_2, M_2 - \Omega^2 J_{13}^c, -M_1 - \Omega^2 J_{23}^c]^T \quad (25)$$

The component Eqs. (14)–(18) and associated boundary conditions are stated collectively as

$$\mathbf{Mh}_{tt} + \Omega\mathbf{Gh}_t + (\mathbf{L} - \Omega^2\tilde{\mathbf{L}})\mathbf{h} = \mathbf{f}$$

$$\mathbf{h}|_{t=0} = \mathbf{h}_o; \ \mathbf{h}_t|_{t=0} = \dot{\mathbf{h}}_o \quad (26)$$

$$B_i w = 0 \quad r = \gamma, 1$$

$$C_i(u, v) = 0 \quad z = 0, 1 \quad (27)$$

The inner product defined on H is

$$(\mathbf{x}, \mathbf{y}) = (x_1, y_1)_P + (x_2, y_2)_S + (x_3, y_3)_S + x_4 y_4^* + x_5 y_5^* + x_6 y_6^* + x_7 y_7^* \quad (28)$$

Downloaded 04 May 2010 to 171.66.16.27. Redistribution subject to ASME license or copyright; see http://www.asme.org/terms/Terms_Use.cfm

where $(x_1, y_1)_P = \int_P x_1 y_1^* dA$, $(x_2, y_2)_S = \int_S x_2 y_2^* dz$, and the superscript * denotes complex conjugation. With this inner product, H is a Hilbert space and all associated mathematical results apply in the extended operator context. This inner product yields the symmetry relationships

$$(\mathbf{L}\mathbf{h}_1, \mathbf{h}_2) = (\mathbf{h}_1, \mathbf{L}\mathbf{h}_2) \quad (\mathbf{M}\mathbf{h}_1, \mathbf{h}_2) = (\mathbf{h}_1, \mathbf{M}\mathbf{h}_2)$$

$$(\mathbf{G}\mathbf{h}_1, \mathbf{h}_2) = -(\mathbf{h}_1, \mathbf{G}\mathbf{h}_2) \quad (\tilde{\mathbf{L}}\mathbf{h}_1, \mathbf{h}_2) = (\mathbf{h}_1, \tilde{\mathbf{L}}\mathbf{h}_2) \quad (29)$$

Operators $\mathbf{L}$, $\mathbf{M}$, and $\tilde{\mathbf{L}}$ are symmetric, and $\mathbf{G}$ is skew-symmetric. Furthermore, $\mathbf{M}$ is positive-definite, and $\mathbf{L}$ is positive-definite provided (27) precludes rigid body motion of the disk and spindle.

The representation (26) and the associated symmetry and definiteness properties of the extended operators with respect to (28) provide essential structure to the problem. With the symmetries (29), (26) is the canonical form of a continuous gyroscopic system. This structure, which is not evident from the component Eqs. (14)–(20), is the keystone for subsequent analysis. All analytical and approximate methods for stability and response analyses of gyroscopic systems are readily applied with this formulation. The following sections exploit this structure in discussing spinning disk-spindle system eigensolutions, closed-form response analysis, and discretization in the context of gyroscopic continua.

Coupled Disk-Spindle Eigensolutions. The coupled disk-spindle eigenvalue problem results from the separable solution $\mathbf{h}(r, \theta, z, t) = \Psi(r, \theta, z)e^{\lambda t}$

$$\lambda^2\mathbf{M}\Psi + \lambda\Omega\mathbf{G}\Psi + (\mathbf{L} - \Omega^2\tilde{\mathbf{L}})\Psi = \mathbf{0} \quad (30)$$

where components of $\Psi \in H$ satisfy (27). The component equations of (30), which are used for actual calculation of the eigensolutions, are exactly those that would result from use of $w(r, \theta, t) = \Psi_1(r, \theta)e^{\lambda t}$, $u(z, t) = \Psi_2(z)e^{\lambda t}$, and $v(z, t) = \Psi_3(z)e^{\lambda t}$ in (14)–(19). The gyroscopic system structure ensures that the subcritical speed eigenvalues consist of purely imaginary complex conjugate pairs $\lambda_n = \pm i\omega_n$, and the corresponding eigenfunctions are complex conjugates. The eigenfunctions also satisfy orthogonality conditions with respect to (28), as is critical for the subsequent response analysis.

For zero rotation speed, the eigensolutions are governed by the symmetric eigenvalue problem

$$\lambda_o^2\mathbf{M}\Psi_o + \mathbf{L}\Psi_o = 0 \quad (31)$$

Parker and Mote (1996) derived these eigensolutions in closed-form and discussed their qualitative features. The disk-spindle system is subject to critical speed instabilities characterized by vanishing eigenvalues λ. The critical speeds Ω_{cr} and associated eigenfunctions are determined from (30) with $\lambda = 0$

$$\mathbf{L}\Psi_{cr} - \Omega_{cr}^2\tilde{\mathbf{L}}\Psi_{cr} = \mathbf{0} \quad (32)$$

The approach used by Parker and Mote (1996) to obtain closed-form eigensolutions of (31) is directly applicable to (32). In both (31) and (32), symmetry of the operators ensures orthogonality of the extended eigenfunctions in the usual sense

$$(\mathbf{M}\Psi_o^m, \Psi_o^n) = \delta_{mn} \quad (\mathbf{L}\Psi_o^m, \Psi_o^n) = -(\lambda_o^m)^2\delta_{mn}$$

$$(\tilde{\mathbf{L}}\Psi_{cr}^m, \Psi_{cr}^n) = \delta_{mn} \quad (\mathbf{L}\Psi_{cr}^m, \Psi_{cr}^n) = (\Omega_{cr}^m)^2\delta_{mn} \quad (33)$$

Closed-form solutions of (31) and (32) are readily obtained with computer algebra software.

For axisymmetric, rotating disks, the eigenfunctions can be classified as either *coupled,* where the eigenfunction involves both disk and spindle deformation, or *uncoupled,* where the disk deforms, but the spindle does not. To see this, consider the eigensolutions of a rigidly supported rotating disk defined by (14) with $u = v = 0$, $\nabla^4 w_n - \Omega^2\chi(w_n) + \lambda_n^2 w_n = 0$. For a uniform disk and uniform boundary conditions, the w_n have the form $w_n^c = R_n(r)\cos n\theta$ and $w_n^s = R_n(r)\sin n\theta$ where n is an integer. For $n \neq 1$ the coupling integrals in $\mathbf{M}$ and $\tilde{\mathbf{L}}$ vanish. The physical interpretation is that disk vibration in any mode where $n \neq 1$ transmits no net inertial moment to the clamp at the inner disk boundary. Accordingly

$$\Psi^c = [R_n(r)\cos n\theta, 0, 0, 0, 0, 0, 0]^T,$$

$$\Psi^s = [R_n(r)\sin n\theta, 0, 0, 0, 0, 0, 0]^T \quad n \neq 1 \quad (34)$$

are eigenfunctions of (30) with the associated eigenvalue being the rigidly supported disk eigenvalue λ_n. Thus, eigenfunctions having other than one nodal diameter disk deflection do not couple with the spindle. For $n = 1$, the coupling integrals do not vanish and the one nodal diameter disk eigenfunctions couple with the spindle. These conclusions are consistent with Chivens and Nelson (1975). In the current formulation, however, one can state the more general result that these coupling conclusions are independent of all asymmetry in the spindle and clamp; they depend only on axisymmetry of the disk. While the coupled eigenfunctions are complex for $\Omega \neq 0$, the uncoupled eigenfunctions are real for all speeds.

Classical Response Analysis. The extended operator formulation permits use of classical techniques for response analyses. Gyroscopic system modal analysis yields the closed-form response and the extended operator analog of the standard Green's function. The governing Eq. (26) is cast in the state space form (Meirovitch, 1975; D'Eleuterio and Hughes, 1984; Wickert and Mote, 1990)

$$\mathbf{A}\mathbf{s}_t + \mathbf{B}\mathbf{s} = \mathbf{F}$$

$$\mathbf{s} = \begin{Bmatrix} \mathbf{h}_t \\ \mathbf{h} \end{Bmatrix} \quad \mathbf{A} = \begin{bmatrix} \mathbf{M} & \mathbf{0} \\ \mathbf{0} & \mathbf{L} - \Omega^2\tilde{\mathbf{L}} \end{bmatrix}$$

$$\mathbf{B} = \begin{bmatrix} \Omega\mathbf{G} & \mathbf{L} - \Omega^2\tilde{\mathbf{L}} \\ -(\mathbf{L} - \Omega^2\tilde{\mathbf{L}}) & 0 \end{bmatrix}$$

$$\mathbf{F} = \begin{Bmatrix} \mathbf{f} \\ 0 \end{Bmatrix} \quad \mathbf{s}_o = \begin{Bmatrix} \mathbf{h}_t \\ \mathbf{h} \end{Bmatrix}_{t=0} \quad (35)$$

The inner product on elements $\mathbf{s}$, $\mathbf{t}$ of the state space is $\langle \mathbf{s}, \mathbf{t} \rangle = (\mathbf{s}_1, \mathbf{t}_1) + (\mathbf{s}_2, \mathbf{t}_2)$, where $\mathbf{s}_{1,2}$ and $\mathbf{t}_{1,2}$ are elements of H. This inner product renders $\mathbf{A}$ symmetric and $\mathbf{B}$ skew-symmetric. The associated eigenvalue problem is $\lambda\mathbf{A}\Phi + \mathbf{B}\Phi = \mathbf{0}$. Expansion of this eigenvalue problem into its two component equations reveals that the complex state eigenfunctions Φ_n are constructed from the Ψ_n of (30) according to

$$\Phi_n = \begin{Bmatrix} \lambda_n\Psi_n \\ \Psi_n \end{Bmatrix} \quad (36)$$

Symmetry properties of $\mathbf{A}$ and $\mathbf{B}$ ensure the eigenfunction orthogonality relations $\langle \Phi_m, \mathbf{A}\Phi_n \rangle = \delta_{mn}$ and $\langle \Phi_m, \mathbf{B}\Phi_n \rangle = \lambda_n\delta_{mn}$; these relations can be reduced to equivalent ones in terms of the eigenfunctions Ψ_m of (30) and the operators $\mathbf{M}$, $\mathbf{G}$, $\mathbf{L}$, $\tilde{\mathbf{L}}$ with use of (35) and (36). The response is represented by the eigenfunction expansion

$$s(D, t) = \sum_{k=\pm 1}^{\pm\infty} \eta_k(t)\Phi_k(D) \quad (37)$$

where $\eta_{-k} = \eta_k^*$, $\Phi_{-k} = \Phi_k^*$ and $D = \{r, \theta, z\}$ is shorthand for the combined domain of the disk and spindle. Substitution into (35) and use of the orthogonality relations yield

$$\eta_k(t) = \eta_k(0)e^{\lambda_k t} + \int_0^t e^{\lambda_k(t-\tau)}F_k(\tau)d\tau$$

$$\eta_k(0) = \langle \Phi_k^*, \mathbf{A}\mathbf{s}_o \rangle$$

$$= [\lambda_k^*(\Psi_k^*, \mathbf{M}\mathbf{h}_t|_{t=0}) + (\Psi_k^*, (\mathbf{L} - \Omega^2\tilde{\mathbf{L}})\mathbf{h}|_{t=0})]$$

$$F_k(t) = \langle \Phi_k^*, \mathbf{F} \rangle = \lambda_k^*(\Psi_k^*, \mathbf{f}) \quad (38)$$

Downloaded 04 May 2010 to 171.66.16.27. Redistribution subject to ASME license or copyright; see http://www.asme.org/terms/Terms_Use.cfm

From the lower element of the state vector $\mathbf{s}$ of (37) (i.e., the element corresponding to the displacement), the response to arbitrary excitation is

$$\mathbf{h}(D, t) = \sum_{k=\pm 1}^{\pm\infty} e^{\lambda_k t}\langle \Phi_k^*, \mathbf{A}\mathbf{s}_o\rangle \Psi_k(D) + \sum_{k=\pm 1}^{\pm\infty} \int_0^t e^{\lambda_k (t-\tau)}\langle \Phi_k^*(D), \mathbf{F}(D, \tau)\rangle \Psi_k(D) d\tau = \mathbf{K}(D, t)(\mathbf{A}\mathbf{s}_o) + \int_0^t \mathbf{K}(D, t-\tau)\mathbf{F}(D, \tau) d\tau \tag{39}$$

The second form of (39) is cast in terms of the operator

$$\mathbf{K}(D, t)\mathbf{b} = \sum_{k=\pm 1}^{\pm\infty} e^{\lambda_k t}\langle \Phi_k^*, \mathbf{b}\rangle \Psi_k(D)$$

which maps elements from the state space to the configuration space. This response representation is a generalization of the standard Green's function to include systems described by extended operators. Because the response for such systems is a vector rather than a scalar, the *Green's function operator* $\mathbf{K}$ replaces the usual form of a *scalar Green's function* kernel in a standard integral expression. Using $\lambda_k = i\omega_k$ and $\Psi_k = \Psi_k^r + i\Psi_k^i$, the response for zero initial conditions is expressed entirely in terms of real quantities as

$$\mathbf{h}(D, t) = \sum_{k=1}^{\infty} \int_0^t 2\omega_k \{ [(\Psi_k^r, \mathbf{f})\Psi_k^r + (\Psi_k^i, \mathbf{f})\Psi_k^i] \sin \omega_k (t-\tau) + [(\Psi_k^r, \mathbf{f})\Psi_k^i + (\Psi_k^i, \mathbf{f})\Psi_k^r] \cos \omega_k (t-\tau) \} \tag{40}$$

where $\mathbf{f} = \mathbf{f}(D, \tau)$. Response to initial conditions can be expressed similarly. This form is simplest for actual calculations, while the purpose of (39) is to show the Green's function structure.

To better see the underlying structure of (39) and (40), consider excitation with separable spatial and temporal dependence

$$\mathbf{f}(D, t) = [e_w(r, \theta) f_w(t), e_u(z) f_u(t), e_v(z) f_v(t), f_{u^c}(t), f_{v^c}(t), f_\phi(t), f_\psi(t)]^T \tag{41}$$

and zero initial conditions. The response is

$$\mathbf{h}(D, t) = \sum_{k=\pm 1}^{\pm\infty} \begin{bmatrix} w_k & & & & \\ & u_k & & & \\ & & \cdots & & \\ & & & \phi_k & \\ & & & & \psi_k \end{bmatrix} \times \int_0^t \lambda_k^* e^{\lambda_k (t-\tau)} \begin{bmatrix} (\bar{w}_k, e_w)_P & (\bar{u}_k, e_u)_S & \cdots & \bar{\phi}_k & \bar{\psi}_k \\ (\bar{w}_k, e_w)_P & (\bar{u}_k, e_u)_S & \cdots & \bar{\phi}_k & \bar{\psi}_k \\ \cdots & \cdots & \cdots & \cdots & \cdots \\ (\bar{w}_k, e_w)_P & (\bar{u}_k, e_u)_S & \cdots & \bar{\phi}_k & \bar{\psi}_k \\ (\bar{w}_k, e_w)_P & (\bar{u}_k, e_u)_S & \cdots & \bar{\phi}_k & \bar{\psi}_k \end{bmatrix} \times \begin{Bmatrix} f_w(\tau) \\ f_u(\tau) \\ \cdots \\ f_\phi(\tau) \\ f_\psi(\tau) \end{Bmatrix} d\tau \tag{42}$$

To see how the individual factors in (42) generalize familiar analogs in conventional modal analysis, the response of a gyroscopic system governed by a scalar field variable $h(D, t)$ to the excitation $f(D, t) = e(D) f_h(t)$ is

$$h(D, t) = \sum_{k=\pm 1}^{\pm\infty} \psi_k(D) \int_0^t \lambda_k^* e^{\lambda_k (t-\tau)} (\psi_k^*, e) f_h(\tau) d\tau \tag{43}$$

where ψ_k are the complex eigenfunctions. $F_k(t) = (\psi_k^*, e) f_h(\tau)$ in (43) represents the modal force, the convolution integral yields the response of the kth modal coordinate $\eta_k(t)$, and the modal coordinate is weighted by the eigenfunction to yield the contribution of the kth eigenfunction to the physical response. Similar interpretations exist for the analogous factors in (42). The inner product matrix in (42) represents the degree to which the *spatial* distribution of individual disk, spindle, and clamp forces excite a particular eigenfunction. These spatial modal excitation factors are weighted by the appropriate temporal dependence in the matrix multiplication which serves to sum contributions of disk, spindle, and clamp forces to the total modal force. Note that rows of the inner product matrix are identical, so all elements in the column vector of modal forces are identical. For uncoupled eigenfunctions, all columns of the inner product matrix except the first vanish. Thus, if the excitation consists solely of spindle and clamp excitation ($e_w = 0$) (i.e., the excitation is applied at "nodes" of the uncoupled eigenfunctions), the matrix in (42) vanishes for all uncoupled eigenfunctions and they do not participate in the response. Recalling that disk asymmetries, but not spindle or clamp asymmetries, leads to disk-spindle coupling in eigenfunctions having other than one nodal diameter disk deflection (Parker and Mote, 1996), however, unavoidable disk asymmetries occurring in practice may allow spindle and clamp excitations to drive other than the $n = 1$ eigenfunctions. The diagonal matrix in (42) reveals that uncoupled eigenfunctions (only $w_k \neq 0$) excited by disk forces do not affect spindle and clamp response. Physically, this is because the spindle and clamp deflections are "nodes" of the uncoupled eigenfunctions.

The foregoing development is directly applicable to other gyroscopic systems governed by extended operators. Such systems occur whenever distributed systems are coupled to discrete inertial elements. Important practical examples include band/wheel systems such as band saws, belt/pulley drives, and rotating disks or traveling continua coupled to discrete mass-spring systems.

Discretization. Weighted residual discretization techniques are readily applicable to the extended operator formulation. Because such techniques restrict the error residual of a comparison function series expansion to be orthogonal to chosen weighting functions, their application to Eqs. (14)–(20) in the absence of the extended operator structure is hampered by the lack of an appropriate inner product. With the extended operator structure and the inner product (28) defined on the extended space H, however, discretization of (26) proceeds in the usual fashion. The required comparison functions are elements (22) of H with components w, u, v that satisfy (27). The stationary system and critical speed eigenfunctions generate sets of comparison functions. Furthermore, symmetry of the operators in (31) and (32) ensures that these sets are complete, so each constitutes a natural basis for weighted residual expansion. Though it is common to use the stationary system eigenfunctions for gyroscopic system discretization, the critical speed eigensolutions are an equally viable option. With the basis functions Ψ_i and the expansion $\mathbf{h}_m = \sum_{i=1}^{m} c_i(t)\Psi_i(r, \theta, z)$, Galerkin discretization of (26) yields

$$[M_{ij}]\ddot{\mathbf{c}} + \Omega[G_{ij}]\dot{\mathbf{c}} + [L_{ij} - \Omega^2 \tilde{L}_{ij}]\mathbf{c} = \mathbf{g}$$

$$M_{ij} = (\mathbf{M}\Psi_j, \Psi_i) = M_{ji} \quad G_{ij} = (\mathbf{G}\Psi_j, \Psi_i) = -G_{ji}$$

$$L_{ij} = (\mathbf{L}\Psi_j, \Psi_i) = L_{ji} \quad \tilde{L}_{ij} = (\tilde{\mathbf{L}}\Psi_j, \Psi_i) = \tilde{L}_{ji}$$

$$g_i = (\mathbf{f}, \Psi_i) \tag{44}$$

Downloaded 04 May 2010 to 171.66.16.27. Redistribution subject to ASME license or copyright; see http://www.asme.org/terms/Terms_Use.cfm

Table 1 Dimensional parameters used in example problem

Dimensional Parameters	
$a = 0.1016m$	$\rho_s = 9.155kg/m$
$b = 0.2032m$	$m = 7.656kg$
$l = 0.4064m$	$\bar{J}^c_{11} = \bar{J}^c_{22} = 0.0282kg-m^2$
$h = 0.001m$	$\bar{J}^c_{33} = 0.0355kg-m^2$
$D = 18.45N-m$	$\bar{J}^d_{11} = \bar{J}^d_{22} = 0.0282kg-m^2$
$\rho_d = 8.030kg/m^2$	$\bar{J}^d_{33} = 0.0202kg-m^2$
$EI = 21110N-m^2$	$\bar{d}_1 = 0.0132m$
$\nu = 0.28$	$\bar{\delta}_1 = \bar{\delta}_2 = \bar{\delta}_3 = 0$

The operator symmetries (29) ensure the matrix symmetries in (44). All matrices are independent of rotation speed and need only be calculated once, a useful feature for examining a range of operating speeds.

When the zero speed or critical speed eigenfunctions are used in the discretization, the previously discussed division into coupled and uncoupled eigenfunctions yields the structure

$$\mathbf{M}_{cc}\ddot{\mathbf{c}}_c + \Omega\mathbf{G}_{cc}\dot{\mathbf{c}}_c + (\mathbf{L}_{cc} - \Omega^2\tilde{\mathbf{L}}_{cc})\mathbf{c}_c = \mathbf{g}_c \qquad (45)$$

$$(w_i, w_i)_P\ddot{c}_{u_i} + [(\nabla^4 w_i, w_i)_P - \Omega^2(\chi(w_i), w_i)_P]c_{u_i} = (q_d, w_i)_P \qquad (46)$$

where c_{c_i} and c_{u_i} are associated with the coupled and uncoupled eigenfunctions. The coupled and uncoupled eigenfunctions do not interact, and (45) and (46) are analyzed separately. The diagonalized equations (46) associated with the uncoupled eigenfunctions are exactly as for the rigidly supported spinning disk discretized by stationary disk eigenfunctions. For response analyses, the uncoupled eigenfunctions can be omitted from the Galerkin expansion if the disk is not excited directly ($q_d = 0$) or if only spindle response is of interest (uncoupled modes do not contribute).

Table 2 Dimensionless natural frequencies and critical speeds of the coupled eigenfunctions for an axisymmetric disk-spindle system. ω_n is the dimensional natural frequency.

Natural frequency	$\Omega = 0$ (exact)	$\Omega = 0.75(\Omega_{crit})_1 = 6.6323$
$\omega = \omega_n\sqrt{\frac{\rho_d b^4}{D}}$ $(\lambda = i\omega)$	8.4616	2.1302
	8.4616	14.536
	13.355	16.697
	13.355	17.187
	73.532	72.375
	73.532	76.243
	91.136	93.598
	91.136	94.787

Critical speed	$(\Omega_{crit})_1$	$(\Omega_{crit})_2$
rotational stress neglected	8.8304	46.134
rotational stress included	8.8430	163.91

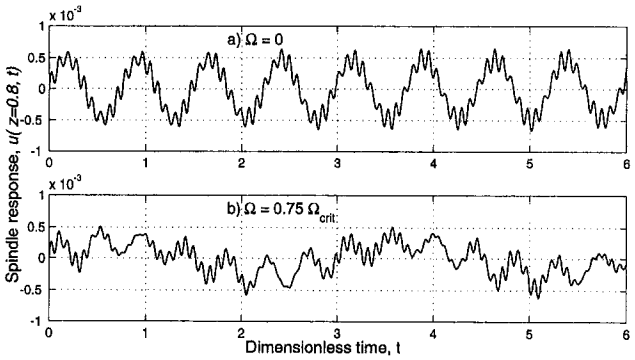

Fig. 2 Impact response $u(0.8, t)$ for a collocated unit impact at $t = 0$. Rotation speeds are indicated, where $\Omega_{crit} = 8.8430$ is the lowest critical speed.

An alternative discretization approach is to expand w, u, and v separately as

$$w = \sum_{k=1}^{n} c_k(t)w_k(r, \theta) \quad u = \sum_{k=1}^{n} d_k(t)u_k(z)$$

$$v = \sum_{k=1}^{n} e_k(t)v_k(z) \qquad (47)$$

Substitution of these series in the system kinetic and potential energy expressions and use of Lagrange's equations would lead to discretized equations similar to (44). The basis functions can be drawn from the known eigenfunctions of the uncoupled disk and spindle systems or from finite element-type functions. Compared to the foregoing Galerkin discretization, this approach suffers the disadvantages that: 1) it requires more terms in the discretization because disk and spindle deflections are expanded in separate series, and 2) the qualitative features of the eigenfunctions and response are less identifiable because the discretization takes place as the first step. With the extended eigenfunction expansion, the familiar interpretation of each generalized coordinate representing a single mode response is retained.

Example: Cantilevered Disk-Spindle System. The utility of the extended operator formulation is demonstrated by a Galerkin solution for the natural frequencies, critical speeds, impact response, and frequency response of an axisymmetric ($\xi = 1$; $J^{c,d}_{ij} = 0, i \neq j$; $\delta_i = 0$) cantilevered disk-spindle system clamped at $z = 0$ with the clamp/disk mounted at the free end $z = 1$. Parameters are given in Table 1. Twelve coupled eigenfunctions associated with the first six degenerate, zero-speed natural frequencies are used as basis functions.

Table 2 compares the exact zero-speed natural frequencies with those at a rotation speed of 75 percent of the first critical speed. All degenerate zero-speed natural frequency pairs split as rotation is introduced, with one increasing and the other decreasing. The fundamental frequency is the most drastically affected by rotation, though gyroscopic splitting is evident for all degenerate zero-speed frequencies. The critical speeds in Table 2, calculated from the eigenvalue problem $[\mathbf{L}_{cc} - \Omega^2_{crit}\tilde{\mathbf{L}}_{cc}]\mathbf{c}_c = \mathbf{0}$, accentuate the importance of rotational stresses: though the first critical speed is unaffected by stress, the second critical speed is dramatically increased when stresses are included. More complete natural frequency, vibration mode, and critical speed results are presented in Parker and Sathe (1999).

As examples of forced response, consider two cases of point loading applied to the spindle: impact excitation and harmonic excitation. Figure 2 shows the spindle response $u\ (z = 0.8,\ t)$ for the collocated, dimensionless unit impact $q_u(z, t) = \delta(z - 0.8)\delta(t)$. The zero-speed response is dominated by the fundamental and third natural frequencies ($\omega_{1,3} \approx 8.5, 73.5$). A richer

Downloaded 04 May 2010 to 171.66.16.27. Redistribution subject to ASME license or copyright; see http://www.asme.org/terms/Terms_Use.cfm

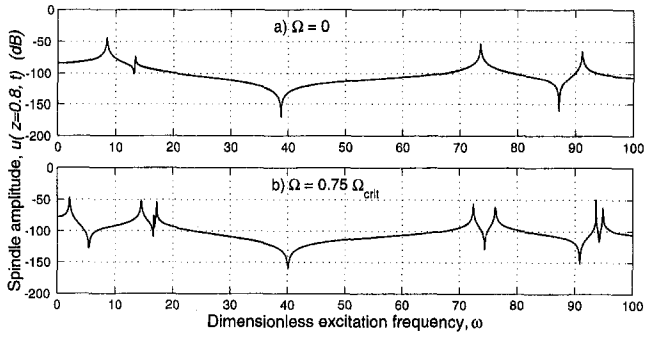

Fig. 3 Frequency response magnitude of the spindle at $u(0.8, t)$ for collocated harmonic excitation. The rotation speeds are indicated, where $\Omega_{crit} = 8.8430$ is the lowest critical speed.

spectrum exists for the rotating system. In particular, the lower fundamental frequency ($\omega_1 \approx 2.1$) is evident. Steady-state response amplitude $u\ (z = 0.8,\ t)$ for the excitation $q_u(z,\ t) = \delta(z - 0.8)\ \sin\ \omega t$ is shown in Fig. 3. Gyroscopic splitting is evident in the additional peaks for $\Omega = 0.75(\Omega_{crit})_1$ in accordance with the natural frequencies of Table 2. Notice that the split frequencies $\omega_{3,4}$ and $\omega_{7,8}$ are each higher than the corresponding zero-speed frequency. This is not the case for $\omega_{1,2}$ and $\omega_{5,6}$ which exhibit the conventional gyroscopic system behavior of one split frequency decreasing with speed and one increasing. The difference derives from qualitative differences between the eigenfunctions and rotational stress stiffening that acts to increase all natural frequencies: the eigenfunctions associated with $\omega_{3,4}$ and $\omega_{7,8}$ are dominated by disk deflection, and are thus more affected by the rotational stress stiffening; while the eigenfunctions associated with $\omega_{1,2}$ and $\omega_{5,6}$ are dominated by spindle deflection, and so disk stress has less influence.

Summary and Conclusions

1 The complete set of governing equations for the spinning disk-spindle system of Fig. 1 are derived. The equations of motion (14) – (20) constitute the coupled model. Certain asymmetries of practical interest are included: center of mass offset, nondiagonal clamp and disk inertia tensors, spindle asymmetry, and general disk and spindle boundary conditions.

2 With the use of extended operators acting on an extended response variable of the form (22), the governing disk-spindle equations are cast in the canonical form for gyroscopic continua. With a natural inner product defined on the extended space, the extended inertia ($\mathbf{M}$), elastic stiffness ($\mathbf{L}$), and rotational stiffness ($\tilde{\mathbf{L}}$) operators are symmetric, and the gyroscopic operator ($\mathbf{G}$) is skew-symmetric. This structure is critical because it permits straightforward application of all known results and analytical methods for gyroscopic systems to spinning disk-spindle systems.

3 Modal analysis yields the closed-form response for arbitrary disk, spindle, and clamp forces. The response solution leads to a Green's function operator that extends the conventional Green's function to hybrid continuous/discrete systems described by extended operators. For axisymmetric disks, the uncoupled eigenfunctions participate in the response only if the disk is excited by direct force application. Disk asymmetries occurring in practice, however, may lead to expanded coupling that negate this conclusion.

4 A major feature of the extended operator formulation is that approximate eigenvalue and response solutions are achievable by classical Galerkin discretization. The lack of conventional structure in terms of differential operators having symmetry and definiteness properties with respect to a suitably defined inner product limits application of such methods to the component Eqs. (14) – (20). The zero-speed and critical-speed extended eigenfunctions are solvable in closed form, and provide the necessary set of complete comparison functions.

5 The formulation in terms of extended operators provides the necessary structure for analysis of complex disk-spindle phenomena such as nonlinearities, time-varying effects, and dissipation. Perturbation, averaging, and other approximate methods can be applied by natural extensions that parallel their use for systems not requiring extended operators. Such methods are not readily applied without the extended operator structure. For example, Renshaw and Mote's (1996) and Parker's (1998) techniques for critical speed stability predictions are immediately applicable with the extended operator formulation.

References

Chivens, D.R., and Nelson, H.D., 1975, "The Natural Frequencies and Critical Speeds of a Rotating, Flexible Shaft-Disk System," ASME *Journal of Engineering for Industry,* Vol. 97, pp. 881–886.

D'Eleuterio, G.M.T., and Hughes, P.C., 1984, "Dynamics of Gyroelastic Continua," ASME *Journal of Applied Mechanics,* Vol. 51, pp. 415–422.

Dopkin, J.A., and Shoup, T.E., 1974, "Rotor Resonant Speed Reduction Caused by Flexibility of Disks," ASME *Journal of Engineering for Industry,* Vol. 96, pp. 1328–1333.

Eversman, W., 1968, "Transverse Vibrations of a Clamped Spinning Membrane," *AIAA Journal,* Vol. 6, pp. 1395–1396.

Flowers, G.T., and Wu, F., 1996, "Disk/Shaft Vibration Induced by Bearing Clearance Effects: Analysis and Experiment," ASME *Journal of Vibration and Acoustics,* Vol. 118, pp. 204–208.

Klompas, N., 1978, "Significance of Disk Flexing in Viscous-Damped Jet Engine Dynamics," ASME *Journal of Engineering for Power,* Vol. 100, pp. 647–654.

Meirovitch, L., 1975, "A Modal Analysis for the Response of Linear Gyroscopic Systems," ASME *Journal of Applied Mechanics,* Vol. 42, pp. 446–450.

Parker, R.G., 1998, "On the Eigenvalues and Critical Speed Stability of Gyroscopic Continua," ASME *Journal of Applied Mechanics,* Vol. 65(1), pp. 134–140.

Parker, R.G., and Mote, C.D., Jr., 1996, "Vibration and Coupling Phenomena in Asymmetric Disk-Spindle Systems," ASME *Journal of Applied Mechanics,* Vol. 63, pp. 953–961.

Parker, R. G., and Sathe, P. G., 1999, "Free Vibration and Stability of a Spinning Disk-Spindle System," ASME *Journal of Vibration and Acoustics,* in press.

Renshaw, A.A., and Mote, C.D., Jr., 1996, "Local Stability of Gyroscopic Systems Near Vanishing Eigenvalues," ASME *Journal of Applied Mechanics,* Vol. 63, pp. 116–120.

Shen, I.Y., and Ku, C.-P.R., 1997, "A Nonclassical Vibration Analysis of a Multiple Rotating Disk and Spindle Assembly," ASME *Journal of Applied Mechanics,* Vol. 64, pp. 165–174.

Vance, J.C., 1988, *Rotordynamics of Turbomachinery,* Wiley, New York, NY.

Wickert, J. A., and Mote, C. D., Jr., 1990, "Classical Vibration Analysis of Axially Moving Continua," ASME JOURNAL OF APPLIED MECHANICS, Vol. 57, pp. 738–744.

Wilgen, F.J., and Schlack, A.L., Jr., 1979, "Effects of Disk Flexibility on Shaft Whirl Stability," ASME *Journal of Mechanical Design,* Vol. 101, pp. 298–303.

Wu, F., and Flowers, G.T., 1992, "A Transfer Matrix Technique for Evaluating the Natural Frequencies and Critical Speeds of a Rotor With Multiple Flexible Disks," ASME *Journal of Vibration and Acoustics,* Vol. 114, pp. 242–248.

Downloaded 04 May 2010 to 171.66.16.27. Redistribution subject to ASME license or copyright; see http://www.asme.org/terms/Terms_Use.cfm

Local Similarity in Nonlinear Random Vibration

S. Krenk
Department of Structural Engineering and Materials,
Technical University of Denmark,
Lyngby, Denmark

J. B. Roberts
School of Engineering,
University of Sussex,
Falmer, Brighton,
Sussex, England

A response analysis procedure is developed for oscillators with highly nonlinear stiffness and light nonlinear damping excited by non-white wide-band random noise based on local similarity between the random response and the deterministic response at the same energy level of the corresponding undamped oscillator. The analysis consists of three parts: introduction of modified phase plane variables, derivation of an approximate general form of the probability density of the response energy for non-white excitation, and derivation of the spectral density function of the response from the conditional covariance function for a given energy level. The use of modified phase plane variables leads to a completely symmetric formulation and reformulates the stiffness nonlinearity as a nonlinear variation of the instantaneous angular frequency, and thereby a local rescaling of time. The probability density is obtained by averaging the full Fokker-Plank-Kolmogorov equation using local similarity, thus avoiding some theoretical problems associated with the traditional averaging of the stochastic differential equations. The use of local similarity with the exact undamped solution in the derivation of the conditional spectral density leads to a spectral density estimate, that contains the higher harmonic components explicitly. Comparisons of theoretical predictions with digital simulation estimates of both the probability and spectral densities for the Duffing oscillator demonstrate the accuracy of the theory.

1 Introduction

Nonlinear random vibrations have been the subject of intensive studies over the last 30 years. Two main approaches have been stochastic equivalent linearization, in which the nonlinear components of the system are replaced by linear equivalents, Roberts and Spanos (1990), and stochastic averaging, introduced by Stratonovich (1963) and reviewed by Roberts and Spanos (1986). Stochastic equivalent linearization is often used in connection with an assumption of Gaussian response. This generally provides robust estimates of the variance of the response but, as many nonlinear characteristics are not accounted for, fails to give an accurate representation of the probability distribution function and the spectral density of the response.

In contrast, the standard stochastic averaging method can give accurate estimates of non-Gaussian response distributions. Stochastic averaging relies on the fact that oscillations of lightly damped systems to wide-band excitation are of a narrow-band character, i.e., the response is in the form of slowly modulated regular oscillations. The standard method uses a polar representation of the original variables x and $\dot{x}$ in terms of amplitude and phase, via the transformation $(x, \dot{x}) = a(\cos \varphi, -\omega_0 \sin \varphi)$, where $\varphi = \omega_0 t + \theta$, and ω_0 is a representative angular velocity that may represent an overall mean value or can depend on the current amplitude (e.g., Iwan and Spanos (1978) and Bouc (1994)). For light damping the amplitude, a, and the phase, θ, are slowly varying quantities. Although useful, the amplitude representation has the drawback that free oscillations with nonlinear stiffness do not correspond to constant amplitude a. As a consequence the standard method is incapable of yielding information on the effect of strong nonlinearities in stiffness such as the occurrence of higher harmonics (see Roberts and Spanos, 1986).

The latter deficiency of the stochastic averaging method can be remedied by considering the energy envelope of the response, rather than the amplitude. In sample functions of the response of a lightly damped oscillator to wide-band excitation oscillations occur which have a shape similar to that corresponding to those occurring in free, undamped vibration. Using this similarity, and the assumption of a white noise excitation, Stratonovich (1963) developed the stochastic averaging method with a formulation based on energy in conjunction with the rapidly varying displacement. This leads to a Markov process model for the energy envelope. Roberts introduced an alternative polar formulation in which the energy envelope is complemented by a phase process (Roberts, 1978), and extended the method to include the effect of the shape of the spectral density, for non-white excitation processes (Roberts, 1982, 1983, 1989; Dimentberg et al., 1995). Later developments have included the effect of parametric excitation (Cai, 1995). In these studies the effect of the spectral density of the excitation process appears through a sum of contributions related to the harmonic components of the free undamped oscillations.

In the analysis of nonlinear systems it is desirable to obtain not only the probability density function of the response but also its spectral density function. The two basic features of the spectral density function of the response of systems with nonlinear stiffness are the presence of higher harmonics and widening of the resonant frequency bands due to the change of the resonant frequency with the intensity of the response. The equivalent linearization procedure, described, e.g., by Roberts and Spanos (1990), fails to represent these two nonlinear characteristics of the spectrum. In a perturbation procedure proposed by Krenk (1985) the higher harmonics were represented via an expansion in terms of generalized Hermite polynomials. Each new term in the expansion adds a new harmonic as well as contributions to harmonics already present in the expansion. The terms are orthogonal when constructed in terms of a normal process. However, no explicit provision was made for the change of fundamental frequency with response intensity, and thus the predicted spectral density is too narrow.

Recently, approximate methods have been proposed which, in combination with the standard stochastic averaging method, yield estimates of the spectral density of the response (Bouc,

Contributed by the Applied Mechanics Division of THE AMERICAN SOCIETY OF MECHANICAL ENGINEERS for publication in the ASME JOURNAL OF APPLIED MECHANICS.

Discussion on the paper should be addressed to the Technical Editor, Professor Lewis T. Wheeler, Department of Mechanical Engineering, University of Houston, Houston, TX 77204-4792, and will be accepted until four months after final publication of the paper itself in the ASME JOURNAL OF APPLIED MECHANICS.

Manuscript received by the ASME Applied Mechanics Division, Jan. 13, 1998; final revision, Sept. 1, 1998. Associate Technical Editor: A. A. Ferri.

 Copyright © 1999 by ASME

Downloaded 04 May 2010 to 171.66.16.27. Redistribution subject to ASME license or copyright; see http://www.asme.org/terms/Terms_Use.cfm

1994; and Fogli et al., 1996). The spectral density is constructed from spectral densities conditional on the amplitude level. While successful in representing the spectral density around the fundamental resonance, the higher harmonics in the response are either missing or must be added by a separate procedure. The cause of this problem can be traced to the implicit or explicit representation of the fundamental oscillation as a simple harmonic, i.e., an oscillation with constant angular velocity.

In the present paper the idea of local similarity between the oscillations occurring in the stochastic response and free undamped oscillations at the same energy level is developed to provide an approximate evaluation of the response probability density function. The shape of the oscillation is represented via the variation of the angular velocity as a function of the phase angle, and the dependency of this variation with energy level, thus accounting accurately for the effect of large nonlinearities in stiffness. The local similarity is used to derive an approximate probability density function by averaging the two-dimensional Fokker-Planck-Kolmogorov equation, and not the stochastic differential equations as is usually done. An advantage of this new approach is that difficulties encountered in earlier attempts, based on a perturbation analysis (e.g., Roberts, 1982), are completely circumvented. As a by-product this approach also leads to a unique definition of equivalent damping in terms of energy. Local similarity of the response is also used in an approximate identification of the correlation function for given energy level, leading to an explicit approximate formula for the spectral density of the response containing the higher harmonics associated with strong stiffness nonlinearity. The theoretical results for both the probability density function and spectral density function of the response are compared with corresponding digital simulation estimates in the specific case of a Duffing oscillator, confirming the accuracy of the theory.

2 State Variable Representation

A nonlinear system will be considered with response $x(t)$ to an excitation $y(t)$ described by the second-order differential equation

$$\ddot{x} + h(x, \dot{x})\dot{x} + g(x) = y(t). \tag{1}$$

The damping is represented in the form $h(x, \dot{x})\dot{x}$, and $g(x)$ is a nonlinear stiffness term. The damping $h(x, \dot{x})$ is assumed to be a positive function of x and $\dot{x}$, while the stiffness depends only on x. The mechanical energy of the system is

$$E(x, \dot{x}) = \tfrac{1}{2}\dot{x}^2 + G(x) \tag{2}$$

with the potential energy associated with the non-linear stiffness given by

$$G(x) = \int_0^x g(\xi)d\xi. \tag{3}$$

Before proceeding to the stochastic response analysis, we shall recast the second-order equation of motion (1) into a symmetric state variable form that illustrates the equivalence between non-linear stiffness and an instantaneous angular velocity $\omega(x)$.

2.1 Modified Phase Plane and Angular Velocity. In the case of an undamped oscillator with no excitation E is constant, and $\sqrt{2E}$ is therefore suitable as a radial distance in a modified phase plane. A quadratic axisymmetric representation of the modified phase plane is

$$2E = \dot{x}^2 + 2G(x) = z_1^2 + z_2^2 = 2E\sin^2\varphi + 2E\cos^2\varphi \tag{4}$$

with the vector components

$$z_1 = \operatorname{sgn}(x)\sqrt{2G(x)} = \sqrt{2E}\cos\varphi,$$
$$z_2 = \dot{x} = -\sqrt{2E}\sin\varphi. \tag{5}$$

The objective of this transformation is to obtain a phase plane representation, in which the path of lightly damped oscillations appears as a regular curve, approaching a circle as the damping level goes to zero.

In undamped oscillations the energy E is constant, and the path is described completely by the phase as a function of time $\varphi(t)$. The corresponding angular velocity $\omega = d\varphi/dt$ is determined by use of the polar representation (5), from which

$$\frac{dz_1}{dt} = \frac{d\varphi}{dt}\frac{dx}{dt}. \tag{6}$$

This relation in turn implies that the angular velocity can be determined as

$$\omega = \frac{d\varphi}{dt} = \frac{dz_1}{dx} = \frac{|g(x)|}{\sqrt{G(x)}}. \tag{7}$$

In terms of the modified phase plane coordinates z_1, z_2 the relation (6) takes the form $\dot{z}_1 = \omega z_2$, and the equation of motion (1) becomes

$$\dot{z}_2 + hz_2 + \omega z_1 = y(t). \tag{8}$$

These two first-order differential equations are conveniently combined into the matrix format

$$\frac{d}{dt}\begin{bmatrix} z_1 \\ z_2 \end{bmatrix} = \begin{bmatrix} 0 & \omega \\ -\omega & -h \end{bmatrix}\begin{bmatrix} z_1 \\ z_2 \end{bmatrix} + \begin{bmatrix} 0 \\ y(t) \end{bmatrix}. \tag{9}$$

This format is completely similar to that of a linear oscillator, apart from the fact that the angular frequency ω is now a function of the response, $\omega = \omega(x)$. For free undamped oscillations a complete analogy with a harmonic oscillation can be established by introducing an equivalent nonuniform nondimensional time ωt. Figure 1 illustrates the paths of free undamped vibrations in the phase plane and the modified phase plane for a nonlinear system with increasing stiffness. The points indicate equal parts of the oscillation period. The modified phase plane is obtained by stretching the x coordinate of the classical phase plane by the factor $dz_1/dx = \omega(x)$. It is seen that the curves at larger amplitudes correspond to a more nonlinear transformation, and larger differences in the point spacing.

2.2 Period of Oscillation. At any energy level the period of a free undamped oscillation plays the role of a characteristic time. The energy relation (2) is written in the form

$$\frac{dx}{dt} = \sqrt{2(E - G(x))} \tag{10}$$

and the period then follows by the well known integral

$$T(E) = \int_0^T dt = 2\int_{x_{\min}}^{x_{\max}} \frac{dx}{\sqrt{2(E - G(x))}} \tag{11}$$

where $x_{\min}(E)$ and $x_{\max}(E)$ are the minimum and maximum displacement at energy level E, respectively.

The mean value of the kinetic energy over a period of free undamped oscillation can similarly be evaluated from (10) by the integral

$$\langle \tfrac{1}{2}\dot{x}^2 \rangle_t = \frac{1}{T(E)}\int_{x_{\min}}^{x_{\max}} \sqrt{2(E - G(x))}\, dx. \tag{12}$$

The integrand vanishes in the upper and lower limit, and therefore differentiation with respect to the energy level E gives

Downloaded 04 May 2010 to 171.66.16.27. Redistribution subject to ASME license or copyright; see http://www.asme.org/terms/Terms_Use.cfm

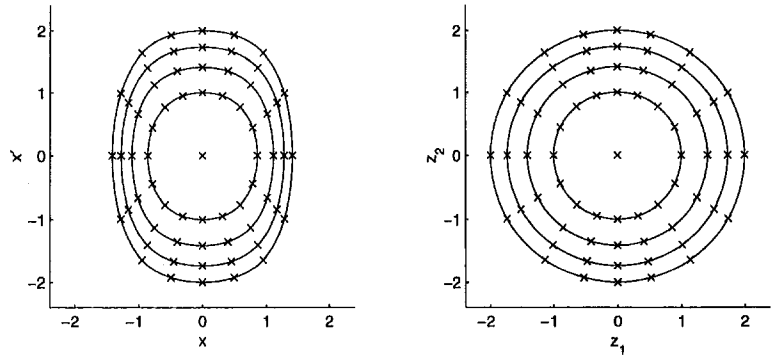

Fig. 1 Classical phase plane (*a*) and modified phase plane (*b*). Energy levels E = 0.5, 1.0, 1.5, 2.0.

$$\frac{d}{dE}\left(T(E)\left\langle\frac{1}{2}\dot{x}^2\right\rangle_t\right) = \int_{x_{\min}}^{x_{\max}} \frac{dx}{\sqrt{2(E - G(x))}} = \frac{1}{2}T(E) \quad (13)$$

where the last equality follows from Eq. (11). This equation is integrated to give

$$s(E) = \frac{\langle\dot{x}^2\rangle_t}{E} = \frac{1}{T(E)}\frac{1}{E}\int_0^E T(e)de. \quad (14)$$

The function $s(E)$ is the ratio of the mean kinetic energy to half the total energy for the energy level E. The function $s(E)$ will play an important role in the explicit formulation of the probability density function and the spectral density function. For a linear system $s(E) = 1$, and for a nonlinear system it follows from (14) that $s(E)$ is the ratio between the mean value of $T(e)$ over energy levels from zero to the current and the period $T(E)$ at the current energy level. For hardening spring stiffness the period decreases with energy level, and thus $s(E) > 1$. Conversely, $s(E) < 1$ for a softening spring.

3 Probability Density of the Energy

The probability density function $p_{x,\dot{x}}(x, \dot{x})$ of simultaneous values of the response x and $\dot{x}$ of a system of the form (1) to ideal white-noise excitation satisfies a two-dimensional Fokker-Planck-Kolmogorov (FPK) partial differential equation. For systems in which the damping is only a function of the energy there is a classical closed-form solution (Caughey, 1991), and also a few other special systems have explicit solutions (see, e.g., Lin and Cai, 1995). However, for non-white excitation and general damping approximate procedures must be used, and usually only the averaged one-dimensional problem is analytically tractable. The procedure used here for general damping and non-white excitation consists in setting up an equivalent two-dimensional FPK equation for the full system, and then reducing the dimension by appealing to local similarity with a free undamped oscillation. This procedure has the advantage of defining an equivalent energy based damping as part of the averaging, and avoids difficulties with order of magnitude arguments encountered in the currently used procedure of averaging stochastic differential equations with a non-white input (see, e.g., Roberts, 1982).

The excitation will be modeled as a stationary random process with zero mean and covariance function

$$R_y(\tau) = E\{y(t)y(t + \tau)\} \quad (15)$$

where $E\{\ \}$ denotes the expected value. The corresponding spectral density $S_y(\omega)$ is defined by

$$S_y(\omega) = \frac{1}{2\pi}\int_{-\infty}^{\infty} R_y(\tau)\cos(\omega\tau)d\tau. \quad (16)$$

In the special case of white noise the spectral density is a constant $S_y(\omega) = S_0$ and $R_y(\tau) = 2\pi S_0\delta(\tau)$.

3.1 The Full FPK Equation. In principle, equivalent stochastic differential equations can be obtained for any choice of state variables but, in view of the following reduction by averaging for constant energy, the energy and phase angle (E, φ) are selected here. Differentiation of the polar representation in (5) with respect to time gives

$$\begin{bmatrix} \dot{E}/\sqrt{2E} \\ \dot{\varphi}\sqrt{2E} \end{bmatrix} = \begin{bmatrix} \cos\varphi & -\sin\varphi \\ -\sin\varphi & -\cos\varphi \end{bmatrix}\begin{bmatrix} \dot{z}_1 \\ \dot{z}_2 \end{bmatrix} \quad (17)$$

and substitution of $(\dot{z}_1, \dot{z}_2)$ from (9) then leads to the stochastic differential equations

$$\frac{d}{dt}\begin{bmatrix} E \\ \varphi \end{bmatrix} = \begin{bmatrix} -2Eh\sin^2\varphi \\ \omega - h\cos\varphi\sin\varphi \end{bmatrix} - \begin{bmatrix} (2E)^{1/2}\sin\varphi \\ (2E)^{-1/2}\cos\varphi \end{bmatrix} y(t) \quad (18)$$

where the angular velocity $\omega(E, \varphi)$ is defined in Eq. (7).

When the excitation is a stationary wide-band process $y(t)$, the stochastic differential Eqs. (18) can be approximated by an equivalent set of diffusion equations as shown in the Appendix. The corresponding two-dimensional FPK equation for the probability density function $p_{E,\varphi}(E, \varphi)$ follows from (A4) as

$$\frac{\partial}{\partial E}\left[-m_E p_{E,\varphi} + \frac{1}{2}\frac{\partial}{\partial E}(B_{EE}p_{E,\varphi}) + \frac{1}{2}\frac{\partial}{\partial\varphi}(B_{E\varphi}p_{E,\varphi})\right] + \frac{\partial}{\partial\varphi}\left[-m_\varphi p_{E,\varphi} + \frac{1}{2}\frac{\partial}{\partial E}(B_{\varphi E}p_{E,\varphi}) + \frac{1}{2}\frac{\partial}{\partial\varphi}(B_{\varphi\varphi}p_{E,\varphi})\right] = 0 \quad (19)$$

with drift and diffusion coefficients given by (A7) and (A8). The reduction of this partial differential equation for $p_{E,\varphi}(E, \varphi)$ to an ordinary differential equation for the marginal probability density function $p_E(E)$ for the energy rests on the following similarity arguments.

3.2 Probability Density Transformations. The general relations between the joint probability density functions for the traditional phase plane coordinates x, $\dot{x}$, the modified phase plane coordinates z_1, z_2, and the polar variables E, φ follow directly from the Jacobi determinant of the transformations defined by Eq. (5). With the Jacobi determinants

$$\left|\frac{\partial(z_1, z_2)}{\partial(x, \dot{x})}\right| = \omega, \quad \left|\frac{\partial(z_1, z_2)}{\partial(E, \varphi)}\right| = 1 \quad (20)$$

the relations between the joint probability densities are

Downloaded 04 May 2010 to 171.66.16.27. Redistribution subject to ASME license or copyright; see http://www.asme.org/terms/Terms_Use.cfm

$$p_{E,\varphi}(E, \varphi) = p_{z_1,z_2}(z_1, z_2) = \frac{1}{\omega(E, \varphi)} p_{x,\dot{x}}(x, \dot{x}). \quad (21)$$

It follows, from the assumption of light damping, that the local shape of the response curve at energy level E follows, approximately, that of a free undamped oscillation. Then the probability of observing a particular value of the phase angle, φ, is proportional with the time interval $dt = \omega^{-1} d\varphi$, where ω is the angular velocity. Under this similarity assumption the probability density function $p_{E,\varphi}(E, \varphi)$ is given by

$$p_{E,\varphi}(E, \varphi) = p_{\varphi|E}(\varphi | E) p_E(E) = \frac{1}{\omega(E, \varphi) T(E)} p_E(E) \quad (22)$$

where the period $T(E)$ is introduced to normalise the probability density with respect to the phase angle.

Under the similarity assumption the probability density $p_{x,\dot{x}}(x, \dot{x})$ is determined from Eqs. (21) and (22) as

$$p_{x,\dot{x}}(x, \dot{x}) = p_{x,\dot{x}}(E) = \frac{1}{T(E)} p_E(E). \quad (23)$$

The important difference between the relations (22) and (23) is that, while the probability density $p_{x,\dot{x}}$ depends only on E, the probability density $p_{E,\varphi}$ depends explicitly on the phase angle φ via the angular velocity $\omega(E, \varphi)$.

3.3 Averaging the FPK Equation. If the two-dimensional FPK Eq. (19) is integrated with respect to the phase angle φ over the interval $[0, 2\pi]$, the terms in the second set of brackets and the last term in the first set of brackets are eliminated, while the remaining terms are replaced with mean values over the phase angle. Under the similarity assumption, resulting in Eq. (22), the remaining terms in Eq. (19) will be integrals with respect to $(\omega T)^{-1} d\varphi$, and they can therefore be converted directly to time averages, using the identity

$$\int_0^{2\pi} \left(\quad \right) \frac{d\varphi}{T(E)\omega(E, \varphi)} = \frac{1}{T(E)} \int_0^T \left(\quad \right) dt = \left\langle \quad \right\rangle_t. \quad (24)$$

The resulting differential equation for $p_E(E)$, corresponding to vanishing probability flux, is then determined in terms of the averaged drift coefficient $m(E) = \langle m_E(E, \varphi) \rangle_t$ and the averaged diffusion coefficient $B(E) = \langle B_{EE}(E, \varphi) \rangle_t$ as

$$-m(E) p_E(E) + \frac{1}{2} \frac{d}{dE} (B(E) p_E(E)) = 0. \quad (25)$$

The averaged drift and diffusion coefficients follow from (A7) and (A8),

$$m(E) = -2E\langle \sin^2 \varphi h \rangle_t + \int_{-\infty}^{0} \langle \sin \varphi_{t+\tau} \sin \varphi_t + \cos \varphi_{t+\tau} \cos \varphi_t \rangle_t R_y(\tau) d\tau \quad (26)$$

$$B(E) = 2E \int_{-\infty}^{\infty} \langle \sin \varphi_{t+\tau} \sin \varphi_t \rangle_t R_y(\tau) d\tau. \quad (27)$$

Equation (25) is the averaged FPK equation for the probability density $p_E(E)$. Although its solution is straightforward in principle, it is of interest to formulate the solution of the general problem with arbitrary damping and non-white excitation as a generalization of the classical solution for energy based damping and white noise excitation.

3.4 Equivalent Damping. Let us first consider the equivalent damping introduced via the first term in the drift coefficient $m(E)$ given by Eq. (26). The damping is introduced via the time average $2E\langle \sin^2 \varphi h \rangle_t = \langle \dot{x}^2 h \rangle_t$. This is the energy dissipation rate, averaged over time. The equivalent damping coefficient $h_{eq}(E)$ then follows from the time average appearing in Eq. (26) as

$$h_{eq}(E) = \frac{\langle \dot{x}^2 h \rangle_t}{\langle \dot{x}^2 \rangle_t} = \frac{\frac{1}{T} \int_0^T \dot{x}^2 h(x, \dot{x}) dt}{\frac{1}{T} \int_0^T \dot{x}^2 dt}. \quad (28)$$

The definition of equivalent damping in terms of the time average $\langle \dot{x}^2 h \rangle_t$ is here derived as a consequence of the integration of the two-dimensional FPK Eq. (19) with respect to the phase angle φ. It corresponds to the result that would follow from an energy balance argument. Results using the definition of equivalent damping in terms of $\langle \dot{x}^2 h \rangle_t$ were found by Hennig and Roberts (1986) to be in better agreement with numerical simulations than alternative definitions of equivalent damping based on $\langle |\dot{x}| h \rangle_t$ and $\langle h \rangle_t$.

It follows from (14) that the denominator $\langle \dot{x}^2 \rangle_t$ in (28) can be written as $s(E)E$, and thus the first term in the drift coefficient (26) is $-s(E) h_{eq}(E) E$.

3.5 Non-white Excitation. The influence of the wide-band spectrum of the excitation on the response statistics is contained in the moment and diffusion coefficients given by Eqs. (26) and (27). Evaluation of these integrals require the representation of the shape of the free undamped oscillation at any energy level in terms of harmonic components. In principle these components can be computed from the function $\omega(\varphi, E)$, but in practice it may be more convenient to obtain this representation from a deterministic perturbation analysis of the free undamped oscillation response or by numerical integration. The necessary harmonic representation is

$$\sin \varphi(t) = \sum_{j=1}^{\infty} s_j \sin \left(2\pi \frac{jt}{T(E)} \right),$$

$$\cos \varphi(t) = \sum_{j=1}^{\infty} c_j \cos \left(2\pi \frac{jt}{T(E)} \right), \quad (29)$$

for a linear system $s_1 = c_1 = 1$, while the other coefficients vanish. For nonlinear systems the coefficients contain the higher order harmonics.

The sine and cosine expansions are closely related to the kinetic and potential energy, respectively. By substitution of the series representations given by Eq. (29)

$$\frac{\left\langle \frac{1}{2} \dot{x}^2 \right\rangle_t}{E} = \langle \sin^2 \varphi \rangle_t = \tfrac{1}{2} \sum_{j=1}^{\infty} s_j^2$$

$$\frac{\langle G(x) \rangle_t}{E} = \langle \cos^2 \varphi \rangle_t = \tfrac{1}{2} \sum_{j=1}^{\infty} c_j^2. \quad (30)$$

Thus the function $s(E)$ for the mean value of the kinetic energy, introduced in (14), is the sum of the squared sine coefficients,

$$s(E) = \sum_{j=1}^{\infty} s_j^2, \quad (31)$$

and the trigonometric identity,

$$\sum_{j=1}^{\infty} s_j^2 + c_j^2 = 2, \quad (32)$$

corresponds to a separation of mean energy into kinetic and potential parts.

The moment and diffusion coefficients are expressed in terms of the spectral density of the excitation process by substitution of the harmonic representation given in Eq. (29) into integrals in (26) and (27). For this purpose it is convenient to introduce the notation $\omega_E = 2\pi/T(E)$ for the mean angular velocity at energy level E.

Downloaded 04 May 2010 to 171.66.16.27. Redistribution subject to ASME license or copyright; see http://www.asme.org/terms/Terms_Use.cfm

$$m(E) = -s(E)h_{eq}(E)E + \frac{\pi}{2}\sum_j (s_j^2 + c_j^2)S_y(j\omega_E) \quad (33)$$

$$B(E) = 2\pi E \sum_j s_j^2 S_y(j\omega_E) \quad (34)$$

For nonlinear systems the shape of the free oscillation acts as a filter through which the excitation process is passed. These results correspond to those obtained by Roberts (1982, 1983) by averaging the energy process under the classical assumption of damping of order ϵ^2 and excitation of order ϵ. In this approach the right-hand sides of the differential equations for E and φ are averaged over the period $T(E)$, defined by Eq. (11). However, the angular velocity $\omega(E, \varphi)$ is neither constant nor small, and this has led to some uncertainty regarding the influence of this term on the averaging procedure (see, e.g., Roberts, 1989). This difficulty is circumvented in the method followed here.

3.6 Probability Density for Non-white Excitation. Although the solution of the reduced FPK Eq. (25) is now simple in principle, it is desirable to cast it in the simplest possible form. This is done by first considering the case of white noise, and then generalizing the procedure to white-noise excitation spectrum.

For the special case of white-noise input the drift and diffusion coefficients (33) and (34) are

$$m(E) = -s(E)h_{eq}(E)E + \pi S_0,$$

$$B(E) = 2\pi s(E)ES_0. \quad (35)$$

Substitution of these expressions into the reduced FPK Eq. (25) gives

$$[s(E)h_{eq}(E)E - \pi S_0]p_E(E) + \frac{d}{dE}[s(E)E\pi S_0 p_E(E)] = 0. \quad (36)$$

The last term can be divided into two factors in such a way that differentiation of the first cancels the term $\pi S_0 p_E(E)$. The appropriate factor is identified by writing the differentiation relation (13) in the form

$$\frac{d}{dE}(T(E)s(E)E) = T(E). \quad (37)$$

When using this relation, the last term in (36) can be rewritten as

$$\frac{d}{dE}\left[T(E)s(E)E\frac{\pi S_0}{T(E)}p_E(E)\right] = \pi S_0 p_E(E) + T(E)s(E)E\frac{d}{dE}\left[\frac{\pi S_0}{T(E)}p_E(E)\right]. \quad (38)$$

The first term on the right will now cancel the second term in (36), leading to the convenient compact equation

$$\frac{h_{eq}(E)}{\pi S_0}\left[\frac{\pi S_0}{T(E)}p_E(E)\right] + \frac{d}{dE}\left[\frac{\pi S_0}{T(E)}p_E(E)\right] = 0. \quad (39)$$

From this the solution is immediately seen to be

$$p_E(E) = \frac{CT(E)}{\pi S_0}\exp\left(-\int_0^E \frac{h_{eq}(e)}{\pi S_0}\,de\right). \quad (40)$$

The classical exact solution for $p_{x,\dot{x}}(E)$ by Caughey (1971) for this particular case is obtained by use of (23), confirming the consistency of the present approach.

The procedure used to obtain the solution (40) for white noise can be generalized to non-white excitation by introducing an effective spectral density of the excitation, defined by

$$S_*(E) = \sum_j \frac{s_j^2}{s(E)} S_y(j\omega_E). \quad (41)$$

When this weighted spectral density is used to replace S_0 in the previous argument, the role of $h_{eq}(E)$ is taken by the effective damping

$$h_*(E) = h_{eq}(E) + \frac{\pi}{s(E)E}\sum_j \left(\frac{s_j^2}{s(E)} - \frac{s_j^2 + c_j^2}{2}\right) S_y(j\omega_E). \quad (42)$$

The additive term is the difference between a relative weighting of the input spectral density with the sine coefficients and a similar weighting with both sine and cosine coefficients.

With these definitions the general solution for non-white excitation takes the form

$$p_E(E) = \frac{CT(E)}{\pi S_*}\exp\left(-\int_0^E \frac{h_*(e)}{\pi S_*}\,de\right). \quad (43)$$

This approximate solution for non-white excitation is of the same form as the exact white-noise result (40), and leads via the similarity assumption (23) to the joint probability density

$$p_{x,\dot{x}}(E) = \frac{C}{\pi S_*}\exp\left(-\int_0^E \frac{h_*(e)}{\pi S_*}\,de\right) \quad (44)$$

for the original state variables $(x, \dot{x})$.

4 Spectral Density of the Response

For light damping, i.e., $h \ll \omega$, the energy E of the oscillation remains nearly constant over several periods, and the spectral properties of the response can be derived from the $\dot{x} = z_2$ component in the modified z_1, z_2 phase plane. Let the time origin be chosen such that at time t the energy is E and the phase angle is φ_t. The response at time $t + \tau$ may be divided into two parts, one corresponding to free decay of the response at time t, and another generated by the excitation in the time interval $[t, t + \tau]$. The excitation process is assumed to be wide-band, and thus the response generated by the excitation in the time interval $[t, t + \tau]$ is effectively uncorrelated with the response at time t. Thus, a conditional covariance function of the velocity $\dot{x}$ can be estimated over some periods for given energy level E from the correlated part of the response.

A similar idea was used based on amplitude a in the x, $\dot{x}$ phase plane by Fogli et al. (1996) for white-noise excitation of a system with bilinear stiffness and linear damping. The results for the spectral density were very good around the fundamental frequency, but due to an approximation in the derivation, the contributions from the higher harmonics were lost. In the present approach the full nonlinear response, as expressed in the modified phase plane, is used and therefore the higher harmonics appear in the spectrum with the weights predicted by the harmonic representation given in Eq. (29*a*).

4.1 Conditional Covariance Function. The correlated part of the response at time $t + \tau$ is estimated from the free vibration decay of the energy. In the absence of external excitation the energy balance equation is

$$\dot{E} + h\dot{x}^2 = 0. \quad (45)$$

In this expression the factor $\dot{x}^2$ is replaced by its time average, given by Eq. (14) as $\langle \dot{x}^2 \rangle_t = s(E)E$. The factors $s(E)$ and

Downloaded 04 May 2010 to 171.66.16.27. Redistribution subject to ASME license or copyright; see http://www.asme.org/terms/Terms_Use.cfm

$h(E)$ only vary slowly with E, and the decay of the correlated energy is then approximately given by

$$E_{t+\tau} \cong E_t \exp(-s_E h_E \tau). \tag{46}$$

The corresponding correlated response components then are

$$\dot{x}_t = \sqrt{2E} \sin \varphi_t, \quad \dot{x}_{t+\tau} \cong \exp(-\tfrac{1}{2} s_E h_E \tau)\sqrt{2E} \sin \varphi_{t+\tau}. \tag{47}$$

The time t is uniformly distributed on the time-axis, and therefore the conditional covariance function is given by the time average

$$R_{\dot{x}}(\tau \mid E) \cong 2E \exp(-\tfrac{1}{2} s_E h_E \tau)\langle \sin \varphi_t \sin \varphi_{t+\tau} \rangle_t. \tag{48}$$

This expression looks similar to that for the covariance function of a linear system excited by white noise, where the sine product combines with a cosine function of time. In the nonlinear case the phase angle is a nonlinear function of time, and the last factor containing the time average therefore contains higher harmonics in this case. The argument is only approximate as the exponential factor implicitly assumes the damping to be uniformly distributed over the period. In the linear case the correction is known to correspond to a small shift in the phase angle, leading to a horizontal tangent and finite curvature of $R_{\dot{x}}(\tau)$ at $\tau = 0$. For nonlinear oscillators the approximation is also restricted to light damping, as the functions $s(E)$, $h(E)$, and $\varphi(E, t)$ refer to a constant energy level E.

When the harmonic representation given by $(29a)$ is substituted into Eq. (48) an approximate conditional covariance function of the response velocity $\dot{x}(t)$ is obtained as

$$R_{\dot{x}}(\tau \mid E) \cong E \exp(-\tfrac{1}{2} s_E h_E \tau) \sum_j s_j^2 \cos(j\omega_E \tau) \tag{49}$$

In each term a phase shift is identified by the requirement that the contribution to the response process $x(t)$ should be differentiable. This identifies the dominating terms of the conditional covariance function of the $x(t)$ process as

$$R_x(\tau \mid E) \cong E\omega_E^{-2} \exp(-\tfrac{1}{2} s_E h_E \tau) \sum_j (s_j/j)^2 \cos(j\omega_E \tau). \tag{50}$$

At any particular energy level E, the conditional covariance function is the sum of covariance functions, each corresponding to white noise excitation of a linear oscillator with resonance frequency at the harmonics. The magnitude of the harmonics is represented via the coefficients s_j/j, determined from the harmonic representation given by Eq. $(29a)$ of the free undamped velocity. The damping ratio relative to critical, for the jth harmonic, is given by

$$\zeta_j = \tfrac{1}{2} s_E h_E / j\omega_E. \tag{51}$$

Thus, the higher harmonic components are less resonant than the fundamental mode. Note, that the damping ratio depends directly on the shape of the oscillation via the shape parameter $s(E)$.

Consistency requires that the sample functions $x(t)$ to be differentiable with a continuous derivative. This implies that the covariance function $R_x(\tau)$ must be continuously differentiable at $\tau = 0$. Thus the approximate expression (50) for the conditional covariance function is complemented by analogy with the well-known white-noise response covariance function. First it is observed that ω_E is the undamped resonant angular frequency. The equivalent damped angular frequencies of the higher harmonics are

$$\Omega_j = j\sqrt{1 - \zeta_j^2}\, \omega_E. \tag{52}$$

With this definition of the damped angular frequency a consistent extension of the expression (50) for the conditional covariance function is

$$R_x(\tau \mid E) \cong E \exp\left(-\frac{1}{2} s_E h_E \tau\right) \sum_j \left(\frac{s_j}{j\omega_E}\right)^2 \times \left[\cos(\Omega_j \tau) + \frac{\zeta_j}{\sqrt{1 - \zeta_j^2}} \sin(\Omega_j \tau)\right]. \tag{53}$$

The corresponding conditional covariance function for the derivative process $\dot{X}(t)$ follows as the negative of the second derivative,

$$R_{\dot{x}}(\tau \mid E) \cong E \exp\left(-\frac{1}{2} s_E h_E \tau\right) \sum_j s_j^2 \times \left[\cos(\Omega_j \tau) - \frac{\zeta_j}{\sqrt{1 - \zeta_j^2}} \sin(\Omega_j \tau)\right]. \tag{54}$$

The approximate conditional covariance functions given by Eqs. (53) and (54) are constructed by analogy with the linear white noise response, and thus the shape of the input spectrum is only represented via the energy level E.

4.2 Unconditional Covariance and Spectral Density. The unconditional covariance function follows from an integration, weighted with the probability density function from (43).

$$R_x(\tau) = \int_0^\infty R_x(\tau \mid E) p_E(E) dE \tag{55}$$

The spectral density of the process $X(t)$ is given by the cosine transform of the covariance function. The spectral density function is therefore given as the integral

$$S_x(\omega) = \int_0^\infty S_x(\omega \mid E) p_E(E) dE \tag{56}$$

of the conditional spectral density $S_x(\omega \mid E)$, following from a transformation of Eq. (53). The resulting conditional spectral density is

$$S_x(\omega \mid E) \cong \frac{s_E h_E E}{\pi} \sum_j \frac{s_j^2}{(j^2\omega_E^2 - \omega^2)^2 + s_E^2 h_E^2 \omega^2}. \tag{57}$$

This conditional spectral density for the response process $x(t)$ leads to a velocity process $\dot{x}(t)$ with harmonic components with participation factors s_j according to Eq. $(29a)$. The absolute width of the resonance peaks is determined by $s_E h_E$, independent of the index j.

5 Example

To illustrate the application of the methods described above the case of a Duffing oscillator with linear damping is considered. The equation of motion is

$$\ddot{X} + 2\zeta\omega_n \dot{X} + \omega_n^2 X(1 + \kappa X^2) = Y(t) \tag{58}$$

where the parameters are the undamped natural frequency ω_n and the linear damping ratio ζ corresponding to the limit of vanishing amplitude, and a nonlinear stiffness coefficient κ. The Duffing oscillator is a particular form of the Eq. (1) with linear damping and a cubic nonlinear stiffness term. It is often used as an approximation corresponding to the first term of a general nonlinear stiffness. The stochastic response of a system with nonlinear stiffness represented by a hyperbolic sine and nonlinear damping was recently investigated by Krenk (1998).

The differential equation is normalized by introducing the nondimensional time $\tau = \omega_n t$ and a nondimensional amplitude $x = \sqrt{\kappa} X$. In this notation the equation of motion takes the simple form

Downloaded 04 May 2010 to 171.66.16.27. Redistribution subject to ASME license or copyright; see http://www.asme.org/terms/Terms_Use.cfm

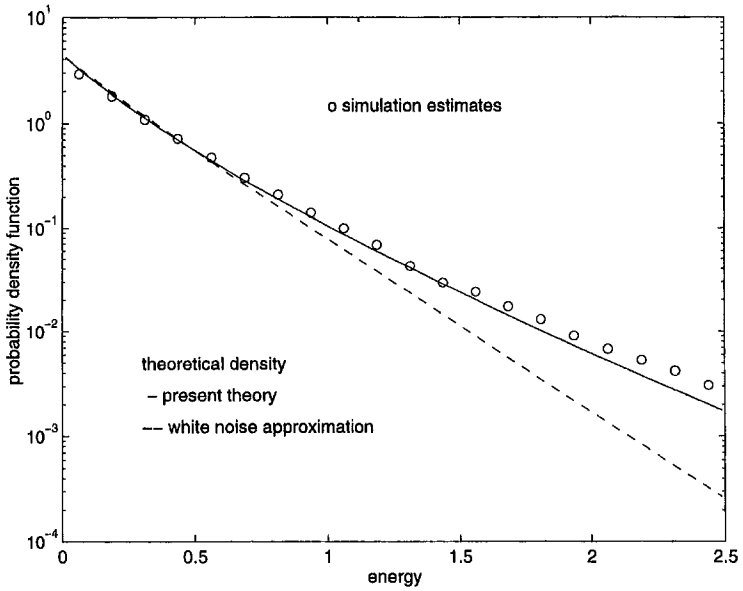

Fig. 2(*a*) Probability distribution of the energy response. $\omega_p/\omega_0 = 2.0$, $y_0 = 0.3$.

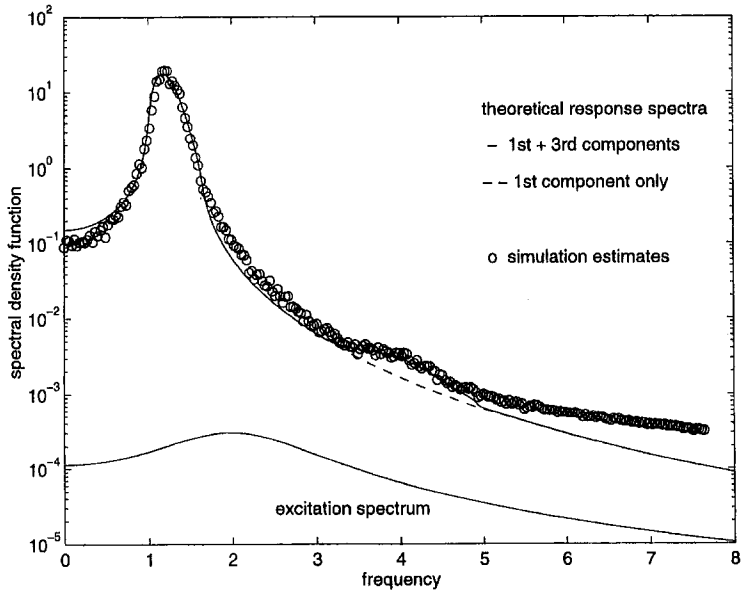

Fig. 2(*b*) Power spectrum of the displacement response. $\omega_p/\omega_0 = 2.0$, $y_0 = 0.3$.

$$\ddot{x} + 2\zeta\dot{x} + x + x^3 = y(t) \tag{59}$$

with the normalized input process $y = \sqrt{\kappa}Y/\omega_n^2$, and differentiation with respect to τ.

The free undamped vibration solution of this equation can be expressed in terms of the Jacobian elliptic function cn( ) as

$$x = x_0 \,\mathrm{cn}\,(\tilde{\omega}\tau|m) \tag{60}$$

where x_0 is the amplitude of oscillation, and the parameters are

$$\tilde{\omega} = (1 + x_0^2)^{1/2}, \quad m = \frac{x_0^2}{2(1 + x_0^2)}. \tag{61}$$

The energy is found from (59) and (60) at the point of maximum displacement as $E = \frac{1}{2}x_0^2(1 + \frac{1}{2}x_0^2)$, and the period of oscillation is given by $T(E) = 4K(m)/\tilde{\omega}$, where $K(m)$ is the complete elliptic integral. The functions $\sin\varphi$ and $\cos\varphi$, defined by (5), can be expressed in terms of the Jacobian functions cn( ) and sn( ), using formulae given, e.g., in Gradshteyn and Ryzhik (1965).

$$\cos\varphi = \frac{x_0}{\sqrt{2E}}\,\mathrm{cn}\,(\tilde{\omega}\tau|m)\sqrt{1 + \frac{1}{2}x_0^2\,\mathrm{cn}^2\,(\tilde{\omega}\tau|m)}$$

$$\sin\varphi = -\frac{x_0}{\sqrt{2E}}\,\mathrm{sn}\,(\tilde{\omega}\tau|m)\sqrt{1 + x_0^2 - \frac{1}{2}x_0^2\,\mathrm{sn}^2\,(\tilde{\omega}\tau|m)} \tag{62}$$

Although explicit Fourier expansions are known for the individual Jacobian functions, the Fourier coefficients s_j and c_j needed in the present theory are most conveniently calculated numerically in this example.

5.1 Simulation of Wide-Band Excitation. A family of wide-band excitation processes corresponding to second-order filtering of white noise is considered. A weak resonant peak around the angular frequency is obtained by combining two independent processes $\nu_1(\tau)$ and $\nu_2(\tau)$ with identical statistical properties to form the excitation process

$$y(t) = y_0[\nu_1(t)\cos\omega_p t + \nu_2(t)\sin\omega_p t]. \tag{63}$$

The trigonometric functions lead to a simple relation between

Downloaded 04 May 2010 to 171.66.16.27. Redistribution subject to ASME license or copyright; see http://www.asme.org/terms/Terms_Use.cfm

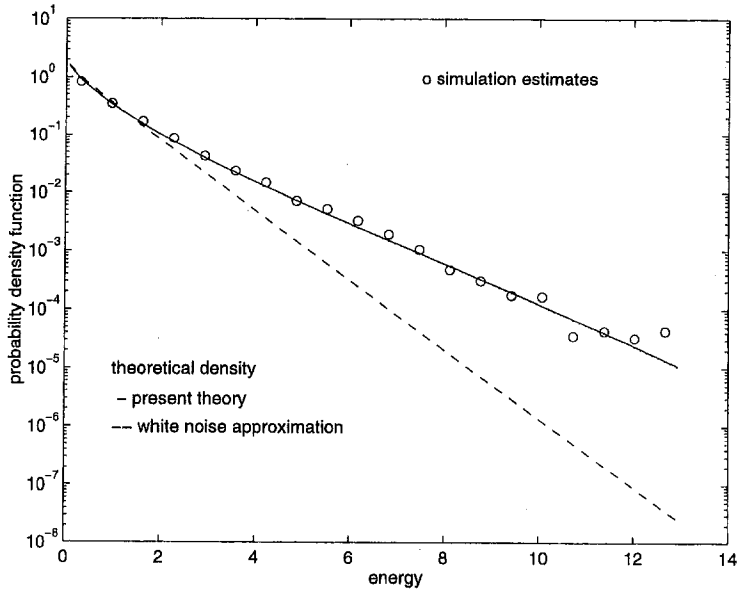

Fig. 3(*a*) Probability distribution of the energy response. $\omega_p/\omega_0 = 2.0$, $y_0 = 0.5$.

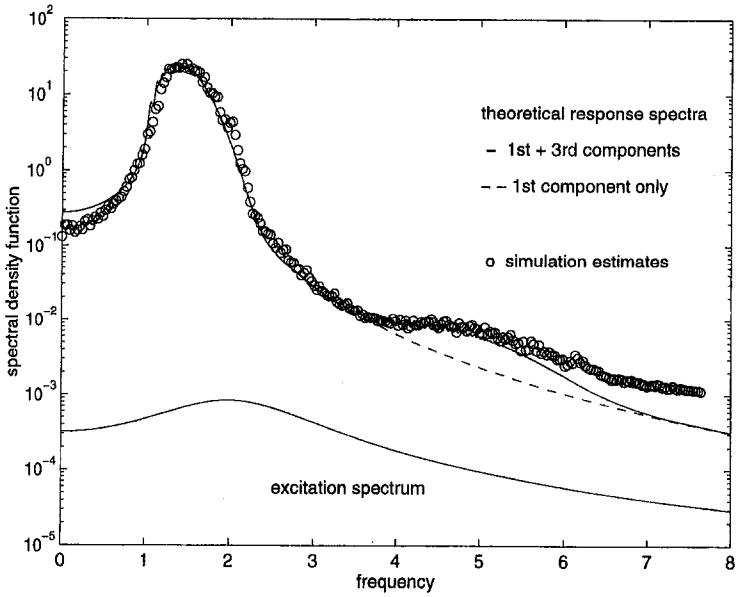

Fig. 3(*b*) Power spectrum of the displacement response. $\omega_p/\omega_0 = 2.0$, $y_0 = 0.5$.

the covariance functions, $R_y(\tau) = 2y_0^2 R_\nu(\tau)\cos(\omega_p\tau)$, corresponding to splitting the spectral density of the ν-process into two parts and shifting one ω_p to the left and the other ω_p to the right. In this example the ν-processes are generated from normalized white noise by a first-order low-pass filter,

$$\dot{\nu} + \beta\nu = \beta n(t) \tag{64}$$

resulting in the power spectral density

$$S_\nu(\omega) = \frac{1}{2\pi}\frac{\beta^2}{\beta^2 + \omega^2}. \tag{65}$$

The spectral density of the excitation process $y(t)$ is a combination of the shifted spectral densities,

$$S_y(\omega) = \frac{\beta^2 y_0^2}{2\pi}\left[\frac{1}{\beta^2 + (\omega - \omega_p)^2} + \frac{1}{\beta^2 + (\omega + \omega_p)^2}\right]. \tag{66}$$

For small β the spectrum has a single peak in the neighborhood of the frequency ω_p. There are three parameters for this spectrum: the peak bandwidth parameter β, the peak position parameter ω_p, and the excitation intensity parameter y_0.

The present formulation of the excitation process allows for exact simulation of discrete sample points by using (63) in connection with the following one-step auto-regressive representation of the ν-process,

$$\nu(\tau + \Delta\tau) = \nu(\tau)\exp(-\beta\Delta\tau) + (\tfrac{1}{2}\beta(1 - \exp(-2\beta\Delta\tau)))^{1/2} n_j, \tag{67}$$

with independent standard normal variables n_j. The relation (67) is easily verified directly, using that $R_\nu(0) = \frac{1}{2}\beta$ and $R_\nu(\Delta\tau) = \frac{1}{2}\beta\exp(-\beta\Delta\tau)$. After generating discrete sample points of the excitation process $y(j\Delta\tau)$ the response $x(j\Delta\tau)$ was obtained by use of the fourth-order Runge-Kutta algorithm. In the results reported here $\Delta\tau = 0.1$ was chosen throughout. The probability density function was estimated from time histories with a total of 100,000 sample values, and the spectral density functions were estimated from 200 blocks, each containing 1024 sample points.

Downloaded 04 May 2010 to 171.66.16.27. Redistribution subject to ASME license or copyright; see http://www.asme.org/terms/Terms_Use.cfm

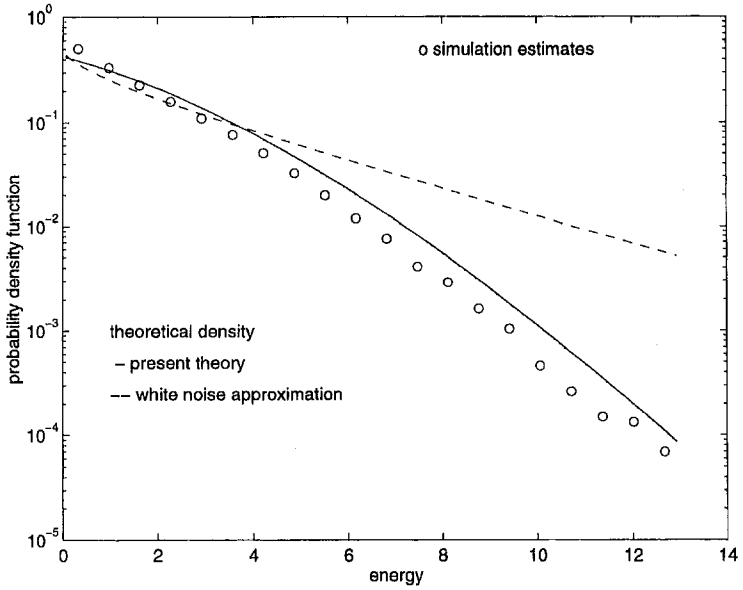

Fig. 4(*a*) Probability distribution of the energy response. $\omega_p/\omega_0 = 5.0$, $y_0 = 0.8$.

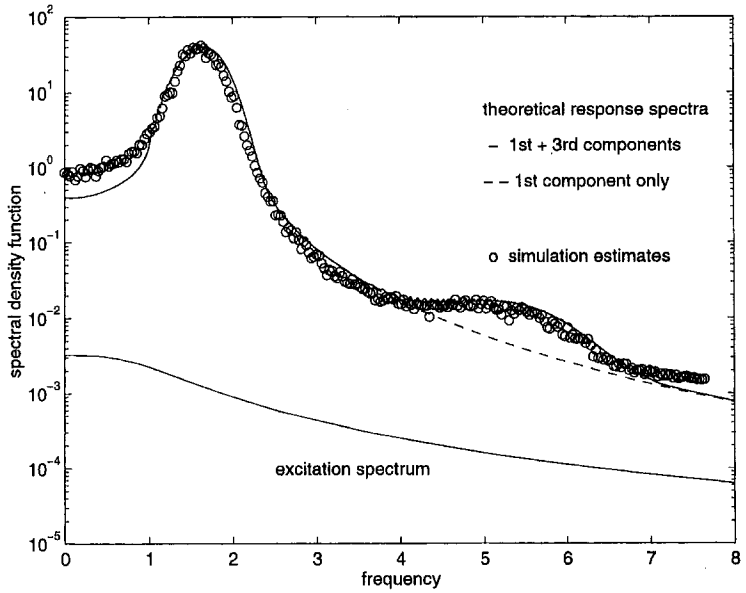

Fig. 4(*b*) Power spectrum of the displacement response. $\omega_p/\omega_0 = 5.0$, $y_0 = 0.8$.

5.2 Typical Results. Typical theoretical and simulated results for the probability density and the spectral density are shown in Figs. 2, 3, and 4. All the results correspond to the linear damping ratio $\zeta = 0.025$ and the excitation bandwidth parameter $\beta = 1.0$, while different values of the peak position parameter ω_p and the excitation intensity parameter y_0 are used to illustrate the influence of deviations from white noise excitation, and the effect of the nonlinear stiffness, respectively.

Figure 2(*a*) shows a comparison between the probability density of the energy E, as calculated by the present theory, and estimated from simulation. Here $\omega_p/\omega_0 = 2.0$ and $y_0 = 0.3$. For comparison, the corresponding result using a white-noise approximation, with the input spectral density $S_y(\omega)$ replaced by $S_y(1)$, is also shown. There is good agreement between the present theory and the simulation results, and a significant improvement on the white-noise approximation. Evidently the effect of the input spectrum is to increase the probability of the response reaching large amplitudes. This trend can be predicted from simple physical reasoning. When $\omega_p/\omega_0 = 2.0$ the resonant frequency lies to the left of the peak in the input spectrum (see Fig. 2(*b*)). Thus, increasing amplitude in the response is associated with increasing frequency of oscillation, which in turn is associated with higher levels in the input spectrum. Thus, at higher amplitudes more energy is fed into the oscillator with the result that the probability of reaching higher levels increases, relative to the white-noise input case.

Figure 2(*b*) shows a comparison between the spectral density of the displacement amplitude, as computed by the present method via Eq. (57) and corresponding simulation estimates. For comparison the spectral density function of the excitation process is also shown. If only the first harmonic component ($j = 1$) is included in the prediction, excellent agreement with the simulation estimates is obtained in the vicinity of the primary resonance. Bearing in mind the small level of damping present in this example, the broadening effect at the primary resonance, caused by the frequency of the oscillations in the response increasing as the amplitude of the oscillation increases, is clearly seen. If the next term ($j = 3$) is included, the theory predicts a secondary resonant peak, corresponding to the third harmonic component in the response oscillations. Both the magnitude and

Downloaded 04 May 2010 to 171.66.16.27. Redistribution subject to ASME license or copyright; see http://www.asme.org/terms/Terms_Use.cfm

location of this peak are well predicted by the theory. Again it is broadened by the effect of the frequency of oscillation changing with amplitude. It is noted that simulation studies for entirely linear cases, where the output spectrum is known exactly, suggest that the deviations between theory and simulation at very low and very high frequencies, as seen in Fig. 2(*b*) (and in Figs. 3(*b*) and 4(*b*), to be discussed) are attributable, at least in part, to accuracy limitations inherent in the implementation of the simulation.

Figures 3(*a*) and 3(*b*) show the effect of increasing the level of the excitation to $y_0 = 0.5$, with all the other parameters as for Figs. 2(*a*) and 2(*b*). There is excellent agreement with the simulation estimates, and as expected the departure of the probability density from the white noise result is more pronounced. The relative magnitude of the secondary spectral peak and the broadening effect referred to earlier show an increase, reflecting the increase in the non-linear character of the response. Again there is excellent agreement between simulation results and the present theory in the vicinity of the primary and secondary resonant peaks.

Finally, Figs. 4(*a*) and 4(*b*) show results for a case where the primary resonant frequency lies to the right of the peak in the input spectrum with $\omega_p/\omega_0 = 0.5$ and $y_0 = 0.8$. Using the physical argument given earlier, to explain the trend shown in Fig. 2(*a*), one would expect an opposite trend here and the results confirm this. The probability of reaching large amplitudes is attenuated, due to the fall off in the input spectral level as the frequency increases. Once again a good agreement between theoretical predictions and simulation estimates is obtained, especially in the case of the response spectral density.

6 Conclusions

A unified approach has been presented for the probability density and the spectral density of random response of highly nonlinear oscillators to non-white excitation. The theory is based on the notion of local similarity between the expected response and a free undamped oscillation with the same level of mechanical energy. The similarity assumption enables the joint probability density of any pair of state variables to be expressed in terms of the marginal probability density of the mechanical energy alone, while the two-dimensional distributions are obtained via the instantaneous angular frequency, as predicted from a free undamped oscillation. The similarity hypothesis makes it possible to obtain the differential equation for the probability of the energy by averaging of the full two-dimensional Fokker-Planck-Kolmogorov equation. This procedure is simple and avoids averaging of the stochastic differential equations, where asymptotic estimates of the "order of magnitude" of the individual terms are needed, but not fully established for the case of non-white excitation. The general, although approximate, result for the probability density is given in (43) and (44) in a compact form, where a complete analogy to the white noise case is established by the introduction of a weighted spectral excitation density (41) and a modified effective damping (42). Although seemingly restricted to lightly damped systems, it is interesting to observe that the exact white noise result is recovered for any magnitude of the damping, provided that any non-linear damping is given in terms of the mechanical energy in the form $h(E)\dot{x}$. Thus, the results appear to be asymptotically valid independently in the limits of vanishing damping or infinitely wide-band excitation spectrum.

The power spectral density of the nonlinear response is also obtained from the local similarity assumption, which is used to predict the slowly decaying fully correlated part of the response. For wide band excitation the remaining part of the response is assumed to be fully uncorrelated, leading to a simple formulation of the conditional correlation function, conditional on the energy level. The corresponding response spectral density clearly shows the higher harmonic components, corresponding to the higher harmonics of free undamped oscillations. The unconditional spectral density is found by integration over the energy probability density. The variation of the free-vibration frequencies with energy level leads to broadening of the peaks in the spectral density.

Numerical simulations of both energy probability density and power spectral density for nonlinear response to non-white excitation demonstrate, that the theory is able to capture the influence of the non-white excitation, and to predict the widening of the basic resonance peak and the occurrence of a higher harmonic component at three times the basic frequency due to the non-linear stiffness.

Acknowledgment

Financial support from the Danish Technical Research Council and the European Union via the "Network for Stochastic Mechanics in Structural and Mechanical Engineering" under the Human Capital and Mobility Programme is gratefully acknowledged.

References

Bouc, R., 1994, "The power spectral density of response for a strongly non-linear random oscillator," *Journal of Sound and Vibration,* Vol. 175, pp. 317–331.

Cai, G.Q., 1995, "Random vibration of nonlinear systems under nonwhite excitations," *Journal of Engineering Mechanics,* Vol. 121, pp. 633–639.

Caughey, T.K., 1971, "Nonlinear theory of random vibrations," *Advances in Applied Mechanics,* Vol. 11, C.S. Yih, ed., Academic Press, New York, pp. 209–253.

Dimentberg, M., Cai, G.Q., and Lin, Y.K., 1995, "Application of quasi-conservative averaging to a non-linear system under non-white excitation," *International Journal of Non-Linear Mechanics,* Vol. 30, pp. 677–685.

Fogli, M., Bresollette, P., and Bernard, P., 1996, "The dynamics of a stochastic oscillator with impacts," *European Journal of Mechanics, A Solids,* Vol. 15, pp. 213–241.

Gardiner, C.W., 1985, *Handbook of Stochastic Methods,* Springer-Verlag, Berlin.

Gradshteyn, I.S., and Ryzhik, I.M., 1965, *Table of Integrals Series and Products,* Academic Press, New York.

Hennig, K., and Roberts, J.B., 1986, "Averaging methods for randomly excited non-linear oscillations," *Random Vibrations—Status and Recent Developments,* I. Elishakoff and R.H. Lyon, eds., Elsevier, Amsterdam, pp. 149–161.

Iwan, W.D., and Spanos, P.-T., 1978, "Response Envelope Statistics for Nonlinear Oscillators With Random Excitation," ASME JOURNAL OF APPLIED MECHANICS, Vol. 45.

Krenk, S., 1985, "Generalized Hermite polynomials and the spectrum of non-linear random vibration," *IUTAM Symposium on Probabilistic Methods in the Mechanics of Solids and Structures,* S. Eggwertz and N. Lind, eds., Springer-Verlag, Berlin. pp. 71–80.

Krenk, S., 1998, "Energy and spectral density in non-linear random response," *Proceedings of the Fourth International Conference on Stochastic Structural Dynamics,* Aug. 6–9, Notre Dame, IN, Balkema, Rotterdam.

Lin, Y.K., and Cai, G.Q., 1995, *Probabilistic Structural Dynamics,* McGraw-Hill, New York.

Roberts, J.B., 1978, "The energy envelope of a randomly excited non-linear oscillator," *Journal of Sound and Vibration,* Vol. 60, pp. 177–185.

Roberts, J.B., 1982, "A stochastic theory for nonlinear ship rolling in irregular seas," *Journal of Ship Research,* Vol. 26, pp. 229–245.

Roberts, J.B., 1983, "Energy methods for non-linear systems with non-white excitation," *IUTAM Symposium on Random Vibrations and Reliability,* K. Hennig, ed., Akademie-Verlag, Berlin, pp. 285–294.

Roberts, J.B., 1989, "Prediction of ship roll motion in irregular seas using stochastic process theory," *Proceedings of the 47th Session of the International Statistical Institute,* Vol. C1, Paris, pp. 497–515.

Roberts, J.B., and Spanos, P.D., 1986, "Stochastic averaging: an approximate method of solving random vibration problems," *International Journal of Non-Linear Mechanics,* Vol. 21, pp. 111–134.

Roberts, J.B., and Spanos, P.D., 1990, *Random Vibration and Statistical Linearization,* John Wiley and Sons, New York.

Stratonovich, R.L., 1963, *Topics in the Theory of Random Noise,* Vols. 1 and 2, Gordon and Breach, New York.

APPENDIX

Equivalent Diffusion Equations

The stochastic differential Eqs. (18) are of the form

$$\frac{d}{dt} Z_j(t) = a_j(Z_k, t) + b_j(Z_k, t)y(t), \quad j = 1, 2 \quad \text{(A1)}$$

with $Z_1 = E$ and $Z_2 = \varphi$. For wide-band excitation this set of

Downloaded 04 May 2010 to 171.66.16.27. Redistribution subject to ASME license or copyright; see http://www.asme.org/terms/Terms_Use.cfm

equations can be replaced by a corresponding set of diffusion, or Ito, equations of the form

$$dZ_j = m_j(Z_k, t)dt + \sigma_j(Z_k, t)dW \tag{A2}$$

where $W(t)$ is a normalized Wiener process (Gardiner, 1985). The coefficients of this equation describe the drift and the diffusion of the vector process by specifying the first two moments of the increments,

$$E\{dZ_j\} = m_j(Z_l, t)dt,$$

$$E\{dZ_j dZ_k\} = \sigma_j(Z_l, t)\sigma_k(Z_l, t)dt = B_{jk}(Z_l, t)dt. \tag{A3}$$

For this type of process the joint probability density $p(z_k)$ satisfies the FPK equation

$$\frac{\partial p}{\partial t} = \frac{\partial}{\partial z_j}\left(-m_j p + \frac{1}{2}\frac{\partial}{\partial z_k}(B_{jk}p)\right) \tag{A4}$$

completely defined by the drift vector m_j and the diffusion matrix B_{jk}, in combination with suitable boundary conditions.

When the coefficients $b_j(Z, t)$ depend on the response vector Z_k, these terms contribute to the drift vector m_j, even if $Y(t)$ is a white noise process. The drift vector and diffusion matrix are determined from their definition in terms of the moments of the increments in Eq. (A3) (see, e.g., Gardiner, 1985),

$$m_j(z_t) = a_j(z_t) + \int_{\Delta t}^{0} b_k(z_{t+\tau})\frac{\partial}{\partial z_k} b_j(z_t)R_y(\tau)d\tau \tag{A5}$$

$$B_{jk}(z_t) = \int_{\Delta t}^{\Delta t} b_j(z_{t+\tau})b_k(z_t)R_y(\tau)d\tau \tag{A6}$$

The time increment Δt is assumed to be longer than the correlation time of the excitation process, determined from the covariance function $R_y(\tau)$. In the present context the wide-band properties of the excitation process implies that this function decreases to negligible values for times exceeding some time interval Δt that is less than the characteristic period of the system $T(E)$, as determined by (11). For the nonlinear oscillator, described by the stochastic differential Eqs. (18) the integrals in (A5) and (A6) are

$$m_j - a_j = \int_{-\infty}^{0} \begin{bmatrix} \sin\varphi_{t+\tau}\sin\varphi_t + \cos\varphi_{t+\tau}\cos\varphi_t \\ -(\cos\varphi_{t+\tau}\sin\varphi_t + \sin\varphi_{t+\tau}\cos\varphi_t)/2E \end{bmatrix} \times R_y(\tau)d\tau \tag{A7}$$

and

$$B_{jk} = \int_{-\infty}^{\infty} \begin{bmatrix} 2E\sin\varphi_{t+\tau}\sin\varphi_t & \sin\varphi_{t+\tau}\cos\varphi_t \\ \cos\varphi_{t+\tau}\sin\varphi_t & \cos\varphi_{t+\tau}\cos\varphi_t/2E \end{bmatrix} \times R_y(\tau)d\tau. \tag{A8}$$

In the reduced formulation (25) only the coefficients $m(E) = \langle m_1\rangle_t$ and $B(E) = \langle B_{11}\rangle_t$ remain.

Downloaded 04 May 2010 to 171.66.16.27. Redistribution subject to ASME license or copyright; see http://www.asme.org/terms/Terms_Use.cfm

Load Identification Through Structural Modification

P. W. Möller
Ph.D. Research Associate,
Department of Solid Mechanics,
Chalmers University of Technology,
S-412 96 Goteborg, Sweden
e-mail: moller@solid.chalmers.se

A load identification problem in structural dynamics has in general multiple solutions. Therefore, additional information, such as the locations of the unknown forces, has to be supplied a priori in order to make a unique solution possible. The present study focuses on cases where such information is not readily available. First, it is shown that, given (tentatively) the spatial shape and position of the load, the Betti reciprocal theorem together with a reference load case may be used to calculate the required magnitude of the unknown load so that the response fits the measurement data as well as possible in a defined sense. In this manner a large number of trial loads may be evaluated with only little computational effort, since no equation system needs to be solved. Second, the situation where several loads, each reproducing the same measurement data, have been identified is investigated. An optimization problem with added discrete masses as design variables is suggested. The solution of this problem yields a structure such that each set of responses generated by each one of the previously identified loads is clearly distinguishable at the transducer positions. The proposed method is a novel approach and should be useful in the load identification problem for an existing structure. A numerical example illustrates the application of the method.

1 Introduction

1.1 General. Inverse problems where the analyst is prompted to find the action (source) that has produced an observed reaction (response) have a long history in science and engineering. Galiullin, (1984) claims that Newton's formulation of the law of gravity from Kepler's data was one of the first inverse problems in dynamics that was treated. Today this type of task is regularly encountered in various sciences, such as in geophysics (Menke, 1989), in medicine (see, e.g., Tarantola, 1987; Menke, 1989), in mechanics of materials (Bui, 1994), and in computational mechanics (see, e.g., Imregun and Visser, 1991; Mottershead and Friswell, 1993; Friswell and Mottershead, 1995), to mention a few.

Here we are concerned with the so-called load identification problem in structural dynamics, which is not only an inverse problem but also ill-posed, since the response typically is a continuous vector valued function of the spatial coordinates, whereas the response is defined at a few points only. Thus, there is in general no unique solution. Moreover, solutions are frequently found to be unstable in the sense that small perturbations of input data, result in large changes in calculated force magnitudes. This ill-conditioning is a prevailing nuisance when a harmonic load operates in the vicinity of an eigenfrequency or close to an antiresonance frequency of the structure. In addition, spatial aliasing, (see Breitfeld, 1996), caused by poorly placed, or too few, transducers may result in bad conditioning.

1.2 Previous Work. The load identification problem has been investigated in several works in the past. D'Cruz, Crisp and Ryall (1992) studied a rectangular viscoelastic plate with a single transverse harmonic point load, and showed that it is sufficient to measure the transverse displacement at three discrete points to determine the magnitude, phase, and location of the force. It is of some interest to note that in an earlier paper D'Cruz et al. (1991) concluded that with an *elastic* plate, it takes at least four displacement readings to calculate the force location and magnitude. Choi and Chang (1996) determined the location and magnitude of an impact load on a beam in a nested loop algorithm. In the outer loop, the location is estimated by minimizing a nonlinear function with a quasi-Newton method, while the magnitude is calculated in the inner loop. Bateman et al. (1992) and Carne et al. (1992) determined the forces on an unsupported structure subjected to an impact, from calculated eigenmodes and measured accelerations. In this case the load location is either known or without interest, and the evaluated magnitudes are those of the load resultants. A few works, (e.g., Shih et al., 1989; Zhang et al., 1990; Kompella et al., 1994), consider the possibility to determine the number of forces or the force locations in a more general setting. Shih et al. (1989) and Zhang et al. (1990) use the "Best Approximation Subspace" technique, described by Zhang et al. (1988) to locate a given number of incoherent forces. It is noted that this approach presumes that the number of sources is known and that there is a candidate set of points for their locations.

Apart from the aforementioned studies, most reports on load identification consider cases where the load locations are known a priori. This information is needed to determine a unique solution in an otherwise general case, and the problem type is usually referred to as indirect force measurement (see, e.g., Hillary and Ewins, 1984; Law and Chan, 1997; Lee and Park, 1995; Okubo et al., 1985; Fabunmi, 1986; Starkey and Merrill, 1989; Hansen and Starkey, 1990; Karlsson, 1996; Desanghere and Snoeys, 1985; Verhoeven, 1988). In particular, several reports deal with the ill-conditioning, and numerical experiments may be found in Hillary and Ewins (1984), Lee and Park (1995), Okubo et al. (1985), Starkey and Merrill (1989), Hansen and Starkey (1990), Karlsson (1996), and Desanghere and Snoeys (1985). Hillary and Ewins (1984) postulate that indirect force measurements based on measured strains are less ill-conditioned than approaches where measured displacements or accelerations are used. Contrary to this, Law et al. (1997) get better predictions of the forces between a vehicle and a bridge deck when acceleration measurements, rather than bending moments, are used in the analysis. Lee and Park (1995) present an error

Contributed by the Applied Mechanics Division of THE AMERICAN SOCIETY OF MECHANICAL ENGINEERS for publication in the ASME JOURNAL OF APPLIED MECHANICS.

Discussion on the paper should be addressed to the Technical Editor, Professor Lewis T. Wheeler, Department of Mechanical Engineering, University of Houston, Houston, TX 77204-4792, and will be accepted until four months after final publication of the paper itself in the ASME JOURNAL OF APPLIED MECHANICS.

Manuscript received by the ASME Applied Mechanics Division, Jan. 21, 1998; final revision, July 21, 1998. Associate Technical Editor: M. Ortiz.

 Copyright © 1999 by ASME

Downloaded 04 May 2010 to 171.66.16.27. Redistribution subject to ASME license or copyright; see http://www.asme.org/terms/Terms_Use.cfm

analysis that shows that frequencies close to a resonance or an antiresonance frequency are prone to result in an inaccurate determination of force magnitude. In the former case the stability problem is caused by inaccuracies in the frequency response function (FRF) matrix, while at antiresonance problems arise from rank deficiency of the FRF submatrix. Numerical results that conform with this error analysis may be found in Okubo et al. (1985).

A few methods to predict situations where stability problems may be present have been suggested. Fabunmi (1986) uses a scalar measure, related to the number of participating eigenmodes in the vibration, to determine the number of unknown forces that can be accurately determined. This method predicts that close to a resonance frequency, only a single force magnitude can be determined, no matter how many transducers that are used. Starkey and Merrill (1989) suggest that the condition number of the FRF matrix, premultiplied by its own transpose, can be used to estimate the sensitivity to perturbations in data. The maximum column norm is utilized to calculate the condition number, and it is verified by means of numerical examples that the result correlates to the errors in calculated force magnitudes. The concept introduced by Starkey and Merrill (1989) was extended to modal based indirect force measurements by Hansen and Starkey (1990). An alternative approach is suggested by Karlsson (1996) who shows that the ratio between the smallest and the largest singular value of the FRF matrix is correlated to the error in calculated force magnitudes.

Regularization may be utilized to improve conditioning. Lee and Park (1995) show how this can be accomplished by artificial damping in the FRF matrix. Only the stability at antiresonance may be improved in this manner, since the difficulties at resonance frequencies pertain to inexact elements in the FRF matrix. Another approach is to add a penalty, expressed in terms of the calculated load, to a least-square formulation of the problem. This type of regularization, known as Tikhonov's method or damped least squares, was used by Busby and Trujillo (1987) in a modal based load identification. In a more recent work Busby and Trujillo (1997) also use first-order regularization, where the penalty is in terms of the derivative of the force rather than the force itself, and an optimal value for the penalty parameter is determined by the so-called L-curve method (see, e.g., Hansen, 1992). While regularization effectively improves conditioning, it inevitably smooths the solution in a manner that cannot be predicted beforehand. Since an actual disturbance may be quite erratic, forces evaluated in this manner may have little physical significance.

A comprehensive review of indirect force calculation methods and the difficulties that arise, is given by Dobson and Rider (1990). In particular one may note that they claim that "*The computations of excitation forces using measured data is in its infancy and few successful applications of any method have been published.*"

1.3 Outline of Present Study. The present work is an attempt to approach the load identification problem in a general manner, in the sense that both the distribution and the locations of the forces are assumed to be unknown. Since the finite element method has become a standard tool of analysis in the engineering community, a discrete model of the structure is utilized throughout the paper; the continuous problem could in principal be treated analogously, but seems to be of less practical interest. The identification problem is defined in Section 2. For large discrete models one may systematically establish a large number of trial load cases with assumed force distributions, but yet unknown magnitudes. The Betti reciprocal theorem may then be used to determine the respective magnitudes without having to solve an equation system, as is shown in Section 3. Given several solutions to the same load identification problem, each of them reproducing the same experimentally observed data to within some specified tolerance, further measurements are required to distinguish between the alternatives. In Section 4 we suggest a novel approach in which the transducer locations remain fixed, but the structure is modified by adding discrete masses prior to new measurements. Optimal locations for the masses so added are determined by solving a minimization problem where the objective function has been constructed so as to separate the responses from each candidate load case as well as possible. A numerical example is provided in Section 5.

2 Problem Definition

Adopting linear elasticity theory (i.e., linearized strains, small displacements, and Hooke's law), we will consider an undamped discrete N-degree-of-freedom system

$$\mathbf{M}\ddot{\mathbf{u}} + \mathbf{K}\mathbf{u} = \mathbf{f}. \tag{1}$$

The majority of approaches to the load identification problem operates in the frequency domain, so for simplicity we assume that the loads are harmonic with a common frequency ω_p, and write

$$\mathbf{f} = \mathbf{f}_a \sin \omega_p t. \tag{2}$$

In case of a more general load, a Fourier decomposition followed by an analysis for each separate term, is necessary.

Let $\bar{\mathbf{u}}_M$ be a vector with $M \ll N$ experimentally determined displacement components. It is observed that $\bar{\mathbf{u}}_M$ may have been calculated from some other measured quantity, e.g., accelerations, and is polluted by measurement errors and scattering. The load identification problem now requires that we find a load vector amplitude $\mathbf{f}_a$ such that the amplitude $\mathbf{u}_a$ of the solution $\mathbf{u}$ of (1) satisfies

$$\mathbf{R}\mathbf{u}_a = \bar{\mathbf{u}}_M. \tag{3}$$

Here $\mathbf{R}$ is an operator that restricts the N-vector $\mathbf{u}_a$ to the M measured quantities.

Most solution methods proposed for the load identification problem may be classified as belonging to one of two approaches, viz. a modal method and a frequency response function method (see, e.g., Dobson and Rider, 1990). Both approaches require us to supply additional information in order to make a unique solution possible. Here, however, we focus on cases where supplementary data is not readily available. First, in Section 3 it is shown how the amplitudes for a large number of trial load cases, with only little computational effort, may be determined so that the responses and measured data agree as well as possible in a defined sense. Second, in Section 4 we suggest an original method to distinguish between loads, each of which reproduce measured data; prior to a new measurement, the structure is modified such that the responses of the respective loads is clearly distinguishable at the transducer locations.

3 Load Case Evaluation

3.1 Reference Load Case. Consider a load case $\mathbf{f}_r$ (subscript r for reference) with point forces applied in each of the M measurement points (and in the direction of the measured quantity) where the force magnitudes have been determined such that the response $\mathbf{u}_r$ conforms to the measured values. We shall subsequently refer to $(\mathbf{u}_r, \mathbf{f}_r)$ as the reference load case. Hence, we have

$$(\mathbf{K} - \omega_p^2\mathbf{M})\mathbf{u}_r = \mathbf{f}_r \tag{4}$$

where

$$\mathbf{R}\mathbf{u}_r = \bar{\mathbf{u}}_M, \tag{5}$$

i.e., the restriction of the reference solution to the measured degrees of freedom, equals the measured values by construction.

Downloaded 04 May 2010 to 171.66.16.27. Redistribution subject to ASME license or copyright; see http://www.asme.org/terms/Terms_Use.cfm

Note that the load vector $\mathbf{f}_r$ is relatively easy and cheap to construct: a point load could be applied to each measured degree-of-freedom, one at a time, and a linear combination of the M response vectors so obtained is formed such that the resulting vector takes on the values $\bar{\mathbf{u}}_M$ at the measured degrees-of-freedom.

3.2 Trial Load Cases. Let us next consider a set of trial load cases with assumed shapes (spatial load distributions) $\mathbf{f}_{ti}$ (subscript t for trial), but unknown magnitudes s_i

$$(\mathbf{K} - \omega_p^2\mathbf{M})\mathbf{u}_{ti} = s_i\mathbf{f}_{ti} \quad i = 1, 2, \ldots . \tag{6}$$

Premultiplying the reference solution $\mathbf{u}_r$ by the transpose of a trial load $s_i\mathbf{f}_{ti}^T$, utilizing (4) and (6), and observing that $\mathbf{K}$ and $\mathbf{M}$ are symmetric, we obtain

$$s_i\mathbf{f}_{ti}^T\mathbf{u}_r = \mathbf{u}_{ti}^T\mathbf{f}_r \tag{7}$$

which is an application of the Betti reciprocal theorem. Let us now decompose $\mathbf{u}_{ti}$ into a vector that coincides with $\bar{\mathbf{u}}_M$ at the measurement points and a deviation whose restriction to the M points is denoted $\bar{\mathbf{e}}_i$. Observing that $\mathbf{f}_r$ has nonzero components at the M points only, we obtain

$$s_i\mathbf{f}_{ti}^T\mathbf{u}_r = \bar{\mathbf{u}}_M^T\bar{\mathbf{f}}_r + \bar{\mathbf{e}}_i^T\bar{\mathbf{f}}_r \tag{8}$$

where $\bar{\mathbf{f}}_r$ is the restriction of $\mathbf{f}_r$ to the M points. The load factor s_i may now be determined such that the deviation $\bar{\mathbf{e}}_i$ becomes orthogonal to the reference load, i.e.,

$$s_i = \frac{\bar{\mathbf{u}}_M^T\bar{\mathbf{f}}_r}{\mathbf{f}_{ti}^T\mathbf{u}_r}. \tag{9}$$

Note that the numerator in (9) is a constant and thus needs to be calculated once only.

Hence, the reciprocal theorem Eq. (7) allows us to calculate load factors s_i for a large number of trial load cases, such that the deviations from measurement data are minimized in the implied manner, without actually solving (6). In case the trial loads $\mathbf{f}_{ti}$ have been normalized with respect to some common value, the load factors for various trial loads are directly comparable and thus immediately reveal the required magnitude.

4 Structure Modification

By nature the load identification problem has no unique solution, which means that further information has to be supplied in order to identify the correct load case. Typically, the location of the load is assumed to be known and the problem then reduces to determination of the load magnitude. In the previous section it was shown how the magnitudes s_i for a large number of trial load cases could be evaluated without actually evaluating the cases in terms of structural responses. Having identified two or several load cases that produce structural responses that conform to the same measured data, one is faced with the problem of choosing between the various cases. The most obvious and straightforward way to accomplish this is probably to increase the number of measurement points or to change their positions. In this section, however, we shall investigate the possibility to modify the structure itself, while keeping the transducers fixed.

4.1 A Minimization Problem. Assume that we have found n trial load cases, each of which results in responses that conform to the same measured data. Let us denote by $\bar{\mathbf{u}}_{ti}$ the response vector restricted to the transducer degrees-of-freedom for the ith case ($i = 1, 2, \ldots, n$). Presumably the quantities

$$\epsilon_i = \|\bar{\mathbf{u}}_M - \bar{\mathbf{u}}_{ti}\|_2 \quad i = 1, 2, \ldots, n \tag{10}$$

where $\|\ \|_2$ denotes the Euclidean vector norm, are all small or otherwise some of the load cases would not have been considered as possible solutions. Estimates of modeling and measurement errors may be used to determine a suitable threshold value of ϵ_i; the load cases considered here all yield values below this threshold. It then follows that the values

$$\epsilon_{ij} = \|\bar{\mathbf{u}}_{tj} - \bar{\mathbf{u}}_{ti}\|_2 \quad i, j = 1, 2, \ldots, n \tag{11}$$

are small as well; i.e., the respective responses in each measured degree-of-freedom are nearly equal. Our mission is then to change the structure such that the values ϵ_{ij} increase as much as possible. If we succeed to accomplish this, some, possibly all, estimated trial force magnitudes must change in order to keep ϵ_i of (10) small. Thus, provided that the structure modification does not affect the exciting force sought for, load cases for which the magnitude significantly changes may be discarded.

One common way to compare two vectors, ignoring the respective magnitudes and focusing on the represented shapes only, is by means of the Modal Assurance Criterion; see, e.g , Allemang and Brown (1982) which is evaluated through a so-called MAC-number. For a pair of vectors, say $\bar{\mathbf{u}}_{ti}$ and $\bar{\mathbf{u}}_{tj}$, this number is given by

$$\mathrm{MAC}_{ij} = \frac{(\bar{\mathbf{u}}_{ti}^T\bar{\mathbf{u}}_{tj})^2}{(\bar{\mathbf{u}}_{ti}^T\bar{\mathbf{u}}_{ti})(\bar{\mathbf{u}}_{tj}^T\bar{\mathbf{u}}_{tj})}. \tag{12}$$

Inspecting the right-hand side of (12), we note that the MAC-number may be understood as the squared cosine of the angle between the two vectors. However, it can also be shown (Möller and Friberg, 1998) that MAC_{ij}, apart from a constant, is proportional to $-\epsilon_{ij}$ of (11). Hence, we expect the MAC-numbers, for each possible pair of vectors $\bar{\mathbf{u}}_{ti}$ and $\bar{\mathbf{u}}_{tj}$, to be high, i.e., close to unity, but search for values close to zero, that is, response vectors that are as orthogonal to each other as possible. Let $\mathbf{M}_{\mathrm{MAC}}$ denote a matrix with MAC-numbers for each pair of vectors; the element in row i and column j pertains to $\bar{\mathbf{u}}_{ti}$ and $\bar{\mathbf{u}}_{tj}$, i.e.,

$$[\mathbf{M}_{\mathrm{MAC}}]_{ij} = \mathrm{MAC}_{ij}. \tag{13}$$

Furthermore, let $\mathbf{I}$ denote the identity matrix of order n and define

$$\mathbf{A} = \mathbf{M}_{\mathrm{MAC}} - \mathbf{I} \tag{14}$$

Our problem may now be expressed as a minimization problem, viz. minimize

$$\Pi = \max\{[\mathbf{A}]_{ij}\} \tag{15}$$

where $\max\{[\mathbf{A}]_{ij}\}$ denotes the largest element of $\mathbf{A}$. Note that $\mathbf{A}$ has zero diagonal and that the off-diagonal elements by construction are in the interval [0, 1].

4.2 Objective Function Gradient. There are several methods available to solve (15). Most of them, albeit not all, will require us to provide the gradient of Π. Since minimization algorithms that utilize function value evaluations only, typically require significantly many more iterations than gradient-based methods, and an equation system has to be solved in each iteration in order to calculate the objective function (cf. Eqs. (6), and (12)–(15)), we have chosen to use a method of the latter type. However, much of the computational advantage is lost if the gradient has to be evaluated numerically, so in this section we derive an explicit expression for it.

The kth element of the gradient vector is given by

$$[\nabla\Pi]_k = \frac{\partial}{\partial d_k}\mathrm{MAC}_{ij} \tag{16}$$

where d_k is the kth design variable, affecting the structure, and MAC_{ij}, $i \neq j$, is the element in the ith row and jth column of the matrix $\mathbf{A}$. By the chain rule we have

Downloaded 04 May 2010 to 171.66.16.27. Redistribution subject to ASME license or copyright; see http://www.asme.org/terms/Terms_Use.cfm

$$\frac{\partial}{\partial d_k}\mathrm{MAC}_{ij} = \sum_m \left\{ \frac{\partial \mathrm{MAC}_{ij}}{\partial (\bar{\mathbf{u}}_{ti})_m} \frac{\partial (\bar{\mathbf{u}}_{ti})_m}{\partial d_k} + \frac{\partial \mathrm{MAC}_{ij}}{\partial (\bar{\mathbf{u}}_{tj})_m} \frac{\partial (\bar{\mathbf{u}}_{tj})_m}{\partial d_k} \right\} \quad (17)$$

where $(\bar{\mathbf{u}}_{ti})_m$ and $(\bar{\mathbf{u}}_{tj})_m$ are the mth elements of $\bar{\mathbf{u}}_{ti}$ and $\bar{\mathbf{u}}_{tj}$, respectively, and where

$$\frac{\partial \mathrm{MAC}_{ij}}{\partial (\bar{\mathbf{u}}_{ti})_m} = \frac{2\mathrm{MAC}_{ij}}{\bar{\mathbf{u}}_{ti}^T \bar{\mathbf{u}}_{tj}} \left[(\bar{\mathbf{u}}_{tj})_m - (\bar{\mathbf{u}}_{ti})_m \frac{\bar{\mathbf{u}}_{ti}^T \bar{\mathbf{u}}_{tj}}{\bar{\mathbf{u}}_{ti}^T \bar{\mathbf{u}}_{ti}} \right]. \quad (18)$$

The expression for the derivative of MAC_{ij} with respect to the mth component of $\bar{\mathbf{u}}_{tj}$ is obtained analogously.

To complete the derivation, we need the derivatives of the response vectors, since these appear in (17). For brevity, let $\mathbf{f}_a$ and $\mathbf{u}_a$ denote the amplitude of the load and response, respectively; then

$$\frac{\partial \mathbf{f}_a}{\partial d_k} = (\mathbf{K} - \omega_p^2 \mathbf{M}) \frac{\partial \mathbf{u}_a}{\partial d_k} + \left(\frac{\partial}{\partial d_k}\mathbf{K} - \omega_p^2 \frac{\partial}{\partial d_k}\mathbf{M} - 2\omega_p \frac{\partial \omega_p}{\partial d_k}\mathbf{M} \right)\mathbf{u}_a \quad (19)$$

is obtained, cf. (4). Assuming that variation of the design variables does neither perturb the amplitude nor the frequency of the load, we get

$$\frac{\partial \mathbf{u}_a}{\partial d_k} = (\mathbf{K} - \omega_p^2 \mathbf{M})^{-1} \left(\omega_p^2 \frac{\partial}{\partial d_k}\mathbf{M} - \frac{\partial}{\partial d_k}\mathbf{K} \right)\mathbf{u}_a \quad (20)$$

from (19). It is observed that in some applications the load may be caused by the structure itself, e.g., in a revolving machinery, in which case the load amplitude and possibly its frequency in fact may be altered by a design change; in such cases it is not possible to obtain the response derivative by the above procedure, unless the frequency and amplitude derivatives are known (which is not very likely, since by assumption the load itself is unknown).

The matrix derivatives in (20) do of course depend on the choice of design variables, which is the topic of the subsequent section.

4.3 Design Variables and Matrix Derivatives. The easiest way to modify the structure is probably to add, or possibly remove, mass, which will be considered here. Let us henceforth denote the mass matrix of the original structure by $\mathbf{M}_0$ and assume that the mass matrix is affine in the K_d design variables d_i, i.e.,

$$\mathbf{M} = \mathbf{M}_0 + \sum_{i=1}^{K_d} d_i \mathbf{M}_i, \quad (21)$$

where $\mathbf{M}_i$ is the contribution due to a unit change in the ith design variable. Typically, $\mathbf{M}_i$ will correspond to a discrete mass and hence be diagonal with nonzero elements in positions associated with a few translational, and possibly rotational, degrees-of-freedom only. We then have

$$\frac{\partial}{\partial d_k}\mathbf{M} = \mathbf{M}_k \qquad \frac{\partial}{\partial d_k}\mathbf{K} = \mathbf{0} \quad (22)$$

and thus the matrix-by-vector product in the right-hand side of (20) reduces to a few, typically two to six, scalar multiplications and additions only. Furthermore, since the original solution requires us to factorize the matrix $\mathbf{K} - \omega_p^2\mathbf{M}$, the derivative of a response vector according to (20) is evaluated with little extra computational effort.

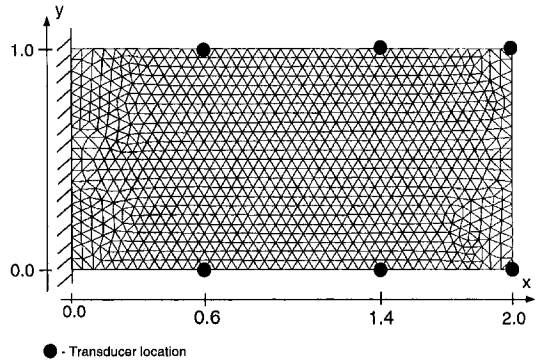

Fig. 1 Geometry and finite element discretization of clamped undamped plate in numerical example; positions of the six transducers are indicated

5 Numerical Experiment

A numerical example is presented in order to illustrate the outlined ideas. We consider a cantilevered plate, Fig. 1, with length, width, and thickness of 2.0 m, 1.0 m, and 0.1 m, respectively. Isotropic material properties with $E = 210$ GPa and $\nu = 0.3$ are used. The mass density is $\rho = 7800$ kg/m^3 meaning that the total weight of the plate is 1560 kg.

A shell element with five degrees-of-freedom in each node is used to discretize the plate; the element may be regarded as a degenerated solid element and is described in detail by Bathe (1996). The mesh, shown in Fig. 1, consists of 468 triangular elements with quadratic basis functions. There are 997 nodes, and 45 of the 4985 nodal variables are prescribed to zero in order to model the clamping. The first ten eigenmodes of the discrete model are described in Table 1.

The role of the unknown load will be played by a transverse harmonic point load

$$P = 0.5 \sin(\omega_p t)\mathrm{MN} \quad \omega_p = 695 \text{ rad/s} \quad (23)$$

which is applied at the upper right corner of the plate, i.e., at $(x, y) = (2.0 \text{ m}, 1.0 \text{ m})$ (cf. Fig. 1 and 2). Note that the frequency of the unknown load is between the second and fourth eigenfrequencies of the structure, and that its third eigenmode is not excited by transverse loads. From Fig. 2 it is conceivable that the frequency of the load is above the first bending and first torsional mode, but below the second bending mode. Six transducer locations are utilized as shown in Fig. 1; their positions and the calculated vertical deflections are given in Table 2.

The reference load case $(\mathbf{u}_r, \mathbf{f}_r)$, defined in Section 3.1, was computed and as trial loads $\mathbf{f}_{ti}$ we chose vertical unit point forces 0.2 m apart along the lines $y = 0.0$ m, $y = 0.5$ m, and $y = 1.0$ m. Subsequently, the respective required magnitudes s_i of those loads were calculated according to (9). Trial load case deflections were solved for, with the cases sorted according to ascending load magnitude; this process was terminated once four cases with $\epsilon_i < 3 \times 10^{-3}$ (cf. (10)) had been found. The load cases so identified are shown in Table 3.

Table 1 Eigenmodes of discrete plate in Fig. 1

Mode	ω [rad/s]	f [Hz]	Comment
1	134.37	21.386	1st bending
2	559.25	89.007	1st torsion
3	797.79	126.97	1st in-plane
4	829.44	132.01	2nd bending
5	1757.2	279.67	2nd in-plane
6	1806.0	287.43	2nd torsion
7	2288.0	364.15	3rd bending
8	2747.0	437.20	3rd in-plane
9	3421.1	544.48	3rd torsion
10	3511.2	558.82	lateral bending

Downloaded 04 May 2010 to 171.66.16.27. Redistribution subject to ASME license or copyright; see http://www.asme.org/terms/Terms_Use.cfm

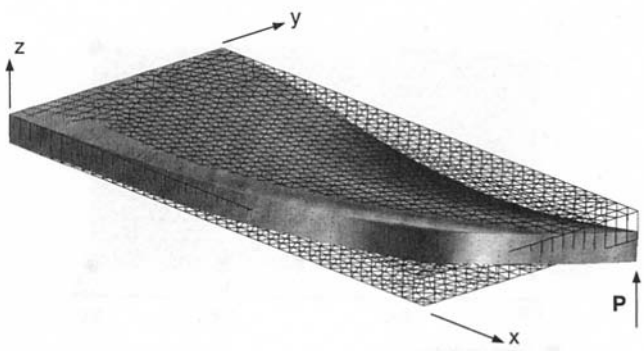

Fig. 2 Deflection of plate due to a harmonic point load (to be identified). Note that the load is π radians out of phase with the first bending and the first torsional eigenmode.

The MAC-matrix, see (12) and (13), for the considered four load cases became

$$\mathbf{M}_{\mathrm{MAC}} = \begin{bmatrix} 1.000 & 0.942 & 0.864 & 0.831 \\ 0.942 & 1.000 & 0.889 & 0.765 \\ 0.864 & 0.889 & 1.000 & 0.934 \\ 0.831 & 0.765 & 0.934 & 1.000 \end{bmatrix} \tag{24}$$

which shows that the respective deflections are well correlated at the measurement points. At this stage, 30 design variables were introduced, viz. discrete point masses 0.2 m apart along the lines $y = 0.0$ m, $y = 0.5$ m, and $y = 1.0$ m. Each variable was normalized to 100 kg of mass and constrained to be in the interval [0.0, 1.0]. For reasons explained in Section 4.2, we prefer to solve (15) with a gradient based minimization method; to this end we use sequential quadratic programming as implemented in the software package IDESIGN, (see Arora, 1989). Naturally, in a practical situation with physical masses it is hardly feasible to use that many discrete masses, but from calculated gradients during the optimization, one may determine the variables that have the greatest impact on the result. In this manner it was found that the masses in the three points $(x, y) = (1.6$ m, 0.0 m), $(x, y) = (1.8$ m, 0.0 m) and $(x, y) = (2.0$ m, 0.0 m) affected the result the most. Performing the optimization with the corresponding three variables only, we obtained the masses 100 kg, 100 kg, and 4.26 kg at the respective locations, and the final MAC-matrix became

$$\mathbf{M}_{\mathrm{MAC}} = \begin{bmatrix} 1.000 & 0.749 & 0.606 & 0.372 \\ 0.749 & 1.000 & 0.451 & 0.062 \\ 0.606 & 0.451 & 1.000 & 0.605 \\ 0.372 & 0.062 & 0.605 & 1.000 \end{bmatrix}. \tag{25}$$

Hence, compared to the initial state, the deflections of the respective trial load cases are now much better separated (cf. (24)) and thus in a physical experiment these three masses could preferably be used.

In order to check the actual results, new trial load magnitudes were calculated so as to fit the respective deflections to the newly obtained "measurement" data, and the results are shown in the last column of Table 3. It is readily seen that for three of the loads the required magnitudes change dramatically, while in the fourth case (i.e., the load searched for) the originally determined magnitude does not change at all. Thus, it should be possible to discard all but one of the trial loads as a possible solution. Note that in a practical situation with physically added masses, this conclusion relies on the assumption, as mentioned earlier, that the structure modification does not alter the mechanism generating the unknown load.

Table 2 Transducer locations and "measured" z-displacements of plate in Fig. 2; the locations are also indicated in Fig. 1

Location		
x-coord. [m]	y-coord. [m]	Displ. [mm]
0.6	0.0	1.376
1.4	0.0	7.358
2.0	0.0	15.69
0.6	1.0	−8.428
1.4	1.0	−15.32
2.0	1.0	−7.675

Table 3 Locations and magnitudes of trial point loads. "Initial" and "Final" refer to the original and modified structures, respectively

Location [m]		Magnitude [MN]	
x-coord.	y-coord.	Initial	Final
2.0	1.0	0.5000	0.5000
1.2	0.0	−0.7566	−0.0899
1.6	0.0	−0.3827	0.1596
1.6	1.0	0.2791	−0.0377

6 Concluding Remarks

A novel approach to the load identification problem in structural dynamics has been described. As opposed to most previous works on the problem, we focus on the case where not only the magnitude, but also the location of the load is unknown. It is shown how the Betti reciprocal theorem may be used to estimate the load magnitude for an assumed spatial load shape so as to best fit measured data. This procedure involves only little computational effort which means that a large number of trial loads with different positions may systematically be investigated. Those with unreasonable magnitude from a physical point of view, can then be dispensed with at an early stage.

When several cases of loads, each reproducing the same original set of measurement data to within some threshold, have been identified, further measurements are needed to distinguish between the possible cases. Here we have suggested that the transducers remain fixed, but the structure be modified prior to new measurements. To this end a minimization problem, with added discrete masses as design variables, is formulated. By minimizing off-diagonal elements in a matrix that contains the MAC-numbers for the deflections caused by the previously identified load cases, the pertinent parts of the responses are separated at the measurement locations. The reason is that the MAC-number may be interpreted, apart from an additive constant, as the negative of a normalized difference between two vectors. One can then determine the best case of loads causing the measured vibrations of the original structure.

Acknowledgment

This study was initiated by Prof. Bengt Å. Åkesson at the Department of Solid Mechanics at Chalmers University of Technology. Financial support was given by the Swedish Research Council for Engineering Sciences (TFR) through their contract 93-622.

References

Allemang, R. J., and Brown, D. L., 1982, "A Correlation Coefficient for Modal Vector Analysis," *Proceedings of the 1st International Modal Analysis Conference,* pp. 110–116.

Arora, J. S., 1989, "IDESIGN User's Manual, Version 3.5.2," Technical Report No. ODL-89.7, Optimal Design Laboratory, College of Engineering, The University of Iowa.

Bateman, V. I., Carne, T. G., and McCall, D. M., 1992, "Force Reconstruction for Impact Tests of an Energy-Absorbing Nose," *International Journal of Analytical and Experimental Modal Analysis,* Vol. 7, pp. 41–50.

Downloaded 04 May 2010 to 171.66.16.27. Redistribution subject to ASME license or copyright; see http://www.asme.org/terms/Terms_Use.cfm

Bathe, K.-J., 1996, *Finite Element Procedures,* Prentice-Hall, Englewood Cliffs, NJ.

Breitfeld, T., 1996, "A Method for Identification of a Set of Optimal Measurement Points for Experimental Modal Analysis," *International Journal of Analytical and Experimental Modal Analysis,* Vol. 11, pp. 1–9.

Bui, H. D., 1994, *Inverse Problems in the Mechanics of Materials: An Introduction,* CRC Press, Boca Raton, FL.

Busby, H. R., and Trujillo, D. M., 1987, "Solution of an Inverse Dynamics Problem Using an Eigenvalue Reduction Technique," *Computers & Structures,* Vol. 25, pp. 109–117.

Busby, H. R., and Trujillo, D. M., 1997, "Optimal Regularization of an Inverse Dynamics Problem," *Computers & Structures,* Vol. 63, pp. 243–248.

Carne, T. G., Bateman, V. I., and Mayes, R. L., 1992, "Force Reconstruction Using a Sum of Weighted Accelerations Technique," *Proceedings of the 10th International Modal Analysis Conference,* pp. 291–298.

Choi, K., and Chang, F.-K., 1996, "Identification of Impact Force and Location Using Distributed Sensors," *AIAA Journal,* Vol. 34, pp. 136–142.

D'Cruz, J., Crisp, J. D. C., and Ryall, T. G., 1991, "Determining a Force Acting on a Plate—An Inverse Problem," *AIAA Journal,* Vol. 29, pp. 464–470.

D'Cruz, J., Crisp, J. D. C., and Ryall, T. G., 1992, "On the Identification of a Harmonic Force on a Viscoelastic Plate From Response Data," ASME JOURNAL OF APPLIED MECHANICS, Vol. 59, pp. 772–729.

Desanghere, G., and Snoeys, R., 1985, "Indirect Identification of Excitation Forces by Modal Coordinate Transformation," *Proceedings of the 3rd International Modal Analysis Conference,* pp. 685–690.

Dobson, B. J., and Rider, E., 1990, "A Review of the Indirect Calculation of Excitation Forces From Measured Structural Response Data," *Proceedings of the Institution of Mechanical Engineers Part C: Journal of Mechanical Engineering Science,* Vol. 204, pp. 69–75.

Fabunmi, J. A., 1986, "Effects of Structural Modes on Vibratory Force Determination by the Pseudoinverse Technique," *AIAA Journal,* Vol. 24, pp. 504–509.

Friswell, M. I., and Mottershead, J. E., 1995, *Finite Element Model Updating in Structural Dynamics,* Kluwer Academic Publishers, Dordrecht, The Netherlands.

Galiullin, A. S., 1984, *Inverse Problems of Dynamics,* Mir Publishers, Moscow.

Hansen, M., and Starkey, J. M., 1990, "On Predicting and Improving the Condition of Modal-Model-Based Indirect Force Measurement Algorithms," *Proceedings of the 8th International Modal Analysis Conference,* pp. 115–120.

Hansen, P. C., 1992, "Analysis of Discrete Ill-Posed Problems by Means of the *L*-Curve," *SIAM Review,* Vol. 34, pp. 561–580.

Hillary, B., and Ewins, D. J., 1984, "The Use of Strain Gauges in Force Determination and Frequency Response Function Measurements," *Proceedings of the 2nd International Modal Analysis Conference,* pp. 627–634.

Imregun, M., and Visser, W. J., 1991, "A Review of Model Updating Techniques," *Shock and Vibration Digest,* Vol. 23, pp. 9–20.

Karlsson, S. E. S., 1996, "Identification of External Structural Loads From Measured Harmonic Responses," *Journal of Sound and Vibration,* Vol. 196, pp. 59–74.

Kompella, M. S., Davis, P., Bernhard, R. J., and Ufford, D. A., 1994, "A Technique to Determine the Number of Incoherent Sources Contributing to the Response of a System," *Mechanical Systems and Signal Processing,* Vol. 8, pp. 363–380.

Law, S. S., and Chan, T. H. T., 1997, "Moving Force Identification: A Time Domain Method," *Journal of Sound and Vibration,* Vol. 201, pp. 1–22.

Lee, H., and Park, Y.-S., 1995, "Error Analysis of Indirect Force Determination and a Regularisation Method to Reduce Force Determination Error," *Mechanical Systems and Signal Processing,* Vol. 9, pp. 615–633.

Menke, W., 1989, *Geophysical Data Analysis: Discrete Inverse Theory,* Academic Press, New York.

Möller, P. W., and Friberg, O., 1998, "An Approach to the Mode Pairing Problem," *Mechanical Systems and Signal Processing,* Vol. 12, pp. 515–523.

Mottershead, J. E., and Friswell, M. I., 1993, "Model Updating in Structural Dynamics: A Survey," *Journal of Sound and Vibration,* Vol. 167, pp. 347–375.

Okubo, N., Tanabe, S., and Tatsuno, T., 1985, "Identification of Forces Generated by a Machine Under Operating Condition," *Proceedings of the 3rd International Modal Analysis Conference,* pp. 920–927.

Shih, C. Y., Zhang, Q., and Allemang, R. J., 1989, "Force Identification by Using Principle and Modal Coordinate Transformation Method," *Vibration Analysis—Techniques and Applications, ASME Publication DE 18-4,* pp. 303–309.

Starkey, J. M., and Merrill, G. L., 1989, "On the Ill-Conditioned Nature of Indirect Force-Measurement Techniques," *International Journal of Analytical and Experimental Modal Analysis,* Vol. 4, pp. 103–108.

Tarantola, A., 1987, *Inverse Problem Theory: Methods for Data Fitting and Model Parameter Estimation,* Elsevier, Amsterdam.

Verhoeven, J., 1988, "Excitation Force Identification of Rotating Machines Using Operational Rotor/Stator Amplitude Data and Analytical Synthesized Transfer Functions," ASME *Journal of Vibration, Acoustics, Stress, and Reliability in Design,* Vol. 110, pp. 307–314.

Zhang, Q., Allemang, R. J., and Brown, D. L., 1990, "Modal Filter: Concept and Applications," *Proceedings of the 8th International Modal Analysis Conference,* pp. 487–496.

Zhang, Q., Wang, W., Allemang, R. J., and Brown, D. L., 1988, "Prediction of Mass Modification for Desired Natural Frequencies," *Proceedings of the 6th International Modal Analysis Conference,* pp. 1026–1032.

Downloaded 04 May 2010 to 171.66.16.27. Redistribution subject to ASME license or copyright; see http://www.asme.org/terms/Terms_Use.cfm

The Modal Formulation and Adaptive-Passive Control of the Nonself-Adjoint One-Dimensional Acoustic System With a Mass-Spring Termination

V. Jayachandran
Graduate Competitive Fellow,
Department of Mechanical Engineering,
University of Delaware,
Newark, DE 19716
Student Mem. ASME

J. Q. Sun
Associate Professor,
Department of Mechanical Engineering,
University of Delaware,
Newark, DE 19716
Mem. ASME

This paper investigates the use of mass-spring type of impedances as absorbing elements for interior noise control. The general modal formulation for a one-dimensional acoustic system terminated by a spring-supported piston is presented. The boundary value problem has a nonself-adjoint operator which renders the mode functions unorthogonal. This is overcome by defining an associated self-adjoint operator in Hilbert space and using an operator-theoretic formulation of the problem. Orthogonal mode functions and an expansion theorem are presented which can be used to construct a series solution for the forced response. A numerical study is performed for the case of single frequency excitation in which the impedance parameters are optimized by minimizing the cost function. The results from the numerical simulations indicate the feasibility of interior noise control using tunable mechanical impedances, and provide guidelines and restrictions in designing such a system.

1 Introduction

The control of low frequency interior noise in aircraft and automobiles is an important problem that has been the focus of extensive research in the last two decades (Tichy, 1991; Nelson and Elliott, 1992). The application of active absorption methods towards such ends has received considerable attention in the recent past. The direct surface impedance control of speakers to produce sound absorbing surfaces has been studied in Furstoss et al. (1997), Radcliffe and Gogate (1995), and Darlington and Avis (1996). Wu et al. (1993) have used actively absorbing coatings for echo minimization. The active control of the reflection coefficient of speakers has been investigated in Guicking and Karcher (1984); and Meynial (1996). A method for active enhancement of passively absorptive surfaces has been developed in Marc et al. (1996) and Beyene and Burdisso (1997).

The analytical and numerical study of the impedance conditions in active absorption systems has been performed by some researchers in Nelson and Elliott (1992), Lacour et al. (1997), and Jayachandran and Sun (1998). They have shown that under optimal conditions, the acoustic impedance at the secondary sources is purely imaginary. Hence, there is no net loss of power at the interface of the secondary sources and the acoustic medium, and sound level reduction is achieved by unloading the primary noise sources (Nelson and Elliott, 1992; Jayachandran and Sun, 1998; Swanson, 1988). The disadvantage of using active sources for global control is that if the control solution is suboptimal, it can actually cause the sound level to go up. Furthermore, active sources need to be actuated and hence, have an energy requirement. Finally, the control algorithm and hardware are quite complex, and there are always concerns regarding stability in such systems.

Adaptive-passive techniques for sound absorption have been studied by some researchers and promise to be a viable alternative to active control schemes, especially over a relatively narrow range of frequencies. Passive elements do not inject power into the system and hence, cannot cause instability. Rather, they achieve sound level reductions by acting as energy sinks and/or by shifting the resonance frequencies of a system. They are fail-safe and reliable. Mechanically, an acoustic absorptive element can be modeled as a piston supported by a spring and a damper. In active noise control systems that use velocity sources as control elements, the impedance condition at the control sources is mechanically equivalent to pure damping (refer to Appendix A for the proof). The purely imaginary nature of the optimal impedance (Nelson and Elliott, 1992; Lacour et al., 1997; Jayachandran and Sun, 1998) implies that the presence of *real* mechanical damping in the support structure of a passive absorptive element will make its performance suboptimal. In the search for optimal impedance conditions which are passively realizable, we restrict our study to mass-spring type of elements.

The use of mass-spring type of absorptive elements for attenuation of interior noise has not been studied extensively. In the 1-D case, a tunable Helmholtz resonator mounted on the side wall of a duct is the closest example of such an application and that too has been investigated only for the case of single frequency excitation. Some recent studies in this area are reported in Matsuhisa et al. (1992) and Bedout et al. (1997). Note that the presence of the Helmholtz resonator on the side wall does not affect the modal behavior of the acoustic medium in the duct. However, if mass-spring elements are mounted on the walls of an acoustically excited enclosure, they will modify the modal behavior of the system. In the one dimensional situation, this would correspond to a duct terminated by a spring-supported piston. To the knowledge of the authors, this type of problem has not been studied extensively in the past. Fahy and Schofield (1980) and Doria (1995) have studied the problem of attenuation of noise in an enclosure using wall-mounted reso-

Contributed by the Applied Mechanics Division of THE AMERICAN SOCIETY OF MECHANICAL ENGINEERS for publication in the ASME JOURNAL OF APPLIED MECHANICS.

Discussion on the paper should be addressed to the Technical Editor, Professor Lewis T. Wheeler, Department of Mechanical Engineering, University of Houston, Houston, TX 77204-4792, and will be accepted until four months after final publication of the paper itself in the ASME JOURNAL OF APPLIED MECHANICS.

Manuscript received by the ASME Applied Mechanics Division, Dec. 19, 1997, final revision, Sept. 25, 1998. Associate Technical Editor: R. C. Benson.

 Copyright © 1999 by ASME

Downloaded 04 May 2010 to 171.66.16.27. Redistribution subject to ASME license or copyright; see http://www.asme.org/terms/Terms_Use.cfm

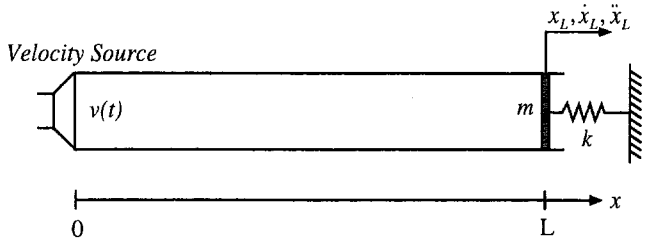

Fig. 1 The one-dimensional duct with a velocity source and an absorbing impedance termination

nators. These studies provide practical guidelines for design and placement of the resonators for bringing down the noise level at a specific enclosure resonance. However, these studies treat the resonators as coupled volume velocity sources. In another interesting study, Kuntz et al. (1991) have developed and tested the use of resonators for cabin tone level reduction in propfan-powered aircraft. In this work, the resonators are used for increasing the sidewall transmission loss for noise attenuation. Martin and Bodrero (1997) have studied the optimization of impedance locations on the walls of a 3-D enclosure for maximum noise attenuation. However, they do not look at tunable impedances and rather concentrate on optimal placement of given impedance patches.

In this paper, we present an analytical model of a one-dimensional acoustic system terminated by a mass-spring type of absorptive element. Such an element modifies the modal behavior of the system. Hence, a modal model is developed to obtain the acoustic response of the system. The modal solution is intuitive to interpret and provides insight into the physics of the problem. The boundary value problem studied in this paper contains a nonself-adjoint operator which renders the mode functions non-orthogonal. Some researchers have studied the case with a damped end condition, which has a different non-self-adjoint operator (Hull et al., 1990; Hull et al., 1991; Hull and Radcliffe, 1992; Hull, 1994; Singh et al., 1989; Prater and Singh, 1990). Yang et al. have presented solution techniques for non-self-adjoint distributed dynamic systems with general boundary conditions, in terms of transfer functions as well as eigenfunction expansions (Yang and Tan, 1992; Yang, 1996; Yang and Wu, 1997).

The first part of this paper provides a modal modeling study of an acoustic duct whose end is subjected to inertial and elastic loading without damping. The approach is based on a mathematical paper by Fulton (1977). The modeling process is described in detail and then specialized to the problem analyzed in the paper. The analysis is extendable to mathematically analogous problems, e.g., the longitudinal vibration of beams loaded at their ends by tuned stiffness and inertial elements.

The second part of this paper present results from a numerical study that investigates the use of tunable mass-spring elements for sound reduction in a duct. The problem studied is that of single-frequency excitation; however, the model presented in this paper can be used for any type of periodic excitation. The remainder of the paper is outlined as follows. In Section 2, we state the problem. In Section 3, we present the mathematical theory for solving the boundary value problem, discuss briefly the impedance optimization and the extension of the theory to analogous problems. In Section 4, we present a numerical study in which the impedance parameters are optimized by minimizing the sound pressure level in a duct under single frequency excitation. The paper is concluded in Section 5.

2 Mathematical Modeling

Consider a one dimensional acoustic problem in a finite duct as shown in Fig. 1. The primary noise field is caused by a velocity source of amplitude $v(t)$ located at one end of the duct, and an interior acoustic source distribution, $q_{\text{vol}}(x, t)$. The duct is terminated by a mechanical impedance in the form of a piston of mass, m, with surface area, A, supported by a spring of stiffness, k. The acoustic pressure in the duct is governed by the wave equation. The left hand end ($x = 0$) is governed by an inhomogeneous Neumann boundary condition. The right hand end ($x = L$) is governed by a mixed type homogenous Robin boundary condition obtained from dynamic balance and momentum conservation (refer to Appendix A). The governing equation and boundary conditions for the acoustic pressure, $u(x, t)$, are

$$u'' - \frac{1}{c_o^2}\ddot{u} = -\rho_o \dot{q}_{\text{vol}}, \tag{1}$$

$$u'(0, t) = -\rho_o \dot{v},$$

$$\frac{m}{\rho_o}u'(L, t) - Au(L, t) + \frac{k}{\rho_o}\int_{-\infty}^{t}\int_{-\infty}^{t} u'(L, t)dtdt = 0, \tag{2}$$

where c_o is the speed of sound, ρ_o is the density of the air, u' represents a spatial derivative and $\dot{u}$ represents a temporal derivative. Time integrations are performed from $t = -\infty$ since we are interested in looking at steady state behavior in the presence of a periodic excitation. In order to homogenize the first boundary condition, we introduce a new variable q, and a particular solution, u_p, such that $u(x, t) = -\rho_o u_p(x)\dot{v} + q(x, t)$ and the particular solution satisfies

$$u_p'(0) = 1,$$

$$u_p'(L) = u_p(L) = 0. \tag{3}$$

The new variable, q, is now governed by the following equation and boundary conditions

$$q'' - \frac{1}{c_o^2}\ddot{q} = \rho_o u_p''\dot{v} - \frac{\rho_o}{c_o^2}u_p\frac{\partial^3 v}{\partial t^3} - \rho_o \dot{q}_{\text{vol}}, \tag{4}$$

$$q'(0, t) = 0,$$

$$\frac{m}{\rho_o}q'(L, t) - Aq(L, t) + \frac{k}{\rho_o}\int_{-\infty}^{t}\int_{-\infty}^{t} q'(L, t)dtdt = 0. \tag{5}$$

The choice of the particular solution is postponed till later. The next section describes in detail the process of obtaining the modal solution for the acoustic pressure in the duct. For the sake of simplicity, the subsequent analysis will assume that the primary noise is caused by the velocity source alone, i.e., $q_{\text{vol}}(x, t) = 0$.

3 Modal Solution Technique

The homogeneous boundary conditions in Eq. (5) motivate us to look for an eigenvalue problem in the spatial domain and to obtain a series solution for the forced response. If the series solution is constructed using orthogonal eigenfunctions, it greatly simplifies numerical computations.

To obtain such a solution, we take a Fourier transform of the above system of equations and solve the resulting problem in the frequency domain. Hence, we have

$$\hat{q}'' + \kappa^2\hat{q} = jk c_o\rho_o\hat{v}[u_p\kappa^2 + u_p''], \tag{6}$$

$$\hat{q}'(0, \kappa) = 0,$$

$$(K - M\kappa^2)\hat{q}'(L, \kappa) = \kappa^2\hat{q}(L, \kappa), \tag{7}$$

where $\kappa = (\omega/c_o)$, $M = (m/\rho_o A)$, $K = (k/\rho_o A c_o^2)$, and $\hat{q}(x, \kappa)$ and $\hat{v}(\kappa)$ are the Fourier transforms of $q(x, t)$ and $v(t)$, respectively. In order to obtain the solution to the above problem, we must first solve the unforced problem to obtain eigenfunctions and then build up the forced response on the basis of these eigenfunctions. The eigenvalue problem defined

Downloaded 04 May 2010 to 171.66.16.27. Redistribution subject to ASME license or copyright; see http://www.asme.org/terms/Terms_Use.cfm

by Eqs. (6) and (7) differs from the Sturm-Liouville form due to the presence of the eigenparameter in the second boundary condition. It can be shown that the eigenfunctions are not orthogonal and that the convergence of a series solution in terms of these eigenfunctions cannot be guaranteed. Many authors have in the past looked at eigenvalue problems with non-orthogonal eigenfunctions (Churchill, 1942; Morgan, 1953; Bauer, 1953; Walter, 1973; Schneider, 1974; Fulton, 1977; Ibrahim and Sleeman, 1981; Hinton, 1979; Hull et al., 1990; Yang, 1996; Yang and Wu, 1997). The next section contains a brief discussion on a technique obtained from the mathematics literature for deriving the series solution to Eqs. (6) and (7), using eigenfunction expansion techniques.

3.1 Modal Analysis of Two-point Boundary Value Problems with Eigenparameter in the Boundary Conditions. Consider a general form of the above eigenvalue problem (Walter, 1973; Schneider, 1974; Fulton, 1977; Ibrahim and Sleeman, 1981; Hinton, 1979),

$$L(u) = -u'' + gu = \lambda u, \tag{8}$$

$$\cos \alpha u(a) + \sin \alpha u'(a) = 0,$$

$$-(\beta_1 u(b) - \beta_2 u'(b)) = \lambda(\beta_1' u(b) - \beta_2' u'(b)), \tag{9}$$

where, $\alpha \in [0, \pi)$, $\beta_1, \beta_2, \beta_1', \beta_2' \in R$, and $g(x) \in C[a, b]$. Walter (1973) gives this problem an operator-theoretic formulation by associating a self-adjoint operator A with Eq. (8), and then develops an associated eigenfunction expansion. Schneider (1974) takes a different approach and solved the problem using the theory of S-Hermitian boundary value problems. Fulton (1977) carries over the method used by Titchmarsh (1946) to this problem and derives a number of convergence theorems. Fulton's method, as with Walter's formulation, requires that

$$\rho = \begin{vmatrix} \beta_1' & \beta_1 \\ \beta_2' & \beta_2 \end{vmatrix} > 0. \tag{10}$$

It is the approach due to Fulton that we shall utilize in this paper for the modal formulation of the system.

We begin by defining a Hilbert space (Soule, 1968; Mate, 1989) $H = L_2[a, b] \oplus C$ of two-component vectors, where $L_2[a, b]$ represents the space of real-valued square integrable functions on $a \le x \le b$, and C represents the unitary space which consists of all complex scalars. Now, we define the following inner product

$$(F, G) = \int_a^b F_1(x)\bar{G}_1(x)dx + \frac{1}{\rho} F_2\bar{G}_2, \tag{11}$$

for $F = (F_1(x), F_2)^T$, $G = (G_1(x), G_2)^T \in H$. Here, $\bar{G}_1$ represents the complex conjugate of G_1, etc. We also define

$$R_b(u) = \beta_1 u(b) - \beta_2 u'(b),$$

$$R_b'(u) = \beta_1' u(b) - \beta_2' u'(b). \tag{12}$$

Using the above notation, in order to obtain an operator theoretic formulation of the eigenvalue problem, we define an operator

$$A(F) = \begin{pmatrix} -F_1''(x) + g(x)F_1(x) \\ -R_b(F_1) \end{pmatrix} \tag{13}$$

whose domain, D, is defined as

$$D(A) = \left\{ \begin{matrix} F \in H | F_1(x), F_1'(x) \in AC[a, b], L(F_1) \in L_2[a, b], \\ \cos \alpha F_1(a) + \sin \alpha F_1'(a) = 0, F_2 = R_b'(F_1) \end{matrix} \right\}, \tag{14}$$

where $AC[a, b]$ denotes the set of absolutely continuous functions in $[a, b]$. Hence, the eigenvalue problem in Eqs. (8) and (9) can be written as $A(F) = \lambda F$. It can be shown that the bilinear functional associated with this operator is symmetric and that the operator is self-adjoint. Consequently, all the eigenvalues are real and the corresponding eigenfunctions will be orthogonal. To obtain the eigenvalues and eigenfunctions, we construct two solutions $\phi(x, \lambda)$ and $\chi(x, \lambda)$ that satisfy the following conditions

$$\phi(a, \lambda) = \sin \alpha, \phi'(a, \lambda) = -\cos \alpha,$$

$$\chi(b, \lambda) = \beta_2'\lambda + \beta_2, \chi'(b, \lambda) = \beta_1'\lambda + \beta_1, \tag{15}$$

for $\lambda \in C$, and define $\omega(\lambda) = \phi(x, \lambda)\chi'(x, \lambda) - \phi'(x, \lambda)\chi(x, \lambda)$. It is clear that for all $\lambda \in C$, $\chi(x, \lambda)$ satisfies the second boundary condition in Eq. (9). It can be shown that $\omega(\lambda)$ is independent of $x \in [a, b]$. Setting $x = b$, we get

$$\omega(\lambda) = \lambda R_b'(\phi(\lambda)) + R_b(\phi(\lambda)). \tag{16}$$

It can be proved that the zeros of $\omega(\lambda)$ are real and simple. Let λ_n $(n = 1, 2, \ldots,)$ denote these zeros. The eigenelements of A are given by

$$\Phi_n = \begin{pmatrix} \phi(x, \lambda_n) \\ R_b'(\phi(\lambda_n)) \end{pmatrix}. \tag{17}$$

These eigenelements satisfy orthogonality conditions, i.e., $(\Phi_n, \Phi_m) = 0$ for $n \neq m$. The normalized eigenfunctions are given by $\Psi_n = (\Phi_n/\|\Phi_n\|) = \left(\frac{\psi_n}{R_b(\psi_n)}\right)$. It can be shown that $\|\Phi_n\|^2 = (1/\rho)R_b'(\phi(\lambda_n))(\partial\omega/\partial\lambda)(\lambda_n)$.

Now, we present the following expansion theorem: (i) For $F \in H$

$$\|F\|^2 = \sum_{n=1}^{\infty} |c_n(F)|^2, \tag{18}$$

where, $c_n(F) = (F, \Psi_n)$, and (ii) for $F \in D(A)$

$$F = \sum_{n=1}^{\infty} (F, \Psi_n)\Psi_n, \tag{19}$$

the series being absolutely and uniformly convergent in the first component for $x \in [a, b]$ and absolutely convergent in the second component. An important corollary is

$$F_1(x) = \sum_{n=1}^{\infty} \left(\int_a^b F_1\psi_n dx \right) \psi_n(x), \tag{20}$$

with mean square convergence in $[a, b]$ for any $F_1(x) \in L_2[a, b]$. For proofs and detailed analyses, the reader is referred to (Fulton, 1977; Titchmarsh, 1946). These results may now be used to obtain orthogonal eigenfunctions for the 1-D acoustic problem.

3.2 Modal Solution for the One-Dimensional Acoustic Problem with a Mass-Spring Termination. Recall the problem described by Eqs. (6) and (7). Comparing the variables and parameters with those in Section 3.1, we have $\lambda \equiv \kappa^2$, $g = 0$, $a = 0$, $b = L$, $\alpha = (\pi/2)$, $\beta_1 = 0$, $\beta_2 = K$, $\beta_1' = 1$, $\beta_2' = -M$ and $\rho = K$. Hence the solution technique will only work for $K > 0$ which is the case we are interested in. We now define

$$R_b(\hat{q}) = -K\hat{q}'(L),$$

$$R_b'(\hat{q}) = \hat{q}(L) + M\hat{q}'(L), \tag{21}$$

and derive $\phi(x, \lambda) = \cos \sqrt{\lambda}x$. Hence, we get

$$\omega(\lambda) = \lambda \cos \sqrt{\lambda}L + \sqrt{\lambda}(K - M\lambda) \sin \sqrt{\lambda}L. \tag{22}$$

The eigenvalues λ_n, $n = 1, 2, \ldots$, are obtained by solving the

Downloaded 04 May 2010 to 171.66.16.27. Redistribution subject to ASME license or copyright; see http://www.asme.org/terms/Terms_Use.cfm

transcendental equation $\omega(\lambda) = 0$. Now, using $\kappa_n = \sqrt{\lambda_n}$, the eigenfunctions for this problem are obtained as

$$\Phi_n = \begin{pmatrix} \cos \kappa_n x \\ \cos \kappa_n L - M\kappa_n \sin \kappa_n L \end{pmatrix}. \tag{23}$$

We also derive,

$$\|\Phi_n\|^2 = -\frac{\sin \kappa_n L}{\kappa_n} \frac{\partial \omega}{\partial \lambda}(\lambda_n). \tag{24}$$

The normalized eigenfunctions are given by $\Psi_n = (\Phi_n/\|\Phi_n\|)$.

Now, consider the forced vibration problem in Eqs. (6) and (7). In order to construct a series solution, we must expand the dependent variable and forcing function in terms of the orthonormal eigenfunctions. We rewrite the problem as

$$(\kappa^2 - A)\hat{Q} = j\kappa c_o \rho_o \hat{v}\Theta, \tag{25}$$

where

$$\hat{Q} = \begin{Bmatrix} \hat{q}(x) \\ R_b'(\hat{q}) \end{Bmatrix}, \quad \Theta = \begin{Bmatrix} \theta_1(x) \\ \theta_2 \end{Bmatrix} = \begin{Bmatrix} u_p(x)\kappa^2 + u_p''(x) \\ 0 \end{Bmatrix}. \tag{26}$$

Enforcing $\theta_2 = 0$ ensures that Eq. (25) exactly represents the forced response problem under consideration. We now choose a particular solution $u_p = -((L - x)^2/2L)$ and construct the following series solution

$$\hat{Q}(x, \kappa) = \sum_{n=1}^{N} \hat{q}_n(\kappa)\Psi_n. \tag{27}$$

We also expand

$$\Theta = \sum_{n=1}^{N} t_n(\kappa)\Psi_n. \tag{28}$$

Since $\theta_1(x) \in L_2[0, L]$, we are assured of the convergence of the first component of Θ in the above series due to the corollary in Eq. (20), even though $\theta_2 \neq R_b'(\theta_1) \Rightarrow \Theta \notin D(A)$. The coefficients, t_n, are now obtained as

$$t_n(\kappa) = \begin{Bmatrix} -\frac{1}{\|\Phi_n\|}\left(\frac{\kappa^2 L^2}{6} + 1\right), & n = 1, \\ -\frac{1}{\|\Phi_n\| L\kappa_n^3}[L\kappa^2\kappa_n - (\kappa^2 - \kappa_n^2)\sin \kappa_n L], & n > 1. \end{Bmatrix} \tag{29}$$

The problem under consideration can now be written as

$$(\kappa^2 - A)\sum_{n=1}^{N} \hat{q}_n(\kappa)\Psi_n = j\kappa c_o \rho_o \hat{v} \sum_{n=1}^{N} t_n(\kappa)\Psi_n. \tag{30}$$

Due to the orthogonality of the eigenfunctions,

$$\hat{q}_n(\kappa) = j\kappa c_o \rho_o \hat{v} \frac{t_n(\kappa)}{\kappa^2 - \kappa_n^2}. \tag{31}$$

It is shown in Appendix B that the second component of Eq. (30) that corresponds to the boundary condition at $x = L$ is satisfied by the series solution. The solution in the time domain may now be obtained by convolution as

$$Q(x, t) = \rho_o \int_{-\infty}^{\infty} \dot{v}(t - \tau)h(x, \tau)d\tau, \tag{32}$$

where,

$$h(x, t) = \sum_{n=1}^{N} \Psi_n F^{-1}\left\{ \frac{t_n\left(\frac{\omega}{c_o}\right)}{\left(\frac{\omega}{c_o}\right)^2 - \kappa_n^2} \right\}, \tag{33}$$

and F^{-1} represents the inverse Fourier transform. Now, if the excitation signal is harmonic and given by $v(t) = v_o e^{j\gamma t}$, we get

$$Q(x, t) = -j\gamma v_o \rho_o e^{j\gamma t} \int_{-\infty}^{\infty} e^{-j\gamma\tau} h(x, \tau)d\tau, \tag{34}$$

$$= -\left[\sum_{n=1}^{N} \frac{t_n\left(\frac{\gamma}{c_o}\right)}{\left(\frac{\gamma}{c_o}\right)^2 - \kappa_n^2} \Psi_n \right] j\gamma v_o \rho_o e^{j\gamma t}. \tag{35}$$

Similarly, for any periodic $v(t) = \sum_{i=1}^{M} v_i e^{j\gamma_i t}$, the solution is given by

$$Q(x, t) = -\sum_{i=1}^{M} \left[\sum_{n=1}^{N} \frac{t_n\left(\frac{\gamma_i}{c_o}\right)}{\left(\frac{\gamma_i}{c_o}\right)^2 - \kappa_n^2} \Psi_n \right] j\gamma_i v_i \rho_o e^{j\gamma_i t}. \tag{36}$$

The overall pressure solution in the duct may now be obtained by combining the homogeneous and particular solutions. Jayachandran et al. (1998) have shown that constructing the particular solution on the basis of the acoustic eigenfunctions does not affect the numerical accuracy of global performance measures such as the acoustical potential energy of the system. Hence, when the excitation is as given above and when we expand the particular solution in terms of the eigenfunctions, the overall pressure can now be written as

$$u(x, t) = -\sum_{i=1}^{M} \sum_{n=1}^{N} j\gamma_i v_i \rho_o \zeta_n(\gamma_i)\Psi_n e^{j\gamma_i t}, \tag{37}$$

where

$$\zeta_n(\gamma_i) = \frac{t_n\left(\frac{\gamma_i}{c_o}\right)}{\left(\frac{\gamma_i}{c_o}\right)^2 - \kappa_n^2} + d_n, \tag{38}$$

and d_n represent the modal coefficients obtained in expanding the particular solution.

3.3 Impedance Optimization. We define a global measure of the sound pressure level in the duct as

$$J = \frac{1}{T}\int_0^T \int_0^L u\bar{u}dxdt, \tag{39}$$

where T is a time period over which the average is computed. This quantity is proportional to the total acoustical potential energy in the duct and is used as a cost function. For single frequency excitation, $J = J_o$, where

Downloaded 04 May 2010 to 171.66.16.27. Redistribution subject to ASME license or copyright; see http://www.asme.org/terms/Terms_Use.cfm

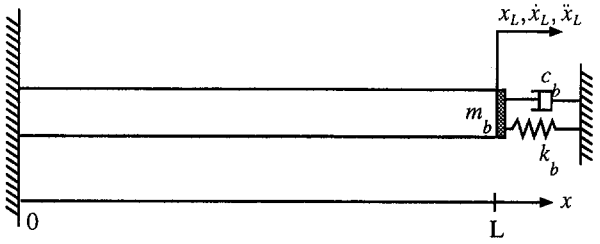

Fig. 2 The beam with a general end impedance condition

$$J_o = \int_0^L u(x)\bar{u}(x)dx. \tag{40}$$

In the case of a general periodic excitation, a suitable cost function may be determined by integrating Eq. (39) with $T = T_L$, where T_L is the lowest common multiple of the time periods of all the superposed harmonic excitations. In this case, after scaling, we obtain the following cost function,

$$J = \sum_{i=1}^{M} \gamma_i^2 v_i^2 \sum_{n=1}^{N} \zeta_n(\gamma_i)^2. \tag{41}$$

Optimal end impedance conditions may be determined by minimizing J with respect to the impedance parameters. This can be done numerically by searching over the inertia and stiffness parameter spaces for the minimum value of J.

The accuracy of the modal model was compared for the single-frequency excitation case with the exact solution and is observed to perform well for most values of piston mass and support stiffness. The proofs in the preceding sections guarantee that a solution built upon the modified eigenfunctions will converge. As the values of k and m are increased, the eigenvalues must be computed to a higher degree of accuracy to ensure the accuracy of the numerically computed dependent variables.

3.4 Extension to Analogous Problems: An Example. As an example of the extension of the above analysis to analogous problems, we now consider the longitudinal vibration of a beam with inertial and elastic loading at its end. Figure 2 shows the schematic of a beam with a general terminal impedance. The governing equation and boundary conditions for the axial displacement, $u(x, t)$, of the beam are given by

$$\ddot{u} - \frac{E}{\rho}u'' = \frac{1}{\rho A}F(x, t) \tag{42}$$

$$u(0, t) = 0,$$

$$AEu'(L, t) = -m_b\ddot{u}(L, t) - c_b\dot{u}(L, t) - k_b u(L, t), \tag{43}$$

where E is the modulus of elasticity, ρ is the density of the bar, A is the area of cross section of the bar, $F(x, t)$ is the distribution of the excitation, and m_b, c_b and k_b represent the inertia, damping and stiffness of the end impedance condition, respectively. Hull (1994) has studied the case when $m_b = k_b = 0$ and derived eigenfunctions and an expansion theorem for the problem. If instead, the end loading has m_b, $k_b \neq 0$ and $c_b = 0$, then the modal solution technique described in previous sections may be used for obtaining a series solution for the vibration of the beam. In that case, following steps similar to the acoustic problem and taking the Fourier transform of the above equations, we finally arrive at the following set of equations

$$\hat{u}'' + \kappa^2\hat{u} = -\frac{1}{EA}\hat{F}(x, \kappa), \tag{44}$$

$$\hat{u}(0) = 0,$$

$$\hat{u}'(L) = (M_b\kappa^2 - K_b)\hat{u}(L), \tag{45}$$

where $\kappa = (\omega/c_o)$, $c_o = \sqrt{(E/\rho)}$, $M_b = (m_b c_o^2/AE)$ and $K_b = (k_b/AE)$. The above problem can now be solved using the theory presented in Section 3.1.

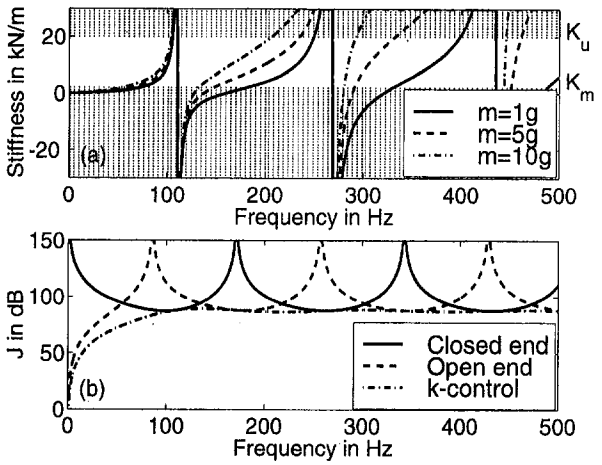

Fig. 3 (*a*) Optimal stiffness curves for different piston masses. Shaded sections show regions that are outside the tuning range. (*b*) *J*-curves for closed, open and optimal stiffness end conditions.

4 Acoustic Control of a 1-D Duct Under Single Frequency Excitation

In this section, we numerically study the effect of the piston impedance on the sound level in the duct for the case of single frequency excitation. The optimal values of stiffness and inertia are determined as a function of excitation frequency by minimizing the cost function, J, defined in Eq. (40). The study is performed using the exact solution since it allows us to look at parameter values which would not be accessible by the modal modeling technique, e.g., negative stiffnesses. The primary source amplitude is taken as unity, and we set $L = 1$ m, $A = 0.01$ m^2.

4.1 Stiffness Control. In this section, the cost function is minimized by optimizing the stiffness. Figure 3(a) shows the optimal stiffness curves for different values of piston mass. It is observed that increasing the inertia makes a bigger portion of the stiffness curves positive, which can be realized passively. Since any practical implementation would impose an upper and lower bound on the tuning range of stiffness, the figure also shows the bounds whose magnitudes are represented by K_u and K_m, respectively. It can be seen that the bounded stiffness curves tend to saturate more at higher frequencies.

Figure 3(b) shows the J-curves corresponding to optimal stiffness conditions as well as open and rigid end conditions. In the latter cases, the duct resonances are clearly visible as peaks. The J-curves for optimal stiffness conditions are always the same irrespective of the piston mass, and the response is seen to be smoothed out uniformly to that of the duct at antiresonances. Figure 4 shows the J-curves for different piston masses when we impose the bounds $[K_m, K_u] = [0, 10]$ kN/m. Increasing the piston mass is observed to improve the attenuation in the low frequency region. However, the upper frequency limit of attenuation is lowered. Next, we observe from Fig. 5 that for a fixed piston mass, increasing K_u raises the upper frequency limit of attenuation. Choosing a suitable combination of m and K_u, we now look at the effect of varying K_m. Figure 6 shows that as K_m is increased, the performance at the lower end of the frequency range starts to suffer. Hence, depending on the piston mass and stiffness bounds, we can define a finite frequency range $[F_m, F_u]$, where the attenuation is effective.

4.2 Inertia Control. Next, we study the sound level when the inertia is optimized by minimizing J. Similar to the previous case, Figs. 7(a) and 7(b) show optimal inertia curves and the

Downloaded 04 May 2010 to 171.66.16.27. Redistribution subject to ASME license or copyright; see http://www.asme.org/terms/Terms_Use.cfm

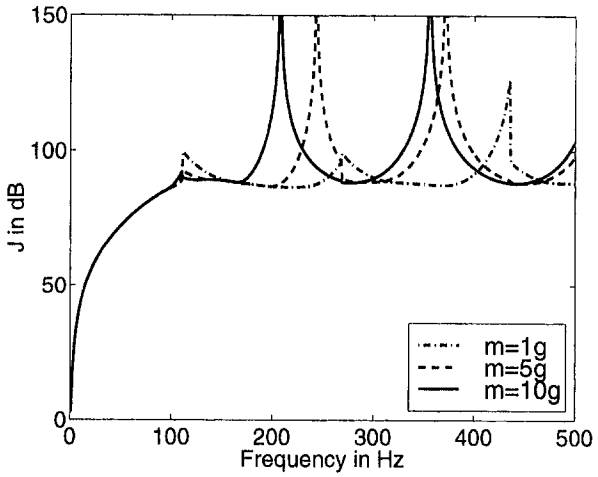

Fig. 4 *J*-curves for different piston masses with K_u = 10 kN/m and K_m = 0 kN/m

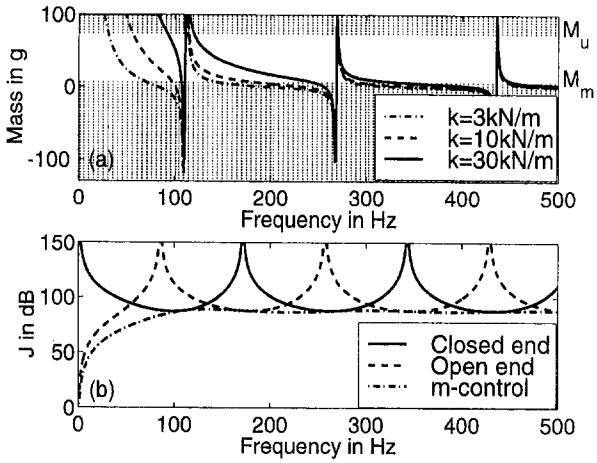

Fig. 7 (*a*) Optimal inertia curves for different support stiffnesses. Shaded sections show regions that are outside the tuning range (*b*) *J*-curves for closed, open and optimal inertia end conditions

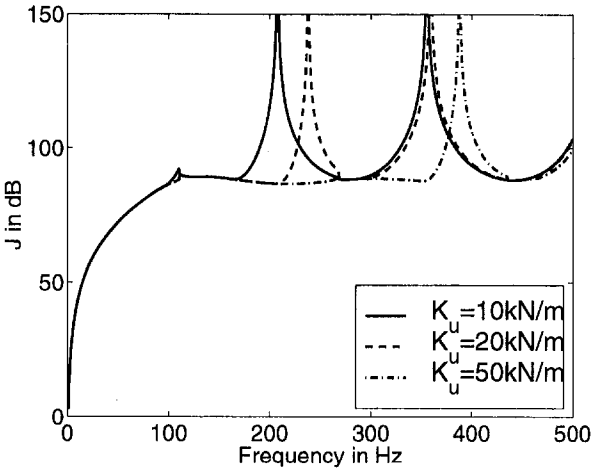

Fig. 5 *J*-curves for m = 10 g, K_m = 0 kN/m and different values of K_u

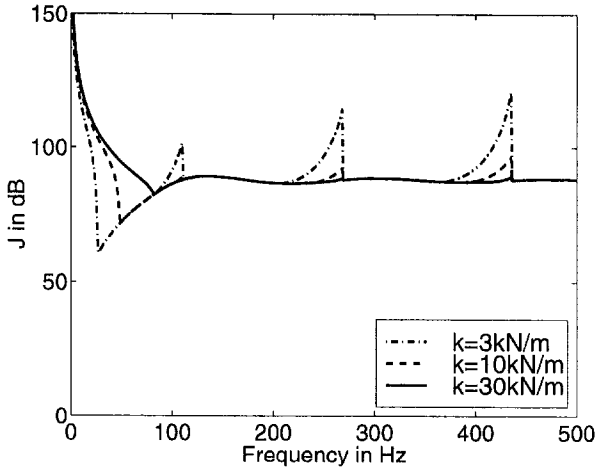

Fig. 8 *J*-curves for different support stiffnesses with M_u = 100 g and M_m = 0 g

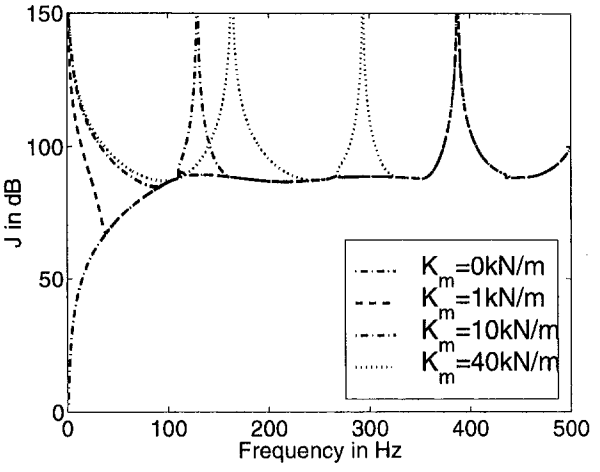

Fig. 6 *J*-curves for m = 10 g, K_u = 50 kN/m and different values of K_m

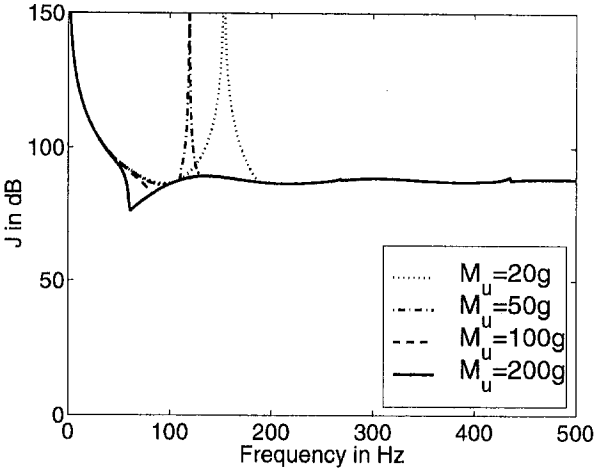

Fig. 9 *J*-curves for k = 30 kN/m, M_m = 0 g and different values of M_u

corresponding *J*-curves, respectively. Also, M_u and M_m represent upper and lower bounds on the tunable inertia. The figure shows that the piston mass tends to saturate at low frequencies. Interestingly, the *J*-curve under inertia control is observed to be identical to that for stiffness control.

Figure 8 shows the *J*-curves for different support stiffnesses when we impose the bounds, $[M_m, M_u] = [0, 10]$ g. Increasing the stiffness is observed to improve the attenuation at higher frequencies. However, it makes the performance at low frequencies worse. Next, we observe from Fig. 9 that when the support

Downloaded 04 May 2010 to 171.66.16.27. Redistribution subject to ASME license or copyright; see http://www.asme.org/terms/Terms_Use.cfm

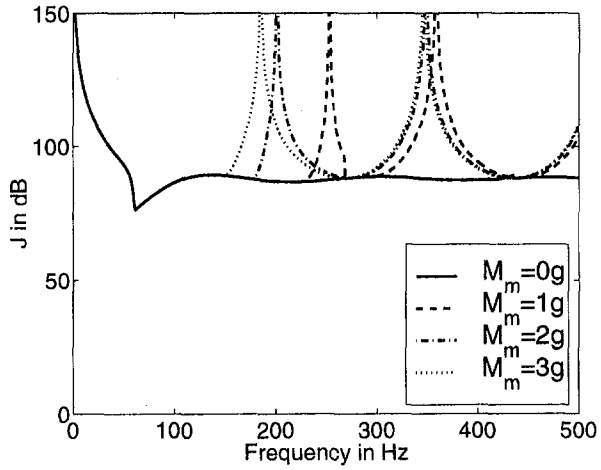

Fig. 10 *J*-curves for k = 30 kN/m, M_u = 200 g and different values of M_m

stiffness is fixed, increasing M_u improves the performance at lower frequencies. Finally, we note from Fig. 10 that increasing M_m lowers the upper frequency bound of attenuation. In fact, even a very small value of M_m = 1 g makes the performance deteriorate significantly. Hence, the inertia must necessarily be tunable from a very small value if attenuation is required over a wide range of frequencies. This clearly indicates that a light-weight tunable piston is desirable for such applications.

4.3 Discussion of Results. The effect of optimal impedance tuning is to cut out the tones and lower the noise level to that of the system at antiresonances. The numerical simulations indicate that for significant attenuation over a large frequency range, the termination impedance must be tunable over a wide range of values. The stiffness and inertia parameters are observed to have opposite trends with respect to the control bandwidth (refer to Table 1), and can be used in a complementary manner. It is also observed that in the presence of reasonable upper and lower bounds for the impedance parameters, the effective frequency range of attenuation can be quite small.

The above discussions suggest that the adaptive-passive method for sound attenuation may be a viable strategy when the excitation frequency is restricted to a small range. A practically implementable tunable absorber may be designed in this case for global noise reduction in the 1-D domain. As compared to active techniques, the algorithm used for computing the command signal would be simpler since it depends only on the excitation frequency and not on the strength of the primary sources. The practical implementation of the tunable impedances and the control algorithms involved are a separate subject for discussion and have not been addressed in this modeling paper.

5 Conclusions

A modal model for a one-dimensional acoustic duct with a mass-spring type of impedance termination has been derived. The mathematical modeling of the system gives rise to a boundary value problem with a nonself-adjoint operator which makes the eigenfunctions unorthogonal. Using an operator-theoretic formulation of the problem and defining an associated self-adjoint operator in Hilbert space, orthogonal mode functions and an expansion theorem are obtained. These are then used for obtaining a series solution for the system response under forced excitation. For the case of periodic excitation, a cost function proportional to the acoustical potential energy in the duct has been derived. This cost function can be minimized for optimal noise attenuation in the duct. The solution approach may also be extended to other analogous problems such as the vibration of longitudinal beams with inertial-elastic end loading.

In the second part of the paper, a numerical study to investigate the practical feasibility of adaptive-passive control using tunable mass-spring type of absorbers has been performed. The one-dimensional case is studied and the results indicate that for attenuation over a broad frequency range, the absorber parameters must be tunable over a very large range. On the other hand, if attenuation is desired only for a narrow operating frequency range, it may be possible to design a tunable absorber which is practically implementable. The present study has yet to be extended to higher dimensional systems.

Table 1 Relationship between the desired bandwidth and the tuning parameters

Desired Effect	k-control	m-Control
$F_m \downarrow$	$m \uparrow$, $K_m \downarrow$	$k \downarrow$, $M_u \uparrow$
$F_u \uparrow$	$m \downarrow$, $K_u \uparrow$	$k \uparrow$, $M_m \downarrow$

Acknowledgments

This work is supported in part by a grant (CMS-963467) from the National Science Foundation, and a grant from the State of Delaware Research Partnership program and Lord Corporation. We would also like to acknowledge the support for Vijay Jayachandran by the University of Delaware Competitive Fellowship.

References

Bauer, W. F., 1953, "Modified Sturm-Liouville Systems," *Quarterly of Applied Mathematics,* Vol. 11, pp. 273–282.

Bedout, J. M., Franchek, M. A., Bernhard, R. J., and Mongeau, L., 1997, "Adaptive-Passive Noise Control with Self-Tuning Helmholtz Resonators," *Journal of Sound and Vibration,* Vol. 202, No. 1, pp. 109–123.

Beyene, S., and Burdisso, R. A., 1997, "A New Hybrid Passive/Active Noise Absorption System," *Journal of the Acoustical Society of America,* Vol. 101, No. 3, pp. 1512–1515.

Churchill, R. V., 1942, "Expansions in Series of Non-Orthogonal Functions," *American Mathematical Society Bulletin,* Vol. 48, pp. 143–149.

Darlington, P., and Avis, M. R., 1996, "Noise Control in Resonant Sound Fields Using Active Absorbers," *Inter-Noise 96,* Liverpool, England, pp. 1121–1126.

Doria, A., 1995, "Control of Acoustic Vibrations of an Enclosure by Means of Multiple Resonators," *Journal of Sound and Vibration,* Vol. 181, No. 4, pp. 673–685.

Fahy, F. J., and Schofield, C., 1980, "A Note on the Interaction Between a Helmholtz Resonator and an Acoustic Mode of an Enclosure," *Journal of Sound and Vibration,* Vol. 72, No. 3, pp. 365–378.

Fulton, C. T., 1977, "Two-point Boundary Value Problems with Eigenvalue Parameter Contained in the Boundary Conditions," *Proceedings of the Royal Society of Edinburgh,* Vol. 77A, pp. 293–308.

Furstoss, M., Thenail, D., and Galland, M. A., 1997, "Surface Impedance Control for Sound Absorption: Direct and Hybrid Passive/Active Strategies," *Journal of Sound and Vibration,* Vol. 203, No. 2, pp. 219–236.

Guicking, D., and Karcher, K., 1984, "Active Impedance Control for One-Dimensional Sound," ASME *Journal of Vibration, Acoustics, Stress, and Reliability in Design,* Vol. 106, pp. 393–396.

Hinton, D. B., 1979, "An Expansion Theorem for an Eigenvalue Problem with Eigenvalue Parameter in the Boundary Condition," *Quarterly Journal of Mathematics, Oxford Series (2),* Vol. 30, pp. 33–42.

Hull, A. J., 1994, "A Closed Form Solution of a Longitudinal Bar with a Viscous Boundary Condition," *Journal of Sound and Vibration,* Vol. 169, No. 1, pp. 19–28.

Hull, A. J., and Radcliffe, C. J., 1992, "Experimental Verification of the Non-self-Adjoint State Space Duct Model," ASME *Journal of Vibration and Acoustics,* Vol. 114, pp. 404–408.

Hull, A. J., Radcliffe, C. J., and MacCluer, M. R., 1991, "State Estimation of the Nonself-Adjoint Acoustic Duct System," ASME *Journal of Dynamic Systems, Measurement, and Control,* Vol. 113, pp. 122–126.

Hull, A. J., Radcliffe, C. J., Miklavcic, M., and MacCluer, C. R., 1990, "State Space Representation if the Nonself-Adjoint Acoustic Duct System," ASME *Journal of Vibration and Acoustics,* Vol. 112, pp. 483–488.

Ibrahim, R., and Sleeman, B. D., 1981, *Ordinary and Partial Differential Equations: Proceedings of the Sixth Conference held at Dundee, Scotland, March 31–April 4, 1980,* Chapter, "A Regular Left-Definite Eigenvalue Problem with Eigenvalue Parameter in the Boundary Conditions," pp. 158–167, Springer-Verlag, Berlin, New York.

Downloaded 04 May 2010 to 171.66.16.27. Redistribution subject to ASME license or copyright; see http://www.asme.org/terms/Terms_Use.cfm

Jayachandran, V., Hirsch, S. M., and Sun, J. Q., 1998, "On the Numerical Modeling of Interior Sound Fields by the Modal Function Expansion Approach," *Journal of Sound and Vibration,* Vol. 210, No. 2, pp. 243–254.

Jayachandran, V., and Sun, J. Q., 1998, "Impedance Characteristics of Active Interior Noise Control Systems," *Journal of Sound and Vibration,* Vol. 211, No. 4, pp. 716–727.

Kuntz, H. L., Prydz, R. A., Balena, F. J., and Gatineau, R. J., 1991, "Development and Testing of Cabin Sidewall Acoustic Resonators for the Reduction of Cabin Tone Levels in Propfan-Powered Aircraft," *Noise Control Engineering Journal,* Vol. 37, No. 3, pp. 129–142.

Lacour, O., Thenail, D., and Galland, M. A., 1997, "Actively Silencing a Cavity by Acoustic Impedance Changes," *Sixteenth Biennial Conference on Mechanical Vibration and Noise, ASME Design Engineering Technical Conferences,* Sacramento, California.

Marc, F., Denis, T., and Marie-Annick, G., 1996, "Actively Enhanced Porous Layers for Free Field Acoustic Absorption," *3rd ICIM/ECSSM'96,* Lyon, France, pp. 734–739.

Martin, V., and Bodrero, A., 1997, "An Introduction to the Control of Sound Fields by Optimising Impedance Locations on the Wall of an Acoustic Cavity," *Journal of Sound and Vibration,* Vol. 204, No. 2, pp. 331–357.

Mate, L., 1989, *Hilbert Space Methods in Science and Engineering,* IOP Publishing Ltd.

Matsuhisa, H., Ren, B., and Sato, S., 1992, "Semiactive Control of Duct Noise by a Volume-Variable Resonator," *JSME International Journal, Series III,* Vol. 35, No. 2, pp. 223–228.

Meynial, X., 1996, "Active Materials for Application in Room Acoustics," *3rd ICIM/ECSSM'96,* Lyon, France, pp. 968–973.

Morgan, G. W., 1953, "Some Remarks on a Class of Eigenvalue Problems with Special Boundary Conditions," *Quarterly of Applied Mathematics,* Vol. 11, pp. 157–165.

Nelson, P. A., and Elliott, S. J., 1992, *Active Control of Sound,* Academic Press Limited, San Diego, CA.

Prater, G. J., and Singh, R., 1990, "Eigenproblem Formulation, Solution and Interpretation for Non-Proportionally Damped Continuous Beams," *Journal of Sound and Vibration,* Vol. 143, No. 1, pp. 125–142.

Radcliffe, C. J., and Gogate, S. D., 1995, "An Analytical Active Acoustic Sink Controller Model for Wide Band Noise Control Applications," *ASME Annual Winter Meeting,* San Francisco, California.

Schneider, A., 1974, "A Note on Eigenvalue Problems with Eigenparameter in the Boundary Conditions," *Mathematische Zeitschrift,* Vol. 136, pp. 163–167.

Singh, R., Lyons, W. M., and Prater, G. J., 1989, "Complex Eigensolution for Longitudinally Vibrating Bars with a Viscously Damped Boundary," *Journal of Sound and Vibration,* Vol. 133, No. 2, pp. 364–367.

Soule, J. L., 1968, *Linear Operators in Hilbert Spaces,* Gordon and Breach Science Publishers Inc, New York.

Swanson, D. C., 1988, "The Role of Impedance Coupling in Achieving Global Active Attenuation of Noise," *ASME Winter Annual Meeting,* Chicago, Illinois.

Tichy, J., 1991, "Current and Future Issues of Active Noise Control," *Journal of Acoustical Society of Japan (E),* Vol. 12, No. 6, pp. 255–262.

Titchmarsh, E. C., 1946, *Eigenfunction Expansions Associated with Second Order Differential Equations,* Oxford University Press.

Walter, J., 1973, "Regular Eigenvalue Problems with Eigenvalue Parameter in the Boundary Condition," *Mathematische Zeitschrift,* Vol. 133, pp. 301–312.

Wu, Z., Bao, X.-Q., Varadan, V. K., and Varadan, V. V., 1993, "Broadband Active Acoustic Absorbing Coating with an Adaptive Digital Controller," *Journal of Smart Materials and Structures,* Vol. 2, pp. 40–46.

Yang, B., 1996, "Integral Formulas for Nonself-Adjoint Distributed Dynamic Systems," *AIAA Journal,* Vol. 34, No. 10, pp. 2132–2139.

Yang, B., and Tan, C. A., 1992, "Transfer Functions of One-Dimensional Distributed Parameter Systems," ASME JOURNAL OF APPLIED MECHANICS, Vol. 59, No. 4, pp. 1009–1014.

Yang, B., and Wu, X., 1997, "Transient Response of One-Dimensional Distributed Systems: A Closed Form Eigenfunction Expansion Realization," *Journal of Sound and Vibration,* Vol. 208, No. 5, pp. 763–776.

APPENDIX A

In this appendix, we derive the boundary condition at the impedance termination of the duct. We will also compare this condition with the boundary condition in the vicinity of the control sources in active noise control systems.

Consider the right hand end of the duct in Fig. 1. From momentum conservation, we get

$$u'(L, t) = -\rho_o \dot{w}(L, t), \tag{46}$$

where w is the local velocity of the acoustic medium. Now, if we allow the presence of damping of magnitude c in the piston, then from force balance conditions, we get

$$m\ddot{x}_L = Au(L, t) - c\dot{x}_L - kx_L, \tag{47}$$

where x_L defines the motion of the piston. By continuity, we have $w(L, t) = \dot{x}_L$. Hence, from the above two equations, we get the following mixed boundary condition

$$-\frac{m}{\rho_o} u'(L, t) = Au(L, t) + \frac{c}{\rho_o}\int_{-\infty}^{t} u'(L, t)dt + \frac{k}{\rho_o}\int_{-\infty}^{t}\int_{-\infty}^{t} u'(L, t)dtdt, \tag{48}$$

which in the absence of damping gives rise to the second boundary condition in Eq. (2). Now, for the case of single frequency forced excitation, we have $u = u(x)e^{j\omega t}$ and the boundary condition reduces to

$$\left(-\frac{m}{\rho_o}\omega^2 + j\frac{c}{\rho_o}\omega + \frac{k}{\rho_o}\right)u'(L) = A\omega^2 u(L), \tag{49}$$

where ω is the excitation frequency. Setting $\omega = \kappa c_o$ and $C = (c/\rho_o c_o A)$, we get

$$(-M\kappa^2 + jC\kappa + K)u'(L) = \kappa^2 u(L). \tag{50}$$

On the other hand, in case of impedance optimization studies in active noise control systems, the right hand boundary is modeled as a controllable impedance Z. In this case, the boundary condition is

$$\frac{Z}{c_o\rho_o} u'(L) = -j\kappa u(L). \tag{51}$$

If we multiply both sides of the above equation by $j\kappa$ and compare it with Eq. (50), we can see that $Z \equiv (C/A)$, i.e., the impedance condition is equivalent to a massless piston supported by a damper with damping ZA.

APPENDIX B

This appendix proves that the second component of the series solution developed in Section 3.2 actually satisfies the boundary condition. Writing Eq. (30) in explicit form, we get

$$\sum_{n=1}^{\infty}(\kappa^2 - A)\frac{t_n}{\kappa^2 - \kappa_n^2}\begin{pmatrix}\psi_n(x)\\ R_b'(\psi_n)\end{pmatrix} = \sum_{n=1}^{\infty} t_n \begin{pmatrix}\psi_n(x)\\ R_b'(\psi_n)\end{pmatrix}. \tag{52}$$

The second part of the above equation can now be written as

$$\sum_{n=1}^{\infty}\frac{t_n}{\kappa^2 - \kappa_n^2}\{\kappa^2 R_b'(\psi_n) + R_b(\psi_n)\} = \sum_{n=1}^{\infty} t_n R_b'(\psi_n). \tag{53}$$

Using $\psi_n(x) = (\cos \kappa_n x/\|\Phi_n\|)$, and simplifying the above equation, we get

$$\sum_{n=1}^{\infty}\frac{t_n}{\kappa^2 - \kappa_n^2}\frac{1}{\|\Phi_n\|}\{\omega(\lambda_n)\} = 0, \tag{54}$$

which is true since λ_n are the zeros of $\omega(\lambda)$.

Downloaded 04 May 2010 to 171.66.16.27. Redistribution subject to ASME license or copyright; see http://www.asme.org/terms/Terms_Use.cfm

On Dynamic Cycle Collapse of Circular Plates

P. D. Chinh
Institute of Mechanics,
224 Doi can,
Hanoi, Vietnam

The upper bound kinematic method, which is based on a reduced kinematic formulation and involves construction of fictitious elastic moment fields and potential incremental collapse mechanisms, is used to evaluate the dynamic cycle collapse loads for a symmetrically loaded circular plate. The respective nonshakedown curves are constructed. A point load effect is discussed.

1 Introduction

It is known that, in comparison with the plastic limit design for a structure subjected to quasi-static loads, the shakedown design generally is more conservative (Prager, 1948; Symonds and Neal, 1952; Koiter, 1963; Martin, 1975; König, 1987). Moreover, the shakedown analysis applies to the broader class of dynamic problems, which lie outside the reach of the plastic limit analysis (Ceradini, 1980; Pham, 1996). Practical structures are often subjected to certain dynamic fluctuating loads (in particular, the quasi-periodic dynamic ones (Pham, 1992), see also the particular cases in the examples that followed), in addition to the quasi-static ones, because of the actions of the working machines and the environment. Despite it's indispensable role in such important cases, the shakedown theory still has not found widespread applications in engineering practice as those of the plastic limit theory. Our recent works, including this one, aim to bring some contributions toward filling this gap, in particular, we are concerned here with the plates under quasi-periodic dynamic transverse loads.

The loading conditions for some structures may be complex and there may be stress concentrations in certain places (especially for dynamic processes, the stress field may be far from homogeneous). In those cases local plastic deformations appear inevitable, but may not cause global collapse of the whole structure and the shakedown design is required. Shakedown design would not permit repeated plastic deformations, but only a limited amount of local plastic deformations in a few cycles before a residual stress field formed inside a structure so it would response elastically to external loads (between the given limits) afterwards. In the sense of safety, the shakedown analysis would indicate how far a loaded structure is from one of the principal and dangerous collapse modes—the nonshakedown one.

Let $\mathbf{M}^e(\mathbf{x}, t)$ be the fictitious elastic moment response of a plate to the given loads (in assumption of its perfectly elastic behavior), which should be confined to a bounded loading domain $\mathcal{L}$ of the moment fields over S ($\mathbf{x} \in S$ designates a point in the plate's midplane). $\bar{\boldsymbol{\kappa}} \in \mathcal{K}$ is any plastic curvature field over S; $\Delta\boldsymbol{\kappa}(\mathbf{x}) \in C$ is a compatible curvature increment (over a cycle, by the terminology of Koiter (1963)) field.

The reduced upper bound shakedown kinematic theorem (without time integrals) for the plates (Pham, 1997a) can be stated in the generalized variables ($\mathbf{M}^e$, $\bar{\boldsymbol{\kappa}}$, $\Delta\boldsymbol{\kappa}$) as (at $k_s < 1$ the structure can not shake down)

$$k_s^{-1} = \text{Max}\ \{A, I\}, \tag{1}$$

where

$$A = \sup_{\mathbf{M}^e \in \mathcal{L}, \bar{\boldsymbol{\kappa}} \in \mathcal{K}, \mathbf{x} \in V, t, t'} \frac{3[\mathbf{M}^e(\mathbf{x}, t) - \mathbf{M}^e(\mathbf{x}, t')] : \bar{\boldsymbol{\kappa}}(\mathbf{x})}{4D(\bar{\boldsymbol{\kappa}}(\mathbf{x}))}, \tag{2}$$

$$I = \sup_{\mathbf{M}^e \in \mathcal{L}, \Delta\boldsymbol{\kappa} \in C} \frac{\int_S \max_{t_x} \mathbf{M}^e(\mathbf{x}, t_x) : \Delta\boldsymbol{\kappa}(\mathbf{x}) dS}{\int_V D(\Delta\boldsymbol{\kappa}(\mathbf{x})) dS}, \tag{3}$$

where the dissipation function in the case of the isotropic Tresca plate has the particular form

$$D(\boldsymbol{\kappa}) = \tfrac{1}{2} M_Y(|\kappa_1| + |\kappa_2| + |\kappa_1 + \kappa_2|)$$

with κ_1, κ_2 being the principal components of the curvature tensor $\boldsymbol{\kappa}$, and M_Y, the yield moment.

A appears to reflect the alternating plasticity collapse mode, while I represents the incremental collapse one. Formula (3) involves the compatible incremental collapse fields $\Delta\boldsymbol{\kappa}$ like the plastic limit kinematic theorem with (compatible) collapse mechanisms, so the respective kinematic method of limit analysis (Hodge, 1963; Save and Massonnet, 1972; Johnson and Mellor, 1973) can be used there. The particular feature of (3) is that one should maximize the inside-integral expressions over time separately for every point $\mathbf{x} \in S$ and given $\Delta\boldsymbol{\kappa}$ before taking the operations of integration and supremum. Note that in difference with $\Delta\boldsymbol{\kappa}(\mathbf{x})$ in (3), the field $\bar{\boldsymbol{\kappa}}(\mathbf{x})$ in (2) is not restricted to compatibility.

2 Axisymmetric Bending of a Circular Plate

For axisymmetric bending of an isotropic circular plate of radius a ($0 \le r \le a$), formula (3) becomes

$$A = \frac{3}{4} \sup_{M^e \in \mathcal{L}, \bar{\kappa}_r, t, t'} \frac{[M_r^e(r, t) - M_r^e(r, t')]\bar{\kappa}_r + [M_\theta^e(r, t) - M_\theta^e(r, t')]\bar{\kappa}_\theta}{\frac{1}{2} M_Y(|\bar{\kappa}_r| + |\bar{\kappa}_\theta| + |\bar{\kappa}_r + \bar{\kappa}_\theta|)}. \tag{4}$$

For that simple expression, the supremum should be attained at $\bar{\kappa}_r = 0$ or $\bar{\kappa}_r = \pm\infty$, and $\bar{\kappa}_\theta = 0$ or $\bar{\kappa}_\theta = \pm\infty$, so

$$A = \max\ \{A_r, A_\theta\}, \tag{5}$$

$$A_r = \frac{3}{4} \max_{M^e \in \mathcal{L}, r, t, t'} \frac{M_r^e(r, t) - M_r^e(r, t')}{M_Y},$$

$$A_\theta = \frac{3}{4} \max_{M^e \in \mathcal{L}, r, t, t'} \frac{M_\theta^e(r, t) - M_\theta^e(r, t')}{M_Y}, \tag{6}$$

Contributed by the Applied Mechanics Division of THE AMERICAN SOCIETY OF MECHANICAL ENGINEERS for publication in the ASME JOURNAL OF APPLIED MECHANICS.

Discussion on the paper should be addressed to the Technical Editor, Professor Lewis T. Wheeler, Department of Mechanical Engineering, University of Houston, Houston, TX 77204-4792, and will be accepted until four months after final publication of the paper itself in the ASME JOURNAL OF APPLIED MECHANICS.

Manuscript received by the ASME Applied Mechanics Division, Jan. 30, 1998; final revision, May 14, 1998. Associate Technical Editor: R. C. Becker.

 Copyright © 1999 by ASME

Downloaded 04 May 2010 to 171.66.16.27. Redistribution subject to ASME license or copyright; see http://www.asme.org/terms/Terms_Use.cfm

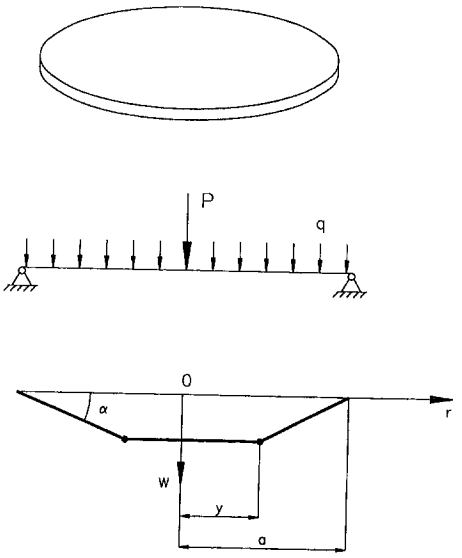

Fig. 1 A loaded simply supported circular plate and a truncated conical incremental collapse mechanism

$$I = \sup_{M^e \in \mathcal{L}, \Delta\kappa \in C} \frac{\int_0^a \max_{t_r} [M_r^e(r, t_r)\Delta\kappa_r(r) + M_\theta^e(r, t_r)\Delta\kappa_\theta(r)]rdr}{\frac{1}{2}M_Y \int_0^a [|\Delta\kappa_r| + |\Delta\kappa_\theta| + |\Delta\kappa_r + \Delta\kappa_\theta|]rdr}. \tag{7}$$

Suppose the plate is simply supported around the edge and subjected to a quasi-periodic dynamic uniformly distributed transverse load (see Fig. 1 with $p \equiv 0$):

$$q(t) = q_0 + q_1 \sin \omega t, \tag{8}$$

where q_0, q_1, and ω are arbitrary quasi-static functions of time, which vary between certain limits

$$q_0^- \le q_0 \le q_0^+, \quad 0 \le q_1 \le q_1^+, \quad 0 \le \omega \le \omega^+ \tag{9}$$

(ω^+ is appropriately smaller than the first natural frequency of the plate), which should determine the load domain $\mathcal{L}$. Note that the frequency ω of a working machine acting upon a structure often increases from 0 to its working value, and can be operated to vary over time.

Without losing generality, presume $q_0^+ \ge |q_0^-|$ (so the potential collapse mechanisms are in the downward (positive) direction). Denote

$$q_0^- = \bar{h} q_0^+ \quad (-1 \le \bar{h} \le 1),$$

$$k^4 = \frac{h\rho}{D_h}\omega^2, \quad (k^+)^4 = \frac{h\rho}{D_h}(\omega^+)^2, \quad D_h = \frac{Eh^3}{12(1-\nu^2)}, \tag{10}$$

where E, ν are the elastic moduli; ρ, the mass density; and h, the thickness of the plate. The parameter $\bar{h}$ indicates the extent of the loading domain $\mathcal{L}$.

Then the fictitious elastic response of the plate to the load (8) can be found from the respective elastic stationary vibration problem

$$M_r^e(r, t) = q_0 \cdot Q_{0r}(r) + q_1 \cdot Q_r(k, r) \sin \omega t,$$
$$M_\theta^e(r, t) = q_0 \cdot Q_{0\theta}(r) + q_1 \cdot Q_\theta(k, r) \sin \omega t, \tag{11}$$

where

$$Q_{0r}(r) = \frac{3+\nu}{16}(a^2 - r^2),$$

$$Q_{0\theta}(r) = \tfrac{1}{16}[(3+\nu)a^2 - (1+3\nu)r^2],$$

$$Q_r(k, r) = \frac{1}{k^3 d}\left[k^2 I_0(ka)J_0(kr) - k^2 J_0(ka)I_0(kr) - \frac{1-\nu}{r} I_0(ka)J_1(kr) + \frac{1-\nu}{r} kJ_0(ka)I_1(kr) - \frac{1-\nu}{a} kI_1(ka)J_0(kr) + \frac{1-\nu}{a} kJ_1(ka)I_0(kr) + \frac{(1-\nu)^2}{ar} I_1(ka)J_1(kr) - \frac{(1-\nu)^2}{ar} J_1(ka)I_1(kr)\right],$$

$$Q_\theta(k, r) = \frac{1}{k^3 d}\left[k\frac{1-\nu}{r} I_0(ka)J_1(kr) - k\frac{1-\nu}{r} J_0(ka)I_1(kr) - \frac{(1-\nu)^2}{ar} I_1(ka)J_1(kr) + \frac{(1-\nu)^2}{ar} J_1(ka)I_1(kr) + \nu k^2 I_0(ka)J_0(kr) - \nu k^2 J_0(ka)I_0(kr) - \frac{(1-\nu)\nu}{a} kI_1(ka)J_0(kr) + \frac{(1-\nu)\nu}{a} kJ_1(ka)I_0(kr)\right],$$

$$d = 2kJ_0(ka)I_0(ka) - \frac{1-\nu}{a} J_0(ka)I_1(ka) - \frac{1-\nu}{a} J_1(ka)I_0(ka).$$

J_0, J_1, I_0, I_1 are Bessel functions.

Substituting (11) into (6) and taking into account (9), we get

$$A_r = \frac{3}{4M_Y} \cdot \sup_{0 \le r \le a, 0 < k \le k^+} [(q_0^+ - q_0^-)|Q_{0r}(r)| + 2q_1^+ |Q_r(k, r)|],$$

$$A_\theta = \frac{3}{4M_Y} \cdot \sup_{0 \le r \le a, 0 < k \le k^+} [(q_0^+ - q_0^-)|Q_{0\theta}(r)| + 2q_1^+ |Q_\theta(k, r)|]. \tag{12}$$

For an evaluation of I from (7), using the result of plastic limit analysis (e.g., Save and Massonnet, 1972; Lubliner, 1990), we take an admissible (compatible) incremental collapse mechanism, which transforms the circular plate into a truncated conical shell with the base angle α and a yield curve around a central circle of radius y ($0 \le y < a$, Fig. 1) ($w(r)$ is the respective deflection of the plate)

$$w(r) = \begin{cases} \alpha(a - y), & 0 \le r < y \\ \alpha(a - r), & y \le r \le a \end{cases} \tag{13}$$

$$\Delta\kappa_r = -\frac{\partial^2 w}{\partial r^2} = \alpha\delta(r - y),$$

$$\Delta\kappa_\theta = -\frac{1}{r}\frac{\partial w}{\partial r} = \begin{cases} 0, & 0 \le r < y \\ \dfrac{\alpha}{r}, & y \le r \le a \end{cases} \tag{14}$$

($\delta(r)$ is Delta Dirac function).

Having substituted (14) into (7) and maximized it over $0 \le y < a$, we get

Downloaded 04 May 2010 to 171.66.16.27. Redistribution subject to ASME license or copyright; see http://www.asme.org/terms/Terms_Use.cfm

$$I = \frac{1}{aM_Y} \cdot \sup_{0 \le y < a, 0 < k \le k^+} \left\{ q_0^+ \left[yQ_{0r}(y) + \int_y^a Q_{0\theta}(r)dr \right] + q_1^+ \left[y|Q_r(k, y)| + \int_y^a |Q_\theta(k, r)|\, dr \right] \right\}$$

$$= \frac{1}{aM_Y} \cdot \sup_{0 \le y < a, 0 < k \le k^+} \left\{ q_0^+ \left[\frac{3 + \nu}{16}(a^3 - y^3) - \frac{1 + 3\nu}{48}(a - y)^3 \right] + q_1^+ \left[y|Q_r(k, y)| + \int_y^a |Q_\theta(k, r)|\, dr \right] \right\}. \quad (15)$$

Numerical results, including those of the examples that follow, indicate that the supremums in (12), (15) (and also in (21), (22)) are always reached at $k = k^+$, if k^+ is smaller than the principal natural frequency of the structure. That fact also supports the engineering common sense that the dynamic loads become increasingly dangerous as their frequency increases (up to the principal natural frequency of the structure), at constant values of loads' amplitudes. The ranges of k that correspond to certain high-frequency intervals (between the structure's natural frequencies) seem to have little practical value and will not be considered here for numerical illustrations.

Now we come to some numerical illustrations of the formulae (1), (5), (12), (15). Take $\nu = 0.25$ and bring in the dimensionless parameters

$$\bar{k} = k^+ a, \ \bar{q}_0 = q_0^+ \frac{a^2}{5.4M_Y}, \quad \bar{q}_1 = q_1^+ \frac{a^2}{5.4M_Y} \quad (16)$$

($\bar{q}_0 = 1$ corresponds to the plastic limit load $q_0^+ = 5.4M_Y/a^2$ for the plate at $q_1^+ = 0$).

Graphics of the nonshakedown curves $k_s = 1$ (i.e., the lower envelope of the curves $A_r = 1$, $A_\theta = 1$, and $I = 1$), above which the plate should fail, are presented in the plane of dimensionless load amplitudes $\bar{q}_0$, $\bar{q}_1$, for $0 \le \bar{q}_1 \le 0.1$, at the frequency parameter limits $\bar{k} = 1.9$, 1.98, 2.03 (Fig. 2), and at the loading range parameters $\bar{h} = 0, -0.5, -1$ (Fig. 3). The dynamic effect is strong: at the ranges of the frequency limit $\bar{k}$, even at relatively small values of the limit amplitude of the dynamic fluctuating part ($0 \le \bar{q}_1 \le 0.1$), the nonshakedown limit on the amplitude of the quasi-static part $\bar{q}_0$ can be reduced drastically. The nonshakedown curve descends considerably at increasing values of the frequency parameter limit $\bar{k}$ (Fig. 2). Besides the parameters $\bar{q}_0$, $\bar{q}_1$, $\bar{k}$, which determine the maximal moments, the parameter $\bar{h}$, indicating the size of the range of the quasistatic load, also influences the shakedown behavior of the plate: At decreasing values of $\bar{h}$ (increasing range $\bar{h} \le \bar{q}_0 \le 1$), the domain under the curve $k_s = 1$ decreases in size correspondingly (Fig. 3).

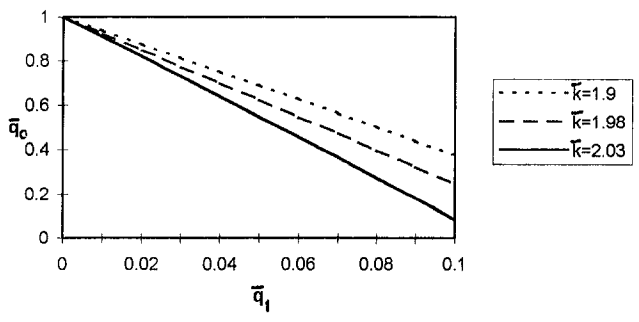

Fig. 2 The nonshakedown curves in the plane of dimensionless load amplitudes $\bar{q}_0$, $\bar{q}_1$ at various values of the load frequency parameter limit $\bar{k}$

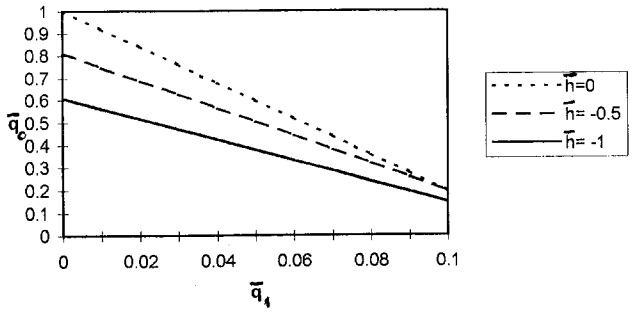

Fig. 3 The nonshakedown curves in the plane of dimensionless load amplitudes $\bar{q}_0$, $\bar{q}_1$ at various values of the load range parameter $\bar{h}$

3 The Point Load Effect

Consider the same plate under combined actions of central quasistatic point load p and uniformly distributed dynamic fluctuating load q (see Fig. 1)

$$p = p_0, \ q = q_1 \sin \omega t, \quad (17)$$

where p_0, q_1, ω are arbitrary quasi-static functions of time, which vary between the limits (9) and

$$0 \le p_0 \le p_0^+. \quad (18)$$

The fictitious elastic response of the plate to the loads (17) is

$$M_r^e(r, t) = p_0 \cdot P_{0r}(r) + q_1 \cdot Q_r(k, r) \sin \omega t,$$
$$M_\theta^e(r, t) = p_0 \cdot P_{0\theta}(r) + q_1 \cdot Q_\theta(k, r) \sin \omega t, \quad (19)$$

where

$$P_{0r}(r) = \frac{1}{4\pi}(1 + \nu) \ln \frac{a}{r},$$
$$P_{0\theta}(r) = \frac{1}{4\pi}\left[(1 + \nu) \ln \frac{a}{r} + 1 - \nu\right]. \quad (20)$$

k, Q_r, and Q_θ are defined in the previous section.

One observes the logarithmic singularity of the elastic field at the center of the plate from (20). The assumptions of elementary plate theory do not hold near the point of application of a concentrated load. Still, (20) should predict correct assymptotic behavior of the elastic field, except for a certain small domain around the point $r = 0$. Moreover, that singularity should not limit our ability to use (19) to determine the plastic limit load p_0 (at $q_1 \equiv 0$) and the incremental collapse loads from (7). That is because the singularity is local, while the plastic limit and incremental collapse modes are global. Mathematically, as the singular elastic field $\mathbf{M}^e$ enters (7) through an inside-integral expression, the integration operation would eliminate the infinity due to the singularity, and the result would become finite. In particular, substituting (19) into (7) and taking the same admissible incremental collapse mechanism (13), (14), we obtain

$$I = \frac{1}{aM_Y} \cdot \sup_{0 \le y < a, 0 < k \le k^+} \left\{ p_0^+ \left[yP_{0r}(y) + \int_y^a P_{0\theta}(r)dr \right] + q_1^+ \left[y|Q_r(k, y)| + \int_y^a |Q_\theta(k, r)|\, dr \right] \right\}$$

Downloaded 04 May 2010 to 171.66.16.27. Redistribution subject to ASME license or copyright; see http://www.asme.org/terms/Terms_Use.cfm

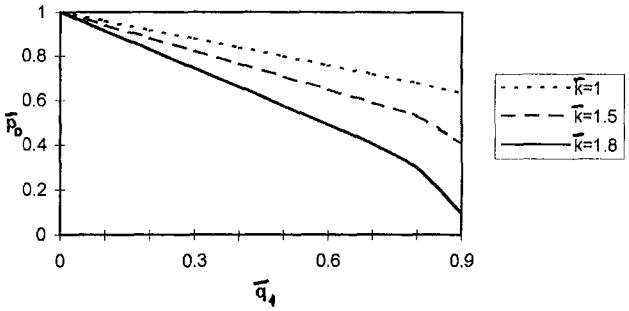

Fig. 4 The nonshakedown curves in the plane of dimensionless load amplitudes $\bar{p}_0$, $\bar{q}_1$ at various values of the frequency parameter limit $\bar{k}$

$$= \frac{1}{aM_Y} \cdot \sup_{0 \le y < a, 0 < k \le k^+} \left\{ p_0^+ \frac{a - y}{2\pi} + q_1^+ \left[y|Q_r(k, y)| + \int_y^a |Q_\theta(k, r)|\, dr \right] \right\}. \quad (21)$$

In the specific case $q_1^+ = 0$, Eq. $I = 1$ yields the plastic limit load for the plate loaded by a concentrated load at its center $p_0^+ = 2\pi M_Y$.

However, when one substitutes (19) into (6), one finds that $A_r, A_\theta \to \infty$ when $r \to 0$, even at infinitesimal variation of the load p_0, which means the plate should fail because of alternating plasticity at any range of p_0. The classical shakedown theory is of less use in dealing with the problems involving singularities, where the elastic stresses can go up to infinity (one can not find, by Melan's theorem, a residual stress distribution that when imposed upon the elastic field would keep the resulting field inside the yield surface near a varying singularity). Distinct from the global plastic limit or incremental collapse modes, the alternating plasticity one is local. For a complete treatment of the problem one needs to consider more exact fields near the presumed singularity and use a more refined material model to deal with the high strain level, and check for local damage and possible spread of the damage to the global collapse of the structure.

Still, in the specific case of constant (static) load $p = p_0 = p_0^+ = \text{const}$, the nonvarying singularity in (20) should disappear in the final expressions of (6), which take the simple forms

$$A_r = \frac{3q_1^+}{2M_Y} \cdot \max_{0 \le r \le a, 0 < k \le k^+} |Q_r(k, r)|,$$
$$A_\theta = \frac{3q_1^+}{2M_Y} \cdot \max_{0 \le r \le a, 0 < k \le k^+} |Q_\theta(k, r)|, \quad (22)$$

while (21) remains valid also for this case.

The nonshakedown curves $k_s = 1$ for the case in the plane of dimensionless load amplitudes

$$\bar{p}_0 = p_0^+ \frac{1}{2\pi M_Y}, \quad \bar{q}_1 = q_1^+ \frac{a^2}{M_Y} \quad (23)$$

($\bar{p}_0 = 1$ corresponds to the plastic limit load $p_0^+ = 2\pi M_Y$ at $q_1^+ = 0$) are presented in Fig. 4 at various values of the frequency parameter limit $\bar{k} = 1, 1.5, 1.8$. Again, we see that the dynamic effect is sensible.

4 Closure

The shakedown theory is shown to be helpful in dealing with the structures subjected to practical quasi-periodic dynamic loading. The proposed approach is simple and can use the available results of the respective kinematic method in plastic limit analysis for circular plates. The dynamic effects are observed to be strong, and the load amplitude-frequency diagrams appear useful for engineering study of plates in dynamic working conditions. The classical shakedown theory does not suffice to solve the problems with singularities resulted from the point loads, where additional refined analysis is required to check for the local fracture and possible spread of the local damage to the ultimate global collapse of the structures.

The kinematic approach used is the upper bound one. For the simple loading schemes considered here, with the reduced kinematic formulation (1)–(3) and the available collapse mechanism (13), (14) from plastic limit analysis, we might get close estimations of the nonshakedown loads for the particular problems considered here. Efforts are needed to explore further the kinematic approach for possible better estimates for more complicated loading schemes, and more complicated structures. Note here also a theoretically more refined kinematic reduced formulation for sufficiently general loading processes is constructed in Pham (1997b).

Acknowledgments

This work was supported by the Program of Basic Research in Natural Science.

References

Ceradini, G., 1980, "Dynamic shakedown in elastic-plastic bodies," *ASCE J. Engng. Mech. Div.*, Vol. 106, pp. 481–499.

Hodge, P. G., Jr., 1963, *Limit Analysis of Rotationally Symmetric Plates and Shells,* Prencice-Hall, Englewood Cliffs, NJ.

Johnson, W., and Mellor, P. B., 1973, *Engineering Plasticity,* Van Nostrand Reinhold, London.

Koiter, W. T., 1963, "General theorems for elastic-plastic solids," *Progress in Solids Mechanics,* I. N. Sneddon and R. Hill, eds., North-Holland, Amsterdam, pp. 165–221.

König, A., 1987, *Shakedown of Elastic-Plastic Structures,* Elsevier, Amsterdam.

Lubliner, J., 1990, *Plasticity theory,* McMillan, New York.

Martin, J. B., 1975, *Plasticity: Fundamentals and General Results,* MIT Press, Cambridge, MA.

Pham, D. C., 1992, "Extended shakedown theorems for elastic plastic bodies under quasiperiodic dynamic loading," *Proc. R. Soc. Lond.,* Vol. A439, pp. 649–658.

Pham, D. C., 1996, "Dynamic shakedown and a reduced kinematic theorem," *Int. J. Plasticity,* Vol. 12, pp. 1055–1068.

Pham, D. C., 1997a, "Evaluation of shakedown loads for plates," *Int. J. Mech. Sci.,* Vol. 39, pp. 1415–1422.

Pham, D. C., 1997b, "Reduced forms of shakedown kinematic theorem for elastic-perfectly plastic bodies," *Proc. R. Soc. Lond.,* Vol. A453, pp. 2259–2269.

Prager, W., 1948, "Problem types in the theory of perfectly plastic materials," *J. Aero. Sci.,* Vol. 15, pp. 337–341.

Save, M. A., and Massonnet, C. E., 1972, *Plastic Analysis of Plates, Shells and Disks,* North-Holland, Amsterdam.

Symonds, P. S., and Neal, B. G., 1952, "Recent progress in the plastic limit methods of structural analysis," *J. Franklin Inst.,* Vol. 252, pp. 469–492.

Downloaded 04 May 2010 to 171.66.16.27. Redistribution subject to ASME license or copyright; see http://www.asme.org/terms/Terms_Use.cfm

Vibration Control of a Rotating Shaft: An Analytical Solution

S. M. Yang[1]
Mem. ASME

G. J. Sheu

Institute of Aeronautics
and Astronautics,
National Cheng Kung University,
Taiwan, R.O.C.

It has been shown that a rotating shaft in the Rayleigh beam model has only a finite number of whirl speeds and vibration modes when the rotating speed is higher than half of the whirl speed. The system's unbalanced response can therefore be written analytically by the vibration modes and the generalized coordinates. This paper presents an analytical controller design of optimal sensor/actuator location and feedback gain for minimizing the steady-state unbalanced response. Because all of the critical speeds and vibration modes are included in the controller design, there will be no residual mode, hence no spillover. An example is used to illustrate that the controller design in collocated or noncollocated configuration not only guarantees the closed-loop stability but also effectively suppresses the unbalanced response.

1 Introduction

Structural control is often aimed at increasing the control-induced damping and stiffness so as to achieve the desired vibration suppression performance. Because of the interaction between structural vibration and sensor/actuator/controller dynamics, simultaneous optimization of both may be necessary for improving system performance.

There have been many studies on the vibration control of beam systems. Schulz and Heimbold (1983) studied the vibration control of a cantilever beam by maximizing the control-induced dissipation energy with an optimal set of sensor and actuator location. Similar work were also studied by Kondoh et al. (1990) and Lee and Chen (1994). Yang and Mote (1991) developed a method to predict the stability of a gyroscopic system and showed that, as commonly believed, the system is stable in collocated sensor/actuator configuration. Yang and Lee (1993) recently developed an analytical model for optimal sensor/actuator location and feedback gain in a structural control system with piezoelectric sensor/actuator. Yang and Liu (1995) also presented a frequency domain stability criterion for controller design in distributed parameter models. All of the above, however, were on the vibration suppression for the transient response of a cantilever beam in classical beam model. What remains needed is the optimal design of sensor/actuator location and feedback gain for minimizing the steady state response of a rotating system.

Most of the efforts in controller design of a rotating system have been emphasized on magnetic bearing and control algorithm but with little attention to sensor/actuator locations. LQR algorithms were recently applied to rotor systems by Palazzolo et al. (1989) and Fan et al. (1993), but the controller order is too high to implement in practice. Even if implementable, it is optimal or near optimal only to the model at a preselected sensor/actuator location and at a specific rotating speed. The optimal sensor/actuator location, however, may change with the rotating speed because of the gyroscopic effects. Poorly chosen sensor/actuator locations will result in unrealistic or unattainable performance. A classical PD controller design for a one-mode rotor system was recently discussed by Kasarda et al. (1990) in which the design parameters were the location and feedback gain of a magnetic bearing. Sheu et al. (1995) also recently developed a controller design methodology that combines the experimental design method and PD control technique. However, the above controller design was based on the discretization of sensor/actuator location by the finite element method [Nelson (1980)]. No analytical study on the vibration suppression of rotor system is presented as yet.

In all of the previous analytical work of a rotating shaft (Bauer, 1980; Zu and Han, 1992; Shiau and Hwang, 1993), the number of whirl speed was found, or believed, to be infinite. In theory, a continuous system requires an infinite number of vibration modes to describe its dynamics. However, a recent study of a rotating shaft (Yang et al., 1996) showed that there are only a finite number of whirl speeds when the rotating speed is higher than half of the whirl speed. The unbalanced response can therefore be written analytically by a finite number of vibration modes and the corresponding generalized coordinates. This paper presents a controller design of optimal sensor/actuator location and velocity feedback gain to minimize the steady-state unbalanced response of rotating systems. Because the number of critical speeds and vibration modes are finite, all can be included in the controller design. Therefore, there will be no residual mode. Spillover stability often seen in vibration control of flexible systems (Balas, 1978; Yang and Liu, 1994) can then be prevented. An example is employed to illustrate the optimal controller design.

2 Rotor Dynamics

The equation of a rotating circular shaft modeled by a Rayleigh beam with rotary inertia and gyroscopic effects are derived in Yang et al. (1996) as

$$\rho A\ddot{\bar{U}} - \rho I\frac{\partial^2\ddot{\bar{U}}}{\partial x^2} + C\dot{\bar{U}} + i2\bar{\Omega}\rho I\frac{\partial^2\dot{\bar{U}}}{\partial x^2} + \mathrm{EI}\frac{\partial^4\bar{U}}{\partial x^4} = e(x)\rho A\bar{\Omega}^2 e^{i\bar{\Omega}t} \quad (1)$$

where ρ is the mass density, A is the cross-sectional area, I is the transverse moment of inertia, C is the system's damping, E is Young's modulus, $\bar{\Omega}$ is the rotating speed, and $e(x)$ is the mass eccentricity distribution. Without the loss of generality, the phase angle of unbalanced mass is zero. $\bar{U}(x, t)$ is a complex variable defined by $\bar{U}(x, t) = V(x, t) + iW(x, t)$ where V and W represent the transverse deflections of the shaft as shown in Fig. 1. The nondimensional form is

[1] To whom correspondence should be addressed. e-mail: smy@mail.iaa.ncku.edu.tw

Contributed by the Applied Mechanics Division of THE AMERICAN SOCIETY OF MECHANICAL ENGINEERS for publication in the ASME JOURNAL OF APPLIED MECHANICS.

Discussion on the paper should be addressed to the Technical Editor, Professor Lewis T. Wheeler, Department of Mechanical Engineering, University of Houston, Houston, TX 77204-4792, and will be accepted until four months after final publication of the paper itself in the ASME JOURNAL OF APPLIED MECHANICS.

Manuscript received by the ASME Applied Mechanics Division, June 13, 1996; final revision, Aug. 20, 1998. Associate Technical Editor: M. Shinozuka.

 Copyright © 1999 by ASME

Downloaded 04 May 2010 to 171.66.16.27. Redistribution subject to ASME license or copyright; see http://www.asme.org/terms/Terms_Use.cfm

$$\ddot{U} - \left(\frac{1}{2l}\right)^2 \dot{U}'' + c\dot{U} + i2\Omega\left(\frac{1}{2l}\right)^2 \dot{U}'' + U'''' = \epsilon(\zeta)\Omega^2 e^{i\Omega\tau}, \quad (2)$$

where the nondimensionalized parameters are

$$U(\zeta, \tau) = \frac{\bar{U}(x, t)}{L}, \quad \text{shaft deformation}$$

$$\zeta = \frac{x}{L}, \quad \text{axial location}$$

$$c = \frac{C}{\left(\frac{\rho AEI}{L^4}\right)^{1/2}}, \quad \text{damping coefficient}$$

$$\epsilon(\zeta) = \frac{e(x)}{L}, \quad \text{eccentricity}$$

$$\tau = t\left(\frac{EI}{\rho AL^4}\right)^{1/2}, \quad \text{time}$$

$$\Omega = \frac{\bar{\Omega}}{\left(\frac{EI}{\rho AL^4}\right)^{1/2}}, \quad \text{rotating speed}$$

$$l = \frac{L}{r}, \quad \text{slenderness ratio.}$$

The dots and the primes in Eq. (2) denote the partial differentiation with respect to dimensionless time τ and location ζ, respectively.

It has been shown in Yang et al. (1996) that the whirl speed of a rotating shaft in a Rayleigh beam model with the boundary conditions: (1) short-short (2) long-long (3) long-free (4) free-free (5) long-short, and (6) short-free bearings can be written analytically by a function of two parameters: the whirl ratio (λ) defined by the rotating speed over the whirl speed

$$\lambda = \frac{\Omega}{\omega} \quad (3)$$

and the slenderness ratio (l) defined by the length of the shaft over its radius,

$$\omega_n \approx \left[\frac{(n\pi)^4}{1 + \left(\frac{n\pi}{2l}\right)^2 (1 - 2\lambda)}\right]^{1/2}, \quad n = 1, 2, 3, \ldots. \quad (4)$$

There will be finite whirl speeds, not infinite, in a rotating system when $\lambda > \frac{1}{2}$, and the number of whirl speed (n_{cr}) is the largest integer satisfying

$$n_{cr} \leq \frac{2l}{\pi}\left(\frac{1}{2\lambda - 1}\right)^{1/2}. \quad (5)$$

The case of $\lambda = 1$ corresponds to synchronous forward whirl, and it is of primary importance because the unbalanced excitation is synchronous with rotating speed. The whirl speed at this mode is also called the primary critical speed. The steady-state response from unbalanced mass effect can therefore be written in an analytical form by a set of finite number of vibration modes and the corresponding generalized coordinates.

3 Velocity Feedback

From Eq. (2), the equation of motion for a rotating shaft under velocity feedback can be described as

$$\ddot{U} - \left(\frac{1}{2l}\right)^2 \dot{U}'' + c\dot{U} + i2\Omega\left(\frac{1}{2l}\right)^2 \dot{U}'' + U'''' = \mathrm{F}(\zeta, \tau) + \epsilon(\zeta)\Omega^2 e^{i\Omega\tau}. \quad (6)$$

The control force $F(\zeta, \tau)$ from n-discrete actuators is

$$F(\zeta, \tau) = \sum_{k=1}^{n} \delta(\zeta - \zeta_{ak}) f_k(\tau), \quad (7)$$

where ζ_{ak} is the location of the kth actuator, n is the number of actuator, $f_k(\tau)$ is the control input, and $\delta(\zeta - \zeta_{ak})$ represents the Dirac delta function. The unbalanced response of a rotating shaft can be expressed by

$$U(\zeta, \tau) = [\mathbf{\Phi}(\zeta)]^T \{\mathbf{q}(\zeta)\} \quad (8)$$

where $[\mathbf{\Phi}(\zeta)]$ is the vibration mode vector and $\{\mathbf{q}(\zeta)\}$ is the generalized coordinate vector. Both are of dimension $n_{cr} \times 1$. Substituting Eq. (8) into Eq. (6), the equation of motion can be written in a matrix form

$$[\mathbf{M}]\{\ddot{\mathbf{q}}(\tau)\} + ([\mathbf{D}] + i\Omega[\mathbf{G}])\{\dot{\mathbf{q}}(\tau)\} + [\mathbf{K}]\{\mathbf{q}(\tau)\} = [\mathbf{B}(\zeta_a)]\{\mathbf{f}(\tau)\} + \{\mathbf{N}(\tau)\}, \quad (9)$$

where the generalized matrices $[\mathbf{M}]$, $[\mathbf{D}]$, and $[\mathbf{K}]$ are the diagonal, symmetric, positive definite mass, damping, and stiffness matrices with dimension $n_{cr} \times n_{cr}$, respectively. $[\mathbf{G}]$ is the gyroscopic matrix of same dimension. $[\mathbf{B}(\zeta_a)]$ is the control influence matrix, $\{\mathbf{f}(\tau)\}$ the control input vector, and $\{\mathbf{N}(\tau)\}$ the unbalanced force vector. They are

$$[\mathbf{M}] = \mathrm{diag}\left[\int_0^1 \phi_j(\zeta)\left[\phi_j(\zeta) - \left(\frac{1}{2l}\right)^2 \phi_j''(\zeta)\right] d\zeta\right]$$

$[\mathbf{D}] = \mathrm{diag}\,[2\xi_j\Omega_{cr(j)}]$ where $\Omega_{cr(j)}$ is the jth critical speed

$$[\mathbf{G}] = \mathrm{diag}\left[\int_0^1 2\left(\frac{1}{2l}\right)^2 \phi_j(\zeta)\phi_j''(\zeta) d\zeta\right]$$

$$[\mathbf{K}] = \mathrm{diag}\left[\int_0^1 \phi_j(\zeta)\phi_j^{(4)}(\zeta) d\zeta\right]$$

$$[\mathbf{B}(\zeta_a)] = [\phi_j(\zeta_{ak})], \quad j = 1, \ldots, n_{cr} \text{ and } k = 1, \ldots, n$$

$$\{\mathbf{f}(\tau)\}^T = [f_k(\tau)]$$

$$\{\mathbf{N}(\tau)\}^T = \left[\int_0^1 \epsilon(\zeta)\Omega^2 e^{i\Omega\tau}\phi_j(\zeta) d\zeta\right]$$

For velocity feedback with r-measurements at ζ_s, the control input becomes

$$\{\mathbf{f}(\tau)\} = -[\mathbf{g}][\mathbf{C}(\zeta_s)]\{\dot{\mathbf{q}}(\tau)\} \quad (10)$$

where $[\mathbf{C}(\zeta_s)]$ is the sensor distribution matrix,

$$[\mathbf{C}(\zeta_s)] = [\phi_j(\zeta_{sm})], \quad j = 1, \ldots, n_{cr} \text{ and } m = 1, \ldots, r$$

and $[\mathbf{g}]$ is an $n \times r$ constant gain matrix. Therefore, the closed-loop system becomes

$$[\mathbf{M}]\{\ddot{\mathbf{q}}(\tau)\} + ([\mathbf{D}] + [\mathbf{B}(\zeta_a)][\mathbf{g}][\mathbf{C}(\zeta_s)] + i\Omega[\mathbf{G}])\{\dot{\mathbf{q}}(\tau)\} + [\mathbf{K}]\{\mathbf{q}(\tau)\} = \{\mathbf{N}(\tau)\}. \quad (11)$$

In the case of noncollocated sensor/actuator, $[\mathbf{B}(\zeta_a)]$ and $[\mathbf{C}(\zeta_s)]$ may not necessarily be in the same column space so that the closed-loop system is no longer guaranteed stable. The

Downloaded 04 May 2010 to 171.66.16.27. Redistribution subject to ASME license or copyright; see http://www.asme.org/terms/Terms_Use.cfm

control-induced damping matrix can then split into a symmetric matrix

$$[\mathbf{D}_c] = \tfrac{1}{2}\{[\mathbf{B}(\zeta_a)][\mathbf{g}][\mathbf{C}(\zeta_s)] + ([\mathbf{B}(\zeta_a)][\mathbf{g}][\mathbf{C}(\zeta_s)])^T\} \quad (12)$$

and a skew symmetric matrix

$$[\mathbf{G}_c] = \tfrac{1}{2}\{[\mathbf{B}(\zeta_a)][\mathbf{g}][\mathbf{C}(\zeta_s)] - ([\mathbf{B}(\zeta_a)][\mathbf{g}][\mathbf{C}(\zeta_s)])^T\} \quad (13)$$

that represent the damping and the gyroscopic effect from velocity feedback, respectively. The closed loop system becomes

$$[\mathbf{M}]\{\ddot{\mathbf{q}}(\tau)\} + ([\mathbf{D}] + [\mathbf{D}_c] + [\mathbf{G}_c] + i\Omega[\mathbf{G}])\{\dot{\mathbf{q}}(\tau)\} + [\mathbf{K}]\{\mathbf{q}(\tau)\} = \{\mathbf{N}(\tau)\}. \quad (14)$$

By the generalized Kelvin-Tait-Chetaev theorem (Yang, 1993), the system is asymptotically stable if $([\mathbf{D}] + [\mathbf{D}_c])$ is positive definite, independent of $[\mathbf{G}]$ or $[\mathbf{G}_c]$. The steady-state unbalanced response $U(\zeta, \tau)$ can be obtained explicitly as

$$U(\zeta, \tau) = |U(\zeta)|\, e^{i(\Omega\tau - \theta)}, \quad (15)$$

where $|U(\zeta)|$ is the vibration amplitude, and θ is the phase lag induced by velocity feedback. The controller design is to determine the optimal sensor location ζ_s, actuator location ζ_a, and feedback gain $[\mathbf{g}]$ such that the steady-state unbalanced vibration can be minimized.

4 Optimal Design

The measure of vibration suppression performance can be evaluated by the integrating the steady-state vibration amplitude over the shaft length

$$W(\Omega, \zeta_s, \zeta_a, [\mathbf{g}]) = \int_0^1 |U(\zeta)|^2 d\zeta. \quad (16)$$

The performance index depends on the rotating speed (Ω), the location of sensor/actuator (ζ_s, ζ_a), and the feedback gain ($[\mathbf{g}]$). For a given rotating speed, the optimal sensor/actuator location (ζ_s^*, ζ_a^*) and feedback gain ($[\mathbf{g}^*]$) can be obtained by solving the optimization problem

$$\min_{\zeta_s, \zeta_a, [\mathbf{g}]} W(\Omega, \zeta_s, \zeta_a, [\mathbf{g}]), \quad (17)$$

subject to the constraints

$$(1) \quad \text{stability criteria } ([\mathbf{D}] + [\mathbf{D}_c]) > 0, \quad (18a)$$

$$(2) \quad \text{admissible region } 0 \le \zeta_s \le 1,\ 0 \le \zeta_a \le 1, \quad (18b)$$

$$(3) \quad \text{saturation limit } 0 \le g_{ij} \le 1. \quad (18c)$$

(ζ_s^*, ζ_a^*) will change with the rotating speed because of the change of the antinode(s) location. In a desired operation range that covers several critical speeds, some tradeoffs among the vibration modes are needed. The performance index can then be defined by

$$S(\zeta_s, \zeta_a, [\mathbf{g}]) = \sum_{j=1}^{n_d} \mu_j W_j(\Omega_{cr(j)}, \zeta_s, \zeta_a, [\mathbf{g}]), \quad \sum_{j=1}^{n_d} \mu_j = 1, \quad \mu_j \ge 0, \quad (19)$$

where n_d is the number of vibration modes within the desired operation range and μ_j is a constant indicating the relative weighting of the jth mode that can be determined a priori from engineering experiences or design requirements. The problem of optimal sensor/actuator locations (ζ_s^*, ζ_a^*) and feedback gain ($[\mathbf{g}^*]$) can be formulated by

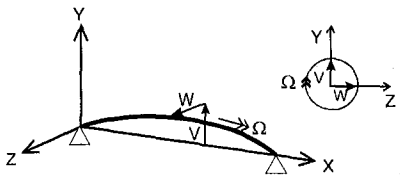

Fig. 1 Schematic diagram of a rotating shaft system

$$\min_{\zeta_s, \zeta_a, [\mathbf{g}]} S(\zeta_s, \zeta_a, [\mathbf{g}]), \quad (20)$$

subject to the constraints in Eq. (18).

5 Example of Vibration Suppression

Consider a rotating shaft of slenderness ratio $l = 4$ with linear eccentricity distribution $\epsilon(\zeta) = \epsilon_0(1 + \zeta)$, and the boundary condition is short-short bearings. According to Eq. (5), there will be only two critical speeds ($n_{cr} = 2$) at $\Omega_{cr} = 10.73$ and 63.78 with the corresponding vibration modes $\phi_1(\zeta) = \sin(\pi\zeta)$ and $\phi_2(\zeta) = \sin(2\pi\zeta)$. The coefficient matrices of the open-loop system in Eq. (9) can then be calculated. For systems with damping ratio $\xi_1 = \xi_2 = 0.1$ percent, the amplitude and phase lag response are plotted in Fig. 2. The first mode is dominant at the lower speed range, until q_1 and q_2 intersects at $\Omega = 55$ where the second mode becomes significant. The unbalanced response $U(\zeta, \tau)$ can be calculated by Eq. (15) and plotted in Fig. 3 for $\Omega = 40$ and 60. This is the first time that the steady-state unbalanced response of a rotating system can be written explicitly by a set of finite modes. The vibration amplitude becomes apparent when the rotating speed ($\Omega = 60$) is close to the second critical speed at $\Omega_{cr2} = 63.78$. The controller design is to place one pair of sensor/actuator in optimal location (ζ_s, ζ_a) with a feedback gain (g) such that the vibration amplitude can be minimized. In the following, two sensor/actuator configurations are applied to search for the optimal location and feedback gain.

In collocated sensor/actuator configuration ($\zeta_s = \zeta_a$), there is only one parameter ζ_s to search because the feedback gain is always the higher the better, provided within the saturation limit. Figure 4 shows the optimal sensor/actuator location calculated by solving the optimization problem in Eq. (17) with the sequential quadratic programming (SQP) method in a finite difference gradient. For systems with low damping ($\xi_i = 0.1$ percent), there is an overshoot in the sensor/actuator location, similar to that in step response. At the speed where the first mode is dominant (say, $\Omega < 55$), the optimal location is at its antinode ($\zeta = 0.5$). However, the optimal location will be shifted to the antinode of the second mode ($\zeta = 0.75$) at higher speed. When operating between the two critical speeds, the optimal location is at neither of the antinodes. This result validates that the optimal sensor/actuator location is dependent on the rotating speed. Previous studies of controller design by using LQR is valid only at a specific speed, not at a speed range with more than one critical speed.

For systems in noncollocated configuration, the optimal sensor location ζ_s, actuator location ζ_a, and feedback gain (g) are shown in Fig. 5. At lower speed where the first mode is dominant, the optimal sensor/actuator locations become collocated instead, and they are at the antinode $\zeta_s = \zeta_a = 0.5$. When $\Omega > \Omega_{cr1}$, the magnitude of q_1 approaches a constant while the influence of q_2 becoming more apparent as shown in Fig. 2. The sensor and actuator locations thus become noncollocated and split into two branches. The farther apart the sensor and actuator, the more gyroscopic effect to be induced. Their relative distance is determined by the control-induced gyroscopic effect in Eq. (13) and also by the stability constraint in Eq. (18a). That is why they are kept at a constant distance in order to guarantee stability as shown in Fig. 5.

Downloaded 04 May 2010 to 171.66.16.27. Redistribution subject to ASME license or copyright; see http://www.asme.org/terms/Terms_Use.cfm

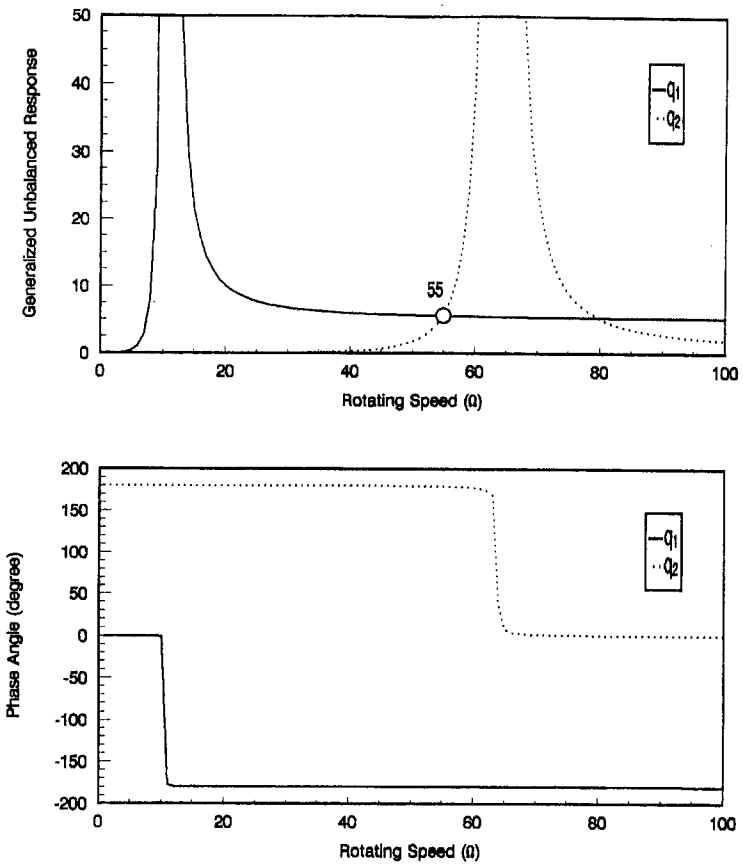

Fig. 2 Amplitude and phase lag of the generalized unbalanced response $\{q(\tau)\}$

At the speed range between the two critical speeds, the influence of the first mode on system dynamics is gradually overtaken by the second mode. When the second mode dictates the system at Ω_{cr2}, the optimal sensor/actuator locations coalesce again at the antinode ($\zeta = 0.75$). Because of the control-induced gyroscopic effect, however, the optimal locations split again right after Ω_{cr2} and they are kept at a distance because of the stability constraint. Both remain in (0.5, 1) so that there is no zero crossing between the sensor and actuator locations. At $\Omega > \Omega_{cr2}$, the optimal sensor location remains in the vicinity of the second mode's antinode while the actuator is more sensitive to speed. This result was previously predicted by Yang et al. (1995) in a discrete model, but the prediction in distributed parameter model has not been reported as yet. It is surprising to find that the feedback gain remains constant at all rotating speeds, although it is treated as a design parameter along with the sensor/actuator locations. This can be explained by that the sensor/actuator locations are in-phase and the control input is always constructive to vibration suppression. As a result, the feedback gain is as large as possible in order to achieve the best system performance within the saturation limit.

Figure 6 shows the unbalanced response under the optimal sensor and actuator locations in collocated and noncollocated configurations of Figs. 4 and 5. At the critical speeds, the steady-state vibration response becomes apparent and the optimal sensor/actuator locations are at their antinodes. The vibration suppression performance achieved by either configuration are almost identical, despite that each configuration has a distinct optimal sensor/actuator location. Compared with the open-loop response, the controller is shown to be effective for vibration suppression. Spillover instability, in theory, is by no means a

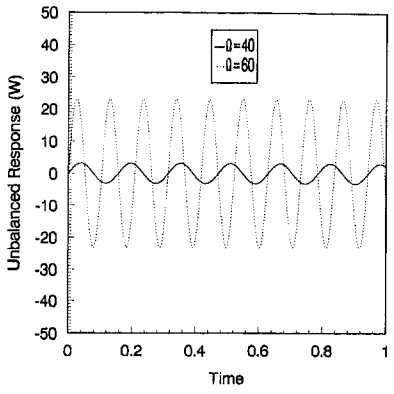

Fig. 3 Steady-state unbalanced responses at $\Omega = 40$ and 60

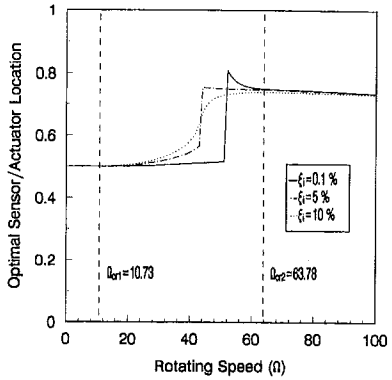

Fig. 4 Optimal sensor/actuator location (ζ_s, ζ_a) from different damping ratio in collocated design

Downloaded 04 May 2010 to 171.66.16.27. Redistribution subject to ASME license or copyright; see http://www.asme.org/terms/Terms_Use.cfm

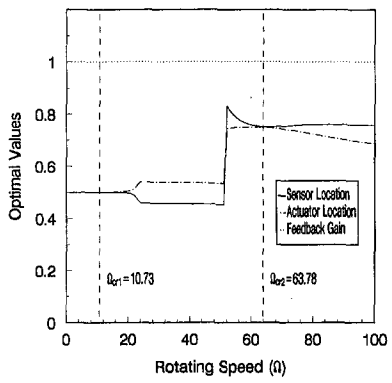

Fig. 5 Optimal sensor/actuator locations (ζ_s, ζ_a) and the feedback gain (g) in noncollocated design

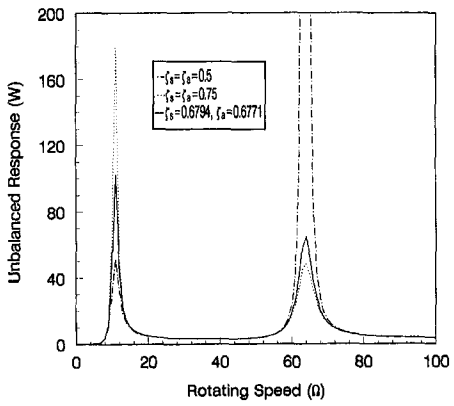

Fig. 7 Unbalanced response of three configurations: (1) $\zeta_s = \zeta_a = 0.5$, (2) $\zeta_s = \zeta_a = 0.75$, and (3) optimal design for S index $\zeta_s = 0.6794$, $\zeta_a = 0.6771$

concern since all of the vibration modes are included in the system model and hence in the controller design.

If the two modes are to be suppressed simultaneously in equal weighting, the performance index defined by Eq. (19) has $\mu_1 = \mu_2 = \frac{1}{2}$. The optimal sensor/actuator locations obtained by solving the optimization problem at Eq. (20) are $\zeta_s = 0.6794$ and $\zeta_a = 0.6771$, and the unbalanced response is plotted in Fig. 7. This optimal design is shown to be effective for controlling all modes simultaneously within the operation range. The case of sensor/actuator location at $\zeta_s = \zeta_a = 0.5$ (the antinode of the first mode) is effective for the vibration suppression of the first mode but it is fruitless for the second mode. Similarly for sensor/actuator location at $\zeta_s = \zeta_a = 0.75$ is by no means applicable in controlling the first mode. Only with an optimal set of sensor/actuator locations, can the steady-state unbalanced response be effective minimized.

6 Conclusions

1 Vibration control of a rotating shaft in Rayleigh beam model is studied analytically in this paper by calculating the optimal sensor/actuator location and feedback gain. An example is employed to illustrate that the controller design not only guarantees the closed-loop stability but also effectively suppresses the steady-state unbalanced response. Because all of the critical speeds and vibration modes are included in the controller design, there will be no residual mode, hence no spillover.

2 The structural dynamics of a rotating system is dependent on the rotating speed, and so is the optimal sensor/actuator location. In collocated configuration, the optimal sensor/actuator location is at the antinode of the dominant vibration mode.

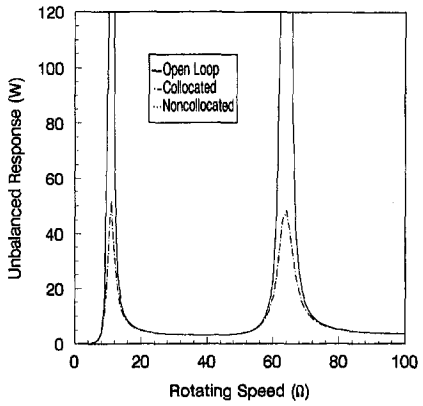

Fig. 6 Unbalanced response of the open loop, the optimal collocated design, and the optimal noncollocated design; the last two are almost identical

At the speeds where some of the vibration modes are "equally" important, the optimal location should be determined by the optimization of Eq. (17). It is at neither of the antinodes. The feedback gain, however, is as large as possible. In the absence of sensor/actuator dynamics, the closed-loop system is stable for any sensor/actuator location with infinite gain margin.

3 In noncollocated configuration, the optimal sensor and actuator locations are affected not only by the rotating speed but also by the control-induced gyroscopic effect. When operating near one of the critical speeds, the optimal locations become collocated at the antinode of that critical mode. At the other speeds, the optimal locations are, as expected, noncollocated, and they are kept at a constant distance to ensure the closed-loop system stability. The actuator location is more sensitive than the sensor location to rotating speed and to system performance. By comparison, the feedback gain is the least sensitive to system performance. Controller design of rotor systems should therefore be emphasized more on sensor/actuator location than on feedback gain. Under the stability constraint, the sensor and actuator locations are placed in a way such that they remain in-phase and the control input is always constructive for vibration suppression.

4 The analytical study shows that the controller is capable of suppressing the vibration modes simultaneously in a desired operation range. One can achieve the desired system performance by tailoring the relative weighting of the modes in a desired speed range. Compared with LQR-based controller design, neither preselected sensor/actuator location nor state estimation is needed.

5 It should be noted that the controller design is based on the Rayleigh beam model where the rotary inertia is considered. However, in the cases where the shear deformation becomes increasingly significant at higher modes of vibration, one may not have the close-form solution of the natural frequencies and vibration modes for nonsimply supported boundary conditions. Consequently, the analytical controller design may be difficult, if not impossible, to derive. Model reduction technique is then required and control spillover will have to be examined for closed-loop instability.

References

Balas, M. J., 1978, "Feedback Control of Flexible Systems," *IEEE Transactions on Automatic Control,* Vol. AC-23, No. 4, pp. 673–679.

Bauer, H. F., 1980, "Vibration of a Rotating Uniform Beam, Part I: Orientation in the Axis of Rotation," *Journal of Sound and Vibration,* Vol. 72, No. 2, pp. 177–189.

Fan, G. W., Nelson, H. D., Crouch, P. E., and Mignolet, M. P., 1993, "LQR-Based Least-Squares Output Feedback Control of Rotor Vibrations Using the Complex Mode and Balanced Realization Methods," ASME *Journal of Engineering for Gas Turbines and Power,* Vol. 115, pp. 314–323.

Kasarda, M. E. F., Allaire, P. E., Humphris, R. R., and Barrett, L. E., 1990, "A Magnetic Damper for First Mode Vibration Reduction in Multimass Flexible

Downloaded 04 May 2010 to 171.66.16.27. Redistribution subject to ASME license or copyright; see http://www.asme.org/terms/Terms_Use.cfm

Rotors," ASME *Journal of Engineering for Gas Turbines and Power,* Vol. 112, pp. 463–469.

Kondoh, S., Yatomi, C., and Inoue, K., 1990, "The Positioning of Sensors and Actuators in the Vibration Control of Flexible Systems," *JSME International Journal,* Series C, Vol. 33, No. 2, pp. 145–152.

Lee, A. C., and Chen, S. T., 1994, "Collocated Sensor/Actuator Positioning and Feedback Design in the Control of Flexible Structure System," ASME *Journal of Vibration and Acoustics,* Vol. 116, pp. 146–154.

Nelson, H. D., 1980, "A Finite Rotating Shaft Element Using Timoshenko Beam Theory," ASME *Journal of Mechanical Design,* Vol. 102, pp. 793–803.

Palazzolo, A. B., Lin, R. R., Kascak, A. F., and Alexander, R. M., 1989, "Active Control of Transient Rotordynamic Vibration by Optimal Control Methods," ASME *Journal of Engineering for Gas Turbines and Power,* Vol. 111, pp. 264–270.

Schulz, G., and Heimbold, G., 1983, "Dislocated Actuator/Sensor Positioning and Feedback Design in Flexible Structures," *Journal of Guidance, Control, and Dynamics,* Vol. 6, No. 5, pp. 361–367.

Sheu, G. J., Yang, C. D., and Yang, S. M., 1995, "Experiment-Aided Controller Design of Rotor Systems with a Magnetic Bearing," ASME *Journal of Vibration and Acoustics,* to appear.

Shiau, T. N., and Hwang, J. L., 1993, "Generalized Polynomial Expansion Method for the Dynamic Analysis of Rotor-Bearing Systems," ASME *Journal of Engineering for Gas Turbines and Power,* Vol. 115, pp. 209–217.

Yang, B., and Mote, C. D., 1991, "Frequency-Domain Vibration Control of Distributed Gyroscopic Systems," ASME *Journal of Dynamic Systems, Measurement, and Control,* Vol. 113, pp. 18–25.

Yang, S. M., 1993, "Stability Criteria of Structural Control Systems with Noncollocated Velocity Feedback," *AIAA Journal,* Vol. 31, No. 7, pp. 1351–1353.

Yang, S. M., and Lee, Y. J., 1993, "Optimization of Non-collocated Sensor/Actuator Location and Feedback Gain in Control Systems," *Smart Materials and Structures,* Vol. 2, pp. 96–102.

Yang, S. M., and Liu, Y. C., 1994, "Optimal Output Feedback Control of Slewing Structures with Spillover Stabilization," *Journal of the Astronautical Sciences,* Vol. 42, No. 4, pp. 473–485.

Yang, S. M., and Liu, Y. C., 1995, "Frequency Domain Control of Flexible Beams with Piezoelectric Actuator," ASME *Journal of Dynamic Systems, Measurement, and Control,* Vol. 117, pp. 541–546.

Yang, S. M., Sheu, G. J., and Yang, C. D., 1995, "Vibration Control of Rotor Systems with Noncollocated Sensor/Actuator by Experimental Design," ASME *Journal of Vibration and Acoustics,* to appear.

Yang, S. M., Sheu, G. J., and Yang, C. D., 1996, "Analytical Solution of Whirl Speed and Mode Shape for Rotating Shafts," presented at ASME IGTI Turbo Expo '96 Conference, Paper No. 96-GT-264.

Zu, J. W. Z., and Han, R. P. S., 1992, "Natural Frequencies and Normal Modes of a Spinning Timoshenko Beam with General Boundary Conditions," ASME JOURNAL OF APPLIED MECHANICS, Vol. 59, pp. S197–S204.

Downloaded 04 May 2010 to 171.66.16.27. Redistribution subject to ASME license or copyright; see http://www.asme.org/terms/Terms_Use.cfm

Journal of Applied Mechanics

Brief Notes

A Brief Note is a short paper that presents a specific solution of technical interest in mechanics but which does not necessarily contain new general methods or results. A Brief Note should not exceed 1500 words *or equivalent* (a typical one-column figure or table is equivalent to 250 words; a one line equation to 30 words). Brief Notes will be subject to the usual review procedures prior to publication. After approval such Notes will be published as soon as possible. The Notes should be submitted to the Technical Editor of the JOURNAL OF APPLIED MECHANICS. Discussions on the Brief Notes should be addressed to the Editorial Department, ASME, United Engineering Center, 345 East 47th Street, New York, N. Y. 10017, or to the Technical Editor of the JOURNAL OF APPLIED MECHANICS. Discussions on Brief Notes appearing in this issue will be accepted until two months after publication. Readers who need more time to prepare a Discussion should request an extension of the deadline from the Editorial Department.

Exact Connection Between Deflections of the Classical and Shear Deformation Laminated Plate Theories

Z.-q. Cheng[1] **and S. Kitipornchai**[2]

1 Introduction

It has long been recognized that the classical two-dimensional laminated plate theory yields inadequate results for analysis of composite plates in many engineering problems. To address this issue, many approaches have been proposed to account for the effects of transverse shear flexibility. (See reviews of Noor and Burton (1989), Reddy and Robbins (1994), and Reddy (1997).) The global response characteristics predicted by shear deformation theories are quite accurate. However, the field equations of shear deformation theories are complicated, compared with the classical laminated plate theory.

This note extends Hu's (1963) method proposed for Reissner's (1948) sandwich plate theory to Reddy's (1984) third-order laminated plate theory. The field equations are then simplified. As a result, an exact differential relationship is established between the deflection of Reddy's theory and of the classical theory of symmetrically laminated plates with transversely isotropic polygonal laminae and simply supported edges. Solutions of the first-order shear deformation theory for laminated plates are simply and explicitly expressed in terms of Kirchhoff deflection of the classical theory. The exact connections include the results obtained by Reddy and Wang (1998, in press[3]) for isotropic single-layer plates as a special case.

2 Field Equations

Consider a symmetrically laminated plate consisting of homogeneous anisotropic laminae with uniform thickness. The undeformed midplane is chosen as the reference plane defined by $x_3 = 0$ and the x_3-axis is normal to it, where $\{x_i\}$ $(i = 1, 2, 3)$ is a Cartesian coordinate system. Throughout unless otherwise unspecified, a comma followed by a subscript denotes a derivative with respect to the corresponding spatial coordinate. The Einsteinian summation convention applies to repeated subscripts of tensor components, with Latin subscripts ranging from 1 to 3 while Greek subscripts are either 1 or 2.

Reddy's (1984) third-order theory for symmetric laminates is based on the following displacement field:

$$v_\alpha(x_i) = -x_3 u_{3,\alpha} + g\varphi_\alpha, \quad v_3(x_i) = u_3, \tag{1}$$

where the deflection u_3 and the generalized displacement φ_α are independent of x_3, and

$$g(x_3) = x_3\left(1 - \frac{4x_3^2}{3h^2}\right), \quad \varphi_\alpha = u_{3,\alpha} + \psi_\alpha. \tag{2}$$

The displacement field (1) is essentially same as the one in Reddy's (1984) original work in the case of symmetric laminates, where the function ψ_α was used through a substitution of Eq. $(2)_2$. For the bending problem of a laminated plate under an arbitrarily distributed normal load $q(x_\alpha)$, the field equations are expressed as

$$M_{\alpha\beta,\alpha\beta} + q = 0, \quad P_{\alpha\beta,\beta} - R_\alpha = 0, \tag{3}$$

where, denoting h as the total thickness of a plate,

$$M_{\alpha\beta} = \int_{-h/2}^{h/2} \sigma_{\alpha\beta} x_3 dx_3, \quad P_{\alpha\beta} = \int_{-h/2}^{h/2} \sigma_{\alpha\beta} g dx_3,$$

$$R_\alpha = \int_{-h/2}^{h/2} \sigma_{\alpha 3} g_{,3} dx_3, \tag{4}$$

$$\sigma_{\alpha\beta} = H_{\alpha\beta\omega\rho} e_{\omega\rho}, \quad \sigma_{\alpha 3} = 2E_{\alpha 3\omega 3} e_{\omega 3}, \quad e_{ij} = \tfrac{1}{2}(v_{i,j} + v_{j,i}). \tag{5}$$

For a transversely isotropic material with its isotropy plane being normal to the reference plane (Librescu, 1975),

$$H_{\alpha\beta\omega\rho} = \frac{\nu E}{1-\nu^2}\delta_{\alpha\beta}\delta_{\omega\rho} + \frac{E}{2(1+\nu)}(\delta_{\alpha\omega}\delta_{\beta\rho} + \delta_{\alpha\rho}\delta_{\beta\omega}),$$

$$E_{\alpha 3\omega 3} = \mu'\delta_{\alpha\omega}, \tag{6}$$

[1] Associate Professor, Department of Modern Mechanics, University of Science and Technology of China, Hefei, Anhui 230026, P.R. China. Currently Vicising Fellow at the University of Queensland.

[2] Professor, Department of Civil Engineering, The University of Queensland, Brisbane Qld 4072, Australia.

[3] The authors thank one of the reviews for drawing their attention to this work.

Contributed by the Applied Mechanics Division of THE AMERICAN SOCIETY OF MECHANICAL ENGINEERS for publication in the ASME JOURNAL OF APPLIED MECHANICS. Manuscript received by the ASME Applied Mechanics Division, July 22, 1997; final revision, Jan. 19, 1998. Associate Technical Editor: R. C. Benson.

 Copyright © 1999 by ASME

Downloaded 04 May 2010 to 171.66.16.27. Redistribution subject to ASME license or copyright; see http://www.asme.org/terms/Terms_Use.cfm

where E and ν denote Young's modulus and Poisson's ratio in the plane of isotropy, respectively, and μ' denotes the shear modulus in the plane normal to the isotropy plane.

Equations (4) may be written in an alternative form as, through Eqs. (1), (5), and (6),

$$\begin{bmatrix} M_{\alpha\beta} \\ P_{\alpha\beta} \end{bmatrix} = \begin{bmatrix} -a_1 + b_1 & a_2 - b_2 \\ -a_2 + b_2 & a_3 - b_3 \end{bmatrix} \begin{bmatrix} u_{3,\omega\omega} \\ \varphi_{\omega,\omega} \end{bmatrix} \delta_{\alpha\beta} + \begin{bmatrix} -b_1 & b_2 \\ -b_2 & b_3 \end{bmatrix} \begin{bmatrix} u_{3,\alpha\beta} \\ \frac{1}{2}(\varphi_{\alpha,\beta} + \varphi_{\beta,\alpha}) \end{bmatrix}, \quad R_\alpha = c\varphi_\alpha, \quad (7)$$

where

$$[a_1, a_2, a_3] = \int_{-h/2}^{h/2} [x_3^2, x_3 g, g^2] \frac{E}{1 - \nu^2} dx_3,$$

$$[b_1, b_2, b_3] = \int_{-h/2}^{h/2} [x_3^2, x_3 g, g^2] \frac{E}{1 + \nu} dx_3,$$

$$c = \int_{-h/2}^{h/2} \mu' (g_{,3})^2 dx_3. \quad (8)$$

With the expressions of Eqs. (7), the field equations (3) are then expressed in terms of three displacement functions u_3 and φ_α as

$$-a_1 u_{3,\alpha\alpha\beta\beta} + a_2 \varphi_{\alpha,\alpha\beta\beta} + q = 0, \quad (9)$$

$$-a_2 u_{3,\alpha\beta\beta} + \tfrac{1}{2} b_3 \varphi_{\alpha,\beta\beta} + (a_3 - \tfrac{1}{2} b_3)\varphi_{\beta,\beta\alpha} - c\varphi_\alpha = 0. \quad (10)$$

Following Hu's (1963) technique proposed for analysis of sandwich plate problems, two new functions, w and f, are introduced such that

$$\varphi_\alpha = (u_3 + w)_{,\alpha} + \epsilon_{\alpha\omega} f_{,\omega}, \quad (11)$$

where $\epsilon_{\alpha\omega}$ is the two-dimensional permutation tensor. The expression of Eq. (11) is sufficient; however, w and f will not be uniquely determined. The Cauchy-Riemann equations

$$(u_3^* + w^*)_{,\alpha} + \epsilon_{\alpha\omega} f^*_{,\omega} = 0 \quad (12)$$

always give a solution $[f^* + i(u_3^* + w^*)]$ which is an analytic function of the complex variable $(x_1 + ix_2)$. The expression (11) remains unchanged when changing $(u_3 + w)$ and f simultaneously by the increments $(u_3^* + w^*)$ and f^*.

Substituting Eq. (11) into Eqs. (9) and (10) yields

$$[(a_2 - a_1)u_3 + a_2 w]_{,\alpha\alpha\beta\beta} + q = 0, \quad (13)$$

$$[(a_3 - a_2)u_{3,\beta\beta} - cu_3 + a_3 w_{,\beta\beta} - cw]_{,\alpha} + \epsilon_{\alpha\omega}(\tfrac{1}{2} b_3 f_{,\beta\beta} - cf)_{,\omega} = 0. \quad (14)$$

Equations (14) are Cauchy-Riemann equations, which can be interpreted in an alternative form

$$\tfrac{1}{2} b_3 f_{,\beta\beta} - cf + i[(a_3 - a_2)u_{3,\beta\beta} - cu_3 + a_3 w_{,\beta\beta} - cw] = F(x_1 + ix_2), \quad (15)$$

where $F(x_1 + ix_2)$ is an analytic function. Furthermore, viewing Eq. (15) as a nonhomogeneous partial differential equation with respect to unknowns (u_3, w, f), its solution is composed of the sum of a homogeneous general solution and an arbitrary particular solution. Since both the real and imaginary parts of the function $F(x_1 + ix_2)$ are harmonic functions, the particular solution (u_3^*, w^*, f^*) can be taken as

$$u_3^* = 0, \quad -c(f^* + iw^*) = F(x_1 + ix_2), \quad (16)$$

and therefore it fulfills the Cauchy-Riemann condition (12). As a result of Eqs. $(16)_1$ and (12), the particular solution has trivial contribution to u_3 and φ_α, and thus to displacements and stresses of laminated plates. Consequently, the particular solution of Eq. (15) can be discarded. Only the corresponding homogeneous part of Eq. (15) is of interest, i.e.,

$$\tfrac{1}{2} b_3 f_{,\beta\beta} - cf = 0,$$

$$(a_3 - a_2)u_{3,\beta\beta} - cu_3 + a_3 w_{,\beta\beta} - cw = 0. \quad (17)$$

3 Simply Supported Edges

In view of the field equations (13) and (17), the unknown f has been decoupled with other two unknowns u_3 and w. This important simplification is very useful in some applications, such as in problems seeking fundamental solutions (e.g., Qin, 1993). Here it must be indicated that the unknown f is coupled with u_3 and w through boundary conditions in the majority of problems. For simply supported edges of polygonal plates; however, the unknown f can be separately determined.

Assuming that a laminated plate is simply supported on its boundary Γ, the boundary condition is expressed as

$$u_3 = 0, \quad P_{NN} = 0, \quad \varphi_T = 0, \quad M_{NN} = 0, \quad u_{3,T} = 0, \quad (18)$$

where the upper case subscripts N and T denote normal and tangential directions, respectively, on the boundary Γ. No implicit summation applies to the repeated upper case subscripts. For a laminated polygonal plate, Eq. $(18)_5$ is identically satisfied due to Eq. $(18)_1$, while Eqs. $(18)_{2,4}$ can be recast as, through Eqs. $(7)_1$ and $(18)_{1,3}$,

$$u_{3,NN} = 0, \quad \varphi_{N,N} = 0. \quad (19)$$

With the aid of Eqs. (11) and $(17)_2$, Eqs. $(18)_3$ and $(19)_2$ can be further rewritten, together with Eqs. $(18)_1$ and $(19)_1$, as

$$u_3 = 0, \quad u_{3,NN} = 0, \quad w = 0, \quad w_{,NN} = 0, \quad f_{,N} = 0, \quad (20)$$

where only three of the first four and the fifth conditions of Eqs. (20) are necessary in determining solutions of bending problems. It is shown by Eqs. (20) that the unknowns u_3, w, and f have been decoupled for the simply supported boundary.

4 Deflection Connection

Applying the Gauss theorem in the plane Ω for the function $f_{,\alpha}$, i.e.,

$$\iint_\Omega f_{,\alpha\alpha} d\Omega = \oint_\Gamma f_{,\alpha} n_\alpha d\Gamma = \oint_\Gamma f_{,N} d\Gamma, \quad (21)$$

it can be concluded, through Eqs. $(17)_1$ and $(20)_5$ that

$$f \equiv 0, \quad \text{on } \Omega. \quad (22)$$

This means that for bending problems of simply supported polygonal laminates, only two functions u_3 and w need to be solved. The field equations for u_3 and w are (13) and $(17)_2$, consistently associated with three of the boundary conditions $(20)_{1-4}$.

While taking $g(x_3) = 0$, it can be seen from Eqs. (1) that the displacement field is the one for the classical Kirchhoff plate theory. In this case, $a_2 = a_3 = 0$ from Eq. $(8)_1$, the Kirchhoff plate equation governing the deflection u_3^K reduces from Eq. (13) to (see also Reddy, 1997)

$$-a_1 u^K_{3,\alpha\alpha\beta\beta} + q = 0, \quad (23)$$

and the associated boundary conditions are

$$u_3^K = 0, \quad u^K_{3,NN} = 0. \quad (24)$$

Based on the uniqueness theorem of solution, it can be concluded from the analogy between the field equations (13) and

Downloaded 04 May 2010 to 171.66.16.27. Redistribution subject to ASME license or copyright; see http://www.asme.org/terms/Terms_Use.cfm

(23) and between the boundary conditions $(20)_{1-4}$ and (24) that

$$(a_2 - a_1)u_3 + a_2 w = -a_1 u_3^K. \quad (25)$$

Eliminating the function w from Eqs. $(17)_2$ and (25) gives

$$(a_1 a_3 - a_2^2)u_{3,\alpha\alpha} - ca_1 u_3 = a_1 a_3 u_{3,\alpha\alpha}^K - ca_1 u_3^K. \quad (26)$$

This is an exact relationship connecting the deflections of the Reddy (1984) and Kirchhoff theories for simply supported polygonal plates with transversely isotropic symmetric laminae. Once the Kirchhoff deflection solution u_3^K is given, the solution u_3 of the third-order Reddy's theory can be solved through Eq. (26) associated with the boundary condition $(20)_1$. Another unknown w is then simply obtained from Eq. (25).

In the case of the first-order theory for laminated plates (see, e.g., Reddy, 1997), taking $g(x_3) = x_3$ in Eq. $(8)_1$ yields $a_1 = a_2 = a_3$. This provides explicit expressions of u_3^F and w^F in terms of Kirchhoff deflection u_3^K as, from Eqs. (26) and (25),

$$u_3^F = u_3^K - \frac{a_1}{c} u_{3,\alpha\alpha}^K, \quad w^F = -u_3^K, \quad (27)$$

where

$$c = \kappa \int_{-h/2}^{h/2} \mu' dx_3, \quad (28)$$

κ is the shear correction factor. Therefore, once the Kirchhoff deflection is given, the solution of the first-order laminated plate theory is readily obtained through simple manipulation of differentiation. It should be noted that Eq. $(20)_2$ is not an essential condition, unless $q = 0$, for describing the simply supported edges in the first-order theory, as can be shown through derivation of the boundary condition from Eqs. (18).

For the particular case of sandwich plates, Hu (1963) gave the relationship between Reissner sandwich plate deflection and classical Kirchhoff thin plate deflection in the same form as Eqs. (27), where a_1 is the flexural rigidity of sandwich plates and $c = \mu_c h$, with μ_c being the shear modulus of the sandwich core. (See also the work of Liu and Cheng (1993) for sandwich plates, where the same form of relationship as in Eqs. (27) is shown in the linear counterpart of their nonlinear boundary value problem.) In the work of Cheng et al. (1993a, b, 1994), it has been shown that the dimensionless field equations and boundary conditions have same forms for the sandwich plate theory (Reissner, 1948) and for the first-order shear deformation theory (Reissner, 1945; Mindlin, 1951) of single-layer plates. Therefore, the relationship (27) also applies to Reissner-Mindlin single-layer plate theory. Equations (26) and $(27)_1$ represent generalizations of Hu's (1963) connection concerning sandwich plates to the cases of Reddy and the first-order laminated plate theories. Recently, the relationship $(27)_1$ was revisited by Wang (1995) for Reissner sandwich plate theory and by Wang and Alwis (1995) for Reissner-Mindlin theory of single-layer plates through a different approach.

It is worth noting that a different procedure from the present was used by Librescu (1975) and Reissner (1985) to decouple Eqs. (9) and (10) for the case of first-order plate theory. By introducing a potential function, one of the resulting equations (see also Librescu and Stein, 1992) is the same as Eq. $(17)_1$ and the linear counterpart of another is

$$a_1 u_{3,\alpha\alpha\beta\beta}^F - q + \frac{a_1}{c} q_{,\alpha\alpha} = 0. \quad (29)$$

Equation (29) is consistent with the present result by eliminating u_3^K through Eqs. (23) and $(27)_1$. Conversely, however, it is insufficient to find the relationship $(27)_1$.

Acknowledgment

This work was partly supported by the National Natural Science Foundation of China.

References

Cheng, Z. Q., Wang, X. X., and Huang, M. G., 1993a, "Large Deflections of Rectangular Hoff Sandwich Plates," *International Journal of Solids and Structures,* Vol. 30, pp. 2335–2346.

Cheng, Z. Q., Wang, X. X., and Huang, M. G., 1993b, "Nonlinear Flexural Vibration of Rectangular Moderately Thick Plates and Sandwich Plates," *International Journal of Mechanical Sciences,* Vol. 35, pp. 815–827.

Cheng, Z. Q., Wang, X. X., and Huang, M. G., 1994, "Postbuckling of Rectangular Moderately Thick Plates and Sandwich Plates," *Applied Mathematics and Mechanics,* Vol. 15, pp. 605–610.

Hu, H. C., 1963, "On Some Problems of the Antisymmetrical Small Deflection of Isotropic Sandwich Plates," *Acta Mechanica Sinica,* Vol. 6, pp. 53–60 (in Chinese).

Librescu, L., 1975, *Elastostatics and Kinetics of Anisotropic and Heterogeneous Shell-Type Structures,* Noordhoff, Leyden, The Netherlands.

Librescu, L., and Stein, M., 1992, "Postbuckling of Shear Deformable Composite Flat Panels Taking Into Account Geometrical Imperfections," *AIAA Journal,* Vol. 30, pp. 1352–1360.

Liu, R. H., and Cheng, Z. Q., 1993, "Nonlinear Bending of Simply Supported Rectangular Sandwich Plates," *Applied Mathematics and Mechanics,* Vol. 14, pp. 217–234.

Mindlin, R. D., 1951, "Influence of Rotatory Inertia and Shear on Flexural Motions of Isotropic Elastic Plates," ASME JOURNAL OF APPLIED MECHANICS, Vol. 18, pp. 31–38.

Noor, A. K., and Burton, W. S., 1989, "Assessment of Shear Deformation Theories for Multilayered Composite Plates," ASME *Applied Mechanics Reviews,* Vol. 42, pp. 1–13.

Qin, Q. H., 1993, "Nonlinear Analysis of Reissner Plates on an Elastic Foundation by the BEM," *International Journal of Solids and Structures,* Vol. 30, pp. 3101–3111.

Reddy, J. N., 1984, "A Simple Higher-Order Theory for Laminated Composite Plates," ASME JOURNAL OF APPLIED MECHANICS, Vol. 51, pp. 745–752.

Reddy, J. N., 1997, *Mechanics of Laminated Composite Plates: Theory and Analysis,* CRC Press, Boca Raton, FL.

Reddy, J. N., and Robbins Jr, D. H., 1994, "Theories and Computational Models for Composite Laminates," ASME *Applied Mechanics Reviews,* Vol. 47, pp. 147–169.

Reddy, J. N., and Wang, C. M., 1998, "Deflection Relationships Between the Classical and Third-Order Plate Theories," *Acta Mechanica,* in press.

Reissner, E., 1945, "The Effect of Transverse Shear Deformation on the Bending of Elastic Plates," ASME JOURNAL OF APPLIED MECHANICS, Vol. 12, pp. A69–A77.

Reissner, E., 1948, "Finite Deflections of Sandwich Plates," *Journal of the Aeronautical Sciences,* Vol. 15, pp. 435–440.

Reissner, E., 1985, "Reflections on the Theory of Elastic Plates," ASME *Applied Mechanics Reviews,* Vol. 38, pp. 1453–1464.

Wang, C. M., 1995, "Deflection of Sandwich Plates in Terms of Corresponding Kirchhoff Plate Solutions," *Archive of Applied Mechanics,* Vol. 65, pp. 408–414.

Wang, C. M., and Alwis, W. A. M., 1995, "Simply Supported Polygonal Mindlin Plate Deflections Using Kirchhoff Plates," *Journal of Engineering Mechanics,* Vol. 121, pp. 1383–1385.

On the Elastic Constants of Transversely Isotropic, Quasi-Symmetric Composites

P. D. Chinh[1]

Estimates for the elastic constants of transversely isotropic composites and the subclass of quasi-symmetric ones are given in unified simple forms from a common framework constructed also for the elastic moduli of three-dimensional isotropic composites and the transport properties.

The transversely isotropic composites are formed from n transversely isotropic components whose phase boundaries are

[1] Institute of Mechanics, 224 Doi Can, Hanoi, Vietnam.

Contributed by the Applied Mechanics Division of THE AMERICAN SOCIETY OF MECHANICAL ENGINEERS for publication in the ASME JOURNAL OF APPLIED MECHANICS. Manuscript received by the ASME Applied Mechanics Division, Oct. 9, 1997; final revision, June 16, 1998. Associate Technical Editor: J. N. Reddy.

Downloaded 04 May 2010 to 171.66.16.27. Redistribution subject to ASME license or copyright; see http://www.asme.org/terms/Terms_Use.cfm

(23) and between the boundary conditions $(20)_{1-4}$ and (24) that

$$(a_2 - a_1)u_3 + a_2 w = -a_1 u_3^K. \quad (25)$$

Eliminating the function w from Eqs. $(17)_2$ and (25) gives

$$(a_1 a_3 - a_2^2)u_{3,\alpha\alpha} - ca_1 u_3 = a_1 a_3 u_{3,\alpha\alpha}^K - ca_1 u_3^K. \quad (26)$$

This is an exact relationship connecting the deflections of the Reddy (1984) and Kirchhoff theories for simply supported polygonal plates with transversely isotropic symmetric laminae. Once the Kirchhoff deflection solution u_3^K is given, the solution u_3 of the third-order Reddy's theory can be solved through Eq. (26) associated with the boundary condition $(20)_1$. Another unknown w is then simply obtained from Eq. (25).

In the case of the first-order theory for laminated plates (see, e.g., Reddy, 1997), taking $g(x_3) = x_3$ in Eq. $(8)_1$ yields $a_1 = a_2 = a_3$. This provides explicit expressions of u_3^F and w^F in terms of Kirchhoff deflection u_3^K as, from Eqs. (26) and (25),

$$u_3^F = u_3^K - \frac{a_1}{c} u_{3,\alpha\alpha}^K, \quad w^F = -u_3^K, \quad (27)$$

where

$$c = \kappa \int_{-h/2}^{h/2} \mu' dx_3, \quad (28)$$

κ is the shear correction factor. Therefore, once the Kirchhoff deflection is given, the solution of the first-order laminated plate theory is readily obtained through simple manipulation of differentiation. It should be noted that Eq. $(20)_2$ is not an essential condition, unless $q = 0$, for describing the simply supported edges in the first-order theory, as can be shown through derivation of the boundary condition from Eqs. (18).

For the particular case of sandwich plates, Hu (1963) gave the relationship between Reissner sandwich plate deflection and classical Kirchhoff thin plate deflection in the same form as Eqs. (27), where a_1 is the flexural rigidity of sandwich plates and $c = \mu_c h$, with μ_c being the shear modulus of the sandwich core. (See also the work of Liu and Cheng (1993) for sandwich plates, where the same form of relationship as in Eqs. (27) is shown in the linear counterpart of their nonlinear boundary value problem.) In the work of Cheng et al. (1993a, b, 1994), it has been shown that the dimensionless field equations and boundary conditions have same forms for the sandwich plate theory (Reissner, 1948) and for the first-order shear deformation theory (Reissner, 1945; Mindlin, 1951) of single-layer plates. Therefore, the relationship (27) also applies to Reissner-Mindlin single-layer plate theory. Equations (26) and $(27)_1$ represent generalizations of Hu's (1963) connection concerning sandwich plates to the cases of Reddy and the first-order laminated plate theories. Recently, the relationship $(27)_1$ was revisited by Wang (1995) for Reissner sandwich plate theory and by Wang and Alwis (1995) for Reissner-Mindlin theory of single-layer plates through a different approach.

It is worth noting that a different procedure from the present was used by Librescu (1975) and Reissner (1985) to decouple Eqs. (9) and (10) for the case of first-order plate theory. By introducing a potential function, one of the resulting equations (see also Librescu and Stein, 1992) is the same as Eq. $(17)_1$ and the linear counterpart of another is

$$a_1 u_{3,\alpha\alpha\beta\beta}^F - q + \frac{a_1}{c} q_{,\alpha\alpha} = 0. \quad (29)$$

Equation (29) is consistent with the present result by eliminating u_3^K through Eqs. (23) and $(27)_1$. Conversely, however, it is insufficient to find the relationship $(27)_1$.

Acknowledgment

This work was partly supported by the National Natural Science Foundation of China.

References

Cheng, Z. Q., Wang, X. X., and Huang, M. G., 1993a, "Large Deflections of Rectangular Hoff Sandwich Plates," *International Journal of Solids and Structures,* Vol. 30, pp. 2335–2346.

Cheng, Z. Q., Wang, X. X., and Huang, M. G., 1993b, "Nonlinear Flexural Vibration of Rectangular Moderately Thick Plates and Sandwich Plates," *International Journal of Mechanical Sciences,* Vol. 35, pp. 815–827.

Cheng, Z. Q., Wang, X. X., and Huang, M. G., 1994, "Postbuckling of Rectangular Moderately Thick Plates and Sandwich Plates," *Applied Mathematics and Mechanics,* Vol. 15, pp. 605–610.

Hu, H. C., 1963, "On Some Problems of the Antisymmetrical Small Deflection of Isotropic Sandwich Plates," *Acta Mechanica Sinica,* Vol. 6, pp. 53–60 (in Chinese).

Librescu, L., 1975, *Elastostatics and Kinetics of Anisotropic and Heterogeneous Shell-Type Structures,* Noordhoff, Leyden, The Netherlands.

Librescu, L., and Stein, M., 1992, "Postbuckling of Shear Deformable Composite Flat Panels Taking Into Account Geometrical Imperfections," *AIAA Journal,* Vol. 30, pp. 1352–1360.

Liu, R. H., and Cheng, Z. Q., 1993, "Nonlinear Bending of Simply Supported Rectangular Sandwich Plates," *Applied Mathematics and Mechanics,* Vol. 14, pp. 217–234.

Mindlin, R. D., 1951, "Influence of Rotatory Inertia and Shear on Flexural Motions of Isotropic Elastic Plates," ASME JOURNAL OF APPLIED MECHANICS, Vol. 18, pp. 31–38.

Noor, A. K., and Burton, W. S., 1989, "Assessment of Shear Deformation Theories for Multilayered Composite Plates," ASME *Applied Mechanics Reviews,* Vol. 42, pp. 1–13.

Qin, Q. H., 1993, "Nonlinear Analysis of Reissner Plates on an Elastic Foundation by the BEM," *International Journal of Solids and Structures,* Vol. 30, pp. 3101–3111.

Reddy, J. N., 1984, "A Simple Higher-Order Theory for Laminated Composite Plates," ASME JOURNAL OF APPLIED MECHANICS, Vol. 51, pp. 745–752.

Reddy, J. N., 1997, *Mechanics of Laminated Composite Plates: Theory and Analysis,* CRC Press, Boca Raton, FL.

Reddy, J. N., and Robbins Jr, D. H., 1994, "Theories and Computational Models for Composite Laminates," ASME *Applied Mechanics Reviews,* Vol. 47, pp. 147–169.

Reddy, J. N., and Wang, C. M., 1998, "Deflection Relationships Between the Classical and Third-Order Plate Theories," *Acta Mechanica,* in press.

Reissner, E., 1945, "The Effect of Transverse Shear Deformation on the Bending of Elastic Plates," ASME JOURNAL OF APPLIED MECHANICS, Vol. 12, pp. A69–A77.

Reissner, E., 1948, "Finite Deflections of Sandwich Plates," *Journal of the Aeronautical Sciences,* Vol. 15, pp. 435–440.

Reissner, E., 1985, "Reflections on the Theory of Elastic Plates," ASME *Applied Mechanics Reviews,* Vol. 38, pp. 1453–1464.

Wang, C. M., 1995, "Deflection of Sandwich Plates in Terms of Corresponding Kirchhoff Plate Solutions," *Archive of Applied Mechanics,* Vol. 65, pp. 408–414.

Wang, C. M., and Alwis, W. A. M., 1995, "Simply Supported Polygonal Mindlin Plate Deflections Using Kirchhoff Plates," *Journal of Engineering Mechanics,* Vol. 121, pp. 1383–1385.

On the Elastic Constants of Transversely Isotropic, Quasi-Symmetric Composites

P. D. Chinh[1]

Estimates for the elastic constants of transversely isotropic composites and the subclass of quasi-symmetric ones are given in unified simple forms from a common framework constructed also for the elastic moduli of three-dimensional isotropic composites and the transport properties.

The transversely isotropic composites are formed from n transversely isotropic components whose phase boundaries are

[1] Institute of Mechanics, 224 Doi Can, Hanoi, Vietnam.

Contributed by the Applied Mechanics Division of THE AMERICAN SOCIETY OF MECHANICAL ENGINEERS for publication in the ASME JOURNAL OF APPLIED MECHANICS. Manuscript received by the ASME Applied Mechanics Division, Oct. 9, 1997; final revision, June 16, 1998. Associate Technical Editor: J. N. Reddy.

 Copyright © 1999 by ASME

Downloaded 04 May 2010 to 171.66.16.27. Redistribution subject to ASME license or copyright; see http://www.asme.org/terms/Terms_Use.cfm

cylindrical surfaces, with generators orthogonal to the components' common plane of isotropy. The statistically homogeneous composites have the effective elastic transverse plain-strain area and shear moduli K_c and μ_c, longitudinal Young's modulus E_c and Poisson's ratio ν_c, and shear modulus $\bar{\mu}_c$. The respective elastic constants of the constituents are K_α, μ_α, E_α, ν_α, and $\bar{\mu}_\alpha$ ($\alpha = 1, \ldots, n$). The geometry of composite's transverse plane is of random nature, so there is no unique formula for an effective property expressed through the components' properties and their volume proportions v_α. Still, from the dual minimum energy and complimentary energy principles, and choosing appropriate trial fields, one can construct tight upper and lower bounds for the effective constants, given the restrictions on the geometry of a class of composites (Hill, 1963; Walpole, 1966; Pham, 1993, 1997). E.g., in this way, Hashin-Shtrikman bounds for the area modulus K_c (Hashin, 1965) can be given as (Pham, 1997)

$$P_K(\mu_{\max}) \geq K_c \geq P_K(\mu_{\min}), \tag{1}$$

$$P_K(\mu_0) = \left(\sum_{\alpha=1}^{n} \frac{v_\alpha}{K_\alpha + \mu_0} \right)^{-1} - \mu_0, \tag{2}$$

$$\mu_{\max} = \max \{\mu_1, \ldots, \mu_n\}, \quad \mu_{\min} = \min \{\mu_1, \ldots, \mu_n\}. \tag{3}$$

The bounds (1)–(3) in the two-component case are attained by certain matrix composites called coated cylinder assemblages (Hashin and Rosen, 1964) and therefore are verified to be the optimal ones.

There is an interesting class of composites called quasi-symmetric ones, in which the phases' microgeometries are statistically indistinguishable except for possible differences in their volume fractions (Miller, 1969; Beran and Silnutzer, 1971; Milton, 1982; Bruno, 1990; Pham, 1994, 1997). Such quasi-symmetric composites do not have distinct inclusion and matrix phases (roughly speaking, the phases are geometrically equal) in contrast with the asymmetric composite cylinder model of Hashin and Rosen where the continuous matrix phase surrounds separated inclusions from the other phase and has greater influence on the composite's effective moduli. The respective bounds for quasi-symmetric mixtures have the simple form in the two-component case (Pham, 1997)

$$P_K(\mu^u) \geq K_c \geq P_K(\mu^l), \tag{4}$$

$$\mu^u = \max \{v_1\mu_1 + v_2\mu_2, v_1\mu_2 + v_2\mu_1\}, \tag{5}$$

$$\mu^l = \min \{(v_1/\mu_1 + v_2/\mu_2)^{-1}, (v_1/\mu_2 + v_2/\mu_1)^{-1}\}. \tag{6}$$

The lower bounds (4), (6) has been verified to be optimal over half the ranges of the parameters, in particular when (Pham, 1997)

$$v_1/\mu_1 + v_2/\mu_2 \leq v_1/\mu_2 + v_2/\mu_1. \tag{7}$$

The bounds appear relatively tight compared with certain realizable geometries within the class (Pham, 1997). The bounds for the subclass of multicomponent circular cylinder cell materials have the very simple form (Pham, 1996, 1997)

$$P_K(\mu_s^u) \geq K_c \geq P_K(\mu_s^l),$$

$$\mu_s^u = \sum_{\alpha=1}^{n} v_\alpha\mu_\alpha, \quad \mu_s^l = \left(\sum_{\alpha=1}^{n} v_\alpha/\mu_\alpha\right)^{-1}. \tag{8}$$

Those circular cylinder cell composites are expected to approximate the situation, that the fibers of approximately circular cross sections from different phases, which have the same patterns of sizes and forms, are combined in a random fashion into compact mixtures (without a binding matrix).

It is interesting to note that the respective bounds for the transverse shear modulus μ_c (Pham, 1997), the elastic moduli of three-dimensional isotropic composites, and the conductivity properties (Pham, 1993, 1994, 1996, 1997) have almost the identical structure as that of relations (1)–(8). The only slight differences are in the particular arguments of the respective property P-functions.

The Longitudinal Shear Modulus $\bar{\mu}_c$

Following the variational approach (Hill, 1963; Hashin, 1965; Christensen, 1979; Pham, 1993), the longitudinal shear modulus $\bar{\mu}_c$ can be defined as

$$\bar{\mu}_c\boldsymbol{\gamma}^0 \cdot \boldsymbol{\gamma}^0 = \inf \int_V \bar{\mu}\boldsymbol{\gamma} \cdot \boldsymbol{\gamma} d\mathbf{x} \quad (\bar{\mu} = \bar{\mu}_\alpha \quad \text{in} \quad V_\alpha \in V), \tag{9}$$

where the infimum is sought over the vector gradient shear strain field

$$\boldsymbol{\gamma} = \{\gamma_{12}, \gamma_{13}\} = \left\{ \frac{\partial}{\partial x_2} u_1(x_2, x_3), \frac{\partial}{\partial x_3} u_1(x_2, x_3) \right\} \tag{10}$$

satisfying restriction

$$\int_V \boldsymbol{\gamma} d\mathbf{x} = \boldsymbol{\gamma}^0 = \text{const.} \tag{11}$$

$u_1(x_2, x_3)$ is the longitudinal displacement and x_2 and x_3 are the coordinates in the transverse plane.

Respectively, $\bar{\mu}_c$ can also be determined from the complementary problem

$$\bar{\mu}_c^{-1}\boldsymbol{\tau}^0 \cdot \boldsymbol{\tau}^0 = \inf \int_V \bar{\mu}^{-1}\boldsymbol{\tau} \cdot \boldsymbol{\tau} d\mathbf{x}, \tag{12}$$

where the infimum is sought over the shear stress field $\boldsymbol{\tau}(\mathbf{x}) = (\tau_{12}, \tau_{13})$, which is subjected to the restrictions

$$\nabla \cdot \boldsymbol{\tau} = 0, \quad \int_V \boldsymbol{\tau} d\mathbf{x} = \boldsymbol{\tau}^0 = \text{const.} \tag{13}$$

Equations (10)–(13) have mathematically the same forms as those for the problem of two-dimensional conductivity (Pham, 1997) with the shear moduli taking the places of the conductivities, the shear strain—the gradient field and the shear stress—of the flux vector. Thus the results from the latter problem can be transformed to the former as well. In particular, the bounds for the transversely isotropic composites read

$$P_{\bar{\mu}}(\bar{\mu}_{\max}) \geq \bar{\mu}_c \geq P_{\bar{\mu}}(\bar{\mu}_{\min}), \tag{14}$$

$$P_{\bar{\mu}}(\bar{\mu}_0) = \left(\sum_{\alpha=1}^{n} \frac{v_\alpha}{\bar{\mu}_\alpha + \bar{\mu}_0} \right)^{-1} - \bar{\mu}_0, \tag{15}$$

$$\bar{\mu}_{\max} = \max \{\bar{\mu}_1, \ldots, \bar{\mu}_n\}, \quad \bar{\mu}_{\min} = \min \{\bar{\mu}_1, \ldots, \bar{\mu}_n\}. \tag{16}$$

The bounds for quasi-symmetric two-component mixtures have the form

$$P_{\bar{\mu}}(\bar{\mu}^u) \geq \bar{\mu}_c \geq P_{\bar{\mu}}(\bar{\mu}^l),$$

$$\bar{\mu}^u = \max \{v_1\bar{\mu}_1 + v_2\bar{\mu}_2, \quad v_1\bar{\mu}_2 + v_2\bar{\mu}_1\},$$

$$\bar{\mu}^l = \min \{(v_1/\bar{\mu}_1 + v_2/\bar{\mu}_2)^{-1}, \quad (v_1/\bar{\mu}_2 + v_2/\bar{\mu}_1)^{-1}\}. \tag{17}$$

The bounds for multicomponent circular cylinder cell materials are

$$P_{\bar{\mu}}(\bar{\mu}_s^u) \geq \bar{\mu}_c \geq P_{\bar{\mu}}(\bar{\mu}_s^l),$$

$$\bar{\mu}_s^u = \sum_{\alpha=1}^{n} v_\alpha\bar{\mu}_\alpha, \quad \bar{\mu}_s^l = \left(\sum_{\alpha=1}^{n} v_\alpha/\bar{\mu}_\alpha\right)^{-1}. \tag{18}$$

We see that Eqs. (14)–(18) have almost the identical structure as that of Eqs. (1)–(8) for the area modulus.

Downloaded 04 May 2010 to 171.66.16.27. Redistribution subject to ASME license or copyright; see http://www.asme.org/terms/Terms_Use.cfm

The Elastic Moduli E_c and ν_c

Hill (1964) established the relations for the two-component composites

$$(K_c^{-1} - v_1K_1^{-1} - v_2K_2^{-1})\frac{\nu_1 - \nu_2}{K_1^{-1} - K_2^{-1}} = \nu_c - v_1\nu_1 - v_2\nu_2$$
$$= -\frac{1}{4}(E_c - v_1E_1 - v_2E_2)\frac{K_1^{-1} - K_2^{-1}}{\nu_1 - \nu_2}, \quad (19)$$

and then deduced the following bounds:

$$\frac{v_1v_2}{v_1/K_2 + v_2/K_1 + 1/\mu_0} \geq \frac{E_c - v_1E_1 - v_2E_2}{4(\nu_1 - \nu_2)^2}$$
$$\geq \frac{v_1v_2}{v_1/K_2 + v_2/K_1 + 1/\mu_0'}, \quad (20)$$

$$\frac{v_1v_2}{v_1/K_2 + v_2/K_1 + 1/\mu_0} \geq \frac{\nu_c - v_1\nu_1 - v_2\nu_2}{(\nu_1 - \nu_2)(1/K_2 - 1/K_1)}$$
$$\geq \frac{v_1v_2}{v_1/K_2 + v_2/K_1 + 1/\mu_0'} \quad (21)$$

for the transversely isotropic composites, taking $\mu_0 = \mu_{\max}$, $\mu_0' = \mu_{\min}$ (see Eqs. (3) at $n = 2$).

Inequalities (20), (21) give also respective bounds for two-component quasi-symmetric mixtures (if one takes $\mu_0 = \mu^u$, $\mu_0' = \mu^l$—see Eqs. (5), (6)) and circular cylinder cell ones (if one choses $\mu_0 = \mu_s^u$, $\mu_0' = \mu_s^l$— see Eq. (8) at $n = 2$). From the relations (19)–(21) one can see that the extremal geometries for K_c also yield the respective extremal values of E_c, ν_c. However, while the configuration that possesses the maximal (minimal) value of K_c also got the maximal (minimal) value of E_c, it may have maximal or minimal (and vice versa) value of ν_c depending on the product $(\nu_1 - \nu_2)(K_2^{-1} - K_1^{-1})$ being positive or negative. Hashin-Rosen's coated cylinder assemblage provides optimal geometries for the moduli K_c, $\bar{\mu}_c$, E_c, ν_c (Hashin and Rosen, 1965) and μ_c (Pham, 1999) of two-component transversely isotropic composites. As the lower bound (4), (6) for K_c of two-component quasi-symmetric mixtures is optimal over the range (7), the respective bounds for E_c and ν_c of the composites are also optimal over that range.

Note that we still do not have the respective bounds for the elastic constants E_c, ν_c in the general multicomponent case.

Relations similar to those of (19)–(21) between the elastic constants and the thermal expansion coefficients and the specific heats (Christensen, 1979) should help to derive the respective bounds for the thermal properties of the composites.

References

Beran, M. J., and Silnutzer, N. R., 1971, "Effective electrical, thermal and magnetic properties of fiber reinforced materials," *J. Composite Mater.*, Vol. 5, pp. 246–249.

Bruno, O. P., 1990, "The effective conductivity of an infinitely interchangeable mixture," *Commun. Pure Appl. Math.*, Vol. 43, pp. 769–807.

Christensen, R. M., 1979, *Mechanics of Composite Materials*, John Wiley and Sons, New York.

Hashin, Z., 1965, "On elastic behaviour of fibre reinforced materials of arbitrary transverse phase geometry," *J. Mech. Phys. Solids*, Vol. 13, pp. 119–134.

Hashin, Z., and Rosen W., 1964, "The Elastic Moduli of Fiber-Reinforced Materials," ASME JOURNAL OF APPLIED MECHANICS, Vol. 31, pp. 223.

Hill, R., 1963, "Elastic properties of reinforced solids: some theoretical principles," *J. Mech. Phys. Solids*, Vol. 11, pp. 357–372.

Hill, R., 1964, "Theory of mechanical properties of fiber-strengthened materials: I. Elastic behaviour," *J. Mech. Phys. Solids*, Vol. 12, pp. 199–212.

Miller, M. N., 1969, "Bounds for the effective elastic bulk modulus of heterogeneous materials," *J. Math. Phys.*, Vol. 10, pp. 2005–2013.

Milton, G. W., 1982, "Bounds on the elastic and transport properties of two-component composites," *J. Mech. Phys. Solids*, Vol. 30, pp. 177–191.

Pham, D. C., 1993, "Bounds on the effective shear modulus of multiphase materials," *Int. J. Engng. Sci.*, Vol. 31, pp. 11–17.

Pham, D. C., 1994, "Bounds for the effective conductivity and elastic moduli of fully-disordered multicomponent materials," *Arch. Rational Mech. Anal.*, Vol. 127, pp. 191–198.

Pham, D. C., 1996, "On macroscopic conductivity and elastic properties of perfectly-random cell composites," *Int. J. Solids Struct.*, Vol. 33, pp. 1745–1755.

Pham, D. C., 1997, "Overall properties of planar quasisymmetric randomly inhomogeneous media: estimates and cell models," *Phys. Rev. E*, Vol. 56, pp. 652–660.

Pham, D. C., 1999, "Estimates for the transverse shear modulus of unidirectional composites" *Eur. J. Mech. A/Solids*, in press

Walpole, L. J., 1966, "On bounds for the overall elastic moduli of inhomogeneous systems," *J. Mech. Phys. Solids*, Vol. 14, pp. 152–162.

A Theory of Continuum Damage Mechanics for Anisotropic Solids

U. Lee[1]

This paper develops a fracture mechanics based continuum damage theory for initially anisotropic *solids by extending the author's previous damage theory for* isotropic *solids. The concepts of strain energy equivalence principle (SEEP) and equivalent line-crack modeling are used to develop the effective continuum elastic properties of a damaged solid in terms of the undamaged anisotropic elastic properties and a scalar damage variable.*

1 Introduction

A material failure process is often assumed to involve general degradation of elastic properties due to the highly localized nucleation and growth of damage. Despite the nonuniqueness of damage definitions, there have been extensive researches on continuum damage mechanics. Extensive treatments of continuum damage mechanics can be found in the recent book by Krajcinovic (1996).

Most theories of continuum damage mechanics have been developed for initially *isotropic* solids, in part due to the fact that the assumption of initial isotropy in many existing anisotropic damage models has been merely made for convenience (Ortiz, 1985).

Recently Lee et al. (1997) developed a continuum damage theory (simply, Lee's damage theory) that permits *anisotropic* behavior of the damaged *isotropic* material, while using a *scalar* damage variable. Lee's damage theory is on the basis of both the principle of strain energy equivalence and the concept of equivalent fictitious microcrack representation of a local damage. Similar concepts can be also found in the recent work by Mazars and Pijaudier-Cabot (1996). The *strain energy equivalence principle* (SEEP) means that a material volume cell (MVC) of the damaged material containing a local damage and its equivalent continuum model (ECM) should contain equal strain energy when they are subjected to identical global displacements on their boundaries. In Lee's damage theory, first SEEP is used to develop the effective continuum elastic properties of a damaged solid in terms of the undamaged isotropic elastic properties as well as a new definition of scalar damage variable. Secondly, a local damage is modeled as an equivalent

[1] Professor, Department of Mechanical Engineering, Inha University, 253 Yonghyun-Dong, Nam-Ku, Inchon 402-751, South Korea. Mem. ASME.

Contributed by the Applied Mechanics Division of THE AMERICAN SOCIETY OF MECHANICAL ENGINEERS for publication in the ASME JOURNAL OF APPLIED MECHANICS. Manuscript received by the ASME Applied Mechanics Division, Nov. 18, 1997; final revision, Aug. 12, 1998. Associate Technical Editor: J. N. Reddy.

Downloaded 04 May 2010 to 171.66.16.27. Redistribution subject to ASME license or copyright; see http://www.asme.org/terms/Terms_Use.cfm

The Elastic Moduli E_c and ν_c

Hill (1964) established the relations for the two-component composites

$$(K_c^{-1} - v_1K_1^{-1} - v_2K_2^{-1})\frac{\nu_1 - \nu_2}{K_1^{-1} - K_2^{-1}} = \nu_c - v_1\nu_1 - v_2\nu_2$$
$$= -\frac{1}{4}(E_c - v_1E_1 - v_2E_2)\frac{K_1^{-1} - K_2^{-1}}{\nu_1 - \nu_2}, \quad (19)$$

and then deduced the following bounds:

$$\frac{v_1v_2}{v_1/K_2 + v_2/K_1 + 1/\mu_0} \geq \frac{E_c - v_1E_1 - v_2E_2}{4(\nu_1 - \nu_2)^2}$$
$$\geq \frac{v_1v_2}{v_1/K_2 + v_2/K_1 + 1/\mu_0'}, \quad (20)$$

$$\frac{v_1v_2}{v_1/K_2 + v_2/K_1 + 1/\mu_0} \geq \frac{\nu_c - v_1\nu_1 - v_2\nu_2}{(\nu_1 - \nu_2)(1/K_2 - 1/K_1)}$$
$$\geq \frac{v_1v_2}{v_1/K_2 + v_2/K_1 + 1/\mu_0'} \quad (21)$$

for the transversely isotropic composites, taking $\mu_0 = \mu_{\max}$, $\mu_0' = \mu_{\min}$ (see Eqs. (3) at $n = 2$).

Inequalities (20), (21) give also respective bounds for two-component quasi-symmetric mixtures (if one takes $\mu_0 = \mu^u$, $\mu_0' = \mu^l$—see Eqs. (5), (6)) and circular cylinder cell ones (if one choses $\mu_0 = \mu_s^u$, $\mu_0' = \mu_s^l$— see Eq. (8) at $n = 2$). From the relations (19)–(21) one can see that the extremal geometries for K_c also yield the respective extremal values of E_c, ν_c. However, while the configuration that possesses the maximal (minimal) value of K_c also got the maximal (minimal) value of E_c, it may have maximal or minimal (and vice versa) value of ν_c depending on the product $(\nu_1 - \nu_2)(K_2^{-1} - K_1^{-1})$ being positive or negative. Hashin-Rosen's coated cylinder assemblage provides optimal geometries for the moduli K_c, $\bar{\mu}_c$, E_c, ν_c (Hashin and Rosen, 1965) and μ_c (Pham, 1999) of two-component transversely isotropic composites. As the lower bound (4), (6) for K_c of two-component quasi-symmetric mixtures is optimal over the range (7), the respective bounds for E_c and ν_c of the composites are also optimal over that range.

Note that we still do not have the respective bounds for the elastic constants E_c, ν_c in the general multicomponent case.

Relations similar to those of (19)–(21) between the elastic constants and the thermal expansion coefficients and the specific heats (Christensen, 1979) should help to derive the respective bounds for the thermal properties of the composites.

References

Beran, M. J., and Silnutzer, N. R., 1971, "Effective electrical, thermal and magnetic properties of fiber reinforced materials," *J. Composite Mater.*, Vol. 5, pp. 246–249.

Bruno, O. P., 1990, "The effective conductivity of an infinitely interchangeable mixture," *Commun. Pure Appl. Math.*, Vol. 43, pp. 769–807.

Christensen, R. M., 1979, *Mechanics of Composite Materials*, John Wiley and Sons, New York.

Hashin, Z., 1965, "On elastic behaviour of fibre reinforced materials of arbitrary transverse phase geometry," *J. Mech. Phys. Solids*, Vol. 13, pp. 119–134.

Hashin, Z., and Rosen W., 1964, "The Elastic Moduli of Fiber-Reinforced Materials," ASME JOURNAL OF APPLIED MECHANICS, Vol. 31, pp. 223.

Hill, R., 1963, "Elastic properties of reinforced solids: some theoretical principles," *J. Mech. Phys. Solids*, Vol. 11, pp. 357–372.

Hill, R., 1964, "Theory of mechanical properties of fiber-strengthened materials: I. Elastic behaviour," *J. Mech. Phys. Solids*, Vol. 12, pp. 199–212.

Miller, M. N., 1969, "Bounds for the effective elastic bulk modulus of heterogeneous materials," *J. Math. Phys.*, Vol. 10, pp. 2005–2013.

Milton, G. W., 1982, "Bounds on the elastic and transport properties of two-component composites," *J. Mech. Phys. Solids*, Vol. 30, pp. 177–191.

Pham, D. C., 1993, "Bounds on the effective shear modulus of multiphase materials," *Int. J. Engng. Sci.*, Vol. 31, pp. 11–17.

Pham, D. C., 1994, "Bounds for the effective conductivity and elastic moduli of fully-disordered multicomponent materials," *Arch. Rational Mech. Anal.*, Vol. 127, pp. 191–198.

Pham, D. C., 1996, "On macroscopic conductivity and elastic properties of perfectly-random cell composites," *Int. J. Solids Struct.*, Vol. 33, pp. 1745–1755.

Pham, D. C., 1997, "Overall properties of planar quasisymmetric randomly inhomogeneous media: estimates and cell models," *Phys. Rev. E*, Vol. 56, pp. 652–660.

Pham, D. C., 1999, "Estimates for the transverse shear modulus of unidirectional composites" *Eur. J. Mech. A/Solids*, in press

Walpole, L. J., 1966, "On bounds for the overall elastic moduli of inhomogeneous systems," *J. Mech. Phys. Solids*, Vol. 14, pp. 152–162.

A Theory of Continuum Damage Mechanics for Anisotropic Solids

U. Lee[1]

This paper develops a fracture mechanics based continuum damage theory for initially anisotropic *solids by extending the author's previous damage theory for* isotropic *solids. The concepts of strain energy equivalence principle (SEEP) and equivalent line-crack modeling are used to develop the effective continuum elastic properties of a damaged solid in terms of the undamaged anisotropic elastic properties and a scalar damage variable.*

1 Introduction

A material failure process is often assumed to involve general degradation of elastic properties due to the highly localized nucleation and growth of damage. Despite the nonuniqueness of damage definitions, there have been extensive researches on continuum damage mechanics. Extensive treatments of continuum damage mechanics can be found in the recent book by Krajcinovic (1996).

Most theories of continuum damage mechanics have been developed for initially *isotropic* solids, in part due to the fact that the assumption of initial isotropy in many existing anisotropic damage models has been merely made for convenience (Ortiz, 1985).

Recently Lee et al. (1997) developed a continuum damage theory (simply, Lee's damage theory) that permits *anisotropic* behavior of the damaged *isotropic* material, while using a *scalar* damage variable. Lee's damage theory is on the basis of both the principle of strain energy equivalence and the concept of equivalent fictitious microcrack representation of a local damage. Similar concepts can be also found in the recent work by Mazars and Pijaudier-Cabot (1996). The *strain energy equivalence principle* (SEEP) means that a material volume cell (MVC) of the damaged material containing a local damage and its equivalent continuum model (ECM) should contain equal strain energy when they are subjected to identical global displacements on their boundaries. In Lee's damage theory, first SEEP is used to develop the effective continuum elastic properties of a damaged solid in terms of the undamaged isotropic elastic properties as well as a new definition of scalar damage variable. Secondly, a local damage is modeled as an equivalent

[1] Professor, Department of Mechanical Engineering, Inha University, 253 Yonghyun-Dong, Nam-Ku, Inchon 402-751, South Korea. Mem. ASME.

Contributed by the Applied Mechanics Division of THE AMERICAN SOCIETY OF MECHANICAL ENGINEERS for publication in the ASME JOURNAL OF APPLIED MECHANICS. Manuscript received by the ASME Applied Mechanics Division, Nov. 18, 1997; final revision, Aug. 12, 1998. Associate Technical Editor: J. N. Reddy.

 Copyright © 1999 by ASME

Downloaded 04 May 2010 to 171.66.16.27. Redistribution subject to ASME license or copyright; see http://www.asme.org/terms/Terms_Use.cfm

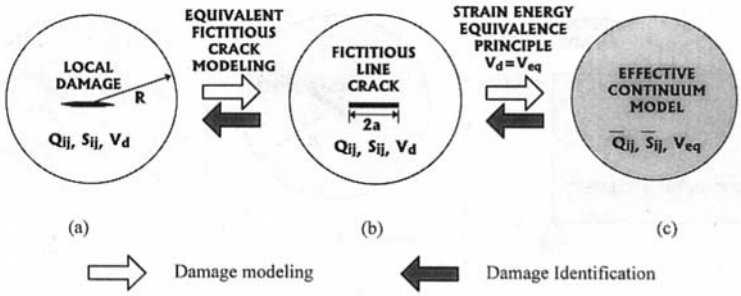

Fig. 1 General features of the present continuum damage theory: (*a*) a local damage within a material volume cell (MVC), (*b*) equivalent fictitious line-crack model, and (*c*) effective continuum model (ECM) based on strain energy equivalence principle (SEEP)

fictitious elliptical microcrack. This process makes it possible to approximately represent the current geometry and growth direction of a local damage in terms of the aspect ratio and orientation of equivalent elliptical microcrack, respectively, and to utilize the strain energy formulated in fracture mechanics for a MVC containing an elliptical crack.

In these days anisotropic materials, such as composite materials and piezoelectric materials, are increasingly used for structural applications. Thus, the purpose of this paper is to develop a continuum damage mechanics for *anisotropic* solids by extending Lee's damage theory developed for *isotropic* solids.

2 Continuum Modeling of Local Damage

In the development of continuum damage theory for initially anisotropic solids, the same principles, assumptions, and modeling procedure that were introduced for initially isotropic solids in Lee et al. (1997) will be used in this paper without duplicating if not necessary. Since most fracture surfaces can be considered as the continual propagation and coalescence of thin film-like microcracks, it may be pertinent to represent a local damage as the line through-crack (simply, line crack) for plane problems. Thus, in this paper, discussion will be confined to the anisotropic plane problems with line cracks. The present study may be readily generalized to other crack problems including the three-dimensional problems.

Figure 1 shows the general features of the present damage theory, a damaged MVC having the characteristic radius of R. The MVC will be modeled as an ECM by determining its effective continuum elastic properties on the basis of SEEP. From SEEP, the strain energy V_d contained in MVC is set to be equal to the strain energy V_{eq} in ECM,

$$V_{eq}(\bar{\mathbf{S}};\, \sigma) = V_d(\mathbf{S},\, \mathcal{D};\, \sigma), \tag{1}$$

where $S_{ij}(i, j = 1, 2, 6)$ represent the elastic compliance for the undamaged state of three-dimensional anisotropic solids and $\bar{S}_{ij}$ $(i, j = 1, 2, 6)$ represent the damaged state. In Eq. (1), $\mathcal{D}$ is the scalar damage variable which will be defined later on. The effective continuum elastic compliance $\bar{S}_{ij}$ is to be determined in terms of S_{ij} and $\mathcal{D}$ from Eq. (1).

Consider a two-dimensional anisotropic solid lying in the 1–2 plane and assume the generalized plane stress state. For the damaged state, the line crack is assumed to be aligned with direction "1" as illustrated in Fig. 2(*b*). In the following, the subscripts 1 and 2 will represent the crack coordinates, as shown in Fig. 2(*b*), if not mentioned otherwise. The stress-strain relation for an undamaged anisotropic solid can be written in terms of S_{ij} as

$$\{\epsilon\} = [S]\{\sigma\}, \tag{2}$$

while, for the ECM of damaged solid, it can be written in terms of $\bar{S}_{ij}$ as

$$\{\epsilon\} = [\bar{S}]\{\sigma\}. \tag{3}$$

In Eqs. (2) and (3), the contracted notations for stresses σ_i $(i = 1, 2, 6)$ and strains ϵ_i $(i = 1, 2, 6)$ are used for plane problems, i.e., $\sigma_1 = \sigma_{11}$, $\sigma_2 = \sigma_{22}$, $\sigma_6 = \tau_{12}$, $\epsilon_1 = \epsilon_{11}$, $\epsilon_2 = \epsilon_{22}$, and $\epsilon_6 = \gamma_{12}$.

The strain energy that can be stored in a undamaged MVC can be written in terms of S_{ij} as

$$V_o = \tfrac{1}{2}\pi R^2\{\sigma\}^T[S]\{\sigma\}. \tag{4}$$

Similarly, the strain energy that can be stored in an ECM of *damaged* anisotropic solid can be written in terms of $\bar{S}_{ij}$ as

$$V_{eq} = \tfrac{1}{2}\pi R^2\{\sigma\}^T[\bar{S}]\{\sigma\}. \tag{5}$$

Due to the degradation of elastic moduli, a damaged solid may not store as much strain energy as a undamaged solid can store. The strain energy V_d that can be stored in a damaged MVC is obtained from

$$V_d = V_o \pm V_c, \tag{6}$$

depending on if the traction or displacement is specified on the boundary of a damaged MVC (Sih and Liebowitz, 1967). The crack energy V_c for generating a line crack of length $2a$ in an infinite two-dimensional anisotropic is available from Sih and Liebowitz (1967) and it can be expressed as

$$V_c = \tfrac{1}{2}\pi a^2\begin{Bmatrix}\sigma_1\\ \sigma_2\\ \sigma_6\end{Bmatrix}^T\begin{bmatrix}0 & 0 & 0\\ 0 & S_{22}\delta_{22} & 0\\ 0 & 0 & S_{11}\delta_{66}\end{bmatrix}\begin{Bmatrix}\sigma_1\\ \sigma_2\\ \sigma_6\end{Bmatrix} \tag{7}$$

where

$$\delta_{22} = (\alpha_1^2 + \beta_1^2)\beta_2 + (\alpha_2^2 + \beta_2^2)\beta_1, \quad \delta_{66} = \beta_1 + \beta_2. \tag{8}$$

In Eq. (8), α_i and β_i are determined from the four roots $r_{1,2} = \alpha_1 \pm i\beta_1$ and $r_{3,4} = \alpha_2 \pm i\beta_2$ of an algebraic equation given as

$$S_{11}r^4 - 2S_{16}r^3 + (2S_{12} + S_{66})r^2 - 2S_{26}r + S_{22} = 0. \tag{9}$$

Substituting Eqs. (4) and (7) into Eq. (6), the strain energy V_d is obtained as

$$V_d = \tfrac{1}{2}\pi R^2\{\sigma\}^T[S_{ij}(1 + \bar{e}_{ij}\mathcal{D})]\{\sigma\}$$

$$(i, j = 1, 2, 6;\ \text{no sum}) \tag{10}$$

where $\bar{e}_{ij}$ are defined as

$$\bar{e}_{22} = \delta_{22},\ \bar{e}_{66} = \frac{S_{11}}{S_{66}}\delta_{66},\ \text{and other } \bar{e}_{ij} = 0. \tag{11}$$

The parameters $\bar{e}_{ij}$ certainly depend on undamaged elastic compliance S_{ij} and crack orientation because they are calculated by

Downloaded 04 May 2010 to 171.66.16.27. Redistribution subject to ASME license or copyright; see http://www.asme.org/terms/Terms_Use.cfm

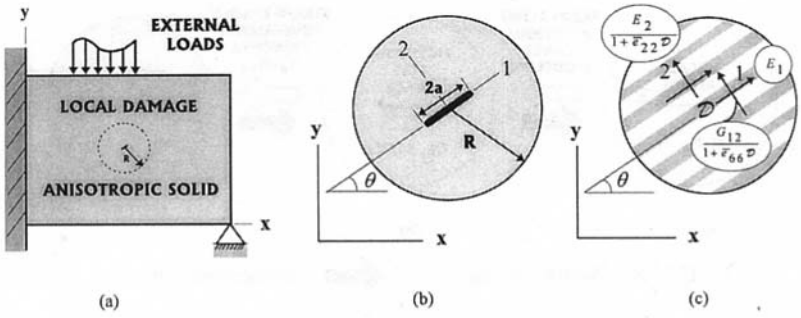

Fig. 2 Identification of local damage: (*a*) current state of a local damage within a structure, (*b*) direction of equivalent line crack, and (*c*) effective engineering constants with respect to crack coordinates

assuming that the line crack is aligned with the direction "1," one of the local coordinates. In Eq. (10), the scalar damage variable $\mathcal{D}$ is defined as

$$\mathcal{D} = \left(\frac{a}{R}\right)^2. \tag{12}$$

The present definition of damage variable $\mathcal{D}$ is found to be identical to that defined in Lee's damage theory. Thus, the damage evolution equation proposed in Lee's damage theory is still valid for anisotropic solids.

Equating Eq. (5) to Eq. (10) on the basis of SEEP yields the effective continuum elastic compliance $\bar{S}_{ij}$ in a simple form as

$$\bar{S}_{ij} = S_{ij}(1 + \bar{e}_{ij}\mathcal{D}) \quad (i, j = 1, 2, 6; \text{ no sum}). \tag{13}$$

Equation (13) implies that initially anisotropic solids behave anisotropic after damaged, while initially orthotropic (in which one plane of material symmetries is aligned with the line crack) and isotropic solids behave orthotropic after damaged by the line crack. The effective engineering constants of ECM are derived from Eq. (13) and are listed in Table 1 for initially anisotropic, orthotropic, and isotropic solids.

The strain energy V_d of Eq. (10) can be rederived in terms of strains and reduced stiffness Q_{ij} as

$$V_d = \tfrac{1}{2}\pi R^2\{\epsilon\}^T[Q_{ij}(1 - e_{ij}\mathcal{D})]\{\epsilon\}$$

$$(i, j = 1, 2, 6; \text{ no sum}) \tag{14}$$

where the reduced stiffness Q_{ij} are defined in terms of the stiffness C_{ij} for three-dimensional solids as follows (Tsai, 1988):

$$Q_{ij} = C_{ij} - \frac{C_{i6}C_{j6}}{C_{66}} \quad (i, j = 1, 2, 6). \tag{15}$$

On the basis of SEEP, the effective continuum elastic stiffness $\bar{Q}_{ij}$ are then obtained from

$$\bar{Q}_{ij} = Q_{ij}(1 - e_{ij}\mathcal{D}) \quad (i, j = 1, 2, 6; \text{ no sum}) \tag{16}$$

where the parameters e_{ij} are listed in Table 2. It is shown from Table 2 that the parameters e_{ij} for initially isotropic solids are identical to that derived in Lee et al. (1997). The notations for anisotropic material properties used in Tables 1 and 2 can be found in the book by Tsai (1988).

Table 1 Effective continuum engineering constants for generalized plane stress problems, depending on the type of material symmetry

Effective engineering constants	Type of initially undamaged solids		
	Anisotropic	Orthotropic	Isotropic
$\bar{E}_1$	E_1	E_1	E
$\bar{E}_2$	$\frac{E_2}{1+\bar{e}_{22}\mathcal{D}}$	$\frac{E_2}{1+\bar{e}_{22}\mathcal{D}}$	$\frac{E}{1+2\mathcal{D}}$
$\bar{G}_{12}$	$\frac{G_{12}}{1+\bar{e}_{66}\mathcal{D}}$	$\frac{G_{12}}{1+\bar{e}_{66}\mathcal{D}}$	$\frac{G}{1+\mathcal{D}/(1+\nu)}$
$\bar{\nu}_{12}$	ν_{12}	ν_{12}	ν
$\bar{\nu}_{16}$	$\frac{\nu_{16}}{1+\bar{e}_{66}\mathcal{D}}$	-	-
$\bar{\nu}_{26}$	$\frac{\nu_{26}}{1+\bar{e}_{66}\mathcal{D}}$	-	-

Downloaded 04 May 2010 to 171.66.16.27. Redistribution subject to ASME license or copyright; see http://www.asme.org/terms/Terms_Use.cfm

Table 2 Values of parameters e_{ij} depending on the type of material symmetry

Parameters	Type of initially undamaged solids		
(e_{ij})	Anisotropic	Orthotropic	Isotropic
e_{11}	$\frac{Q_{12}^2}{Q_{11}} S_{22}\bar{e}_{22} + \frac{Q_{16}^2}{Q_{11}} S_{66}\bar{e}_{66}$	$\left(\frac{\nu_{12}^2}{1-\nu_{12}\nu_{21}}\right)\frac{E_2}{E_1}\bar{e}_{22}$	$\frac{2\nu^2}{1-\nu^2}$
e_{22}	$Q_{22}S_{22}\bar{e}_{22} + \frac{Q_{26}^2}{Q_{22}} S_{66}\bar{e}_{66}$	$\left(\frac{1}{1-\nu_{12}\nu_{21}}\right)\bar{e}_{22}$	$\frac{2}{1-\nu^2}$
e_{66}	$\frac{Q_{26}^2}{Q_{66}} S_{22}\bar{e}_{22} + Q_{66}S_{66}\bar{e}_{66}$	$\bar{e}_{66}$	$\frac{1}{1+\nu}$
e_{12}	$Q_{22}S_{22}\bar{e}_{22} + \frac{Q_{16}Q_{26}}{Q_{12}} S_{66}\bar{e}_{66}$	$\left(\frac{1}{1-\nu_{12}\nu_{21}}\right)\bar{e}_{22}$	$\frac{2}{1-\nu^2}$
e_{16}	$\frac{Q_{12}Q_{26}}{Q_{16}} S_{22}\bar{e}_{22} + Q_{66}S_{66}\bar{e}_{66}$	-	-
e_{26}	$Q_{22}S_{22}\bar{e}_{22} + Q_{66}S_{66}\bar{e}_{66}$	-	-

3 Identification of Local Damage

In the preceding section, the elastic behavior of a damaged solid is represented by the effective continuum elastic compliance $\bar{S}_{ij}$ or stiffness $\bar{Q}_{ij}$. In effect, a solid with embedded damages (equivalently, line cracks) is smeared smoothly into an equivalent continuum with elastic compliance $\bar{S}_{ij}$ or stiffness $\bar{Q}_{ij}$. For damage analysis in conjunction with conventional stress analysis, it requires us to know the effective elastic properties, $\bar{S}_{ij}$ or $\bar{Q}_{ij}$, which are dependent of the current state of local damage. Unfortunately, the damage inside of solids is not accessible. Hence, it requires a innovative method by which the local damage state can be identified.

Since a local damage is modeled as an equivalent line crack, to identify a local damage is equivalent to identifying the size and growth direction of a line crack. As the growth of damage size (a) is governed by the damage evolution equation introduced in Lee et al. (1997), the present discussion will be confined to the identification of crack orientation (θ) with respect to the global coordinates (x-y), as shown in Fig. 2.

As can be seen from Table 1 and also from Fig. 2(c), the effective Young's modulus $\bar{E}_1$ in the direction "1" of crack coordinates does not change due to the presence of the line crack, but the effective Young's modulus $\bar{E}_2$ in the direction "2" and the effective shear modulus $\bar{G}_{12}$ are reduced in magnitude by the factors of $(1 + \bar{e}_{ii}\mathcal{D})$ $(i = 2, 6)$. As the stress analysis is typically conducted in the course of damage analysis it may be reasonable to use the current stress and strain informations at a damaged local point for identifying the crack orientation.

To determine the current crack orientation (θ), assume that current damage value ($\mathcal{D}$) and current stresses and strains (σ_I and ϵ_J) with respect to the global coordinates are known at a local damage. After estimating the crack orientation with respect to the global coordinates, say θ_0, the coordinates transformation is used to compute the stresses and strains with respect to the estimated crack coordinates, i.e., σ_i and ϵ_j. The effective elastic moduli for the damaged state are then estimated from σ_i and ϵ_j as follows:

$$E_1^* = \frac{\sigma_1}{\epsilon_1}, \quad E_2^* = \frac{\sigma_2}{\epsilon_2}, \quad G_{12}^* = \frac{\sigma_6}{\epsilon_6}. \tag{17}$$

The undamaged compliance with respect to global coordinates, S_{IJ}, are assumed to be known in advance. Then, by using the coordinates transformation, the compliance with respect to estimated crack coordinates, S_{ij}, can be calculated from S_{IJ} with ease. Using calculated S_{ij}, the parameters $\bar{e}_{22}$ and $\bar{e}_{66}$, and the elastic moduli E_1, E_2, and G_{12} for the undamaged state can be computed. If the estimated crack orientation θ_0 is correct, then the following three relations from Table 1 may be satisfied.

$$\frac{E_1^*}{E_1} = 1, \quad \frac{E_2^*}{E_2} = \frac{1}{1 + \bar{e}_{22}\mathcal{D}} < 1,$$

$$\frac{G_{12}^*}{G_{12}} = \frac{1}{1 + \bar{e}_{66}\mathcal{D}} < 1 \tag{18}$$

However, the estimated crack orientation θ_0 may not exactly satisfy Eq. (18) at once. Hence, the best estimation of θ may be found from an error minimizing approach as

$$\text{Minimize} \left\{ f(\theta) = \left(\frac{E_1^*}{E_1} - 1\right)^2 + \left(\frac{E_2^*}{E_2} - \frac{1}{1 + \bar{e}_{22}\mathcal{D}}\right)^2 + \left(\frac{G_{12}^*}{G_{12}} - \frac{1}{1 + \bar{e}_{66}\mathcal{D}}\right)^2 \right\}. \tag{19}$$

Once the crack orientation is identified, the corresponding damaged zone can be converted to an effective continuum by using Eq. (13) or (16). Since the effective continuum elastic properties are defined with respect to the crack (local) coordinates (1–2), they will be transformed back with respect to the global coordinates (x-y), for the next step process of damage analysis.

Acknowledgment

This study was supported by the 1998 Inha University Research Fund.

Downloaded 04 May 2010 to 171.66.16.27. Redistribution subject to ASME license or copyright; see http://www.asme.org/terms/Terms_Use.cfm

References

Krajcinovic, D., 1996, *Damage Mechanics,* Elsevier, New York.

Lee, U., Lesieutre, G. A., and Lei, F., 1997, "Anisotropic damage mechanics based on strain energy equivalence and equivalent elliptical microcracks," *International Journal of Solids and Structures,* Vol. 34, No. 33–34, pp. 4377–4397.

Mazarz, J., and Pijaudier-Cabot, G., 1996, "From damage to fracture mechanics and conversely: A combined approach," *International Journal of Solids and Structures,* Vol. 33, No. 20–22, pp. 3327–3342.

Ortiz, M., 1985, "A Constitutive theory for the inelastic behavior of concrete," *Mechanics of Materials,* Vol. 4, No. 1, pp. 67–93.

Sih, G. C., and Liebowitz, H., 1967, "Mathematical theories of brittle fracture," *Fracture,* Vol. II, H. Liebowitz, ed., Academic Press, New York, Chapter 2.

Tsai, S. W., 1988, *Composite Design,* 4th Design, Think Composites, Dayton, OH.

Closed-Form Integrals for Constant and Linear Elements in the Eigenstrain Method

P. A. Kelly[1] and D. Nowell[2]

1 Introduction

The eigenstrain technique (Mura, 1982) is a powerful tool for solving three-dimensional crack problems. The first step in this solution procedure is to use the concept of the eigenstrain to derive the integral equation which expresses the requirement that the crack surfaces of an open crack cannot bear any normal/shear stress. Assuming that the crack lies in the $z = 0$ plane and occupies the region S, this integral equation may be written in the form (Lee and Keer, 1986)

$$C\sigma^o_{zz}(x_o, y_o) = \int_S u(x, y)\left[\frac{1}{r^3(x_o, y_o, x, y)} + G(x_o, y_o, x, y)\right] dS \quad (1)$$

where C is a material parameter and $u(x, y)$ is the crack-surface-opening displacement. The function σ^o_{zz} represents the stress arising at an arbitrary point (x_o, y_o) due to the imposed loading, i.e., in an uncracked geometry. G is a bounded function of the material and geometric parameters, for example to take account of free boundaries or material interfaces, $r = \sqrt{(x - x_o)^2 + (y - y_o)^2}$, and the integration is carried out over the entire crack. The integral equation is to be solved for the unknown displacement function $u(x, y)$, and must be satisfied at all points (x_o, y_o) on the crack.

In order to solve (1), the arbitrarily shaped crack front is approximated by a many-sided polygon Γ, Γ is divided into N triangular elements, and the integral in (1) is taken over each individual triangle, Fig. 1 (see Hills et al. (1996) for a discussion of quadrilateral elements). Thus, satisfying (1) at N collocation points (x^K_o, y^K_o), usually taken to be the centroids of the triangles, as in Fig. 1, one has

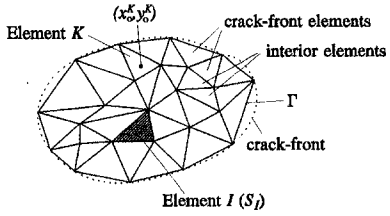

Fig. 1 Triangulation of crack

$$C\sigma^o_{zz}(x^K_o, y^K_o) = \sum_{I=1}^{N} \int_{S_I} u(x, y)\left[\frac{1}{r^3(x^K_o, y^K_o, x, y)} + G(x^K_o, y^K_o, x, y)\right] dS_I \quad (K = 1 \ldots N) \quad (2)$$

where S_I is the Ith triangle. The two most commonly used procedures for solving (2), the *weight function* method and the *piecewise linear* method, will be discussed next.

First, it is assumed that the opening-displacement function $u(x, y)$ over element I is of the form

$$u(x, y) = \hat{u}^I w(x, y),$$
$$w(x, y) = \sqrt{(d(x, y)/a)[2 - \alpha(d(x, y)/a)]} \quad (3)$$

where $\hat{u}^I$ is a constant displacement, $w(x, y)$ is the *weight* function, a is half the largest distance between any two points on Γ, and d is the minimum distance between (x, y) and Γ. The weight function ensures that the opening displacement in the vicinity of the crack front vanishes in a square-root fashion $(\sqrt{d})$ as the crack front is approached, which is a requirement of the classical singular elastic solution. The precise form of $w(x, y)$ depends on the parameter α in (3); Murakami and Nemat-Nasser (1982) suggest a value of $\alpha = 1$. Taking $\hat{u}^I$ outside the integral sign, the integral in (2) is evaluated numerically for each element S_I, and thus (2) is solved for the N values of $\hat{u}^I$.

In the second method (Dai et al., 1996), one must distinguish between *crack front* elements, i.e., those with a side or a triangle-vertex touching Γ, and the remaining *interior* elements, Fig. 1. It may be assumed that $u(x, y)$ behaves as described above in the case of crack front elements, i.e., according to (3), so that the correct crack front asymptotic displacement is maintained. For the interior elements, however, use is made of the linear nonconforming element familiar to users of the finite element method, and $u(x, y)$ is assumed to vary linearly over each element. Typical interior elements are shown in Fig. 2. Each has *three* collocation points, positioned symmetrically within each element at

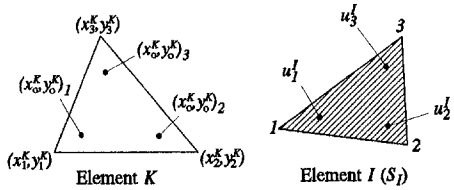

Fig. 2 Linear triangular elements: collocation in element K, integration over element I

[1] Department of Engineering Science, School of Engineering, University of Auckland, Private Bag 92019, Auckland, New Zealand.

[2] Department of Engineering Science, University of Oxford, Parks Road, OX1 3PJ, UK.

Contributed by the Applied Mechanics Division of THE AMERICAN SOCIETY OF MECHANICAL ENGINEERS for publication in the ASME JOURNAL OF APPLIED MECHANICS. Manuscript received by the ASME Applied Mechanics Division, Feb. 2, 1998; final revision, June 30, 1998. Associate Technical Editor: M.-J. Pindera.

Downloaded 04 May 2010 to 171.66.16.27. Redistribution subject to ASME license or copyright; see http://www.asme.org/terms/Terms_Use.cfm

References

Krajcinovic, D., 1996, *Damage Mechanics,* Elsevier, New York.

Lee, U., Lesieutre, G. A., and Lei, F., 1997, "Anisotropic damage mechanics based on strain energy equivalence and equivalent elliptical microcracks," *International Journal of Solids and Structures,* Vol. 34, No. 33–34, pp. 4377–4397.

Mazarz, J., and Pijaudier-Cabot, G., 1996, "From damage to fracture mechanics and conversely: A combined approach," *International Journal of Solids and Structures,* Vol. 33, No. 20–22, pp. 3327–3342.

Ortiz, M., 1985, "A Constitutive theory for the inelastic behavior of concrete," *Mechanics of Materials,* Vol. 4, No. 1, pp. 67–93.

Sih, G. C., and Liebowitz, H., 1967, "Mathematical theories of brittle fracture," *Fracture,* Vol. II, H. Liebowitz, ed., Academic Press, New York, Chapter 2.

Tsai, S. W., 1988, *Composite Design,* 4th Design, Think Composites, Dayton, OH.

Closed-Form Integrals for Constant and Linear Elements in the Eigenstrain Method

P. A. Kelly[1] and D. Nowell[2]

1 Introduction

The eigenstrain technique (Mura, 1982) is a powerful tool for solving three-dimensional crack problems. The first step in this solution procedure is to use the concept of the eigenstrain to derive the integral equation which expresses the requirement that the crack surfaces of an open crack cannot bear any normal/shear stress. Assuming that the crack lies in the $z = 0$ plane and occupies the region S, this integral equation may be written in the form (Lee and Keer, 1986)

$$C\sigma^o_{zz}(x_o, y_o) = \int_S u(x, y)\left[\frac{1}{r^3(x_o, y_o, x, y)} + G(x_o, y_o, x, y)\right] dS \quad (1)$$

where C is a material parameter and $u(x, y)$ is the crack-surface-opening displacement. The function σ^o_{zz} represents the stress arising at an arbitrary point (x_o, y_o) due to the imposed loading, i.e., in an uncracked geometry. G is a bounded function of the material and geometric parameters, for example to take account of free boundaries or material interfaces, $r = \sqrt{(x - x_o)^2 + (y - y_o)^2}$, and the integration is carried out over the entire crack. The integral equation is to be solved for the unknown displacement function $u(x, y)$, and must be satisfied at all points (x_o, y_o) on the crack.

In order to solve (1), the arbitrarily shaped crack front is approximated by a many-sided polygon Γ, Γ is divided into N triangular elements, and the integral in (1) is taken over each individual triangle, Fig. 1 (see Hills et al. (1996) for a discussion of quadrilateral elements). Thus, satisfying (1) at N collocation points (x^K_o, y^K_o), usually taken to be the centroids of the triangles, as in Fig. 1, one has

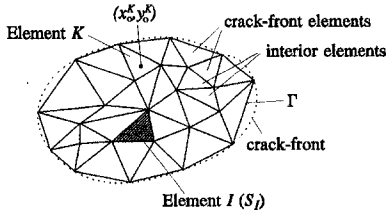

Fig. 1 Triangulation of crack

$$C\sigma^o_{zz}(x^K_o, y^K_o) = \sum_{I=1}^{N} \int_{S_I} u(x, y)\left[\frac{1}{r^3(x^K_o, y^K_o, x, y)} + G(x^K_o, y^K_o, x, y)\right] dS_I \quad (K = 1 \ldots N) \quad (2)$$

where S_I is the Ith triangle. The two most commonly used procedures for solving (2), the *weight function* method and the *piecewise linear* method, will be discussed next.

First, it is assumed that the opening-displacement function $u(x, y)$ over element I is of the form

$$u(x, y) = \hat{u}^I w(x, y),$$
$$w(x, y) = \sqrt{(d(x, y)/a)[2 - \alpha(d(x, y)/a)]} \quad (3)$$

where $\hat{u}^I$ is a constant displacement, $w(x, y)$ is the *weight* function, a is half the largest distance between any two points on Γ, and d is the minimum distance between (x, y) and Γ. The weight function ensures that the opening displacement in the vicinity of the crack front vanishes in a square-root fashion $(\sqrt{d})$ as the crack front is approached, which is a requirement of the classical singular elastic solution. The precise form of $w(x, y)$ depends on the parameter α in (3); Murakami and Nemat-Nasser (1982) suggest a value of $\alpha = 1$. Taking $\hat{u}^I$ outside the integral sign, the integral in (2) is evaluated numerically for each element S_I, and thus (2) is solved for the N values of $\hat{u}^I$.

In the second method (Dai et al., 1996), one must distinguish between *crack front* elements, i.e., those with a side or a triangle-vertex touching Γ, and the remaining *interior* elements, Fig. 1. It may be assumed that $u(x, y)$ behaves as described above in the case of crack front elements, i.e., according to (3), so that the correct crack front asymptotic displacement is maintained. For the interior elements, however, use is made of the linear nonconforming element familiar to users of the finite element method, and $u(x, y)$ is assumed to vary linearly over each element. Typical interior elements are shown in Fig. 2. Each has *three* collocation points, positioned symmetrically within each element at

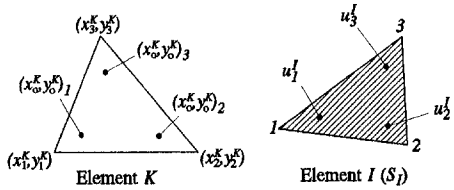

Fig. 2 Linear triangular elements: collocation in element K, integration over element I

[1] Department of Engineering Science, School of Engineering, University of Auckland, Private Bag 92019, Auckland, New Zealand.

[2] Department of Engineering Science, University of Oxford, Parks Road, OX1 3PJ, UK.

Contributed by the Applied Mechanics Division of THE AMERICAN SOCIETY OF MECHANICAL ENGINEERS for publication in the ASME JOURNAL OF APPLIED MECHANICS. Manuscript received by the ASME Applied Mechanics Division, Feb. 2, 1998; final revision, June 30, 1998. Associate Technical Editor: M.-J. Pindera.

 Copyright © 1999 by ASME

Downloaded 04 May 2010 to 171.66.16.27. Redistribution subject to ASME license or copyright; see http://www.asme.org/terms/Terms_Use.cfm

$$(x_o^K, y_o^K)_m = [(x_1^K + x_2^K + x_3^K)/6 + x_m^K/2,$$
$$(y_1^K + y_2^K + y_3^K)/6 + y_m^K/2], \quad m = 1 \ldots 3 \quad (4)$$

where (x_m^K, y_m^K), $m = 1 \ldots 3$ are the coordinates of the vertices of element K. The values of $u(x, y)$ at the corresponding points within element I are taken to be, respectively, $\hat{u}_1^I$, $\hat{u}_2^I$, and $\hat{u}_3^I$, Fig. 2. The opening displacement is now represented as a linear interpolation of these values, according to

$$u(x, y) = \sum_{k=1}^{3} N_k(x, y)\hat{u}_k^I \quad (5)$$

and the *shape functions* are

$$N_k(x, y) = \frac{1}{\Delta}[a_k + b_k x + c_k y] - \frac{1}{3}, \quad (6)$$

where Δ is the area of element I,

$$a_k = x_i^I y_j^I - x_j^I y_i^I, \quad b_k = y_i^I - y_j^I, \quad c_k = x_j^I - x_i^I, \quad (7)$$

(x_k^I, y_k^I), $k = 1 \ldots 3$ are the coordinates of the vertices of element I, and i, j, are related to k through

$$\{i, j, k\} = \{1, 2, 3\}, \{2, 3, 1\} \quad \text{or} \quad \{3, 1, 2\}. \quad (8)$$

Expression (5), or (3) in the case of crack-front elements, is now substituted into (2), the integral is evaluated numerically for each element, and hence the corresponding values of $\hat{u}^I$ (for crack-front elements) and $\hat{u}_k^I$, $k = 1 \ldots 3$ (for interior elements) are evaluated.

Note that when the collocation point lies within the element S_I, i.e., when $K = I$, the dominant integral in (2) (that involving the $1/r^3$ term) is divergent in the usual sense, and one needs to evaluate its finite part. There are a number of ways of evaluating the finite part of this integral, but perhaps the most efficient is to take the first few terms of the Taylor series of u about the collocation point (x_o, y_o), add and subtract these terms from u (Krishnasamy et al., 1990), and then to evaluate the resulting contour integrals (Dai et al., 1993), giving

$$\text{F.P.} \int_{S_I} \frac{u(x, y)dS_I}{r^3(x_o^I, y_o^I, x, y)} = L_o u(x_o^I, y_o^I) + M_x \frac{\partial u}{\partial x}\bigg|_{(x_o^I y_o^I)} + M_y \frac{\partial u}{\partial y}\bigg|_{(x_o^I y_o^I)} + I_1(x_o^I, y_o^I) \quad (9)$$

where

$$I_1 = \int_{S_I} \frac{1}{r^3}\left[u(x, y) - u(x_o^I, y_o^I) - (x - x_o^I)\frac{\partial u}{\partial x}\bigg|_{(x_o^I y_o^I)} - (y - y_o^I)\frac{\partial u}{\partial y}\bigg|_{(x_o^I y_o^I)}\right] dS_I \quad (10)$$

and the functions/integrals L_o, M_x, and M_y are given in the Appendix. The surface integral I_1 is not singular and may be evaluated numerically (this is strictly true only under certain mild conditions—it will certainly be regular if the second derivatives of $u(x, y)$ are continuous).

This paper is concerned with the evaluation of the dominant integral in (2). The evaluation of this integral constitutes the main work in solving (2), and the integral is difficult to solve when the distance l between the collocation point and a side of element I is small, as it is of order $1/l$. The integrals associated with the function $G(x_o^K, y_o^K, x, y)$ are regular and may be conveniently evaluated using the quadrature rules for triangular regions given by Grundmann and Möller (1978).

This paper presents three main results:

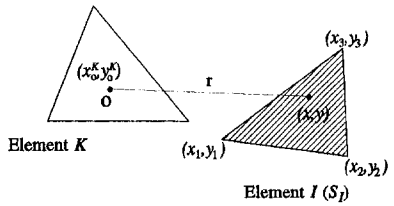

Fig. 3 Integration over the constant element *I*

1 closed-form expressions for the dominant integral for the case of a *constant* element, i.e., one over which the displacement is constant ($u(x, y) = \hat{u}^I$, $w(x, y) = 1$ in (3)),
2 closed-form expressions for the dominant integral associated with the piecewise linear method, evaluated for all interior elements, for $K = I$ and $K \neq I$, and
3 the reduction of integral I_1 to an analytic component and a circumferential line integral.

The results which follow have been tested by using them to solve a number of crack problems for which the exact (or approximate) solution is known. They increase the accuracy of the eigenstrain method, and greatly decrease the time required to obtain a solution. Their derivation is fairly lengthy and the interested reader is referred to Kelly (1997) for full details.

2 Constant Element

The constant element is the two-dimensional element corresponding to the one-dimensional boundary element used in a variety of two-dimensional crack problems, and is of corresponding importance. First, label the nodes of element S_I 1, 2, and 3 in a *counterclockwise* sense with, respectively, coordinates (x_1, y_1), (x_2, y_2), and (x_3, y_3), (Fig. 3). One then obtains (dropping the superscript K)

$$\int_{S_I} \frac{dS_I}{r^3(x_o, y_o, x, y)} = -\frac{\Delta_{123}}{2}\left[\frac{l_{o1}}{\Delta_{o31}\Delta_{o12}} + \frac{l_{o2}}{\Delta_{o12}\Delta_{o23}} + \frac{l_{o3}}{\Delta_{o23}\Delta_{o31}}\right] \quad (11)$$

where Δ_{pqr} is the area of the triangle formed by the points (x_p, y_p), (x_q, y_q), and (x_r, y_r) (Δ_{pqr} is positive if the points are taken, respectively, in a counterclockwise direction, negative otherwise), i.e.,

$$\Delta_{pqr} = \tfrac{1}{2}[(x_r - x_q)(y_p - y_q) - (x_p - x_q)(y_r - y_q)], \quad (12)$$

and l_{pq} is the length of the line joining (x_p, y_p) and (x_q, y_q). As the collocation point approaches an element side, one of Δ_{o12}, Δ_{o31}, or Δ_{o23} vanishes, and the $1/l$ singularity discussed above is explicit in the right-hand side of (11). One of these three terms vanishes also when (x_o, y_o) lies on the extrapolation of one of the triangle sides. Taking the limiting values of the integral, one finds that, if the point (x_o, y_o) is in line with the nodes (x_i, y_i) and (x_j, y_j), then

$$\int_{S_I} \frac{dS_I}{r^3(x_o, y_o, x, y)} = -\frac{\Delta_{123}}{2}\left\{\frac{l_{ok} + f_{ijk}}{\Delta_{ojk}\Delta_{oki}}\right\}$$
$$((x_o, y_o) \text{ in line with side } ij) \quad (13)$$

where the set $\{i, j, k\}$ are defined by (8), and

Downloaded 04 May 2010 to 171.66.16.27. Redistribution subject to ASME license or copyright; see http://www.asme.org/terms/Terms_Use.cfm

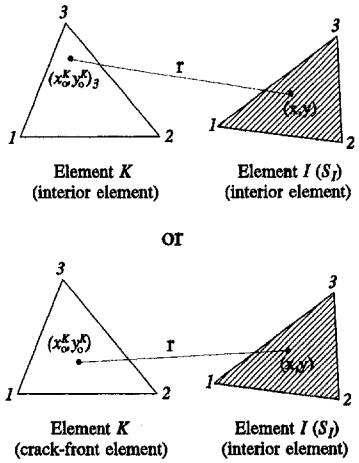

Fig. 4 Integration over the interior linear element *I*

$$f_{pqr} = \begin{cases} \dfrac{\lambda}{y_q - y_p}\left[-l_{pq}(y_r - y_o) + 2\Delta_{123}(x_q - x_p)/l_{pq}\right] \\ \quad \text{when } y_q \neq y_p \\ -|x_o - x_r| \\ \quad \text{when } y_q = y_p \end{cases}$$

$$\lambda = \begin{cases} +1, & l_{op} < l_{oq} \\ -1, & l_{op} > l_{oq}. \end{cases} \tag{14}$$

These results pertain to the case when the collocation point lies *outside* the triangle S_I. When $K = I$, integral (11) may be evaluated through (9), (10). The result for this case is well known (Murakami and Nemat-Nasser, 1983) and is included here for completeness:

$$\int_{S_I} \frac{dS_I}{r^3(x_o, y_o, x, y)} = L_o, \tag{15}$$

and the function L_o is given in the Appendix.

3 Linear Element

In the case of the piecewise linear element, Fig. 4, substituting (5) into (2) yields

$$\sum_{k=1}^{3} \hat{u}_k^I \int_{S_I} \frac{N_k(x, y)dS_I}{r^3(x_o^K, y_o^K, x, y)} = \sum_{k=1}^{3} \hat{u}_k^I \left\{ \Psi_o + \frac{1}{\Delta_{123}}\left[l_{ij}\Psi_1 + \frac{\Phi_{ijk}}{l_{jk}}\Psi_2 + \frac{\Phi_{jik}}{l_{ik}}\Psi_3 \right] \right\} \tag{16}$$

where

$$\Psi_o = \left(\frac{\Delta_{123}}{6\Delta_{oij}} - 1\right)\left[\frac{l_{oi}\Delta_{ojk} + l_{oj}\Delta_{oki} + l_{ok}\Delta_{oij}}{\Delta_{ojk}\Delta_{oki}}\right]$$

$$\Psi_1 = \ln\left(\frac{-\Phi_{oij} - l_{ij}l_{oi}}{+\Phi_{oji} - l_{ij}l_{oj}}\right), \quad \Psi_2 = \ln\left(\frac{-\Phi_{ojk} + l_{jk}l_{oj}}{+\Phi_{okj} + l_{jk}l_{ok}}\right),$$

$$\Psi_3 = \ln\left(\frac{-\Phi_{oik} + l_{ik}l_{oi}}{+\Phi_{oki} + l_{ik}l_{ok}}\right). \tag{17}$$

i, j, are related to k through (8), and the function Φ_{pqr} is defined by

$$\Phi_{pqr} = (x_r - x_q)(x_p - x_q) + (y_r - y_q)(y_p - y_q). \tag{18}$$

Again, the case where the collocation point lies on the extrapolation of an element side must be considered separately. One has

$$\Psi_o \to \left(\frac{\Delta_{123}}{6}\right)\left[\frac{l_{ok} + f_{ijk}}{\Delta_{ojk}\Delta_{oki}}\right], \quad \Psi_1 \to \left|\ln\left(\frac{l_{oi}}{l_{oj}}\right)\right|, \quad \text{as } \Delta_{oij} \to 0$$

$$\Psi_o \to \left(\frac{\Delta_{123}}{6\Delta_{oij}} - 1\right)\left[\frac{l_{oi} + f_{jki}}{\Delta_{oki}}\right], \quad \Psi_2 \to -\left|\ln\left(\frac{l_{oj}}{l_{ok}}\right)\right|,$$

$$\text{as } \Delta_{ojk} \to 0$$

$$\Psi_o \to \left(\frac{\Delta_{123}}{6\Delta_{oij}} - 1\right)\left[\frac{l_{oj} + f_{kij}}{\Delta_{ojk}}\right], \quad \Psi_3 \to -\left|\ln\left(\frac{l_{oi}}{l_{ok}}\right)\right|,$$

$$\text{as } \Delta_{oki} \to 0 \tag{19}$$

and f_{pqr} is given by (14). Again, these results pertain to the case when the collocation point lies outside the triangle S_I. The finite part may be evaluated through (9), (10) as

$$\sum_{k=1}^{3} \hat{u}_k^I \int_S \frac{N_k(x, y)dS}{r^3[(x_o^I, y_o^I)_m, x, y]} = \sum_{k=1}^{3} \hat{u}_k^I \left\{ N_k(x_o^I, y_o^I)_m L_o + \frac{b_k M_x + c_k M_y}{\Delta_{123}} \right\}, \quad m = 1 \ldots 3 \tag{20}$$

where b_k, c_k are given by (7) and the functions L_o, M_x, and M_y are listed in the Appendix. Note that, from (6, 7),

$$N_k(x_o^I, y_o^I)_m = \begin{cases} 1 & \text{when } m = k \\ 0 & \text{when } m \neq k. \end{cases} \tag{21}$$

4 Elements With a Weight Function

The finite part of the dominant integral associated with elements with a weight function is considered in this section. Surface integral I_1, Eq. (10), is usually solved by invoking a polar or degenerate coordinate transform (Hills et al., 1996), and by numerically solving the resulting double integral. In fact, I_1 can be reduced to a line integral, and this result is presented here. Thus the evaluation of the finite part integral, $K = I$, for all elements (weight function method), or crack front elements (piecewise linear method), only involves the use of a simple one-dimensional, such as the Gauss-Legendre, quadrature.

The minimum distance d from a point (x, y) within an element to a line segment pq on Γ, with end points/nodes (x_p, y_p) and (x_q, y_q), is given by

$$d(x, y) = \frac{A \text{ sgn } (A)}{l_{pq}} \tag{22}$$

where

$$A(x, y) = (x_q - x_p)(y_j - y) - (y_q - y_p)(x_j - x), \quad j = p \text{ or } q, \tag{23}$$

l_{pq} is the length of the line segment, and sgn $(\cdot)$ is the sign function, i.e.,

$$\text{sgn } (z) = \begin{cases} +1, & \text{when } z > 0 \\ -1, & \text{when } z \leq 0. \end{cases} \tag{24}$$

Substituting (22) into (3), (9) can be rewritten as

Downloaded 04 May 2010 to 171.66.16.27. Redistribution subject to ASME license or copyright; see http://www.asme.org/terms/Terms_Use.cfm

$$\text{F.P.} \int_{S_I} \frac{u(x, y)dS_I}{r^3(x_o^I, y_o^I, x, y)}$$

$$= \hat{u}^I \left\{ L_o w(x_o^I, y_o^I) + \frac{1 - \alpha d(x_o^I, y_o^I)/a}{l_{pq} w(x_o^I, y_o^I)} \operatorname{sgn} [A(x_o^I, y_o^I)] \right.$$

$$\left. \times [(y_q - y_p)M_x - (x_q - x_p)M_y] + I_1(x_o^I, y_o^I) \right\}. \quad (25)$$

Integral I_1, Eq. (10), may be reduced to a line integral by changing to polar coordinates (r, θ), centred at the collocation point (x_o^I, y_o^I). Integrations in the radial direction (using, for example, the integrals listed in Gradshteyn and Ryzhik (1994, Section 2.26)), and part of the integration in the circumferential direction, may be evaluated in closed form, and one obtains

$$I_1 = -L_o\sqrt{1 - p_o} + \int_0^{2\pi} \Phi(\theta)d\theta \quad (26)$$

where

$$\Phi(\theta) = -\frac{\sqrt{1 - p_o - 2q_oR - s_oR^2}}{R} + \sqrt{s_o}\left\{ \arcsin \frac{-s_oR - q_o}{\sqrt{s_o(1 - p_o) + q_o^2}} - \arcsin \frac{-q_o}{\sqrt{s_o(1 - p_o) + q_o^2}} \right\}$$

$$+ \frac{q_o}{\sqrt{1 - p_o}} \ln \left(\frac{1 - p_o - q_oR + \sqrt{(1 - p_o)(1 - p_o - 2q_oR - s_oR^2)}}{2(1 - p_o)} \right) \quad (27)$$

and

$$p_o = 1 - \frac{A(x_o^I, y_o^I)}{l_{pq}} \left[2 \operatorname{sgn} [A(x_o^I, y_o^I)] - \alpha \frac{A(x_o^I, y_o^I)}{l_{pq}} \right]$$

$$q_o = \frac{g_o}{l_{pq}} \left[\operatorname{sgn} [A(x_o^I, y_o^I)] - \alpha \frac{A(x_o^I, y_o^I)}{l_{pq}} \right]$$

$$s_o = \alpha \left(\frac{g_o}{l_{pq}} \right)^2$$

$$g_o = (x_q - x_p) \sin \theta - (y_q - y_p) \cos \theta. \quad (28)$$

Here R is the radial distance between the collocation point (x_o^I, y_o^I) and the point *on* the boundary of the element defined by θ. If this point lies on the triangle side with end points (x_i, y_i) and (x_{i+1}, y_{i+1}), then

$$R(\theta) = \frac{(x_{i+1} - x_i)(y_i - y_o^I) - (y_{i+1} - y_i)(x_i - x_o^I)}{(x_{i+1} - x_i) \sin \theta - (y_{i+1} - y_i) \cos \theta}. \quad (29)$$

As mentioned earlier, the integral in (26) may be evaluated using the Gauss-Legendre quadrature and, depending on the precise shape of the element and position of the collocation point, between 20–40 Gauss points should prove sufficient for a highly accurate solution.

Note that some investigators (Dai et al., 1997) use a combination of weight function *and* linear interpolation for crack front elements, i.e., $u(x, y)$ in the form

$$u(x, y) = w(x, y) \sum_{k=1}^{3} N_k(x, y)\hat{u}_k^I \quad (30)$$

with $w(x, y)$ given by (3) with $\alpha = 0$. Here, again, I_1 can be reduced to a line integral by a change to polar coordinates (using, for example, the integrals listed in Gradshteyn and Ryzhik (1994, Section 2.22)).

Acknowledgment

This work was supported by EPSRC contract No. GR/K87913.

References

Dai, D. N., Hills, D. A., and Nowell, D., 1993, "Eigenstrain methods in three dimensional crack problems: an alternative integration procedure," *J. Mech. Phys. Solids.*, Vol. 41, pp. 1003–1017.

Dai, D. N., Hills, D. A., and Nowell, D., 1996, "Formulation and implementation of the eigenstrain method employing higher order elements," *Int. J. Sols. Struct.*, Vol. 33, No. 3, pp. 331–342.

Dai, D. N., Hills, D. A., and Nowell, D., 1997, "Modelling of growth of three-dimensional cracks by a continuous distribution of dislocation loops," *Computational Mechanics*, Vol. 19, pp. 538–544.

Gradshteyn, I. S., and Ryzhik, I. M., 1994, *Table of Integrals, Series and Products*, 5th Ed; Academic Press, Boston.

Grundmann, A., and Möller, H. M., 1978, "Invariant Integration Formulas for the *n*-Simplex by Combinatorial Methods," *Siam J. Numer. Anal.*, Vol. 15, No. 2, pp. 282–290.

Hills, D. A., Kelly, P. A., Dai, D. N., and Korsunsky, A. M., 1996, *Solution of Crack Problems: The Distributed Dislocation Technique;* Klewer, Dordrecht, The Netherlands.

Kelly, P. A., 1997, "The distributed dislocation-loop technique: Some basic problems," Univ. of Oxford, OUEL Report No. 2147/97.

Krishnasamy, G., Schmerr, L. W., Rudolphi, T. J., and Rizzo, F. J., 1990, "Hypersingular boundary integral equations: Some applications in acoustic and elastic wave scattering, ASME JOURNAL OF APPLIED MECHANICS, Vol. 57, pp. 404–414.

Lee, J. C., and Keer, L. M., 1986, "Study of a three-dimensional crack terminating at an interface," ASME JOURNAL OF APPLIED MECHANICS, Vol. 53, pp. 311–316.

Mura, T., 1982, *Micromechanics of Defects in Solids,* Martinus Nijhoff Publishers, Dordrecht, The Netherlands.

Murakami, Y., Nemat-Nasser, S., 1982, "Interacting Dissimilar Semi-elliptic Surface Flaws Under Tension and Bending," *Engng. Fract Mech.*, Vol. 16, pp. 373–386.

Murakami, Y., and Nemat-Nasser, S., 1983, "Growth and Stability of Interacting Surface Flaws of Arbitrary Shape," *Engng. Fract. Mech.*, Vol. 17, No. 3, pp. 193–210.

APPENDIX

The functions L_o, M_x, and M_y are given by (see Hills et al., 1996, Appendix)

$$L_o = \text{F.P.} \int_{S_I} \frac{dS_I}{r^3}$$

$$= \sum_{i=1}^{3} \frac{(x_{i+1} - x_i)(\cos \theta_{i+1} - \cos \theta_i) + (y_{i+1} - y_i)(\sin \theta_{i+1} - \sin \theta_i)}{(x_{i+1} - x_i)(y_i - y_o) - (y_{i+1} - y_i)(x_i - x_o)}$$

$$M_x = \text{F.P.} \int_{S_I} (x - x_o) \frac{dS_I}{r^3} = \sum_{i=1}^{3} \left[-\frac{y_{i+1} - y_i}{l_i} \right] \Theta_i$$

$$M_y = \text{F.P.} \int_{S_I} (y - y_o) \frac{dS_I}{r^3} = \sum_{i=1}^{3} \left[+\frac{x_{i+1} - x_i}{l_i} \right] \Theta_i \quad (31)$$

where (x_i, y_i), $i = 1 \ldots 3$, are the coordinates of the nodes/vertices of the triangular element S_I, (x_o, y_o) are the coordinates of the collocation point within the element, and

$$\Theta_i = \ln \frac{r_{i+1}[(x_{i+1} - x_i) \cos \theta_{i+1} + (y_{i+1} - y_i) \sin \theta_{i+1} + l_i]}{r_i[(x_{i+1} - x_i) \cos \theta_i + (y_{i+1} - y_i) \sin \theta_i + l_i]}$$

$$\tan \theta_i = \frac{y_i - y_o}{x_i - x_o}$$

Downloaded 04 May 2010 to 171.66.16.27. Redistribution subject to ASME license or copyright; see http://www.asme.org/terms/Terms_Use.cfm

$$r_i = \sqrt{(x_i - x_o)^2 + (y_i - y_o)^2}$$
$$l_i = \sqrt{(x_{i+1} - x_i)^2 + (y_{i+1} - y_i)^2}$$
$$(x_4, y_4) = (x_1, y_1). \quad (32)$$

The function L_o has dimensions 1/length whereas the functions M_x and M_y are dimensionless.

Comments on Stability Properties of Conservative Gyroscopic Systems

P. Lancaster[1] and W. Kliem[2]

A conjecture of Renshaw and Mote concerning gyroscopic systems with parameters predicts the eigenvalue locus in the neighborhood of a double-zero eigenvalue. In the present paper, this conjecture is reformulated in the language of generalized eigenvectors, angular splitting, and analytic behavior of eigenvalues. Two counter-examples for systems of dimension two show that the conjecture is not generally true. Finally, splitting or analytic behavior of eigenvalues is characterized in terms of expansion of the eigenvalues in fractional powers of the parameter.

1 Introduction

An interesting paper of Renshaw and Mote (1996) concerns the stability of the zero eigenvalue of gyroscopic systems, and a two-part conjecture is formulated giving a sufficient (and computationally feasible) condition for "stability" and "instability" of this eigenvalue. Here, we show by simple examples that both parts of the conjecture are false.

For our present purposes, the systems in question can operate on a space of dimension $n < \infty$. Indeed, for the specific examples presented here, $n = 2$. For convenience, we use the language of vectors and matrices and define a gyroscopic system to be an $n \times n$ matrix-valued function

$$L(\lambda) = \lambda^2 M + \lambda G + K$$

where M, G, K are real $n \times n$ matrices with $M > 0$ (M is positive definite), $M^T = M$ (where T denotes the transposed matrix), $G^T = -G$, and $K^T = K$. The parameter λ may take complex values (i.e., $\lambda \in \mathbb{C}$). We also define

$$L^{(1)}(\lambda) = 2\lambda M + G$$

An eigenvalue of $L(\lambda)$ is a number λ_0 for which $L(\lambda_0)$ is singular, and each eigenvalue has associated eigenvectors, i.e., nonzero vectors x_0 for which $L(\lambda_0)x_0 = 0$. Denote the complex conjugate of a number λ or matrix A by $\bar{\lambda}$, $\bar{A}$, respectively. We also write $A^* = \bar{A}^T$, the conjugate transpose.

The reader will easily verify that

$$L(\lambda)^T = L(-\lambda), \quad L(\lambda)^* = L(-\bar{\lambda})$$

These relations imply that the distribution of eigenvalues of $L(\lambda)$ in the complex plane is symmetric with respect to both the real and imaginary axes.

Contributed by the Applied Mechanics Division of THE AMERICAN SOCIETY OF MECHANICAL ENGINEERS for publication in the ASME JOURNAL OF APPLIED MECHANICS. Manuscript received by the ASME Applied Mechanics Division, Aug. 27, 1997; final revision, Dec. 10, 1997. Associate Technical Editor: S. W. Shaw.

The notion of a generalized eigenvector is important for this discussion, and, although this expression is not used by Renshaw and Mote (1996), it is helpful in understanding the conjecture in question. Let λ_0 be an eigenvalue of $L(\lambda)$. Following Lancaster and Tismenetsky (1985; see especially Chap. 14); we say that x_1 is a *generalized eigenvector* associated with λ_0 if x_1 is a solution of the equation (with singular coefficient matrix)

$$L(\lambda_0)x_1 = -L^{(1)}(\lambda_0)x_0 \quad (1)$$

for some eigenvector x_0. If Eq. (1) has no solution x_1 for any possible choice of x_0, then there are *no generalized eigenvectors* associated with λ_0.

Notice that, in the special case $\lambda_0 = 0$, an eigenvector x_0 satisfies $Kx_0 = 0$, and the generalized eigenvector equation is

$$Kx_1 = -Gx_0 \quad (2)$$

There is a generalized eigenvector associated with the zero eigenvalue if and only if (2) has a solution x_1 (possibly $x_1 = 0$) for some $x_0 \neq 0$ satisfying $Kx_0 = 0$.

2 Parameter Dependence

Suppose now that M, G, K (and hence L) depend analytically on an independent real parameter α which takes values in an interval (c, d). When α is fixed, an eigenvalue $\lambda(\alpha)$ and eigenvector $x(\alpha)$ satisfy $x(\alpha) \neq 0$, and

$$L(\lambda(\alpha), \alpha)x(\alpha) = 0$$

As α varies in (c, d), *eigenvalue functions* $\lambda(\alpha)$ are generated. They are known to depend continuously on α. A number $\alpha_0 \in (c, d)$ is a *critical value* of α if there is a *multiple* eigenvalue $\lambda_0 = \lambda(\alpha_0)$; and λ_0 is said to be multiple if either:

(a) there is a generalized eigenvector x_1 associated with λ_0, or
(b) the nullspace of $L(\lambda_0)$ has dimension $g > 1$,

or both (a) and (b) hold.

Although eigenvalue functions $\lambda(\alpha)$ are continuous in α, they may not be analytic functions of α at a critical value α_0. Indeed, the real and imaginary parts of $\lambda(\alpha)$ may not have a well-defined tangent at a critical α_0. These ideas are at the heart of the problem. To make the issues more precise, suppose that α_0 is critical and $\lambda_0 = \lambda(\alpha_0)$ is a multiple eigenvalue on the imaginary axis and, as α converges to α_0 from one side (for convenience, suppose α decreases to α_0 and write $\alpha \to \alpha_0^+$). It is assumed that as $\alpha \to \alpha_0^+$, certain eigenvalue functions $\lambda(\alpha) \to \lambda(\alpha_0)$ along the imaginary axis. We are concerned with continuation of the eigenvalue functions $\lambda(\alpha)$ when $\alpha < \alpha_0$. Several phenomena may occur, and two are of interest:

1 There may be "*angular splitting*" of the eigenvalue paths. In this case, there is no tangent to the paths of the real and imaginary parts of $\lambda(\alpha)$ at $\alpha = \alpha_0$. Also, for $\alpha < \alpha_0$, $\lambda(\alpha)$ is no longer pure imaginary, and (because of the symmetry of aforementioned eigenvalues) at least one eigenvalue has positive real part, i.e., produces instability.

2 For a two-sided neighborhood of α_0, say $(\alpha_0 - \epsilon, \alpha_0 + \epsilon)$, $\epsilon > 0$, all eigenvalues are pure imaginary. In this case, the system *may* remain stable. We refer to this as *(pure imaginary) analytic behavior* at α_0.

The conjecture of Renshaw and Mote (1996) is now very close to:

I If there are no generalized eigenvectors at $\lambda_0 = \lambda(\alpha_0)$ then there is pure imaginary analytic behavior at α_0.
II If there is a generalized eigenvector at $\lambda_0 = \lambda(\alpha_0)$ then there is angular splitting at α_0.

Downloaded 04 May 2010 to 171.66.16.27. Redistribution subject to ASME license or copyright; see http://www.asme.org/terms/Terms_Use.cfm

$$r_i = \sqrt{(x_i - x_o)^2 + (y_i - y_o)^2}$$
$$l_i = \sqrt{(x_{i+1} - x_i)^2 + (y_{i+1} - y_i)^2}$$
$$(x_4, y_4) = (x_1, y_1). \quad (32)$$

The function L_o has dimensions 1/length whereas the functions M_x and M_y are dimensionless.

Comments on Stability Properties of Conservative Gyroscopic Systems

P. Lancaster[1] and W. Kliem[2]

A conjecture of Renshaw and Mote concerning gyroscopic systems with parameters predicts the eigenvalue locus in the neighborhood of a double-zero eigenvalue. In the present paper, this conjecture is reformulated in the language of generalized eigenvectors, angular splitting, and analytic behavior of eigenvalues. Two counter-examples for systems of dimension two show that the conjecture is not generally true. Finally, splitting or analytic behavior of eigenvalues is characterized in terms of expansion of the eigenvalues in fractional powers of the parameter.

1 Introduction

An interesting paper of Renshaw and Mote (1996) concerns the stability of the zero eigenvalue of gyroscopic systems, and a two-part conjecture is formulated giving a sufficient (and computationally feasible) condition for "stability" and "instability" of this eigenvalue. Here, we show by simple examples that both parts of the conjecture are false.

For our present purposes, the systems in question can operate on a space of dimension $n < \infty$. Indeed, for the specific examples presented here, $n = 2$. For convenience, we use the language of vectors and matrices and define a gyroscopic system to be an $n \times n$ matrix-valued function

$$L(\lambda) = \lambda^2 M + \lambda G + K$$

where M, G, K are real $n \times n$ matrices with $M > 0$ (M is positive definite), $M^T = M$ (where T denotes the transposed matrix), $G^T = -G$, and $K^T = K$. The parameter λ may take complex values (i.e., $\lambda \in \mathbb{C}$). We also define

$$L^{(1)}(\lambda) = 2\lambda M + G$$

An eigenvalue of $L(\lambda)$ is a number λ_0 for which $L(\lambda_0)$ is singular, and each eigenvalue has associated eigenvectors, i.e., nonzero vectors x_0 for which $L(\lambda_0)x_0 = 0$. Denote the complex conjugate of a number λ or matrix A by $\bar{\lambda}$, $\bar{A}$, respectively. We also write $A^* = \bar{A}^T$, the conjugate transpose.

The reader will easily verify that

$$L(\lambda)^T = L(-\lambda), \quad L(\lambda)^* = L(-\bar{\lambda})$$

These relations imply that the distribution of eigenvalues of $L(\lambda)$ in the complex plane is symmetric with respect to both the real and imaginary axes.

Contributed by the Applied Mechanics Division of THE AMERICAN SOCIETY OF MECHANICAL ENGINEERS for publication in the ASME JOURNAL OF APPLIED MECHANICS. Manuscript received by the ASME Applied Mechanics Division, Aug. 27, 1997; final revision, Dec. 10, 1997. Associate Technical Editor: S. W. Shaw.

The notion of a generalized eigenvector is important for this discussion, and, although this expression is not used by Renshaw and Mote (1996), it is helpful in understanding the conjecture in question. Let λ_0 be an eigenvalue of $L(\lambda)$. Following Lancaster and Tismenetsky (1985; see especially Chap. 14); we say that x_1 is a *generalized eigenvector* associated with λ_0 if x_1 is a solution of the equation (with singular coefficient matrix)

$$L(\lambda_0)x_1 = -L^{(1)}(\lambda_0)x_0 \quad (1)$$

for some eigenvector x_0. If Eq. (1) has no solution x_1 for any possible choice of x_0, then there are *no generalized eigenvectors* associated with λ_0.

Notice that, in the special case $\lambda_0 = 0$, an eigenvector x_0 satisfies $Kx_0 = 0$, and the generalized eigenvector equation is

$$Kx_1 = -Gx_0 \quad (2)$$

There is a generalized eigenvector associated with the zero eigenvalue if and only if (2) has a solution x_1 (possibly $x_1 = 0$) for some $x_0 \neq 0$ satisfying $Kx_0 = 0$.

2 Parameter Dependence

Suppose now that M, G, K (and hence L) depend analytically on an independent real parameter α which takes values in an interval (c, d). When α is fixed, an eigenvalue $\lambda(\alpha)$ and eigenvector $x(\alpha)$ satisfy $x(\alpha) \neq 0$, and

$$L(\lambda(\alpha), \alpha)x(\alpha) = 0$$

As α varies in (c, d), *eigenvalue functions* $\lambda(\alpha)$ are generated. They are known to depend continuously on α. A number $\alpha_0 \in (c, d)$ is a *critical value* of α if there is a *multiple* eigenvalue $\lambda_0 = \lambda(\alpha_0)$; and λ_0 is said to be multiple if either:

(a) there is a generalized eigenvector x_1 associated with λ_0, or
(b) the nullspace of $L(\lambda_0)$ has dimension $g > 1$,

or both (a) and (b) hold.

Although eigenvalue functions $\lambda(\alpha)$ are continuous in α, they may not be analytic functions of α at a critical value α_0. Indeed, the real and imaginary parts of $\lambda(\alpha)$ may not have a well-defined tangent at a critical α_0. These ideas are at the heart of the problem. To make the issues more precise, suppose that α_0 is critical and $\lambda_0 = \lambda(\alpha_0)$ is a multiple eigenvalue on the imaginary axis and, as α converges to α_0 from one side (for convenience, suppose α decreases to α_0 and write $\alpha \to \alpha_0^+$). It is assumed that as $\alpha \to \alpha_0^+$, certain eigenvalue functions $\lambda(\alpha) \to \lambda(\alpha_0)$ along the imaginary axis. We are concerned with continuation of the eigenvalue functions $\lambda(\alpha)$ when $\alpha < \alpha_0$. Several phenomena may occur, and two are of interest:

1 There may be "*angular splitting*" of the eigenvalue paths. In this case, there is no tangent to the paths of the real and imaginary parts of $\lambda(\alpha)$ at $\alpha = \alpha_0$. Also, for $\alpha < \alpha_0$, $\lambda(\alpha)$ is no longer pure imaginary, and (because of the symmetry of aforementioned eigenvalues) at least one eigenvalue has positive real part, i.e., produces instability.

2 For a two-sided neighborhood of α_0, say $(\alpha_0 - \epsilon, \alpha_0 + \epsilon)$, $\epsilon > 0$, all eigenvalues are pure imaginary. In this case, the system *may* remain stable. We refer to this as *(pure imaginary) analytic behavior* at α_0.

The conjecture of Renshaw and Mote (1996) is now very close to:

I If there are no generalized eigenvectors at $\lambda_0 = \lambda(\alpha_0)$ then there is pure imaginary analytic behavior at α_0.
II If there is a generalized eigenvector at $\lambda_0 = \lambda(\alpha_0)$ then there is angular splitting at α_0.

 Copyright © 1999 by ASME

Downloaded 04 May 2010 to 171.66.16.27. Redistribution subject to ASME license or copyright; see http://www.asme.org/terms/Terms_Use.cfm

The following examples show that both statements are not generally true.

Example 1. Let

$$M = \begin{bmatrix} 1 & 0 \\ 0 & 1 \end{bmatrix}, \quad G = \begin{bmatrix} 0 & 1 \\ -1 & 0 \end{bmatrix}, \quad K = \begin{bmatrix} \alpha & 0 \\ 0 & \alpha^2 \end{bmatrix}.$$

Then

$$L(\lambda, \alpha) = \begin{bmatrix} \lambda^2 + \alpha & \lambda \\ -\lambda & \lambda^2 + \alpha^2 \end{bmatrix}.$$

Let $\alpha_0 = 0$ so that $\det L(\lambda, \alpha_0) = \lambda^4 + \lambda^2$ and there is a zero eigenvalue λ_0 of algebraic multiplicity two. Since $K(\alpha_0) = 0$, x_0 can be an arbitrary nonzero 2-vector and equation (2) is

$$\begin{bmatrix} 0 & 0 \\ 0 & 0 \end{bmatrix} x_1 = \begin{bmatrix} 0 & -1 \\ 1 & 0 \end{bmatrix} x_0. \tag{3}$$

There is no solution of (3) when $x_0 \neq 0$, i.e. there is no generalized eigenvector at λ_0.

However,

$$\det L(\lambda, \alpha) = \lambda^4 + (1 + \alpha + \alpha^2)\lambda^2 + \alpha^3 = 0$$

can be solved for $\lambda(\alpha)$ by elementary methods giving for those two $\lambda(\alpha)$ for which $\lambda(\alpha) \to \lambda_0 = 0$ as $\alpha \to \alpha_0$,

$$\lambda(\alpha) = \pm i\alpha^{1/2}\left\{\alpha + \begin{pmatrix}\text{(higher integer powers}\\ \text{with real coefficients)}\end{pmatrix}\right\}. \tag{4}$$

This means that there is angular splitting at $\alpha_0 = 0$ ($\lambda(\alpha)$ is pure imaginary when $\alpha > 0$ and real when $\alpha < 0$). This example contradicts part I of the conjecture.

Example 2. Let

$$M = \begin{bmatrix} 1 & 0 \\ 0 & 1 \end{bmatrix}, \quad G = \begin{bmatrix} 0 & 1 \\ -1 & 0 \end{bmatrix}, \quad K = \begin{bmatrix} 0 & \alpha \\ \alpha & -2 \end{bmatrix}$$

Then

$$\det L(\lambda, \alpha) = \lambda^4 - \lambda^2 - \alpha^2 = 0 \tag{5}$$

Let $\alpha_0 = 0$ and $\lambda_0 = 0$. We may take $x_0 = \left[\begin{smallmatrix}2\\0\end{smallmatrix}\right]$, and Eq. (2) is

$$\begin{bmatrix} 0 & 0 \\ 0 & -2 \end{bmatrix} x_1 = -\begin{bmatrix} 0 & 1 \\ -1 & 0 \end{bmatrix}\begin{bmatrix} 2 \\ 0 \end{bmatrix} = \begin{bmatrix} 0 \\ 2 \end{bmatrix}$$

This equation has a solution $x_1 = \left[\begin{smallmatrix}1\\-1\end{smallmatrix}\right]$, so *there is a generalized eigenvector.* However, for eigenvalues $\lambda(\alpha)$ satisfying $\lambda(\alpha) \to 0$ as $\alpha \to 0$, Eq. (5) gives

$$\lambda(\alpha) = \pm i\left\{\alpha + \begin{pmatrix}\text{(higher integer powers}\\ \text{with real coefficients)}\end{pmatrix}\right\}. \tag{6}$$

The behavior at $\alpha_0 = 0$ is pure-imaginary analytic and shows that conjecture II is false.

Another counter-example in this direction is

$$M = \begin{bmatrix} 1 & 0 \\ 0 & 1 \end{bmatrix}, \quad G = \begin{bmatrix} 0 & 3 \\ -3 & 0 \end{bmatrix}, \quad K = \begin{bmatrix} -\alpha^2 & 0 \\ 0 & -1 \end{bmatrix}$$

3 Concluding Remarks

The notion of "angular splitting" as defined here can be characterized in another way. A general theorem of analytic perturbation theory ensures that the eigenvalue functions $\lambda(\alpha)$ have power series expansions about a critical α_0 in (generally) *fractional powers* of $\alpha - \alpha_0$. Thus, in some complex neighborhood of α_0, an expansion

$$\lambda_\sigma(\alpha) = \lambda_0 + \sum_{j=1}^{\infty} a_j\{(\alpha - \alpha_0)^{1/k}\}^j, \quad \sigma = 0, 1, 2, \ldots, k-1$$

holds, where k is a positive integer, and the fractional powers $(\alpha - \alpha_0)^{1/k}$ can take k distinct values (accounting for the suppressed index σ on the right-hand side). A general result of this kind can be found in Baumgärtel (1985). This expansion admits analytic dependence of λ on α. This is the case $k = 1$. *Angular splitting* can occur only if $k > 1$ (as in (4)). There is *pure-imaginary analytic behavior* at α_0 if and only if $k = 1$ and all coefficients a_j, $j = 0, 1, 2, \ldots$ are pure-imaginary (as in (6)).

References

Baumgärtel, H., 1985, *Analytic Perturbation Theory for Matrices and Operators,* Section 9.3, Birkhäuser Verlag, Basel (OT 15), Switzerland.

Lancaster, P., and Tismenetsky, M., 1985, *The Theory of Matrices,* Academic Press, Orlando, FL.

Renshaw, A. A., and Mote, Jr., C. D., 1996, "Local Stability of Gyroscopic Systems Near Vanishing Eigenvalues," ASME *Journal of Applied Mechanics,* Vol. 63, pp. 116–120.

[1] Department of Mathematics and Statistics, The University of Calgary, Calgary, Alberta, T2N 1N4 Canada.

[2] Department of Mathematics, Technical University of Denmark, DK-2800 Lyngby, Denmark.

A Simplified Variation of Parameters Approach to Euler's Equations

D. L. Richardson[1] and J. W. Mitchell[1]

A normalized form of Euler's equations is rewritten in a variation of parameters approach using amplitudes and angular displacement as parameters. This new form is compact and yields a more accurate numerically integrated solution over longer simulation times than does a conventional integration of the Euler equations.

1 Introduction

Variational methods have played an important role in solving ordinary differential equations since their introduction by John Bernoulli in the late 17th century. Perhaps the most famous application of a variational method, the variation of orbital elements or the variation of constants, was performed by Leonhard Euler between 1748 and 1752 to describe the mutual perturbations of Jupiter and Saturn. However, it was not until 1782 that Joseph-Louis Lagrange fully and completely developed the method of the variation of parameters (VOP) in an application involving cometary motion. His approach is widely used today, particularly in astrodynamics applications where perturbed two-body motion is considered.

Because the moment-free rigid-body motion equations developed by Euler in 1754 admit an analytical solution, it seemed desirable to apply Lagrange's method of the variation of parameters to these equations. It was hoped that the resulting differential equations would enjoy the same numerical robustness that characterizes

[1] Department of Aerospace Engineering and Engineering Mechanics, University of Cincinnati, Cincinnati, OH 45221-0070.

Contributed by the Applied Mechanics Division of THE AMERICAN SOCIETY OF MECHANICAL ENGINEERS for publication in the ASME JOURNAL OF APPLIED MECHANICS. Manuscript received by the ASME Applied Mechanics Division, Aug. 4, 1997; final revision, July 8, 1998. Associate Technical Editor: N. C. Perkins.

Downloaded 04 May 2010 to 171.66.16.27. Redistribution subject to ASME license or copyright; see http://www.asme.org/terms/Terms_Use.cfm

The following examples show that both statements are not generally true.

Example 1. Let

$$M = \begin{bmatrix} 1 & 0 \\ 0 & 1 \end{bmatrix}, \quad G = \begin{bmatrix} 0 & 1 \\ -1 & 0 \end{bmatrix}, \quad K = \begin{bmatrix} \alpha & 0 \\ 0 & \alpha^2 \end{bmatrix}.$$

Then

$$L(\lambda, \alpha) = \begin{bmatrix} \lambda^2 + \alpha & \lambda \\ -\lambda & \lambda^2 + \alpha^2 \end{bmatrix}.$$

Let $\alpha_0 = 0$ so that $\det L(\lambda, \alpha_0) = \lambda^4 + \lambda^2$ and there is a zero eigenvalue λ_0 of algebraic multiplicity two. Since $K(\alpha_0) = 0$, x_0 can be an arbitrary nonzero 2-vector and equation (2) is

$$\begin{bmatrix} 0 & 0 \\ 0 & 0 \end{bmatrix} x_1 = \begin{bmatrix} 0 & -1 \\ 1 & 0 \end{bmatrix} x_0. \tag{3}$$

There is no solution of (3) when $x_0 \neq 0$, i.e. there is no generalized eigenvector at λ_0.

However,

$$\det L(\lambda, \alpha) = \lambda^4 + (1 + \alpha + \alpha^2)\lambda^2 + \alpha^3 = 0$$

can be solved for $\lambda(\alpha)$ by elementary methods giving for those two $\lambda(\alpha)$ for which $\lambda(\alpha) \to \lambda_0 = 0$ as $\alpha \to \alpha_0$,

$$\lambda(\alpha) = \pm i\alpha^{1/2}\left\{\alpha + \begin{pmatrix}\text{(higher integer powers} \\ \text{with real coefficients)}\end{pmatrix}\right\}. \tag{4}$$

This means that there is angular splitting at $\alpha_0 = 0$ ($\lambda(\alpha)$ is pure imaginary when $\alpha > 0$ and real when $\alpha < 0$). This example contradicts part I of the conjecture.

Example 2. Let

$$M = \begin{bmatrix} 1 & 0 \\ 0 & 1 \end{bmatrix}, \quad G = \begin{bmatrix} 0 & 1 \\ -1 & 0 \end{bmatrix}, \quad K = \begin{bmatrix} 0 & \alpha \\ \alpha & -2 \end{bmatrix}$$

Then

$$\det L(\lambda, \alpha) = \lambda^4 - \lambda^2 - \alpha^2 = 0 \tag{5}$$

Let $\alpha_0 = 0$ and $\lambda_0 = 0$. We may take $x_0 = \begin{bmatrix} 2 \\ 0 \end{bmatrix}$, and Eq. (2) is

$$\begin{bmatrix} 0 & 0 \\ 0 & -2 \end{bmatrix} x_1 = -\begin{bmatrix} 0 & 1 \\ -1 & 0 \end{bmatrix}\begin{bmatrix} 2 \\ 0 \end{bmatrix} = \begin{bmatrix} 0 \\ 2 \end{bmatrix}$$

This equation has a solution $x_1 = \begin{bmatrix} 1 \\ -1 \end{bmatrix}$, so *there is a generalized eigenvector.* However, for eigenvalues $\lambda(\alpha)$ satisfying $\lambda(\alpha) \to 0$ as $\alpha \to 0$, Eq. (5) gives

$$\lambda(\alpha) = \pm i\left\{\alpha + \begin{pmatrix}\text{(higher integer powers} \\ \text{with real coefficients)}\end{pmatrix}\right\}. \tag{6}$$

The behavior at $\alpha_0 = 0$ is pure-imaginary analytic and shows that conjecture II is false.

Another counter-example in this direction is

$$M = \begin{bmatrix} 1 & 0 \\ 0 & 1 \end{bmatrix}, \quad G = \begin{bmatrix} 0 & 3 \\ -3 & 0 \end{bmatrix}, \quad K = \begin{bmatrix} -\alpha^2 & 0 \\ 0 & -1 \end{bmatrix}$$

3 Concluding Remarks

The notion of "angular splitting" as defined here can be characterized in another way. A general theorem of analytic perturbation theory ensures that the eigenvalue functions $\lambda(\alpha)$ have power series expansions about a critical α_0 in (generally) *fractional powers* of $\alpha - \alpha_0$. Thus, in some complex neighborhood of α_0, an expansion

$$\lambda_\sigma(\alpha) = \lambda_0 + \sum_{j=1}^{\infty} a_j\{(\alpha - \alpha_0)^{1/k}\}^j, \quad \sigma = 0, 1, 2, \ldots, k-1$$

holds, where k is a positive integer, and the fractional powers $(\alpha - \alpha_0)^{1/k}$ can take k distinct values (accounting for the suppressed index σ on the right-hand side). A general result of this kind can be found in Baumgärtel (1985). This expansion admits analytic dependence of λ on α. This is the case $k = 1$. *Angular splitting* can occur only if $k > 1$ (as in (4)). There is *pure-imaginary analytic behavior* at α_0 if and only if $k = 1$ and all coefficients a_j, $j = 0, 1, 2, \ldots$ are pure-imaginary (as in (6)).

References

Baumgärtel, H., 1985, *Analytic Perturbation Theory for Matrices and Operators,* Section 9.3, Birkhäuser Verlag, Basel (OT 15), Switzerland.

Lancaster, P., and Tismenetsky, M., 1985, *The Theory of Matrices,* Academic Press, Orlando, FL.

Renshaw, A. A., and Mote, Jr., C. D., 1996, "Local Stability of Gyroscopic Systems Near Vanishing Eigenvalues," ASME *Journal of Applied Mechanics,* Vol. 63, pp. 116–120.

[1] Department of Mathematics and Statistics, The University of Calgary, Calgary, Alberta, T2N 1N4 Canada.

[2] Department of Mathematics, Technical University of Denmark, DK-2800 Lyngby, Denmark.

A Simplified Variation of Parameters Approach to Euler's Equations

D. L. Richardson[1] and J. W. Mitchell[1]

A normalized form of Euler's equations is rewritten in a variation of parameters approach using amplitudes and angular displacement as parameters. This new form is compact and yields a more accurate numerically integrated solution over longer simulation times than does a conventional integration of the Euler equations.

1 Introduction

Variational methods have played an important role in solving ordinary differential equations since their introduction by John Bernoulli in the late 17th century. Perhaps the most famous application of a variational method, the variation of orbital elements or the variation of constants, was performed by Leonhard Euler between 1748 and 1752 to describe the mutual perturbations of Jupiter and Saturn. However, it was not until 1782 that Joseph-Louis Lagrange fully and completely developed the method of the variation of parameters (VOP) in an application involving cometary motion. His approach is widely used today, particularly in astrodynamics applications where perturbed two-body motion is considered.

Because the moment-free rigid-body motion equations developed by Euler in 1754 admit an analytical solution, it seemed desirable to apply Lagrange's method of the variation of parameters to these equations. It was hoped that the resulting differential equations would enjoy the same numerical robustness that characterizes

[1] Department of Aerospace Engineering and Engineering Mechanics, University of Cincinnati, Cincinnati, OH 45221-0070.

Contributed by the Applied Mechanics Division of THE AMERICAN SOCIETY OF MECHANICAL ENGINEERS for publication in the ASME JOURNAL OF APPLIED MECHANICS. Manuscript received by the ASME Applied Mechanics Division, Aug. 4, 1997; final revision, July 8, 1998. Associate Technical Editor: N. C. Perkins.

 Copyright © 1999 by ASME

Downloaded 04 May 2010 to 171.66.16.27. Redistribution subject to ASME license or copyright; see http://www.asme.org/terms/Terms_Use.cfm

the VOP astrodynamics equations. We have indeed found this to be the case through a careful selection of VOP system parameters.

A VOP approach to Euler's equations and to the general orientational motion of rigid bodies has been investigated several times since the mid-1970s. Early work by Kraige and Junkins (1976) and Donaldson and Jezewski (1977) used the body's kinetic energy and angular momentum as the primary parameters in a general VOP scheme. The resulting equations were algebraically complex. The later work of Kraige and Skaar (1977) and Kraige (1978) did introduce less complexity to the form of the variational equations. More recently, Bond (1996) investigated a VOP scheme for rigid-body motion that utilized the case of symmetric, torque-free motion as the analytical basis for generating the parameters. Taken altogether, we felt that there was still room for improvement through a more judicious selection of parameters developed from the analytical solution to the general problem of torque-free rotation.

In the following, we present our development of Euler's equations in a VOP form using parameters that we feel are more natural and intrinsic to the problem. Our resulting VOP equations are not algebraically complex making them desirable for use in numerical simulations. We apply our approach to the constant-torque problem to demonstrate how our VOP equations provide greater accuracy integrations over longer simulation periods independent of the numerical propagation method chosen.

2 Formulation

2.1 Analytical Solution. The classical Euler's equations for rigid-body motion are given by the coupled first-order system

$$\left.\begin{aligned} I_1\dot{\omega}_1 &= (I_2 - I_3)\omega_2\omega_3 + M_1,\\ I_2\dot{\omega}_2 &= (I_3 - I_1)\omega_1\omega_3 + M_2,\\ I_3\dot{\omega}_3 &= (I_1 - I_2)\omega_1\omega_2 + M_3. \end{aligned}\right\} \tag{1}$$

The ω_i are the components of the angular velocity of the body expressed in a body-fixed principal-axis coordinate frame. The I_i and M_i are the principal-axis moments of inertia and external moment components, respectively.

Rewriting Eqs. (1), we have

$$\left.\begin{aligned} \dot{\omega}_1 &= -A_1\omega_2\omega_3 + M_1/I_1,\\ \dot{\omega}_2 &= A_2\omega_1\omega_3 + M_2/I_2,\\ \dot{\omega}_3 &= -A_3\omega_1\omega_2 + M_3/I_3, \end{aligned}\right\} \tag{2}$$

where

$$\left.\begin{aligned} A_1 &= (I_3 - I_2)/I_1,\\ A_2 &= (I_3 - I_1)/I_2,\\ A_3 &= (I_2 - I_1)/I_3, \end{aligned}\right\} \tag{3}$$

and $I_3 > I_2 > I_1$.

Upon performing a change of variables defined by the relations

$$\Omega_i = \omega_i/\sqrt{A_i} \quad \text{and} \quad \frac{d\tau}{dt} = \sqrt{A_1A_2A_3}\,, \tag{4}$$

the Euler equations become the normalized expressions

$$\left.\begin{aligned} \Omega_1' &= -\Omega_2\Omega_3 + G_1,\\ \Omega_2' &= \Omega_1\Omega_3 + G_2,\\ \Omega_3' &= -\Omega_1\Omega_2 + G_3, \end{aligned}\right\} \tag{5}$$

where the prime indicates $d/d\tau$ and G_i are the rescaled external moments.

Two independent integrals of motion, c_1 and c_2, of the unperturbed equations are obtained from the expressions

$$\left.\begin{aligned} \frac{d}{d\tau}\left(\frac{1}{2}\Omega_1^2\right) &= \Omega_1\Omega_1' = -\Omega_1\Omega_2\Omega_3,\\ \frac{d}{d\tau}\left(\frac{1}{2}\Omega_2^2\right) &= \Omega_2\Omega_2' = \Omega_1\Omega_2\Omega_3,\\ \frac{d}{d\tau}\left(\frac{1}{2}\Omega_3^2\right) &= \Omega_3\Omega_3' = -\Omega_1\Omega_2\Omega_3. \end{aligned}\right\} \tag{6}$$

and, by inspection, are seen to be

$$\left.\begin{aligned} \Omega_1^2 + \Omega_2^2 &= c_1^2,\\ \Omega_2^2 + \Omega_3^2 &= c_2^2. \end{aligned}\right\} \tag{7}$$

These integrals of motion are related to the classical integrals of energy T and angular momentum H by

$$c_1^2 = \frac{2TI_3 - H^2}{(I_3 - I_1)(I_3 - I_2)} \geq 0, \tag{8}$$

$$c_2^2 = \frac{H^2 - 2TI_1}{(I_3 - I_1)(I_2 - I_1)} \geq 0. \tag{9}$$

The solutions for the Ω_i of the unperturbed system are developed by first considering the second of Eqs. (5). Combining this with Eqs. (7) gives

$$\Omega_2' \triangleq c_1c_2\sqrt{1 - s^2}\,\sqrt{1 - k^2s^2}\,, \tag{10}$$

with $s = \Omega_2/c_1$ and $k = c_1/c_2 \geq 0$ where k is called the modulus. By restricting k such that $0 \leq k < 1$ and integrating Eq. (10), we obtain

$$\mathrm{sn}^{-1}(s) = c_2(\tau - \tau_0) \triangleq u. \tag{11}$$

Using this result along with Eqs. (7) produces the solutions for the Ω_i:

$$\left.\begin{aligned} \Omega_1 &= c_1\mathrm{cn}(u),\\ \Omega_2 &= c_1\mathrm{sn}(u),\\ \Omega_3 &= c_2\mathrm{dn}(u) \end{aligned}\right\} \tag{12}$$

It is seen that c_1, c_2, and τ_0 form a natural set of elements (parameters) for the characterization of the solution to the moment-free Euler equations. The variable u is viewed as the intrinsic angular variable for this problem.

2.2 Variation of Parameters. The variations of the two independent integrals of motion, c_1 and c_2, are obtained by direct differentiation of Eqs. (7) along with substitutions from Eqs. (5), yielding

$$\left.\begin{aligned} c_1' &= \frac{1}{c_1}(\Omega_1G_1 + \Omega_2G_2) = \mathrm{cn}(u)G_1 + \mathrm{sn}(u)G_2,\\ c_2' &= \frac{1}{c_2}(\Omega_2G_2 + \Omega_3G_3) = k\,\mathrm{sn}(u)G_2 + \mathrm{dn}(u)G_3. \end{aligned}\right\} \tag{13}$$

From a numerical perspective, integrating directly for the argument u is somewhat more algebraically desirable than integrating the variational equation for τ_0 and then forming u. Accordingly, we develop u' directly by manipulation of Ω_1 and Ω_2 from Eqs. (12) to produce

$$\mathrm{cn}(u)\Omega_2' - \mathrm{sn}(u)\Omega_1' = c_1u'\mathrm{dn}(u)$$

$$- \frac{c_1\mathrm{dn}(u)}{kk_c^2}[E(u) - k_c^2u - k^2\mathrm{sn}(u)\mathrm{cn}(u)/\mathrm{dn}(u)]k'. \tag{14}$$

Downloaded 04 May 2010 to 171.66.16.27. Redistribution subject to ASME license or copyright; see http://www.asme.org/terms/Terms_Use.cfm

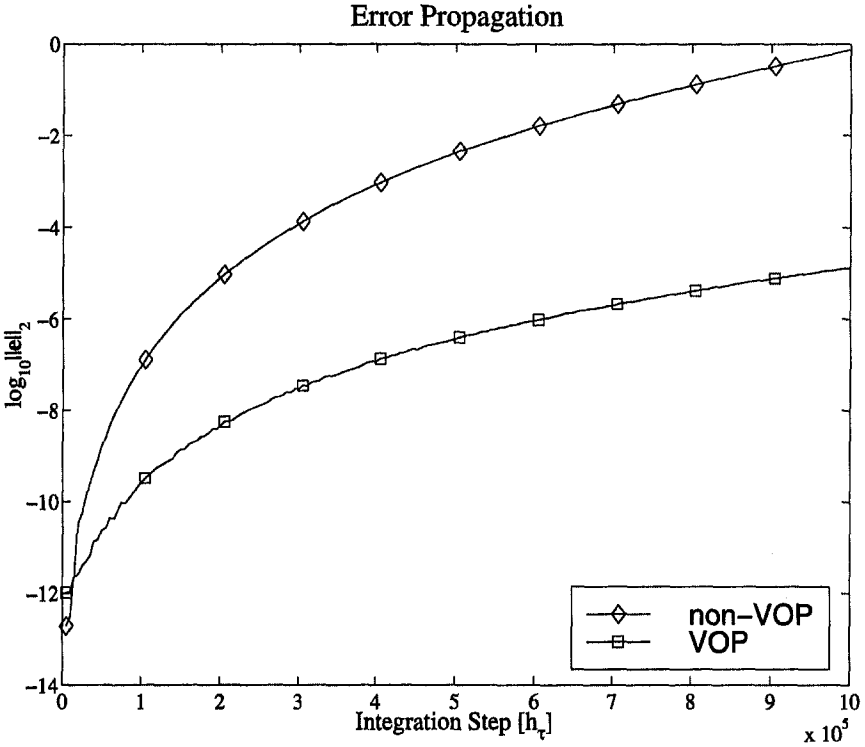

Fig. 1 Two-norm errors for numerical integrations of the modified Euler equations (non-VOP) and the variation of parameters equations (VOP) for approximately 3000 cycles of Ω_3

In the above expression, $k_c^2 = 1 - k^2$ is the complementary modulus, $E(u)$ is the incomplete elliptic integral of the second kind, and k' is given by

$$k' = \frac{1}{c_2}\left[\mathrm{cn}(u)G_1 + k_c^2\mathrm{sn}(u)G_2 - k\,\mathrm{dn}(u)G_3\right]. \quad (15)$$

After some algebraic manipulation, we arrive at the desired expression

$$u' = \frac{1}{c_1 k_c^2}\left[k(c_2^2 - c_1^2) - \mathrm{sn}(u)\mathrm{dn}(u)G_1 + k_c^2\mathrm{cn}(u)\mathrm{dn}(u)G_2 + k^3\mathrm{sn}(u)\mathrm{cn}(u)G_3 + [E(u) - k_c^2 u][\mathrm{cn}(u)G_1 + k_c^2\mathrm{sn}(u)G_2 - k\,\mathrm{dn}(u)G_3]\right]. \quad (16)$$

In summary, the variation of parameters solution to the perturbed Euler system of normalized Eqs. (5) is given by Eqs. (12) with the differential equations for the parameters given by Eqs. (13) and (16).

3 A Numerical Demonstration

We demonstrate the numerical behavior of our variation of parameters solution by comparisons to numerically generated solutions of the normalized Euler system of Eqs. (5). The solution to the problem of a constant torque applied to the body is of interest in satellite attitude determination applications (Williams and Tanygin, 1996). We chose this problem to illustrate the robustness of our VOP formulation. To this end, we selected the external moment components G_i to be constants of the same order of magnitude as the Ω_i components. We used

$$G_1 = G_2 = G_3 = 1.0. \quad (17)$$

We completed our system initialization by specifying values at $\tau = 0$ as

$$c_1(0) = 0.5, \quad c_2(0) = 1.0, \quad u(0) = 0.0, \quad (18)$$

which produced the initial conditions

$$\Omega_1(0) = c_1, \quad \Omega_2(0) = 0.0, \quad \Omega_3(0) = c_2. \quad (19)$$

Using these initial conditions, the variational equations (Eqs. (12) through (16)) and Euler's equations (Eqs. (5)) were integrated numerically using a Runge-Kutta 4/5 scheme. Both systems of equations were integrated with the same fixed step size. This step size h was taken to be approximately 1/400th of the initial $\mathrm{dn}(u)$ period as specified by the initial conditions, i.e., $h = K/200$, where $K \equiv K(k)$ is the complete elliptic integral of the first kind. In this case, we have $K(0.5) \approx 1.686$.

Both sets of double precision (IEEE Standard 754) integrations were compared to an extended precision (16-byte) integration of Eqs. (5). The extended precision step size was approximately 1/4000th of the initial $\mathrm{dn}(u)$ period. This integration was performed by using a 16th-degree first-order Chebyshev procedure (Richardson et al., 1998).

For each integration, we computed and graphed the two-norm error,

$$e = \sqrt{(\Delta\Omega_1)^2 + (\Delta\Omega_2)^2 + (\Delta\Omega_3)^2}, \quad (20)$$

where $\Delta\Omega_i = \Omega_i^* - \Omega_i$ is the difference of Ω_i when compared with the extended precision result, Ω_i^*. Figure 1 shows the error propagation results.

From this figure, it is seen that the variation of parameters solution maintains an accuracy of several orders of magnitude better than that produced by direct integration of the normalized Euler equations. This behavior was expected largely because of similar behaviors that have been observed in the numerical integration of various sets of VOP equations used in astrodynamics applications.

4 Concluding Remarks

In this paper, a variation of parameters solution is developed for a normalized form of the arbitrarily perturbed Euler's equa-

Downloaded 04 May 2010 to 171.66.16.27. Redistribution subject to ASME license or copyright; see http://www.asme.org/terms/Terms_Use.cfm

tions for attitude motion. The three parameters of the variation, two amplitudes, and an angular displacement lead to a very compact form that yields higher numerical accuracy over longer simulation intervals than did direct integration of Euler's equations for the same fixed step size. This improved accuracy is the result of the reformulation using the variation of parameters and thus independent of the numerical integration scheme.

While the accuracy of the integration did improve, one disadvantage of this method is additional computational overhead. Much of this overhead is due to the calculation of the necessary special functions. This additional computation is consistent with the variation of parameters integrations of the orbital elements in astrodynamics applications and is expected. For applications involving algebraically complex moment components, the variational equations will produce comparable execution timings.

With regard to step size, the reader should note that the normalized Euler equations and the variation of parameters equations both contain the same spectral content. Consequently, the variation of parameters equations cannot be integrated using step sizes that are substantially greater than that needed for the normalized equations.

Acknowledgment

This research was supported by the National Aeronautics and Space Administration under GSRP grant NGT-51639.

References

Bond, V. R., 1996, "A Variation of Parameters Approach for the Solution of the Differential Equations for the Rotational Motion of a Rigid Body," *Proceedings of the 6th AAS/AIAA Spaceflight Mechanics Meeting: Advances in the Astronautical Sciences,* Vol. 93, Part II, p. 1113, abstract (full paper not published).

Donaldson, J. D., and Jezewski, D. J., 1977, "An Element Formulation for Perturbed Motion About the Center of Mass," *Celestial Mechanics,* Vol. 16, pp. 367–387.

Kraige, G. L., and Junkins, J. L., 1976, "Perturbation Formulations for Satellite Attitude Dynamics," *Celestial Mechanics,* Vol. 13, pp. 39–64.

Kraige, G. L., and Skaar, S. B., 1977, "A Variation of Parameters Approach to the Arbitrarily Torqued, Asymmetric Rigid Body Problem," *Journal of the Astronautical Sciences,* Vol. 25, pp. 207–226.

Kraige, G. L., 1978, "The Development and Numerical Testing of a Variation of Parameters Approach to the Arbitrarily Torqued, Asymmetric Rigid Body Problem," Report No. VPI-E-78-9, Virginia Polytechnic Institute, Blacksburg, VA, pp. 1–85.

Richardson, D. L., Schmidt, D., and Mitchell, J. W., 1998, "Improved Chebyshev Methods for the Numerical Integration of First-Order Differential Equations," *Proceedings of the 8th AAS/AIAA Spaceflight Mechanics Meeting: Advances in the Astronautical Sciences,* Vol. 99, Part II, pp. 1533–1544.

Williams, T., and Tanygin, S., 1996, "Dynamics of a Near-Symmetrical Spacecraft Driven by a Constant Thrust," *Proceedings of the 6th AAS/AIAA Spaceflight Mechanics Meeting: Advances in the Astronautical Sciences,* Vol. 93, Part II, pp. 925–944.

A Circular Inhomogeneity Problem Revisited

K. W. Lee[1], S. T. Choi,[1] and Y. Y. Earmme[2]

1 Introduction

A circular inclusion whose elastic moduli are different from the infinite matrix has been a subject of many researchers. Most recent works incluse those by Honein and Herrmann (1990) and Chao (1994). A circular inclusion in an infinite matrix under a point force was analyzed by Dundurs and Hetenyi (1961) and Hetenyi and Dundurs (1962) and the similar one with an edge dislocation was dealt with by Dundurs and Mura (1964).

A simple approach to obtain the stresses and displacements of the two semi-infinite materials bonded together along the straight boundary (i.e., along the x-axis) under the point force, an edge dislocation, and a point moment was proposed by Suo (1989). The method has an advantage over those of the aforementioned works by taking the complex potential of the bimaterial problem to be the sum of the complex potential of the corresponding homogeneous material with the same singularity source and the perturbed complex potential due to the existence of the other materials, to make the solution procedure simple and straightforward. Honein and Herrmann (1990) obtained the solution of an inclusion in an infinite matrix by substituting the solution of the corresponding homogeneous problem into an algebraic expression, which they referred to as "heterogenization". However it seems that the advantage of the complex potential method is not fully utilized so that the solution procedure is quite complicated compared to the procedure by Suo (1989).

It is the purpose of this study to show that the solution procedure for an inclusion in the infinite matrix, guided by the method of Suo (1989) is simple and straightforward, and the solution can be written in a compact form.

2 Solution Procedure and Result

The components of the stresses and displacements in the polar coordinates are expressed in terms of the complex potentials $\Phi(z)$, $\Psi(z)$, and $\Omega(z)$ as follows:

$$\sigma_{rr} + \sigma_{\theta\theta} = 2[\Phi(z) + \bar{\Phi}(\bar{z})],$$

$$\sigma_{rr} + i\sigma_{r\theta} = \Phi(z) + \Omega\left(\frac{1}{\bar{z}}\right) + \bar{z}\left(\bar{z} - \frac{1}{z}\right)\bar{\Psi}(\bar{z}),$$

$$2\mu \frac{\partial}{\partial\theta}(u_x + iu_y) = iz\left[\kappa\Phi(z) - \Omega\left(\frac{1}{\bar{z}}\right) - \bar{z}\left(\bar{z} - \frac{1}{z}\right)\bar{\Psi}(\bar{z})\right]. \quad (1)$$

The complex potential $\Omega(z)$ is defined by

$$\Omega(z) = \bar{\Phi}\left(\frac{1}{z}\right) - \frac{1}{z}\bar{\Phi}'\left(\frac{1}{z}\right) - \frac{1}{z^2}\bar{\Psi}\left(\frac{1}{z}\right), \quad (2)$$

whence

$$\Psi(z) = \frac{1}{z^2}\Phi(z) - \frac{1}{z}\Phi'(z) - \frac{1}{z^2}\bar{\Omega}\left(\frac{1}{z}\right). \quad (3)$$

When a singularity is in an infinite homogeneous isotropic material, the solution $\Phi_o(z)$ and $\Omega_o(z)$ are listed in the word of Suo (1989), however in the case of circular inclusion, $\Omega(z)$ is defined by Eq. (2), which is different from that of Suo (1989), so that we obtain $\Phi_o(z)$ and $\Omega_o(z)$ as follows:

$$\Phi_o(z) = -\frac{Q_o}{z - s}, \quad \Omega_o(z) = \frac{z^2\bar{Q}_o + \hat{\kappa}Q_o}{z(z\bar{s} - 1)} - \frac{\bar{Q}_o(z - s)}{(z\bar{s} - 1)^2}, \quad (4)$$

where, $z = x + iy$, $s = x_o + iy_o$ (the position of the singularity), Q_o and $\hat{\kappa}$ are defined as

(i) for a point force P $(= P_x + iP_y)$

[1] Ph.D. Student, Department of Mechanical Engineering, ME3053, Korea Advanced Institute of Science and Technology, 373-1, Yusung-Gu, Kusong-Dong, Taejon 305-701, South Korea.

[2] To whom correspondence should be addressed. Professor, Department of Mechanical Engineering, ME3013, Korea Advanced Institute of Science and Technology, 373-1, Yusung-Gu, Kusong-Dong, Taejon 305-701, South Korea. e-mail: yyearmme@cais.kaist.ac.kr. Mem. ASME.

Contributed by the Applied Mechanics Division of THE AMERICAN SOCIETY OF MECHANICAL ENGINEERS for publication in the ASME JOURNAL OF APPLIED MECHANICS. Manuscript received by the ASME Applied Mechanics Division, June 1, 1998; final revision, Oct. 4, 1998. Associate Technical Editor: M. J. Pindera.

Downloaded 04 May 2010 to 171.66.16.27. Redistribution subject to ASME license or copyright; see http://www.asme.org/terms/Terms_Use.cfm

tions for attitude motion. The three parameters of the variation, two amplitudes, and an angular displacement lead to a very compact form that yields higher numerical accuracy over longer simulation intervals than did direct integration of Euler's equations for the same fixed step size. This improved accuracy is the result of the reformulation using the variation of parameters and thus independent of the numerical integration scheme.

While the accuracy of the integration did improve, one disadvantage of this method is additional computational overhead. Much of this overhead is due to the calculation of the necessary special functions. This additional computation is consistent with the variation of parameters integrations of the orbital elements in astrodynamics applications and is expected. For applications involving algebraically complex moment components, the variational equations will produce comparable execution timings.

With regard to step size, the reader should note that the normalized Euler equations and the variation of parameters equations both contain the same spectral content. Consequently, the variation of parameters equations cannot be integrated using step sizes that are substantially greater than that needed for the normalized equations.

Acknowledgment

This research was supported by the National Aeronautics and Space Administration under GSRP grant NGT-51639.

References

Bond, V. R., 1996, "A Variation of Parameters Approach for the Solution of the Differential Equations for the Rotational Motion of a Rigid Body," *Proceedings of the 6th AAS/AIAA Spaceflight Mechanics Meeting: Advances in the Astronautical Sciences,* Vol. 93, Part II, p. 1113, abstract (full paper not published).

Donaldson, J. D., and Jezewski, D. J., 1977, "An Element Formulation for Perturbed Motion About the Center of Mass," *Celestial Mechanics,* Vol. 16, pp. 367–387.

Kraige, G. L., and Junkins, J. L., 1976, "Perturbation Formulations for Satellite Attitude Dynamics," *Celestial Mechanics,* Vol. 13, pp. 39–64.

Kraige, G. L., and Skaar, S. B., 1977, "A Variation of Parameters Approach to the Arbitrarily Torqued, Asymmetric Rigid Body Problem," *Journal of the Astronautical Sciences,* Vol. 25, pp. 207–226.

Kraige, G. L., 1978, "The Development and Numerical Testing of a Variation of Parameters Approach to the Arbitrarily Torqued, Asymmetric Rigid Body Problem," Report No. VPI-E-78-9, Virginia Polytechnic Institute, Blacksburg, VA, pp. 1–85.

Richardson, D. L., Schmidt, D., and Mitchell, J. W., 1998, "Improved Chebyshev Methods for the Numerical Integration of First-Order Differential Equations," *Proceedings of the 8th AAS/AIAA Spaceflight Mechanics Meeting: Advances in the Astronautical Sciences,* Vol. 99, Part II, pp. 1533–1544.

Williams, T., and Tanygin, S., 1996, "Dynamics of a Near-Symmetrical Spacecraft Driven by a Constant Thrust," *Proceedings of the 6th AAS/AIAA Spaceflight Mechanics Meeting: Advances in the Astronautical Sciences,* Vol. 93, Part II, pp. 925–944.

A Circular Inhomogeneity Problem Revisited

K. W. Lee[1], S. T. Choi,[1] and Y. Y. Earmme[2]

1 Introduction

A circular inclusion whose elastic moduli are different from the infinite matrix has been a subject of many researchers. Most recent works incluse those by Honein and Herrmann (1990) and Chao (1994). A circular inclusion in an infinite matrix under a point force was analyzed by Dundurs and Hetenyi (1961) and Hetenyi and Dundurs (1962) and the similar one with an edge dislocation was dealt with by Dundurs and Mura (1964).

A simple approach to obtain the stresses and displacements of the two semi-infinite materials bonded together along the straight boundary (i.e., along the x-axis) under the point force, an edge dislocation, and a point moment was proposed by Suo (1989). The method has an advantage over those of the aforementioned works by taking the complex potential of the bimaterial problem to be the sum of the complex potential of the corresponding homogeneous material with the same singularity source and the perturbed complex potential due to the existence of the other materials, to make the solution procedure simple and straightforward. Honein and Herrmann (1990) obtained the solution of an inclusion in an infinite matrix by substituting the solution of the corresponding homogeneous problem into an algebraic expression, which they referred to as "heterogenization". However it seems that the advantage of the complex potential method is not fully utilized so that the solution procedure is quite complicated compared to the procedure by Suo (1989).

It is the purpose of this study to show that the solution procedure for an inclusion in the infinite matrix, guided by the method of Suo (1989) is simple and straightforward, and the solution can be written in a compact form.

2 Solution Procedure and Result

The components of the stresses and displacements in the polar coordinates are expressed in terms of the complex potentials $\Phi(z)$, $\Psi(z)$, and $\Omega(z)$ as follows:

$$\sigma_{rr} + \sigma_{\theta\theta} = 2[\Phi(z) + \bar{\Phi}(\bar{z})],$$

$$\sigma_{rr} + i\sigma_{r\theta} = \Phi(z) + \Omega\left(\frac{1}{\bar{z}}\right) + \bar{z}\left(\bar{z} - \frac{1}{z}\right)\bar{\Psi}(\bar{z}),$$

$$2\mu \frac{\partial}{\partial\theta}(u_x + iu_y) = iz\left[\kappa\Phi(z) - \Omega\left(\frac{1}{\bar{z}}\right) - \bar{z}\left(\bar{z} - \frac{1}{z}\right)\bar{\Psi}(\bar{z})\right]. \quad (1)$$

The complex potential $\Omega(z)$ is defined by

$$\Omega(z) = \bar{\Phi}\left(\frac{1}{z}\right) - \frac{1}{z}\bar{\Phi}'\left(\frac{1}{z}\right) - \frac{1}{z^2}\bar{\Psi}\left(\frac{1}{z}\right), \quad (2)$$

whence

$$\Psi(z) = \frac{1}{z^2}\Phi(z) - \frac{1}{z}\Phi'(z) - \frac{1}{z^2}\bar{\Omega}\left(\frac{1}{z}\right). \quad (3)$$

When a singularity is in an infinite homogeneous isotropic material, the solution $\Phi_o(z)$ and $\Omega_o(z)$ are listed in the word of Suo (1989), however in the case of circular inclusion, $\Omega(z)$ is defined by Eq. (2), which is different from that of Suo (1989), so that we obtain $\Phi_o(z)$ and $\Omega_o(z)$ as follows:

$$\Phi_o(z) = -\frac{Q_o}{z - s}, \quad \Omega_o(z) = \frac{z^2\bar{Q}_o + \hat{\kappa}Q_o}{z(z\bar{s} - 1)} - \frac{\bar{Q}_o(z - s)}{(z\bar{s} - 1)^2}, \quad (4)$$

where, $z = x + iy$, $s = x_o + iy_o$ (the position of the singularity), Q_o and $\hat{\kappa}$ are defined as

(i) for a point force P $(= P_x + iP_y)$

[1] Ph.D. Student, Department of Mechanical Engineering, ME3053, Korea Advanced Institute of Science and Technology, 373-1, Yusung-Gu, Kusong-Dong, Taejon 305-701, South Korea.

[2] To whom correspondence should be addressed. Professor, Department of Mechanical Engineering, ME3013, Korea Advanced Institute of Science and Technology, 373-1, Yusung-Gu, Kusong-Dong, Taejon 305-701, South Korea. e-mail: yyearmme@cais.kaist.ac.kr. Mem. ASME.

Contributed by the Applied Mechanics Division of THE AMERICAN SOCIETY OF MECHANICAL ENGINEERS for publication in the ASME JOURNAL OF APPLIED MECHANICS. Manuscript received by the ASME Applied Mechanics Division, June 1, 1998; final revision, Oct. 4, 1998. Associate Technical Editor: M. J. Pindera.

 Copyright © 1999 by ASME

Downloaded 04 May 2010 to 171.66.16.27. Redistribution subject to ASME license or copyright; see http://www.asme.org/terms/Terms_Use.cfm

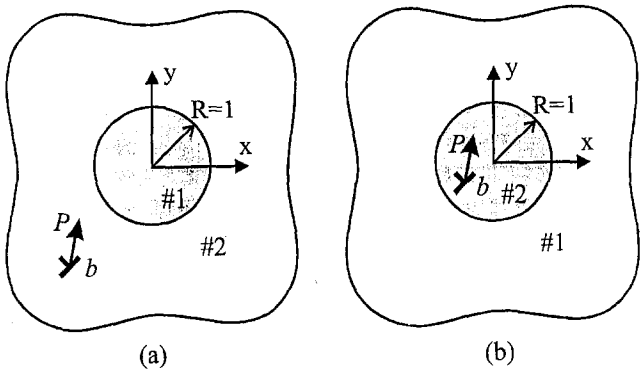

Fig. 1 A singularity interacting with a circular inclusion perfectly bonded in an infinite matrix; (a) case 1: the singularity in the infinite matrix, (b) case 2: the singularity inside the circular inclusion

$$Q_o = \frac{1}{2\pi(\kappa + 1)} [P_x + iP_y],$$

$$\hat{\kappa} = \kappa = \begin{cases} 3 - 4\nu & \text{for plane strain} \\ (3 - \nu)/(1 + \nu) & \text{for plane stress} \end{cases} \tag{5}$$

(ii) for an edge dislocation b $(= b_x + ib_y)$

$$Q_o = \frac{i\mu}{\pi(\kappa + 1)} [b_x + ib_y], \quad \hat{\kappa} = -1. \tag{6}$$

Here, ν and μ respectively are the Poisson's ratio and the shear modulus.

Let us consider the circular inclusion of unit radius embedded in an infinite matrix under a singularity such as a point force and an edge dislocation either in the inclusion or in the matrix, as shown in Fig. 1(a) and 1(b). The complex potentials $\Phi_{(i)}(z)$ and $\Omega_{(i)}(z)$ for each material (i = 1 or 2) are assumed to be

$$\Phi(z) = \begin{cases} \Phi_{(1)}(z) = \Phi_1(z) + \Phi_o(z) \\ \Phi_{(2)}(z) = \Phi_2(z) + \Phi_o(z), \end{cases} \tag{7a}$$

$$\Omega(z) = \begin{cases} \Omega_{(1)}(z) = \Omega_1(z) + \Omega_o(z) \\ \Omega_{(2)}(z) = \Omega_2(z) + \Omega_o(z). \end{cases} \tag{7b}$$

For definiteness of the problem, $\Phi_o(z)$ and $\Omega_o(z)$ are assumed to be the solution of the corresponding homogeneous material with the subscript 2, hence the inclusion is denoted by the subscript 2 when the singularity is in the inclusion, while the matrix by the subscript 2 when the singularity is in the matrix. The continuity of $\sigma_{rr} + i\sigma_{r\theta}$ and $\partial(u_x + iu_y)/\partial\theta$ across the interface is used to determine $\Phi_{(i)}(z)$ and $\Omega_{(i)}(z)$ with the argument of the analytic continuation properly employed. The procedure is basically identical to that of Suo (1989), however, the only difference from the work of Suo (1989) is that $f(z)$ and $g(z)$ (to be shown below) are introduced due to the existence of the circular boundary in the problem. The details are suppressed here and the results are as follows:

$$\Phi_{(1)}(z) = (1 + \Lambda)[\Phi_o(z) + f(z)] + \frac{g(z)}{1 - \beta},$$

$$\Omega_{(1)}(z) = (1 + \Pi)\Omega_o(z) + \frac{g(z)}{1 + \beta} \tag{8}$$

for material 1, and

$$\Phi_{(2)}(z) = \Phi_o(z) + \Pi\Omega_o(z) + f(z) + \frac{g(z)}{1 + \beta},$$

$$\Omega_{(2)}(z) = \Omega_o(z) + \Lambda[\Phi_o(z) + f(z)] + \frac{g(z)}{1 - \beta} \tag{9}$$

for material 2, where $\Lambda = [(\alpha + \beta)/(1 - \beta)]$ and $\Pi = [(\alpha - \beta)/(1 + \beta)]$. Here α and β are the Dundurs' parameters defined by

$$\alpha = \frac{\mu_1(\kappa_2 + 1) - \mu_2(\kappa_1 + 1)}{\mu_1(\kappa_2 + 1) + \mu_2(\kappa_1 + 1)},$$

$$\beta = \frac{\mu_1(\kappa_2 - 1) - \mu_2(\kappa_1 - 1)}{\mu_1(\kappa_2 + 1) + \mu_2(\kappa_1 + 1)}. \tag{10}$$

The undetermined functions $f(z) = \sum_{n=0}^{\infty} f_n/z^n$ and $g(z) = \sum_{n=0}^{\infty} g_n/z^n$ are analytic except at the origin and the constants f_n and g_n are determined so as to satisfy the boundary conditions.

(a) Case of a singularity in the matrix (Fig. 1(a))

The boundedness of the stresses in the inclusion and the circumferential gradients of the displacements at infinity yields

$$f(z) = f_o = -\frac{2\beta}{1 + \alpha - 2\beta} S_1 + i\frac{2\alpha}{1 - \alpha} S_2,$$

$$g(z) = g_o = \frac{(1 + \alpha)(3\beta - \alpha)}{1 + \alpha - 2\beta} S_1 - i\frac{(\alpha + \beta)(1 + \alpha)}{1 - \alpha} S_2, \tag{11}$$

where, S_1 and S_2 represent the real and the imaginary part of Q_o/s $(= \Phi_o(0))$, respectively, and $i = \sqrt{-1}$.

(b) Case of a singularity in the inclusion (Fig. 1(b))

The boundedness of the circumferential gradients of the displacements at infinity and the single-valuedness of the displacements in the inclusion result in

$$f(z) = f_o + \frac{f_1}{z},$$

$$f_o = \frac{\Pi(1 - \hat{\kappa}_2)}{\Pi - 1} |s|^2 S_1 - i\frac{\Pi(1 + \hat{\kappa}_2)}{\Pi + 1} |s|^2 S_2,$$

$$f_1 = Q_o \frac{(\alpha - \beta)\hat{\kappa}_2 - (\alpha + \beta)}{1 - \alpha},$$

$$g(z) = g_o + \frac{g_1}{z},$$

$$g_o = -(1 + \alpha) f_o,$$

$$g_1 = Q_o \frac{(\alpha + \beta)[(1 + \beta) - (\alpha - \beta)\hat{\kappa}_2]}{1 - \alpha}. \tag{12}$$

3 Concluding Remarks

Guided by the work of Suo (1989) for a bimaterial bonded along the x-axis, we present here the result in a compact form for the solution of a circular inclusion (or inhomogeneity) in an infinite matrix having a singularity either in the inclusion or the matrix. The present result is reduced to the solution of Dundurs and Hetenyi (1961) with $P_y = 0$ and $y_o = 0$. The present solution differs from that of Hetenyi and Dundurs (1962) with $P_x = 0$ and $y_o = 0$ in the following sense: let $\Phi^H_{(1)}(z)$ and $\Psi^H_{(1)}(z)$ denote the solutions of Hetenyi and Dundurs (1962). It is found that $\Phi^H_{(1)}(z) = \Phi_{(1)}(z) - iS_2(1 + \Lambda)(\alpha - \beta)/(1 - \alpha)$, $\Psi^H_{(1)}(z) = \Psi_{(1)}(z)$, yielding the identical result except for the rigid body rotation. In other words, there exists a discontinuity in the displacement along the interface by an

Downloaded 04 May 2010 to 171.66.16.27. Redistribution subject to ASME license or copyright; see http://www.asme.org/terms/Terms_Use.cfm

amount of the rigid body rotation in their work. This is confirmed by the finite element analysis performed (but not presented here) by us. When an edge dislocation is in the matrix, the present solution of course gives the same result as Dundurs and Mura (1964). The present solution is also in agreement with that of Honein and Herrmann (1990) although the results of the latter work are expressed in so quite a complicated way that it is hard to grasp the structure of the solution.

Acknowledgments

Financial support by KOSEF (The Korea Science and Engineering Foundation) under contract 94-0200-02-02-3 is hereby acknowledged.

References

Chao, R.-M., 1994, "Potential Functions of an Edge Dislocation Associated With a Circular Inclusion," ASME JOURNAL OF APPLIED MECHANICS, Vol. 61, pp. 218–219.

Dundurs, J., and Hetenyi, M., 1961, "The Elastic Plane With a Circular Insert, Loaded by a Radial Force," ASME JOURNAL OF APPLIED MECHANICS, Vol. 28, pp. 103–111.

Dundurs, J., and Mura, T., 1964, "Interaction Between an Edge Dislocation and a Circular Inclusion," *J. Mech. Phys. Solids,* Vol. 12, pp. 177–189.

Hetenyi, M., and Dundurs, J., 1962, "The Elastic Plane with a Circular Insert, Loaded by a Tangentially Directed Force," ASME JOURNAL OF APPLIED MECHANICS, Vol. 29, pp. 362–368.

Honein, T., and Herrmann, G., 1990, "On Bonded Inclusions With Circular or Straight Boundaries in Plane Elastostatics," ASME JOURNAL OF APPLIED MECHANICS, Vol. 57, pp. 850–856.

Suo, Z., 1989, "Singularities Interacting With Interfaces and Cracks," *Int. J. Solids Structures,* Vol. 25, No. 10, pp. 1133–1142.

Nature of Stress Singularities at the Reentrant Wedge Corner for a Branched Crack Problem

A. S. Selvarathinam[1,2,3] and J. G. Goree[2,3]

The solution of the branched crack problem for an isotropic material, employing the dislocation method as developed by Lo (1978), results in a singular integral equation in which the slope of the crack-opening displacement is the unknown. In this brief note, using the function-theoretic method, the behavior of this unknown function is investigated at the corner where the branched and main crack meet and it is shown that the order of stress singularity obtained at the reentrant corner of the branched crack is given by the Williams' (1952) characteristic equation for the isotropic wedge.

1 Introduction

The solution of branched crack (Fig. 1) problems employing conformal mapping and dislocation methods result in a singular integral equation, with either the crack-opening displacement or the slope of the crack-opening displacement as the unknown. Chatterjee (1975) solved the branched crack problem employing conformal mapping technique, and was the first to investigate the order of the stress singularity at the reentrant wedge corner (C in Fig. 1). Several authors (e.g., Lo, 1978; Karihaloo et al., 1980; Hayashi and Nemat-Nasser, 1980), who employed the dislocation technique to solve the branched crack problem, have acknowledged that the order of singularity at the reentrant corner should be given by Williams' (1952) characteristic equation but without presenting a formal proof. In this brief note the order of singularity at the corner where the branched and main crack meet is investigated using the function-theoretic method as developed by Muskhelishvili (1992), and it is shown that the order of stress singularity is given by the Williams' (1952) characteristic equation. This proof not only shows that the formulation adopted by the authors (Lo, 1978; Karihaloo et al., 1980; Hayashi and Nemat-Nasser, 1980) satisfies the boundary condition at the reentrant wedge corner but also helps in establishing an effective numerical scheme for solving the singular integral equation as discussed in Selvarathinam (1995, 1998).

It should be noted that the singularity at the branched crack corner can also be obtained employing eigenfunction analysis as discussed in Grenestedt and Hallstrom (1997) for a general case of bi-material wedge. However, the objective of the present analysis is to obtain the singularities directly from the integral formulation itself.

2 Analysis

2.1 An Overview of the Problem. The solution of the branched crack problem (Fig. 1) in terms of the slope of the crack-opening displacement results in a singular integral equation of the following form:

$$2\int_0^l \frac{\bar{\Theta}(t_o)e^{i\theta}\,dt_o}{t-t_o} + \int_0^l M(t, t_o; \Theta(t_o))dt_o + \sigma^{\infty}_{\theta\theta}(z) + i\sigma^{\infty}_{r\theta}(z) = 0, \quad (1)$$

where $\Theta(t_o)$ (an unknown complex function) is the slope of the crack-opening displacement, $M(t, t_o, \Theta(t_o))$ contains the terms which arise due to the interaction between the branched and the main cracks, and $\sigma^{\infty}_{\theta\theta}(z)$, $\sigma^{\infty}_{r\theta}(z)$ are the remote loading terms. In Eq. (1), $i = \sqrt{-1}$.

From the geometry of the crack problem (Fig. 1) it can be seen that the kink tip (A) has the well-known square root singularity. At the other end of the kink, i.e., at the origin, the upper side of the kink indicated by the letter "U" is similar to the external corner of a wedge, and hence according to Williams (1952) does not give rise to any stress singularity. The lower side of the kink, "C," resembles an internal corner of a wedge, and hence (following Williams, 1952) one would expect it to give rise to singular stresses, with the order of the singularity given by Williams' (1952), characteristic equation. A formal proof verifying this is developed in the following sections.

2.2 Extension of a Theorem for a Singular Integral to Include a Bounded Integral. To understand the behavior of a singular integral near an end point an asymptotic analysis has to be performed on the integrals near the end points, as discussed in Muskhelishvili (1992, Chapter 4). This results in a term which is unbounded at the end point and another term which remains bounded. Bounded integrals, on the other hand, are bounded in the entire range of integration. Moreover, near the integration end points, the bounded integrals can be analyzed in the same manner as the singular integrals. This analysis, which is the key to obtain the asymptotic solution, is shown below. Following Muskhelishvili (1992), consider the behavior of a Cauchy integral of the form

[1] To whom correspondence should be addressed. Presently at MAES, University of Tennessee, Knoxville, TN 37996-2030.

[2] Department of Mechanical Engineering, Clemson University, Clemson, SC 29634-0921.

[3] Mem. ASME.

Contributed by the Applied Mechanics Division of THE AMERICAN SOCIETY OF MECHANICAL ENGINEERS for publication in the ASME JOURNAL OF APPLIED MECHANICS. Manuscript received by the ASME Applied Mechanics Division, June 28, 1996; final revision, Nov. 7, 1998. Associate Technical Editor: J. L. Bassani.

Downloaded 04 May 2010 to 171.66.16.27. Redistribution subject to ASME license or copyright; see http://www.asme.org/terms/Terms_Use.cfm

amount of the rigid body rotation in their work. This is confirmed by the finite element analysis performed (but not presented here) by us. When an edge dislocation is in the matrix, the present solution of course gives the same result as Dundurs and Mura (1964). The present solution is also in agreement with that of Honein and Herrmann (1990) although the results of the latter work are expressed in so quite a complicated way that it is hard to grasp the structure of the solution.

Acknowledgments

Financial support by KOSEF (The Korea Science and Engineering Foundation) under contract 94-0200-02-02-3 is hereby acknowledged.

References

Chao, R.-M., 1994, "Potential Functions of an Edge Dislocation Associated With a Circular Inclusion," ASME JOURNAL OF APPLIED MECHANICS, Vol. 61, pp. 218–219.

Dundurs, J., and Hetenyi, M., 1961, "The Elastic Plane With a Circular Insert, Loaded by a Radial Force," ASME JOURNAL OF APPLIED MECHANICS, Vol. 28, pp. 103–111.

Dundurs, J., and Mura, T., 1964, "Interaction Between an Edge Dislocation and a Circular Inclusion," *J. Mech. Phys. Solids,* Vol. 12, pp. 177–189.

Hetenyi, M., and Dundurs, J., 1962, "The Elastic Plane with a Circular Insert, Loaded by a Tangentially Directed Force," ASME JOURNAL OF APPLIED MECHANICS, Vol. 29, pp. 362–368.

Honein, T., and Herrmann, G., 1990, "On Bonded Inclusions With Circular or Straight Boundaries in Plane Elastostatics," ASME JOURNAL OF APPLIED MECHANICS, Vol. 57, pp. 850–856.

Suo, Z., 1989, "Singularities Interacting With Interfaces and Cracks," *Int. J. Solids Structures,* Vol. 25, No. 10, pp. 1133–1142.

Nature of Stress Singularities at the Reentrant Wedge Corner for a Branched Crack Problem

A. S. Selvarathinam[1,2,3] and J. G. Goree[2,3]

The solution of the branched crack problem for an isotropic material, employing the dislocation method as developed by Lo (1978), results in a singular integral equation in which the slope of the crack-opening displacement is the unknown. In this brief note, using the function-theoretic method, the behavior of this unknown function is investigated at the corner where the branched and main crack meet and it is shown that the order of stress singularity obtained at the reentrant corner of the branched crack is given by the Williams' (1952) characteristic equation for the isotropic wedge.

1 Introduction

The solution of branched crack (Fig. 1) problems employing conformal mapping and dislocation methods result in a singular integral equation, with either the crack-opening displacement or the slope of the crack-opening displacement as the unknown. Chatterjee (1975) solved the branched crack problem employing conformal mapping technique, and was the first to investigate the order of the stress singularity at the reentrant wedge corner (C in Fig. 1). Several authors (e.g., Lo, 1978; Karihaloo et al., 1980; Hayashi and Nemat-Nasser, 1980), who employed the dislocation technique to solve the branched crack problem, have acknowledged that the order of singularity at the reentrant corner should be given by Williams' (1952) characteristic equation but without presenting a formal proof. In this brief note the order of singularity at the corner where the branched and main crack meet is investigated using the function-theoretic method as developed by Muskhelishvili (1992), and it is shown that the order of stress singularity is given by the Williams' (1952) characteristic equation. This proof not only shows that the formulation adopted by the authors (Lo, 1978; Karihaloo et al., 1980; Hayashi and Nemat-Nasser, 1980) satisfies the boundary condition at the reentrant wedge corner but also helps in establishing an effective numerical scheme for solving the singular integral equation as discussed in Selvarathinam (1995, 1998).

It should be noted that the singularity at the branched crack corner can also be obtained employing eigenfunction analysis as discussed in Grenestedt and Hallstrom (1997) for a general case of bi-material wedge. However, the objective of the present analysis is to obtain the singularities directly from the integral formulation itself.

2 Analysis

2.1 An Overview of the Problem. The solution of the branched crack problem (Fig. 1) in terms of the slope of the crack-opening displacement results in a singular integral equation of the following form:

$$2\int_0^l \frac{\bar{\Theta}(t_o)e^{i\theta}\,dt_o}{t-t_o} + \int_0^l M(t, t_o; \Theta(t_o))dt_o + \sigma^{\infty}_{\theta\theta}(z) + i\sigma^{\infty}_{r\theta}(z) = 0, \quad (1)$$

where $\Theta(t_o)$ (an unknown complex function) is the slope of the crack-opening displacement, $M(t, t_o, \Theta(t_o))$ contains the terms which arise due to the interaction between the branched and the main cracks, and $\sigma^{\infty}_{\theta\theta}(z)$, $\sigma^{\infty}_{r\theta}(z)$ are the remote loading terms. In Eq. (1), $i = \sqrt{-1}$.

From the geometry of the crack problem (Fig. 1) it can be seen that the kink tip (A) has the well-known square root singularity. At the other end of the kink, i.e., at the origin, the upper side of the kink indicated by the letter "U" is similar to the external corner of a wedge, and hence according to Williams (1952) does not give rise to any stress singularity. The lower side of the kink, "C," resembles an internal corner of a wedge, and hence (following Williams, 1952) one would expect it to give rise to singular stresses, with the order of the singularity given by Williams' (1952), characteristic equation. A formal proof verifying this is developed in the following sections.

2.2 Extension of a Theorem for a Singular Integral to Include a Bounded Integral. To understand the behavior of a singular integral near an end point an asymptotic analysis has to be performed on the integrals near the end points, as discussed in Muskhelishvili (1992, Chapter 4). This results in a term which is unbounded at the end point and another term which remains bounded. Bounded integrals, on the other hand, are bounded in the entire range of integration. Moreover, near the integration end points, the bounded integrals can be analyzed in the same manner as the singular integrals. This analysis, which is the key to obtain the asymptotic solution, is shown below. Following Muskhelishvili (1992), consider the behavior of a Cauchy integral of the form

[1] To whom correspondence should be addressed. Presently at MAES, University of Tennessee, Knoxville, TN 37996-2030.

[2] Department of Mechanical Engineering, Clemson University, Clemson, SC 29634-0921.

[3] Mem. ASME.

Contributed by the Applied Mechanics Division of THE AMERICAN SOCIETY OF MECHANICAL ENGINEERS for publication in the ASME JOURNAL OF APPLIED MECHANICS. Manuscript received by the ASME Applied Mechanics Division, June 28, 1996; final revision, Nov. 7, 1998. Associate Technical Editor: J. L. Bassani.

 Copyright © 1999 by ASME

Downloaded 04 May 2010 to 171.66.16.27. Redistribution subject to ASME license or copyright; see http://www.asme.org/terms/Terms_Use.cfm

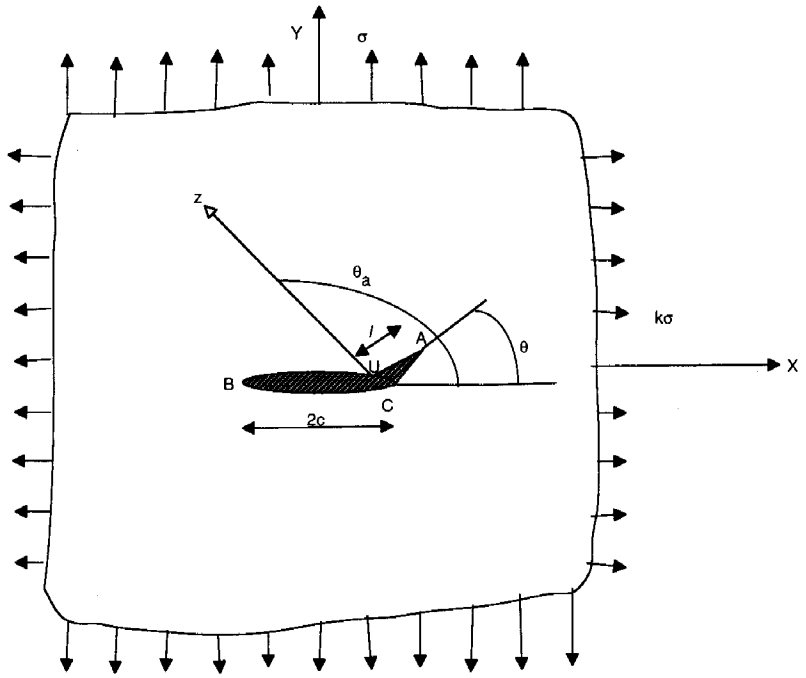

Fig. 1 Geometry of the branched crack problem

$$F(z) = \int_0^l \frac{\alpha(t_o)}{(t_o - z)}\, dt_o \tag{2}$$

near the limits of integration (0 or l). Let $\alpha(t_o)$ be bounded every where in the region of integration 0–l. In other words $\alpha(t_o)$ satisfies the Hölder condition in the range 0–l except at the end points 0 and l. Near the end points $\alpha(t_o)$ can be assumed to be of the form

$$\alpha(t_o) = \frac{\lambda(t_o)}{t_o^{\alpha}(l - t_o)^{\beta}} \tag{3}$$

where $\lambda(t_o)$ is bounded in the entire range of integration. α and β are always between 0 and 1 in order to have bounded integrals. If the above conditions are satisfied, then near the end of the integration limit (for example, near $t_o = 0$) $F(z)$ can be written as follows (Muskhelishvili 1992, see Eq. (29.5), p. 74):

$$\lim_{z\to 0} F(z) = \lim_{z\to 0} \int_0^l \frac{\lambda(t_o)}{t_o^{\alpha}(l - t_o)^{\beta}} \frac{dt_o}{t_o - z} = \frac{\pi\lambda(0)e^{i\pi\alpha}}{\sin(\pi\alpha)} \lim_{z\to 0} \frac{1}{z^{\alpha}} + bf, \tag{4}$$

where bf is a bounded function. A similar relation can be written for the behavior of the function at the other end l. The restriction that $0 < \alpha, \beta < 1$ imposed by Muskhelishvili (1992) is strictly for singular integrals. For bounded integrals this restriction can be relaxed. If the integral is bounded at the end "0" then the restriction that $\alpha > 0$ can be removed for the lower end (i.e., $\alpha < 1$ only) and hence α can have negative values. Therefore, in the limit, the integral (given by (4)) has a part that vanishes and a bounded part. Hence any asymptotic value for a Cauchy integral, given in the range $0 < \alpha < 1$, can be extended for the range $-\infty \le \alpha < 1$. However, the above formula is valid only when α is not zero, in which case a logarithmic singularity occurs at the end point.

2.3 Proof for Verification of Order of Stress Singularity at C (Fig. 1). In order to verify the order of stress singularity at the wedge corner it is sufficient to examine the sum of the hoop and radial stresses. From Muskhelishvili (1992), the sum of the hoop and radial stresses can be written as

$$\sigma_{rr}(z) + \sigma_{\theta\theta}(z) = 4\Re[\Phi(z)], \tag{5}$$

where $\Phi(z)$ is the stress function obtained by solving the branched crack problem shown in Fig. 1. The derivation of $\Phi(z)$ is given in detailed form in Lo (1978) and Selvarathinam (1995). Since all the stresses vanish at the external corner of the wedge (U, Fig. 1),

$$\Re\Phi(z) = \Re[I_1(z) + I_2(z) + I_3(z) + I_4(z) + I_5(z) + I_6(z) + I_7(z) + C_1] = 0 \tag{6}$$

where

$$I_1(z) = \frac{1}{2}\int_0^l \frac{\Theta(t_o)}{(z - z_o)}\, dt_o,$$

$$I_2(z) = -\frac{1}{2}\int_0^l \frac{\Theta(t_o)}{(z - \bar{z}_o)}\, dt_o,$$

$$I_3(z) = \frac{1}{2}\int_0^l \frac{\Theta(t_o)X(z_o)}{X(z)(z - z_o)}\, dt_o,$$

$$I_4(z) = \frac{1}{2}\int_0^l \frac{\Theta(t_o)\overline{X(z_o)}}{X(z)(z - \bar{z}_o)}\, dt_o,$$

$$I_5(z) = -\frac{1}{2}\int_0^l \frac{\overline{\Theta(t_o)}(z_o - \bar{z}_o)}{(z - \bar{z}_o)^2}\, dt_o,$$

$$I_6(z) = -\frac{1}{2}\int_0^l \frac{\overline{\Theta(t_o)}(z_o - \bar{z}_o)\overline{X(z_o)}}{X(z)(z - \bar{z}_o)}\, dt_o,$$

$$I_7(z) = \frac{1}{2}\int_0^l \frac{\overline{\Theta(t_o)}(z_o - \bar{z}_o)(\bar{z}_o + c)}{X(z)X(\bar{z}_o)(z - \bar{z}_o)^2}\, dt_o,$$

$$C_1 = -\frac{1}{4} + \frac{(z + c)}{2X(z)}$$

where, $X(z)$ is given as

Downloaded 04 May 2010 to 171.66.16.27. Redistribution subject to ASME license or copyright; see http://www.asme.org/terms/Terms_Use.cfm

$$X(z) = \sqrt{z(z + 2c)}\ ,\ z = te^{i\theta_a},\ z_o = t_o e^{i\theta}.$$

The above integrals are the same as those obtained by Lo (1978) for $\Phi(z)$, and were also derived in Selvarathinam (1995).

Employing the limiting value of each integral near the end point, i.e., $z = 0$, the asymptotic values of each can be written down. Integrals with $X(z)$ in their denominator require special attention. It is these integrals that have to be evaluated using the behavior for bounded integrals as discussed in Section 2.2. Integrals that do not have $X(z)$ can be evaluated by employing Eq. (4) directly.

It should be noted that $X(z)$ is a sectionally holomorphic function which is discontinuous across the line BC or BU. If "z" tends to "U" from the upper side of the main crack then,

$$X(z) = e^{i(\theta_a/2)}\sqrt{2tc}. \tag{7}$$

where "c" is half the length of the main crack. On the other hand if "z" approaches "C" from the lower side of the main crack then,

$$X(z) = -e^{i(\theta_a/2)}\sqrt{2tc}\ . \tag{8}$$

Details of the derivation of the asymptotic limits of integrals $I_i(z)$, $i = 1, \ldots, 7$, are given in Selvarathinam (1995). Substituting the resulting asymptotic values in Eq. (6) and after some lengthy manipulations the following equation is obtained.

$$\lim_{t\to 0} \Re\left[\left\{\frac{-\beta(0)e^{-i[\alpha(\theta_a-\pi)-(\pi/2))]}\sin[\theta(\alpha-1)+\pi\alpha]}{l^\beta \sin(2\pi\alpha)} - \frac{\overline{\beta(0)}e^{-i[\alpha(\theta_a-\pi)-(\pi/2))]}e^{-i[\theta(\alpha-2)]}\sin(\theta)(1-\alpha)e^{-i\pi\alpha}}{l^\beta \sin(2\pi\alpha)} + (Bf)t^\alpha\right\}\frac{1}{t^\alpha} + (A_1 + iA_2)\frac{1}{\sqrt{t}}\right] = 0 \tag{9}$$

where, Bf, A_1, and A_2 are bounded functions.

Setting the coefficient of $1/t^\alpha$ and it's complex conjugate to zero a pair of equation is obtained which can be written in matrix form as follows:

$$\begin{bmatrix} \sin[\theta(\alpha-1)+\pi\alpha] & e^{-i[\theta(\alpha-2)]}\sin(\theta)(1-\alpha)e^{-i\pi\alpha} \\ e^{-i[\theta(\alpha-2)]}\sin(\theta)(1-\alpha)e^{i\pi\alpha} & \sin[\theta(\alpha-1)+\pi\alpha] \end{bmatrix} \begin{bmatrix} \beta(0) \\ \overline{\beta(0)} \end{bmatrix} = \begin{bmatrix} 0 \\ 0 \end{bmatrix}. \tag{10}$$

If $\beta(0)$ and $\overline{\beta(0)}$ do not vanish, then the determinant of the above equation must vanish (i.e., at least one nontrivial solution exists). Therefore,

$$\sin[\theta(\alpha-1)+\pi\alpha] + (1-\alpha)\sin(\theta) = 0 \tag{11}$$

$$\sin[\theta(\alpha-1)+\pi\alpha] - (1-\alpha)\sin(\theta) = 0, \tag{12}$$

which are the characteristic equations obtained by Williams' (1952) for an isotropic wedge. If Eqs. (11) or (12), or both, are satisfied by choosing "α" suitably, the coefficient of $1/t^\alpha$ term vanishes. Also by setting the coefficient of $1/t^{1/2}$ to zero, $A_1 = 0$ is obtained.

If "z" approaches the internal corner of the wedge "C" in Fig. 1 it can be shown that the stresses are $1/t^\alpha$ singular.

3 Conclusions

It has been shown, through the function-theoretic method, that the stresses at the reentrant wedge corner where the main crack and the branched crack meet are singular and that the order of the stress singularity is given by the Williams' characteristic equation.

Acknowledgment

The support of AFOSR through Grant F49620-93-1-0256 (Dr. W. F. Jones, Monitor) are gratefully acknowledged by the authors.

References

Chatterjee, S.N., 1975, "The Stress Fields in the Neighborhood of a Branched Crack in an Infinite Elastic Sheet," *International Journal of Solids and Structures*, Vol. 11, pp. 521–538.

Grenestedt, J.L., and Hallstrom, S., 1997, "Crack Initiation from Homogeneous and Bimaterial Corners," ASME JOURNAL OF APPLIED MECHANICS, Vol. 64, pp. 811–818.

Hayashi, K., and Nemat-Nasser, S., 1981, "Energy Release Rate and Crack Kinking," *International Journal of Solids and Structures*, Vol. 17, pp. 107–114.

Karihaloo, B.L., Keer, L.M., and Nemat-Nasser, S., 1980, "Crack Kinking Under Nonsymmetric Loading," *Engineering Fracture Mechanics*, Vol. 13, pp. 879–888.

Lo, K.K., 1978, "Analysis of Branched Cracks," ASME JOURNAL OF APPLIED MECHANICS, Vol. 45, pp. 797–803.

Muskhelishvili, N., 1992, *Singular Integral Equations*, Dover, New York.

Selvarathinam, A.S., 1995, "A Generalized Linear Elastic Fracture Model for Advanced Materials," Ph.D. dissertation, Clemson University, Clemson, SC.

Selvarathinam, A.S., and Goree, J.G., 1998, "T-stress Based Fracture Model for Cracks in Isotropic Material," *Engineering Fracture Mechanics*, In press.

Timoshenko, S.P., and Goodier, J.N., 1982, *Theory of Elasticity*, McGraw-Hill, New York.

Williams, M.L., 1952, "Stress Singularities Resulting From Various Boundary Conditions in Angular Corners of Plates in Extension," ASME JOURNAL OF APPLIED MECHANICS, Vol. 19, pp. 526–528.

Synthesis of Nonlinear Constitutive Functions, Applications to the Electromagnetic Control of Snapping

S. S. Antman[1]

The purpose of this note is to illustrate the principle that by using electromagnetic feedbacks for solids sensitive to such effects, one can readily synthesize artificial materials with useful nonlinear responses unlikely to be found in natural materials. Here we synthesize the material of a straight magnetostrictive column that undergoes specified kinds of snap bucklings at specified compressive loads. Such snap bucklings can be used, for example, for switches or for the rapid deployment of obstacles in a fluid flow with the aim of controlling it.

To fix ideas, consider the planar equilibrium states of a uniform inextensible, unshearable elastic column of scaled length 1 with one end clamped and the other end unconstrained and subjected to a compressive dead force of magnitude λ acting parallel to the straight line describing the natural state of the clamped column. (See Fig. 1.) A typical configuration of the column is modelled by a plane curve with arc-length parameter s. Let $\theta(s)$ be the angle between the tangent to this curve at s and the natural state. Let $M(\mu)$ be the bending couple needed to produce the curvature μ at any point of this column. We assume that $M(0) = 0$ and that M vanishes only at 0. Then the

[1] Department of Mathematics, Institute for Physical Science and Technology, and Institute for Systems Research, University of Maryland, College Park, MD 20742-4015.

Contributed by the Applied Mechanics Division of THE AMERICAN SOCIETY OF MECHANICAL ENGINEERS for publication in the ASME JOURNAL OF APPLIED MECHANICS. Manuscript received by the ASME Applied Mechanics Division, Jan. 22, 1998; final revision, Nov. 7, 1998. Associate Technical Editor: J. T. Jenkins.

Downloaded 04 May 2010 to 171.66.16.27. Redistribution subject to ASME license or copyright; see http://www.asme.org/terms/Terms_Use.cfm

$$X(z) = \sqrt{z(z + 2c)}\ , z = te^{i\theta_a},\ z_o = t_o e^{i\theta}.$$

The above integrals are the same as those obtained by Lo (1978) for $\Phi(z)$, and were also derived in Selvarathinam (1995).

Employing the limiting value of each integral near the end point, i.e., $z = 0$, the asymptotic values of each can be written down. Integrals with $X(z)$ in their denominator require special attention. It is these integrals that have to be evaluated using the behavior for bounded integrals as discussed in Section 2.2. Integrals that do not have $X(z)$ can be evaluated by employing Eq. (4) directly.

It should be noted that $X(z)$ is a sectionally holomorphic function which is discontinuous across the line BC or BU. If "z" tends to "U" from the upper side of the main crack then,

$$X(z) = e^{i(\theta_a/2)}\sqrt{2tc}. \tag{7}$$

where "c" is half the length of the main crack. On the other hand if "z" approaches "C" from the lower side of the main crack then,

$$X(z) = -e^{i(\theta_a/2)}\sqrt{2tc}\ . \tag{8}$$

Details of the derivation of the asymptotic limits of integrals $I_i(z)$, $i = 1, \ldots, 7$, are given in Selvarathinam (1995). Substituting the resulting asymptotic values in Eq. (6) and after some lengthy manipulations the following equation is obtained.

$$\lim_{t\to 0} \Re\left[\left\{\frac{-\beta(0)e^{-i[\alpha(\theta_a-\pi)-(\pi/2))]}\sin[\theta(\alpha-1)+\pi\alpha]}{l^\beta \sin(2\pi\alpha)} - \frac{\overline{\beta(0)}e^{-i[\alpha(\theta_a-\pi)-(\pi/2))]}e^{-i[\theta(\alpha-2)]}\sin(\theta)(1-\alpha)e^{-i\pi\alpha}}{l^\beta \sin(2\pi\alpha)} + (Bf)t^\alpha\right\}\frac{1}{t^\alpha} + (A_1 + iA_2)\frac{1}{\sqrt{t}}\right] = 0 \tag{9}$$

where, Bf, A_1, and A_2 are bounded functions.

Setting the coefficient of $1/t^\alpha$ and it's complex conjugate to zero a pair of equation is obtained which can be written in matrix form as follows:

$$\begin{bmatrix} \sin[\theta(\alpha-1)+\pi\alpha] & e^{-i[\theta(\alpha-2)]}\sin(\theta)(1-\alpha)e^{-i\pi\alpha} \\ e^{-i[\theta(\alpha-2)]}\sin(\theta)(1-\alpha)e^{i\pi\alpha} & \sin[\theta(\alpha-1)+\pi\alpha] \end{bmatrix} \begin{bmatrix} \beta(0) \\ \overline{\beta(0)} \end{bmatrix} = \begin{bmatrix} 0 \\ 0 \end{bmatrix}. \tag{10}$$

If $\beta(0)$ and $\overline{\beta(0)}$ do not vanish, then the determinant of the above equation must vanish (i.e., at least one nontrivial solution exists). Therefore,

$$\sin[\theta(\alpha-1)+\pi\alpha] + (1-\alpha)\sin(\theta) = 0 \tag{11}$$

$$\sin[\theta(\alpha-1)+\pi\alpha] - (1-\alpha)\sin(\theta) = 0, \tag{12}$$

which are the characteristic equations obtained by Williams' (1952) for an isotropic wedge. If Eqs. (11) or (12), or both, are satisfied by choosing "α" suitably, the coefficient of $1/t^\alpha$ term vanishes. Also by setting the coefficient of $1/t^{1/2}$ to zero, $A_1 = 0$ is obtained.

If "z" approaches the internal corner of the wedge "C" in Fig. 1 it can be shown that the stresses are $1/t^\alpha$ singular.

3 Conclusions

It has been shown, through the function-theoretic method, that the stresses at the reentrant wedge corner where the main crack and the branched crack meet are singular and that the order of the stress singularity is given by the Williams' characteristic equation.

Acknowledgment

The support of AFOSR through Grant F49620-93-1-0256 (Dr. W. F. Jones, Monitor) are gratefully acknowledged by the authors.

References

Chatterjee, S.N., 1975, "The Stress Fields in the Neighborhood of a Branched Crack in an Infinite Elastic Sheet," *International Journal of Solids and Structures*, Vol. 11, pp. 521–538.

Grenestedt, J.L., and Hallstrom, S., 1997, "Crack Initiation from Homogeneous and Bimaterial Corners," ASME JOURNAL OF APPLIED MECHANICS, Vol. 64, pp. 811–818.

Hayashi, K., and Nemat-Nasser, S., 1981, "Energy Release Rate and Crack Kinking," *International Journal of Solids and Structures*, Vol. 17, pp. 107–114.

Karihaloo, B.L., Keer, L.M., and Nemat-Nasser, S., 1980, "Crack Kinking Under Nonsymmetric Loading," *Engineering Fracture Mechanics*, Vol. 13, pp. 879–888.

Lo, K.K., 1978, "Analysis of Branched Cracks," ASME JOURNAL OF APPLIED MECHANICS, Vol. 45, pp. 797–803.

Muskhelishvili, N., 1992, *Singular Integral Equations*, Dover, New York.

Selvarathinam, A.S., 1995, "A Generalized Linear Elastic Fracture Model for Advanced Materials," Ph.D. dissertation, Clemson University, Clemson, SC.

Selvarathinam, A.S., and Goree, J.G., 1998, "T-stress Based Fracture Model for Cracks in Isotropic Material," *Engineering Fracture Mechanics*, In press.

Timoshenko, S.P., and Goodier, J.N., 1982, *Theory of Elasticity*, McGraw-Hill, New York.

Williams, M.L., 1952, "Stress Singularities Resulting From Various Boundary Conditions in Angular Corners of Plates in Extension," ASME JOURNAL OF APPLIED MECHANICS, Vol. 19, pp. 526–528.

Synthesis of Nonlinear Constitutive Functions, Applications to the Electromagnetic Control of Snapping

S. S. Antman[1]

The purpose of this note is to illustrate the principle that by using electromagnetic feedbacks for solids sensitive to such effects, one can readily synthesize artificial materials with useful nonlinear responses unlikely to be found in natural materials. Here we synthesize the material of a straight magnetostrictive column that undergoes specified kinds of snap bucklings at specified compressive loads. Such snap bucklings can be used, for example, for switches or for the rapid deployment of obstacles in a fluid flow with the aim of controlling it.

To fix ideas, consider the planar equilibrium states of a uniform inextensible, unshearable elastic column of scaled length 1 with one end clamped and the other end unconstrained and subjected to a compressive dead force of magnitude λ acting parallel to the straight line describing the natural state of the clamped column. (See Fig. 1.) A typical configuration of the column is modelled by a plane curve with arc-length parameter s. Let $\theta(s)$ be the angle between the tangent to this curve at s and the natural state. Let $M(\mu)$ be the bending couple needed to produce the curvature μ at any point of this column. We assume that $M(0) = 0$ and that M vanishes only at 0. Then the

[1] Department of Mathematics, Institute for Physical Science and Technology, and Institute for Systems Research, University of Maryland, College Park, MD 20742-4015.

Contributed by the Applied Mechanics Division of THE AMERICAN SOCIETY OF MECHANICAL ENGINEERS for publication in the ASME JOURNAL OF APPLIED MECHANICS. Manuscript received by the ASME Applied Mechanics Division, Jan. 22, 1998; final revision, Nov. 7, 1998. Associate Technical Editor: J. T. Jenkins.

 Copyright © 1999 by ASME

Downloaded 04 May 2010 to 171.66.16.27. Redistribution subject to ASME license or copyright; see http://www.asme.org/terms/Terms_Use.cfm

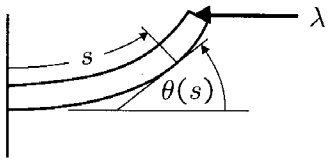

Fig. 1 A buckled state of the column

equilibrium of this column is governed by the boundary value problem

$$M(\theta'(s))' + \lambda \sin \theta(s) = 0, \quad (1)$$

$$\theta(0) = 0, \quad M(\theta'(1)) = 0, \quad (2)$$

where the prime denotes differentiation with respect to s. Note that the second condition of (2) is equivalent to $\theta'(1) = 0$. (If the Bernoulli-Euler law $M(\mu) = EI\mu$ holds, where EI is the constant bending stiffness of the column, then this boundary value problem can be solved in closed form in terms of elliptic functions, as in Love (1927).)

The boundary value problem (1), (2) has nontrivial solutions, which correspond to buckled states. These solutions are most easily visualized in a bifurcation diagram, which is a plot of curves of λ versus some convenient measure of the amplitude of the solutions θ. The lowest branch of such a bifurcation diagram is shown in Fig. 2. It has wiggles, which would not be present for a Bernoulli-Euler column. The wiggles are the source of snapping: According to the standard doctrine, if the load λ is slowly raised from zero to a high value λ_D, then the rod buckles at the bifurcation point A with the amplitude slowly increasing until λ reaches (the vicinity of) λ_B, at which the configuration suddenly jumps from that corresponding to B (or its reflection) to that corresponding to C (or its reflection). (This dynamical process takes place rapidly, with oscillations about C rapidly damping out). A further increase in λ corresponds to a movement along the branch CD. If λ is then slowly lowered from λ_D to zero, then a configuration starting at D snaps from E to F.

As already noted, it can be advantageous to design structures with specified snappings. We therefore confront the inverse problem of finding a constitutive function M such that the first bifurcating branch, like Fig. 2, is specified. Antman and Adler (1987) reduced this problem to the solution of a linear Volterra integral equation. The solution of this equation produces a graph for M. There is, however, no assurance that any natural material has such a graph. Our objective here is show how to synthesize such a material by using feedbacks to control the response of

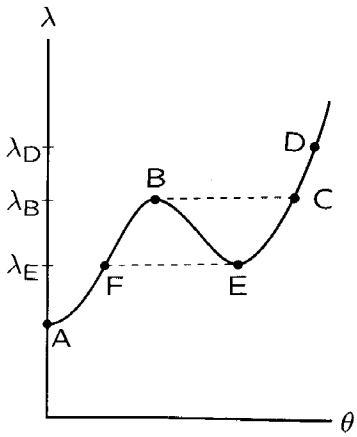

Fig. 2 The lowest branch of a bifurcation diagram for the buckled column

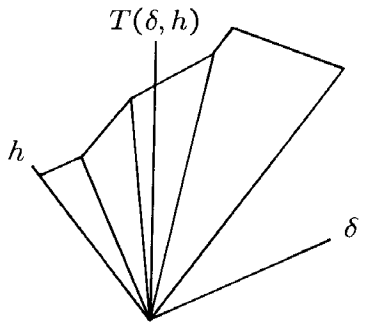

Fig. 3 A piecewise linear approximation of the graph of (Piola-Kirchhoff) tension $T(\delta, \eta)$ as a function of elongation δ and magnetic field h for a magnetostrictive material like Metglas. This graph is obtained by assigning values to the parameters of (3). This piecewise linear approximation is introduced only for the sake of visualization; in the experimental data for the tension test the edges appearing here are rounded off.

a column made of a natural material sensitive to electromagnetic effects.

We illustrate our methods with a magnetostrictive material such as Metglas for which tension tests show that the tensile Piola-Kirchhoff (engineering) stress $T(\delta, h)$ due to elongation δ and magnetic field h has a form like that shown in Fig. 3. The discussion given in the next paragraph of the properties of Metglas and how Fig. 3 models them is not central to aims of this note.

The properties of Metglas are described, e.g., by Clark et al. (1989), Hathaway et al. (1984), Savage et al. (1982), and Spano et al. (1982). (Metglas is a registered trademark of the Allied Chemical Corporation.) Figure 3 can be inferred from their data. At the end of the paper we discuss adjustments needed to handle the magnetostrictive material Terfenol. The function T is even in h. There are critical values $h_c < h_s$ of h such that as h increases in the interval $[h_c, h_s]$, the effects of magnetization diminish to zero, so that $T(\delta, h_s) = T(\delta, 0)$. When h exceeds the saturation field h_s, $T(\delta, h)$ remains at its saturation value $T(\delta, 0)$. For our purpose of using the magnetic field to control material properties, we may accordingly limit our attention to h's in the interval $[0, h_c]$. The graph in Fig. 3 is obtained by fixing values for the parameters $\alpha > \beta > \gamma > 0$ and $E > e > 0$ in the piecewise linear function

$$T(\delta, h) = \begin{cases} E\left(\delta - \dfrac{h}{\alpha}\right) & \text{for } \delta \le \dfrac{h}{\beta}, \\ Eh\left(\dfrac{1}{\beta} - \dfrac{1}{\alpha}\right) + e\left(\delta - \dfrac{h}{\beta}\right) & \text{for } \dfrac{h}{\beta} \le \delta \le \dfrac{h}{\gamma}, \\ Eh\left(\dfrac{1}{\beta} - \dfrac{1}{\alpha}\right) + eh\left(\dfrac{1}{\gamma} - \dfrac{1}{\beta}\right) + E\left(\delta - \dfrac{h}{\gamma}\right) & \text{for } \dfrac{h}{\gamma} \le \delta. \end{cases} \quad (3)$$

Here E is the maximal tangent modulus and e is the minimal tangent modulus. For Metglas, e is of the order of $E/10$. This marked reduction in modulus is the virtue of Metglas. The modulus E is approximately the elastic modulus for iron. h_c is of the order of 1 Oe. All the activity shown in Fig. 3 takes place for T well below the plastic yield stress. (There do not seem to be any experimental results on the behavior of Metglas under compression. Since Metglas is typically fabricated in thin strips, such experiments would be quite tricky. Theoretical considerations, however, indicate that the magnetic field does not

Downloaded 04 May 2010 to 171.66.16.27. Redistribution subject to ASME license or copyright; see http://www.asme.org/terms/Terms_Use.cfm

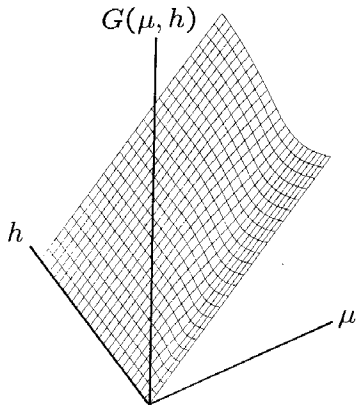

Fig. 4 Graph of the function G for the bending couple when T has the form of Fig. 3

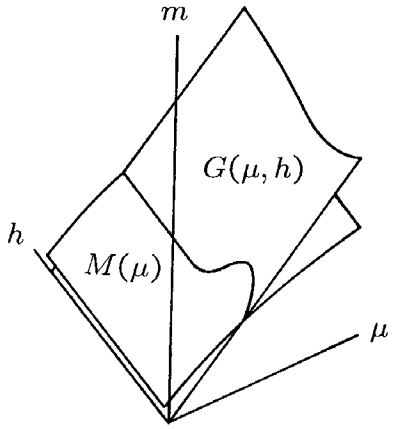

Fig. 5 Intersections of the surfaces $m = G(\mu, s)$ and $m = M(\mu)$ in (μ, h, m)-space. The M shown here is a concave function of μ.

alter the tangent modulus when the material is in compression. The model (3) and Fig. 3 reflect this fact. Below we discuss the different response of Terfenol.)

If we model the column (in a traditional way) as a three-dimensional rod with an inextensional line of centroids for which planar sections are constrained to remain planar, undeformed, and normal to the deformed line of centroids, then in a planar deformation, the stretch of a fiber at distance x from the line of centroids is $1 - x\theta'(s)$ and we can generate the constitutive function G for the bending couple corresponding to T by the classical formula

$$G(\mu, h) = -\int_{\mathcal{A}} xT(-x\mu, h)dxdy \tag{4}$$

where $\mathcal{A}$ denotes the cross section. It is not difficult to show that G is odd in μ when $\mathcal{A}$ is symmetric about the line $x = 0$. In this case, G has the form shown in Fig. 4 when T has the form of Fig. 3. In particular, if the cross section $\mathcal{A}$ is the rectangle for which $-\epsilon \le x \le \epsilon$, $0 \le y \le b$, then a lengthy but straightforward computation (reminiscent of that used to produce the engineering theory of elastoplastic beams; cf. Crandall and Dahl (1959)) shows that (3), (4) yield

$$b^{-1}G(\mu, h) = \begin{cases} \dfrac{2}{3}E\epsilon^3\mu & \text{for } h \ge \epsilon\beta\mu, \\ \dfrac{1}{3}(E+e)\epsilon^3\mu + \dfrac{1}{2}(E-e)\epsilon^2\dfrac{h}{\beta} - \dfrac{1}{6}(E-e)\dfrac{h^3}{\beta^3\mu^2} & \text{for } \epsilon\gamma\mu \le h \le \epsilon\beta\mu, \\ \dfrac{2}{3}E\epsilon^3\mu - \dfrac{1}{2}\epsilon^2(E-e)\left(\dfrac{1}{\gamma}-\dfrac{1}{\beta}\right)h + \dfrac{1}{6}(E-e)\left(\dfrac{1}{\gamma^3}-\dfrac{1}{\beta^3}\right)\dfrac{h^3}{\mu^2} & \text{for } h \le \epsilon\gamma\mu \end{cases} \tag{5}$$

for $\mu \ge 0$. Note that the G of (5) is continuously differentiable.

Let M be the constitutive function delivering a prescribed bifurcation branch, or more generally, let it be any artificial constitutive function that we wish to synthesize. For those values of μ for which the equation

$$G(\mu, h) = M(\mu) \tag{6}$$

has a (possibly multiple) solution for h as a function of μ, denoted $\hat{h}(\mu)$, we can construct $M(\mu)$ to be $G(\mu, \hat{h}(\mu))$. The function $\hat{h}$ is the feedback; it tells how to adjust the magnetic field (by using solenoids) in response to strains that are monitored. Graphically, solution curves of (6) are just projections onto the (μ, h)-plane of intersections of the surfaces $m = G(\mu, h)$ and $m = M(\mu)$ in three-dimensional (μ, h, m)-space, as illustrated in Fig. 5.

The rather mild effect shown in Fig. 5 is a consequence of the mild curvature of the surface of Fig. 4, which in turn is a consequence of the lack of oddness of T as a function of δ. We can get much stronger effects by replacing the constitutive equation for G, based on (3), with ones based on magnetostrictive devices that directly influence flexure. For example, suppose that the column is a composite column (like a bimetallic strip) consisting of two columns attached so that different magnetic fields h^+ and h^- can be independently delivered to each constituent column. Then in place of $G(\mu, h)$, we would obtain a constitutive function for the bending couple of the form $J(\mu, h^+, h^-)$ (with $J(\mu, h, h) = G(\mu, h)$) and in place of (6) we would have

$$J(\mu, h^+, h^-) = M(\mu). \tag{7}$$

In particular, suppose that (3) holds for $x > 0$ with h replaced by h^+, and (3) holds for $x < 0$ with h replaced by h^-. Then a careful computation shows that

$$J(\mu, h^+, h^-) = G(\mu, h^-) + \tfrac{1}{2}(\epsilon^2 Eb/\alpha)(h^+ - h^-) \quad \text{for} \quad \mu > 0. \tag{8}$$

Equation (7) lacks some of the simplicity of a graphical inter pretation of (6) because $m = J(\mu, h^+, h^-)$ is represented by a three-dimensional surface in four-dimensional space of (μ, h^+, h^-, m). But we gain the great advantage that (7) now is an underdetermined single equation for the two unknowns h^+ and h^-. For example, if (8) holds, then by taking h^+ to be any feedback function of the form $f(\mu)$ with values in $[0, h_c]$, we can make the graph of J as a function of (μ, h^-) be the sum of the graph of G, the graph of a linear function in h^-, and the graph of the arbitrary function f. This means that we can expect to synthesize M by finding feedback magnetic fields $h^\pm$ satisfying (7) for a range of μ's far larger than those for which we can use (6). (Note that for the snapping process discussed above, the curvature μ has one sign throughout the column.)

Downloaded 04 May 2010 to 171.66.16.27. Redistribution subject to ASME license or copyright; see http://www.asme.org/terms/Terms_Use.cfm

Comments

(i) The magnetostrictive material Terfenol is manufactured in bulk, whereas Metglas is manufactured in strips. Since Terfenol is brittle in tension, in its engineering applications it is usually kept under a compressive prestress. Its constitutive function giving the *compressive* stress as a function of (δ, h) has a graph similar to Fig. 3 (see, e.g., Dozor et al. (1997), Moffett et al. (1991), and Wun-Fogle et al. (1990)). The same sorts of syntheses can be obtained with Terfenol provided that its inability to sustain tension is respected (and its hysteresis is ignored or compensated for). For example, to control the snap buckling of a column, we could construct the column as a bimetallic strip by welding a column of terfenol to a column of another metal that can sustain tension. By placing an obstacle on the Terfenol side of the composite column, we can ensure that any unilateral buckling that could occur keeps the Terfenol under compression.

(ii) In using formula (3), we are tacitly assuming that the h at any section can be prescribed. In practice, this means that (a) the column is so thin that h is nearly constant across a section and does not have to be found as the solution of some rod-theoretic version of Maxwell's equations, and (b) h can be effectively prescribed at each s by wrapping solenoids around short segments of the column.

(iii) A technique similar to that leading to (6) allows the feedback linearization of the quasi-linear wave equation governing the longitudinal motion of a nonlinearly elastic rod

$$\rho A w_{tt} = T(w_s, h)_s \tag{9}$$

where ρA is the (constant) mass density per unit undeformed length, $w(s, t)$ is the longitudinal displacement at (s, t), and where, for simplicity of exposition, we assume that the rod is uniform and that it is unforced. If we take the feedback h to satisfy

$$T(\delta, h) = a^2\delta + b, \tag{10}$$

where $a \neq 0$ and b are constants, then (10) converts (9) into a linear wave equation, which faithfully transmits signals and prevents the shocks that the natural material would be subject to. Equation (10) describes the intersection of the graph of T with a plane.

(iv) Antman and Adler (1987) complicated their development by restricting their attention to M's that are increasing functions of their arguments. Since we are treating artificial materials, we have no need for such restrictions. (The buckling of columns with M's that are not everywhere increasing, which have nonconvex energies, has been treated by James (1981).) Moreover, Antman and Adler excluded multivalued solutions M. As Fig. 5 indicates, the feedbacks h satisfying (6) may often give rise to such multivalued M's, so such an exclusion is not needed.

(v) Clearly, analogous results can be obtained for materials that are sensitive to electrical effects. For such materials the electric field replaces the magnetic field as the control variable.

Acknowledgment

I am grateful to A. E. Clark, J. B. Restorff, M. L. Spano, J. Teter, and M. Wun-Fogle of the Magnetic Materials Group of the Carderock Division of NSWC for helpful discussions, and to C. B. Bright of Etrema Products, Inc., for supplying me with useful literature. The preparation of this note was supported in part by ARO-MURI97 Grant No. DAAG55-97-1-0114 to the Center for Dynamics an Control of Smart Structures and by NSF Grant DMS9623261.

References

Antman, S. S., and Adler, C. L., 1987, "Design of Material Properties that Yield a Prescribed Global Buckling Response," ASME JOURNAL OF APPLIED MECHANICS, Vol. 109, pp. 263–268.

Clark, A. E., and Wun-Fogle, M., 1989, "A new method of magnetostrictivity and magnetostriction measurement," *IEEE Trans. Magnetics,* Vol. 25, pp. 3611–3613.

Crandall, S. H., and Dahl, N. C., 1959, *An Introduction to the Mechanics of Solids,* McGraw-Hill, New York.

Dozor, D. M., Gerver, M. J., and Swenbeck, R., 1997, "Nonlinear Modeling for Control of Terfenol-D Based Actuators," *Proc. 4th SPIE Conf. on Smart Materials and Structures,* Vol. 3039, pp. 644–654.

Hathaway, K. B., and Spano, M. L., 1984, "Measurement of high magnetomechanical coupling factors by resonance techniques," *J. Appl. Phys.,* Vol. 55, pp. 1765–1767.

James, R. D., 1981, "The Equilibrium and Post-Buckling Behavior of a Curve Governed by a Non-Convex Energy," *J. Elasticity,* Vol. 11, pp. 239–269.

Love, A. E. H., 1927, *Mathematical Theory of Elasticity,* Cambridge University Press, Cambridge, UK.

Moffett, M. B., Clark, A. E., Wun-Fogle, M., Lindberg, J. F., Teter, J. P., McLaughlin, E. A., 1991, "Characterization of Terfenol-D for magnetostrictive transducers," *J. Acoust. Soc. Am.,* Vol. 89, pp. 1448–1455.

Savage, H. T., and Spano, M. L., 1982, "Theory and application of highly magnetoelastic Metglas 2605SC," *J. Appl. Phys.,* Vol. 53, pp. 8092–8097.

Spano, M. L., Hathaway, K. B., and Savage, H. T., 1982, "Magnetostriction and magnetic anisotropy of field annealed Metglas 2605 alloys via dc M-H loop measurements under stress," *J. Appl. Phys.,* Vol. 53, pp. 2667–2669.

Wun-Fogle, M., Savage, H. T., Antman, S. S., and Kabacoff, L. T., 1990, "The effect of longitudinal stress and torsional strain on the magnetization of amorphous magnetoelastic wires," *Anales de Fisica, Serie B,* Vol. 86, pp. 277–283.

Downloaded 04 May 2010 to 171.66.16.27. Redistribution subject to ASME license or copyright; see http://www.asme.org/terms/Terms_Use.cfm